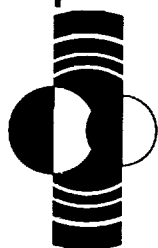


Lunar and Planetary Science XXV



*Abstracts of papers submitted to the
Twenty-fifth Lunar and Planetary
Science Conference*

(NASA-CR-195743) THE TWENTY-FIFTH
LUNAR AND PLANETARY SCIENCE
CONFERENCE. PART 1: A-G Abstracts
Only (Lunar and Planetary Inst.)
572 p

N94-35395
--THRU--
N94-35433
Unclas

G3/91 0002940

PART 1 A - G



National Aeronautics and
Space Administration

Lyndon B. Johnson Space Center
Houston, Texas

LPI / USRA

LUNAR AND PLANETARY INSTITUTE
UNIVERSITIES SPACE RESEARCH ASSOCIATION

LUNAR AND PLANETARY SCIENCE XXV

**Abstracts of Papers Submitted to the
TWENTY-FIFTH LUNAR AND PLANETARY SCIENCE CONFERENCE**

Sponsored by

**National Aeronautics and Space Administration
Lunar and Planetary Institute
NASA Johnson Space Center**

March 14–18, 1994

Part 1

**Compiled by
Lunar and Planetary Institute
3600 Bay Area Boulevard
Houston TX 77058-1113**

The Lunar and Planetary Institute is operated by the Universities Space Research Association under Contract No. NASW-4574 with the National Aeronautics and Space Administration.

Material in this volume may be copied without restraint for library, abstract service, educational, or personal research purposes; however, republication of any paper or portion thereof requires the written permission of the authors as well as appropriate acknowledgment of this publication.

Preface

This volume contains abstracts accepted by the Program Committee of the Twenty-Fifth Lunar and Planetary Science Conference.

The Program Committee was co-chaired by Douglas Blanchard (*NASA Johnson Space Center*) and David Black (*Lunar and Planetary Institute*); other members were Nadine Barlow (*Lunar and Planetary Institute*), James Bell (*NASA Ames Research Center*), Donald Bogard (*NASA Johnson Space Center*), Bruce Bohor (*U.S. Geological Survey, Denver*), Bruce Campbell (*Smithsonian Institution*), Mark Cintala (*NASA Johnson Space Center*), Tammy Dickinson (*NASA Headquarters*), Deborah Domingue (*Lunar and Planetary Institute*), Charles Hohenberg (*Washington University*), Walter Kiefer (*Lunar and Planetary Institute*), Marilyn Lindstrom (*NASA Johnson Space Center*), Glenn MacPherson (*Smithsonian Institution*), Renu Malhotra (*Lunar and Planetary Institute*), Scott Murchie (*Lunar and Planetary Institute*), Laurence Nyquist (*NASA Johnson Space Center*), Patricia Rogers (*NASA Headquarters*), Sue Smrekar (*Jet Propulsion Laboratory*), Allan Treiman (*Lunar and Planetary Institute*), Faith Vilas (*NASA Johnson Space Center*), Paul Warren (*University of California, Los Angeles*), and Michael Zolensky (*NASA Johnson Space Center*).

Papers are arranged alphabetically by the last name of the first author. There are four indexes: author, lunar sample number, meteorite, and keyword.

This abstract volume was compiled by the staff of the Publications and Program Services Department of the Lunar and Planetary Institute. Computer service support was provided by the LPI's Computer Center.

Logistics and administrative support for the conference was provided by the staff of the Publications and Program Services Department, Lunar and Planetary Institute.

CONTENTS

Magnetic Properties of Zagami and Nakhla <i>D. P. Agerkvist, L. Vistisen, M. B. Madsen, and J. M. Knudsen</i>	1
Martian Fluvio-Thermal Erosion: Experimental Project <i>J. Aguirre-Puente, F. Costard, and N. Makhloufi</i>	3
Radiative Signals from Impact of Shoemaker-Levy on Jupiter <i>T. J. Ahrens, G. S. Orton, T. Takata, and J. D. O'Keefe</i>	5
Chondrules from Chondrules? An Ion Probe Trace Element Study <i>C. M. O'D. Alexander</i>	7
Evidence for Short SiC Lifetimes in the ISM <i>C. M. O'D. Alexander</i>	9
C1 and Alkali Metasomatism in Unequilibrated Ordinary Chondrites <i>C. M. O'D. Alexander, J. C. Bridges, and R. Hutchison</i>	11
Distributions of the Preatmospheric Sizes of Antarctic and Non-Antarctic Chondrites <i>V. A. Alexeev</i>	13
On Calculation of Cosmic-Ray Exposure Ages of Meteorites <i>V. A. Alexeev</i>	15
Short Life of Small Meteorites in the Cosmic Space? <i>V. A. Alexeev</i>	17
Meteorites as Differential Detectors of Events Over a Long Time Scale <i>V. A. Alexeev and G. K. Ustinova</i>	19
New Prospects for Analyzing Lunar Pyroclastic Glass <i>C. C. Allen, L. P. Keller, J. P. Bradley, D. E. Brownlee, and D. S. McKay</i>	21
Reduction of Lunar Mare Soil and Pyroclastic Glass <i>C. C. Allen, R. V. Morris, and D. S. McKay</i>	23
Calorimetric Thermometry of Meteoritic Troilite: Preliminary Thermometer Relationships <i>J. H. Allton, S. J. Wentworth, and J. L. Gooding</i>	25
C-, N-, O-, Si-, and Ti-Isotopic Ratios of Low Density Graphite Grains from Murchison Indicate a Supernova Origin <i>S. Amari, E. Zinner, and R. S. Lewis</i>	27
Lithospheric Controls on the Formation of Valles Marineris <i>F. S. Anderson and R. E. Grimm</i>	29
Bunte Breccia-like Deposits Within the Manson Impact Structure (Iowa); Evidence for Impact into a Shallow Marine Environment? <i>R. R. Anderson and B. J. Witzke</i>	31
Surface Characteristics of Steep-Sided Domes on Venus and Terrestrial Silicic Domes: A Comparison <i>S. W. Anderson, D. A. Crown, J. J. Plaut, and E. R. Stofan</i>	33

Cryptomaria in the Schiller-Schickard, Mare Humorum and Western Oceanus Procellarum Areas: Studies Using Dark-Halo Craters <i>I. Antonenko and J. W. Head</i>	35
Computer Simulation of Low Pressure Melting in Meteoritic Igneous Systems <i>A. A. Ariskin and M. I. Petaev</i>	37
Oblique Impact: Atmospheric Effects <i>N. A. Artem'eva and V. V. Shuvalov</i>	39
Laboratory Simulations of Large-Scale Vortex Flows Generated at Impacts on Venus and on Earth <i>V. I. Artem'ev, V. A. Rybakov, S. A. Medveduk, and B. A. Ivanov</i>	41
The Surface and Interior of Phobos <i>E. Asphaug and W. Benz</i>	43
Stratigraphy of Small Volcanoes and Plains Terrain in Vellamo Planitia, Venus <i>J. C. Aubele</i>	45
Stepping into Space: Getting Involved in Pre-College Outreach <i>J. C. Aubele and P. H. Schultz</i>	47
A Mercury Orbiter Mission: Report on the European Space Agency's Assessment Study <i>A. Balogh, R. Grard, G. Scoon, and M. Hechler</i>	49
Gravity Studies of Mead Crater, Venus <i>W. B. Banerdt, N. J. Rappaport, W. L. Sjogren, and R. E. Grimm</i>	51
Mars Soil: Nanophase Minerals and Formation Processes <i>A. Banin</i>	53
The Hypsometric Distribution of Impact Craters on Venus <i>M. Banks, S. Emerson, R. G. Strom, and G. G. Schaber</i>	55
Observational and Computational Evidence for Gravitationally Stable Particle Accretions in the Perseid Meteor Stream <i>J. C. Barentine</i>	57
Impact Craters as Indicators of Subsurface H ₂ O on Mars <i>N. G. Barlow</i>	59
A Quantitative Assessment of an Impact Generated Ring Vortex <i>O. S. Barnouin and P. H. Schultz</i>	61
Concentric Wrinkle Ridge Pattern Around Sif and Gula <i>A. T. Basilevsky</i>	63
Preliminary Stratigraphic Basis for Geologic Mapping of Venus <i>A. T. Basilevsky and J. W. Head</i>	65
Geology and Morphometry of Large Impact Craters of Venus <i>A. T. Basilevsky, B. A. Ivanov, P. G. Ford, and C. M. Weitz</i>	67
Variations in Mars' North Residual Polar Cap Frost Coverage in Mariner 9 and Viking Images <i>D. S. Bass, K. E. Herkenhoff, and D. A. Paige</i>	69

Single Agglutinates: A Comparative Study of Compositions of Agglutinitic Glass, Whole-Grain, Bulk Soil, and FMR <i>A. Basu, R. Robinson, D. S. McKay, D. P. Blanchard, R. V. Morris, and S. J. Wentworth</i>	71
Deep Melting and Residual Garnet in the Sources of Lunar Basalts: Lu-Hf Isotopic Systematics <i>B. L. Beard, G. A. Snyder, and L. A. Taylor</i>	73
CoMA: A Cometary Matter Analyzer for In Situ Analysis with High Mass Resolution <i>P. Beck and J. Kissel</i>	75
Solar Wind Gases in a Metal Separate from Lunar Soil 68501: A Followup Study <i>R. H. Becker and R. O. Pepin</i>	77
The Partitioning of Na Between Melilite and Liquid: An Experimental Study with Applications to Type B CAIs <i>J. R. Beckett and E. M. Stolper</i>	79
High Spatial Resolution Telescopic Multispectral Imaging and Spectroscopy of the Moon: I. The Serenitatis/Tranquillitatis Border Region <i>J. F. Bell III and B. R. Hawke</i>	81
High Resolution Visible to Short-Wave Near-Infrared CCD Spectra of Mars During 1990 <i>J. F. Bell III, K. Bornhoeft, and P. G. Lucey</i>	83
Absolute Calibration and Atmospheric vs. Mineralogic Origin of Absorption Features in 2.0 to 2.5 μm Mars Spectra Obtained During 1993 <i>J. F. Bell III, J. B. Pollack, T. R. Geballe, D. P. Cruikshank, and R. Freedman</i>	85
Wavelength Calibration Techniques and Subtle Surface and Atmospheric Absorption Features in the Mariner 6, 7 IRS Reflectance Data <i>J. F. Bell III, T. L. Roush, T. Z. Martin, and R. Freedman</i>	87
Ordinary Chondrites in Space and Time <i>J. F. Bell</i>	89
Geologic Map of Callisto <i>K. C. Bender, R. Greeley, J. W. Rice Jr., and D. E. Wilhelms</i>	91
Pre-Impact Orbital Evolution of P/Shoemaker-Levy 9 <i>L. A. M. Benner and W. B. McKinnon</i>	93
Post-Shock Cooling and Annealing Within L-Group Ordinary Chondrites <i>M. E. Bennett and H. Y. McSween Jr.</i>	95
Primitive Material in Lunar Highland Soils <i>P. H. Benoit, J. D. Batchelor, S. J. Symes, and D. W. G. Sears</i>	97
Natural Thermoluminescence Profiles in Meteorites: Cosmogenic and Terrestrial Profiles in Falls and Finds <i>P. H. Benoit, Y. Chen, and D. W. G. Sears</i>	99
Shoemaker-Levy 9 and the Tidal Disruption of Comets <i>W. Benz and E. Asphaug</i>	101
Refractory Carbides in Interstellar Graphite <i>T. J. Bernatowicz, S. Amari, and R. S. Lewis</i>	103

Origin of Amorphous Rims on Lunar Soil Grains <i>T. J. Bernatowicz, R. H. Nichols Jr., and C. M. Hohenberg</i>	105
Craters in Aluminum 1100 Targets Using Glass Projectiles at 1–7 km/s <i>R. P. Bernhard, T. H. See, F. Hörz, and M. J. Cintala</i>	107
A Martian Mantle with Peridotitic Versus Chondritic Mg/Si and Al/Ca Ratios: Implications for Mantle Mineralogy and Melting Reactions <i>C. M. Bertka</i>	109
Thermal Inertias in the Upper mm of the Martian Surface Derived Using the Phobos Shadow <i>B. H. Betts, B. C. Murray, and T. Svitek</i>	111
Magellan LOS Gravity of Venus Plains Regions: Lithospheric Properties and Implications for Global Tectonics <i>D. L. Bindschadler</i>	113
The Unique Carbonaceous Chondrite Acfer 094: The First CM3 Chondrite (?) <i>A. Bischoff and T. Geiger</i>	115
Reflectance Spectra of Mars Soil Analogs Measured Under Reduced Atmospheric Pressures and Temperatures <i>J. L. Bishop and C. M. Pieters</i>	117
Spectroscopic and Geochemical Analyses of Sediments from Lake Hoare, Antarctica and Applications to Dry Valleys on Mars <i>J. L. Bishop, P. A. J. Englert, D. W. Andersen, C. Kralik, C. Koeberl, C. M. Pieters, H. Froeschl, and R. A. Wharton Jr.</i>	119
A Mineralogical Instrument for Planetary Applications <i>D. F. Blake, D. T. Vaniman, and D. L. Bish</i>	121
Infrared Spectrophotometry of Io Between 3 and 13 μm in 1993 <i>D. L. Blaney, M. S. Hanner, R. Russell, D. Lynch, and J. Hackwell</i>	123
Measuring Track Densities in Lunar Grains Using Image Analysis <i>G. E. Blanford, D. S. McKay, R. P. Bernhard, and C. K. Schulz</i>	125
A Spectral Survey of the Crisium Region of the Moon <i>D. T. Blewett, B. R. Hawke, P. G. Lucey, and P. D. Spudis</i>	127
Venus: Influence of Surface Roughness on the Threshold for Windblown Sand Derived from Magellan Data <i>D. G. Blumberg and R. Greeley</i>	129
Mars Cartographic Coverage: Status Prior to Mars-94 Mission <i>N. N. Bobina and G. A. Burba</i>	131
Geometrical Transformation of Panoramas of Mars Surface Received from Phobos-2 Space Station <i>I. M. Bockstein, M. A. Kronrod, and Yu. M. Gektin</i>	133
Fe and Mn Systematics in Experimental Analogues of Murchison and a 65% H Chondrite-35% CM Chondrite <i>J. S. Boesenberg and J. S. Delaney</i>	135

³⁹ Ar- ⁴⁰ Ar Ages of Four Ureilites <i>D. D. Bogard and D. H. Garrison</i>	137
Bromine in Interplanetary Dust Particles <i>J. Bohsung, P. Arndt, and E. K. Jessberger</i>	139
The Solubility of Platinum in Silicate Melts: Experiments Under Oxidizing Conditions <i>A. Borisov, H. Palme, and B. Spettel</i>	141
Phosphorus Chemistry in the Atmospheres of Jupiter and Saturn <i>S. Borunov, V. Dorofeeva, I. K. Khodakovsky, P. Drossart, E. Lellouch, and Th. Encrenaz</i>	143
Axial Focusing of Seismic Energy from a Large Impact on Earth: Preliminary Numerical Simulations <i>M. B. Boslough and E. P. Chael</i>	145
Comet Shoemaker-Levy 9: An Upper Bound on Its Mean Density <i>A. P. Boss</i>	147
Midplane Temperatures and Solar Nebula Evolution <i>A. P. Boss</i>	149
Injection of Presolar Grains into the Solar Nebula by a Stellar Shock Wave <i>A. P. Boss and P. N. Foster</i>	151
Provenance of the Spacewatch Small Earth-Approaching Asteroids <i>W. F. Bottke Jr., M. C. Nolan, R. Greenberg, A. M. Vickery, and H. J. Melosh</i>	153
Spacing Distributions and Intersection Angles for Kilometer Scale Lineations on the Plains of Venus <i>D. D. Bowman, C. G. Sammis, and W. B. Banerdt</i>	155
Vapor Transport, Weathering, and the Highlands of Venus <i>R. A. Brackett, B. Fegley Jr., and R. E. Arvidson</i>	157
Reflectance Spectroscopy of Individual Interplanetary Dust Particles <i>J. P. Bradley, D. E. Brownlee, and L. P. Keller</i>	159
Rb-Sr Dating of Alkaline and Mafic Intrusives from the Pretoria Saltpan Impact Crater and Environs <i>D. Brandt, W. U. Reimold, and C. B. Smith</i>	161
Your Own Educational Outreach Program: It's Not as Hard as You Think <i>R. H. Brazzle, B. M. Barker, L. C. McLeod, and C. M. Hohenberg</i>	163
Metamorphic Effects in the Matrices of CO ₃ Chondrites: Compositional and Mineralogical Variations <i>A. J. Brearley</i>	165
Metamorphism in the CO ₃ Chondrites: Trace Element Behavior in Matrices and Rims <i>A. J. Brearley, S. Bajt, and S. R. Sutton</i>	167
Pancake Domes on Venus and the Seafloor <i>N. T. Bridges</i>	169

Release of Light Nitrogen from Apollo 12023 <10 μm Fraction by a Combination of Pyrolysis-Combustion <i>D. R. Brilliant, I. A. Franchi, and C. T. Pillinger</i>	171
The ^{15}N -rich Low-temperature Nitrogen Component in Lunar Soils—An Ammonia Related Species? <i>D. R. Brilliant, A. D. Morse, J. Higgins, I. A. Franchi, and C. T. Pillinger</i>	173
'Space Weathering' and the Ordinary Chondrites <i>D. T. Britt and B. E. Clark</i>	175
Cat Mountain: Spectra and Petrology of an L5 Impact-Melt Breccia <i>D. T. Britt and D. A. Kring</i>	177
Tectonics of Artemis Corona, Venus: Implications for Formation and Evolution <i>C. D. Brown and R. E. Grimm</i>	179
Alteration and Formation of Rims on the CM Parent Body <i>L. B. Browning, H. Y. McSween Jr., and M. Zolensky</i>	181
Eureka!! Aerogel Capture of Meteoroids in Space <i>D. E. Brownlee, F. Hörz, L. Hrubsch, J. A. M. McDonnell, P. Tsou, and J. Williams</i>	183
Identification and Analysis of Cometary IDPs <i>D. E. Brownlee, D. J. Joswiak, S. G. Love, J. P. Bradley, A. O. Nier, and D. J. Schlutter</i>	185
Considerations for Planetary Gamma-Ray Spectroscopy of the Surface of Mercury <i>J. Brückner, U. Fabian, and M. Wieder</i>	187
Lava Flow Rheology: A Comparison of Data and Theory <i>B. C. Bruno, S. M. Baloga, G. J. Taylor, and M. J. Tatsumara</i>	189
Venus Climate Stability and Volcanic Resurfacing Rates <i>M. A. Bullock, D. H. Grinspoon, and J. B. Pollack</i>	191
Modified Lava Domes on Venus <i>M. H. Bulmer and J. E. Guest</i>	193
Thematic Map Types Possible for Mars: Mars-94 Mission Cartographic Perspectives <i>G. A. Burba</i>	195
Zhamanshin Astrobleme: Review and First Results of 1992 Landscape and Geomorphic Survey <i>G. G. Burba Jr. and V. A. Meshcherskaya</i>	197
Questions Concerning the Oxidation of Ferrous Iron in Carbonaceous Chondrites <i>T. H. Burbine and R. G. Burns</i>	199
Are Steep Slopes on Venus Preserved as a Result of Chemical Cementation of Pore-Spaces in Surface Rocks? <i>K. Burke, B. Fegley Jr., and V. L. Sharpton</i>	201
Schwertmannite on Mars: Deposition of This Ferric Oxyhydroxysulfate Mineral in Acidic Saline Meltwaters <i>R. G. Burns</i>	203

Crustal Recycling Due to Mantle Flow-Driven Crustal Thickening: A Preliminary Assessment <i>J. D. Burt, E. M. Parmentier, and J. W. Head</i>	205
Modelling the Formation of Venusian Channels <i>D. B. J. Bussey, S. A. Sørensen, and J. E. Guest</i>	207
Light Element Isotopic Composition in the Wind of a Typical AGB Star <i>M. Busso, R. Gallino, C. M. Raiteri, and G. J. Wasserburg</i>	209
Martian Polar Regions: 35-cm Radar Images <i>B. J. Butler, D. O. Muhleman, and M. A. Slade</i>	211
Fluvial Processes in Ma'adim Vallis and the Potential of Gusev Crater as a High Priority <i>N. Cabrol, R. Landheim, R. Greeley, and J. Farmer</i>	213
Comparative Results from Giant Impact Studies <i>A. G. W. Cameron</i>	215
Dielectric Properties of Venus: Results from Emissivity Modeling and Terrestrial Field Measurements <i>B. A. Campbell</i>	217
Multiple-Wavelength Lunar Radar Images: Analysis of Regolith Properties <i>B. A. Campbell and B. R. Hawke</i>	219
Siderophile Trace Elements in Silicate Melts: Significance and Status of Unusual Oxidation States <i>C. J. Capobianco, J. A. DeAro, M. J. Drake, and V. J. Hillgren</i>	221
Low-Temperature Cooling Histories of Vigarano CAIs: Constraints from Compositions of Metal Particles <i>I. Casanova and L. Grossman</i>	223
Impact Craters on Mars: The Relative Roles of Atmospheric and Subsurface Volatiles <i>J. Cave, J. Guest, and N. Barlow</i>	225
Impact Crater Morphology on Martian Volcanoes <i>J. Cave, J. Guest, B. J. Moore, J. Carroll, and N. Barlow</i>	227
Evidence for Episodic Tectonic Construction of Ovda Regio, Venus <i>D. J. Chadwick and G. G. Schaber</i>	229
Refined Volcanic and Tectonic History of the Valles Marineris, Mars <i>D. J. Chadwick, G. J. Leonard, and K. L. Tanaka</i>	231
Wax Modeling of Thermal Erosion in Low-Viscosity Lava Flows <i>D. Challis, S. Williams, and R. Greeley</i>	233
Lunar Mineral Feedstocks from Rocks and Soils: X-Ray Digital Imaging in Resource Evaluation <i>J. G. Chambers, A. Patchen, L. A. Taylor, S. J. Higgins, and D. S. McKay</i>	235
First Galileo Image of the Asteroid 243 Ida <i>C. R. Chapman, M. J. S. Belton, J. Veverka, G. Neukum, J. Head, R. Greeley, K. Klaasen, D. Morrison, and the Galileo Imaging Team</i>	237

3-D Perspective Imaging: A Tool for Geologic Mapping of Venus <i>M. G. Chapman, R. L. Kirk, and J. M. Barrett</i>	239
Subpixel Resolution from Multiple Images <i>P. Cheeseman, B. Kanefsky, J. Stutz, and R. Kraft</i>	241
Hypervelocity Impacts and the Magnetism of Small Bodies in the Solar System <i>G. Chen, T. J. Ahrens, and R. Hide</i>	243
The Abundance of Thallium and Premordial Lead in Selected Meteorites—The Search for ²⁰⁵ Pb <i>J. H. Chen and G. J. Wasserburg</i>	245
The Orbital Evolution of Ordinary Chondrites Over the Last 50 Million Years <i>Y. Chen, P. H. Benoit, and D. W. G. Sears</i>	247
Exploration of the Morphological Distribution of the Spectral Units in the Gruithuisen Domes Region <i>S. D. Chevrel, P. C. Pinet, and J. W. Head</i>	249
Determination of Nanogram Amounts of C ₆₀ by High Pressure Liquid Chromatography <i>L. P. F. Chibante, W. S. Wolbach, and D. Heymann</i>	251
MORO: A European Moon Orbiting Observatory <i>A. F. Chicarro and G. D. Racca</i>	253
Formation of IAB-IIICD Iron Meteorites <i>B.-G. Choi and J. T. Wasson</i>	255
Thermal-Infrared Multi-Spectral Observations of Mars <i>P. R. Christensen</i>	257
Grain Rims on Ilmenite in the Lunar Regolith: Comparison to Vapor Deposits on Regolith Silicates <i>R. Christoffersen, D. S. McKay, and L. P. Keller</i>	259
Block Distributions on the Lunar Surface: A Comparison Between Measurements Obtained from Surface and Orbital Photography <i>M. J. Cintala and K. M. McBride</i>	261
Acid Waters as Agents of Change on a Cold Early Mars <i>B. C. Clark</i>	263
Infrared Spectral Observations of Smaller (50 km) Main Belt S, K, and M Type Asteroids <i>B. E. Clark, J. F. Bell, D. J. O'Connor, and F. P. Fanale</i>	265
Remote Geochemical Experiment Package for Discovery Class Missions <i>P. E. Clark, L. G. Evans, and J. I. Trombka</i>	267
Oxygen Isotopes in Kaidun <i>R. N. Clayton, T. K. Mayeda, A. V. Ivanov, and G. J. MacPherson</i>	269
The Role of Low Temperature Hydrothermal Convection in the Physical and Chemical Evolution of the Martian Crust and Groundwater <i>S. M. Clifford</i>	271
An X-Ray Diffraction and Reflectance Spectroscopy Study of Iron Sulphides <i>E. A. Cloutis and M. J. Gaffey</i>	273

Minimum Discharge Rates Required for Sustained Water Flow on the Martian Surface <i>G. D. Clow</i>	275
Triton's Lineaments: Complex Morphology and Stress Patterns <i>G. Collins and P. Schenk</i>	277
On the Possible Role of Elemental Carbon in the Formation of Reduced Chondrules <i>H. C. Connolly Jr., R. H. Hewins, R. D. Ash, G. E. Lofgren, and B. Zanda</i>	279
Astronomy Laboratory Exercise Based on SkyGlobe™ <i>M. Connors</i>	281
Return of an Earth-Grazing Asteroid <i>M. Connors</i>	283
Has the Tidal Bulge on Ariel Shifted in Longitude? <i>G. Consolmagno, D. M. Davis, and P. Nyffenegger</i>	285
Unusual Concentrations of Rampart Craters at the Mouths of Outflow Channels, Mars <i>F. Costard</i>	287
Affinity and Petrogenesis of a Unique Vitrophyric Olivine-Augite Mare Basalt from the Apollo 15 Coarse Fines <i>T. C. Cox and G. Ryder</i>	289
Geologic History of Isidis Planitia and Syrtis Major Planum, Mars <i>R. A. Craddock</i>	291
The Origin of Phobos and Deimos <i>R. A. Craddock</i>	293
The Influence of Body Shape on the Deformation and Breakup of Comet Shoemaker-Levy 9 Fragments as They Enter the Jovian Atmosphere <i>D. A. Crawford, T. G. Trucano, M. B. Boslough, M. E. Kipp, and J. M. McGlaun</i>	295
Palimpsests on Ganymede: An Endogenic Origin? <i>S. K. Croft</i>	297
Post-Impact Hydrothermal Systems: Manson Impact Structure, Manson, Iowa <i>L. J. Crossey, A. M. Kudo, and P. McCarville</i>	299
Geology of the Guinevere Planitia Quadrangle of Venus <i>D. A. Crown, E. R. Stofan, and J. J. Plaut</i>	301
The Distribution of Hot Spots and Its Relation to Global Geology: Venus, Earth, and Mars <i>L. S. Crumpler</i>	303
Calderas on Mars: Classification, Characteristics, and Processes Related to Mechanisms of Formation <i>L. S. Crumpler, J. W. Head, and J. C. Aubele</i>	305
What Initiated Planetesimal Formation? <i>J. N. Cuzzi, A. R. Dobrovolskis, and R. C. Hogan</i>	307
NMR Spectroscopy of Experimentally Shocked Coconino Sandstone and the Effect of Pore Water <i>R. T. Cygan, M. B. Boslough, and R. J. Kirkpatrick</i>	309

The Planetary Data System Educational CD-ROM Demonstration <i>M. A. Dale-Bannister</i>	311
High-Resolution Transmission Electron Microscopy Study of Meteoritic and Terrestrial Nano-Diamond Microstructures <i>T. L. Daulton, D. D. Eisenhour, R. S. Lewis, and T. J. Bernatowicz</i>	313
Alteration of Allende Type B1 CAIs: When, Where, and How <i>A. M. Davis, S. B. Simon, and L. Grossman</i>	315
Morphometries and Possible Terrestrial Analogs of Small Martian Volcanoes <i>P. A. Davis and K. L. Tanaka</i>	317
The Occurrence of Blue Luminescing Enstatite in E3 and E4 Chondrites <i>J. M. DeHart and G. E. Lofgren</i>	319
Ponding and Lacustrine Deposition in Lower Mangala Valles, Mars <i>R. A. De Hon</i>	321
An Oxygen Fugacity Grid for Nebular and Planetary Geochemistry <i>J. S. Delaney, S. R. Sutton, and S. Bajt</i>	323
Abundance and Diffusivity of Sulfur in Lunar Picritic Magmas <i>J. W. Delano, B. Z. Hanson, and W. B. Watson</i>	325
The Fretted Terrain of the Nilosyrtris Mensae Region of Mars: Clues to the Timing of Dichotomy Formation and the Emplacement of the Northern Plains <i>J. E. DeTroye and S. H. Williams</i>	327
High-Temperature Vaporization of Olivine and Serpentine <i>Yu. P. Dikov, O. I. Yakovlev, M. V. Gerasimov, and F. Wlotzka</i>	329
Geologic History of the Thaumasia Region of Mars <i>J. M. Dohm and K. L. Tanaka</i>	331
Magnetic Field in the Protosun and Protostars Vicinities <i>A. Z. Dolginov</i>	333
Soil Texture at the Lunar Surface: Regional Analysis with Polarimetric Images <i>A. Dollfus</i>	335
The Role of Hapke's Bidirectional Surface Reflection Model in Determining Atmospheric Abundances at Mercury <i>D. L. Domingue, A. L. Sprague, and D. M. Hunten</i>	337
A Search for Further Concentrations of Organic Materials in EET A79001 <i>C. Douglas, I. P. Wright, C. T. Pillinger, and M. M. Grady</i>	339
Found: Star and Linear Dunes on Mars <i>K. S. Edgett and D. G. Blumberg</i>	341
Suggestions for Interaction Between Scientists, K-12 Students and Educators: Mars Education Program in Arizona <i>K. S. Edgett, P. R. Christensen, and S. Schmidt</i>	343

Heating by Light and the Size Distribution of Chondrules <i>D. D. Eisenhour, T. L. Daulton, and P. R. Buseck</i>	345
Carrier Phases of Isotopically Anomalous Nitrogen in Acapulco Metal: C- and N-Isotopic Compositions Vary with Graphite Morphology <i>A. El Goresy, E. Zinner, and K. Marti</i>	347
Carbonates in the CI-Chondrite Ivuna: Implications for Aqueous Alteration Processes on the CI-Parent Body <i>M. Endress and A. Bischoff</i>	349
Apollo 16 Lunar Glasses: Normative Composition and Origin <i>W. v. Engelhardt</i>	351
Gamma Ray Spectra from the Mars Observer Gamma Ray Spectrometer: Cruise Data Analysis <i>P. A. J. Englert, N. Chakravarty, O. Ivanova, E. A. Beck, J. Brückner, S. H. Bailey, F. C. McCloskey, and W. V. Boynton</i>	353
C/O Atomic Ratios in Antarctic Micrometeorites: A Progress Report <i>C. Engrand, M. Perreau, and M. Maurette</i>	355
Effects of Aerosols Scattering on Spectral Characterization of the Martian Surface <i>S. Erard</i>	357
Projectile Shape and Velocity: Impact on Ejecta Distribution and Composition <i>N. J. Evans and T. J. Ahrens</i>	359
Theoretical Analysis of the Explosive Emplacement of Basaltic Magma in Lava Fountain Eruptions: Implications for Pyroclast Dispersal on Earth, Venus and Mars <i>S. A. Fagents and L. Wilson</i>	361
Mg and Ti Isotopic Compositions of CAI's from the Unusual Chondrite Acfer 214 <i>A. Fahey and F. Wlotzka</i>	363
Will the Real Asteroid Size Distribution Please Step Forward <i>P. Farinella and D. R. Davis</i>	365
Exopaleontology and the Search for a Fossil Record on Mars <i>J. D. Farmer and D. J. Des Marais</i>	367
Diaplectic Transformation in Clinopyroxene (Puchezh-Katunka Astrobleme, Russia) <i>V. Feldman, S. Kotelnickov, L. Sazonova, and E. Guseva</i>	369
Modeling the Space Weathering-Induced Optical Alteration of Lunar Soils: First Results <i>E. M. Fischer, C. M. Pieters, and S. F. Pratt</i>	371
Grain-Size Fractions of SiC in Murchison ARR: A Method for the Analysis of Carbon and its Isotopes by Stepped Combustion <i>A. V. Fisenko, A. B. Verchovsky, L. F. Semjenova, J. W. Arden, and C. T. Pillinger</i>	373
Isotopic and Elemental Fractionations Produced During Evaporation of the Allende Carbonaceous Chondrite <i>C. Floss, A. El Goresy, G. Kransel, W. Rammensee, H. Palme, and E. Zinner</i>	375
Narrow-Field Imaging of the Lunar Sodium Exosphere <i>B. Flynn and S. A. Stern</i>	377

Does the Kuiper Belt Contribute Significantly to the Zodiacal Cloud and the Stratospheric Interplanetary Dust?	379
<i>G. J. Flynn</i>	
Hydrated Interplanetary Dust Particles: Element Abundances, Mineralogies, and Possible Relationships to Anhydrous IDPs	381
<i>G. J. Flynn, S. R. Sutton, S. Bajt, W. Klöck, K. L. Thomas, and L. P. Keller</i>	
Nitrogen Solubility in Aubrite and E Chondrite Melts	383
<i>R. A. Fogel</i>	
SIMS Analysis of Orthopyroxene in Diogenites: An Attempt to Define a Fractionation Sequence	385
<i>G. W. Fowler, J. J. Papike, and C. K. Shearer</i>	
Impact Basins in Southern Daedalia, Mars: Evidence for Clustered Impactors?	387
<i>H. Frey and J. H. Roark</i>	
Effects Due to Overlapping Large Impact Basins on Mars	389
<i>H. Frey, A. M. Reidy, J. H. Roark, and S. Stockman</i>	
Constraints on the Physical Details of Nakhlite Formation	391
<i>R. C. Friedman, T. J. McCoy, and G. J. Taylor</i>	
Estimating Surface Roughness: Evaluation of an Empirical Backscatter Model	393
<i>L. Gaddis</i>	
Spectral Unit Map of the Moon with Improved Galileo SSI Mosaics	395
<i>L. Gaddis, A. McEwen, and T. Becker</i>	
Influence of Variable Oxygen and Sulfur Fugacity on Partitioning of Ni, Cu and Cr Among Olivine, Silicate Melt and Sulfide Melt	397
<i>G. A. Gaetani and T. L. Grove</i>	
Nature and Origins of the Olivine-Dominated A- and S(I)-type Asteroids	399
<i>M. J. Gaffey</i>	
Interstellar Graphite in Tieschitz	401
<i>X. Gao, C. Alexander, P. Swan, and R. Walker</i>	
Solar Proton Produced Neon in Shergottite Meteorites	403
<i>D. H. Garrison, M. N. Rao, and D. D. Bogard</i>	
Quantifying Shapes of Volcanoes on Venus	405
<i>J. B. Garvin</i>	
Mesoscale Roughness of Venus	407
<i>J. B. Garvin and J. J. Frawley</i>	
Volcano Morphometry and Volume Scaling on Venus	409
<i>J. B. Garvin and R. S. Williams Jr.</i>	
Ida: Distribution and Origin of Surface Blocks	411
<i>P. Geissler, J.-M. Petit, and R. Greenberg</i>	

High-Temperature Vaporization of Gypsum and Anhydrites: Experimental Results <i>M. V. Gerasimov, Yu. P. Dikov, O. I. Yakovlev, and F. Wlotzka</i>	413
Trapping of Carbon Dioxide from a Hot Atmosphere by Condensing Silicates <i>M. V. Gerasimov, Yu. P. Dikov, O. I. Yakovlev, and F. Wlotzka</i>	415
Preliminary Analysis of Associations of Small Volcanic Edifices with Major Geologic Features by Latitude on the Surface of Venus <i>K. Gerlach, M. Safford, Evergreen High School Astronomical Research Class, Sahuaro High School Astronomical Research Class, G. Komatsu, J. Johnson, J. Lockwood, and M. Ellison</i>	417
Morphological Mapping of Two Distinct Corona Chains <i>R. C. Ghail</i>	419
Plate Tectonics, Venusian Style <i>R. C. Ghail and L. Wilson</i>	421
A Reappraisal of Metamorphism in the Vredefort Dome, South Africa, and Its Implications for the Origin and Evolution of the Dome <i>R. L. Gibson, W. U. Reimold, Th. Wallmach, and W. P. Collison</i>	423
Intratessera Volcanism of Alpha and Tellus Tesserae on Venus <i>M. S. Gilmore and J. W. Head III</i>	425
Composition and Petrography of a Muong Nong-type Georgia Tektite <i>B. P. Glass, C. Koeberl, and H. Povenmire</i>	427
A Theoretical Study of SO ₂ Transport by Explosive Volcanism on Venus <i>L. S. Glaze</i>	429
Hot Belts of Venus and the Early Earth <i>M. Z. Glukhovsky and V. M. Moralev</i>	431
The Linear Polarization of Light Scattered from Icy Satellite Surfaces: The Diagnostic Potential of Galileo PPR Measurements <i>J. D. Goguen</i>	433
Application of an Alkylammonium Method for Characterization of Phyllosilicates in CI Chondrites <i>D. C. Golden, D. W. Ming, M. E. Zolensky, and S. V. Yang</i>	435
High Resolution Transmission Electron Microscopy (HRTEM) of Nanophase Ferric Oxides <i>D. C. Golden, R. V. Morris, D. W. Ming, and H. V. Lauer Jr.</i>	437
Structure and Rheology of Partially Molten Ammonia-Water Ices <i>D. L. Goldsby and D. L. Kohlstedt</i>	439
Constraints on the Largest Marsquake <i>M. P. Golombek</i>	441
Extension Across Tempe Terra and Sirenum Provinces on Mars from Measurements of Fault Scarp Widths <i>M. P. Golombek, K. L. Tanaka, D. J. Chadwick, B. J. Franklin, and P. A. Davis</i>	443
"Flindersite" Bearing Impact Ejecta Layer from South Australia <i>V. A. Gostin and M. Zbik</i>	445

"Flindersites", Distant Ejecta Impactites from South Australia <i>V. A. Gostin and M. Zbik</i>	447
Diamonds from Acfer 182: Morphology, C and N Stable Isotopic Composition and Cathodoluminescence Properties <i>M. M. Grady, M. R. Lee, C. M. O'D. Alexander, J. W. Arden, and C. T. Pillinger</i>	449
A Search for Nitrates in Nakhla <i>M. M. Grady, I. P. Wright, and C. T. Pillinger</i>	451
A Galileo Multi-Instrument Spectral Analysis of 951 Gaspra <i>J. C. Granahan, F. P. Fanale, M. S. Robinson, R. W. Carlson, L. W. Kamp, K. P. Klaasen, P. R. Weissman, M. Belton, D. Cook, K. Edwards, A. S. McEwen, L. A. Soderblom, B. T. Carcich, P. Helfenstein, D. Simonelli, P. C. Thomas, and J. Veverka</i>	453
Ganymede and Callisto Spectral Data Cubes <i>J. C. Granahan, K. Polk, and F. P. Fanale</i>	455
Early Fluvial Degradation in Terra Tyrrhena, Mars: Constraints from Styles of Crater Degradation on the Earth <i>J. A. Grant and P. H. Schultz</i>	457
Erosion of Ejecta at Meteor Crater, Arizona: Further Constraints from Ground Penetrating Radar <i>J. A. Grant and P. H. Schultz</i>	459
Solar UV Photon Interaction with the Surface of Mars <i>R. Grard</i>	461
The Carson Quadrangle, Venus <i>R. Greeley, K. Bender, D. Senske, and J. Guest</i>	463
Do Lava Flows Erode? Preliminary Assessment <i>R. Greeley, R. S. Harris, S. D. Kadel, D. A. Williams, and J. E. Guest</i>	465
Dust on Mars: New Values for Wind Threshold <i>R. Greeley, M. Lacchia, B. White, R. Leach, D. Trilling, and J. Pollack</i>	467
Morphology and Geology of Asteroid Ida: Preliminary Galileo Imaging Observations <i>R. Greeley, R. Sullivan, R. Pappalardo, J. Head, J. Veverka, P. Thomas, P. Lee, M. Belton, and C. Chapman</i>	469
Constraints on Flash Heating from Melting Kinetics <i>J. P. Greenwood and P. C. Hess</i>	471
Ratio of First and Second Generation Fold Wavelengths on Lavas May Indicate Flow Composition <i>T. K. P. Gregg and J. H. Fink</i>	473
$^{40}\text{Ar}/^{39}\text{Ar}$ Dating of Samples from the Cat Mountain Meteorite <i>J. A. Grier, T. D. Swindle, and D. A. Kring</i>	475
The Sudbury Structure: Additional Constraints on Its Origin and Evolution <i>R. A. F. Grieve and A. Deutsch</i>	477

Wanapitei Impact Structure: Reconstruction of the Event <i>R. A. F. Grieve and T. Ber</i>	479
Mars—It's What's Inside That Counts <i>L. L. Griffith and R. E. Arvidson</i>	481
Proposal for a Topographic Survey of Gusev Crater <i>E. A. Grin, N. A. Cabrol, and G. Dawidowicz</i>	483
Dike Emplacement at Zones of Neutral Buoyancy on Venus <i>E. B. Grosfils and J. W. Head</i>	485
Modes of Origin for Giant Radiating Lineament Systems on Venus <i>E. B. Grosfils and J. W. Head</i>	487
Radial Lineament Systems on Venus: Constraining Models of Global Stress <i>E. B. Grosfils and J. W. Head</i>	489
A Possible Atmospheric Water Source for the Fluvial Valleys on Alba Patera <i>V. C. Gulick and C. P. McKay</i>	491
Ferrosilicate, Fayalite and Magnesioferrite Formation by Isothermal Annealing of an Iron-contaminated Mg-SiO Smoke <i>F. Guofoi and F. J. M. Rietmeijer</i>	493
Meteoritic Constraints on the 500 Ma Disruption of the L Chondrite Parent Body <i>H. Haack, K. Keil, E. R. D. Scott, M. D. Norman, and P. Farinella</i>	495
X-Ray Diffraction Line Broadening in Experimentally Shocked Orthopyroxenes <i>K. Hackbarth, A. Deutsch, and D. Stöffler</i>	497
Restoration of a Planetary Gamma-Ray Data Map <i>E. L. Haines, R. G. Radocinski, C. L. Lawson, and A. E. Metzger</i>	499
The Geology and Evolution of Hecate Chasma, Venus <i>V. E. Hamilton and E. R. Stofan</i>	501
Are There Correlations Between Emissivity, Topography, and Age at Coronae on Venus? <i>V. E. Hamilton, P. R. Christensen, and E. R. Stofan</i>	503
Electron Microprobe Analyses of Low Vanadium Basalt Glasses <i>B. Hanson and J. W. Delano</i>	505
The Refractive Index of the Regolith of Mercury <i>B. Hapke</i>	507
Investigations of the ^{182}Hf - ^{182}W Systematics <i>C. L. Harper Jr. and S. B. Jacobsen</i>	509
Martian Atmospheric Interaction with Bolides: A Test for an Ancient Dense Martian Atmosphere <i>W. K. Hartmann and S. Engel</i>	511
Melt Inclusions in PAT91501: Evidence for Crystallization from an L-Chondrite Impact Melt <i>R. P. Harvey and E. Roedder</i>	513

Spectral and Radar Studies of the Schiller-Schickard Region of the Moon <i>B. R. Hawke, D. T. Blewett, and B. A. Campbell</i>	515
Atmospheric Effects on the Mapping of Martian Thermal Inertia and Thermally Derived Albedo <i>J. N. Hayashi, B. M. Jakosky, and R. M. Haberle</i>	517
Effects of Fine Particles (<25 μm) on Reflectance Spectra from 0.3 to 25 μm <i>J. E. Hays and J. F. Mustard</i>	519
Large Igneous Provinces: A Planetary Perspective <i>J. W. Head III</i>	521
Lunar Mare Deposits: Mechanisms of Emplacement, Stratigraphy, and Implications for the Nature and Evolution of Source Regions and Secondary Crusts <i>J. W. Head</i>	523
NOAH: A Program to Visualize Lava Flooding of the Venus Crust <i>J. W. Head and P. Haggerty</i>	525
Mars: Formation and Evolution of Magma Reservoirs <i>J. W. Head and L. Wilson</i>	527
Geology of the Lavinia Planitia Area, Venus <i>J. Head, K. Magee, S. Keddle, M. Gilmore, and A. Yingst</i>	529
Kawelu Planitia, Venus: Geology and Mechanisms for the Formation of a Major Volcanic Region <i>M. B. Helgerud and D. Senske</i>	531
New Laboratory Measurements of Mid-IR Emission Spectra of Simulated Remote Planetary Surfaces <i>B. G. Henderson, P. G. Lucey, and B. M. Jakosky</i>	533
Geologic Map of the MTM-85280 Quadrangle, Mars <i>K. E. Herkenhoff</i>	535
Gravity Analysis of Impact Basins at Spacecraft Altitudes: Lessons from Chicxulub <i>R. R. Herrick and V. L. Sharpton</i>	537
^{26}Al , ^{10}Be , and Mg Isotopes in the Grant Iron Meteorite <i>G. F. Herzog, A. E. Souzis, S. Xue, J. Klein, and R. Middleton</i>	539
Overturn of Magma Ocean Ilmenite Cumulate Layer (II): Implications for Lunar Thermal and Magmatic Evolution <i>P. C. Hess and E. M. Parmentier</i>	541
Possible Origin of Si-bearing Metal in Chondrites <i>R. H. Hewins, B. Zanda, H. C. Connolly Jr., and M. Bourot-Denise</i>	543
Search for Extractable Fullerenes in Clays from K/T Boundaries of New Zealand <i>D. Heymann, L. P. F. Chibante, W. S. Wolbach, and R. E. Smalley</i>	545
Petrographic Characterization of Lunar Soils: Application of X-Ray Digital-Imaging to Quantitative and Automated Analysis <i>S. J. Higgins, A. Patchen, J. G. Chambers, L. A. Taylor, and D. S. McKay</i>	547

Tektites Found in the Ruins of the Maya City of Tikal, Guatemala <i>A. R. Hildebrand, H. Moholy-Nagy, C. Koeberl, L. May, F. Senftle, A. N. Thorpe, P. E. Smith, and D. York</i>	549
High Pressure and Temperature Metal-Silicate Partitioning Behavior of Moderately Siderophile Elements: Implications for the Early History of the Earth <i>V. J. Hillgren, M. J. Drake, and D. C. Rubie</i>	551
Possible Spinel Absorption Bands in S-Asteroid Visible Reflectance Spectra <i>T. Hiroi, F. Vilas, and J. M. Sunshine</i>	553
The Ammonia-Water Phase Diagram and Phase Volumes to 4 Kbars <i>D. L. Hogenboom, J. S. Kargel, T. C. Holden, and J. Ganasan</i>	555
An Experimental Study of KREEP Basalt Evolution <i>B. Holmberg and M. J. Rutherford</i>	557
Recipes for Impact Cratering <i>K. A. Holsapple</i>	559
Galileo Magnetic Field Signature: No Evidence That Gaspra is Differentiated <i>L. L. Hood and C. P. Sonett</i>	561
Evidence for an Interstellar Nitride Grain with Highly Anomalous Isotopic Compositions of C, N and Si <i>P. Hoppe, R. Strebel, P. Eberhardt, S. Amari, and R. S. Lewis</i>	563
Shocked Materials from the Dutch Peak Diamictite, Utah <i>F. Hörz, T. E. Bunch, and V. R. Oberbeck</i>	565
Experimental Impacts into Teflon Targets and LDEF Thermal Blankets <i>F. Hörz, M. J. Cintala, M. E. Zolensky, R. P. Bernhard, and T. H. See</i>	567
Simulation of Gravity-dominated Collisions <i>K. Housen</i>	569
On the Formation of Enstatite in Unequilibrated Enstatite Chondrites <i>W. Hsu and G. Crozaz</i>	571
Group A5 Chondrules in Ordinary Chondrites: Their Formation and Metamorphism <i>S. Huang, P. H. Benoit, and D. W. G. Sears</i>	573
NIMS Science Objectives and Observational Plans for Ganymede During the Galileo Tour <i>J. Hui, H. H. Kieffer, and the NIMS Team</i>	575
Characterization of Lava-Flow Surface Textures in Different Eruptive Environments on Venus <i>L. K. Hultgrien and L. R. Gaddis</i>	577
The Non-Terrestrial Origin of the Moon <i>M. Humayun and R. N. Clayton</i>	579
Potassium Isotopic Composition of Some Australasian Tektites <i>M. Humayun, R. N. Clayton, and C. Koeberl</i>	581
Presolar Al ₂ O ₃ with a Large Excess of ¹⁷ O and Depleted ¹⁸ O <i>G. R. Huss, A. J. Fahey, R. Gallino, and G. J. Wasserburg</i>	583

Silicon Carbide in Unequilibrated Ordinary Chondrites <i>G. R. Huss, A. J. Fahey, and G. J. Wasserburg</i>	585
A Search for ^{26}Al in Chondrites: Chondrule Formation Time Scales <i>I. D. Hutcheon, G. R. Huss, and G. J. Wasserburg</i>	587
Grain Charging and Plasma Potentials in a Dusty Plasma with a Dust Grain Size Distribution <i>T. W. Hyde and L. A. Bringol</i>	589
Extended Grain Lattice Formation Within a Dusty Plasma <i>T. W. Hyde and W. M. Richter</i>	591
Dynamics of Two Interacting Objects Orbiting the Sun <i>S. I. Ipatov</i>	593
New Phosphides in the Kaidun Meteorite <i>A. V. Ivanov, M. E. Zolensky, G. J. MacPherson, S. V. Yang, and N. N. Kononkova</i>	595
Dynamic Fragmentation of a Comet in the Jovian Atmosphere <i>B. A. Ivanov and H. J. Melosh</i>	597
Dynamics of Fluidized Ejecta Blankets on Mars <i>B. A. Ivanov, B. C. Murray, and A. S. Yen</i>	599
Induced Thermoluminescence Study of Experimentally Shock-loaded Quartz <i>A. I. Ivliev, L. L. Kashkarov, and D. D. Badjukov</i>	601
Shock-Thermal History of Erevan Howardite Matter on Data of Thermoluminescence Analysis of Silicate Minerals <i>A. I. Ivliev, L. L. Kashkarov, and Yu. Yu. Korotkova</i>	603
Relationships Among Radar Backscatter, Microwave Emissivity, Altitude, and Geology in Ovda Regio, Venus <i>N. R. Izenberg and R. E. Arvidson</i>	605
Size and Distribution of Shocked Mineral Grains in the Pierre Shale (Late Cretaceous) of South Dakota Related to the Manson, Iowa, Impact Event <i>G. A. Izett and W. A. Cobban</i>	607
Dust Evolution from Comets and Asteroids: Their Velocities at Earth Orbit Intersection <i>A. A. Jackson and H. A. Zook</i>	609
New Sulfur Isotopic Measurements of Meteorites and Possible Nebular Relations <i>T. Jackson, S. G. Bobias, and M. H. Thiemens</i>	611
Dating the Giant Moon-forming Impact with ^{146}Sm - ^{147}Nd Systematics <i>S. B. Jacobsen and C. L. Harper Jr.</i>	613
Mars Atmospheric Escape and Isotopic Fractionation: Synthesis of Data and Models <i>B. M. Jakosky, J. G. Luhmann, and J. H. Jones</i>	615
Siderophile and Volatile Elements in Apollo 17 Impact Melt Rocks <i>O. B. James</i>	617
Life Cycle of Venusian Coronae <i>D. M. Janes and S. W. Squyres</i>	619

The Structural Changes of Water Ice I During Warmup <i>P. Jenniskens and D. F. Blake</i>	621
Buoyant Mantle Flow and Rift Associated Volcanism: Application to Venus <i>K. Jha and E. M. Parmentier</i>	623
Resolution Analysis of Magellan Cycle 5 Gravity Data <i>C. L. Johnson and D. T. Sandwell</i>	625
Backscatter Cross Sections of Venusian FEB Crater Deposits <i>J. R. Johnson and V. R. Baker</i>	627
Longitudinal Surface Property Variations Along Venusian FEB Flows: Isabella <i>J. R. Johnson and V. R. Baker</i>	629
Preliminary Geologic Mapping of Venus Quadrangle V59 (Barrymore) <i>J. R. Johnson, G. Komatsu, and V. R. Baker</i>	631
Searching for Rare Highland Igneous Rocks at Apollo 14: Fragments of Magnesian-Suite Assemblages <i>B. L. Jolliff</i>	633
Evidence for the Nature of the Igneous Precursor of Ferroan Plutonic Rocks from North Ray Crater, Apollo 16 <i>B. L. Jolliff and L. A. Haskin</i>	635
Sampling the Apollo 17 Highlands Using Soils and Lithic Fragments <i>B. L. Jolliff, K. M. Rockow, R. L. Korotev, and L. A. Haskin</i>	637
The Compositional Similarity Between Sioux County and Experimentally Produced Partial Melts of the Murchison Chondrite Favors a Partial Melting Origin for Primitive Eucrites <i>J. H. Jones, B. Z. Hanson, G. A. McKay, A. J. G. Jurewicz, J. W. Delano, and D. W. Mittlefehldt</i>	639
Reduced, Plagioclase-rich Chondrules in the Lancé and Kainsaz CO3 Chondrites <i>R. H. Jones and A. J. Brearley</i>	641
An Additional Alba Patera Structure in Tempe Terra, Mars? <i>H.-P. Jons</i>	643
Textural Constraints on the Formation of Alteration Phases in CM Chondrites <i>L. H. Joseph, L. B. Browning, and M. E. Zolensky</i>	645
¹⁴ C Terrestrial Ages of Achondrites from Victoria Land, Antarctica <i>A. J. T. Jull, E. Cielaszyk, S. T. Brown, and D. J. Donahue</i>	647
Evidence for an Implanted Solar Component of ¹⁴ C in Lunar Samples <i>A. J. T. Jull, D. Lal, and D. J. Donahue</i>	649
Partial Melting of the St. Severin (LL) and Lost City (H) Ordinary Chondrites: One Step Backwards and Two Steps Forwards <i>A. J. G. Jurewicz, J. H. Jones, and D. W. Mittlefehldt</i>	651
Preliminary Results of Sulfide Melt/Silicate Wetting Experiments in a Partially Melted Ordinary Chondrite <i>S. R. Jurewicz and J. H. Jones</i>	653

Radar Imaging of "Overspread" Bodies Using Coherent Frequency Hopping <i>R. Jurgens, L. Robinett, M. Slade, D. Strobert, and B. Flores</i>	655
The Effect of Oxygen Fugacity on the Partitioning of Nickel and Cobalt Between Melt and Metal <i>A. A. Kadik</i>	657
The CO ₂ Formation in Terrestrial Magmas During the Fluid-Absent Melting of Carbon-bearing Rocks <i>A. A. Kadik and S. N. Shilobreeva</i>	659
Compositional Similarities Between Undergrouped Loongana 001 and CV4 Coolidge <i>G. W. Kallemeyn</i>	661
Geochemistry of LEW88774 and Two Other Unusual Ureilites <i>G. W. Kallemeyn and P. H. Warren</i>	663
Isotopic, Chemical and Textural Properties of Acid Residues from Various Meteorites <i>N. Kano, K. Yamakoshi, and H. Matsuzaki</i>	665
An Alluvial Depositional Analog for Some Volcanic Plains on Venus <i>J. S. Kargel</i>	667
Cosmic-Ray Exposure History of the Erevan Howardite Matter by Track Data <i>L. L. Kashkarov and N. N. Korotkova</i>	669
Some General Characteristics of the Early Radiation-Thermal History of Carbonaceous and Ordinary Chondrite Matter on Data of Track Studies <i>L. L. Kashkarov, N. N. Korotkova, and G. V. Kalinina</i>	671
Structural Characteristics and Classification of Double-Type Coronae and Corona-like Features on Venus <i>K. Kauhanen and T. Törmänen</i>	673
Dione Regio Venus: A Comparison to Other Regional Highlands <i>S. T. Keddie and J. W. Head</i>	675
The Geology and Stratigraphy of Dione Regio, Venus <i>S. T. Keddie and J. W. Head</i>	677
Sapas Mons: Evolution of a Type-Shield Volcano on Venus <i>S. T. Keddie and J. W. Head</i>	679
Structural Evolution of Danu Montes, Venus: Deformation Around a Curved Boundary <i>M. Keep and V. L. Hansen</i>	681
Xenon Isotopic Measurements in Shallowater: <i>In Situ</i> Pulsed Laser Volatilization and the Search for the Carrier of Radiogenic ¹²⁹ Xe <i>K. Kehm, C. M. Hohenberg, and R. H. Nichols Jr.</i>	683
The Nature of Agglutinitic Glass in the Fine-Size Fraction of Lunar Soil 10084 <i>L. P. Keller and D. S. McKay</i>	685
Electron Energy-loss Spectroscopy of Carbon in Interplanetary Dust Particles <i>L. P. Keller, J. P. Bradley, K. L. Thomas, and D. S. McKay</i>	687

Compositional Evidence in Favor of a Genetic Link Between the Nysa and Hertha Asteroid Families <i>M. S. Kelley, M. J. Gaffey, and J. G. Williams</i>	689
Modelling Lava Flow Cooling Using a Finite-Difference Numerical Approximation <i>R. M. Kent and H. Pinkerton</i>	691
Modelling the Flow and Heat Transfer of Magma in Dikes Using Computational Fluid Dynamics <i>R. M. Kent and H. Pinkerton</i>	693
Production of Superparamagnetic Fe ⁰ on the Lunar Surface <i>J. F. Kerridge</i>	695
Formation of Venusian Crustal Plateaus Over Mantle Downwellings <i>J. G. Kidder and R. J. Phillips</i>	697
Mantle Plumes on Venus: New High Rayleigh Number Models and Applications to Magellan Observations <i>W. S. Kiefer</i>	699
Isolation of Cosmic-Ray-produced Nitrogen in Meteoritic Silicates and Some Implications <i>J. S. Kim, Y. Kim, and K. Marti</i>	701
Genetic Relationship of Acapulcoites and Lodranites? A Study of Nitrogen and Xenon Isotopic Signatures <i>Y. Kim and K. Marti</i>	703
Splotches on Venus: Distribution, Properties, and Classification <i>R. L. Kirk and D. J. Chadwick</i>	705
⁵⁷ Fe Mössbauer Studies of the Kinetics of Pyrite Decomposition on the Surface of Venus <i>G. Klingelhöfer, B. Fegley Jr., and K. Lodders</i>	707
Optimization of the Miniaturized Backscattering Mössbauer-Spectrometer MIMOS <i>G. Klingelhöfer, P. Held, J. Foh, F. Schlichting, R. Teucher, E. Kankleit, E. N. Evlanov, O. F. Prilutski, G. V. Veselova, and E. A. Duzheva</i>	709
Geochemical and Mineralogical Constraints on the Parent Objects of Micrometeorites <i>W. Klöck and T. Presper</i>	711
Heating Experiments Simulating Atmospheric Entry of Micrometeorites <i>W. Klöck, G. J. Flynn, S. R. Sutton, S. Bajt, and K. Neuking</i>	713
Wave Tectonics on the Moon and Symmetries-Antisymmetries of Mare Orientale Region <i>G. G. Kochemasov</i>	715
Ni-rich Cr Spinel in Spherule Beds from the Barberton Mountain Land (South Africa) are of Terrestrial Origin: Evidence Against Impact Origin of Spherule Layers <i>C. Koeberl and W. U. Reimold</i>	717
Mineralogical, Petrological, and Geochemical Studies of Drill Cores from the Manson Impact Structure: A Progress Report <i>C. Koeberl, R. R. Anderson, R. H. Boer, J. D. Blum, C. P. Chamberlain, A. Kracher, W. U. Reimold, B. Träxler, and A. Vormaiier</i>	719

Ames Structure, Oklahoma: An Economically Important Impact Crater <i>C. Koeberl, W. U. Reimold, and R. A. Powell</i>	721
Magnesium Isotopic Fractionation in the Olivines from Allende Chondrules and Isolated Grains <i>A. Koga, H. Nagahara, H. Yurimoto, and O. Koike</i>	723
Al-Mg Isotopic and REE Clues to the Formation of a Type B1 CAI from Allende Meteorite <i>O. Koike, H. Yurimoto, and H. Nagasawa</i>	725
Longitudinal Profiles of Plains Channels on Venus <i>G. Komatsu and V. R. Baker</i>	727
Geochemical Comparison of Four Cores from the Manson Impact Structure <i>R. L. Korotev, K. M. Rockow, B. L. Jolliff, and L. A. Haskin</i>	729
The Ionized Luminous Column Created During the Flight of a Comet Through Jovian Atmosphere <i>I. B. Kosarev and I. V. Nemtchinov</i>	731
Lunar and Planetary Mission Scenario for H-II Launch Vehicle <i>H. Koshiishi, R. Kouda, K. Matushima, and A. Takano</i>	733
Towards Formation of Shells and Rays in Cometary Ionosphere <i>N. Ya. Kotsarenko and O. P. Verkhoglyadova</i>	735
Aspect of Lunar Resources Exploration <i>R. Kouda and H. Koshiishi</i>	737
Mercury: Mid-Infrared (7.3–13.5 μm) Spectroscopic Observations Showing Features Characteristic of Plagioclase <i>R. W. H. Kozłowski, A. L. Sprague, F. C. Witteborn, D. P. Cruikshank, D. Wooden, and K. D. Snyder</i>	739
Fate of Halogens at the Surface of Tektites <i>U. Krähenbühl and M. Langenauer</i>	741
Small Grains with High Lead Concentration in Chainpur <i>J. L. A. M. Kramer, A. C. Kik, and R. D. Vis</i>	743
Uniqueness of a Solution of a Steady-state Photochemical Problem: Applications to Mars <i>V. A. Krasnopolsky</i>	745
H ₂ O-H ₂ SO ₄ System in Venus' Clouds and OCS, CO, and H ₂ SO ₄ Profiles in Venus' Troposphere <i>V. A. Krasnopolsky and J. B. Pollack</i>	747
First Measurement of Helium on Mars: Implications for the Problem of Radiogenic Gases on the Terrestrial Planets <i>V. A. Krasnopolsky, S. Bowyer, S. Chakrabarti, G. R. Gladstone, and J. S. McDonald</i>	749
Model for Ascending of Mantle Diapirs Forming Coronae on Venus <i>M. A. Kreslavsky</i>	751

Silica- and Merrihueite/Roedderite-bearing Chondrules and Clasts in Ordinary Chondrites: New Occurrences and Possible Origin <i>A. N. Krot and J. T. Wasson</i>	753
Ab Initio Calculations of Thermodynamics and Kinetics of Gas-Phase Reactions Relevant to the Early Solar Nebula <i>J. D. Kubicki, J. R. Beckett, G. A. Blake, and E. M. Stolper</i>	755
Isostasy Models and Correlations of Geoid and Topography Data for Characteristic Highlands on Venus <i>A. B. Kucinskas and D. L. Turcotte</i>	757
Mars, A Carbon Rich Planet? Behavior of H and C During Early Core Formation <i>K. Kuramoto and T. Matsui</i>	759
Fractionated Trace Element Abundances in Micrometeorites from Antarctica <i>G. Kurat, C. Koeberl, and M. Maurette</i>	761
Preliminary Report on Spinel-rich CAIs in an Antarctic Micrometeorite <i>G. Kurat, P. Hoppe, and M. Maurette</i>	763
Non-Steady Modeling of Comet's Wake in the Rarefied Layers of the Jovian Atmosphere <i>M. Ju. Kuzmitcheva and O. P. Popova</i>	765
Volcanism and Tectonism in Rusalka Planitia and Atla Regio, Venus <i>M. G. Lancaster and J. E. Guest</i>	767
Stratigraphic Assessment of Gusev Crater as an Exobiology Landing Site <i>R. Landheim, N. A. Cabrol, R. Greeley, and J. D. Farmer</i>	769
Mossbauer and Spectral (Visible and Near-IR) Data for Fe ³⁺ -Substituted Rutile <i>H. V. Lauer Jr., R. V. Morris, and R. K. Vempati</i>	771
An Experimental Study of Iron Sulfide Kinetics in H ₂ -H ₂ S Gas Mixtures and Application to Iron Sulfide Condensation in the Solar Nebula <i>D. Lauretta and B. Fegley Jr.</i>	773
The Massive O, B Star of Second Generation May be Source of Interstellar Diamond, SiC and Graphite in Chondrites <i>A. K. Lavrukhina and A. V. Fisenko</i>	775
On Forming Mg-26 and Cr-53 Anomalies in Some Meteoritic Minerals <i>A. K. Lavrukhina and G. K. Ustinova</i>	777
Characterizing Errors Using the Spectral Mixture Framework <i>M. E. Lawler and J. B. Adams</i>	779
Impact-Related Low-Emissivity Anomalies on Venus <i>S. L. Lawson and J. J. Plaut</i>	781
Project Artist: Integrating Astronomy and Planetary Sciences Into the Elementary and Middle School Curriculum <i>L. A. Lebofsky and N. R. Lebofsky</i>	783
The Nature of Low Albedo Asteroids from 3- μ m Spectrophotometry <i>L. A. Lebofsky, D. T. Britt, E. S. Howell, and A. S. Rivkin</i>	785

Mapping Regolith and Blocks on Asteroid 243 Ida: The Effects of Photometric Viewing Geometry <i>P. Lee, J. Veverka, M. J. S. Belton, P. C. Thomas, B. T. Carcich, R. Greeley, R. Sullivan, R. Pappalardo, and the Galileo SSI Team</i>	787
Progress in the Development of the GMM-2 Gravity Field Model for Mars <i>F. G. Lemoine, D. E. Smith, F. J. Lerch, M. T. Zuber, and G. B. Patel</i>	789
Preliminary Solutions for the Lunar Gravity Field from Analysis of Lunar Orbiter Tracking Data <i>F. G. Lemoine, D. E. Smith, M. T. Zuber, D. D. Rowlands, and S. K. Fricke</i>	791
Precision Noble Gas Measurements on Presolar Diamonds from the Murchison Meteorite <i>R. S. Lewis</i>	793
Exploring Meteorite Mysteries: A Teachers' Guide with Activities <i>M. Lindstrom, J. Allen, A. Treiman, J. Burch, K. Crowell, K. Stocco, B. Swaby, R. Luksch, and K. Tobola</i>	795
Pigeonholing Planetary Meteorites: The Lessons of Misclassification of EET87521 and ALH84001 <i>M. M. Lindstrom, A. H. Treiman, and D. W. Mittlefehldt</i>	797
Thumbprint Terrain in Isidis Planitia: Formed in a Glacial Paleolake Environment <i>J. F. Lockwood and J. S. Kargel</i>	799
On the Origin of Enstatite Chondrite Chondrules Based on Their Petrography and Comparison with Experimentally Produced Chondrules <i>G. E. Lofgren, J. M. DeHart, and P. J. Burkett</i>	801
Liquidus Equilibria of Lunar Analogs in the Garnet Stability Field <i>J. Longhi</i>	803
A Model for Forecasting Lava Flow Lengths <i>R. Lopes-Gautier and C. R. J. Kilburn</i>	805
Galileo's Near Infrared Mapping Spectrometer (NIMS) Science Objectives and Observational Plans for Io <i>R. Lopes-Gautier, R. Carlson, W. Smythe, L. Soderblom, and the Galileo NIMS Team</i>	807
Morphology of Meteoroid and Space Debris Craters on LDEF Metal Targets <i>S. G. Love, D. E. Brownlee, N. L. King, and F. Hörz</i>	809
Scarp Heights of Martian Channels from Shadow Measurements <i>B. K. Lucchitta and J. Dembosky</i>	811
Small Time Differences in Differentiated Meteorites Recorded by the ^{53}Mn - ^{53}Cr Chronometer <i>G. W. Lugmair, C. MacIsaac, and A. Shukolyukov</i>	813
Terrain Simulator <i>W. Luo, R. Arvidson, and R. Becker</i>	815
Dry Deformation of Diabase: Implications for Tectonics on Venus <i>S. J. Mackwell, M. E. Zimmerman, D. L. Kohlstedt, and D. S. Scherber</i>	817

Magnetic Properties Experiments Designed for Use with a Mössbauer Spectrometer and an APX Spectrometer on Mars <i>M. B. Madsen, J. M. Knudsen, S. Faurschou Hviid, H. P. Gunnlaugsson, D. P. Agerkvist, L. Vistisen, J. Madsen, G. Klingelhöfer, E. Kankeleit, V. N. Khromov, E. Evlanov, O. Prilutski, and B. Zubkov</i>	819
A Model for the Origin of Flood Volcanism and "Passive" Rifting in the Lada Terra-Lavinia Planitia Region on Venus <i>K. P. Magee and J. W. Head</i>	821
Venus: Morphology and Morphometry of Volcanism in Rifting Environments <i>K. P. Magee and J. W. Head</i>	823
Alternative Thermal Histories for Type B Ca-Al-rich Inclusions <i>S. V. Maharaj and R. H. Hewins</i>	825
Radial Compaction of the Dust Subdisk in a Protoplanetary Disk as a Possible Way to Gravitational Instability <i>A. B. Makalkin</i>	827
Numerical Simulation of Tidal Capture of a Lunar-Mass Planetoid by an Earth-like Planet: Two-Dimensional Limits of a Prograde Stable Capture Zone <i>R. J. Malcuit and R. R. Winters</i>	829
Extreme Potassium Enrichment in Plagioclase from Lithic Clasts in the Lewis Cliff 86001 Monomict Eucrite <i>J. L. Mann and J. S. Delaney</i>	831
Geologic Mapping of the Sif Mons Southern Flank, Venus (Preliminary Results) <i>A. G. Marchenko</i>	833
Apollo—The Next Generation: Activities to Accompany the Lunar Sample Disk <i>L. Martel and G. J. Taylor</i>	835
Evidence for a Mineralogical Change in Relation with the Martian Global Geomorphic Dichotomy in the Tharsis-Mare Sirenum Region <i>P. Martin, P. C. Pinet, R. Bacon, and A. Rousset</i>	837
Experimental and Theoretical Investigation of Shock Induced Outgassing of Dolomite <i>I. Martinez, U. Schärer, F. Guyot, A. Deutsch, and U. Hornemann</i>	839
Trojan Collisional Families as a Source for Short-Period Comets <i>F. Marzari, V. Vanzani, and P. Farinella</i>	841
Effects of Meteoroid Shape on Cosmogenic-Nuclide Production Rates <i>J. Masarik and R. C. Reedy</i>	843
Numerical Simulations of Gamma-Ray Emission from the Martian Surface <i>J. Masarik and R. C. Reedy</i>	845
The Highbury Structure, A New Impact Crater in N.W. Zimbabwe <i>S. Master, W. U. Reimold, D. Brandt, C. Koeberl, D. Robertson, and L. A. G. Antoine</i>	847
I-Xe Dating of El Taco Inclusions <i>K. J. Mathew and F. Begemann</i>	849

Production Rate of Nitrogen in Moon and Meteorites <i>K. J. Mathew and S. V. S. Murty</i>	851
Cosmogenic ^{26}Al in Deep-Sea Stony Spherules <i>H. Matsuzaki and K. Yamakoshi</i>	853
GVDR Data Product: A Summary of All Magellan Observations of Venus Surface Characteristics <i>M. J. Maurer and R. A. Simpson</i>	855
Erosion and Deposition in the Martian Highlands: Aeolis and Arabia <i>T. A. Maxwell and R. A. Craddock</i>	857
Depth of Formation of Lunar and Terrestrial Anorthosites and Gabbros from Compositional Profiles of Exsolved Pyroxenes <i>I. S. McCallum and H. E. O'Brien</i>	859
Post-Impact Hydrothermal Alteration of the Manson Impact Structure <i>P. McCarville and L. J. Crossey</i>	861
The Galileo Mission Near Infrared Mapping Spectrometer (NIMS) Investigation of the Galilean Satellites <i>T. B. McCord, R. Carlson, and the NIMS Team</i>	863
Low-FeO Ordinary Chondrites: A Nebular Origin and New Chondrite Parent Body <i>T. J. McCoy, K. Keil, E. R. D. Scott, G. K. Benedix, A. J. Ehlmann, T. K. Mayeda, and R. N. Clayton</i>	865
Eureca's Hypervelocity Impact Score: Microcrater Flux Decreases But the Large Crater Flux Increases in Specific Directions <i>J. A. M. McDonnell</i>	867
Evidence for Pre-Nectarian Impact Basin in Northwestern Oceanus Procellarum <i>A. McEwen, P. Davis, and A. Howington-Kraus</i>	869
Global Color Views of Mars <i>A. S. McEwen, L. A. Soderblom, T. L. Becker, E. M. Lee, J. D. Swann, R. Aeschliman, and R. M. Batson</i>	871
V, Cr and Mn Partition Coefficients Between Mantle Minerals and Silicate Melt <i>E. A. McFarlane, M. J. Drake, and D. C. Rubie</i>	873
Lunar Ferroan Anorthosite Subgroups <i>J. J. McGee</i>	875
Evolution of a Hot Spot, Central Eistla Regio, Venus <i>G. E. McGill</i>	877
Production of Ferroan Andesites by the Experimental Partial Melting of an LL Chondrite <i>J. C. McGuire, A. J. G. Jurewicz, and J. H. Jones</i>	879
Apatite Fission-Track Age of Marquez Dome Impact Structure, Texas <i>J. F. McHone and R. B. Sorkhabi</i>	881
Synthetic and Natural Nakhla Pyroxenes: Parent Melt Composition and REE Partition Coefficients <i>G. McKay, L. Le, and J. Wagstaff</i>	883

Venusian Channel Gradients as a Guide to Vertical Tectonics <i>L. C. McLeod and R. J. Phillips</i>	885
The Distribution and Source of Na in Two Type B1 CAIs <i>G. P. Meeker</i>	887
Determination of Bulk-Carbon Contents in Seven IIIAB Iron Meteorites <i>A. Meibom, K. L. Rasmussen, O. S. Hansen, P. Hornshøj, and N. Rud</i>	889
Discovery Day, Introducing Space Science to the High School <i>R. C. Melchior and J. O. Annexstad</i>	891
Crater Chains on the Moon: Records of Comets Split by the Earth's Tides? <i>H. J. Melosh and E. A. Whitaker</i>	893
Genetic Links Between Equatorial and South Polar Regions on Mars? <i>E. Merényi, W. M. Calvin, K. S. Edgett, and R. B. Singer</i>	895
A Successful Planetary Science "SPACE" Education Program for Students in Grades 3–8 <i>J. A. Merrell, D. Kenealy, and D. Nash</i>	897
An Absolute Normalization for Modeled Neutron Flux Distribution <i>A. E. Metzger, D. M. Drake, E. L. Haines, J. Mazarik, and R. C. Reedy</i>	899
The Pasamonte <i>Polymict</i> Eucrite—A Reclassification <i>K. Metzler, K.-D. Bobe, H. Palme, B. Spettel, and D. Stöffler</i>	901
Isotope Source Table for a 25 M _⊙ Type II Supernova <i>B. S. Meyer</i>	903
Textural and Mineralogical Heterogeneity of Silicate Inclusions in Tsarev Chondrite <i>L. F. Migdisova, A. A. Yaroshevsky, M. A. Nazarov, and N. N. Kononkova</i>	905
Cr, Mn and Ca Distributions for Olivine in Angritic Systems: Constraints on the Origins of Cr-rich and Ca-poor Core Olivine in Angrite LEW87051 <i>T. Mikouchi, G. McKay, and L. Le</i>	907
Mineral Paragenesis of the Ureilites: Evidence for High Pressure in a Large Parent Body <i>O. B. Mitreikina, O. V. Chryukina, N. G. Zinovieva, and L. B. Granovsky</i>	909
ALH84001 Cumulate Orthopyroxenite: A Previously Unappreciated Martian Meteorite <i>D. W. Mittlefehldt</i>	911
Two Types of Shocked Quartz and Graphite at Barringer Impact Crater <i>Y. Miura</i>	913
Lunar Landing Site and Exploration by Japanese Lunar Project <i>Y. Miura and Lunar Working Group of Japan</i>	915
Japanese Found Meteorites Similar to Antarctic Meteorite Collection <i>Y. Miura, K. Yanai, and O. G. Iancu</i>	917
New SNC Meteorite ALH84001: Evidence for SNC Meteorite from Noble Gases <i>Y. N. Miura, N. Sugiura, and K. Nagao</i>	919

Chemical Zoning of Olivine in Several Pallasites Suggestive of Faster Cooling <i>M. Miyamoto and H. Takeda</i>	921
Partition Coefficients for Al, Ca, Ti, Cr, and Ni in Olivine Obtained by Melting Experiment on an LL6 Chondrite <i>M. Miyamoto, T. Mikouchi, and G. A. McKay</i>	923
Thermal Infrared Observations of Mars from Palomar Mountain <i>J. Moersch, T. Hayward, J. Houck, P. Lee, J. Miles, P. Nicholson, M. Smith, S. Squyres, and J. Van Cleve</i>	925
Geology of the Mahuca Tholus Quadrangle, Venus <i>H. J. Moore, S. T. Arriola, and E. J. Israel</i>	927
Rhenium-Osmium Isotope Systematics in IIAB and IIIAB Iron Meteorites <i>J. W. Morgan, M. F. Horan, R. J. Walker, M. I. Smoliar, and J. N. Grossman</i>	929
Thermal Conductivity of Planetary Lithospheres: New Estimates from Measurements on Mantle Xenolith Samples <i>P. Morgan and S. Y. O'Reilly</i>	931
Use of Mars Climate History to Demonstrate Causes and Consequences of Global Change on Earth: A Teaching Module for Middle School Students <i>P. Morgan, R. A. Lynch, and G. P. Johnson</i>	933
REE Characteristics of an Igneous Inclusion in the Yamato-75097 L6 Chondrite <i>N. Morikawa, K. Misawa, N. Nakamura, and K. Yanai</i>	935
Ferromagnetic Resonance Spectra of H ₂ -Reduced Minerals and Glasses <i>R. V. Morris and C. C. Allen</i>	937
Hematite Formed from Pyroxene on Mars by Meteoritic Impact <i>R. V. Morris, J. F. Bell III, and H. V. Lauer</i>	939
Mössbauer Mineralogy of Calcined Murchison Meteorite <i>R. V. Morris, M. E. Zolensky, T. Hiroi, and M. E. Lipschutz</i>	941
Toward Systematic Estimation of the Origins of Regolith Materials that Might be Sampled During a Lunar Highland Geologic Traverse <i>B. E. Moss and L. A. Haskin</i>	943
Carbon in the Metal of Bishunpur and Other Ordinary Chondrites <i>S. Mostefaoui and C. Perron</i>	945
Impact Craters on Martian Volcanoes <i>P. J. Mouginis-Mark</i>	947
Morphology of Venus Calderas: Sif and Maat Montes <i>P. J. Mouginis-Mark</i>	949
Radar Imaging of the Ice Deposits on Mercury's Poles <i>D. O. Muhleman, B. J. Butler, and M. A. Slade</i>	951
Photoclinometric Studies of Crater and Groove Morphology on Phobos <i>D. C. Munro and L. Wilson</i>	953

Spectral Units of Martian Soil: Possible Discrimination of Mobile Sediments and Substrate <i>S. Murchie and J. Mustard</i>	955
The HST Spectrum of Phobos: Comparison with Mariner 9, Viking, and Phobos 2 Results and with Meteorite Analogs <i>S. Murchie and B. Zellner</i>	957
He, Ne and Ar from the Solar Wind and Solar Energetic Particles in Metal Separates from Fayetteville and Acfer111 <i>Ch. Murer, H. Baur, P. Signer, and R. Wieler</i>	959
Limits on the Mafic Mineralogy of Mars Through MGM Analysis of ISM Spectra <i>J. F. Mustard and J. M. Sunshine</i>	961
Mare-Highland Mixing Relationships Along the Southwestern Shores of Oceanus Procellarum <i>J. F. Mustard, J. W. Head, and I. Antenenko</i>	963
Why Chondrules Do Not Show and Some CAIs Show Significant Isotopic Fractionation <i>H. Nagahara</i>	965
Diffusion Measurement on Double-Layered Single Crystals of Olivine, Orthopyroxene, and Zircon Synthesized by Epitaxial Overgrowth <i>H. Nagasawa and M. Morioka</i>	967
High-Temperature Shock Effects on Carbonaceous Chondrites <i>T. Nakamura, K. Tomeoka, T. Sekine, and H. Takeda</i>	969
Argon Degassing and Crustal Production Rates on Venus <i>N. Namiki and S. C. Solomon</i>	971
The Impact Crater Density on Volcanoes and Coronae on Venus: Implications for Volcanism and Global Resurfacing <i>N. Namiki and S. C. Solomon</i>	973
Mid-Infrared Spectra of Condensed SO ₂ Phases: Lab Data and Applications to Galileo Mapping of Io <i>D. Nash and B. Betts</i>	975
Shape, Size, and Distribution of Magnetic Particles in Bjurböle Chondrules <i>D. F. Nava</i>	977
P-rich Sulfide, Barringerite, and Other Phases in Carbonaceous Clasts of the Erevan Howardite <i>M. A. Nazarov, F. Brandstätter, and G. Kurat</i>	979
Chemistry of Carbonaceous Xenoliths from the Erevan Howardite <i>M. A. Nazarov, F. Brandstätter, G. Kurat, B. Spettel, and H. Palme</i>	981
Utilization of ICP-MS Analytical Techniques for Determination of Siderophile-Element Abundances: Potential Uses for the Planetary Geochemist <i>C. R. Neal and L. A. Taylor</i>	983
The Hermes Mercury Orbiter Mission <i>R. M. Nelson, L. J. Horn, J. R. Weiss, and W. D. Smythe</i>	985
Atmospheric Oscillations Initiated by the Penetration of a Comet or an Asteroid into Gaseous Envelope of a Planet <i>I. V. Nemtchinov and T. V. Loseva</i>	987

Waves Created by Comet Impact Into Ocean <i>I. V. Nemtchinov, A. V. Teterev, and S. P. Popov</i>	989
The Inner Solar System Impact Record: Lunar, Terrestrial-Planet, and Asteroid Size-Frequency Data Comparison <i>G. Neukum and B. Ivanov</i>	991
Patterns of Brittle Deformation Under Extension on Venus <i>G. A. Neumann and M. T. Zuber</i>	993
The Depletion of W in the Earth's Primitive Mantle, A Stumbling Block for High Temperature Equilibrium Core Formation? <i>H. E. Newsom, P. D. Noll Jr., S. A. Maehr, and K. W. W. Sims</i>	995
Trapped Noble Gases in Native Gold; Radiogenic He and Fission Xe in U-rich Minerals Accompanying Placer Gold <i>S. Niedermann, O. Eugster, Ch. Thalmann, R. Frei, J. D. Kramers, L. Bruno, and B. Hofmann</i>	997
A Search for Solar Energetic Particle Helium in Interplanetary Dust Particles <i>A. O. Nier and D. J. Schlutter</i>	999
Geology of Akkriva Colles Area on Venus: Venera 15/16 SAR Images Analysis <i>A. M. Nikishin, N. N. Bobina, and G. A. Burba</i>	1001
Recent Histories of Lunar Cores 15009 and 79002/1 Using Cosmogenic Radionuclides ^{10}Be , ^{26}Al , and ^{36}Cl <i>K. Nishiizumi, R. C. Finkel, M. W. Caffee, P. Sharma, J. Masarik, R. C. Reedy, and J. R. Arnold</i>	1003
Interstellar Corundum and Spinel from the Tieschitz Ordinary Chondrite <i>L. Nittler, C. Alexander, X. Gao, R. Walker, and E. Zinner</i>	1005
Sudbury Igneous Complex: Evidence Favoring Endogenous Magma Rather Than Impact Melt <i>M. D. Norman</i>	1007
Alkali Element Constraints on Earth-Moon Relations <i>M. D. Norman, M. J. Drake, and J. H. Jones</i>	1009
Formation of Iron Metal and Grain Coagulation in the Solar Nebula <i>J. A. Nuth III and O. Berg</i>	1011
Measurement of the Decay Rate of the SiH Feature as a Function of Temperature <i>J. A. Nuth III and G. F. Kraus</i>	1013
Pre-Bombardment Crystallization Ages of Basaltic Clasts from Antarctic Howardites EET87503 and EET87513 <i>L. E. Nyquist, C.-Y. Shih, H. Wiesmann, and B. M. Bansal</i>	1015
New Data Supporting a $^{146,147}\text{Sm}$ - $^{142,143}\text{Nd}$ Formation Interval for the Lunar Mantle <i>L. E. Nyquist, H. Wiesmann, B. M. Bansal, and C.-Y. Shih</i>	1017
Galileo's Near Infrared Mapping Spectrometer (NIMS) Science Observation Plan for Europa <i>A. Ocampo, D. Matson, and the NIMS Team</i>	1019
Calorimetric Thermobarometry of Experimentally Shocked Quartz <i>K. D. Ocker, J. L. Gooding, and F. Hörz</i>	1021

Penetration of Large Bolides into Dense Planetary Atmospheres—Role of Hydrodynamic Instabilities <i>J. D. O'Keefe, T. Takata, and T. J. Ahrens</i>	1023
Lithophile Element Diffusion Profiles in Phosphate Phases in IIIAB Iron Meteorites: A Clue to Trace Elements in Metal During Core Formation <i>E. J. Olsen and I. M. Steele</i>	1025
I Don't Believe All the Irregularly Shaped Small Bodies in the Solar System are the Result of Collisions <i>W. A. Oran</i>	1027
Depositional Patterns at the Mouths of the Martian Outflow Channels (Dao, Harmahkis, Maja, and Ares Valles, Mars) <i>G. G. Ori</i>	1029
Constraints on the Origin of the Offset Dikes (Sudbury Impact Structure, Canada) from U-Pb Data <i>M. Ostermann, U. Schärer, and A. Deutsch</i>	1031
Chromium Isotopic Anomalies in Stepwise Dissolution of Orgueil <i>U. Ott, F. A. Podosek, J. C. Brannon, T. J. Bernatowicz, and C. R. Neal</i>	1033
Refractory Siderophiles in Antarctic Unequilibrated Ordinary Chondrites <i>H. Ozaki and M. Ebihara</i>	1035
New Thermal Models for High-Latitude Impact Craters on Mercury: Implications for Water Ice <i>D. A. Paige, S. E. Wood, and A. R. Vasavada</i>	1037
Noble Gas Composition of Tektites from Bedias, Texas <i>R. L. Palma, K. D. Ocker, and M. N. Rao</i>	1039
Re-Os Calibration for Isochron Determinations <i>D. A. Papanastassiou, H. H. Ngo, and G. J. Wasserburg</i>	1041
ALH 84001 A "SNC Orthopyroxenite": Insights from SIMS Analysis of Orthopyroxene and Comparisons to Diogenites <i>J. J. Papike, G. W. Fowler, G. D. Layne, M. N. Spilde, and C. K. Shearer</i>	1043
Orthopyroxene as a Recorder of Lunar Mg-Suite Norite Petrogenesis: Preliminary Ion Microprobe Studies of Apollo 17 Fragments <i>J. J. Papike, G. W. Fowler, and C. K. Shearer</i>	1045
Extensional Tectonics of Arden Corona, Miranda: Evidence for an Upwelling Origin of Coronae <i>R. Pappalardo, R. Greeley, and S. J. Reynolds</i>	1047
Modelling the Transition Between Hawaiian-Style Lava Fountaining and Strombolian Explosive Volcanic Activity <i>E. A. Parfitt and L. Wilson</i>	1049
The Role of Magma Recycling in Controlling the Behavior of Hawaiian-Style Lava Fountains <i>E. A. Parfitt, L. Wilson, and J. W. Head III</i>	1051
Apron Heights Around "Stepped Massifs" in the Borealis Basin of Mars <i>T. J. Parker and D. S. Gorsline</i>	1053

Formation of Complex Ridged Terrain Through Progressive Compressional Deformation in the Northern Ovda Region of Venus <i>T. J. Parker and R. S. Saunders</i>	1055
High Spatial Resolution Sulphur Isotopic Analysis of Troilite in Ordinary Chondrites by Ion Microprobe <i>B. A. Paterson, H. Y. McSween Jr., and L. R. Riciputi</i>	1057
The Composition of SEPs Implanted in Regolith Minerals Depends on Implantation Ranges <i>A. Pedroni</i>	1059
Anomalous Metal and Sulfide Abundances in the Regolith-Breccia Acfer111 <i>A. Pedroni, B. Spettel, and F. Wlotzka</i>	1061
A New Imaging Resonance Ionization Mass Spectrometer for Isotopic and Trace Analysis <i>M. J. Pellin, R. N. Thompson, Z. Ma, A. M. Davis, R. S. Lewis, and R. N. Clayton</i>	1063
Heavy Xenon Isotopes on the Moon and in the Solar Wind <i>R. O. Pepin</i>	1065
The Thick Festoon Flow and Adjacent Dark Flow, Ovda Regio, Venus <i>J. L. Permenter and R. L. Nusbaum</i>	1067
Lamellar Olivine in the Divnoe Achondrite: EPMA and TEM Studies <i>M. I. Petaev and A. J. Brearley</i>	1069
Numerical Model of a Genetic Link Between Acapulco and Y791493 Primitive Achondrites. I: Phase Equilibria and Major Element Constraints <i>M. I. Petaev, A. A. Ariskin, and J. A. Wood</i>	1071
Numerical Model of a Genetic Link Between the Acapulco and Y791493 Primitive Achondrites. II: Implications to the Origin of Acapulcoites and Lodranites <i>M. I. Petaev, A. A. Ariskin, and J. A. Wood</i>	1073
Mg and Ti Partition Coefficients for Anorthite-CAI Liquid: Dependence on Oxygen Fugacity and Melt Composition <i>M. T. Peters, E. Shaffer, and D. S. Burnett</i>	1075
The Distribution of Lithologic Units in the Western Highlands of the Moon <i>C. A. Peterson, B. R. Hawke, P. G. Lucey, G. J. Taylor, and P. D. Spudis</i>	1077
Venus Resurfacing History: Constraints from Halo Ejecta Deposits <i>R. J. Phillips, N. R. Izenberg, and J. S. Alexopoulos</i>	1079
FeO and MgO in Plagioclase of Lunar Anorthosites: Igneous or Metamorphic? <i>W. C. Phinney</i>	1081
Young Vesta (Regolith)? <i>C. M. Pieters and R. P. Binzel</i>	1083
Geophysical Studies of the Montagnais Impact Crater <i>M. Pilkington, L. F. Jansa, and R. A. F. Grieve</i>	1085
Arachnoid-like Feature on Oldoinyo Lengai, an Active Carbonatite Volcano in Northern Tanzania <i>H. Pinkerton, J. B. Dawson, and D. M. Pyle</i>	1087

Lava Flow Morphology and Chemistry <i>H. Pinkerton, J. B. Dawson, and D. M. Pyle</i>	1089
Topographic and Surface Roughness Properties of Steep-Sided Domes on Venus and Earth from Radar Remote Sensing and Field Measurements <i>J. J. Plaut, E. R. Stofan, D. A. Crown, and S. W. Anderson</i>	1091
Atmospheric vs. Solar Noble Gas Abundances: Isotopic Fractionation in Low Energy Argon Ion Implantation <i>K. V. Ponganis, Th. Graf, and K. Marti</i>	1093
Prolonged Biospheric Effects of Sulfur Vaporization by the K/T Chicxulub Impact <i>K. O. Pope, A. C. Ocampo, K. H. Baines, and B. A. Ivanov</i>	1095
Systematics of Xe Isotopes in a Two-layer Earth with Mass Transport <i>D. Porcelli and G. J. Wasserburg</i>	1097
Attempt to Observe the Sodium Exosphere of Mercury During the 1993 Solar Transit <i>A. E. Potter, D. Talent, H. Kurokawa, S. Kawakami, and T. H. Morgan</i>	1099
Discovery and Description of a Muong Nong-type Georgia Tektite <i>H. Povenmire, B. P. Glass, and R. Strange</i>	1101
Pb Isotopic Systematics of Troctolitic Anorthosite 62237 <i>W. R. Premo and M. Tatsumoto</i>	1103
Young Tectonism and Volcanism on Venus: Age Estimates from Crater Densities <i>M. Price, J. Suppe, F. Bilotti, and G. Watson</i>	1105
LEW 88774: A New Type of Cr-rich Ureilite <i>M. Prinz, M. K. Weisberg, and C. E. Nehru</i>	1107
Surface Expression of Gravitational Relaxation of Topography: South Scarp of Lakshmi Planum, Venus <i>A. A. Pronin and M. A. Kreslavsky</i>	1109
Solid-Solid Trace-Element Partitioning Between Exsolved Pyroxenes in Cumulate Eucrites <i>A. Pun and J. J. Papike</i>	1111
Studies of Mafic Intrusives in the Vredefort Impact Structure, South Africa: Implications for Craton Wide Igneous Activity at 1.1 Ga Ago <i>G. Q. J. Pybus, W. U. Reimold, and C. B. Smith</i>	1113
Cythorean Dextral Transform Fault Zone from Concave Arc to Concave Arc? <i>J. Raitala</i>	1115
Relative Change in Cross-Sectional Area and Albedo with Rotational Phase for 532 Herculina and 45 Eugenia <i>K. L. Reed, M. J. Gaffey, and L. A. Lebofsky</i>	1117
Cosmogenic-Nuclide Depth Profiles in the Lunar Surface <i>R. C. Reedy and J. Masarik</i>	1119
First Observations of Shatter Cones in the Direct Vicinity of the Bushveld Complex <i>W. U. Reimold and R. C. A. Minnitt</i>	1121

The Dynamical Evolution of Magnetized Solar Nebula <i>M. Reyes-Ruiz and T. F. Stepinski</i>	1123
Terrestrial Polar Beach Processes: Martian Paleolake Analogs <i>J. W. Rice Jr.</i>	1125
Analog and Interpretations for the Martian Thumbprint Terrain and Sinuous Ridges <i>J. W. Rice Jr. and J. D. Mollard</i>	1127
Searching for a Principal Component Mixing Model for Chondritic Interplanetary Dust Particles: The Use of Size Analyses <i>F. J. M. Rietmeijer</i>	1129
Sulfide and Layer Silicate Grain Size Distributions Constrain the Unique Petrogenesis of a Type CM Interplanetary Dust Particle <i>F. J. M. Rietmeijer</i>	1131
Lineament Analysis of Fortuna Tessera; A Preliminary Evaluation of a Complex Ridged Terrain, Venus <i>K. M. Riley and R. C. Anderson</i>	1133
Hydrated E-class and M-class Asteroids <i>A. S. Rivkin, D. T. Britt, E. S. Howell, and L. A. Lebofsky</i>	1135
The Weathering Process on Venus Takes 2–3 Hundred Million Years: Evidence from Radiothermal Emissivity Signatures at Coronae <i>C. A. Robinson</i>	1137
SO ₂ and CH ₄ Levels in the Venusian Atmosphere, Measured by Pioneer Venus: Caused by Plinian-Style Volcanic Activity at Maat Mons? <i>C. A. Robinson and G. D. Thornhill</i>	1139
Volumes and Depth of Burial of the Lesser Tharsis Volcanoes <i>M. S. Robinson and H. Garbeil</i>	1141
Mass Spectra of Sputtered Sugars: Testing the Assignment of Polyoxymethylene as a Constituent of Comet Halley <i>M. S. Robinson and T. J. Wdowiak</i>	1143
Mariner 10 Multispectral Images of the Moon and Mercury <i>M. S. Robinson, B. R. Hawke, P. G. Lucey, and K. Edwards</i>	1145
The Lesser Tharsis Volcanoes: Clues to Martian Edifice Building Eruptions <i>M. S. Robinson, P. J. Mouginis-Mark, and S. K. Rowland</i>	1147
Geology and Distribution of Rock Types at the Apollo 17 Landing Site from a 2–4 mm Perspective <i>K. M. Rockow, B. L. Jolliff, R. L. Korotev, and L. A. Haskin</i>	1149
Compositional Differences Between Impact-Melt Breccias of the North and South Massifs at Apollo 17 <i>K. M. Rockow, R. L. Korotev, B. L. Jolliff, and L. A. Haskin</i>	1151
Luna 24 Regolith Breccias—A Possible Source of the Fine Size Material of the Luna 24 Regolith <i>O. D. Rode and M. M. Lindstrom</i>	1153

Antarctic Weathering of the CK Chondrites EET90004, 90007, and 90022: Nickel and Sulfur Mobility <i>C. S. Romanek, R. A. Socki, E. K. Gibson Jr., and J. H. Allton</i>	1155
The Chondritic Regolith Breccia (H3-6) Acfer 153: Petrography and <i>In-Situ</i> Nuclear Track Investigations <i>J. Romstedt and K. Metzler</i>	1157
Thermal Isostasy Process and Lithospheric Structure on Venus <i>P. Rosenblatt and P. C. Pinet</i>	1159
Thermal Emission Measurements (5–25 μm) of Hawaiian Palagonitic Soils with Implications for Mars <i>T. L. Roush and J. F. Bell III</i>	1161
Thermal Emission Measurements (5–25 μm) of Palagonite/Fe-substituted Montmorillonite Intimate Mixtures: Applications to Mars <i>T. L. Roush and J. B. Orenberg</i>	1163
Transmission Measurements (4000–400 cm^{-1} , 2.5–25 μm) of Crystalline Ferric Oxides and Ferric Oxyhydroxides: Implications for Mars <i>T. L. Roush, J. F. Bell III, and R. V. Morris</i>	1165
More Shock Recovery Experiments on Mesosiderite Analogs <i>L. R. Rowan and D. W. Mittlefehldt</i>	1167
Contact Metamorphism in Ordinary Chondrite Impact Breccias: Implications for the Impact Heating of Chondrite Parent Bodies <i>A. E. Rubin</i>	1169
Comparison of Mars Sinuous Ridges with Terrestrial Linear Dunes: Observations from the Field <i>S. W. Ruff</i>	1171
Chondrule Formation in Radiative Shock <i>T. V. Ruzmaikina and W. H. Ip</i>	1173
Energy Partitioning in Catastrophic Collisions <i>E. V. Ryan and D. R. Davis</i>	1175
Past Geological Exploration of the Earth and Future Geological Exploration of the Planets <i>G. Ryder</i>	1177
The Petrogenetic Interpretation of Tiny Fragments of Evolved Lunar Rocks: An Analog Analysis of the Abriachan Granite, Scotland <i>G. Ryder and J. Gillis</i>	1179
Detectability of Lunar Tephra Deposits: Examples from the Apollo 17 Landing Site <i>D. E. Sabol Jr., J. B. Adams, M. O. Smith, and P. C. Pinet</i>	1181
Igneous Inclusions from Ordinary Chondrites: High Temperature Residues and Shock Melts <i>R. O. Sack, M. S. Ghiorso, and M. E. Lipschutz</i>	1183
Search for ^{26}Mg Isotopic Anomaly in Unequilibrated Chondrites and Unique Meteorites <i>S. Sahijpal, J. N. Goswami, L. L. Kashkarov, N. N. Korotkova, and M. A. Nazarov</i>	1185

Small Volcanic Edifices on Venus: Morphology, Diameter, and Elevation Distributions <i>Sahuaro High School Astronomical Research Class, J. F. Lockwood, Evergreen High School Research Class, M. Ellison, J. Johnson, and G. Komatsu</i>	1187
Terrestrial Basaltic Counterparts for the Venus Steep-Sided or "Pancake" Domes <i>S. E. H. Sakimoto</i>	1189
Thermal Gradients and Kirchhoff's Law <i>J. W. Salisbury, A. E. Wald, and D. M. D'Aria</i>	1191
Formation of Continuous Ridges on Icy Satellites by Cooling Gravity-Current Volcanism <i>S. Sasaki, R. Kono, and Y. Iwase</i>	1193
Scientific Analysis and Display of Magellan Venus Data with McIDAS-eXplorer <i>R. S. Saunders, S. S. Limaye, L. A. Stromovsky, R. Krauss, E. Wright, D. Santeck, and P. Fry</i>	1195
Genesis and Parameters of Ultramylonite and Pseudotachylite (Puchezh-Katunky Astrobleme, Russia) <i>L. Sazanova and N. Korotaeva</i>	1197
Venus: Fractured Craters Revisited, and the Evidence for Minimal Geologic Activity Over the Past 300 m.y. <i>G. G. Schaber, R. G. Strom, and D. J. Chadwick</i>	1199
Venusian Parabolic Halos: Numerical Model Results <i>C. J. Schaller and H. J. Melosh</i>	1201
Lobate Thrust Scarps and the Thickness of Mercury's Lithosphere <i>P. Schenk and H. J. Melosh</i>	1203
The Stereo View of the Solar Sytem <i>P. Schenk, D. Wilson, R. Morris, and T. J. Parker</i>	1205
Hole Size from Impacts at Scaled Velocities of 7 to 21 km/s <i>R. M. Schmidt and K. R. Housen</i>	1207
Calculation of Hugoniot Curves and Post-Shock Temperatures for H- and L-Chondrites <i>R. T. Schmitt, A. Deutsch, and D. Stöffler</i>	1209
Chicxulub as an Oblique Impact <i>P. H. Schultz</i>	1211
Atmospheric Containment of Crater Growth <i>P. H. Schultz and O. S. Barnouin</i>	1213
Penetrating and Escaping the Atmospheres of Venus and Earth <i>P. H. Schultz and S. Sugita</i>	1215
Comparative Rock Mass Strengths of Basalt and Tuff and Some Planetological Implications <i>R. A. Schultz</i>	1217
Outstanding Tectonic Problems in the Valles Marineris Region of Mars <i>R. A. Schultz</i>	1219

Distribution of Siderophile and Other Trace Elements in Melt Rock at the Chicxulub Impact Structure <i>B. C. Schuraytz, D. J. Lindstrom, R. R. Martinez, V. L. Sharpton, and L. E. Marín</i>	1221
Preliminary Description of Double Drive Tube 68002/68001 <i>C. Schwarz, R. V. Morris, and R. L. Korotev</i>	1223
1:1 Million-scale Geologic Maps of Mars' Tharsis Montes <i>D. H. Scott, J. R. Zimbelman, and J. M. Dohm</i>	1225
Evaporation and Recondensation of Volatiles During Chondrule Formation <i>E. R. D. Scott</i>	1227
Evaporation and Recondensation During Chondrule Formation <i>D. W. G. Sears and M. E. Lipschutz</i>	1229
Numerical Ocean Tides on Titan: Spherical Case <i>W. D. Sears</i>	1231
Current Activities and Results of the Long Duration Exposure Facility Meteoroid and Debris Special Investigation Group <i>T. H. See, K. S. Leago, J. L. Warren, R. P. Bernhard, and M. E. Zolensky</i>	1233
NIMS-Callisto Science Objectives and Observational Plans <i>M. Segura, J. Sunshine, T. McCord, and the NIMS Team</i>	1235
SEM Study of Metal Grain Surface in Ordinary Chondrites. I. Primary Sculptures <i>V. P. Semenenko and B. V. Tertichnaya</i>	1237
SEM Study of Metal Grain Surface in Ordinary Chondrites: II. Secondary Sculptures <i>V. P. Semenenko and B. V. Tertichnaya</i>	1239
Examination of the Relation Between Rifting and Volcanism in the Juno Dorsum Region of Venus <i>D. A. Senske</i>	1241
Radar Characteristics of Geologic Units in the Carson Quadrangle, Venus <i>D. Senske, R. Greeley, and K. Bender</i>	1243
The Global Geology of Venus: Classification of Landforms and Geologic History <i>D. A. Senske, R. S. Saunders, E. R. Stofan, and members of the Magellan Science Team</i>	1245
Pyrolysis Typing of Meteoritic Organic Matter <i>M. A. Sephton, C. T. Pillinger, and I. Gilmour</i>	1247
Student Explorer Demonstration Initiative: Affordable Access to Space <i>J. Sevier and P. Coleman</i>	1249
Nebula Matter Differentiation as a Result of Condensation <i>A. I. Shapkin and Yu. I. Sidorov</i>	1251
The Problem of High Precision Measurements of $^{142}\text{Nd}/^{144}\text{Nd}$: The Terrestrial Record of ^{146}Sm <i>M. Sharma, D. A. Papanastassiou, G. J. Wasserburg, and R. F. Dymek</i>	1253

Constraints on Excavation and Mixing During the Chicxulub Impact Event <i>V. L. Sharpton, L. E. Marín, B. C. Schuraytz, P. D. Spudis, and G. Ryder</i>	1255
Light Lithophile Elements (Li, Be, B) in Lunar Picritic Glasses. Implications for Lunar Mantle Dynamics and the Origin of the Moon <i>C. K. Shearer, G. D. Layne, and J. J. Papike</i>	1257
The Earth-Moon Connection. Clues Preserved in Lunar Picritic Magmas <i>C. K. Shearer, J. J. Papike, and H. E. Newsom</i>	1259
Innovative Instrumentation for Mineralogical and Elemental Analyses of Solid Extraterrestrial Surfaces: The Backscatter Mössbauer Spectrometer/X-Ray Fluorescence Analyzer (BaMS/XRF) <i>T. D. Shelfer, R. V. Morris, T. Nguyen, D. G. Agresti, and E. L. Wills</i>	1261
A Ferroelectric Model for the Low Emissivity Highlands on Venus <i>M. K. Shepard, R. E. Arvidson, R. A. Brackett, and B. Fegley Jr.</i>	1263
Ion Microprobe Studies of Lunar Highland Cumulate Rocks: Preliminary Results <i>J. W. Shervais</i>	1265
Remote Sensing Assessment of the Lunar Soil Maturation <i>V. V. Shevchenko</i>	1267
Tektite-Obsidian-like Glasses from Space <i>M. Shima, M. Honda, A. Okada, T. Okada, Y. Kobayashi, M. Ebihara, Y. N. Miura, and K. Nagao</i>	1269
Is There Umov Effect for the Moon in Polarization Minimum? <i>Yu. G. Shkuratov and N. V. Opanasenko</i>	1271
Pu-Xe Ages of Eucrites <i>A. Shukolyukov and F. Begemann</i>	1273
Unusual Refractory Inclusions from a CV3 Chondrite Found Near Axtell, Texas <i>S. B. Simon, L. Grossman, and J. F. Wacker</i>	1275
Geoid/Topography Admittance on Venus from Models of Convection with No Crustal Deformation <i>M. Simons, B. H. Hager, and S. C. Solomon</i>	1277
The Magellan Quasi-Specular Bistatic Radar Experiment <i>R. A. Simpson, G. H. Pettengill, and P. G. Ford</i>	1279
Venus Gravity Field Determination: Progress and Concern <i>W. L. Sjogren and A. S. Konopliv</i>	1281
Pre-Allende Planetesimals with Refractory Compositions: The CAI Connection <i>W. R. Skinner</i>	1283
Rounding of Chondrules by Abrasion: A Cautionary Note Regarding Textural Evidence <i>W. R. Skinner and H. C. Connolly Jr.</i>	1285
Access to Large Planetary Science Data Bases <i>S. Slavney, T. Stein, and R. E. Arvidson</i>	1287

The Topography of Mars: A Re-Evaluation of Current Data <i>D. E. Smith and M. T. Zuber</i>	1289
The Mass of Mars, Phobos, and Deimos, from the Analysis of the Mariner 9 and Viking Orbiter Tracking Data <i>D. E. Smith, F. G. Lemoine, and S. K. Fricke</i>	1291
The Imager for MESUR Pathfinder (IMP) <i>P. H. Smith, D. T. Britt, L. R. Dose, R. B. Singer, M. G. Tomasko, F. Gliem, H. U. Keller, J. M. Knudsen, and L. A. Soderblom</i>	1293
Interpretation of Magellan Gravity Data for Large Volcanic Swells on Venus: Implications for Interior Structure <i>S. E. Smrekar</i>	1295
The Status of Mercury Exploration <i>W. Smythe, R. Lopes-Gautier, A. Ocampo, and R. Nelson</i>	1297
A Sortie for Pristine Rocks at Mare Tranquillitatis: A Ferroan Anorthosite, A New Group D Basalt, and the Isotopic Composition of Group D High-Ti Basalts <i>G. A. Snyder, E. A. Jerde, L. A. Taylor, D.-C. Lee, and A. N. Halliday</i>	1299
A Basaltic Safari Across the Cayley Plains and Over the Descartes Mountains: Still Searching for a Pristine Highlands Basalt at Apollo 16 <i>G. A. Snyder, J. Karner, E. A. Jerde, and L. A. Taylor</i>	1301
Silicate Liquid Immiscibility in Anorthosite Suites: Viewing the Moon from Wyoming and Labrador <i>G. A. Snyder, J. Mitchell, L. A. Taylor, and E. C. Simmons</i>	1303
Petrology and Chemistry of the Magnesian Suite: Further Evidence of Liquid Immiscibility and Metasomatism in the Western Highlands of the Moon <i>G. A. Snyder, C. R. Neal, L. A. Taylor, and A. N. Halliday</i>	1305
Chronology and Petrogenesis of the Western Highlands Alkali Suite: Cumulates from Quartz Monzodiorite (QMD) Liquids <i>G. A. Snyder, L. A. Taylor, and A. N. Halliday</i>	1307
Rb-Sr Isotopic Systematics of Lunar Ferroan Anorthosite 62237 <i>G. A. Snyder, L. A. Taylor, and A. N. Halliday</i>	1309
Evolved QMD-Melt Parentage for Lunar Highlands Alkali Suite Cumulates: Evidence from Ion-Probe Rare-Earth Element Analyses of Individual Minerals <i>G. A. Snyder, L. A. Taylor, E. A. Jerde, and L. R. Riciputi</i>	1311
Journey to the Center of the Regolith: Petrology and Mineral Chemistry of a New Ferroan Anorthosite from Drive Tube 68002/68001 <i>G. A. Snyder, L. A. Taylor, and A. D. Patchen</i>	1313
Crystal Sizes in Magma Oceans: Application to the Suspension Problem <i>V. S. Solomatonov and D. J. Stevenson</i>	1315
Gravity Anomalies over Volcanoes on Venus: Implications for Lithospheric Thickness and Volcano History <i>S. C. Solomon, P. J. McGovern, M. Simons, and J. W. Head</i>	1317

The Bimodal Size Distribution of Near-Earth Asteroids <i>D. H. Speidel</i>	1319
Laser Fusion ^{40}Ar - ^{39}Ar Dating of Pseudotachylites from the Vredefort Impact Structure: New Evidence for a Major Formation Event at 2.0 Ga <i>J. G. Spray and S. P. Kelley</i>	1321
Return to Mercury: The Discovery-Mercury Polar Flyby Mission <i>P. D. Spudis, J. B. Plescia, and A. D. Stewart</i>	1323
^{41}K Excess in Efremovka CAIs <i>G. Srinivasan, J. N. Goswami, and A. A. Ulyanov</i>	1325
Trajectory Calculation of Individual Particles from LDEF Impacts <i>F. J. Stadermann</i>	1327
Spectral Variation Within Mare Tranquillitatis: Implications for Stratigraphy and Mixing Mechanisms <i>M. I. Staid, C. M. Pieters, and J. W. Head</i>	1329
Longitudinal Variations of the Linear Polarization in Jupiter's Polar Regions at the System III and IV Periods <i>O. M. Starodubtseva, L. A. Akimov, V. V. Korokhin, and V. G. Teffel</i>	1331
Reflectance Spectra of Particle Size Separates of Lunar Soils: Is the Difference Controlled by Reduced Iron? <i>L. V. Starukhina, Yu. G. Shkuratov, O. D. Rode, and C. M. Pieters</i>	1333
Chemical Zoning and Exsolution in Olivine of the Pavlodar Pallasite: Comparison with Springwater Olivine <i>I. M. Steele</i>	1335
Crystal Structure of Chladniite $\text{Na}_2\text{CaMg}_7(\text{PO}_4)_6$, from Carlton (IIICD) Iron Meteorite <i>I. M. Steele</i>	1337
Oscillatory Zoning in Forsterite from Carbonaceous and Unequilibrated Ordinary Chondrites: Implications for Origin of Some Forsterite <i>I. M. Steele</i>	1339
New TOF-SIMS Results on Hydrated Interplanetary Dust Particles <i>T. Stephan, E. K. Jessberger, H. Rulle, K. L. Thomas, and W. Klöck</i>	1341
Carbonate Formation on Mars: Implications of Recent Experiments <i>S. K. Stephens, D. J. Stevenson, L. F. Keyser, and G. R. Rossman</i>	1343
Noachian and Hesperian Modification of the Original Chryse Impact Basin Topography <i>S. Stockman and H. Frey</i>	1345
Classification and Nomenclature of Impact Metamorphic Rocks: A Proposal to the IUGS Subcommittee on the Systematics of Metamorphic Rocks <i>D. Stöffler and R. A. F. Grieve</i>	1347
Status of the Small Body Mapping Program <i>P. J. Stooke</i>	1349
Promoting Planetary Science Among Elementary School Students <i>M. M. Strait</i>	1351

The Global Resurfacing History of Venus <i>R. G. Strom, G. G. Schaber, and D. D. Dawson</i>	1353
Impact Ejecta Vapor Cloud Interference Around Venus Craters <i>S. Sugita and P. H. Schultz</i>	1355
Isotopic Composition of Nitrogen in the PCA91002 Chondrite <i>N. Sugiura and S. Zashu</i>	1357
New Evidence for Compositional Diversity on the Marius Hills Plateau from Galileo Multi-Spectral Imaging <i>J. M. Sunshine, C. M. Pieters, and J. W. Head</i>	1359
Microanalysis of Iron Oxidation States Using X-Ray Absorption Spectroscopy <i>S. R. Sutton, S. Bajt, and J. S. Delaney</i>	1361
Brownlee's Particles of Cosmic Origins in Deep Sea Sediments <i>Y. Suzuki, M. Noma, H. Sakurai, K. Yamakoshi, H. Matsuzaki, N. Kano, and K. Nogami</i>	1363
Radiation Emitted During the Flight: Application to Assessment of Bolide Parameters from the Satellite Recorded Light Flashes <i>V. V. Svetsov</i>	1365
The Thermal History of the Lunar Regolith at the Apollo 16 and 17 Sites <i>S. J. Symes, P. H. Benoit, and D. W. G. Sears</i>	1367
Comet Shoemaker-Levy 9 Impact on Jupiter—The First Ten Minutes <i>T. Takata, J. D. O'Keefe, T. J. Ahrens, and G. S. Orton</i>	1369
Orthopyroxene with Dusty Core and Clear Rims in Acapulco and Its Related Formation Process to Lodranites <i>H. Takeda and M. Miyamoto</i>	1371
Mineralogy of Apollo 12 Low-Ti Basalts in Relation to Lunar Meteorites from Mare Region <i>H. Takeda, T. Arai, and K. Saiki</i>	1373
Inhomogeneous Distribution of Materials in Lodranites-Acapulcoites and IAB Irons and Their Common Formation Processes <i>H. Takeda, M. Otsuki, A. Yamaguchi, M. Miyamoto, M. Otsuki, M. Tomobuchi, and T. Hiroi</i>	1375
Strain Measurements of Impact Craters on Tempe Terra, Mars <i>K. L. Tanaka and M. P. Golombek</i>	1377
Eolian History of the Hellas Region of Mars <i>K. L. Tanaka and G. J. Leonard</i>	1379
Experimental and Theoretical Examination of Cosmic Dust Grain Deceleration <i>W. G. Tanner Jr., W. M. Alexander, and S. Stephenson</i>	1381
Slow Emplacement of Flood Basalts: Evidence from Fractal Properties of Lava Flows <i>G. J. Taylor, B. C. Bruno, and S. Self</i>	1383

Planar Deformation Features in Quartz Grains from Resurge Deposit of the Lockne Structure, Sweden <i>A. M. Theriault and M. Lindström</i>	1385
New Studies of Mass Independent Isotopic Fractionation Processes and Their Occurrence in the Early Solar System, Mars, and the Earth <i>M. H. Thiemens</i>	1387
First Observation of a Mass Independent Isotopic Fractionation in a Condensation Reaction <i>M. H. Thiemens, R. Nelson, Q. W. Dong, and J. A. Nuth III</i>	1389
Anatomy of a Cluster IDP (II): Noble Gas Abundances, Trace Element Geochemistry, Isotopic Abundances, and Trace Organic Chemistry of Several Fragments from L2008#5 <i>K. L. Thomas, S. J. Clemett, G. J. Flynn, L. P. Keller, D. S. McKay, S. Messenger, A. O. Nier, D. J. Schlutter, S. R. Sutton, R. M. Walker, and R. N. Zare</i>	1391
The Anatomy of a Cluster IDP (I): Carbon Abundance, Bulk Chemistry, and Mineralogy of Fragments from L2008#5 <i>K. L. Thomas, L. P. Keller, W. Klock, J. Warren, G. E. Blanford, and D. S. McKay</i>	1393
Ida: Topography, Slopes and Grooves <i>P. Thomas, J. Veverka, M. J. S. Belton, and Galileo Imaging Science Team</i>	1395
Deformation of Large Bolides During Atmospheric Passage: Comparison of SPH and Analytic Models <i>P. J. Thomas, L. Brookshaw, and G. Starkey</i>	1397
Teaching Planetary Surface Processes and Mapping to Advanced 5th and 6th Grade Students <i>P. Thompson, S. Murchie, R. Herrick, B. Schuraytz, and G. Ryder</i>	1399
Magellan Mission Progress Report <i>T. W. Thompson and Magellan Flight Team</i>	1401
A Simple Model for Particle Support in Pyroclastic Flows <i>G. D. Thornhill</i>	1403
Properties of Lava Flows Associated with Coronae in S.E. Aphrodite Terra, Venus <i>K.-A. Tomkinson and L. Wilson</i>	1405
Semi-Objective Determination of Lithologic End-Members in Geologic Environment (Spectral Mixture Analysis) <i>S. Tompkins, J. F. Mustard, C. M. Pieters, and D. W. Forsyth</i>	1407
4.56 Ga U-Th-Pb Age of MET 78008 Ureilite <i>N. Torigoye, M. Tatsumoto, and K. Yanai</i>	1409
Areal Distribution of Double-Type Coronae and Corona-like Features on Venus, and Their Relation to Topography, Tesserae and Deformation Belts <i>T. Törmänen and K. Kauhanen</i>	1411
Two Source Areas for the SNC Meteorites: Petrologic, Chemical, and Chronologic Evidence <i>A. H. Treiman</i>	1413
Chemical Weathering on Venus: Preliminary Results on the Interaction of Basalt with Carbon Dioxide <i>A. H. Treiman and C. C. Allen</i>	1415

The Parent Magma of Xenoliths in Shergottite EETA79001: Bulk and Trace Element Composition Inferred from Magmatic Inclusions <i>A. H. Treiman, D. J. Lindstrom, and R. R. Martinez</i>	1417
The Temperature of Nitrogen on Pluto <i>K. A. Tryka, R. H. Brown, D. P. Cruikshank, and T. C. Owen</i>	1419
Purity and Cleanness of Aerogel as a Cosmic Dust Capture Medium <i>P. Tsou, R. H. Fleming, P. M. Lindley, A. Y. Craig, and P. Blake</i>	1421
How Does Venus Lose Its Heat? <i>D. L. Turcotte</i>	1423
Stress and Flexural Modeling of Alba Patera, Mars <i>E. P. Turtle and H. J. Melosh</i>	1425
Excitation Functions of the Neon Isotopes in Chondrites and Achondrites <i>G. K. Ustinova</i>	1427
On Possible Disturbance of the Solar Modulation Mechanism Over a Long-Time Scale <i>G. K. Ustinova and A. K. Lavrukhina</i>	1429
Shock Deformation in Talc and Its Possible Significance for Investigations of Astroblemes <i>A. A. Valter</i>	1431
A Silicate Lava Model for Io's Hotspots <i>G. J. Veeder, D. L. Blaney, T. V. Johnson, and D. L. Matson</i>	1433
Nitrogen and Carbon Components in C ₈ : A Possible Presence of Nitrogen-Free Diamonds in C ₈ <i>A. B. Verchovsky, J. Newton, I. P. Wright, J. W. Arden, and C. T. Pillinger</i>	1435
Impact Erosion of Atmospheres <i>A. M. Vickery</i>	1437
A Quick Look Method of Detecting Water of Hydration in Small Solar System Bodies <i>F. Vilas</i>	1439
Fireworks Around Naked T Tauri Stars <i>A. V. Vityazev and G. V. Pechernikova</i>	1441
Generalized Coagulation Equation and Mass-Spectrum of Protoplanet <i>A. Vityazev, Yu. Kukhareno, A. Bashkurov, and G. Pechernikova</i>	1443
Surface Energy Measurements of Comminuted Silicates: Implications for Cosmochemical Processes <i>R. Voelkel, R. F. Giese, and C. J. van Oss</i>	1445
Depositional Units in Western Maxwell Montes: Implications for Mountain Building Processes on Venus <i>R. W. Vorder Bruegge</i>	1447
Variation in Compressional Structures Across Maxwell Montes: Evidence for a Sequence of Events in a Venusian Orogeny <i>R. W. Vorder Bruegge</i>	1449

Rare Earth Element Distributions in Chassigny: Clues to Its Petrogenesis and Relation to the Nakhilites <i>M. Wadhwa and G. Crozaz</i>	1451
Modeling the Thermal Infrared Directional Emissivity of Large, Close-Packed, Particulate Media <i>A. E. Wald and J. W. Salisbury</i>	1453
TEM Studies on the Dislocations in Olivine of Taizhou Meteorite from Jiangsu Province China <i>H. Wang, W. Rong, F. Zheng, and C. Lin</i>	1455
Chemical and Isotopic Fractionation During the Evaporation of the FeO-MgO-SiO ₂ -CaO-Al ₂ O ₃ -TiO ₂ -REE Melt System <i>J. Wang, A. M. Davis, R. N. Clayton, and T. K. Mayeda</i>	1457
Kinetic Isotopic Fractionation During the Evaporation of the Iron Oxide from Liquid State <i>J. Wang, A. M. Davis, R. N. Clayton, and T. K. Mayeda</i>	1459
Coorbital Bending Waves and Inclination Decay <i>W. R. Ward and J. M. Hahn</i>	1461
Petrologic Insights Regarding Lunar and Planetary Meteorite Launch Processes <i>P. H. Warren</i>	1463
Petrology of LEW88774: An Extremely Chromium-rich Ureilite <i>P. H. Warren and G. W. Kallemeyn</i>	1465
Chondrule Magnetic Properties <i>P. J. Wasilewski and M. V. O'Bryan</i>	1467
The Evolution of Nebular Solids: Evidence from Compound Chondrules and from Igneous Rims on Chondrules in Ordinary Chondrites <i>J. T. Wasson and A. N. Krot</i>	1469
The Abundance and Stable Isotopic Composition of Volatiles Released from Weathering Products During Stepped Heating of Nakhla and Lafayette <i>L. L. Watson, S. Epstein, and E. M. Stolper</i>	1471
Morphologic Studies of Contractional Features on Mars Using Photoclinometrically Derived Elevation Profiles <i>T. R. Watters and M. S. Robinson</i>	1473
Trace Element and Isotopic Measurements of Refractory Inclusions from the Acfer 182 Carbonaceous Chondrite <i>D. Weber, E. K. Zinner, and A. Bischoff</i>	1475
Origin of "Rubble Pile" Cometary Nuclei <i>S. J. Weidenschilling</i>	1477
Primitive Trapped Xe in Lodran Minerals and Further Evidence from EET84302 and Gibson for Break-up of the Lodranite Parent Asteroid 4 Ma Ago <i>A. Weigel and O. Eugster</i>	1479
Agglomeratic Olivine (AO) Chondrules in Ordinary Chondrites <i>M. K. Weisberg and M. Prinz</i>	1481

Radiophysical Properties of Impact Craters on Venus <i>C. M. Weitz, J. J. Plaut, and H. J. Moore</i>	1483
Detectability of Carbonate in Unconsolidated and Indurated Sediments <i>M. L. Wenrich and P. R. Christensen</i>	1485
Provenance of the Terrestrial Planets <i>G. W. Wetherill</i>	1487
Dark-Floored Crater Elevations on Venus: Implications for Crater-centered Volcanism <i>R. W. Wichman</i>	1489
Comet Disruption and Crater Chain Formation in the Earth-Moon System <i>R. W. Wichman and C. A. Wood</i>	1491
Analytical Modeling of Thermal Erosion by Low-Viscosity Lava Flows and Implications for Planetology <i>D. A. Williams and R. Greeley</i>	1493
Mars: Volcanic Eruption Theory and Relationships to Observed Landforms <i>L. Wilson and J. W. Head</i>	1495
Clast Sizes of Basaltic Ejecta from Explosive Eruptions on Asteroids <i>L. Wilson and K. Keil</i>	1497
Lunar LIGO and Gravitational Wave Astronomy on the Moon <i>T. L. Wilson and N. LaFave</i>	1499
Advanced Technology Lunar Telescope <i>T. L. Wilson, W.-K. Chu, and P. C. Chen</i>	1501
Numerical Simulation of Scattering by Discrete Objects <i>P. B. Wong, R. A. Simpson, and G. L. Tyler</i>	1503
A Remotely Operated Planetary Science Observatory to Enhance Space Education <i>C. A. Wood and P. Abell</i>	1505
An Asteroid Family Among the NEAs? <i>C. A. Wood, R. Fevig, and J. Nordlie</i>	1507
Occurrences of Low-Emissivity Surface Material at Low Altitudes on Venus: A Window to the Past <i>J. A. Wood</i>	1509
Identifying Controlling Mineral Phases in Basalt Chemistries: On Beyond Pearce Element Ratio Diagrams <i>A. Woronow</i>	1511
Parental Magma Compositions of Basalts Using an Artificial Neural Network: Theory <i>A. Woronow, A. M. Reid, J. H. Jones, and N. E. Pingitore Jr.</i>	1513
Attempts to Produce Carbon-Free Silica Aerogel for Micrometeoroid Capture Cells <i>I. P. Wright, H.-P. Huang, and C. T. Pillinger</i>	1515
Could the Original Sudbury Structure Have Been Circular? <i>J. Wu, B. Milkereit, D. Boerner, and B. Robertson</i>	1517

Magellan Radar Data for Venus Topographic Mapping <i>S. S. C. Wu and E. A. Howington-Kraus</i>	1519
Windblown Sand on Mars: The Effect of Saltation Threshold on Drift Potentials Derived from Mars GCM <i>P. Xu, R. Greeley, S. Williams, and J. B. Pollack</i>	1521
²⁶ Al and ¹⁰ Be Activities and Exposure Ages of Lodranites, Acapulcoites, Kakangari and Pontlyfni <i>S. Xue, G. F. Herzog, J. Klein, and R. Middleton</i>	1523
Granulitic Matrices in Monomict Eucrites <i>A. Yamaguchi and H. Takeda</i>	1525
Tidal Disruption of Comet Shoemaker-Levy-9 Nuclei Just Before the Impact on Jupiter <i>M. Yanagisawa and T. Konno</i>	1527
AEM Study of the Tetraenaite Rim of Metal Phases in Meteorites <i>C. W. Yang, D. B. Williams, and J. I. Goldstein</i>	1529
Lunar Mare Deposit Volumes, Composition, Age, and Location: Implications for Source Areas and Modes of Emplacement <i>R. A. Yingst and J. W. Head</i>	1531
Advanced Generation Condensation Calculations: Compositions of Fassaite, Spinel and Plagioclase in the Solar Nebula <i>S. Yoneda and L. Grossman</i>	1533
Retention of Sodium Under Transient Heating Conditions—Experiments and Their Implications for the Chondrule Forming Environment <i>Y. Yu and R. H. Hewins</i>	1535
Can Sulfide Minerals Survive the Chondrule-forming Transient Heating Event? <i>Y. Yu, R. H. Hewins, B. Zanda, and H. C. Connolly</i>	1537
Oxygen Isotope Distribution in Fassaite of Allende CAI <i>H. Yurimoto, H. Nagasawa, and O. Matsubaya</i>	1539
Spectrophotometry of Martian Satellites with the Hubble Space Telescope <i>B. Zellner and E. N. Wells</i>	1541
Simultaneous Adsorption of CO ₂ and H ₂ O Under Mars-like Conditions and Applications to the Evolution of the Martian Climate <i>A. P. Zent and R. Quinn</i>	1543
The Complex Thermal History of Enstatite Chondrites <i>Y. Zhang, P. H. Benoit, and D. W. G. Sears</i>	1545
The Unique Thermal History of EL Chondrites and a New Means of Classifying Equilibrated Enstatite Chondrites <i>Y. Zhang, S. Huang, P. H. Benoit, and D. W. G. Sears</i>	1547
Gravitational Relaxation of Planetesimals <i>I. N. Ziglina</i>	1549
Computer Simulation of Lava Flow Emplacement on the Terrestrial Planets <i>J. R. Zimbelman</i>	1551

1:5,000,000-scale Geologic Mapping of the Kawelu Planitia Quadrangle (V16) on Venus <i>J. R. Zimbelman</i>	1553
Mafic Magnetic Volcaniclastic Dunes: A Possible Mars Analog in the Andes of Ecuador <i>J. R. Zimbelman and K. S. Edgett</i>	1555
Evidence for Extraneous Perovskites in CAIs from the Efremovka (CV3) Meteorite: A Combined Petrographic, Trace Element, and Isotopic Study <i>E. Zinner and A. El Goresy</i>	1557
Crystallization in the Silicate Part of the Experimental Melted Ordinary Chondrite Tsarev (L5) <i>N. G. Zinovieva, O. B. Mitreikina, and L. B. Granovsky</i>	1559
Liquid Immiscibility Process of the Experimental Melted Ordinary Chondrite Tsarev (L5) <i>N. G. Zinovieva, O. B. Mitreikina, and L. B. Granovsky</i>	1561
The Chemical Composition of Acapulco and Acapulcoites <i>J. Zipfel and H. Palme</i>	1563
Mineralogy of an Unusual CM Clast in the Kaidun Meteorite <i>M. E. Zolensky, A. V. Ivanov, S. V. Yang, R. A. Barrett, and L. Browning</i>	1565
Mineralogy of Artificially Heated Carbonaceous Chondrites <i>M. E. Zolensky, M. E. Lipschutz, and T. Hiroi</i>	1567
Near-Surface Atmosphere of Venus: New Estimations of Redox Conditions Based on New Data <i>M. Yu. Zolotov</i>	1569
Phase Relations in the Fe-Ti-Mg-O Oxide System and Hematite Stability at the Condition of Venus' Surface <i>M. Yu. Zolotov</i>	1571
Lunar Horizon Glow and the Clementine Mission <i>H. A. Zook and A. E. Potter</i>	1573
Rheology, Tectonics, and the Structure of the Venus Lithosphere <i>M. T. Zuber</i>	1575
Formation of Fold and Thrust Belts on Venus Due to Horizontal Shortening of a Laterally Heterogeneous Lithosphere <i>M. T. Zuber, E. M. Parmentier, and G. A. Neumann</i>	1577
Author Index	liii
Sample Index	lxiv
Meteorite Index	lxv
Keyword Index	lxix

CHIT TO
P. 5

Magnetic Properties of Zagami and Nakhla.

D.P. Agerkvist, L. Vistisen, M.B. Madsen and J.M. Knudsen Niels Bohr Institute for Astronomy, Physics and Geophysics, Blegdamsvej 17, DK-2100 Copenhagen Ø, Denmark.

Both Zagami and Nakhla contain a small amount of a ferrimagnetic mineral, titanomagnetite. Does the magnetic phase in the Martian dust also contain titanium?

Introduction: In coming missions to Mars (US Pathfinder 1996, Russian Rover 1996) efforts will be made to study the strongly magnetic (ferrimagnetic) phase known to exist in the Martian soil [1,2].

Most SNC meteorites are known to contain titanomagnetite. If the SNC meteorites really are Martian rocks, we may thus assume that the rocks of Mars contain titanomagnetite. The magnetic phase in the red soils of Mars may or may not have been inherited directly from the titanomagnetite in the Martian surface basalts.

We have therefore initiated an investigation of the magnetic properties of the meteorites Zagami and Nakhla. Preliminary results from the study of the magnetization as function of an applied field will be presented and Mössbauer spectra included.

Experimental: On two small samples of the meteorites Zagami (0.0278 g) and Nakhla (0.0126 g) we have measured the hysteresis loops up to 1.6 T at room temperature. The measurements were performed in an Vibrating Sample Magnetometer (VSM). The curves are shown on the figure.

It is important to note that the magnetization given in the figure is the magnetization of the bulk sample of the respective meteorites. No separation of magnetic phase has been attempted. Contrary to this, the Mössbauer spectra also shown on the figure correspond to a rather careful separation of the magnetic phase.

Results and Discussion: Both magnetization curves shown in the figure consist of a magnetically ordered (ferrimagnetic) phase, and a paramagnetic component. The paramagnetic component in Zagami is mainly due to pyroxene, in Nakhla to a mixture of pyroxene and olivine. The interesting aspect from our point of view is the hysteresis loop present for both Zagami and Nakhla. (There is an asymmetry in both loops. The reason for this has not been found, but it is probably due to a systematic error in the VSM). The ferrimagnetic curve is most significant in Nakhla. In Zagami the ferrimagnetic phase only causes a small bending of the line corresponding to the paramagnetic phase. The results of magnetization measurements on the bulk samples are consistent with the results of Mössbauer spectra of the magnetic separates from the two meteorites. The magnetite in Zagami contains so much Ti ($\text{Fe}_{3-x}\text{Ti}_x\text{O}_4$, $x \sim 0.7$) that it is close to being paramagnetic at room temperature. The sample from Nakhla shows a hyperfine splitting corresponding to a Ti content of $x \leq 0.1$.

Conclusion: From the magnetic properties experiment on the Viking landers it was estimated that the spontaneous magnetization σ of the Martian soil is in the range 1

Magnetic properties of Zagami and Nakhla. D.P. Agerkvist et al.

$\text{Am}^2/\text{kg soil} \leq \sigma \leq 7 \text{ Am}^2/\text{kg soil}$. The magnetization of Nakhla and Zagami is evidently substantial lower. If the Martian soil formed by direct comminution from basaltic rocks with a composition as Nakhla and Zagami, the soil would not stick to both permanent magnets brought by the Viking landers.

However, by chemical weathering of similar terrestrial rocks the magnetic phase may basically survive and be concentrated in the weathering products [3]. In this case the magnetic phase still contains titanium as found in the underlying rocks. On the other hand, if the iron has been completely dissolved in abundant liquid water, the magnetic phase may have formed via precipitation of Fe(III)-compounds (e. g. $\gamma\text{-FeOOH}$). In this case the magnetic phase will not contain Ti. A basic problem in the future exploration of the magnetic phase on Mars will though be to investigate - by means of X-ray fluorescence - if the Ti ions in the soil of Mars correlate with the magnetic phase.

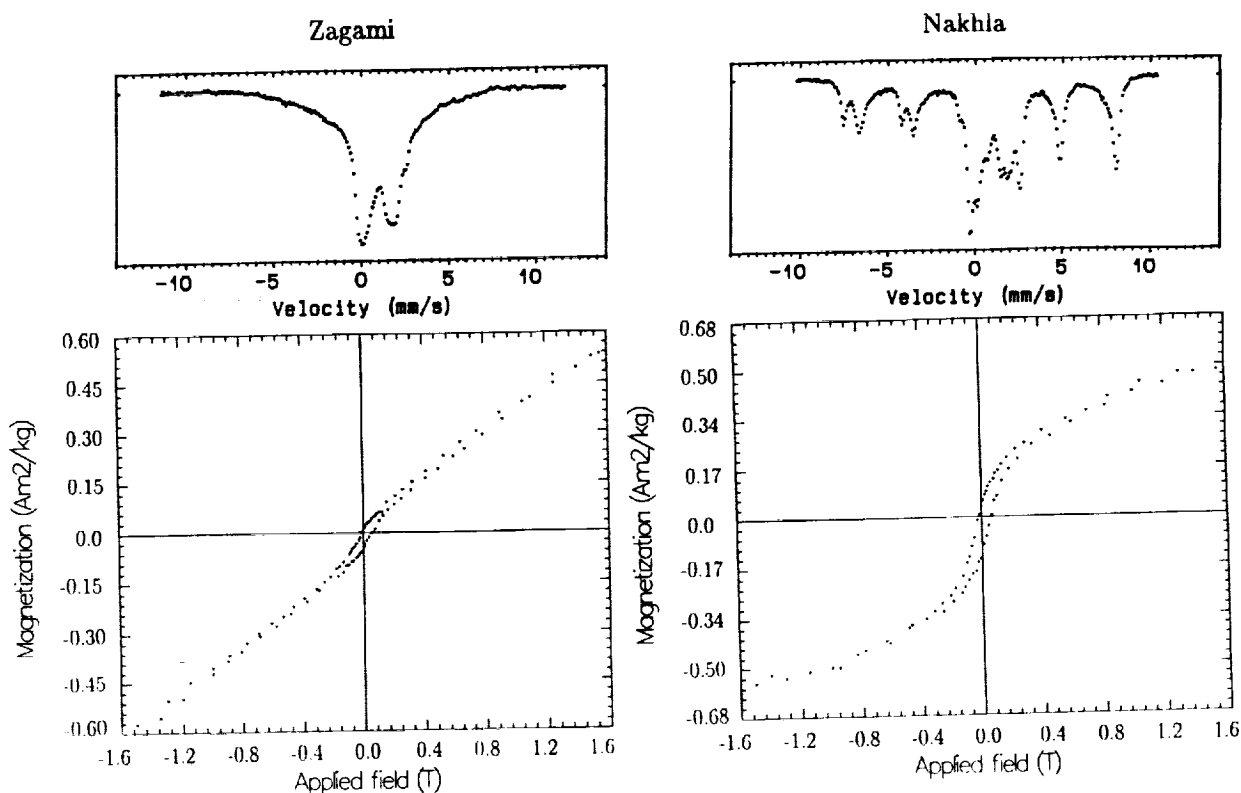


Figure 1: Magnetization as a function of applied field and Mössbauer spectra for Zagami and Nakhla, room temperature

Acknowledgements: The Novo Nordisk Foundation and the Danish Natural Science Research Council are gratefully acknowledged for support.

References: [1] Hargraves R.B., Collinson D.W., Arvidson R.E. and Spitzer C.R., *J. Geophys. Res.* 82, no 28 (1977), 4547. [2] Madsen M.B., Knudsen J.M., Vistisen L., Hargraves R.B. *Lunar Planet. Sci. Conf. XXIV* (1993), 917. [3] Allan J.E.M., Coey J.M.D., Resende M. and Fabris J.D., *Phys. Chem. Minerals* 15 (1988), 470.

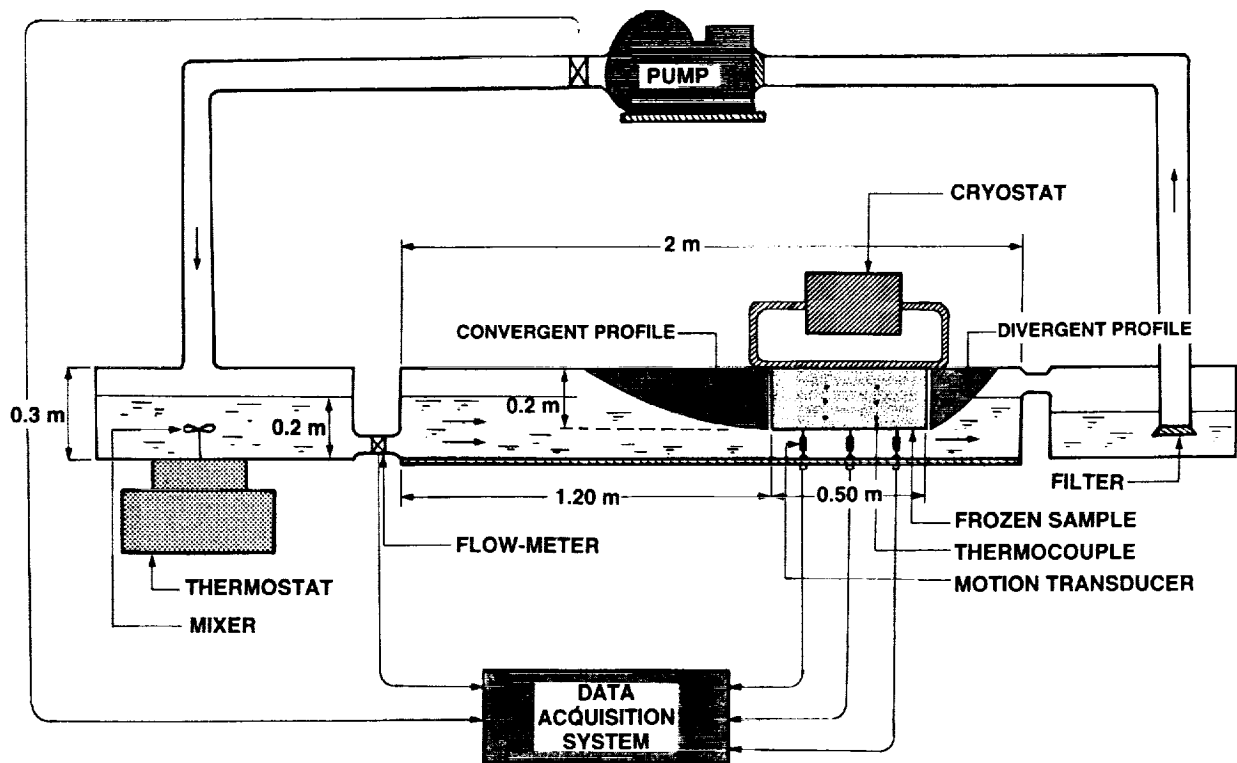
MARTIAN FLUVIO-THERMAL EROSION: EXPERIMENTAL PROJECT. J. Aguirre-Puente, F. Costard and N. Makhloufi. Centre de Géomorphologie, CNRS, rue des Tilleuls, 14000 Caen, France.

Introduction: Fluvio-thermal erosion on Mars has been proposed by F. Costard (1), based on a comparison between Martian outflow channels and fluvial outbursts in Siberia. These analogies leads to the hypothesis that Martian outflow channels were eroded by the action of liquid water against a ground ice. The dynamics of these flows under cold climate induces the propagation of a thawing line in the ground ice and a fast bank recession (~25m/year) with removal of sediments (2). Our research program has been essentially focused on the modeling of some periglacial processes in a Martian environment. Generally, the modeling of an erosional process is difficult because it is the result of an interaction of several elementary phenomena. An ablation model with immediate removal of sediments has been first proposed (3,4,5). An experimental study must complete our theoretical approach. Despite the limits of the preliminary tests, the study of the thermal erosion will allow to better understand both, the Martian thermokarst and outflow channel formations. This paper presents the designed experimental device.

Conception of the experimental setup: The purpose of the experimental study is to measure the propagation of the thawing line in a simulated Martian ground ice and the thermal erosion rate. A general overview of the experimental configuration is presented in the included figure. To test our theoretical fluvio-thermal modelisation (ablation model), we propose to built a hydraulic channel in a small scale. The flow must erode a frozen rectangular block (about 0.5x0.3x0.2 m) supported by a mechanical framework. The frozen sample, in thermal contact with the water during the experimentation undergoes a strong thermal action. The channel discharge has been calculated to be enough to produce a turbulent regime and to insure the immediate removal of the thawed sediments. The velocity near the ground ice sample is about 0.8 m.s⁻¹. To obtain these conditions, the upstream comes from a water thermostated tank. A pump insures the recycling of the water. Temperature measurements will be done with regularly spaced thermocouples. A data acquisition system will insure the information acquisition and the control of the experiment. The hydraulic channel will be located in the freezer hall facility (18 x8x5 m) in view to conduct the experiment under controlled conditions (mean air temperature: about -10°C). We plan to perform this experiment with a ground ice temperature of -5°C; later, more various temperatures and sophisticated compositions and porosities will be introduced. A water temperature of 1°C and 5°C will be used.

Conclusion: This paper presents the thermo-mechanical study necessary to conduct a fluvio-thermal simulation. Measurements will be confronted with our previous ablation model and with terrestrial measurements in Arctic regions. If this first experimental study agrees with theory, the estimations of thermal erosion rate for Martian outflow channels will be reliable. The experimentation will give us necessary elements to refine the studies and to conduct the experimental study in a simulated Martian environment (6) - DLR Space Simulator, Germany -. Our recent insertion in the Martian Simulation Group (with German and Russian scientists) allows us to consider this type of experimentation.

This work is supported by Programme National de Planétologie de l'Institut National des Sciences de l'Univers (CNRS, France).



General overview of the experimental study.

Water temperature : $T = 5^{\circ}\text{C}$ and $T = 1^{\circ}\text{C}$

Ground ice temperature : $t = -5^{\circ}\text{C}$

Channel cross section : 0.3 m

Channel discharge : $Q = 24 \text{ l s}^{-1}$

Water velocity in the channel : $v = 0.4 \text{ ms}^{-1}$

Water velocity beneath the frozen sample: $v = 0.8 \text{ ms}^{-1}$

Reynolds number: $Re = 3 \cdot 10^5$

References : (1) Costard F. (1989) LPSC XX, 189. (2) Are F.E. (1983) Proc. 4th Int. Conf. on Permafrost, 24. (3) Aguirre-Puente J., Costard F. and Posado-Cano R. (1990) LPSC XXI, 7. (4) Aguirre-Puente J., Costard F. and Posado-Cano R. (1993) LPSC XXIV, 5. (5) Aguirre-Puente J., Costard F. and Posado-Cano R. (1994) submitted to Icarus. (6) Möhlmann D. and Kochan H. (1993) Workshop on the Int. Coord. of the Expl. of Mars, IACG, Wiesbaden, 29.

2941

P- 2

RADIATIVE SIGNALS FROM IMPACT OF SHOEMAKER-LEVY ON JUPITER;

Thomas J. Ahrens , *Glenn S. Orton , Toshiko Takata and John D. O'Keefe, Lindhurst Laboratory of Experimental Geophysics, Seismological Laboratory, California Institute of Technology, Pasadena, CA 91125; *Jet Propulsion Laboratory, Caltech, Pasadena, CA 91109

Background. We used the temperature and internal energy fields calculated by Takata et al [1] in the plume to calculate the greybody thermal radiation emitted versus wavelength, to predict what might be observed by several spectral sensors operating from different platforms when fragments of Comet Shoemaker-Levy-9 (SL-9) impact Jupiter in July 1994 [1-5].

A SPH code was used by Takata et al [6] to calculate the full three-dimensional flow and thermodynamic fields in the comet fragment and the atmosphere of Jupiter. We determined the fragment penetration depth, energy partitioning between the atmosphere and the impactor, and energy density deposited per unit length over the trajectory.

Once the impactor had disintegrated and stopped, and the strong atmospheric shock decayed, the flow is driven by buoyancy effects. We then used our SPH code to calculate the flow and thermodynamic fields---pressure, article velocity, temperature and internal energy distributions in the plume.

The calculations for 2 and 10 km cometary fragment yielding maximum deposition of depths of ~175 and ~525 km, respectively (1 bar = 0 km depth). We also calculated that 0.7 and 0.6 of the initial kinetic energy of the 10- and 2-km diameter bolides, respectively, are deposited as internal energy in Jupiter's atmosphere.

Radiative Signatures. The radiation upon entry from the heated atmosphere and vaporized cometary media within the temporary conical cavity will be multiply Rayleigh scattered by the H₂ and He of Jupiter's atmosphere, and obscured by the several Jovian cloud decks. Moreover, as pointed out by Field and Ferrara [7], the radiant flux may also be reflected from one or more Galilean satellites depending upon their position during impact. The observed color temperature during entry of a cometary fragment into Jupiter's atmosphere will be in excess of 10⁴ K. The details of the spectrum will depend on the degree of ionization which occurs in the bolide material and in Jupiter's atmosphere [8,9]. In any case, the ~10⁴ K temperature seen in the impact flash during bolide entry will occur (because of radiative cooling) for only a minute or so.

Because the optical radiation from the (~10sec) entry of a SL-9 fragment into Jupiter will emit radiation anisotropically , we chose to model only the radiation from the second SPH calculation describing the plume. Moreover, the entry flash may be partially obscured in many directions by the asymmetry of the entry hole, opacity of ionized gas, and the NH₃, NH₄SH, and H₂O cloud layers.

Starting with plume calculations of 2-and 10-km SL-9 fragments, we have considered each particle as a greybody radiator disc and calculated the total normal radiative power as a function of wavelength at a series of times (e.g. Figure 1). Since we are not accounting for the absorption of CH₄ or Rayleigh scattering from H₂, the present calculations are an upperbound to the actual radiating power. However, most of the hot materials, shown in Figure 2 a,b, are at, or above, the elevations such that there will be minimal absorption effects of clouds. We observe that in the case of the 2 km comet nucleus fragment impact (Figure 2b) that its particle velocity is such that it should achieve an altitude of 3000 km within several minutes.

Predictions. In July 1994, the Galileo spacecraft will be in a good position (1.6 AU away from Jupiter) to observe with the Solid State Imaging Experiment [10] the plumes from Shoemaker-Levy-9 fragment collisions directly. The flux emitted by the plume associated with a 2-km diameter fragment is some 30% of the solar visible flux reflected by Jupiter. It is comparable to both Jupiter's reflected solar flux near 1 micron and an order of magnitude or more higher than Jupiter's near-infrared reflected flux, and Jupiter's average 5- and 7.8-micron thermal emission. Using our 2-and 10-km results, we infer that the plume from impact of a 2-km diameter fragment yields a radiant

RADIATIVE SIGNALS FROM SHOEMAKER-LEVY: Ahrens, T. J., Orton, G. S., Takata, T. and O'Keefe, J. D.

power equivalent to 3% of Jupiter's total flux and some 10% of Jupiter's average thermal emission at 5 and 7.8 microns. Thus, observations by Galileo instruments are technically feasible for a large number of the fragments if they are as dense as we have assumed.

Direct earth-based observations of the impact-induced plume may be possible as it rises above Jupiter's horizon as seen from the earth (prior to dawn at the impact point). However, observation of the inner Galilean satellites brightnesses as a function of time may detect a reflection of the plume illumination superimposed on the solar illumination. The plume generated by a 1-km diameter fragment would increase Io's visible flux by some 10% in the visible and by 1% or less in the near infrared. The plume generated by the 0.5-km fragment illuminates Io only 0.01-0.03% more than the sun between the visible and near infrared. However, at wavelengths of 5 microns and longer, the 0.5 km fragment induced plume illuminates Io some 1-3% more than the sun. Clearly, the most favorable spectral band for indirect detection of impact-induced plumes is in the near or middle infrared.

For SL-9 fragments with diameters <1 km, impact-induced plume brightnesses are expected to be decreased by plume and atmospheric opacity effects [9]. In these cases, the wavelength of peak spectral power is likely to be diagnostic of fragment size. Our present study indicated the wavelength of maximum plume intensity, λ_m , and fragment diameter, d , are related by the Wein's law type relation: $\lambda_m d^3 \approx 5 \times 10^{11} \text{ cm}^4$.

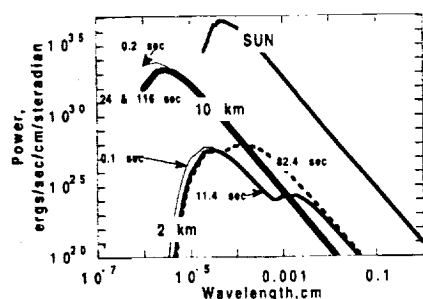


Fig. 1 Calculated spectra from Shoemaker-Levy-9 impact-induced plumes for 2 and 10 km diameter fragments. The peak power from the 2 km fragments radiates at the approximately same power level as the total Jupiter disk. The total power from the sun, considered as a point source is shown, for comparison.

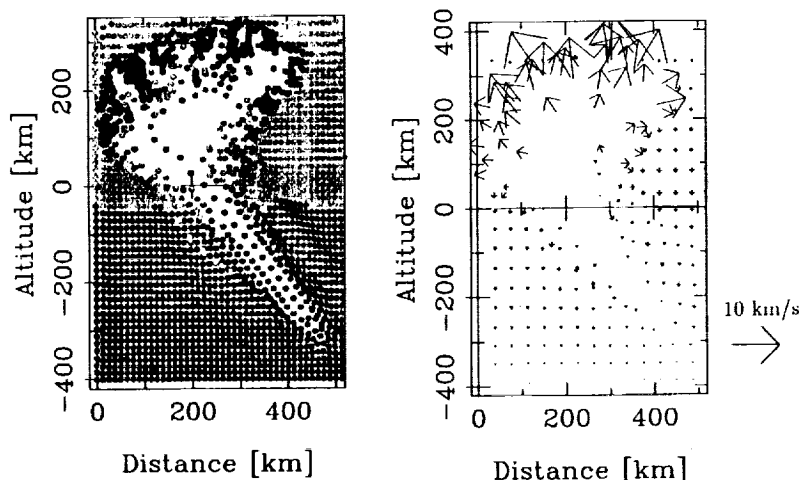


Fig. 2 (a) Impact plume (75 secs.) configuration for 2 km fragment impacting at 40° from zenith. (b) Particle velocity field for plume at same time.

- REFERENCES: [1] Shoemaker, C. S. et al. (1993) *IAU Circ.*, 5725. [2] Marsden, B.G. and Nakano, S. (1993) *IAU Circ.*, 5800; Yeomans, D.K. and Chodos, P. (1993) *Minor Planet Circ.*, 22197; Yeoman, D. K. and Chodos, P. (1993) *IAU Circ.*, 5909. [3] Chapman, C. R. (1993) *Nature*, 363, 492. [4] Scotti, J. V. and Melosh, H. J. (1993) *Nature*, 365, 7333; Sekanina, Z. et al. (1993) *Astron. J.* [5] Sekanina, Z. (1993) *Science*, 262, 382-387; Sekanina and Yeomans, D. K. (1985) *Astron. J.*, 90, 2335. [6] Takata, T. et al. (1994) *25th LPSC*. [7] Field, G. B. and Ferrara, A. (1993). [8] Zahnle, K. and MacLow, M. M. submitted (1994) *ICARUS*. [9] Chevalier, R. A. and Sarazin, C. L. submitted (1994) *Astrophys. J.* [10] (1992) *Space Science Reviews*, 60, Russell, C.T., ed.

CHONDRULES FROM CHONDRULES ? AN ION PROBE TRACE ELEMENT STUDY. C. M. O'D. Alexander. McDonnell Center for Space Sciences, Washington University, St Louis, MO 63130, U.S.A.

Inter-element correlations, particularly between the refractory elements, observed in INAA bulk chondrule data have led to the now generally accepted conclusion that the chondrule precursors were nebular condensates [e.g.1] rather than pre-existing crystalline rocks. Here the trace element abundances of the major UOC chondrule silicate phases, measured by ion microprobe, are used to re-examine the issue of chondrule precursors. It is shown that random sampling of a previous generation of chondrules could produce the observed range of bulk composition [2,3].

Ion probe measurements of porphyritic chondrule olivines tend to fall into two groups, 'normal' and incompatible-rich. The incompatible-rich olivines (Fo>97, low Cr and Mn) appear to have formed under highly reducing conditions. All porphyritic chondrule olivines and low-Ca pyroxenes have surprisingly unfractionated REEs compared to the patterns expected from equilibrium distribution coefficients [4]. The distribution coefficients of many trace elements in olivine and low-Ca pyroxene are strongly dependent on the cooling rate [5]. In particular, the LREEs become less fractionated, with respect to the HREEs, as the cooling rate increases. The ion probe results for chondrule minerals are consistent with porphyritic chondrules having cooled at about 1000°C/hr or even faster [2,3], in agreement with previous estimates based on zoning profiles [6].

As might be expected, ion probe measurements show that the refractory lithophiles, with the exception of Mg, are all highly incompatible in silicate melts and are, as a result, concentrated in the chondrule glasses [2,3]. The refractory lithophiles in the glass have, in most cases, essentially chondritic relative abundances suggesting that neither vapor phase nor crystal-liquid fractionation played a major role in the formation of chondrules or their precursors.

Based largely on the observation that the refractory lithophiles are concentrated in the chondrule glasses it is suggested that previously reported correlations between these elements in bulk chondrule analyses are due to chondrules themselves, as opposed to refractory condensates, having been their own immediate precursors. In this model, it is envisioned that chondrules formed by randomly sampling fragments of a previous generation of chondrules. If correct, the correlations between the incompatible elements in the bulk analyses result from chondrules incorporating variable amounts of glass when they formed.

Other correlations amongst the lithophile elements in the bulk chondrule data have been reported. It is possible that some of these correlations are artifacts produced by the variable dilution of the lithophiles, whose abundances would otherwise be relatively constant but uncorrelated, by reduced and oxidized Fe. For this reason the bulk chondrule data have been recalculated on an Fe-free basis and are shown in Fig. 1. Also, in Fig. 1 are the results of a simple Monte Carlo model, which sampled at random the ion probe measurements, to simulate chondrules. The similar distribution of compositions between the natural and simulated chondrules supports the hypothesis that chondrules formed by the random sampling of a previous generation of chondrules (Fig. 1).

As can be seen in Fig. 1, the previously described inverse correlation between the refractory lithophile element abundances, such as Sm, and the Fa/Fs content of the chondrule minerals all but disappears from the Fe-free data and the correlation Mg-Al correlation becomes rather weak. The inverse correlation of the Sc/Cr ratio with the Fa/Fs content of chondrule minerals remains but, in the context of this model, could be explained by the mixing of incompatible-rich olivines (Fo>97, high Sc, low Cr) with the 'normal' olivines (Fo<97, low Sc, high Cr which correlates with Fa content) and by Cr being lost in chondrule metal from the more reduced chondrules. Finally, it has been argued that the upper limit of about one observed in the atomic Na/Al ratios of chondrule glasses is due to an albitic precursor. However, it is possible that this upper limit simply reflects that for Na to be incorporated into the structure of the melt it must take part in the coupled substitution $\text{NaAlO}_2 \rightarrow \text{SiO}_2$ [7].

- [1] Grossman J.N. and Wasson J.T. (1983) In *Chondrules and their Origins* (ed. E.A. King), pp. 88-121. [2] Alexander C.M.O'D (1992) *Meteoritics* 27, 197. [3] Alexander C.M.O'D (1993) *G.C.A.*, in press. [4] Alexander C.M.O'D (1991) *Meteoritics* 26, 312. [5] Kennedy A.K. et al. (1993) *E.P.S.L* 115, 177-195. [6] Jones R.H. (1990) *G.C.A.* 54, 1785-1802. [7] Taylor M. and Brown G.E. (1979) *G.C.A.* 43, 61-75.

CHONDRULES FROM CHONDRULES?: Alexander C.M.O'D.

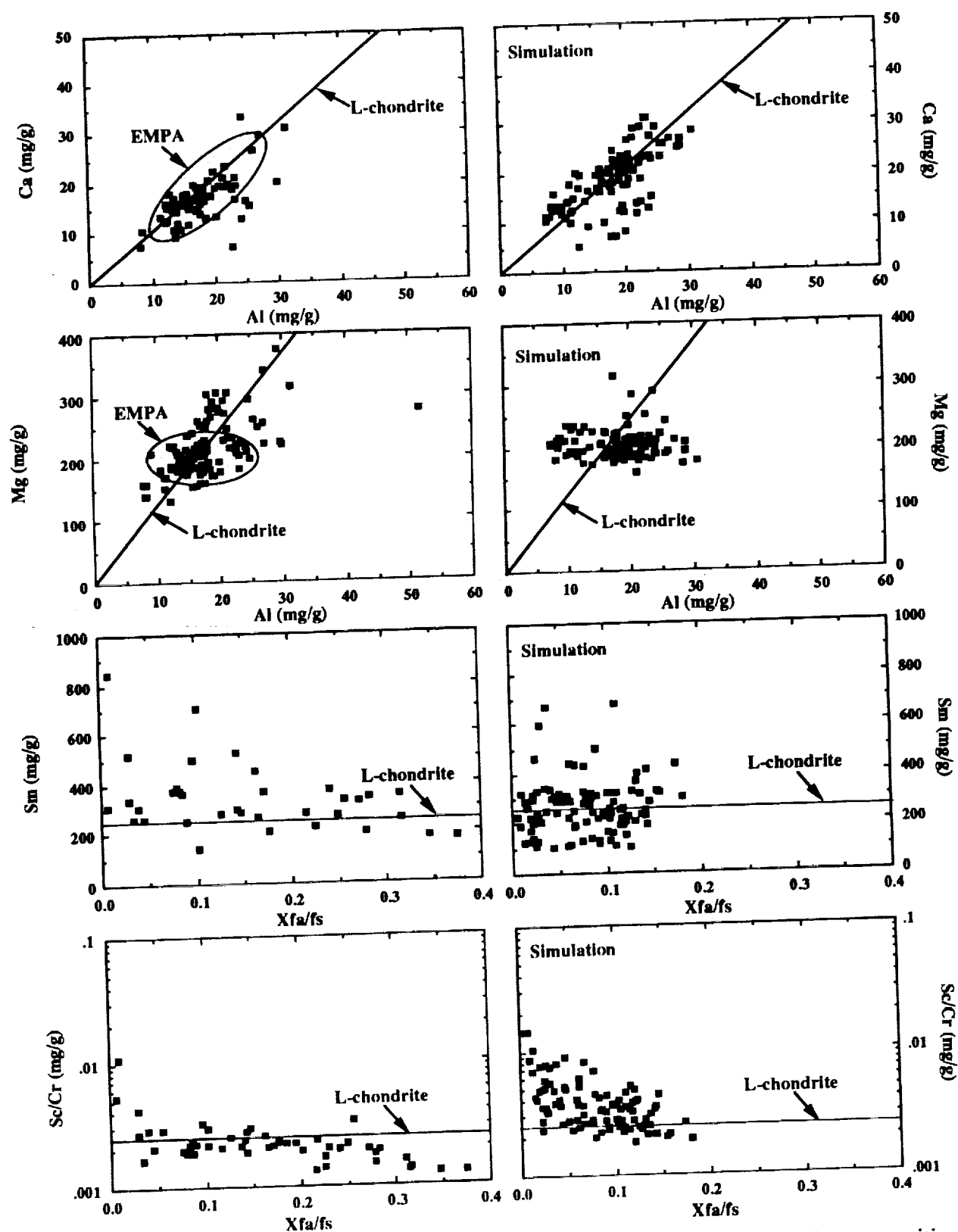


Fig. 1 Comparison of bulk chondrule INAA data taken from the literature with the compositions simulated chondrules formed by randomly sampling the ion probe data.

EVIDENCE FOR SHORT SiC LIFETIMES IN THE ISM; C. M. O'D. Alexander, McDonnell Center for the Space Sciences, Physics Department, Washington University, One Brookings Drive, St. Louis, MO 63130 USA.

The KJ series of presolar SiC size separates isolated from the Murchison meteorite exhibit pronounced variations in the absolute abundances and isotopic compositions of their noble gases with grain size [1,2]. In the case of ^{21}Ne , its variation in abundance with grain size appears to reflect differences in the cosmic ray exposure ages of grains, from 13Ma to 133Ma with increasing size, while they resided in the interstellar medium (ISM). These ages are significantly shorter than typical theoretical estimates of 500Ma for the residence times of refractory grains in the ISM [e.g.3] but are consistent with an observed under abundance of SiC in the ISM [4]. Another remarkable feature of the SiC noble gas data is the linear correlation between the cosmic ray exposures of the size separates and their ^{22}Ne contents. The ^{22}Ne is thought to have formed in the He-shell of AGB stars [5] so there is no obvious reason why it should correlate with exposure age. The observation that only about 5% of SiC grains carry essentially all the ^4He and ^{22}Ne [e.g.6] led to the suggestion that these same gas-rich grains also carry the ^{21}Ne and that most of the meteoritic SiC has been degassed in the Solar System [2]. However, this explanation requires that the gas-rich grains be up to 1Ga old, much older than theoretical expectations, does not explain why only very old gas-rich grains survived degassing and cannot explain the variations with size of the other noble gases, including He, which do not show linear correlations with exposure age. Here an alternative model for the variation of noble gas abundances with size is outlined which is based on the premise that the measured cosmic ray exposure ages are related to the mean residence time of SiC of different sizes in the ISM.

The presolar SiC found in meteorites was probably produced by numerous stars [e.g.7] and presumably accumulated in the reservoir from which the solar system formed. If star formation in the galaxy approximates a steady state, the rate at which SiC was added to the reservoir is likely to have been, on average, constant. This being so, the 133Ma mean exposure age of the Murchison KJG fraction suggests that the reservoir had been accumulating grains of this size for at least twice this length of time.

While SiC grains reside in the reservoir they are continually bombarded by cosmic rays and their ^{21}Ne contents rise accordingly. At the same time, grains are being continuously removed and replaced by SiC that has a zero age. Consequently, the average exposure age of the SiC in the reservoir will evolve, but given enough time both the concentration and average exposure age will reach a steady state.

In the larger grain sizes, at least, ^4He and ^{22}Ne are carried by only about 5% of the grains [6], because the stars that form gas-rich grains are relatively rare. The concentration of grains injected into the reservoir by a particular star will decay with time at rates that are approximately inversely proportional to their size. As a result, when the solar system forms the grains from this star will be depleted in the finer fractions compared to the coarser ones and the extent of the relative depletion will depend on the age of the grains. Here, then, is a means of varying the gas abundances with size and in the same direction as the exposure ages.

Changes in the $^4\text{He}/^{22}\text{Ne}$ ratio with size require that a minimum of two gas-rich populations be present, here only two are assumed, and that they have different ages. At present, it is not known how the noble gases, other than spallogenic ^{21}Ne , were trapped in the SiC but it seems likely that they were implanted by stellar winds after SiC growth was complete [1,2]. At low wind energies, implanted gas concentrations will vary as $1/r$, but as the energies increase and implantation depths approach the dimensions of the smaller grains this relationship will flatten and gas concentrations could even start to increase with size. Changing the energies of the winds is thus another means of varying the gas concentrations with grain size. Finally, for the sake of simplicity it is assumed that, when it forms, SiC always has the same initial size distribution [8].

A simple mathematical model based on the ideas outlined above has been fitted to the pure s-process KJ noble gas data by solving for the ages of the two gas-rich populations, the energies (keV/amu) of the winds that irradiated them and the noble gas fluences they 'saw' (Table 1). As can be seen the fit is quite successful (Fig. 1) except, perhaps, for ^4He . Using the results of the fit and assuming all stars produce the same amount of SiC one can estimate the gas abundances as a function of size in the two populations and compare these to the single grain data [e.g.6] (Fig. 2). The predicted gas concentrations of the population A grains are consistent with the less gas rich grains. The predicted gas concentrations for the population B grains are higher than observed in any grains and may, in fact, exceed the saturation levels for SiC, an effect that will have to be included in future models.

[1] Lewis R.S. et al. (1990) *Nature*, **248**, 293. [2] Lewis R.S. et al. (1993) *G.C.A.*, in press. [3] Scab C.G. (1988) In *Dust in the Universe* (eds. Bailey M.E. and Williams D.A.), pp.303. [4] Whittet D.C.B. et al. (1990) *Mon. Not. Roy. Astr. Soc.* **244**, 427. [5] Gallino R. et al. (1990) *Nature*, **248**, 298. [6] Nichols R.H. et al. (1993) *Meteoritics*, **28**, 410. [7] Alexander C.M.O'D. (1993) *G.C.A.*, **57**, 2869. [8] Little-Marenin I.R. (1986) *Ap. J.*, **307**, L15.

Fig. 1 Comparison of the s-process gas concentrations measured by [2] with those predicted by the fit.

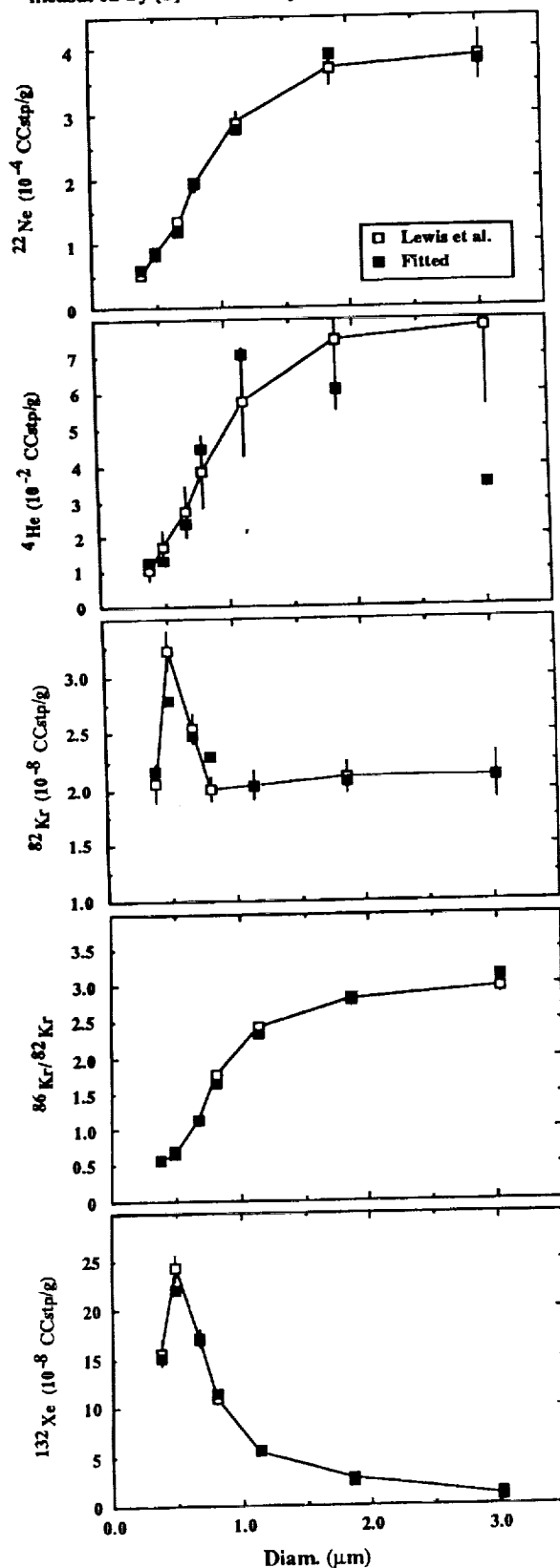
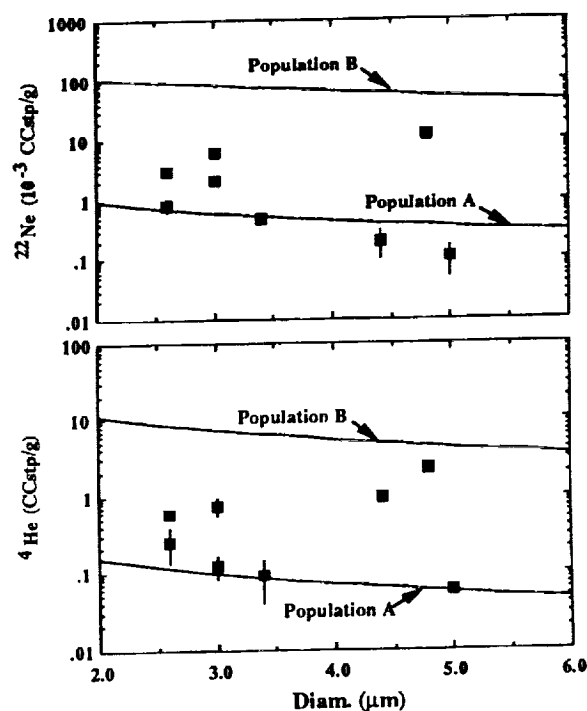


Table 1. Summary of results of the fit to the pure s-process KJ data [2]. The age is the age before the solar system formed. The isotopic ratios are the ratios in the winds. The absolute ^{22}Ne fluences were calculated assuming all stars produce similar amounts of SiC. The wind energies include the 1 sigma in the energy distributions.

	Pure s-process	
	Population A	Population B
Age (m.y.)	31.1	84.9
$^4\text{He}/^{22}\text{Ne}$	2.1×10^2	1.2×10^2
^{22}Ne (ccSTP/ μm^2)	5.7×10^{-15}	5.4×10^{-13}
$^{36}\text{Ar}/^{22}\text{Ne}$	1.9×10^{-3}	1.6×10^{-3}
$^{82}\text{Kr}/^{22}\text{Ne}$	3.5×10^{-4}	7.8×10^{-5}
$^{86}\text{Kr}/^{82}\text{Kr}$	0.61	3.4
$^{132}\text{Xe}/^{22}\text{Ne}$	2.8×10^{-3}	5.6×10^{-8}
Energy (keV/amu)	6.9 ± 0.3	56.6 ± 31.6

Fig. 2 Comparison of the predicted gas concentrations with those measured in single grains [e.g. 6].



C1 AND ALKALI METASOMATISM IN UNEQUILIBRATED ORDINARY CHONDRITES; C.M.O'D. Alexander, McDonnell Center for the Space Sciences, Washington University, St Louis, MO 63130, J.C. Bridges and R. Hutchison, Mineralogy Department, The Natural History Museum, London SW7 5BD

Mineralogical changes, probably driven by hydrous fluids, occur within the UOCs, but are subtle and little documented. Furthermore, the meteorites involved need not be the lowest types on the petrographic sub-scale, 3.0-3.9, based on thermoluminescence [1]. Evidence of this alteration was found in five UOCs: the presence of smectite in Semarkona (LL3.0) and Bishunpur (LL3.1) [2], and post-accretion oxidation and C1- (\pm H₂O) metasomatism in Tieschitz (H3.6) [3-5], Sharps (H3.4) [4], Bishunpur [6] and Parnallee (LL3.6) [7]. The latter produces C1-bearing species such as chlorapatite, scapolite, nepheline or feldspathoid, and "white-matrix". We show that white matrix and altered chondrule mesostases in Tieschitz are enriched in F, Cl, K, Rb and Ba, and describe new examples of alteration in Chainpur (LL3.4) and Parnallee.

Tieschitz The bulk composition of white matrix resembles Bishunpur scapolite (Table 2), but TEM observations show that white matrix is not scapolite, but is dominated by a lamellar intergrowth of two unidentified phases [4], or, in some areas, nepheline [8]. Hutchison observed incipient alteration of chondrule mesostases [5] to a product physically and chemically resembling white matrix. We therefore analysed, by ion-probe, unaltered and altered mesostases co-existing in five porphyritic chondrules, plus three areas of interchondrule white matrix. All of the mesostases consist of glassy or cryptocrystalline material containing dendrites of Ca-pyroxene. In back-scattered electron images, "glassy" unaltered mesostases have smooth surfaces and are bright but altered mesostases appear blocky and dark. The presence of phenocrysts and dendrites throughout a chondrule precludes the possibility that different, immiscible liquids were involved. Chemical data are presented (Table 1) which show that, compared with unaltered mesostases, altered mesostases are enriched in F, Cl, K, Rb and Ba. There is no enrichment in Na.

Chainpur A radiating pyroxene chondrule was found to have altered mesostasis of two compositional types (Fig. 1, Table 2). One has high SiO₂ and Cl (<4.6 wt%), but lower Na₂O, but the reverse is true of the other. Both types tend to decompose under the electron beam, which may account for the low totals obtained. Similar low totals in Tieschitz white matrix were attributed to porosity [8]. The representative analyses do not correspond to mineral species, but the higher SiO₂ type is close to the composition of Bishunpur scapolite and Tieschitz white matrix. The mesostasis contains crystallites of Ca-pyroxene (Wo₁₆En₃₇) and may not be fully crystalline.

Parnallee A barred chondrule comprises olivines (Fo₇₂₋₇₆) intergrown with plagioclase (An₇₀₋₈₇) and minor pyroxene. At their margins, the feldspathic areas have partially altered to material with the composition of Cl-bearing nepheline. Much of the feldspar is also deficient in Si.

Conclusions Our observation of Cl-bearing phases in Chainpur brings the number of UOCs in which secondary alteration has been recognised to six. These UOCs are of different chemical groups and petrologic types, so alteration probably was fairly widespread. In Tieschitz, at least, K, Rb and Ba were introduced into altered chondrule mesostases, so the fluid was enriched in these elements. The association of volatile Rb with refractory Ba indicates that the alteration was not driven by condensation or evaporation. This, and the

CHONDRITE METASOMATISM: Alexander, C.M.O'D. et al.

juxtaposition of white matrix with altered mesostases around the margins of chondrules, indicates that alteration was a parent body process. Transport presumably was accomplished by F, Cl and H₂O. A genetic relationship between altered mesostases and white matrix [5] is confirmed by their high F, Cl, K, Rb and Ba contents (Table 1). Relative to other UOCs, Tieschitz is depleted in Na and K. It is possible that although local elemental enrichments were produced, the bulk meteorite was leached.

References [1] Sears, D.W.G. et al. (1980) *Nature* **287**, 791. [2] Alexander, C.M.O'D et al. (1989) *GCA* **53**, 3045. [3] Christophe Michel-Levy, M. (1976) *EPSL* **30**, 143. [4] Alexander, C.M.O'D et al. (1989) *EPSL* **95**, 187. [5] Hutchison, R. (1992) *Meteoritics* **27**, 236. [6] Alexander, C.M.O'D et al. (1987) *Mineralog. Mag* **51**, 733. [7] Kennedy, A.K. et al. (1992) *EPSL* **113**, 191. [8] Ashworth, J.R. (1981) *Proc. R. Soc. Lond.* **A374**, 179. [9] Alexander, C.M.O'D. (1987) Unpubl. Ph.D. Thesis, University of Essex

Table 1:

	2U	2A	4U	4A	5U	5A	8U	8A	9U	9A	A/U	WM4	WM9	WM10
F	13.0	720	20.6	297	13.5	224	16.9	30.4	61.4	155	1.8-55	43.1	44.5	26.6
Cl	69.4	3267	666	5440	162	5223	1331	5708	99.5	4032	4.3-47	3706	3426	2379
K	185	5868	538	2733	254	4589	597	4263	253	3646	5.1-32	5467	5261	5794
Rb	1.44	7.08	0.77	3.57	0.87	5.25	0.38	10.8	2.19	9.82	4.5-28	9.54	8.71	10.0
Ba	1.28	15.6	2.10	15.6	1.50	128	3.07	28.6	1.14	27.6	7.4-85	19.3	9.79	9.51

Elemental abundances (ppm) in unaltered (U) and altered (A) mesostases, Tieschitz chondrules 2, 4, 5, 8 and 9. A/U is the range of values. WM4, WM9 and WM10 are interchondrule white matrix, near chondrules 4, 9 and 10. Data from the Washington University, St Louis, ion-probe. The absolute values may need correction, but the ratio A/U should be unaffected, indicating that all elements are enriched in altered relative to unaltered mesostatis.

Table 2:

	C(a)	C(b)	P(ne)	B(sc)	T(wm)
SiO ₂	53.3	46.1	44.0	59.0	56.2
Al ₂ O ₃	23.9	25.5	32.5	20.3	18.3
TiO ₂	0.05	1.21	-	-	n.d.
FeO	0.98	1.58	0.3	3.22	4.75
MgO	1.24	0.22	0.4	0.40	3.32
CaO	1.48	2.65	1.4	3.05	3.85
Na ₂ O	8.89	12.1	18.0	11.0	8.9
K ₂ O	0.91	0.80	0.1	0.81	0.4
P ₂ O ₅	0.03	0.22	-	-	n.d.
Cl	4.64	2.07	0.9	3.67	n.d.
Sum	95.4	92.5	97.6	101.5	95.7

Representative analyses of Cl-bearing materials. C(a) and C(b), WDS microprobe analyses of (a) Si- and Cl-rich, (b) Si- and Cl-poor mesostatis, Chainpur chondrule (Fig. 1). P(ne) EDS analysis, nepheline in Parnallee chondrule. B(sc) Bishunpur scapolite [6]. T(wm) Tieschitz white matrix [9].



Fig.1

Back-scattered electron image, Chainpur RPx chondrule, with mesostasis. H = 4 spots, high Si, Cl; L = 3 spots, low Si, Cl.

DISTRIBUTIONS OF THE PREATMOSPHERIC SIZES OF ANTARCTIC AND NON-ANTARCTIC CHONDRITES. V.A.Alexeev. Vernadsky Inst. of Geochem and Analyt. Chem., Russian Academy of Sciences, Moscow, Russia

The similarity of distributions of the cosmogenic (Ne-22/Ne-21)c ratios of Antarctic and non-Antarctic ordinary chondrites suggests the similarity of distributions of the preatmospheric masses of these two populations of meteorites.

It is well known the clear difference of mass distributions of Antarctic and non-Antarctic meteorites [1,2]. For example, average value of mass of non-Antarctic stone falls is found about 100 times that of Antarctic finds: $2750 \pm 200\text{g}$ and $29 \pm 2\text{g}$ respectively (Fig 1). Somewhat, this difference results from comparison of distribution of total weight values of all collected fragments of each meteorite in the case of non-Antarctic meteorites with distribution of weight values of individual fragments of Antarctic ones. However this difference remains valid also at comparison of weights of individual fragments. Thus, non-Antarctic meteorites have much more fragments of big mass than Antarctic ones (Table 1). These differences may be explained by easiness of collection of small fragments on the Antarctic ice and destruction of big fragments due to weathering of Antarctic meteorites [3].

Distribution of the preatmospheric sizes of meteorites may be estimated out of distribution of the ratio of cosmogenic isotopes of (Ne-22/Ne-21)c. This ratio varies mainly in interval of 1.05-1.25 for the most of stone meteorites [4]. In this case the big values of ratio are typical for small meteorites or small depth of location. For studying the distribution of (Ne-22/Ne-21)c ratios we used the values of Ne-22c and Ne-21c obtained at calculations of exposure ages of ordinary chondrites [5]. Initial data on contents of noble gas isotopes were taken from compilation [6]. However many of noble gas analyses were carried out more than 25 years ago. At that time instrumental fractionation as well as background corrections were based on an atmosphere Ne-20/Ne-22 ratio of 10.3 rather than the presently accepted value of 9.8 [7]. We have analysed distributions of the (Ne-22/Ne-21)c values for analyses made since 1962 up to now. It was found the systematical decrease of this ratio on an average by $3.8 \pm 0.8\%$ for analyses published in or before 1967 (Fig 2, Table 2). Therefore, we used only noble gas data obtained after 1967 at comparison of (Ne-22/Ne-21)c ratio distribution of non-Antarctic chondrites with that of Antarctic chondrites.

The obtained distributions of (Ne-22/Ne-21)c ratios for ordinary chondrites are shown on Fig 3. We can see, histogram for non-Antarctic meteorites for measurements after 1967 appreciably displaces in the direction of the higher (Ne-22/Ne-21)c values as against that of all measurements. We used the non-parametric statistical tests for comparison of these distributions. The found average (median) values of the (Ne-22/Ne-21)c ratios for measurements after 1967 are given in the Table 3. It is seen all average values agree well within the error limits. This fact allows to suppose the similarity of the (Ne-22/Ne-21)c ratio distributions. The same conclusion was made after use the Kolmogorov-Smirnov test. The obtained data suggest the similarity of distributions of preatmospheric sizes of Antarctic and non-Antarctic chondrites.

Table 1. The numbers of fragments with mass of $\geq m$ of Antarctic and non-Antarctic stone meteorites

Meteorites	$m \geq 16\text{kg}$	$m \geq 64\text{kg}$
non-Ant.(1813)	>250	>65
Antarct.(≈ 7000)	11	3

Table 3. Average values of $(\text{Ne-22}/\text{Ne-21})_c$ ratios in different groups of meteorites analysed after 1967. Errors correspond to confidence probability of 0.95. The number of meteorites is shown in parenthesis.

Meteorites	$(\text{Ne-22}/\text{Ne-21})_c$
non-Ant. H	1.105 ± 17 (161)
L+LL	1.111 ± 9 (184)
H+L+LL	1.109 ± 8 (345)
Antarct. H	1.117 ± 26 (63)
L+LL	1.114 ± 14 (59)
H+L+LL	1.114 ± 12 (122)

Table 2. Average values of $(\text{Ne-22}/\text{Ne-21})_c$ ratios in non-Antarctic ordinary chondrites for noble gas data obtained in different time. Standard deviation is ± 10 .

	Analyses		$\Delta, \%$
	before 1967	after 1967	
H falls	1.070 ± 6	1.110 ± 5	3.7 ± 0.7
finds	1.067 ± 9	1.100 ± 6	3.0 ± 1.0
L falls	1.076 ± 4	1.120 ± 4	4.0 ± 0.6
finds	1.048 ± 6	1.107 ± 6	5.5 ± 0.8
H and L	1.068 ± 6	1.109 ± 5	3.8 ± 0.8

$$\Delta = \frac{R(>67) - R(\leq 67)}{R(>67) + R(\leq 67)} \cdot 200\%, \quad \text{where}$$

$R(\leq 67)$ and $R(>67)$ are average $(\text{Ne-22}/\text{Ne-21})_c$ values, obtained from analyses before and after 1967 respectively

REFERENCES: [1] Koeberl Ch., Cassidy W.A. GCA, 1991, v.55, No 1, 3. [2] Graf Th. et al. GCA, 1990, v.54, No 9, 2521. [3] Alexeev V.A. LPS XXIII, 1992, 15; LPS XXII, 1991, 11. [4] Schultz L., Kruse H. Meteoritics, 1989, v.24, No 4, 155. [5] Schultz L. et al. GCA, 1991, v.55, 53.



Fig 2

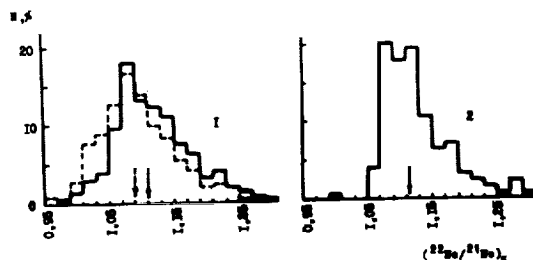


Fig 3

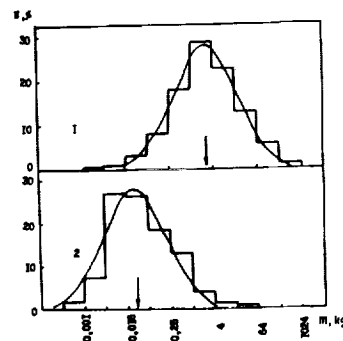


Fig 1

Fig 1 Mass distributions of stone meteorites. 1 - 835 non-Antarctic stone falls; 2 - 1047 Antarctic finds (Allan Hills). Arrows show the average values of distributions.

Fig 2 The average values of $(\text{Ne-22}/\text{Ne-21})_c$ ratio of non-Antarctic H-chondrites (falls) vs. year of measurements. Hatched areas correspond to the average values (± 10) for measurements before and after 1967.

Fig 3 Distribution of $(\text{Ne-22}/\text{Ne-21})_c$ values in ordinary chondrites. 1 - non-Antarctic (528) and 2 - Antarctic (122) meteorites. Solid lines - measurements only after 1967; dotted lines - all measurements. Arrows show the median values.

ON CALCULATION OF COSMIC-RAY EXPOSURE AGES OF METEORITES.
V.A.Alexeev. *Vernadsky Inst. of Geochem. and Analyt. Chem.,
Russian Academy of Sciences, Moscow, Russia*

For exclusion the systematic error in calculation of cosmic-ray exposure ages of meteorites the values of cosmogenic Ne-21c and (Ne-22/Ne-21)c ratio calculated out of noble gas data obtained before 1967 must be multiplied by 1.08 and 1.038 respectively.

Study of the distributions of cosmic-ray exposure ages can give some information on conditions of these cosmic bodies formation. For L- and H-chondrites we see as a whole exponential decrease of the number of meteorites with increase of the exposure age (with $\tau \approx 30\text{My}$ [1]). H-chondrites show also clear peak in the region of $\approx 7\text{My}$. At the present time the attempts to find out the "thin structure" in exposure age distributions of H- and L-chondrites are undertaken for discovery of possible clusters resulted from simultaneous origin of the meteorite groups [2,3]. In this attempts it is necessary to take into consideration the uncertainties of age values which can leads to the incorrect conclusions.

Now exposure ages are usually calculated with production rates of Eugster [4] on contents of cosmogenic He-3, Ne-21 and Ar-38 (with small correction for Ar-38 [5,6]). However, many noble gas measurements were carried out more than 25 year ago and content the systematic error [7]. It was found the systematical decrease of the cosmogenic (Ne-22/Ne-21)c ratios on an average by $3.8 \pm 0.8\%$ for analyses published in or before 1967 in comparison with those for analyses after 1967 [8]. This effect must be born in mind in calculations of the exposure ages.

For determination the possible systematic deviation in contents of cosmogenic Ne-21 calculated on data published before 1967 we select those H chondrites which were analysed both before and after 1967. For each such meteorite the average value of cosmogenic Ne-21 was calculated: $(\text{Ne-21})_{\text{av}} = \sum (\text{Ne-21})_i / n$, where $(\text{Ne-21})_i$ are contents of cosmogenic Ne-21 for the different years of measurements in the meteorite and n is the number of Ne-21 measurements for given meteorite. Then the relative contents of cosmogenic Ne-21 were calculated in this meteorite: $R_i = (\text{Ne-21})_i / (\text{Ne-21})_{\text{av}}$. Such procedure was made for all selected meteorites and histograms were constructed for R_i values for analyses both before and after 1967 (Fig 1). The obtained distributions are close to normal ones and for every histogram the Gaussian curve was calculated by the method of successive approximations. The difference between positions of the maxima is $8 \pm 2\%$. Thus if we want for more statistical validity of conclusions to use the noble gas data published in or before 1967 we must calculated contents of cosmogenic Ne-21 multiply by 1.08 and calculated cosmogenic Ne-22/Ne-21 ratios multiply by 1.038. This will allow to avoid the discussed above systematic deviations.

We made this procedure for H-chondrites falls and finds with exposure ages of $t \leq 12\text{My}$ (the region of peak). The obtained results (Fig.2) showed a shift of peak after corrections in the direction of higher ages; the peak for corrected ages became narrower. Apparently presence of different uncertainties at determination of the exposure ages stipulates the resolving power on the exposure age scale of 20-30%, close to the width of H-chondrite peak.

REFERENCES

1. Alexeev V.A. LPS XXIII, 1992, 17.
2. Graf Th., Marti K. LPS XXIII, 1992, 433.
3. Graf Th., Marti K. LPS XX, 1989, 353.
4. Eugster O. Geochim. Cosmochim. Acta, 1988, v.52, 1649.
5. Graf Th., Marti K., LPS XX, 1989, 353.
6. Alexeev V.A. LPS XXII, 1991, 11.
7. Schultz et al. Geochim. Cosmochim. Acta, 1991, v.55, 59.
8. Alexeev V.A. This volume.

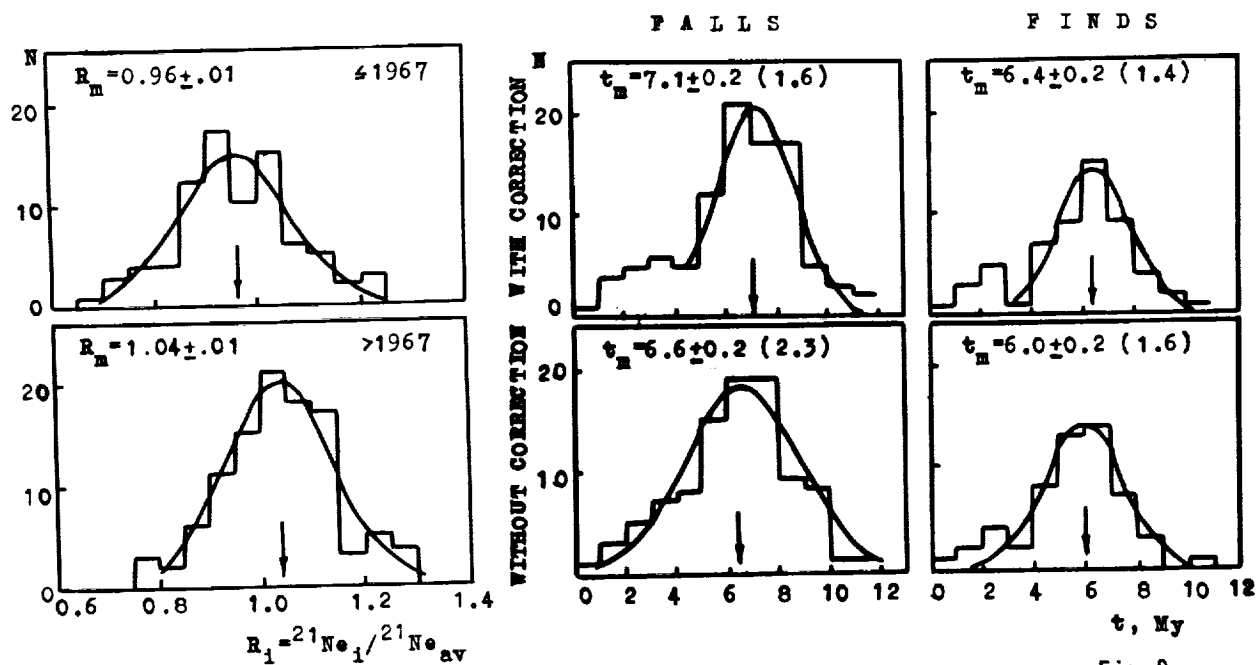


Fig 1

Fig 2

Fig.1. Distributions of cosmogenic $(\text{Ne-21})_i / (\text{Ne-21})_{av}$ ratios of H-chondrites which were investigated on noble gas content both before and after 1967. Arrows show the maximum positions of Gaussian curves (R_m).

Fig.2. Distributions of exposure ages (t) of H-chondrites (falls and finds) with $t < 12\text{My}$. Above - the ages were calculated with corrections of cosmogenic Ne-21 contents and Ne-22/Ne-21 ratios of meteorites measured before 1967; below - without corrections. The errors are standard deviation of average value (first number) and parameter of σ in Gaussian equation (the number in parenthesis).

SHORT LIFE OF SMALL METEORITES IN THE COSMIC SPACE ?
 V.A.Alexeev. V.I.Vernadsky Inst. of Geochem. and Analyt. Chem.,
 Russian Academy of Sciences, Moscow, Russia.

An analysis of distribution in the ordinary chondrites of the average values of track production rates, due to galactic cosmic rays, suggests short time of life of small meteorites in the cosmic space.

An analysis of the dispersion of ratios of cosmogenic isotopes of He-3/Ne-21 and Ne-22/Ne-21 depending on the cosmic-ray exposure ages of meteorites showed the increasing dispersion at decreasing age [1]. This effect was explained by presence of significant portion of meteorites of small preatmospheric sizes (of small shielding depths) mainly among meteorites of small exposure ages. It is known, the shielding depth of the investigated sample in the preatmospheric body of the meteorite stipulates not only the values of cosmogenic isotope ratios of He-3/Ne-21 and Ne-22/Ne-21 [2] but also the production rate of tracks by galactic cosmic rays [3]. In this report we investigated the distribution of the average values of track production rates of ρ_{av}/T as a function of cosmic-ray exposure ages of T in ordinary chondrites (H,L, and LL).

The average track density values of ρ_{av} were estimated according to data published in [4]. Calculations were made according to formula: $\rho_{av} = N/S$, where the N is a total number of tracks detected on the area of S of all investigated pyroxene or feldspar grains in the meteorite. We used also the exposure ages calculated in our early studies [5]. The obtained distribution is shown in Fig 1 to a scales line and logarithmic. The points correspond to meteorites with number of investigated grains of $n < 3$; circles are for $n \geq 3$. We can not see the meteorites with high values of ρ_{av}/T in the region of high exposure ages. For example, more than 20% of meteorites with $T < 15$ My (10 among 48) have $\rho_{av}/T \geq 4 \times 10^5 \text{ cm}^{-2} \text{ My}^{-1}$ whereas none of 45 meteorites with $T \geq 15$ My have not such track production rates. For calculation of "boundary" regression line we choose the points with $n \geq 3$ which deviate from calculated for these points regression line in log-scale not more than $\pm 5\%$ (the filled circles in Fig 1). The such way obtained regression line have form: $\lg(\rho_{av}/T) = 6.35 - 0.034 T$.

For estimation of preatmospheric sizes of meteorites located along the regression line, we calculated the distributions of weighted mean (for volume of found meteorite) value of ρ_{av}/T depending on preatmospheric radius (R_0) of meteorite for different ablation of A. Calculations were made at simplifying assumptions that 1) ablation was uniform and 2) form of fallen meteorite is spherical. The ρ_{av}/T values were calculated according to the formula: $\rho_{av}/T = (\sum_{i=1}^R \rho_i \Delta V_i) / (4\pi R^3/3)$, where R (in cm) is the radius of fallen meteorite (see Fig 2). The ρ_i is track density at depth of d_i in preatmospheric body of radius of R_0 at $T=1\text{My}$ [3]. This value of ρ_i was taken identical for all volume of $\Delta V_i = 4\pi(r_{i+1}^3 - r_i^3)/3$. As there was demonstrated in [4], mass ablation estimates range between 27% and 99.9% with a weighted mean ablation of about 85%. Therefore we carried out the calculations for ablation of A=25; 50; 85; 99 and 99.9% (Fig 3). We can see, the high average track production rates ($\sim 10^6 \text{ cm}^{-2} \text{ My}^{-1}$)

SHORT LIFE... Alexeev V.A.

inherent only small bodies (with $R_0 \sim 5$ cm) out of dependence on value of ablation. For big meteorites ($R_0 \sim 30-50$ cm) probability of detection of samples with high track production rates ($\geq 10^5 \text{ cm}^{-2} \text{ My}^{-1}$) is extremely small. The obtained data allows us to suggest the short life of small meteorites in the cosmic space before capture by the Earth.

The considered effect may be understood in the framework of model according to which meteorites may be fragments of main-belt asteroids, derived by cratering collisions. In this case dispersion of the velocities of fragments at collisions of asteroids stipulates the different times of the evolution of these fragment orbits to the earth-crossing orbits. Smaller fragments obtain higher velocities, whereby the time of transfer of this fragments to the earth-crossing orbits is decreased and therefore their exposure ages will be mainly small.

REFERENCES: [1] Alexeev V.A. LPS XXIV, 1993, 9. [2] Graf Th. et al. GCA, 1990, v.54, 2521. [3] Bhattacharya et al. JGR, 1973, v.78, 8356 [4] Bhandari N. et al. Nucl. Tracks, 1980, v.4, 213 [5] Alexeev V.A. LPS XXIII, 1992, 15; XXIV, 1993, 11

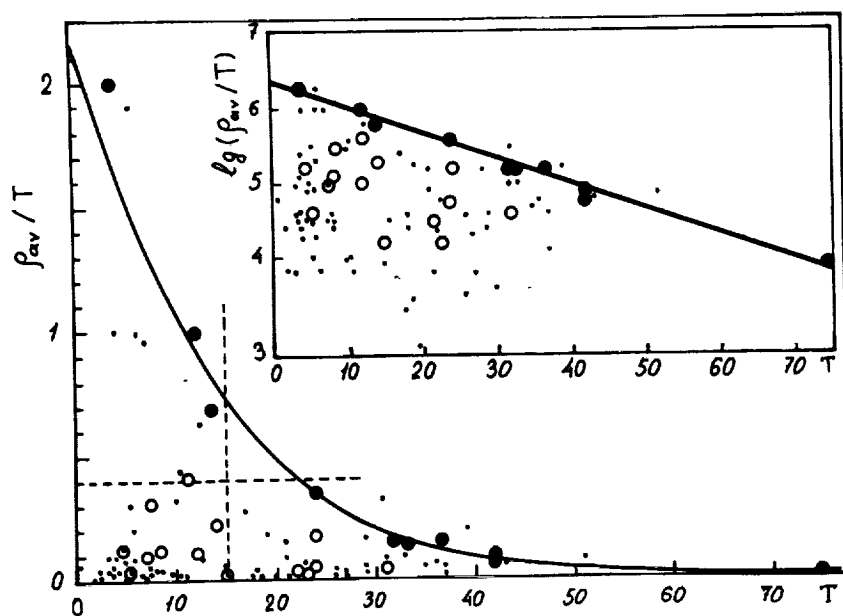


Fig 1

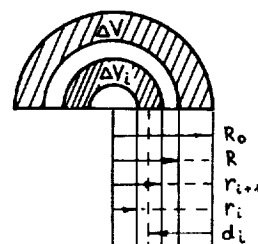


Fig 2

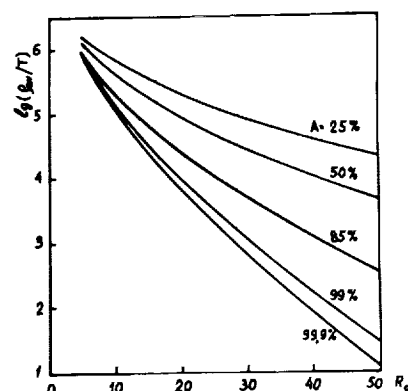


Fig 3

Figure captions

- Fig 1. Distribution of the average values of track production rates in ordinary chondrites (ρ_{av}/T , $10^6 \text{ cm}^{-2} \text{ My}^{-1}$) vs. exposure ages of meteorites (T , My). Points correspond to the meteorites with number of investigated samples of pyroxene or feldspar of $n < 3$; circles are those for $n \geq 3$.
- Fig.2. Schematic diagram for calculation of weighted mean value of ρ_{av}/T . The ΔV is volume lost at ablation and/or also not found after fall of meteorite; $d_i = (R_0 - (r_{i+1} + r_i))/2$.
- Fig.3. Weighted mean track production rate in fallen meteorite (ρ_{av}/T , $10^6 \text{ cm}^{-2} \text{ My}^{-1}$) vs. preatmospheric radius (R_0 , cm) for different values of ablation (A , %).

METEORITES AS DIFFERENTIAL DETECTORS OF EVENTS OVER A LONG TIME SCALE; V.A.Alexeev and G.K.Ustinova, Institute of Geochemistry and Analytical Chemistry, RAS, Moscow 117334 Russia

An effective approach to temporal localization of events during meteorite life is developed due to use of the statistical distributions of various meteoritic features and properties, in particular, contents of cosmogenic nuclides, in dependence on their cosmic-ray exposure or radiation age.

The history of meteorites abounds in diverse events having played, perhaps, a key role in forming their characteristics and peculiarities. However, the observed effects of the events in meteorites are integral by their nature, i.e., they are accumulated over the whole life of the meteorites, so there is no possibility to attach those events to any definite period of time. Nevertheless, a constructive approach is elaborated in the previous works /1,2/ allowing us to decide this problem. The fact is that meteorites have different cosmic-ray exposure and radiogenic ages, so searching for an effect statistically, among great numbers of the meteorites with different ages, one can distinguish the moment when this effect exists and when it does not yet/or already exist. Therefore, such a statistical approach converts the meteorites, as integral detectors, into the differential ones of events in their history over a long-time scale /3/. In the present paper some irradiation effects in ordinary chondrites in accordance with the radioactivity of long-lived nuclides are considered. The fulfilled analysis of Al-26, Be-10 and Mn-53 radioactivity in 435 Antarctic and non-Antarctic H- and L,LL-chondrites with different cosmic-ray exposure ages has shown that the average equilibrium radioactivity \bar{A}_0 of Mn-53 in the chondrites with $t \leq 8$ My is appreciably higher than in those with $t > 8$ My (see it in Fig.1 for the non-Antarctic H-chondrites /1,2/). This effect is not observed for Al-26 and Be-10 ($T_{1/2}$ of which are 0.705 and 1.51 My, respectively, versus 3.7 My of Mn-53), namely, the magnitude $\Delta = [\bar{A}_0(t \leq 8) - \bar{A}_0(t > 8)] / \bar{A}_0(t > 0)$ is equal to $17.3 \pm 3.3\%$ for Mn-53 and only to $4.1 \pm 3.2\%$ for Be-10 and $4.8 \pm 2.2\%$ for Al-26. Such a situation could be conditioned by temporal variations of galactic cosmic rays several million years ago, i.e., by their higher intensity $\sim 2-6$ My ago due to relaxation of the solar modulation mechanism /4,5/. If so, the higher Mn-53 average radioactivity should be observed, on the whole, in H-chondrites (whose average cosmic-ray exposure age t is ~ 7.8 and ~ 7.5 for the Antarctic and non-Antarctic chond-

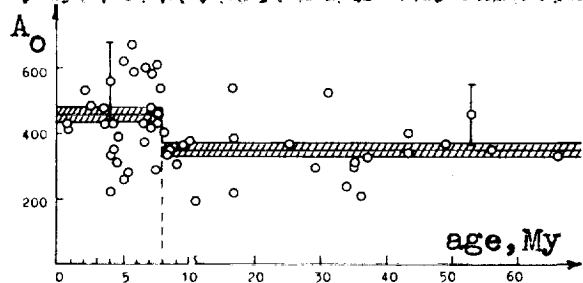


Fig.1- Distribution of Mn-53 equilibrium radioactivity (dpm/kgFeNi) in non-Antarctic H-chondrites with different cosmic-ray exposure age (dashed belts mark its average values ($\bar{A}_0 \pm \sigma$) in the chondrites with $t \leq 8$ and $t > 8$ My) /1,2/

52-91 ABS ONLY

NEW PROSPECTS FOR ANALYZING LUNAR PYROCLASTIC GLASS

C. C. Allen, Lockheed Engineering & Sciences Co., Houston, TX L. P. Keller and J.P. Bradley, MVA, Inc., Norcross, GA D.E. Brownlee, University of Washington, Seattle, WA and D. S. McKay, NASA/Johnson Space Center, Houston, TX ✓

2942

p. 2

Pyroclastic glass particles of diverse compositions are sparsely distributed in the lunar soil. Numerous suspected pyroclastic deposits have been pinpointed on the nearside. However, a dearth of pure samples large enough for spectral study, coupled with the kilometer spatial resolution of Earth-based telescope spectrometry, make it difficult to remotely analyze these deposits or tie most glasses to specific sources. Two developments should soon improve this situation. First, the technique of microscope photometry combined with microprobe analysis for the first time allows correlation of the reflectance spectra and chemical compositions of individual glass particles. Second, the Clementine spacecraft will provide multispectral images of pyroclastic deposits at much higher spatial resolution than is currently achievable. These developments, combined with traditional laboratory and telescope studies, should allow compositions of many pyroclastic deposits and sources of many soil particles to be determined.

Pyroclastic Glass. Lunar pyroclastic glass particles, tens to hundreds of micrometers in diameter, span a large range of chemical compositions. Delano (1) has identified 25 distinct glasses in lunar soil. Among these glasses, thin section colors range from green to yellow to orange to red with increasing TiO_2 content. Some of these compositions are also represented by devitrified black particles, darkened by myriad submicrometer ilmenite and spinel crystals.

Of these diverse glass types the reflectance spectra of only three are known (2,3). Sample 74220 is the high-Ti "orange soil" from Shorty Crater. Sample 74001 is a core dominated by almost pure concentrations of black glass, the devitrified equivalent of 74220. Sample 15401 contains predominantly low-Ti green glass. No other pyroclastic glasses have been found in sufficient quantity (10 mg \approx 10,000 particles) to permit classical reflectance spectrometry (C.M. Pieters, personal communication).

If reflectance spectra could be correlated to chemical composition it might allow remote analysis of many lunar pyroclastic glass deposits. Such determinations could be ambiguous, however, if the deposits are heterogeneous. The extensive Taurus-Littrow dark mantle, for example, contains mainly black glass like 74001, mixed with orange glass similar to 74220. This determination was made based on telescopic measurements (4, 5) with 5-20 km spatial resolutions. Homogeneous deposits of smaller dimensions, if they exist on the Moon, cannot be identified by Earth-based measurements.

Microscope Photometry. We have for the first time collected reflectance spectra of individual pyroclastic glass spheres as small as $\sim 20 \mu\text{m}$ in diameter. Measurements were made over the wavelength range of 380- to 800-nm relative to a BaSO_4 reference standard. Spectra were obtained by scanning over the wavelength range in 5 nm steps. Measuring apertures were optimized to individual particle diameters. Further details of the microscope photometric technique are reported by Bradley et al. (6).

Figure 1 shows typical spectra of $\sim 100 \mu\text{m}$ diameter glass particles from samples 74220 (orange), 74001 (black), and 15401 (green). The orange glass spectrum is characterized by a gradual rise from the UV to around 600 nm, followed by a steep rise and a broad absorption feature longward of 700 nm. The green glass shows a rapid rise to approximately 560 nm, followed by a deep absorption feature centered in the infrared. These bands have been correlated with the abundances and oxidation states of iron and titanium in the glasses (7). The black glass spectrum is essentially flat throughout the measured range. The locations of absorption features closely match those measured for bulk samples (2,3), though the bulk samples exhibit more pronounced red slopes.

NEW PROSPECTS FOR ANALYZING LUNAR GLASS: Allen C.C. et al.

The peak reflectivities of individual glass particles depend on size and degree of roughness, with broken particles having the most prominent spectral features. Values for green glass range from 7-16%, while orange glass ranges from 8-40%. In both cases slope trends and peak locations are similar among all particles. Black glasses all have nearly identical spectra.

Particles which have been measured by microscope photometry can subsequently be classified by chemical type using the electron microprobe. Thus, chemical compositions can be correlated with reflectance spectra even for extremely rare particles. We intend to use this combination of techniques to quantify the colors of the entire range of pyroclastic glasses, using individual particles picked from lunar soil samples.

Clementine. The Clementine spacecraft, due to map the moon from polar orbit in 1994, will carry four multispectral sensors. The high resolution camera, with an optimum resolution of 23 m, has been targeted to all identified pyroclastic deposits on the nearside. It will provide multispectral images through filters centered at 415, 560, 650, and 750 nm.

We analyzed our spectra of individual particles to determine if the three glass types could be distinguished using only data from the Clementine filter passbands. To emphasize spectral features and minimize albedo differences, reflectivity ratios among several bands were compared. Figure 2 shows a plot of 650/560 nm ratios vs. 750/560 nm ratios. This presentation was chosen to emphasize differences among the spectral types.

Figure 2 demonstrates a strong clustering of reflectivity ratios according to particle composition. We conclude that Clementine data would be adequate to differentiate among deposits of essentially pure orange, black, and green glass. With a resolution of 23 m, the Clementine high-resolution sensor could locate such concentrations in larger deposits which are heterogeneous at telescope resolution.

Determining the chemical compositions of pyroclastic glass deposits will significantly aid our understanding of lunar volcanism. Similarly, locating the sources of individual glass particles in lunar soils will place new constraints on models of regolith development.

References. (1) Delano, 1986, *PLPSC16*, D201 (2) Adams et al., 1974, *PLSC5*, 171 (3) Heiken et al., 1991, *Lunar Sourcebook*, p.211 (4) Gaddis et al., 1985, *Icarus*, 61, 461 (5) Hawke et al., 1991, *PLPSC21*, 377 (6) Bradley et al., 1994, this volume (7) Bell et al., 1976, *PLSC7*, 2543

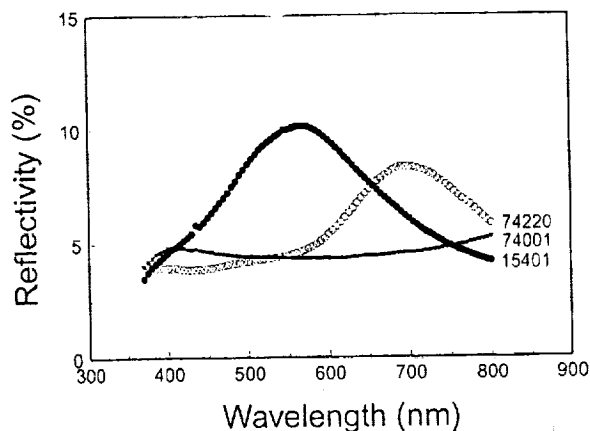


Figure 1. Representative spectra of individual pyroclastic glass particles ~100 μm in diameter

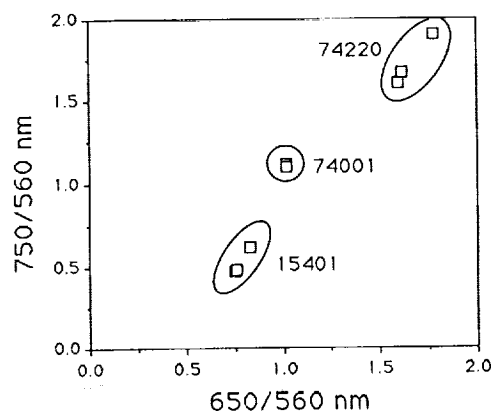


Figure 2. Pyroclastic glass particle color ratios using Clementine filter passbands

p. 2
2943

REDUCTION OF LUNAR MARE SOIL AND PYROCLASTIC GLASS

C.C. Allen, Lockheed ESC, Houston, TX R.V. Morris and D.S. McKay, NASA/JSC, Houston, TX

Mare soil and orange and black pyroclastic glass were reduced in hydrogen gas at temperatures of 900-1100°C. The experiments support studies of regolith maturation, lunar volcanism, and the production of oxygen on the Moon. The most reactive component in the high-Ti soil was FeO in ilmenite, which was completely reduced to iron metal at all temperatures. Vitreous orange glass crystallized and was partially reduced to iron metal, pyroxene, and minor olivine. Initially devitrified black glass was similarly reduced and converted to iron metal, pyroxene, and minor olivine. The degree of reaction in both glasses increased with temperature.

Lunar Samples. Sample 75061 is a high-Ti mare soil which contains pyroxene, plagioclase, ilmenite, minor olivine, agglutinates, and a trace of glass (1). Sample 74220 is the Apollo 17 "orange soil," an essentially pure pyroclastic glass deposit (1). Orange spheres, which comprise the bulk of this sample, are completely glassy. Black spheres are the same glass partly recrystallized to olivine, ilmenite, and spinel.

Experimental/Analytical. The samples were reduced in a vertical tube furnace, with weight change continually monitored, as in previous tests with lunar simulants (2). All samples were run "as received." Samples (200-300 mg) were placed into the hot furnace and reduced in flowing hydrogen for three hours. The fO_2 was kept below the iron-wüstite buffer.

Bulk samples and thin sections were examined by SEM and EDS. Minerals were identified by XRD. Iron Mössbauer spectroscopy (FeMS) was used to indicate the oxidation states and relative abundances of iron in the glass and mineral phases. The abundances of alpha iron metal in the reduced samples were also determined by vibrating sample magnetometry (VSM).

Results - Mare Soil. Lunar mare soil 75061 was reduced in three experiments at 900-1050°C. Sample weights decreased rapidly for the first 20 minutes and then fell more slowly, remaining essentially constant after the first hour. The total weight losses ranged from 2.6-3.0 wt.%, increasing slightly with increasing temperature.

Most of the weight loss was due to reduction of ferrous oxide to iron metal, with concomitant release of oxygen. This sample contained FeO in several phases, including pyroxene, ilmenite, olivine, and agglutinitic and pyroclastic glass. The VSM data indicated that 47-54% of the Fe^{2+} in the starting sample was reduced to alpha iron metal. This was equivalent to the loss of 1.9-2.2% of the starting sample weight as oxygen. The XRD and FeMS spectra (Fig. 1) show that a portion of the remaining Fe^{2+} was reduced to gamma iron in experiments above the transition temperature of 911°C.

The most reactive phase in this Ti-rich soil was ilmenite. In our experiments the Fe^{2+} in ilmenite was completely reduced. No ilmenite remained in these samples, to the detection limit of FeMS and XRD. All ilmenite grains examined by SEM showed characteristic phase separation and reduction textures (Fig. 2). Other FeO-bearing phases showed much less evidence of reduction. Olivine grains exhibited small-scale reduction textures in SEM images. Olivine peaks in the FeMS spectra became smaller with increasing temperature. Agglutinitic glass underwent partial reduction, with increasing concentrations of iron metal particles as reduction temperature increased from 900 to 1050°C. Minor reduction of pyroxene was documented in the 1050°C experiment by SEM and FeMS.

These results are in close agreement with data from previous reduction experiments utilizing crushed lunar basalt (3). They also provide an extreme "end member" for studies of reduction as a cause of lunar soil maturation.

REDUCTION OF LUNAR SOIL AND GLASS: Allen C.C. et al.

Results - Pyroclastic Glass. Pyroclastic glass 74220 was reduced in four experiments at 900-1100°C. Weight loss was rapid for the first 10-20 minutes, and then became more gradual. Total losses ranged from 2.2-5.4 wt.%, increasing steadily with temperature.

The XRD and FeMS spectra of all reduced glass samples were dominated by the peaks of iron metal (Fig. 3). The metal occurred as micrometer-scale blebs scattered throughout each glass particle (Fig. 4). The VSM data indicated that 32-68% of the Fe^{2+} in the starting sample was reduced to alpha iron, with the percentage increasing with temperature. This was equivalent to the loss of 1.7-3.3% of the starting sample weight as oxygen. A significant portion of the remaining Fe^{2+} formed gamma iron.

Orange glass underwent devitrification in all of the experiments. Pyroxene crystals grew steadily with temperature, from less than 1 μm across in the 900°C sample to well over 10 μm at 1100°C. At this temperature the orange glass was totally devitrified to pyroxene and iron metal, plus minor olivine and titanium oxide (Fig. 4). Black glass spheres also underwent striking changes. At higher temperatures ever greater amounts of FeO in the glass and crystals were reduced to metal. Ilmenite was reduced to iron plus titanium oxide and olivine to iron plus pyroxene. In the 1100°C sample, spheres which were initially crystalline were almost indistinguishable from those which were initially vitreous.

Reduction and devitrification experiments on orange and black glass provide constraints on conditions during lunar pyroclastic eruptions. They also support the contention that pyroclastic glass would be an ideal feedstock for lunar oxygen production (4).

References. (1) Heiken and McKay, 1974, *PLSC5*, 843 (2) Allen et al., 1993, *Icarus*, 104, 291 (3) Gibson et al., 1994, submitted *JGR* (4) Hawke et al., 1990, *PLPSC20*, 249

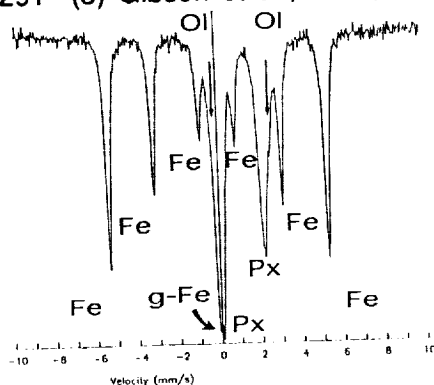


Figure 1. FeMS spectrum of mare soil 75061, reduced at 1050°C



Figure 2. Ilmenite from mare soil 75061, reduced at 1050°C

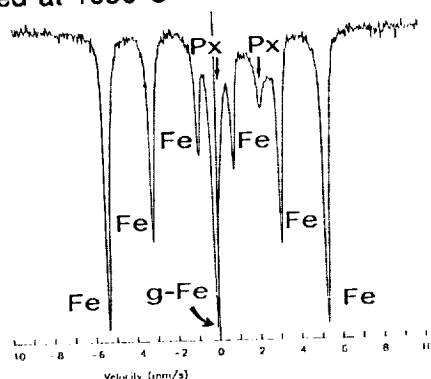


Figure 3. FeMS spectrum of pyroclastic glass 74220, reduced at 1100°C



Figure 4. Pyroclastic glass from 74220, reduced at 1100°C

CALORIMETRIC THERMOMETRY OF METEORITIC TROILITE: PRELIMINARY THERMOMETER RELATIONSHIPS. Judith H. Allton¹, Susan J. Wentworth¹, and James L. Gooding². ¹C23, Lockheed Engineering and Sciences Co., Houston, TX 77058. ²SN2, NASA/Johnson Space Center, Houston, TX 77058 USA.

Summary. Thermodynamic properties of the α/β phase transformation in terrestrial troilite (FeS), as measured by differential scanning calorimetry (DSC), vary systematically with prior thermal history of the troilite, as imposed under laboratory conditions. Both the transition temperature and enthalpy change for the α/β transformation decrease with increasing maximum temperature of prior heat treatment. DSC measurements on troilite from various meteorites indicate clear differences in the α/β thermodynamic properties that are consistent with differences in the natural thermal histories of the meteorites.

Introduction. Our previous work [1,2] established the feasibility of DSC as a technique for measuring solid-state phase changes in troilite as possible indicators of troilite thermal histories. Here we report new data that confirm the separation of elemental compositions from thermal history as influences on DSC data for troilite. In addition, we present new evidence that thermal histories can be preserved in troilite samples that are stored at temperatures near 300 K.

Experimental Procedure. Individual samples of terrestrial troilite (from Del Norte County, California) were heated under Ar at 10 K/min and to various maximum temperatures up to the 1000 K operating limit of our DSC instrument [1,2]. After cooling at 10 K/min, each sample was re-heated at 10 K/min, under Ar, to the same maximum temperature as before; calorimetric data were collected and calibrated using temperature and enthalpy standards. Calibrated DSC analyses were performed on troilite extracted from the Mundrabilla (octahedrite) and PAT91501 (L7 chondrite) meteorites; DSC analyses were also made for bulk silicate powder of EET83213 (L3 chondrite). After heating, representative troilite samples were prepared as polished grain mounts and subjected to elemental analysis by electron microprobe.

Results and Interpretations. Troilite exhibits two solid-state phase transitions [1,2] but preliminary parameterization of data is based only on the stronger of the two, namely, the α/β transformation. Results for Del Norte clearly show systematic changes in the α/β transformation as a function of previous thermal history. Both the temperature and enthalpy change of the α/β transformation vary inversely with maximum temperature of prior heating (Fig. 1).

To test survivability of the α/β "memory" of thermal history, we analyzed a troilite sample that had been stored in air at about 300 K for more than one year

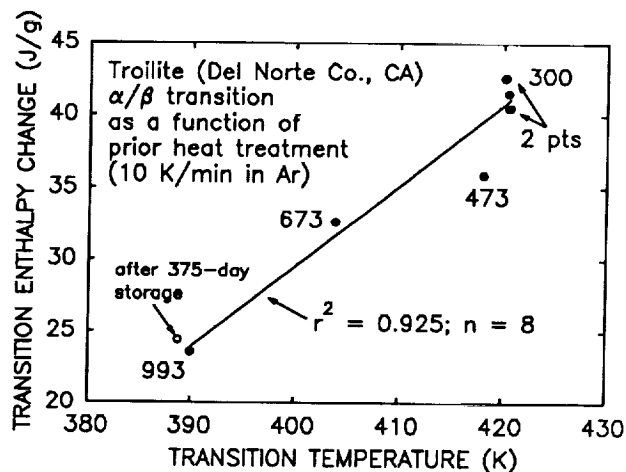


Figure 1. Thermometer relationship, based on the α/β phase transformation, determined for artificially heated samples of Del Norte troilite. The three-digit number by each point indicates the Kelvin temperature experienced during prior heat treatment of the sample. The cluster of points labelled "300" indicates scatter measured for replicate samples of the natural (unheated) troilite. Filled circles depict a series of samples that were analyzed within a few days of heat treatment; the open circle represents a sample analyzed more than one year after heat treatment.

Calorimetric Thermometry of Meteoritic Troilite: Allton J. H. et al.

after it was artificially heated to 993 K. As shown in Fig. 1, the thermodynamic properties measured for the α/β transformation of previously heated troilite were essentially the same for a sample analyzed 375 days after heating compared with a separate sample analyzed only 6 days after heating to the same maximum temperature. Although a one-year baseline cannot be claimed as significant on the cosmic timescale, it at least demonstrates that troilite thermal memory does not rapidly degrade under mild storage conditions.

Results for meteoritic troilite show appreciable scatter for a given meteorite but, nonetheless, indicate systematic differences among individual meteorites (Fig. 2). Dissolved impurities might be expected to depress the temperatures and enthalpies of first-order phases changes, but the systematic differences in the troilite α/β transformations are not attributable simply to compositional differences. If trace elements controlled the α/β transformation, PAT91501 troilite, which is lowest in trace elements (Table 1), should probably not possess properties intermediate between those of Mundrabilla and Del Norte (Fig. 2). The Del Norte and Mundrabilla samples contain similar levels of trace elements (Table 1) but exhibit substantially different properties for the α/β transformation. Although trace-element chemistry probably plays a minor role, the systematic differences among the meteoritic troilites probably reflect separate, distinctive thermal histories.

Application of the preliminary Del Norte "thermometer" (Fig. 1) to the meteorite data (Fig. 2) suggests a trend of maximum planetary temperatures that decrease from Mundrabilla to PAT91501 to EET83213, which is qualitatively consistent with petrology. Iron meteorites probably cooled from 1800 K [3] but chondrites probably accreted at < 1000 K [4]. After further calibration, including possible effects of heating/cooling rates, more precise calorimetric thermometry of meteoritic troilite should become possible.

Acknowledgments. Troilite samples were provided by C. Moore (Del Norte), E. Scott (Mundrabilla), and the Meteorite Working Group (PAT91501; EET83213 powder prepared by E. Jarosewich). This work was supported by the NASA Planetary Materials and Geochemistry Program (J. Gooding, PI).

References. [1] Allton J. H. and Gooding J. L. (1993) *Lunar Planet. Sci. XXIV*, Lunar and Planetary Institute, Houston, TX, 21. [2] Allton J. H. et al. (1993) *Meteoritics*, 28, 315. [3] Haack H. and Scott E. R. D. (1992) *J. Geophys. Res.*, 97, 14,727. [4] Haack H. et al. (1992) *Geophys. Res. Lett.*, 19, 2235.

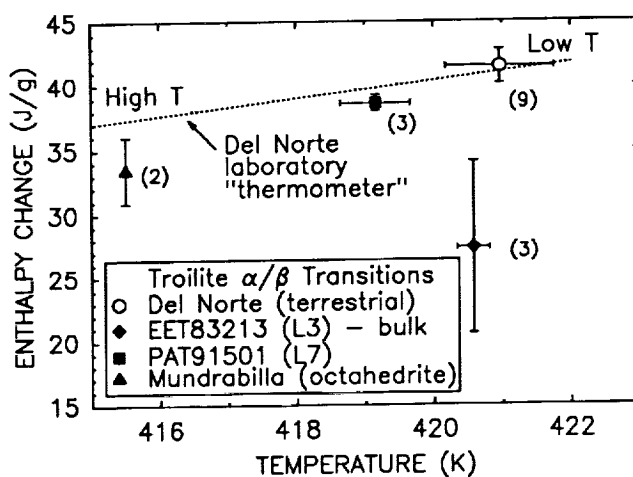


Figure 2. Thermodynamic properties of the α/β phase transformation in natural (not previously heated) troilite from various meteorites compared with the laboratory thermometer relationship determined for terrestrial troilite (Fig. 1). Each point represents the average result for the number of replicate samples shown in parentheses; error bars indicate one standard deviation of the mean. Results for EET83213, based on bulk samples of the meteorite, plot systematically low on the y-axis as a consequence of incomplete corrections for matrix effects.

Table 1. Trace-element compositions of troilite determined by electron microprobe (wt. %; 10-grain avg. \pm 1 std. dev.)

	Ni	Cr	Mn
Del Norte	0.41 \pm 0.17	0.01 \pm 0.01	0.01 \pm 0.01
Mundrabilla	0.04 \pm 0.03	0.52 \pm 0.27	0.07 \pm 0.04
PAT91501	0.10 \pm 0.04	0.06 \pm 0.04	0.02 \pm 0.01

C-, N-, O-, Si-, AND Ti-ISOTOPIC RATIOS OF LOW DENSITY GRAPHITE GRAINS FROM MURCHISON INDICATE A SUPERNOVA ORIGIN;
 Sachiko Amari^{1,2}, Ernst Zinner¹ and Roy S. Lewis², ¹McDonnell Center for the Space Sciences and the Physics Department, Washington University, One Brookings Dr., St. Louis, MO 63130, ²Enrico Fermi Institute; University of Chicago, 5630 Ellis Ave., Chicago IL 60637

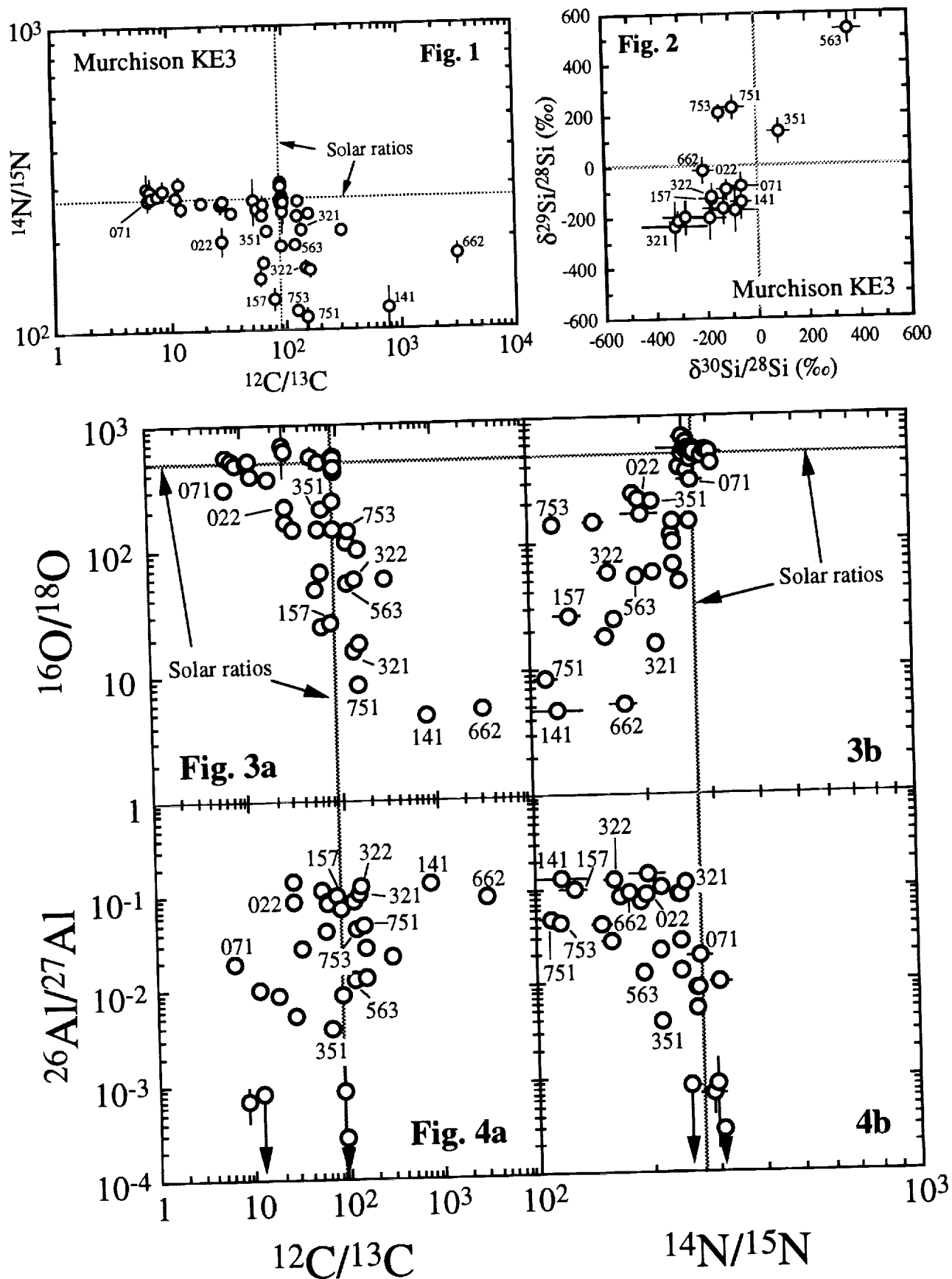
Interstellar graphite grains larger than 3 μm and with densities 1.57-2.12 g/cm³ have extremely large $^{18}\text{O}/^{16}\text{O}$ ratios, ranging up to 100 \times solar. These excesses, together with large variations in the Si-isotopic ratios and ^{49}Ti excesses, suggest a supernova origin for these grains.

Interstellar graphite from the Murchison CM2 meteorite has shown a bewildering variety of isotopic compositions in C, N, O, Mg, Si and the noble gases, indicating that it originated from several types of stellar sources [1,2]. One problem with identifying particular stellar sources is that, unlike interstellar SiC, graphite generally has low concentrations of other elements, which makes it difficult if not impossible to make correlated isotopic measurements of several elements in single grains. An exception are grains of low density, which have higher trace element contents and thus offer the chance to measure O, Si and Mg isotopes in addition to those of C and N [3,4]. Here we report correlated isotopic measurements of C, N, O, Mg and Si in individual grains from Murchison separate KE3 (1.57-2.12 g/cm³; nominal grain size $\geq 3 \mu\text{m}$). Of the grains found in KE3 we selected round grains for isotope analyses by ion microprobe spectrometry. In a few unusually large grains we succeeded in also analyzing Ca and Ti isotopes.

The C- and N-isotopic compositions of 47 grains are shown in Fig. 1. Most grains have isotopically heavy to normal C, and heavy to normal N. Si-isotopes were measured in 46 grains; 14 of them have anomalies outside of 2σ errors (Fig. 2). While most grains have deficits in ^{29}Si and ^{30}Si , a few have excesses in ^{29}Si and two grains excesses in both ^{29}Si and ^{30}Si , which are larger than 400‰ in grain 563. We determined $^{16}\text{O}/^{18}\text{O}$ ratios in 40 grains (Fig. 3); 26 of them have ^{18}O excesses, ranging up to a factor of 100, much larger than ^{18}O excesses previously observed [4,5]. We also measured $^{16}\text{O}/^{17}\text{O}$ ratios in 23 grains; they are normal with the sometimes fairly large errors. However, it is clear that, if anomalies in the $^{16}\text{O}/^{17}\text{O}$ ratio exist, they are much smaller than those in $^{16}\text{O}/^{18}\text{O}$. There is a rough correlation between the $^{16}\text{O}/^{18}\text{O}$ and $^{14}\text{N}/^{15}\text{N}$ and $^{12}\text{C}/^{13}\text{C}$ ratios; grains with ^{18}O excesses have the tendency to be enriched in ^{12}C and ^{15}N (Fig. 3). Of 38 grains analyzed for Mg-Al, 27 have large ^{26}Mg excesses with inferred $^{26}\text{Al}/^{27}\text{Al}$ ratios ranging up to 0.15 (Fig. 4). While $^{25}\text{Mg}/^{24}\text{Mg}$ ratios are usually normal, three grains have ^{25}Mg excesses: #022: $654 \pm 250\%$; #157: $1585 \pm 602\%$; #753: $562 \pm 111\%$ (2σ errors). Of the 8 grains in which we measured Ca and Ti, all have ^{49}Ti excesses, ranging up to $1720 \pm 972\%$ (2σ) in grain 141. Grain 662, the grain with the largest $^{12}\text{C}/^{13}\text{C}$ ratio and largest ^{18}O excess (Fig. 3) has, in addition to a ^{49}Ti excess of $862 \pm 90\%$, excesses of $175 \pm 72\%$ and $429 \pm 132\%$ (2σ) in ^{42}Ca and ^{43}Ca , respectively. The low density graphite grains show a similarity in their C, N, Si and Ti isotopic compositions to SiC grains of type X for which a supernova origin has been invoked [6]. The case for a SN origin of the graphite grains is strengthened by the large ^{18}O excesses observed in these grains. While Wolf-Rayet stars can have ^{18}O enrichments on their surface during the WN-WC transition, it appears doubtful that ^{18}O excess of more than a factor 10 can be achieved [7]. Massive pre-SN stars, on the other hand, have a $^{16}\text{O}/^{18}\text{O}$ ratio of ~ 5 in the He-burning zone, the only layer with C/O > 1 [8]. This ratio is comparable to the smallest ratios observed in the carbon grains of this study.

References: [1] Amari S. *et al.* (1993) *Nature* **365**, 806 [2] Amari S. *et al.* (1994) in preparation [3] Amari S. *et al.* (1993) LPS XXIV, 29 [4] Amari S. *et al.* (1993) *Meteoritics* **28**, 316 [5] Hoppe P. *et al.* (1992) *Meteoritics* **27**, 235 [6] Amari S. *et al.* (1992) *Ap. J.* **394**, L43 [7] Arnould M., pers. commun. [8] Weaver T. A. and Woosley S. E. (1993) *Phys. Rep.* **227**, 65.

MURCHISON GRAPHITE OF SUPERNOVA ORIGIN: Amari et al.



LITHOSPHERIC CONTROLS ON THE FORMATION OF VALLES MARINERIS. F. Scott Anderson and Robert E. Grimm, Department of Geology, Arizona State University, Tempe, AZ 85287-1404.

Introduction. Rifting hypotheses for Valles Marineris are based upon the idea that tectonic tensional stresses, most likely associated with the formation of Tharsis, opened the troughs [1]. On Earth, variations in crustal thickness and composition, heat flow, and extension rate are known to control rift style [2-4]. As the first of several quantitative studies of Valles Marineris, we adopt a simple one-dimensional model [4] to test the hypothesis that reasonable values of these parameters alone can account for the general morphology and timing of the rift.

Model. The 1D model calculates the change in vertically integrated strength of the lithosphere after a proscribed extensional strain, including time-dependent thermal advection and conduction. The strength of the lithosphere is assumed to be controlled by frictional sliding near the surface and by ductile creep at depth. The latter is sensitive to temperature, composition, and strain rate, whereas the former largely depends only on gravity. Rifts where extension is rapid and vertical advection of heat dominates over conduction are weakened due to uplifted isotherms, resulting in a localized runaway of deformation. Such deformation is characteristic of the "narrow mode" of rifting like the Rio Grande or slightly more complex, anastomosing structures like East Africa. Rifts where extension is slow are strengthened due to the replacement of weak crust by strong mantle at quasi-steady-state temperatures. It is assumed that it is then easier for deformation to move outwards rather than continue in the same location, where the entire process repeats. Such broad lateral sequences of rifts are termed the "wide" mode and are typified by the northern Basin and Range. "Core-complex mode", which is characteristic of parts of the southern Basin and Range, is predicted for narrow rifts in which temperatures are high enough to result in flow of the lower crust [4].

Application to Mars. A range of strain rate, heat flux, and crustal thicknesses values were tested. A minimum strain rate may be computed from the minimum estimated strain and the maximum estimated formation interval. A minimum strain rate of $\sim 4 \times 10^{-18} \text{ s}^{-1}$ follows from the two-billion-year formation interval of Valles Marineris [1] and a final strain of .25, typical of the strains in individual troughs such as Ius and Tithonium. A minimum extension rate of $\sim 10^{-3} \text{ cm/yr}$ follows for an extending region 100 km wide. Parameterized convection models for the global thermal evolution of Mars [5] predict that heat flux varied considerably over the period of Chasmata formation (30-100 mW/m²), and indirect mapping of lithospheric thickness around the planet suggests that strong regional variations in heat flux were present [6]. The regional crustal thickness around Valles Marineris is taken to be 40-60 km [7]. The lithosphere was assumed to be composed of a diabase crust [8] overlying a dunite upper mantle [9].

Different combinations of these parameters will uniquely determine the rift style, but the exact mode for Valles Marineris is unclear. The morphology of Valles Marineris is least similar to that of a core complex. Perhaps the most intuitive choice is a narrow rift, due to the great length of the Ius-Melas-Coprates string of canyons. However, the possibility that Valles Marineris is a wide rift should not be ruled out, as two to possibly five incipient parallel troughs are present. These arguments suggest that Valles Marineris is one of three possible cases: (i) A narrow rift, (ii) An incipient wide rift that stopped extending shortly after formation, (iii) A rift that is on the narrow-wide rift boundary. Solutions that exclude the core complex mode alone provide significant constraints without discriminating between wide and narrow rift modes.

Results. Figure 1 shows the calculations for Valles Marineris as functions of crustal thickness H and heat flux Q (cf. Fig. 12 in [4]). Positive values for the change in vertically integrated strength, representing wide rifting, are contoured for different values of extension rate v_x . The contours may be interpreted as the maximum rifting velocity allowable at a given Q and H to achieve wide rifting. It is important to note that wide rifting cannot occur in this model without a ductile lower crust; therefore wide rifting is easier on Earth than on Mars because of the more felsic composition and greater radioactive heat generation in terrestrial continental crust. However, the slow extension rates likely for Mars partially offset this. The transition to core complex from wide rift is clear where the strength difference changes from positive to negative, but the direct transition from narrow rift is implied from the inflection of the strength difference curve, which, for the case $v_x = 0.01$, is shown as a dashed line in Fig. 1. Similar extensions of other v_x may be inferred.

Rejection of the core complex mode alone for Valles Marineris constrains the heat flux and crustal thickness to lie within $QH < 3000 \text{ mW/m}^2\text{-km}$ for $v_x = 0.01 \text{ cm/yr}$; this agrees well with the expected ranges of Q and H . For

VALLES MARINERIS: Anderson and Grimm

higher v_x , the direct transition from narrow to core complex mode lies approximately along the axis of the curves and is only slightly more restrictive. Taken together, $Q < 80 \text{ mW/m}^2$ at the time of rifting. If Valles Marineris is interpreted as an aborted wide rift, then Q lies in the range $30\text{--}80 \text{ mW/m}^2$ for $v_x = 0.01 \text{ cm/yr}$; if it is a narrow rift, then $Q < 40 \text{ mW/m}^2$. A higher extension rate of 0.1 cm/yr restricts the wide rift mode to close to 60 mW/m^2 and the narrow rift mode to less than this value. Wide rifting at rates characteristic of terrestrial extension, $\geq 1 \text{ cm/yr}$, are completely ruled out.

Concluding Discussion. The 1D extension model confirms that narrow rifts can be produced on Mars at the expected range of heat flow and crustal thickness and composition appropriate for the time of canyon formation; in particular, $Q < 60\text{--}80 \text{ mW/m}^2$. However, wide rifts are more difficult to initiate, and are restricted to extension rates $< 0.1 \text{ cm/yr}$.

This work provides the foundation to address three principal outstanding questions for Valles Marineris: (1) Why are the canyons so deep? (2) What was the nature of lithospheric weakness (aquifers, pre-existing structures) that localized extension within a presumably more homogeneous regional stress field? (3) Did the rift propagate with time, as suggested by the inability of the best stress models to extend at both ends of the canyon system simultaneously [10]? Finite-element modeling in both section and plan view will provide sufficient flexibility to answer these questions.

References [1] B.K. Luchitta et al, in *Mars* (eds. H. Kieffer, B. Jakosky, C. Snyder, and M. Matthews), Ch. 14, Univ. of Ariz. Press, 1992; [2] N. Kusznir and R. Park, *Spec. Pub. Geol. Soc. Lond.*, 28, 35, 1987; [3] P. England, *JGR*, 88, 1145, 1983; [4] W.R. Buck, *JGR*, 96, 20161, 1991; [5] G. Schubert et al, in *Mars* (op. cit), Ch 5; [6] S. Solomon and J. Head, *JGR* 95, 11073, 1990; [7] G. Balmino et al., *JGR*, 87, 9735, 1982; [8] Y. Caristan, *JGR*, 87, 6781, 1982; [9] P. Chopra and M. Paterson, *Tectonophys.*, 78, 543, 1981; [10] W. Banerdt et al., *JGR*, 87, 9723, 1982.

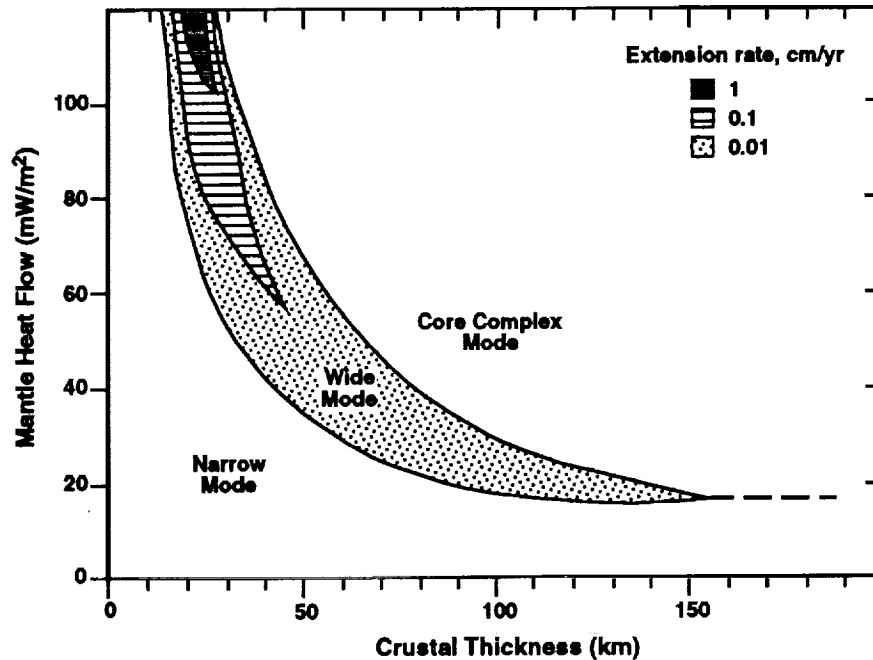


Figure 1. Rift mode on Mars. Expected range of heat flow ($30\text{--}100 \text{ mW/m}^2$) and crustal thickness ($40\text{--}60 \text{ km}$) agree with either narrow or wide mode but not core complex. Wide rifting further requires $v_x < 0.1 \text{ cm/yr}$.

BUNTE BRECCIA-LIKE DEPOSITS WITHIN THE MANSON IMPACT STRUCTURE (IOWA): EVIDENCE FOR IMPACT INTO A SHALLOW MARINE ENVIRONMENT?

ANDERSON, Raymond R. and WITZKE, Brian J., Iowa D.N.R. Geological Survey
Bureau, 109 Trowbridge Hall, Iowa City, Iowa 52242-1319.

Ongoing study of 12 research cores recovered from the Manson Impact Structure (MIS) in north-central Iowa has advanced our understanding of the largest intact impact structure in the U.S. and one of the best preserved complex craters in the world. Of the impact rocks encountered in the cores, one of the most enigmatic is the **Phanerozoic Clast Breccia (PCB)**, a poorly consolidated polymict breccia that is preserved as the upper impact unit in all areas of the MIS. The **PCB** is a matrix-supported breccia with clasts ranging in size from mm to in excess of 100 m. Clasts are dominated by Cretaceous marine rocks, with subordinate Paleozoic carbonate-dominated sedimentary rock clasts, minor clasts of Proterozoic Red Clastics, and very rare clasts of Proterozoic crystalline rocks and impact meltrock. The abundance of each clast lithology is inversely related to its pre-impact depth of burial. Parallel deformation features and other indicators of a hypervelocity impact are very rare in these clasts. The matrix is a light gray, calcareous, sandy, silty shale that contains scattered common Cretaceous Foraminifera in some samples. **PCB** clast composition varies within the MIS, especially near its base, reflecting lithologies in underlying breccia units. The **PCB** is compositionally similar to the Bunte Breccia described from the Ries Crater (Germany) [1, 2]. Ries Bunte Breccia is a polymict breccia composed of clastic material derived from all stratigraphic horizons of the target, however "the frequency of (clasts from) a given target horizon is inversely proportional to its pre-impact position in the Ries target" [1, p. 42]. It is interpreted as a mixture of proximal impact ejecta and material excavated by secondary cratering processes, mobilized and emplaced by turbulent debris surge. At the Ries Crater, Bunte Breccia is found only in the area immediately outside the crater rim. At Manson all impact materials not structurally preserved within the crater have been removed by post-impact erosion. However, unlike Ries Bunte Breccia, the **PCB** is found inside the crater, recovered in cores from the Terrace Terrane, the Crater Moat, and even in the Central Peak Pit. In fact, petrographic examination of all drill cores and most available cutting samples collected during the drilling of water wells within the MIS show the **PCB** to be preserved as the uppermost impact-related unit in most areas of the crater (Figure 1). Manson **PCB** appears to be Bunte Breccia that was originally deposited outside the MIS, but subsequently remobilized and transported into the crater as debris flows. The **PCB** was transported back into the Manson crater with sufficient energy to carry it for at least 17 km, across the Terrace Terrane, to the floor of the Crater Moat (about 2 km below the crater rim), and up at least 2 km to the top of the Central Peak, where it is preserved in the Central Peak depression.

Another clastic unit similar to the **PCB** was reported in the Chesapeake Bay Impact Crater [3]. The Chesapeake Bay Crater is thought to have been formed by an impact into a thick sequence of unconsolidated sediment overlain by about 200-500 m of sea water. The **PCB**-like unit, informally called the *Exmore boulder bed* or *Exmore breccia*, was interpreted as a Bunte Breccia-like material that was originally deposited outside the crater, but was swept back into the crater by the return of water displaced by the impact (Powars, 1994, pers. comm.). Like the *Exmore breccia*, a likely mechanism for driving the **PCB** debris flows into the Manson Crater is water, surging back into the crater following an impact into a shallow-marine environment. Stratigraphic investigations and paleogeographic reconstructions suggest that the Late Cretaceous Pierre Seaway had regressed out of Iowa and its eastern margin lay in central South Dakota at about 73 Ma, the age recently suggested for the Manson Impact and its proposed ejecta blanket in the Crow Creek Mbr of the Pierre Shale Fm [4]. The probable departure of the seas from the Iowa area at that time (demonstrated by the subaerial unconformity separating the Claggett and Bearpaw marine cycles) and the evidence suggesting that the Manson Crater was formed in a marine environment, raise questions concerning the 73 Ma age for the Manson impact.

Evidence for marine conditions at the time of the Manson impact does not necessarily preclude a K-T boundary age. Although most previous Late Cretaceous paleogeographic reconstructions suggest that the sea had regressed from the Midcontinent prior to the K-T boundary, the eastward erosional truncation of upper-most Cretaceous strata across North and South Dakota has removed direct evidence of eastern sedimentation. However, two lines of evidence are suggestive that a seaway remained along the eastern margin of the Western Interior at K-T time:

- 1) Nonmarine strata of the Hell Creek-Ludlow Fms progressively thin eastward between Maastrichtian-Paleocene units (the thinning trend extrapolates a K-T shoreline position in the eastern Dakotas).
- 2) Marine-related fish occurrences in upper-most Maastrichtian channels of the Hell Creek Fm provide indirect evidence that a seaway persisted across parts of the Dakotas at K-T time (see [5]).

It appears likely that the western-derived clastic wedge (Hell Creek Fm) had not advanced into the eastern Dakotas or western Iowa at K-T time, leaving open the possibility that a K-T impact in the Manson area would have occurred in a shallow marine setting. Biostratigraphic and depositional studies of Cretaceous rocks in the Manson Structure are needed to determine the timing and environmental setting of the impact, and to independently evaluate significant discrepancies between published radiometric dates from Manson (65 vs 73 Ma).

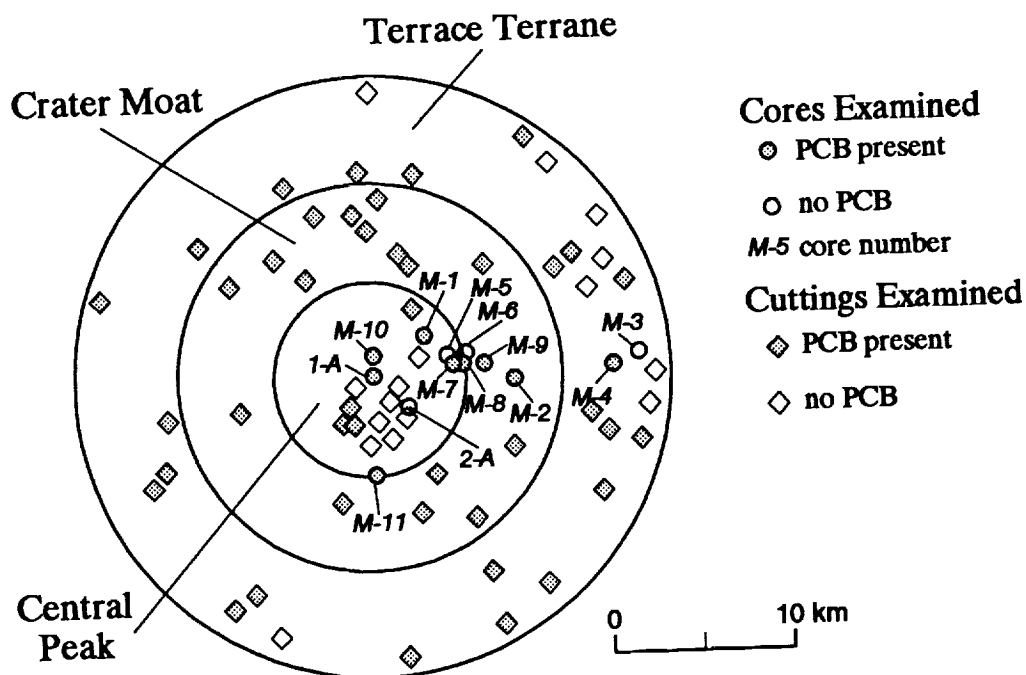


Figure 1. Location of Phanerozoic Clast Breccia (PCB) as identified by petrographic analysis

References Cited:

- [1] Hörz, F. (1982) *GSA SP-190*, 39-54. [2] Newsom, H.E., Graup, G., Iseri, D., Geissman, J.W., and Keil, K. (1990) *GSA SP-247*, p 195-206. [3] Powars, D.S., Poag, C.W., and Mixon, R.B. (1993) *GSA Abs. with Prog.*, **25**, 6, A-378. [4] Izett, G.A., Cobban, W.A., Obradovich, J.D., and Kunk, M.J. (1993) *Science* **262**, 729-732. [5] Bryant, L.J. (1989) *Univ. Calif. Publ. Geol. Sci.* **134**, 107p.

SURFACE CHARACTERISTICS OF STEEP-SIDED DOMES ON VENUS AND TERRESTRIAL SILICIC DOMES: A COMPARISON *Steven W. Anderson*, Black Hills State University, Spearfish SD 57799-9102, *David A. Crown*, Department of Geology and Planetary Science, University of Pittsburgh, Pittsburgh, PA 15260, *Jeffrey J. Plaut and Ellen R. Stofan*, Jet Propulsion Laboratory, California Institute of Technology, 4800 Oak Grove Drive, Pasadena, CA 91109

A silicic composition for steep-sided Venusian domes has recently been proposed on the basis of similarities in thickness, planform, and gross topographic profile to terrestrial rhyolitic and dacitic domes [1-4]. However, there are significant morphologic, volcanologic, and remote sensing characteristics that do not support direct comparison. For example, domes on Venus lack typically observed structures and morphological units, are an order of magnitude or more larger in volume and have smoother surfaces than terrestrial silicic lava domes [5-7].

In order to evaluate the validity of the silicic model for Venusian domes, we measured and analyzed topographic profiles, boulder-size distributions, and structural elements present on the surfaces of recent rhyolitic and dacitic domes in the western United States. These data show that steep-sided domes on Venus lack the progression in surface morphologies, characteristic large block size, and topographic variability found on terrestrial dome surfaces. Our study suggests that these discrepancies preclude direct comparison of domes on Venus and Earth, and that a re-evaluation of the silicic model for the origin of Venusian domes is required.

Lava domes at the Medicine Lake Highland Volcano and Long Valley Caldera

Our study concentrates on two large eruptive centers in the western United States. The Medicine Lake Highland volcano in northern California contains several rhyolitic and dacitic lava domes, with volumes ranging from $<3000 \text{ m}^3$ to $>1 \text{ km}^3$ [8,9]. The largest of these domes, Glass Mountain, shows a progression from early dacitic to late rhyolitic compositions. Many of the domes have little or no vegetation present on their surfaces and have been emplaced within the past 10000 years [9]. The Inyo dome chain in eastern California consists of 5 rhyolitic domes erupted along an en echelon dike [10]. Three of these domes, Obsidian, Deadman, and Glass Creek, were erupted 550-650 years ago [11]. The domes vary in volume from approximately 0.04 km^3 to 0.3 km^3 [11,12]. Anderson and Fink [8] calculated effusion rates ranging from 0.03 to $106 \text{ m}^3/\text{s}$ for rhyolitic domes in these two areas.

Surface Morphologies and Structures on Terrestrial Silicic Domes

Surface morphology maps of lava domes at Medicine Lake and Inyo have been compiled from aerial photographs as a basis for comparison to Venusian domes and for later field characterization. We have mapped four distinct morphologies consistently present on the various domes. **Vent regions** are characterized by high relief (>10 meters), the presence of fractures, and divergence of flow paths. Vent regions may also contain one or more crease structures, fractures indicative of spreading [8]. **Ridged areas** are characterized by regularly-spaced compressional ridges, with wavelengths between 10 and 15 meters and amplitudes of 1 to 5 meters. Small crease structures (1-10 meters in length) are typically present on ridge crests, with axial valleys oriented parallel to the direction of maximum compression [8]. **Jumbled regions** have more subdued topography and lack the characteristic structures present in vent regions and ridged areas [6]. Jumbled areas appear to represent a transitional zone between vent and ridged areas. **Flow fronts** on silicic domes typically have tens of meters of relief. They are commonly steeper than the angle of repose, owing to numerous, nearly vertical cliff faces. Most domes show a spatial progression of morphologies from vent regions in dome interiors, to jumbled regions, to ridged areas, to flow fronts, although the aerial extent of the various units may vary between domes.

Silicic lava domes exhibit three main surface lava textures. **Finely vesicular pumice (FVP)** is a carapace-forming unit that may occur in all of the morphologic units. The thickness of the FVP unit varies from 1-20 m, and is formed by vesiculation of the lava flow surface during eruption [12-14].

STEEP-SIDED DOMES AND TERRESTRIAL SILICIC DOMES: Anderson S.W. et al.

Coarsely vesicular pumice (CVP) is a volatile-rich layer of magma from the flow interior that may rise buoyantly to the surface in the form of diapirs [12,13]. The CVP unit forms as volatiles released during crystallization concentrate beneath the flow's cooled crust [12,13]. CVP is rarely found in the vent or jumbled regions, but is common in ridged areas and flow fronts. **Dense obsidian** is found in minor amounts on the flow surface and at flow fronts, and is commonly associated with CVP. Obsidian forms in the interior of the lava flow at depths where the weight of overburden prevents the vesiculation of magma, and is typically sandwiched between FVP and CVP units [12,13].

We have further characterized the vent, jumbled, and ridged morphologic units on the basis of their topographic profiles (measurements made at 25 cm intervals) and boulder-size distributions. We measured ~25 meter orthogonal transects at 19 different vent, jumbled, and ridged areas on silicic lava flows at Inyo and Medicine Lake Highland. Calculated RMS heights and average boulder sizes range from 30-82 and 30-82 cm respectively in vent regions, 30-56 and 27-71 cm in jumbled regions, and 43-187 and 18-36 cm in ridged areas. We consider RMS height and boulder-size measurements in vent regions to be minimum values, as many vent features are larger than the scale of the transects. The RMS height calculations confirm interpretations from aerial photographs that jumbled areas have the most subdued topography. Boulder-size measurements from Obsidian dome show a decrease in average boulder size with distance from the vent, suggesting that large features produced in the vent region become progressively degraded during surface flow, due to increased fracturing during cooling and transport.

Surface Characteristics of Steep-sided Venusian Domes

Preliminary analysis of the geologic characteristics of steep-sided Venusian domes using Magellan SAR images and altimetry data indicates that domes are typically characterized by smooth surfaces, pits, and radial, concentric and polygonal fractures [5]. Domes are circular to highly irregular in plan view with generally steep margins. Typically, domes are flat-topped or concave, but variations in relief on the upper surfaces are common. Two types of pits are observed: 1) centrally located collapse pits that may have concentric fractures, and 2) pits with prominent raised rims that are randomly located on dome surfaces and are most likely indicative of secondary eruptions.

Many aspects of Venusian dome morphology do not directly support comparisons with terrestrial silicic domes. For example, domes in southern Guinevere Planitia are generally comparable in radar roughness to their surroundings, whereas the surfaces of silicic domes on Earth are extremely rough [5,7]. Venusian domes are also directly associated with volcanic vents from which thin, lobate flows of similar morphology to terrestrial basaltic flows emanate. The domes also occur in groups with low shields, which are interpreted to be due to basaltic volcanism. Thin, lobate flows appear to originate from some domes, a relationship not observed at terrestrial silicic domes.

Conclusions

These results show that Venusian and terrestrial silicic domes have significantly different surface morphologies. Surface morphologies at silicic domes in the Inyo chain and at the Medicine Lake Highland volcano appear to exhibit complex relationships between cooling, fracturing and flow. Our study questions direct comparisons between terrestrial and Venusian domes based simply on morphology, and suggests that the silicic model for Venusian domes can only be validated through analysis of the relationships between morphology and emplacement mechanisms.

References: [1] Pavri, B., et al. (1992) *J. Geophys. Res.*, 97, 13445-13478. [2] McKenzie, D., et al. (1992) *J. Geophys. Res.*, 97, 15967-15976. [3] Head, J.W., et al., (1992) *J. Geophys. Res.*, 97, 13153-13198. [4] Guest, J.E., et al., (1992) *J. Geophys. Res.*, 97, 15949-15966. [5] Crown, D.A., et al., (1993) *Lunar Planet. Sci. Conf.*, XXIV, 355-356, LPI, Houston. [6] Plaut, J.J., et al., (1993) *EOS, Trans. Amer. Geophys. Union*, 74, 379. [7] Plaut, J.J., et al., (1994) this volume. [8] Anderson, S.W., and Fink, J.H. (1992) *Geol. Soc. Am. Bull.*, 104, 615-625. [9] Donnelly-Nolan, J.M. (1988) *J. Geophys. Res.*, 93, 4412-4420. [10] Fink, J.H. (1985) *J. Geophys. Res.*, 90, 11127-11133. [11] Sampson, D.E. (1987) *Geol. Soc. Am. Spec. Pap.*, 212, 89-102. [12] Fink, J.H., and Manley, C.R. (1987) *Geol. Soc. Am. Spec. Pap.*, 212, 77-88. [13] Fink, J.H. (1984) *Geol. Soc. Am. Bull.*, v. 94, 350-384. [14] Anderson, S.W., and Fink, J.H. (1990) *IAVCEI Proc. in Volc.*, 2, 25-46.

CRYPTOMARIA IN THE SCHILLER-SCHICKARD, MARE HUMORUM AND WESTERN OCEANUS PROCELLARUM AREAS: STUDIES USING DARK-HALO CRATERS:

Irene Antonenko and James W. Head, Dept. Geol. Sci., Brown Univ., Providence, RI 02912 USA

Summary: A number of dark halo craters were identified in the Schiller-Schickard area, a known cryptomare. Statistical considerations of these DHC's indicate that deposit thicknesses overlying the cryptomaria are consistent with those expected from an Orientale ejecta origin for this unit. Cryptomare thicknesses in Schiller-Schickard were found to be about 1.4 km, and NW of Humorum about 1.0-1.2 km, values comparable to other known maria. Similar approaches for adjacent regions west of Procellarum show evidence for patchy cryptomaria there.

Background: Dark halo craters (DHC) are evidence for the presence of cryptomaria underlying highlands material (1). Spectroscopy (2) and multispectral imaging (3) permit the confident identification of mare components and their mapping over the surface. The size and geometry of DHCs offers clues to the three-dimensional geometry of cryptomaria deposits and the deposits that overly them. Here we examine three areas using DHCs as such a tool. Craters must occur in a specific size range to produce a dark halo in the cryptomaria area. Small craters that do not penetrate to the cryptomare will not produce a dark halo; large craters penetrating through the cryptomare to the underlying highland material, will have highland ejecta which obscures the dark halo signature. The smallest observed DHCs should define the top of the cryptomare, and therefore the thickness of the overlying ejecta, while the largest observed DHCs should define the bottom. Thus, the thickness of the cryptomare can be obtained from the difference between the depth of the mare base and the thickness of the overlying ejecta.

Schiller-Schickard Area: Twenty-seven DHCs have been found in this region, located approximately 1400 km SE of Orientale. They are distributed somewhat evenly, ranging in distance 1000-1900 km from the center of Orientale. Depths of excavation for the 27 craters were estimated from their diameter, using Pike's depth/diameter equations (4). The minimum depths, so calculated, are plotted as a function of distance from Orientale (Fig. 1). Column heights represent the thickness of the overlying deposit (interpreted to be the Orientale ejecta unit) as determined from the size of the smallest DHC in each 100 km distance interval. These results are compared to theoretical ejecta decay models for an Orientale diameter of 900 km (6, 5), and of 620 km (6). The data are generally consistent with theoretical predicted values for ejecta from Orientale and thus support an Orientale source for the ejecta. Craters far from Orientale deviate from predicted values and this may be the result of the paucity of DHCs at this distance; i.e., the smallest craters observed are not necessarily the smallest craters possible.

Cryptomare thickness estimates can be plotted as a function of distance from Orientale (Fig. 2). Column heights represent the maximum depths minus the minimum depths for each 100 km distance interval. If a distance interval contains only one DHC, no value is thus entered. Cryptomare thickness determined by this technique can be seen to vary from about 1000-2000 m, with the average being approximately 1.4 km. This is a typical thickness for mare (7, 8).

North of Mare Humorum Area: This region is located just north and NE of Humorum, near the crater Gassendi. We have identified numerous DHCs in this area (Fig. 3), mostly south of Procellarum, over an area of about 200,000 km², about 3/4 the size of the Schiller-Schickard cryptomaria. This information further supports the hypothesis that this area is the site of a cryptomare deposit (9-11). We have used the major craters identified spectrally (9, 10) as containing mare components to make preliminary estimates of deposit thicknesses. One DHC, Gassendi G, was found to have pure highland debris exposed in the central part of the crater floor. This was interpreted to mean that the crater had penetrated to the pre-mare substrate (10). Application of Pike's equations (4) to the diameter of this crater yields a deposit depth estimate of 1540 m. If the overlying unit is Orientale ejecta and its thickness is comparable to that found at this range (~1400 m) in the Schiller-Schickard area, then we estimate the cryptomare thickness to be ~1040 m at Gassendi G. Examination of a DHC near Gassendi G suggests penetration into mare at depths of about 300 m, indicating a local cryptomare thickness of about 1240 m.

West of Oceanus Procellarum Area: Three DHCs are located west of Oceanus Procellarum (Fig. 3), and they occur as single isolated occurrences, rather than in clusters seen in Schiller-Schickard and NW of Humorum. We are investigating two hypotheses for this distribution: 1) The sparsity of DHCs may be due to the fact that this area is much closer to Orientale, the ejecta should be thicker, and only a few large craters will be able to penetrate to a cryptomare surface. 2) The cryptomaria exposed by the DHCs are small, disconnected, and widespread, more typical of the present distribution of mare ponds in this region (12-14). On the basis of our initial analysis and the results of mixing models using Galileo multispectral image data, we presently favor the latter hypothesis.

Conclusions: Ongoing analyses confirm earlier studies suggesting the presence of cryptomaria in the southwestern lunar nearside and provide additional evidence for their widespread nature, their configuration and deposit thickness, and the thickness of overlying units. Mare volcanism is shown to be an areally and volumetrically significant process in this area prior to the Orientale basin-forming event ~3.84 b.y. ago, a process of potentially comparable significance to that occurring in post-Orientale times.

LUNAR CRYPTOMARE: I. Antonenko and J. W. Head

References: 1) P. Schultz and P. Spudis, *PLPSC 10*, 2899, 1979. 2) J. Bell and B. Hawke, *PLPSC 12*, 665, 1981. 3) J. Head *et al.*, *JGR*, 98, 17149, 1993. 4) R. Pike, *GRL*, 1, 291, 1974. 5) T. McGetchin *et al.*, *EPSL*, 20, 226, 1973. 6) P. Schultz *et al.*, *PLPSC 12*, 181, 1981. 7) R. Dehon, *PLPSC 10*, 2935, 1979. 8) J. Head, *Moon and Planets*, 26, 61, 1982. 9) P. Lucey *et al.*, *PLPSC*, 21, 391, 1991. 10) B. Hawke *et al.*, *GRL*, 20, 419, 1993. 11) J. Mustard *et al.*, *LPSC 23*, 957, 1992.; *ibid.*, this volume. 12) R. Greeley *et al.*, *JGR*, 98, 17183, 1993. 13) L. Gaddis and J. Head, *LPSC 12*, 321, 1981. 14) A. Yingst and J. Head, this volume.

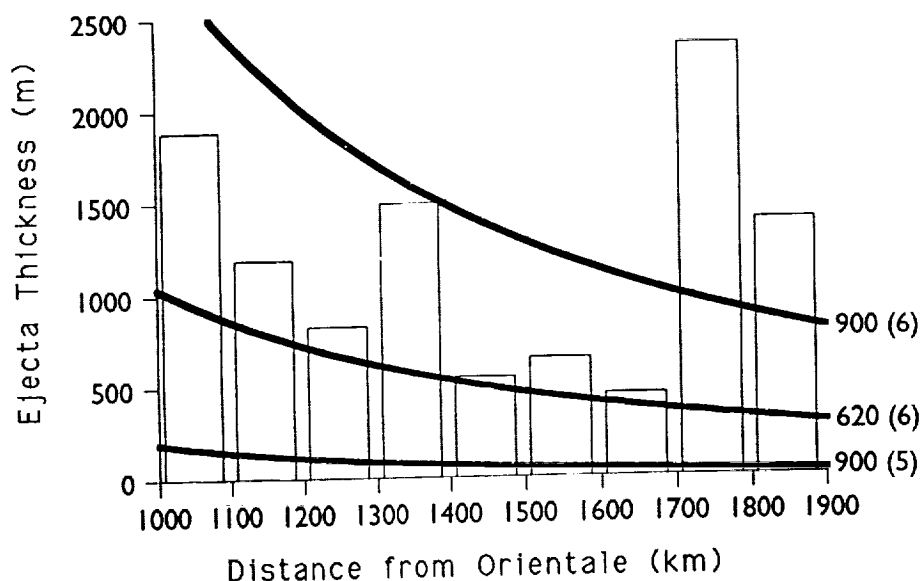


Fig. 1. Estimation of unit thickness overlying cryptomaria.

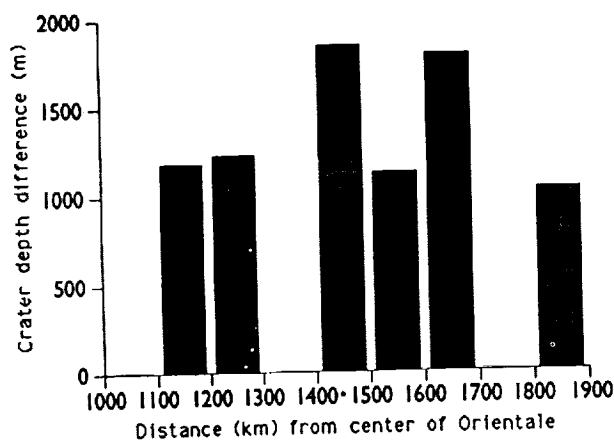


Fig. 2. Estimation of cryptomare thickness from DHC excavation geometry.

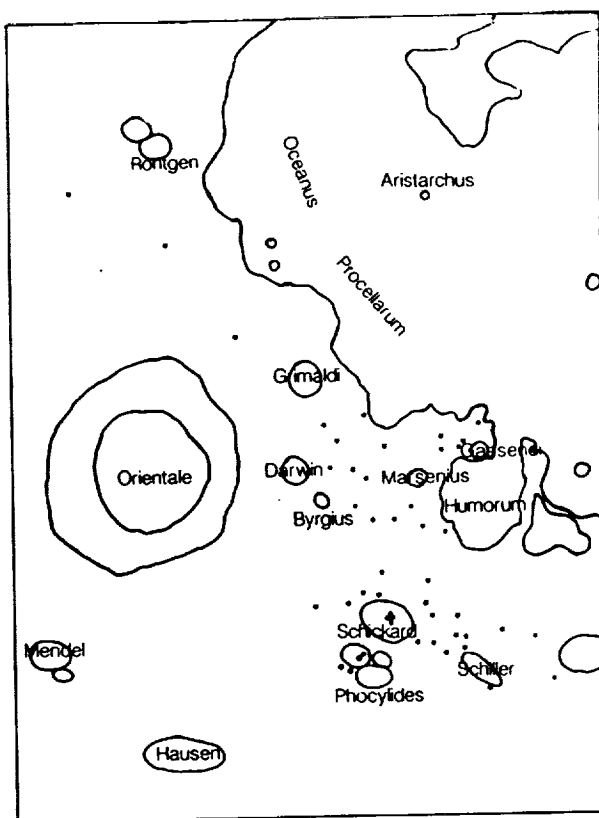


Fig. 3 Sketch map showing the location of DHCs in the area W of Humorum and W of Procellarum.

COMPUTER SIMULATION OF LOW PRESSURE MELTING IN METEORITIC IGNEOUS SYSTEMS. Alexei A. Ariskin and Mikhail I. Petaev, Vernadsky Institute of Geochemistry and Analytical Chemistry, Russian Academy of Sciences, Kosygin St.-19, Moscow 117975, Russia, and Harvard-Smithsonian Center for Astrophysics, 60 Garden st., Cambridge, MA 02138

Abstract. [1,2] demonstrated use of the LUNAMAG program in simulating the effect of extremely low oxygen fugacities on mineral-melt boundaries in achondritic systems. Herein we describe and test an extension of LUNAMAG, the Meteorite Melting Model (MMM), which is better suited for the accurate calculation of low pressure equilibrium melting in high-Mg systems. Both programs determine phase compositions and temperature, for specified values of oxygen fugacity and degree of melting (5-100%) [3]. LUNAMAG and MMM are based on sets of empirically fitted expressions that describe mineral-melt equilibria for major elements as a function of temperature and liquid composition. Special subroutines to simulate the precipitation of metallic iron phase and trace element partitioning are also provided [1,3].

Basis for the Model. The empirical basis for MMM is a library of 1-atm melting experiments that have been carried out on natural samples, ranging from komatiites and norites through basalts to andesites, including low-alkali compositions ($\text{Na}_2\text{O}+\text{K}_2\text{O} \leq 5\%$). We selected only the most reliable experiments, those with run durations >48 hours in the $1100^\circ\text{--}1500^\circ\text{C}$ temperature range. To assemble the data we used the latest version of the INFOREX-2.1 (1993) database, which was developed to archive experimental information on phase equilibria available in the literature [4]. Expressions of the form $\ln K = A/T + B + C \ln(Si/O)_{\text{melt}}$ for each mineral component were fitted by least squares regression to the experimental data (Table 1): here K is the equilibrium constant for the reaction describing the melting of that component and Si/O is, literally, the ratio of abundances of those two elements in the melt. Components in solid minerals were assumed to form ideal solutions; melt component activities were calculated using the two-lattice model [5]. When these expressions are used to predict the temperatures at which particular minerals begin to crystallize in systems that have been studied experimentally, agreement is found with the experimental data to $\pm 10\text{--}15^\circ\text{C}$ for each mineral.

Test of Model on High-Mg Systems. To test the MMM we attempted to reproduce the results of a set of 1-atm melting experiments made on 5 high-Mg terrestrial, synthetic, and meteoritic compositions (Table 2). Data from these experiments had not been used in establishing the parameters of Table 2. Preliminary calculations showed that agreement was excellent for the crystallization histories of olivine and plagioclase, but within the relatively narrow compositional range of these 5 samples there are systematic disagreements of $\sim 10^\circ\text{C}$ for the appearance of augite and $\sim 20^\circ$ for orthopyroxene between the calculated and experimental data. When corrections of these magnitudes are applied to the calculations affecting pyroxene minerals, the models of 1-atm mineral-melt equilibria shown in Fig. 1 are obtained. Results for the Murchison chondrite (Fig. 1D,E) and the high-Mg Kapoeta eucrite (Fig. 1F) show that the MMM can correctly predict the appearance of olivine, plagioclase, low-Ca pyroxene, and augite as a function of the amount of melt present. Thus the model can be used for the calculation of both the proportions of phases and the liquid lines of descent for major and trace elements during equilibrium melting of various high-Mg achondrites [12].

Future Work. Needed are improvements in the accuracy of the expressions for mineral-melt equilibrium constants, and incorporation into the system of new expressions for pigeonite and spinel. An observed discrepancy between experimental and modeled oxygen fugacities when Fe metal precipitation is simulated in Murchison (Fig. 1E) may mean that the equation for iron-silicate melt equilibrium equation requires correction [1]. To model sulfide melting, more experimental data is needed on sulfide-silicate melt equilibrium in systems of interest.

References. [1] Ariskin, A.A. et al. (1992) *Lunar Planet. Sci.* **XXIII**, 35-36. [2] Petaev, M.I. et al. (1994) *Meteoritics*, 29 (in press). [3] Ariskin A.A. et al. (1993) *Computers & Geosciences*, **19**, 1155-1170. [4] Ariskin A.A. et al. (1992) *Amer. Mineral.*, **77**, 668-669. [5] Nielsen, R.L. and Dungan, M.A. (1983) *Contrib. Mineral. and Petrol.*, **84**, 310-326. [6] Ryerson, F.J. et al. (1988) *J. Geophys. Res.*, **93B**, 3421-3436. [7] Jaques, A.L. and Green, D.H. (1980) *Contrib. Mineral. and Petrol.*, **73**, 287-310. [8] Takahashi, E. (1986) *J. Geophys. Res.*, **91B**, 9367-9382. [9] Jarosewich, E. (1990) *Meteoritics*, **25**, 323-337. [10] Jurewich, A.J.G. et al. (1993) *Geochim. et Cosmochim. Acta*, **57**, 2123-2139. [11] Bartels, K.S. and Grove, T.L. (1991) *LPSC XXI*, 351-365. [12] Petaev, M.I. et al. (1994) *This volume*.

SIMULATION OF MELTING IN METEORITES: Ariskin, A.A. and Petaev, M.I.

Table 1. Parameters in expressions for equilibrium constants controlling mineral-melt equilibria. *n*: number of experiments included in the multiple regression fitting

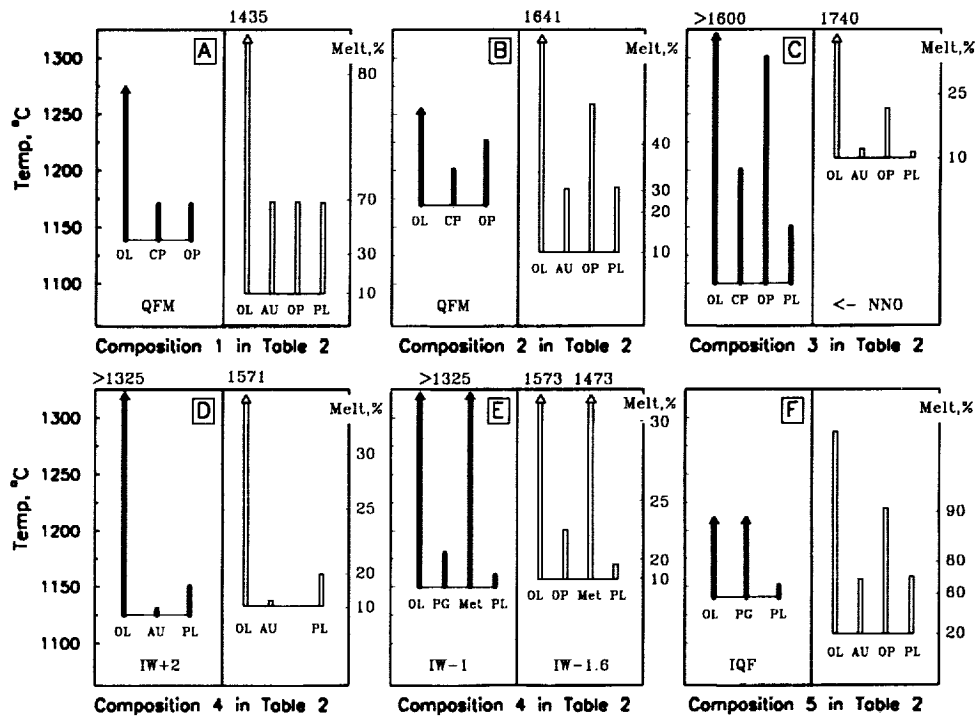
Component	A	B	C
=====			
<i>Plagioclase-Melt (n=142)</i>			
FeAl ₂ Si ₂ O ₈	15214.56	-13.52	-3.36
CaAl ₂ Si ₂ O ₈	18648.75	-16.14	-6.08
NaAlSi ₃ O ₈	9887.96	-3.12	1.92
=====			
<i>Olivine-Melt (n=166)</i>			
Fe ₂ SiO ₄	6753.55	-4.66	0.00
Mn ₂ SiO ₄	6417.98	-4.51	0.00
Mg ₂ SiO ₄	5502.20	-2.54	0.00
Ca ₂ SiO ₄	3064.80	-5.81	0.00
=====			
<i>Augite-Melt (n=70)</i>			
FeSiO ₃	6799.49	-3.53	1.58
MnSiO ₃	4061.15	-3.03	0.00
MgSiO ₃	8973.99	-5.18	0.22
CaSiO ₃	2831.50	-3.03	-1.26
=====			
<i>Orthopyroxene-Melt (n=29)</i>			
FeSiO ₃	4682.54	-1.65	1.59
MnSiO ₃	3842.95	-2.50	0.00
MgSiO ₃	7396.49	-3.13	0.66
CaSiO ₃	11714.03	-10.53	-0.58
=====			

Table 2. System compositions used to test the Meteoritic Melting Model

Comp	1	2	3	4	5
=====					
SiO ₂	46.76	48.63	44.72	38.11	49.37
TiO ₂	1.91	1.20	0.16	0.17	0.74
Al ₂ O ₃	10.55	6.00	3.61	2.82	9.90
FeO	11.45	8.34	8.14	29.35	19.49
MnO	0.19	0.13	0.12	0.26	0.51
MgO	18.08	29.24	39.43	26.14	10.39
CaO	8.58	5.22	3.46	2.48	9.14
Na ₂ O	1.86	0.96	0.30	0.31	0.46
K ₂ O	0.40	0.22	0.02	0.05	-
P ₂ O ₅	0.22	0.06	0.03	0.30	-
=====					

1 - Picrite [6], 2 - Peridotite [7], 3 - Peridotite [8],
4 - Murchison chondrite [9] minus FeS,
5 - Kapoeta eucrite [11]

Fig 1. Temperature ranges in which various minerals coexist stably with melt; a comparison of experimental data (left boxes, solid bars) with calculated models (right boxes, open bars). Bases on which the bars rest represent limits of the experiments and calculations, not system solidus temperatures. Degrees of melting shown to right of each box are applicable to calculated models



OBLIQUE IMPACT: ATMOSPHERIC EFFECTS. N.A.Artem'eva, V.V.Shuvalov. Institute for Dynamics of Geospheres, Russian Academy of Sciences, Leninsky prosp., 38-6, Moscow, 117979.

The impacts of asteroids and comets on the Earth cause large-scale disturbances of the Earth's atmosphere. Only 1% or less of the energy of bolides is taken up directly during the passage through the atmosphere, and the vaporized, melted and solid ejecta transfer up to 40% of their energy to the atmospheric air [1]. It may be the reason why the latter effect has been investigated in detail - from the fundamental work [2] to the encyclopedia [3], and the former has received only occasional attention in the literature. For example, O'Keefe and Ahrens [1] mentioned, that the penetration of the bolide produces a short-lived hole in the atmosphere with diameter approximately equal to that of the bolide. The gas in this hole flows radially inward filling the hole and upward propelling the air and ejecta particles to high altitudes. In [4] it was emphasized that the presence of a tail of a highly rarefied cavity promotes the escape of the ejecta to the upper layers of the Venusian atmosphere. The interaction of airblast waves with a thin heated channel and the accompanying reconstruction of the ejecta flow has been investigated numerically in [5], and the more realistic problem has been solved in [6,7] for the case of vertical impact on Mars and on the Earth. The results of the above mentioned computer simulation indicate the powerful upward stream that is many times greater than the well known asymmetry of the "facula" due to the atmospheric inhomogeneity.

Now we have improved the previous model [7] - the real wake, real impact with crater formation, heat and light transfer are taken into account. Fig.1 demonstrates the 50 km/s vertical impact of 1 km silicate body on the Earth. The vapor plume, consisting of the body and surface material, is expanded within the "hole" (rarefied wake). The shape of the plume and blast wave is far from spherical mainly because of the wake influence. Although vertical impact is a convenient object for numerical simulation due to its cylindrical symmetry, in real situations an impact is most likely to be oblique.

Relatively simple 3DE hydrocode enables us to make computer simulation of the oblique impact of the same asteroid falling with inclination angle 45° onto a silicate Earth covered by atmosphere. For the sake of simplicity we have restricted ourselves to the simplest model: the wake can be treated as a time-dependent cylindrical explosion with the energy $V^2/2$ per unit mass of the atmosphere, and the ejecta - as an explosion of a hemisphere that is 10 times as massive and 4 times as great as the asteroid and its thermal energy is equal to the half of the asteroid's kinetic energy. The scale height of the atmosphere is taken to be $H=8.4$ km.

Fig.2 presents the isolines of the relative density ρ/ρ_i at XZ-section of the flow, where ρ_i is the atmospheric density at the corresponding height z immediately after the impact, Fig.3 presents ρ/ρ_i at 1.25 sec following the impact. As shown in Fig.2, the wake ranges in thickness from 20 km at the height 50 km to 4 km near the surface, and its density in a thin central channel is ~ 10 times lower than that of the ambient gas. Fig.3 depicts an absence of strong vertical flow: the blast waves occupy considerably greater region than it has been suspected for an explosion without wake (dashed lines), with strong disturbances toward the wake. Also the velocity is a maximum not on the upper edge of the ejecta flow but within the wake (35 km/s versus 15 km/s).

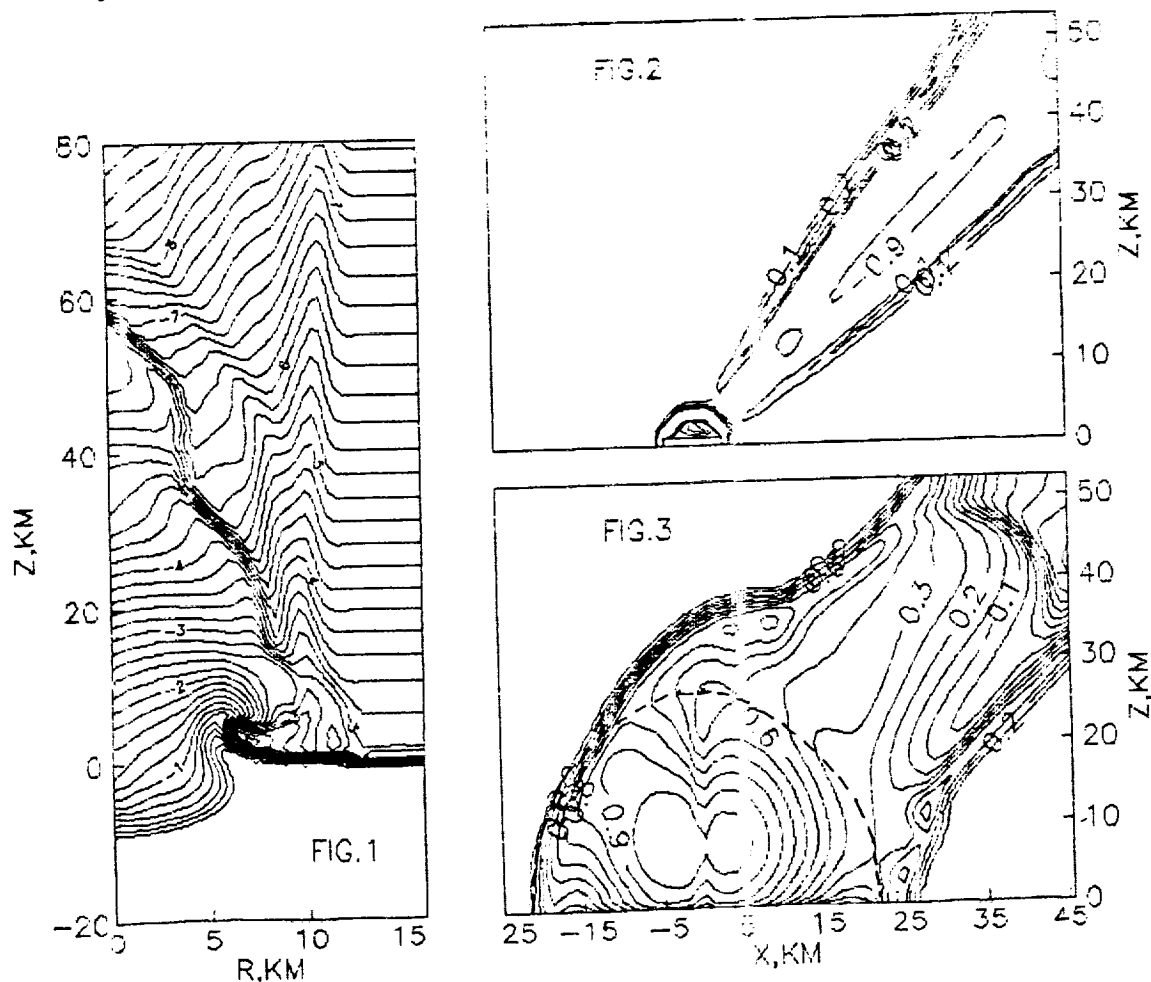
So the interaction of the atmospheric shock waves generated during the flight and the following impact of the bolide alters the final flow

OBLIQUE IMPACT: ATMOSPHERIC EFFECTS. N.A.Artem'eva, V.V.Shuvalov.

pattern radically. This doesn't mean that the ejecta pathways change dramatically too, but it's not unlikely. The complex spatial flow can modify the mass and velocity distribution of high-energy ejecta, its deposition in the stratosphere and largely influence the long-term consequences of impact phenomena. In our model we do not take into account radiation at all. But it is well known that the fireball is a powerful source of light and heat pulse, that causes fire storms on the Earth's surface. As the fireball is distorted in shape, the area of fires may be significantly increased.

Whereas essentially all impacts are vertical in relation to crater formation except gently inclined ones [3], they are significantly oblique in relation to atmospheric effects. Our simulation is only the first step on the road to extensive studies. At a later time we try to adjust our physical model.

References: [1] O'Keefe J.D., Ahrens T.J. (1982), GSA Special Paper No 190, p.103-120. [2] Zeldovich Ya.B., Raizer Yu.P. (1967), Physics of Shock Waves and High Temperature Hydrodynamic Phenomena, Academic Press, N.Y. [3] Melosh H.J. (1989), Impact Cratering, Oxford Univ. Press, N.Y. [4] Ivanov B.A. et al. (1986), J. Geophys. Res., v.91, No B4, p.413-430. [5] Bergelson V.I. et al. (1987), Meteoritica, No 48, p.137-141 (in Russian). [6] Nemchinov I.V., Shuvalov V.V. (1992), Solar System Research, v.26, No 4, p.333-343. [7] Nemchinov I.V. et al. (1993), LPSC XXIV (abstracts), p.1067-1068.



LABORATORY SIMULATIONS OF LARGE-SCALE VORTEX FLOWS GENERATED AT IMPACTS ON VENUS AND ON EARTH. V.I.Artem'ev, V.A.Rybakov, S.A.Medveduk, and B.A.Ivanov. Institute for Dynamics of Geospheres, Russian Academy of Sciences, Leninsky prosp., 38-6, Moscow, 117979.

The analysis of the Magellan Mission data suggests that ejecta emplacement and crater formation on Venus are closely related to the atmospheric effects. The formation of the parabolic impact crater related features is supposed to be determined to the injection of small particles to the upper atmosphere and their transport by E-W zonal winds. We propose here another model of ejecta long distant transportation: the escape of ejecta particles to high altitudes can be performed by large-scale atmospheric vortex flows.

Collisions of large meteoroids with planets having dense atmospheres (Venus and Earth) are accompanying by substantial atmospheric disturbances. The impact-generated atmospheric flows with vertical size exceeding the scale height of the atmosphere may be responsible for global propagation of solid ejecta and dust.

In [1] a model for the formation of the parabolic impact crater related features is developed based on the injection of small particles to the upper atmosphere. The vorticity generation at impacts on Venus has been attributed to the interaction of atmospheric blast waves with radiatively heated surface (the thermal layer effect) [2], and to the atmospheric disturbances by the outward moving ejecta [3]. In [4,5] it was emphasized that a disturbance of the atmosphere by falling meteoroid *before* the impact (i.e. a formation of the wake of shock-heated gas downstream of the meteoroid) promotes the escape of the ejecta to the upper layers of the Venusian atmosphere; in experiments [6] the near-surface vortex flow has been generated by detonation of an oblique line charge burst simulated the atmospheric wake.

In general, the baroclinity of the gasdynamic flow ($\nabla 1/\rho \times \nabla p \neq 0$, where ρ and p are density and pressure) is responsible for vorticity generation. A complex time-spatial character of energy release during atmospheric flight and at impact of the meteoroid - the inhomogeneity of the atmosphere, the presence of heated channels and layers, crossing shock fronts *etc.* - results in such a baroclinity and hence in vorticity generation. In our experiments we make an effort to simulate the vortex flows resulting from the interactions of impact-generated air blast wave and wake.

The spherical shock wave is produced on action of a focused laser radiation onto a surface. The energy of the laser driven blast is $\mathcal{E} \approx 10$ J. The atmospheric wake is simulated by electrical explosion of a thin wire. On modeling of the impact on the Earth the atmospheric pressure and density in laboratory are the same as in real atmosphere. In this case the energy \mathcal{E} corresponds to the energy of impact-generated air blast E as follows: $\mathcal{E} = (l/L)^3 \cdot E$, where l and L are the linear scales in laboratory and in atmosphere. The explosion energy for 100 m-stony asteroid falling with velocity ~ 15 km/s is about $E \approx 10^{24}$ erg. In this case $L = 10$ km in atmosphere corresponds to $l \approx 5$ cm in laboratory. The energy expended for formation of the atmospheric wake can be estimated in the case considered as $E_a \approx 2\rho_a H / (\rho_m D) \cdot E \approx 0.1 \cdot E$, where $H \approx L = 10$ km is the scale height of the Earth's atmosphere, and $D = 100$ m is the asteroid's diameter. Thus the energy of electrical explosion simulating the wake must be $\mathcal{E}_a / l \approx 0.1 \cdot \mathcal{E} / l \approx 0.2$ J/cm.

Fig.1 represents the results of the laboratory simulation of the impact on the Earth: the shadowgraphs of the flow generated on blast-wake interaction at the consecutive points of time. The "experimental" time τ corresponds to the "real" time t as $\tau = l/L \cdot t \approx 5 \cdot 10^{-6} \cdot t$. In Fig.1a one can see the expanding wake just before the impact, two next pictures illustrate the

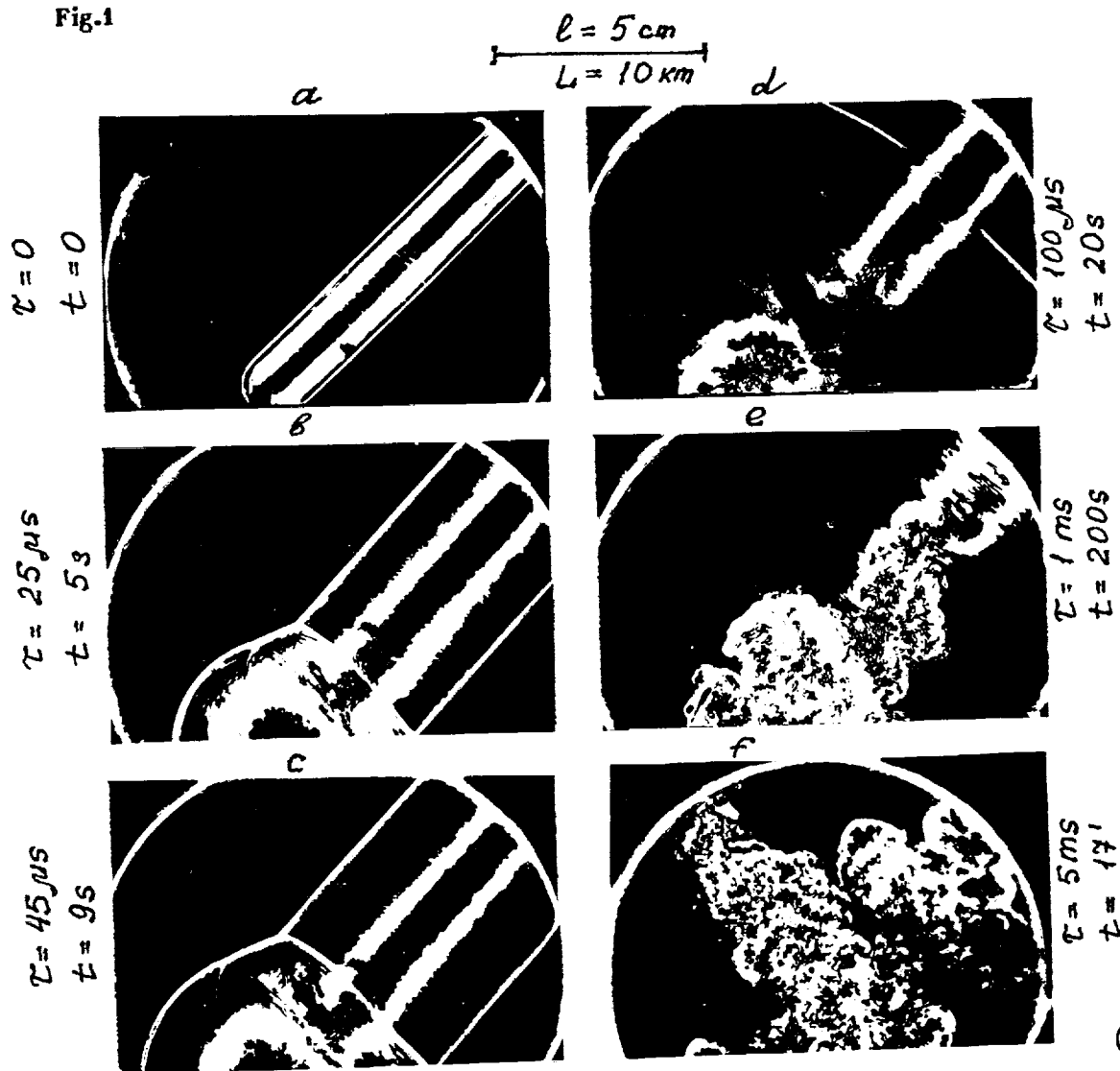
LARGE-SCALE VORTEXES AT IMPACTS: V.I.Artem'ev *et al.*

interaction of spherical and cylindrical air blast waves. In Fig.1d and Fig.1e are shown the initial stages of the large-scale vorticity formation: initially the near-surface part of the wake and then the whole wake is destroyed by vortexes. On the later stage (Fig.1f, $\tau=5$ ms, $t=17$ min) a system of large-scale toroidal vortexes oriented normally to the initial direction of the wake is formed.

In simulation of the impact of 3 km-projectile on Venus the energy of atmospheric explosion is taken to be comparable to the energy dissipated in the wake. In this case the results are qualitatively the same as for the impact on the Earth. Notice that in both cases we neglect the atmospheric inhomogeneity. The vertical scale of vortex flows (especially at impact on Venus) in fact exceeds the scale height of atmospheres, therefore in more improved simulation a vertical decrease of the atmospheric density will be taken into account.

References: [1] Campbell D.B. *et al.* (1992), J. Geophys. Res., 97, No E10, p.16249-16277. [2] Ivanov B.A. *et al.* (1992), LPSC XXIII, p.575-576. [3] Barnouin O.S. and Schultz P.H. (1993), LPSC XXIV. [4] Ivanov B.A. *et al.* (1986), J. Geophys. Res., 91, No B4, p.413-430. [5] Ivanov B.A. *et al.* (1992), J. Geophys. Res., 97, No E10, p.16167-16181. [6] Ivanov B.A. and Provalov A.A. (1993), LPSC XXIV.

Fig.1

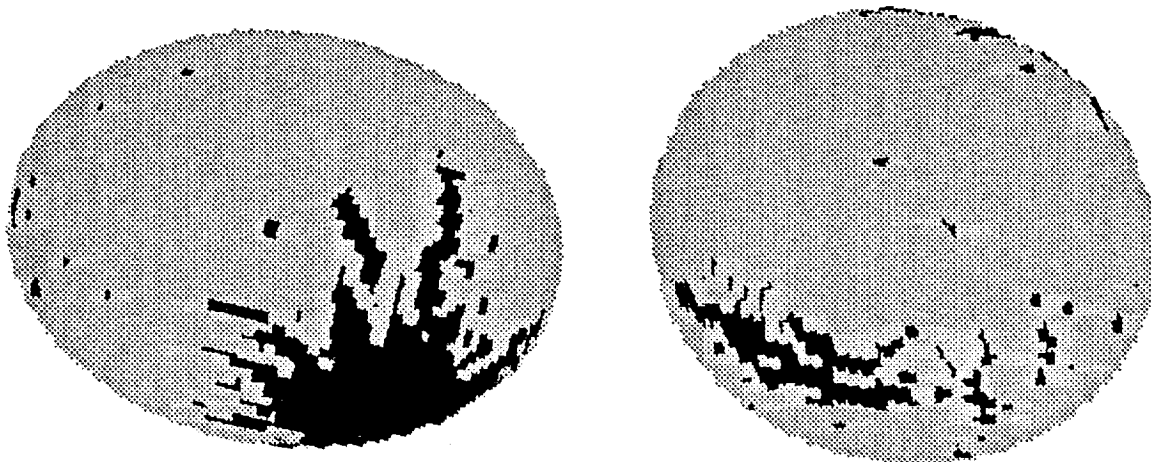


C-2.

P-2 THE SURFACE AND INTERIOR OF PHOBOS: E. Asphaug, NASA Ames Research Center 245-3, Moffett Field CA 94035, and W. Benz, Steward Observatory, University of Arizona, Tucson AZ 85721

The impact crater Stickney dominates one hemisphere of the Martian moon Phobos; its diameter (11 km) is about half the size of the body ($19 \times 22 \times 27$ km). Besides demarking a threshold between cratering and catastrophic disruption, this impact reveals a great deal about the target's interior. Because Phobos has an unusually low density yet exhibits no direct evidence for volatiles such as water ice, it has been supposed that it sequesters volatiles in the deep interior, or that it is made of some exotic substance, or that it is a loosely-aggregated rubble-pile. The network of fracture grooves created by the Stickney impact constrain which, if any, of these models accord with observation.

We first model Phobos as a homogeneous elastic ellipsoid using the smooth particle hydrocode SPH3D with fracture (Benz and Asphaug, *Icarus*, in press), which is the first hydrocode capable of resolving the dynamical growth of explicit cracks. We use the fracture constants and equation of state for laboratory basalt, substituting a density of 1.95 g/cm^3 . A 6 km/s impactor is introduced with the appropriate trajectory (normal incidence at the current center of Stickney) and a size determined by gravity crater scaling¹. The outcome of this impact is shown in Figs. 1a and 1b, which are surface plots of the damaged ellipsoid 12 seconds after impact, viewed from two sides. Dark regions are fully-damaged computational cells (i.e., cracks) and lighter regions are intact rock. By this time fracture is complete, but the crater bowl has only just begun to develop, with flow velocities of a few m/s.

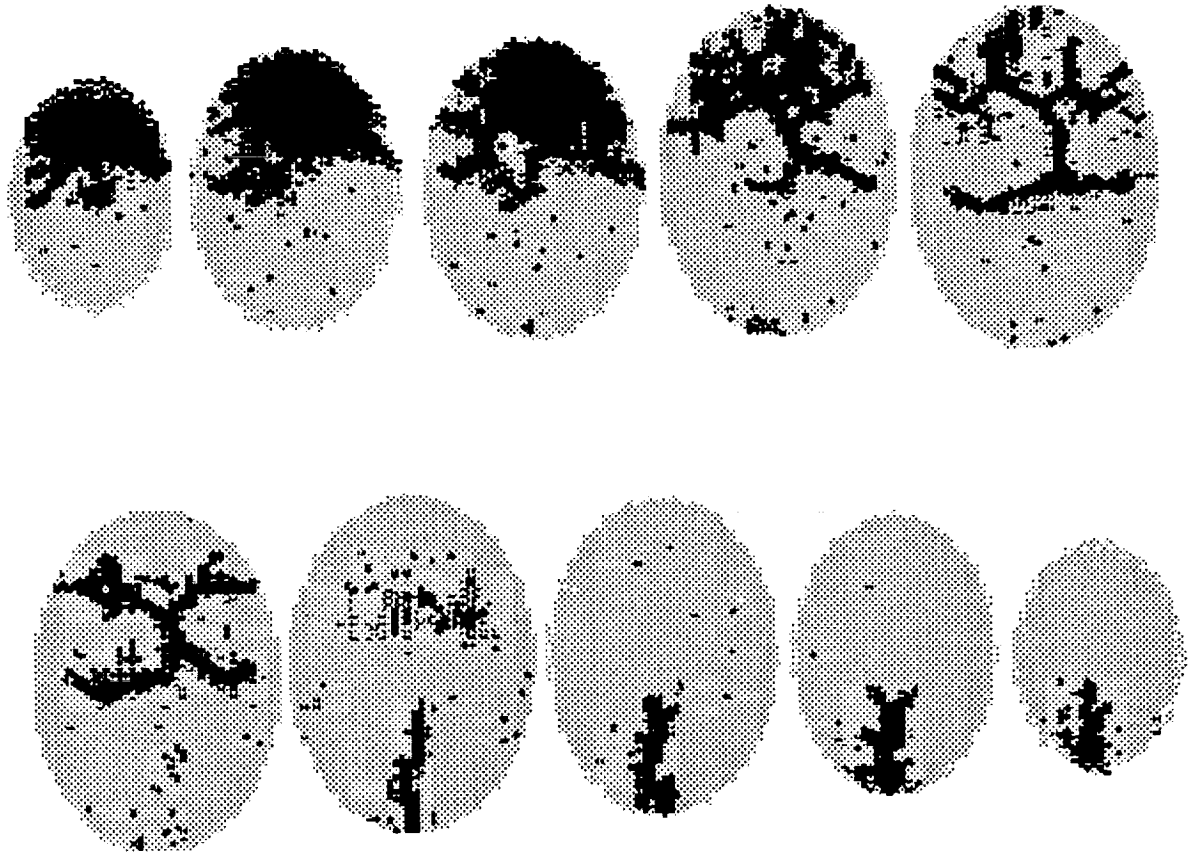


The fracture grooves antipodal to the crater (1b) do not appear until the final stages of the calculation, when reflected impact stresses come to focus. The fracture orientation is sensitive to the impact locus. Phobos shows a more complex fracture pattern than our simulation, with a general trend correlated with the axis of greatest tidal stress. Nonetheless we feel we have captured the major features of the event.

The damaged region is not quite as large as the predicted size of the final crater, suggesting that strength may indeed play some role in this impact. To test this hypothesis we tried a larger impactor (strength-scaled) to see what would happen. None of the body survived fragmentation, a large fraction escaped, and what remained was transformed into something quite different from the present Phobos. Hence, although the crater does not form purely in the gravity regime, gravity scaling is far closer to the truth than strength scaling. This study confirms the earlier work of Asphaug and Melosh² — who used a significantly different numerical method and fracture model, in axial symmetry — that the impact took place essentially in the gravity regime, with a correspondingly slow cratering flow and a retention of crater ejecta. It is worth noting that the crater flow fields predicted by both numerical models are in very good agreement with analytical crater scaling in the gravity regime³.

THE SURFACE AND INTERIOR OF PHOBOS: E. Asphaug and W. Benz

The fracture grooves in Fig. 1 extend deep into the interior, as shown in Fig. 2 below. This series of figures is a slice through the final target, again with damaged regions (cracks) shaded darkest. The slices are 1 km thick, beginning near the crater (i.e., near the bottom front of Fig. 1a) and proceeding into the least-damaged hemisphere, where one can see the antipodal fracture groove. The grooves of Phobos are not mere surface features, but extend deep into the body. Although fractures permeate Phobos, they do not disconnect it (except the near-crater zone), and hence our final target retains a significant fraction of its original strength.



We finally modeled Phobos as an ellipsoid of rock-like density (2.7 g/cm^3) with a random distribution of small "holes" removed to simulate a heterogeneous interior, so that the bulk density was 1.95 g/cm^3 . The result was dramatically different. Instead of forming the highly organized pattern of fractures seen in Fig. 1 (and on Phobos itself), the impact produced a crater and not much else. In heterogeneous targets (such as rubble-piles) the impact stresses scatter rapidly and are evidently unable to lead to coherent rupture. Hence, the existence of fracture grooves on Phobos, especially those far from the crater (Fig. 1b), leads us to conclude that the target is homogeneous, at least down to a scale smaller than the width of the grooves themselves, i.e. tens of meters. And this, in turn, places a rigorous constraint on the evolution and composition of this ever-mysterious small body.

REFERENCES: ¹ Holsapple and Schmidt, *JGR* 92, pp. 6350-6376, 1987. ² Asphaug and Melosh, *Icarus* 101, pp. 144-164, 1993. ³ Housen, Schmidt and Holsapple, *JGR* 88, pp. 2485-2499, 1983.

STRATIGRAPHY OF SMALL VOLCANOES AND PLAINS TERRAIN IN VELLAMO PLANITIA, VENUS

AUBELE, JAYNE C., *Department of Geological Sciences, Brown University, Providence, RI 02912*

Objectives: (1) to analyze the relationship between fields of small volcanoes and plains terrain on Venus by using the tool of geologic mapping; and (2) to use stratigraphic relationships interpreted from the mapping to test theories of the geologic evolution, formation and resurfacing of the plains terrain. **Results:** Newly defined plains unit in Vellamo Planitia contains all of the small volcanoes in the area, is well-defined with consistent stratigraphic relationships, and may represent a potentially widespread period of edifice-building and a stratigraphic marker unit.

INTRODUCTION The plains terrain on Venus covers approximately 80% of the surface [1]; and the mechanism of formation, total crustal contribution, and age (or range of ages) represented by the plains is presently uncertain or unknown. Fundamental questions and theories regarding the thermal evolution of the planet [2,3] can only be tested by an understanding of plains stratigraphy. While the Venus plains can be assumed, by analogy with Moon and Mars, to be volcanic in origin with subsequent surface modification by tectonism, impact cratering, and aeolian processes [4-8], there is a paucity of individual volcanic centers, particularly large volcanic edifices, occurring within the lowland plains terrain [9,10]. The volcanic features that do commonly occur are lava channels [11,12] and clusters of small, predominantly shield-type, volcanoes [1,18]. These volcanoes are the most abundant geologic feature on Venus, and were initially recognized on Arecibo and Goldstone Earth-based images [13,14] and first examined in detail using the Venera 15/16 data [15-17]. These clusters of volcanoes may be similar to volcanic "fields" in the terrestrial volcanological sense of the term [18]; and they appear to have some volume of volcanic flows, or possibly a small component of pyroclastic material [1], covering a larger area in association with each "field" of edifices. Although lava channels appear to be related to the mechanism of formation of some plains terrain, there is embayment and stratigraphic evidence for variations in age of local fields of small volcanoes and associated plains units. A major question that is the focus of the VMAP research reported here is the relationship between material extruded or intruded in association with these "shield fields" and the formation or resurfacing of the plains terrain with which they are associated.

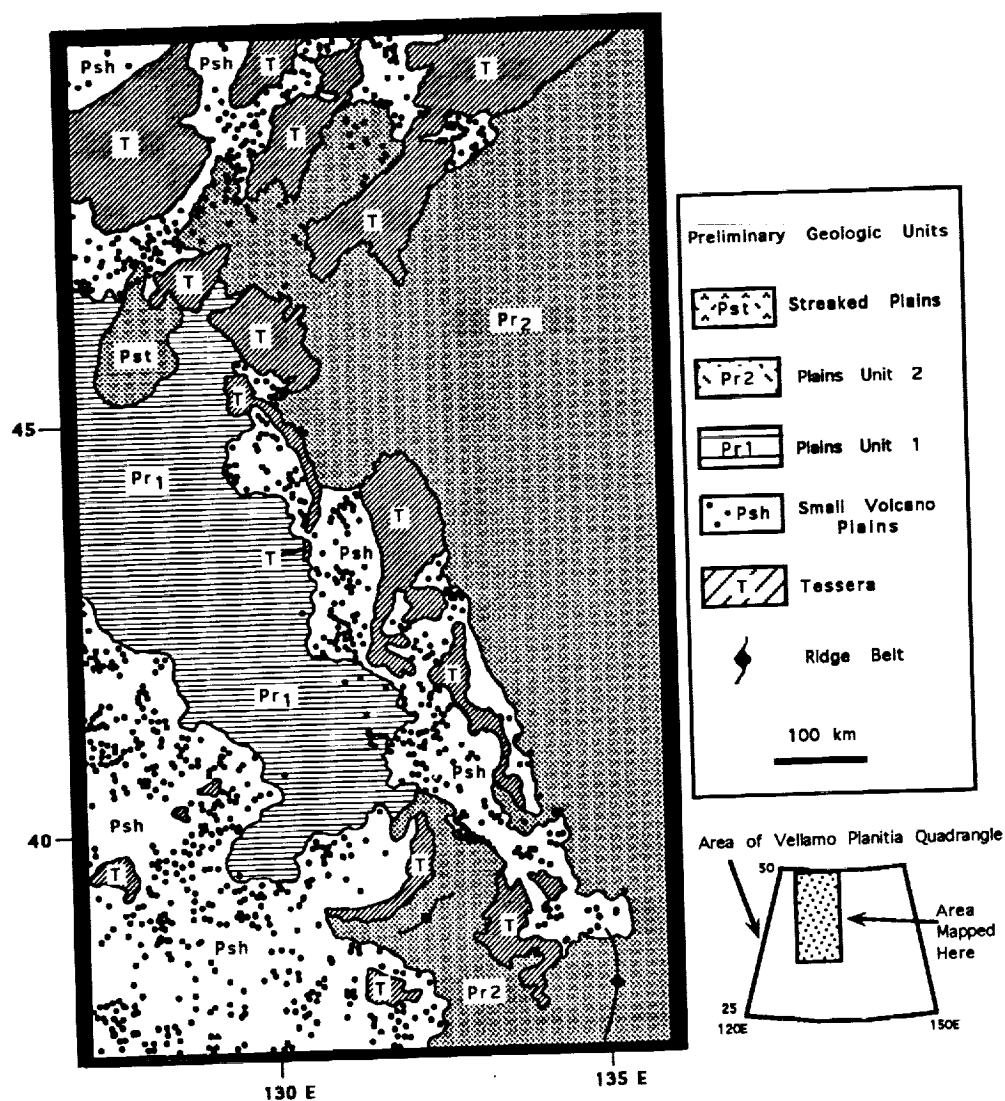
DATA AND PRELIMINARY ANALYSIS Venus quadrangle V12, Vellamo Planitia, centered at 37°N and 135°E, was selected for mapping on the following basis: (1) presence of a large number of small volcanoes; (2) occurrence of the small volcanoes in association with lowland plains terrain; and (3) low abundance of large-scale volcanic or tectonic features that might complicate the geologic evolution of the surface and obscure stratigraphic evidence. Vellamo Planitia Quadrangle is situated at the intersection of major terrain units of geologic significance. The western half of the quadrangle consists of a large number of clusters of small volcanoes and isolated patches of tessera, while the eastern half consists of extensive ridged plains with 2 previously identified coronae [19] and ridge belts. Four possible stratigraphic models can be tested on the basis of stratigraphic relationships interpreted from geologic mapping: (1) the small volcanoes are the source of flows that form or resurface the plains; (2) the small volcanoes and the plains have been formed simultaneously; (3) the small volcanoes predate plains terrain; and (4) the small volcanoes postdate the plains. **Small Volcano Plains Unit.** The portion of the quadrangle shown in Figure 1 is a critical area where abundant clusters of small volcanoes and extensive plains units intersect; and the stratigraphic relationship between tessera, small volcanoes and plains can be determined. Five geologic units occur in this area. As has been reported by other workers in other areas, tessera (Complex Ridged Terrain) appears to be the oldest stratigraphic unit in the area. Remnants of tesserae are embayed by three plains units. The oldest of these plains units appears to contain all of the small volcanoes in the area. This unexpected and newly defined plains unit has been informally named "Small Volcano Plains" unit on the preliminary map. It is a discrete geologic unit with well-defined contacts and consistent stratigraphic relationships. This was an unexpected result of the mapping. Prior to detailed mapping, it was assumed that local clusters of small volcanoes would show relative stratigraphic and contact relationships with small areas of plains. However, all of the small volcanoes in V12 occur on this distinct and mappable plains unit. The "small volcano plains" unit overlays and embays tesserae throughout the mapped area; and it is overlain by two units of younger ridged plains that contain few volcanic edifices. Where small volcanoes occur within the ridged plains units, they are clearly isolated outliers of the small volcano plains which have been embayed and surrounded. The two ridged plains units (Pr1 and Pr2) are distinguished by difference in radar backscatter and embayment relationships along contacts. However, the orthogonal system of small-scale ridges that occur in both units crosses the contact boundaries without showing a systematic change. This may indicate that the difference in radar characteristics of Pr2 simply reflects a resurfacing event of Pr1 or that the small-scale ridges represent a continuing or late-stage deformational process. Ridge-belts, however, occur only in the youngest ridged plains unit and do not cross the "small volcano plains". Altimetry profiles show that the younger ridged plains are locally topographically higher than the older "small volcano plains".

Implications. Preliminary results from mapping Vellamo Planitia Quadrangle indicate that the small volcanoes in this region are uniquely associated with (and are probably the source of) a distinctive plains unit that postdates tessera terrain and predates the more extensive ridged plains terrain. The "small volcano plains" unit mapped in this area is a potential stratigraphic marker. It is well-defined regionally and its temporal relationships with adjoining units are consistent; however, its total areal extent and relationship with other areas of small volcano concentration is unknown. Continuing analysis will address the following: What is the nature of the "small volcano plains" material and emplacement? What are its distinctive characteristics in the Magellan physical properties data sets? What are the detailed characteristics of the individual small volcanoes that occur within this unit? Does the unit represent a regional or

AUBELE, J.C. STRATIGRAPHY OF SMALL VOLCANOES AND PLAINS, VENUS

a global period of small volcanic edifice building or a resurfacing event that occurred prior to the formation of the extensive ridged plains?

[1]Guest et al, JGR 97, 15949, 1992; [2]Schaber et al, JGR 97, 13257, 1992; [3]Phillips et al, JGR 97, 15923, 1992; [4]Squyres et al, JGR, 97, 13579, 1992; [5]McGill, LPI 789 (abst), 67, 1992; [6]Arvidson et al, JGR 97, 13303, 1992; [7]Greeley et al, JGR 97, 13319, 1992; [8]Campbell et al, JGR 97, 16249, 1992; [9]Head et al, JGR 97, 13153, 1992; [10]Crumpler et al, Sci 261, 591, 1993; [11]Baker et al, JGR 97, 13421, 1992; [12]Parker et al, LPSC XXIII (abst), 1035, 1992; [13]Campbell et al, Sci 246, 273, 1989; [14]Jurgens et al, GRL 15, 6, 577, 1988; [15]Slyuta et al, Aston. Vestnik 22(4), 287, 1988 (in Russ); [16]Aubele & Slyuta, EMP 50/51, 493, 1990; [17]Garvin & Williams, GRL 17, 9, 1381, 1990; [18]Aubele et al, LPSC XXIII (abst), 47, 1992; [19]Stofan et al, JGR 97, 13347, 1992



Preliminary Geologic Map of A Part of the Vellamo Planitia Quadrangle, Venus
Jayne C. Aubele

Part of the preliminary geologic map of the Vellamo quadrangle. Units shown in stratigraphic order. In this area the stratigraphic relationship between tessera, small volcano plains, and late ridged plains can be determined. The small volcano plains unit is recognized as widespread, both here and regionally on Venus, and predates the ridged plains.

STEPPING INTO SPACE: GETTING INVOLVED IN PRE-COLLEGE OUTREACH

Aubele, Jayne C. and Schultz, Peter H., *R.I. Space Grant Program and Department of Geological Sciences, Brown University, Providence, RI 02912*

The RI Space Grant Program provides scholarships for graduate and undergraduate students from a variety of space-related science disciplines. These students devote a portion of their time to pre-college science education outreach programs which are designed with teacher-input and are tailor-made for individual schools or classrooms. Our programs and presentations use one of the following philosophies: (1) Hot Topic - sharing science information in the context of popular current events; (2) Student to Student - one-on-one interaction between kids and science majors; and (3) Special Focus - special projects designed for individual needs. This flexible approach, combined with our diverse graduate and undergraduate students, allows us to "reach" pre-college teachers and children throughout the state.

The Rhode Island Space Grant Program is part of the nationwide NASA National Space Grant College and Fellowship Program and is designed to enhance learning opportunities in space-related science at all levels of education, from elementary school through graduate school. Our objectives are: (1) to encourage undergraduate students to explore space-related science as a career; (2) to enable graduate students to pursue an education in space-related science or engineering; and (3) to use space-related science as a vehicle for increasing scientific literacy among the children and pre-college educators of Rhode Island through diverse outreach activities. All three goals are interrelated in our program and a flexible approach to outreach allows us to interact with many different groups.

An underlying theme in all of our activities is to stimulate, encourage and enable grass-roots efforts in science education throughout the state by tailor-made Space Grant / teacher / student partnerships designed for individualized needs. We have found that the most effective outreach programs involve student to student. We fund undergraduate and graduate students from a variety of space-related science and engineering disciplines and they devote a portion of their time to science education outreach activities, including visits to school classrooms and presentations of special workshops and short-courses designed for pre-college students and teachers. The undergraduate and graduate students gain financial support, improve their communication skills and become more excited about their science; and in turn, they use their enthusiasm and energy to excite children about science and to act as a resource for teachers who wish to present science topics in the classroom. These interactions enable kids to see exactly what scientists are like and what they do; and since a large part of our activities present Space Grant personnel as science role models for children, we have strived to include as many women and minority students as possible. Currently our undergraduate scholars and graduate fellows consist of 4 women and 4 men and include African-American, Asian American and Hispanic students. The wide range in scientific disciplines represented by these students has made it easy to fit into a variety of school and grade level curricula, and the ethnic and racial diversity of our fellows and scholars has allowed us to design outreach programs specifically for target groups such as middle-school age girls, and African-American and Hispanic children.

Over the past three years we have offered a variety of school presentations, workshops, short-courses and special events aimed at pre-college teachers or their students. Topics for teachers have ranged from Astronomy for Secondary School Teachers to a Teacher's Science Overnight, short-courses based on the Dinomation exhibit at our local Zoo and the movie *Jurassic Park*, and workshops on Using Space to Teach Science for the entire faculty of some schools and the RI State Dept. of Education Math/Science Collaboratives and Advisory Board. Recognizing that today's student teachers will reach many more children than we can, we have established a program with Rhode Island College, Department of Elementary Education (RIC produces almost 90% of the elementary teachers in Rhode Island public schools). We present space-related science teaching methods workshops for all teachers-in-training every semester at Rhode Island College. Topics for pre-college students have ranged from Mars surface to Earth's oceans (as seen by satellite), archaeoastronomy, light and holography, the big bang, plans for a lunar base and a mission to Mars, airplanes and rockets, Earth and Moon, using art to understand physical science, and building a receiving station for weather satellite images. Special projects have focused on an African-American science club and science in Spanish for Hispanic students, with particular emphasis on partnerships with inner-city schools that lack the facilities or resources for classroom science or field trips. Recognizing that middle school is a time when children commonly lose interest in science, we have designed special short-courses for this critically important age group. We track and evaluate all of these diverse projects and programs by presenter and participant evaluation and, where possible, by the achievements and test scores of the teachers and children. A few of our programs and workshops are described in detail as examples of the usefulness of this flexible approach.

HOT TOPICS Our teacher's workshops have been geared to excite teachers with information and possibilities that they can draw on to make their own classroom projects work, thereby enhancing the spirit of personal

Aubele and Schultz STEPPING INTO SPACE: PRE-COLLEGE OUTREACH

discovery. For example, the hit book and movie *Jurassic Park* (and every child's fascination with dinosaurs) were used as a basis for a 2-day teacher's workshop held in August and based on the science issues of "Jurassic Park". Researchers in biology, paleontology, geology and mathematics gave presentations on chaos theory, DNA and genetic engineering, dinosaur physiology, mass extinctions, the Jurassic Period, and theories of dinosaur extinction. The full two days began with breakfast and a field trip to one of the largest excavated dinosaur trackways in the world, located in nearby Connecticut, and concluded with lengthy discussions over pizza after a special showing of the movie *Jurassic Park*. We had to limit the number to the first 40 teachers to enroll - a number reached just two days after our mass mailing went out - and they included teachers from all grade levels and from schools in every part of Rhode Island. They gave up 2 days of their summer vacation but took home lots of information, hand-outs, copies of *Earth Magazine*, and ideas about teaching science in their classrooms this fall.

This approach, sharing "hot-topic" research in the context of entertainment, rather than producing specific curriculum products, found favor with the teachers. Their evaluations were uniformly enthusiastic: "I liked this well-developed, innovative approach, I think this format is a pleasant change of pace from the usual teacher workshop fare". "I enjoyed using a book I had read to learn about new research". "I found the information useful for my own background in designing and teaching a dinosaur unit". "Congratulations on presenting an outstanding opportunity to RI educators...this is the kind of non-text learning experience that can keep science fresh for teachers and their students."

STUDENT TO STUDENT Public schools in economically disadvantaged urban neighborhoods frequently have no science resources. We have set up "partnership" programs with several such elementary and middle schools in Providence. Our graduate and undergraduate students have visited and worked with every grade level and every class in these partnership schools - showing the kids what is possible. Teacher's evaluations noted that "the kids were so excited they could barely contain themselves and talked about the visit for weeks after" and "the Space Grant visitor was so enthusiastic about the subject matter, she captivated the children"... "this presentation allowed the children to extend their knowledge and get answers to their questions"... "this gave the students a positive attitude toward both the material presented and those involved in science!"

Student to student is particularly effective when the visitor becomes a role model. Our women graduate and undergraduate students have taken part in 3 math/science workshops for middle school girls. We funded a group of African-American and Hispanic middle school children from economically disadvantage neighborhoods to visit Brown University science departments for hands-on fun every day for a week during the summer. But, more importantly, we were able to provide mentors from among our graduate fellows who accompanied the kids every day, ate lunch with them, and shared their experiences and reasons for studying science.

An urban elementary school with a high population of Spanish-speaking children became a focus for one of our Hispanic undergraduate scholars. She put together a program in association with the bilingual teachers at the school and has visited the classrooms once a week for a full year presenting a range of science topics and exercises in both English and Spanish. According to their teacher, "this has been a wonderful experience for the children - they look forward to her visit each week and come prepared with information and questions...not always just about science!"

SPECIAL FOCUS With teacher-input we have offered a range of short-courses for several individual schools or classrooms. For example, an after-school science club in one school planned an entire Mars mission with the weekly visits of our engineering graduate fellow and geology undergraduate scholar. One of several mini-courses we designed and presented was requested by a 6th grade teacher on "Using math to solve real science problems".

Our most ambitious project to date has been a 3 year association with all 20 elementary schools of the Warwick RI Public School System and their science teachers and science supervisor. The Warwick school system is one of only two in the country with designated science teachers for grades 1-6 in all elementary schools. In conjunction with the "Space and Planets" section of their science curriculum, our graduate and undergraduate students have given presentations to all 3rd through 6th grade science classes. Each year we have face-to-face contact with approximately 6400 Warwick children and 400 Warwick classroom teachers in a 2-month period. The children then choose a space science topic, research it, and produce an individual or group poster or story board (with video) depending on their grade level and in association with the school art teachers. In 1992, 45 children were presented with gold medals from RI Space Grant in an award ceremony covered by the local newspapers and TV news; and 2 children and 4 teachers were awarded trips to the Smithsonian Air and Space Museum and Goddard Spaceflight Center. The winners for 1993 will be announced soon, and a gallery showing of their posters is planned. This sustained involvement in association with strongly supportive and interested science teachers has made it possible to track science testing scores for children in the Warwick elementary schools. They have increased by an unprecedented 11 points since the start of active involvement by the RI Space Grant program in "using space and art to teach science".

A MERCURY ORBITER MISSION: REPORT ON THE EUROPEAN SPACE AGENCY'S ASSESSMENT STUDY

A. Balogh, The Blackett Laboratory, Imperial College, London, U.K; R. Grard, Space Science Department of ESA, ESTEC, Noordwijk, The Netherlands; G. Scoon, Future Mission Studies Division, ESTEC, Noordwijk, The Netherlands; M Hechler, European Space Operations Centre, Darmstadt, Germany

An assessment study of a Mercury orbiter mission has been undertaken by the European Space Agency, as one of the candidates for its Medium 3 mission, to be considered for launch in the early years of the next decade. The mission's objectives include the mapping of Mercury's magnetic field, its complete imaging, the determination of its surface composition by measuring its gamma ray emission, and a comprehensive survey of the Hermean magnetosphere. The objectives of the study are to define a set of scientific objectives and to derive representative requirements from these; to establish the principal technical characteristics and to design, in outline, a configuration for the spacecraft; and to establish a mission scenario. A Mercury Orbiter mission presents formidable technical challenges. To send a spacecraft to Mercury, and place it in orbit around the planet, requires a large delta-V capability and a long cruise, as well as the use of two Venus and two Mercury flybys, prior to orbit insertion. The thermal problem, once the spacecraft is in orbit around Mercury, requires special design techniques: partly because of the large solar input (the solar constant is up to a factor 11 larger than at the Earth), but even more so because of the high level of heat radiated by the sunlit side of the low albedo planet. We present in this paper a brief outline of the scientific objectives and the preliminary spacecraft and mission designs.

The origin of Mercury's magnetic field, identified by Mariner 10, is not well understood, and remains a challenge for theories of planetary magnetism and evolution. Prior to the Mariner 10 flyby, it had been assumed that the planetary interior solidified very early in Mercury's history, thus preventing the operation of a classical dynamo. In the light of the unambiguous detection of a planetary field, a number of possible models have been proposed, in order to explain it either by modifying the composition of the core (to prevent complete freezing out) or by attempting to devise mechanisms which could provide the stable current systems needed for the formation of the field. One such model is based on the very large thermal gradients between the dayside and nightside hemispheres, maintained by the slow rotation of the planet. In most models, the magnetic field contains not only a dipole term, but significant higher order terms as well. A complete mapping of the planetary field is required to provide observational constraints on the various models and thus information on Mercury's interior and history.

The Hermean surface is very much lunar-like in the sense that it is pockmarked with impact craters of different sizes. There are, however, major differences: while smooth plains covering large areas are stratigraphically similar to the lunar mare, the intercrater plains of older age are a new feature. Furthermore, the Caloris basin with a diameter of 1300 km and the hilly structures near the antipodal point are unique to Mercury. Without a comprehensive understanding of these outstanding issues, we are unable to reconstruct the history of the early solar system. This also means that it is a matter of urgency in planetary science to complete the high-resolution imaging observations initiated by Mariner 10. Recent ground-based radar observations of Mercury indicated the possible presence of buried water ice in the polar regions. A most direct way to confirm (or deny) this conjecture is to compare the crater morphologies (particularly if a polar-orbiting phase can be incorporated in this mission) with those of the so-called rampant craters on Mars with softened rim structures. The modification of rampant craters above a latitude of about 35 deg is most likely the result of fluid flows generated by the water melted at impact. The polar crater zones are consequently one of the high-priority targets

A MERCURY ORBITER MISSION: Balogh A. et al.

for the imaging experiment. The chemical composition of the Hermean surface, retaining important information on the processes which formed it, also needs to be explored by detecting the signatures of the different elements through their induced gamma ray emission spectra.

The intrinsic magnetic field of the planet, while much weaker than that of the Earth, is nevertheless sufficiently strong to present an obstacle to the solar wind flow, thus creating a magnetosphere which differs in several important respects from that of the Earth. These differences make it a unique "laboratory" in which to study magnetospheric phenomena on time and length scales dramatically different from those in other planetary magnetospheres. The very tenuous atmosphere and the almost certainly insignificant ionosphere provide boundary conditions which result in very different patterns of current flow and energy transfer from the solar wind to the magnetosphere. The pressure balance between the planetary magnetic field and the solar wind provides the basic scaling law for the size of the magnetosphere. The field is weaker than that of the Earth by three orders of magnitude, and, while the solar wind velocity is not greatly different at the heliospheric distance of Mercury, its density is, on average, about 8 times larger than at 1 AU. These figures yield a scale size for the Hermean magnetosphere which is about 5 % that of the terrestrial magnetosphere.

From the point of view of comparative studies, the Hermean magnetosphere can be ranked among the most tantalizing systems. For example, the substorm generation process now under much debate (e.g., whether near-tail current disruption should hold the key or not) can be clarified by comparing the substorm effects at Earth and Mercury. This is because the lack of a significant ionosphere on Mercury will automatically rule out mechanisms invoking magnetosphere-ionosphere coupling as a key element, as far as the Hermean magnetosphere is concerned. Even so, solar wind interaction must lead to the development of a magnetospheric current system. How such an electric current system would flow and how should it be connected with the planetary surface (as a function of local electrical conductivities) must await detailed magnetic field and plasma observations by the Mercury Orbiter.

In order to address these objectives, a representative high priority payload has been defined. The instruments included are a multi-spectral imaging camera, a gamma ray detector, a magnetometer, plasma electron and ion detectors, plasma wave detectors and an ion emitter for spacecraft charge control. As a guideline, about half the resources allocated to the payload are for the planetary objectives, and the other half for the magnetospheric and space physics objectives. The nominal mass of the payload is 40 kg. The spacecraft design concept is primarily driven by requirements to carry the fuel needed for the large delta-V capability and to cope with the thermal environment. The spinning spacecraft, of dry mass of about 540 kg, is based on the ESA's Cluster spacecraft which already carries some 2.2 km/s delta-V capability. The propellant mass required for the baseline Mercury Orbiter mission is about 820 kg, corresponding to a total delta-V of 2.7 km/s. The total power foreseen in Mercury orbit is about 400 W. Communications are provided by a despun antenna of 1.47 m diameter, in both S- and X bands. The downlink rates are variable from 2 to 8 kbps, limited by the planned use of ESA 15 m ground stations. Following a transfer orbit from the Earth, using two Venus flybys and two Mercury flybys, the spacecraft will be injected into Mercury orbit with an apherm of 100,000 km. The orbit is then rotated, to a 200 x 16,800 km polar orbit, with a pericentre at 30° latitude north. In order to maintain the nominal orbit, fuel corresponding to 72 m/s is needed. The resulting orbit will provide full surface coverage, below 5,000 km altitude, in 150 days. In 264 days, a sampling time of 471 hours can be achieved over the north pole at altitudes below 1,200 km.

Widespread scientific interest has been expressed in the mission. At the conclusion of the study, expected in April 1994, the scientific and programme committees of the Agency will take a decision concerning whether to follow up with an industrial Phase A study.

GRAVITY STUDIES OF MEAD CRATER, VENUS

W. Bruce Banerdt, Nicole J. Rappaport, and William L. Sjogren (Jet Propulsion Laboratory, California Institute of Technology, Pasadena, CA 91109)
Robert E. Grimm (Arizona State University, Tempe, AZ 85287)

Mead Crater, with an outer ring diameter of 280 km and a depth of about 1 km, is the largest crater identified on Venus [1] (Figure 1). It presents perhaps the only opportunity for investigating the structure of the crust and lithosphere of Venus (and the effects of a large impact upon them) using gravity data, as the altitude of the Magellan spacecraft precludes the detection of gravity signals with spatial wavelengths much less than about two hundred kilometers. In November of 1992 Magellan's periapsis passed over Mead Crater, making it possible to acquire high-quality, high-resolution doppler tracking data. In this abstract we will describe some preliminary analyses of this data.

The gravity data set consists of 13 X-band Doppler radio tracks spanning 21 orbits (6178–6198). The quality of the X-band data was excellent, having an average noise of less than 0.2 mm/sec for 2-second data samples. Ten orbits had a definite signature for the crater, whereas the three orbits at the beginning and end of the span had essentially no crater signature. Figure 3 shows an example the doppler residuals (orbit 6186) relative to GM and to a 36th degree and order field [2]. The orbits crossed the crater (located at 57.5° E. latitude, 12.5° N. longitude) in a north-south direction and the spacecraft was at an altitude of 182 km over the crater. It can be seen that the negative signal from the crater (roughly 5° wide, centered at latitude 12.5) is superimposed on a strong regional signal; only a fraction of the regional signal is absorbed by the 36×36 field. In order to better isolate the crater anomaly, the residuals were reduced relative to a 60th degree and order field [3] (Figure 4). When this is done, the regional "background" becomes less than a milligal, and a negative anomaly of 3 mgal is centered over the crater. However, the 60×60 field itself contains a part (1–2 mgal) of the crater signal (Figure 2). Thus we estimate the total gravity anomaly at spacecraft altitude to be 4–5 mgal.

Several preliminary approaches have been used to interpret the gravity data. By comparing the 60th degree and order field to that computed from a global harmonic representation of the gridded topography, we find that the regional gravity is considerably subdued relative to the predicted gravity from topography, whereas the observed crater signal is relatively more prominent in the observed field. This indicates that the regional topography is considerably more compensated than the crater itself at wavelengths greater than about 600 km. Line of sight (LOS) accelerations were also computed using an orbit simulation program [4]. Topography within two crater radii of the center of Mead was used, tapered at the edges, and a nominal crustal thickness of 20 km was assumed for the compensation depth [5,6]. The best fit to the observed LOS accelerations are obtained from models with 0–30% compensation. This implies either little or no uplift of the moho, much deeper compensation (e.g., thicker crust), or perhaps some sort of low-density fill within the crater.

Considerable uncertainties remain in these models due to incomplete topographic coverage of the area, especially over the topographically rough rim deposits. The models are particularly sensitive to the amount of mass in the rim, as the crater itself is relatively shallow. We are currently working on extending both the spherical harmonic and LOS studies using a more complete representation of the topography derived from specially-processed cycle-3 altimetry data and stereo modeling.

References: [1] Schaber et al., *J. Geophys. Res.*, **97**, 13,257, 1992; [2] Nerem et al., *Geophys. Res. Lett.*, **20**, 599, 1993; [3] Konopliv et al., *Geophys. Res. Lett.*, **20**, 2403, 1993; [4] Phillips et al., *J. Geophys. Res.*, **83**, 5455, 1978; [5] Zuber, *J. Geophys. Res.*, **92** (17th LPSC suppl.), E541, 1987; [6] Banerdt and Golombek, *J. Geophys. Res.*, **93**, 4759, 1988.

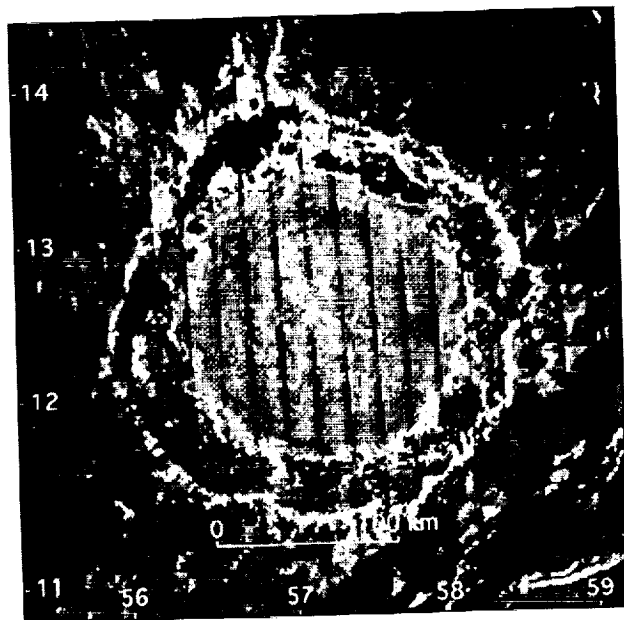


Figure 1: Radar image of Mead Crater. Image is 350 km across (C1MIDR-15N060).

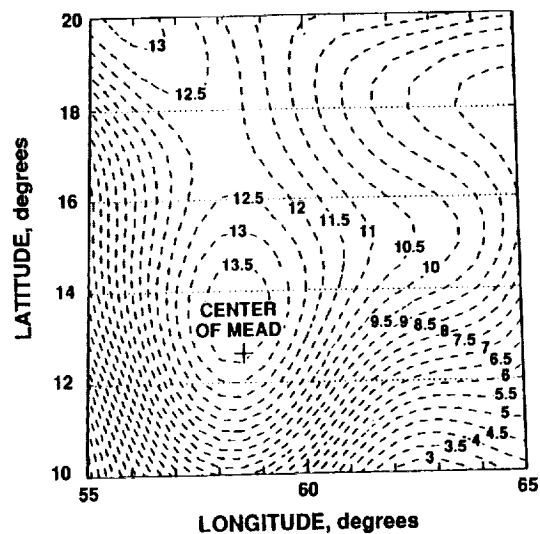


Figure 2: Radial acceleration at 182 km from PMGN60J. Contour interval is -0.5 mgal.

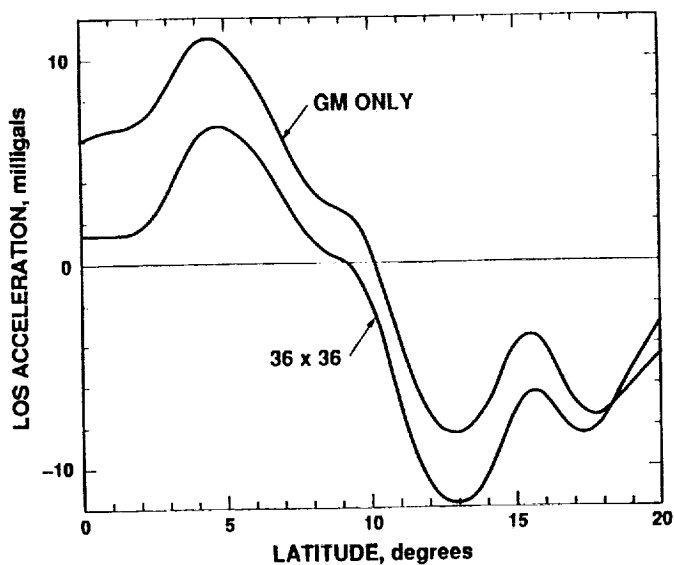


Figure 3: Magellan LOS acceleration profiles over Mead Crater derived from doppler residual relative to GM only, and to a 36×36 field [2]. Orbit number 6186.

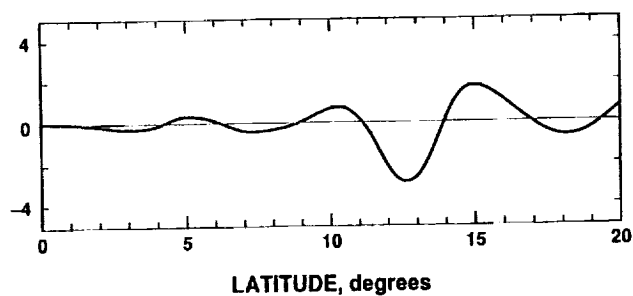


Figure 4: Magellan LOS acceleration profiles over Mead Crater derived from doppler residual relative to a 60^{th} degree and order field (PMGN60J). Orbit number 6186.

MARS SOIL: NANOPHASE MINERALS AND FORMATION PROCESSES; A. Banin, The Hebrew University, Rehovot 76100, Israel

A single "geological unit" consisting of fine, weathered material is covering large portions of the surface of Mars in a homogeneous, presumably thin, blanket of soil. Rocks and boulders are exposed on the surface and are surrounded and covered by fine loose soil material. Homogeneity of the soil material over the planet is manifested by the similarity of spectral fingerprints of the bright regions on Mars, the almost identical chemical composition found in the two Viking Lander sites, the resemblance of the physical and mechanical properties and of the chemical reactivity shown in the Viking Biology experiments conducted at the two landing sites.

The mineralogical nature of Mars soil is far from being understood, nor are the formation time and weathering processes known. Quantitatively, the two major mineral-forming elements in Mars soil are silicon and iron, constituting 44% and 19% of the soil as SiO_4 and Fe_2O_3 , respectively (1). The silicate phases have been studied only briefly, mostly because of their limited spectral fingerprinting in the VIS and NIR. Much attention was given to the iron minerals in the soil, due to their pronounced absorption in the VIS and NIR, making them easily detectable by telescopic observations (2,3). In the following, the available information on Mars soil mineralogy, mostly obtained by remote sensing, will be reviewed and it will be hypothesized that it leads to the suggestion that nanophase short-range-ordered ("amorphous") phases of the silicates and iron oxides abound in the soil. This then raises several questions: Why are the major minerals in Mars soil poorly crystalline? What are the weathering pathways? Why did not the secondary silicate and iron oxides in Mars soil "ripe" and develop into well crystallized phases despite the long period of time since aqueous-weathering took place? Is it the kinetics? Antarctic weathering analogs do not support this. Alternatively - is it possible that the minerals in the thin top layer of Mars soil, which is what we have sampled and analyzed up to now, were produced by a slow on-going weathering processes of volcanic materials proceeding on the surface of Mars over hundreds of millions of years?

Earlier studies (4) have identified 60% "silicate" in the soil, using the Mariner 9 IRTM data. Montmorillonite (a smectitic aluminosilicate clay mineral) was suggested as a major component of the dust and soil on Mars, on the basis of more detailed analysis of the IRTM (Mariner 9) data (5). Non-weathered basalt was rejected as it did not fit the spectral features. Nontronite and montmorillonite were initially suggested as the major silicate components on the basis of the elemental analyses of the soil (6). This was supported by successful simulations of the Viking Labeled Release (LR) experiment using iron-enriched montmorillonite (7) and the similarity of this clay's reflectance spectra in the visible range to those of Mars soil (8). Another candidate was suggested, primarily on the basis of spectral telescopic data, to be palagonite, a weathering product of volcanic glass (9-12). However, several palagonites tested did not simulate the reactivity of Mars soil as observed in the LR experiment (13). A magnesium containing silicate (saponite?) was detected in the analyses of the NIR spectra at $2.2\mu\text{m}$ (2). However, the typical doublet of well-crystallized standard montmorillonite at $10\mu\text{m}$ was not observed in the IR spectra of Mars, leading to the conclusion that no crystalline smectite is present in the soil (3) or, alternatively that it constitutes less than 15%-20% of the soil (14). If these observations are further corroborated, they suggest that most of the weathered silicates in Mars soil are of the low-crystallinity or amorphous varieties. No definitive identification of this phase was given until now. It is interesting to note in this context that a poorly crystalline silicate-aluminum mineraloid was detected in non-metamorphosed inclusions in EETA 79001, one of the SNC meteorites (15). Furthermore, the possibility that the silicate "rust" (iddingsite) found in the interior of Nakhla is of preterrestrial origin has not been completely ruled out, since this SNC meteorite is a fall with very limited terrestrial weathering. The "rust" is a silicate alteration-product produced perhaps by the action of fluids enriched in halides on olivine. The very limited data are consistent with di- or tri- octahedral phyllosilicates with excess Fe and Si (16).

Iron, the second most abundant element in Mars soil, appears to be primarily present in its oxidized form (ferric), strongly suggesting chemical weathering of the basaltic parent material. The typical reflectance spectrum of Mars in the visible/short wave NIR range (12,17,18) bears the strong fingerprinting of oxidized iron and has been reproduced more or less faithfully in laboratory measurements of many different iron-containing phases. They include "amorphous" iron oxides (19), palagonite (9,10), nanophase hematite deposited in silica matrix (11), and iron-enriched smectites (8,13). One conclusion from the abundance of spectral analogs is that unambiguous identification of the iron mineral(s) in Mars soil, on the basis of reflectance only, is not possible at present. A more important conclusion is that the accumulating evidence shows that iron in the weathered component of Mars soil is mostly present in poorly crystallized clusters of oxy-hydroxy ferric iron, or as crystalline minerals but in extremely small particle size range ("nanophases" or "nanocrystals"). Recent telescopic observations have detected typical hematite features at 860 nm, and possibly other crystallized iron oxides (12,20). However, these features are very weak and estimates of the content of hematite and/or other crystalline phases are in the range of 1-3% or less. The content of the magnetic mineral in the soil is also estimated to be in the range of 1-3%. It may be maghemite, magnetite or nanophase hematite that is typically superparamagnetic. However, the bulk of the iron oxide-oxyhydroxide in the soil is amorphous or short-range ordered and is characterized by extremely small particle sizes.

As a whole, the evidence now leads to the suggestion that much of the silicon- and iron-containing phases in Mars soil are short-range-ordered or "amorphous" i.e. do not have well developed crystallinity. This hypothesis is based on accumulating excellent telescopic observations during the late 1980s (1988-1990 Mars-Earth oppositions) and detailed laboratory studies on soil analogs. It opens a new and intriguing question—what is the peculiar mode of weathering that

MARS SOIL: NANOPHASE MINERALS AND FORMATION PROCESSES; Banin, A.

has produced these amorphous silicates and iron oxides? More specifically, what is the cause of the limited growth of crystals of secondary silicate and iron oxide minerals in the weathered soil on Mars. Given that currently the most accepted model for the soil formation is during earlier epoch (~3.5 billion years ago) when Mars was "warm and wet" (e.g. 21,22), it is puzzling that only a minor portion of the silicates and iron oxides have crystallized and developed a more thermodynamically stable mineralogical composition and particle size distribution.

Similar silicate and iron oxide entities are found on Earth only as transitory phases, which "ripe" rapidly (geologically speaking) to more stable minerals. Palagonites represent such a transitory assemblage of minerals produced as the initial weathering product of volcanic glass. The maximal age of palagonite deposits on Earth is in the range of $1-10 \times 10^6$ years.

Is it possible then that the peculiar nature of the Martian dust and soil is due to its being a relatively "young" weathering product that has formed, and continues to form at an extremely slow rate, over the last several hundred millions to a billion years? It is then plausible that this "recent" (in Mars time scale of changes) and non-evolved weathering product is coating or burying ancient, more evolved weathered mineral assemblages that formed in the earlier "warm and wet" epoch of Mars. This suggestion apparently goes against the "common wisdom" on weathering. The low temperature and aridity of the Mars environment preclude hydrolytic-weathering as a significant process (22). However, "surface-weathering", involving gas phase-solid phase reactions taking place at the atmosphere-rock microscopic interface may proceed, albeit at a very slow rate, even there. Such surface weathering may involve just the unfrozen water layers (with a thickness of 1-3 molecular layers, (24)), sorbed on the surface of any rock or solid phase by virtue of the surface potential exerted by the solid. These weathering reactions are, generally speaking, driven by the same chemical driving forces that act on rocks in the more humid environments on Earth with which we are familiar. Overall, these processes can be viewed as reequilibration of minerals formed under magmatic conditions of high temperature and low redox, with their new conditions of lower temperature, higher redox potential, higher water activity, and, frequently under soil conditions, more varied and less fractionated ionic environment. So it is expected that the end products of these weathering processes may be similar to those found in the more water-rich environments of Earth. A major difference in rate is, however, expected. The lack of excess liquid water on Mars may cause chemical saturation of the aqueous-phase thus slowing down the overall rate of dissolution. Furthermore, the low temperature prevailing in these extremely cold environments may slow down the intrinsic rate of the reactions, causing the processes to proceed at a very slow pace. Still, in Mars-like environments on Earth (e.g. Dry Valleys, Antarctica) where hydrolytic-weathering processes involving excess water are limited or non-existent, the products of the surface-weathering mechanisms become quantitatively important, given enough time to proceed (25). The data available for Antarctic soils cover a period of ~3 million years only (25). Mars surface may be of much older age, perhaps up to 1 billion years old. The global surface stability (lack of plate tectonics) facilitates the accumulation of weathering products over long periods. Even at an extremely slow linear rate of rock-surface weathering of 0.3 nm/yr (i.e., about one molecular layer per year), an average layer of 30 cm could be weathered on Mars over the last 10^9 years. Wind abrasion rates on Mars are estimated at 1 $\mu\text{m}/\text{yr}$ (27) i.e. 3-4 orders-of-magnitude faster than the assumed hydration-front penetration rate, thus the assumption of a linear-rate of advancement of the weathering front (rather than a square-root-of-time dependence), is warranted. This leads to higher overall rate of weathering than arrived at under diffusion-limited conditions (22). Particularly susceptible to the surface-weathering processes are the more recently erupted volcanic materials. Estimated at $26.4 \times 10^6 \text{ km}^3$ during Amazonian (27), these materials may have supplied the highly unstable minerals that weathered and produced a thin coating of dust and soil remotely sensed on much of the planet's surface. This "recent" (in Mars time-scale of changes) and non-evolved weathering products may be coating or burying ancient, more evolved weathered minerals assemblages that may have formed in an earlier "warm and wet" epoch of Mars.

References: (1) Clark, B.C. et al. (1982) JGR 87, 10059-10067. (2) Singer, R.B. (1985) Adv. Space Res. 5, 59-66. (3) Roush, T.L. et al. (1993) in Remote Geochemical Analysis, K. Pieters and P. Engelhart, Eds., Cambridge Univ. Press, pp367-393. (4) Hanel, R. et al. (1972) Icarus 17, 423-442. (5) Toon, O.B. et al. (1977) Icarus 30, 663-696. (6) Toulmin, P.III et al. (1977) JGR 82, 4625-4634. (7) Banin, A. and Rishpon, J. (1979) J. Mol. Evol. 14, 133-152. (8) Banin, A., et al. (1993) JGR-Planets, in press. (9) Allen, C.C. et al. (1981) Icarus 45, 347-369. (10) Singer, R.B. (1982) JGR 87, 10159-10168. (11) Morris, R.V., et al. (1989) JGR 94, 2760-2778. (12) Bell, J.F.III et al. (1991) JGR 95, 14,447-14,461. (13) Banin, A. et al. (1988) Origins of Life 18, 239-265. (14) Orenberg, J. and Handy, J. (1992) Icarus 96, 219-225. (15) Gooding, J.L. and Muenow, D.W. (1986) Geochim. Cosmochim. Acta 50, 1049-1059. (16) Gooding, J.L. et al. (1991) Meteoritics 26, 135-143. (17) Singer, R.B. et al. (1979) JGR 84, 8415-8426. (18) McCord, T.B. et al. (1982) JGR 87, 3021-3032. (19) Evans, D.L. and Adams, J.B. (1979) PLPSC 10, 1829-1834. (20) Singer, R.B. et al. (1990) LPSC XXI, 1164-1165. (21) Banin, A. et al. (1992) Ch. 18 in "Mars", H.H. Kiefer, B.M. Jakosky C. Snyder and M.S. Matthews, Eds., Univ. of Arizona Press, pp. 594-625. (22) Gooding, J.L. et al. (1992) Ch. 19 in "Mars", H.H. Kiefer, B.M. Jakosky C. Snyder and M.S. Matthews, Eds., Univ. of Arizona Press, pp. 626-653. (23) Singer, A. and Banin, A. (1990) Sci. Geol. Mem. 88, 173-181. (24) Banin, A. and Anderson, D.M. (1975) Nature 255, 261-262. (25) Allen, C.C. and Conca, J.L. (1991) PLPSC 21, 711-717. (26) Arvidson et al. (1979) Nature 278, 533-535. (27) Greely, R. and Schneid, D. (1992) Science 254, 996-998. (28) The work reported here was supported in part by the NASA Exobiology Research Program and by grants from the National Research Council Washington D.C. and the Hebrew University.

THE HYPSONOMETRIC DISTRIBUTION OF IMPACT CRATERS ON VENUS; M. Banks, S. Emerson, R.G. Strom, Univ. of Arizona, Tucson, AZ, and G.G. Schaber, U.S.G.S., Flagstaff, AZ.

The spatial and hypsometric distribution of impact craters on Venus places important constraints on resurfacing models. Phillips, et al. (1992) have shown that the spatial distribution of impact craters on Venus cannot be distinguished from a random distribution. This is illustrated by Figure 1 which shows cylindrical projections of 5 Monte Carlo simulations of 932 spatially random points compared to the distribution of the 932 craters on 98% of Venus. If the spatial distribution can not be distinguished from a random one, then one would expect that the distribution of impact craters with respect to elevation should also be indistinguishable from a random one. Figure 2 is a histogram showing the percentage of all observed craters and the percentage of surface area in 500-m elevation bins. The histogram shows no more than a 1.6% difference between the percentage of craters and the percentage of surface area in any 500-m bin containing a crater. Multinomial chi square statistical tests were performed of the data set. In these tests probability values (P values) greater than 0.05 show "no evidence against a random distribution" of craters with respect to elevation. The P value for all categories of altitude is 0.17. However, this test is not as reliable because the 5 highest altitude categories contain too few craters per category. To achieve statistical stability the five highest altitude categories were combined and the observed, expected, difference, and "normalized difference" for altitude categories were compared. This is statistically more trustworthy and yields a P value of 0.31. Thus, both tests indicate that there is "no evidence against a random distribution" of impact craters with respect to elevation, with the more reliable test indicating a greater probability of randomness. These results are not in agreement with an earlier report of possible ancient terrains on Venus (Schultz, 1993), or crater density variations of about 10% within 2-km elevation bands (Herrick, 1993). Our results support a remarkably random distribution of craters with elevation and agree with the observed spatially random distribution of the crater population. Therefore, on average, the highlands and lowlands have the same crater density and age. In reality, there are surely age differences within each venusian terrain that can be determined by stratigraphic relations, but the correspondence in average ages suggests that the differences are not great on an absolute time scale. Even recent activity has not had a statistically significant effect on the crater population, which remains largely intact since it was formed. Consequently, it is not possible to determine relative or absolute ages of local or regional areas by crater densities, because the crater population has a spatially and hypsometrically random distribution with stochastic variations.

VENUS CRATER HYPSONOMETRIC DISTRIBUTION, Banks *et al.*

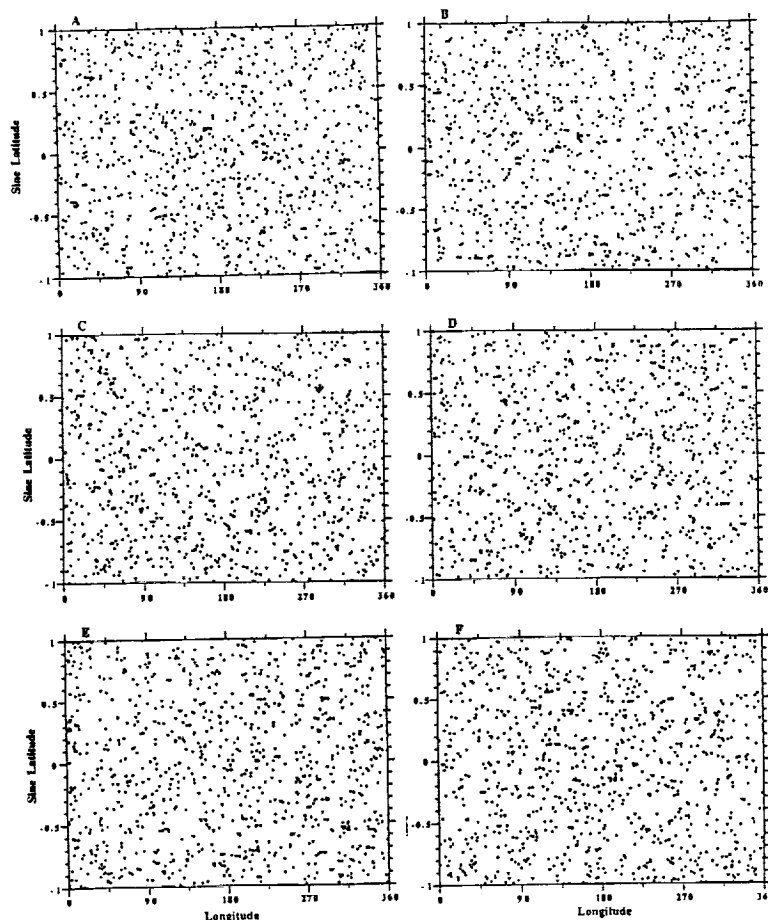


Fig. 1. Cylindrical projections of 5 Monte Carlo simulations of 932 spatially random points compared to the distribution of the 932 craters on 98% of Venus. Note the "clusters" and "holes" due to stochastic variations. Venus is B.

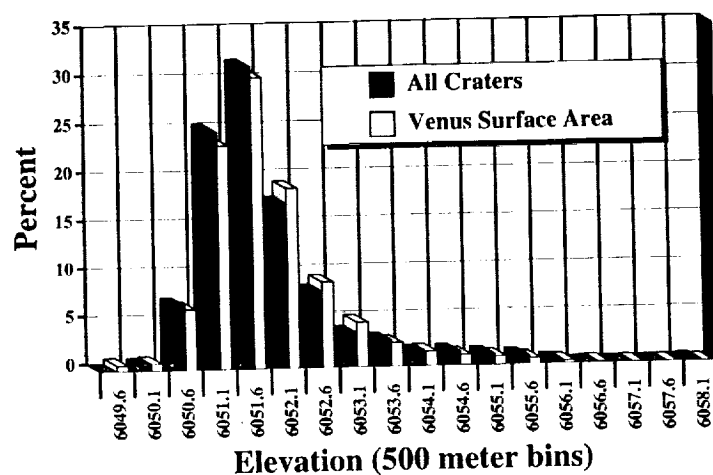


Fig. 2. Histogram showing the percentage of all observed craters and the percentage of surface area in 500-m elevation bins.

References: Herrick, R.R., *Lunar Planet. Sci. Conf. XXIV*, Abstract, 645-646, 1993; Phillips, R.J. et al., *J. Geophys. Res.*, 97, E10, 15,923-15,948, 1992; Schultz, P.H., *Lunar Planet. Sci. Conf. XXIV*, 1255-1256, 1993.

OBSERVATIONAL AND COMPUTATIONAL EVIDENCE FOR GRAVITATIONALLY STABLE PARTICLE ACCRETIONS IN THE PERSEID METEOR STREAM; J. C. Barentine, Cortez High School

Recent results in the field of meteoroid dynamics in Short Period Comet (SPC) streams have yielded a new model of the stream of Comet P/Swift-Tuttle (1992t). Unusually high Zenithal Hourly Rates (ZHRs) noted in the Perseid meteor shower, of which P/Swift-Tuttle is the parent body, in c.1861-65 and c. 1988-92 suggest a localized accretion of particles preceding and following the comet during its 135-year period. A computer simulation of the stream appears to confirm the existence of the accretions through gravitational theory. The model was tested in the shower of 1993, in which outside predictions of meteoroid "storm" were not fulfilled. The lack of increased activity conforms well to the projections of the model, in which the particle groupings correspond roughly to the L4 and L5 Lagrange points.

After the apparition of 1862, the orbit of P/Swift-Tuttle was deduced by Sciaparelli with a return postulated for 1982. In 1973, B. Marsden linked the comet with an earlier observation of Comet Kegler 1737III, changing the perihelion date to T=November 1992.

The comet's particle shower, the Perseids features a slow rise and fall in activity about a maximum which occurs on or about August 12 UTC. The reliability of the shower's strength, with normal rate of ZHR ~100, is an indicator that the overall stream density is high. Observers reported a new maximum feature in observations beginning in 1988, with the "early" maximum several hours before the normal peak. This new yearly attribute grew in intensity until 1991, when observers in east Asia reported a rate of ZHR>500 on c. 1991 August 11.7 UTC. The unusually high rate of the early maximum continued into 1992.

These data suggested a new orbital feature within the particle stream which was moving at or near the orbital velocity of the parent body. The density of this feature was concluded to increase with respect to time by the parallel rise in Perseid shower activity. The apparent relative motion of this particle mass indicates a gravitational relationship which allows the component particles to remain near the mass without being dispersed into the local medium. If the proper forces were exerted on the stream, it is possible that this feature could exist for several thousand years. Observations similar to those of 1988-92 were noted in 1861-62, in advance of P/Swift-Tuttle's 1862 return. This allows that the feature predates the aforementioned perihelion passage. Based on high ZHR's in the showers of 1864-65, a similar accretion mass likely exists following the comet as well. The foundation for these proposed accretions was set by way of the observational evidence noted.

The standard correction was applied to data collected from observers worldwide during the 1993 shower and the ZHRs displayed in Fig. 1, showing the high central stream concentration. This central peak, though, does not appear to be of a "storm" nature. The line shown was a smoothing spline fit, with $\lambda=0.01$.

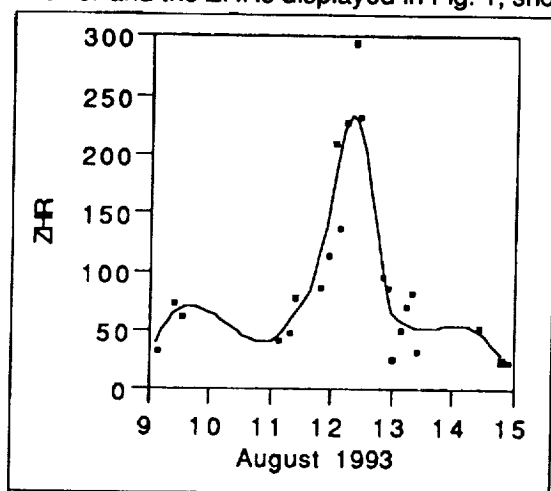


Fig. 1. ZHRs from the 1993 Perseid meteor shower during the period 9 to 15 August UTC. Data points represent averaged values computed in decimal day intervals by the equation in Fig.1.

To test the model against gravitational mechanics theory, a computer simulation was devised. The software used was the commercially-available *Dance of the Planets* (copyright 1989 Applied Research & Computing, Inc.) This program was chosen due to its wide use among both amateur and professional astronomers to facilitate easy reproduction of the results reported here. The orbital elements of P/Swift-Tuttle and 9 test particles included in the simulation are given in Fig. 2. The masses of the particles are assumed to be nearly zero, and are treated in the same manner as the comet itself in relation to the larger masses of the Sun and planets. The dates of perihelion of the particles were set in intervals of 0.1d, five ahead of and four following the comet for a total system of 10 masses. The gravitational influence of the nine planets was allowed to act upon this system and is responsible for the subsequent results. The Poynting-Robertson effect

PARTICLE ACCRETIONS IN THE PERSEID METEOR STREAM : J.C. Barentine

was not taken into account in this simulation, leading to a purely gravitational solution. Although excluding forces lowers the accuracy of the simulation to a certain extent, the degree of accuracy attained is enough to encompass the results presented herein. No claims are made which place particles in exact locations; the precise margin of error is unknown, but presumed low as gravity is the primary source of displacement. The program effectively solves the equations of motion through Newtonian and Keplerian mechanics and integrates the products over time.

The initial setting of the simulation was for the date 6 January 4609 BC (the setting 06\27.00\ -4609 in *Dance* 's mode of time). Execution of the program was performed on a personal computer operating at 33MHz and independently confirmed on a second computer. The simulation ran ~37500 years of time and was displayed through orbital diagrams. An image at T=34609 years is shown in Fig. 3. Particle compression begins

as they fall into three distinct areas of space: ahead of, proximal to, and behind the comet itself. Finally, two main areas of accretion exist, ~60 degrees ahead of and behind P/Swift-Tuttle. During the simulation, individual particles were seen to move from one accretion "lobe", passing the comet, into the other lobe, and back in spirals lasting over 5,000 years. Settling into the final configuration does not appear to halt the particles' passage. Despite repeated passes near the Jovian planets, which ordinarily would severely deform ordinary cometary orbits, these accretions appear to be relatively stable, regardless of Jovian perturbations.

As the "storm" feature of the Perseid stream predicted to coincide with a locally-dense region of particles did not appear in 1993, the model can be analyzed to provide information regarding when this predicted feature will actually appear in the shower observations. Assuming that the simulation provides a reasonably accurate description of the orbital features of P/Swift-Tuttle, including the relative positions of the accretion lobes, a feature of this type is most likely to appear in 1994-95, being roughly equidistant in time from the comet's perihelion T=December 12.3 1992 as the 1991 East Asia feature is. The possibility exists that it may go unnoticed; this stems largely from the compression density of the feature,

which may cause it to pass the node at Earth's orbit either before or after the August shower date. However, its density is most likely similar to that of the preceeding accretion lobe; if so, it will be observed on time.

A new view of such particle streams has emerged which suggests an equally novel approach toward studying the gravitational forces acting on these particles. The particle streams of other short-period comets whose parent bodies are still active ejectors should

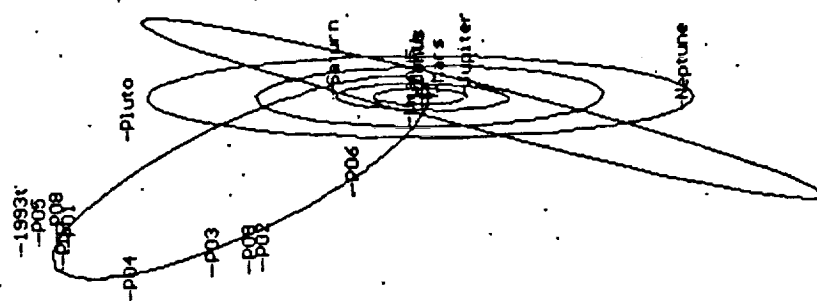


Fig. 3. Orbital diagram from the described simulation at T=34609 yrs., clearly displaying areas of accretion. Test particles are denoted as "P" and a two-digit identification number.

show similar results upon long-term examination of their meteor showers. Currently, the Leonid (P/Temple-Tuttle) and the Taurid (P/Encke) streams are candidates for further work, as well as an examination of the gravitational forces which allow the accretions to remain relatively stable.

Object	e	q	I	W	w	T
1992t	.958216	.9636	113.4266	139.4442	153.0016	1992.12123
P01	.958216	.9636	113.4266	139.4442	153.0016	1992.12118
P02	.958216	.9636	113.4266	139.4442	153.0016	1992.12119
P03	.958216	.9636	113.4266	139.4442	153.0016	1992.12120
P04	.958216	.9636	113.4266	139.4442	153.0016	1992.12121
P05	.958216	.9636	113.4266	139.4442	153.0016	1992.12122
P06	.958216	.9636	113.4266	139.4442	153.0016	1992.12124
P07	.958216	.9636	113.4266	139.4442	153.0016	1992.12125
P08	.958216	.9636	113.4266	139.4442	153.0016	1992.12126
P09	.958216	.9636	113.4266	139.4442	153.0016	1992.12127

Figure 2. Orbital elements for Comet P/Swift-Tuttle and the nine test particles from the computer simulation described in the text.

IMPACT CRATERS AS INDICATORS OF SUBSURFACE H₂O ON MARS.

N. G. Barlow, Lunar and Planetary Institute, 3600 Bay Area Blvd., Houston, TX 77058.

Impact craters provide remotely sensed information about the third dimension (depth) of a planetary surface. Changes in the morphologies of Martian impact craters and their ejecta blankets have been attributed to changes in subsurface properties (1) or to interaction with the atmosphere (2). A combination of crater studies conducted by the author and colleagues, including studies of ejecta blanket morphologies, rampart ejecta blanket sinuosity, and regional crater depth variations, strongly suggest that subsurface volatiles dominate in influencing the observed features.

Ejecta Studies: Barlow and Bradley (3) conducted a study of 3819 craters surrounded by an ejecta blanket distributed across the entire Martian surface. Ejecta morphologies were subdivided into seven classes: single lobe rampart, double lobe rampart, multiple lobe rampart, radial, diverse, pancake, and amorphous. Of these seven classes, the diverse and pancake morphologies are found within specific diameter ranges in localized regions of the planet. The radial morphology is associated with small craters (generally <6-km-diameter in the equatorial region), craters on the flanks of volcanoes, and very large craters (generally >60-km-diameter). Amorphous morphologies are found around large craters as well but appear to represent highly weathered ejecta blankets. Double lobe rampart craters dominate in the 40°-65°N latitude range, with a lower concentration in the 40°-65°S latitude range. Double lobe craters exhibit diameters primarily in the 8-50 km range. Single lobe craters occur primarily in the 8-20 km diameter range within the equatorial region of Mars, giving way to multiple lobe rampart craters at larger crater diameters (16-45 km). However, at higher latitudes, single lobe craters extend over a larger diameter range (up to 60 km diameter) and multiple lobe craters are rare to non-existent.

Ejecta Sinuosity Studies: Barlow (4) and Bridges and Barlow (5) computed the degree of sinuosity exhibited by 1582 single lobe, 251 double lobe and 380 multiple lobe craters across Mars. These studies found that the single lobe morphology displays lower degrees of sinuosity than the multiple lobe morphology. The outer lobe of the double lobe morphology is similar in sinuosity to single lobe. Inner lobe(s) of double lobe and multiple lobe craters are less sinuous than the outer lobe(s). Resolution does play some role in the actual sinuosity values, but the above relationships are seen to hold when resolution effects are taken into consideration. The only statistical variation of sinuosity is seen among the rampart ejecta classes--no significant variation in sinuosity with latitude, longitude, diameter, or terrain is seen for craters within a particular ejecta class.

Crater Depth Studies: Pike and Davis (6) derived a globally averaged depth-diameter relationship for fresh Martian impact craters. Recent photoclinometric studies of crater depths (7, 8) reveal that depth-diameter ratios can vary considerably across the Martian surface, probably as the result of changes in target properties. In areas of thick, friable deposits such as the Medusae Fossae formation, craters are deeper than in the equatorial plains or highlands. At high northern latitudes, preliminary studies suggest that fresh craters are shallower than similarly sized craters at lower latitudes. The lower depth-diameter ratio of craters at high latitudes has been suggested by previous morphologic studies to be the result of relaxation (9) and is consistent with theoretical models of near-surface ice deposits in these regions of the planet (10, 11).

Summary and Discussion: The diameter-latitude variation of single lobe and multiple lobe rampart morphologies is consistent with the theoretical distribution of subsurface ice and water on Mars (10, 11), but is difficult to explain using the theory of atmospheric entrainment of ejecta (2). Barlow and Bradley (3) therefore prefer the theory that the rampart crater ejecta morphologies on Mars result from impact and vaporization of subsurface volatiles. The results from the sinuosity and crater depth studies also are consistent with subsurface volatiles. Combining the results of these studies, we propose that single lobe craters are formed from impact into predominantly ice-

MARTIAN IMPACT CRATERS AND SUBSURFACE H₂O: Barlow N.G.

rich targets, multiple lobe craters excavate to depths containing liquid-water/brines, double lobe craters result from impact into layered targets where the upper layer has a higher volatile-to-clast ratio than the lower layer, and radial craters result from excavation of material with an overall low volatile-to-clast ratio (i.e., dry materials). If multiple lobe craters result from excavation into liquid reservoirs, larger sinuosity values than those resulting from impact into ice-rich terrain would be expected. Observation of lower depth-to-diameter ratios and rampart morphologies around smaller craters at high latitudes supports the proposal of theoretical models and other geologic evidence that ice occurs at or very near the surface at high latitudes (>35°-40° latitude).

References:

- (1) Carr, M. H. et al. (1977) *JGR*, **82**, 4055-4065. (2) Schultz, P. H. (1992) *JGR*, **97**, 11623-11662. (3) Barlow, N. G. and Bradley, T. L. (1990) *Icarus*, **87**, 156-179. (4) Barlow, N. G. (1994) Submitted to *JGR*. (5) Bridges, N. T. and Barlow, N. G. (1989) *LPSC XX*, 105-106. (6) Pike, R. J. and Davis, P. A. (1984) *LPSC XV*, 645-646. (7) Barlow, N. G. (1992) *LPSC XXIII*, 63-64. (8) Barlow, N. G. (1993) *LPSC XXIV*, 61-62. (9) Squyres, S. W. and Carr, M. H. (1986) *Science*, **231**, 249-252. (10) Fanale, F. P. (1976) *Icarus*, **28**, 179-202. (11) Clifford, S. M. (1993) *JGR*, **98**, 10973-11016.

A QUANTITATIVE ASSESSMENT OF AN IMPACT GENERATED RING VORTEX Olivier S. Barnouin and Peter H. Schultz, Dept. Geol. Sci., Brown University, Providence, R.I. 02912

Introduction: Studies show the importance of an atmosphere in the ejecta emplacement process [1,2,3,4,5] where an advancing ejecta curtain displaces atmosphere to form two ring vortices at its upper edge [3,6,7]. The stronger vortex forms near the target surface and can dominate the ejecta emplacement process by entraining and depositing sufficiently the fine ejecta thereby producing contiguous ramparts and/or flow lobes over a wide range of scales [3,4]. Theoretical studies [6,7] analytically estimated the circulation in the lower vortex generated by the advancing impermeable ejecta curtain and the decay of the flow velocity in the vortex. These attempts to quantify the formation and evolution of the lower vortex only qualitatively replicate observations made at both small and large scales. A refined theoretical assessment in conjunction with new experiments performed at the Ames Vertical Gun Range (AVGR) provide a new framework for predictions at large scales depending on target and atmospheric conditions during impact.

Theory: For a small enough vortex, the impermeable ejecta curtain advancing through an atmosphere can be considered a semi-infinite plate [9]. A similarity solution exists for an incompressible fluid under these conditions, and dimensional analysis gives a circulation:

$$\Gamma = 3.7 V_e H t^{1/3} \quad (1)$$

where V_e and H are the curtain velocity and height at time t after impact [9]. The exact time, impermeable length, and velocity of the curtain when the curtain becomes porous must be known in order to estimate the circulation accurately. High speed video images allows approximating these parameters at the time when the vortex essentially no longer gains momentum from the curtain. Since the height H measured does not account for partial permeability of the ejecta curtain [10], the circulation estimated using the latter variables should be greater than its actual value.

The motion of the lower vortex can be predicted by Helmholtz's law which states that a vortex moving in an irrotational flow will continue unaffected unless acted upon by another flow. Since the upper ring vortex is disrupted extremely rapidly [1,2,3], the lower vortex should continue to move radially outward at the velocity imparted to it when the curtain becomes porous. However, this prediction does not hold true if viscous forces at the target surface significantly reduce the advance of the vortex. These forces may be important for small circulation Reynolds numbers ($Re = \Gamma/\nu$ where ν is the kinematic viscosity) but are not important for high Re where the viscous drag at the surface of the target are confined to a thin boundary layer.

Two models estimating the decay time for the flow velocity in the ring vortex are considered. The first is the Oseen or Lamb vortex model for two dimensional flow [7]:

$$V_\theta = \Gamma(1 - \exp(-r^2/4\nu t))/2\pi r \quad (2)$$

where V_θ is the azimuthal velocity at r , the radial distance from core axis of the vortex, and t , time. This model has two forms: 1) ν is equal to the kinematic viscosity and the flow in the vortex is laminar; 2) ν is replaced by $K^2(\Gamma/\nu)^{-1/2}$ where K is a constant and the flow in the vortex is turbulent [11]. As in [12], the radius R for an impact generated ring vortex is very much greater than the radius of its core r and eq.(2) should successfully describe the decay of these. However in [12], the ring vortex was allowed to move parallel to its axis and did not expand laterally as for impacts. Thus, the simple Oseen or Lamb vortex may not describe the behavior of ring vortices generated by impacts.

To overcome this problem, a second modified Oseen vortex model includes the effect of the laterally expanding ring by ensuring that the kinematic energy initially imparted to the vortex is conserved, excepting for internal energy losses due to viscous decay already included in eq.(2). Because this energy must be conserved over the volume of a toroid, the circulation in the vortex must reduce by the square root of the radial distance $R(t)$ to give:

$$V_\theta = \Gamma(R_0/R(t))^{1/2}(1 - \exp(-r^2/4\nu t))/2\pi r \quad (3)$$

where R_0 is the vortex radius when the curtain becomes impermeable. As for eq.(2), ν in eq.(3) can be modified for turbulent flow with Γ multiplied by the energy conservation factor indicated in eq.(3).

The long-term behavior of a ring vortex does not only depend on viscous decay as described by the Oseen vortex model. For some cases when Re of the vortex exceeds a certain critical value [8], a ring vortex will break into a number of waves [8,13,14]. This occurs because at higher Re , certain instability modes grow rapidly in the vortex core [14]. An interesting feature is that once the critical Re is achieved, the growth rate of the waves seem to be unaffected by the magnitude of Re [8].

Observations: A series of quarter space experiments were undertaken at AVGR in order to test the theory above. Ring vortices were generated by using a coarse sand target, but unnecessary complications due to extensive ejecta entrainment in the vortex flow were avoided. A Venturi pressure gauge was used to measure the flow past the quarter space plate to obtain two maximum vortex flow velocities in the lower ring vortex passing by the gauge.

As Fig. 1 shows, the experiments indicate that the outward motion of the lower ring vortex is unaffected by

IMPACT GENERATED RING VORTEX: Barnouin, O.S. and Schultz, P.H.

viscous drag affects, confirming theoretical expectations.

Table 1 compares the initially generated circulation obtained by eq.(1) to that obtained by eq.(2) and eq.(3), for both laminar and turbulent flow for three sample experiments. The magnitude of Γ from eq.(2) and eq.(3) for laminar flow are much less than values from eq.(1). Hence, flow in the these ring vortices are not laminar. Model (2) for turbulent flow generates Γ values which are still significantly less than Γ obtained from eq.(1). Model (3) for turbulent flow does the best job in duplicating the values from eq.(1). Furthermore, the values of Γ obtained by the latter model for both vortex velocities measured, very nearly equal each other as expected theoretically. The discrepancy between Γ calculated by eq.(1) and eq.(3) for the turbulent case for shot 931010 and 931015 may be explained by the overestimation of H in eq.(1) described above. Thus, the modified energy-conserving Oseen vortex model appears to describe adequately the decay of the vortex prior to its possible breakdown.

Although the observed vortices are turbulent, their Re are not sufficient to cause the breakdown of the lower ring vortex into dominant wave modes. At higher atmospheric pressures with fine grained target, the large Re results in an initially stable circular lower ring vortex that scours the inner rim and generates flow lobes attributed to the break up of the ring vortex into waves [3].

Discussion: Laboratory results illustrate certain aspects of the behavior of impact -generated ring vortices that should apply at large scale. First, they indicate that these vortices are turbulent. Second, they show that the outward motion of the ring vortex is unaffected by the surface. The breakdown of the vortex cannot be then attributed to surface shear effects; rather its occurrence reflects instabilities in the vortex flow as described in [9,13,14]. Third, prior to the vortex break up by these instabilities, the magnitude of the flow in the vortex can be described by eq. (3) although it should be modified for incompressible flows. Fourth, multiple lobes can be explained by a variety of means: 1.) Concentric contiguous distal ramparts result from a simply decaying circular ring vortex enhanced by a bimodal target distribution [3,7]; 2) A contiguous rampart surrounded by multi-lobate flow-like structures could indicate vortex breakdown: sudden growth of a vortex core instability growth forms the rampart while the unstable ring vortex forms the flow lobes ; 3) Several lobate structures could be a combination of the above processes plus flow separation at the distal ejecta edges and autosuspension [3].

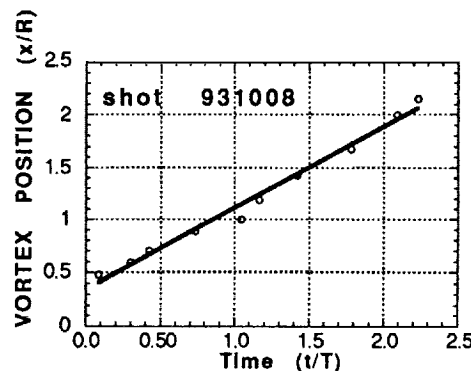


Fig. 1: Vortex position as function of time indicating a constant advancing velocity .

Table 1: Comparison of circulations obtained from ring vortex flow velocities measured

shot	Γ from eq(1)	Γ from laminar flow	Γ from eq(2) for flow	Γ from turbulent flow	Γ from eq(2) for flow	Γ from laminar flow	Γ from eq(3) for flow	Γ from turbulent flow	Γ from eq(3) for flow
931009	0.0460	0.0070	0.005	0.0232	0.0159	0.0165	0.0160	0.0545	0.0485
931010	0.0851	0.0049	0.003	0.0143	0.0084	0.0091	0.0078	0.0266	0.0200
931015	0.0951	0.0070	0.005	0.0251	0.0147	0.0108	0.0094	0.0384	0.0294

Values for Γ are in m^2/s

References: [1] Schultz, P.H. and D.E. Gault (1979) *JGR* 84, 7669-7687. [2] Schultz, P.H. and D.E. Gault (1982) *GSA* special paper 190, p. 153-174. [3] Schultz, P.H. (1992a) *JGR* 97, 11623-11662. [4] Schultz, P.H. (1992b) *JGR* 97, 16183-16248. [5] Schultz, P.H. and J. Grant (1989) *LPSC XX*, 972-973. [6] Barnouin, O.S. and P.H. Schultz (1992) *LPSC XXIII*, 65-66. [7] Barnouin, O.S. and P.H. Schultz (1993), *LPSC XXIV*, 63-64. [8] Saffman, P.G. (1978) *JFM* 84, 625-639. [9] Anton, L. (1939) *Ing. Archiv.* 10, 411-427. [10] Schultz, P.H. and Barnouin, O.S.(1994), *LPSC XV*, (in this issue). [11] Owen, P.R. (1970) *Aero. Quart.* XXI, 69-78. [12] Sallet, D.W. and Widmayer, R.S. (1974) *Z. Flugwiss.* 22, 207-215. [13] Widnall, S.E. and Sullivan, J.P. (1973) *Proc. R. Soc. Lond. A* 322, 335-353. [14] Widnall, S.E. and Tsai, C.Y. *Phil. Trans. R. Soc. Lond. A* 287, 273-305.

CONCENTRIC WRINKLE RIDGE PATTERN AROUND SIF AND GULA; A.T.Basilevsky; Vernadsky Institute, Moscow, 117975, Russia

Summary. Wrinkle ridges were mapped on plains around Sif and Gula Montes. Their trends show a prominent concentric pattern around Sif and Gula topographic rise. Wrinkle ridges correspond to a quite early stage of the Venus stratigraphy while Sif and Gula are relatively young and their lavas are not deformed by the ridges. This probably means that during the time of wrinkle ridge emplacement at the place where now are Sif and Gula there was a topographic rise or other object prominent enough to diverge the wrinkle ridges.

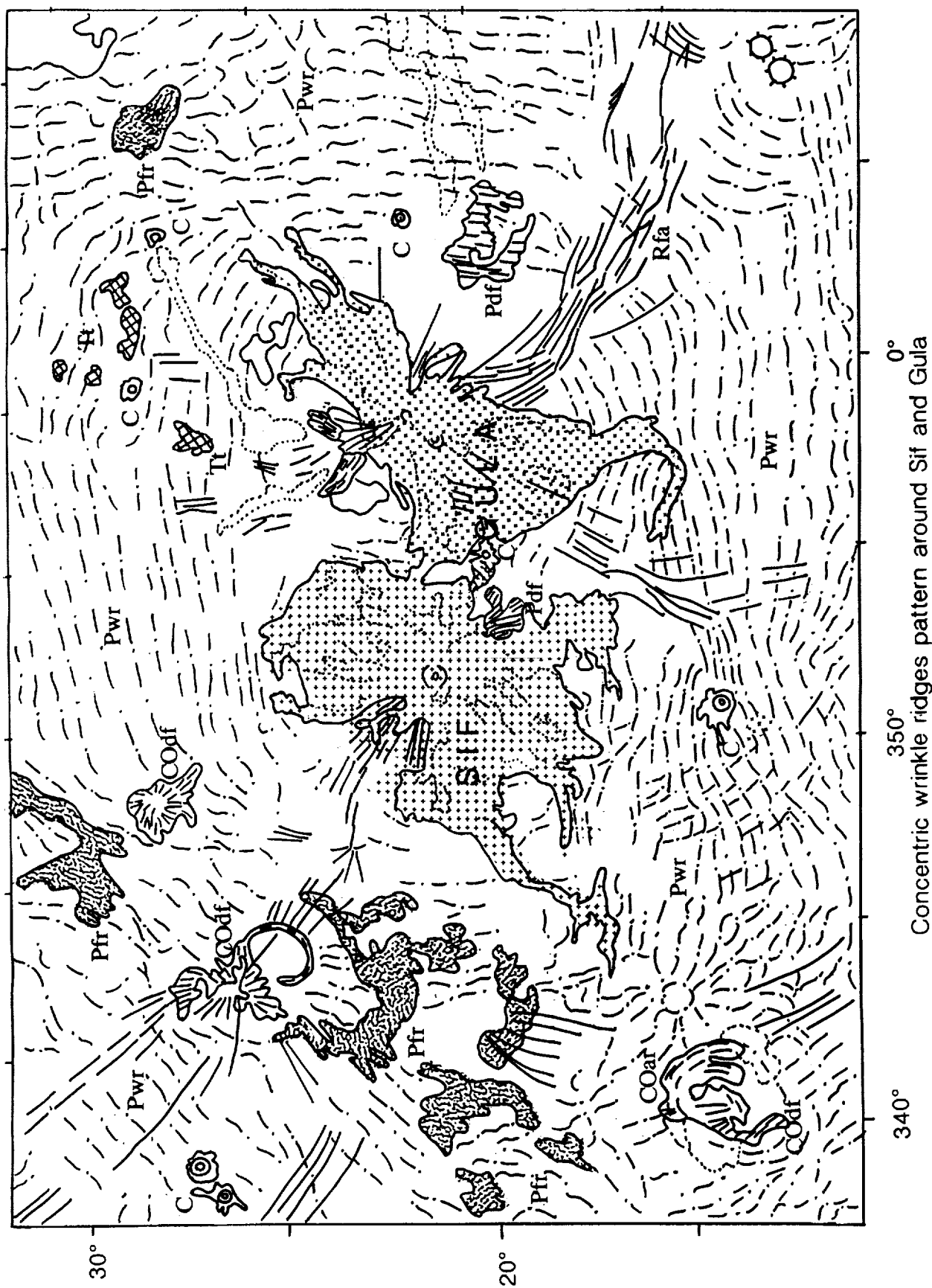
Introduction. Wrinkle ridges are abundant on most venusian plains [1,2]. Plains with wrinkle ridges (Pwr) is a distinct stratigraphic unit manifesting one of the major, if not the largest, episodes of volcanic resurfacing of Venus of about 500 m.y. ago [3,4]. Previous studies showed both evidence for existence of two or more differently oriented sets of these compressional features with butting and zig-zagging relations indicating on their formations at different times [5] and globally organized distribution of wrinkle ridge trends indicate a global stress control [6] that probably favors the idea of wrinkle ridge formation more or less synchronously, but of course not instantly, all around the planet. Our study is a step in inferring the history of tectonic stresses in the area of two outstanding volcanic edifices of Venus - Sif Mons and Gula Mons.

Data. We have mapped all recognizable wrinkle ridges at the area centered on Sif Mons and Gula Mons from 11 to 32 deg N and from 337 to 10 deg E based on C1-MIDRP's but involving F-MIDRP's for reliable identification of the features. The resulting picture was photographically reduced and generalized and superposed on the generalized geologic map of this area (see Figure). The units predating Pwr in this area are tessera (Ti), densely fractured terrains in coronae (COdf) and among the plains (Pdf), and plains with broad ridges and fractures (Pfr). They are also typical for other areas of Venus [3,4]. Lavas emerging from Sif and Gula edifices and fractures of the Guor Linea rift zone (Rfa) are the units postdating Pwr.

Discussion and conclusion. The results of our mapping show that wrinkle ridges at the plains around Sif and Gula form a prominent pattern which is concentric to the Sif-and-Gula rise thus resembling a concentric pattern of wrinkle ridge trends around Aphrodite Terra [6]. In some areas, e.g. SW of Sif, wrinkle ridges form at least two sets with different orientation but this does not violate the general concentric pattern. Diverging compressional features around topographic highs is the expected phenomenon [5]. The surprising part of this is the fact that lavas composing Sif and Gula constructs are definitely younger than Pwr and not involved in the ridging. These two giant volcanoes because of their topographic prominence and association with the rift system are believed to represent the latest part of geologic history of Venus [7]. Meanwhile extreme rarity of impact craters deformed by the regional network of wrinkle ridges [8] is evidence that the wrinkle ridge emplacement occurred within a very short period of time after the plain-forming lavas eruptions. This observation places the ridge emplacement close to about 500 m.y. ago [8]. This situation evidently means that during the time of wrinkle ridge emplacement at the place where are now Sif and Gula there was a topographic rise or some other object prominent enough to diverge passively the wrinkle ridges. Alternatively the wrinkle ridges pattern around Sif and Gula might be controlled in a more active way due to coupling of lithosphere with the upwelling and horizontally spreading plume or due to outward stresses around gravitationally relaxing topographic rise [9,10]. Actually all these options are very much interrelated in demanding the upwelling plume at the time of wrinkle ridge emplacement. This implies, in turn, that the rising hot plume in the planet's mantle, which supposedly caused the Sif and Gula volcanism, produced its geologic effect on Venus' surface during a few hundred million years.

REFERENCES. 1) Solomon S.C. et al., *Science*, 252, 297-312, 1991; 2) Solomon S.C. et al., *JGR*, 97, 13,199-13,255, 1992; 3) Basilevsky A.T. & Head J.W., (in preparation); 4) Basilevsky A.T. & Head J.W., *LPSC XXV Abstracts*, this volume, 1994; 5) McGill G.E., *GRL*, 20, 2407-2410, 1993; 6) Bilotti F. et al., *LPSC XXIV Abstracts*, 107-108, 1993; 7) Head J.W. et al., *JGR*, 97, 13,153-13,197, 1992; 8) Schaber G.G. et al., *JGR*, 97, 13,257-13,301, 1992; 9) Senske D.A. et al., *JGR*, 97, 13,395-13,420, 1992; 10) Grimm R.E. & Phillips R.J., *JGR*, 97, 16,035-16,054, 1992.

WRINKLE RIDGES AROUND SIF AND GULA: Basilevsky A.T.



PRELIMINARY STRATIGRAPHIC BASIS FOR GEOLOGIC MAPPING OF VENUS; A. T. Basilevsky^{1,2} and J. W. Head², 1) Vernadsky Institute, Moscow 117975 Russia, 2) Dept. Geol. Scis., Brown Univ., Providence, RI 02912 USA

SUMMARY. The age relations between geologic formations have been studied at 36 1000x1000 km areas centered at the dark paraboloid craters. The geologic setting in all these sites could be characterized using only 16 types of features and terrains (units). These units form a basic stratigraphic sequence (from older to younger): 1) Tessera (Tt); 2-3) Densely fractured terrains associated with coronae (COdf) and in the form of remnants among plains (Pdf); 4) Fractured and ridged plains (Pfr); 5) Plains with wrinkle ridges (Pwr); 6-7) Smooth and lobate plains (Ps/Pl); and 8) Rift-associated fractures (Fra). The stratigraphic position of the other units is determined by their relation with the units of the basic sequence: 9) Ridge belts (RB), contemporary with Pfr; 10-11) Ridges of coronae and arachnoids annuli (COar/Aar), contemporary with wrinkle ridges of Pwr; 12) Fractures of coronae annuli (COaf) disrupt Pwr and Ps/Pl; 13) Fractures (F) disrupt Pwr or younger units; 14) Craters with associated dark paraboloids (Cdp), which are on top of all volcanic and tectonic units except the youngest episodes of rift-associated fracturing and volcanism; 15-16) Surficial streaks (Ss) and surficial patches (Sp) are approximately contemporary with Cdp. These units may be used as a tentative basis for the geologic mapping of Venus including VMAP. This mapping should test the stratigraphy and answer the question of whether this stratigraphic sequence corresponds to geologic events which were generally synchronous all around the planet or whether the sequence is simply a typical sequence of events which occurred in different places at different times.

INTRODUCTION. High-resolution global Magellan imagery provides an opportunity to analyze the stratigraphic relations among various features and terrains on Venus. In this work an analysis of stratigraphic relationships between 36 impact craters with dark paraboloids and other geologic formations at these localities has been done. The age relations were analyzed at the areas of about 1000x1000 km centered at the craters. Due to the nature of impact cratering the study areas seem to be randomly distributed on the surface of Venus.

STRATIGRAPHIC UNITS. We could characterize practically all geologic situations in all 36 sites using only 16 major types of features and terrains (units, see figure): 1) Tessera (Tt) represents intersecting ridges and grooves and forms continental-like blocks and small islands standing above and embayed by adjacent plains; 2-3) Densely fractured terrains associated with coronae (COdf) or forming outliers among the younger plains (Pdf); 4) Fractured and ridged plains (Pfr) forming remnants usually among plains with wrinkle ridges; a typical characteristic of Pfr is the presence of relatively broad (5-10 km wide) ridges tens of km long; 5) Ridge belts (RB) consisting of clusters of densely spaced 5-10-km-wide ridges; 6) Plains with wrinkle ridges (Pwr); 7) Ridges of corona annulus (COar), outline sectors of annulus of many coronae, typically are in structural alignment with neighboring wrinkle ridges of plains; 8) Ridges of arachnoid annulus (Aar), practically are a part of Pwr wrinkle ridges network; 9) Smooth plains (Ps); 10) Lobate plains (Pl); 11) Fractures of corona annulus (COaf), usually sparsely spaced thus differing from COdf; 12) Fractures (F), identified as a separate unit only if they disrupt Pwr or younger units; 13) Rift-associated fractures (Fra), form swarms and clusters of subparallel and anastomosing faults as a rule in association with topographic troughs (chasmata); 14) Craters with associated dark paraboloids (Cdp), represent the youngest 10% of the Venus impact crater population [4]; 15) Surficial streaks (Ss), commonly darker than the background terrain, have been interpreted to be of eolian origin [5]; Surficial patches (Sp), radar-dark, tend to be in local topographic lows and against or behind positive topographic obstacles.

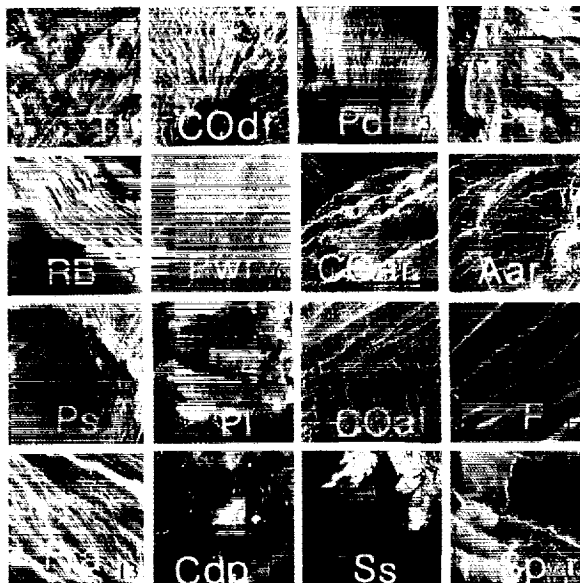
STRATIGRAPHIC RELATIONS AMONG THE UNITS. We used standard techniques for the determination of relative stratigraphic position [6] for each of the 36 areas establishing a stratigraphic column at each site, and then examined the relationship (correlation) between the columns to search for common themes in the sequence of events. The results of our analysis have shown that the stratigraphic sequences in all studied sites are quite similar and may be combined into a model of Venus regional and global stratigraphy (Table).

DISCUSSION. The similarity of stratigraphic columns in all 36 studied sites means that either this unit's sequence corresponds to geologic events which were generally synchronous all around the planet, or the sequence simply reflects a typical sequence of events which occurred in different places at different times, thus representing a regional tectono-magmatic cycle. The systematic mapping of Venus (VMAP program) gives a chance to resolve this alternative. Prioritizing approaches for this seems to be: 1) global-wide mapping of stratigraphically sliced structural trends (ridges, faults, tessera-forming elements) to judge whether they display a globally organized system or they are dominated by regional components; 2) analysis of relations of major stratigraphic units with such geologically instant phenomena as formation of major channels (e.g. 6,800 km long Hildr channel) [1] or crater-associated dark paraboloids [2,4]; 3)

CONCLUSION. This study has shown that major mapped stratigraphic units can be identified on Venus. Mapping of such units in 36 randomly distributed regions shows evidence for a distinctive regional and global stratigraphic sequence. This sequence, in turn, provided evidence for a stratigraphic model that highlights several major themes in the history of Venus: "catastrophic" tessera formation in the period prior about 500 m.y. ages, subsequent episodes of plains-forming volcanism alternated with episodes of extensional fracturing and compressional ridging, and geologically recent rifting and some associated volcanism. The systematic mapping gives a chance to test and improve our stratigraphic model and to resolve the alternative of the global vs. regional character of observed time sequence of geologic events.

References: [1] Baker V.R. *et al.*, *JGR*, 97,13,421-13,444, 1992. [2] Basilevsky A.T. *GRL*, 20, 883-886, 1993. [3] Ivanov M.A. and Basilevsky A.T., *GRL*, 20, 2579-2592, 1993. [4] Campbell D.B. *et al.*, *JGR*, 97,16249-16,277, 1992. [5] Greeley R. *et al.*, *JGR*, 97, 13,319-13,345, 1992. [6] Wilhelms D.E., in *Planetary Mapping*, R. Greeley and R.M. Batson eds., 208-260, Cambridge University Press, NY 1990.

VENUS REGIONAL AND GLOBAL STRATIGRAPHY



Units	Stratigraphic Column	Events	Processes	
Ss, Sp Cdp Fra, F, Ps, Pl.		<ul style="list-style-type: none"> • Wind Streaks • Debris Sheets • Paraboloid Craters • Local Intense Fracturing • Smooth Plains 	<ul style="list-style-type: none"> • Rifting • Associated Volcanism 	C A T E R I C A C T I V I T Y
COaf F Ps, Pl.		<ul style="list-style-type: none"> • Minor Fractures • Smooth Plains Emplacement 	<ul style="list-style-type: none"> • Minor Extensional Tectonics • Basaltic Volcanism 	
Pwr Aar, COar		<ul style="list-style-type: none"> • Wrinkle Ridge Formation • Coronae/Arachn. Ridges • Plains Emplace. 	<ul style="list-style-type: none"> • Compressional Tectonics • Volcanism 	
RB Pfr		<ul style="list-style-type: none"> • Ridge Belt Formation • Plains Emplacement 	<ul style="list-style-type: none"> • Compressional Tectonics • Volcanism 	
COfd Pdf		<ul style="list-style-type: none"> • Plains Fracturing • Plains Emplacement 	<ul style="list-style-type: none"> • Vast Extensional Tectonism • Corona Formation • Volcanism 	
Tt		<ul style="list-style-type: none"> • Tessera-Forming Deformation • Tessera Precursor Formation 	<ul style="list-style-type: none"> • Vast Extensional and Compressional Deformation 	I M P O S T C O S M O G R A P H I C

GEOLOGY AND MORPHOMETRY OF LARGE IMPACT CRATERS OF VENUS; A.T.Basilevsky⁽¹⁾, B.A.Ivanov⁽²⁾, P.G.Ford⁽³⁾ and C.M.Weitz⁽⁴⁾; (1)Vernadsky Institute, Moscow, 117975, Russia; (2)Institute of Dynamics of Geospheres, Moscow, Russia; (3)MIT, Cambridge, MA 02139; (4)Brown University, Providence, R.I., 02912.

SUMMARY. Photogeologic analysis of the 3 largest craters on Venus (Mead, Isabella and Meitner) showed a presence of wrinkle ridges on the crater's floor. It seems to contradict the crater relaxation model which predicts the crater floor uprise. The precise altimetry of large impact craters shows the presence not of floor uprising but shallow central depressions. This may be caused by the subsidence of the uplifted blocks of dense mantle material beneath the crater center.

INTRODUCTION. The low resurfacing rate typical for the last 0.5 b.y. of Venus' history and global coverage of this planet by the Magellan high resolution radar survey make Venus an interesting place to study impact craters formed by projectiles large enough to penetrate through the planet's massive atmosphere. Our study is concentrated on the analysis of SAR imagery and altimetry data for the largest four impact craters of Venus: Mead, D=280 km; Isabella, 175 km; Meitner, 150 km; Klenova, 140 km. We used in our analysis full resolution mosaics and altimetry data specially processed to distinguish separate nearby echos placed in the nadir zone surfaces with different elevations.

PHOTOGEOLOGIC DESCRIPTION. Crater Mead (12.5° N, 57.2° E) is a double-ring basin among the plains with wrinkle ridges (Pwr). Remnants of densely fractured terrain (Pdf) and ridge belts (RB) are observed among Pwr. Both Pdf and RB are embayed by Pwr. The outer ring of the Mead basin is the crater rim consisting of degraded remnants of knobby crater ejecta alternating with plains, areas of which have wrinkle ridges, and areas which seem to be covered with aeolian debris mantle hiding the wrinkle ridges. Remnants of the Mead ejecta look superimposed on the said remnants of ridge belts (11.5° N, 58.7° E). The inner ring of the basin (D=180 km) is an inward-looking scarp of sinuous outline. The annular area between the outer and inner rings looks quite similar to the rim area: patches of plains alternating with knobby ejecta. In some cases plains of the crater rim merge into plains of the inter-ring annulus (11.8° N, 56.1° E). Wrinkle ridges are seen at some places of the inter-ring plains too. In the western part of the inter-ring annulus Pwr look as if they are embaying the ejecta patches. The basin floor inside the circle scarp is more radar-bright than the inter-ring and rim area plains. The scarp cuts the terrace of the inter-ring annulus and, in turn, looks as though embayed by the said brighter plains of the basin floor. The latter in its north-central part is complicated by sinuous lineaments, at least part of which are wrinkle ridges, but they are shorter, more narrow and more irregularly oriented than the wrinkle ridges of the surrounding plains. These observations provide the possibility of deducing a scenario of geologic history of the crater Mead area: The Mead basin was superposed on the plains with ridge belts (RB). Then younger plains later deformed by wrinkle ridges (Pwr) were emplaced outside the crater, in the inter-ring annulus, and probably on the basin floor. Then the inner scarp was formed and the brighter plains were emplaced in the depression outcircled by this scarp. It is not clear whether all wrinkle ridges of this area were emplaced in one episode or in two separate episodes, first, wrinkle ridges of the regional network and inter-ring annulus, and, second, the wrinkle ridges of the basin floor.

Crater Isabella (29.7° S, 204.1° E) is a double-ring basin superimposed on the plains with wrinkle ridges (Pwr). The outer ring is the crater rim, mostly covered with knobby ejecta. In the southern sector of the crater the blocky material of the crater floor merges with the knobby material of the crater rim. This part of the ejecta is a source of two extended outflows. The central part of the basin is outlined by the annulus of lineaments (fractures?) which forms the inner ring of about 80 km in diameter. Between the lineaments circle and the outer rim there is an alternation of plains and blocky material of the primary crater floor. Inside the inner ring there are plains with a subradial system of wrinkle ridges. The latter were definitely formed after the basin excavation and emplacement of the plains of the basin floor. Meanwhile the wrinkle ridges of the regional network on the plains outside crater Isabella were formed before this crater was emplaced. This is proved by the overlapping of the wrinkle ridges by the crater outflow (33° S, 205° E) and by the intrusion

of the outflow material into the fracture which belongs to the system disrupting wrinkle ridges of the regional network.

Crater Meitner (55.6° S, 321.6° E) is a double-ring basin. The outer ring is the crater rim covered with knobby ejecta. Among the ejecta there are volcanic domes, some of which look partly covered by ejecta, and some which look emplaced after the ejecta. No outflows are seen in association with crater Meitner. The inner ring ($D=90$ km) is an annulus of knobby terrain elevated over the basin floor. The area between the inner and outer rings is plains with knobs among them similar to those which make the inner ring. The basin floor inside the inner ring is plains with wrinkle ridges forming a concentric system on the periphery and a subradial system in the center. Small domes similar to the volcanic domes of the venusian plains are seen on the basin floor. Crater Meitner is superposed on the plains with wrinkle ridges with predominant NE trending. The wrinkle ridges are covered by the crater ejecta and in some cases show through the ejecta. In the eastern sector of the ejecta a wrinkle ridge showing through the ejecta comes very close to the inward-looking crater rim scarp with no changes in the ridge prominence and its NE trending. If the wrinkle ridges were formed after the crater the stress forming this on-rim ridge would be impossible. In the NW sector the emplacement of the ejecta seems to be controlled by the preexisting wrinkle ridges. So crater Meitner like crater Isabella has on its floor a set of wrinkle ridges formed after the crater emplacement while the wrinkle ridges of the regional network were formed in a different episode before the crater formation.

DISCUSSION. The presence of wrinkle ridges on the craters' floors seems to contradict the model of crater relaxation [1] predicting the crater floor uprising in this process. If this prediction was correct we would see fractures rather than ridges on the crater floor. Moreover the precise radar altimetry for the venusian craters larger than 70 km in diameter [2] did not show the evidence of the floor uprising predicted by [2]. The reason for this disagreement between the prediction and observations could be the initial state of compensation of large venusian craters which seems to be different from that supposed by [1].

It is well known from terrestrial experience that in the center of complex craters the structural uplift of rocks exists with an amplitude of $D/10$ relative to the initial depth [3, 4]. If we adopt the same amplitude for Venus, craters with diameters 150 to 300 km would have an uplift with 15 to 30 km amplitude. So for the largest craters the significant uplift of the dense mantle material might exist just after a crater formation. Geophysical evidence of the mantle uplift have been analyzed for lunar basins by Bratt *et.al.* [5]. According to [5] the mantle uplift subsides down with time. If this style of relaxation is the case for Venus, one may propose the model of initially overcompensated craters with the downward subsiding of the mantle uplift (and the crater floor) due to viscous relaxation. In this case the maximum depth of a crater may increase, not decrease, with geologic time.

CONCLUSION. The Magellan specially processed altimetry profiles [2] demonstrate the relatively small central depression at the flat floor of some of the Venusian craters larger 70 km. These depressions may be a manifestation of the "downward mantle relaxation." If so: (i) a viscous relaxation model for initially overcompensated craters may give an additional possibility of estimating rheological properties of Venus rock; and (ii), the surface layer of these craters' floor should be affected by compression rather than extension.

REFERENCES. 1. Grimm, R.E., and Solomon, S.C. (1988) *J. Geophys. Res.*, 93, 11,911-11,929; 2. Ivanov B.A., and P.G.Ford.(1993) *LPSC* 24, 681-690; 3. Ivanov B.A. and A. T. Basilevsky (1979) *LPSC* X, 607-609; 4. Grieve, R.A.F., P. B. Robertson, and M.R.Dence (1981) Constraints on the formation of ring structures, based on terrestrial data, In *Multi-Ring Basins* (P.H.Schultz and R.B.Merrill eds.), pp.37-57, Pergamon Press, New York; 5. Bratt, S.R., S.C.Solomon, and J.W.Head (1985) *J.Geophys.Res.*, 90, 12,415-12,433.

VARIATIONS IN MARS' NORTH RESIDUAL POLAR CAP FROST COVERAGE IN MARINER 9 AND VIKING IMAGES D. S. Bass (UCLA), K. E. Herkenhoff (JPL) and D. A. Paige (UCLA)

A comprehensive study of orbiter images of Mars' north residual polar cap frost has been undertaken to determine whether frost differences can be used to qualify interannual cycles of deposition-and-erosion. Examination of Mariner 9 and Viking Orbiter north polar data shows dramatic changes in frost coverage at the cap edge between images obtained at approximately the same solar longitude. Further study should lead to conclusions regarding residual cap frost distribution and its relationship to interannual cycles.

Current research concerning the nature of Mars' residual polar ice and associated layered terrains has not included a systematic study of frost coverage as observed in Mariner 9 and Viking Orbiter datasets. Limited regions have been examined, yielding evidence that points to interannual variations of deposition-and-erosion cycles rather than seasonal cycles. It has been reported that high resolution Viking photos show large disappearances of frost on the north polar cap [1]. Further, Kieffer [2] and Paige *et al.* [3] have noted the disappearance of a frost outlier near Chasma Boreale at 80.2 N, 44 W. Comparisons of Mariner 9 images with those taken approximately three years later by the Viking 2 Orbiter show a marked increase in frost coverage, suggesting that layered deposits may be forming in these areas over an interannual time scale.

We have begun a detailed study of residual cap frost changes as observed in Mariner 9 and Viking data. By examining Mariner 9 data of the north polar cap from $L_S=90$ to $L_S=180$, we have found eleven high resolution and four low resolution images that show changes in frost coverage when compared to Viking photo mosaics. In each case, there is more bright frost in the Viking images than in the Mariner 9 photos. cursory examination of approximately 200 Viking observations of the north polar cap show even more dramatic differences in the residual cap outline.

For example, a Mariner 9 image (center: 80.1 N, 265.6 W) taken at $L_S=97$ has less bright frost than that in a Viking mosaic (center: 82 N, 265 W) at $L_S=117$ and $L_S=134$ (Figures 1, 2). The darkest regions in the figures are sand, while the intermediate areas constitute polar layered deposits, and the brightest regions are composed of exposed water ice. Clearly, the Viking orbiter image has substantially more bright frost than the Mariner 9 image. Further, the Mariner 9 photo shows less bright frost on the plateaus and also in the troughs than the Viking mosaic. The faint outline of frost in the lower right-hand corner of the Viking image (Figure 2) is also interesting to note, as the similar although brighter feature is visible in the earlier Mariner 9 photo. The differences are quite pronounced, leading to the questions of whether dust has been deposited on top of the ice or whether the ice has sublimed, exposing a fresh surface. An extended database of frost distribution differences should provide answers to these questions.

References

- [1] James, P. B. and Martin, L. (1985) *Bul. Amer. Astron. Soc.*, 17, 735.
- [2] Kieffer, H. H. (1990) *JGR*, 96, 1481-1493.
- [3] Paige, D. A. *et al.* (1994) *JGR*, in press.

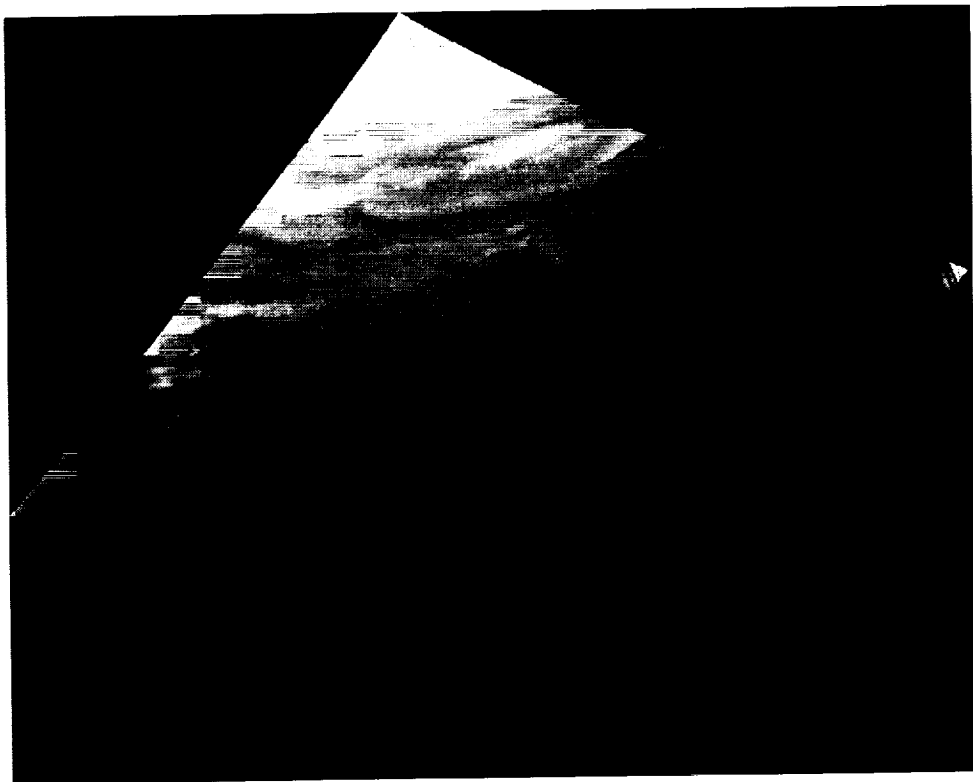


Figure 1. A high resolution Mariner 9 B camera image (picno 675b07) centered at 80.1 N, 265.6 W ($L_s=97$). Image projection is polar stereographic and shows a region of approximately 440 km by 286.5 km. The dark regions are dune material, the intermediate is polar layered deposits, and the bright regions in the lower left-hand corner are comprised of frost. Image shows less bright frost coverage at cap edge when compared to Viking image taken at approximately the same season three Mars years later.



Figure 2. Viking mosaic of two images from orbits 765A ($L_s=117$) and 801A ($L_s=134$) in the same region as Figure 1. Mosaic polar stereographic projection centered at 82 N, 265 W. Image shows significantly more bright frost than Figure 1. Also note faint outline of frost outlier in lower right-hand corner.

2946

SINGLE AGGLUTINATES: A COMPARATIVE STUDY OF COMPOSITIONS OF AGGLUTINITIC GLASS, WHOLE-GRAIN, BULK SOIL, AND FMR; A. Basu, R. Robinson (Dept. Geol. Sci., Indiana U., Bloomington, IN 47405), D.S. McKay, D.P. Blanchard, R.V. Morris (NASA-JSC, Houston, TX 77058), and S.J. Wentworth (LESC, Houston, TX 77058)

INTRODUCTION. Previous workers on *single agglutinates* have variously interpreted the composition of agglutinitic glass to represent impact melts of (a) bulk soil, (b) mixed components in finer sizes, and (c) micro-targets [1,3,4,8,10]. Separately, Papike has argued in favor of fusion of the finest fraction of bulk soils [13].

SAMPLES AND ANALYSIS. We hand-picked 34 single agglutinates from the mature Apollo 16 soil 61181 ($I/FeO = 82$) and measured the FMR and chemical composition (INAA for Fe, Sc, Sm, Co, Ni, Cr) of each agglutinate particle. Thirteen of these single agglutinates were selected for electron beam microanalysis and imaging. We have analyzed $<1\mu m$ spots (for Na, Mg, Al, Si, P, S, K, Ca, Ti, Cr, Mn, Fe, Ni, Ba) on pure glassy areas (approximately ten in each particle) selected on the basis of optical and BSE images (avoiding all clasts and inclusions) with a CAMECA SX50 electron microprobe to obtain average glass compositions of each single agglutinate.

GLASS COMPOSITIONS AND 61181 SOIL COMPOSITION. Our data show a very strong negative correlation between $(Al_2O_3 + CaO)$ and $(MgO + FeO)$ and a positive correlation between MgO and FeO, suggesting that the distribution of felsic and mafic minerals in the target generally control the composition of the melt (figs. 1,2). MgO (11.91%) in the glass of particle #48 is about twice the average of the rest. Relative to average agglutinitic glass in this soil, this grain has higher SiO_2 and much lower Al_2O_3 and CaO indicating that some bronzitic pyroxene dominated the micro-target that melted to form the glass of particle #48.

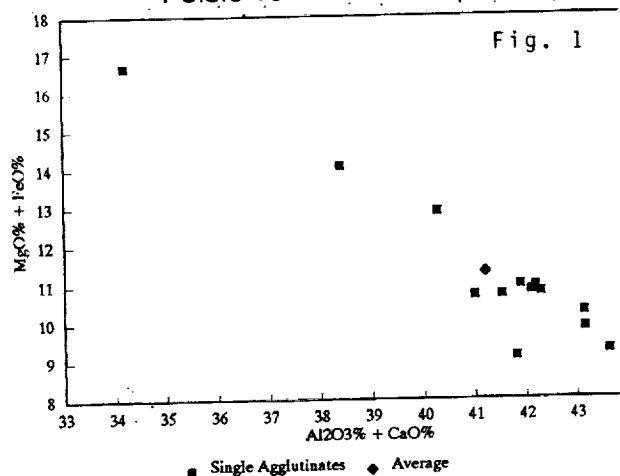
Our average agglutinitic glass composition deviates from that of the bulk soil composition [12]. Specifically, Na_2O , K_2O , and BaO are depleted in the glass relative to the bulk soil, suggesting that fine grained mare basalt mesostasis material or fine grained matrix of KREEPy breccias did not melt preferentially to produce these agglutinates (although preferential vapor loss of these components is also a possibility). However, P_2O_5 , TiO_2 , MnO and NiO are enriched in the glass suggesting that melted apatite, ilmenite, and some meteoritic component are enriched in the glass.

COMPARISON WITH WHOLE-GRAIN COMPOSITION. No correlation is evident between the total Fe content of each grain and the concentration of either Ni in the grains or SO_2 in the glass (fig. 3). If S and Ni primarily represent meteoritic components, then the total Fe in the 13 grains is largely indigenous (i.e. of lunar sources). The lack of correlation between concentrations of Ni in the glass and that in the whole agglutinate further confirms that the projectile composition does not significantly control composition of agglutinitic glass. An enrichment of S in the glass could come from incorporation of S vapor-coated submicron grains in the glass [9]. There is a weak but not a 1:1 correlation between FeO in the glass and the whole particle (fig. 4) indicating that the clast population in an agglutinate represents the micro-target from which the glass was produced, only in part. This suggests that dust grains on the lunar surface are distributed somewhat inhomogeneously at the scale of single agglutinate production by micrometeoritic bombardment.

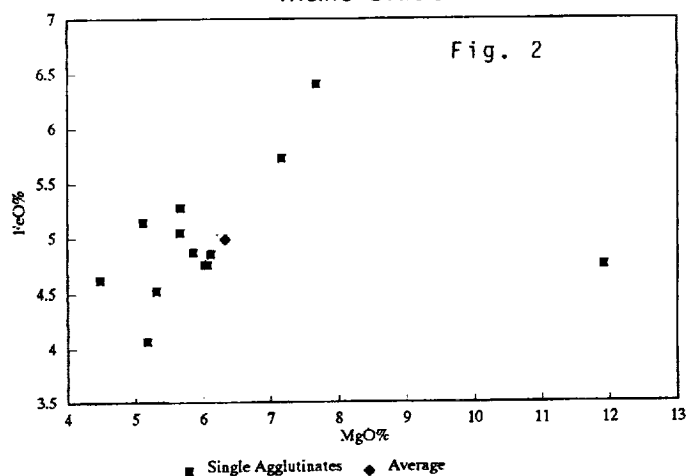
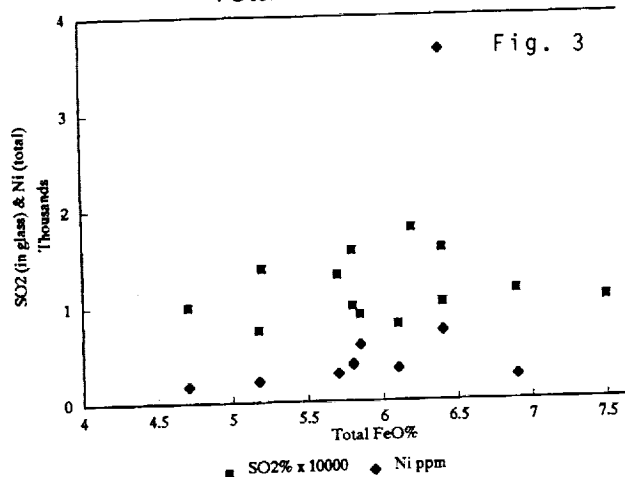
COMPARISON WITH WHOLE-GRAIN FMR (I_0/FeO). I_0/FeO depends primarily on the production of single domain Fe° by reduction of FeO from silicate and oxide minerals in micrometeoritic impact melts of lunar dust impregnated with solar wind hydrogen [5,6,10]. The process is independent of the composition of any Fe-bearing micro-target. A plot of major oxides in agglutinitic glass vs. I_0/FeO confirms that bulk compositions of agglutinitic glass are independent of maturity. If however, some agglutinates are repeatedly melted i.e. recycled into newer agglutinates, FeO in the glass will be further reduced and partitioned into single domain Fe° . Ideally then, glass in the more mature agglutinates will tend to have lesser concentrations of FeO and more Fe° than the glass in a less mature agglutinate of the same bulk composition.

REFERENCES : [1] Basu, A. & McKay, D.S. (1985) PLPSC 16th, D87-D94; [2] Basu, A. and Meinschein (1976) PLSC 7th, 337-349; [3] Blanchard, D.P. & Morris, R.V. (1984) LPSC XV, 66-67; [4] Gibbons, R.V. et al. (1976) PLSC 7th, 405-422; [5] Heiken et al. (1991) Lunar Sourcebook, Cambridge. 736p; [6] Housely, R.M. et al. (1972) PLSC 3rd, 1065-1076; [7] Housely, R.M. et al. (1973) PLSC 4th, 2737-2750; [8] Hu, H.-N. & Taylor, L.A. (1977) PLSC 8th, 3645-3656; [9] Keller, L.P. and McKay, D.S. This Volume; [10] McKay, D.S. & Basu, A. (1982) LPSC XIII, 489-490; [11] Morris, R.V. (1978) PLPSC 9th, 2287-2297; [12] Morris, R.V. et al. (1983) Handbook of Lunar Soils, NASA-JSC 19069. Houston. 914p; [13] Papike, J.J. (1981) LPSC XII, 805-807.

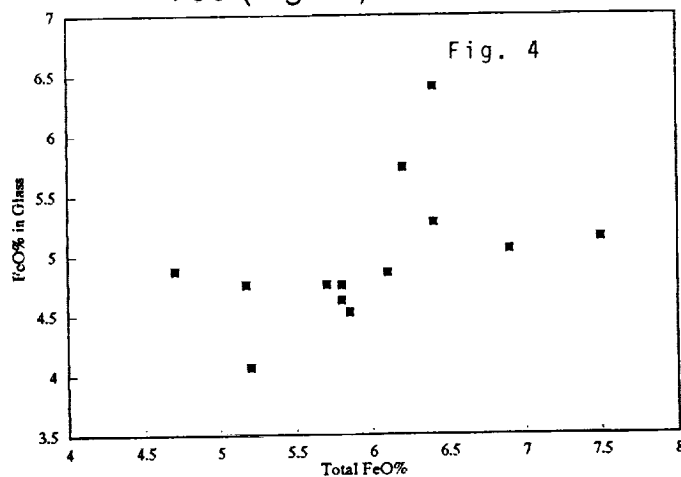
Felsic vs. Mafic Components



Mafic Oxides

Total FeO vs. SO_2 & Ni

FeO (in glass) vs. Total FeO



DEEP MELTING AND RESIDUAL GARNET IN THE SOURCES OF LUNAR BASALTS: Lu-Hf ISOTOPIC SYSTEMATICS; Brian L. Beard, Gregory A. Snyder, and Lawrence A. Taylor, University of Tennessee, Planetary Geosciences Institute, Department of Geological Sciences, Knoxville, TN 37996

Combined Lu/Hf concentration and Hf isotopic data are powerful tools for determining the source region mineralogy from which basalts are derived. For example, Salters and Hart [1] concluded that mid-ocean ridge basalts were derived with garnet as a residue phase, in order to explain the low Lu/Hf ratio measured in MORB relative to the high Lu/Hf ratio required in the source based on their high initial ϵ_{Hf} values. Unruh et al. [2] conducted a similar type of analysis for lunar mare basalts and determined that mare basalts require residual ilmenite in the source. However, this analysis was conducted prior to many modern determinations for Lu and Hf mineral-melt partition coefficients [e.g., 3, 4, and references reported in 5] and re-interpretation of these data would seem timely. Mare basalts have high initial positive ϵ_{Hf} values (+40 to +5), but Lu/Hf ratios much less than chondrite ($[\text{Lu}/\text{Hf}]_n$ 0.49 to 0.74; [2]). The high positive ϵ_{Hf} values imply derivation from a source that had a Lu/Hf ratio greater than chondrite for a significant period of time. To explain the low Lu/Hf ratio of mare basalts relative to the high Lu/Hf ratio required in their source, we suggest that there must be a Lu-retentive phase in the lunar mantle, such as garnet; ilmenite is Hf-retentive relative to Lu [3,4]. The presence of garnet in the source region of mare basalts implies that melting began at a minimum depth of 275 km.

Calculations of the Lu/Hf ratio of liquids produced from melting different sources with varying modal and melting proportions indicate that a source similar to that proposed by Snyder et al. [6] for mare basalts, except with garnet instead of plagioclase, can produce the required low Lu/Hf ratios in liquids, given that their source must have a high Lu/Hf ratio (Fig. 1). Considering the extremely low Lu/Hf D-value ratio of ilmenite (0.17; [3]) it is unlikely that ilmenite can be in the residue after partial melting unless garnet is in the residue as well (Fig 1). In figure 1 the $[\text{Lu}/\text{Hf}]_n$ (chondrite normalized Lu/Hf) of the source (y-axis) is calculated assuming derivation from a 4.4 b.y. old source with an ϵ_{Hf} value of 0 and the crystallization ages and initial ϵ_{Hf} values of [2], if this 4.4 Ga source was assumed to have an ϵ_{Hf} value less than 0 [e.g., 7], then the samples would plot at even higher $[\text{Lu}/\text{Hf}]_n$ SOURCE values. Note that the sources used in these melting calculations only differ by the presence of garnet (solid lines) or plagioclase (dashed lines). Similar melting calculations performed using the Sm-Nd system are equivocal because the Sm-Nd system does not effectively discriminate between these different source mineralogies (Fig. 2).

Garnet is not required in the source if the Lu/Hf ratio of the lunar mantle was decreased just prior to melting by a metasomatic process. However, considering the relatively high Sm/Nd ratios of these mare basalts (all similar to or greater than chondrite), if this metasomatism occurred then it must have been accomplished by a fluid that had a low Lu/Hf ratio but a Sm/Nd ratio similar to chondrite. This requirement seems highly unlikely.

Although the presence of garnet in the source region of mare basalts is speculative, garnet could be produced by subsolidus reactions involving plagioclase and pyroxene, if these phases are subjected to

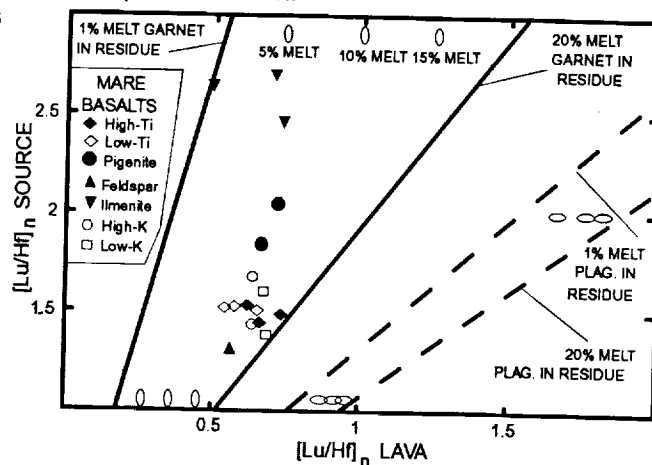


Figure 1: Chondrite normalized Lu/Hf ($[\text{Lu}/\text{Hf}]_n$ LAVA) ratio measured for mare basalts (x-axis) relative to the calculated $[\text{Lu}/\text{Hf}]_n$ of the source based on the initial ϵ_{Hf} value of the lava (y-axis; see text for calculation method). Melting fields calculated from non-modal batch melting of 1% (left side) to 20% (right side) material with garnet in the residue (solid lines), and 1% (left side) to 20% (right side) material with plagioclase in the residue (dashed lines); modes and melting proportions and D-values for these calculations are in table 1. Ovals indicate, from left to right, 5%, 10%, and 15% partial melts. All mare basalt data from Unruh et al. [2].

ROLE OF GARNET IN THE LUNAR MANTLE: Hf ISOTOPIC CONSTRAINTS: Beard, Snyder, and Taylor

the correct P and T conditions. Pressures >12 kbar can stabilize garnet [8], which corresponds to a depth of approximately 275 km [9]. If garnet in the upper mantle of the Moon was a result of phase transformations involving plagioclase, then it is interesting to speculate on how plagioclase was brought down to such depths. A likely scenario for bringing plagioclase into the deep lunar mantle is by convective overturn of the lunar magma ocean cumulate pile [e.g., 10]. Such convection, however it occurred, does not require complete mixing of the cumulate pile. For example, the geochemical similarities of high-Ti mare basalts from different areas on the Moon point to source regions that have maintained their chemical integrity. Indeed, experimental models of convection reveal that complete homogenization is unlikely to occur unless convection is prolonged [11].

In any event, the low measured Lu/Hf ratio in mare basalts relative to the high Lu/Hf ratio of their source, calculated from the measured $^{176}\text{Hf}/^{177}\text{Hf}$ of these basalts, requires a phase in the source that is Lu retentive relative to Hf. Garnet has the correct Lu and Hf partition coefficients to produce such a relationship. The presence of garnet in the source region of mare basalts requires that the initial minimum depth of melting began at 275 km.

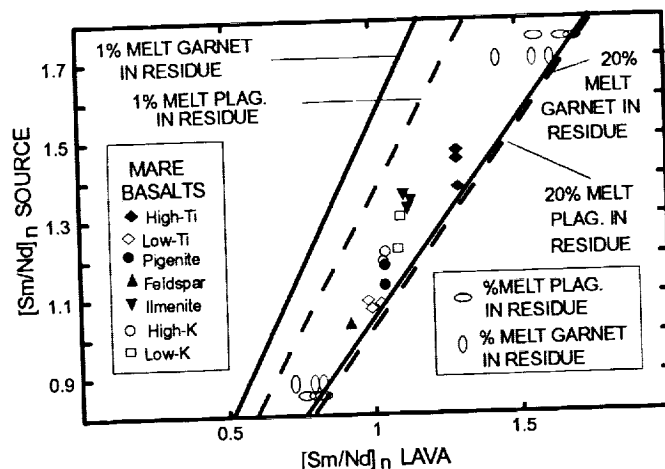


Figure 2: Chondrite normalized Sm/Nd ($[\text{Sm}/\text{Nd}]_n$ LAVA) ratio measured for mare basalts (x-axis) relative to the calculated $[\text{Sm}/\text{Nd}]_n$ of the source (y-axis) based on the initial ϵ_{Nd} value of the lava. The $[\text{Sm}/\text{Nd}]_n$ of the source is calculated assuming derivation from a source with an ϵ_{Nd} value of 0 at 4.4 Ga and the crystallization ages and initial ϵ_{Nd} values of [2]. Melting fields are as in Fig 1. All mare basalt data from Unruh et al. [2].

Table 1: D-values and melting and modal proportions used in calculating melting fields in figures

Mineral	D-values				— Model 1 —		— Model 2 —	
	Sm	Nd	Lu	Hf	Mode	Melt	Mode	Melt
Olivine	0.0006	0.0001	0.03	0.013	0.40	0.25	0.40	0.25
Cpx	0.17	0.104	0.30	0.15	0.10	0.30	0.10	0.30
Pigenite	0.011	0.0058	0.11	0.063	0.40	0.25	0.40	0.25
Ilmenite	0.0023	0.0012	0.070	0.406	0.05	0.10	0.05	0.10
Plag	0.017	0.0236	0.0068	0.0128	—	—	0.05	0.10
Garnet	0.1225	0.0316	7.37	0.1908	0.05	0.10	—	—

D-values for olivine, pigenite, plagioclase (Plag), and ilmenite are from [6], garnet and clinopyroxene (cpx) D-values are from [5]. Model 1 modal and melting proportions are for the liquid field labeled garnet in residue and model 2 modal and melting proportions are for the liquid field labeled plagioclase in residue in figures 1 and 2. Note, melting proportions between these two mantle models only differ in if garnet or plagioclase is present.

REFERENCES

- [1] Salters, V.J.M. and Hart, S.R. (1989) *Nature*, 342, 420-422; [2] Unruh, D.M., et al. (1984) *J. Geophys. Res.*, 89, B459-477; [3] Nakamura, Y., et al. (1986) *J. Geophys. Res.*, 91, D239-D250; [4] McKay, G., et al. (1986) *J. Geophys. Res.*, 91, D229-D237; [5] Beard, B.L. and Johnson, C.M. (1993) *Earth and Planet. Sci. Letts.*, 119, 495-509; [6] Snyder, G.A., et al. (1993) *Geochim. Cosmochim. Acta*, 56, 3809-3823; [7] Paces, J.B., et al. (1991) *Geochim. Cosmochim. Acta*, 55, 2025-2043; [8] Ringwood, A.E. and Essene, E. (1970) *Proc. Apollo 11 Lunar Sci. Conf.*, 769-799; [9] Warren, P.H. (1985) *Ann. Rev. Earth and Planet. Sci.*, 13, 201-240; [10] Spera, F.J. (1992) *Geochim. Cosmochim. Acta*, 56, 2253-2265; [11] Ottino, J.M. (1990) *Annu. Rev. Fluid Mech.*, 22, 207-253.

COMA: A COMETARY MATTER ANALYZER FOR IN SITU ANALYSIS WITH HIGH MASS RESOLUTION; P. Beck and J. Kissel, Max-Planck-Institut für Kernphysik, Postfach 103980, D-69029 Heidelberg, FRG

Introduction: Comets were not thermally processed and thus are unique bodies from the origin of the solar system. Other than asteroids, comets release their material as they approach the sun thereby making it accessible for *in situ* analysis. The fly-byes of the VEGA and Giotto space probes provided a wealth of new information [1-3]. Among a variety of instruments most sensitive dust impact analyzers were used to determine chemical composition and density of the small dust particles down to 10^{-15} g [4-5]. Since these missions it became knowledge what was intelligent speculation before the encounter of comet p/Halley: Cometary dust consists of particles with a stony (Mg, Si, S, Ca, Fe etc.) nucleus and a cover of volatile, organic (H, C, O, N) material. Detailed analyses [6] indicated that the elemental composition of the dust is even more primitive than CI-Chondrites, the most unaltered meteorite class. The isotopic composition of carbon with $^{12}\text{C}/^{13}\text{C}$ ranging up to 4500 (compared to a normal about 90) in some dust particles point towards a connection with presolar grains [7]. Now, after this mission the next two logical steps in exploration comets would be a.) to analyze other comets for their diversity and b.) to analyze one other comet in greater detail.

With respect to dust a Time-of-Flight Secondary-Ion-Mass-Spectrometer (TOF-SIMS) was developed for the comet-mission CRAF and was named Cometary Matter Analyzer (CoMA). This mission was cancelled in January 1992. ESA now plans the Comet-Rendezvous-Mission ROSETTA as her third CORNERSTONE mission. It offers the next chance for detailed *in situ* comet exploration. CoMA is the ideal instrument for analyzing cometary dust. Detailed objectives for the CoMA instrument are to

- determine the elemental composition of solid cometary matter to characterize comets in the framework of solar system chemistry;
- determine the isotopic composition of key elements such as H, Li, C, Mg in order to establish boundary conditions for models of the origin and evolution of comets;
- determine the elemental and isotopic composition of the neutral and ionized atmosphere of the comet and compare it with the data from the particles;
- gain insight into the molecular composition of particles with emphasis on organic matter;
- investigate the chemical states of the elements;
- investigate the variation of the chemical and isotopic composition between individual particles;
- characterise changes in composition that occur as functions of time and orbital position.

The Cometary Matter Analyzer Instrument: The high dust impact velocities of the Halley mission provided impact generated positive ions for mass spectroscopy with the PUMA and PIA instruments. During a rendezvous mission dust particles will be collected and subsequently the material has to be ionised within the instrument for isotopic, elemental and molecular analysis. TOF-SIMS has been proven as the most sensitive method available for that purpose. Fig.1 shows the principle schematic of the CoMA instrument. The physical parts of the instrument consist of the *dust-collector* system, the *primary-ion-system* and the *time-of-flight mass-spectrometer*.

The Dust Collector: The task of this unit is to handle the targets onto which cometary dust particles are collected. A single target wheel houses about 30 target groups, each group containing four targets. They are individually delectable to meet the demands of the different features of the dust grains. The system moves the target mechanically from the *store-* to the *collect-, clean- and analyze-* positions. A target group consists of three targets for dust collection and one for adsorbing cometary gases. Foils coated with highly porous metal blacks are the means of choice to achieve minimal destruction of the collected dust grains [8]. The coatings have a thickness of 20–100 μm , various densities and inelastic and chemical properties. Platinum black structures are best suited for high-velocity particles (> 100 m/s). Fluffy particles of low velocity (< 100 m/s) are collected by ruthenium black covered foils. Each target has markers on it to establish a reference system such that collected particles can repeatedly be found and analyzed. A shutter at the entrance of the dust collector prevents undesirable contamination.

Cometary Matter Analyzer; P.Beck and J.Kissel

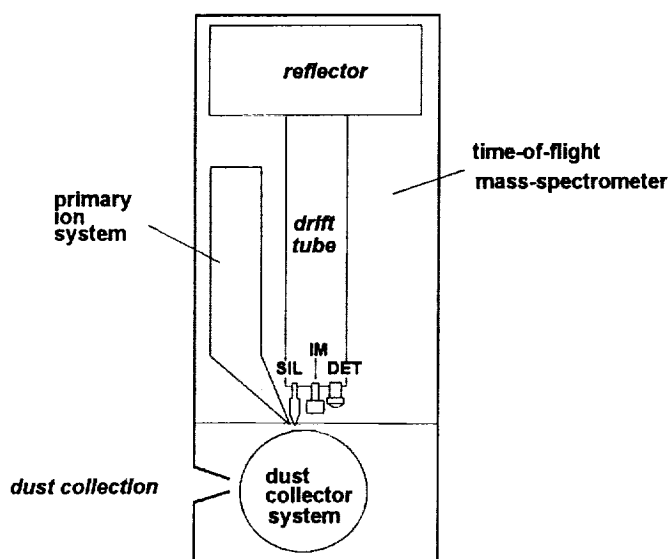


Fig.1: Principle Schematic of CoMA. SIL: secondary ion extraction lens; IM: ion mirror; DET: detector

The Primary-Ion-System: The pulsed primary ion gun has to ionize dust material in order to analyze it with the TOF-mass-spectrometer. $^{115}\text{In}^+$ ions are produced using a liquid metal ion source (LMIS) that is already well tested for space applications [9-10]. This source consists of a heated reservoir containing a tungsten needle covered with indium and an extraction electrode. With a weight of about 1g and a power consumption of less than 700 mW it is well suited for space experiments. The divergent 10 keV ion beam (some μA) is transformed to a parallel beam with an extraction lens. Chopping and bunching provides the short (< 4 ns) ion

pulse needed for high mass resolution of $m/\Delta m > 10,000$ at $m > 150$ Da. An enclosing lens focuses the ion pulse to a $15\ \mu\text{m}$ spot on the sample. For cleaning and depth profiling a DC mode is also implemented.

The Time of Flight Mass Spectrometer: Secondary ions (positive and negative ion-modes are possible!) starting from the analyzed target-spot first are accelerated into the secondary ion extraction lens and then move through the flight tube into a reflector [11]. To increase the flight-time the ions are sent to an ion mirror and back to the reflector again. With a two stage reflector sufficiently high mass resolution as well as second order energy compensation are achieved. Finally, the secondary ions are detected by a two stage channel-plate (accuracy < 1 ns, dead time < 3 ns) with an integrated non-linear preamplifier.

During the experiment session the beam is electrically scanned over an area of about $100 \times 100\ \mu\text{m}^2$ above micrometer sized dust-grains. The full $5 \times 5\ \text{mm}^2$ of the target area is mechanically positioned. With about 50 ions per primary ion pulse and 5000 pulses per second, a full mass spectrum of 10^6 particle ions is obtained within 20 minutes. Faster operational modes are implemented for target scans to locate collected particles on one of the 30 different target groups. In a separate instrument location the full DC beam is used for depth profiling. For more details see [12]. Future instrumental improvements may lead to a spot size of the primary beam of only 100 nm at a mass resolution of $m/\Delta m > 2500$.

References:

- (1) M.Grewing, F. Praderie, R. Reinhard (eds.), *Exploration of Halley's Comet*, Springer Verlag, Berlin, pp 984, (1988).
- (2) W.F. Huebner (ed.): *Physics and Chemistry of Comets*, Springer Verlag, Berlin, pp. 376, (1990).
- (3) R.L. Newburn, Jr. M. Neugebauer, J. Rahe (eds.), *Comets in the Post-Halley Era*, Kluwer, Dordrecht, , pp 1360, (1991).
- (4) J. Kissel et al., *Nature* **321**, 280-282, (1986).
- (5) J. Kissel et al., *Nature* **321**, 336-338, (1986).
- (6) E. Jessberger et al., *Nature* **332**, 691-695, (1988).
- (7) E. Jessberger and J. Kissel, in: *Comets in the Post-Halley Era*, R.L. Newburn, Jr., M. Neugebauer, J. Rahe (eds.) Kluwer, Dordrecht, 1075-1092, (1991).
- (8) D.E. Brownlee and J. Kissel, in: Mason J.W. (ed.), *Comet Halley: Investigations, Results, Interpretations*, Vol. 2, *Dust, Nucleus, Evolution*, Ellis Horwood, New York, p. 89, (1990).
- (9) P. Beck, in: F.G. Rüdener (ed.), *Austrian Research Centre Report 2308*, 119-127 (1992).
- (10) G. Rüdener, H.M.Fehrer, R.Schmidt, H. Arends, *ESA Journal* **17**, 147-157, (1993).
- (11) Wollnik, in: *Ion Formation from Organics Solids IFOS III* (Benninghofen A. ed.), Springer Proc. in Physics **9**, (1986).
- (12) H. Zschegg, J. Kissel, G.H. Natour, E. Vollmer, *Astrophys. Space Sci.* **195**, 447-661, (1992).

SOLAR WIND GASES IN A METAL SEPARATE FROM LUNAR SOIL 68501: A FOLLOWUP STUDY; R. H. Becker and R. O. Pepin, School of Physics and Astronomy, University of Minnesota, Minneapolis, MN 55455.

Noble gases and nitrogen were analyzed in a 90-95% pure metal separate from lunar soil 68501 by step-wise combustion and pyrolysis. Helium and neon appear essentially unfractionated with respect to one another, yielding the solar He/Ne ratio in the total gas and in all but the highest temperature steps. However, they are depleted relative to Ar by a factor of 5. Argon, krypton and xenon exhibit mass-dependent fractionation relative to solar abundance ratios, but appear unfractionated, both in bulk and in early temperature steps, when compared to abundance ratios in 71501 ilmenite, derived by chemical etching and suggested to represent abundance ratios in solar wind. Total spallation-corrected Kr and Xe show no isotopic fractionation relative to SW Kr and Xe compositions derived from this same 71501 ilmenite, supporting the idea that these gases may not have undergone a mass-dependent fractionation. The depletion of He and Ne in the lunar metal is in contrast to what has been seen in analyses of metal separates from meteorites. Nitrogen has a $\delta^{15}\text{N}$ value of $\sim +80\%$ in the bulk sample, with the solar N component considerably heavier than that but difficult to determine accurately.

We originally undertook analysis of lunar regolith metal [1] with the expectation that step-wise combustive release would not lead to elemental or isotopic fractionation of the implanted solar noble gases in the metal, for reasons having to do with the properties of noble gas diffusion in metal [1,2]. We also expected the implanted noble gases to have undergone little or no fractionation while on the moon, for the same reasons. Extraction of apparently unfractionated solar He, Ne and Ar from metal from the gas-rich Weston meteorite [2] supported these expectations. The results from an impure metal separate from 68501 [1], however, suggested the presence of fractionated heavy noble gases overprinting a solar He, Ne and Ar component, even for the lowest temperature steps. We pointed out that the fractionated gases might be due to the fairly large silicate component (20-25%) in that sample, but also considered that they might reside in the metal [1]. Results of step-wise combustion of a cleaner separate (5-10% silicate content) of 68501 metal are presented here. They confirm the pattern of relative abundance ratios seen in [1], and that the gases are almost certainly present in the metal rather than the silicates. They turn out to be open to two very different interpretations, however.

One possibility is that only He and Ne in the metal are unfractionated, with the remaining noble gases dominated by the overprint of a strongly mass-fractionated component. These is illustrated by the conventional normalization of the bulk sample data shown in Table 1. He/Ar and Ne/Ar are normalized to solar ratios from [3], Kr/Ar and Xe/Ar to ratios from [4]. In the first three steps, from 330°-410°C, where laboratory-induced diffusion should be at a minimum, He/Ar and Ne/Ar are within 15% of the solar values, yet Kr/Ar and Xe/Ar ratios are 1.8 and 3 times their solar values even in this relatively low-temperature regime [5]. The presence of a strongly fractionated solar component would account for the elemental abundance patterns seen in the total gas and most individual steps. It would also explain why spallation-corrected $^{36}\text{Ar}/^{38}\text{Ar}$ ratios (assuming a uniform distribution of spallogenic Ar in the metal [5]) are well below $^{36}\text{Ar}/^{38}\text{Ar}$ in solar wind (SW) as determined from other samples [6], even in the earliest steps where solar energetic-particle (SEP) Ar should not be a factor. However, we see no significant mass-dependent isotopic fractionation in Kr and Xe in the metal sample [5]. One could argue that all elemental fractionation occurred relative to Xe, with little or no actual Xe loss, but if elemental abundances require that a mass-fractionated heavy gas component be present, the Kr isotopic pattern at least should reflect a mass fractionation due to Kr loss. Yet the total metal Kr isotopic pattern is within error that of the unfractionated SW component determined by Wieler and Baur [7].

Table 1. Atom ratios relative to Ar in total metal, normalized to "solar" ratios.

	$^4\text{He}/^{36}\text{Ar}$	$^{22}\text{Ne}/^{36}\text{Ar}$	$^{36}\text{Ar}/^{38}\text{Ar}$	$^{84}\text{Kr}/^{36}\text{Ar}$	$^{132}\text{Xe}/^{36}\text{Ar}$
Conventional normalization	0.205	0.227	1.00	2.06	3.83
<u>Alternate normalization</u>	<u>0.205</u>	<u>0.227</u>	<u>1.00</u>	<u>1.01</u>	<u>1.09</u>

SOLAR WIND IN LUNAR METAL: Becker R. H. and Pepin R. O.

The alternative interpretation assumes that the Ar:Kr:Xe elemental abundance pattern seen in lunar ilmenite 71501 represents the actual flux ratios of these elements in the recent solar wind [8]. With this assumption, Ar, Kr and Xe in the 68501 metal are essentially unfractionated (see Alternative normalization in Table 1, which assumes "solar" Ar:Kr:Xe ratios of 16730:8.97:1 from [9]). In this normalization, it is reasonable to find that Kr and Xe isotopic ratios have not suffered mass fractionation effects. The argon isotopic result mentioned above can be accounted for by a spallation-correction using Ne_{sp} amounts derived on a step-by-step basis, rather than assuming a uniform Ar_{sp} distribution [5]. This interpretation of the data is more in keeping with our original expectations of finding unfractionated solar gases in lunar metal.

Note, however, that He and Ne are depleted in the metal in this second interpretation by a factor of 5 relative to the other gases. It is generally considered that loss of solar wind gases occurs either by processes such as sputtering, flaking and abrasion which don't significantly differentiate among gases or isotopes of a gas, but may enrich the more deeply-implanted SEP component over SW, or by diffusion, which leads to elemental and isotopic fractionations as well as enhancement of SEP (see, for example, [10,11]). It would appear that in metal there is a third possible process, presumably diffusion without fractionation. He/Ar and Ne/Ar ratios in our individual steps vary from initially solar values to about a factor of 50 lower at the highest temperatures, representing either a lunar or laboratory-induced separation. However, He/Ne varies hardly at all except at the highest temperatures. This depletion process is evident in our lunar metal, but does not appear to have occurred in meteoritic metal samples [2,10,11], for reasons we don't yet understand. SEP accounts for about 40% of the He and Ne now in the lunar metal, but could have been as low as 8% in the originally implanted gas, if the depletions of He and Ne seen are primarily due to loss of the SW component. This is consistent with the Kr isotopic composition in the metal, which yields an upper limit of 15% SEP in the Kr as measured [5].

Nitrogen in the metal, as with the other gases measured, can be interpreted in more than one way. There is undoubtedly a meteoritic component in the nitrogen, which is almost certainly lighter [12,13] than the total nitrogen and therefore lighter than the solar N component. Because we do not know the average $\delta^{15}N$ value of the meteoritic component, or its abundance, we cannot subtract it out accurately enough to determine the $\delta^{15}N$ value of the solar component. Additionally, since we don't know how much solar N should even be in the sample, because the primary flux ratio of N/Ar in the solar wind is not known, we could not determine whether there have been significant losses of the solar component with associated fractionation of isotopes, even if the meteoritic component were well determined. However, it is possible to make educated guesses with regard to these unknown quantities. Our best estimates lead us to believe that the primary flux ratio of N/Ar is likely to be an order of magnitude or more above the Cameron solar value [4], and that the $\delta^{15}N$ of recent solar wind is around +200‰ or higher. If we are wrong about the degree of retention of Ar, Kr and Xe in the sample, the first of these two conclusions may be incorrect. The second conclusion however is not very sensitive to this particular assumption, and should still be pretty much valid.

References: [1] Becker R.H., Lunar Planet. Sci. XX, 54-55 (1989). [2] Becker R.H. and Pepin R.O., Earth Planet. Sci. Lett. **103**, 55-68 (1991). [3] Bochsler P. and Geiss J., Trans. Int. Astron. Union XVII, 120-123 (1977). [4] Cameron A.G.W., in Essays in Nuclear Astrophysics, pp. 23-43 (1982). [5] Becker R.H. and Pepin R.O., manuscript submitted to Meteoritics. [6] Benkert J.-P. *et al.*, Jour. Geophys. Res. **98**, 13147-13162 (1993). [7] Wieler R. and Baur H., manuscript submitted to Meteoritics. [8] Wieler R. *et al.*, Lunar Planet. Sci. XXIII, 1525-1526 (1992). [9] Wieler R., personal communication (1993). [10] Pedroni *et al.*, Lunar Planet. Sci. XXIII, 1049-1050 (1992). [11] Murer Ch. *et al.*, Lunar Planet. Sci. XXV, this volume. [12] Franchi I.A. *et al.*, Geochim. Cosmochim. Acta **57**, 3105-3121 (1993). [13] Prombo C.A. and Clayton R.N., Geochim. Cosmochim. Acta **57**, 3749-3761 (1993).

THE PARTITIONING OF Na BETWEEN MELILITE AND LIQUID: AN EXPERIMENTAL STUDY WITH APPLICATIONS TO TYPE B CAIs; J.R. Beckett and E.M. Stolper, Division of Geological and Planetary Sciences, California Institute of Technology, Pasadena, CA 91125.

Introduction. Many Ca-, Al-rich inclusions (CAIs) contain alteration products formed under subsolidus conditions [1], including the sodic phases nepheline and sodalite [2,3]. The alteration processes have generally been viewed as post-dating all melting events, but textural and isotopic evidence [3] suggest that multiple stages of melting and alteration were involved, leading to the possibility that Na and other volatile elements were present in the melt during crystallization of the igneous phases. This is consistent with significant concentrations of Na₂O in melilite (Mel) and anorthite (An) in some apparently unaltered inclusions. To constrain the composition of melt from which Mel in CAIs crystallized and to evaluate the role of volatilization, it is necessary to understand the partitioning behavior of Na₂O between Mel and liquid (Liq). We determined experimentally the partition coefficients for Na₂O between Mel and Liq using procedures of [4] and a bulk Na₂O content analogous to those observed in CAIs [5].

Experimental Techniques. A glass starting material (CaO=29.26±0.14(2σ) wt%; MgO=10.06±0.15; Al₂O₃=28.68±0.23; SiO₂=30.11±0.32; TiO₂=1.34±0.09; Na₂O=0.47±0.01) corresponding in composition to an average Type B inclusion [6] but with 0.5 wt% Na₂O was synthesized from an oxide mix. Each sample was held at 1420°C for 3 hrs, cooled at 1°C/hr in air, and quenched into deionized H₂O. Synthetic Mel, An and glass (Gl) were analyzed by electron probe. Samples lost variable amounts of Na (1/3-1/2 of total) during the course of experiments but rapid diffusion of Na in the melt [7] and slow cooling rates led to glasses homogeneous with respect to Na₂O and allowed equilibrium to be maintained at the growing Mel-Liq interfaces.

Experimental Results. Runs were quenched in the T range 1208-1353°C. All run products contain spinel, Mel and Gl. The Mel is zoned with X_{AK} and Na₂O increasing from core to rim of individual crystals (maximum range from core-to-rim = Ak18-67; 0.06-0.39 wt% Na₂O). X_{AK} and Na₂O also increase at the crystal-Liq interface with decreasing T. Fig. 1 shows a linear relationship between T and X_{AK} of rim melilites. Values of T-X_{AK} of [8] for experiments conducted under identical conditions on an Na-free CAI bulk composition are similar and the inferred T for core Mel (Ak18; 1400°C) is consistent with the equilibrium appearance T of Mel in the Na-free system (1399-1405°C; [6]). One sample (1208°C) contained An (0.09 wt% Na₂O). Pyroxene was not observed although it is expected at lower temperatures [e.g., 8]. Na₂O in Gl ranges from 0.21-0.38 wt% and is homogeneous (±0.004-8 wt% 1σ) within each sample. Other elements in Gl are also homogeneous, except for the 1208°C run. In this experiment, Gl compositions are quite variable (e.g., TiO₂ ranges from 2.5 to 4.7 wt%) probably due to crystallization of An.

Experimentally determined Mel/Liq partition coefficients for Na₂O (D_{Na}) are 0.59-1.52 for Ak30-67 (Fig. 2) and a linear function of X_{AK}/X_{Ge} (Ge: Gehlenite), reflecting crystal-chemical control. A simple linear relationship between D_{Na} and X_{AK}/X_{Ge} is expected based on the exchange reaction $\text{Ca}_2\text{MgSi}_2\text{O}_7(\text{Mel}) + \text{AlO}_{3/2}(\text{Liq}) + \text{NaO}_{1/2}(\text{Liq}) = \text{CaO}(\text{Liq}) + \text{MgO}(\text{Liq}) + \text{NaCaAlSi}_2\text{O}_7(\text{Mel})$, assuming ideal ionic activities for trace elements in Mel, and approximately constant T and melt composition [see 4]. In our experiments, the dependence of D_{Na} on T, melt composition, and nonideality in Mel is secondary but these effects are probably important for data of [9,10] where melt and Mel have much higher Na₂O (Fig. 3).

Discussion. The experimentally determined D_{Na} are applicable to Vigarano Type B inclusion 1623-8 because Mel (Fig. 4) and bulk compositions [3] are similar to those of our experiments. There are also relevant reconnaissance data [3] on three Allende Type B1's. From our D_{Na} and Mel from 1623-8 [3], we calculate wt% Na₂O in the melt during Mel crystallization of 0-0.5% with Na₂O = 0.10±0.09(1σ) for X_{AK}<0.35 and 0.19±0.08(1σ) for X_{AK}>0.35. These calculations suggest: (1) Although Vigarano Type B inclusion 1623-8 shows little petrographic evidence for the pervasive alteration that characterizes altered Allende inclusions, the calculated

MELILITE/LIQUID PARTITIONING: Beckett, J.R. and Stolper, E.M.

concentrations of Na_2O in liquids from which early-crystallized Mel (i.e., low Ak) formed are comparable to those of bulk altered Allende CAIs [5]. This result is consistent with previous suggestions [3] that the last melting event to have affected inclusions such as 1623-8 may have obliterated an altered precursor similar to an Allende CAI but a substantial fraction of the Na_2O originally present in the precursor was retained. The evolution of 1623-8 is similar to chondrules in that loss of Na_2O during melting was limited [11], probably due to rapid heating and cooling. (2) The highly variable Na_2O of low Ak Mel may reflect highly variable Na concentrations in the precursor or multiple partial melting and alteration events involving low-Na and high Na precursors (i.e., some of the gehlenitic Mel is relict, predating alteration and the last melting event).

Mel from Allende Type B1's [3] imply a somewhat different pattern of melt compositions. Calculated Na_2O of the melt are near zero for $X_{\text{Ak}} < 0.35$, rise to ~ 0.13 wt% between Ak35 and Ak50 then decrease to ~ 0.07 by Ak70. Na-poor gehlenitic Mel, mostly in the Mel-rich outer mantle, may be relict phases from an earlier melting event that predated alteration. Alternatively, they could have crystallized within an Na_2O -depleted near surface zone and reflect volatilization during the initial stages of a heating event rapid enough to prevent diffusive rehomogenization of Na_2O in the melt.

References. [1] Hutcheon, I.D. and Newton, R.C. (1981) *LPS XII*, 491-3. [2] Wark, D.A. (1981) *LPS XII*, 1145-7. [3] MacPherson, G.J. and Davis, A.M. (1993) *GCA* 57, 231-44. [4] Beckett, J.R. *et al.* (1990) *GCA* 57, 1755-74. [5] Grossman, L. and Ganapathy, R. (1975) *Proc. Lunar Sci. Conf.* 6th, 1729-36. [6] Stolper, E. (1982) *GCA* 46, 2159-80. [7] Tsuchiyama, A. *et al.* (1981) *GCA* 45, 1357-67. [8] Stolper, E. and Paque, J.M. (1986) *GCA* 50, 1785-1806. [9] Pan, V. and Longhi, J. (1989) *AJS* 289, 1-16. [10] Pan, V. and Longhi, J. (1990) *CMP* 105, 569-84. [11] Hewins, R.H. (1989) *Proc. NIPR Symp. Antarct. Meteorites*, 2, 200-220.

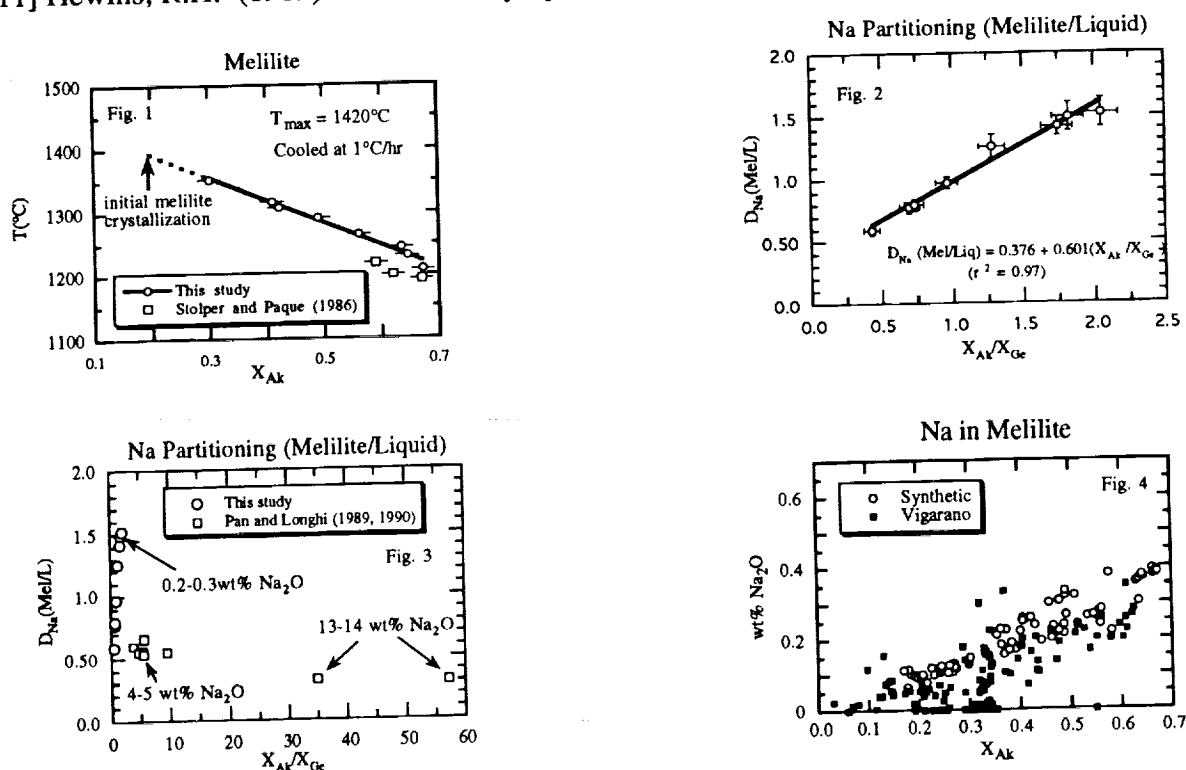


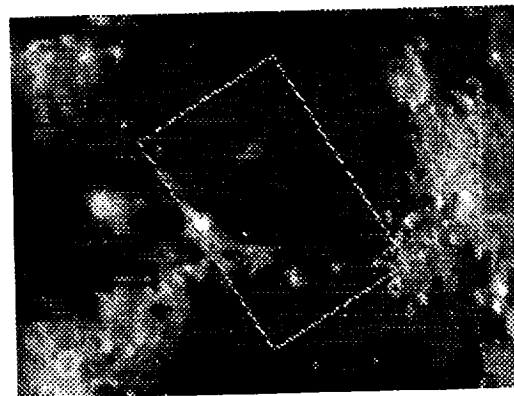
Fig. 1. T vs. X_{Ak} at the rim of Mel in contact with melt. Fig. 2. D_{Na} vs. $X_{\text{Ak}}/X_{\text{Ge}}$ (this study). Fig. 3. D_{Na} vs. $X_{\text{Ak}}/X_{\text{Ge}}$ (this study and [9-10]). Wt% Na_2O in melt is indicated. Fig. 4. Wt% Na_2O vs. X_{Ak} for synthetic (this study) and meteoritic (Vigarano inclusion 1623-8 [3]) Mel.

2947
HIGH SPATIAL RESOLUTION TELESCOPIC MULTISPECTRAL IMAGING AND SPECTROSCOPY OF THE MOON: I. THE SERENITATIS/TRANQUILLITATIS BORDER REGION; J.F. Bell III (NRC/NASA Ames Research Center, Moffett Field, CA 94035) and B.R. Hawke (PGD/SOEST, University of Hawaii, Honolulu, HI 96822).

The region of the Moon near the border between Mare Serenitatis and Mare Tranquillitatis is one of the most geologically and compositionally complex areas of the nearside. The geologic history of this region has been shaped by impacts of widely-varying spatial scale and temporal occurrence, by volcanism of variable style and composition with time, and by limited tectonism. We have been studying this region as part of a larger multi-remote-sensing-technique effort to understand the composition, morphology, geology, and stratigraphy of the Moon at spatial scales of 2 km or less [cf. 1, 2]. We have been aided in this effort by the proximity of this area to the Apollo 11, 15, and 17 landing sites and by the occurrence of one of the primary lunar spectroscopic "standard areas" within our scene (MS2). Here, we report some of the findings from the multispectral imaging and spectroscopy part of this effort [3].

The reflectance spectra analyzed here were obtained with the UHPGD near-IR circular variable filter (CVF) spectrometer with a cooled InSb detector. The data were obtained at a spectral resolution of $\Delta\lambda/\lambda \approx 1.25\%$ over the wavelength range 0.65 to 2.6 μm using the University of Hawaii 2.24-m telescope at Mauna Kea Observatory. The CVF was stepped through 112 wavelengths over the course of about 90 seconds, and anywhere from 2 to 6 independent measurements were made of each region. Observations were carried out on October 29 and 30 UT, 1985, at a lunar phase angle of 10° and 20° respectively. The 2.24-m telescope was configured at $f/35$, yielding at spot size of 1.3 km diameter on the Moon using the smallest aperture and assuming 0.65 arcsec seeing. Spectra were obtained of 20 regions in the Serenitatis/Tranquillitatis region [4] as well as of the Apollo 16 landing site.

Telescopic multispectral CCD images of the Serenitatis/Tranquillitatis region were obtained using a 384x576 pixel Photometrics cooled CCD camera. The camera and an uncooled narrowband filter wheel were mounted to the University of Hawaii Planetary Patrol 61-cm telescope at Mauna Kea Observatory. Images were obtained in 8 narrowband transmission filters, chosen to maximize the potential spectral differences between the units in the different regions. Observations were carried out on August 7 1990 UT at a lunar phase angle of 10° . The Planetary Patrol telescope was configured at $f/13.5$, yielding a plate scale of 0.573 arcsec per 23 μm CCD pixel. This translates to a 1.66 km/pixel resolution at the lunar equator and a 200x310 arc sec field of view. The boundaries of our study region are shown in Figure 1.



Multiple independent measurements of the near-IR spectrum of each region were averaged to produce a final "raw" spectrum with associated error bars. The spectra were converted into scaled reflectance units by taking a ratio of each region relative to Apollo 16 and then multiplying by the ratio of Apollo 16 to the Sun derived from spectral studies of returned Apollo 16 lunar samples. For many of these spectra, one or more linear continua were removed by fitting straight lines to the data at local maxima near 0.8 and 1.5 and 2.6 μm . Spectroscopic analyses include (1) determination of band center positions and band widths using derivative

LUNAR SPECTROSCOPY: BELL J.F. III AND HAWKE B.R.

analysis and polynomial curve fitting; (2) determination of band depth, width, and area using standard methods [5,6]; and (3) calculation of simple linear mixing models [7].

The imaging data reduction process included subtraction of the dark (bias + dark current) values from all images and then division of a normalized (mean = 1.0) flatfield frame from each Moon and sky image at the appropriate wavelength. The sky image was then subtracted from the Moon image for each filter. Finally, the multispectral images are spatially co-registered into an image cube with an estimated registration accuracy of 0.25 pixel. This was achieved using a flux-conserving procedure whereby each image is convolved with a sinc² function having a width consistent with the estimated point spread function of our images. A relative calibration is achieved by ratioing all the images to the spectrum of MS2 as observed in the scene. Thus, we can compare spectra extracted from these multispectral images with previously-obtained spectroscopic data sets also presented as spot/MS2 ratios.

Analysis techniques used on these images included (1) generation of simple ratio images between different wavelengths in order to examine spectral slope and absorption band variations; (2) extraction of 6 to 8 channel spectra ("pseudospectra") from the image cube for comparison with other spectroscopic data sets; and (3) creation of simple linear mixing models using a small number of endmembers. We followed the mixing technique of [7] and [2] for spatial mapping of spectral heterogeneity and for the analysis of compositional variations focusing on specific processes (e.g., soil maturation, highlands-mare mixing, etc.).

Major findings to date [3,8] include the observation that the 1- μ m band in the 43-km crater Plinius' central peak and NE wall regions is clearly composed of two features: a short-wavelength component centered near 0.92 μ m and a longer-wavelength component centered near 1.0 μ m. The 0.92 μ m feature is weaker than the 1.0 μ m band in the NE wall spectrum; however, the two bands have comparable strengths in the central peak. The presence of a 0.92 μ m band in these spectra indicates that parts of Plinius are composed of highlands-like materials. This interpretation is confirmed by mixing analyses of the imaging data, which clearly show that the Plinius peak and several regions on the floor have a Haemus-like highlands signature. Also seen in the endmember images is an indication that low-Ti (central Serenitatis) mare exists on several regions of the floor and S-SW crater rim. The implication is that the mare is relatively shallow in this part of the Serenitatis-Tranquillitatis border. It is puzzling, however, that there are no indications of highlands material in the Plinius ejecta. This may be due to inadequate spatial resolution (the highlands component of the ejecta is unresolved) or more likely to the effects of vertical mixing, where the spectral signature of the pre-existing mare materials now completely dominates the mixed highlands-mare signal. The nearby 18-km crater Dawes has little or no highlands signature in its spectra. It registers a very high fraction of immature endmember materials, however, and one interpretation of this is that the brightness of its ejecta blanket is due to maturation rather than compositional effects.

Our study demonstrates the value of both high spatial and spectral resolution observations of geologically and spectroscopically interesting regions of the Moon for extending compositional, stratigraphic, and morphologic interpretations gleaned from previous data sets. While the Clementine mission should obtain spectacular high spatial resolution multispectral views of the Moon, it is important to note that higher spectral resolution observations of these regions will substantially add to our understanding of the Moon at fine spatial scales.

References: [1] Bell, J.F. III and B.R. Hawke (1991) *LPSC XXII*, 75. [2] Campbell, B.A. *et al.* (1992) *PLPS*, 22nd, 259. [3] Bell, J.F. III and B.R. Hawke (1994) submitted to *Icarus*. [4] Jaumann, R. (1991) *Ph.D. Dissertation*. [5] Clark and Roush (1984) *J. Geophys. Res.*, 89, 6329. [6] Lucey, P.G. *et al.* (1986) *J. Geophys. Res.*, 91, D344. [7] Adams, J.B. *et al.* (1986) *J. Geophys. Res.*, 91, 8098. [8] Bell, J.F. III and B.R. Hawke (1992) *LPSC XXIII*, 77.

P-2
HIGH RESOLUTION VISIBLE TO SHORT-WAVE NEAR-INFRARED CCD SPECTRA OF MARS DURING 1990; James F. Bell III (NRC/NASA Ames, Moffett Field CA), Karl Bornhoeft (PGD/SOEST, Univ. of Hawaii), and Paul G. Lucey (PGD/SOEST, Univ. of Hawaii)

The 0.4 to 1.0 μm spectrum of Mars is dominated by a steep red, relatively featureless spectral slope. Earlier lower spectral resolution observations [e.g., 1-3] interpreted the red color and the lack of absorption features in the spectra as evidence of poorly crystalline ferric oxide minerals. More recent higher spectral resolution observations and re-interpretations of older data sets have revealed measurable spectral structure, however [4-7]. For example, absorption features near 0.65 and 0.86 μm were detected and spatially mapped in data obtained during the 1988 opposition. These absorptions were interpreted as evidence for crystalline hematite on Mars, occurring as an accessory phase in abundances of 3-6% in the soil. We are attempting to verify the existence of these subtle crystalline Fe^{3+} absorption features and to map their spatial distribution in regions of the planet not imaged in 1988.

During the 1990 opposition, we obtained imaging spectroscopic data of Mars from the University of Hawaii 2.24 m telescope at Mauna Kea Observatory [8]. The data were obtained with the Wide Field Grism Spectrograph (WFGS), a facility instrument operated by the Institute for Astronomy at the University of Hawaii. WFGS uses an 800 \times 800 CCD and a transmission grating ruled on a prism. We used a grating blazed at 4800 \AA in first order to obtain data from 0.50 to 0.94 μm at a spectral resolution of $R = 200$ to 350. WFGS is a field widened spectrograph that can accommodate a variety of user-designed slits. Our Moon/Mars slit design had projected dimensions of 0.29" \times 153", allowing for high spectral resolution and adequate cross-slit spatial sampling of the Martian disk. A typical Mars image cube consists of approximately 20 \times 30 spatial pixels at \approx 160 useful wavelengths.

On 9-10 November 1990 UT we obtained 11 image cubes of all or parts of the Martian disk centered near 100-140° W longitude. Mars subtended 17.8" during this time, was at a phase angle of 17°, and the season was late northern winter ($L_s = 330^\circ$). We also obtained 10 scans of the standard star κ Cetus (Type G5V, $M_V = +4.82$) and numerous bias and flatfield calibration frames. As an aid in reconstruction of the slit-scan images, we also obtained a number of red filter CCD images of Mars with the grism out of the path. Wavelength calibration was performed using Hg-Cd-Zn and Ne calibration lamps.

Data reduction procedures are similar to those used for 1988 WFGS data described previously [9, 10]. These procedures include bias and dark current removal, flatfield (pixel-to-pixel non-uniformity) corrections, assembly of the individual slit positions into image cubes, and spatial reconstruction of the imaging data.

Table 1. 1990 Mars MKO/WFGS Imaging Spectroscopic Observations

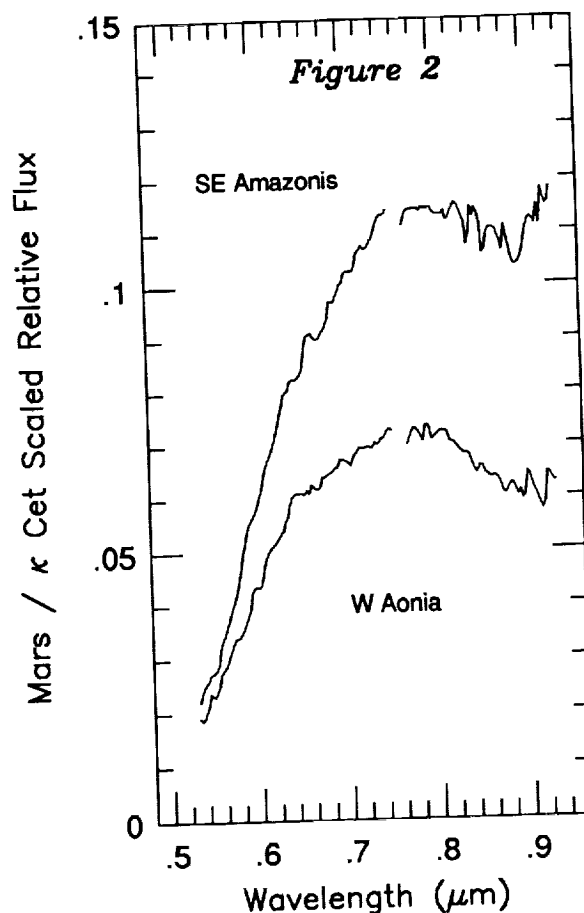
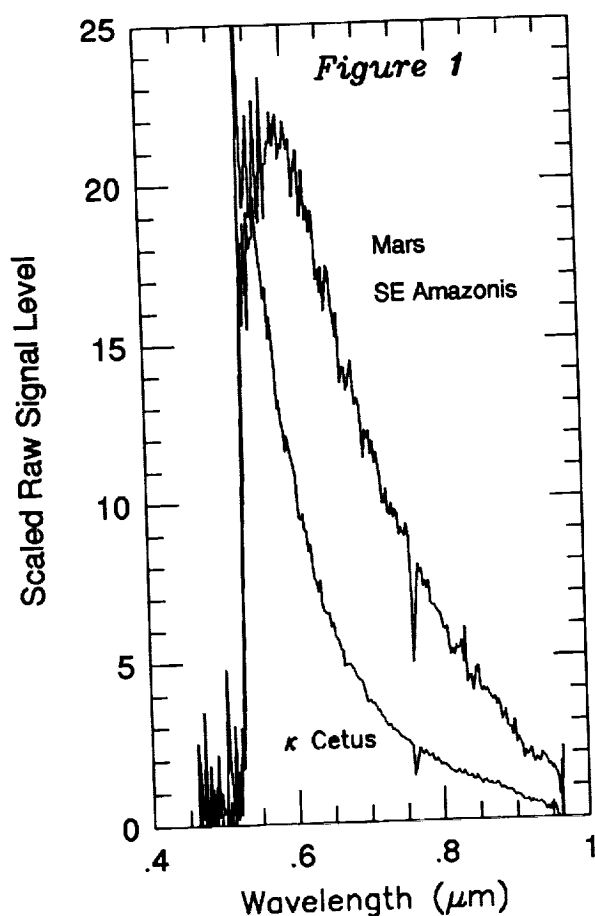
Date (UT)	L_s	Phase	# Mars Cubes	# Spectra	# Star Cubes	# Spectra
9 Nov. 1990	330°	17°	5	\approx 4000	4	\approx 30
10 Nov. 1990	330°	16°	6	\approx 6000	5	\approx 35

Figure 1 shows an example of the raw data obtained on 11/9/90 UT for a Mars bright region in southeast Amazonis and for the standard star κ Cetus. These data have had bias and flatfield corrections applied. A number of high frequency features can be seen in the spectra, some of which are associated with poor signal to noise at the shortest wavelengths and some of which are due to absorptions in the Earth's atmosphere or in the Solar or κ Cet spectra [e.g., 11].

Figure 2 shows some representative bright and dark region spectra extracted from the same image cube as Figure 1. The spectra are (Mars / κ Cet), which is a good approximation of (Mars /

Sun) as κ Cet is a G class main sequence star with a spectrum described as "very close to solar" by Hardorp [12]. The spectra have been smoothed slightly using a gaussian convolution program in order to eliminate some of the high frequency noise.

Several interesting features are immediately apparent in the spectra of Figure 2. First, both bright and dark regions exhibit the characteristic red slope typical of Mars. Second, absorption features are evident near 0.6 to 0.7 μm and 0.8 to 0.9 μm in both spectra. The longer wavelength band is centered near 0.867 μm (derived using a 2nd order polynomial fit) in the bright region and near 0.893 μm in the dark region. And finally, the dark region spectrum exhibits a more negative spectral slope in the 0.75 to 0.94 μm region than the bright region. These observations are consistent with the interpretations that (a) the bright regions exhibit a ferric spectral signature due to a small amount of crystalline hematite (having bands near 0.65 and 0.86 μm) in a matrix of a much more poorly crystalline ferric phase that primarily accounts for the color [e.g., 4,5] and (b) this particular dark region also exhibit much of this ferric character but also shows evidence of absorption at slightly longer wavelengths that would be expected for more ferrous-bearing compositions. Evidence will be sought in the data for additional compositional heterogeneity among and between bright and dark regions.



- References:** [1] McCord, T.B. and J.A. Westphal (1971) *Astrophys. J.*, 168, 141. [2] McCord, T.B. et al. (1978) *J. Geophys. Res.*, 83, 5433. [3] Singer, R.B. (1982) *J. Geophys. Res.*, 87, 10159. [4] Morris, R.V. et al. (1989) *JGR*, 94, 2760. [5] Bell, J.F. III et al. (1990) *J. Geophys. Res.*, 95, 14447. [6] Singer, R.B. et al. (1990) *LPSC XXI*, 1164. [7] Bell, J.F. III (1992) *Icarus*, 100, 575. [8] Bell, J.F. III et al. (1991) *LPSC XXII*, 77. [9] Bell, J.F. III et al. (1990) *PLPSC XX*, 479. [10] Bell, J.F. III et al. (1992) *Exp. Astron.*, 2, 287. [11] Kurucz, R.L. et al. (1984) *NSO Solar Flux Atlas*, Harvard Univ. Press, 239 pp. [12] Hardorp, J. (1978) *Astron. Astrophys.*, 63, 383.

2949

ABSOLUTE CALIBRATION AND ATMOSPHERIC VS. MINERALOGIC ORIGIN OF ABSORPTION FEATURES IN 2.0 TO 2.5 μm MARS SPECTRA OBTAINED DURING 1993; James F. Bell III (NRC/NASA Ames, Moffett Field CA), James B. Pollack (NASA Ames), Thomas R. Geballe (JAC/UKIRT, Hilo HI), Dale P. Cruikshank (NASA Ames), and Richard Freedman (Sterling Software, Palo Alto CA).

For over twenty years the origin of weak absorption features in the spectrum of Mars near 2.3 μm ("K" Band: 1.9-2.5 μm) has been debated. This spectral region contains gaseous absorption features predominantly from CO_2 and CO on Mars as well as from molecules like H_2O , CO_2 , CH_4 , and CO in the telluric and solar atmospheres [e.g., 1-4]. Putative mineralogic absorption features in Mars spectra at these wavelengths have been interpreted as evidence for specific Mg-bearing clay silicates or amphiboles [5,6] and bicarbonate-bearing minerals such as scapolite [7]. Spectra from other wavelength regions have been used to infer the existence of smectite clays on Mars based on features in the visible and in the mid-IR [e.g., 8-10] and to place limits on the abundance and distribution of anhydrous and hydrous carbonate-bearing minerals [e.g., 11-14].

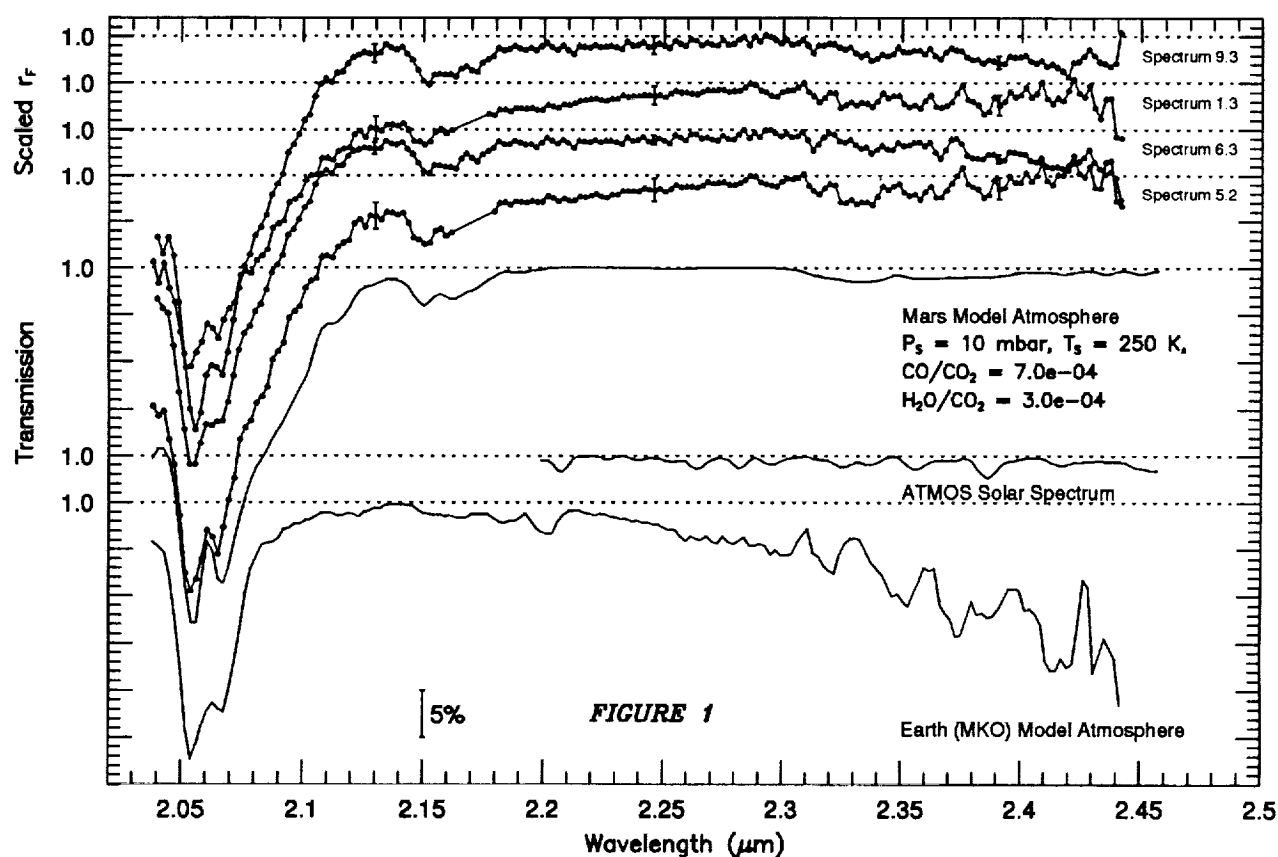
We obtained new high resolution ($R \approx 300$ to 370) reflectance spectra of Mars during the 1993 opposition from Mauna Kea Observatory using the UKIRT CGS4 spectrometer. Fifty spectra of 1600-2000 km surface regions and a number of standard star spectra were obtained in the 2.04 to 2.44 μm wavelength region on 4 February 1993 UT. S/N in the raw data ranged from 30 to 300. Near-simultaneous observations of bright standard stars were used to perform terrestrial atmospheric corrections and an absolute flux calibration. Using the known magnitude of the stars and assuming blackbody continuum behavior, the flux from Mars could be derived. To derive radiance factor values (observed flux / expected Lambertian flux) we assumed that the solar continuum flux followed an empirically-derived relationship [15] and we used the technique of [16] to derive the expected Lambertian flux at Mars. The absolutely-calibrated spectra exhibit a S/N precision of from 35 to 90 depending on the radiance factor of the region observed. The errors on the absolute flux level are from 6 to 10% (1σ) and those on the radiance factor values are from 8 to 12%, assuming a 5% uncertainty in the absolute flux distribution of the Sun.

A radiative transfer model [17] and the HITRAN spectral line data base [18] were used to compute atmospheric transmission spectra for Mars and the Earth in order to simulate the contributions of these atmospheres to our observed data. Also, we examined the ATMOS solar spectrum in the near-IR [19] to try to identify absorption features in the spectrum of the Sun that could be misinterpreted as Mars features. Scaled radiance factor spectra are shown in Figure 1, along with Earth and Mars model atmospheric spectra and the solar spectrum for comparison.

Eleven absorption features were detected in our Mars spectra. Six were attributed all or in part to Mars atmospheric CO_2 or CO (2.052, 2.114, 2.151, 2.331, 2.356, and 2.365 μm). Four others were interpreted as evidence for telluric (H_2O , CH_4) or possibly solar/stellar spectral contamination (2.316, 2.384, 2.414, and 2.432 μm). One band at 2.297 μm appears to be mineralogic in origin. Three of the bands (2.331, 2.356, and 2.365 μm) appear to have widths and depths that are consistent with additional, non-atmospheric absorptions, although a solar contribution at these wavelengths and at 2.297 μm cannot be entirely ruled out.

Our data provide no conclusive identification of the mineralogy responsible for the absorption features we detected. However, examination of terrestrial spectral libraries and previous high spectral resolution mineral studies [e.g., 20, 21] indicates that the most likely origin of these features is either CO_3^{2-} , HCO_3^- , or HSO_4^- anions in framework silicates or possibly (Fe, Mg)-OH bonds in sheet silicates. If the latter is correct, then an explanation for the extremely narrow widths of the cation-OH features in the Mars spectra as compared to terrestrial minerals must be

devised. One possibility involves dehydroxylation [22], but this situation has not yet been fully examined spectroscopically. Unfortunately, we can provide no conclusive resolution of the debate over scapolite on Mars. Our data [23] apparently confirm earlier observations by [7] that there are subtle, narrow absorption features in the Martian K band spectrum that cannot be explained solely by atmospheric absorption. We do not favor assigning a specific mineralogy at this time based on these bands because (a) our understanding of the spectral nature of many other minerals at such high spectral resolution is lacking; (b) we cannot be certain that the stellar and solar spectra are not introducing artifacts; and (c) placing stringent constraints on surface mineralogy from spectrally limited data may not prove consistent with other observational, geologic, or geochemical constraints gleaned from previous spacecraft and telescopic data.



- References: [1] Connes, J. *et al.* (1969) *CNES Near-IR Spectral Atlas of the Planets*. [2] Park, J.H. *et al.* (1981) NASA RP-1084. [3] Farmer, C.B. *et al.* (1987) JPL Publication 87-32. [4] Crisp, D. (1990) *J. Geophys. Res.*, 95, 14577. [5] McCord, T.B. *et al.* (1978) *J. Geophys. Res.* 83, 5433. [6] McCord, T.B. *et al.* (1982) *J. Geophys. Res.* 87, 3021. [7] Clark, R.N. *et al.* (1990) *J. Geophys. Res.*, 95, 14463. [8] Banin, A. *et al.* (1985) *J. Geophys. Res.*, 90, C771-C774. [9] Hunt, G. *et al.* (1973) *Icarus*, 18, 459. [10] Toon, O.B. *et al.* (1977) *Icarus*, 30, 663. [11] Roush, T.L. *et al.* (1986) *LPSC XVII*, 732. [12] Blaney, D.L. and T.B. McCord (1989) *J. Geophys. Res.*, 94, 10159. [13] Pollack, J.B. *et al.* (1990) *J. Geophys. Res.* 95, 14595. [14] Calvin, W.M. *et al.* (1994) *J. Geophys. Res.*, in press. [15] Smith, E.V.P. and D.M. Gottlieb (1974) *Space Sci. Rev.* 16, 771. [16] Roush, T.L., *et al.* (1992) *Icarus* 99, 42. [17] Pollack, J.B. *et al.* (1993) *Icarus*, 103, 1. [18] Rothman, L.S. *et al.* (1987) *Appl. Optics*, 26, 4058. [19] Farmer, C.B. and R.H. Norton (1989) NASA RP-1224, vol. 1. [20] Clark, R.N. *et al.* (1993) U.S. Geological Survey Open File Report 93-592. [21] Swayze, G.A. and R.N. Clark (1990) *J. Geophys. Res.*, 95, 14481. [22] Burns, R.G. (1993) *Geochim. Cosmochim. Acta* 57, 4555. [23] Bell III, J.F. *et al.* (1994) submitted to *Icarus*.

WAVELENGTH CALIBRATION TECHNIQUES AND SUBTLE SURFACE AND ATMOSPHERIC ABSORPTION FEATURES IN THE MARINER 6, 7 IRS REFLECTANCE DATA; J.F. Bell III (NRC/NASA Ames, Moffett Field CA), T.L. Roush (San Francisco State University/NASA Ames), T.Z. Martin (Jet Propulsion Laboratory/Caltech), J.B. Pollack (NASA Ames), and R. Freedman (Sterling Software, Palo Alto CA).

1994 marks the 25th anniversary of the Mariner 6 and 7 flyby missions to Mars. Despite its age, the Mariner 6,7 Infrared Spectrometer (IRS) data are a unique set of measurements that can provide important information about the Martian surface, atmospheric, and atmospheric aerosol composition. For certain mid-IR wavelengths, the IRS spectra are the only such spacecraft data obtained for Mars. At other wavelengths, IRS measured surface regions different from those measured by Mariner 9 or Phobos 2 and under different dust opacity conditions. The IRS instrument was described by [1,2] and initial results on surface features were presented by [3], on atmospheric features and topography by [4,5] and on aerosols and polar deposits by [6,7]. For many years after this initial set of papers, the IRS data went ignored.

Recently, a data set restoration was carried out by T.Z. Martin [8-10] and the IRS data have become available in digital form. This has led to several re-examinations of the IRS data using modern computational and spectroscopic techniques [11-14].

We are interested in examining the IRS reflectance data in the 1.8 to 3.0 μm region because there are numerous diagnostic absorption features at these wavelengths that could be indicative of hydrated silicate minerals (*e.g.*, clays, amphiboles, hydroxides) or of carbonate- or sulfate-bearing minerals [*e.g.*, 15]. Groundbased telescopic data and recent Phobos ISM measurements have provided controversial and somewhat contradictory evidence for the existence of mineralogic absorption features at these wavelengths [16-20]. Our goal is to determine whether any such features can be seen in the IRS data and to use their presence or absence to re-assess the quality and interpretations of previous telescopic and spacecraft measurements.

As part of the data set restoration exercise, Martin [8] performed a wavelength calibration of the data using fiduciary spikes in the CVF, atmospheric absorption features, and absorption features detected in a polystyrene film occasionally viewed by the IRS. We have attempted to test the quality of this calibration by comparing the IRS channel 2, left segment (1.8 to 3.6 μm) reflectance data to the Mars atmospheric transmission predicted using a radiative transfer model. We included CO_2 , CO , and H_2O in a single layer, no-dust model atmosphere and used the HITRAN line database to derive absorption coefficients at very fine frequency spacing. The absorption coefficients were converted to transmission using the molecular abundance derived from the incidence and emission values provided with the IRS spectra. The modeled transmission data were then convolved to the resolution of the IRS CVFs [2].

An example comparison is shown in Figure 1. The data are raw Mariner 7 spectra 92 and 98 that have not had instrumental artifacts (such as near 3.4 μm) removed. In general, it is apparent that the IRS spectra show both strong and weak Mars absorption features. For example, the CO_2 triplet near 2.0 μm and doublet near 2.7 μm are both well resolved, as are weak CO_2 features near 2.15 and 2.6 μm and the weak CO absorption envelope near 2.35 μm . In all, 9 features were isolated in the spectra to test the nominal wavelength calibration provided by [8]. Figure 2 shows the correlation between the models and the data. The fit is very good near the 2.7 μm CO_2 band but it deviates significantly at shorter wavelengths. The trend in Figure 2 indicates that the spectrum may need to be fit with 2 or 3 independent wavelength calibration segments. This may indicate that the CVF experienced a skip of some kind while rotating or that there were occasional speed changes in the rotation rate.

This preliminary examination indicates that substantial refinements in the wavelength calibration of the data can be achieved by using model atmosphere wavelengths as tie points in a fitting routine. This is an essential step for the interpretation of weak absorption features seen in the data which have center positions that are very sensitive indicators of composition. Unfortunately, as pointed out in [8], for accurate compositional interpretations it is necessary to perform an independent wavelength calibration for each spectrum. We are currently devising an automated scheme to accomplish this for all of the Mariner 6,7 IRS data in channel 2.

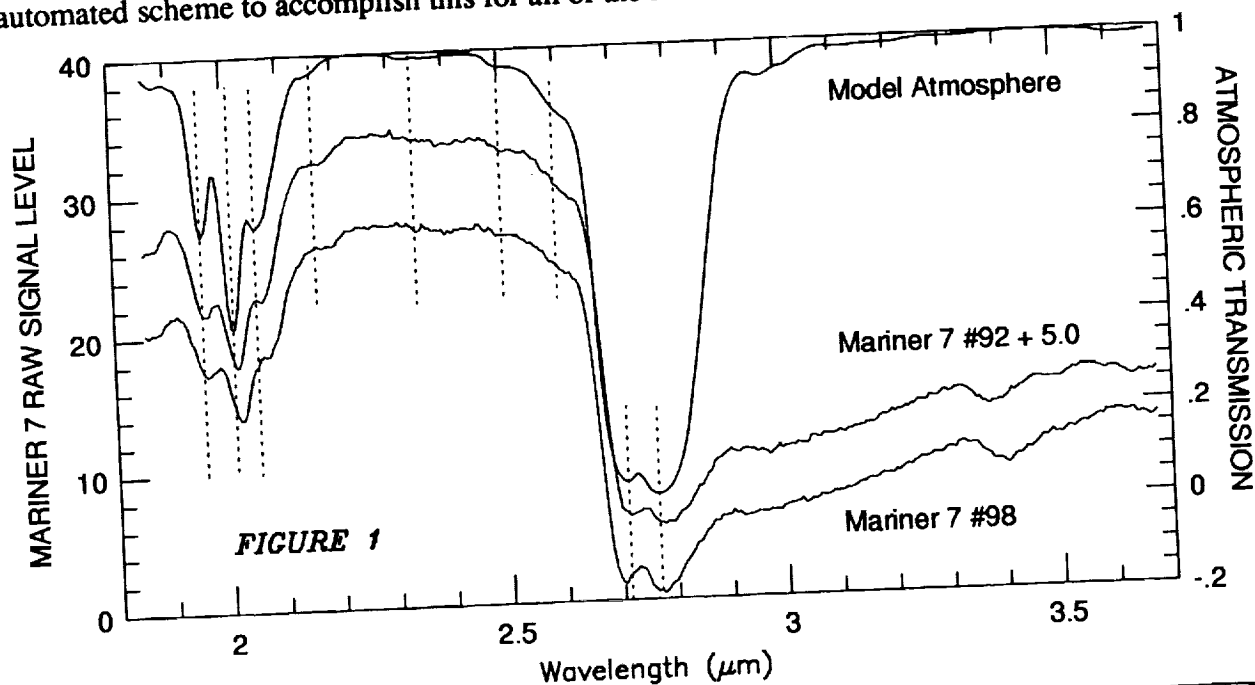
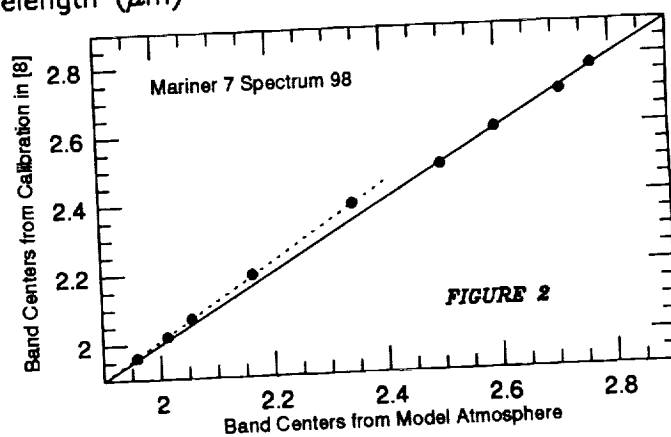


Figure 1 (top) shows Mariner 7 spectra 92 and 98 (with the wavelength calibration provided by Martin [8]) compared to a model atmosphere spectrum calculated at the same viewing geometry. Dashed lines indicate model band centers. Figure 2 (right) shows the correlation between band center wavelengths for spectrum 98 in Fig. 1 to those derived from the radiative transfer model. The solid line represents 100% correlation; the dashed line demonstrates a typical level of difference (or error) between the wavelengths derived by the two methods.



- References: [1] Herr, K.C. and G.C. Pimentel (1969), Chapter 6 in NASA SP-225. [2] Herr, K.C. et al. (1972) *Appl. Optics*, 11, 493. [3] Pimentel, G.C. et al. (1974) *JGR*, 79, 1623. [4] Horn, D. et al. (1972) *Icarus*, 16, 543. [5] Herr, K.C. et al. (1970) *Astron. J.*, 75, 883. [6] Herr, K.C. and G.C. Pimentel (1969) *Science*, 166, 496. [7] Herr, K.C. and G.C. Pimentel (1970) *Science*, 170, 47. [8] Martin, T.Z. (1994) *JGR*, in press. [9] Martin, T.Z. (1985) *B.A.A.S.*, 17, 723. [10] Martin, T.Z. (1985) *LPSC XVI*, 523. [11] Roush, T.L. et al. (1986) *LPSC XVII*, 732. [12] Calvin, W.M. et al. (1994) *JGR*, in press. [13] Calvin, W.M. and T.Z. Martin (1994) submitted to *JGR*. [14] Roush, T.L. et al. (1992) *LPSC XXIII*, 1179. [15] Gaffey, S.J. et al. (1993) in *Remote Geochemical Analysis* (C. Pieters and P. Englert, Eds.), pp. 43-77. [16] McCord, T.B. et al. (1982) *JGR*, 87, 3021. [17] Clark, R.N. et al. (1990) *JGR*, 95, 14463. [18] Bell, J.F. III and D. Crisp (1993) *Icarus*, 104, 2. [19] Murchie, S. et al. (1993) *Icarus*, in press. [20] Bell, J.F. III et al. (1994) submitted to *Icarus*.

ORDINARY CHONDRITES IN SPACE AND TIME

Jeffrey F. Bell (Planetary Geosciences Division, Dept. of Geology and Geophysics, Univ. of Hawaii, Honolulu HI 96822)

The origin of the H, L, and LL chondrites has remained one of the most enduring controversies in planetary science over the last 30 years. Recently, attention has focused on the spectroscopic discovery of a possible OC parent body in the main asteroid belt. A variety of more obscure recent discoveries clarify this question and point the way toward a sensible unified theory of the origin of these objects and the reasons they dominate the meteorite fall statistics.

OCs in the main belt: For some years the only good spectral analogs for OCs among the observed (i.e. bright) asteroids were a few objects assigned to spectral class Q. Curiously, all the good examples of this class were on Earth-crossing orbits, leading to suggestions that these objects did not originate in the main belt but rather from the Oort Cloud or undiscovered asteroids in the Earth-Sun or Venus-Sun Trojan points. However, with the extension of spectral surveys to smaller objects, a main-belt asteroid with a Q-class spectrum has been discovered [1]. This object (3628 Boznemcova) is near the 3:1 Jupiter resonance (long suspected to be a principal source of meteorites) and is about 7 km in diameter. The existence of surviving main-belt OC source bodies in this location and size range was predicted by the author's model of asteroid evolution [2]. In this model, large asteroids in the inner belt have all been melted, and only small objects can survive as unaltered chondrites. Alternatively, Binzel has suggested that Boznemcova was recently created from a larger OC asteroid and lacks the "weathered" regolith that camouflages OCs as S-class asteroids. This idea conflicts with a large body of data showing that weathering effects in chondritic regoliths are small. For instance, the IR spectral maps of 243 Ida returned by Galileo are uniform to within a few percent, ruling out any fresh OC-like region larger than about 100m [3]. Frequent low-velocity impacts on Ida should be excavating fresh bedrock from below the weathered regolith; yet there are no fresh halos or rays surrounding the youngest craters such as are seen on the Moon.

Some hints from CCs: Recent lab spectral studies [4] suggest that some rare highly metamorphosed carbonaceous chondrites are close spectral analogs to the F-B-C-G asteroid classes, suggesting that the more common CM/CI meteorites come from a yet undiscovered outer-belt spectral class composed entirely of small asteroids. This discovery brings the outer belt into line with the inner belt: in both regions the most common meteorites come from small (=weak, =primitive) asteroids, and only a few rare meteorites come from large (=strong, =metamorphosed) objects.

OCs in near-Earth space: Initial Spacewatch Camera results as analysed by D. L. Rabinowitz show a population of ≈ 10 -meter objects near the Earth about 100 times that predicted by extrapolation of the abundance curve for larger Earth-crossers [5]. The abundance vs. size curve for these objects is unusually steep, apparently joining the flatter distribution of larger Earth-crossers at a diameter of about 100m. This population also seems to be more concentrated toward the Earth's orbit than larger Earth-crossers. Theorists have attempted to explain this population as ejecta from Mars [6] or the Moon [7]. Both these interpretations conflict with the very small abundance of Mars and Moon samples in the meteorite collection. The "Rabinowitz Objects" must either be ordinary chondrites or some rarer class of meteorite which is filtered out by the Earth's atmosphere. It appears most likely that they are predominantly OCs, in which case future spectral observations will reveal a large predominance of Q-class objects in this size range.

OCs in lunar history: The abundance curve for near-Earth objects as extended by Spacewatch exhibits the "kink" near 100m diameter previously seen in lunar and martian crater distributions and attributed by some workers to an increasing proportion of unrecognized secondary craters at smaller sizes, e.g. [8]. The similarity of the Spacewatch and lunar crater abundance curves strongly suggests that secondary cratering is a minor contributor, as other lunar geologists

have long argued, e.g. [9]. It is more likely that this change in slope represents the transition between metal-dominated projectiles (=S asteroids = iron meteorites) and silicate-dominated projectiles (=Q asteroids = ordinary chondrites). This idea was proposed in early interpretations of Ranger photographs [10] but has been dormant until recently [11].

The OC bombardment of Gaspra and Ida: The crater abundance curve on Gaspra shows a differential power law with index -4.3, appreciably steeper than the theoretically derived value of -3.5 which was expected in the absence of secondary cratering [12] but similar to the actual slope found in Spacewatch data and lunar craters over this size range. At larger sizes there may be a transition to a flatter slope as on the planets, but this is doubtful due to the difficulty of distinguishing very large craters on such a small object [13]. Ida is much more heavily cratered and its crater abundance curve is similar to those of Phobos and Deimos [14], suggesting that saturation has obscured the original production function.

Towards a new paradigm: From the recent results discussed above, it appears that the abundance vs. size distribution of objects in the size range 10m to ~100m everywhere in the inner solar system follows a common and unexpectedly steep slope. If this slope is the true size spectrum of OCs, the dominance of OCs in the terrestrial meteorite collections is simply an artifact of the narrow size range sampled. The difference in slope between this size range and the flatter "classical asteroid" abundance curve (dominated by S-types) suggests that collisional evolution is strongly controlled by strength variations in the projectile/target population, in the sense that more fragile materials take up steeper size distributions richer in smaller objects. A traditional "unexamined paradigm" in meteorite and asteroid science has been that the size distributions of all types of material are roughly parallel. The picture now emerging seems to require 1) steeper abundance curves for more fragile materials; 2) a power-law with index -4.3 for ordinary chondrites (Q asteroids) in the ≤ 100 m size range; 3) a transition to shallower populations dominated by highly metamorphosed chondrites (C) and metal-rich igneous materials (S,M) at ≈ 100 m. Asteroid spectroscopists and meteoriticists should ponder deeply the implications of a model in which the asteroid and meteorite populations are necessarily anticorrelated.

REFERENCES: [1] Binzel et al (1993), *Science* 262, 1541. [2] Bell (1986), *Meteoritics* 21, 333; Bell et al. (1989), *ASTEROIDS II*, 942. [3] Carlson et al. (1993), *BAAS* 25, 1137. [4] Hiroi et al. (1993) *LPSC XXIV*, 659. [5] Rabinowitz, *Astrophys. J.* 407, 412. [6] Vickery and Melosh (1993) *Meteoritics* 28, 453. [7] Gladman and Burns (1993) *BAAS* 25, 1117. [8] Shoemaker (1965), *JPL TR #32-700*, Pt. II, 75. [9] Neukum and Wise (1976) *Science* 194, 1382. [10] Kuiper, Strom, and Le Poole (1966), *JPL TR #32-800*, Pt II, 169. [11] Bell (1991), *BAAS* 23, 1140; Bell (1993), *BAAS* 25, 1127. [12] Neukum et al (1992), *BAAS* 24, 932; Chapman et al. (1993) *LPSC XXIV*, 269. [13] Greenberg et al (1993) *BAAS* 25, 1138. [14] Belton et al. (1993) *BAAS* 25, 1136.

GEOLOGIC MAP OF CALLISTO; K. C. Bender and R. Greeley, Department of Geology, Arizona State University, Tempe, Arizona 85287-1404, J. W. Rice, Jr., Department of Geography, Arizona State University, Tempe, Arizona 85287, D. E. Wilhelms, Hyde St., San Francisco, CA 94109

A 1:15M scale photogeologic map of Callisto, the second largest and outermost Galilean satellite of Jupiter, has been completed (Figure 1). Callisto's density of 1.86 g/cm^3 suggests a high proportion of water-ice to silicates. The satellite's geology is surprisingly simple for a body 4840 km in diameter. Most of it is mapped as an apparently uniform geologic unit (ctu) on which only 128 craters >60 km across and seven multi-ring features are superposed. This paucity of large craters is very unlike the crater size-frequency distribution on the terrestrial planets, and may reflect impacts by comets and not asteroids [1].

Each of the two largest multi-ring features, the younger [2] ~1100 km Valhalla and the ~700 km Asgard, possess an inner palimpsest (units vi, ai), which probably represents the relaxed transient impact crater, and an outer concentric deposit (units vo, ao), which probably consists of ejecta. These Valhalla and Asgard Formations are less densely cratered than the cratered terrain (unit ctu) [3]. Structural symbols trace ring arcs surrounding these deposits and five smaller rings features that lack mappable deposits. Isolated light plains interpreted as palimpsests (unit lp) probably mark additional impact sites. Some crater chains (catenae) may have been created by the impact of disrupted comets like Shoemaker-Levy 9 [4], and others by the secondary impact of ejecta from a visible or nearly vanished (palimpsest) impact site.

The only unit considered endogenic forms small, elongate, smooth patches (unit sp), light toned at the bases of some scarps NE of Valhalla and dark toned within the cratered terrain (unit ctu). Water or slurry probably rose in response to disruption of the crust by the Valhalla impact [3,5,6,7].

The map probably portrays a generally ancient surface. Impacts are thought to have created Valhalla and Asgard about 4 b.y. ago [2], and the same is probably true of the isolated palimpsests (unit lp) and most of the craters (units c1 and c2). Only rayed craters (unit c3) and possibly the smooth plains are likely to have formed during the last 3 billion years.

This map has been used to aid in planning the Galileo imaging targets for Callisto. Within the constraints of the selected tour and the sharing of resources among various instruments, the following targets are candidates for imaging by the Galileo SSI: a) Valhalla, at high resolution (~50 m/pxl); b) Asgard, at moderate (1 km/pxl) and high (~100 m/pxl) resolutions; c) Adlinda and the ring feature NW of it at moderate (1 km/pxl) resolution; d) a scarp NE of Valhalla with smooth plains material at high (~100 m/pxl) resolution; e) a number of sites within the cratered terrain at high resolution; f) filling Voyager gaps (at Voyager or better resolutions) at 300°W longitude, SW of Valhalla, and portions of the South Pole.

References: [1] Chapman, C.R. and McKinnon W.B.(1986) in *Satellites*, Burns, J.A. and Matthews, M.S. eds, Univ. Ariz. Press, 548. [2] Passey, Q.R.(1982) Ph.D. Diss., Caltech, 89. [3] Remsberg, A.R.(1981) *LPSC Absts*, XII, 874. [4] Melosh, H.J. and P. Schenk (1993) *Nature*, 365 (in press), 735. [5] Melosh, H.J.(1982) *JGR*, 87, 1880. [6] Stooke, P.J.(1990) *LPSC Absts*, XX, 568. [7] Schenk, P.(1992) *EOS*, 73, 179.

DESCRIPTION OF MAP UNITS

Plains Materials

- (sp) Smooth plains- small mostly elongate patches. Light and dark albedo and lower crater frequency than surrounding terrain. *Interpretation:* Ice extruded from interior
- (lp) Light plains- elliptical or circular patches. Higher albedo and usually lower crater frequency than surrounding terrain. *Interpretation:* palimpsests originating by the viscous relaxation of a transient impact crater
- (ctu) Cratered terrain, undivided-most heavily cratered unit. Average albedo 0.2. *Interpretation:* ancient crustal materials, consisting of ice and rock/dust, brecciated by extensive impact cratering

GEOLOGIC MAP OF CALLISTO: Bender K.C. et al.

Valhalla Formation

- (vi) Inner facies- bright elliptical patch lacking structure. *Interpretation:* palimpsest like those of unit lp
 (vo) Outer facies- multiple discontinuous concentric ridges. Lower crater frequency than on surrounding terrain. *Interpretation:* impact ejecta blanket

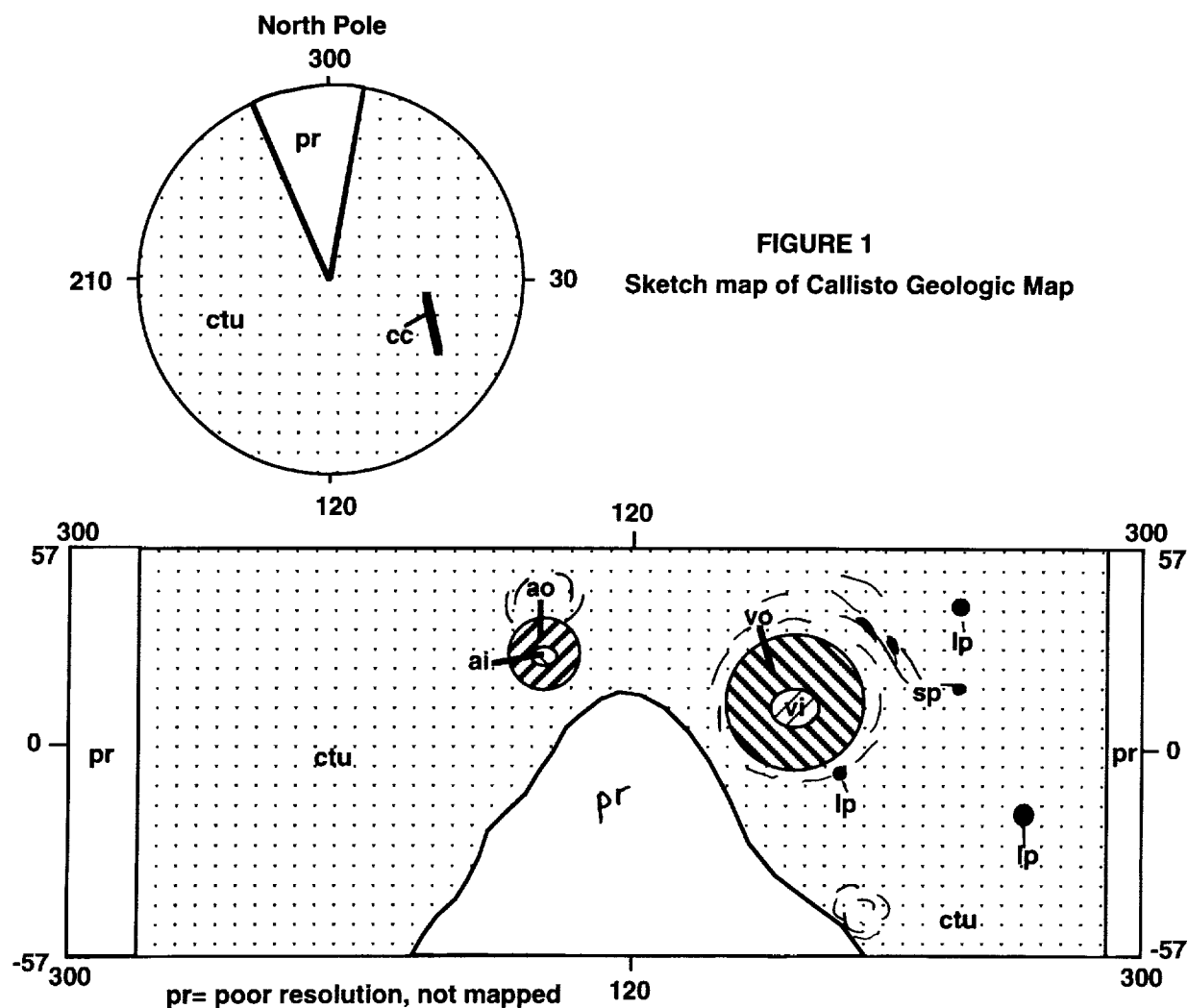
Asgard Formation

- (ai) Inner facies- bright elliptical patch. A few arcuate structures at margin. *Interpretation:* palimpsest like those of unit lp
 (ao) Outer facies- multiple discontinuous inward-facing concentric scarps. Lower crater frequency than on surrounding terrain. *Interpretation:* impact ejecta blanket

Crater Materials

Craters >60 km in diameter mapped. *Interpretation:* formed by impact, degree of degradation approximates relative age (c1 oldest to c3 youngest)

- (c3) Class three- includes crater floor, complete rim and all visible ejecta
 (c2) Class two- includes crater floor and complete rim
 (c1) Class one- includes crater floor and all visible rim
 (cc) Crater catena- includes floors and rims of craters aligned in linear chains



PRE-IMPACT ORBITAL EVOLUTION OF P/SHOEMAKER-LEVY 9; Lance A.M. Benner and William B. McKinnon, Department of Earth and Planetary Sciences and McDonnell Center for the Space Sciences, Washington University, Saint Louis, MO 63130-4899, lance@wunder.wustl.edu.

We investigate the orbital evolution of P/Shoemaker-Levy 9 as a temporarily captured satellite and focus on its heliocentric motion prior to capture by Jupiter, and on its joviocentric motion after capture but prior to impact. We numerically integrate the comet's motion backward and forward in time using the orbital elements determined by D.K. Yeomans and P.W. Chodas (solution 28) [1]. We include the gravitational effects of Jupiter, Saturn, and the Sun, and Jupiter's oblateness J_2 and J_4 . Assuming that no orbital energy changes occurred during the 1992 disruption, we find that the comet's joviocentric orbit prior to the July, 1992 perijove was not hyperbolic. Integration of the nominal solution 28 elements indicates that Shoemaker-Levy was captured by Jupiter in 1970 and has since completed nine irregular, eccentric, and steeply inclined orbits about the planet. The comet's nominal pre-capture heliocentric orbit originated interior to that of Jupiter and crossed the asteroid belt; however, varying the initial elements within the formal uncertainties indicates that a pre-capture orbit between Jupiter and Saturn is also possible. The range of pre-capture heliocentric eccentricities ($e \sim 0.1 - 0.3$) and inclinations ($i \sim 1^\circ - 4^\circ$) are consistent with a short-period comet or asteroid, but not with a highly inclined and eccentric long-period comet.

Figure 1 shows Shoemaker-Levy's heliocentric trajectory extending 21 Jovian years prior to the 1994 collision; for comparison, the radial distance in astronomical units from Jupiter and the Sun during this interval appears in Figure 2. Shoemaker-Levy orbits Jupiter backward in time for ~ 2 Jovian years, and "escapes" into an orbit interior to that of the planet. Prior to capture, the comet frequently approached within ~ 1.5 AU of Jupiter when it experienced the distinct changes in its heliocentric orbit that are visible in Fig. 1. Discrete changes in Shoemaker-Levy's heliocentric eccentricity and inclination also occurred during the closest approaches to Jupiter. The discrete changes in Shoemaker-Levy's heliocentric elements, as well as the sensitivity of the orbit to initial conditions noted above, are hallmarks of chaotic dynamics. Indeed, temporary gravitational capture orbits are, in general, chaotic [2]. Using the method of divergent trajectories in phase space [3], we find P/Shoemaker-Levy 9 to be fundamentally chaotic with a Lyapunov time of ~ 1.3 Jovian years.

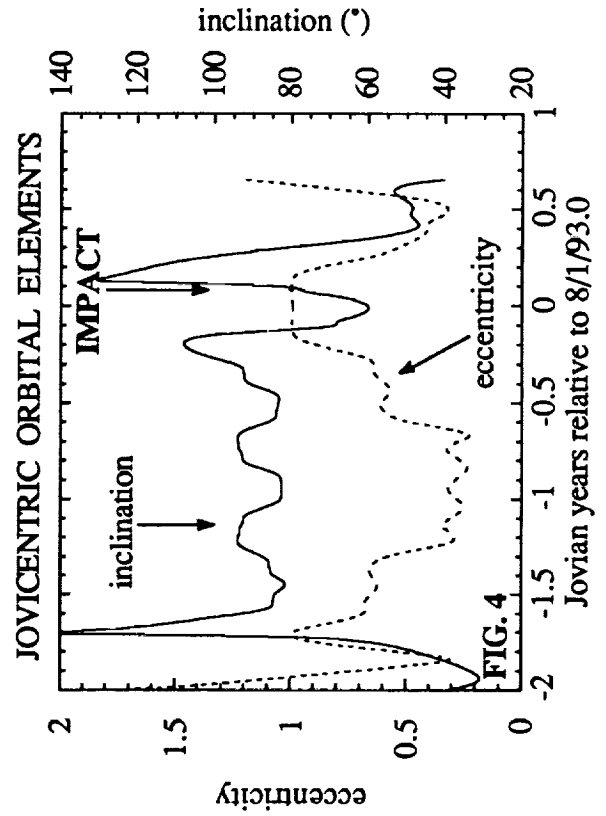
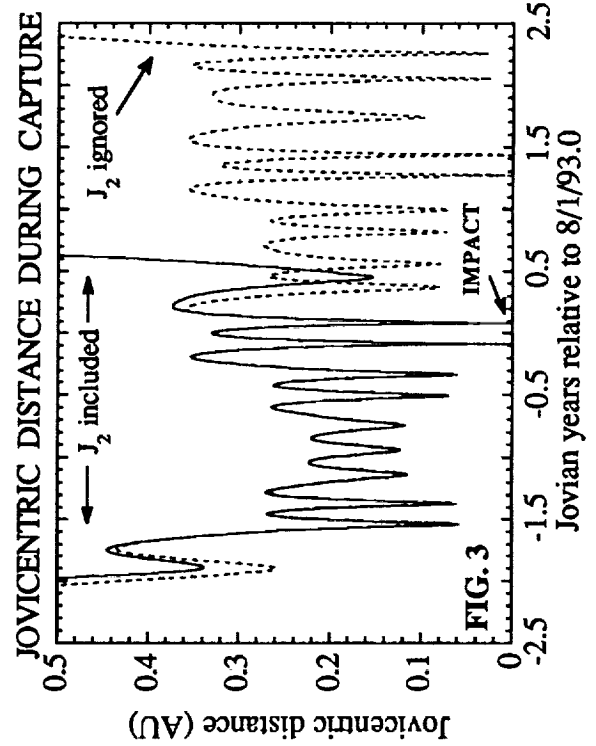
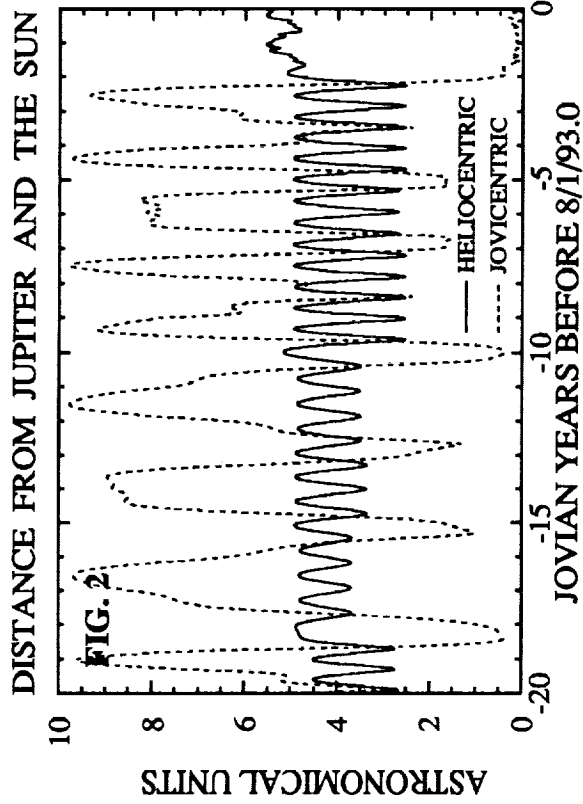
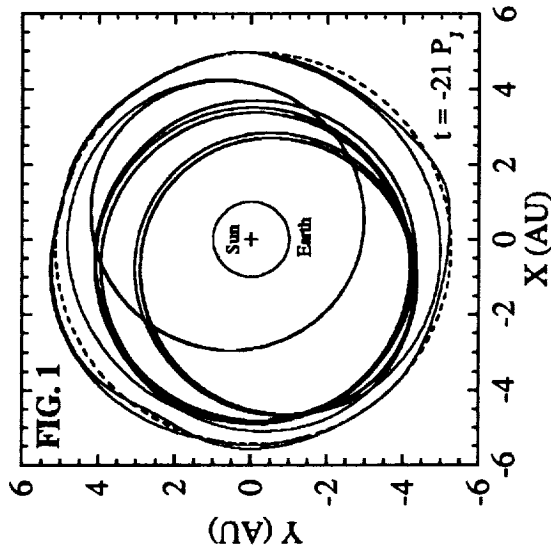
Figure 3 shows Shoemaker-Levy's joviocentric distance after capture, including that which would result if the 1994 collision with Jupiter is ignored. If the impact is ignored, the comet passes within $\sim 0.5 R_J$ of the planet's center and completes one additional, distant orbit prior to escaping to an orbit between that of Jupiter and Saturn. Consequently, any orbital energy dissipation that P/Shoemaker-Levy 9 experienced when it fragmented in 1992 was insufficient to bind it into permanent orbit about Jupiter. For comparison, the distance that would result ignoring Jupiter's oblateness is also included. The motion backward in time changes only slightly, but because of the comet's extremely close approach to Jupiter in 1994, the trajectories including and ignoring oblateness rapidly diverge forward in time.

Capture by Jupiter occurs when the comet's joviocentric eccentricity decreased below unity, indicating (temporarily) bound motion (Fig. 4). Shoemaker-Levy's subsequent joviocentric orbit is strongly perturbed by the Sun because of the comet's generally large distance from the planet. The orbit alternates between prograde and retrograde motion and is highly inclined, common characteristics of weakly bound and unbound satellites, and ones that we have observed in our simulations of Triton's capture by Neptune [3]. At the time of impact, the orbital inclination is $\sim 78^\circ$ and the eccentricity near unity.

REFERENCES: [1] Yeomans, D.K., and P.W. Chodas, posted on the Comet Shoemaker-Levy 9 bulletin board 11/4/93; [2] Murison, M.A.(1989), *Astron. J.* **98**, 2346-2359; [3] Wisdom, J. (1983), *Icarus* **56**, 51-74; [4] Benner, L.A.M., and W.B. McKinnon, submitted to *Icarus*.

EVOLUTION OF P/SHOEMAKER-LEVY 9: Benner L.A.M. and McKinnon W. B.

CAPTURE OF P/SHOEMAKER-LEVY 9



POST-SHOCK COOLING AND ANNEALING WITHIN L-GROUP ORDINARY CHONDRITES. Marvin E. Bennett and Harry Y. McSween Jr., Department of Geological Sciences, University of Tennessee, Knoxville, TN 37996-1410.

Two cation-exchange thermometers were applied to electron microprobe data from a petrologically diverse suite of L-group ordinary chondrites in an attempt to determine the effects of post-shock cooling and annealing on mineral re-equilibration. All analyses were taken from matrix minerals, which should be more sensitive to secondary thermal effects than those within chondrules. Fe - Mg exchange between olivine and spinel [1] was utilized to monitor cooling rates of high-temperature mineral phases. Ni exchange between metal and troilite [2] provided information on post-shock annealing within the low-temperature mineral portion. Both thermometers have been calibrated at temperatures and pressures appropriate for meteorite study.

Samples selected for this study reflect the diverse thermal and shock history recorded in L-group ordinary chondrites. Hallingeborg, Björbole, and Ausson are low-shock (below S4 shock stage, [3]) chondrites that lack evidence of post-shock melting. Kyushu and McKinney are high-shock chondrites (above S4 stage) that contain small melt pockets of metal, sulfides, and silicates. In addition, McKinney has a shock-blackened texture produced by rapid injection of metal and sulfide into surrounding fractures [3]. Y793421, Y75097, and EET87555 are L chondrite breccias that contain small, isolated melt inclusions. Shaw contains numerous small silicate melt dikes that have been injected into surrounding brecciated materials (the previously described 'gray lithology' [4]). PAT91501 has a cumulus texture and a mineralogy reflecting a possible history of partial to complete melting [5].

Fig. 1 is a summary of the temperatures obtained by both geothermometers. The lengths of the bars indicate the ranges of temperature recorded for six to ten mineral pairs from each sample. Both analytical and calibration errors for the two thermometers are approximately 50°C.

Low-shock samples yield olivine-spinel temperatures appropriate for slowly cooled, unequilibrated L chondrites (650-700°C). The range of metal-sulfide temperatures correlate with the rate of post-shock annealing and not with petrologic type. Hallingeborg (L3, S3) shows the greatest variation in metal-sulfide temperatures while Björbole (L-LL4, S1) displays the smallest variation in temperature range. Faster cooling from an initially higher degree of post-shock reheating (for Hallingeborg), with slower cooling from an initially lower degree of reheating (for Björbole), could explain this apparent trend. Ausson (L5, S2) has a temperature range that is intermediate between the above samples. The two Yamato breccias also plot in the same region as the unequilibrated chondrites. Since these breccias contain melted L chondrite inclusions the low temperatures recorded by both thermometers could indicate very slow rates of cooling from samples that originated beneath a thick, thermally insulating blanket of regolith.

High-shock samples record olivine-spinel temperatures within the range of equilibrated L chondrites (~750°C, from [6]). Kyushu displays a wider range of metal-sulfide temperatures than seen in the unequilibrated chondrites owing to the proximity of large shock-induced melt pockets to several analyzed mineral pairs. McKinney displays a much narrower range in sulfide-metal temperatures due to the rapid heating (with subsequent rapid cooling) of metal and sulfide prior to portions being injected into pre-existing fractures. The breccia EET87555 has a mean for both thermometers that falls within the same temperature range as the high-shock samples. The extreme range of temperatures seen in this sample, however, suggests that the fragments that comprise this breccia formed from thermally diverse sources and that, once accreted, the sample was not buried to any great depth within the parent body.

PAT91501 is a sample chondrite melt. The high temperatures recorded by the olivine-spinel thermometer are consistent with other evidence suggesting an origin in a melt sheet within an impact crater on the parent body [6]. Metal-sulfide temperatures are similar to those in unequilibrated L chondrites. Such temperatures could have been produced if this melt sheet were covered by regolith material, resulting in slower cooling of these phases. Slow cooling is also consistent with the coarse grained, cumulate texture of this sample.

Olivine-spinel temperatures recorded in the gray lithology of Shaw are intermediate between the unmelted equilibrated samples and the PAT melt inclusion. Either the dike material was not wholly

POST-SHOCK COOLING AND ANNEALING

Bennett, M.E. and McSween, H.Y., Jr

melted before it was shock-injected into the surrounding breccia or the breccia acted as an insulator to allow these minerals to equilibrate to lower temperatures. Metals and sulfides are absent from this portion of Shaw. The temperatures that this mineral pair preserves are directly correlated to distance from this lithology. Pairs adjacent to the melt dike record higher temperatures (near 750°C). Those within a centimeter of the dike record lower temperatures (~550°C).

References: [1] Sack R.O. and Ghiorso M.S. (1991) *Am. Mineral.* **76**, 827-847. [2] Bezmen N.I. et al. (1978) *Geochem. Intern.* **15**, 120-127. [3] Stöffler D. et al. (1991) *Geochim. Cosmochim. Acta* **55**, 3845-3867. [4] Taylor G.J. et al. (1979) *Geochim. Cosmochim. Acta* **43**, 323-337. [5] Harvey R.P. (1993) Submitted to *Meteoritics*. [6] McSween H.Y., Jr. et al. (1988) in *Meteorites and the Early Solar System*, 102-113.

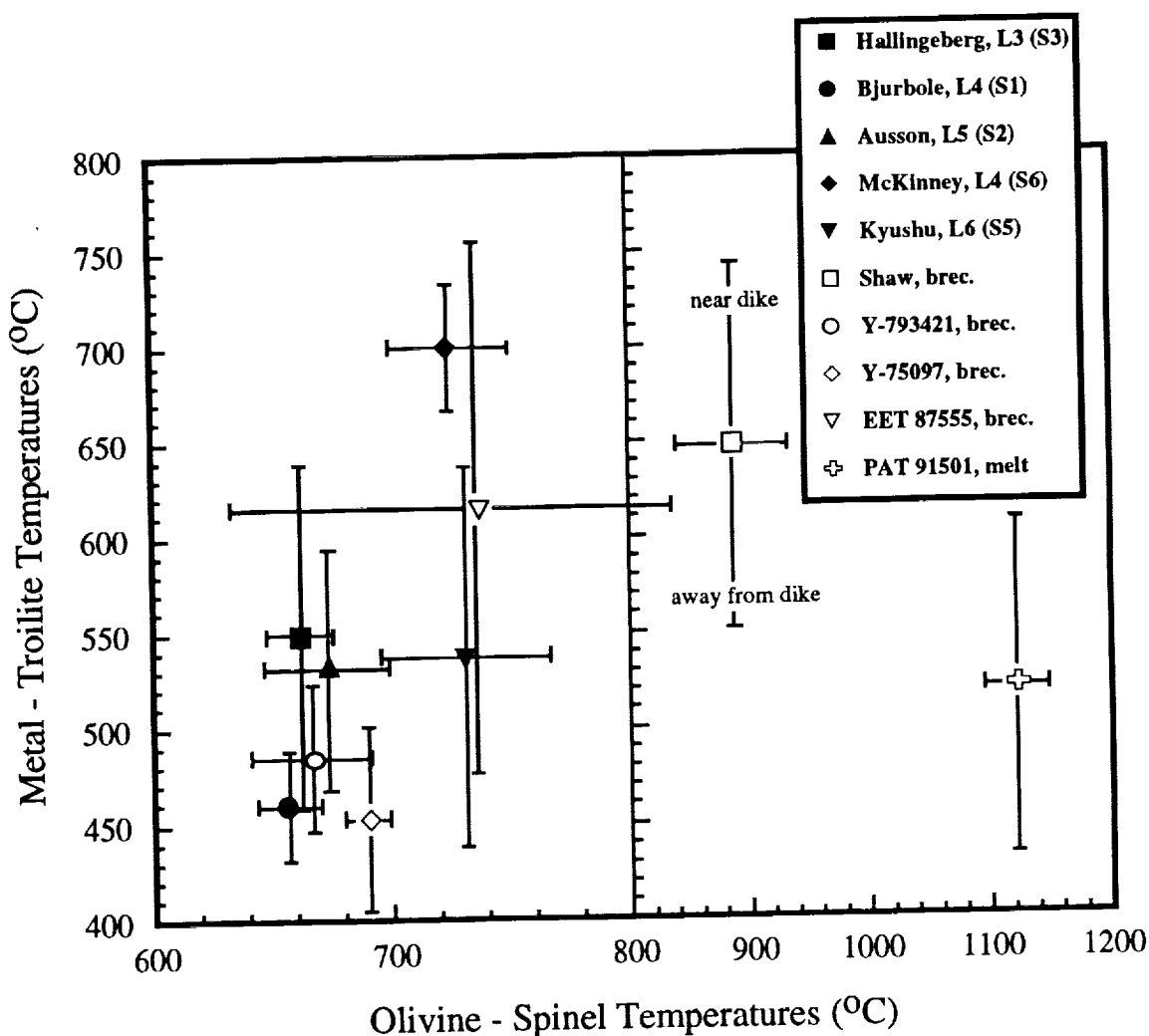


Figure 1. Means and temperature ranges for two thermometers plotted for unmelted chondrites (solid symbols) and breccias and melt inclusions (open symbols). Errors for each thermometer would extend each bar 40 to 50°C.

PRIMITIVE MATERIAL IN LUNAR HIGHLAND SOILS. P.H. Benoit¹, J.D. Batchelor^{1,2}, S.J. Symes¹, and D.W.G. Sears¹. ¹Cosmochemistry Group, Department of Chemistry and Biochemistry, University of Arkansas, Fayetteville, AR 72701, USA. ²Analytical Services, Reynold's Electric and Engineering, P.O. Box 98521, Las Vegas, NV 89193.

The surface of the Moon, the source of all current lunar samples, has been heavily processed since its formation. The lunar highlands are particularly interesting in this regard; they represent the first material to crystallize on the Moon and they are the most heavily modified by subsequent impact processing. In fact, virtually all lunar highland samples are heavily brecciated. In this paper we present induced thermoluminescence data for Apollo 16 and 17 soil samples and 16 lunar rocks (including three lunar meteorites); we find that there is feldspar in the lunar soils which has been less thermally processed than most highland rock samples. On the basis of these data we suggest that simple comminution to produce soil is thermally a less extreme process than brecciation and hence the least thermally altered highland material in the lunar collection may be found in the lunar soil.

Introduction. The search for "primitive" lunar highlands material in the lunar sample collection has been a difficult and only partially successful one. A number of monomict breccias have been recognized which can be considered as chemically "pristine" [1]. However, these breccias have been subjected to a fair degree of thermal processing associated with the brecciation event(s). Even rarer are the true igneous highland rocks, which show no signs of brecciation. The collection of lunar highland samples is thus heavily dominated by brecciated, if not partially or wholly impact-melted, material.

Induced thermoluminescence (TL) measurements are useful in the study of the thermal history of brecciation and regolith processing; we have previously conducted studies of ordinary chondrite regolith breccias [2] and present results for lunar cores at the current meeting [3]. There are two separate types of data obtained from the TL glow curves. The maximum intensity of the TL signal (TL sensitivity) reflects the abundance of phosphors in the sample. In the case of most lunar, achondrite, and ordinary chondrite samples feldspar is the dominant phosphor. The peak temperature in the glow curve reflects the average degree of order in the feldspar. Ordered high-Ca feldspar has a TL peak temperature of 90°C, while the disordered form has a peak temperature of 240°C [4].

The induced TL data were collected using the same technique and apparatus that we have used to study achondrites [4]. Sample processing was limited to gentle grinding. Thermoluminescence sensitivity values are reported relative to Dhajala (H3.8) which was used as a laboratory standard throughout these and previous measurements. Our samples include various depth intervals in the lunar cores 60009/10, 60013/14, and 70001-70009, the impact melt rocks 14310, 60315 and 68415, and the lunar highland meteorites ALHA 81005, Y82192 and MAC 88104/5 in addition to various mare basalt samples.

Results. Our results are summarized in Fig. 1. Although a number of rock samples show inflections at low glow curve temperatures which may be caused by polymorphs of quartz (e.g., 60315, 12021), no other glow curve peaks aside from those associated with feldspar were observed. As noted by Symes *et al.* [5] the highland rock samples have higher TL sensitivities than the mare basalt samples but have TL peak temperatures which are similar to the mare basalts. While the TL sensitivities of the two Apollo 16 cores are very similar to those of the highland rock samples, their TL peak temperatures are significantly lower. The Apollo 17 core samples show low sensitivity levels similar to mare basalts, but also have significantly lower TL peak temperatures than either the mare basalts or the highland rock samples.

Discussion. As described by Symes *et al.* [5], the hiatus between the highland and mare basalt samples in TL sensitivity reflects differences in feldspar abundance between these two broad classes of lunar samples, with the highland rock samples having much higher feldspar abundances compared to mare basalts [1]. The high peak temperatures of the highland rock samples are, however, related to thermal history. It is apparent that the feldspar of highland cumulate rocks crystallized from a magma and cooled slowly, allowing the growth of large crystals. Under such conditions feldspar should be highly ordered, as is the case for terrestrial analogues. The high degree of feldspar disorder, as shown by their high TL peak temperatures, in the three impact melts (14310, 60315, and 68415) is not unexpected; virtually all the feldspar in these rocks crystallized during very rapid cooling. The variation in the peak temperatures of these samples may reflect mixing of disordered feldspar crystallized from the melt with more ordered surviving clasts. Alternatively, the variation may reflect differing degrees of feldspar order as a result of different cooling rates, with 68415 having a lower cooling rate than 60315 and 14310; the differences in texture between 68415 and 14310 (an impact melt breccia) is evidence for this possibility [1]. The explanation for the difference between 60315 and 68415 is less certain, but 60315 contains more mesostasis than 68415 and hence may have cooled more rapidly.

All three of the lunar highland meteorites in the present study are regolith breccias. Of the three, Y82192 and ALHA 81005 have very similar TL parameters while MAC 88104/5 has lower TL sensitivity and a higher peak temperature. It is likely that these observations reflect the different cooling histories of these meteorites. While MAC 88104/5 has relatively pristine interstitial maskelynite glass, the equivalent glass in Y82192 and ALHA 81005 is completely devitrified to submicrometer-sized crystals of plagioclase [6]. The

PRIMITIVE MATERIAL IN LUNAR HIGHLAND SOILS: Benoit et al.

higher TL sensitivity and lower peak temperatures of Y82192 and ALHA 81005 compared to MAC 88104/5 reflects the abundance of devitrified glass. In any case, although these meteorites have lower TL peak temperatures than two of the impact melts, it is clear that they still contain high abundances of disordered feldspar and hence have been heavily thermally processed compared to the supposed ordered parent rocks.

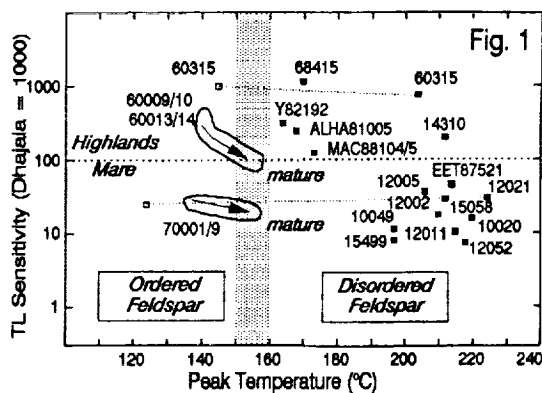
The lunar cores have the lowest TL peak temperatures of any of the lunar materials yet measured. In addition, however, as described by Symes *et al.* [3] we observe a trend of increasing TL peak temperature and decreasing sensitivity as a function of soil maturity. Thus, the lunar samples in our present database with the lowest TL peak temperatures are core samples from immature intervals in the stratigraphy. In the case of the 60009/10 core (Fig. 2), the TL parameters generally correlate with the abundance of the ferroan anorthosite component, calculated from bulk chemical analyses [7]. However, as is apparent from the grouping on the basis of maturity in Fig. 2, this trend is largely produced by a fortuitous correlation between ferroan anorthosite content and regolith maturity in this core.

There are two non-exclusive explanations for the low TL peak temperatures of feldspar from immature portions of the lunar cores. One possibility is that feldspar in these portions of the core have somehow been annealed at fairly high temperatures and slowly cooled, thus converting disordered feldspar to ordered feldspar. Since the only significant heat source is impact processing, however, this does not explain why it is the immature rather than the mature portions of the cores which have the highest degree of feldspar order. Another possibility is essentially a mixing model. In this case, primary ordered feldspar, produced by slow cooling after crystallization from a magma, is the source of much of the feldspar in the cores. Not surprisingly, much of this feldspar is associated with the ferroan anorthosite component (Fig. 2). During regolith processing a portion of the primary ordered feldspar is converted to disordered feldspar (in addition to some converted to non-luminescent glass). Thus, with increasing degrees of regolith processing, the average degree of feldspar disorder increases, which is reflected in the larger TL peak temperatures of mature portions of the cores.

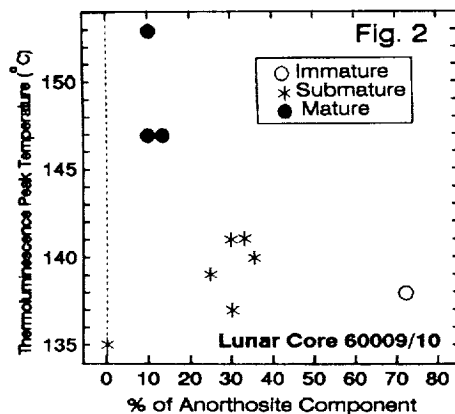
In conclusion, our data indicate that the average degree of order in feldspar is greater in lunar cores (soils) than in any highland rocks examined to date and that the average degree of order is greatest in the most immature portions of the cores. We suggest that these data are best explained by relatively small amounts of thermal processing in the soil samples compared to the lunar breccias (rocks). Thus, from the standpoint of thermal reprocessing, portions of the lunar soil are more pristine than any of the highland rocks that we have yet measured.

Acknowledgements. We wish to thank the curators of the lunar processing laboratory for their assistance in sampling and D.A. McKay for discussions. This study supported by NASA grant NAGW - 3519.

Fig. 1 (top). Induced TL sensitivity vs. TL peak temperature for lunar core and rock samples. The soil samples from cores 60009/10, 60013/14, and 70001-70009 have significantly lower TL peak temperatures than lunar rock samples. This indicates the presence of a greater amount of ordered feldspar in the soil samples compared to the rock samples. **Fig. 2 (bottom).** In the 60009/10 core there is a correlation between induced TL parameters (exemplified by TL peak temperature) and anorthosite component (taken from [7]). However, this alone cannot explain the trends observed in Fig. 1 and the apparent correlation is probably the result of a correlation between anorthosite component and maturity in this core.



[1] Taylor G.J., Warren P., Ryder G., Delano J., Pieters C., and Lofgren G. (1991) in *The Lunar Sourcebook*, G.H. Heiken, D.T. Vaniman, and B.M. French, eds., Cambridge University Press, 183-284. [2] Haq M., Hasan F.A., Sears D.W.G., Moore C.B., and Lewis C.F. (1989) *Geochim. Cosmochim. Acta* **53**, 1435-1440. [3] Symes S., Benoit P.H., and Sears D.W.G. (1994) this meeting. [4] Batchelor J.D. and Sears D.W.G. (1991) *Geochim. Cosmochim. Acta* **55**, 3831-3844. [5] Symes S., Benoit P.H., Batchelor J.D., and Sears D.W.G. (1992) *Meteoritics* **27**, 294. [6] Takeda H., Mori H., Saito J., and Miyamoto M. (1991) *Geochim. Cosmochim. Acta* **55**, 3009-3017. [7] Korotev R.L. (1991) *Proc. Lunar Planet. Sci.* **21st**, 229-289.



NATURAL THERMOLUMINESCENCE PROFILES IN METEORITES: COSMOGENIC AND TERRESTRIAL PROFILES IN FALLS AND FINDS. P.H. Benoit¹, Y. Chen^{1,2}, and D.W.G. Sears¹.
¹Cosmochemistry Group, Department of Chemistry and Biochemistry, University of Arkansas, Fayetteville, AR 72701, USA. ²Institute of Geological New Technology, Chinese Academy of Sciences, Wushan, Guangzhou 510640, PRC.

The recent history of meteoroid bodies in space has been explored through their long-term radiation exposure as determined by cosmic-ray tracks or abundances of cosmogenic nuclides. Natural thermoluminescence (TL) levels of meteorites and lunar samples also reflect radiation exposure, although unlike cosmogenic noble gases natural TL cannot be used to determine exposure times for most meteorites due to the relatively rapid attainment of equilibrium. Unlike cosmogenic nuclides, however, TL is sensitive to recent thermal history; hence, natural TL levels are generally controlled by solar heating which, in turn, is determined by orbital history. In this paper we present new data on natural TL profiles of a number of meteorite falls and finds. We find that, as expected from our previous lunar core data, cosmogenic natural TL profiles in meteorite falls are generally very shallow. Much larger profiles, however, can be produced in meteorite finds, especially those with large terrestrial ages, as a result of terrestrial thermal profiles. These data indicate that (a) cosmogenic TL profiles are generally not significant compared to thermal effects in typical meteoroid bodies and (b) the terrestrial history of larger meteorite finds can be studied through terrestrial TL profiles.

Introduction. We have previously reported natural TL results for lunar cores [1] and discussed the implications of these data for meteoroid bodies irradiated in space [2]. In the present paper we discuss some recently acquired data on several modern falls which generally support the previous work. In addition, however, we extend the theory of TL decay to discuss the effect of temperature gradients in large meteorite finds.

Cosmogenic TL Profiles. The natural TL profiles observed for lunar cores (up to 300 cm below the surface) are fairly flat, compared to the more steep profile calculated from only the primary and secondary proton flux [3]. The discrepancy probably reflects the fact that TL is produced by a variety of energetic events, including cosmogenic nuclear reactions, i.e., as a result of interaction of secondary neutrons with the target material. If we use the lunar core profile instead of the calculated proton-induced profile and correct for 4π irradiation (e.g., thick target accelerator experiments [4]) we find that the expected TL profile in typical meteoroid sized bodies is also very modest. In fact, for a fairly large meteoroid-sized body (100 cm radius) of H chondrite composition our calculations indicate a total variation in TL levels of no more than 25% from surface to center.

Previous work on Lost City and Ucera (approximately 50 cm and 6 cm terrestrial radii, respectively) shows a total variation in natural TL levels of about 22% and essentially 0%, respectively [5]. Compared to our calculated profiles, these data indicate that Ucera was no larger than 20 cm prior to atmospheric entry whereas Lost City was at least 100 cm in radius during irradiation in space. The larger size for Lost City is also supported by the asymmetrical shape of the TL profile, which decreases linearly from one side of the meteorite to the opposite side. These data are independent of atmospheric entry heating; we observe steep decreases in TL levels only within 0.3 cm of fusion crust and these decreases are quite distinct from the more gentle slopes observed in interior profiles.

We have also recently acquired data for samples from St. Severin and Jilin. We find that the TL profile for St. Severin is essentially flat and this TL profile suggests that St. Severin was no larger than about 20 to 25 cm during irradiation. In comparison, cosmogenic nuclide profiles [6] suggest a radius of about 30 cm for St. Severin.

Six samples of Jilin show a very large variation in natural TL (45% total variation). A large degree of variation in natural TL is expected from the large size of the terrestrial body but its magnitude is greater than that predicted in our current calculated profiles using the radius of about 85 cm derived from cosmogenic nuclide abundances [7]. We find, however, that the variation is accentuated by a single sample with a very high TL level; this sample is from the surface of the meteorite. The remainder of the samples, from various depths in the meteorite, show a total variation of only 25% with TL decreasing with depth as expected from the calculated profiles. This degree of variation is about that expected for a meteoroid body with a radius of about 100 cm during irradiation. The source of the very high TL in the surface sample is unknown, but could be related to solar flare irradiation effects.

Terrestrial Profiles. As has been noted elsewhere [e.g., 1,2,8], aside from the fairly shallow cosmogenic profiles natural TL levels are largely governed by temperature, either temperature in space (in the case of modern falls) or on Earth (in the case of older finds). Due to the relatively rapid attainment of thermal equilibrium from solar heating compared to the typical orbital times of meteoroid bodies it is not expected that pre-terrestrial thermal profiles would be observed in most modern falls. In larger terrestrial finds, however, it is possible that temperature gradients are established, i.e., that one face of the meteorite may be consistently warmer due to solar heating than other faces which are protected by soil, ice, etc. If such

THERMOLUMINESCENCE PROFILES IN METEORITES: Benoit P.H. et al.

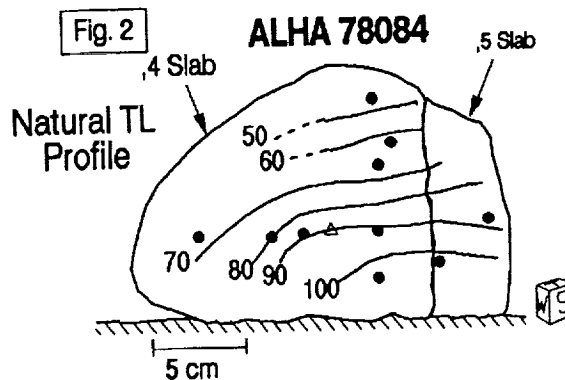
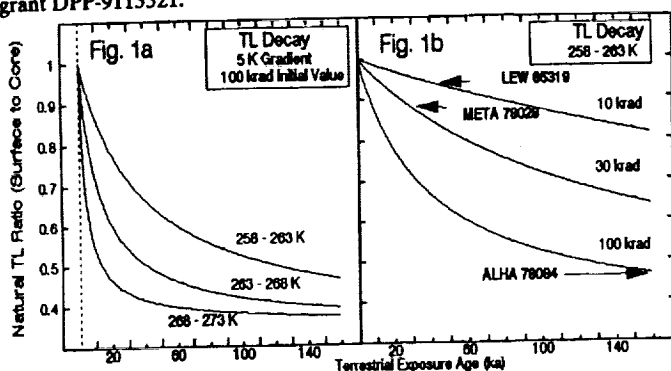
temperature gradients are maintained over extended periods of time the rate of TL decay will be different for different portions of the meteorite due to this thermal gradient. In an example calculation, we assume a five °C difference between two samples of the same meteorite which began with the exact same initial TL level. As expected, the difference in TL between the two samples increases as a function of time (Fig. 1). Two variables determine the rate of TL decay and thus can modify this calculation, namely, the absolute temperatures (Fig. 1a) and the level of initial TL (Fig. 1b). For Antarctic meteorites (with relatively low TL decay rates due to the low absolute temperatures averaged over long periods of time) one can use the highest level of TL observed in a meteorite as an indicator of the initial TL level. It is more difficult to make assumptions about which absolute temperatures are appropriate (Fig. 1a) but Schultz [9] has observed a difference of about 5 - 10 °C between air temperatures and the relatively warm interior of a meteorite on the ice surface with typical interior temperatures being about -10 °C. Thus the 258 - 263 K curve in Fig. 1a is probably a fairly good model of the TL response of samples from the surface and the interior portions of an Antarctic meteorite find, although, as mentioned below, not all Antarctic meteorites have necessarily experienced significant thermal gradients over much of their terrestrial history.

We have measured TL profiles in three large Antarctic ordinary chondrite finds. In two of these meteorites, namely, META 78028 (L6, 20.7 kg) and LEW 85319 (H5, 11.5 kg) the TL profiles are essentially flat, indicating that (a) these meteorites were small bodies (<20 - 25 cm radii) during irradiation in space, as discussed above and (b) there is no evidence for a long-term terrestrial thermal profile in these meteorites. The lack of a terrestrial thermal profile might be due to long-term homogenization of their terrestrial thermal history, by continuous "tumbling" by ice movement for instance. Perhaps more likely, however, is that their flat profiles reflect small terrestrial surface exposure ages. Meteorites completely surrounded by ice will not have any differential thermal profiles; hence their long-term TL profiles will be governed solely by pre-terrestrial cosmogenic effects. One can obtain an upper limit for terrestrial surface exposure age from Fig. 1b, with the assumptions mentioned above. We find that META 78028 and LEW 85319 could not have been exposed on the ice surface for more than 40 ka. In comparison, the ^{36}Cl -derived terrestrial age of these meteorites is 70 ± 40 and 70 ± 70 ka, respectively [10].

In contrast, ALHA 78084 (H4, 14.3 kg) has a very strong natural TL profile which is clearly related to its orientation on the ice, with the lowest TL levels being nearest to the upper, solar-heated face of the meteorite (Fig. 2). Using the same assumptions used above (Fig. 1b) we find that this it would require more than 140 ka to produce this profile. This meteorite has a ^{36}Cl -derived terrestrial age of 140 ± 70 ka [10]. If we assume that the temperature gradient across the meteorite was greater than the 5 °C used in Fig. 1 the TL-determined surface exposure age would be <140 ka. However, it is apparent that, within the error limits and assumptions of both ^{36}Cl and TL, this meteorite has spent a significant fraction of its terrestrial history on the surface of the ice in the orientation in which it was found. This, in turn, suggests that the Allan Hills Mid-western icefield, the find locality of this meteorite, has been a stable "platform" over at least this period of time.

Summary. As expected from our previous work on lunar core samples, we find that cosmogenic TL profiles of meteorites tend to be fairly shallow. Meteoroid bodies with radii <25 cm should have essentially flat TL profiles and TL measurements on samples from various small meteorite falls confirms this. We find, however, that very steep TL profiles can be produced in meteorite finds with long terrestrial ages due to thermal profiles caused by differential solar heating. In the case of Antarctic meteorites these profiles can be used as indicators of surface exposure ages up to about 160 ka under certain conditions.

Acknowledgments. We wish to thank the curators at the Muséum National D'Histoire Naturelle (Paris) and at Johnson Space Center and the Meteorite Working Group of NASA for their efforts in sampling. This study supported by NASA grant NAGW-3519 and NSF grant DPP-9115521.



- References.** [1] Benoit P.H. and Sears D.W.G. (1993) *Lunar Planet. Sci.* 24, 95. [2] Benoit P.H. and Sears D.W.G. (1994) *Earth Planet. Sci. Lett.* (in press). [3] Michel R. et al. (1991) *Meteoritics* 26, 221. [4] Honda M. (1962) *J. Geophys. Res.* 67, 4847. [5] Vaz J.E. (1971) *Nature Phys. Sci.* 230, 23. [6] Graf et al. (1990) *Geochim. Cosmochim. Acta* 54, 2521. [7] Heusser et al. (1985) *Earth Planet. Sci. Lett.* 72, 263. [8] Benoit et al. (1993) *Meteoritics* 28, 196. [9] Schultz L. (1990) *LPI Tech. Rpt.* 90-03, 56. [10] Nishiizumi K. et al. (1989) *Earth Planet. Sci. Lett.* 93, 299, and unpublished data.

2951

SHOEMAKER-LEVY 9 AND THE TIDAL DISRUPTION OF COMETS W. Benz,
University of Arizona; and E. Asphaug, NASA Ames Research Center

The break-up of Periodic Comet Shoemaker-Levy 9 into multiple pieces following its grazing encounter with Jupiter in July 1992 can be used to study tidally-induced fracture in comets. This spectacular event allows us not only to set limits on the size, strength and density of Shoemaker-Levy 9 itself, but provides invaluable guidance to numerical modeling of such encounters.

In an extensive treatment of tidal breakup which assumed self-gravitating, homogeneous, perfectly elastic bodies, Dobrovolskis^{1,2} derived simple analytical expressions for the tidally-induced surface and central stresses. Both can be cast in such a way that Poisson's ratio is the only material dependent constant entering in these expressions. For various cometary radii, densities and Poisson's ratios, we compute upper limits to the comet's tensile strength for either surface or central fracture. Fig. 1, computed for a closest approach distance of $1.3R_J$ and a cometary radius of 5 km, displays both upper limits to the tensile strength of the comet as a function of its density. For both stresses we found the two Poisson ratios ($0 \leq \nu \leq 0.5$) that maximized and minimized our upper limits. These two curves for both central and surface strength are shown on Fig. 1. Since all materials have Poisson ratios between 0 and 0.5, the space between the curves can be seen as uncertainties in the derivation of our upper limits due to unknown cometary material properties.

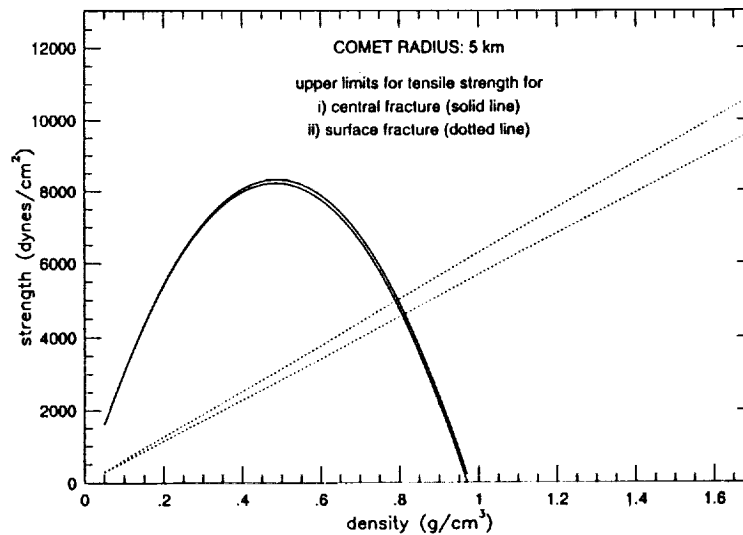


Fig. 1

For densities higher than 0.8 g/cc, fracture starts on the surface, whereas for lower densities, fracture initiates at the center. Note that the greatest strength still resulting in central fracture is strongly peaked at a density of about 0.5 g/cc, as denser comets are shielded by self-gravity and lower-density comets do not build up tidal stresses as high. Thus, if comets come with a large distribution of intrinsic strength, the ones most likely to be tidally disrupted are those with a density near 0.5 g/cm³. The linear increase in the upper strength limit for greater density comets is the result of the linear dependence of tidal force on cometary mass. For comparison purpose, the tensile strength of water ice² in laboratory samples is 2×10^7 dynes/cm² or 2500 larger than our upper limit for central fracture. However, if one accounts for the fact that strength of an object scales³ like $R^{-\alpha}$ with $0.5 \leq \alpha \leq 0.24$, we obtain a corresponding strength for a 5km pure ice block of 8.9×10^4 or 1.5×10^6 dynes/cm² depending on α (for an assumed laboratory sample of 10 cm). These numbers are still between 10 to 190 times larger than our upper limits.

Whether both surface and central failure must be initiated as a criterion for breakup, or either one of them is sufficient, remains a subject of disagreement. To resolve this debate, we model the details of cometary breakup using a three-dimensional Smooth Particle Hydrodynamics (SPH)⁴ code modified to simulate fracture in small solid objects⁵. At the lower stresses associated with brittle failure, we use a rate-dependent strength based on the nucleation of incipient flaws whose number density is given by a Weibull distribution. These flaws nucleate fracture once a local strain threshold has been exceeded. The effect of growing cracks on the dynamics is described by a new state variable D ("damage")⁶, $0 \leq D \leq 1$ which affects the stress tensor in such a way that a totally damaged region cannot sustain any tensile or shear stress.

TIDAL FRACTURE OF COMETS; W. Benz and E. Asphaug

This scheme was extensively tested on numerous analytical and experimental results with great success. For example, our code is only one currently available correctly predicting central cores of the appropriate mass laboratory impact experiments⁵.

Figure 2 illustrates the outcome of the two modes of fracture. We plotted velocity vectors at particle locations in a narrow equatorial slice for a case where fracture initiates on the surface (left panel) and in the center (right panel). As can be seen from this Figure, surface fracture results in a slow erosion of the outer layers on the near and far side of the comet, whereas central fracture actually breaks the comet into 2 hemispheres. From these results, we conclude that in order for an object to be broken up into many sizeable fragments, fracture has to initiate in the center. Indeed, surface fracture by eroding the near and far side of the object actually reduces the size over which tidal stresses can act, thus effectively shielding the inner parts from further disruption.

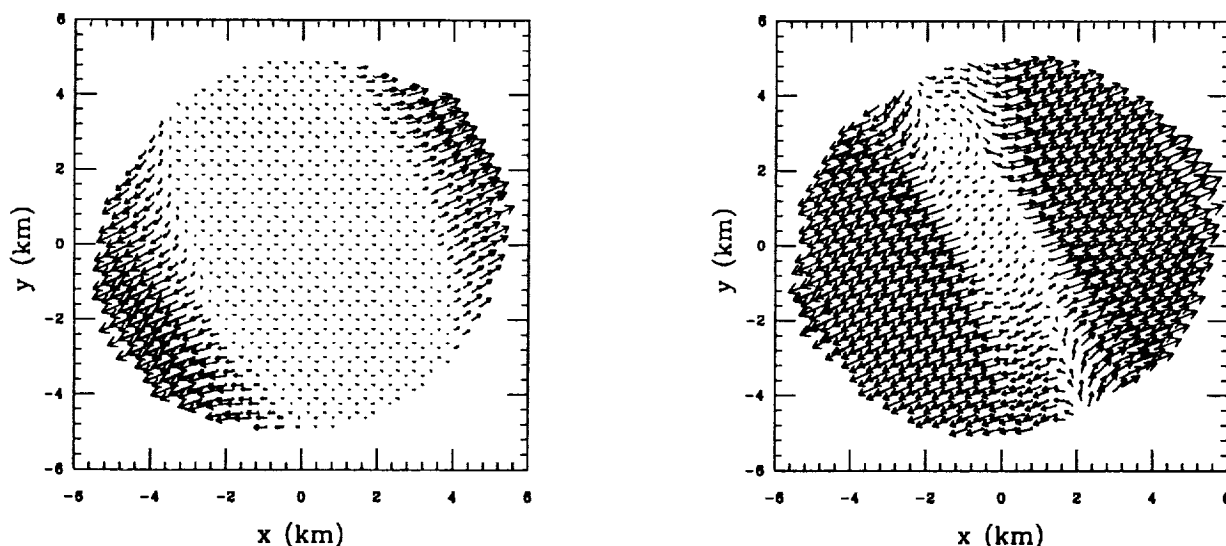


Fig. 2

Using the requirement that fracture has to initiate in the central region together with Fig. 1, implies a very strict upper bound for comet Shoemaker-Levy's density of 0.8 g/cm^3 . It is important to recall that our upper limits for both strength and density are very conservative ones. Indeed, we assumed in deriving these numbers that breakup occurred at closest approach and that all the fragments can be obtained in one episode of fragmentation. Thus, we argue that although the radius of comet Shoemaker-Levy might be quite large (5km), the mass involved may not be that large owing to the low density of the material.

These results have been obtained assuming the comet is made of a homogeneous material and obeys the usual laws of elasticity as a single object. Clearly, this may not be the case as for example, if comets are made out of a collection of loosely bound smaller entities, then fracture initiates at the boundaries between these "cometesimals" and the comet breaks up into a subset of the original fragments. We are currently investigating numerically the breakup of these heterogeneous comets.

References: (1) Dobrovolski, A.R. (1982) *Icarus*, **52**, 136-148.; (2) Dobrovolski, A.R. (1982) *Icarus*, **88**, 24-38; (3) Housen K., and K. Holsapple (1990) *Icarus*, **84**, 226-253; (4) Benz, W. (1991) in *Numerical Modeling of Nonlinear Stellar Pulsations. Problems and Prospects*, ed. J.R. Buchler (Dordrecht: Kluwer Academic Press), p. 269-288; (5) Benz, W., and E. Asphaug (1994) *Icarus*, in press.; (6) Grady, D.E., and M.E. Kipp (1980) *Int. J. Rock Mech. Min. Sci. Geomech. Abstr.* **17**, 147-157;

REFRACTORY CARBIDES IN INTERSTELLAR GRAPHITE; Thomas J. Bernatowicz¹, Sachiko Amari¹ and Roy S. Lewis², ¹*McDonnell Center for the Space Sciences & Physics Department, Washington University, St. Louis MO 63130-4899, USA*; ²*Enrico Fermi Institute, University of Chicago, Chicago IL 60637-1433, USA*.

Previous transmission electron microscope (TEM) investigations of interstellar graphite (C- α) grains [1] have shown that they sometimes contain small (tens of nm) crystals of TiC. The laboratory study of these polymineralic assemblages, coupled with thermodynamic modelling, opens the possibility of exploring grain formation conditions (composition, temperature and pressure) in stellar atmospheres in unprecedented detail. Here we report preliminary results of TEM studies on suites of interstellar graphitic spherules in the KFC1 density separate (2.15-2.20 g/cc) from the carbonaceous chondrite Murchison, aimed at expanding the database on the composition and abundance of 'interstellar grains within grains.' The approach used here results in greatly increased mineralogical data on interstellar graphite and is complementary to previous work on individual spherules in which isotopic data were also obtained [1]. Details of the extraction procedure for KFC1 have been described previously [2]. KFC1 consists largely of well-graphitized spherules (mean diameter \approx 1-2 μ m). The ¹²C/¹³C ratios (from 0.02-80 times the solar value of 89) measured in several hundred individual spherules clearly establish their pre-solar origin [3]. In preparation for TEM study of the graphite, an 8mm diameter gelatin cylinder was affixed to a pre-cleaned glass slide with RTV silicone cement. The graphite particles were then deposited from suspension in an area $<1\text{mm}^2$ on the glass within the cylinder; the deposit was imbedded in resin (which was detached from the slide after curing) and sliced into sections 50nm thick with an ultramicrotome equipped with a diamond knife. Each slice thus produced contained ultra-thin sections of many (>30) graphite grains. The slices were retrieved on Cu TEM grids covered with holey C films, and were examined for the composition and structure of their included graphite sections in many different orientations using a JEOL-2000FX TEM equipped with a Noran (EDS) X-ray detector sensitive to elements with $Z \geq 5$.

Internal study of the KFC1 spherules (e.g., by direct imaging and convergent beam diffraction) reveals that they typically have a composite structure, with an amorphous C core surrounded by a well-graphitized shell. Whether this structural transition represents a change in kinetics during spherule growth or some post-formational surface transformation (e.g., caused by subsequent irradiation by energetic photons) is unknown, but the frequency of such spherules suggests that mechanisms involved in their formation must be rather pervasive. A noteworthy exception to this rule occurs in the case of spherules having refractory carbide inclusions at their centers that evidently served as heterogeneous nucleation sites for carbon; in these cases the spherules are well-graphitized throughout. However, randomly distributed refractory carbide crystals (5-70 nm) occur in many, perhaps most, of the KFC1 spherules. They have been observed in one-third of the 34 spherules studied to date, but this is certainly a lower limit due to the difficulty of detecting these small crystals (because of poor contrast) when they are in non-diffracting orientations.

X-ray spectra of the included crystals show that they are typically refractory carbides of Ti, Zr and Mo in variable proportions, suggestive of solid solution among these elements. Compositions range from pure Ti carbides to Mo and Zr carbides with only a few percent Ti. In Figure 1 we show data from three KFC1 graphite spherules (designated A, G and Q) from a single slice, each having more than one carbide crystal. The elemental data are displayed as atomic ratios relative to Ti that have been normalized to the corresponding ratios in the solar system. It is evident that all of these crystals have Zr/Ti and Mo/Ti much greater than solar values, up to factors of several thousand. While the s-process can produce significant enhancements in these ratios (e.g., between 1 and 2 orders of magnitude above the solar values in the He-shells of AGB stars [4]), it is difficult to produce enhancements as great as those observed. Because the relative proportions of Ti, Zr and Mo vary appreciably from crystal to

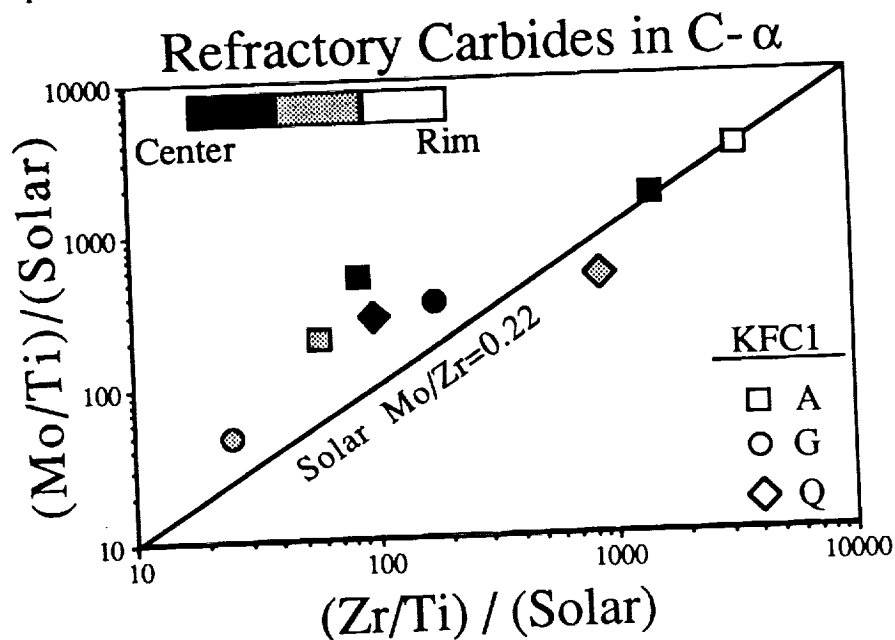
INTERSTELLAR REFRACTORY CARBIDES; Bernatowicz, T. J. *et al.*

crystal within the same graphite spherule, it appears likely that the Mo and Zr enrichments relative to Ti are in part due to chemical fractionation accompanying formation of the crystals. In particular, such chemical variation arises as a natural consequence of differences in condensation temperatures amongst the Zr, Mo and Ti carbides. There is, however, no tendency for crystals near the center of a given graphite spherule to be more refractory (i.e., to have higher Zr/Ti and Mo/Ti) than crystals near the rim (Fig. 1). The simplest explanation for these observations is that the crystals formed prior to carbon condensation, and subsequently (in the case of crystals that did not serve as heterogeneous nucleation sites for carbon) were randomly incorporated into growing carbon spherules.

Equilibrium condensation models [5-7] show that the relative condensation temperatures of Zr, Mo and Ti carbides and graphite depend in a complicated manner on the C/O gas ratio, pressure and degree of metal enrichment above solar obtaining in the stellar atmosphere. Despite restriction to equilibrium conditions, the models enjoy some success. For example, with C/O near unity under moderately low pressure, the formation of pure Zr, Mo and Ti carbides may occur prior to graphite condensation, consistent with the above observations. In the case of Zr and Mo, this is particularly favorable when the s-process has enriched these elements one to two orders of magnitude relative to solar proportions [8]. There is thus reason to believe that in the future, refined thermodynamic models (taking, e.g., solid solution into account) coupled with elemental data on refractory interstellar grains should be able to place realistic constraints on physical conditions and compositions of stellar atmospheres.

REFERENCES: [1] Bernatowicz T. *et al.* (1991) *Ap. J.* **373**, L73; [2] Amari S. *et al.* (1993), *GCA*, in press. [3] Amari S. *et al.* (1993), *Nature* **365**, 806; [4] Gallino R. (1993), pers. comm; [5] Sharp C. and Wasserburg G. J. (1993) *Lunar Planet. Sci. XXIV*, 1281; [6] Lodders K. and Fegley B. (1992), *Meteoritics* **27**, 250; [7] Lodders K. and Fegley B. (1993), *Meteoritics* **28**, 387; [8] Lodders K. and Fegley B. (1993), pers. comm; [8] Anders E. and Grevesse N. (1989), *GCA* **53**, 197.

Figure 1: Mo/Ti and Zr/Ti atomic ratios in carbides from three KFC1 graphite spherules compared to solar [8] ratios (Solar Zr/Ti=0.0048, Mo/Ti=0.0011). Fractional errors in solar-normalized elemental ratios are <30% for all values less than 1000, and ~50% for greater values. Shading of symbols indicates approximate location of carbide crystals in a given spherule; none of the crystals are located in the exact centers of their host spherule.



ORIGIN OF AMORPHOUS RIMS ON LUNAR SOIL GRAINS; Thomas J. Bernatowicz, Robert H. Nichols Jr. and Charles M. Hohenberg, *McDonnell Center for the Space Sciences & Physics Department, Washington University, St. Louis MO 63130-4899, USA*

In a recent paper, Keller and McKay [1] have challenged the generally accepted idea that the ~50nm amorphous rims on lunar soil grains are the result of solar wind (SW) ion damage [2]. They instead propose that these rims are almost entirely impact-derived rock vapor deposits (based on compositional differences between grain rims and interiors observed in Apollo 11, 16 and 17 silicate soil particles), and conclude that SW radiation effects are of minor importance relative to vapor deposition. A decisive test of this hypothesis should be provided by a study of the surfaces of ilmenite (FeTiO_3) in mature lunar soils, since this mineral (not investigated by Keller and McKay) is compositionally distinct from silicates and constitutes only a minor fraction of the regolith. Specifically, the vapor deposition model implies that any amorphous rims observed on ilmenites should be dominantly silicate vapor deposits.

To test this prediction, we have performed complementary noble gas and TEM studies of 7 ilmenite grains (90-125 μm) separated [3] from the mature lunar soil 71501 (with a modal ilmenite abundance of 8% [4]). The grains were imbedded in resin and partially sliced with a diamond-blade ultramicrotome to produce sections thin enough (70 nm) for study in the TEM. The remainder of each grain was then individually analyzed for noble gases using the same laser extraction techniques as in a recent study [5] of 90 ilmenites from 71501. All of the grains in the present study are rich in SW gases (0.04 - 0.4 ccSTP $^4\text{He/g}$) and have He and Ne concentrations and Ne isotopic ratios within the range observed in the much larger ilmenite suite. The interiors of the grain sections are heavily shattered by the slicing, but portions (tens of μm) of the outermost surface of the grain immediately adjacent to the embedding resin are frequently preserved to a depth of 1-2 μm . This allows for comparative elemental analysis of the surfaces exposed to SW and the unexposed ilmenite beneath them. We performed energy dispersive X-ray analyses of the grain surfaces (73 analyses) and near-surface interiors (49 analyses) with a 20 nm, 200kV electron beam, using a Noran detector sensitive to elements with $Z \geq 5$.

The interior analyses reveal substantial Mg and minor Cr substitution for ferrous iron in these ilmenites ($\text{Mg/Ti}=0.04\text{-}0.17$; $\text{Cr/Ti}\approx 0.01$), but $(\text{Fe}+\text{Mg}+\text{Cr})/\text{Ti}$ is unity within analytical uncertainty. Compared to the interior composition, the outermost 50nm of surface is typically enriched in Mg, Al, Si, S and Ca. These excess abundances are displayed in Fig. 1 as the mean difference between surfaces and interiors in terms of atomic ratios relative to Ti. Titanium is chosen as the reference element because its atomic abundance is less than that of all of the other major elements in 71501 [6] and because it is the dominant cation in ilmenite. Not included in the figure are analyses of surface glass splashes (which comprise at most a few percent of the surface and thus are not representative of the bulk surface composition). In Fig. 1 the ilmenites are ordered by increasing abundance of surface Si, the most abundant excess element. It is evident that the excess elements are far less abundant than Ti (mean excess $/\text{Ti} < 0.2$), so that the surfaces are compositionally similar to ilmenite. In the sense that the surfaces of the ilmenites are dominated by Ti, as opposed to Si and the other major elements in the bulk soil, the idea that vapor deposits entirely constitute the amorphous rims on lunar grains is seen to fail. On the other hand, the present work shows that there is indeed some vapor contamination of grain surfaces, as revealed by the element excesses. Within analytical uncertainty, the mean Mg/Si and Al/Si ratios in the excess are identical to those in the bulk soil [6] and to the ratios measured in the surface glass splashes. On this basis, it is reasonable to ascribe these excess surface elements to contamination by impact-generated rock vapor. Sulfur, on the other hand, is surface-enriched by

LUNAR AMORPHOUS RIMS. Bernatowicz T. J. *et al.*

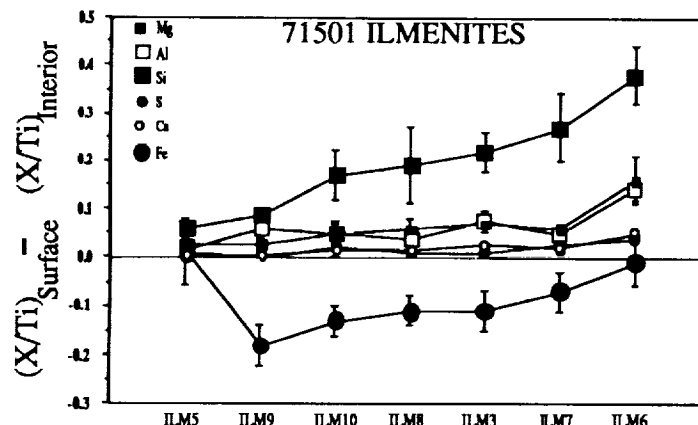
an order of magnitude relative to the bulk soil, consistent with the observations of Keller and McKay [1]. Based on the surface abundances of Mg, Al and Si, all of the calculated excesses are probably low by 3-5% due to Ti that may have accompanied these elements in the vapor deposits, but this does not affect the conclusion that the surface composition of the ilmenites is essentially that of the interior, except for minor rock vapor contamination.

The surfaces of all of the ilmenites, regardless of degree of vapor contamination, are disordered to depths of 30-80nm as revealed by high resolution imaging and convergent beam diffraction. In addition to amorphous regions, the surfaces typically have randomly oriented ilmenite crystallites (<10nm) that are presumably the result of surface recrystallization. In the most contaminated grain (ILM6) there are also surface blebs (20-50nm) of metallic Fe, most likely formed by reduction of impact vapor iron on contact with the SW hydrogen-saturated grain surface. We may plausibly attribute the surface disorder of the ilmenite grains to SW ion damage, since the surface concentration [5] of SW He inferred for the most gas-rich ilmenites in 71501 is up to 5×10^{-3} ccSTP/cm², equivalent to a flat target He fluence of 10^{17} atom/cm². Simulation experiments [2] show that such fluences produce severe radiation damage in ilmenite, consistent with our observations. To our knowledge this is the first observation of SW ion damage in ilmenite. Thus, not only do the present results reject the vapor deposition model for the origin of lunar grain amorphous rims, but they also give new evidence in favor of the SW ion damage model.

Returning to the discussion of Fig. 1, we note that, on the average, there is a 10% deficiency of Fe relative to Ti in the ilmenite surfaces compared to their interiors. Vapor addition of Ti to the grain surfaces cannot account for this, since Fe should be at least twice as abundant as Ti in vapor generated from the bulk soil [6]. Detailed investigation of the disordered grain surfaces, the crystalline interiors and the region between them revealed no reservoir for this missing Fe. Given that Mg/Si and Al/Si in the surface vapor deposits are unfractionated relative to the bulk soil, we are forced to conclude that the Fe has been preferentially removed. Whether this occurred on the lunar surface or during the heavy liquid separation used to isolate the ilmenite [3] remains to be determined.

REFERENCES: [1] Keller L. and McKay D. (1993) *Science* **261**, 1305; [2] Bibring P. *et al.* (1974), *EPSL* **22**, 205. [3] Benkert J. *et al.* (1993), *J. Geophys. Res.* **98**, 13,147; [4] Heiken G. and McKay D. (1974), *Proc. 5th Lun. Sci. Conf.* v.3, 843; [5] Nichols R. *et al.* (1994) *Geochim. Cosmochim. Acta* **58**, in press; [6] LSPET (1973), *Science* **182**, 659.

Figure 1:



p. 2
CRATERS IN ALUMINUM 1100 TARGETS USING GLASS PROJECTILES AT 1-7 KM/S; R.P. Bernhard¹, T.H. See¹, F. Hörz², and M.J. Cintala², ¹Lockheed-ESC, C23, 2400 NASA Road.1, Houston, TX 77058, ²NASA Johnson Space Center, Solar System Exploration, Houston, TX 77058

INTRODUCTION: We report on impact experiments using soda-lime glass spheres of 3.2 mm diameter (D_p) and aluminum targets (1100 series). The purpose is to assist in the interpretation of LDEF instruments and in the development of future cosmic-dust collectors in low-Earth orbit. Because such instruments demand understanding of both the cratering and penetration process, we typically employ targets with thicknesses that range from massive, infinite half-space targets, to ultrathin films (e.g., [1]). This report addresses a subset of cratering experiments that were conducted to fine-tune our understanding of crater morphology as a function of impact velocity (V). Also, little empirical insight exists about the physical distribution and shock-metamorphism (unmelted / melted / vaporized / fractionated) of the impactor residues as a function of encounter speed, despite their recognized significance in the analysis of space-exposed surfaces [2, 3, 4].

Soda-lime glass spheres were chosen as a reasonable analog to extraterrestrial silicates, and aluminum 1100 was chosen for targets, which among the common Al-alloys, best represents the physical properties of high-purity aluminum (i.e., one of the choice materials for stacked, thin-film collectors). These materials complement existing impact studies that typically employed metallic impactors and less ductile Al-alloys (see [5] or [6] for summaries). We have completed dimensional analyses of the resulting craters and are in the process of investigating the detailed distribution of the unmelted and melted impactor residues via SEM methods, as well as potential compositional modifications of the projectile melt(s) via electron microprobe. The following progress report concentrates on the dimensional analysis.

RESULTS: Figure 1 shows "low" velocity (<4.5 km/s) craters in cross-section (at identical scales; V indicated by insert). Note that the craters' depth-diameter relationship (P/D_c) changes from relatively deep structures at <3 km/s, to aspect ratios that closely resemble "hemispherical" structures ($P/D_c = 0.5$) typical for $V > 4$ km/s [5]. Measurements of the depth-diameter ratios are plotted in Figure 2 and the experimental craters are obviously not perfect hemispheres. Craters in aluminum resulting from 5-7 km/s impacts typically yield an average of $P/D_c \approx 0.56$. Although the experimental trends in Figure 2 seem to indicate that relative crater depth increases again with increasing velocity, this is not the case as demonstrated by depth-diameter measurements of ~ 400 craters in aluminum 6061-T6 alloy from LDEF [7]. Average values for P/D_c of 0.589, 0.581 and 0.574 were observed on surfaces from the trailing, leading and space-facing directions that have mean encounter velocities of ~ 22 , 13, and 17 km/s, respectively. LDEF results and experimental observations suggest that the relationship of $P = 0.5 D_c$ is only approximately correct, when calculating projectile sizes from crater diameters or depths.

Figure 3 illustrates the relationship of crater diameter (D_c ; measured at the initial target surface) to impact velocity. The slope of a linear regression line through the D_c measurements reveals a velocity exponent of 0.564, modestly smaller than the 0.666 resulting from generally larger craters of [5], and substantially larger than the 0.44 from much smaller events [8]. The cause of these variances is unknown at present.

Finally, Figure 4 presents select "high-velocity" craters (>4.7 km/s) in plan view, providing a preview of the ongoing SEM and microprobe studies that concentrate on the characterization of the projectile residues. The hummocky

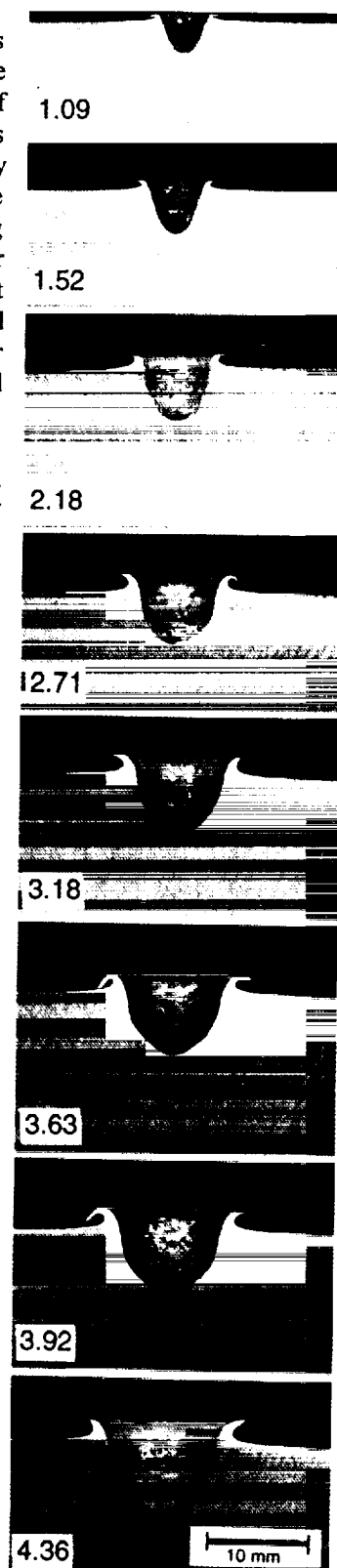


Figure 1.

CRATERS IN Al 1100 TARGETS WITH GLASS PROJECTILES: Bernhard, R.P. *et al.*

interior of the 4.7 km/s crater is composed of unmelted glass fragments that float on top of a glass liner. The number of unmelted fragments decreases with increasing speed and the projectile is completely molten at $V > 6$ km/s. Note the substantial radial velocity component of the melt: starting at ~ 5.8 km/s an increasingly larger area of the crater bottom is devoid of melt, because larger and larger melt fractions will drape the walls and/or be ejected from the crater altogether. These observations suggest limited utility of massive targets as dust collectors, because large fractions, possibly all, of the projectile may escape the crater cavity at very high encounter speeds typical for low-Earth orbit. The projectile residue remaining in $\sim 50\%$ of all LDEF craters is below detection thresholds via SEM-EDX methods [2].

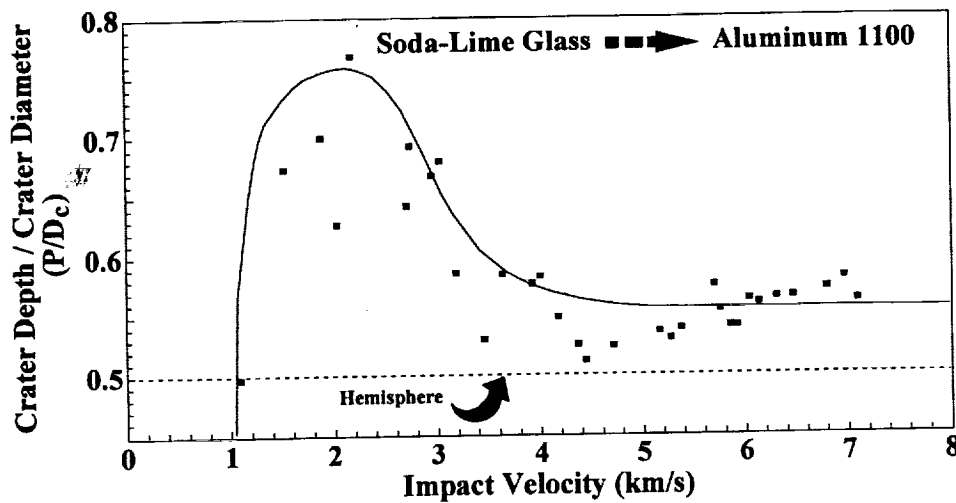


Figure 2.

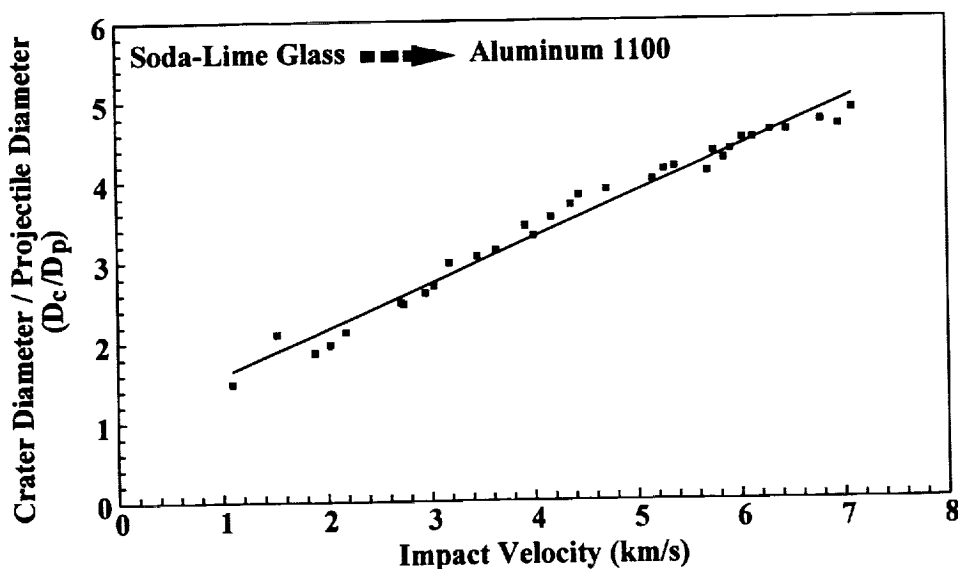


Figure 3.

REFERENCES: 1) Hörz *et al.* (1994), *Int. J. Impact Engng.*, Vol. 15, No. 3, in press, 2) Bernhard, R.P. *et al.* (1993), *LDEF 2nd Post Retrieval Symp.*, NASA-CP 3194, 551-573, 3) Amari *et al.* (1993), *LDEF 2nd Post Retrieval Symp.*, NASA-CP 3194, 513-528, 4) Simon, C.G. *et al.* (1993), *LDEF 2nd Post Retrieval Symp.*, NASA-CP 3194, 677-692, 5) Cour-Palais, B.G. (1987), *Int. J. Imp. Engng.*, 5, 221-237, 6) Watts, A. *et al.* (1993), NASA NCR-188259, 92 pp. 7) Love, S.G. *et al.* (1994) *Int. J. Imp. Engng.*, submitted, 8) Iglseider, H. and Igenbergs, E. (1990), *Int. J. Imp. Engng.*, 10, 271-280.

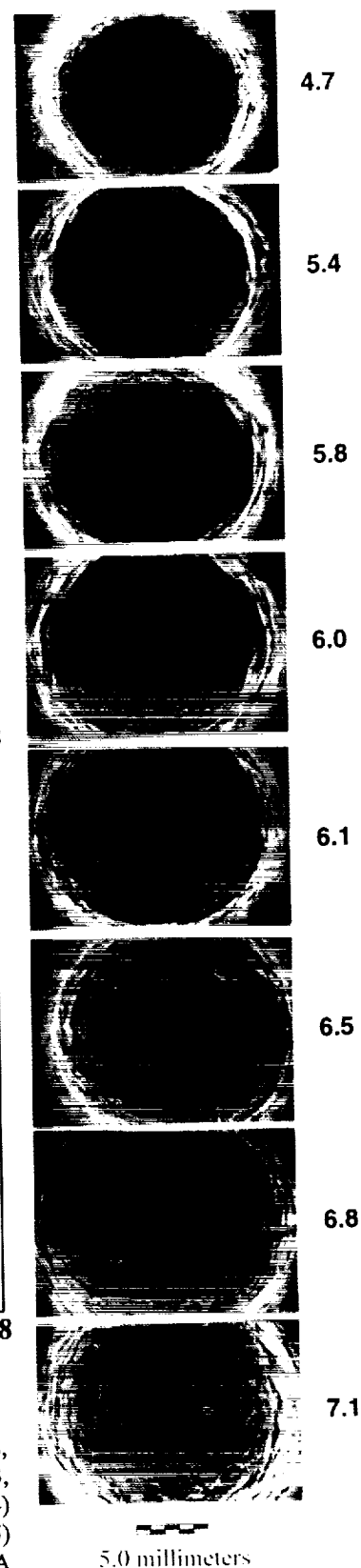


Figure 4.

A MARTIAN MANTLE WITH PERIDOTITIC VERSUS CHONDRITIC Mg/Si and Al/Ca RATIOS: IMPLICATIONS FOR MANTLE MINERALOGY AND MELTING REACTIONS

C.M. Bertka Geophysical Laboratory, Carnegie Institution of Washington, 5251 Broad Branch Rd. N.W., Washington DC 20015

INTRODUCTION:

Mantle compositions derived from cosmochemical arguments for the Earth, Venus and Mars, share a similarity to chondritic compositions. If a carbonaceous chondrite Mg/Si atomic ratio is assumed, then the largest major element difference between the mantles of these terrestrial planets can be described by variations in their mg#, the atomic ratio $\text{Mg}/(\text{Fe}+\text{Mg}) \times 100$ (1). Earth and Venus models are iron-poor, mg# 76 to 99, relative to Mars, mg# 67 to 78 (1,2,3). The Earth's mantle composition has also been predicted from the composition of peridotite nodules. The mg# of these samples fall largely within 87 to 92, but their atomic Mg/Si is higher than chondritic, ~1.3-1.4 vs. 1.1 and their atomic Al/Ca is lower than chondritic, ~1.2 vs. 1.3-1.4 (4,5). Previous experimental studies to determine the mineralogy and melting phase relations of an iron-rich Martian mantle have been performed with the Dreibus and Wanke (3) SNC (shergottites, nakhlites, chassignites) parent body composition (DW) (6). The DW composition has chondritic ratios of Mg/Si and Al/Ca and mg# 75. In this study the subsolidus mineralogy and partial melting phase relations of four iron-rich bulk mantle compositions in the system CMASNF have been experimentally determined at 15 kbar. Peridotitic (atomic ratio Mg/Si=1.3, Al/Ca=1.2) and chondritic (Mg/Si=1.1, Al/Ca=1.3) compositions with mg#s of both 75 and 85 and $\text{Na}_2\text{O}=0.5$ wt% were studied (Table 1). The composition of a partial melt produced at 15 kbar and near solidus temperatures from the most iron-rich peridotite composition studied was also determined.

EXPERIMENTAL TECHNIQUE:

Experiments were performed in an end-loaded piston cylinder apparatus with a 0.5" diameter solid-media pyrex-NaCl-AlSiMag cell assembly. Starting materials were synthesized from spec pure oxides ground under ethanol in an agate mortar for one hour, reduced in a gas mixing furnace (1000°C , $f\text{O}_2$ at one log unit below QFM) for 24 hours, and reground under ethanol in an agate mortar to less than 5 μm . Approximately 10 mgs of a starting composition was sealed in graphite-lined platinum capsules. Run duration varied from 48 hours at near solidus temperatures to 3 hours at near liquidus temperatures. The partial melt composition of the iron-rich peridotite was determined using the diamond technique (7). A sintered diamond chip weighing 0.14 mgs was placed in the center of the peridotite mix and sealed in a graphite-lined platinum capsule. Run duration for this experiment was 48 hours.

RESULTS:

The mg# 75 compositions MB and PB have solidus temperatures at 15 kbar that are $\sim 20^\circ\text{C}$ lower than the solidus temperatures of the mg# 85 compositions MA and PA. The mineral assemblage at the 15 kbar solidi of the chondritic compositions MA and MB and at the solidus of the mg# 85 peridotite composition PA is a lherzolite, clinopyroxene + orthopyroxene + olivine. The clinopyroxene stable at the solidus of the MA, MB and PA compositions is pigeonite with a CaSiO_3 component (Wo) of <20 mole%. The mineral assemblage at the 15 kbar solidus of the mg# 75 peridotitic composition PB is a spinel wehrlite, spinel + clinopyroxene + olivine. The clinopyroxene stable at the solidus of the PB composition is augite with Wo >25 mole%. Clinopyroxene melts out of all of the assemblages at 40 to 60°C above the solidus. Like the melt produced at $\sim 20^\circ\text{C}$ above the solidus of the DW mantle composition, the partial melt composition produced at 40°C above the solidus of the mg# 75 peridotite composition PB (in equilibrium with a spinel wehrlite assemblage), is a picritic alkali basalt. However, the PB partial melt has a higher mg# (54.5) and is richer in CaO (11.5 wt%) and Al_2O_3 (15.0 wt%) than the DW partial melt (mg# 47.8, CaO 9.6 wt%, Al_2O_3 13.0 wt%).

MARTIAN MANTLE PERIDOTITIC VS CHONDRITIC

Bertka, C.M.

DISCUSSION:

The calculated STP densities of the mg# 75 compositions MB and PB fall within the range of Martian mantle density proposed by Goettel (2), 3.44 ± 0.06 g/cc. The calculated STP densities of the mg# 85 compositions MA and PA fall slightly below Goettel's estimate, by 0.027 and 0.013 g/cc respectively. If the Goettel density estimate is accepted, then these results imply that the Martian mantle has an mg# <85. However, the mineral assemblages produced in this study bracket feasible 15 kbar Martian mantle assemblages. The absence of spinel from the lherzolite assemblages PA, MA and MB may be attributed to the high Na₂O abundance of the bulk mantle compositions which results in the stability of aluminous-rich pyroxenes. The addition of Cr₂O₃ to these mantle compositions or the reduction of Na₂O abundance will stabilize spinel.

The melting reaction that takes place at the 15 kbar solidi of the model mantle compositions is determined by their stable mineral assemblages. Recent work at mantle pressures in both iron-free and iron-rich, mg#<90, systems has shown that a melting reaction that produces orthopyroxene occurs when the stable clinopyroxene is pigeonite with Wo <20 mole% (8-12). All of the model mantle compositions studied have pigeonite stable at their 15 kbar solidus except the mg# 75 peridotite composition PB. We may predict that a melting reaction that produces orthopyroxene is present in the spinel stability field of the Martian interior unless the interior has an iron-rich, mg#<85, peridotite composition. The PB melting reaction at 15 kbar is augite + spinel = olivine + liquid. Orthopyroxene is absent below the solidus and is not produced above the solidus by the melting reaction. Preliminary experiments with the PB composition in the garnet stability field at 25 and 30 kbar indicate that orthopyroxene is absent from the subsolidus assemblage, but pigeonite is stable. Therefore, orthopyroxene may be produced above the solidus by the melting reaction. If the Martian mantle has an iron-rich peridotite composition, then orthopyroxene may only be present in residual source regions that have experienced partial melting in the garnet stability field.

References: 1) BVSP (1981) in *Basaltic Volcanism on the Terrestrial Planets*, Pergamon Press. 2) Goettel K.A. (1981) *Geophys. Res. Lett.*, 8, 497. 3) Dreibus G. and Wanke H. (1985) *Meteoritics* 20, 367. 4) Jagoutz E. et al. (1979) *Proc. Lunar Planet. Sci. Conf. 10th*, 2031. 5) Maaloe S. and Aoki K. (1977) *Contrib. Mineral. Petrol.*, 63, 161. 6) Bertka C.M. and Holloway J.R. (1994) *Contrib. Mineral. Petrol.*, in press. 7) Johnson K.T.M. and Kushiro I. (1992) *Geophys. Res. Lett.*, 19, 1703. 8) Herzberg C. et al. (1990) *J. Geophys. Res.*, B95, 15,779. 9) Bertka C.M. et al. (1991) *abst. EOS*, 72, 317. 10) Kinzler K.J. and Grove T.L. (1992) *J. Geophys. Res.*, B97, 6,885. 11) Bertka C.M. and Holloway J.R. (1993) *J. Geophys. Res.*, B98, 19,755. 12) Longhi J. and Kinzler K.J. (1993) *abst. EOS*, 74, 658.

Table 1. Starting Compositions

model mantle	Chondritic		Peridotitic	
	MA	MB	PA	PB
oxide (wt%)				
SiO ₂	47.9	43.7	43.0	38.8
Al ₂ O ₃	3.4	3.1	3.5	3.1
FeO	10.9	18.7	11.9	20.3
MgO	34.6	31.5	37.9	34.2
CaO	2.7	2.5	3.3	3.0
Na ₂ O	0.5	0.5	0.5	0.5
Mg/Si	1.1	1.1	1.3	1.3
Al/Ca	1.3	1.3	1.2	1.2
mg#	85.0	75.0	85.0	75.0

THERMAL INERTIAS IN THE UPPER MM OF THE MARTIAN SURFACE DERIVED USING THE PHOBOS SHADOW; B. H. Betts¹, B. C. Murray, and T. Svitek², California Institute of Technology. ¹Now at the San Juan Institute, 31872 Camino Capistrano, San Juan Capistrano, CA 92675. ²Now at Orbital Sciences Corp.

The first ever thermal images of the shadow of Mars' moon Phobos on the surface of Mars, in addition to simultaneous visible images, were obtained by the Soviet Phobos '88 Termoskan instrument. The best observed shadow occurrence was on the flanks of Arsia Mons. For this occurrence, we combined the observed decrease in visible illumination of the surface with the observed decrease in brightness temperature to calculate thermal inertias of the Martian surface. We refined our preliminary model [1,2] by adding downward atmospheric infrared flux and non-isothermal starting conditions, and we have now compared our results to atmospherically corrected diurnal inertia results [3]. Most of our derived inertias fall within the range 0.9 to 1.4 ($10^{-3} \text{ cal cm}^{-2} \text{ s}^{-1/2} \text{ K}^{-1}$), corresponding to 5 to 10 micrometer dust particles for a homogeneous surface [3,4,5]. Dust at the surface is consistent with previous theories of Tharsis as a current area of dust deposition [6,7,8]. Viking IRTM-derived inertias are based upon diurnal temperature variations and are sensitive to centimeter depths, whereas the shadow-derived inertias sample the upper tenths of a millimeter of the surface due to the short (about 20 second) duration of the eclipse. The shadow-derived inertias are significantly lower than those originally derived from Viking IRTM measurements (inertias of 2 to 3.5) [8]. However, they are very similar to *Haberle and Jakosky's* [3] atmospherically corrected *Palluconi and Kieffer* [8] IRTM inertias. Thus, if near surface (mm versus cm scales) layering exists at all in this region, it is not very significant.

Termoskan was an optical-mechanical scanning radiometer with one visible channel (0.5-1.0 μm) and one thermal infrared channel (8.5-12.0 μm) (see [1,9] for more information). The instrument was fixed to the spacecraft, pointing in the antisolar direction. We have analyzed the best observed and least complicated of four observed shadow occurrences (Figure 1). The elongated shape of the shadow in the Termoskan panoramas was due to the instantaneous field of view of the instrument "following the shadow" because of a combination of unusual orbital geometry (the spacecraft and Phobos were nearly co-orbiting) and the antisolar orientation of the instrument.

We used the observed drop in the visible flux within the shadowed area to model the solar insolation as a function of both actual time since the beginning of eclipse and position in the scan. We then used this in three different one dimensional, finite difference thermal models for homogeneous surfaces (adapted from [10]). Model 1 was our preliminary model from [1,5]. Model 2 did not assume that the pre-eclipse temperatures were constant with depth as Model 1 did. Model 3 added a downward atmospheric flux term to Model 2, and thus is the most realistic of the three.

By comparing the model results with the temperature drops observed in the infrared scan, we find most of the data fall between inertias of 0.85 and 1.2 (in units of $10^{-3} \text{ cal cm}^{-2} \text{ s}^{-1/2} \text{ K}^{-1}$) for Model 1, between 1.0 and 1.55 for Model 2, between 0.75 and 1.2 for Model 3 with a downward atmospheric flux of 20% of the absorbed pre-eclipse flux, and 0.9 and 1.35 for Model 3 with a 10% downward flux value (see Figure 2). The actual atmospheric flux is relatively uncertain, but probably was slightly less than 10% (based upon [3] and an approximate optical depth of .4). In any case, our main conclusions remain unchanged for the range of most likely values.

Our results show that non-isothermal Model 2 raises the derived inertias from the less realistic isothermal Model 1. Adding atmospheric downward flux in Model 3 reduces the derived inertias. Ironically, for this case, these two additions to the model roughly cancel each other out. The inertias derived from all the models are consistent with dust sized particles.

A representative *Palluconi and Kieffer* [8] IRTM inertia for the shadowed region is 2.4. Using the suggested *Haberle and Jakosky* [3] corrections, this inertia becomes 1.34 for an optical depth 0.2 and 0.81 for an optical depth of 0.4 (with 0.3 to 0.5 typical of the period analyzed by [8]). Thus, the *Haberle and Jakosky* corrected *Palluconi and Kieffer* inertias agree with our model results for the shadowed region to within the uncertainty of their corrections.

Therefore, if layering of the upper mm versus the upper few cm exists at all, it is probably not as significant as was first thought [1]. Also, consistent with the theoretical considerations of [3], our

PHOBOS SHADOW ANALYSES OF THE MARTIAN SURFACE: Betts, B.H. et al.

modeling shows that for the inertias involved, atmospheric downward flux has considerably less effect upon eclipse derived inertias than upon diurnally derived inertias.

REFERENCES: [1] Murray, B.C. et al., *Planetary and Space Science*, Vol. 39 (1/2), 237-265, 1991; [2] Betts, B. H. et al., *LPSC XXI*, 1990; [3] Haberle, R. M., and B. M. Jakosky, *Icarus*, 90, 187-204, 1991; [4] Kieffer, H. H. et al., *J. Geophys. Res.*, 78, 4291-4312, 1973; [5] Jakosky, B. M., *Icarus*, 99, 117-124, 1986; [6] Kieffer, H. H. et al., *J. Geophys. Res.*, 82, 4249-4291, 1977. [7] Zimbelman, J. R. and H. H. Kieffer, *J. Geophys. Res.*, 84, 8239-8251, 1979; [8] Palluconi, F. D., and H. H. Kieffer, *Icarus*, 45, 415-426, 1981; [9] Betts, B. H., Ph.D. thesis, Caltech, 1993; [10] Clifford, S. M. et al., Houston, Tex., 1987.

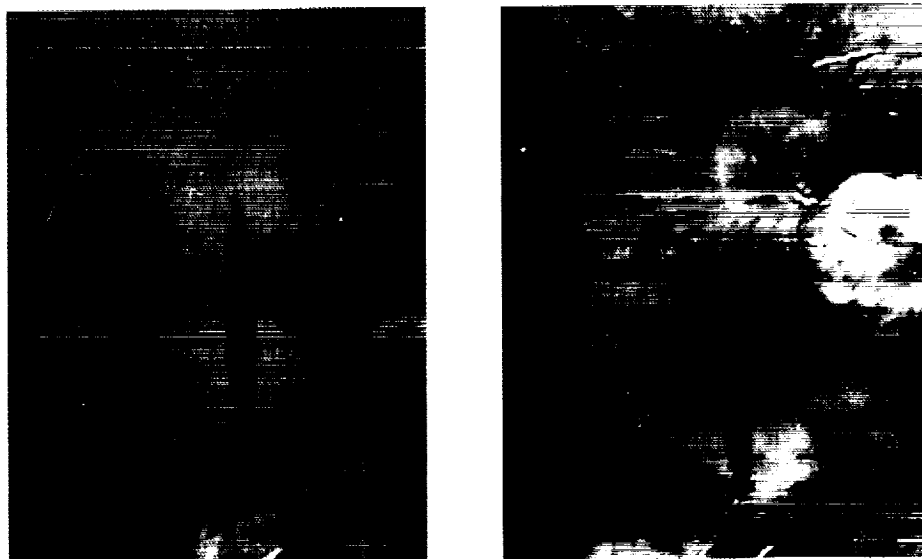


Figure 1: Phobos shadow images. Termoskan visible (left) and thermal (right) images showing the analyzed Phobos shadow occurrence on the flanks of Arsia Mons. West at top. The shadow is observed first (further West) in the visible, then later (to the East) in the thermal. This is due to the delay in cooling after the onset of the shadow. The shadow is centered approximately upon 14°S, stretching from 120°W to 110°W. Local times of day within the shadow vary from about 9.3 H to 10.1 H.

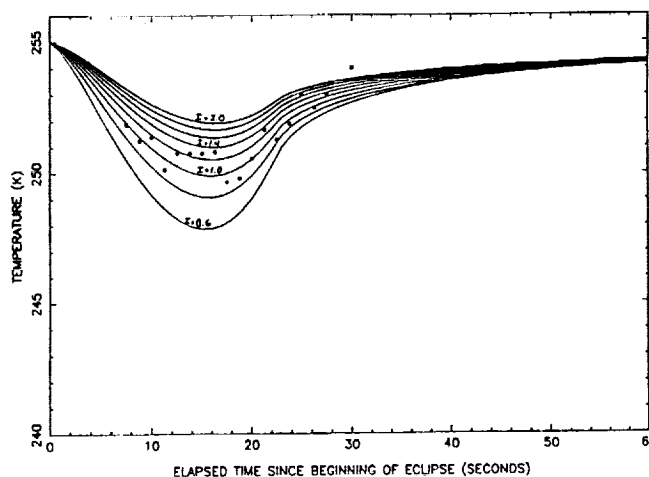


Figure 2: The lines in this plot are model surface temperatures for various thermal inertias (from 0.6 to 1.3). This model run used a downward atmospheric flux of 10% of the absorbed pre-eclipse solar flux. The dots are experimental data retrieved from thermal infrared channel. They are derived from 10 line averages of temperature drops at the center of the shadow relative to comparable points outside the shadow. The temperature drops have been subtracted from 255 K to facilitate comparison with our model results. We chose 255 K for the model because it is a typical temperature from the region surrounding the shadow. Most of the experimental data values fall between model curves corresponding to thermal inertias of 0.90 to 1.35 (in units of $10^{-3} \text{ cal cm}^{-2} \text{ s}^{-1/2} \text{ K}^{-1}$).

MAGELLAN LOS GRAVITY OF VENUS PLAINS REGIONS: LITHOSPHERIC PROPERTIES. AND IMPLICATIONS FOR GLOBAL TECTONICS. D.L. Bindshadler, Dept. Earth and Space Sciences, University of California, Los Angeles, CA 90024-1567, bindsch@mgnvax.ess.ucla.edu

Although the plains of Venus represent over 70% of the surface area of the planet, they have remained largely unstudied. These regions are an important constraint on models for Venus tectonics. "Catastrophic" models postulate that Venus' plains were resurfaced ~500 million years ago [1], while "steady-state" models imply a spectrum of ages for plains [2]. With regards to the plains, one can identify two end-member possibilities. In the first, the plains are tectonically homogeneous and at approximate thermal equilibrium with the interior. Such a scenario might arise, for example, as the result of a catastrophic overturn of the Venus mantle [3] and subsequent resurfacing. In the second, they are tectonically diverse regions characterized by a complex loading history, and may be significantly heterogeneous with respect to thermal gradient and apparent elastic thickness. This latter possibility would tend to suggest a more protracted period of Venusian tectonics. In addition, lowlands with relatively large negative gravity anomalies have been suggested to be regions of mantle downwelling [4]. The high spatial resolution of Magellan altimetry and line of sight (LOS) gravity data can be used to test these hypotheses for Venus' plains regions. Initial results for the Rusalka Planitia region (10°S - 15°N, 155°-180°E; north of Central Aphrodite Terra) include a best-fit apparent depth of compensation of 135 ± 38 km and very low coherence of gravity and topography at spatial wavelengths less than ~700 km. Preliminary analysis suggests that the effective elastic thickness of the lithosphere in this region is large, perhaps more than 40 km. The large ADC is primarily an expression of the longest wavelengths in gravity and topography and suggests either a very thick thermal lithosphere, or dynamic support of long-wavelength topography by mantle downwelling.

LOS gravity data are obtained from Magellan via two-way coherent Doppler tracking of the spacecraft by Deep Space Network stations [5]. To obtain the highest possible spatial resolution, LOS anomalies are used to model the vertical gravity field over localized regions of Venus using a linear inversion technique made available by R.J. Phillips and R.E. Grimm. Once a suitable solution for the local vertical gravity is obtained, the relationships between gravity and topography can be examined in both the spatial and spectral domains. In the spectral domain, both admittance and coherence of gravity and topography are calculated [6] and can be compared to simple models of lithospheric and crustal properties (e.g., Airy isostatic or elastic flexure models).

As part of the initial analysis of Magellan gravity data, I am studying the gravity and topography of several lowland plains regions. Results obtained for Rusalka Planitia show a substantial negative gravity anomaly (Fig. 1) associated with the topographic low, a large apparent depth of compensation (135 ± 38 km), and very low coherence of gravity and topography at wavelengths less than ~700 km (Fig. 2.). A lack of coherence at these long wavelengths is suggestive of a strong elastic lithosphere, comparable in strength to old oceanic lithosphere on Earth. Values of spectral admittance between gravity and topography shows that an Airy model based on the ADC estimate overpredicts gravity at all but the longest wavelengths ($> \sim 1000$ km). This is consistent with a model in which there is downwelling convective flow at long wavelengths beneath the plains lithosphere, as well as shorter-wavelength loads emplaced at the surface and/or on an intra-lithospheric density interface such as a Venus Moho. If similar results are obtained for the other plains regions under study, this would tend to support more "catastrophic" models of plains formation.

Following the approach of Forsyth [6] and coworkers [7], it may also be possible to confirm the presence of a mantle downwelling and to place constraints on its physical properties. Current efforts are focused on obtaining estimates of lithospheric thickness and producing local inversions for a number of plains regions. Results of analysis of Rusalka Planitia and of other near-equatorial plains regions (including parts of Guinevere, Aino, Niobe, and possibly Navka Planitiae) will be presented in March.

References: [1] Schaber, G.G., *et al.*, (1992), *J. Geophys. Res.* **97**, 13, 257-13,302. [2] Phillips, R.J., *et al.*, (1992) *J. Geophys. Res.* **97**, 15,923-15,948. [3] Parmentier, E.M., and P.C. Hess, (1992), *Geophys. Res. Lett.* **19**, 2015-2018. [4] Bindshadler, D.L., *et al.*, (1990) *Geophys. Res. Lett.* **17**, 1345-1348; Bindshadler, D.L., *et al.*, (1992) *J. Geophys. Res.* **97**, 13,495-13,532; Phillips, R.J., *et al.*, (1991), *Science* **252**, 651-658. [5] Konopliv, A.S., *et al.*, (1993), *Geophys. Res. Lett.* **20**, 2403-2406. [6] Forsyth, D.W., (1985), *J. Geophys. Res.* **90**, 12623-12632. [7] Bechtel, T.D., *et al.*, (1987), *Geophys. J. R. astr. Soc.* **90**, 445-465; Zuber, M.T., *et al.*, (1989), *J. Geophys. Res.* **94**, 9353-9367.

LOS GRAVITY OF VENUS PLAINS

Bindschadler, D.L.

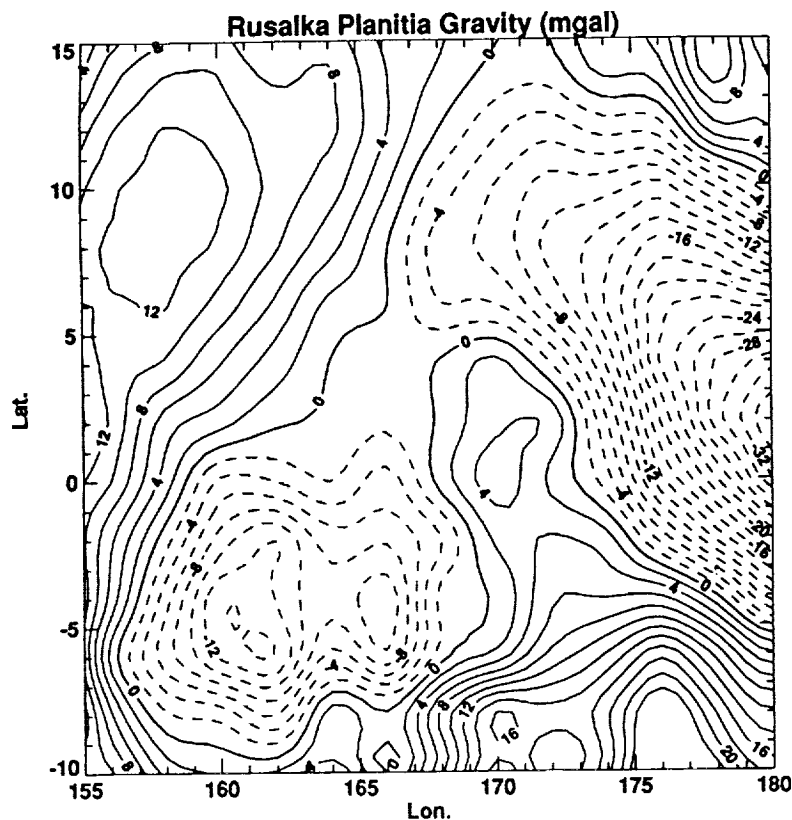


(Fig. 1) Contours of vertical gravity at an altitude of 250 km above the surface as obtained from inversion of LOS data. Contour interval is 2 mgal. Negative contours are dashed.

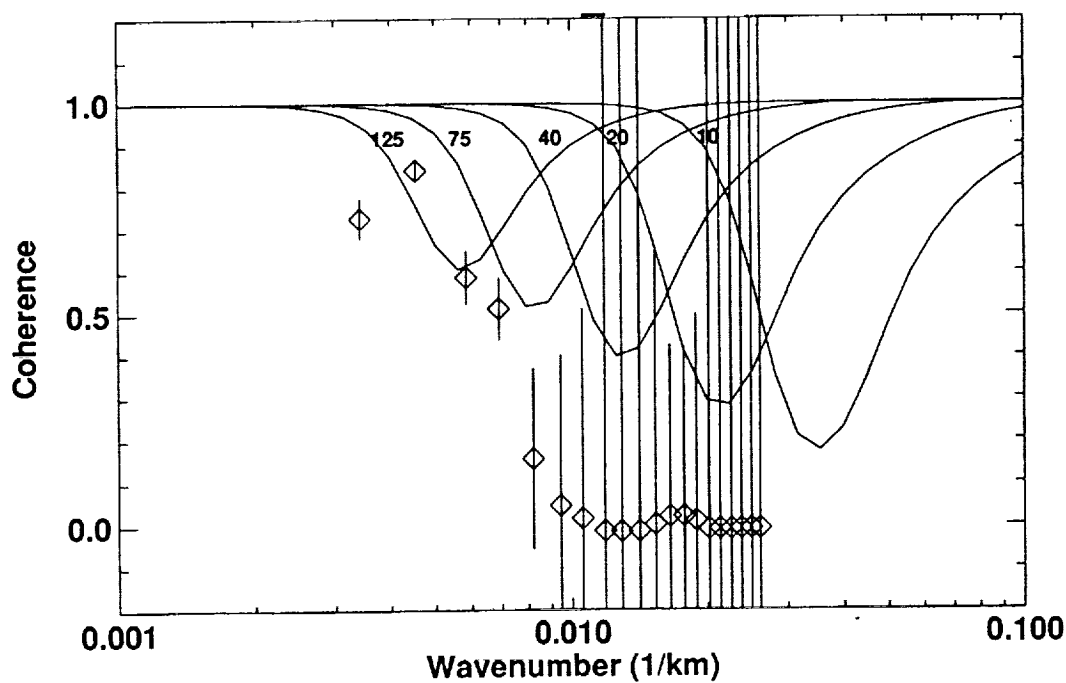


(Fig. 2) Free-air coherence of gravity and topography. Solid lines are theoretical curves for elastic plates of varying thickness (10-125 km) with loading equally partitioned between the top and bottom of the plate. They provide a poor fit to observations and are included solely for reference. Incoherence at wavelengths < 700 km suggests a thick elastic lithosphere.

THE UNIQUE CARBONACEOUS CHONDRITE ACFER 094: THE FIRST CM3 CHONDRITE (?) A. Bischoff and T. Geiger, Institut für Planetologie, Wilhelm-Klemm-Str. 10, 48149 Münster, Germany.

Acfer 094 is a small sample (82 grams) recovered from the Sahara and has recently been classified as a CO(CM)-chondrite [1,2]. Based on chemical and mineralogical investigations and isotope studies Acfer 094 can be characterized as follows: The sample has trace element characteristics of a CM2-meteorite [1,3], but the oxygen isotopes are very different to that of CM2-chondrites and are more closely related to the CO-samples [1]. Initial stable isotope studies indicate that Acfer 094 contains isotopically anomalous carbon and nitrogen [4]. Mineralogically, Acfer 094 is a breccia consisting of abundant chondrules (mean chondrule diameter: 165 μm), olivine aggregates, Ca,Al-rich inclusions, and fragments embedded in an extremely fine-grained, sulfide-rich groundmass [5,6]. Most chondrules contain Fa-poor olivine ($\text{Fa}_{<2}$), but olivines in the matrix exist having a broad peak at Fa_{37-50} (Fig. 1). These latter grains (usually <5 μm in size) appear somewhat clastic and are different in appearance to matrix olivines known for example from Allende. A significant abundance of phyllosilicates like in CM2 chondrites can be ruled out [5,6]. It is suggested that Acfer 094 is a CM3 chondrite.

Discussion

About 63 vol.% of Acfer 094 are fine-grained materials (<50 μm in size [6]). From CO3 chondrites it is known that the average matrix abundance is 33.7 vol.% [7]. The abundances of fine-grained components in CM2 chondrites is about 70 vol.% [8,9]. Comparing the data of Acfer 094 with those of CO and CM chondrites it is obvious that Acfer 094 is more closely related to CM chondrites.

This is also the case by comparing the abundances of various chondrule types. Porphyritic chondrules (POP, PO, PP) together contribute about 90% of the chondrules; 2% of barred-olivine chondrules occur. The percentage of the nonporphyritic radial-pyroxene/cryptocrystalline (RP/C) chondrules (about 8%) is certainly higher in Acfer 094 than reported for CO-chondrites (2-3% [10,11]). The abundance of non-porphyritic chondrules is similar to that of CM-chondrites (3-8% [10]).

Based on defocused-beam microprobe analyses of the bulk matrix of Acfer 094 we rule out the occurrence of significant portions of phyllosilicates, since high totals were obtained (typically 90 wt%), although the matrix shows some porosity. This clearly does not speak for a type 2 chondrite. Although the matrix is extremely fine-grained it is suggested that olivine and pyroxene (and not phyllosilicates) are the most abundant phases. Based on the fact that a broad peak between 37 and about 50 mol% Fa in the olivine distribution exists (please note that there is only one peak (at Fo-rich olivines) in the distribution of olivines from chondrules; Fig. 1) it is suggested that the matrix olivines belong to an own primitive matrix component, similarly to matrix olivines in CV and CO chondrites [5,12]. These results are clearly consistent with type 3 chondrites.

Formation and evolution of the Acfer 094 parent body

The Acfer 094 precursor material was formed in a reservoir of the solar nebula that was chemically similar to that, where the components of the CM2 chondrites derived from; however, the formation and evolution process of the parent body was different from that of the CM2 chondrites. Based on observations of Metzler et al. [9] major precursor materials of the CM2 chondrites were affected by aqueous alteration processes in the nebula or on relatively small and uncompacted pre-existing precursor planetesimals, that were destroyed and dispersed, prior to the accretion of dust mantles and CM2 parent body formation. In the case of the precursor components of the Acfer 094 parent body this aqueous alteration process did not take place to such an extent (if at all) as found in the CM2 chondrites. Based on the existence of probably anhydrous accretionary dust mantles around chondrules it is clear that no major aqueous processing occurred prior to accretion. Also, significant aqueous activity on a meteorite parent

ACFER 094: THE FIRST CM3 CHONDRITE (?): Bischoff A. and Geiger T.

body can be ruled out. However, the parent body of Acfer 094 was affected by heavy impact activities. This is indicated by the brecciated nature of the chondrite, the abundant clastic matrix, the lack of fragments of primary accretionary rock [9], and the loss of accretionary dust mantles around many coarse-grained components.

Acfer 094 has an oxygen isotope composition, which is similar to that of type 3 carbonaceous chondrites basically consisting of anhydrous minerals. The bulk rock lies somewhat below (probably due to some terrestrial weathering processes) the mixing line AM of Clayton and Mayeda [13] connecting a weighted mean of the oxygen isotopic composition of anhydrous silicates (A) and the matrix composition of Murchison (M). Clayton and Mayeda [13] assumed that the isotopic composition of CM2 chondrites could be established by reactions of anhydrous silicates with a liquid rich in ^{18}O and ^{17}O . In the case of Acfer 094 reactions of this kind (or with a gas) were not as significant as it was the case for the CM2 chondrites. Therefore, Acfer 094 might be a primitive CM chondrite, whose components escaped major hydrous processes in the solar nebula or on small preexisting parent planetesimals. Acfer 094 may be the first CM3 chondrite.

References:

- [1] Bischoff et al. (1991), *Meteoritics* 26, 318-319. [2] Wlotzka (1991) *The Meteoritical Bulletin*, *Meteoritics* 26, 255-262. [3] Spettel et al. (1992), *Meteoritics* 27, 290-291. [4] Newton et al. (1992), *Meteoritics* 27, 267-268. [5] Geiger and Bischoff (1992), *Meteoritics* 27, 223. [6] Newton et al. (1994), *Meteoritics* (in preparation). [7] McSween (1977), *Geochim. Cosmochim. Acta* 41, 477-491. [8] McSween (1979), *Geophys. Space Phys.* 17, 1059-1078. [9] Metzler et al. (1992), *Geochim. Cosmochim. Acta* 56, 2873-2897. [10] Grossman et al. (1988), in "Meteorites and the Early Solar System", (eds. J.F. Kerridge and M.S. Matthews), 619-659, Univ. Arizona Press, Tucson. [11] Rubin (1989), *Meteoritics* 24, 179-189. [12] Scott et al. (1988), in "Meteorites and the Early Solar System" (eds. J.F. Kerridge and M.S. Matthews), 718-745, Univ. Arizona Press, Tucson. [13] Clayton and Mayeda (1984), *Earth Planet. Sci. Lett.* 67, 151-161.

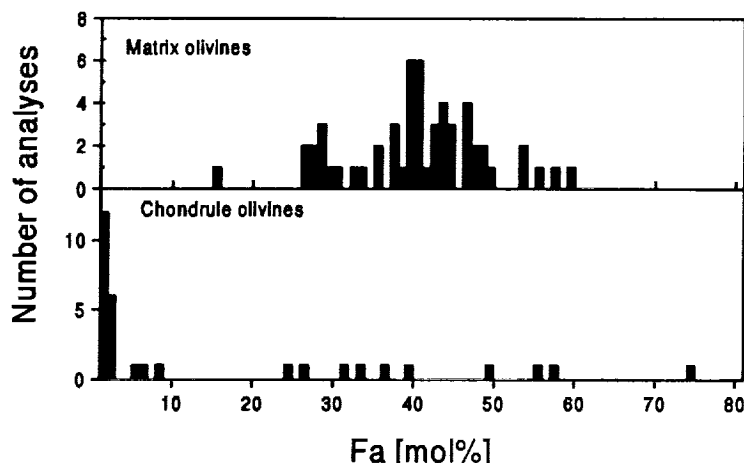


Fig. 1: The composition of olivines within chondrules and matrix of Acfer 094.

REFLECTANCE SPECTRA OF MARS SOIL ANALOGS MEASURED UNDER REDUCED ATMOSPHERIC PRESSURES AND TEMPERATURES; Janice L. Bishop and Carlé M. Pieters;
Departments of Chemistry and Geological Sciences, Brown University, Providence, RI 02912.

Reflectance spectra of Mars soil analogs measured under reduced temperatures and pressures are presented here. It is important to study analogs of soils on other planets under conditions representative of that planet, since soils are sensitive to their chemical and physical environment. Moisture in soils is responsible for prominent water features that hinder identification of mineral features in reflectance spectra measured under ambient conditions on Earth. The experiments presented here encompass atmospheric pressures ranging from one bar to about 10^{-5} bar, and temperatures ranging from 23 °C to about -50 °C. The analog materials used in these experiments include ferrihydrite-bearing montmorillonites, ferric sulfate-bearing montmorillonites and ferrihydrite prepared in the laboratory, as well as palagonitic soil from Haleakala crater, Maui. Each of these samples exhibit spectral changes at 1.9 μm , 2.7 - 4 μm and 6 μm due to loss of adsorbed water as a result of lowering the pressure and the temperature of the sample environment.

Introduction. Spectral experiments on particulate, ferric-containing analogs to Martian soil (Fe^{3+} -doped smectites and palagonites) have been performed to facilitate interpretation of remotely acquired spectra. Spectroscopic analyses in the visible to near infrared have shown that ferrihydrite-bearing montmorillonites prepared in the laboratory exhibit important similarities to the soils on Mars[1]. The chemical composition and visible to infrared reflectance spectra of montmorillonites containing ferric sulfate compare well with the surface material on Mars. These analogs are especially promising because of the shape of the visible features and the strength of the 3 μm band[2]. Spectral measurement of palagonitic soils indicate that these are also good Mars soil analog candidates[3,4]. Each of these materials contains structural OH bonded to metal cations, adsorbed H_2O , and bound H_2O .

Previous experiments involving a variety of Mars analogs under differing environmental conditions have examined the influence of exposure history on water content and absorption features due to H_2O [5,6]. These experiments have shown that reflectance spectra of ferrihydrite, montmorillonites doped with ferric sulfate, and palagonitic soils contain sufficient bound H_2O to retain a strong 3 μm band under dry conditions, which is similar to that observed in spectra of Mars.

When the effects of the environment on bound water in clays, oxides and salts are understood, the hydration bands measured via reflectance spectroscopy can be used to gain information about the chemical composition and moisture content of real soil systems. Such information is especially useful in interpreting observations of Mars where subtle spatial variations in the strengths of cation-OH and H_2O absorptions have been observed in telescopic [7] and ISM [8,9] spectra.

Methods. Infrared reflectance spectra were measured in these experiments using a Nicolet 740 FTIR, and attachments from Specac and Connecticut Instruments. This system allows spectral measurements to be made of particulate samples under a controlled atmospheric environment down to pressures of 10^{-3} torr and temperatures, currently, to about -50 °C.

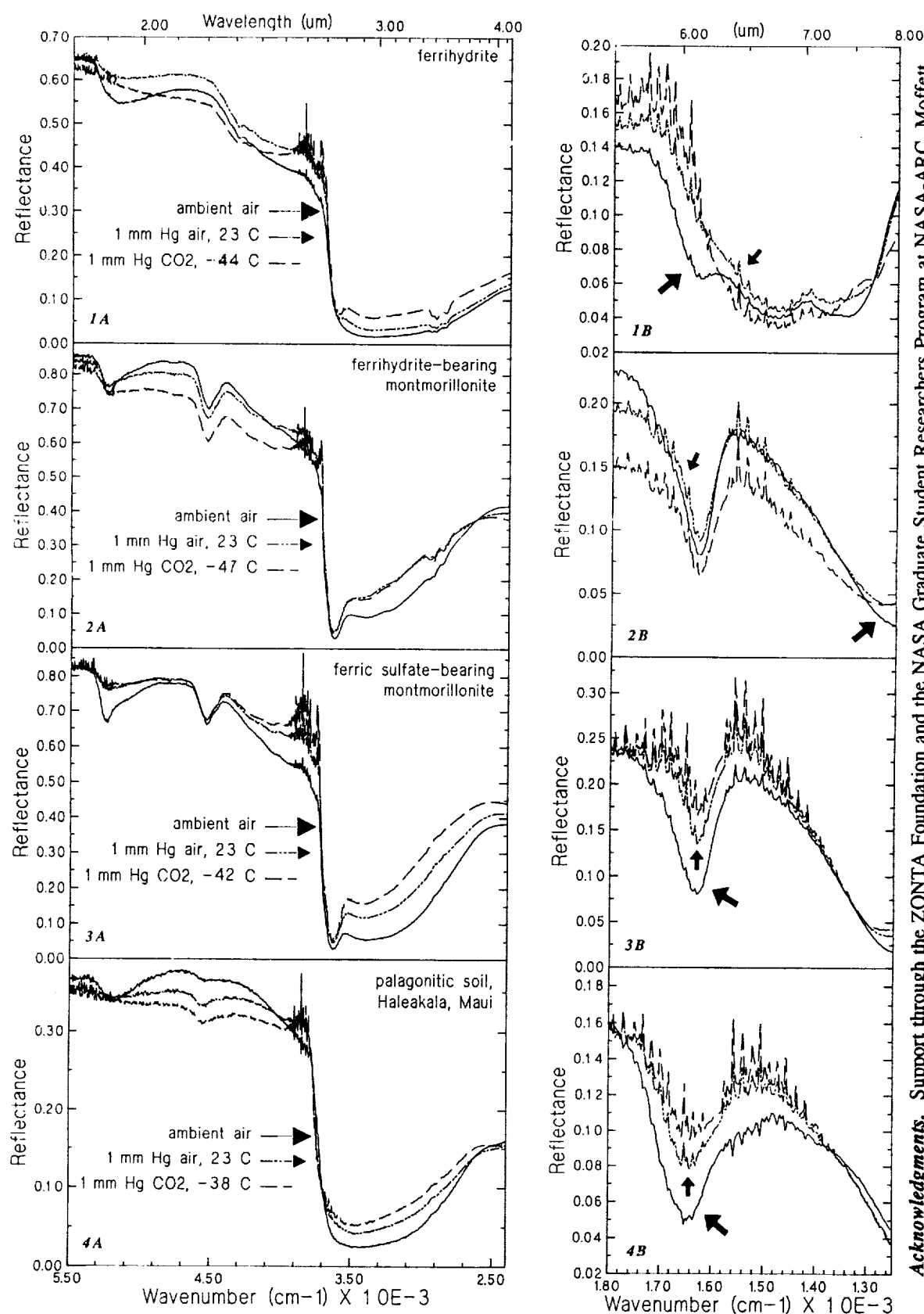
Results and Discussion. Reflectance spectra are shown from 5500 cm^{-1} to 2500 cm^{-1} (1.8 - 4 μm) in Figures 1A, 2A, 3A and 4A of ferrihydrite, ferrihydrite-bearing montmorillonite, ferric sulfate-bearing montmorillonite and palagonitic soil, respectively. In each figure the solid line is the spectrum measured under an ambient pressure and temperature environment, the patterned line is the spectrum measured under ambient temperature and about 1 mm Hg air pressure, the dashed line is the spectrum measured under about -40 °C and about 1 mm Hg CO_2 pressure. These spectra have not been smoothed and exhibit atmospheric water features due to difficulties in calibrating the decrease in H_2O molecules in the pathlength. Spectral changes observed for these samples under reduced pressures and temperatures include: (i) the feature near 1.9 μm in these spectra becomes weaker and appears to broaden toward longer wavelengths, (ii) a weak broad band associated with H_2O near 2.4 μm is reduced in intensity and allows better resolution of the cation-OH features in the 2.2 - 2.5 μm region and (iii) the intensity of the strong broad 3 μm band decreases especially near 3.2 μm and sharpens near 2.75 μm (structural OH) and near 2.95 μm (bound H_2O).

Reflectance spectra are shown from 1800 cm^{-1} to 1250 cm^{-1} (5.5 - 8 μm) in Figures 1B, 2B, 3B and 4B as in the previous figures. The spectra of ferrihydrite in Figure 1B exhibit a decrease in intensity near 6 μm and a sharpening of the weak features near 7.25 μm and 7.75 μm under reduced temperature and pressure conditions. The spectra of the ferrihydrite-bearing montmorillonite, the ferric sulfate-bearing montmorillonite and the palagonitic soil show a decrease in intensity near 6 μm as the temperature and pressure are reduced. A slight shift in the Christiansen feature toward shorter wavelengths under reduced temperatures and pressures is also observed.

Conclusions. Reflectance spectra of selected Mars soil analogs under low temperature and pressure environments have shown changes in the character of a number of spectral features. Under ambient temperature and pressure conditions adsorbed water in and on particulate samples is responsible for many broad spectral absorptions. Removing these adsorbed water molecules by examining Mars analog soils under reduced temperatures and pressures allows the measurement of infrared spectra that more accurately resemble infrared spectra of these samples in a Martian environment.

References. [1] Bishop J., Pieters C. & Burns R. (1993) *GCA* 57, 4583. [2] Bishop J., Pieters C. & Burns R. (1993) *MSATT, LPI Tech. Rpt. 93-06*, 6. [3] Singer (1982) *JGR* 87, 10159. [4] Morris *et al.* (1990) *JGR* 95, 14427. [5] Murchie S. *et al.* (1992) *LPSC XXII*, 941. [6] Bishop J. *et al.* (1993) *MSATT, LPI Tech. Rpt. 93-06*, 4. [7] Bell J. & Crisp D. (1993) *Icarus* 104, 2. [8] Arnold G. (1992) *DLR-Nachrichten* 69, 25. [9] Murchie S. *et al.* (1993) *Icarus* 105, 454.

Reflectance Spectra (low P, T) of Mars Soil Analogs: Bishop J. L. & Pieters C. M.



Acknowledgments. Support through the ZONTA Foundation and the NASA Graduate Student Researchers Program at NASA-ARC, Moffett Field, is greatly appreciated by J. Bishop. NASA support for this research under grant NAGW-28 is gratefully acknowledged by C. Pieters. RELAB is a multi-user facility supported by NASA under grant NAGW-748. The Nicolet system was funded under a grant from the Keck Foundation.

SPECTROSCOPIC AND GEOCHEMICAL ANALYSES OF SEDIMENTS FROM LAKE HOARE, ANTARCTICA AND APPLICATIONS TO DRY VALLEYS ON MARS; *Janice L. Bishop¹, Peter A. J. Engler², David W. Andersen², Claudia Kralik³, Christian Koeberl³, Carlé M. Pieters¹, Heinz Froeschl⁴ and Robert A. Wharton, Jr.⁵* ¹Brown University, Providence, RI; ²San Jose State University, San Jose, CA; ³Institute for Geochemistry, University of Vienna, Vienna, Austria; ⁴Universität für Bodenkultur, Vienna, Austria; ⁵Desert Research Institute, University of Nevada, Reno, NV.

The sedimentary records from ice-covered lakes in the Antarctic dry valleys may provide information about sedimentation in the dry valley regions on Mars, where ice-covered lakes may have existed in the past. Antarctic lake bottom sediments have been examined using reflectance spectroscopy and neutron activation analysis to study sedimentation processes in the dry valleys. Sediment cores were sampled from three locations (two aerobic, one anaerobic) in Lake Hoare, a perennially ice-covered lake in the Taylor Valley (77 °S, 162 °E). Organic material was found at the surface of each core. Thin layers of organic and carbonate-rich mats were also found dispersed throughout the cores. The core sediments are comprised of quartz, feldspar, polycrystalline rock fragments and monocrystalline accessory minerals. Na/K ratios and Sc concentrations are nearly constant for all of the samples measured. Variations in the Fe, Zn and Sr levels indicate non-uniform sedimentation processes. Quartz, pyroxenes, clays, carbonates and organic materials have been identified in the sediments from reflectance spectra. The reflectance spectra indicate diversity in the dominant mineralogy as a function of depth in the cores. Variation in the quartz grain size is also observed throughout the cores; organic-rich layers have very fine quartz particles and other sand layers have quartz grain sizes on the order of 100 µm or larger.

Introduction. Perennially ice-covered lakes exhibit important differences from non-ice-covered lakes, such as the presence of coarse sand in the center of the lake[1]. Studying lake bottom samples from the dry valleys in Antarctica provides information about sedimentation that may be relevant to understanding soils on Mars. Geophysical evidence on the surface of Mars indicates the presence of water there at one time[2]. Ice-covered lakes may have formed as the planet cooled and sediments exposed from these lakes may be contributing to the current surface material on Mars. The sedimentary record also bears information about former climates on Earth and thus, understanding sedimentary records for Mars-like lakes in Antarctica might lead to climatic information about Mars as well[3].

Sedimentation patterns developed for Lake Hoare, Taylor Valley, Antarctica, are based on mineralogical and grain size analyses of sediment cores from the lake bottom and of material collected in sediment traps in the lake, as well as on observations of sediments in the ice sheet[1,4,5]. These studies suggest that the lake bottom sediments are similar to the sediment found on top of the ice cover and the dominant means of transport is via sediment percolation from meltwater pools. Fine-grained sediment and organic material is thought to deposit slowly and continuously across the lake bottom. Sudden and localized deposition of coarser-sized sediment occurs through cracks in the ice or bubble channels.

The samples employed in these studies were collected in cores from aerobic (DH-1, DH-2) and anaerobic (DH-4) regions of the lake. The locations of these dive holes are described in[1]. The frozen cores were carefully melted and separated by sediment layers. Organic mat layers were found near the top of each core. Some cores contained organics intermixed with sediments at depth as well. The sediments from the aerobic lake regions are cream to tan colored, while those from the anaerobic region are a darker gray-green color.

Grain Size and Mineralogy. The sediments range from fine- to coarse-grained sand that is subquartzose with variable mineral contents. An average sample contains roughly equal amounts of quartz, feldspar, polycrystalline rock fragments (mostly felsic plutonic rocks with lesser amounts of mafic volcanics and metamorphic rocks), and monocrystalline accessory minerals (mostly orthopyroxene and clinopyroxene with variable amounts of biotite, chlorite, olivine and hornblende). The rock fragment percentage increases with increasing grain size, while the abundance of the accessories decreases with increasing grain size.

Some samples contain both sand and microbial mat. These samples have organic matter and biogenic carbonate with varying amounts of terrigenous sediment. Sand within the mat layers resembles the sand samples described above. Suspended silt and clay are most abundant in samples with the highest organic-matter content, suggesting slow sediment accumulation rates for these samples[1].

Geochemistry. A preliminary study of another DH-2 core showed variability in some major and minor elements throughout the core[6]. The elements Al, Sc, Fe, Zn and Cu exhibit variable concentrations in Antarctic lakes due to precipitation out of the lake water into the sediment and other processes taking place at the sediment-water interface[7]. In the cores examined here Sc levels remain constant near 20 ppm, and Fe and Zn concentrations vary by about a factor of two, but tend to parallel each other.

Snow contains small quantities of salts (Na⁺, Ca²⁺, Mg²⁺, K⁺, Cl⁻ and SO₄²⁻), which influence the salt composition of soils[8]. Salt fractionation is controlled by relative humidity and other properties of the salts, such that the least deliquescent salts will remain in the soil and the more deliquescent will percolate through the soil to the ice-cemented layer[8]. Analyses of Na, Ca, Mg, K, Cl and S in the cores are underway to assess whether these salts vary with either depth in the core or sediment grain size. Na/K ratios exhibit little variation within and among the cores examined in this study.

A decrease in Sr concentration was observed in water near the bottom of Lake Bonney (also located in the Taylor Valley), indicating precipitation of a Sr-bearing phase in the lake-bottom sediments[9]. Sr concentrations vary

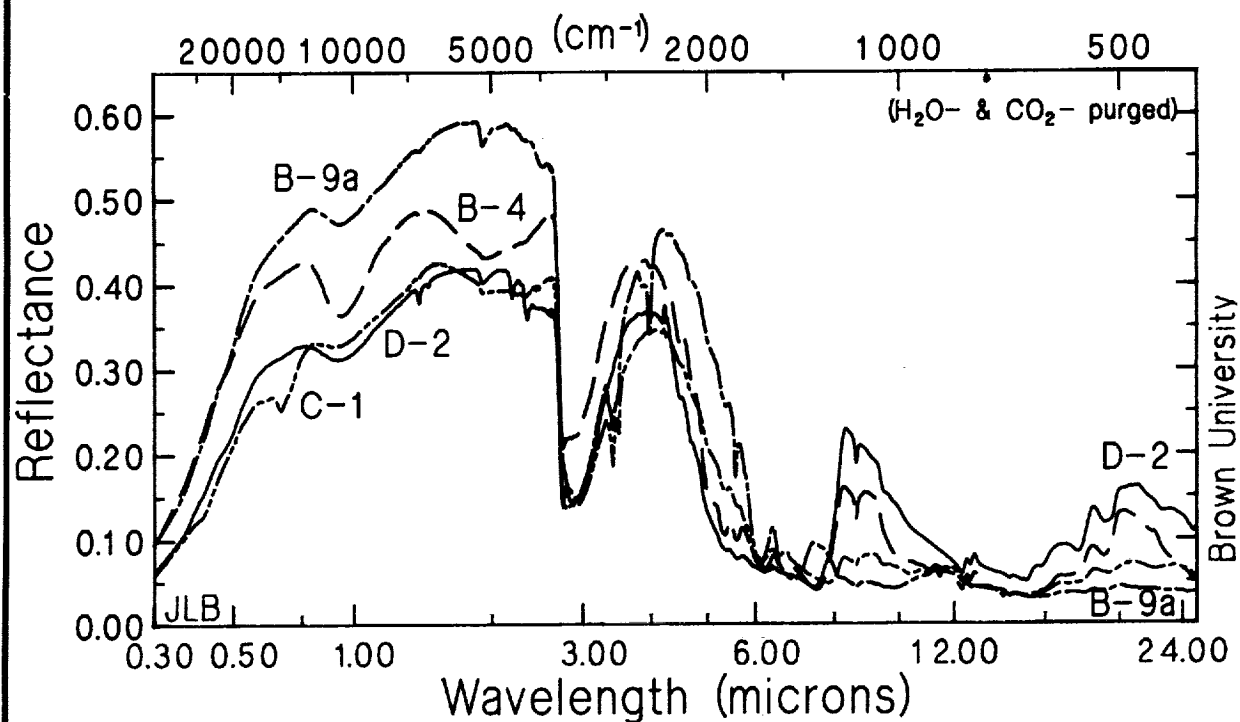
Spectroscopic and Geochemical Analyses of Antarctic Sediments: Bishop J. L. et al.

between 250 and 400 ppm in samples from core C (DH-4), and between 350 and 500 ppm in samples from core D (DH-1); however, core B (DH-2) shows a much broader range of Sr values including a high of 357 ppm in the surface sediment, a gradual decrease to a low of 11 ppm at 11-12 cm and a high of 326 ppm again at 28 cm depth. In core B the surface organic layer has only 75 ppm Sr, while some -1 mm thick organic layers have over 500 ppm Sr.

Reflectance Spectroscopy. Reflectance spectra indicate the presence of quartz, pyroxenes, clays, carbonates and organic materials in these sediments. Interpreting spectral data of soils is complicated because soils composed of multiple materials mix non-linearly and the spectral properties depend on the particle size distributions of the soil components and the manner in which the components are mixed in the soil, as well as the spectral properties of the individual components. Spectroscopic experiments involving mixtures of variable grain size separates of pyroxenes and olivine have shown that soils containing a higher abundance of small particles exhibit spectral properties dominated by the mineral having the small particle sizes; however, soils containing a higher abundance of larger particles exhibit spectral properties less directly related to one mineral [10,11].

Figure 1 includes reflectance spectra from 0.3 to 25 μm of samples B-4, B-9a, C-1 and D-2, which exhibit a number of different spectral features. The spectrum of sample B-4 includes strong pyroxene features in the near infrared at 1 μm and 2 μm , no indication of organic features at 3.4 μm or 6 μm and strong features due to quartz from 5 to 10 μm . Sample B-9a exhibits spectral features indicating a dominance of very fine-grained quartz and organics in the sediment, as well as smaller amounts of montmorillonite and carbonates. Many of the core C samples, from the anaerobic zone, show an absorption near 0.7 μm , which is similar to that found in vegetation. This is likely to be due to the algal mats observed dispersed throughout the core. This feature is most pronounced in the spectrum of sample C-1; also present in this spectrum are pyroxene features at 1 μm and 2 μm , strong organic features at 3.4 μm and 6 μm , and strong features due to fine-grained quartz from 5 to 10 μm . The spectrum of D-2 exhibits an absorption near 1 μm , but no absorption near 2 μm ; this spectrum also exhibits the strong near infrared montmorillonite and carbonate features, as well as features due to quartz in the mid-range infrared.

Figure 1: Reflectance Spectra (0.3 to 25 μm) of Lake Hoare Sediments, Antarctica.



Acknowledgments. The authors wish to thank J. Mustard for assistance in interpreting the spectral features. Support from the ZONTA Foundation and the NASA Graduate Student Researchers Program at NASA-ARC, Moffett Field, is greatly appreciated by J. Bishop. NASA support for this research under grant NAGW-28 is gratefully acknowledged by C. Pieters. RELAB is a multi-user facility supported by NASA under grant NAGW-748. The Nicolet system was funded under a grant from the Keck Foundation. This project was in part made possible by funding from the University of Vienna to P. Englert. Support is also acknowledged from NSF (OPP-9211773) and NASA (NCA2-799, NAGW-1947) to R. Wharton.

References. [1] Andersen D., Wharton R., Jr. & Squyres S. (1993) in *Phys. Biogeochem. Proc. Antarc. Lakes, Antarctic Research Series* 59, 71. [2] Carr M. (1981) *The Surface of Mars*. [3] Wharton R., Jr. et al. (1992) *J.G.R.* 97, 3503. [4] Nedell S. et al. (1987) *Sedimentology* 34, 1093. [5] Squyres S. et al. (1991) *Sedimentology* 38, 363. [6] Bishop J. et al. (1990) *LPSC XXI*, 91. [7] Masuda N., Nishimura M. & Torii T. (1982) *Nature* 298, 154. [8] Wilson A. (1981) in *Dry Valley Drilling Project, Antarctic Research Series*, ed. L. McGinnis. 33, 185. [9] Jones L. & Faure G. (1978) *Chem. Geol.* 22, 107. [10] Pieters C. et al. (1993) *LPSC XXIV*, 1147. [11] Mustard J. et al. (1993) *LPSC XXIV*, 1041.

513-91 ABS JULY
2953

P-2

A MINERALOGICAL INSTRUMENT FOR PLANETARY APPLICATIONS. David F. Blake,¹ David T. Vaniman² and David L. Bish² ¹Planetary Biology Branch, MS 239-4, NASA/Ames Research Center, Moffett Field, CA 94035-1000, ²EES-1, MS D462, Los Alamos National Laboratory, Los Alamos, NM 87545

The mineralogy of a planetary surface can be used to identify the provenance of soil or sediment and reveal the volcanic, metamorphic and/or sedimentological history of a particular region. We have discussed elsewhere the applications^{1,2} and the instrument design of possible X-ray diffraction and X-ray fluorescence (XRD/XRF) devices for the mineralogical characterization of planetary surfaces.³ In this abstract we evaluate some aspects of sample-detector geometry and sample collection strategies.

For XRD/XRF, the two X-ray photon - sample interactions of interest are coherent Bragg diffraction and X-ray fluorescence. In our prototype design, diffracted primary-beam X-rays and secondary fluorescence X-rays are detected by one or several X-ray sensitive CCD arrays operated in single-photon counting mode.⁴ A diffraction pattern can be generated by displaying an image made only of X-rays having the energy of the primary X-ray beam. An X-ray fluorescence analysis can be obtained by summing all of the X-rays recorded by the CCD which have energies lower than that of the primary beam into a multichannel analyzer.

In order to obtain an optimal angular dispersion for X-ray powder diffraction the CCD arrays may be arranged as shown in Figure 1 (edge and plan views). In this arrangement, the sample powder is collected on an adhesive tape that can be advanced for collection of subsequent samples. The tape mechanism can be rotated around the axis of the direct beam to improve particle statistics. The direct beam is allowed to pass through a narrow slit (0.126 cm) between a set of 1-cm 512 X 512 CCD arrays. These CCD arrays supply the "flat plate" for collection of the diffracted Cu radiation. In the geometry shown, the CCD plates are capable of covering the 2θ range from 4° to 50° , including most of the characteristic diffraction peaks for a broad range of mineral types (oxides, silicates, complex water-rich ices) that might be encountered on a range of extraterrestrial objects. For accurate analysis, particularly in quantitative studies of mineral mixtures, a pattern precision of 0.05° is desirable. In the edge-view configuration shown in Figure 1, the actual angular range encompassed by each pixel varies from $0.123^\circ 2\theta$ at pixel 1 to $0.052^\circ 2\theta$ at pixel 512. These precisions are acceptable for prototype work, but they can be easily cut in half - within the acceptable range for a highly accurate XRD instrument-by substituting 1024 X 1024 CCD arrays that are commercially available but rather expensive for prototype studies.

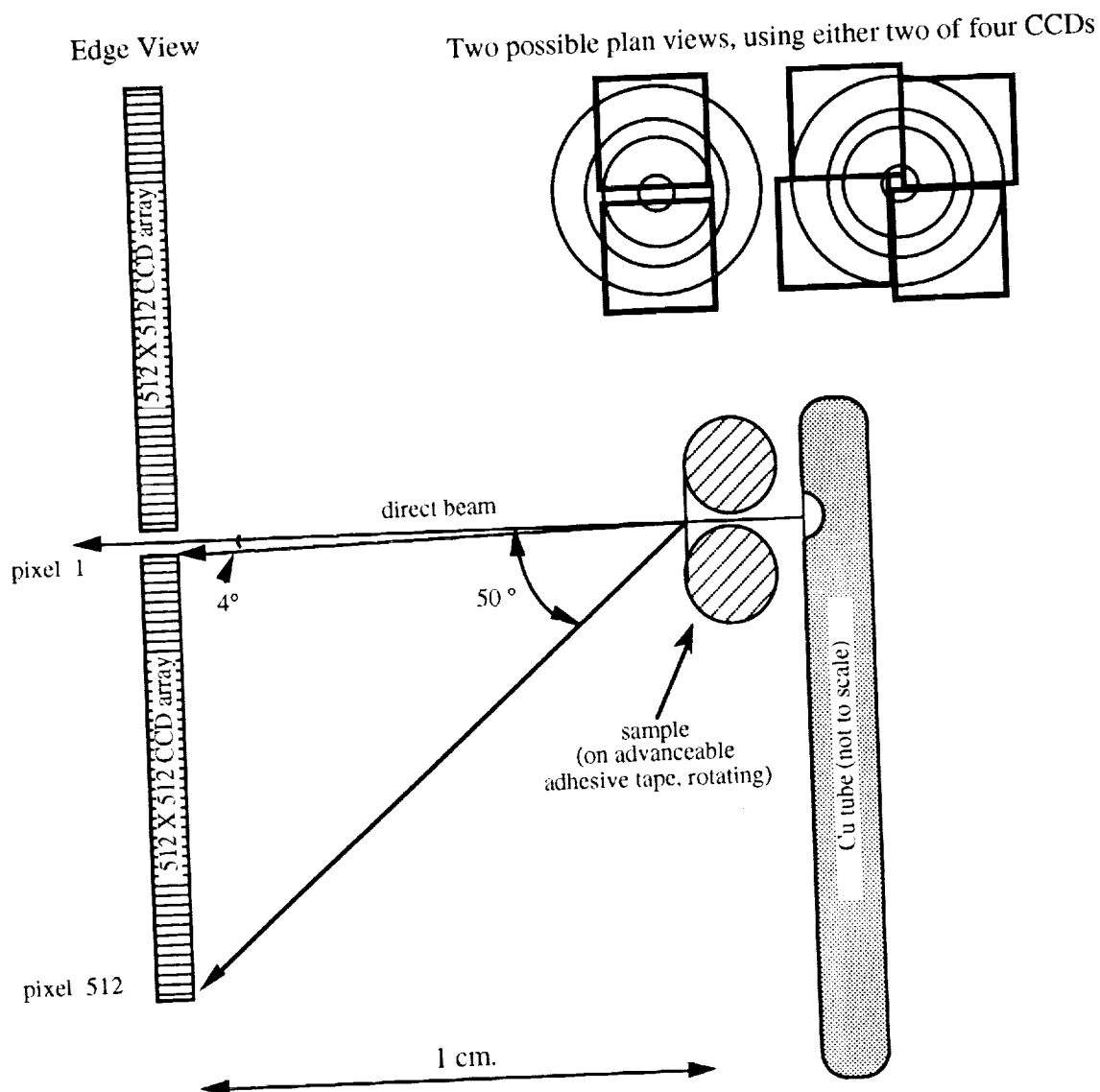
The flat-plate geometry presents some problems in XRD pattern interpretation because of the different solid angles subtended by each of the 262,144 pixels in a 512 X 512 array. However, the increasing angular resolution at higher 2θ makes this geometry attractive for small instrument applications. Commercial diffraction instrument manufacturers are currently working on software improvements that may facilitate the use of flat-plate geometries in XRD. With regard to data reduction, our goal is to develop applications of both determinative and quantitative Rietveld analysis⁵ that will make the optimal use of such geometries.

A critical aspect of instrument development is sample collection and manipulation. The option shown in Figure 1 is based on drum-fed adhesive tape mounted in a rotating sample head. The sample head can be swung away from the analysis position to be pressed against powders (from passive dust collectors, abrasive chucks or regolith surfaces). Disposable adhesive plates or fibers provide other options as sample holders. Many other sample acquisition systems are possible but the test of each must be ruggedness and simplicity. Since the XRD/XRF technique is non-destructive, the instrument is amenable to inclusion in a sequential analysis strategy in which the sample is passed on to another instrument after analysis.

XRD/XRF INSTRUMENT FOR PLANETARY APPLICATIONS: Blake, D.F. et al.

1. Vaniman, D.T., D.L. Bish and S.J. Chipera (1991). LPSC XXII, 1429-1430.
2. Vaniman, D.T., D.L. Bish and S.J. Chipera (1991). Clay Min. Soc. 28th Ann. Mtng., 157.
3. D.F. Blake, C. Bryson and F. Freund (1992). LPSC XXIII, 117-118.
4. Luppino, G.A. et al (1987). Optical Engineering 26 No. 10, 1048-1054.
5. Bish, D.I. and J.E. Post (1993). Am. Min., Vol. 78 Nos. 9-10, 932-940.

Figure 1. (insert, upper right) Plan view of two possible configurations of CCD detector arrays. The direction of view is directly down the X-ray beam path toward the detector array. A crystalline powder pattern is shown superimposed onto arrays using two and four detectors. The remainder of the figure shows an edge view of the instrument illustrating the diffraction angles subtended by the CCD arrays.



INFRARED SPECTROPHOTOMETRY OF IO BETWEEN 3 AND 13 μm IN 1993. D. L. Blaney*, M. S. Hanner*, Jet Propulsion Laboratory, California Institute of Technology, R. Russell*, D. Lynch*, and J. Hackwell* Aerospace Corp., *Visiting Scientist at the NASA Infrared Telescope Facility

Much remains unknown about the variability of Io's surface composition and volcanic activity. The 3 - 13 μm spectral region contains both reflected solar radiation that is sensitive to SO_2 frost and emission from volcanic thermal anomalies. We observed Io at the NASA Infrared Telescope Facility, Mauna Kea Hawaii on February 7 and 8, 1993 UT using the Aerospace Corp. liquid-He-cooled spectrograph covering the wavelength region 3-13 μm with a resolving power of 30-120. The instrument uses two 58-element Blocked Impurity Band (BIB) linear arrays and all spectral elements are observed simultaneously [1,2]. The primary standard was Alpha Boo. An absolute radiometric calibration based on Vega was made by using a spectrum of Alpha Boo / Vega provided by Martha Hanner from another observing run combined with the flux density from Vega [3]. The longitude ranges on Io covered were 225°-260° West longitude on February 7 (Trailing Hemisphere with the Loki Volcanic Center at 309°W) and 70°-105° West longitude on February 8 (Leading Hemisphere).

Thermal Emission Conclusions: The thermal emission from both hemispheres were of comparable magnitudes (see figure 1). On the leading hemisphere, the emission varied less than 2% on February 8. On the trailing hemisphere on February 7, the thermal emission increased throughout the night by roughly 30%. This rise is consistent with the expected increase caused by the volcanic region Loki increasing its observed area as it comes closer to the center of the disk. These values show a low level of activity at Loki, consistent with other observations of Io in 1992 and 1993. [4,5,6]

SO_2 Frost Conclusions: The absorption feature due to SO_2 frost is present at 4.08 μm (see figure 1). The band depth, measured using the ratio of the values at 3.47 μm (continuum) and at 4.08 μm (band minim), was roughly 50% on both the leading and trailing hemisphere and ranged between 45-55% in the regions measured (see figure 2). **The leading and trailing hemisphere SO_2 frost distribution differs from observations collected between 1976 and 1982** discussed in Howell et al. [7] (see figure 2). The spectra in Howell et al. [7] show almost a factor of 2 difference in the band strength between the leading hemisphere and the trailing hemisphere. Comparing the two sets of observations, the SO_2 frost distribution on the trailing hemisphere has changed dramatically between 1982 and 1993. Recent HST images [8] indicate that the gross albedo pattern caused by SO_2 frost has changed little since Voyager. However, Howell et al. concluded that the depth of the 4 μm feature requires regions other than the bright SO_2 frost deposits to have SO_2 frost or absorbate (i.e. the 4 μm feature is sensitive to optically thin deposits that aren't seen in the visible). Therefore, the infrared distribution of SO_2 frost may be variable even if the large bright frost deposits are stable. Io's volcanic activity is an obvious source of this variability. The relationship between volcanic activity and SO_2 frost distribution is unknown. The Howell et al. measurements have no long wavelength (8-12 μm) data collected contemporaneously so no statements can be made on volcanic activity. Additional observations with improved longitude and temporal coverage are needed. Part of this work was done at JPL/Caltech, under contract to NASA.

References : [1] Warren D.W. and Hackwell J.A., "A Compact Prism Spectrograph Suitable for Broadband Infrared Spectral Surveys with Array Detectors", SPIE, 1155, 314, 1989. [2] Hackwell et al., "A Low Resolution Array Spectrograph for the 2.9 -13.5 μm Spectral Region", Proc. SPIE Conf. 1235 on Instrumentation in Astronomy VII, 1990. [3] Rieke et al., "An absolute photometric system at 10 and 20 μm ", Astron. J., 90, 900, 1985. [4] Veeder et al., Io's heat flow from infrared radiometry: 1983-1993, submitted to JGR Planets, 1993. [5] Spencer, J.R. et al., Volcanic activity on Io at the time of the Ulysses encounter, *Science*, 257, 1507-1510, 1992. [6] Spencer, J.R., et al. Infrared imaging of Io: Volcanic activity 1989-1993, *Io: An International Conference*, (San Juan Capistrano, CA), 105-106, 1993. [7] Howell et al., "Sulfur Dioxide on Io: Spatial Distribution and Physical State, *Icarus*, 57, 82, 1984. [8] Sartoretti P. and M. McGrath, Disk-Resolving Imaging of Io with the HST. San Jan Capistrano Io Meeting, June, 1993

IO INFRARED SPECTROPHOTOMETRY: Blaney, D. L. et al.

Figure 1. The infrared spectra of Io between 3-13 μm . The turn down at 4.08 μm is caused by SO_2 frost or absorbate on the surface the rise in emission at longer wavelengths is caused by thermal anomalies due to tidal heating.

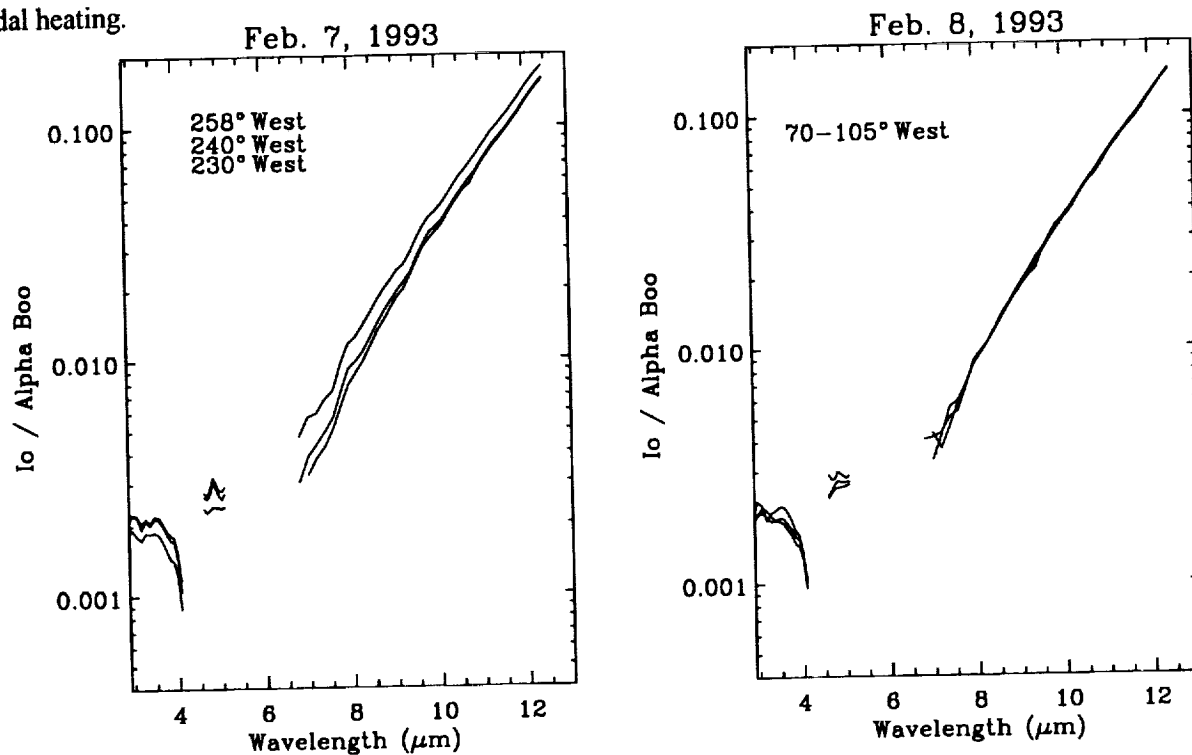
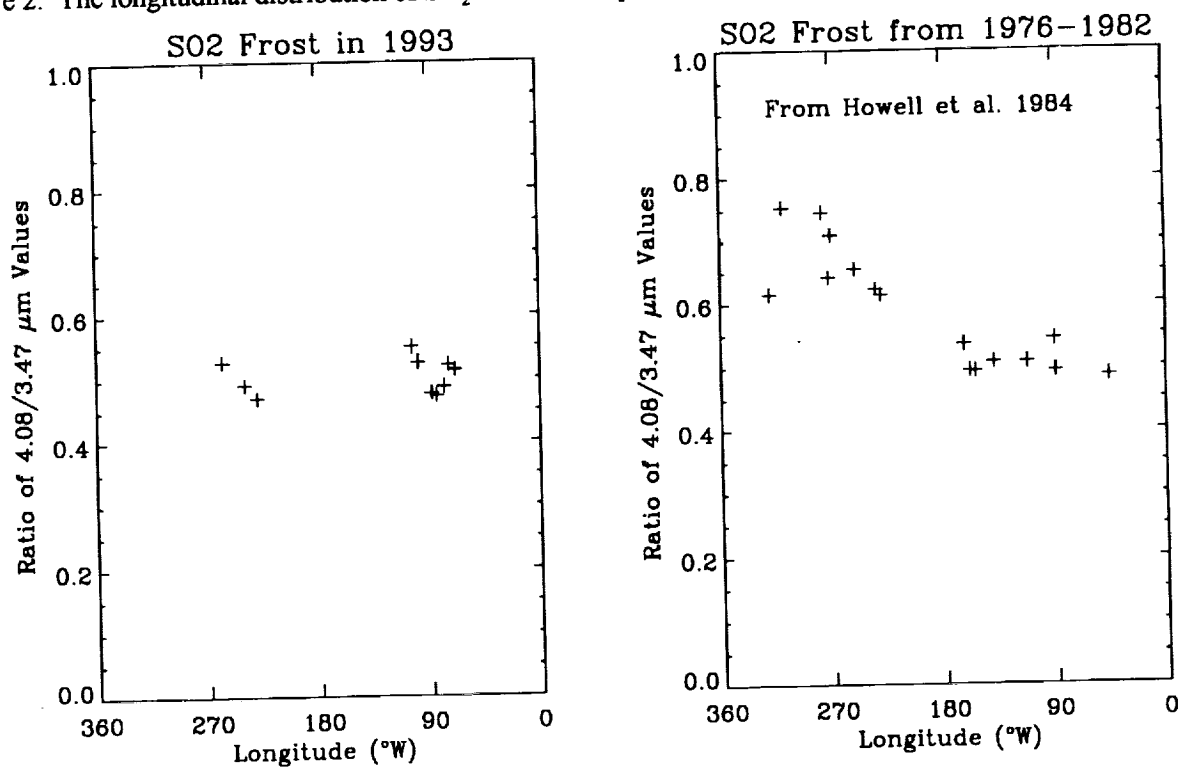


Figure 2. The longitudinal distribution of SO_2 in 1993 compared to the distribution between 1977 and 1982.



2954

2 MEASURING TRACK DENSITIES IN LUNAR GRAINS USING IMAGE ANALYSIS; G.E. Blanford¹, D.S. McKay², R.P. Bernhard³, and C.K. Schulz¹, ¹University of Houston-Clear Lake, Houston, TX 77058, ²NASA/JSC SN, Houston, TX 77058, ³Lockheed, 2400 NASA Rd. 1, Houston, TX 77058

We have used digitized scanning electron micrographs and computer image analysis programs to measure track densities in lunar soil grains. Tracks were formed by highly ionizing solar energetic particles and cosmic rays. We used sample 60009, 6049 that was previously studied by Blanford *et al.* (1979) [1]. Back-scattered electron images produced suitable high contrast images for analysis. The images were digitized to 512 x 512 pixels with gray scale 0-255 (8 bit). We ascertained gray-scale thresholds of interest: 0-230 for tracks, 231 for masked regions, and 232-255 for background. We used computer counting and measurement of area to obtain track densities. We found an excellent correlation with manual measurements for track densities below $1 \times 10^8 \text{ cm}^{-2}$. For track densities between $1 \times 10^8 \text{ cm}^{-2}$ to $1 \times 10^9 \text{ cm}^{-2}$ we found that a regression formula using the percentage area covered by tracks gave good agreement with manual measurements

Measurement of track densities in lunar samples has been a very rewarding technique for measuring exposure ages and soil maturation processes [2]. However measuring track densities is labor intensive because quantitative scientific results require counting tracks and measuring areas on micrographs. The sophistication and ready availability of image processing software can reduce this tedious labor.

To establish analytical conditions we used a polished section from Apollo 16 double drive tube 60009, 6049 at a position estimated to be 546 mm below the lunar surface. This sample had been etched for 15 hours in 1 N NaOH at 118°C. We used an ISI SEM with the polished sample oriented perpendicular to the electron beam. The same condenser lens setting and aperture were used for all images. The microscope is not equipped with a Faraday cup and we could not be sure of reproducing the same beam current for each microscope session. We set a fixed working distance of 8 mm and coarse focused by adjusting the sample height. We calibrated magnification with a stage micrometer and verified that it remained consistent within 1.5%. Back-scattered electron (BSE) images naturally showed a high contrast between tracks and background. We purposely chose to exploit this property and took digital images that appeared to the naked eye to be almost binary. Using the computer we could set the contrast and brightness to numerically reproducible settings.

We produced digital images and analyzed them using an eXL computer manufactured by Oxford Instruments, formerly Link Analytical. Digital images were collected as a Kalman average for 90 sec. We worked at 4 different magnifications, 4600x, 6800x, 10000x, and 15000x. After acquiring the image, we created a mask for the image to obscure parts of the image we did not wish to analyze such as areas off the edge of the grain, large cracks, *etc.* We could "paint" the image using this mask to some useful gray-scale level.

We used a set of procedures referred to as "feature scan" to count tracks. A "feature" is defined in terms of connected areas (pixels) within defined limits of gray-scale. Because we took high contrast images, it was relatively simple to define these limits. By trial and error the limits were set to obtain track counts that were consistent with manual track counts on several standard images. The program counted every connected "feature" within the gray-scale thresholds, but it distinguished some as too big and others as too small. Trial and error were used to set these size criteria.

The "single image phase analysis" subset of routines prepares a histogram of pixel number versus the image gray-scale levels and allows the user to interactively set thresholds that are color coded. The routine displays the area covered by each threshold region in pixels, in square micrometers, and percentage of total area. Using this routine, we could determine the total area of the image, the area of the mask, and the percentage area covered by tracks.

Figure 1 shows a correlation diagram of track density measurements using image analysis with conventional measurements from a photomicrograph. The correlation is excellent for track densities below $1 \times 10^8 \text{ cm}^{-2}$. Furthermore, the correlation is not sensitive to the magnification used within the range tested

TRACK DENSITIES USING IMAGE ANALYSIS: Blanford G.E. *et al.*

(but there is better statistical accuracy for lower track density grains when measured at lower magnifications). However, above track densities of $1 \times 10^8 \text{ cm}^{-2}$ the image analysis technique shows saturation. It is not hard to understand why this is true because tracks overlap at high densities. The human counter can distinguish overlapping tracks to some extent. The software however lumps many tracks into single "features" on the digital image and the computer under counts. However, the area covered by the tracks should be proportional to the number of tracks. We performed a linear regression between track density versus the percentage area covered by tracks for images taken at 10000x. There was a correlation coefficient $r = 0.98$. Consequently, we used this regression line to determine track densities from $1 \times 10^8 \text{ cm}^{-2}$ to $1 \times 10^9 \text{ cm}^{-2}$. Even this method is likely to fail at higher track densities. Figure 2 shows the 10000x data from Fig. 1 together with corrected points using the regression formula. The rectangles surrounding each point represent one standard deviation statistical uncertainty.

We have shown that we can reliably measure track densities in lunar grains using image analysis techniques. It is difficult to assess exactly how much more time efficient this method will be, but we believe it will be very significant. When conditions had been established, we collected and analyzed 125 images in ~12 hours. Even during these sessions, however, we keystroked the procedures rather than use macros to speed up the process. Automating track counting may allow application of this technique to important problems in regolith dynamics including the ratio of radiation exposure to reworking in various surface and core samples and in regolith breccias.

[1] Blanford G.E. *et al.* (1979) *Proc. Lunar and Planetary Sci. Conf. 10th*, 1333. [2] Heiken G. *et al.* (ed.) (1991) *Lunar Sourcebook: A User's Guide to the Moon*.

Figure 1. Graph of track densities in lunar soil grains from sample 60009, 6049 at a depth of 546 mm from the lunar surface from images taken at 4600x, 6800x, 10000x, and 15000x. The ordinate has values determined from counts using "feature scan." The abscissa has values determined by manual counting.

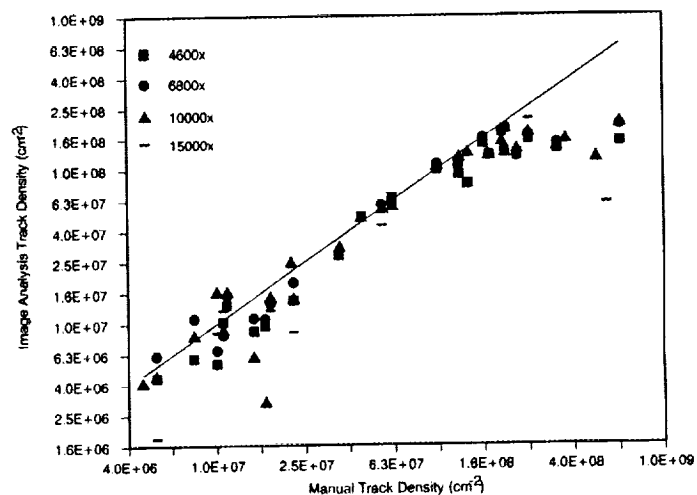
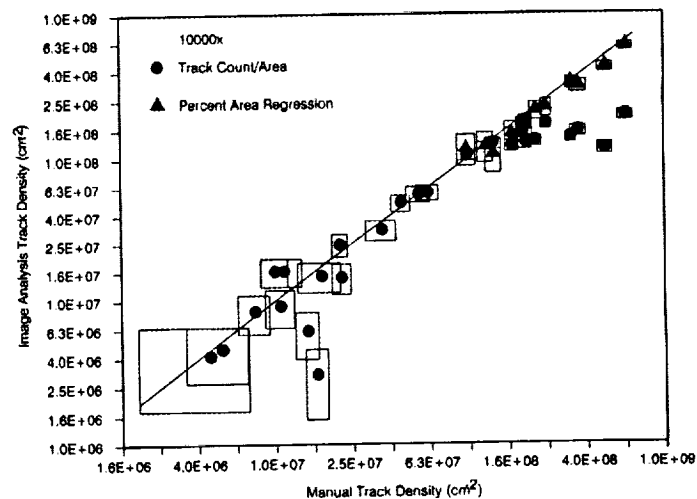


Figure 2: The correlation of manually counted and image analysis determined track densities for data taken at 10000x. Circles represent data obtained using feature scan and triangles represent data using a linear regression formula of the percentage area. Rectangles give one standard deviation uncertainty based on counts or the error in the regression formula.



A SPECTRAL SURVEY OF THE CRISIUM REGION OF THE MOON;

D. T. Blewett, B. R. Hawke, P. G. Lucey, Planetary Geosciences, Univ. of Hawaii, 2525 Correa Rd., Honolulu, HI 96822; P. D. Spudis, Lunar & Planetary Inst., Houston, TX 77058

This report presents preliminary results of a near-IR spectral study concerning a variety of surface units in the Crisium region, including Mare Crisium, the terra associated with the Crisium Basin, northern portions of Mare Fecunditatis, and the light plains deposits north of the crater Taruntius. Issues to be addressed include (1) the nature and origin of light plains deposits, (2) the existence and distribution of possible cryptomaria, (3) the origin of geochemical anomalies in the region, (4) the composition of highlands units associated with the Crisium Basin, and (5) the stratigraphy of the Crisium target site.

INTRODUCTION: The Crisium Basin is a multiring impact structure on the eastern portion of the Moon's Earth-facing hemisphere. Stratigraphic relations deduced from photogeologic mapping [e.g., 1, 2] indicate that the basin formed in Nectarian time. The basin-forming impact may have occurred at 3.895 Ga, based on the dating of material returned by the Luna 20 spacecraft [3]. The rings and deposits of the Crisium Basin have been discussed by [2].

DATA & ANALYSIS: Near-infrared (0.6-2.5 μm) reflectance spectra were collected with the Planetary Geosciences CVF spectrometer mounted on the University of Hawaii 0.61m and 2.24 m telescopes at Mauna Kea Observatory. Moonlight is admitted to the spectrometer detector through a circular focal plane aperture; apertures used in the observations described here correspond to spot sizes of 2-25 km at the center of the lunar disc. Data collection and reduction techniques were standard and are described elsewhere [4]. In order to derive mineralogical information, an analysis focusing on the mafic mineral absorption band near 1 μm was conducted for each spectrum [5]. In addition, spectral mixing relationships were studied using a linear model [6].

RESULTS and DISCUSSION: Findings for individual lunar features are given below.

I. Crisium highlands

A. Proclus crater. Proclus (16.1° N, 46.8° E; 28 km diam.) is a Copernican age crater with a markedly asymmetric ray pattern located in the highlands west of Crisium. A spectrum of the east rim of Proclus was presented by Pieters [7], who interpreted it as indicative of noritic anorthosite. It was noted, however, that the spectral parameters fell outside the range typical of other noritic anorthosite spectra. The interior of Proclus was observed for this study. This spectrum was determined to have a band minimum located at 0.93 μm and a band depth of about 4%, consistent with noritic anorthosite.

B. Circum-Crisium massifs. Spectra were obtained for locations in the highlands massifs bounding the Crisium basin to the north, southwest and south. These spectra have band minima located at 0.92-0.94 μm , with band depths of 2-4%. A noritic anorthosite composition is indicated, though slightly steeper continuum slopes in several spectra with deeper bands may attest to the presence of anorthositic norite.

C. Eimmart A. This 7 km crater (24.0° N, 65.7° E) is on the rim of a highlands crater northeast of Crisium, just at the edge of Mare Anguis. Previous work interpreting a spectrum for Eimmart A [7, 8] noted its extremely strong (21%) absorption band, and favored an olivine/pyroxene mixture to account for the position of the band minimum and broad band shape. On this basis, Eimmart A was proposed as the possible source crater for the Antarctic meteorite ALHA81005 [7, 8, 9].

D. Taruntius peak. Located at 5.6° N, 46.5° E, the 56 km-diam. Copernican age crater Taruntius lies southwest of Crisium and the central peak of Taruntius probably exposes pre-Crisium material. A spectrum for the peak has spectral characteristics generally consistent with a noritic anorthosite or anorthositic norite. The band depth (5.6%) is greater than that of the circum-Crisium highlands spectra described above, and the continuum slope is steeper. This suggests that the material exposed in the peak is slightly more mafic (anorthositic norite) than that composing the circum-Crisium highlands.

II. Light Plains and Cryptomaria

A. Light plains northeast of Taruntius. Orbital geochemical data, in conjunction with

SPECTRAL SURVEY OF CRISIUM REGION: Blewett D.T. *et al.*

morphological considerations, led to the suggestion that the light plains NE of Taruntius were formed by the extrusion of post-Crisium Basin mare units followed by contamination of these deposits by highlands material [10, 11]. Spectra for two spots on the plains have band minima longward of $0.95\ \mu\text{m}$ and band depths of 6-7%, clearly indicating a significant mare basalt component. Further evidence for mare basalt is provided by the dark-halo impact crater Taruntius C (~12 km) on the northwest rim of Taruntius. A spectrum of this crater has a band minimum of $0.98\ \mu\text{m}$ and a 7% depth, demonstrating that mare basalt was excavated from beneath the deposits of Taruntius.

B. "Arrowhead" shaped plains. A triangular patch of plains material is found in the circum-Crisium highlands due north of Taruntius at $\sim 10^\circ\text{N}$, 46.3°E . A number of factors distinguish this area: it has a low albedo compared to the surrounding highlands and is distinctive in multispectral images (cited by [12]). Additionally, this area possesses a high Mg/Al ratio, similar to that of mare soils, as determined from Apollo orbital geochemical measurements [13]. The area corresponds to exposures of Imbrian age (units Ip and Its) on the geological map of the region [12]. A reflectance spectrum of the arrowhead plains has a stronger absorption band (~5%) than the nearby highlands massifs, demonstrating a greater abundance of pyroxene in the plains surface. In order to evaluate the possibility of a mare basalt component in the plains, a linear mixing analysis [6] was conducted on the spectrum. The endmembers employed were a mature mare spectrum ("Mare Crisium C" [14]) and a spectrum for a typical mature highlands soil (Apollo 16). The model indicates that a roughly 50-50 mixture of the mare and highlands spectra produce a reasonable fit to the spectrum of the arrowhead plains.

C. Dark highlands southwest of Crisium. The highlands along the eastern shore of Mare Tranquillitatis contain a distinctive strip of low-albedo plains, at $\sim 9.5^\circ\text{N}$, 43.5°E . This "smooth terra material (Its)" unit has been described as having an uncertain origin, possibly thin mare flows mantling the terra [12]. The spectrum obtained for this area has spectral parameters similar to that of the arrowhead plains described above. The relatively strong absorption band indicates a mare basalt component and a mixing analysis determined that approximately equal amounts of flux were contributed to the dark highlands spectrum by mare and highlands spectral types.

III. Mare Basalt Deposits

A. Picard. Extensive work on the stratigraphy, geologic history and remote sensing characteristics of Mare Crisium has been published [14, 15]. Additional spectra for several features in the mare have been collected. The crater Picard (14.6°N , 54.7°E ; 23 km diam.) is located in western Mare Crisium. It has been proposed [15] that the floor of Picard contains mature non-mare soil, based on the floor's relatively high brightness, and on its high $0.95/0.56\ \mu\text{m}$ ratio value. If this is the case, then it could be inferred that the Picard impact penetrated the mare deposits and exposed subjacent highlands material. However, spectra for the center of the crater have band minima at $0.96\text{-}0.97\ \mu\text{m}$ and band depths measuring 12-13%. Thus the reflectance spectra show that the floor is composed largely of mare basalt.

B. Luna 16 region. Two reflectance spectra were obtained for mare surfaces in the vicinity of the site sampled by Luna 16 in Mare Fecunditatis. A spectrum for a fresh crater has spectral parameters expected for an immature mare basalt. The absorption band is very strong (22%) and the band minimum occurs just longward of $0.95\ \mu\text{m}$. A spectrum for a mature surface was found to have a band minimum at $1.01\ \mu\text{m}$, and a band depth of 4.5%.

- References: [1] D. E. Wilhelms (1987) U.S. Geol. Survey Prof. Pap. 1348. [2] P. Spudis *et al.* (1989) *LPS XX*, 1042. [3] T. Swindle *et al.* (1991) *Proc. LPS 21st*, 167. [4] T. B. McCord *et al.* (1981) *J. Geophys. Res.* **86**, no. B11, 10883. [5] P. G. Lucey *et al.* (1986) *Proc. LPSC 16th*, D344. [6] R. B. Singer and T. B. McCord (1979) *Proc. LPSC 10th*, 1835. [7] C. Pieters (1986) *Rev. Geophys.* **24**, no.3, 557. [8] C. Pieters (1993) in *Rem. Geochem. Analysis*, C. Pieters and P. Englert, eds., Cambridge Univ. Press, ch. 14. [9] C. Pieters *et al.* (1983) *Geophys. Res. Lett.* **10**, no.9, 813. [10] B. R. Hawke and P. D. Spudis (1980) *Proc. Conf. Lunar Highlands Crust*, 467. [11] B. R. Hawke *et al.* (1985) *Earth, Moon, Planets* **32**, 257. [12] D. E. Wilhelms (1972) USGS Map I-722. [13] E. Schonfeld (1981) *Proc. LPSC 12th*, 809. [14] C. Pieters *et al.* (1979) *Proc. LPSC 10th*, 2967. [15] J. W. Head *et al.* (1978) in *Mare Crisium*, R. Merrill and J. Papike, eds., Pergamon Press, pp. 43-74.

Venus: Influence of surface roughness on the threshold for windblown sand derived from Magellan data. Dan G. Blumberg and Ronald Greeley, *Department of Geology, Arizona State University, Tempe, AZ 85287-1404*

Summary: Threshold wind speeds are a function of surface roughness, particle characteristics, and planetary environment. Using Magellan radar data, estimates were made for threshold wind speeds at two locations on Venus, volcanic plains at 10°N, 177°E and the Carson Crater area. Results show that the threshold wind speed (u_t) is about 1 m/sec at a height of about 1 m above the surface. This value is in the range measured by landed spacecraft and suggests that aeolian processes could be active currently.

Previous estimates of u_t and the threshold shear velocity u_{*t} for blowing particles on Earth and Venus were based on wind tunnel experiments and theoretical considerations, and assumed an unrestricted, infinite sand supply and a smooth surface [1, 2, 3]. However, surface roughness influences the length of the aerodynamic roughness (z_0) and, thus, the turbulent properties of the boundary-layer wind profile. Surface roughness also influences the threshold wind speed. The aerodynamic roughness length is a function of surface roughness and traditionally is derived from wind and temperature profiles of the near-surface planetary boundary-layer. Such profile data are not available for Venus, nor are they likely to be available in the near future.

The radar backscatter coefficient (σ^0) is primarily a function of surface roughness at a scale comparable to the radar wavelength; local slope and the dielectric constant are also important. Both the wind and the radar backscatter respond to surface roughness at the sub-meter scale; consequently, there is a correlation between z_0 and σ^0 [4, 5]. Using field data from terrestrial studies in which the relationship between z_0 and σ^0 was determined [6], a new correlation was derived to determine z_0 as a function of the S-band backscatter coefficient:

$$\text{Log}(z_0) = -1.221 + 0.0906 \sigma^0_{hh} \quad \text{Eqn. 1}$$

In this study we estimated threshold wind speeds as a function of surface roughness derived from radar backscatter for various surface units at two locations on Venus. The wind speeds were calculated using Eqn. 2 [7] which considers surface roughness, particle size and density, and planetary environment:

$$u_{*t} = [0.139 \rho_p g d / (\rho (1 + 0.776 (\ln(1 + d/z_0))^2))]^{0.5} \quad \text{Eqn. 2}$$

in which g is acceleration due to gravity, d is the particle diameter, ρ is the fluid density, and ρ_p is the density of the particle. These calculations assume that z_0 is an intrinsic property of surface roughness and is not sensitive to atmospheric pressure. To test this assumption, a rough bed was placed in a planetary environment wind tunnel and wind profiles were measured at surface pressures ranging from 5 mb to 1033 mb. The wind profiles were reduced to z_0 values and confirmed the assumption that z_0 does not change as a function of atmospheric pressure.

Study locations on Venus included a bright wind streak in the lee of a dome on volcanic plains at 10°N 177°E, and sites in the vicinity of Carson Crater. The results were then assessed in terms of the affect of local microtopography on the requirements for aeolian processes. Table 1 shows the σ^0 , z_0 , and derived u_{*t} , and u_t values for these sites. From comparison with sites on Earth [5, 6], the z_0 values of the Venus sites are consistent with the smoother terrestrial sites, such as gravel-mantled playas and relatively smooth alluvial fans. The table shows that dark surfaces, including the paraboloid, have u_t values of up to 1 m/sec, whereas the bright streak u_t values are higher by about 30%. The table also shows that the threshold wind speeds are on the

Venus: Influence of surface roughness for windblown sand. D.G. Blumberg and R. Greeley

order of 1 m/sec at a nominal height of 1 m above the surface. This wind speed is in the range measured by the Venera 9 and 10 spacecraft at a similar height, suggesting that aeolian processes can be active today. Only two potential large dune fields were identified in Magellan images so far; therefore, there is still a question as to why aeolian features and dune fields are so abundant on Earth and Mars and markedly less so on Venus. As this study shows current wind speeds can move particles on Venus; hence, there could be a smaller supply of sand-sized particles on Venus or, dunes are present but cannot be detected via Magellan data.

Table 1: Data for Venus study sites; Radar backscatter coefficients (σ^0), derived aerodynamic roughness (z_0), number of pixels sampled at each site (n), derived threshold shear velocities (u_{*t}), and threshold wind speeds (u_t) at a height of 1 m.

Site characteristic	Mean σ^0	Mean z_0	n	u_{*t}	$u_t(z=1m)$
Carson					
Paraboloid	-18.84	0.0013	12	0.036	1.015
Paraboloid	-18.73	0.0014	5	0.037	1.030
Paraboloid	-19.05	0.0012	4	0.035	1.000
Paraboloid	-13.33	0.0037	3	0.050	1.264
Paraboloid edge	-12.63	0.0047	6	0.054	1.335
Bright streak	-7.60	0.0133	3	0.075	1.668
Dome	-22.89	0.0005	3	0.028	0.865
Paraboloid	-21.13	0.0007	3	0.031	0.911
Dark surface north of crater	-21.39	0.0007	3	0.031	0.911
Paraboloid	-12.39	0.0045	3	0.053	1.322
Bright streak	-15.73	0.0022	3	0.042	1.127
Fractured terrain	-21.43	0.0006	5	0.030	0.889
Radar dark plain	-12.53	0.0045	2	0.053	1.322
Tessera					
10°N 177° on volcanic plain					
Bright streak	-12.24	0.0047	3	0.054	1.335

References:

- [1] Bagnold (1941) Methuen. [2] Greeley and Iversen (1985) Cambridge Press. [3] Tsoar and Pye (1990) Unwin Hyman. [4] Greeley et al. (1988) *Geophysical Research Letters*, **15**, 565-568. [5] Greeley et al. (1991) *Acta Mechanica*, **S2**, 77-88. [6] Blumberg and Greeley (1993) *Journal of Arid Environments*, **25**, 39-48. [7] Greeley et al. (1974) *Proc. R. Soc. Lon.*, **341**, 331-360.

MARS CARTOGRAPHIC COVERAGE: STATUS PRIOR TO MARS-94 MISSION
N.N.Bobina, G.A.Burba Vernadsky Inst., Moscow 117975, Russia

Mars surface area (144 mln.sq.km), being slightly less than that of the Earth's continents (149 mln. sq. km), have sufficiently regular cartographic coverage at 1:2,000,000 scale. All maps of Mars surface relief and topography were obtained during the recent 20 years with the space images. Most of these maps were produced by the US Geological Survey, Flagstaff, AZ.

GENERAL IMAGE MAPS. To obtain an overview impression of the current status of Martian mapping on the eve of MARS-94 mission one should know that the whole planet is covered with 1:2,000,000-scale image map (= photomap or controlled photo-mosaics). It consists of 144 sheets covering about 1,000,000 sq. km each. There are the areas on the map with the resolution insufficient for such scale map.

The smaller-scale maps also exist for global coverage - 1:5,000,000 (30 sheets), 1:15,000,000 (3 sheets), and 1:25,000,000 (1 sheet) [1].

Maps in scales large than 1:2,000,000 exist only for restricted areas of the planet (Fig. 1). Most of 1:1,000,000-scale maps are based on the enlarged early Mariner 9 images and are of not up-to-date quality, as they have coarser resolution in comparison with Viking-based 1:2,000,000 maps.

The image maps (controlled photomosaics) of 1:500,000 scale exist for large areas of Mars. There are 169 sheets for the different areas, published up to now. They cover 8.6% of Mars (12.4 mln. sq. km). There are also 3 revised edition sheets, and 5 areas near North pole have sets of two sheets presenting different season appearance of the surface. Each of sheets covers the area of 73,000 sq.km, which is equal to the area of New Hampshire, Vermont, Massachusetts, and Rhode Island taken together. Global coverage of Mars with 1:500,000-scale map needs 1964 sheets, but it is not planned to produce all of them. These maps are based on high-resolution Viking pictures, but the resolution differs between the sheets, and even sometimes within the same sheet.

Mosaics at 1:250,000 scale exist for 4 very small areas connected with Viking landing sites (both final and potential).

GEOLOGIC MAPS cover whole Mars at 1:5,000,000 (30 sheets) and smaller scales. There is a set of 16 sheets of lava flow maps at 1:2,000,000 scale for Tharsis Montes and vicinities. The lava flow maps cover 11% of the Martian globe. Larger scale geologic maps are presented only by seven 1:500,000 sheets.

SUMMARY. Cartographic coverage of Mars is sufficiently regular. But this coverage being at 1:2,000,000 scale should be considered now only as reconnaissance one. Same could be ruled out for the geologic mapping which covers the whole planet only with 1:5,000,000-scale maps. No another (but geologic) thematic maps exist for Mars with more or less regular coverage. The future studies, in particular with MARS-94 mission, should lead to the diversity of the thematic map types [2] for the whole planet or its considerable regions.

REFERENCES: 1. J.L.Inge, R.M.Batson (1992) Indexes of maps the planets and satellites 1992. NASA TM 4395. 2.G.A.Burba (1993) Thematic map types possible for Mars ... - This volume.

MARS CARTOGRAPHIC COVERAGE: Bobina, N.N. and Burba, G.A.

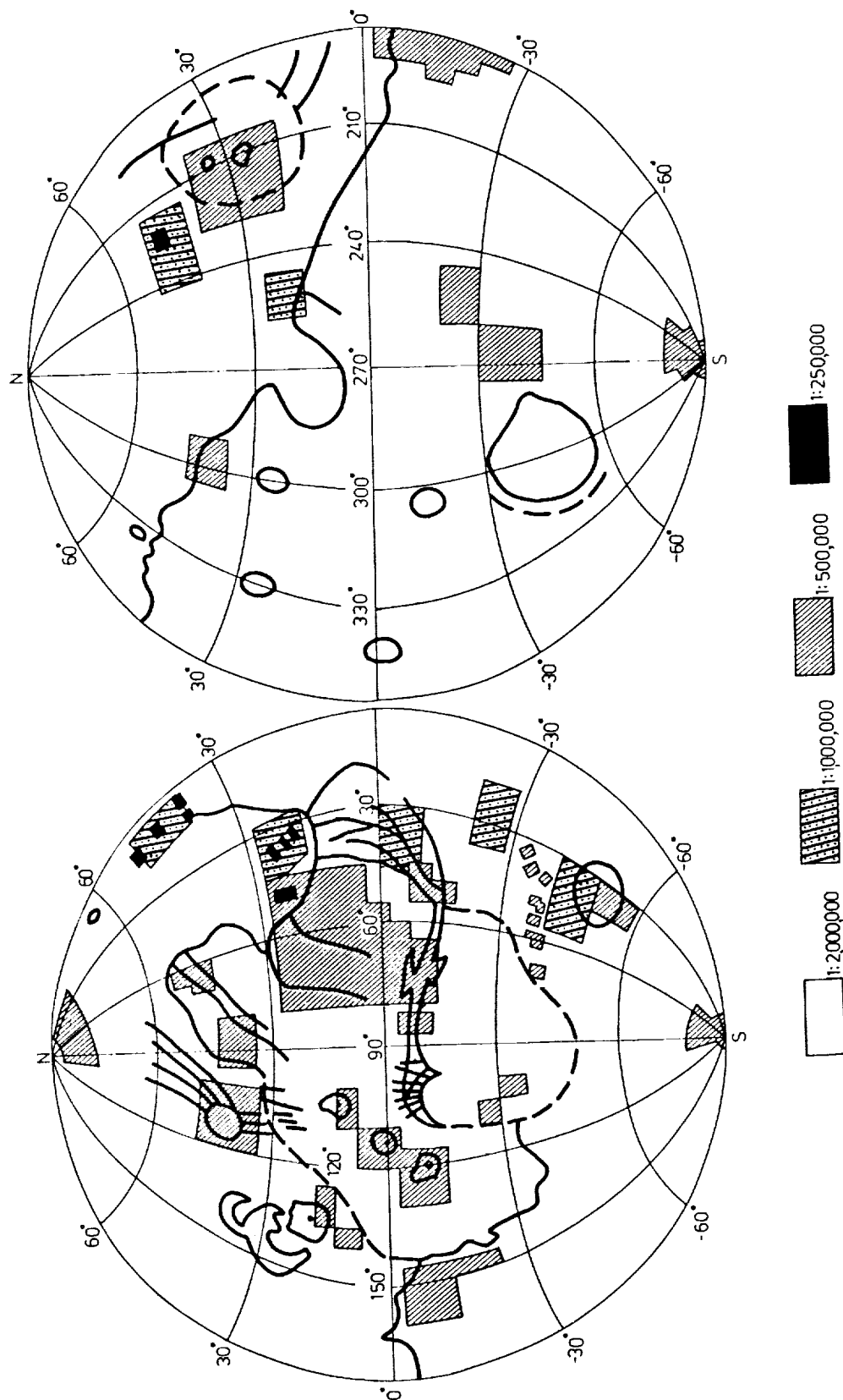


Fig.1. Cartographic Coverage of Mars.
Largest Scale Exists for the Area is shown

GEOMETRICAL TRANSFORMATION OF PANORAMAS OF MARS SURFACE RECEIVED FROM PHOBOS-2 SPACE STATION; I.M.Bockstein, M.A.Kronrod, Institute of Problems of Information Transmission, Russian Academy of Sciences, Moscow, Russia

Yu.M.Gektin, Institute of Space Device Engineering

Methodology of geometrical transformations of planetary images is described that leads to transferring these images to the format of a photographic map available. The results of practical use of the corresponding software for geometrical transformation of Mars surface panoramas obtained from Phobos-2 space station are also presented.

In 1989 Soviet space station Phobos-2 has made four sessions of Mars surface surveying. Two-channel opto-mechanical scanner THERMOSCAN was used for this purpose. It gave possibility to register four surface panoramas in visual and thermal spectral channels. The procedure and the results of pre-processing these images are described in [1].

Now it became necessary to transfer these Mars panoramas to the format of the existing photographic map of Mars surface for interpretation purposes. Since the parameters of Phobos-2 station's orbit for the periods of registration of panoramas are known inexactly, it is impossible to realize the transformation by means of direct calculations according to some exact formulae. That is why we have chosen the following well-known way of transformation:

- a lot of near-located points of correspondence were found on the panorama to be transformed, and on the photographic map;
- triangulation network was constructed across these points;
- affine geometrical transformation was realized inside each triangle of the network. Its parameters were chosen to achieve the coincidence of the vertices of this triangle (i.e., the points of correspondence) on both the map and the transformed panorama. Due to some properties of affine (linear) transformation the deformations of the panorama on either side of borders of the neighbouring triangles were the same, and no ruptures arose in the subject of the panorama.

Practical application of the above-described methodology to geometrical transformation of Mars surface panoramas led us to the necessity to solve a lot of difficult problems. The main problem was to find the points of correspondence on real panorama (Fig. 1a) and real photographic map (Fig. 1b). Since Mars surface consists mostly of craters of approximately the same shape and size, and since these craters look differently in visual and thermal spectral channels, all the attempts to find the points of correspondence automatically were doomed to failure. That is why we decided to find such points (usually, the centers of craters) interactively. IMS-VGA image processing system [2] was used for this purpose. The base of this system was IBM-compatible PC with SuperVGA card; it gave possibility to display gray-scale images and to support the dialogue directly on the screen of computer console. The size of the screen was 512*512 pixels. A program for piece-affine geometrical transformation of images was created as a part of IMS-VGA system. Special subroutine of this program was used to find the points of correspondence. This subroutine enabled user of the system to see both panorama and the photographic map as wholes, to set roughly the positions of each pair of points of correspondence, and then to display and to compare on the console screen the enlarged fragments of the panorama and of the map (with the size of 128*128 pixels, or about 200*200 km). These fragments were centered in chosen positions; the user could shift them up, down, left, or right, rotate panorama fragment to an arbitrary angle, or change its scale. User's task was to achieve the correspondence not only of the central crater (with the point of correspondence inside) but, as far as possible, of all the parts of map and panorama subjects. This decreased strongly the possibility of gross mistakes, when a crater on the panorama was supposed to correspond with quite a different crater of similar shape on the map. In order to reduce the demands of user's skill, approximate position of each new point of correspondence on the panorama was predicted after establishing the rough position of this point on the map. The information about scale and rotation of the panorama in the nearest points of correspondence was used to realize this prediction.

Automatic construction of triangulation network at the second stage of transformation process also caused many problems in practice. After some experiments we have proposed and realized in software the following procedure of triangulation:

TRANSFORMATION OF PANORAMAS OF MARS: Bockstein I.M. et al.

- each of the points of correspondence found at the first stage was connected with the nearest of its neighbouring points that answered the following conditions: it was still not connected to the current point, and the line that connected them did not cross the lines drawn earlier;
 - after each reaching the end of the list of points of correspondence, the first step of the procedure was repeated while it was possible to draw a new line.
 This procedure ensured the construction of the triangulation networks that consisted mainly of the small triangles of almost regular shape. An example of such network is drawn on the photographic map Fig. 1b.

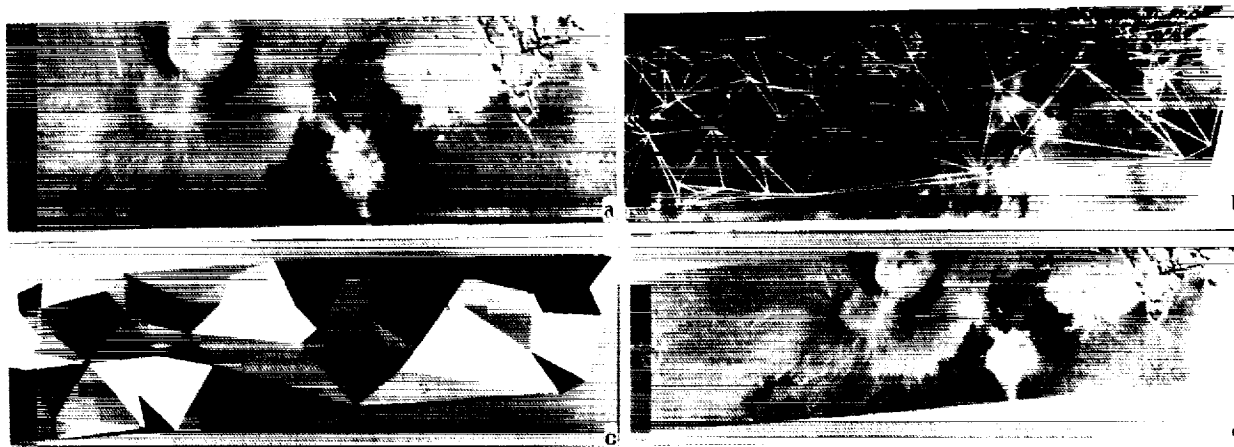


Figure 1. (a) fragment of the panorama of Mars surface (thermal spectral channel); (b) fragment of the photographic map with the triangulation network; (c) mask image; (d) result of the piece-affine geometrical transformation of the shown fragment of panorama

At the stage of piece-affine transformation all the problems were caused by the necessity to determine for each pixel of a panorama the triangle of the network that surrounded this pixel. In order to simplify and to speed up the transformation, we drew in advance a special mask image (Fig. 1c), the size of this image being the same as the size of the photographic map. Mask image consisted of the same triangles as the triangulation network for this map, and the brightness values inside each triangle were equal to its number. For each pixel of the photographic map we found from the mask image the number of triangle that surrounded this pixel, the coordinates of its vertices on the map and on the panorama, and the parameters of affine transformation that led to coincidence of these vertices. The coordinates of a pixel of the panorama that corresponded to the pixel of the map were then found as a result of transformation itself. This mode of calculations ensured the absence of ruptures of the transformed panorama irrespective of its local scaling. Transformation procedure was optimized to achieve maximum speed.

The application of our methodology has led us to success in solving the problem of transferring the panoramas of Mars surface to the format of an arbitrary photographic map. The result of geometrical transformation of the panorama Fig. 1a in order to correspond it with the map Fig. 1b is shown on Fig. 1d. More than 50 points of correspondence were found and used to transform this panorama.

We have to note that the above-described methodology and the created software means can be used very widely. In particular, we intend to use them when working with Mars panoramas that will be obtained in 1995 as a result of surveying this planet by Russian space stations.

[1] Bockstein I.M. et al. Processing of Mars surface images received from Phobos-2 space station. *LPSC XXI*, 1991.

[2] Bockstein I.M. and Kronrod M.A. IMS-VGA interactive image processing system. *Pattern Recognition and Image Analysis*, v. 3, No. 4, 1993.

FE AND MN SYSTEMATICS IN EXPERIMENTAL ANALOGUES OF MURCHISON AND A 65% H CHONDRITE-35% CM CHONDRITE:

Joseph S. BOESENBERG and Jeremy S. DELANEY; Dept Geological Sciences, Rutgers University, New Brunswick, NJ 08903

Partial melting experiments on Murchison and 65% H chondrite-35% CM chondrite analogues can produce eucritic melts with good compositional matches for all major elements and for the Fe/Mn ratio. The H-CM mixture is a good precursor that matches the phase equilibria as well as the oxygen isotope constraints on eucrite precursors. The main problem is an over abundance of Na. The H-CM composition also satisfies many trace element constraints and produces eucritic melts at oxygen fugacities between IW -0.5 and IW -1.5 and at temperatures from 1180 to 1300°C.

INTRODUCTION: Boesenberg and Delaney (1993), following up on the work by [2] and [3], investigated the Mn and Fe systematics of eucritic compositions and the evolution of eucrites from the simple partial melting of a chondritic precursor, specifically a Murchison analogue. We proposed that iron alloying to the platinum wire used in experimental runs could simulate a reducing atmosphere and further simulate the subsequent fractionation of the Fe-metal from a parent body. The effect of Fe removal reduces the Fe/Mn ratio and Fe/(Fe+Mg) of the resulting glass, while preserving most other elements in eucritic proportions. New experiments, using inert platinum-iron wire and at oxygen fugacities of iron-wustite (IW) -0.5 log unit and IW -1.5 log unit confirm that the Fe/Mn and FFM of the minimum melt for a chondritic precursor can be controlled and produce eucritic compositions. Additional experiments tested the new chondritic precursor proposed by [4]. This composition was designed to resolve the major oxygen isotope problem associated with eucrites. No simple chondritic precursor has oxygen isotopes compatible with eucritic precursors [5], but a mixture of H and CM compositions can produce an appropriate oxygen isotope ratio. This mixture also has a bulk composition very similar to the most useful parent body composition [6] and has an initial Fe/Mn ratio compatible with eucrite compositions. Experiments on the CM chondritic meteorite, Murchison, by [2] showed that a eucrite-like composition could be derived from such material. The experiment's of [2], however, showed that the Murchison composition fails to produce appropriate Fe/Mn ratios. In an attempt to account for this discrepancy, [4] calculated a possible eucritic precursor based on oxygen isotopes and the Fe/Mn ratios. The result was a composition containing 65% H chondrite and 35% CM chondrite. This composition satisfies all of the requirements for a precursor except the over abundance of volatiles, specifically Na. The Murchison differs from the 65H-35CM by having approximately 3.5 wt% less SiO₂, 0.1 wt% greater TiO₂, 6 wt% greater FeO, 4 wt% less MgO, 0.6 wt% greater CaO, and 0.55 wt% less Na₂O.

METHODS: The Murchison analogue and 65H-35CM analogue experiments were run using a vertical muffle tube CO-CO₂ gas mixing furnace. The experiments were run at three temperatures (1180°C, 1200°C, and 1300°C), and two oxygen fugacities (IW -0.5 and IW -1.5). Most of the experiments were run for a duration of about one week to allow the experiments to reach equilibrium. Using the partition coefficient calculations of [7] on Fe, Mn, and Mg in the olivines and glasses, all of the experiments showed that they were either at or very near equilibrium.

RESULTS: The results of both the Murchison analogue and the 65H-35CM analogue experiments demonstrate the independent effects of Fe loss and olivine crystallization on the bulk composition (Figure 1A and 1B). They show that with a decreasing oxygen fugacity, more Fe-metal is fractionated from the melt, causing both the Fe/Mn ratio and Fe/(Fe+Mg) (FFM) of the bulk to decrease. This compositional change follows the predicted Fe loss path seen in Figure 1. Equilibrium olivine compositions for points on the Fe loss path have higher Fe/Mn and lower FFM ratios corresponding to those produced in these experiments. The residual liquid compositions have higher FFM ratios reflecting mass balance constraints as well as equilibrium partitioning. These redox controlled Fe changes leave most other elements unaffected, except Cr which is also redox sensitive.

A comparison between the experimental glasses and mean eucrites (Figure 2a and 2b) [8] showed that, in general, the Murchison composition is not as good of a candidate for a precursor as is the 65H-35CM composition. The partial melts of the Murchison precursor have Mn and Al depletion that deviate significantly from eucritic compositions. The 65H-35CM precursor, on the other hand has glass/eucrite ratios of about one for most elements except Na at temperatures of 1180-1200°C. The wide Na₂O variation within both sets of experiments reflects the volatility effects on Na. The 65H-35CM composition is strongly enriched in Na₂O content but shows great variability caused by Na volatilization. The 1300°C

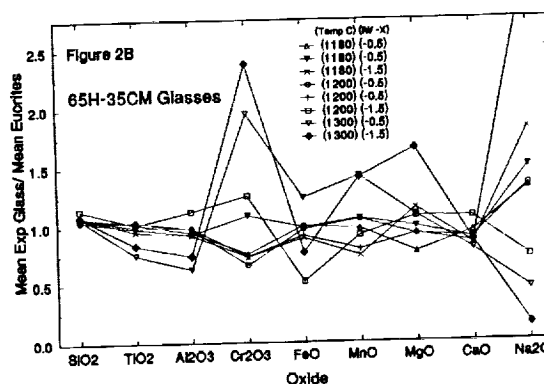
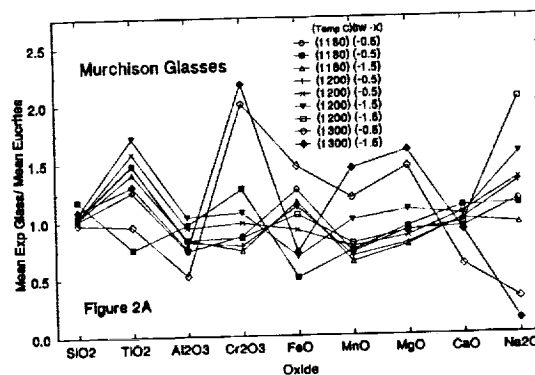
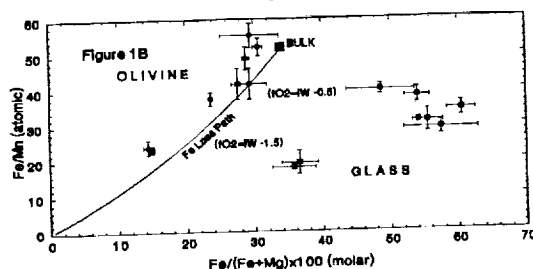
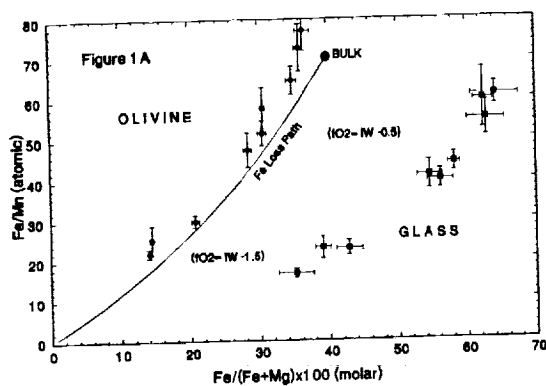
Eucritic melts from H-CM chondrite mixtures: Boesenberg & Delaney

experiments show the more variable compositions caused by the glass becoming increasingly olivine normative at higher temperatures. The higher Cr_2O_3 content of these higher temperature experiments reflects a decrease in the chromite content of the bulk composition, and the presence of Cr^{2+} at these low fugacities. The Cr^{2+} enrichment in the glasses is enhanced in the lower fugacity experiments. The increase of Cr in the melt correlates with a decrease of the silica content of the glasses, reflecting increased solution of Cr^{2+} bearing olivine in the melt. The compositional differences give the 65H-35CM a more appropriate Fe/Mn and FFM for eucrites and better agreement with the TiO_2 content. The Na₂O content of 65H-35CM, however, is far too high for eucrites, since the volatility effect of Na should be negligible on a parent body sized object.

CONCLUSIONS: A eucritic composition that will produce appropriate Fe/Mn ratios and FFM ratios, can be made from chondritic precursors under reducing conditions. The effect of this reduction shows little or no change to the remaining composition. This reduction alters the bulk melt Fe/Mn ratio and FFM along the Fe loss path in the predictable manner. Based on these experiments, the 65H-35CM composition of [4] appears to be a better precursor than a carbonaceous chondrite, such as Murchison, despite the over abundance of Na. The 65H-35CM composition, designed to satisfy oxygen isotope and trace element constraints is also an appropriate precursor for production of eucritic melts at "realistic" oxygen fugacities and temperatures. Comparison of the experiments carried out between IW -0.5 and IW -1.5 suggest that the eucritic melts may be produced at any of these oxygen fugacities.

REFERENCES: [1] Boesenberg and Delaney (1993) LPSC XXIV, 137-138; [2] Jurewicz et al (1993) GCA 57, 2123-2139; [3] Stolper (1977) GCA 41, 587-611; [4] Delaney (1993) Meteoritics 28, 341; [5] Clayton and Mayeda (1983) EPSL 62; [6] Dreibus et al (1979) PLSC 8, 211 [7] Takahashi (1978) GCA 42, 1829-1844; [8] Jarosewich (1990) Meteoritics 25, 323-337.

ACKNOWLEDGEMENTS: NASA: NAG9-304 (JS Delaney) is gratefully acknowledged.



1-2
2955

³⁹Ar-⁴⁰Ar AGES OF FOUR UREILITES; D. D. Bogard¹ and D. H. Garrison²

(¹Code SN1 and ²Lockheed-ES, NASA Johnson Space Center, Houston, TX 77058).

Abstract. Ureilites Novo Urei, Haverö, and Kenna show strong evidence of one or more ⁴⁰Ar degassing events in the time period of 3.3-4.1 Ga ago. These ages may be compared to current interpretations of ureilite chronology. These include the suggestion of metasomatic activity on the parent body 3.7 Ga ago that reset some Sm-Nd ages and the suggestion that ureilites have experienced terrestrial contamination of several trace elements (including Pb and LREE), which makes suspect ages younger than ~4.5 Ga [1, 2].

The detailed isotope chronology of ureilites, critical in deciphering their enigmatic history, has proved elusive. Takahashi and Masuda [3] reported a Rb-Sr isochron age of 4.01 ± 0.06 Ga for the MET78008 ureilite. Goodrich et al. [1] reported that three ureilites defined a Sm-Nd isochron age of 3.74 ± 0.02 Ga, which was interpreted as the probable time of metasomatic activity and introduction of additional LREE and other components. A few other ureilites not showing enhanced LREE defined Sm-Nd model ages of 4.55 Ga. Sr suggested correlation with LREE enrichments and was sufficiently radiogenic to suggest a later introduction. In a U-Th-Pb study of Gualpara by Torigoye et al. [2] most analyses plotted above a 4.5 Ga isochron, which was interpreted as indicating significant terrestrial Pb contamination. They found LREE enrichments only in the acid leaches of the carbon- and metal-rich phases and suggested that a portion of various incompatible elements, including Pb and the LREE, may be terrestrial contamination. This study suggests that the 3.74 Ga isochron is a mixing line and that the formation age of ureilites is ~4.55 Ga.

Because the K-Ar chronometer can be sensitive to metamorphic events, we made ³⁹Ar-⁴⁰Ar determinations on bulk samples (0.12-0.14 g each) of four ureilites. Novo Urei and Kenna (a fall) were included in the group that suggested a Sm-Nd age of 3.74 Ga [1]; PCA86502 was included in the group that gave a Sm-Nd age of 4.55 Ga [1]. Haverö (a fall) has not been dated, but a significant LREE enrichment was reported [3]. The determined [K] for our samples ranged 1.3-20 ppm (Fig. 1); literature data for bulk ureilites range ~0.7-35 ppm [4, 5]. Nevertheless, corrections to ⁴⁰Ar and ³⁹Ar for system blanks were relatively small. Corrections for reactor interferences were sometimes substantial, however, especially at high extraction temperatures where the K/Ca ratio was very small. Uncertainties in blank and reactor corrections, along with uncertainties in measurements of ratios and neutron flux levels, are included in the age uncertainties.

The ³⁹Ar-⁴⁰Ar age spectra (rectangles, left scale) and K/Ca ratios (dashed line, right scale) as a function of cumulative ³⁹Ar release from stepwise temperature extractions for the four ureilites analyzed are shown in Fig. 1. The total age for Haverö is 4.2 Ga; five extractions degassing ~65% of the K sites indicate a quasi-plateau age of 3.0-3.5 Ga. Ages for Novo Urei generally decrease with extraction temperature, suggesting possible redistribution of ⁴⁰Ar; the total age of all extractions is 3.71 Ga. The total age for Kenna is 5.75 Ga, and that for PCA86502 is 5.67 Ga. The higher ages shown by the first few extractions of Haverö and PCA86502 are associated with much higher K/Ca and probably represent contamination by K and adsorbed atmospheric ⁴⁰Ar. The first two extractions of Kenna probably also represent adsorbed atmospheric ⁴⁰Ar. The increased ages at the highest extraction temperatures of all four samples are associated with very low K/Ca ratios (~10⁻⁴) and K concentrations. Although these higher ages may reflect lesser degrees of degassing (e.g., the highest ages for Kenna and Novo Urei are ~4.5 Ga), they may also be due to ⁴⁰Ar contamination. Unusually high total gas pressures were observed at higher extraction temperatures, and these high ages may be due to enhanced ⁴⁰Ar furnace blanks caused by CO-CO₂ released from high temperature carbon reduction of iron oxides.

Because ³⁹Ar-⁴⁰Ar ages shown by low and high temperature extractions may be suspect, we examined the intermediate temperature extractions. Five extractions (5-70% ³⁹Ar release) of Haverö suggest an age of 3.30 Ga. Four extractions of Kenna (~25-80% ³⁹Ar) suggest an age of 4.1 Ga, similar to the Rb-Sr age reported for MET78008 [3]. Extractions of Novo Urei releasing >40% of the ³⁹Ar suggest an age 3.30 Ga. However, because no obvious reason exists to suspect the low temperature extractions of Novo Urei, we note that the age given by the 0-90% ³⁹Ar release is 3.7 Ga, identical to the total age. The lowest ages shown by two extractions of PCA86502 are 4.5-4.6 Ga, identical to the PCA86502 Sm-Nd age [1] and the maximum Ar ages shown by Kenna and Novo Urei. Although interpretation of these spectra is obviously uncertain, we believe that the most recent times of Ar degassing can be roughly inferred. These times are ~3.3 Ga for Haverö, 3.3-3.7 Ga for Novo Urei, and ~4.1 Ga for Kenna, for which Ar degassing may not have been complete.

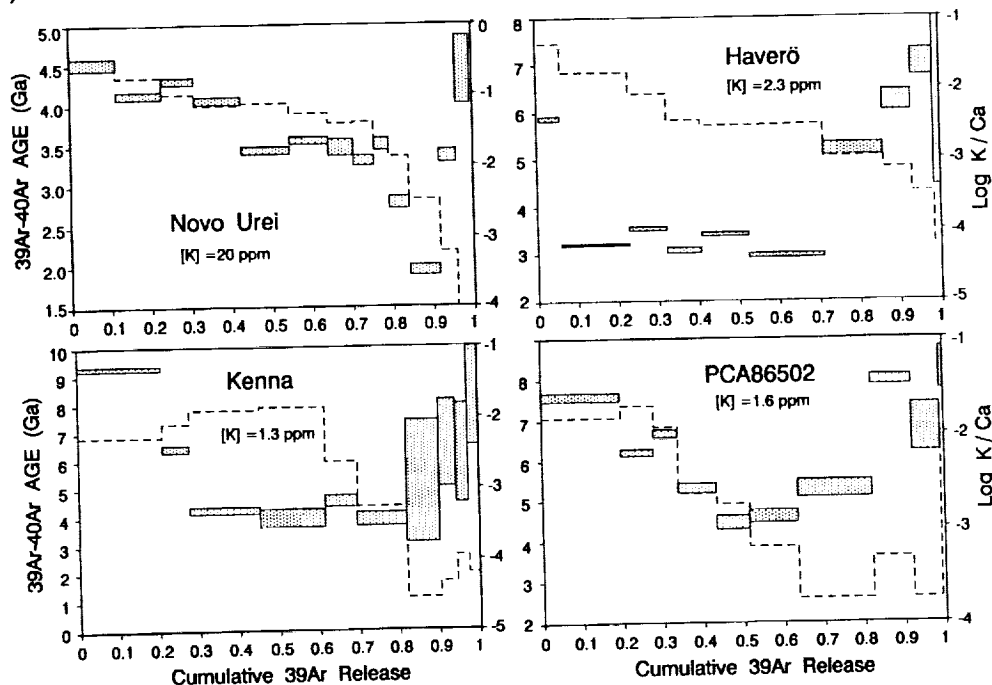
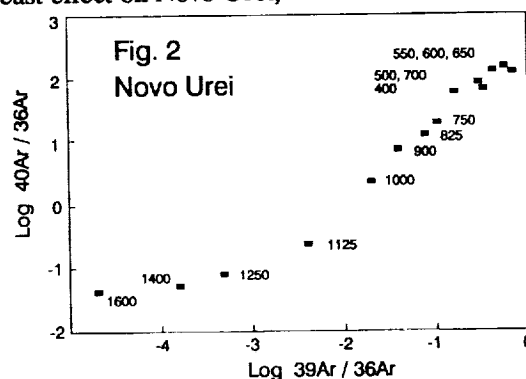
We examined the possibility that some of the excess ⁴⁰Ar might be associated with the large concentrations of trapped Ar known to occur in the diamond/graphite phase of ureilites. A study of Haverö [6]

^{39}Ar - ^{40}Ar AGES OF UREILITES; Bogard & Garrison

gave an upper limit to the trapped $^{40}\text{Ar}/^{36}\text{Ar}$ ratio of 0.0076; the predicted cosmic ratio is considerably smaller. Our Novo Urei and PCA86502 data define trapped $^{36}\text{Ar}/^{38}\text{Ar}$ ratios of 5.26 ± 0.03 and 5.32 ± 0.03 , respectively, similar to the value of 5.20 ± 0.06 reported by [6]. A correlation plot of $^{40}\text{Ar}/^{36}\text{Ar}$ vs. $^{39}\text{Ar}/^{36}\text{Ar}$ for Novo Urei (Fig. 2) shows the significant range in isotopic ratios caused by the preferential release of trapped ^{36}Ar at higher temperatures compared to ^{40}Ar and ^{39}Ar . The large ($>10^3$) variations in $^{40}\text{Ar}/^{36}\text{Ar}$ ratios show that ^{40}Ar is not associated with trapped ^{36}Ar . The other three ureilites give similarly large variations in $^{40}\text{Ar}/^{36}\text{Ar}$; the lowest ratio observed was 0.013 for the 1300°C extraction ($\sim 55\%$ ^{39}Ar release) of PCA86502. Correction for planetary ^{40}Ar assuming $^{40}\text{Ar}/^{36}\text{Ar} = 0.007$ produced no significant changes in the age spectra, even at high extraction temperatures. Thus, we conclude that planetary ^{40}Ar is a negligible component in these ureilites.

The indication of ^{39}Ar - ^{40}Ar degassing ages of 3.3-4.1 Ga for three ureilites that also contain an enhanced LREE component and (excepting Haverö) produce a 3.74 Ga Sm-Nd age [1], suggests that both chronometers may have responded to the same parent body event. On the other hand, it is also possible that the Ar data reflect one or more separate events that did not strongly affect the Sm-Nd system, a situation that commonly occurs in eucrites [7]. Thus the existence of reset Ar ages does not require similarly reset Sm-Nd ages. It seems unlikely that the reset Ar ages could have been caused by terrestrial contamination of incompatible elements (including Pb and LREE), as was suggested by [2] to explain the U-Pb and Sm-Nd results. However, if terrestrial K were also introduced into these ureilites along with other trace elements, and if that K contaminant occupies similar (interstitial?) lattice sites to indigenous K in the ureilites, then it would be possible, in principle, to generate a ^{39}Ar - ^{40}Ar release spectrum showing artificially young ages. Because of its relatively high [K], such a K contaminant would produce the least effect on Novo Urei, whose total ^{39}Ar - ^{40}Ar age is 3.7 Ga.

References: [1] Goodrich, Patchett, Lugmair, & Drake, *G.C.A.* 55, 829, 1991; [2] Torigoye, Misawa, & Tatsumoto, *Meteoritics* 28, 450, 1993, and *G.C.A.* submitted; [3] Takahashi & Matsuda, *Meteoritics* 25, 411, 1990; [4] Wänke, Baddehausen, Spettel, Teschke, Rico, Dreibus, & Palme, *Meteoritics* 7, 579, 1972; [5] Boynton, Starzyk, & Schmitt, *G.C.A.* 40, 1439, 1976; [6] Weber, Begemann, & Hintenberger, *E.P.S.L.* 29, 81, 1976; [7] Bogard & Garrison, *Meteoritics* 26, 320, 1991.



BROMINE IN INTERPLANETARY DUST PARTICLES; Jörg Bohsung, Peter Arndt, Elmar K. Jessberger, Max-Planck-Institut für Kernphysik, PO-Box 103980, 69029 Heidelberg, Germany

During the passage through the atmosphere the chemical composition of interplanetary dust particles (IDPs) may be altered not only by devolatilization upon heating [1] but also by contaminating processes [2]. Given the possible cometary origin of some IDPs, the understanding of such processes is fundamental for the interpretation of IDP trace element data in general. Recently Rietmeijer [3] reported the first observation of Br nanocrystals associated with IDP W7029E5 that conjecturally are of stratospheric origin. To support this interpretation, Rietmeijer presents a linear relationship of Br concentrations of 11 IDPs with theoretical stratospheric residence times. We will criticise Rietmeijer's model but nevertheless demonstrate that with the given data the Br enrichments can be interpreted as being due to contamination. We present a contamination model that predicts a linear relation of the absolute numbers of Br atoms in a given IDP with its capture area and sticking coefficient. A stratospheric contamination would naturally explain the Br enrichments observed in many stratospheric IDPs [e.g. 2, 4-7] and, if unequivocally proven, would discourage from speculations about exotic cosmic scenarios [4,7].

RIETMEIJER'S MODEL: According to [3], Br enrichments due to stratospheric contaminations via surface adsorption would result in a linear correlation of mass normalised Br concentrations to mass normalised atmospheric residence time: $C_{Br}(t)/m \propto t/m$ (Eq. 1). To proof this prediction, Rietmeijer shows the data of a set of 11 particles (Tab. 1) according to Eq. 1 in a log-log plot, using particle masses m

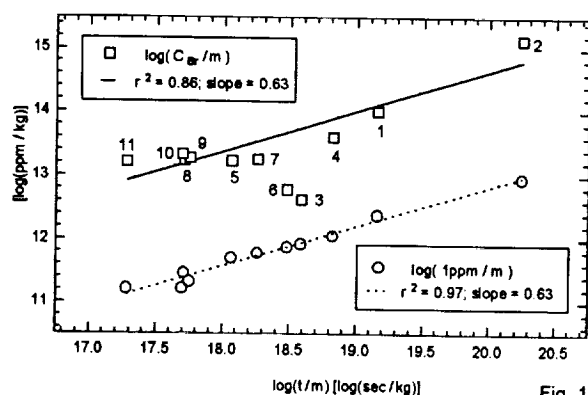


Fig. 1

from [5,7] and residence times t which were calculated using a new model [8,9] for the settling of non-spherical dust particles. In that plot the data points are correlated linearly (Fig. 1, upper line).

CRITICISMS: (1) The straight line does not proof Eq. 1, because it is incorrect to conclude a linear correlation of two variables if only their logarithms are linearly correlated. (2) The correlation itself is merely an artefact. This is obvious from the lower line of Fig. 1 where the same data are plotted assuming a constant ($=1$ ppm) Br concentration: the correlation is independent of the Br contents. Consequently, the real Br abundances are not responsible for the observed correlation but they rather tend to destroy it.

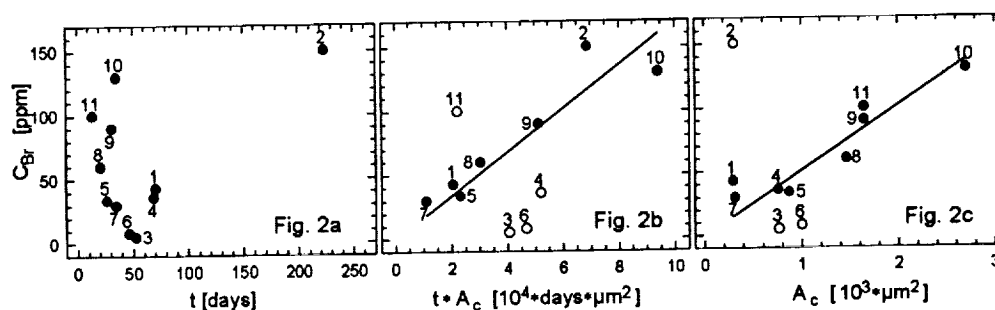
The common cause for the same slopes of both correlation lines is the proportionality of $\log(1/m)$ and $\log(t/m)$. This is expected since in the Rietmeijer model the residence time t increases with decreasing particle mass m . The measured Br abundances then introduce a slight perturbation since the variation of $\log(C_{Br})$ is small compared to that of $\log(1/m)$. (3) The residence time model of Rietmeijer only is valid if the original preterrestrial size and shape of an IDP are known. But at least 2 out of 11 IDPs, W7066*A4 and W7029*A27, are associated with clusters that probably were produced from larger particles by disaggregation during collection [11], and there the model is not applicable.

NEW MODEL: We assume that (1) the original Br abundance of an IDP is low compared to a stratospheric contamination and that (2) the Br contamination rate is constant during the settling process. Then the absolute number of Br atoms $N_{Br}(t)$ should be proportional to the residence time t , to the capture area A_c of the particle and to a sticking coefficient s , which is a measure of the surface morphology and chemistry of a given dust grain: $N_{Br}(t) \propto t \cdot A_c \cdot s$ (Eq. 2). A_c characterises the capture probability and s the probability that the particle holds the Br atom (even after cleaning procedures). As the capture area A_c we take the geometrical contour. There is, however, no good measure for the sticking coefficient s . Therefore we make the third assumption that as a first approximation s is proportional to the particle mass m . This is justified if the number of possible chemical reaction partners for Br increases with the particle mass which is supported by the observation that Br is absent from the surface but rather concentrated in the FeO-rich portion of the volume in one IDP [12]. With this it follows: $N_{Br}(t) \propto t \cdot A_c \cdot m$ (Eq. 3). This contrasts to Eq. (1) which, by use of $C_{Br} \sim N_{Br}/m$ can be transformed to $N_{Br}(t) \propto t \cdot m$ (Eq. 4) and thus does not take into account the capture probability A_c in addition to the sticking probability s represented by the particle mass m .

BROMINE IN INTERPLANETARY DUST PARTICLES; Bohsung et al.

Eq. (3) implicitly assumes short residence time t i.e. that the particle is not Br saturated (slow contamination model). If the contamination process is fast compared to typical residence times, then N_{Br} becomes independent of t (fast contamination model): $N_{Br}(\text{sat}) \propto A_c \cdot m$ (Eq. 5).

In Fig. 2 the three situations as expressed in Eq. 4 (Rietmeijer's model) and Eqs. 3 and 5 (our models) for the set of 11 IDPs used by [3] are depicted after dividing both sides by the mass, i.e. plotting $C_{Br}[\text{ppm}]$ versus $t[\text{days}]$ (Fig. 2a), versus $t \cdot A_c[\text{days} \cdot \mu\text{m}^2]$ (Fig. 2b) and finally versus $A_c[\mu\text{m}^2]$ (Fig. 2c). Capture areas A_c are estimated from geometry data [10]. In Fig. 2a the data points are not correlated whatsoever but scatter rather widely. This already indicates that the original assumption of Rietmeijer [3] is insufficient for any statement on the probability of stratospheric Br contamination processes.



This contrasts to our models depicted in Fig. 2b and Fig. 2c where almost all data points are linearly correlated. Unlike in Fig. 1, the slopes of the correlation lines now are physically significant: they characterise the increase of Br concentration with time and capture area (Fig. 2b) and capture area (Fig. 2c), respectively. A more detailed investigation of Figs. 2b and 2c reveals that in both cases the correlations mainly depend on the variation of the capture area A_c . If at all, the residence time t seem to play only a minor role, since the correlation of Fig. 2c is higher than that of Fig. 2b with only one particle (U2022G17) being far off the correlation line. Therefore we conclude that our simple fast contamination model can explain the observed bromine enrichments as caused by stratospheric contamination. If the

latter is true, then broken cluster particles are no longer problematic: because of the short duration of contamination now one could conceive Br enrichments of the cluster fragments even after their collision with the sampling collector. In conclusion, with our simple model the Br enrichment data – at least for the available rather small set of IDPs – can be understood as due to stratospheric contamination processes, supporting the experimental observations by Rietmeijer [3] that stratospheric Br-salt nanocrystals are associated with IDP W7029E5.

References: [1] Flynn, G., ICARUS 77, 287-310, 1989. [2] Jessberger, E. K., J. Bohsung, S. Chakaveh, and K. Traxel, Earth Planet. Sci. Lett., 112, 91-99, 1992. [3] Rietmeijer F. J. M., J. Geophys. Res., E4, 7409-7414, 1993. [4] Van der Stap, C. C. A. H., Academisch

Nr.	IDP Name	Mass [pg]	C_{Br} [ppm]	Times [days]	A_c [μm^2]
1	W7066*A4	424	43	70.8	292
2	U2022G17	110	150	223.7	307
3	W7013H17	1188	5	53.0	769
4	U2022C18	892	36	68.8	758
5	U2022G2	2000	34	26.8	870
6	U2022B2	1333	8	46.7	1004
7	W7029*A27	1666	30	35.1	314
8	W7013A11	3500	60	20.8	1464
9	U2001B6	4776	90	31.1	1647
10	U2022G1	6056	130	34.8	2700
11	U2015G1	6111	100	13.5	1647

Table 1: Particle masses and Br concentrations from [5,7], residence times from [3]. Capture areas A_c are calculated using particle dimensions and shapes from [10]. Numbers in the first row allow IDP identification in Figs. 1 and 2.

Proefschrift, University of Amsterdam, The Netherlands, 1986. [5] Sutton S. R., and G. J. Flynn, Proc. Lunar Planet. Sci. Conf., 18th, 607-614, 1988. [6] Wallenwein, R., Ch. Antz, E. K. Jessberger, A. Buttewitz, A. Knöchel, K. Traxel and M. Bavdaz, Lunar and Planet. Sci., XX, 1172-1173, 1989. [7] Flynn, G. J., and S. R. Sutton, Proc. Lunar Planet. Sci. Conf., 20th, 335-342, 1990. [8] Rietmeijer F. J. M., J. Volcanol. Geotherm. Res., 55, 69-83, 1993. [9] Wilson, L., and T. C. Huang, Earth Planet. Sci. Lett., 44, 311-324, 1979. [10] Flynn, G. J., and S. R. Sutton, Proc. Lunar Planet. Sci., 21, 541-547, 1991. [11] Cosmic Dust Courier Nr. 7, Code SN2, p. 13, NASA/Johnson Space Center, 1986. [12] Stephan, T., W. Klöck, E. K. Jessberger, and J. Zehnpfennig, Meteoritics, 27, 292, 1992.

THE SOLUBILITY OF PLATINUM IN SILICATE MELTS: EXPERIMENTS UNDER OXIDIZING CONDITIONS; A. Borisov, H. Palme, B. Spettel, MPI für Chemie, Saarstrasse 23, 55122 Mainz, Germany

The effects of oxygen fugacity and temperature on the solubility of Pt in silicate melts of anorthite-diopside eutectic composition at 1 atm total pressure were determined using metal loops. The main Pt-species in the melt is Pt^{2+} . The solubility of Pt was found to increase with temperature in pure O_2 , while the solubility in air seems to be temperature independent. Extrapolations to the high temperatures and low oxygen fugacities, perhaps appropriate for core formation in the Earth, indicate that Pt partition coefficients between iron metal and silicate melts may be very high ($10^7 - 10^{16}$).

Experimental. As in earlier work [1,2,3] liquid silicate droplets (2-3 mm diameter) were equilibrated with 0.5-1.0 mm wide Pt metal band loops inside a furnace with controlled oxygen fugacity. After the experiments metal loops were removed and glasses were analysed for Pt by INAA. Because of the low neutron flux of the TRIGA-reactor ^{199}Au could be used for Pt-analysis. The sensitivity of INAA for Pt-analysis, however, is lower than for Pd or Ir. In addition, Ca-produced ^{47}Sc (159.1 keV) caused interference on the 158.4 keV line of ^{199}Au . For these reasons experiments were restricted to oxidizing conditions with solubilities not lower than one ppm.

Results. Three experimental points at 1400°C reveal decreasing Pt concentrations with decreasing oxygen fugacity, from 17.9 ppm in pure oxygen to 7.6 ppm in air (Fig.1). In an experiment at $10^{-3.4}$ atm the Pt concentration was found to be below the detection limit of the INAA (<1 ppm). Thus, Pt solubility decreases with decreasing $f\text{O}_2$ similar to what was found for Ir, Pd and Au [1,2,3], but in contrast to the results of Amosse et al. [4] and Amosse and Allibert [5] for Pt and Ir. The slope of the correlation of $\log(\text{Pt})$ vs. $\log(f\text{O}_2)$ is 0.54, indicating Pt^{2+} as the main Pt-species in silicate melt. In [5] it was suggested that Pt^0 , at a level of 25 ppb, is the only Pt-species in silicate melts, independent of oxygen fugacity. The decrease of Pt solubility at reducing conditions is supported by one experiment of Fleet et al. [6] at 1300°C and an $f\text{O}_2$ close to QFI. These authors found a Pt content of 70 ppb in silicate melt equilibrated with two immiscible complex FePdIrPt-alloys. Recalculation to the solubility of pure Pt (assuming ideal solid solution of Pt in the alloy) gives values of about 0.3-1.1 ppm, which are an order of magnitude higher than extrapolation of our results to the same conditions. This difference may be explained by different melt compositions, nonideality of the alloys and inaccuracy of our extrapolation.

At constant $f\text{O}_2$ Pt-solubility increases with increasing temperature in pure oxygen and remains constant in air (Fig.2), opposite to the behavior of metals of the Fe group, with decreasing solubilities at increasing temperature (see, for example, [7] for Ni, Co and Mo). Different temperature slopes for different $f\text{O}_2$ are unexpected. For Pd-solubilities the same slope of 5 different $f\text{O}_2$ values was found, within error limits [1].

D^{Pt} (iron metal/silicate melt). The results for Pt-solubility at oxidizing conditions were extrapolated to high temperatures and low oxygen fugacities and corresponding metal/silicate partition coefficients were calculated. Two assumptions were made: (1) Pt-solubility is temperature independent at reducing conditions; (2) only Pt^{2+} is stable in the melt. With these assumptions the following equation could be derived from the experimental results:

$$\log(\text{Pt, ppm}) = 0.5 \cdot \log(f\text{O}_2) + 1.23$$

or converting to D^{Pt} (wt. ratios), (see [1] for details):

$$\log(D^{\text{Pt}}) = -0.5 \cdot \log(f\text{O}_2) + 5.31 - \log(\gamma_{\text{Pt}})$$

The activity coefficient of Pt in iron metal (γ_{Pt}) was taken from [8]. We want to emphasize the extremely low γ_{Pt} in solid iron at low Pt-concentration compared with other nobel metals resulting in a very high D^{Pt} value. For example, at 1300°C the difference between $\log(\gamma_{\text{Pt}}) = -4.53$ [8] and $\log(\gamma_{\text{Pd}}) = -0.67$ [9] alone produces a 4 orders of magnitude higher D^{Pt} value compared with D^{Pd} !

Lines of constant D^{Pt} s are shown in Fig. 3 at $f\text{O}_2$ -conditions more reducing than the IW buffer. These lines cross the IW buffer curve, reflecting a decrease of D^{Pt} with increasing temperature along or parallel to the IW-buffer. However, even at temperatures as high as 3500 K, which was suggested by Murthy in his model of global mantle/core equilibrium [10], Pt solubility is still very low (0.4 ppm). Assuming $\gamma_{\text{Pt}} = 1$ (ideal behavior of Pt in liquid iron at very high temperatures) the calculated D^{Pt} value at $f\text{O}_2 = \text{IW-2}$ is about 10^7 .

Comparing the present results with earlier data [1,2,3] we can establish a sequence of relative metal/silicate partition

THE SOLUBILITY OF PLATINUM... Borisov et al.

coefficients for different nobel metals: $D^{Pt} \gg D^{Ir} \gg D^{Pd} \sim D^{Au}$. It is interesting that sulfide/silicate partition coefficients at 1300°C and QFI follow the same sequence: $D^{Pt} \gg D^{Ir} \sim D^{Pd}$ [6].

Conclusions: The Pt content in upper mantle rocks is about 1% of the CI-chondritic value, and Pt/Ir and Pt/Au ratios are approximately chondritic. Thus, neither the high absolute value of D^{Pt} , nor the high D^{Pt}/D^{Ir} and D^{Pt}/D^{Au} ratios are compatible with a global mantle/core equilibrium as was suggested in [10]. The accretion of a late chondritic veneer to the Earth is probably the best explanation for these data.

References: [1] Borisov A. et al. (1993) *GCA*, in press; [2] Borisov A. et al. (1992) *LPSC XXIII*, 139; [3] Borisov A. et al. (1993) *LPSC XXIV*, 147; [4] Amosse et al. (1990) *Chem. Geology*, 81, 45; [5] Amosse J. and Allibert M. (1993) *GCA*, 57, 2395; [6] Fleet M.E. et al. (1991) *GCA*, 55, 2545; [7] Holzheid A. et al. (1994) *GCA*, submitted; [8] Gudmundsson G. and Holloway J.R. (1993) *Am. Mineral.*, 78, 178; [9] Hultgren R. et al. (1973) Selected values of thermodynamic properties of binary alloys, *American Society for metals, Metals Park, Ohio*; [10] Murthy V.R. (1991) *Science*, 253, 303.

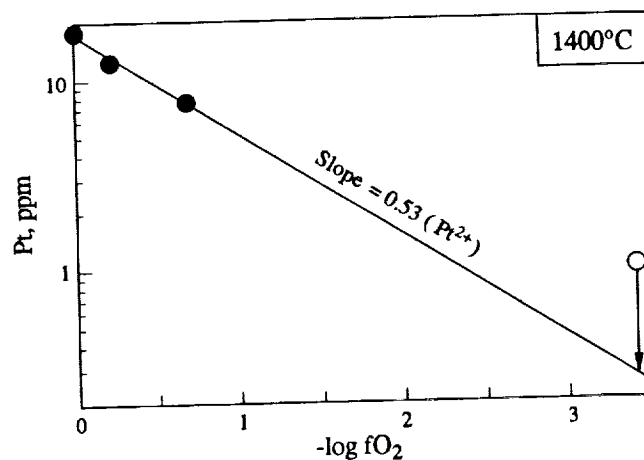


Fig.1. Effect of fO_2 on Pt solubility in silicate melts at 1400°C

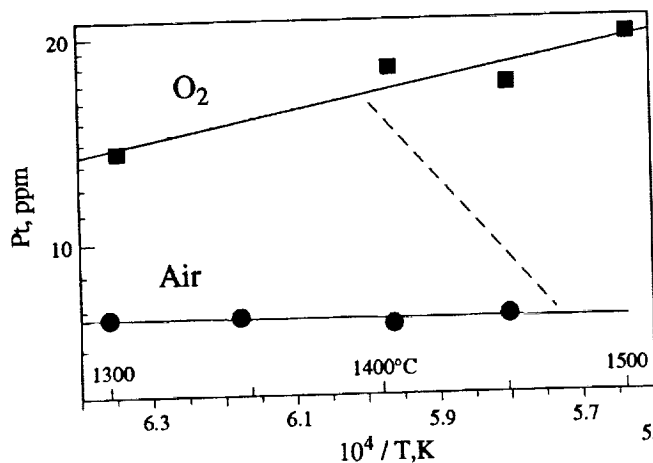
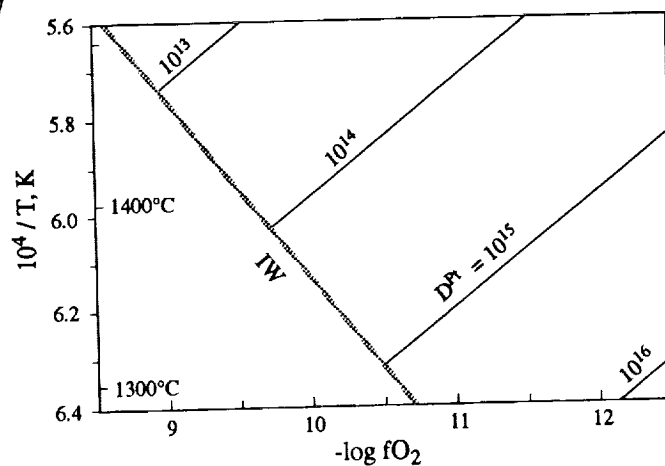


Fig.2. Effect of temperature on Pt solubility in silicate melts at constant fO_2 (O_2 or air). Dashed line indicates typical slope for elements of the Fe-group.

Fig.3. Lines of constant $D^{Pt}(Fe/melt)$ values on $1/T$ vs. $\log(fO_2)$ diagram.



Phosphorus Chemistry in the Atmospheres of Jupiter and Saturn

S.Borunov,* V.Dorofeeva, I.Khodakovsky,[†] P.Drossart, E.Lellouch, Th.Encrenaz*

* *Observatoire de Paris-Meudon, 92195 Meudon Principal Cedex, France*

[†] *Vernadsky Institute of Geochemistry and Analytical Chemistry, Moscow, Russia*

The chemistry of phosphorus compounds in the atmospheres of Jupiter and Saturn is investigated, leading to new distributions of phosphorus species. It is found that phosphine PH_3 is the most abundant gaseous compound in temperature region 300-2000 K. The observed PH_3 abundances are found to be equal to its equilibrium abundances at $T > 600$ K in all the cases which have been analyzed, including a sensitivity study to variations of elemental phosphorus and oxygen abundances. The P_4O_6 abundances are negligible within all the temperature range.

The only phosphorus compound to have been detected on Jupiter and Saturn is PH_3 (see, e.g.[1]). Previous studies [2], [3], [4] have concluded that PH_3 is the stable chemical state of phosphorus only at $T > 1000$ K. In Figures the equilibrium distributions of the main phosphorus gaseous compounds along the jovian adiabat, in case of solar phosphorus and oxygen abundances, for old (above) and update (below) thermochemical data are presented. Similar distributions are for saturnian atmosphere.

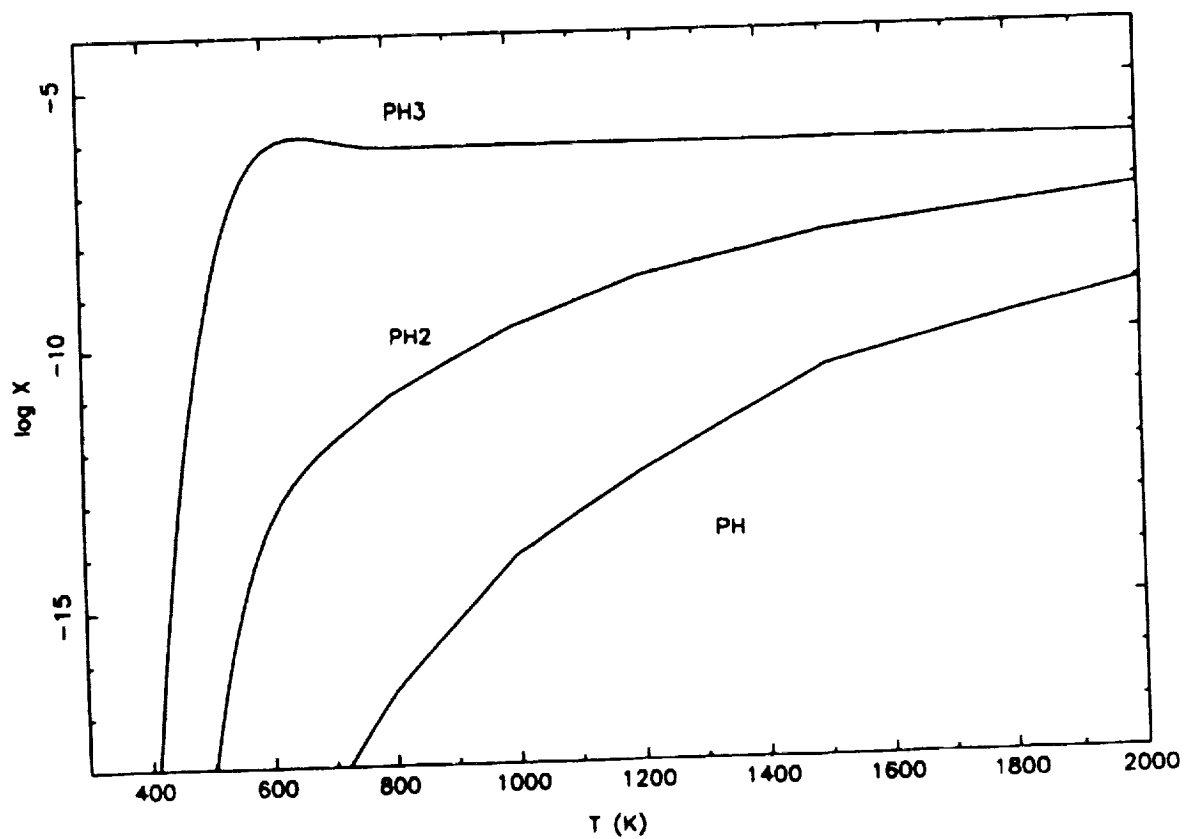
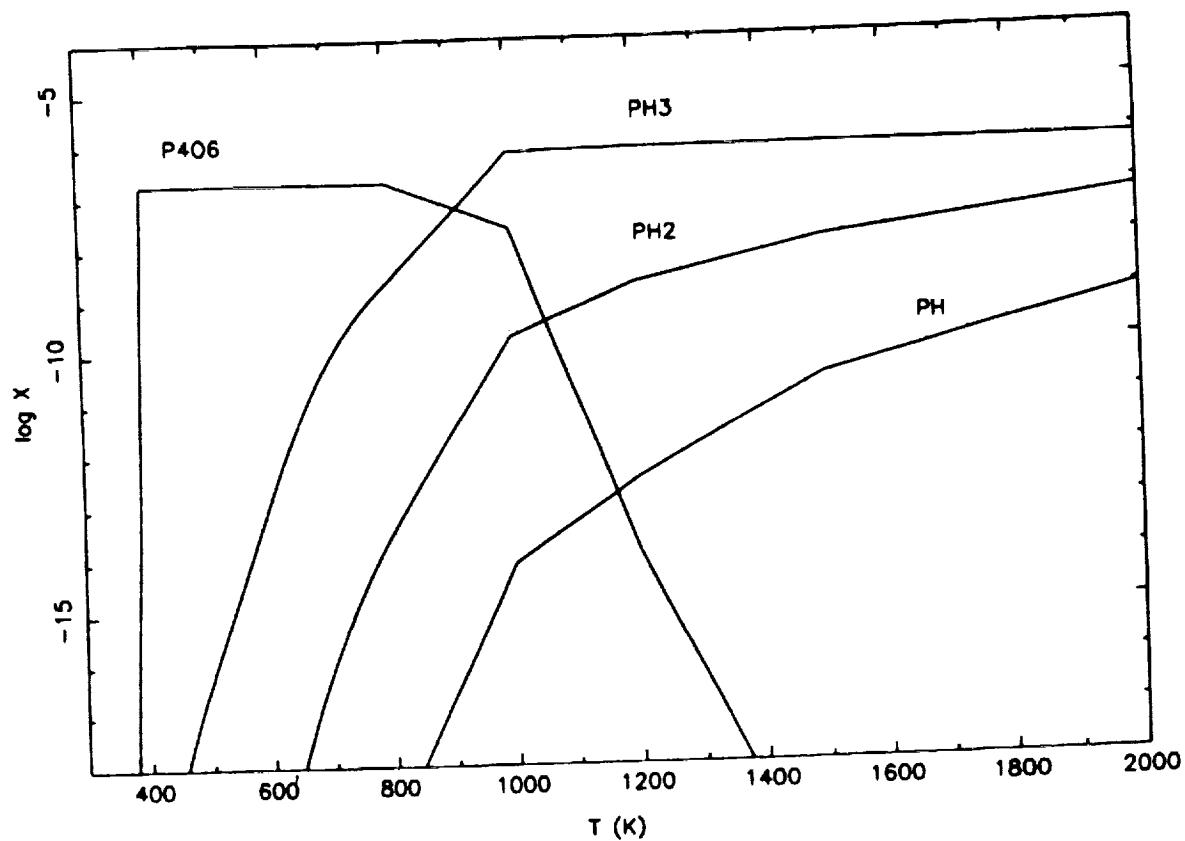
Table 1. T_{cond} (K) of $NH_4H_2PO_4(s)$ at various abundances of phosphorus and oxygen (relative to solar).

Jupiter			Saturn		
Abundances		T_{cond}	Abundances		T_{cond}
O=1.0	P=1.0	535	O=2.5	P=2.5	580
O=1/50	P=1.0	426	O=1.0	P=2.5	556
O=5.0	P=1.0	578	O=10.0	P=2.5	625
O=1.0	P=1/5	524	O=2.5	P=1.0	575
O=1.0	P=5.0	546	O=1.0	P=10.0	592

- References. [1] Encrenaz Th. (1990) Rep.Prog.Phys., **53**, 793. [2] Lewis J. (1969) Icarus, **10**, 393. [3] Barshay S.S. and Lewis J. (1978) Icarus, **33**, 593. [4] Fegley B., Jr. and Prinn R.G. (1985) Jp.J. **299**, 1067.

Phosphorus on Jupiter and Saturn

Borunov S. et al.



AXIAL FOCUSING OF SEISMIC ENERGY FROM A LARGE IMPACT ON EARTH:
PRELIMINARY NUMERICAL SIMULATIONS; M.B. Boslough and E.P. Chael, Sandia
National Laboratories, Albuquerque, NM 87185.

We have proposed a hypothesis and performed preliminary proof-of-principle simulations for the coupling of energy to the earth's mantle from a major impact by axial focusing of seismic waves. Because of the axial symmetry of the explosive source, the phases and amplitudes are dependent only on ray parameter (or takeoff angle) and are independent of azimuthal angle. For a symmetric and homogeneous earth, all the seismic energy radiated by the impact at a given takeoff angle will be refocused (minus attenuation) on the axis of symmetry, regardless of the number of reflections and refractions it has experienced. Mantle material near the axis of symmetry will experience more strain cycles with much greater amplitude than elsewhere, and will therefore experience more irreversible heating. This mechanism may give rise to an isostatic instability leading to uplift, rifting, or volcanism. The situation is very different than for a giant earthquake which has an asymmetric focal mechanism and a larger area. It should be noted that our hypothesis is fundamentally different from those proposed by others [e.g. 1-4] which involve melting and excavation at the impact location.

Along with the appreciation of the importance of impact events on the earth's evolution, there has been increasing speculation that energetic collisions have been responsible for processes as varied as continental flood basalt eruptions, mantle plumes, continental rifting, and geomagnetic pole reversals. The link between impacts and such geophysical processes was first discussed by Seyfert and Sirkin [5], who suggested that impact-induced mantle plumes could be a mechanism for initiating the breakup of plates. Burek and Wanke [6] listed correlations between known Cenozoic impacts and geomagnetic field reversals, unconformity ages, shifts in paleotemperatures, and tectonic episodes. They suggested that major impacts could generate shock-induced phase transitions in the upper mantle, disrupting a delicately-balanced stability down to the core-mantle boundary. Rampino and Strothers [7] proposed a quasi-periodic correlation between mass extinctions and major continental flood basalt volcanism over the last 250 million years and attempted to explain it in terms of episodic showers of impacting comets. Connections between impacts and the internal workings of the earth are supported by correlations of the ages of tektites from strewn fields with geomagnetic field reversals [8], and by a reversal associated with sediments deposited immediately after the impact that formed the Ries Crater [9].

A causal link between major impact events and global processes would probably require a significant change in the thermal state of the earth's interior, presumably brought about by coupling of impact energy. One possible mechanism for such energy coupling from the surface to the deep interior would be through focusing due to axial symmetry. Antipodal focusing of surface and body waves from earthquakes is a well-known phenomenon [10] which has previously been exploited by seismologists in studies of the earth's deep interior [11,12]. Antipodal focusing from impacts on the moon, Mercury, and icy satellites has also been invoked by planetary scientists to explain unusual surface features opposite some of the large impact structures on these bodies [13,14]. For example, "disrupted" terrains have been observed antipodal to the Caloris impact basin on Mercury and the Imbrium basin on the Moon. Very recently there have been speculations that antipodal focusing of impact energy within the mantle may lead to flood basalt and hotspot activity [15,16], but there has not yet been an attempt at a rigorous model.

For the preliminary seismic modeling, the impact was represented as a vertical point force applied at the earth's surface as a delta function in time. The impactor was assumed to yield an

AXIAL FOCUSING OF SEISMIC ENERGY; Boslough M.B. and Chael E.P.

impulse of approximately 3×10^{24} dyne sec, as an estimate of a K/T-sized impact. Synthetic displacement and strain records were generated for such a source by summing the normal modes of the elastic earth model 1066A of Gilbert and Dziewonski [17]. We used the attenuation profile of the model PREM [18] to determine Q values for the 1066A modes. We assumed a vertically-directed point source, so we included only spheroidal modes in the synthetic seismogram calculations. Toroidal modes are not excited by a vertical point force. All spheroidal modes with periods greater than 45 seconds were summed for the synthetics.

The synthetic signals yield estimates of the peak strains at any location in or on the earth. Strains at the surface near the antipode (angular distance = 180°) are orders of magnitude higher than those over most of the rest of the earth's surface. Figure 1 demonstrates that focused arrivals have much greater amplitudes than direct arrivals at the core-mantle boundary. The direct arrival can be seen for a point directly beneath the impact, followed by a long high-amplitude focused trace. Figure 2 plots the peak strains as a function of depth beneath the antipode of the impact, from the surface to the core-mantle boundary. It can be seen that peak strain amplitude varies by two orders of magnitude, and is largest at the top. This would imply that most of the energy is focused at shallow depths. Future work will model the impact using shock-dynamics codes to determine how the impact generates seismic waves.

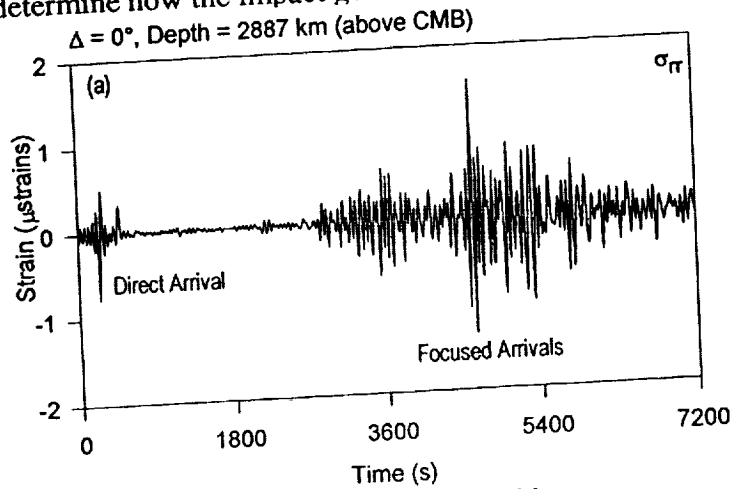


Figure 1. Synthetic strain history

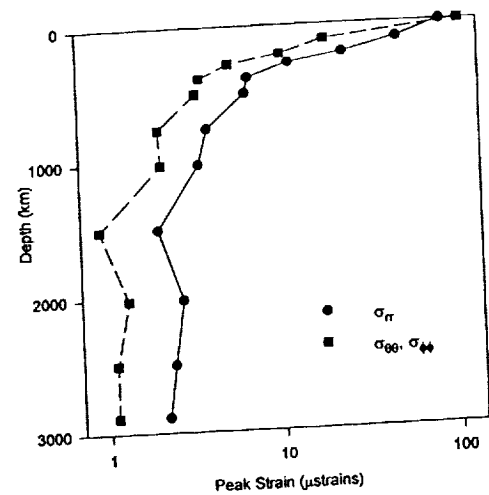


Fig. 2. Peak strain along antipode

References: [1] Green (1972) *Earth and Planet. Sci. Lett.*, 15, 263-270. [2] Alt et al. (1988) *J. Geol.*, 96, 647-662. [3] Oberbeck et al. (1992) *J. Geol.*, 101, 1-19. [4] Negi et al. (1993) *Phys. Earth Planet. Int.*, 76, 189-197. [5] Seyfert and Sirkin (1979) *Earth History and Plate Tectonics*. NY: Harper & Row. [6] Burek and Wanke (1988) *Phys. Earth Planet. Inter.*, 50, 183-194. [7] Rampino and Strothers (1988) *Science*, 241, 663-668. [8] Glass et al. (1979) *Proc. Lunar Planet. Sci. Conf. 10th*, pp. 25-37. [9] Pohl J. (1977) *Geol. Bavarica*, 75, 329-348. [10] Gutenberg and Richter (1934) *Gerlands Beitr. Geophys.*, 43, 56. [11] Rial (1979), Ph.D. Thesis, Caltech. [12] Chael (1983), Ph.D. Thesis, Caltech. [13] Schultz and Gault (1975) *The Moon*, 12, 159-177. [14] Watts et al. (1991) *Icarus*, 93, 159-168. [15] Hagstrum and Turrin (1991) *EOS*, 72 (44), p. 516. [16] Rampino and Caldeira (1992) *Geophys. Res. Lett.*, 19, 2011-2014. [17] Gilbert and Dziewonski (1975) *Phil. Trans. Roy. Soc. Lond. A*, 278, 187-269. [18] Dziewonski and Anderson (1981) *Phys. Earth Planet. Inter.*, 25, 297-356.

Acknowledgments: This work performed at Sandia National Laboratories by the U.S. Dept. of Energy under contract DE-AC04-94AL85000, with funding under the LDRD program

COMET SHOEMAKER-LEVY 9: AN UPPER BOUND ON ITS MEAN DENSITY. A. P. Boss, DTM, Carnegie Institution of Washington, 5241 Broad Branch Road N.W., Washington DC 20015.

The tidal disruption of Comet Shoemaker-Levy 9 (SL-9) after passage well within the Roche limit of Jupiter can be used to set an upper bound on the mean density of the pre-disruption body: if the body was dense enough, its self-gravity would have prevented the divergence of the tidally-fractured rubble. Assuming a perijove radius of $r_P = 1.62R_J$, where R_J is Jupiter's radius, the theoretical upper bounds range from a mean density $\rho_c < 0.702 \text{ g cm}^{-3}$ for a simple analytical model that agrees with numerical (SPH) simulations, to $\rho_c < 1.50 \text{ g cm}^{-3}$ for a more detailed semi-analytical model. Because these upper bounds are proportional to $(1.62R_J/r_P)^3$, an accurate determination of r_P is necessary in order to constrain the mean density by this mechanism. If $r_P \sim 1.62$, the theoretical models imply that prior to disruption, Comet SL-9 was not a body with $\rho > 2 \text{ g cm}^{-3}$ (e.g., an asteroid).

INTRODUCTION. Comet SL-9 appears to have been tidally disrupted into multiple pieces following a close encounter inside the Roche limit of Jupiter [1]. While the pre-disruption body evidently had little tensile strength [2], the fact that the resulting pieces were able to emerge on independent orbits requires that the self-gravity of the comet was too weak to hold a rubble pile together, i.e., the mean density could not have been too large. Previous theoretical models of tidal disruption [3,4,5,6] can then be used to place an upper bound on the mean density of Comet SL-9 prior to disruption [7]. Cometary densities have been estimated on the basis of outgassing rates and non-gravitational orbital perturbations to be significantly lower than that of solid ice, implying a high porosity [8]; specific estimates include 0.6 g cm^{-3} [9] and even 0.3 g cm^{-3} [10] for Comet Halley. However, because of the likelihood of large errors in the quantities used to derive estimates based on outgassing, the error bars for Comet Halley probably range from 0.03 to 4.9 g cm^{-3} [11]. The tidal disruption of Comet SL-9 potentially offers a tighter upper bound on the mean density of a comet, provided the theoretical models can be refined and the perijove radius can be determined.

ASSUMPTIONS. Numerical and analytical models of tidal disruption [3,4,5,6] agree that tidal disruption is possible during a close encounter with the primary body provided that four criteria are met: (1) the mass of the secondary body is much less than that of the primary, (2) the pericenter radius (r_P) is well within the Roche limit, (3) the velocity at infinity is small (i.e., the orbit is nearly parabolic), and (4) the dynamical motions are not dissipated. For Comet SL-9, the first two criteria are certainly met, and the latest orbital solutions imply that the pre-disruption orbit was bound to Jupiter, so that the third criterion is also fulfilled. While the viscosity of cometary ice is high enough to strongly dissipate fluid motions, for a tidal encounter a comet should react as an elastic rather than a viscous body. This follows from comparing the Maxwell time $\tau_M = \rho\nu/\mu$ (ρ = density of secondary, ν = kinematic viscosity, μ = modulus of rigidity) to the encounter time, which is about 10^4 s for Jupiter. An elastic body description is justified [6] if $\tau_M > 10^4 \text{ s}$. For a comet, $\rho \sim 1 \text{ g cm}^{-3}$, $\nu \gg 10^{14} \text{ cm}^2 \text{ s}^{-1}$, and $\mu \sim 3.5 \times 10^{10} \text{ dynes cm}^{-2}$, so that $\tau_M \gg 3 \times 10^3 \text{ s}$. This means that the close encounter occurs so quickly that the comet cannot adjust to the changing tidal forces through viscous flow, and instead will tidally fracture and behave similar to an elastic rubble pile.

THEORETICAL CONSTRAINTS. Three different approaches have been taken to studying the tidal disruption problem, and each yields its own theoretical upper bound on the mean density [7]. All three yield constraints of the form

$$\rho_c < \rho_u \left(\frac{1.62R_J}{r_P} \right)^3,$$

COMET SHOEMAKER-LEVY 9: Boss, A. P.

where ρ_u is the upper bound. An analysis of the scattering of fragments following the encounter [3] produced $\rho_u = 0.934 \text{ g cm}^{-3}$. A simple analytical model [4,5], calibrated by the results of detailed smoothed particle hydrodynamics (SPH) simulations of the tidal disruption of lunar-sized bodies by the Earth (see Fig. 1), yielded $\rho_u = 0.702 \text{ g cm}^{-3}$. A semi-analytical model of the tidal disruption of small fluid bodies [6] leads to $\rho_u = 1.50 \text{ g cm}^{-3}$. All three of these estimates have been normalized to an assumed perijove radius of $r_P = 1.62R_J$ [2,12]. Because of the strong dependence of these upper bounds on r_P , the largest uncertainty in the upper bound may be due to the uncertainty in the perijove radius. However, there is also a large uncertainty due to the factor of two difference between the two extremes for the theoretical models. This uncertainty presumably could be reduced by a concentrated effort, such as the use of an SPH code to study more precisely the physics of a comet being disrupted by Jupiter. Such a more precise determination should also take into account the likelihood that the pre-disruption comet was significantly non-spherical and rotating.

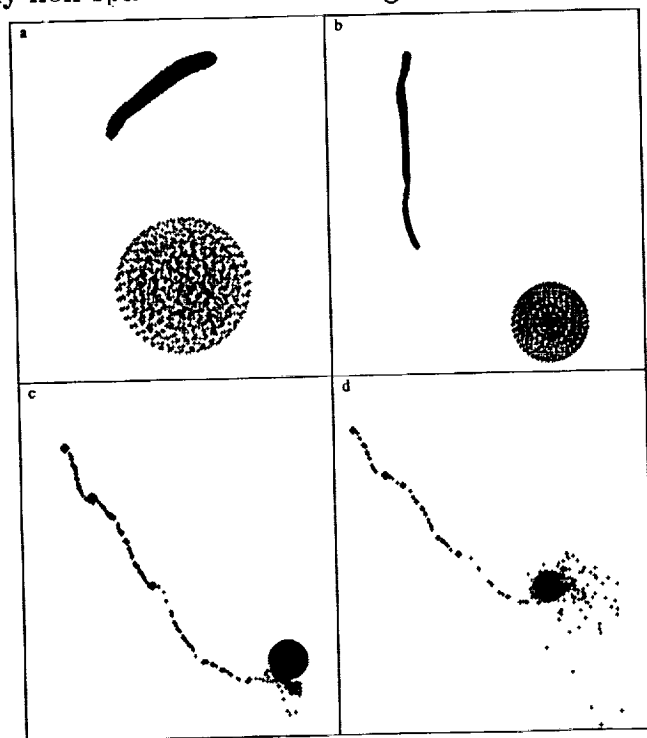


Fig. 1. Tidal disruption of a lunar-sized body by the Earth as calculated by an SPH code [5]. This calculation provides a heuristic analog for the tidal disruption of a comet by Jupiter. Note that the secondary body is tidally distorted into a string-like configuration, similar to the 'string of pearls' appearance of Comet SL-9.

REFERENCES. [1] Marsden, B. G. (1993). *IAU Circular 5800*. [2] Sekanina, Z. (1993). *Science*, **262**, 382. [3] Ziglina, I. N. (1978). *Phys. Solid Earth*, **14**, 467. [4] Boss, A. P. (1991). *LPSC XXII*, 129. [5] Boss, A. P., Cameron, A. G. W., & Benz, W. (1991). *Icarus*, **92**, 165. [6] Sridhar, S., & Tremaine, S. (1992). *Icarus*, **95**, 86. [7] Boss, A. P. (1994). *Icarus*, in press. [8] Grün, E. (1990). In *Asteroids Comets Meteors III*, eds. C.-I. Lagerkvist, H. Rickman, B. A. Lindblad, & M. Lindgren (Uppsala: Uppsala U. Press), 321. [9] Sagdeev, R. Z., Elyasberg, P. E., & Moroz, V. I. (1988). *Nature*, **331**, 240. [10] Rickman, H., & Huebner, W. F. (1990). In *Physics and Chemistry of Comets*, ed. W. F. Huebner (Berlin: Springer-Verlag), 245. [11] Peale, S. J. (1989). *Icarus*, **82**, 36. [12] Chodas, P. W., & Yeomans, D. K. (1993). *B.A.A.S.*, **25**, 1042.

MIDPLANE TEMPERATURES AND SOLAR NEBULA EVOLUTION.

A. P. Boss, DTM, Carnegie Institution of Washington, 5241 Broad Branch Road N.W., Washington DC 20015.

The thermal structure of the solar nebula is important not only for the chemical evolution of grain aggregates that eventually formed meteoritical components, but also for determining the dynamical evolution of the nebula. Improvements to the radiative transfer solution method have allowed a new series of 2D solar nebula models to be computed. The new models confirm previous calculations that produced a relatively warm (midplane temperature $T_m > 1000$ K inside 2.5 AU) inner region in a minimum mass ($0.020 M_\odot$) nebula undergoing mass accretion at $\sim 10^{-6}$ to $10^{-5} M_\odot \text{ yr}^{-1}$. The radial extent of the region with $T_m > 1000$ K shifts inward to about 1.5 AU in a lower mass nebula ($0.0086 M_\odot$). While the surface density appears to be too low for such a nebula to evolve through gravitational torques, thermal ionization of K and Na may allow the generation of significant magnetic fields at the warm nebula midplane.

INTRODUCTION. The extent to which the solar nebula was globally warm enough to account for volatile depletions [1] and other chemical patterns in primitive meteorites can be addressed through theoretical calculations of the thermal structure expected in a minimum mass nebula surrounding a solar-mass protostar. Calculations of the 2D structure of a low-mass nebula still accreting gas and dust from its parent molecular cloud core suggest that midplane temperatures high enough to account for significant volatile depletion may well have occurred [2,3]. Extrapolation of surface temperatures inferred for disks around T Tauri stars to midplane values predicts similar temperature profiles [4].

NUMERICAL METHODS. The 2D equations of gravitational hydrodynamics and radiative transfer are solved by a spatially second-order method [5]. The previous investigation [2,3] was limited by the slow convergence of the radiative transfer equation. Improvements in this solution led to a speed-up by about a factor of 20, and allowed several new models to be calculated and evolved farther in time than the previous model [2,3].

RESULTS. The ability to calculate farther in time means that the models can now be pushed past the transients associated with relaxation of the initial temperature guess toward a quasi-equilibrium temperature distribution, and into a phase where the nebula cools because of the artificial depletion of matter infalling onto the nebula from the envelope (mass is not allowed to enter the grid). This allows the true quasi-equilibrium temperature to be approximated by extrapolation back to $t = 0$, using the cooling trend (Fig. 1a). The first model is a recalculation of the previous model [2,3], in order to see if the new numerical methods have any effect. As shown in Fig. 1b, the midplane temperature in the new model is close to that of the previous model, though slightly higher inside 3 AU. Other models have been calculated with variations in the inner boundary condition on the temperature distribution (1700 K, 1500 K, 500 K), the mass of the central protostar ($1 M_\odot$, $0.5 M_\odot$), the density of the infalling envelope, and the mass of the nebula ($0.020 M_\odot$, $0.0086 M_\odot$ inside 10 AU, see Fig. 1b). The $0.020 M_\odot$ model is warm enough to be stable to the growth of self-gravitational spiral structures [6] that could result in nebula evolution. The model is also largely convectively stable, except in the radial direction in the vicinity of the sharp T_m drop at 2 AU to 4 AU, and near the nebula surface, though the absence of convective instability in the vertical direction could be caused by an incomplete relaxation of the temperature distribution. However, the model is also warm enough to thermally ionize sufficient K and Na atoms to allow the decay time of a magnetic field due to resistive diffusion [7] to be longer than the rotational period (Fig. 2b) – i.e., the Balbus-Hawley instability can operate [8]. While this thermal ionization is limited to the midplane inside about 2.5 AU, other processes [9] may account for sufficient ionization outside 2.5 AU and away from the midplane to allow magnetic fields to grow throughout the nebula.

SOLAR NEBULA MODELS: Boss, A. P.

CONCLUSIONS. Lowering the nebula mass by a factor of 2.3 can lower midplane temperatures significantly. Thermal ionization of elements such as K and Na could result in sufficient ionization to allow the growth of magnetic fields in the inner nebula; ionization by decay of ^{26}Al and ^{40}K and by cosmic rays [9] could maintain the needed ionization elsewhere.

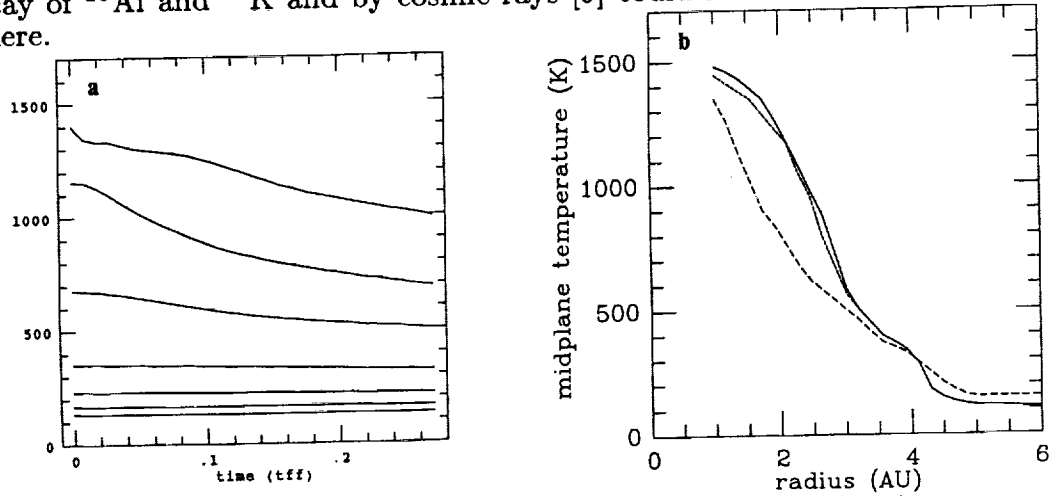


Fig. 1. a: Time evolution of the midplane temperature at various radii (from top: 1.0, 1.7, 2.7, 4.5, 6.3, 8.1, & 9.8 AU) in the $0.0086M_{\odot}$ model, showing initial transients followed by a 'linear' cooling phase. b: Midplane temperature for the new $0.020M_{\odot}$ model (solid line) compared to the previous model [2,3] (short-dashed line) and the new $0.0086M_{\odot}$ model (long-dashed line).

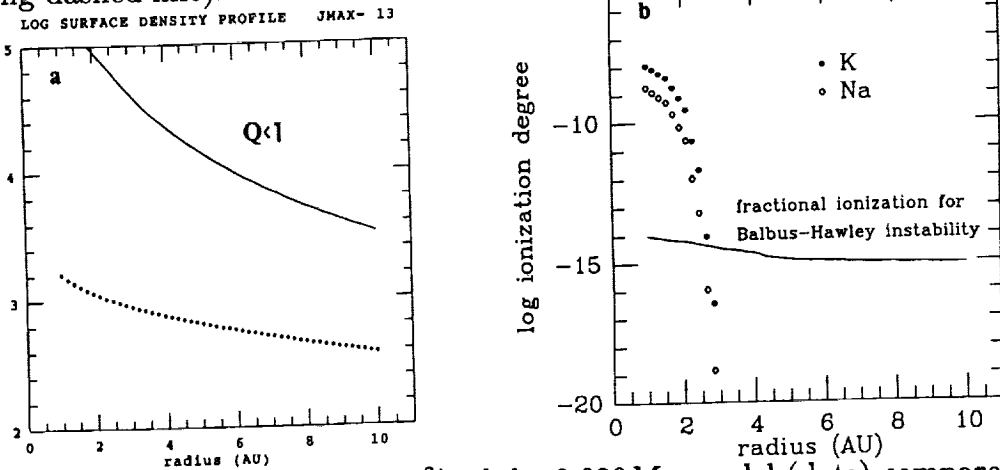


Fig. 2. a: Surface density (σ in g cm^{-2}) of the $0.020M_{\odot}$ model (dots) compared to the critical σ needed for gravitational instability ($Q < 1$) – the model appears to be stable. b: Fractional ionization (n_e/n_H) for the $0.020M_{\odot}$ model due to thermal ionization of K and Na, compared to that needed for growth of a magnetic field on a dynamic timescale (solid line).

REFERENCES. [1] Palme, H., & Boynton, W. V. (1993). In *Protostars & Planets III*, eds. E. H. Levy & J. I. Lunine (Tucson: Univ. Arizona), 979. [2] Boss, A. P. (1993). *LPSC XXIV*, 151. [3] Boss, A. P. (1993). *Ap. J.*, **417**, 351. [4] Cassen, P. (1992). *LPSC XXIII*, 207. [5] Boss, A. P., & Myhill, E. A. (1992). *Ap. J. S.*, **83**, 311. [6] Toomre, A. (1964). *Ap. J.*, **139**, 1217. [7] Jackson, J. D. (1962). *Classical Electrodynamics* (New York: Wiley), 313. [8] Hawley, J. F., & Balbus, S. A. (1992). *Ap. J.*, **400**, 595. [9] Stepinski, T. F. (1991). *LPSC XXII*, 1329.

INJECTION OF PRESOLAR GRAINS INTO THE SOLAR NEBULA BY A STELLAR SHOCK WAVE. A. P. Boss & P. N. Foster, DTM, Carnegie Institution of Washington, 5241 Broad Branch Road N.W., Washington DC 20015.

The ~ 1 Myr time interval between stellar nucleosynthesis of short-lived radioactivities and the incorporation of this material into grain aggregates in the solar nebula implies that the same star that generated these nuclides and isotopes also triggered the collapse of the presolar cloud. The interaction of a shock wave from an AGB star with a quiescent, solar-mass molecular cloud core has been modeled with a 3D gravitational hydrodynamics code. Such shock waves can trigger sustained gravitational collapse, and inject about half of the impacting stellar wind gas and presolar grains into the collapsing protostar. About $0.01M_{\odot}$ of AGB star matter would be injected into the protosolar cloud, consistent with estimates of the dilution of AGB star matter necessary to match solar system abundances of short-lived radioactivities.

INTRODUCTION. The presence of short-lived radioactivities such as ^{26}Al in meteoritical inclusions [1] requires a time interval on the order of 1 Myr between nucleosynthesis and formation of these inclusions [2]. This seems to exclude forming the solar system through the gradual contraction (over ~ 10 Myr) of a magnetically-supported molecular cloud core [3] in favor of a more impulsive means of initiating collapse of the presolar cloud, such as a supernova shock wave [4]. The meteoritical discovery of presolar grains (SiC, graphite, diamond) carrying distinctive isotopic anomalies consistent with nucleosynthesis in a carbon-rich star such as a low-mass asymptotic giant branch (AGB) star [5,6], coupled with the possibility of synthesizing the short-lived radioactivities in an AGB star [7], implies that a late-phase AGB star wind (planetary nebula) may have triggered the formation of the solar system. Previous calculations have shown that a supernova shock wave (1000 km/sec) can destroy a low-mass ($15M_{\odot}$) cloud [8]. Here we investigate the interaction of much gentler AGB star shock waves with solar-mass clouds.

NUMERICAL METHODS. The calculations were performed in 3D with a spatially and temporally second-order accurate gravitational hydrodynamics code [9]. Trajectories of tracers representing gas parcels or presolar grains are also calculated. A central sink cell absorbs the infalling matter and models its gravity as a point source. Isothermal thermodynamics is assumed, as is appropriate for relatively slow (25 km/sec) shock waves. 3D calculations require coarse grids that limit the ability of the calculation to follow the small-scale instabilities (Kelvin-Helmholtz, Rayleigh-Taylor) that are likely to develop. Accordingly, a new set of calculations is underway with a 2D 'piecewise parabolic method' (PPM) hydrodynamics code [10]. This code approximates the fluid variables within a cell with parabolae, as opposed to the linear expansions used in the second-order code. Cell average values are used as inputs for a series of shock problems with contact discontinuities located at each cell's edge. The code then solves the Riemann shock problem analytically for each cell. PPM can resolve shock fronts with just a few (~ 3) cells, about half that needed by other methods, and combined with the increased spatial resolution resulting from a restriction to 2D, the PPM calculations will allow us to follow the shock-cloud interaction more accurately.

RESULTS. The initial clouds are centrally condensed (20:1), spherical or prolate, gravitationally stable ($E_{\text{therm}}/|E_{\text{grav}}| = 0.57, 0.77$), and in uniform rotation ($E_{\text{rot}}/|E_{\text{grav}}| = 0.01, 0.04$). When struck solely by the dynamic (ram) pressure of a stellar shock wave (10 to 25 km/sec), the clouds are marginally unstable to gravitational collapse [11]. When the compressive effects of high temperature (10,000 K) gas behind the shock front are included (Fig. 1), sustained gravitational collapse results, and the central density increases by more than a factor of 10^5 . The trajectories of tracers placed around the periphery of the cloud (inside the shock front) show that roughly half the matter in the portion of the shock front that impacts the cloud is injected into the central protostellar disk (a sphere of radius 200 AU).

INJECTION OF PRESOLAR GRAINS: Boss, A. P. & Foster, P. N.

CONCLUSIONS. The models show that a stellar shock wave with characteristics similar to those of an AGB star wind in the planetary nebula phase is quite capable of inducing a solar-mass molecular cloud core into sustained self-gravitational collapse, without destroying the cloud. The trajectories of test particles indicate that about half of the matter in the stellar shock wave that interacts with the molecular cloud is injected into the protostellar cloud. About $0.01M_{\odot}$ of AGB star matter would be injected into the solar-mass cloud by this mechanism, consistent with estimates of the dilution needed to explain the abundances of short-lived radioactivities generated by AGB star nucleosynthesis [7].

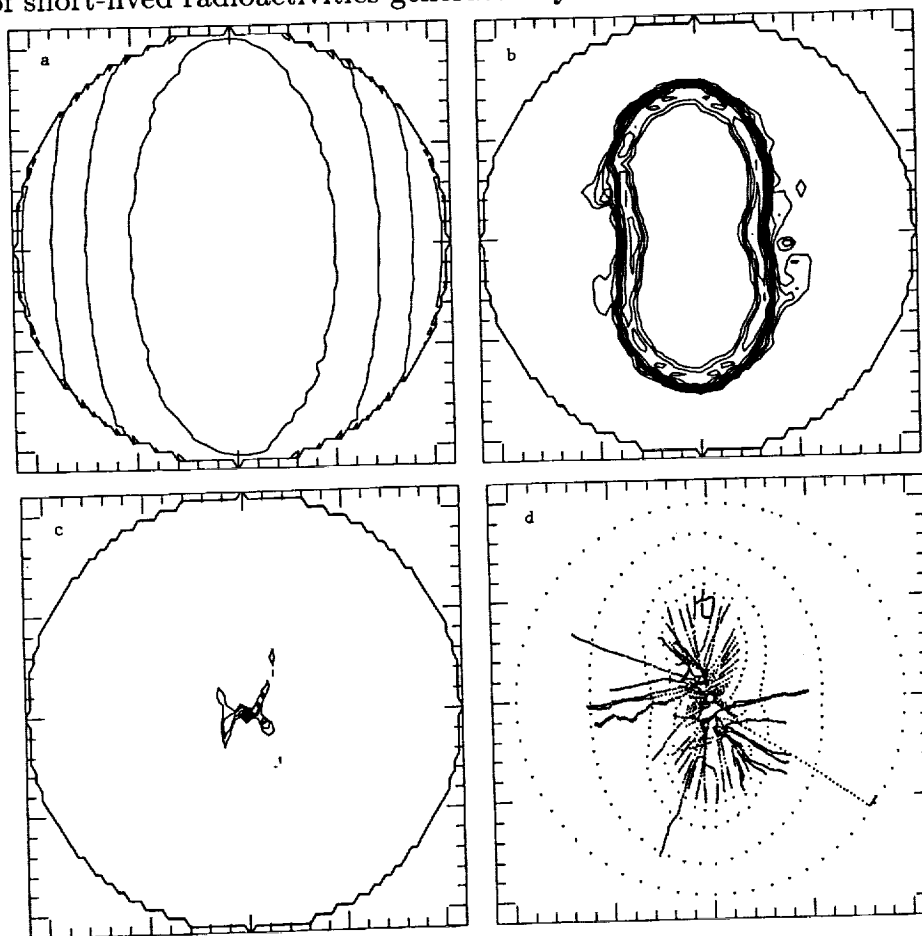


Fig. 1. Equatorial density contours at three times: a: $t = 0$, b: $0.144 t_{ff}$, c: $0.195 t_{ff}$, and d: particle trajectories from $t = 0$ through $0.488 t_{ff}$. The initially prolate molecular cloud (20,000 AU in diameter) is forced into gravitational collapse by a stellar shock wave entering from the right at 10 km/sec, immersed in 10,000 K gas. Roughly half the particles in the stellar shock wave are injected into the collapsing protostellar cloud.

REFERENCES. [1] Lee, T., Papanastassiou, D. A., & Wasserburg, G. J. (1976). *Geophys. Res. Lett.*, **3**, 41. [2] Wasserburg, G. J. (1985). In *Protostars & Planets II*, eds. D. C. Black & M. S. Matthews (Tucson: Univ. Arizona), 703. [3] Shu, F. H., Adams, F. C., & Lizano, S. (1987), *Ann. Rev. Astr. Ap.*, **25**, 23. [4] Cameron, A. G. W., & Truran, J. W. (1977). *Icarus*, **30**, 447. [5] Ott, U. (1993). *Nature*, **364**, 25. [6] Anders, E., & Zinner, E. (1993). *Meteoritics*, **28**, 490. [7] Wasserburg, G. J., Busso, M., Gallino, R., & Raiteri, C. M. (1994). *Ap. J.*, in press. [8] Różycka, M., & Tenorio-Tagle, G. (1987). *Astr. Ap.*, **176**, 329. [9] Boss, A. P., & Myhill, E. A. (1992). *Ap. J. S.*, **83**, 311. [10] Colella, P., & Woodward, P. R. (1984). *J. Comp. Phys.*, **54**, 174. [11] Boss, A. P., & Myhill, E. A. (1993). *LPSC XXIV*, 155.

PROVENANCE OF THE SPACEWATCH SMALL EARTH-APPROACHING ASTEROIDS. W. F. Bottke, Jr., M. C. Nolan, R. Greenberg, A. M. Vickery, and H. J. Melosh, Lunar and Planetary Laboratory, University of Arizona, Tucson, AZ 85721.

Recent discoveries of small Earth-approaching asteroids by the 0.9 m Spacewatch telescope (referred to here as S-SEAs) reveal more bodies with diameter $D < 50$ m than had previously been inferred from the distribution of larger bodies ($D > 100$ m) [1]. Rabinowitz *et al.* found most S-SEAs have perihelia and aphelia near 1 AU, $e \leq 0.35$, and i from 0° to $\sim 30^\circ$. They may also have unusual spectral properties. The apparent overabundance of S-SEAs is not reflected in the lunar cratering record, perhaps because: (a) the S-SEA population is an artifact of observational selection effects, or (b) the current S-SEA population is the product of an anomalous event, or (c) the S-SEA population is not representative of the entire small-body Earth-approaching asteroid population, but rather a sub-population on special orbits. Explanation (c) is quite plausible, because the orbits of the observed S-SEAs would produce much lower impact velocities (and smaller lunar craters) than most Earth-crossing bodies.

Assuming that the S-SEA observations do represent a steady-state excess of small bodies in that orbital space, candidate sources are: impact ejecta from one (or more) terrestrial planets, collisional fragments from the main-belt, or collisional break-up of a larger Earth-crossing asteroid. A source must match the following constraints: (1) the known S-SEA orbits, (2) S-SEA spectra (3) the excess of small bodies in the size distribution, (4) the paucity of special meteorites (*e.g.*, SNCs or lunar meteorites) relative to the overall meteorite record, (5) the frequency of impact events that could create the observed S-SEAs.

To test constraints (1) and (3), we follow the orbital evolution of test bodies using the model of Melosh and Tonks [2] (see also [3-5]), in which both the planets and the test bodies are on keplerian orbits (with uniformly precessing apsides and nodes) around the Sun. In this model, bodies are considered unperturbed unless they enter a planet's sphere of influence, where they either (a) collide with the planet, or (b) experience a ΔV based on a two-body encounter.

We have modified the Melosh and Tonks model to include impact disruption, based on a map (in orbital a, e, i space) of the collision probabilities and mean impact velocities (using the method of Bottke *et al.* [6]) for an asteroid encountering both the 682 largest main-belt asteroids ($D > 50$ km) and the 224 known near-Earth asteroids. By estimating the number of bodies in each asteroid population as a function of size [7, 8] and adopting the strength-scaling laws of Housen and Holsapple [9] to simulate catastrophic disruption of the target body, we obtain the disruption frequency for a given size body on a particular orbit. Fig. 1 shows that bodies with high eccentricities disrupt more frequently than bodies with low eccentricities, due to high impact velocities and the large amount of time spent near aphelion among main-belt projectiles. An asteroid's frequency of disruption drops dramatically when it becomes collisionally decoupled from the main-belt (*i.e.* for aphelion $Q < 1.7$ AU).

Our model confirms well-known evolutionary paths for near-Earth asteroids (NEAs) [5, 11]. Main-belt material reaching the perihelion $q = 1$ AU line random walks along contours of constant Jacobi-constant. These contours closely follow the $q = 1$ AU line, making a transition to the $Q = 1$ AU line at small e . If an asteroid does not impact a planet or collisionally disrupt, it may survive to become Venus-crossing, where multiple planetary perturbations will allow it to freely wander (a, e) space.

The model shows that main-belt objects, which reach the $q = 1$ AU line via the 3:1 and ν_6 resonances ($e \sim 0.6$ and 0.52 , respectively) are unlikely to become S-SEAs; most objects, while evolving down the $q = 1$ AU line, disrupt through impacts with the main-belt population or collide with Earth before reaching the low e orbits of the S-SEAs. Furthermore, though frequent impacts with

PROVENANCE OF SPACEWATCH SEAS

Bottke, W. F. *et al.*

the main-belt would produce fresh collisional debris, there is no reason for the process to create the clear excess of small bodies seen as S-SEAs.

However, planetary ejecta from either the Earth-Moon system (Fig. 2) or Venus could produce a small body excess spanning the current S-SEA orbits within ~ 10 Myr after ejection (see also [12]). Ejecta from these regions is collisionally decoupled from the main-belt, allowing it to survive and maintain its steep size-distribution. Small-body ejecta from Mars does not appear to survive long enough to reach the $q = 1$ AU line, unless it is ejected with high enough velocity to reach $q = 1$ AU almost immediately. A large Martian fragment could survive to reach $q = 1$ AU; break-up there might produce the S-SEA distribution. In fact, a stochastic collisional disruption of any NEA in the same region could also produce the observed S-SEA population. In that case, S-SEA spectra should be consistent with other observed NEAs. More information is needed on the S-SEA size-frequency distribution, their spectra, and their orbits to further constrain source models.

References: [1] Rabinowitz D. L. *et al.* (1993) *Nature* 363, pp. 704-706. [2] Melosh, H. J., and Tonks, W. B. (1993) *Meteoritics* 28, pp. 398. [3] Öpik, E. J. (1951) *Proc. Roy. Irish Acad.* A54, pp. 165-199. [4] Arnold, J. R. (1965) *Astrophys. J.* 141, pp. 1536-1547. [5] Wetherill, G. W. (1985) *Meteoritics* 20, pp. 1-22. [6] Bottke, W. F. *et al.* (1994) *Icarus*, in press. [7] Belton M. J. S. *et al.* (1992) *Science* 257, pp. 1647-1652. [8] Morrison, D. (ed.) (1992). *The Spaceguard Survey*. NASA, Washington, D.C. [9] Housen, K. R., and Holsapple, K. A. (1990) *Icarus* 84, pp. 226-253. [11] Greenberg, R. and Nolan, M. C. (1993) *Resources of Near-Earth Space*, University of Arizona Press, pp. 473-492. [12] Vickery, A. M. and Melosh, H. J. (1993) *Meteoritics* 28, pp. 453.

Fig. 1:

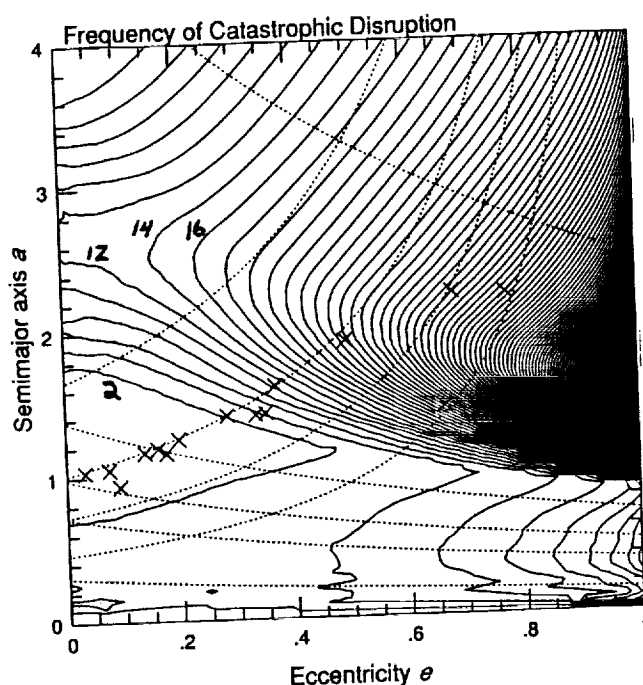


Fig. 2:

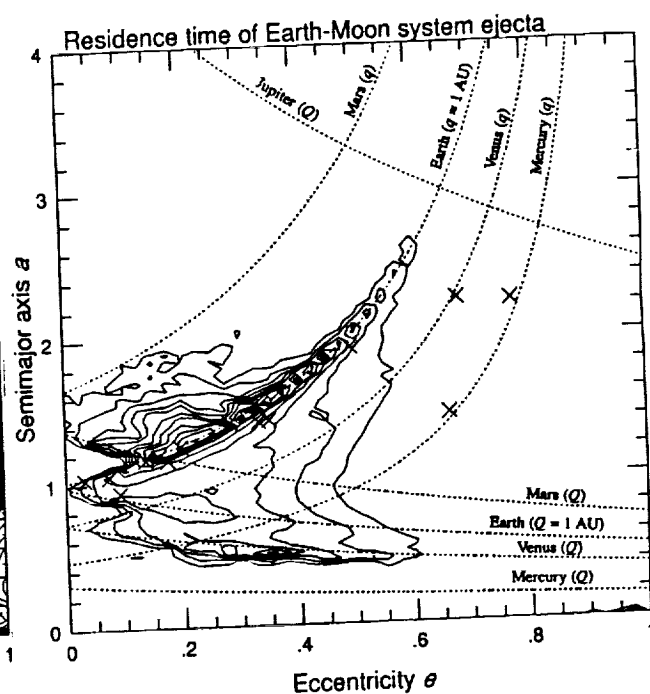


Fig. 1: Map showing frequency of catastrophic disruption based on strength-scaling [9] for a 100 m target asteroid at an inclination of 10° (Contour spacing is $2 \times 10^{-9} \text{ yr}^{-1}$). Dotted lines show where the asteroids have perihelia (q) or aphelia (Q) crossing the orbits of Jupiter or the terrestrial planets. Crosses show the (a, e) positions of the S-SEAs [1]. Note that few S-SEAs along the $q = 1$ AU line are found at the higher disruption frequencies.

Fig. 2: Contour plot showing the "relative" residence time of Earth-Moon system ejecta ($V_\infty = 1 \text{ km/s}$). Note that the higher contours correlate well with the positions of the S-SEAs.

SPACING DISTRIBUTIONS AND INTERSECTION ANGLES FOR KILOMETER SCALE LINEATIONS ON THE PLAINS OF VENUS; D. D. Bowman and C. G. Sammis, University of Southern California, W. Bruce Banerdt, Jet Propulsion Laboratory

Images from the Magellan space probe have revealed broad regions of intricate small scale, regularly spaced, radar-bright lineations on the volcanic plains of Venus. These lineations, which we interpret as tensile cooling fractures, have spacings ranging from 0.5 to 2.0 km. Extensive measurements of lineation spacing have been taken, primarily in the plains to the north of Ovda Regio. According to a shear lag model of fracture formation, the standard deviation of the spacing of the lineations should be $1/3$ the mean spacing. To date, our analysis of the plains of Venus has revealed that the standard deviation is actually closer to $1/4$ the mean. There are two possible explanations for this discrepancy. The shear lag model assumes homogeneous, isotropic cooling, which results in random nucleation. However, if a cooling front advances across the flow, the nucleation spacing may be more regular, resulting in a smaller standard deviation. A second possibility arises because the predicted relation between mean and standard deviation is derived from a one dimensional model of crack nucleation. Nucleation in two dimensions may allow fractures to grow into an otherwise "dead" zone of fracture formation in the 1-D model. In addition to measuring the mean spacing of fractures, we also measure the angle of intersection between two or more superimposed sets of lineations. The intersection angles typically fall between 30° and 45° .

Figure 1 shows a volcanic plains unit with fractures trending to the north and northeast. To facilitate the processing of fracture spacing data, the pixel intensity of the fractures is set to zero using the program "NIH Image". An intensity profile is then taken across the fracture pattern and processed to determine the mean and standard deviation of the lineation spacing. Several highlighted fractures and an example of a profile line can be seen on the right side of the image.

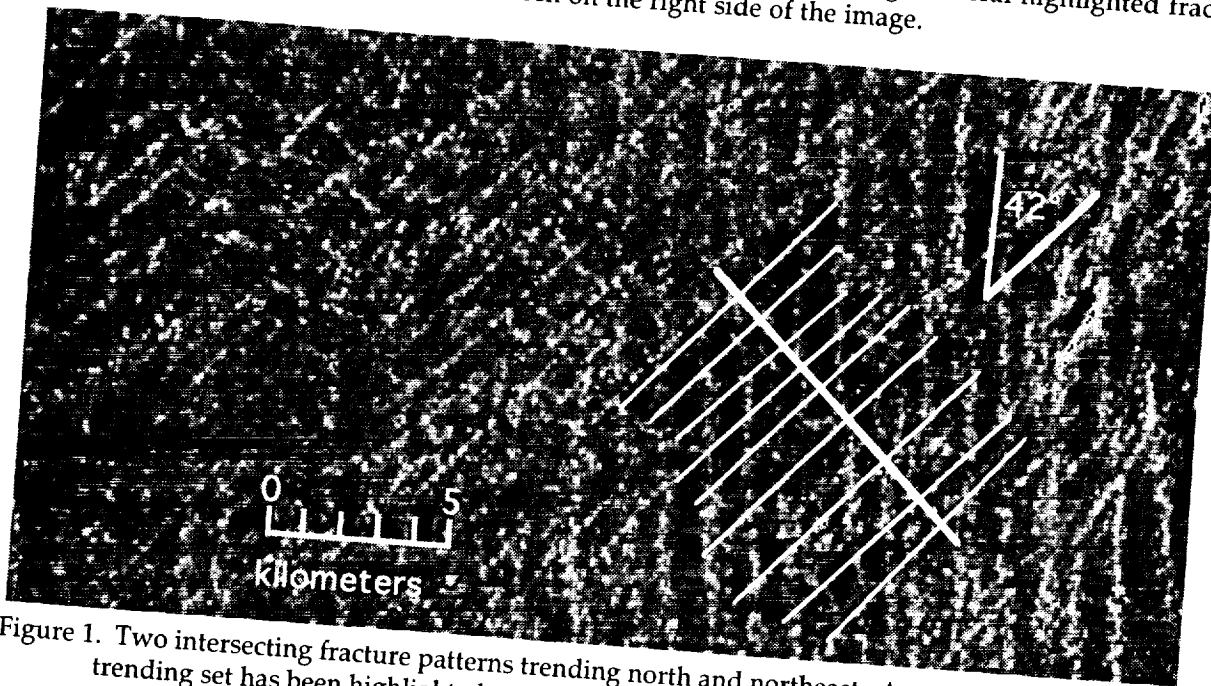


Figure 1. Two intersecting fracture patterns trending north and northeast. A portion of the northeast trending set has been highlighted, with an intensity profile line drawn perpendicular to the fractures. Image taken from F-MIDR 05N076;1.

The standard deviation is plotted as a function of the mean spacing in figure 2. The one dimensional shear lag model predicts a slope of $1/3$ [1]. However, the best fit line has a slope of only $1/4$. This suggests that the fractures are more evenly spaced than would be expected if they were nucleated randomly.

KILOMETER SCALE LINEATIONS ON PLAINS OF VENUS: Bowman et al.

Figure 3 is a histogram of the observed angle between superimposed sets of lineations. The mean angle is 39° , suggesting that one of the sets may have been formed in shear.

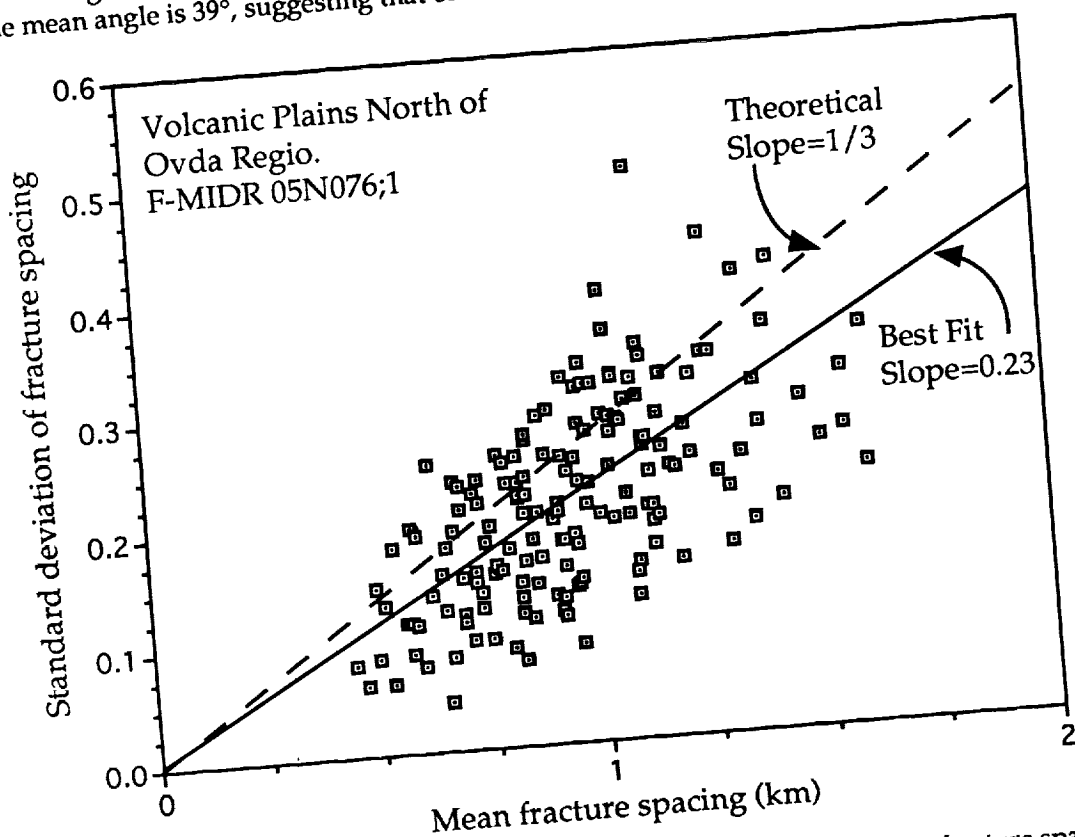


Figure 2. Standard deviation of fracture spacing as a function of mean fracture spacing. The dashed line is the theoretical slope [1], the solid line is a best fit slope

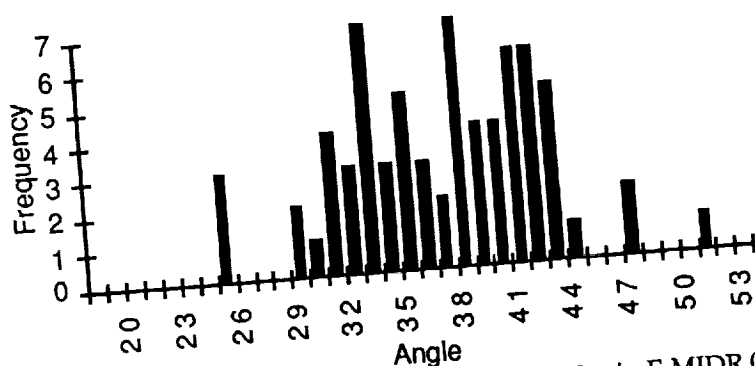


Figure 3. Distribution of fracture intersection angles in F-MIDR 05N076;1

References

- [1] Banerdt W. B. and Sammis C. G. (1992) *JGR*, 97, 16149

VAPOR TRANSPORT, WEATHERING, AND THE HIGHLANDS OF VENUS; Robert A. Brackett, Bruce Fegley Jr., and Raymond E. Arvidson, Department of Earth and Planetary Sciences and McDonnell Center for the Space Sciences, Washington University, St. Louis MO 63130

Introduction A one-dimensional finite-difference vapor transport model shows the diffusive migration of 0.01 to >10 micrometers per year of moderately to highly volatile phases (e.g., metal halides and chalcogenides) from hot lowlands (740 K) to cold highlands (660 K) on Venus. The diffusive transport of volatile phases on Venus has implications for the interpretation of Magellan radar observations, weathering models, and surface geochemistry.

The microwave emissivity of the highlands of Venus (0.3–0.6) is lower than that of the lowlands (0.8–0.9) [1], and has been attributed to highland surfaces with unusual chemical compositions and/or textures including: the presence of pyrite [1], perovskite [2], ferroelectrics [3], decimeter-scale voids [4], or a low-loss soil layer [5]. Here, we investigate the effects of vapor transport of volatile phases and discuss possible mechanisms for producing the inferred highlands signatures.

At the global mean temperature, $T \sim 740$ K, vapor pressures of nearly all metal halides and chalcogenides are 10^{20} times greater than on the Earth ($T \sim 288$ K) [6]. From 0 to 10 km elevation, vapor pressures of metal halides and chalcogenides drop by 1–5 orders of magnitude. The net effect of high vapor pressures and strong concentration gradients is that the venusian highlands act as "cold traps" for volatile vapors [7; 8]. We focus on metal halides and chalcogenides because they are commonly observed in terrestrial volcanic gases and sublimates (see Table 1.) [9–12]. Chalcophilic and volatile elements in volcanic gases are enriched up to 8 orders of magnitude relative to associated basalts for ocean island basaltic volcanism and arc volcanism [10; 13; 14]. Elements with the largest enrichment factors include: Se, S, Cl, Ir, F, Sn, Br, Cd, Au, As, Zn, Cu, Pb, Hg [13; 14]. Metal halides and chalcogenides may also be products of chemical weathering of basaltic minerals.

Model Description Vapor transport is modeled using a one-dimensional box model composed of 100 isothermal 10-km long pairs of boxes (one atmosphere and one solid). The temperature range is 740 K to 660 K. Mass is transferred between atmosphere boxes through eddy diffusion, governed by Fick's Law [15; 16]. The meridional eddy diffusivity, K_{eddy} , of the near-surface atmosphere is estimated as $10^8 \text{ cm}^2 \text{ s}^{-1}$ from observed Venera surface wind velocities, u , [17] as $K_{\text{eddy}} \sim uH$, where H is scale height and by analogy to the terrestrial troposphere [18]. Mass is transferred from surface to atmosphere through Langmuir evaporation. Transfer from the surface to the atmosphere occurs when the partial pressure in a gas reservoir is less than the equilibrium vapor pressure. Evaporation occurs only if solid material is present. Mass is transferred from atmosphere to surface through condensation. If the partial pressure in a gas reservoir exceeds the equilibrium vapor pressure, mass is condensed until the equilibrium vapor pressure is reached. Mass transfer is solved as a function of time using a finite-difference method. The total mass is conserved. Initially, the mass in each gas reservoir is determined from the equilibrium vapor pressure for that reservoir. Each solid box begins with a uniform thickness (i.e., uniform mass).

Model Results Figure 1 shows results for model runs using high, moderate, and low volatility, $K_{\text{eddy}} = 10^8 \text{ cm}^2 \text{ s}^{-1}$, and a uniform initial surface layer thickness of 1 cm spread over the entire grid. The thickness of the surface layer is plotted as a function of time versus elevation above mean Venus radius. Transport of several cm of material to high elevation occurs over time scales of thousands to millions of years (for high and moderate volatility phases). Little transport occurs for low volatility phases. Three general features are observed. First, the hottest reservoir with solid material loses material to colder boxes and gains no material. Also, the average residence time is inversely proportional to T . Therefore, the transition from areas with no surface material to areas with enhanced (greater than initial) surface layer thicknesses is abrupt. Second, material accumulates at the coldest reservoir (highest elevation) because of mass balance and down-gradient vapor transport. Third, transport of material to the highlands occurs nonlinearly due to the exponential dependence of vapor pressure on T . The rate of transport is, to first order, linearly proportional to K_{eddy} . Figure 2 shows the volatility of selected metal halides and chalcogenides compared to the high, medium, and low volatility runs. Table 1 lists metal phases found near terrestrial volcanic vents and fumaroles.

Discussion Sufficiently thick condensate layers would be detectable in Magellan emissivity data. For a two-layer infinite half-space, the microwave emissivity, e , from the surface is

$$e = 1 - [R_1 + R_2(1 - 2R_1/L)^2(1 - R_1R_2/L^2)]^{-1}$$

where R_1 and R_2 are the directional power reflectivities (from Fresnel's laws) of the 1st and 2nd layer, respectively and L is the loss factor in the 1st layer [19], assuming layer thicknesses \geq wavelength of the radar, Rayleigh-Jeans approximation, phase incoherency and no volume scattering in the coating layer. For selected metal halides and chalcogenides, thin (\leq few cm) layers have sufficiently high dielectric constants to match the observed highland emissivities. The microwave dielectric constants of WO_3 , SbSI , PbTe , PbSe , PbO , PbS , Sb_2S_3 , Sb_2Se_3 , PbCl_2 , and TlCl (halides and chalcogenides whose metals are enriched in volcanic emissions [13; 14]) are 6,000–90,000, 2,000–50,000, 400, 280, 200, 190, 180, and 110 respectively [20]. WO_3 and SbSI are ferroelectric [3].

Volatile phases may speed mechanical and chemical weathering. At equilibrium with a saturated fluid, large crystals grow at the expense of small crystals, minimizing Gibbs free energy [21]. Large crystals will exert sufficient pressure to mechanically fracture rock along pores and cracks, analogous to salt weathering on the Earth [21].

Other lines of evidence also suggest the importance of vapor transport on Venus. It is possible that volatiles (perhaps metal halides or chalcogenides) may be detectable as low-altitude hazes on Venus. [22] found increases in the scattering cross-section between altitudes of 5.8 – 6.4 km that are compatible with presence of low-altitude hazes. The failure of several instruments aboard Pioneer Venus Entry Probes at 12.5 km elevation may be due to conductive metal phases shorting out external instruments [8]. A metal halide or chalcogenide is a likely candidate. A highland

VAPOR TRANSPORT, WEATHERING, AND HIGHLANDS OF VENUS; Brackett, R.A. et al.

lander capable of elemental analysis (e.g., XRF or α -particle backscatter) would provide direct evidence of the role of vapor transport.

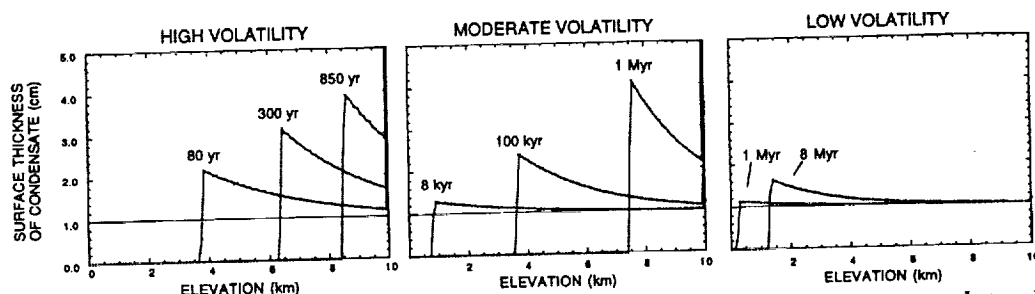


Figure 1. Thickness of surface layer vs. elevation as a function of time. High volatility corresponds to a $P_{vap}(740\text{ K}) = 10^{-3.5}$, $P_{vap}(660\text{ K}) = 10^{-5.2}$. Moderate volatility corresponds to a $P_{vap}(740\text{ K}) = 10^{-6.7}$, $P_{vap}(660\text{ K}) = 10^{-8.7}$. Low volatility corresponds to a $P_{vap}(740\text{ K}) = 10^{-9.6}$, $P_{vap}(660\text{ K}) = 10^{-12.2}$.

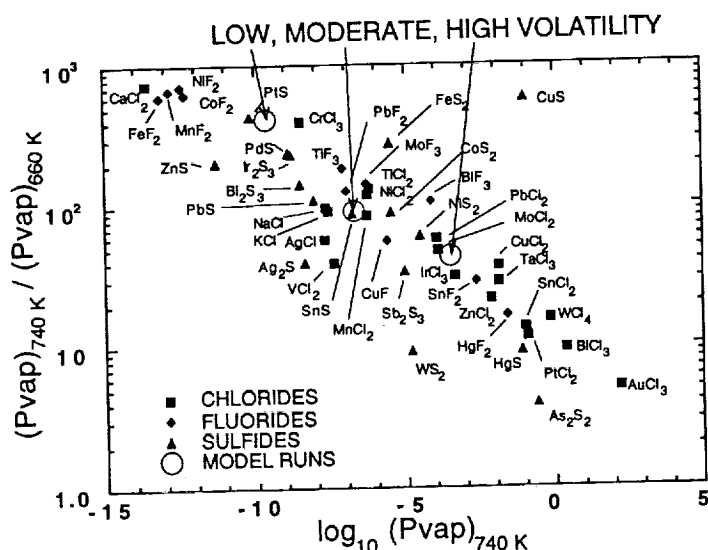


Fig. 2. Ratio of $P_{vap}(740\text{ K})$ to $P_{vap}(660\text{ K})$. Small closed symbols correspond to selected metal halides and sulfides [6]. Large open circles correspond to model runs.

TABLE 1. Metal Phases Observed as Terrestrial Volcanic Sublimates^a

Mineral Name	Chemical Formula
Anglesite	PbSO ₄
Cassiterite	SnO ₂
Chalcocyanite	CuSO ₄
Chloromagnesite	MgCl ₂
Contunnite	PbCl ₂
Covellite	CuS
Cs-K Sulfate	not identified
native elements	As, Pb, S, Se, Te, TI
Fluorite	CaF ₂
Galena	PbS
Galenobismutite	PbBiS ₄
Halite	NaCl
Hieratite	K ₂ SiF ₆
Hydrophilite	CaCl ₂
Lawrencite	FeCl ₂
Magnetite	Fe ₃ O ₄
Massicot	PbO
Mn-bearing wolframite	(Fe,Mn)WO ₄
Nanodite	CuCl ₂
Orpiment	As ₂ S ₃
Re-molybdenite	(Re,Mo)S ₂
Realgar	AsS
Scacchite	MnCl ₂
Scherbinitite	V ₂ O ₅
Se-bearing minerals	not identified
Sphalerite	ZnS
Sylvite	KCl
Tl-bearing minerals	not identified

a. Data taken from [9-12]

References [1] Pettengill G.H. et al. (1988) *JGR*, 93, 14881; [2] Fegley B. et al. (1992) *Proc. LSC* 22, 3; [3] Shepard M.K. et al. (1994) *this volume*; [4] Pettengill G.H. et al. (1992) *JGR*, 97, 13091; [5] Tryka K.A. and Muhleman D.O. (1992) *JGR*, 97, 13379; [6] Knacke O. et al. (1991) *Thermochemical Properties of Inorganic Substances*, Springer-Verlag; [7] Lewis J.S. (1968) *Icarus*, 8, 434; [8] Fegley B., presentation at NASA Ames Pioneer Venus Probe 12.5 km Anomaly Workshop; [9] Stoiber R.E. and Rose W.I. Jr. (1974) *GCA*, 38, 495; [10] Symonds R.B. et al. (1987) *GCA*, 51, 2083; [11] Quisefit J. et al. (1989) *GCA*, 53, 2591; [12] Toutain J. et al. (1990) *J. Volcanol. Geotherm. Res.*, 40, 257; [13] Olmez I. et al. (1986) *JGR*, 91, 653; [14] Lepel E.A. et al. (1978) *JGR*, 83, 6213; [15] von Zahn U. et al. (1983) *Venus*, UA Press; [16] Chapman S. and Cowling T.G. (1970) *The Mathematical Theory of Non-uniform Gases*, Cambridge; [17] McGill G.E. et al. (1983) *Venus*, UA Press; [18] Warneck P. (1988) *Chemistry of the Natural Atmosphere*, Academic Press; [19] Ulaby F.T. et al. (1982) *Microwave Remote Sensing*, Addison-Wesley; [20] Young K.F. and Frederikse H.P.R. (1973) *J. Phys. Chem. Ref. Data*, 2, 313; [21] Wellman H.W. and Wilson A.T. (1965) *Nature*, 205, 1097; [22] Ragert B. and Blamont J. (1980) *JGR*, 85, 8089.

Acknowledgements B.F is supported by the NASA VDAP and Planetary Atmospheres Programs.

REFLECTANCE SPECTROSCOPY OF INDIVIDUAL INTERPLANETARY DUST PARTICLES

J. P. Bradley¹, D. E. Brownlee², and L. P. Keller¹ 1. MVA Inc. 5500/200 Oakbrook Pkwy, Norcross, GA 30093, 2. Dept. of Astronomy, Univ. of Washington, Seattle, WA 98195.

In the absence of actual samples from most Solar System objects, reflectance spectroscopy provides a means of obtaining information about planetary surface compositions and mineralogy [1]. A large data base has been acquired from asteroids in the visible (VIS) and near infrared (IR) spectral range, and similar data have been acquired from all of the major classes of meteorites [1-3]. On the order of fifteen asteroid classes are recognised but most belong to the S, C, P, and D classes [1]. Comparison of meteorite spectra with those of asteroids suggests that meteorites are a highly biased sampling of the asteroids. In contrast to meteorites, interplanetary dust particles (IDPs) collected at 1 AU are derived from a broader range of Solar System objects [4]. Reflectance spectra from IDPs might result in recognition of samples of parent bodies not represented among meteorites. We have obtained the first reflectance spectra from individual IDPs as small as 5 μm over the visible wavelength range 380-800 nm. Many chondritic IDPs are ideal candidates for reflectance spectroscopy because they are extremely fine-grained and homogenous on a scale of micrometers. Spectra have also been collected from particle standards and meteorite fragments. We are now evaluating hardware modifications that will enable us to extend the range of measurement into the near-IR region (800-2100 nm).

Spectra are acquired using a reflected light microscope equipped with a halogen light source, 10X and 50X objectives, aperturing diaphragms, and a photometer unit with a photomultiplier tube (PMT) detector. The spectral response of the microscope photometer system itself is continuously monitored by collecting data from a pressed barium sulfate pellet over the 380 - 800 nm range with a 5 nm measurement interval. Particle data were collected from titanium oxide (Ti_4O_7), fragments of Allende (CV3) matrix, and chondritic IDPs (with diameters between 5 and 30 μm). The spectra were acquired using oblique illumination and measurement of the (scattered) light reflected perpendicular to the surface of the sample. Figure 1 compares a "bulk" spectrum (from a 2 mm diameter region of a pressed pellet) of Ti_4O_7 with that of an individual 20 μm diameter Ti_4O_7 particle. The Ti_4O_7 standard is homogenous, fine-grained ($\sim 0.5 \mu\text{m}$ average grain size), with a low (bulk) reflectivity that has been independently measured at JSC. Between 430 and 800 nm (Fig. 1), the reflectivity of the particle mimics that of the bulk sample. However, below 430 nm there is an abrupt drop-off into the UV. The reason for this drop-off is currently under investigation, but preliminary observations suggest that it is a scattering effect related to particle morphology. (This particle dependent UV drop-off may have implications with regard to interpretation of asteroid reflectance data). Under appropriately optimized conditions, it was possible to routinely determine the reflectivity of Ti_4O_7 particles ($< 25 \mu\text{m}$ diameter) within 1% of the (bulk) reflectivity of Ti_4O_7 between 430 and 850 nm (Fig. 1).

Figures 2 and 3 show reflectance spectra from 4 Allende fragments and 5 chondritic IDPs.

The Allende spectra, collected from particles between 20 and 40 μm diameter, are compatible with bulk spectra of Allende and other CV3 meteorites (see Hiroi *et al.* [3]). The IDPs exhibit a broad range of reflectivities in the visible wavelength range (Fig. 3), although we see evidence of grouping among a much larger population of chondritic IDPs. Some IDPs (e.g. L2005AE11) exhibit generally flat spectra similar to those of carbonaceous chondrite meteorites and C-type asteroids, while others (L2011R7) exhibit a pronounced rise into the infrared similar to P and D asteroids (Fig. 3). Spectra from IDPs whose bulk carbon contents have been determined are also shown in Figure 3. Generally, the most carbon-rich IDPs exhibit the lowest albedos, although there are exceptions. Determination of the spatial distribution and chemical state of the carbon (e.g. amorphous carbon or carbonates) may explain these exceptions.

We have established that it is possible to measure the reflectivities of individual ($< 25 \mu\text{m}$ diameter) IDPs within the visible wavelength range 430 - 800 nm. Noble gas measurements and electron microscopic studies of many of these IDPs have been initiated in order to evaluate spectral reflectivities in terms of mineralogy, petrography, thermal histories, and sources of IDPs.

Reflectance spectra of IDPs, Bradley, Brownlee, and Keller

References

- [1] M. J. Gaffey, T. H. Burbine, and R. P. Binzel (1993) *Meteoritics*, 28, 161-187;
- [2] B. Zellner, D. J. Tholen, and E. F. Tedesco (1985) *Icarus*, 61, 355-416.
- [3] Hiroi, T., Pieters, C. M., Zolensky, M. E. and Lipschutz, M. E. *Science*, 261, 1016-1018 (1993).
- [4] Jackson, A. A. and Zook, H. A. (1992) *Icarus*, 97, 70-84.

Acknowledgements: This work supported by NASA Contract NASW-4831.

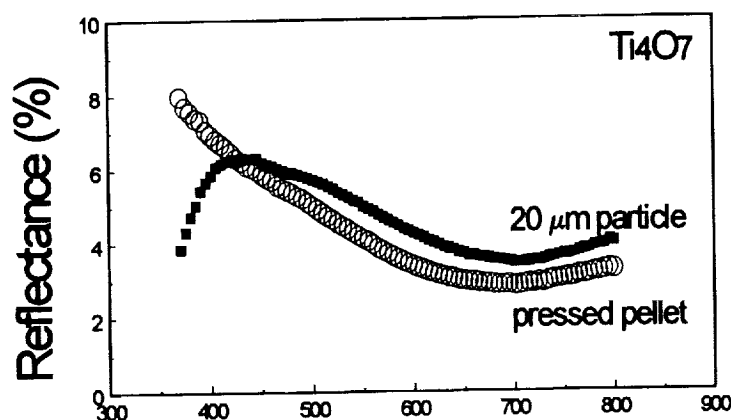


Figure 1. Reflectance spectra of Ti_4O_7 from a pressed pellet and from a typical 20 μm fragment. (Ti_4O_7 sample was provided by Carl Allen, Lockheed, NASA/JSC)

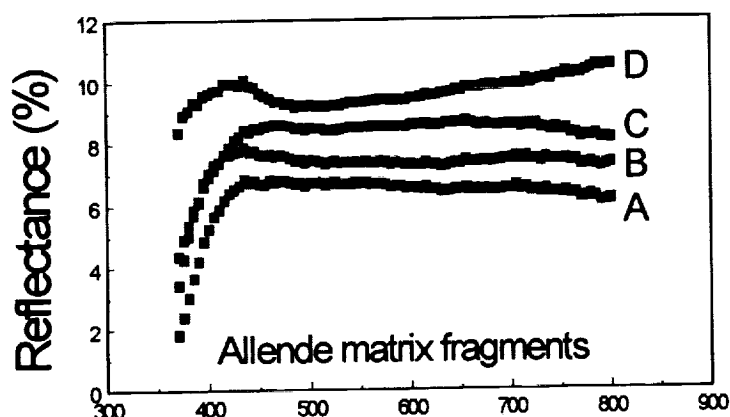


Figure 2. Reflectance spectra from four 20- to 40- μm sized fragments of matrix from the Allende CV3 chondrite. Spectra B, C, and D are shifted from A by 1, 2, and 3 reflectance units, respectively.

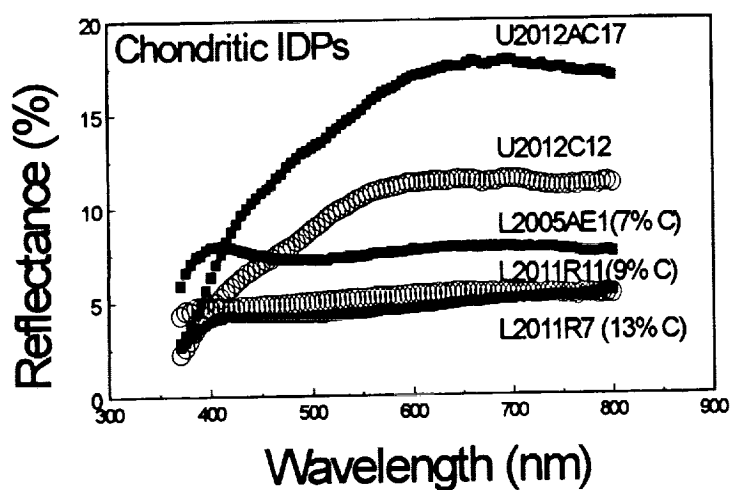


Figure 3. Reflectance spectra from individual chondritic IDPs showing the range of reflectivities and spectral slopes observed in IDPs.

RB-SR DATING OF ALKALINE AND MAFIC INTRUSIVES FROM THE PRETORIA SALTPAN IMPACT CRATER AND ENVIRONS. D. Brandt¹, W.U. Reimold¹ & C.B. Smith². ¹Econ. Geol. Res. Unit, Dept. of Geology; ²Isotope Res. Unit, Bernard Price Institute of Geophys. Res.; Univ. of the Witwatersrand, P.O. WITS, 2050, Johannesburg, R.S.A.

INTRODUCTION: The Pretoria Saltpan crater is a simple, bowl-shaped crater located in the southern portion of the Bushveld Complex, some 40 km NNW of Pretoria, at 25°24'30" S and 28°04'59" E in the Transvaal Province of South Africa. The crater position is approximately 20 kilometers to the west of the margin of the Pienaars River Alkaline Complex (Fig.1). The near-circular structure has a 1.13 km rim-to-rim diameter and exhibits a well-preserved, uptilted granite rim, which is largely overlain by granitic breccia. The breccia overlies Karoo sediment in places, indicating a **post-Karoo** age for the cratering event. Lamprophyre and alkaline volcanic rocks have been mapped in the crater rim [1]. The origin of the Pretoria Saltpan crater has been a matter of controversy for the last century. Two models have been proposed, namely, a cryptovolcanic or meteorite impact origin. The coincidence of the occurrence of the crater with that of mafic and alkaline intrusives has been the main argument against the impact hypothesis and is still forwarded by proponents of an internal origin of the Pretoria Saltpan crater - despite the findings of impact-diagnostic shock metamorphic effects, in Saltpan breccias [2]. Here we report geochronological data for volcanics from the crater rim and crater environs that prove unequivocally that the volcanics in the crater rim are part of a 1.2-1.3 Ga regional event.

PREVIOUS WORK: The geology of the crater environs and the possibility of occurrences of mafic and alkaline rocks in both the wider region and within the crater have been disregarded in previous work. In contrast, our group carried out detailed mapping of the crater rim and its environs, together with comparative petrographic, chemical, and chronological studies on samples from the crater and its environs in order to test the possibility of an association of the basic and alkaline intrusives with the cratering event. Chronological data obtained in the past for samples from the Pienaars River Alkaline Complex, which forms an integral part of the study region, are summarized in Table 1, together with the ages previously determined for various intrusives from the crater rim. From these results it is evident that all intrusives from the crater and the Pienaars River Alkaline Complex were intruded around the same period and may all be part of the same igneous event at about 1.3 Ga ago. The exception to this age are the fission track data for a crater carbonatite [3]. Two different studies yielded reliable and comparable ages for the Saltpan cratering event: 1) ¹⁴C age determinations on algal debris from the upper 20 metres of the core sediments [4] indicated a mean sedimentation rate of about 1 metre/2000 years. This accumulation rate indicates an age of approximately 200 ka for the lowermost crater-fill sediments. 2) A very similar age of 220 ± 52 ka was obtained [5] by fission track dating of glass fragments recovered from a drill-core through the crater interior. These relatively young ages for the cratering event are in excellent agreement with the well-preserved state of the crater. Clearly the crater age is quite different from that of the alkaline and ultramafic intrusives in the general region.

THIS STUDY: Rb-Sr dating was carried out on a phonolite sample from the crater rim, a lamprophyre sample from the crater environs (Sample 21-E), and a peralkaline syenite from the previously undated Roodeplaat Complex (Fig.1). Mineralogical and chemical comparisons of alkaline volcanics and lamprophyre samples from the crater rim and crater environs showed that all these occurrences are very similar [6]. The isotopic data are presented in Fig.2 and Fig.3. All three rock types were altered to some extent. This is related to the scatter of points at the lower end of the data spread (Fig. 3), which indicates some degree of open system behaviour, particularly in plagioclase, the whole-rocks and at least one of the hornblendes. One biotite sample (Bio-3; Fig.2) was visibly altered and was excluded from all regressions. The best age estimate is considered to be 1342 ± 11 Ma for the unaltered biotites, the hornblende (Hld-4), and the clinopyroxene (cpx-9). The initial ratio of 0.7026 is controlled by the clinopyroxene and the hornblende, and is similar to values for megacrysts in the 1180 Ma Premier kimberlite [7]. These rocks are of direct mantle derivation, apparently from a lithospheric source similar to that of the Pretoria area kimberlites.

CONCLUSION: Rb-Sr data for these samples indicate an age of 1342 ± 11 Ma for the alkaline rocks of the Saltpan crater and associated rocks of the Roodeplaat Complex. This is consistent with previous estimates, but is considered to be a more precise determination. These results support the argument that the intrusives of the entire region, including the crater area itself, are more or less coeval and have no association with the cratering event at ca. 200 ka ago.

REFERENCES: [1] Feuchtwanger T. (1973) B.Sc. Hons. Proj., Univ. Wits (unpubl.), 41. [2] Reimold W.U. et al. (1991) LPSC XXII, 1117-1118. [3] Milton D.J. and Naeser C.W. (1971) Nature Phys. Sci. 229, 211-212. [4] Partridge T.C. et al. (1993) Palaeogeog., Palaeoclim., Palaeoecol., 101, 317-337. [5] Storzer D. et al. (1993) LPSC XXIV, 1365-1366. [6] Brandt D. (1993) M.Sc. thesis in prep. [7] Smith C.B. (1983) Ph.D. thesis, Univ. Wits (unpubl.), 436. [8] Snelling N.J. (1963) Ann. Rep. Overs. Geol. Surv., 30. [9] Oosthuysen E.J. and Burger A.J. (1964) Ann. Geol. Surv. S. Afr., 3, 87-106. [10] Harmer R.E. (1985) Trans. geol. Soc. S. Afr., 88, 215-223. [11] Partridge T.C. (1990) Meteoritics, 25, 396. [12] Walraven F. (pers comm.).

DATING OF INTRUSIVES FROM THE PRETORIA SALTPAN IMPACT CRATER: Brandt D. et al.

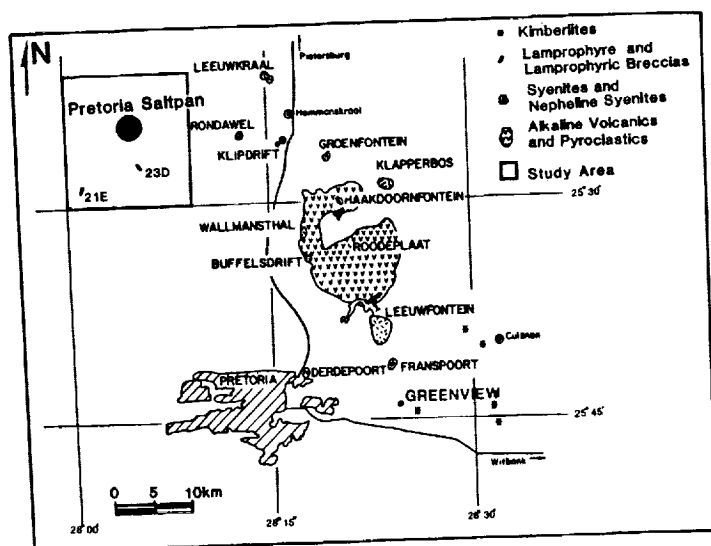


Fig.1 Location of the Pretoria Saltpan and mapped surroundings with respect to identified members (shown as outcrop) of the Pienaars River Alkaline Complex (modified after Harmer, 1985).

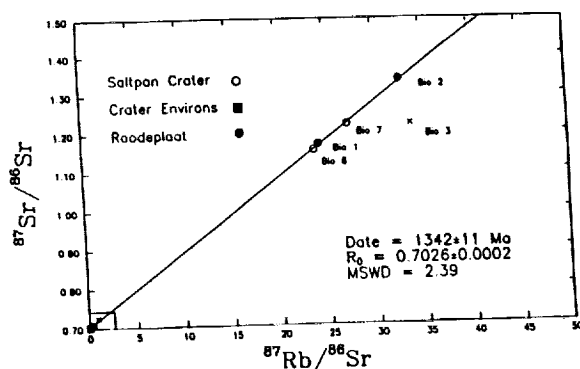


Fig.2 Isochron diagram for studied samples using Cpx 9 and Hld 4 as the lower limit constraints. Crosses indicate samples excluded in these results. This combination gives the best fit isochron age.

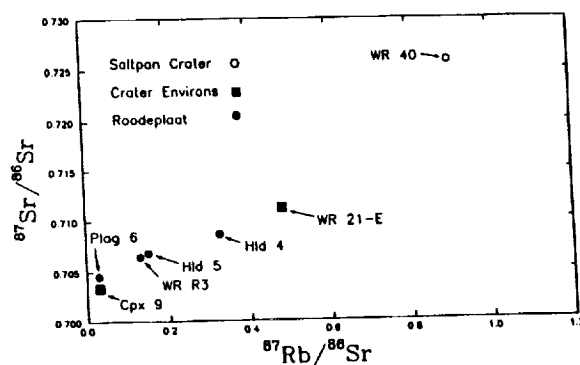


Fig.3 Diagram of the "lower end" values, combinations of which were used to calculate isochron ages (cf. text). Scatter is attributed to alteration.

Rock Unit/Sample	Age in Ma	Type of Determination	Source
Pilanesberg Complex	1250 ± 60	K-Ar, biotite	[8]
Leeuwfontein	1420 ± 70	U-Pb, zircon	[9]
Crater Carbonatite	600 ± 90,	Fission Track, apatite	[3]
	1900 ± 400	Fission track, zircon	
8 Pienaars River Alkaline Complex Samples	1300 ± 143	Rb-Sr, zircon	[10]
Crater Lamprophyre	1360	K-Ar, biotite	[11]
Crater Lamprophyre	1459 ± 22	Rb-Sr, biotite	[12]

Table 1. Age data on alkaline volcanic rocks from the crater and the Pienaars River Alkaline Complex.

YOUR OWN EDUCATIONAL OUTREACH PROGRAM: IT'S NOT AS HARD AS YOU THINK. R.H. Brazzle¹, B.M. Barker¹, L.C. McLeod² and C.M. Hohenberg¹; 1. McDonnell Center for the Space Sciences, and Physics Department, Box 1105; 2. Department of Earth and Planetary Science, Box 1169; Washington University, One Brookings Dr., St. Louis, MO 63130

In recent years, educational outreach programs (specifically in the sciences) have begun popping up at colleges throughout America. A possible motivation for this may be a 1983 report by the U.S. Department of Education popularly titled "A Nation at Risk." This report found that while the *percentage* of people who graduate from high school or college has continually increased in the 20th century, the *quality* of their education has not [1]. Thus, as our society has struggled to become more inclusive educationally, we have sacrificed the quality of that education for all. This report had a special warning about the scientific future of our nation: with the great gains of the "Sputnik challenge" program essentially undone, we face "a new generation of Americans [that is being raised] scientifically and technologically illiterate" [1].

A new U.S. Department of Education report, titled "National Excellence: a Case for Developing America's Talent" was released in November 1993 [3]. This report studied gifted and talented children, and educational programs for these children. It found that while progress has been made since 1971 (the year of a previous government study [2]), only about two-thirds of America's public schools have "gifted programs", and many of these are probably inadequate. These students thus spend most of their time in classes that require little effort. [3-6]

Thus it seems that the future holds mediocrity for America's best students, and scientific illiteracy for all. At Washington University's McDonnell Center for the Space Sciences, we are developing an outreach program that attempts to address both of these problems. Thus we have two general goals for our outreach program: 1) to reach a large number of students with the message "science is ubiquitous, relevant and exciting" and 2) to challenge students who are scientifically talented, and show them a working example of how science is done.

We are not attempting to 'make more scientists'. Rather, we are attempting to give students an honest, clear view of what scientists do. For those students who are serious about science, our program should provide a head start to (and overview of) their own career in science; through this, they may be able to make better decisions concerning subsequent education, etc. For all students, our program should help reduce fears of science, and help guide all students to be members of a scientifically literate citizenry. They will be the politicians and voters of the future, and will be making decisions that affect our nation's scientific pursuits.

Our educational outreach program was made possible by a unique program conceived by NASA called the "Educational Research Fellowship." This fellowship supports a graduate student for fundamental research (as is the case with NASA's Graduate Fellowship Program). However, it makes additional money (\$10,000 annually) available for the formation of an 'education team' (consisting of the PI, graduate student, and undergraduate intern) who are then charged with designing an outreach program. The authors of this abstract are our education team members. We are working on several projects which aim to satisfy these goals:

Specific Projects

In regard to the first goal, we are developing a slide show presentation on the history of the solar system, and the ways we explore it. At first, we are focusing on students at about the 8th or 9th grade level (when many students are taking earth and/or space science courses) but we hope to expand this to accommodate both younger and older students.

We have made \$1,000 available to local teachers in a "curriculum improvement grant," to purchase educational materials which will be used to augment an existing science course. This money came from the \$5,000 budgeted by NASA for our outreach program through their "Educational Research Fellowship" mentioned above. Our reasons for making this money directly available were several-fold: Applying for the grant gave teachers practice in writing proposals for funding, which may become an important skill in the future. The responses from

EDUCATIONAL OUTREACH PROGRAM. Brazzle R. H. *et al.*

teachers provided us with additional ideas for our own program; i.e. we became more aware of the kinds of materials that real teachers need. Finally, the announcement of the award provided an excellent form of 'advertisement' for the rest of our outreach program. The goals we set in announcing this city-wide award were realized, even though the response rate was lower than anticipated.

To fulfill the second goal, we are developing an in-depth tour of our facilities here at the McDonnell Center. This tour is geared towards students studying high school physics and is intended to show them how the physics they're learning is used in real scientific research, as well as introduce them to some of the current methods of scientific research. We have also given a presentation on a specific research project (along with two other Washington University graduate students) at the new St. Louis Science Center, to an audience of local science teachers. We hope to give similar presentations to talented high school students and their teachers in the future.

Finally, we are working to increase teacher awareness of existing NASA resources, and are augmenting these resources for the teachers in the St. Louis metropolitan area. The "National Excellence" report showed that America's top students are bored and unchallenged in their classes; but the authors of the report argue against the practice of "tracking" talented children into special classes. Therefore, fundamentally new materials must be developed to simultaneously challenge a classroom of students who populate a broad 'ability spectrum.' We are developing such materials to distribute to local science teachers through our regional Teacher Resource Center. These written materials are in the spirit of NASA's "educational briefs." In fact, they can be used as background information to get more out of the "briefs." Thus, we hope that these materials will benefit students at all ability levels.

An example of these broad-based materials is an activity on crystal growth. The basic message would be the ordered structure of crystals. More sophisticated students would also learn ideas of solubility. Students with yet higher levels of ability might learn about atomic structure. The most advanced students may be able to redesign or modify the experiment in order to broaden their understanding. This activity (and others like it) is applicable in a wide variety of classrooms, and it contains an essentially arbitrary amount of information for a given student to learn. This makes it ideal for the 'integrated classrooms' advocated in "National Excellence."

Conclusions

We feel that this kind of outreach program is relatively easy to set up; it's also fun, pertinent, and rewarding for all those involved. Our poster presentation will include information on how researchers can set up such a program at their own labs, and how teachers can utilize these programs. Basically, we feel that graduate students are the logical choice to be 'outreachers.' They will be the professors of the future, and the experience of setting up and running an educational outreach program should prove extremely useful (the ultimate test of learning is teaching). We also point out that today's graduate students are products of the educational system described in "A Nation at Risk" and "National Excellence." A graduate student leading an outreach program would represent a continuation of the learning process, a 'working example' to young students of the necessity of being a 'life-long learner.' For more information, please see our poster.

References: [1] *A Nation at Risk*, National Commission on Excellence in Education (1983). [2] "Education of the Gifted and Talented" G.P.O. SuDocs # HE5.2:G36/2/V1&2 (1971). [3] "National Excellence: A Case for Developing America's Talent" G.P.O. SuDocs # ED1.302:EX2 (1993). [4,5,6] News articles about "National Excellence" all appearing on Nov. 5, 1993 from: the New York Times, Newsday, and the St. Louis Post Dispatch.

METAMORPHIC EFFECTS IN THE MATRICES OF CO3 CHONDRITES: COMPOSITIONAL AND MINERALOGICAL VARIATIONS Adrian J. Brearley, Institute of Meteoritics, Department of Earth and Planetary Sciences, University of New Mexico, Albuquerque, New Mexico 87131.

We are examining the mineralogical and compositional variations of fine-grained matrix through the petrologic sequence in the CO3 chondrites to assess possible metamorphic models for these meteorites. We have measured the major and minor element compositions of matrix and rims by electron microprobe and studied the fine-scale mineralogy by transmission electron microscopy. Our data show that there are systematic, but complex, compositional trends in the matrices of these meteorites through the metamorphic sequence. The major elements, Mg and Fe, become progressively more equilibrated with increasing petrologic type and the matrices become progressively enriched in Mg and depleted in Fe. The behavior of the minor elements, Ti, Cr and Al, contrast markedly with Mg and Fe and become increasingly heterogeneous through the metamorphic sequence.

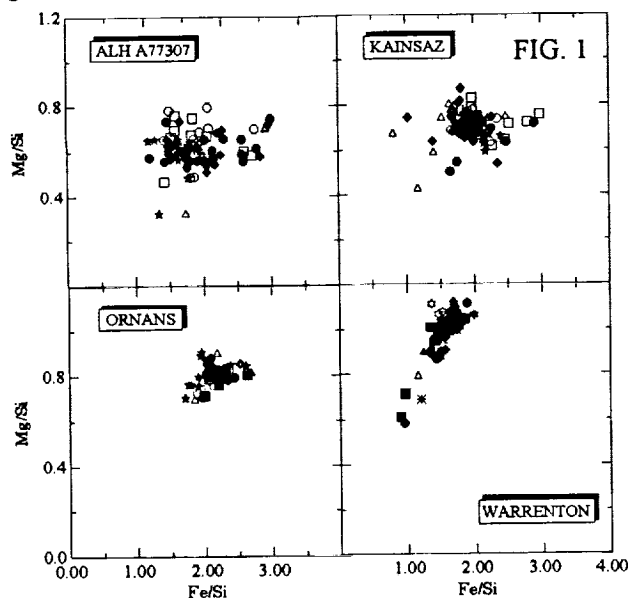
Introduction. It has been recognised for several years that carbonaceous chondrites of the CO3 group define a metamorphic sequence, similar to that observed in the ordinary chondrites [1,2]. Scott and Jones [2] provided detailed petrologic subtypes for individual CO3 chondrites and showed that ALH A77307 (3.0) and Isna (3.7) represent the least and most equilibrated members respectively. The detailed compositional variations in chondrule silicates reported by [2] and [3] provide support for the model that equilibration in these meteorites occurred by diffusional exchange, principally of Fe and Mg, between Mg-rich chondrules and Fe-rich matrix within a parent body environment. The compositional systematics observed in chondrules are now well understood, but the chemical and mineralogical changes which occur in the fine-grained matrix of these meteorites as a response to metamorphism are poorly understood. We have carried out a detailed study of the compositions and mineralogy of these meteorites to examine variations which may develop during metamorphism. These data will provide insights into how fine-grained matrix materials respond to metamorphism in terms of their textures, mineralogy and compositions and will ultimately test the model of in-situ parent body metamorphism.

We have studied 3 CO3 chondrites, Kainsaz (3.1), Ornans (3.3) and Warrenton (3.6), all falls, which span the range of degrees of equilibration found in this group. We have previously obtained data on the least equilibrated CO3 chondrite, ALH A77307, for comparison [3]. Major and minor element compositions of fine-grained rims and matrix were measured by electron microprobe using a 10 μ m beam. These regions were then demounted from the thin sections and were studied by TEM techniques.

Results. Our electron microprobe data show systematic trends in the composition of matrix through the metamorphic sequence. The observed trends are complex and the behavior of different elements is variable, demonstrating that the response of these elements to metamorphism is controlled by several variables. A comparison of data for a number of rims and bulk matrix from each meteorite, normalized to Si and CI values, shows some of the major compositional variations which occur through the metamorphic sequence. The element ratio pattern for ALH A77307 shows strong depletions in Ca, Ti, Mg, Cr, Mn, and Na and a small depletion in S [3]. Al, K, Ni and Fe are all enriched. The element ratio patterns for Kainsaz are, in comparison, much flatter and the relative enrichments and depletions are smaller, with the exception of S, which shows a depletion 2 orders of magnitude larger than that for ALH A77307. Depletions of S of the same magnitude are also observed in Ornans and Warrenton. However, in general the patterns for these two meteorites are more fractionated than Kainsaz, with variable, but significant depletions in Ca, Na, K and Ni and an enrichment in Al. In moving through the metamorphic sequence, several points are clear: 1) there is a significant drop in the concentrations of S and Ni, 2) the Mg/Si ratios of matrix increase systematically through the metamorphic sequence, 3) the bulk Na/Si, K/Si, Ca/Si and Ni/Si ratios for individual rims become increasingly variable in the higher petrologic type chondrites, Ornans and Warrenton and 4) the unfractionated character of matrix in Kainsaz appears, in some respects, anomalous and requires further investigations.

METAMORPHIC EFFECTS IN CO3 CHONDRITE MATRICES: Brearley, A.J.

The elemental variations observed in individual microprobe analyses for matrix and rims have also been examined in detail. These data provide some important additional insights into the response of matrix to increasing degrees of metamorphism. The major elements, Mg and Fe show a sensitive response to increasing degrees of metamorphism. In ALH A77307 the range of Fe/Si and Mg/Si ratios observed is large, but there is no correlation between these two elements, indicating that the matrix is not a simple two component mixture of Mg and Fe-bearing phases. Mineralogically this is certainly the case, as the matrix consists of a complex unequilibrated assemblage of olivines, pyroxenes, amorphous material, sulfides, oxides and iron nickel metal. In Kainsaz, the matrix clearly has a higher Mg/Si ratio than ALH A77307, but the spread in Fe/Si ratios is still large, although, unlike ALH A77307 the bulk of the analyses are much more strongly clustered. Like ALH A77307 there is no correlation between Mg and Fe. In the higher petrologic types, Ornans and Warrenton, the range of Fe/Si and Mg/Si ratios decreases dramatically and there is a clear movement of the matrices to progressively higher Mg/Si and lower Fe/Si ratios. In addition, Mg and Fe progressively develop a positive correlation, which is especially well-developed in Warrenton, indicating that the matrix mineralogy is much simpler in this meteorite. Indeed, TEM studies of the rims and matrix analysed by electron microprobe show that Warrenton matrix consists largely of fine-grained, equilibrated olivine with common, Mg, Al-bearing Cr spinel and accessory kamacite.



Although Mg and Fe show increased homogenization in matrix through the metamorphic sequence, this is not the case for other elements. Cr, Ti and Al show the reverse trend to those observed for Mg and Fe. In ALH A77307, the variation in Cr/Si, Ti/Si and Al/Si ratios is limited throughout matrix and rims, but increases progressively, such that in Warrenton all these elements are highly variable. In addition, Cr and Ti and Cr and Al become progressively better correlated. In ALH A77307 there is no correlation between these elements, whereas in Warrenton Cr shows positive correlations with both Ti and Al. Mineralogically, the correlation of Cr and Al must be the result of the presence of a significant amount of Al-bearing Cr spinel in rims and matrix.

Discussion. The parent body metamorphic model for the CO3 chondrites requires elemental mass transfer between a compositionally homogeneous matrix with heterogeneous chondrule and inclusion silicates. In the CO3 chondrites the bulk of chondrules are Mg-rich varieties [1,2], which based on the data of [2] become progressively more Fe-rich as equilibration proceeds. Fe-Mg exchange between chondrules and matrix requires that the matrix becomes more Mg-rich, exactly what is observed in the CO3 chondrites studied here. In addition, the data for chondrule silicates reported by [2] suggest that their compositions are equilibrating towards a composition of Fa_{40} , exactly the compositions observed for rim olivines in Warrenton in this study. (For comparison [5] reported olivine compositions of Fa_{45-50} for Warrenton). All these data are consistent with an in-situ metamorphic model for the CO3 chondrites. The heterogeneities observed in the distribution of minor elements in the most equilibrated CO3 chondrites requires further investigation, but may be the result of the local crystallization of discrete phases which contain elements such as Ti, Al and Cr, for example Mg-Al-bearing chromite in Warrenton matrix. **Acknowledgments.** Funding was provided by NASA grant NAGW-3347 to J.J. Papike.

References. [1] McSween, H.Y. (1977) GCA 41, 477-491. [2] Scott, E.R.D. and Jones, R.H. (1990) GCA 54, 2485-2502. [3] Jones, R.H. (1993) 2853-2867 [4] Brearley, A.J. (1993) GCA 57, 1521-1550. [5] Keller, L.P. and Buseck, P.R. (1990) GCA 54, 1155-1163.

METAMORPHISM IN THE CO3 CHONDRITES: TRACE ELEMENT BEHAVIOR IN MATRICES AND RIMS. Adrian J. Brearley¹, Saša Bajt^{2,3}, and Steve R. Sutton^{2,3} ¹Institute of Meteoritics, Department of Earth and Planetary Sciences, University of New Mexico, Albuquerque, New Mexico 87131. ²Dept. of Applied Sciences, Brookhaven National Laboratory, Upton, NY 11973. ³Dept. of Geophysical Sciences, University of Chicago, Chicago, IL 60637.

We have measured the concentrations of Ni, Cu, Zn, Ga, Ge and Se in chondrule rims in the three CO3 chondrites Kainsaz, Ornans and Warrenton by SXRF microprobe to examine the behavior of these elements during metamorphic reequilibration. These data have been compared with the trace element compositions of rims in the least equilibrated CO3 chondrite, ALH A77307. Our data show that in the least metamorphosed chondrites, these elements are distributed relatively homogeneously within rims, but as petrologic type increases they become much more heterogeneous. The heterogeneity appears to be controlled by the progressive crystallization of fine-grained matrix sulfides into larger grains.

Introduction. Carbonaceous chondrites of the CO3 group show a range of degrees of metamorphic reequilibration, which defines a petrologic sequence from petrologic type 3.0 (ALH A77307) to petrologic type 3.8 (Isna) [1,2]. We have undertaken a comprehensive study of the mineralogical and chemical changes which occur in the matrices of the CO3 chondrites in order to understand how this fine-grained material responds during metamorphism. These data will test the model that metamorphism occurred *in situ*, within a parent body, and involved elemental mass transfer between Fe-rich matrix and Mg-rich chondrules during metamorphic reheating. We have concentrated our studies on chondrule rims, which are abundant within the CO3 chondrites and have widths between 20-100 μm . In this study we have measured the concentrations of the trace elements Cu, Zn, Ga, Ge and Se, and the minor element Ni by synchrotron X-ray fluorescence microprobe at Brookhaven National Laboratory.

Techniques. We have studied 3 CO3 chondrites, Kainsaz (3.1), Ornans (3.3) and Warrenton (3.6) all falls, which span the range of degrees of equilibration found in this group. Chondrules, which are mantled by well-defined rims, were selected optically or by backscattered electron imaging and their major and minor element compositions were measured by electron microprobe using a 10 μm beam [3]. These regions were then demounted from the thin sections and attached to carbon TEM grids. The trace element concentrations were then determined on the demounted samples by SXRF microprobe at the same locations on the sample used to acquire the electron microprobe data. 3 to 8 analyses were carried out on each rim using a beam size of 8 x 10 μm . To reduce the intensity of the Fe peak in the SXRF spectra a 85 μm thick Al filter was used on the fluorescent beam. After SXRF analysis selected rims were ion milled and studied by transmission electron microscopy. This procedure enables us to obtain major, minor and trace element data, as well as a complete mineralogical characterization, on the same areas of the sample. We anticipate that this combination of data will enable us to establish the behavior of trace elements in terms of their crystal chemical behavior in the fine-grained matrix phases.

Results. We have previously measured the trace element compositions of several rims in the least equilibrated CO3 chondrite ALH A77307 [4], providing a basis for comparison with the more equilibrated CO3 meteorites. A preliminary analysis of the data for Kainsaz, Ornans and Warrenton shows that the behavior of trace elements through the metamorphic sequence is extremely complex. However, in general it is clear that the distribution of trace elements within the rims becomes significantly more heterogeneous through the metamorphic sequence. The complex behavior is illustrated in Fig 1., a plot of Zn (ppm) vs Ni (wt%) for all four meteorites. In ALH A77307 the data show a well-defined positively correlated array, which is not observed in any of the other meteorites. The Kainsaz data show extreme variability, with two populations, high and low Zn respectively. Like the data for ALH A77307, Zn does appear to be positively correlated with

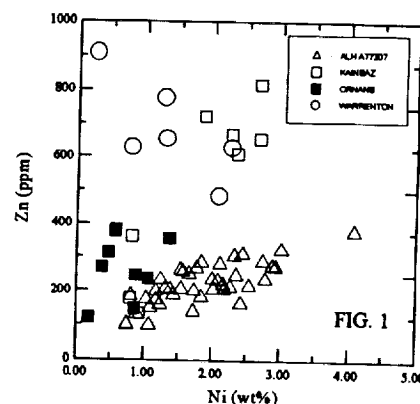
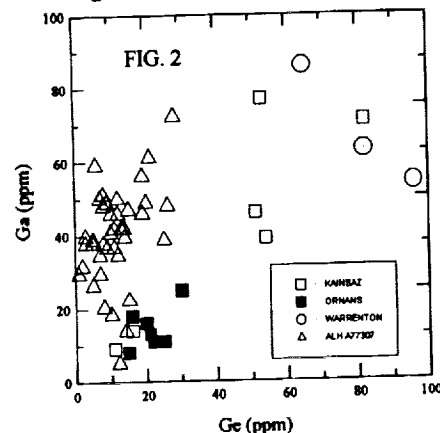


FIG. 1

TRACE ELEMENTS IN CO₃ CHONDRITE MATRICES: Brearley, A.J. *et al.*

Ni, but the trend defines a correlation line with a lower Ni/Zn ratio. Warrenton, the most equilibrated of the four meteorites studied is significantly enriched in Zn in its rims and the data appear to show a negative correlation with Ni, exactly the reverse of the other meteorites studied. Further analyses are required to define this correlation more fully. The behavior of Zn and Ni in Ornans appears to be anomalous, or at least inconsistent with the other meteorites. The scatter in the data is extremely restricted, a surprising result in view of the fact that Kainsaz, which is less equilibrated, shows a large variation in both Ni and Zn concentrations. The data for Ornans do, however, appear to lie on the low Ni and Zn end of the trend defined by the Kainsaz data.

Figure 2 shows Ga (ppm) vs Ge (ppm) which emphasizes the general observations made above. In ALH A77307, Ge shows a positive correlation with Ga, Kainsaz shows two populations of data, also positively correlated and Ornans data shows a highly restricted compositional range, but lies on the same trend as Kainsaz. The Warrenton data lie completely apart at high Ge and Ga values, which may be negatively correlated. For Warrenton the distribution of Ge is extremely heterogeneous. Of the 6 analyses carried out 3 showed high concentrations, whereas data from the other 3 points were below detection limits. This is also true for Se in Warrenton and Kainsaz. Out of 12 analyses (6 from each meteorite) Se was only above detection limits in 3 points (2 for Kainsaz, 1 for Warrenton) and in all cases the concentrations of Se were between a factor of 2 to 4 higher than in Ornans or ALH A77307.



Discussion. The trace element behavior in chondrule rims in CO₃ chondrites is evidently complex, but demonstrates a rapid response to metamorphism. The changes observed in the trace element abundances can reasonably be attributed to changes in the mineralogy of the matrices of these meteorites, which occurred during metamorphism. Cu and Zn are both chalcophile and are strongly correlated in all the meteorites, except Warrenton. This suggests that the dominant Cu and Zn carrying phases are sulfides, probably pentlandite. Pentlandite and pyrrhotite are both abundant in ALH A77307 and both Zn and Cu have a positive correlation with Ni in this meteorite, suggesting that pentlandite is the most likely candidate as a carrier. In Warrenton, however, Zn is negatively correlated with Ni and Cu showing that its behavior has changed during metamorphism and that it is probably not present in sulfides. TEM studies [3] show that Mg-Al-bearing chrome spinel is a common component in rims in Warrenton. Since Zn can readily substitute as a gahnite component into spinel, we suggest that this is the major carrier phase for Zn, rather than sulfides. An additional problem is the heterogeneous distribution, on the 10 μ m scale, of some of the trace elements, such as Cu and Se in Warrenton rims (and Kainsaz to a lesser extent). Both these elements are chalcophile in character and should be present in sulfides. In ALH A77307 sulfides are very fine-grained and are disseminated throughout the matrix [5], so that matrix analyses give extremely uniform concentrations of these elements. In comparison, in Warrenton Se and Cu are either present in extremely high concentrations in some analyses or are below detection limits. TEM studies of Warrenton show that fine-grained sulfides are essentially absent from rims, but BSE studies show that larger (50-100 μ m) sulfide grains do occur. The high concentrations of Cu and Se appear, therefore, to be the result of a sulfide grain being intercepted occasionally by the synchrotron beam as it passes through the sample. These data clearly show that during metamorphism, recrystallization of fine-grained sulfides into heterogeneously distributed, larger grains has occurred. This is consistent with the depletions of S found in chondrule rims in Kainsaz, Ornans and Warrenton, compared with ALH A77307 [3].

Acknowledgments. Funding was provided by NASA grants NAGW-3347 to J.J. Papike and NAG9-106 and NAGW-3651 to Steve Sutton (P.I.).

References. [1] McSween, H.Y. (1977) GCA 41, 477-491. [2] Scott, E.R.D. and Jones, R.H. (1990) GCA 54, 2485-2502. [3] Brearley, this vol. [4] Brearley, A.J., Bajt, S. and Sutton S.R. LPS XXIV 187-188. [5] Brearley, A.J. (1993) GCA 57, 1521-1550.

PANCAKE DOMES ON VENUS AND THE SEAFLOOR; N.T. Bridges, Dept. of Geology and Geography, University of Massachusetts, Amherst, MA 01003

The steep-sided, flat-topped "pancake" domes on Venus are volcanic features of enigmatic origin. There are at least 145 pancakes on the planet, ranging from 10 to 100 km across and up to 1500 m high or more (1). Aspect ratios (height/diameter) and volumes range from 8×10^{-4} - 0.18 and 2×10^9 - 4×10^{12} m³, respectively (2). Genetic models include formation from continuously fed silicic eruptions (1), extrusion of basaltic foams (1), and episodic eruptions of silicic lavas (2). For lack of a better analog, Venusian pancake domes have been compared to terrestrial subaerial domes (1,2). However, these domes are not comparable in size, with the Venusian pancakes generally one to several orders of magnitude larger. However, *Gloria* sonar surveys of the U.S. Exclusive Economic Zone (EEZ) (3,4) off Hawaii reveal a suite of volcanoes more similar in size and morphology to the Venusian pancakes than any other volcano class in the Solar System. Here, Venusian and seafloor pancakes are compared. It is proposed that their similarities may be due to similar ambient eruption environments.

The seafloor near the Hawaiian islands contains hundreds of volcanoes, many of which have steep sides and flat tops (Figures 1 and 2). These "seafloor pancakes" were mapped and measured using *Gloria* side-scan sonar image mosaics and bathymetric maps. The map area, extending from ~15-27° N latitude and 151-163° W longitude, contains 286 pancake-like volcanoes. They generally have flat to curved tops and steep sides, bearing a striking resemblance to the Venusian pancakes. Sixteen (5.6%) of the seafloor pancakes have one or more central craters, 8 (3%) are within a grouping of coalesced domes, 2 (<1%) are truncated, probably because of extensive erosion, 4 (1%) have landslides on their flanks, and 3 (1%) have a secondary volcano on top of them. Similar features exist on the Venusian pancakes (1). The seafloor pancakes range in diameter from ~1 to > 30 km. Their heights vary from less than 30 m (corresponding to the minimum height recorded on bathymetric maps) to over 900 m. Their volumes range from 6×10^7 - 5×10^{11} m³. Thus, though the seafloor pancakes are on average slightly smaller than the Venusian pancakes, they are much larger than most subaerial domes. Some of the Venusian pancakes have lower aspect ratios than the seafloor ones, perhaps simply because the lowest seafloor volcanoes are below the resolution of the bathymetry.

There are also some important differences between the volcanoes on the two planets. Sediment cover on the seafloor volcanoes masks some summit features and subdues the topography. Though there are no samples of the seafloor pancakes, they are probably basaltic like the rest of the ocean floor. On the basis of morphology and dimensions, the Venusian pancake domes are generally thought to be silicic (1,2,5). Finally, these oceanic volcanoes either form in the plate interior from hotspots or are born and later carried away from a spreading ridge. Due to the probable lack of plate tectonics on Venus, the Venusian pancakes are more tectonically analogous to seafloor pancakes that form in the plate interior.

The high pressures beneath the ocean and on Venus result in environments that are more similar to each other than other places in the Solar System. The pressure on Venus is ~90 bars compared to over 400 bars at the ~4500 m depth of the oceanic volcanoes. The high pressures in the two environments result in high ambient densities, so that there is a significant convective heat loss in addition to that due to radiation (6-8). The high pressures also inhibit the exsolution of volatiles that drive explosive volcanism (6). It is therefore likely that the similarities of the Venusian and seafloor pancakes are due in large part to their similar eruptive environments. Composition may also be a factor, and the remarkable similarity between the pancake volcanoes on Venus and the ocean floor reopens the question of the inferred silicic nature of the Venusian pancakes.

Future work will focus on further detailed comparisons between the Venusian and seafloor pancakes. Currently, volcanoes in other part of the EEZ and at the mid-Atlantic Ridge are being studied. Together with theoretical modeling of eruptive and tectonic conditions, this

Pancake Domes: Bridges, N.T.

comparative study should result in a deeper understanding of the mysterious Venusian pancake domes.

References

- (1) Pavri, B. et al. (1992) *J. Geophys. Res.*, **97**, 13,445-13,478. (2) Fink, J.H. et al. (1993) *Geophys. Res. Lett.*, **20**, 261-264. (3) Gardner, J.V. and Normark, W.R. (1989) *Proc. EEZ Resources: Tech. Asses. Conf.*, 22-26. (4) Gardner, J.V. (1992) *Pub. Iss. Energy Marine Geology*. (5) McKenzie, D. et al. (1992) *J. Geophys. Res.*, **97**, 15,967-15,976. (6) Head, J.W. and Wilson, L. (1986) *J. Geophys. Res.*, **91**, 9407-9446. (7) Griffiths, R.W. and Fink, J.H. (1992) *J. Geophys. Res.*, **97**, 19,729-19,737. (8) Griffiths, R.W. and Fink, J.H. (1992) *J. Geophys. Res.*, **97**, 19,739-19,748. (9) Atwater, T. and Severinghaus, J. (1988) *Tec. Map N Cen. Pac. Ocean*; in *Eastern Pac. Ocean and HI, Vol. N of the Geo. of N Amer.*, GSA, Boulder, CO.

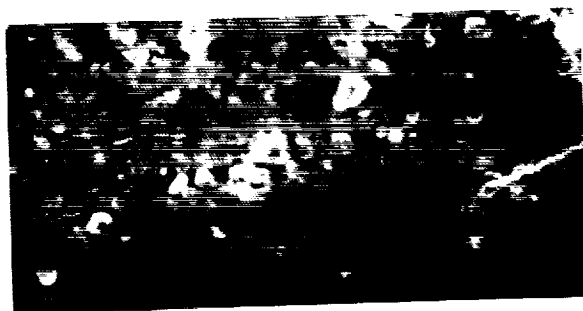


Figure 1: *Gloria* sonar image of pancake lava dome field north of Kauai, Hawaii. Image is about 180 km across.

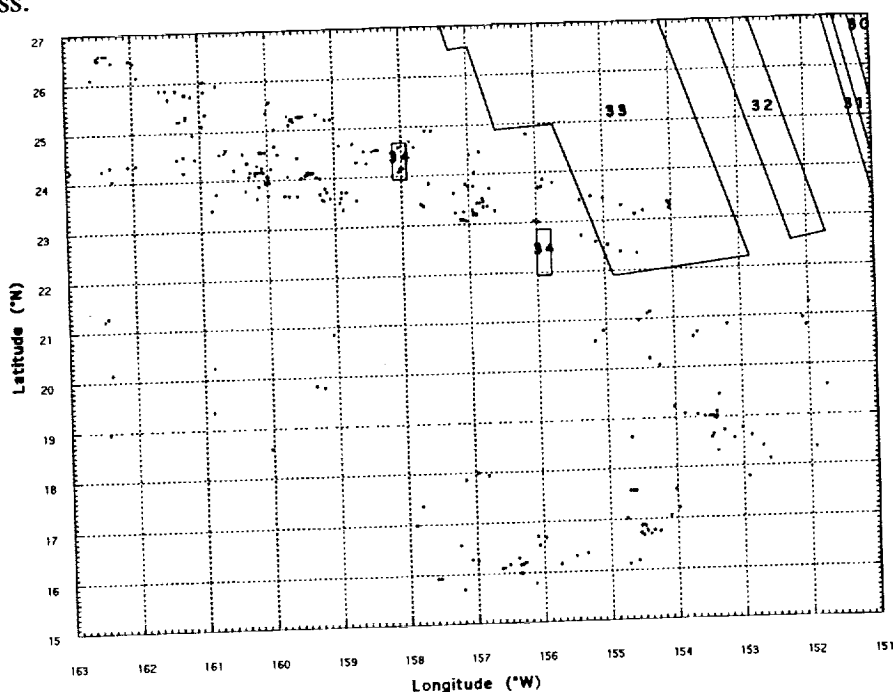


Figure 2: Map of the distribution of seafloor pancakes in the *Gloria* mosaic of the Hawaiian seafloor. Dark line is the boundary of the map area. Numbered boxes are normal magnetic anomalies (9): anomaly 30 ~ 67-68 Ma, anomaly 31 ~ 68.5-69.5 Ma, anomaly 32 ~ 72-73.5 Ma, anomaly 33 ~ 75-80.5 Ma, anomaly 34 ~ < 84.5 Ma.

RELEASE OF LIGHT NITROGEN FROM APOLLO 12023 < 10 μm FRACTION BY A COMBINATION OF PYROLYSIS - COMBUSTION; D.R.Brilliant, I.A. Franchi and C.T. Pillinger, Planetary Sciences Unit, Dept. of Earth Sciences, Open University, Walton Hall, Milton Keynes MK7 6AA, UK.

Release of the component having the most ^{14}N enriched nitrogen in lunar soil 12023 has been found to be affected by the presence of oxygen during stepped heating experiments. The results are consistent with this nitrogen, about 5% of the total being in an oxidisable phase.

The characterisation of different nitrogen carriers remains a serious problem when attempting to determine the reason for the large (20-50%) variation of $\delta^{15}\text{N}$ both within and between lunar samples. Amongst the ideas put forward to explain the observed changes are (i) a secular increase in the $^{15}\text{N}/^{14}\text{N}$ of the solar wind [1] and (ii) a two or multi-component mixing of solar wind nitrogen with a non-solar source(s) [2,3], such as indigenous lunar N [4], interstellar grains from primitive meteorites (5,6) and magnetospheric ions from the terrestrial atmosphere [7]. However, with the exception of the attempt by Brilliant *et al.* [6] to study an acid resistant residue, there have been few efforts to provide any "chemical" information about the nature of putative components. The best which has been offered to date is the observation that the part of the gas enriched in the ^{15}N isotope is liberated at a lower temperature than the portion having more of the ^{14}N isotope; since the concept of the higher temperature component being equated with fossil surfaces has long been discredited [5] but recently reconfirmed [8] and acknowledged [9], other ideas need to be evaluated.

In the current study, we have attempted to combine stepped pyrolysis and combustion to provide information about the rôle of oxygen in nitrogen release which would allow inferences about the chemical nature of the carrier phases. High resolution (10°C and 25°C) extraction procedures were applied to an Apollo 12023 grain size separate of < 10 μm . Note that the small particle fraction was chosen to eliminate the true "volume correlated" component which is only released at temperatures above 1100°C when the sample melts. All samples were analysed with a static vacuum nitrogen mass spectrometer giving better than $\pm 0.2\%$ precision at picomole levels.

When compared directly the isotopic profiles for stepped combustion and stepped pyrolysis are remarkably different. The pyrolysis experiment showed a pronounced second minimum in $\delta^{15}\text{N}$ at 1050°C not seen at all in the combustion. A summary of the observations is given in the Table. Pyrolysis shows there are two isotopically light components in the lunar soil 12023, one (hereinafter called N_{HT}) released at 1050°C, more "stable" than the other by around 150 - 200°C. The N_{HT} carrier is in this case at least 70‰ depleted in ^{15}N relative to its companion and is rendered less stable (combustible?) in the presence of oxygen. The other light N carrier released at ~850°C (hereinafter N_{MT}), which is not apparently affected by oxygen, is much more abundant but unresolved from yet another component enriched in ^{15}N [8] which is even less stable to combustion and pyrolysis (henceforward N_{LT}). On the basis of summing the N yields below and above 900°C, the N_{HT} may be between 6 and 10 ppm by wt of the bulk sample (5% of the total nitrogen).

For the purpose of investigating further N_{HT} the component affected by O_2 , we undertook a high resolution examination of a sample by a dual pyrolysis and combustion method. Two slightly different approaches were employed. Firstly the sample was pyrolysed to a temperature (900°C), believed to be above the release of N_{LT} and N_{MT} ; several combustion steps (at a fixed temperature of 900°C) were then carried out. Secondly, the sample was step pyrolysed as before but at between 860 and 890°C the procedure was stopped, the extraction vessel cooled and a stepped

RELEASE OF LIGHT NITROGEN; Brilliant D.R. *et al.*

combustion begun from low temperature. Both experiments confirmed that release of N_{HT} is enhanced by the presence of oxygen. In the first experiment the release of nitrogen which had been running at approximately 2ng/step, $\delta^{15}N$ ca. -20‰ , up to $900^{\circ}C$ suddenly increased to 12.5 ng, $\delta^{15}N = -66.7\text{‰}$ in the first $900^{\circ}C$ combustion. Once the pyrolysis was resumed the amounts of nitrogen released dropped back to ca. 1ng/step and a minimum $\delta^{15}N$ of -72‰ was reached at $1050^{\circ}C$. In the second type experiment, there was evidence for a peak in the stepped combustion nitrogen release at $700 - 725^{\circ}C$ believed to be N_{HT} ; blank corrections are substantial but there is good evidence from the data to suggest that N_{HT} has a true $\delta^{15}N < -200\text{‰}$. At high temperature above, $860 - 890^{\circ}C$, the combustion resembled the resumed pyrolysis in the first type combination experiment; $\delta^{15}N$ minima of -71‰ and -66‰ at $1050^{\circ}C$ were observed in repeat analyses.

	A12023 < $10\mu m$ Combustion ⁽¹⁾	A12023 < $10\mu m$ Pyrolysis ⁽¹⁾
Total N abundance	215 ppm ⁽²⁾	217 ppm
Abundance < $900^{\circ}C$	188.6 ppm ⁽²⁾	184.7 ppm
Abundance > $900^{\circ}C$	26.5 ppm	32.5 ppm
$\delta^{15}N$ bulk	+15.5‰	+12.4‰
$\delta^{15}N$ maximum	+141‰	+136‰
$\delta^{15}N$ minima	-44‰ (790-810°C)	-26‰ (800-840°C)
	none observed	-93‰ (1000-1050°C)

Footnotes: (1) Note that in both experiments the sample is combusted a number of times at $350^{\circ}C$ to remove any terrestrial contamination; the nitrogen released at $350^{\circ}C$ is not accumulated as part of the yield.

(2) One step lost, on the basis of steps before and after ca. 6 ppm could be added.

Although we have now demonstrated that N_{HT} , the lightest nitrogen in soil 12023, has a release which is facilitated by the presence of oxygen, we have hesitated from identifying the carrier as combustible which might imply carbonaceous. The analytical system we use for nitrogen is able to obtain information on carbon and argon conjointly with the main element of interest. Although carbon measurements are afflicted by significant blank contributions, a release can be discerned coincident with the N_{HT} . In both combination experiments however the C/N ratio cannot be > 4 and could be much less. There is good evidence for a component of ^{36}Ar accompanying N_{HT} ; the $^{36}/^{38}$ ratio is typical of a solar wind value.

We now have strong evidence for the presence of two light nitrogen components (N_{HT} and N_{MT}) in lunar regolith samples. N_{HT} has a lower $\delta^{15}N$ than N_{MT} and is chemically distinguishable, *ie.* affected by oxygen at a temperature as low as $700 - 725^{\circ}C$. If the carrier of N_{HT} is carbonaceous it does not have a high C/N; the existence of accompanying ^{36}Ar however could mean that N_{HT} is of solar wind in origin. The difference in release characteristics could be mineralogical *eg.* N_{HT} might be associated with finely-divided metallic iron. Future efforts will need to consider if N_{HT} is present in ancient lunar breccias, and the N_{MT}/N_{HT} ratio in such specimens.

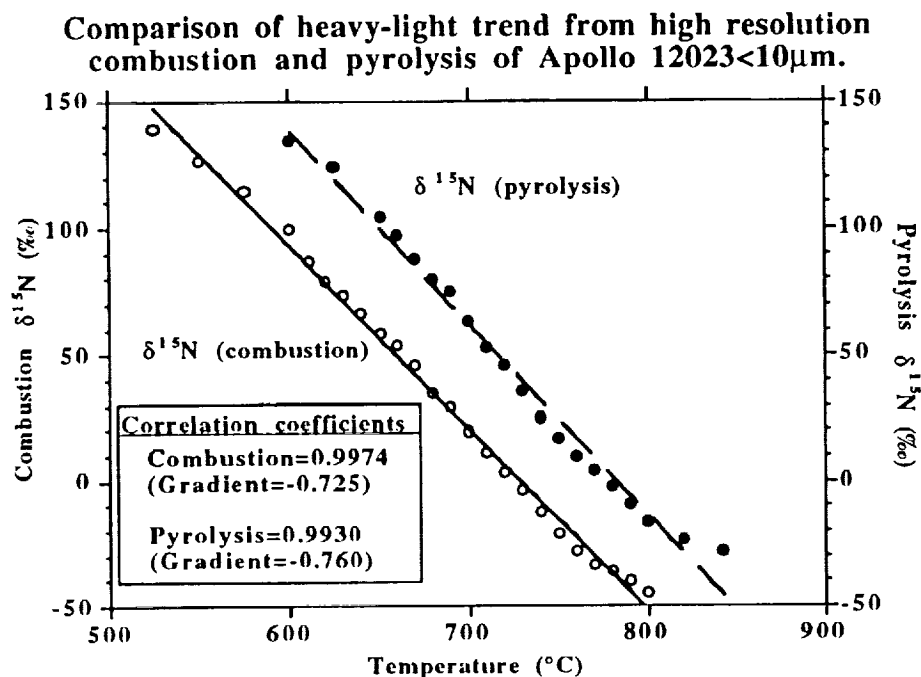
References: [1] Kerridge J.F. (1989), *Science* **245**, 480-86; [2] Geiss J. and Bochsler P. (1982), *Geochim. Cosmochim. Acta* **46**, 529-48; [3] Kerridge J.F. *et al.* (1992), *Proc. Lunar. Planet. Sci.* Vol. **22**, 239-48; [4] Becker R.H. and Clayton R.N. (1975), *Proc. Lunar. Planet. Sci. Conf.* **6th**, 2131-49; [5] Norris S.J. *et al.* (1983), *Meteoritics* **18**, 366-67. [6] Brilliant D.R. *et al.* (1992), *Meteoritics* **27**, 206-7. [7] Geiss J. and Bochsler P. (1991), *The Sun in Time* (eds. C.P. Sonnett, M.S. Giampapa and M.S. Matthews), Univ. of Arizona, Tuscon, 98 - 117. [8] Brilliant D.R. *et al.* (1993), *Proc. Lunar Planet. Sci. Conf.* **24**, 191-2 (including oral presentation). [9] Kerridge J.F. (1993), submitted for publication.

THE ^{15}N -RICH LOW TEMPERATURE NITROGEN COMPONENT IN LUNAR SOILS - AN AMMONIA RELATED SPECIES? D.R. Brilliant, A.D. Morse, J. Higgins, I.A. Franchi and C.T. Pillinger, Planetary Sciences Unit, Dept. of Earth Sciences, The Open University, Walton Hall, Milton Keynes MK7 6AA.

In a companion abstract [1], we have discussed the use of a combination of stepped pyrolysis and stepped combustion to recognise that the most ^{14}N -rich nitrogen (therein called N_{HT}) representing about 5% of the total N in a very fine fraction of Apollo 12023 lunar soil is carried by a component which is oxidisable. By far the major portion of the nitrogen in the sample is released by pyrolysis at substantially lower temperatures than the oxidisable material. The release profile of the lower temperature gas and the trend in isotopic composition during extraction suggest that the most nitrogen is a mixture of two components. One of these, called N_{LT} because it is liberated at the lowest temperature, is enriched in ^{15}N ; the other N_{MT} (medium temperature) is a ^{14}N carrier but not quite as depleted in the heavy isotope as N_{HT} . Herein we discuss the ^{15}N -rich gas N_{LT} , considered by some investigators to be the most recently implanted modern solar wind, but for reasons given below possibly an ammonia related species.

Details of the experiments performed on 12023, $< 10\mu\text{m}$ grains have been given earlier [1]; the results in respect of N_{LT} and N_{MT} are as follows: Using either stepped combustion or pyrolysis, N_{LT} , the nitrogen enriched in ^{15}N , is already being evolved by heating at temperatures as low as 350°C . It is difficult to be precise about how much comes off at 350°C because an essential part of the pyrolysis experiment involved repeated low temperature combustions to ensure the removal of terrestrial contamination. Once the experiment proper begins the isotopic composition of low temperature gas quickly rises to a maximum. We are reluctant to give absolute values for the highest $\delta^{15}\text{N}$ and the temperature at which the maximum release is reached because the amounts of gas can be close to the initial blank. From experience, we are aware that the blank decreases as the experiment proceeds, our policy is therefore to correct yields using the nominal blank (always less than 30 picomoles) and $\delta^{15}\text{N}$ values, only when the gas liberated is more than a factor of 3 above perceived blank. We have not yet refined the errors on the results but it is quite clear that N_{LT} has a $\delta^{15}\text{N} > +141\text{‰}$ and its release is enhanced by the combustion. Evidence supporting this idea is manifold from a direct comparison of the combustion versus the pyrolysis experiments: (i) the $\delta^{15}\text{N}$ for N_{LT} is higher in the former, (ii) it is reached at a lower temperature, (iii) the nitrogen release pattern is broader and less peaked in the combustion and (iv) the latter has an obvious shoulder on its low temperature side. Perhaps the best evidence that N_{LT} is a carrier affected by oxygen is seen in the figure where $\delta^{15}\text{N}$ is plotted against temperature over the interval where N_{LT} and N_{MT} are obviously mixing. The combustion mixing line is shifted by $50\text{--}75^\circ\text{C}$ to lower temperature. N.B. this is not an artifact caused by the reduced release temperature of ^{14}N enriched N_{HT} because this material is $\leq 5\%$ of the gas involved in the combustion and does not "burn" until 725°C . The pyrolysis line in the figure is confirmed by the repeat dual pyrolysis/combustion experiments [1]. From the mixing lines in figure 1, we ought to be able to deconvolute the two component mixtures. However, it is fairly obvious, assuming that the two components have approximately gaussian release, they are only just resolvable by the techniques we employ. Therefore any estimates of the abundance of N_{LT} and N_{MT} will be very dependant on the choice of $\delta^{15}\text{N}$ values for the end-members. A number of models are being considered.

The recognition of N_{LT} as a component, whose release from lunar fines is enhanced by the presence of oxygen, is not consistent with N_{LT} being the most recently implanted solar wind. Whilst the absolute surfaces of lunar silicate grains are oxygen depleted by preferential

THE ^{15}N RICH LOW TEMPERATURE; Brilliant D.R. *et al.*

sputtering [2], because solar wind accumulation is an equilibrium process (implantation balanced by erosion) the implanted atoms currently at the very surface are those earliest implanted [3]. We must therefore look for an alternative explanation. One which could fit our observations is that N_{LT} is ammonia or ammonium ions. The former could be produced analogous to methane [4] in lunar regolith materials. The possibility that the solar wind N and H may also react together to give NH_4^+ , which could substitute for metal cations in the silicate lattice, is appealing. It offers possibilities for the enhanced retention of nitrogen.

Because of our hypothesis that N_{LT} in ammonia/ammonium, we have carried out preliminary investigation of CH_4 from lunar soil 10086 to compare its release characteristics under similar conditions to that used to study N_{LT} . There is good evidence to suggest that methane is liberated over the appropriate temperature range 400 -800 $^{\circ}\text{C}$. Moreover we believe that the carbon in methane is isotopically heavy; Chang *et al.* 1974 [5] suggest a $\delta^{13}\text{C}$ of +15‰, our preliminary results are indicative of values of +60‰. There are a number of ways such as preferential sputtering and preferential diffusion, whereby volatile ammonia could be ^{15}N enriched as a function of lunar regolith evolution. Such ideas will be explored qualitatively and quantitatively elsewhere. We need also to investigate ancient lunar breccias for the presence of an N_{LT} component.

In this paper and its predecessor [1] we have given chemical evidence on the nature of two of the nitrogen carriers N_{LT} and N_{HT} in a lunar soil. The remaining nitrogen carrier N_{MT} appears to be chemically inert. By default N_{MT} may be solar wind elemental nitrogen implanted into silicate minerals.

References: [1] Brilliant D.R. *et al.* (1994) this volume. [2] Pillinger C.T. *et al.* (1976) *EPSL* **33**, 289. [3] Pillinger C.T. *et al.* (1979) *Rep. Prog. Phys.* **42**, 899. [4] Pillinger C.T. *et al.* (1972) *Nature Phys. Sci.* **235**, 108. [5] Chang *et al.* (1974). *Geochim Cosmochim. Acta* **38**, 853-72.

"SPACE WEATHERING" AND THE ORDINARY CHONDRITES. D.T. Britt¹ and B.E. Clark² (1) Lunar and Planetary Laboratory, University of Arizona, Tucson, AZ 85721 (2) McDonald Observatory, University of Texas at Austin, Austin, TX 78712.

Introduction: The role of "space weathering" (broadly defined in this context as regolith processes that alter the reflectance spectra of surface material on atmosphereless bodies) in the controversy over the asteroidal source of the ordinary chondrite meteorites has been the subject of lively debate. There has been general agreement on a few points: (1) The spectra of the ordinary chondrites and the spectra of most S-class asteroids do not match [1]. The possible exceptions are the asteroids in Gaffey's S(IV) class which may be similar to some ordinary chondrites [2]. (2) That known regolith processes (shock, heating, melting, comminution, solar wind implantation, reduction of Fe²⁺) do not alter ordinary chondrite spectra to the spectra of S-class asteroids [1,3,4]. This is not to say that space weathering does not alter the spectra of ordinary chondrites. We have samples of the surface material of ordinary chondrite asteroids. These are the dark matrix portions of the gas-rich ordinary chondrites, and, as their name implies, are all spectrally altered to a greater or lesser extent. This alteration consists of spectral darkening which lowers their reflectance and flattens their absorption features. Fanale and Clark illustrated the spectral effects of lunar "space weathering" and their relationship with S-asteroids and "unweathered" ordinary chondrites graphically in their 1993 LPSC abstract [5] using the parameters of spectral slope, depth of the 1.0 μm band, and albedo. It is useful to examine the observed spectral "weathering" of ordinary chondrites in the same format to understand the relationships (or lack thereof) between weathered ordinary chondrites, lunar material, the S-asteroids, and other asteroid classes.

Method: In the near-IR wavelength range the most immediately apparent spectral features of ordinary chondrites and S-type asteroids are: (1) albedo or reflectance at 0.56 μm ; (2) the slope of the continuum; and (3) the depth of the 1 μm absorption band. The continuum slope is calculated as a linear fit from peak to peak around the mafic mineral band. By convention, the continuum is removed from the spectrum before band center position identification by ratioing the entire spectrum to the continuum slope. The band center is the minimization of the derivative of a polynomial fit to the absorption band near 0.95 μm . The band depth is then measured from the continuum to the band center [3].

Discussion: Shown in **Figure 1** is a plot of continuum slope vs band depth for mature and immature Lunar Mare Basalts, an average of 23 ordinary chondrite meteorites, an average of 39 S-asteroids, an average of 4 gas-rich ordinary chondrites, and an average of 5 black ordinary chondrites. Weathering processes move the spectra of lunar mare basalts from the immature zone in the lower center toward the upper left of the slope/band depth space. This spectral "weathering path" reflects the extremely strong reddening of the mature lunar spectra along with a shallowing of absorption bands. The spectral effect of "space weathering" on ordinary chondrites is different. In both gas-rich and black ordinary chondrites band depth and continuum slope decrease. In the case of the gas-rich ordinary chondrites the continuum slope becomes slightly blue. The overall effect is to move away from the slope/band depth space of S-type asteroids and to move at right angles to the weathering path of lunar material. **Figure 2** shows a similar result in albedo/slope space. Once again the strong reddening of mature lunar material creates a spectral weathering path that goes from the left to right across the plot. In ordinary chondrites "space weathering" causes a reduction of both reflectance (albedo) and continuum slope. The spectral weathering path for this material is toward the lower left, again at right angles to the lunar case and away from the S-type asteroids. The slope/band depth/albedo parameters for an average of six C-type asteroids are also plotted in Figures 1 and 2. "Space weathering" in ordinary chondrites does move in the direction of the parameter space occupied by the C-asteroids. This is not to say that all C-type asteroids are ordinary chondrite parent bodies. What these plots show is that known "space weathering" processes, as exhibited by meteorites in our collections, darken and flatten the spectra of ordinary chondrites. These processes create a spectral weathering path that is different from the path of lunar material and would push large ordinary chondrite parent bodies with "mature" surfaces (if any exist) toward the spectra of C-type asteroids. This suggests that large ordinary chondrite parent bodies that have accumulated a thick regolith would have spectra more similar to C-type asteroids. The implication is that some large anhydrous C-type asteroids in the inner asteroid belt may be ordinary chondrite parent bodies with "mature" space weathered surfaces.

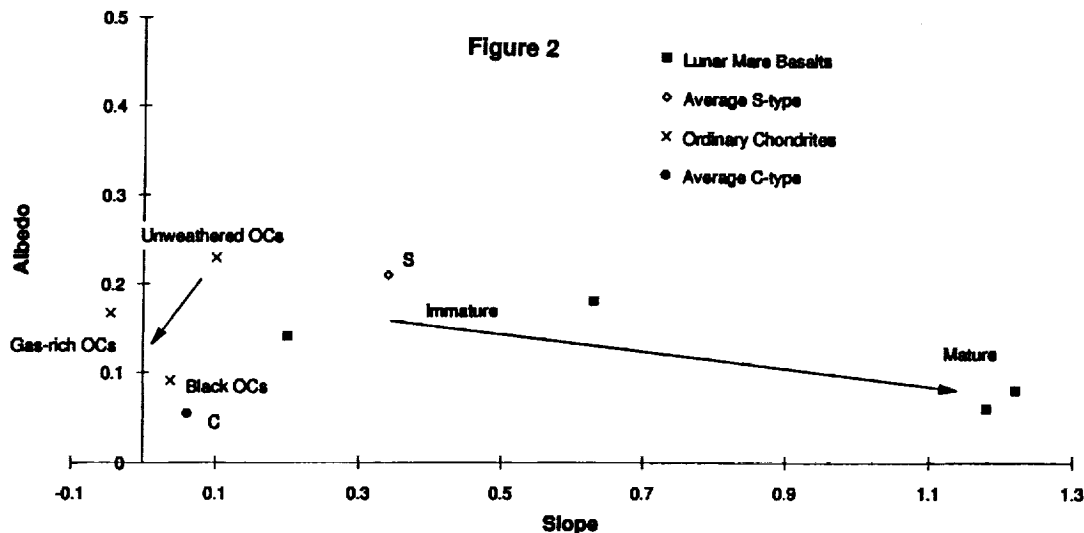
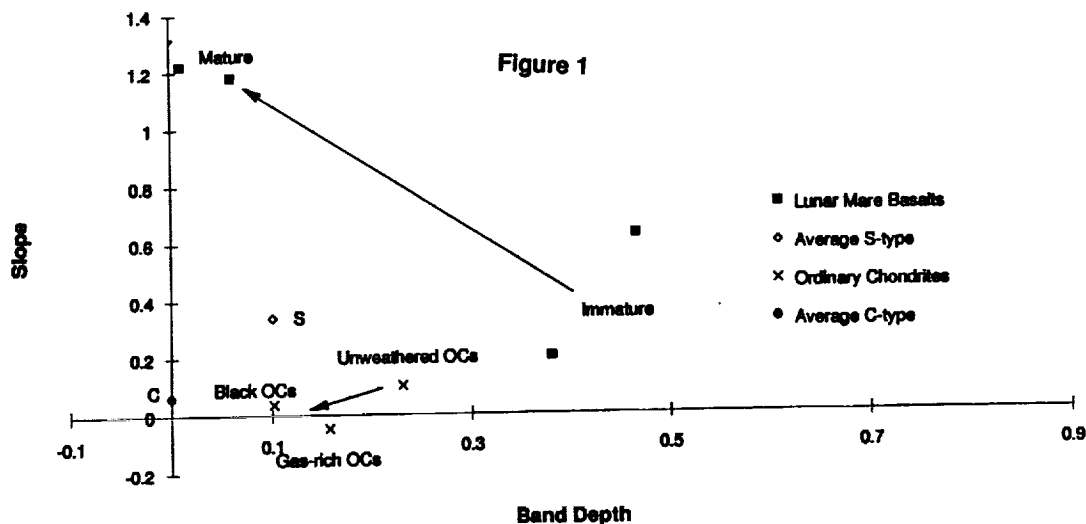
Arguments against significant "space weathering" on large ordinary chondrite parent bodies: (1) There are no large ordinary chondrite parent bodies because they have been ground-down to small sizes by the collisional evolution of the inner asteroid belt [6]: The asteroids that have been observed with ordinary chondrite-like spectra

"SPACE WEATHERING" AND THE ORDINARY CHONDRITES: Britt D.T. and Clark B.E

are uniformly small. These include the main belt asteroid 3628 1979 WD (diameter 7 km) and the NEA 1862 Apollo (diameter 1.5 km). However, these are objects with very low gravity and short collisional lifetimes that are unlikely to develop or retain a regolith. The same collisional evolution process has allowed a number of large inner-belt hydrated C-type asteroids to survive even though they are thought to be composed of relatively weak aqueously altered materials. (2) Impact processes would strip-off weathered material and excavate fresh material: Recent hydrocode modeling suggests that impacts "shake" rather than strip asteroids and are likely to leave accumulated regolith soil intact [7]. The fresh material that is excavated by larger impacts would be subject to the weathering effects of micrometeorite bombardment which effectively saturates and weathers exposed material on the Lunar surface in 10^6 years.

Conclusions: Spectral studies of gas-rich and shock-blackened ordinary chondrites show that space weathering processes darken and flatten ordinary chondrite spectra. This is a different spectral result than is seen in Lunar weathering processes. In spectral parameter space weathering drives ordinary chondrite spectra away from the parameters of S-asteroids and toward the parameters of C-asteroids. If large ordinary chondrite parent bodies have survived collisional evolution and can retain a regolith, their weathered spectral properties would suggest looking for them among anhydrous inner-asteroid belt C-type asteroids.

References: [1] Clark B.E. (1993) Ph.D. Thesis. [2] Gaffey M.J. et al. (1993) *Meteoritics* 28, 161 [3] Bell J.F. and Keil K (1988) *Proc. 18th Lunar Sci. Conf.*, 573. [4] Britt D.T. (1991) Ph.D. Thesis. [5] Fanale F.P. and Clark B.E. (1993) *LPSC XXIV*, 463. [6] Bell J.F. et al. (1989) *Asteroids II*, 921. [7] Asphaug E. (1993) Personal Communication.



CAT MOUNTAIN: SPECTRA AND PETROLOGY OF AN L5 IMPACT-MELT BRECCIA. D.T. Britt and D.A. Kring. Lunar and Planetary Laboratory, University of Arizona, Tucson, AZ, 85721.

The Petrology of Cat Mountain: The Cat Mountain chondrite is an L5 impact melt breccia of rounded highly shocked clasts in an igneous melt matrix [1]. This stone was found near Tucson, Arizona in approximately 1980-82 and was probably recovered within 24 hours after its fall [2]. It was identified as a meteorite in 1992. Cat Mountain is comprised of two lithologies: (1) shocked clasts of L5 material which represent relic fragments of the pre-impact asteroid and (2) a melt matrix surrounding the clasts which was produced by complete shock-melting of other portions of the asteroid.

The Clast Phase: The shock processes that affected the clasts produced dikes of shock-comminuted and shock-melted material. The shock-comminuted silicates were reduced to micron-sized grains, some of which may not have any crystalline order. Silicate grains adjacent to the dikes have undulatory extinction, irregular fractures, multiple planar fractures (some with Fe,Ni-metal and sulfide fillings), or are recrystallized, all of which has reduced the size of uniform crystalline domains. Micron-sized metal and/or sulfide particles are disseminated throughout the dikes. Although veins containing larger crystals of Fe,Ni-metal and sulfides crosscut the clasts, and some metal-sulfide assemblages in chondrules were unaffected by shock processes, most opaque grains in the clasts are $\leq 1 \mu\text{m}$ in size. Four point count lines were analyzed across the clast phase in thin section UA 159,4 to quantify the abundance and distribution of the opaque grains. The lines were separated by approximately $150 \mu\text{m}$ and points were counted every $30.5 \mu\text{m}$. The total number of points was 1218 over an area of 16.7 mm^2 . Of these points 13.6% consisted of metal and sulfide phases. The size and particle distribution of these phases are summarized in Figure 1. In the count of points and particles the opaque population of the clast material is dominated by the smallest fraction.

The Melt Phase: The silicate portion of the impact melt matrix surrounding the relic clasts is dominantly olivine and pyroxene, with grain sizes typically $< 50 \mu\text{m}$, interspersed with a feldspathic mesostasis. Even though the melt matrix contains submillimeter-sized mineral clots, the size distribution of silicate crystals in the melt is more uniform than in unshocked L5 material, which has a bimodal distribution. In addition, there is less crystalline silicate material in the melt than in unshocked L5 material, because of the abundant ($\sim 10\%$) glassy mesostasis. In contrast, the metal and sulfide phases in the melt have a bimodal size distribution. Most particles are either $\leq 1 \mu\text{m}$ in diameter or have lengths that extend beyond 1 mm . In addition, the metals are concentrated in the larger particles while sulfides are concentrated in the smaller particles (excluding those $\leq 1 \mu\text{m}$ in size, which are too small to accurately identify). Five point count lines were analyzed across the melt phase in thin section UA 159,4. These lines were separated by approximately $300 \mu\text{m}$ with points every $30.5 \mu\text{m}$. The total number of points was 3284 over an area of 129 mm^2 . A total of 12.7% of the points consisted of metal and sulfide phases. Shown in Figure 2 are the data from this point count series. The distribution of points is distinctly bimodal with similar peak at the smallest and largest size ranges. The number of particles shows a strong peak at the smallest size range but also shown a distinct hump in the 15-30 and 30-61 μm sizes.

Reflectance Spectra: To link the meteorite's petrology with its reflectance spectra small samples of both the melt and clast phases were taken from areas immediately adjacent to the area sampled by thin section UA 159,4. These samples were ground to a particle size of $< 125 \mu\text{m}$ and bidirectional reflectance spectra over the wavelength range 0.3 to $2.6 \mu\text{m}$ were obtained using the RELAB facility at Brown University. Shown in Figure 3 are the reflectance spectra of the two phases of Cat Mountain. What is apparent are the very large differences in reflectance and band depth between the melt and clast phases. There is almost a factor of two difference in reflectance. The clast phase has a reflectance at $0.55 \mu\text{m}$ of 0.09 and the melt phase has a reflectance of 0.15. The difference in band depth at $1.0 \mu\text{m}$ is even greater with the clast phase having a very attenuated band of 6.7% and the melt phase having a depth of 17.5% which is a normal band depth for an ordinary chondrite. The spectrum of the clast phase with its low reflectance and flattened absorption features is typical for a highly shocked black chondrite, but the melt phase reflectance is much closer to what is normal for ordinary chondrites. The reflectance differences between these two phases are a consequence of the particle size differences in their opaque metal and sulfide grains. Small particle size opaques, particular those with diameters on the order of the wavelength of visible light have been shown to be very effective spectral darkening agents [3]. Both phases have approximately the same areal coverage of opaques, but the clast phase has 52% of its metal and sulfide areal coverage in the smallest size fraction against only 22% for the melt phase. This increase in the smallest sizes makes the same total

SPECTRA AND PETROLOGY OF CAT MOUNTAIN: Britt D.T. and Kring D.A.

amount of opaques much more effective as a spectral darkening agent. The result for the clast phase is more opaque particles per unit area, a much shorter average optical path length, greater absorption of photons, and, as we can see, a flatter and darker spectrum than the melt phase.

Figure 1: Cat Mountain Clast Phase

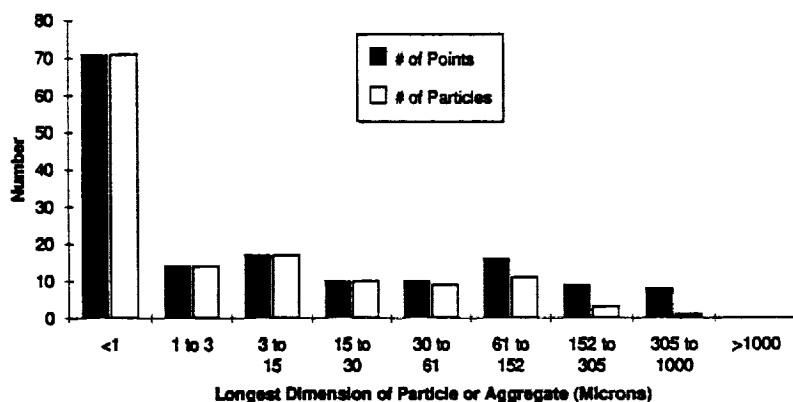
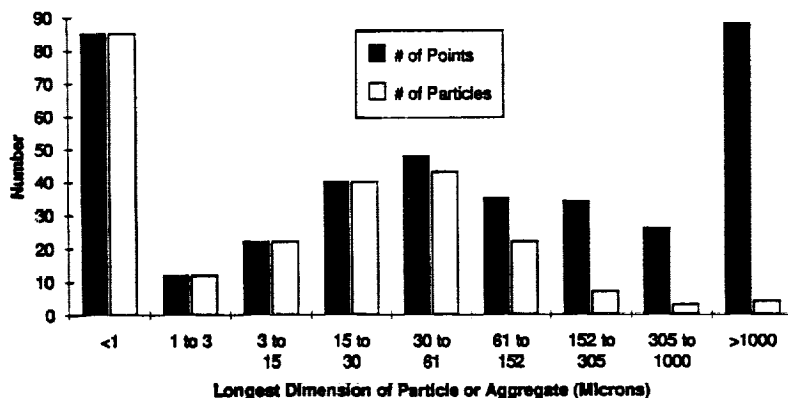
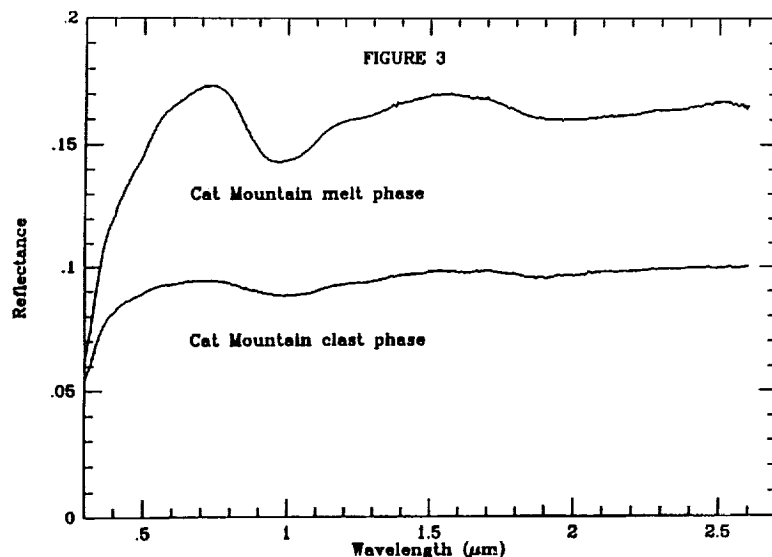


Figure 2: Cat Mountain Melt Phase



Reflectance spectra can also be used as a test for terrestrial weathering. The 0.5/0.6 μm ratio is very sensitive to weathering because the oxidation of the abundant iron in ordinary chondrites increases the absorptions in this wavelength range [4]. The 0.5/0.6 μm ratio of the clast phase in Cat Mountain is 0.96 which is the highest ratio that we have seen for a meteorite find. This ratio tends to confirm the theory that this meteorite was recovered within 24 hours after its fall [2].

References: [1] Kring, D.A. (1993) *LPS XXIV*, 823. [2] Wlotzka, F. (1993) *Meteoritics* 28, 693. [3] Britt, D.T. (1991) Ph.D. Thesis. [4] Salisbury, J.W. and Hunt, G.R. (1974) *JGR* 79, 4439.



TECTONICS OF ARTEMIS CORONA, VENUS: IMPLICATIONS FOR FORMATION AND EVOLUTION

C. David Brown and Robert E. Grimm, Dept. of Geology, Arizona State University, Tempe, AZ 85287-1404.

Introduction. Artemis, the largest corona on Venus at 2600 km diameter, is a feature of particular interest due to the insight on the thermal and mechanical structure of the lithosphere provided by analysis of the presumed flexural topography on its margin. The processes responsible for the peripheral trench-outer rise system and the deformation in the corona interior are also relevant to the general nature of venusian tectonics. It is unlikely that Artemis can be completely explained by the standard corona evolution model of surface uplift by a plume or diapir, transition to a plateau, and eventual gravitational relaxation [1,2]. Elastic flexure modeling has shown the need for large applied bending moments, suggesting the presence of a subducted slab [3]. Inelastic flexure models require an inplane force an order of magnitude larger than that inferred from the geoid, a large moment, and a mantle rheology stronger than that measured for dry olivine in laboratory experiments [4,5]. The extreme conditions imposed by the models indicate that our understanding of the rheology, thermal state, and forces acting on the lithosphere is inaccurate, or the assumption that the topography is flexural and induced by subduction is in error. The present work concentrates on the interpretations of the geologic structures comprising the annulus and interior of Artemis, and their implications for the mechanisms responsible for the formation of the chasma and forebulge. This abstract focuses on C1-MIDRP 30S135, although the conclusions encompass observations of most of Artemis. This study has relied on the Magellan cycles 1 and 2 synthetic aperture radar F- and C1-MIDRPs, shaded relief images created by combining the left- and right-looking SAR images [6], and gridded altimetry data. A schematic map of the preliminary interpretations is illustrated in Figure 1; parenthesized letter callouts in the text denote locations of features that may not be visible in the figure.

Annulus Structures. The Artemis annulus includes structures formed by both shortening and extension [1], but folding is prevalent on the southeastern margin (A) [7]. Evidence for a compressional origin of the structures found in the chasma includes their sinusoidal cross-sections, continuity over ~200 km, and tapered terminations as well as the absence of steep scarps and associated radar layover common to extensional features. Anastomosing graben are observed along the inner trench slope and corona rim (B), and may reflect gravitational sliding [7]. Horsts and graben on the outer trench slope, while ubiquitous at terrestrial subduction zones, are absent along most of the Artemis annulus. This observation might be explained by the influence of a large compressive inplane force. Radial fractures of unknown origin tend to correlate in density with the height of the outer rise (C). The identity of the structures in the trench north of the termination of folding (D) is ambiguous. Outer trench slope graben are found where annulus folding is absent (E). At its northern terminus (F) the Artemis annulus intersects a rift zone.

Interior structures. The interior of Artemis is dominated by a northeast trending belt of deformation superimposed on smooth, unbroken volcanic plains (G). Interpretation of this unit in the context of shortening or extension is made difficult by structures characteristic of both modes of tectonics. Observations in favor of compression include imbricate thrust faults (H), a plunging anticline (I), tapered ridge terminations, sinusoidal and symmetrical cross sections of some ridges, >100 km length of some ridge-trough pairs, and convex outward arcuate fault scarps. The flat trough floors are similar to graben, but this is a result of infilling by lava. The high northeast edge of the deformation belt bows outward into the annulus (J); this shape and the presence of northwest oriented thrust faults is consistent with a compressional origin. The volcanism and low topography are typical of extensional regions; in addition, many flat-topped ridges resemble horsts and some scarps appear to be normal faults. However, it is generally easier to explain such structures as special cases of compressional deformation than to cast the evidence for shortening in terms of an extensional origin [8]. A structure that is especially difficult to explain with extension is a prominent fault scarp paired with a high, smooth ridge (K). A fine scale (~1 km) of deformation parallel to the ridge appears to result from the buckling of a thin surface layer. The length (~300 km), continuity, and splaying behavior of the scarp are characteristic of thrust faults. Features posed as possible fracture zones [9] are located within a "sub-corona" and may be associated with its formation rather than back-arc spreading in the whole of Artemis coupled with rollback subduction at the chasma. The geometry of two parallel shear zones (L) [9] is inconsistent with an Earth-like system of spreading ridges and transform faults. Shear zones like these are rare in Artemis, and a distributed form of spreading in the interior appears unlikely.

Conclusions. The southeast limb of Artemis Chasma is distinguished by folding; this fold belt and the adjacent flexural topography possibly have a common origin in a large northwest directed inplane force. Difficulties with this model are that the magnitude of the required force greatly exceeds the predicted forces due to mantle flow coupling [10], and the trench-forebulge on the northeast and southwest limbs requires an alternative explanation. A compressional origin for the northeast trending interior deformation belt is favored. However, this interpretation is

TECTONICS OF ARTEMIS CORONA Brown C. D. and Grimm R. E.

difficult to reconcile with the low topography of the region; compression resulting from the collapse of the uplifted surface or local downwelling is a possible rationale. The amount of extensional strain in the interior is small relative to shortening, and insufficient to maintain back-arc spreading. The relative ages of the interior and annulus fold belts is not obvious; while the interior belt overthrusts the trench, the annulus folding generally appears more pristine than that of the northeastern portion of the interior deformation. Therefore an ancient episode of back-arc spreading coupled with peripheral rollback subduction seems improbable, and the annulus folding may be unrelated to the flexural topography. It is difficult to speculate on a model of origin for Artemis Chasma that is more consistent with all the observations, but it is anticipated that this analysis will aid the development of such a model.

References. [1] Stofan E. R. *et al.* (1992), *JGR*, 97, 13,347. [2] Squyres S. W. *et al.* (1992), *JGR*, 97, 13,611. [3] Sandwell D. T. and Schubert G. (1992), *JGR*, 97, 16,069. [4] Brown C. D. and Grimm R. E. (1993), *LPS*, XXIV, 199. [5] Brown C. D. and Grimm R. E. (1993), *Eos*, 74, 378. [6] Kirk R. L. (1993), *LPS*, XXIV, 803. [7] Suppe J. and Connors C. (1992), *JGR*, 97, 13,545. [8] Pappalardo R. T. and Greeley R. (1993), *JGR*, submitted. [9] McKenzie *et al.* (1992), *JGR*, 97, 13,533. [10] Phillips R. J. (1990), *JGR*, 95, 1301.

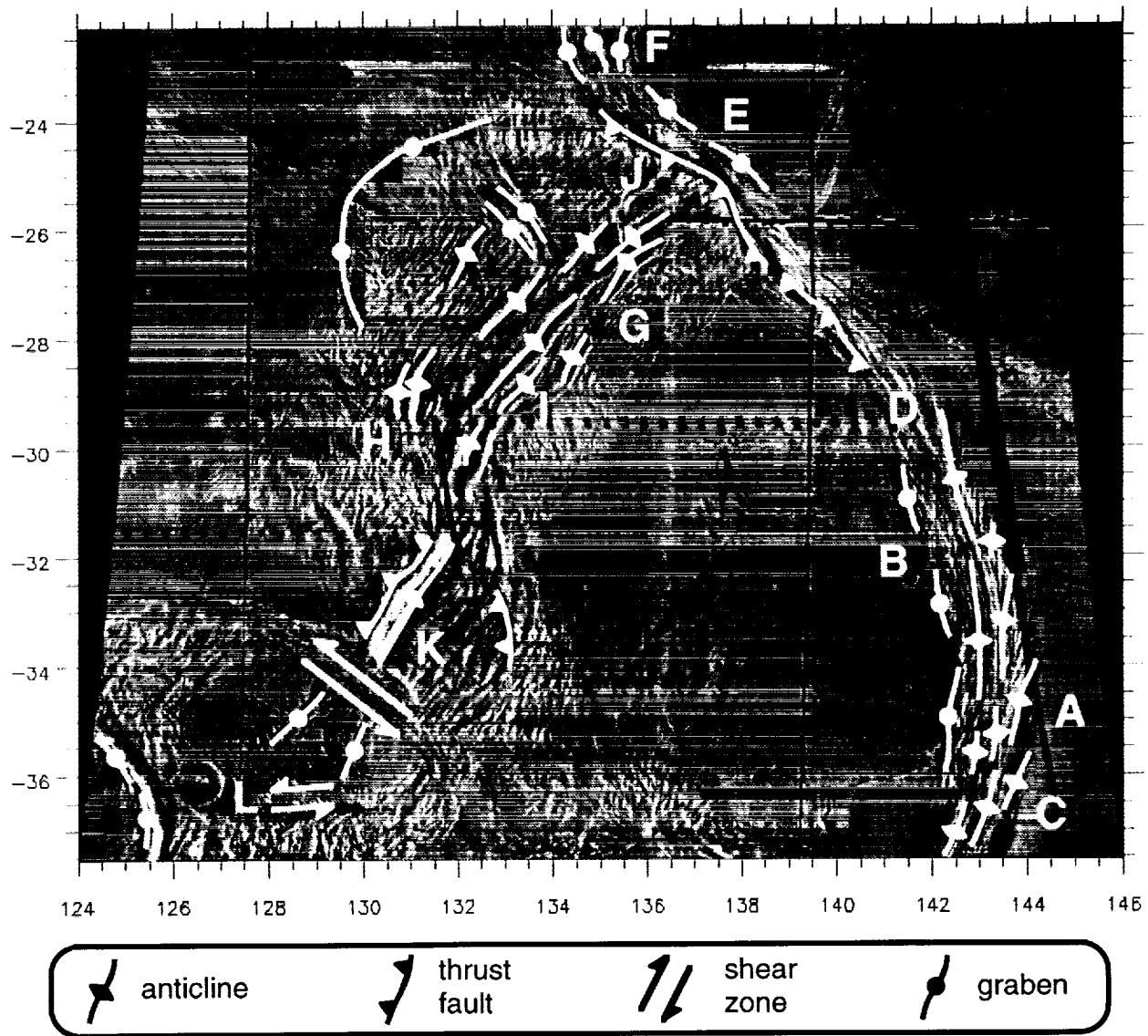


Figure 1. Schematic map of Artemis Corona structural geology. Base image is a shaded relief composite of cycles 1 and 2 C1-MIDRPs 30S135 in an equidistant cylindrical projection. Map symbols are intended to represent the style of tectonics where drawn, and do not necessarily correspond to specific structures.

2 ALTERATION AND FORMATION OF RIMS ON THE CM PARENT BODY Lauren B. Browning¹, Harry Y. McSween, Jr.¹, and Michael Zolensky², ¹ Department of Geological Sciences, University of Tennessee, Knoxville, TN 37996-1410, ² Solar System Exploration Division, NASA Johnson Space Center, Houston, TX 77058.

All types of coarse-grained components in CM chondrites are surrounded by fine-grained dust coatings [1], but the origin of these rims is not yet clear. Although a strictly nebular origin seems likely for rims in the relatively unaltered type 3 chondrites [2], the rims in CM chondrites are dominated by secondary alteration phases. It has been argued that either the coarse-grained cores accreted altered rim materials while still in the nebula [1] or that alteration of primary rim phases occurred on the CM parent body [3]. To constrain the origin of alteration phases in rim material, we have analyzed the textures and mineral associations from 10 CM chondritic falls by optical and scanning electron microscopy. Our results indicate that the secondary phases in CM chondritic rims were produced by parent body fluid-rock interactions which redefined some primary rim textures and may have produced, in some cases, both coarse-grained components and the rims that surround them.

Textural features demonstrate the interactive exchange of alteration fluids between rims, matrix, and chondrules on the CM parent body. For example, most matrix-rim contacts are gradational, suggesting the synchronous alteration of both components. Rim assemblages typically extend into matrix along multiple convoluted avenues and eventually merge with either surrounding matrix or nearby rims. This gradual coalescence of chondrule rims with different CM components is inconsistent with a nebular origin for secondary rim phases because it precludes a clastic origin for CM chondrites. In addition, we have identified several delicate rim extensions (<10 μm thick) that pond into immediately adjacent matrix and probably would not have survived impact and subsequent regolith gardening processes. Both types of rim extensions are most simply explained by the localized migration of precursor rim components in an aqueous medium. Transport of material during fluid-rock interactions on the CM parent body is also supported by documentation of both phyllosilicate veins that bridge chondrules to matrix and the breaching of chondrules by rim-like materials along fractures and within glassy mesostasis.

Several observations suggest the possibility of in situ rim production. For example, tochilinite and phyllosilicates commonly form rims around matrix carbonates [4], which are generally believed to have precipitated from alteration fluids on the CM parent body [5]. This suggests that the rims surrounding matrix carbonates may also have been produced by alteration processes. In addition, tochilinite and phyllosilicates often coat the fractures and peripheries of individual olivine grains within chondrules (Figure 1). Rinds of hydrated Fe-oxides are observed on olivines in partially serpentinized terrestrial rocks [6], and it has been suggested that if sulfur is available in the alteration fluid, then sulfide rims may be formed around dissolving olivine in a similar manner [7]. Unfortunately, conditions favorable for the precipitation of tochilinite, a common S-bearing rim phase, are poorly constrained [8]. However, we observe pseudomorphing of chondrule silicates by tochilinite and serpentine, which indicates that S-bearing phases are important to some olivine dissolution reactions in CM chondrites. Outlines of internal fracture planes in completely pseudomorphed olivines are often delineated by concentrations of fine-grained pentlandite.

Partially replaced chondrule olivines bear a striking resemblance to many rimmed olivines in the matrix which suggests, by analogy, that site-specific precipitation of S-bearing phases may also be responsible for the occurrence of many tochilinite-rich rims around isolated

matrix olivines. The presence of fine-grained rims around fragmented chondrules and isolated matrix olivines is nearly ubiquitous in CM chondrites, but rarely occurs in other chondrite classes [2]. We observe isolated olivine fragments in optic continuity which are separated by rinds of tochilinite; preservation of crystallographic orientation is consistent with the preferential, in situ precipitation of tochilinite-rich rim material at the surface of the dissolving olivine.

Non-silicate rims precipitate around olivines of any composition, but the process is most effective for fayalitic olivines [7]. Most of the remaining olivines in CM chondrites are relatively Mg-rich, which suggests that the precipitation of S-bearing rims on olivines may not have been an important process in the aqueous alteration of CM chondrites, despite the evidence presented above. However, compositionally-zoned olivines with forsteritic cores and fayalitic rims have been observed in CM chondrites and are common in the less-altered chondrite classes [9]. This suggests the possibility that tochilinite and Fe-rich serpentine rims observed around isolated matrix silicates in CM chondrites may reflect the preferential replacement of the outer fayalitic component of compositionally zoned olivines in CM chondrites. Although we currently have no explanation for the association of tochilinite with matrix carbonates, a nebular rim formation seems unlikely.

We therefore conclude that: (1) precursor rim materials in CM chondrites were subjected to pervasive aqueous alteration on the CM parent body; and (2) textures and mineral associations observed in CM chondrites also suggest the possibility of in situ rim production.

References: [1] Metzler K., Bishoff A., and Stoffler D. (1992) *Geochim. Cosmochim. Acta* **56**, 2873-2897. [2] Rubin A. E. (1984) *Geochim. Cosmochim. Acta* **48**, 1779-1789. [3] Brearley A. J. (1991) *Meteoritics* **26**, 323. [4] Bunch T. E. and Chang S. (1980) *Geochim. Cosmochim. Acta* **44**, 1543-1577. [5] Armstrong, J. T. et al. (1982) *Geochim. Cosmochim. Acta* **46**, 575-596. [6] Ramdohr P. (1967) *N. Jb. Miner. Abh.* **107**, 241-265. [7] Siever R. and Woodford N. (1979) *Geochim. Cosmochim. Acta* **43**, 717-724. [8] Zolensky M. (1984) *Meteoritics* **19**, 346-347. [9] Steele I. M. (1986) *Geochim. Cosmochim. Acta* **50**, 1379-1395.



Figure 1: Plane light photograph of tochilinite and phyllosilicates rimming partially altered olivine in a Murchison aggregate.

2957

EUREKA!! AEROGEL CAPTURE OF METEOROIDS IN SPACE

D.E. Brownlee¹, F. Horz², L. Hrubsch³, J.A.M. McDonnell⁴, P. Tsou⁵ and J. Williams⁶ [1] Dept. of Astronomy, Univ. of Washington, Seattle, WA 98195 [2] NASA Johnson Space Center, Houston, TX 77058, [3] L-322, Lawrence Livermore National Lab. 7000 E. Ave., Livermore, CA 94555, [4] Unit for Space Sciences, University of Kent at Canterbury, Kent CT2 7NR, U.K., [5] 283-501, Jet Propulsion Lab, 4800 Oak Grove Dr., Pasadena CA 91109, [6] MST-7 E549, Los Alamos National Lab, Los Alamos, NM 87545

Light gas gun studies have shown that 6 km/s solid mineral and glass test particles can be successively captured in 0.05 g cm⁻³ aerogel without severe heating or fragmentation. In spite of this work, there has been uncertainty in the performance of aerogel for hypervelocity capture of real meteoroids. Natural impacts differ from simulations in that the particles are likely to be structurally weak and they typically impact at higher velocity that can be simulated in the laboratory. We are fortunate now to have had two successful capture experiments using aerogel exposed in space. These experiments provide fundamental data for the assessment of the value of silica aerogel for capture of hypervelocity meteoroids from spacecraft. The first experiment used 0.02 g cm⁻³ aerogel flown on the lid of a Shuttle Get Away Special canister [1]. During its 9 day exposure, the 0.165 m² of aerogel in this Sample Return Experiment (SRE) captured two long "carrot-shaped" tracks and one highly fractured bowl shaped "crater". The second collection was with 0.04 m² of 0.05 g cm⁻³ aerogel exposed on ESA's Eureka freeflying spacecraft that was exposed for 11 months before recovery by the Shuttle. The Eureka aerogel exposure consisted of four 10cm X 10cm module trays that were part of the TiCCE meteoroid collector built by the University of Kent at Canterbury[2]. To date we have found ten "carrot-shaped" tracks and two "craters" on this experiment. The longest tracks in both exposures are over 2 mm long.

The typical impacts on these experiments produced classic carrot shaped tracks that begin with entry holes as big as 100µm and taper to a point with a cone angle of only a few degrees. In every case the projectile can be clearly seen at the end of the track. Under low angle illumination the tracks can easily be located with a stereo microscope and the larger tracks can be seen with the naked eye with appropriate lighting. The first three tracks in the Eureka experiment were found with only 10 minutes of scanning. Unlike simulations, the carrot shaped tracks caused by true meteoroids show no obvious evidence of fracturing. This difference may be due to the higher speed of the natural impacts or differences in the aerogel. Even near the end of the tracks, where the projectiles have slowed down, there is no visual evidence of fracturing. The tracks are simply clean, hollow, carrot-shaped holes in the aerogel with a particle in the end. The particles are rounded objects with high reflectance. Few stratospheric IDPs are light colored and it is likely the apparent brightness of the captured particles as well as their rounded shape is due to a thin coating of compressed aerogel. Most of the larger projectiles have an apparent in-situ diameter of ≈ 10µm, the size of particles expected for the [time]X[area] exposure product of the collectors. At their widest points, the cone shaped cavities are a order of magnitude wider than the projectile diameters and it is probable that the carrot width is determined by jetting at the projectile-aerogel interface, The cone angles and deviation from perfect cone shape vary between

EUREKA!!: Brownlee, D.E. et al.

tracks. It is likely that the track geometry can be used to estimate the velocity of non-fragmenting projectiles. The carrot walls are quite distinct and are presumably composed of either compressed or fused aerogel. The tracks are very straight and would provide a highly accurate record of the meteoroid trajectory if the orientation of the aerogel was known at the time of impact. Most of the carrot tracks are spectacular and simple features and there is no evidence that the projectile fragmented. In a few cases, however, one or more shorter tracks branch from the main carrot and are evidence for fragmentation. In these cases the secondary tracks are faint, short and only slightly deviate from the path of the bulk of the projectile mass.

Two of the TiCCE modules had a $0.1\mu\text{m}$ Al film suspended a millimeter above the aerogel. On these modules several of the projectiles fragmented during passage through the film producing fields of carrot shaped tracks from the resulting miniature "meteor" shower. The smallest tracks seen in these clusters are only $20\mu\text{m}$ long and apparently were made submicron fragments. Most of the tracks in these showers have observable particles at their ends.

One of the SRE impacts and two of the TiCCE impacts are essentially bowl shaped craters surrounded by extensive conchoidal fractures. These are remarkably different from the more common carrot-shaped tracks because they are shallow, large, surrounded large fracture zones and they retain no evidence of a surviving projectile. The biggest of these craters is $800\mu\text{m}$ in diameter, 8 times the diameter of the largest track. Most of these craters are nearly two orders of magnitude larger than the most likely size of the largest projectiles expected to impact either experiment. TiCCE also contains an impact that appears to be an intermediate case between a carrot track and a crater. It could be considered either a short carrot or a deep crater. It has a depth /diameter ratio of about 4 and it is surrounded by extensive fractures. The origin of these large, shallow and barren craters is a mystery. It is conceivable that they are either low velocity impacts or impacts of very high velocity or very fragile particles. Either low specific momentum or an explosion on impact might prevent deep penetration to form a carrot track. If crater formation results from abnormally high speed impact, this would imply that the threshold for crater formation is exceeded by only 20% of $10\mu\text{m}$ meteoroids.

We have extracted one of the carrot track meteoroids and mounted it in epoxy for sectioning. We plan to present data on the TEM analyses of microtome sections of several samples at the meeting. This work will provide data on the composition of natural and space debris impacting spacecraft in low Earth orbit and will provide much needed information on the degree of alteration of bonafide meteoroids captured in low density aerogel. So far the examination of these 14 impacts suggests that low density aerogel is a magic and highly effective media for intact capture of hypervelocity particles in space. Typical meteoroids travel ≈ 100 projectile diameters in the aerogel before stopping and it is obvious that typical projectiles remain intact throughout their penetration. The tracks are easily found, there is no ambiguity in their distinction from artifacts and they clearly provide an excellent record of the particle trajectory. If velocity can indeed be determined from track geometry then this would provide a novel method of determining orbital parameters of collected particles. References: [1] Tsou, P. et al. LPSC XXIV, 1333, 1993, [2] McDonnell, J.A.M., LPSC XXV, 1994.

IDENTIFICATION AND ANALYSIS OF COMETARY IDP'S

D.E. Brownlee, D.J. Joswiak, S.G. Love, Dept. of Astronomy, Univ. of Washington, Seattle, WA 98195, J.P. Bradley, MVA Inc., 5500 Oakbrook Parkway, Atlanta, GA 30093, A.O. Nier, D.J. Schlutter, Dept. of Physics, Univ of Minnesota, Minneapolis, MN, 55455

The thermally stepped He release method of Nier and Schlutter[1] provides a powerful technique for distinguishing cometary IDPs from asteroidal ones in stratospheric collections. The thermal pulse method determines the temperature where most of the He is released from an IDP. This is related to the maximum temperature reached during atmospheric entry which in turn can be used to compute entry speed, a strong discriminator for cometary VS asteroidal origin. Before atmospheric entry, nanogram IDPs contain up to $1 \text{ cc(stp)}\text{g}^{-1}$ of ^4He trapped in sites that is released at various temperatures ranging up to 1100 C. Laboratory heating tests on actual IDPs show that particles that were previously heated strongly retain only He that is released at high temperature while less strongly heated IDPs retain He released both at low and high temperature. The experiments indicate that the temperature where 50% of the total gas has been released provides a good determination of the maximum temperature reached during atmospheric entry over the 500-1000 °C range.

We use the 50% release temperature to calculate the most probable entry speed using the new graph of $(\text{max temperature})/(\text{velocity})/(\text{diameter} \times \text{density product})$ [2] computed from the Love entry code. Entry velocity is a strong discriminator between asteroidal and cometary origin for 10 μm IDPs because most particles reaching the Earth by Poynting Robertson drag from the asteroid belt enter near 12 km/s while typical cometary IDPs have entry speeds above 15 km/s[3]. With recognition of complicating factors such as unknown entry angle, shape factors and possible subliming components, we believe that the velocity measurements are adequate to distinguish typical comet IDPs from asteroidal ones. For 8 μm IDPs entering at 45°, a 16 km/s cometary particle has a peak temperature 265 °C hotter than an asteroid IDP entering at 11.2 km/s and a cometary IDP entering at 20 km/s is 470 C hotter. Although the absolute accuracy of the entry temperature measurement is yet to be established, the relative temperatures of fast and slow IDPs is believed to be accurate to ≈ 100 °C. The identification of high speed cometary IDPs is the most straightforward because only high speed produces strong heating. Anomalously low heating can occur for rare low entry angles but no effect can produce anomalously high temperatures except high velocity. To accurately determine entry speeds it is critical that the density and mass of each must be accurately known. A factor of 3 error in density of a 10 μm IDP produces a temperature error of 300 °C, the common temperature difference of comet and asteroid IDPs.

We are conducting a project to analyze a large set of 5-10 μm IDPs with origins identified with the stepped He release method. Particles are initially analyzed in the SEM and STEM to determine mass, density, elemental composition and morphology and their spectral reflectance is measured by the new technique described by Bradley et al [4]. The particles are subdivided with the microtome and a dozen 0.1 μm slices are preserved for analysis after the bulk of the IDP is consumed in He analysis. We find that $\approx 20\%$ of randomly selected <10 μm IDPs are cometary with much higher comet yields for particles selected on

ID AND ANALYSIS OF COMETARY IDPS: Brownlee, D.E. et al.

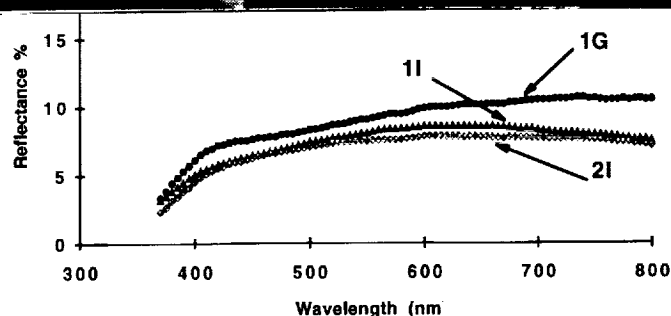
the basis of high porosity and aggregate structure. We expect that study of these particles will provide criteria for identification of comet dust using other properties such as mineralogy, Zn depletion, magnetite formation.

So far the highest velocity IDPs (15-21 km/s) are fine grained porous anhydrous IDPs related to the pyroxene subclass. They all have high abundance of rounded subunits that are composed of glass surrounding <100 nm FeNi metal and sulfide spheruloids. These exotic highly reduced submicron components appear to have been the major particulate in the region where comets formed. The comet IDPs also contain the full range of minerals that have been previously described in the Px subclass. One 20 km/s comet particle contains rare CAI's composed of anorthite and melilite implying that these objects must have existed in the outer solar system. The comet particles have low albedos with spectral reflectances similar to C asteroids although the "best" comet IDPs have been heated above 800 °C during entry and their reflectance properties may have been modified. So far no hydrated comet particles have been identified.

We believe that this work will provide intimate details on the properties of materials that accreted into comets in the outer regions of the solar nebula. We stress however that this work compliments but in no way replaces or detracts from future missions to comets. The collected IDP comet samples are fabulous but they are <10 µm and were heated above 600 °C during atmosphere entry.

References: [1] A.O Nier and D.Schlutter, Meteoritics 28, 675, 1993 [2] S. Love and D.E. Brownlee, Meteoritics in press 1994. [3] H. Zook and A. Jackson, ICARUS 97, 70, 1992 [4] J.P. Bradley, D.E. Brownlee and L. Keller LPSC XXV 1994.

The figure is cometary dust particle U2012 C11 (SEM-left; BSE of section-right). It has a mass of 0.65 ng, a density of 1.8 g/cc, it was heated to 980 °C during atmospheric entry, it contained 0.13 cc/g of He and it entered the atmosphere at 19 km/s. Its spectral reflectance is shown compared to other cometary IDPs.



CONSIDERATIONS FOR PLANETARY GAMMA-RAY SPECTROSCOPY OF THE SURFACE OF MERCURY; J. Brückner, U. Fabian, M. Wieder, Max-Planck-Institut f. Chemie, Mainz, Germany.

To approach basic scientific questions on the origin of Mercury one needs data on its bulk chemical composition, which can be inferred from the elemental composition of the planet's surface. Planetary gamma-ray spectroscopy is a very capable tool to explore the surface of Mercury from an orbiting spacecraft. The gamma rays emitted from the surface carry information on the composition of the surface and the measured gamma-ray data can be used to derive the elemental concentration of many elements present in the surface. A germanium detector would be the best choice for these tasks, provided the problem of cooling can be solved in near future. Otherwise, the usage of suitable scintillation detectors has to be considered. In any case, sufficient information will be obtained to contribute substantially to the exploration of Mercury.

Planetary gamma-ray spectroscopy is considered as a key technique for the exploration of a planet. A gamma-ray spectrometer was on board of the lost Mars Observer spacecraft [1]. NASA is planning on a second mission to Mars and a gamma-ray spectrometer will be on board, again. Currently, the European Space Agency (ESA) is studying a mission to the planet Mercury and among the primary payload a gamma-ray spectrometer is listed.

Little is known about the planet Mercury, since terrestrial observations are very difficult because of the close proximity to the sun and, secondly, so far only one spacecraft, Mariner 10, visited Mercury in three fly-bys. From this visit the high density (5.4 g/cm^3) of Mercury was confirmed, which emphasised the puzzle, that Mercury is too heavy compared to the volume and weight of other terrestrial planets. One plausible assumption is, that Mercury contains a large core (about 70 % metallic phase) and a relatively small mantle (30 % silicate phase). By using the tracking data of an orbiting spacecraft one could measure higher-order terms of the gravitational potential and derive the core size and density distribution. If one could measure the elemental composition of Mercury's surface, a distinction of scenarios of the ancient history of Mercury could be done.

One scenario would be that due to unspecified processes the iron/silicon ratio in the feeding zones of Mercury was changed. However, about a fivefold increase of the Fe/Si ratio is required to account for an iron core of the size needed. One could speculate that in the proximity of the sun the conditions were highly reducing so that other elements like silicon would become metallic and hence contributing to the core phase. As a consequence the Mercury mantle and crust should contain only very little FeO. The elemental composition of the surface should mirror this kind of scenario. An other hypothesis assumes that the accretion of Mercury was similar to other terrestrial planets. Later, Mercury suffered from giant impacts leading to the loss of a substantial portion of the mantle. Also, this would be reflected in the composition of its surface [2].

The average potassium/uranium ratio of the Mercury surface would show if this ratio would decrease with decreasing distance from Sun; e. g. Mars has $K/U = 19000$ and Earth 11000 [3]. These features can only be revealed by determining the elemental composition of the Mercury surface.

Since Mercury has no atmosphere and only a very weak magnetic field the energetic galactic cosmic rays are permanently bombarding its surface. The resulting interactions of the particles with matter are the main sources of gamma rays. Since the production process of secondary particles is very complex, the major portion of the gamma rays belongs to an continuum, a rather featureless distribution of gamma-ray energies spread over a range from about several 10 MeV down to tens of keV. The production of secondary neutrons provides typical reactions inside the surface that result from $(n,n\gamma)$ scattering reactions and (n,γ) capture reactions of fast and thermal neutrons, respectively. These two neutron-induced reactions are a major source for the production of discrete-energy gamma rays that carry information about the nucleus which emitted them. These gamma rays are diagnostic for the composition of the surface material and can be used as an analytical tool. Their specific very sharp energies are used for the identification of the nuclei, i. e. the elements present in the surface, while their intensities reflect the concentration of the elements, i. e. qualitative and quantitative analysis of the planetary surface is possible. The former can be done successfully by using high-resolution gamma-ray detectors, such as high-purity germanium detectors [4].

The Mercury Orbiter of ESA has as primary objectives four instruments: magnetometer, imaging camera, gamma-ray spectrometer, and plasma ion sensor. The spacecraft that has to withstand the strenuous thermal environment (up to 25 W/m^2) of the Mercury orbit, will be a spin-stabilized design. The orbit that has to fulfill requests from all instruments will be polar elliptical with a perihelion of 200 to 300 km and an aphelion of 15000 to 20000 km. This orbit ensures good surface coverage at low altitude for remote sensing and at high altitude for magnetospheric/plasma measurements. The nominal mission will last three Mercury years (263 terrestrial days).

The gamma-ray measurements have to take into account the omni-directional response of the spectrometer and a varying field of view. Since the gamma-ray production in the surface is depth dependent, a self-collimation of the gamma rays restricts the effective field of view as a function of the altitude of the spacecraft. A footprint (or pixel) can be defined as an area on the planet, where 80 % of the radiation originates. Depending on the altitude of the spacecraft the finite size of the planet shrinks the size of the footprint. In its polar orbit, the spacecraft flies over the same footprint at the equator only four times during the nominal mission, except for the polar regions. After each

PLANETARY GAMMA-RAY SPECTROSCOPY OF MERCURY ... Brückner et al.

orbital period (about 13 hours), the planet will be rotated by 3° at the equator, which provides sufficient overlap of adjacent footprints. The gamma-ray spectrometer will make short measurements (20 to 60 sec) over each footprint. During each orbit the spacecraft will fly below 1200 km altitude for about 1/2 hour, i. e. the solid angle under which the planet appears is more than $\pi/2$. Approaching and leaving the planet will provide some additional time of measurements, but, with a smaller solid angle. During the encounter phase (perihelion passage), the data will be stored on board. Afterwards, in the remaining 10 hours (aphelion passage), the data will be downlinked to Earth at a low bit rate. On Earth, the individual spectra together with the position of the spacecraft will be stored in a data base to permit summing of the spectra according to selected criteria. In the beginning of the mission, one can sum spectra of large regions, only, to get good statistics; later on, smaller and smaller regions will be spatially resolved. One straight-forward approach would be to add all spectra measured at a given latitude band and subdivide the bands in smaller areas.

Taking into consideration the given elliptical polar orbit and the given orientation of the spacecraft spin axis, an estimation of the expected planetary gamma-ray flux at the spacecraft and the resulting counting time per surface pixel was accomplished. First, the calculated gamma-ray fluxes from the Moon were taken as a preliminary flux estimation, since Mercury is a very dry body [5]. Second, we used data from our 'Simulation Experiments for Planetary Gamma-Ray Spectroscopy [6]' and scaled the measured gamma-ray continuum, accordingly. Combining the lunar gamma-ray fluxes with the experimentally determined continuum we derived the necessary counting time to achieve an analysis for a given error. The estimation of the counting time for one footprint (for a given altitude) can be seen in Table 1.

One has to keep in mind that the gamma rays are produced in the upper meter of the surface, while due to attenuation only gamma rays that originate from depths down to 40 cm have a chance to escape the surface without scattering. In this respect, gamma-ray spectroscopy provides the only known tool to sample several centimetres of surface in contrast to x-rays, which provide information of the upper micrometer, only.

To achieve excellent measurements of the Mercury gamma-rays, a high-purity germanium (HPGe) detector is considered to be the best option. The advantage of a HPGe detector system is based on its excellent energy-resolution, which facilitates the evaluation of the measured spectra, tremendously. The disadvantages of a HPGe system are: the Ge crystal has to be cooled down to temperatures below 115 K; the Ge crystal is subject to radiation damage induced by cosmic-ray particles or by strong solar flares. If the Ge crystal can be kept below 90 K, one year of good performance can be achieved, provided no strong solar flares occurred, otherwise, the energy resolution can degrade so much that removal of the damage is necessary. This can be done by heating the crystal up to temperatures of 100°C for several hours to obtain the original energy resolution, again [7]. Cooling in the Mercury orbit can only be done by using an active cooling device, such as a Stirling cooler. Right now, it seems that Stirling coolers are not suitable for such a mission (they are either too heavy or need too much power, besides vibrational problems); but, given five years of further development, a spaceproof light-weight Stirling cooler seems to be achievable. Therefore, the option for a HPGe gamma-ray spectrometer can be kept open. In case a suitable Stirling cooler will not be available, a scintillation detector, such as NaI or CsI, could be used since they need no cooling. Of course, their energy resolution is much worse compared to HPGe detectors and puts severe restrictions on the evaluation of the accumulated spectra.

Elem.	Energy [keV]	Composition [w-%]	10 % Error TIME [h]	20 % Error TIME [h]	30 % Error TIME [h]
Si	1779	20.00	0.61	0.15	0.07
K	1461	0.12	0.78	0.19	0.09
U	609.3	5.0E-05	1.30	0.33	0.14
Th	2614	1.9E-04	1.49	0.37	0.17
O	6129	43.50	4.02	1.01	0.45
Mg	1369	4.00	4.47	1.12	0.50
Fe	7632	0.90	53	13	6
Ti	6760	1.40	86	22	10
Na	440	0.35	208	52	23
Ca	6420	10.00	216	54	24

Table 1: Counting times for one pixel at a spacecraft altitude of 400 km.

References: [1] Boynton W. V., et al. (1992), *J. Geophys. Res.*, 97, No. E5, 7681. [2] Cameron A. G. W. (1988), in Mercury, ed. Vilas et al., Univ. Press, Tucson, pp. 692. [3] Wänke H. and G. Dreibus (1988), *Phil. Trans. R. Soc. Lond. A* 325, 545. [4] Brückner J. et al. (1987), Proc. 17th Lunar Planet. Sci. Conf., Part 2, *J. Geophys. Res.* 92, B4, E603. [5] Reedy (1978), Proc. Lunar Planet. Sci. Conf. 9th, *Geochim. Cosmochim. Acta, Suppl.* 10, 2961. [6] Brückner J., et al. (1992), *Lunar Planet. Science XXIII, Houston*, 169. [7] Brückner J. et al. (1991), *IEEE Trans. Nucl. Sci.*, 38, No. 2, 209.

LAVA FLOW RHEOLOGY: A COMPARISON OF DATA AND THEORY; B.C. Bruno¹, S.M. Baloga², G.J. Taylor¹ and M.J. Tatsumura¹ (¹Planetary Geosciences, Dept. of Geology and Geophysics, University of Hawaii, Honolulu, HI 96822; ²Jet Propulsion Laboratory, California Institute of Technology, MS 183-601, Pasadena, CA 91109).

This work involves testing a fluid dynamic model of lava flow emplacement by comparing its predictions against measurements obtained from field and photographic studies of terrestrial flows. This model determines changes in flow thickness and width with distance from the source of the flow for different rheological characteristics based on known or assumed initial parameters. Consequently, these results may be used to infer downstream changes in rheology of unconfined flows from the width and/or thickness of the deposits. Thus, this work can be useful in the study of planetary lavas from photographs and other images.

Theory: The Model & The Solution.

In [1], we find an exact analytic solution for unconfined flows with an arbitrary power-law rheology advancing on an inclined plane. Based on earlier work [2,3], we consider flow movement to be the result of both gravitational transport and hydrostatic pressure, and we examine how these forces combine to drive flow movement in the downstream (x) and cross-stream (y) directions by adopting a volume conservation approach. Simplifying assumptions reduce the equation to the dimensionless form:

$$\frac{\partial}{\partial x}(\alpha h^m) = \frac{\partial}{\partial y} \left(\alpha h^m \frac{\partial h}{\partial y} \right)$$

where h is flow thickness, and $\alpha = \alpha(x)$ and m are prescribed by the rheology of the fluid. Smith [4] solved this equation analytically for a Newtonian fluid ($m=3$) with a constant rheology ($\alpha=1/3\nu$, where ν =viscosity) using a similarity transformation. By invoking additional transformations of the dependent and independent variables, we use this same approach to obtain an analytic solution for flows of arbitrary rheology (i.e., arbitrary m and α). The parameter α is unknown and must be modeled; endmember approximations include constant α , linearly decreasing α , and exponentially decreasing α . These choices for α are somewhat arbitrary, but based on our knowledge that, at least for Newtonian flows, α is inversely related to ν .

Data.

We conducted field studies of 5 basaltic flows on Kilauea volcano. We measured longitudinal profiles of flow thickness and width. Flows are individual pahoehoe breakouts, with lengths ranging from 0.6 - 5 m from the point of breakout. Over this length, ν (and thus α) is assumed constant. We also measured longitudinal width profiles of 4 basaltic flows (alkali basalt to basaltic andesite) from aerial photographs and other images. As flow lengths ranged from 2 - 8 km, we can not assume constant ν .

Results: Data vs. Theory.

1) *Basaltic lava flows have $m \sim 1 - 2$.* Fig. 1 shows a comparison of longitudinal width profiles of sample field data and model predictions, assuming constant rheology. These field data are well approximated by the constant viscosity model, for m between 1 and 2.

2) *Model predicts downstream viscosity increases of 2 - 3 orders of magnitude.* Using m values of 1 and 2, we ran the model for endmember approximations of α . The best fits of the model to sample photographic data are shown for constant α (Fig. 2), linear α (Fig. 3) and exponential α (Fig. 4). In Fig. 2, the data are inconsistent with the model's predictions, indicating non-constant α . Instead, the data are better approximated by linearly or exponentially decreasing α . The downstream ν increases corresponding to the model predictions shown in Fig. 3 and 4 are two and three orders of magnitude, respectively, over a distance of 4 km. The reasonableness of these values [e.g., 5] attests to the validity of this model.

LAVA FLOW RHEOLOGY: Bruno, B.C. et al.

Fig. 1. Plots of half-width $w(x)$, based on field data (+) of (a) ropy pahoehoe and (b) pahoehoe toe. Also shown are the model's predictions for constant α for $m=1/2, 1, 2, 3$ (bottom to top). The data in (a) and (b) both lie between $m=1$ and $m=2$.

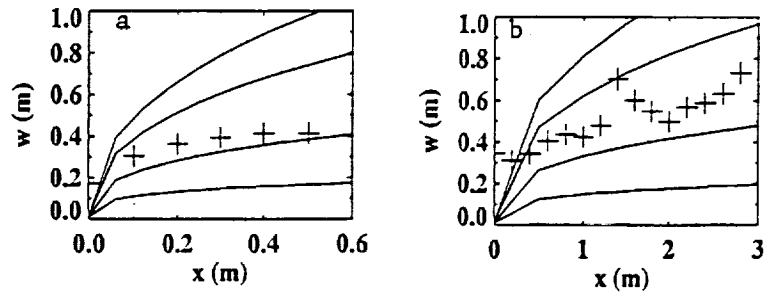


Fig. 2. Plots of half-width $w(x)$, based on photo data (+) of (a) basaltic andesite and (b) alkali basalt. Also shown are the model's predictions for constant α for $m=1$ (bottom curve) and $m=2$ (top curve). This constant α model does not appear to fit the data well.

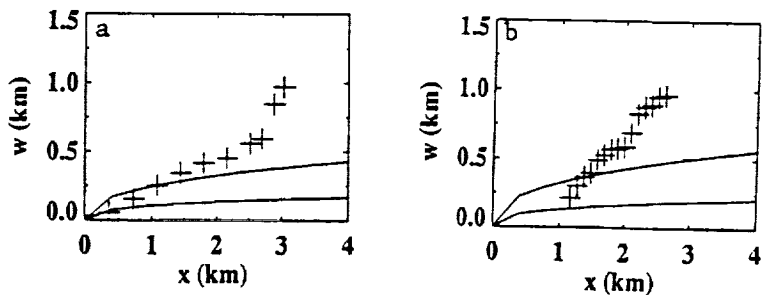


Fig. 3. Plots of half-width $w(x)$, based on photo data (+) of (a) basaltic andesite and (b) alkali basalt. Also shown are the model's predictions for linear α for $m=1$ (bottom curve) and $m=2$ (top curve). The corresponding downstream v increase is approximately 2 orders of magnitude.

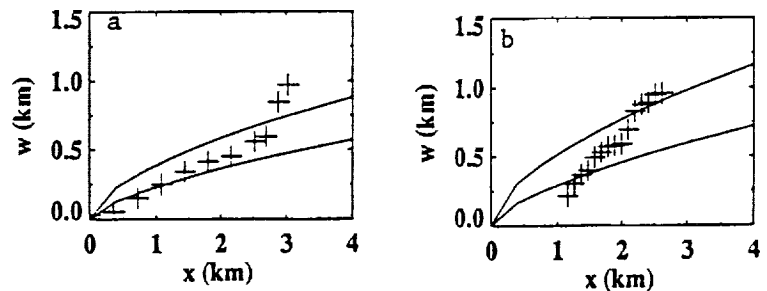
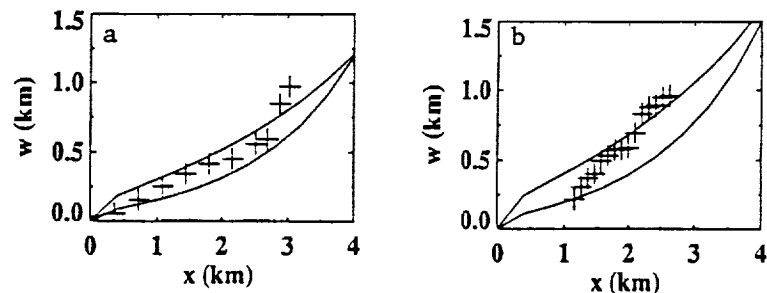


Fig. 4. Plots of half-width $w(x)$, based on photo data (+) of (a) basaltic andesite and (b) alkali basalt. Also shown are the model's predictions for exponential α for $m=1$ (bottom curve) and $m=2$ (top curve). The corresponding downstream v increase is approximately 3 orders of magnitude.



References. (1) Bruno, B.C. et al. (1993), *IAVCEI Abstracts 1993*, pp.13. (2) Baloga, S. and D. Pieri (1986), *JGR* 91, 9543-52. (3) Baloga, S. (1987), *JGR* 92, 9271-79. (4) Smith, P. (1973), *JFM* 58, 275-88. (5) Fink, J. and J. Zimbelman (1990), In *Lava flows and domes. Emplacement mechanisms and hazard implications* (J. Fink, ed.), pp. 157-173.

P. 2

VENUS CLIMATE STABILITY AND VOLCANIC RESURFACING RATES

M. A. Bullock, D. H. Grinspoon, University of Colorado, Laboratory for Atmospheric and Space Physics and the Department of Astrophysical, Planetary and Atmospheric Sciences, Boulder, CO 80309, and J.B. Pollack, NASA Ames Research Center, M/S 245-3, Moffett Field, CA 94035

The climate of Venus is to a large degree controlled by the radiative properties of its massive atmosphere. In addition, outgassing due to volcanic activity, exospheric escape processes, and surface/atmosphere interactions may all be important in moderating the abundances of atmospheric CO₂ and other volatiles. Before the return of detailed radar images of Venus' surface by the Magellan spacecraft, estimates of the magnitude of volcanic source terms were relatively unconstrained. Recent work on the interpretation of the impact cratering record as revealed by Magellan, however, have placed some plausible limits on the magnitude of the volcanic flux [1][2][3]. In addition, the high temperatures and pressures at the surface of Venus have led to the suggestion that heterogeneous reactions between surface minerals and the atmosphere may play an important role in buffering CO₂ and other volatiles [4]. For example, Fegley and Treiman [5] have shown that the surface temperature and pressure on Venus coincide approximately with the P-T equilibrium of the calcite-wollastonite mineral reaction. If this is the case, perturbations to the atmospheric inventory of radiatively active species, caused by volcanic eruptions, may have a significant impact on the climate of Venus and upon the stability of the greenhouse effect. For example, it appears that a small increase in atmospheric CO₂ would increase the magnitude of the greenhouse effect, and at the same time shift the calcite-wollastonite mineral equilibrium to one of both a higher temperature and pressure. In this way, the buffering effect of the surface mineral equilibrium can produce an important feedback on the greenhouse effect.

We have developed an evolutionary climate model for Venus using a systems approach that emphasizes feedbacks between elements in the climate system. Modules for atmospheric radiative transfer, surface/atmosphere interactions, tropospheric chemistry, and exospheric escape processes have so far been developed. Climate feedback loops result from interconnections between modules, in the form of the environmental parameters pressure, temperature, and atmospheric mixing ratios. The radiative transfer module has been implemented by using Rosseland mean opacities in a one dimensional grey radiative-convective model. The model has been solved for the static (time independent) case to determine climate equilibrium points. The dynamics of the model have also been explored by employing reaction/diffusion kinetics for possible surface atmosphere heterogeneous reactions over geologic timescales. It was found that under current conditions, the model predicts that the climate of Venus is at or near an unstable equilibrium point. Without sources, the surface/atmosphere system spontaneously evolves to a cooler, lower pressure state. Assuming that surface carbon and sulfur reservoirs are active, a single volcanic event involving an eruption approximately the size that created the Deccan traps on Earth is sufficient to precipitate a climate catastrophe towards a state of higher surface pressure and temperature. Finally, the effects of constant rate volcanism and corresponding exsolution of volatiles on the stability of the climate model were also explored. Average terrestrial lava abundances of about 200 ppm were assumed for SO₂, and a lower limit of 50 ppm was considered for H₂O. The exospheric escape of H₂O was modeled as a diffusion limited process in which the escape rate is uniquely determined by the abundance and a time constant. Current estimates of hydrogen escape rates place the time constant against escape at about 160 m.y. [6]. By including the constant source and exospheric escape terms in the dynamics of the model, we determined that an injection rate of 3×10^{13} g each of H₂O and SO₂ per year would be sufficient to keep the

current climate in a steady state close to the present point of unstable equilibrium. Using the assumption of volatile abundances described above, this amounts to an upper bound on the yearly volcanic flux of about 18 km^3 , approximately the rate associated with the formation of large igneous provinces on the earth.

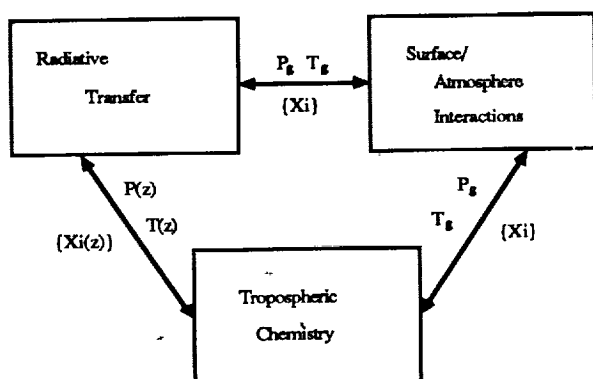


Figure 1. Climate Model Summary.

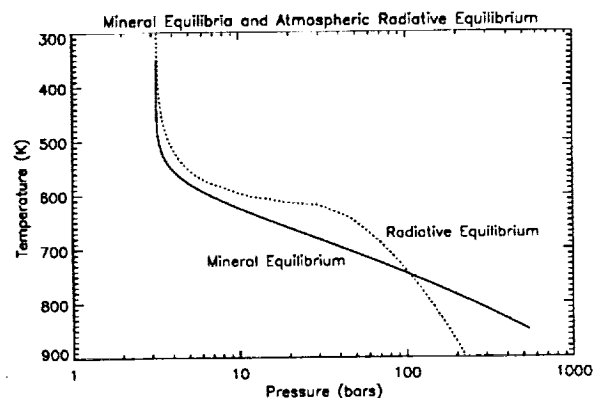


Figure 2. Mineral equilibria and radiative equilibrium curves for surface pressures and temperatures.

References: [1] Bullock, M.A. et al. (1993) *GRL* 20, 2147. [2] Schaber, G.G. et al. (1992) *JGR* 97, 13,257. [3] Phillips, R.J. et al., (1992) *JGR* 97, 15,923. [4] Urey, H.C. *The Planets* (1952). [5] Fegley, B. and A.H. Treiman, (1991) *Proceedings of the Chapman Conference of Comparative Study of Venus and Mars*. [6] Grinspoon, D.H., and J.S. Lewis (1988) *Icarus* 74, 21.

Modified lava domes on Venus; Bulmer MH, Guest JE (Univ. London Obs. NW7 2QS, UK)

During the early stages of the Magellan mission an edifice with scalloped margins was seen situated to the north of Alpha Regio (18.1°S , 5.5°E), whose origin was enigmatic and was thought to have no terrestrial analogue. As more data were examined other edifices with scalloped margins were identified. The radar characteristics and morphologies of many of these edifices were noted to be similar to volcanic domes and fell within a spectrum ranging from unmodified to remnant forms. Many modified domes had deposits associated with them that possessed a range of radar and morphologic characteristics indicative of landslide deposits. Large amphitheatres on the flanks of some domes indicated that large scale collapses had occurred. Other domes showed coalesced scallops giving a stellate plan form. Based on the characteristic margins, the edifices were termed scalloped margin domes¹.

An extensive database has been compiled from a global survey of volcanic domes on Venus. It incorporates information on morphologic and morphometric aspects of domes and large landslide phenomena associated with them. The survey identifies that volcanic domes are more common than suggested in a previous study². Over 320 domes have been located of which over 80% had modified morphologies. A strictly descriptive classification scheme using the form of the upper surface, the planimetric form and the presence of associated deposits was devised, that allowed comparison between dome morphologies. Broadly the modified domes could be described by five groups with different characteristics that appeared to have evolved from three unmodified dome sub-categories (figure 1).

Dome diameters range from < 10 km to 120 km, the majority being between 10 km and 35 km. Domes with diameters greater than 70 km tend to be comprised of several superposed or coalesced domes whose margins are often indistinguishable. Modified domes have heights ranging from 0.4 km to 5.8 km. The mean height is 1.3 km which is 970 m higher than the mean for terrestrial subaerial domes. The distribution of domes as a function of altitude shows that they range from 6050.4 km to 6054.7 km mpr. The majority are located between 6051.0 km and 6052.0 km mpr very close to the mean planetary radius.

Volcanic domes are present over the majority of the surface of the planet though few domes are located in the highlands of Ishtar Terra, Aphrodite Terra and Lada Terra where a general absence of small volcanoes was noted. The lowest areas of the plains are also devoid of domes. An examination of the association of volcanic domes with other geological features revealed 50 % occur in plains. A total of 31 % of modified domes were recorded as associated with volcano-tectonic structures and 56 domes are situated in or on such structures. This association supports the suggestion that volcano-tectonic structures are the surface expressions of magma plumes or reservoirs^{3,4}. Such large volumes of magma could have provided a source for differentiated or volatile enhanced material. The association of 17 % of domes with large volcanoes may be explained by the presence of high level magma reservoirs, the existence of which is supported by the observation of calderas on the summit of many large volcanoes. More evolved magmas could have been formed in such reservoirs. Of the domes associated with large volcanic centres 47% are situated on the summit region such as the domes on the 4.8 km high shield volcano Sapas Mons (9°N , 188°E). Those on the summit of large volcanoes possibly represent the youngest volcanic event. A total of 11 % of domes are situated in fracture zones and have been heavily modified. Only 3 % are associated with tessera, but they are often situated on plains at the margins of upland areas. The number of domes found on tessera and fracture belts coupled with their degree of modification indicates that in zones that had been tectonically deformed many small volcanoes may have been destroyed.

The majority of domes are found in isolation or in pairs. Often circumferential fractures surround one or sometimes two domes situated close together and may have been related to upwarping associated with dome emplacement or with downwarping at the end of an eruption. A total of 10 % of domes occur in clusters often formed of overlapping or coalesced domes. These dome complexes have large diameters ranging between 70 km to 120 km. Other clusters are made up of overlapping pairs of domes such as those to the east of Alpha Regio (30°S , 12°E).

Landslide deposits associated with volcanic domes may have originated from destructive geomorphic processes. On Earth such processes occur on volcanic dome during emplacement (explosive decomposition, directed blasts, pyroclastic flows and surges, lava flows, and rockfalls and rock avalanches) and after dormancy (rockfalls and rock avalanches), exhibiting a broad range of complexity, diversity and magnitude.

Modified lava domes on Venus; Bulmer MH

A descriptive classification using headscarp-debris-apron relationship, surface texture and plan view, was used to compare different landslides around modified domes. Four morphologic groups are identified. Three have morphological and morphometric similarities to terrestrial flow deposits. The term flow is used to describe any fluidized transport or movement of fragmented solid rock, with or without interstitial fluid (e.g. atmospheric gases, magmatic gases, melted rock or fines). Two of the flow deposits are most comparable to terrestrial volcanic debris avalanches and the third, to pyroclastic flows. The fourth group of deposits are similar to deep-seated arcuate, planar, and translational slides on Earth.

The landslide deposits and backscarps indicate that volcanic domes on Venus have been modified primarily by slope failures. The stellate or arcuate margins of domes can be attributed to large scale landslides⁵. The absence of landslide deposits around some domes with scalloped margins can in particular geological settings be explained by younger material having been superposed on the deposits. Elsewhere the deposits may have formed only a thin unconsolidated mantle that was penetrated by the radar or has been reworked by secondary processes. It is also possible that some deposits possess similar radar backscatter coefficients to the surrounding plains.

References: (1) Guest et al (1992) *J. Geophys. Res.*, 15,949-15,966. (2) Pavri et al (1992) *J. Geophys. Res.*, 13,445-13,476. (3) Stofan et al (1992) *J. Geophys. Res.*, 13,347-13,378. (4) Squyres (1992) *J. Geophys. Res.*, 13,611-13,634. (5) Bulmer et al (1994) in press.

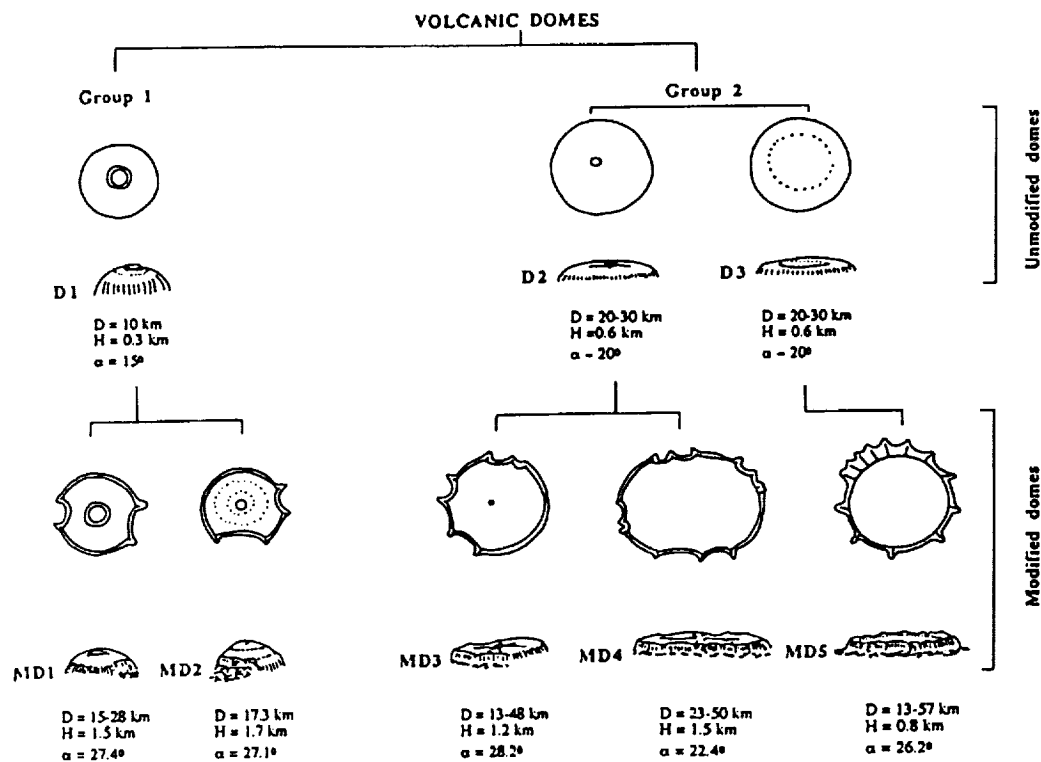


Figure 1 Schematic representation of the modification of volcanic domes. The first group of unmodified domes has one subcategory (D1) from which two subcategories of modified dome develop (MD1, MD2). The second group of unmodified domes has two subcategories (D2, D3). Two subcategories of modified domes (MD3, MD4) develop from D2, and one (MD5) from D3.

THEMATIC MAP TYPES POSSIBLE FOR MARS: MARS-94 MISSION
CARTOGRAPHIC PERSPECTIVES

G.A.Burba Vernadsky Institute, Moscow 117975, Russia

The forthcoming Russia's-spacecraft-based international MARS-94 mission to Mars is planned to image the planet with two TV-cameras designed at DLR, Germany [1,2]. These images could be used to produce the diverse thematic maps of Mars at 1:100,000 to 1:1,000,000 scales [3]. The possible types of such maps are discussed to provide a basis for a future work.

The potential thematic maps of Mars could be divided into two main groups: (i) solid body maps, and (ii) atmosphere maps. SOLID BODY MAPS group consists of two principal subgroups:

- surface characteristic maps, and
- subsurface characteristic maps.

ATMOSPHERE MAPS group consists of one principal subgroup:

- atmosphere characteristic maps.

There are two more subgroups of maps which are intermediate in thematics between the subgroups listed above:

- atmosphere/surface interaction maps, and
- surface/subsurface feature maps.

This classification of five principal subgroups of Martian thematic map types is presented at fig. 1. The short description of the five subgroups is given below.

ATMOSPHERE CHARACTERISTIC MAPS include maps of wind, pressure, temperature, dust, etc. The maps could be of analytic type (portraying direction, speed, value, duration, dynamics, abundance, composition, particle size, etc.), or of synthetic type (zones, types, seasonal parameters, daily changes, etc.).

SURFACE CHARACTERISTIC MAPS include three main families:

- (1) optical characteristics of the surface;
- (2) surface relief and/or topography;
- (3) surface material parameters (other than optical).

SUBSURFACE CHARACTERISTIC MAPS are to portray first of all ground ice. Two families could be outlined:

- (1) depth of ice-bearing layers;
- (2) ice content at the different depths.

ATMOSPHERE/SURFACE INTERACTION MAPS present both gaseous and solid parts of Mars through the three main families of maps:

- (1) aeolian features;
- (2) surface rocks weathering;
- (3) polar caps.

SURFACE/SUBSURFACE FEATURE MAPS include two main families:

- (1) geologic/geomorphic features;
- (2) permafrost features.

REFERENCES: 1. G.Neukum et al. High Resolution Stereo Camera (HRSC), Mars 94 Mission. Consolidated Phase A Conception. Part A: Science Description. DLR, 1990.
2. G.Neukum et al. The HRSC [/WAOSS] Data System Concept. Data Processing & Data Management (Draft Version). DLR, 1991.
3. G.A.Burba et al. Forthcoming mapping of Mars with MARS-94 mission: Study of cartographic products needed to utilize HRSC and WAOSS scientific data and the ways of their cartographic analysis. GEOKHI (Vernadsky Institute), 1992.

THEMATIC MAP TYPES FOR MARS: Burba, G.A.

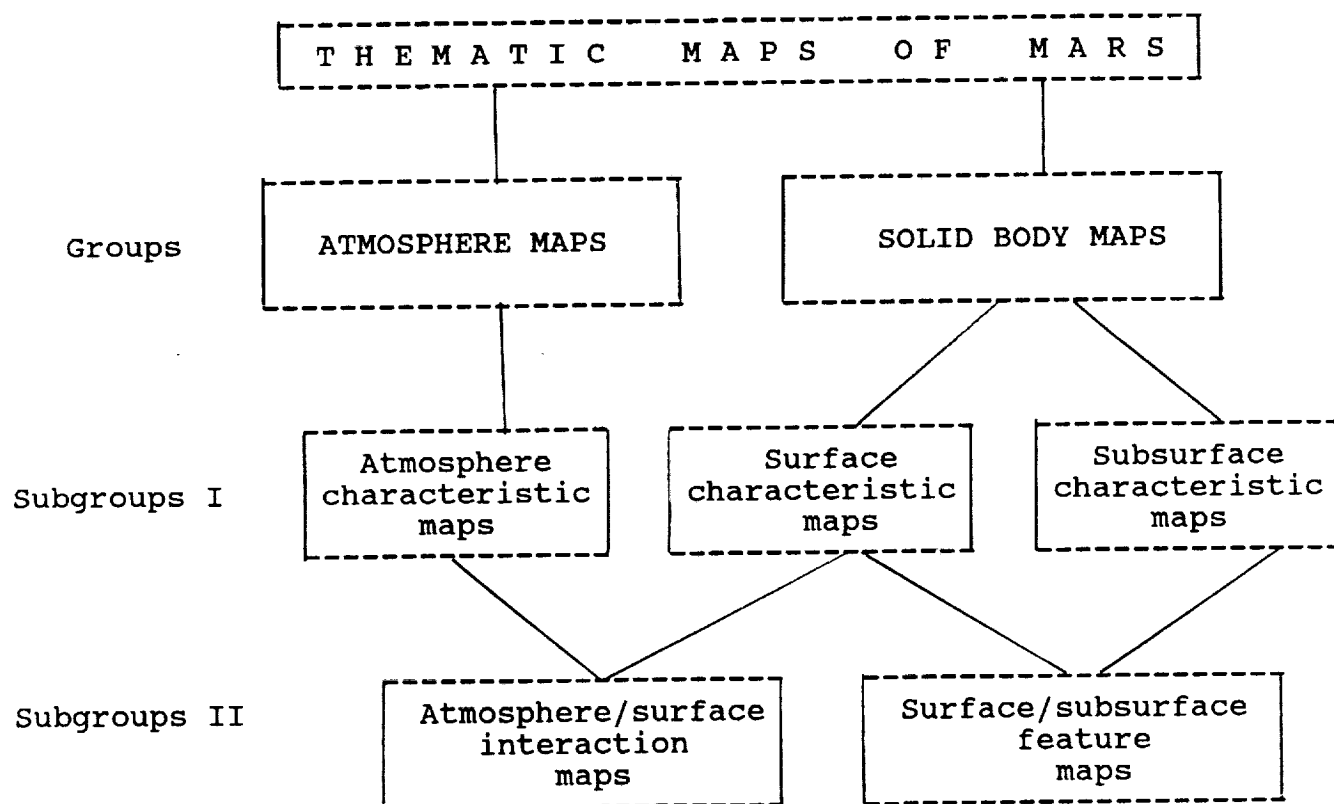


Fig. 1. Classification of possible map types for Mars

Diverse types of thematic maps could be produced for Mars or its areas with the forthcoming image and other data obtained with MARS-94 mission

ZHAMANSHIN ASTROBLEME: REVIEW AND FIRST RESULTS OF 1992
LANDSCAPE AND GEOMORPHIC SURVEY

G.G.Burba, Jr. (1,2), and V.A.Meshcherskaya (1),

(1) Geographical Dept., Lomonosov Univ., Moscow, 119899, Russia

(2) Dept. Agrometeorol., Univ. Nebraska, Lincoln, NE 68583, USA

Zhamanshin impact crater located in Kazakhstan between the Aral Sea and Irghiz River was studied in June 1992 by geographic expedition. An attempt was undertaken to study the natural complexes of the impact structure with the landscape and geomorphic survey. Such approach could help to recognize unknown impact structures through their traces in landscape - the geographic complex which is the most sensible to the changes of the environment.

High degree of knowledge and good expression in topography define Zhamanshin crater as suitable feature for the geographic investigations of the natural complexes of terrestrial impact crater. Zhamanshin is located in semidesert plain of the North Kazakhstan at $48^{\circ}20'N$ and $60^{\circ}58'E$. The topographic levels of the area are within 150-300 m. The crater looks as isometric in plan depression of 100-150 m deep and have rim crest diameter 13 km. It is relict of impact crater aged around 0.75 m.y. [1].

The following tasks were taken in mind during the field trip.

- (1) Definition of modern natural complexes of the area through the geologic/geomorphic and soil/vegetation differences.
- (2) To study gravitational (slope), aeolian, and insolation conditions and hydrologic net patterns.
- (3) Tracing the main directions of material movement with the exogenic processes.
- (4) Estimation of crater's landscapes or their structure (patterns) uniqueness vs. the same at the adjacent regions.
- (5) To look for the correlation between the modern landscape patterns and the original geologic structure of crater.
- (6) To try to estimate the role of catastrophic impact origin for the following evolution of the crater's landscapes.

During the field trips the landscape and geomorphic cross-sections were constructed. They cross the crater N to S and E to W and are 13-16 km long. Trips along crater rim and across the areas outside the crater took place. After that the areas within the crater were studied in accordance with pre-field mapping with multispectral Landsat satellite image. An area about 300 sq. km was surveyed during the field trips. The observations took place at 42 points located at the bottom and rim of the crater and outside the crater. Each point was described in details with geologic/geomorphic data, surface soil, deep section of soil, hydrologic patterns, botanical square. Rock and vegetation samples were collected.

ZHAMANSHIN ASTROBLEME: Burba, G.G., Jr. and Meshcherskaya, V.A.

Preliminary landscape map of Zhamanshin area [2] was produced with pre-field interpretation of May 1986 Landsat image. This map was dramatically modified after the field trip. Six maps of 30 x 30 km area were compiled at 1:170,000 scale: topographic (c.i. 20 m), geologic, surface deposit types, geomorphic, soil, and drainage net. They were used together with field data on vegetation to produce a final landscape map. Many new landscape areas were defined and landscape complexes outlined at the final map. This map shows two principal landscape regions: (i) connected with impact crater, and (ii) non-connected with impact crater. The first region includes three main subregions: (1) crater bottom and inner walls, (2) crater rim/ejecta plateau, and (3) crater rim/ejecta outer slopes. The second region consist of two subregions: (1) NE plains, and (2) SW plains. Ninety smaller landscape divisions took place within the principal areas.

Crater-connected landscape regions look to be intrazonal landscapes. Their patterns did not follow the general regional patterns of the area. The landscapes outside the crater (and its rim/ejecta area) fit the regional picture of geographic zonality. The final landscape map shows that landscape divisions outline the material movement patterns: concentric for crater-related landscapes and elongated-spotty for areas outside the crater and its rim/ejecta area.

Exogenic processes were found to be more active within the crater rim: the long deluvial aprons took place at the foothills of the modern rim. These aprons are larger than the aprons around the isolated remnant hills on the surrounding plains. The summit surfaces of crater rim hills are covered with eluvial material which consist of the welded ejecta breccias. Because of it the destroying of the summit surfaces is weak.

Number of landscape levels were recognized. They are connected with the morphostructure of the crater and have concentric location. The principal landscape divisions of Zhamanshin crater were well recognizable in the field in accordance with the composition and density of the vegetation, soil and surface rock types. The crater bottom is the smooth alluvial-proluvial plain which contains no manifestations of geologic structures. But the concentric patterns of the landscape complexes are sharply recognisable within the bottom both at the Landsat image and in the field.

REFERENCES: 1. P.V. Florensky, A.I. Dabizha (1982) Zhamanshin meteoritic crater. Moscow: Nauka [in Russian].
2. G.G. Burba, V.A. Meshcherskaya (1993) Landscape and geomorphic survey of Zhamanshin area. LPSC XXIV, 221-222.

QUESTIONS CONCERNING THE OXIDATION OF FERROUS IRON IN CARBONACEOUS CHONDRITES

Thomas H. Burbine and Roger G. Burns, Department of Earth, Atmospheric and Planetary Sciences, Massachusetts Institute of Technology, Cambridge, MA 02139

Introduction. It is generally acknowledged that certain carbonaceous chondrites, notably CI and CM chondrites, underwent pre-terrestrial aqueous alteration at or near the surfaces of their parent bodies. The occurrence of ferric-bearing minerals, including cronstedtite in CM chondrites and ferrihydrite-magnetite- Fe^{3+} smectite assemblages in CI chondrites, indicate that oxidation of Fe^{2+} in silicate and sulfide minerals took place when aqueous alteration occurred. Oxidation of dissolved ferrous iron leached from minerals on asteroid surfaces may have been induced either by photochemical oxidation by UV radiation emitted by the young Sun or in primordial atmospheres. However, fundamental problems exist for both models. Questions concerning reaction mechanisms and ages of such pre-terrestrial aqueous alteration processes are discussed here.

Background. The aqueous alteration products observed in CI and CM chondrites [1] indicate that oxidation accompanied the formation of secondary mineral assemblages in these meteorites. Thus, the presence of the Fe^{3+} -bearing serpentine cronstedtite [ideally $\text{Fe}^{2+}_2\text{Fe}^{3+}(\text{SiFe}^{3+})\text{O}_5(\text{OH})_4$] in CM chondrites, as well as magnetite [ideally $\text{Fe}^{2+}\text{Fe}^{3+}_2\text{O}_4$], ferrihydrite [approx. $5\text{Fe}_2\text{O}_3 \cdot 9\text{H}_2\text{O}$] and Fe^{3+} smectites in CI meteorites, all indicate that pre-terrestrial aqueous alteration processes occurred at or near the surfaces of parent bodies of the CI and CM chondrites and were accompanied by oxidation of precursor Fe, FeS, ferromagnesian silicates (olivine and pyroxene) and C minerals. In contrast, products of aqueous oxidation are minor or negligible in most CV, CO, CK and CR chondrites, in which magnetite and, perhaps, minor phyllosilicates are the only pre-terrestrial Fe^{3+} -bearing minerals present.

From electron microscopic observations [2], the following alteration was proposed for the aqueous alteration of olivine, pyroxene, sulfides and Fe-Ni in matrix of CM meteorites. First, sulfur-bearing fluids penetrated chondrite aggregates and reacted with metal grains to form the coherently stratified mackinawite-brucite sheets that constitute tochilinite. Then, fine-grained olivine reacted with fluids to produce Mg-rich serpentine (antigorite). The silica released in this process reacted with tochilinite to form cronstedtite, which resulted in the intimate tochilinite-cronstedtite intergrowths. As alteration continued, the tochilinite was consumed to produce a mixture of cronstedtite, magnetite and troilite. The cronstedtite also reacted with the Mg-rich serpentine to produce a Fe^{2+} -bearing serpentine (greenalite) more magnesian than cronstedtite. More intense aqueous alteration may have produced the ferric-bearing minerals in CI chondrites, which contain little, if any, tochilinite and cronstedtite.

Computer simulations [3] that modeled the interaction of an aqueous phase with the anhydrous minerals found in CV and CM chondrites have been used to produce theoretical mineral assemblages in CM and CI chondrites. The best matches to the alteration products in CM chondrites were produced at temperatures between 1 and 25 °C, total dissolved C concentrations between 10^{-8} and 10^{-2} *m*, and a wide range of rock/fluid ratios. The predicted dominant stable phases are tochilinite, greenalite and antigorite. Matches to the CI chondrites can be produced by altering either CM or CV anhydrous minerals at temperatures between 50 and 150 °C, total dissolved C varying from 10^{-3} to 10^{-2} *m* and a wide range of rock/fluid ratios. The predicted dominant stable phases include sulfides, magnetite, saponite and antigorite, but omitted ferrihydrite.

One characteristic of CM chondrites not addressed by these reaction path calculations is that Mossbauer spectroscopy [4] [5] has identified mixed-valence Fe^{2+} - Fe^{3+} cronstedtite as the predominant phyllosilicate in CM chondrites. All of the theoretical calculations were based on Mg or Fe^{2+} -bearing serpentines and not Fe^{3+} -bearing cronstedtite. The cronstedtite is intimately intergrown with tochilinite (a highly reduced mineral) and appears to be an alteration product of it. The question raised is how Fe^{2+} in tochilinite was oxidized to Fe^{3+} in cronstedtite. It is

OXIDATION OF FERROUS IRON: Burbine T. H. and Burns R. G.

noteworthy that stability diagrams [6] for mineral assemblages in banded iron-formations predict mackinawite (a constituent of tochilinite) and stilpnomelane (a serpentine-like mineral with a 1:1 ratio of Fe^{2+} to Fe^{3+}) to be stable in the pH range 6 to 8 and Eh range -0.2 to -0.4 V, which encompass the computed stability field of tochilinite-serpentine assemblages. Note also that Mossbauer spectroscopy [4] [5] of four CI chondrites has identified major amounts of ferrihydrite coexisting with maghemite and magnetite.

Mechanisms of Aqueous Oxidation. More fundamental to the evolution of the early solar system, however, are questions concerning the mechanisms, rates and ages of aqueous oxidation reactions that produced the ferric-bearing assemblages in CI and CM chondrites. Some insight on such questions may be provided by recent research on the kinetics and mechanisms of aqueous oxidation processes on terrestrial planets [7].

The oxidation of Fe^{2+} can proceed by several mechanisms. These include: (1) solid-state processes involving atmospheric surface interactions which occur without the intervention of water; and (2) reactions that occur in an aqueous medium, including: (a) oxidation of aqueous Fe^{2+} in groundwater by dissolved atmospheric oxygen, where the oxygen is derived from photolysis of CO_2 or water vapor in the atmosphere; and (b) photochemical oxidation in UV light of either Fe^{2+} ions in acidic solutions or FeOH^+ complex ions in near-neutral pH or slightly alkaline solutions.

The slow kinetics of gas-solid (atmosphere-surface and UV irradiation) reactions indicate that oxidation on surfaces of terrestrial planets is facilitated in an aqueous environment. Dissolved iron (as Fe^{2+} ions derived from dissolution of basaltic glass, olivine, pyroxenes and sulfide minerals) are initially oxidized to Fe^{3+} ions by aerated groundwater and then hydrolyzed to insoluble hydrated Fe(III) oxide phases, yielding ferrihydrite, which is a major constituent of CI chondrites. Dissolution rates of ferromagnesian silicate and sulfide minerals are fast in acidic solutions but rates of oxidation of aqueous Fe^{2+} either by UV radiation or by dissolved atmospheric oxygen are very slow in acidic solutions. On the other hand, in slightly acidic, near-neutral pH and alkaline solutions (pH 4.5 to 8), which may be more applicable to the formation of matrix minerals in carbonaceous chondrites [3], rates of oxidation of dissolved Fe^{2+} and hydrolysis of Fe^{3+} ions are rapid, but dissolution rates of primary silicate and sulfide minerals are very slow.

Applications to Parent Bodies. The question arising from the foregoing discussion is which (if any) of these oxidation processes are applicable to a parent body containing anhydrous silicates and ice that were heated by some source (e.g., the decay of ^{26}Al or solar electromagnetic induction.) The present-day surface temperature of asteroids (< 190 K) would be too low to allow liquid water to exist on the surface. These parent bodies would have very tenuous atmospheres that would be in a constant state of flux with water vapor from the sublimation of ice or outgassing continually being lost due to very low escape velocities on asteroids. Heating of the asteroid interior to temperatures above the freezing point of water would allow liquid water to exist inside the asteroid and thereby facilitate aqueous alteration reactions.

However, to oxidize aqueous Fe^{2+} in such an environment by one or more of the proposed mechanisms appears to be very difficult. The very tenuous atmospheres on these asteroids would not allow for any atmosphere-surface interactions. The lack of an atmosphere plus the inability of liquid water to exist near an asteroid's surface appears to rule out oxidation by dissolved atmospheric oxygen. The absence of liquid water at the surface would also minimize oxidation by the high flux of UV radiation emitted from the young Sun.

References. [1] Buseck, P. R. and Hua, X. (1993) *Ann. Rev. Earth and Plan. Sci.*, 115-149. [2] Tomeoka, K. and Buseck, P. R. (1985) *Geochim. Cosmochim. Acta* **49**, 2149-2163. [3] Zolensky, M. E., Bourcier, W. L. and Gooding, J. L. (1989) *Icarus* **78**, 411-425. [4] Fisher, D. S. and Burns, R. G. (1993) *Lunar Planet. Sci. XXIV*, 489-490. [5] Burns, R. G. and Fisher, D. S. (1993) *Proc. Intern. Conf. Mossbauer Spectroscopy, Hyperfine Interact.*, in press. [6] Klein, C. and Bricker, O. P. (1977) *Economic Geology* **72**, 1457-1470. [7] Burns, R. G. (1993) *Geochim. Cosmochim. Acta* **57**, 4555-4574.

ARE STEEP SLOPES ON VENUS PRESERVED AS A RESULT OF CHEMICAL CEMENTATION OF PORE-SPACES IN SURFACE ROCKS?

Kevin Burke¹, Bruce Fegley Jr², and Virgil L. Sharpton³; ¹Dept. of Geosciences, University of Houston, Houston TX 77004,, ²Dept. of Earth & Planetary Sciences and McDonnell Center for the Space Studies, Washington University, St. Louis MO 63130, ³LPI, 3600 Bay Area Blvd, Houston, TX 77058 (713-486-2111)

Introduction. The surface of Venus has sustained approximately a billion years of volcanic, tectonic, and aeolian activity, yet it seems to lack evidence of substantial landform degradation, particularly in comparison to the intensely degraded surfaces of the other two terrestrial planets with atmospheres, Earth and Mars. Average kilometer-scale topographic slopes of 30° are not uncommon on Venus (*Ford and Pettengill, 1992*) and yet evidence of mass movement is sparse (*Malin, 1992*). Those impact structures on Venus that have escaped direct involvement in tectonic or volcanic activity show very little evidence of topographic degradation. They retain bright blocky ejecta deposits and steep rim topography (*Sharpton, 1994*). Despite the evidence of approximately a billion years of endogenic and impact surface processing there are relatively few sites on Venus where loose particulate matter is available to be moved by the wind (*Greeley et al., 1992*). These observations indicate that some process may act to stabilize surface materials on Venus. We propose that cementation of fragmental and other porous rocks has taken place by mineral precipitation as a result of chemical reaction between the atmosphere of Venus and rocks exposed at the planet's surface.

Experimental studies. Two different gas-solid reactions lead to the formation of chemical cement. Anhydrite (CaSO₄) formation via the thermochemical reaction $\text{CaCO}_3 + \text{SO} = \text{CaSO}_4 + \text{CO}$ was studied by heating high purity natural calcite crystals of known weight and surface area and synthetic calcium carbonate powder (ACS reagent grade) in SO₂-CO₂ gas mixtures at ~1 atmosphere total pressure. The gas mixtures nominally contained 1% SO₂ by volume and therefore had a SO₂ number density comparable to that at the surface of Venus. The gas mixtures also typically contained <1 ppm O₂ and ≤ 10 ppm water vapor as impurities but experiments that were done with gas mixtures containing up to 100 ppm O₂ showed that the rates were independent of the O₂ number density within this range. The temperatures of the experiments ranged from 600-850° C because the slow reaction rates led to undetectable amounts of reaction at Venus surface temperatures over laboratory time scales. During the experiment, calcite crystal become coated with a porous layer of anhydrite. The derived growth rate of such a layer is 1µm per year under Venus surface conditions (*Fegley and Prinn, 1989*). Porosity determinations done by the line intercept method applied to SEM photomicrographs show a wide range of layer porosities, ranging up to 25%. However, the anhydrite layers typically have porosities of 5-15%. Consequently, the reaction is not expected to be diffusion controlled and is plausibly controlled by the chemical reaction rate at the calcite-anhydrite interface. The experiments done with the high purity synthetic calcium carbonate powders showed dramatic changes in the sample morphology: Individual particles become sintered or cemented together by the anhydrite and the originally sharp rhombic shaped crystals of the unreacted powder becomes increasingly corroded and welded together into irregularly shaped aggregates as the reaction proceeded.

SLOPE STABILIZATION ON VENUS; Burke *et al.*

Figure 1



Calcite formation via the thermochemical reaction $\text{CaO} + \text{CO}_2 = \text{CaCO}_3$ is being studied in CO_2 at ~ 1 atmosphere total pressure. This reaction is proxy for the formation of calcite, magnesite, and dolomite from the reaction of wollastonite, forsterite, and diopside with CO_2 on Venus (Fegley and Treiman, 1992). Preliminary experimental work by B. Brackett, N. Izenberg, and B. Fegley shows that the silicate + CO_2 reactions are slower than calcite formation from CaO , which is easier to study experimentally. In these experiments, highly reactive CaO is prepared by thermal decomposition of $\text{Ca}(\text{OH})_2$. Conversion of the CaO to CaCO_3 again leads to the cementation of individual grains (Figure 1). The cementation is evident on a macroscopic scale because carbonate formation transforms free flowing powder into a single compact piece that maintains the cylindrical shape of the crucible after removal from the furnace. As yet, no

kinetic data are available for carbonate formation under Venus surface conditions.

Conclusions. Chemical cementation is a plausible means of keeping the global inventory of particulate material on Venus depleted in the presence of ongoing surface activity and may stabilize surface debris and preserve steep slopes associated with impact craters and tectonic features. If so, there may be no correlation between age and surface slope measured over short length scales. Chemical alteration and pore filling may also explain the gradual disappearance of dark haloes and parabolas around impact craters over time scales of 10^8 y as 'fresh' ejected debris is first stabilized then gradually altered to compounds that are chemically similar to the surrounding surface and in equilibrium with the reactive atmosphere. Steep slopes as well as aeolian features, such as dunes and wind streaks, may be stabilized structures that record ancient, rather than recent, events. In the absence of significant atmospherically driven weathering, topographic degradation would be dominated by volcanic processes such as burial under lava, or tectonic processes such as folding and faulting.

Acknowledgements: B.F. is supported by grants from the NASA Planetary Atmospheres and VDAP Programs; V.L.S. is supported by a grant from VDAP. Figure 1 was taken by D. Kremser and K.L. Lodders.

References. Fegley, Jr, B. and A.H. Treiman, 1992, *Geophysical Monograph* 66, 7-71. Malin, M.C., 1992, *J. Geophys. Res.*, 97, 16,337-16,352. Ford, P.G. and G.H. Pettengill, 1992, *J. Geophys. Res.*, 97, 13,091-13,102. Fegley, Jr, B. and R.G. Prinn, 1989, *Nature*, 337, 55-58. Sharpton, V.L., 1994, *Geol. Soc. America Sp. Pap* 293, in press. Greeley, R. and 10 others, 1992, *J. Geophys. Res.*, 97, 13,139-13,346.

SCHWERTMANNITE ON MARS: DEPOSITION OF THIS FERRIC OXYHYDROXYSULFATE MINERAL IN ACIDIC SALINE MELTWATERS

Roger G. Burns, Department of Earth, Atmospheric and Planetary Sciences, Massachusetts Institute of Technology, Cambridge, MA 02139

Introduction. Schwertmannite, $\text{Fe}_8\text{O}_8(\text{OH})_6\text{SO}_4$, a poorly crystalline oxyhydroxysulfate of iron, has been identified on Earth as the primary component of ochrous precipitates from sulfate-rich acidic mine waters. More widespread deposits may occur in arid environments, such as southern and western areas on the Australian continent. Since acidic permafrost probably occurs beneath the Martian regolith, the precipitation of schwertmannite is suggested to occur in equatorial regions of Mars when seepages of saline melt waters become exposed to the martian atmosphere.

Background. Groundwater existing beneath the Martian surface is generally believed to be acidic rather than alkaline [1-4]. Due to minimal plate tectonic activity on Mars, acidic groundwater has probably prevailed near the Martian surface, having originated from: (1) volcanic gases in acid rain; (2) dissolution of sulfide minerals [$\text{FeS}_2 + 7/2 \text{O}_2 + \text{H}_2\text{O} \rightarrow \text{Fe}^{2+} + 2 \text{SO}_4^{2-} + 2 \text{H}^+$; eq. {1}]; (3) aqueous oxidation of Fe^{2+} ions derived from leached basaltic glass, ferromagnesian silicates and sulfides [$\text{Fe}^{2+} + 1/4 \text{O}_2 + \text{H}^+ \rightarrow \text{Fe}^{3+} + 1/2 \text{H}_2\text{O}$; eq. {2}]; and (4) hydrolysis of the Fe^{3+} ions generated by these oxidative weathering processes [$\text{Fe}^{3+} + 2\text{H}_2\text{O} \rightarrow \text{FeOOH} + 3 \text{H}^+$; eq. {3}]. The aqueous solutions with $\text{pH} \leq 6$ have remained unbuffered by wall-rock alteration of basalts such as that occurring in fracture zones associated with seafloor spreading on Earth.

On Earth, natural acidic groundwater systems are comparatively rare but occur, nevertheless, when water seeps through mined sulfide and coal deposits. Outflows of such acid mine-drainage water are invariably associated with ochrous ferric-bearing assemblages. On a much larger scale, oxidative weathering processes associated with acidic groundwater is occurring across the southern half of the Australian continent, yielding deposits of Mars-like yellow-brown hydrous ferric oxide and hydroxysulfate minerals. Similar depositional environments may also occur on the martian surface.

Formation of Schwertmannite in Acid Sulfate-Rich Groundwater. Schwertmannite, recently recognised as a new oxyhydroxysulfate mineral of ferric iron [5-7], is brownish-yellow and has an approximate formula $\text{Fe}_8\text{O}_8(\text{OH})_6\text{SO}_4$. Its crystal structure resembles that of akaganeite ($\beta\text{-FeOOH}$), with SO_4^{2-} ions located in the tunnels formed by double chains of edge-sharing $\text{FeO}_3(\text{OH})_3$ octahedra. Schwertmannite occurs as an ochrous crust on rocks inundated by acidic ($\text{pH} 3.2$) drainage water exiting mined sulfide ore and coal deposits [5]. The mineral forms as a result of aerial oxidation of Fe^{2+} in acid, sulfate-rich effluents produced by the decomposition of primary sulfides. A pH range 3.0 to 4.5 and sulfate concentrations in the range 1 to 3 g l^{-1} are optimum for the formation of schwertmannite [7]. At lower pH s, jarosite may form as an ancillary phase if the concentration of SO_4^{2-} is sufficiently high [8]. Goethite is also a commonly associated phase and may be alteration product of schwertmannite, especially at pH s exceeding 4.5 [e.g., $\text{Fe}_8\text{O}_8(\text{OH})_6\text{SO}_4 + 2 \text{H}_2\text{O} \rightarrow 8 \text{FeOOH} + \text{H}_2\text{SO}_4$; eq. {4}].

Schwertmannite was recently identified as the interlayer phase in smectite clays exchanged with acidic ferric sulfate solutions [9]. Such ferric sulfate-exchanged montmorillonites have spectral features in the visible and near-infrared regions that closely match remote-sensed reflectance spectra of bright regions of Mars, particularly in equatorial regions scanned during the Phobos 2 imaging spectrometer measurements of the martian surface [10].

The suggested occurrence of schwertmannite in equatorial regions of Mars may have resulted from precipitation of this ferric oxyhydroxysulfate phase from acidic saline melt-waters. Relatively high concentrations of dissolved Fe^{2+} , derived from dissolution of basaltic glasses, ferromagnesian silicates and iron sulfides, were oxidized by dissolved atmospheric oxygen. The kinetics of such

aqueous oxidation reactions [4] indicate that rates of oxidation of Fe^{2+} dissolved in ice-cold saline solutions range from about 1 ppm $\text{Fe}^{2+} \text{ yr}^{-1}$ (pH 4.5) to about 1000 ppm $\text{Fe}^{2+} \text{ yr}^{-1}$ (pH 6.0).

Deposition in Arid Environments. In the southeastern part of Western Australia, deep-weathering of basement igneous rocks in the Yilgarn Block comprising Archean komatiitic basalts has yielded saline groundwater systems, drainage of which in a semi-arid climate has resulted in extensive playas [11-16]. The discharging water contains high concentrations of dissolved Al, Si and Fe^{2+} , oxidation and hydrolysis of which generates very acidic groundwater (pH ≥ 2.8), as a result of the ferrolisis reactions (eqs {2} and {3}). The acidity prevents the precipitation of aluminosilicate clay minerals. Instead, jarosite [$\text{KFe}_3(\text{SO}_4)_2(\text{OH})_6$] - alunite [$\text{KAl}_3(\text{SO}_4)_2(\text{OH})_6$] assemblages are precipitated in the pH range 2.8 to 6 from solutions with ionic strengths ranging from 1 M to 5 M, occurring in evaporite deposits with gypsum and halite. Ferrihydrite and schwertmannite, instead of jarosite-alunite assemblages, are deposited from groundwater depleted in dissolved K and Al. A similar situation may exist on Mars where ground water associated with parent iron-rich komatiitic basaltic rocks may also have low Al and K contents.

Two stages were important in the development of the acidic hydrogeochemical and arid weathering environment of southern Australia. Initially, there were periods of laterization/ferric oxide deposition under a warm humid climate during the Tertiary. The laterite profiles are characterized by a surface duricrust of Fe and Al oxides over deep clay silicate zones depleted of alkali and alkaline earth elements. Subsequently, periods of aridity and semi-aridity have continued to the present.

An explanation for the acidic saline groundwater systems on such a large scale and only in Australia lies in the recent climatic history of the continent. After the break from Antarctica began 65 million years ago, Australia moved into the sub-tropic region. The climate through the Eocene was humid and warm, much like that proposed on early Mars, and periods of laterization occurred. Laterite profiles became abundant in Western Australia on deeply weathered bedrock depleted in alkalis and alkaline earths but enriched in Fe, Al and Si. Little chemical weathering is now occurring on the Australian continent today due to arid conditions. However, periodic discharges of anoxic acidic groundwater into the arid environment and oxidation of the dissolved ferrous iron continues to generate ferric-bearing mineral assemblages in contact with the oxygenated atmosphere.

Applications to Mars. A similar scenario may apply to the present-day surface of Mars, in which periodic precipitation of hydronium jarosite, schwertmannite and ferrihydrite may be precursors to nanophase hematite identified in bright regions of the martian surface.

References. [1] Clark, B. C. and Van Hart, D. (1981) *Icarus*, 45, 370; [2] Banin, A., Clark, B. C. and Wanke, H. (1992) In *Mars* (eds. H. H. Kieffer *et al.*, Univ. Arizona Press), p. 54; [3] Plumlee, G. S., Ridley, W. I. and DeBaal, J. D. (1992) *MSATT/LPI Tech. Rept.* 92-04, 31; [4] Burns, R. G. (1993) *GCA*, 57, 4555; [5] Bigham, J. M., *et al.*, (1990) *GCA*, 54, 2743; [6] Bigham, J. M., Calson L. and Murad, E. (1993) *Amer. Mineral.* (in press); [7] Murad, E., *et al.* (1993) *ACS Symp. Ser.*, in press; [8] Burns, R. G. (1988) *Proc. 18th LPSC*, 713; [9] Bishop, J. L., Pieters, C. M. and Burns, R. G. (1993) *MSATT/LPI Tech. Rept.* 93-06, 6; *Icarus* (submitted) [10] Murchie, S., Mustard, J. and Saylor, R. (1993) *MSATT/LPI Tech. Rept.* 93-06, 32; [11] Long, D. T. and Lyons, W. B. (1992) *GSA Today*, 2, 185; [12] Long, D. T. *et al.* (1992) *Chem. Geol.*, 96, 183; [13] Mann, A. W. (1983) *GCA*, 47, 181; [14] McArthur, J. M., *et al.* (1991), *GCA*, 55, 1273; [15] Long, D. T. *et al.* (1992) *Chem. Geol.*, 96, 33; [16] Macumber, R. G. (1992) *Chem. Geol.*, 96, 1; [17] Enver Murad is thanked for providing unpublished manuscripts; research supported by NASA grants NAGW-2049 and NAGW-2220.

CRUSTAL RECYCLING DUE TO MANTLE FLOW-DRIVEN CRUSTAL THICKENING: A PRELIMINARY ASSESSMENT; Jeffrey D. Burt, E. M. Parmentier, and James W. Head, Department of Geological Sciences, Brown University, Providence, RI 02912.

Introduction: Crustal recycling on Earth occurs at convergent plate boundaries. Magellan mission data indicate there is no global plate tectonic system on Venus (1). A fundamental question for Venus is how crust recycles in the absence of plate tectonics. A second fundamental question is the origin of venusian highland regions. Can crustal thickening associated with mantle downwelling cause plateau-like, compressional highlands (2)? What are the relative roles of thermal buoyancy in the mantle and buoyancy due to the gabbro-eclogite phase change in crust in governing the evolution of highland regions? Studies of the effects of the gabbro-eclogite phase transformation on the isostatic elevation of the compressional mountain belts of Venus predict that compressional crustal thickening in the presence of a shallow thermal gradient may lead to eclogite formation in a crustal root and to possible delamination (3), while low water concentrations in venusian rocks may slow the gabbro-eclogite transformation and allow isostatically balanced mountain belts to reach great elevations (4).

We explore the possibility that large compressional highland terrains could be sites of crustal recycling. If horizontally convergent mantle flow at a downwelling leads to crustal thickening, then the gabbroic crustal root thus formed could deepen sufficiently to transform to eclogite. If the crustal root were to become sufficiently negatively buoyant, an instability would form leading to crustal loss into the mantle and contributing to mantle flow. This may develop into a self-sustaining system which for some span of time may act to gather and recycle crustal material into the mantle. In contrast to (5), who consider crustal recycling linked to thermally driven mantle flow, we examine the influence of crustal buoyancy forces due to the gabbro-eclogite phase transformation.

Model: We consider a compositionally buoyant basaltic crust (3000 kg/m^3) of thickness T_c overlying a peridotite mantle (3360 kg/m^3). Both are assumed to behave as viscous fluids, with the mantle viscosity ten times greater than that of the crust. Assuming the model region is small relative to the region of mantle flow, we model the effects of large scale mantle downwelling and horizontal convergence by imposing a horizontal velocity boundary condition (V_c) on one side of the model while fixing the other. Flow is also driven by buoyancy forces resulting from the topography on both the crust-mantle boundary and on the surface. We calculate flow due to both forces using finite element approximations. Changes in density due to the gabbro-eclogite phase change are determined using a basalt stability field defined in P-T space. Latent heat of reaction effects on the temperature field are included (6), but the effects of heat conduction are not. In our results we look for evidence that eclogitic material has formed in sufficient quantities in the crustal root to enable the resulting buoyancy forces to begin to dominate the material flow. The imposed boundary velocity causes continuous horizontal compression and crustal thickening. With an initially uniform crustal thickness, eclogite would eventually form in a broad region at the base of the crust. We wish to consider instead the behavior of an initial thickened region of crust that might be the remnant of earlier magmatic activity.

We introduce an initial, isostatically balanced, crustal thickness variation and examine how this perturbation evolves. The balance of thinning due to relaxation of crustal thickness variations, and thickening due to horizontal shortening focussed on the relative weakness of the crust in the thicker region, governs crustal thickening. The balance of these effects depends upon the viscosities of the crust and mantle and the magnitude of V_c . Larger viscosities reduce buoyancy-driven flow, allowing the convergence velocity to dominate. We seek to define the conditions, or the range of model parameters, which would allow the gabbro-eclogite transformation to affect this balance and lead to crustal thickening. Thus, we examine the conditions leading to the development of a self-sustaining, eclogite-driven downwelling. In this preliminary study we investigate the role of crustal thickness and convergence velocity in promoting the phase change in, and eclogite-driven flow of, the crustal root.

Results: For a 100 km long and 100 km deep model region with a mantle viscosity of 10^{21} Pa s , we present preliminary results for different values of V_c and initial T_c . We have chosen a thermal gradient of 4K/km with a surface temperature of 725 K . The convergence velocities used correspond to rates of 1 km/My and 10 km/My .

For $T_c=20 \text{ km}$ the root of the thickened zone initially lies at 40 km depth. Convergence leads to crustal thickening and deepening of the root, allowing root material to transform to eclogite. Figure 1 shows the crustal thickness ratio between the thick zone and crust away from the initial thickening. Convergence, without the phase change, allows crustal thickness variations to diminish (lower line in Figure 1). When negative buoyancy forces due to eclogite are included, crustal thickness variations still decrease, but more slowly.

Figure 2 (a-c) shows a model beginning with a thicker crust ($T_c=40 \text{ km}$) having a root already lying within the eclogite stability region. Flow due to negative buoyancy forces in the dense crustal root becomes significant relative to convergence flow ($V_c=1 \text{ km/My}$). The sequence of figures illustrates how flow driven at first by convergence becomes dominated by negative buoyancy, increasing the rate of crustal thickening. Figure 2d shows the importance of the phase change in enhancing the crustal thickness variation. Without the phase change, shown by the descending curve, the thickness variation dissipates, while the reverse is true when the phase change is included.

CRUSTAL RECYCLING ON VENUS: Burt, Parmentier, and Head

Discussion: This preliminary work illustrates the manner in which mantle-driven crustal thickening could lead to the formation of a negatively-buoyant crustal root. For an initially thick crust, the body forces in a dense eclogitic root will enhance the crustal thickening effects of convergence. Continuing convergence and thickening increases the amount of eclogite. Flow due to the growing buoyancy forces of the root will eventually become significant relative to convergence-driven flow and lead to the instability of the root and the descent and recycling of root material. This scenario may be appropriate to areas where anomalously thick crust has been created by means such as magmatism and later cooling brings the root within the eclogite stability field.

For a thin crust, the initial zone of thickening relaxes. Continued convergence will cause thickening over a broad region. The wavelength of an eventual instability may not be related to the size of the initial zone of excess crustal thickness. Instead, the instability wavelength will be determined by the relative thicknesses of the basalt and eclogite layers and the mantle and crustal viscosities. It is important to recall that these preliminary models do not yet include the effects of heat conduction or crustal radioactivity, both of which will tend to heat regions of thickening crust therefore inhibiting eclogite formation. Including these effects is the next step in our modelling studies.

References: 1) Solomon, S.C., et al., *JGR*, **97**, 13199-13255, 1992. 2) Bindschadler, D.L., and E.M. Parmentier, *JGR*, **95**, 21329-21344, 1990. 3) Vorder Bruegge, R.W., and J.W. Head, *Geology*, **19**, 885-888, 1991. 4) Namiki, N., and S.C. Solomon, *JGR*, **98**, 15025-15032, 1993. 5) Lenardic, A., W.M. Kaula, and D.L. Bindschadler, *JGR*, **98**, 18697-18706, 1993. 6) Turcotte, D.L. and G. Schubert, *JGR*, **76**, 7980-7987, 1971.

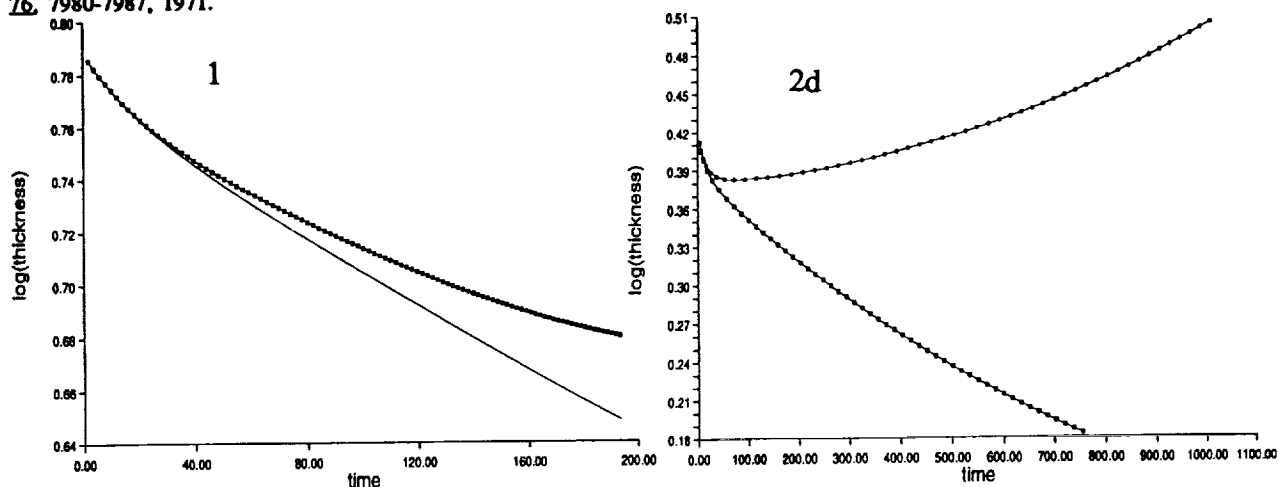
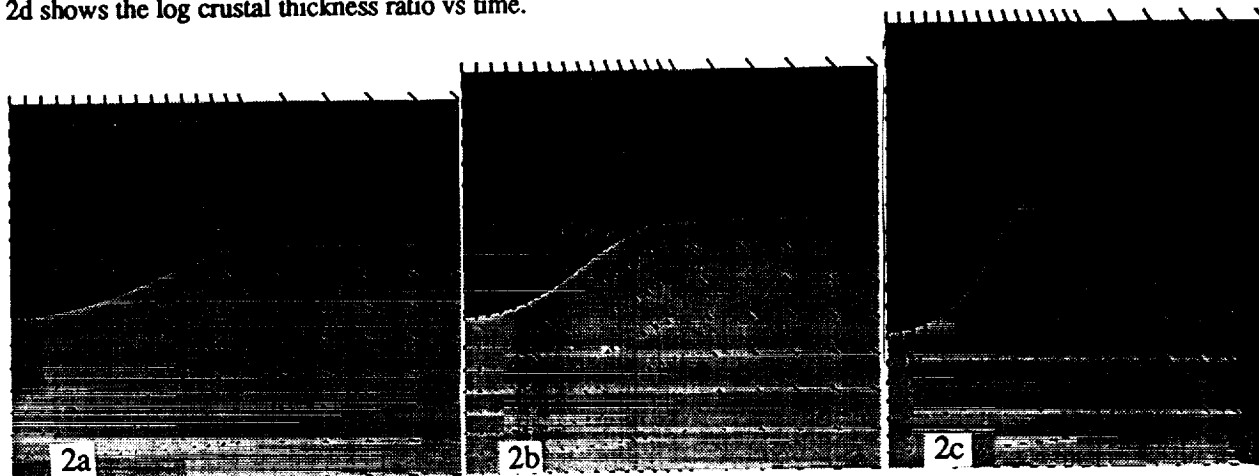


Figure 1. Log of crustal thickness ratio vs time for $T_c=20$ km. Dotted line shows the model including the phase change while solid line shows results without the phase change.

Figure 2. Model evolution for $T_c=40$ km. Light tone is mantle, medium is gabbro, and darkest is eclogite. Flow is shown by lines segments. Timesteps correspond to times of: a) 250, b) 750, and c) 1100 on the scale of figure 2d. 2d shows the log crustal thickness ratio vs time.



MODELLING THE FORMATION OF VENUSIAN CHANNELS; D.B.J. Bussey, S-A. Sørensen, J.E. Guest, University of London Observatory, University College London, London, NW7 2QS, U.K.

Magellan images have revealed the presence of channels on the surface of Venus [1]. Among the processes being considered for their origin are thermal erosion, and the roofing process which may lead to the formation of lava tubes [2]. These processes have been studied initially using simple one dimensional models [3]. However a one dimensional model has limited usefulness and modelling of realistic boundary conditions requires the production of a two dimensional model, one dimension representing depth and the other distance from the vent. The model uses a linear vent and the eruption is assumed to occur at a constant effusion rate, hence the vent is treated as an infinite source of energy, at an energy density corresponding to the eruption temperature, for a length of time equal to the eruption duration.

As this model is two dimensional we are able to enter various velocity profiles to see how channel morphology is affected by the velocity gradient within the lava. Initially the model was run with a constant velocity profile. Alternatives to try include the velocity profile for turbulent flow as well as treating the lava as a Bingham plastic which results in a laminar profile near the ground with a "plug" like constant velocity layer above it [4].

As the lava flows it cools by losing energy to the atmosphere, and to the underlying rock. If cooled sufficiently, a crust will form on the surface of the flow. Therefore the model can be used to study the process of lava tube formation as it gives an estimate for the distance from the vent when crust formation starts. It can also be used to see how much energy is conserved within the flow with the onset of crusting, and how this affects the erosion rate at the base of the flow.

The model was run to simulate a 5 metre thick basaltic type lava flowing over a basaltic substrate. It was assumed that the flow velocity was constant at 1 ms^{-1} and a distance up to 50 kilometres from the vent was considered. Figure 1 shows two temperature profiles, both occurring 50 hours into the eruption. One line shows the temperature gradient within the lava 10 kilometres from the vent, and the other, 50 kilometres. The y axis represents temperature and the x axis distance into the flow with zero corresponding to the surface of the flow and 5 meters the lava/substrate boundary. It can be seen that even at 50 kilometres from the vent, the model predicts that there is still a core region, albeit a small one, still at the eruption temperature. It should also be noted that the thermal boundary layer at the surface of the flow is much greater than the one at the base of the flow. This is expected as the rate of heat loss at the surface is much greater than at the base of the flow.

Whilst, in its present state, this model can only make simple predictions, a fully developed two dimensional model will be able to predict some of the features seen on the venusian surface.

FORMATION OF VENUSIAN CHANNELS: D.B.J. Bussey et al.**REFERENCES:**

- [1] Baker V.R. et al. (1992) *JOURNAL GEOPHYSICAL RESEARCH* **97** pp 13421 - 13444.
[2] Gregg T.K.P. and Greeley R. (1993) *JOURNAL GEOPHYSICAL RESEARCH* **98** pp 10873 - 10882.
[3] Bussey D.B.J. et al. (1993) *LPSC XXIV* pp 237 - 238.
[4] Dragoni M. et al. (1986) *JOURNAL OF VOLCANOLOGY & GEOTHERMAL RESEARCH* **30** pp 305 - 325.

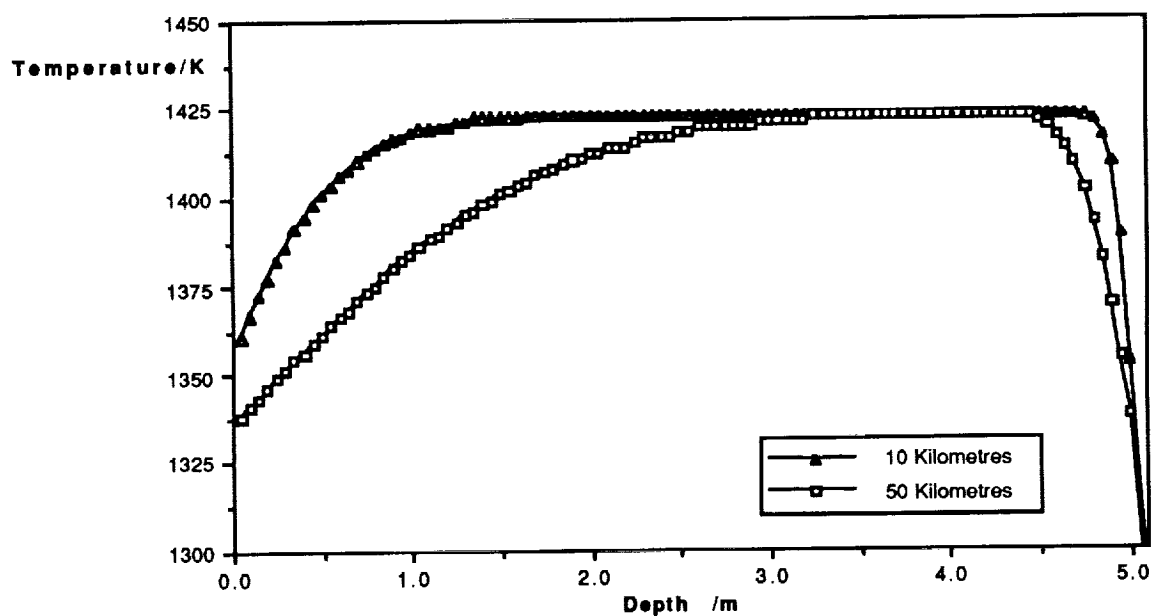


Figure 1. Temperature Profile after 50 Hours

LIGHT ELEMENT ISOTOPIC COMPOSITION IN THE WIND OF A TYPICAL AGB STAR. Maurizio Busso³, Roberto Gallino^{1,2,3}, Claudia M. Raiteri³, and G. J. Wasserburg¹. ¹Lunatic Asylum, Division of Geological and Planetary Sciences, California Institute of Technology, Pasadena, CA 91125, ²Istituto di Fisica Generale, Università di Torino, Via P. Giuria 1, 10125, Torino, Italy, ³Osservatorio Astronomico di Torino, Strada Osservatorio 20, 10025 Pino Torinese, Italy

Interstellar grains very likely condense in the extended mass-losing cool atmospheres of low mass red giants ($M < 3M_{\odot}$) during the time when they are ascending the Asymptotic Giant Branch (AGB). These stars are enshrouded by circumstellar envelopes, being among the most important galactic IR sources. The AGB stars are expected to show a strongly anomalous isotopic composition of the CNO elements and of many other light elements with respect to the solar system. This is due to the occurrence of different mixing episodes that bring to the surface newly synthesized matter from the inner stellar zones. Both the oxygen-rich and the carbon-rich AGB stars should have large isotopic anomalies in light elements as C, N, O, He, Ne, Mg.

All red giant stars suffer for a major I dredge-up episode during their early stages (M stars). A deep convective envelope sets in, penetrating into the partially H-burning inner zones and homogenizing the whole outer structure. Standard evolutionary theory [1] predicts that the stellar atmospheric ^{12}C is reduced by about 1/3 of its initial value, ^{14}N is increased by a factor 2 - 3, ^{15}N is reduced by about 30% and ^{13}C is increased by a factor 2. Thus the carbon isotopic ratio is expected to be considerably lower than solar, in the range $^{12}\text{C}/^{13}\text{C} = 20 - 30$. A ratio close to $^{14}\text{N}/^{15}\text{N} = 1200$ is expected. Spectroscopic observations of M stars [2, 3] partly agree with these expectations, for star of $M > 2 M_{\odot}$. But the lower mass M stars with $M < 2 M_{\odot}$ show much lower values of $^{12}\text{C}/^{13}\text{C}$, that roughly scale with stellar mass. It is then necessary to postulate some sort of extra mixing [4] to further reduce the $^{12}\text{C}/^{13}\text{C}$ ratio to 10 - 20. The same process would also affect nitrogen isotopes, with a resulting increase of the $^{14}\text{N}/^{15}\text{N}$ to about 4,000. In addition, the oxygen abundances are affected by the I dredge-up. While ^{16}O remains essentially unchanged, the envelope convection reaches the inner zones close to the H-shell where a large production of ^{17}O occurs. This causes the surface $^{16}\text{O}/^{17}\text{O}$ ratio to substantially decrease. This ratio is in principle a very sensitive function of the maximum depth reached by the outer convection and of the still highly uncertain reaction rate of $^{17}\text{O}(p,\alpha)^{14}\text{N}$. From a comparative analysis of theory and spectroscopic observations, which is biased by the poor knowledge of the mass of the sample stars [5,6], one can infer that $^{16}\text{O}/^{17}\text{O}$ decreases about exponentially with the initial mass of the star, from its initial value for stars of about $1 M_{\odot}$, down to a factor 20 for stars of $2 M_{\odot}$, and then it increases back, up to about 1/3 the initial $^{16}\text{O}/^{17}\text{O}$ for stars of about $20 M_{\odot}$. Concerning He, all red giants are slightly enriched in ^4He , but a large enrichment is predicted for ^3He for the lower masses [1].

Finally, when the star is on the AGB, its intermediate layers (outside the degenerate C-O core which is the parent of a future white dwarf) are periodically swept by recurrent episodes of convective He-shell burning (the thermal pulses). This is followed by the partial penetration of the external convective envelope which mixes to the surface material enriched in He-burning ashes, mainly ^{12}C . During this process, ashes of the (now inactive) H-shell, containing CNO nuclei in equilibrium abundances are taken to the surface. We note that AGB stars more massive than $4-5 M_{\odot}$, though rare, can give rise to further hydrogen processing, occurring at the base of the convective envelope. Such stars are now recognized to produce abundantly ^7Li , ^{14}N , ^{13}C and ^{26}Al . During AGB evolution the envelope is progressively peeled off by mass loss. This is treated by extensive parametric modeling but understanding is poor. The most widely used simplified treatment [7] involves a free parameter (η); by tuning it to a common value (0.4) it is possible to account very well for the mass loss rates observed in MS, S and C-stars (see observations by [8]; models by [9]). As for the mixing expected after each pulse, (the third dredge-up), we follow the model for this mixing from recent results on AGB evolution [10]. Some typical results concerning the mass loss rate, the C/O ratio and the $^{12}\text{C}/^{13}\text{C}$ ratio versus pulse number are illustrated in Figs. 1 and 2. While C

ISOTOPIC COMPOSITION IN AGB WINDS: Busso M. *et al.*

becomes more and more enriched in ^{12}C during the III dredge-up episodes, no appreciable O composition variation is expected to occur in the envelope of low mass AGB star. As for nitrogen, the ^{14}N produced in the H-burning shell is also mixed with the envelope when the convection zone penetrates below the temporarily inactivated H-shell. We recall that the most important signature of the third dredge-up consists in a strong increase of the heavy s-elements that were built through neutron captures during each convective He-burning instability (thermal pulse). The neutron source in carbon stars is provided by the $^{13}\text{C}(\alpha, n)^{16}\text{O}$ reaction, whereas the temperature of the He shell never becomes sufficiently high to allow ^{22}Ne to be consumed. Consequently, a major consequence of the III dredge-up is to carry essentially pure ^{22}Ne matter into the envelope. Among interstellar dust grains produced in the reducing conditions of carbon rich atmosphere are the SiC grains. The mainstream population of SiC grain shows a $^{12}\text{C}/^{13}\text{C}$ distribution [11,12], that compares nicely [13] with the observed distribution in carbon stars [2]. A debated problem is the interpretation of the isotopic anomaly of Si, however, which shows a linear correlation of $^{29}\text{Si}/^{28}\text{Si}$ versus $^{30}\text{Si}/^{28}\text{Si}$ on a steeper slope ($n = 1.4$) than that predicted by the s-process analysis on the basis of an assumed S/Si initial composition by [14]. We have found that it is possible to match the observed slope using a lower initial S/Si value, a factor of 3 lower than that currently adopted. While the dominant mass loss rate over the whole stellar evolution of AGB stars occurs with $\text{C/O} > 1$, thus providing a source for C, SiC, TiC grains, it should be noted that about 10% of the mass lost is in the region where $\text{C/O} < 1$ and where $^{16}\text{O}/^{17}\text{O}$ was increased in the envelope by the I dredge-up. This could permit oxide grains to form. In particular, the rare Al_2O_3 grains could be produced during the early stage of AGB evolution when $\text{C/O} < 1$.

[1] Iben I. (1977) In *Advanced Stages in Stellar Evolution* (eds. P. Bouvier, A. Maeder) Sauverny: Geneva Observatory). [2] Smith V. V. and Lambert D. L. (1990) *Ap. J. Supp.* **72**, 387. [3] Gilroy K. (1989) *Ap. J.* **347**, 835. [4] Iben I. and Renzini A. (1984) *Phys. Reports* **105**, 329. [5] Dearborn D. S. P (1992) *Physics Reports* **210**, 367. [6] El Eid M. F. (1993) *A & A*, submitted. [7] Reimers D. (1975) *Mem. Roc. Soc. Sci. Liege* VI ser 8, 369. [8] Olofsson *et al.* (1993) *Ap. J. Supp.* **87**, 267. [9] Busso M. *et al.* (1992) *Ap. J.* **399**, 218. [10] Busso M. *et al.* (1993) in progress. [11] Stone J. *et al.* (1990) *EPSL* **107**, 570. [12] Hoppe P. *et al.* (1994) *Ap. J.*, in press. [13] Gallino R. *et al.* (1994) *Ap. J.*, in press. [14] Anders E. and Grevesse N. (1989) *GCA* **53**, 197. Division Contribution 5361 (836). NASA NAGW-3337.

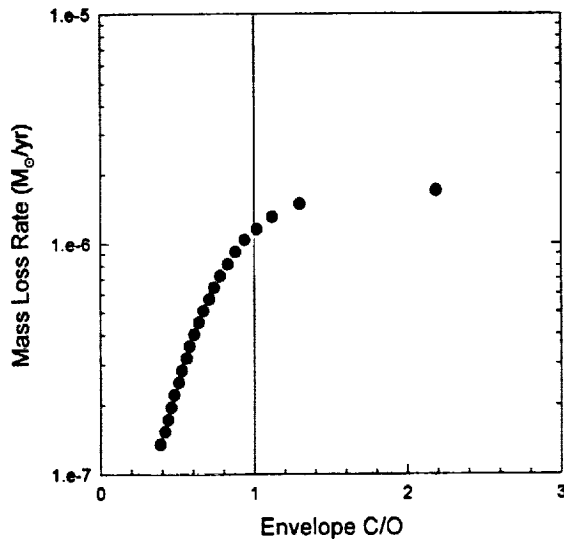


Figure 1. Mass loss rate versus C/O in the envelope for a $1.6 M_{\odot}$ star during the thermal pulses (filled circles) along the AGB track.

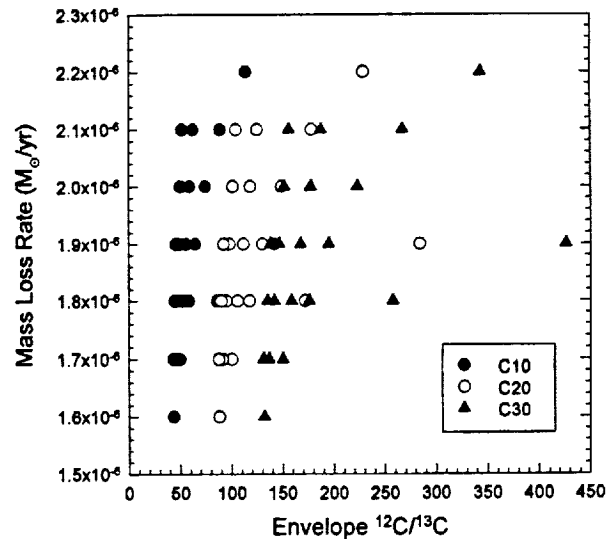


Figure 2. Mass loss rates versus envelope $^{12}\text{C}/^{13}\text{C}$ for AGB stars of twenty initial masses and three $(^{12}\text{C}/^{13}\text{C})_0 = 10, 20$, and 30 at the last pulse before the star leaves the AGB.

MARTIAN POLAR REGIONS: 3.5-CM RADAR IMAGES; B. J. Butler, D. O. Muhleman, California Institute of Technology, M. A. Slade, Jet Propulsion Laboratory

Introduction: We have conducted several unique radar experiments in an effort to further understand the surface of Mars. The experiments were carried out during the oppositions of 1988, and 1992/93. The experiments resulted in well-calibrated, *unambiguous* radar images of the entire visible disk at many viewing geometries. The images were constructed using the Very Large Array (VLA) in Socorro, New Mexico to receive and map radar flux at 3.5 cm which was continuously transmitted from the Jet Propulsion Lab (JPL) 70-m antenna at Goldstone, California and reflected from the surface of Mars. A preliminary description and interpretation of the data from the 1988 experiment has already appeared (1). This mapping technique has also been used in the past to image Mercury (2) and Venus (3), and to obtain echoes from Saturn's largest moon, Titan (4). The entire Martian surface has been imaged, at resolutions as good as 100 km. This abstract and talk will only concern the results for the polar regions of the planet. We imaged south polar regions in 1988, during mid southern summer ($L_s \sim 295^\circ$), and found a highly reflective feature associated with the residual south polar ice cap (RSPIC), which was exposed at the time. The peak normalized cross section of this feature in the same sense circular polarization as that transmitted (SS) was ~ 0.7 . This feature also had a polarization inversion, meaning that more echo energy was returned in the SS polarization than in the opposite sense circular polarization (OS). The most favored mechanism to produce this effect requires a low loss medium with many scattering centers, indicating that the RSPIC had many discontinuities (cracks and voids) in its upper few meters. We imaged north polar regions in 1992/93, during early northern spring ($L_s \sim 20^\circ$), and found no similar features (with high reflectivity OR polarization inversion) associated with the residual north polar ice cap (RNPIC). We think that there are three causes for the difference: 1 - there is some fundamental difference in the structure and/or composition (amount of dust contaminant) in the two residual caps, 2 - the residual CO_2 cap was not sublimated away during the 1992/93 experiments, and absorbed some of the incoming radar energy, and 3 - the north polar regions were imaged with slightly poorer geometry (higher incidence angles).

Observations and Data Reduction: We observed Mars on October 22, 1988, at a distance of ~ 0.46 AU, when the subearth latitude was $\sim -24^\circ$. The range of subearth longitudes was $\sim 40^\circ - 160^\circ$. We again observed the red planet on December 29, 1992, and January 12, 1993, at a distance of ~ 0.63 AU, when the subearth latitude was $\sim +8^\circ$. The range of subearth longitudes was $\sim 337^\circ - 194^\circ$. On each date, periodic observations of quasi-stellar objects were used to calibrate the phases of the observed visibilities, and an observation of a source of known flux was used to calibrate the amplitudes. Because of the rapid rotation of the planet, the data was split into many "snapshots", each of about 10 minutes duration. After subtraction of the thermal emission signature from the surface, the data for each snapshot were then self-calibrated using the phase closure method on the specular spike in the OS visibilities. The data for each polarization were then mapped and the known antenna response ("beam") deconvolved out using a modified CLEAN algorithm. The result is a well-calibrated radar reflection image for each received polarization of the entire visible hemisphere of Mars for each snapshot. Polar (latitudes above 65°) reflectivity images were then constructed by projecting the proper polar region (south for the 1988 data, north for the 1992/93 data) for each snapshot into an individual stereographic image, then averaging these individual images with the appropriate weighting.

Polar Reflectivities: The south polar images show a highly reflective feature in both polarizations whose location corresponds closely to that of the RSPIC, which we resolve. At the time of the observations, the seasonal CO_2 cap had entirely sublimated away, so the feature was due to the RSPIC itself. The peak normalized cross section was $0.716 \pm .009$ for the SS polarization, and $0.312 \pm .014$ for the OS polarization. These reflectivities are very high, particularly considering that they occurred at an incidence angle of $\sim 66^\circ$. The peak polarization ratio (ratio of SS to OS reflectivity) was ~ 2.3 , and the ratio throughout the extent of the highly reflective region was > 1 . The occurrence of high reflectivities and polarization ratios > 1 is an uncommon one in radar studies, but has also been found on the icy Galilean satellites (see (5) for a review), the polar regions of Mercury (1,6), and a portion of the Greenland ice sheet (7). The mechanism to produce this signature is poorly understood, but the effect is probably due to the penetration of the radar wave into a relatively lossless medium which contains many scatterers (8). This implies that the ice in the upper 10's of meters of the RSPIC was very lossless (less than 1% included dust), and contained many scatterers. The scatterers could not have been dust layers or rocks, as too much energy would have been absorbed during the

MARTIAN POLAR REGIONS: 3.5-CM RADAR IMAGES; B. J. Butler *et al.*

many subsurface scattering events to reproduce the high reflectivities. The alternative is that the scatterers were cracks and voids in the ice.

The north polar images tell a significantly different story. There was no region northward of $\sim 75^\circ$ which had a high reflectivity in either polarization, or had a polarization inversion. There were two regions at lower latitudes which had slightly enhanced cross sections (peak OS cross section $\sim .14$), but no polarization inversion (ratio of ~ 0.5). This result was quite surprising to us at first, but we attribute it to the combination of three effects: different geometry, different season, and fundamental structural or compositional difference. Each of these effects will now be discussed.

During the 1988 experiment, the subearth latitude was $\sim -24^\circ$, giving us a relatively good view of the south pole and the RSPIC. During the 1992/93 experiments, the most northerly subearth latitude was $\sim +9^\circ$, so the pole was considerably closer to grazing incidence. This difference in incidence angles may explain part of the discrepancy, but there are indications that this is not the case. First, our Mercury experiment, which showed a north polar feature similar to that at the RSPIC, was at $\sim 79^\circ$ incidence angle, similar to that for the Martian north polar observations. Also, the large extent of the RNPIC implies that there were portions of the cap which were at much lower incidence angles during the experiments, indeed similar to the 66° of the south polar observations. However, in an attempt to correct for the different geometry, we made weighted least squares fits to a cosine law backscatter model for the polar regions. The RSPIC feature shows up clearly in these fits, as expected. In the north, there are features in the SS fits near the southeastern edge of the residual cap, although the peak cross section is about a factor of 6 less than that for the RSPIC feature. This seems to indicate that the geometry is indeed a factor, but the reliability of the fits remains in question, since the excursion in incidence angle for most of the fits is less than 15° , and at high incidence angles.

At the time of the north polar observations, the Martian season was early northern spring, so a significant portion of the entire extent of the seasonal CO_2 cap would be expected to still be present. The seasonal cap at this time is most likely a low porosity polycrystalline layer of CO_2 with very small amounts of included dust, with a depth of $\lesssim 0.5$ m. Assuming that CO_2 ice has the same loss tangent as H_2O ice, we have calculated the amount of absorption caused by such a layer, and we find that for angles other than very near grazing, this absorption cannot explain the difference in the polar reflectivities. It certainly contributes to the difference, but cannot be the only cause.

If the difference is not due entirely to geometry and the seasonal cap, it must imply some fundamental difference between the two residual caps. For our purposes, this difference could either be in the transparency of the two caps (i.e. amount of included dust), or in the number of scatterers (cracks and voids). There has been some indication that the RNPIC is "dirtier" than the RSPIC (9), and we may be seeing the signature of this at 3.5-cm. However, there is still some controversy about the actual amount of dust needed to make the RNPIC "dirtier" (10). If the amount needed is less than a few percent, then it does not affect our measurements significantly, as the loss tangent of the bulk ice/dust mixture would still be very low. If the difference is structural, there must be some difference in the production or destruction rate of scatterers. The production of scatterers is most likely either a thermal process (for the RNPIC only) or due to motion (i.e. glaciation). For the RSPIC to have more scatterers, it must have significantly more underlying relief, and hence more motion. The destruction of most cracks and voids is most likely through filling with CO_2 frost, which is a very fast process (seasonal). However, if there is no communication with the atmosphere, then the cracks and voids are likely closed by simple viscous relaxation. For H_2O ice, this relaxation is a very long process (millions of years). If the upper meters of the RSPIC are CO_2 ice, then this process may be somewhat faster there, but the rheological properties of CO_2 ice are unknown, so this is uncertain.

References: (1) D. O. Muhleman, *et al.*, *Science*, 253, 1508-1513, 1990; (2) B. J. Butler, *et al.*, *J. Geophys. Res.*, 98, 15003-15023, 1993; (3) K. A. Tryka, *et al.*, *LPSC XXII*, 1417-1418, 1990; (4) D. O. Muhleman, *et al.*, *Science*, 248, 975-980, 1990; (5) S. J. Ostro, *et al.*, *J. Geophys. Res.*, 97, 18227-18224, 1992 (6) J. K. Harmon and M. A. Slade, *Science*, 258, 640-643, 1992 (7) E. J. Rignot, *et al.*, *Science*, 261, 1710-1713, 1993 (8) B. Hapke, *Icarus*, 88, 407-417, 1990 (9) D. A. Paige and A. P. Ingersoll, *Science*, 228, 1160-1168, 1985 (10) H. H. Kieffer, *J. Geophys. Res.*, 95, 1481-1493, 1990

FLUVIAL PROCESSES IN MA'ADIM VALLIS AND THE POTENTIAL OF GUSEV CRATER AS A HIGH PRIORITY SITE; Nathalie Cabrol¹, Ragnild Landheim², Ronald Greeley³, and Jack Farmer⁴. ¹ *Observatoire de Meudon*, ² *Department of Botany and Geology, Arizona State University, Tempe, AZ*, ³ *Department of Geology, Tempe, AZ*, ⁴ *NASA Ames Research Center, Moffet Fiels, CA*.

Introduction

According to exobiology site selection criteria for Mars (Farmer et al., 1993), the search for potential extinct/ extant water dependant life should focus on sites where water flowed and ponded. The Ma'adim Vallis/Gusev crater system is of high priority for exobiology research, because it appears to have involved long-term flooding, different periods and rates of sedimentation (Schneeberger, 1989), and probable episodic ponding.

Evidence for non-uniform fluvial processes

Ma'adim Vallis exhibits a series of elevated terraces which lie above the present valley floor (Landheim et al., 1994). The length of the valley, the lateral continuity of the terraces and thickness of terrace deposits suggest that the region experienced long-term, non uniform processes of fluvial erosion and deposition, reflected in geomorphic features along the valley floor, at the valley mouth, and within Gusev crater. Along the downstream course of Ma'adim Vallis at least ten different levels of terraces are visible along the west bank of the valley, and at least eleven on the east bank. These terraces represent a minimum estimate that is likely to increase as higher resolution images become available.

Three levels of terraces are visible within the two 30 km diameter impact craters located at the mouth of Ma'adim Vallis (Landheim et al., 1994). Three terraces (T9-T11) which occur within Gusev crater are interpreted to represent fluvial deposits that are correlated by elevation to fluvial terraces in Ma'adim Vallis. Other levels recognized within Gusev crater are not found in the valley system, but could be associated with upper terraces on the surrounding plateau which are related to small valley networks adjoining Gusev crater on the SW and SE rims. The suggested terrace correlations provide a framework linking the morphology and stratigraphy of deposits within Gusev crater to processes operating within the downstream region of the Ma'adim Vallis.

Early overflowing of the plateau and ponding

Table 1 summarizes our interpretation of the evolution of terracing within the lower 40 km of Ma'adim Vallis. In the early stages represented, the channel floor of Ma'adim Vallis appears to have been about 900 m above the current level. Remnants of five upper terraces (T1-T5) are visible on the plateau. They terminate along the southern margins and continue on the C1 west bank and C3 east bank where they adjoin small fluvial valleys entering Gusev crater. These observations suggest the three large impact craters located at the outlet formed natural dam to flow from Ma'adim Vallis, and that water ponded locally to form a lake which backed up into the lower part of the valley (Cabrol et al., 1993a, 1993b).

The slight sinuosity of terraces T1 to T5 reflects original channel meandering. The terraces also appear to correspond to channelization of the flow by small valley networks on the SW and SE rims of Gusev crater, leading to the setting of two different levels of sedimentation inside the crater, which may be evidence of a crater-lake that overtopped the Gusev north rim. The overtopping generated a catastrophic release of water to the northern plains. This period left less than 200 m thick deposits distributed into five sequences of comparable amplitude (Table 1). The correlative sequences of erosion were observed by the deepening of the valley section, which at T5 is located about 200 m below the primary level, and by its reduction in width.

From terrace level T6, the flow changed direction to enter its present axis. This episode is interpreted to correspond to the opening of the southern rims of C1 and C3 impact craters and to the sedimentation inside these basins, with drainage of the remnant flood plain towards Ma'adim Vallis through small valley networks that are visible on both banks. Because the T6 level is not observed inside Gusev crater, the northern rim of C3 is interpreted to have acted as a dam. The visible thickness of the deposits inside C1 and C3 (Table 1) are twice that observed for previous episodes, suggesting that the increase in erosion was linked to a drop in base level. This event appears to have lowered the channel floor at least 70 m to a level corresponding to that of C1/C3 floor.

After T9, all the terrace levels in Ma'adim Vallis correspond to deposits found in Gusev crater, as described in Landheim et al., (1994). Breaching of the last northern rim of C3 is believed to represent a base level drop of at least 500 meters and appears to correlate to accelerated channel incision into the T9 terrace deposits within Ma'adim Vallis. The depth achieved by this incision event was equivalent to the difference in elevation between Gusev crater and the thickness of the T9 deposits.

The geomorphology of the deposits within Gusev crater provide evidence for loaded flows, especially the shape and thickness of the delta remnants, and the different lobes of sedimentary deposits fronts

FLUVIAL PROCESSES IN MA'ADIM VALLIS; Cabrol, N.A et al.,

within Gusev crater.

Conclusion

During its period of fluvial activity, Ma'adim Vallis experienced different fluvial processes, from slow sedimentation rates to catastrophic release of mud-like flows. The results was accumulation of nearly 900 meters of fluvial sediments which were derived from different source rocks upstream in the region. This exceptional diversity designates Ma'adim vallis-Gusev crater system high priority for exobiology studies.

Table 1 : Terrace n° Elev.(km) Width (km)¹ Volume of sediments

Young	11	floor	2	?
	10	0,04	4,4	0,19
	9	0,5	7,5	3,75
	8	0,03	10	0,3
	7	0,05	13,5	0,6
	6	0,07	19	1,3
	5	0,03	21	0,6
	4	0,06	30	1,5
	3	0,04	33,5	1,3
	2	0,03	47,5	1,4
Old	1	0,04	55	2,2

1-Width considers the distance between the terraces of the same level. The volume of sediments is estimated from this width, the 40 km long sample of the valley, and the elevation of the terraces.

References : Cabrol et al., LPSC XXIV, 241-242 (1993_a); Cabrol et al., (submitted to *Icarus*) (1993_b); Landheim et al., LPSC XXV, (1994); Farmer et al., *Proceedings of the World Space Conference, 29th meeting of the World Space Congress (COSPAR)* (in press); Schneeberger, LPSC XX, 964-965, (1989).

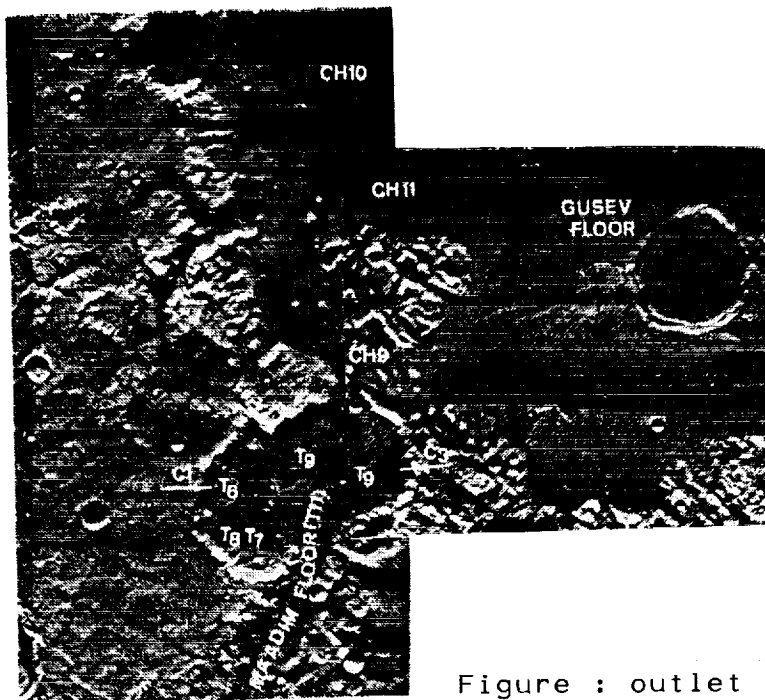


Figure : outlet of Ma'adim Vallis

COMPARATIVE RESULTS FROM GIANT IMPACT STUDIES. A. G. W. Cameron,

Harvard-Smithsonian Center for Astrophysics.

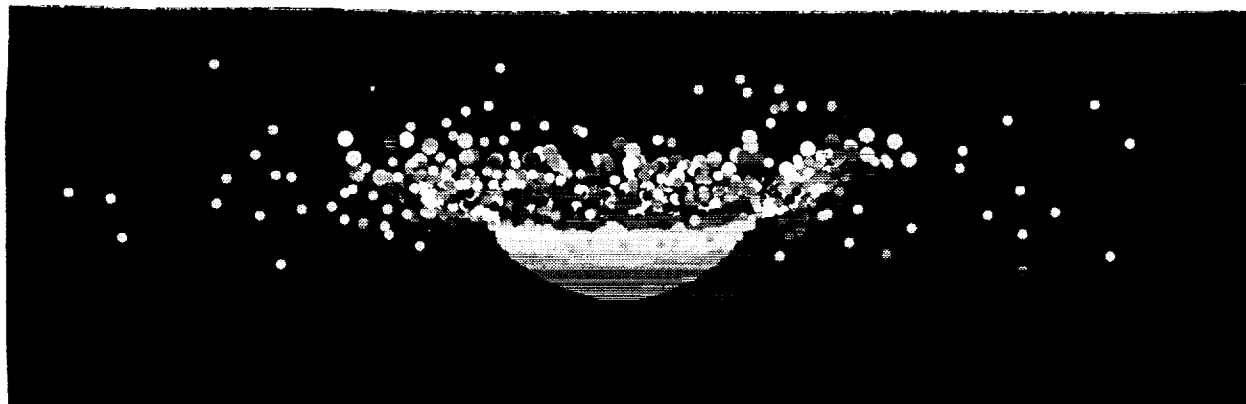
The author's program of simulations of Giant Impacts on the protoearth has nearly finished its current phase; seven of nine simulations have completed at the end of 1993, and an additional simulation of a $0.2 M_{\oplus}$ planet impacting centrally on a $0.8 M_{\oplus}$ planet has been carried out. The results have shown the universality of the development of large hot rock vapor atmospheres around the impacted planet. In the equatorial plane the density distributions of these atmospheres are remarkably similar, being largely independent of the variations in collisional angular momentum (over a factor of two) or of the ratio of projectile to target mass (from 2:8 to 5:5).

During the last eight years the author, together with several colleagues, has carried out a series of numerical investigations of the Giant Impact theory for the origin of the Moon (1-4). Current smooth particle hydrodynamic (SPH) simulations use 10,000 particles with 5,000 particles in the target and 5,000 in the impactor.

So far seven runs (out of nine) have finished; these have target to impactor mass ratios varying from 5:5 to 8:2. The collisional angular momenta range from 1.2 to 2.2 times the present angular momentum of the Earth-Moon system. In addition, one run with a mass ratio of 8:2 was carried out with zero angular momentum, involving a central impact. All of these runs started with zero velocity at infinity, so that the impact occurred at escape speed.

The initial temperatures of all colliding bodies were taken to be 2,000 K, which is high enough realistically to represent a history of collisional accumulation and low enough to suppress thermal evaporation of matter from the surface. After the collision, wherever very hot rock appears in a surface region, rock vapor evaporates and forms a hydrostatic atmosphere around the body. This rock vapor is simply the vapor phase of the dunite equation of state developed by Jay Melosh (3).

A comparative analysis of the computational results is still being carried out, and only a flavor of them can be reported in this abstract. First, the collisional event involving the central impact was rather spectacular. The impactor produced a major compression of the impacted hemisphere; a view of the system from the side at the time of maximum compression is shown here. The impactor struck the target from above and is buried in the other material, making the system look much like a thick but shallow bowl. The rebound from this compression set off wild oscillations of a variety of modes before things settled down with most of the energy converted to heat. The usual rock vapor atmosphere formed around this system due to evaporation.



The top figure on the second page shows the density distribution of the rock vapor atmosphere in the equatorial plane for cases 2 and 6 and the central impact. Case 2 was the collision between two half-protosearths (5:5 mass ratio) and an angular momentum of 2.2 times that of the present Earth Moon system. Case 6 involved a mass ratio of 8:2 and an angular momentum of 1.4 times that of the present Earth-Moon system. The density distributions of these two cases are remarkably similar, and the other numbered cases are in turn quite similar to these two. However, the zero angular momentum case (central impact) falls off a little more rapidly, showing the effect of rotational flattening toward the equatorial plane.

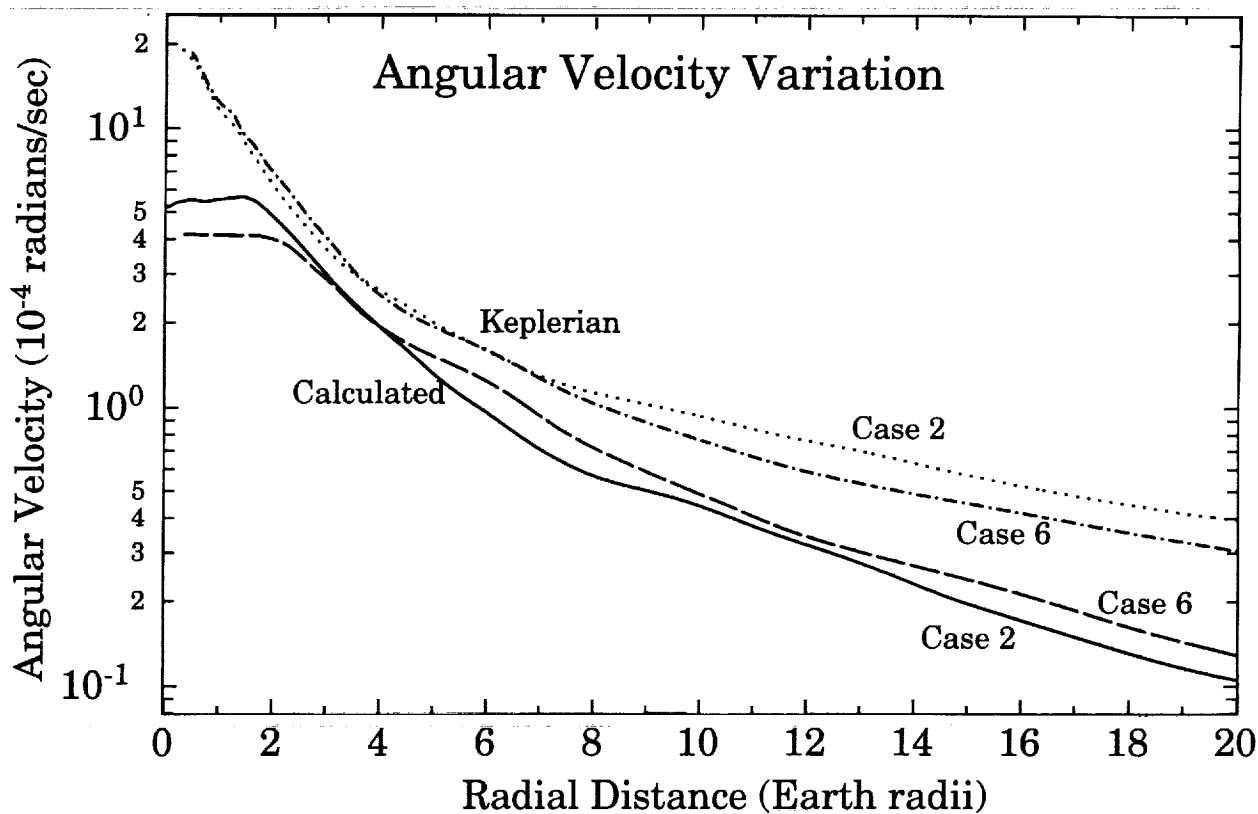
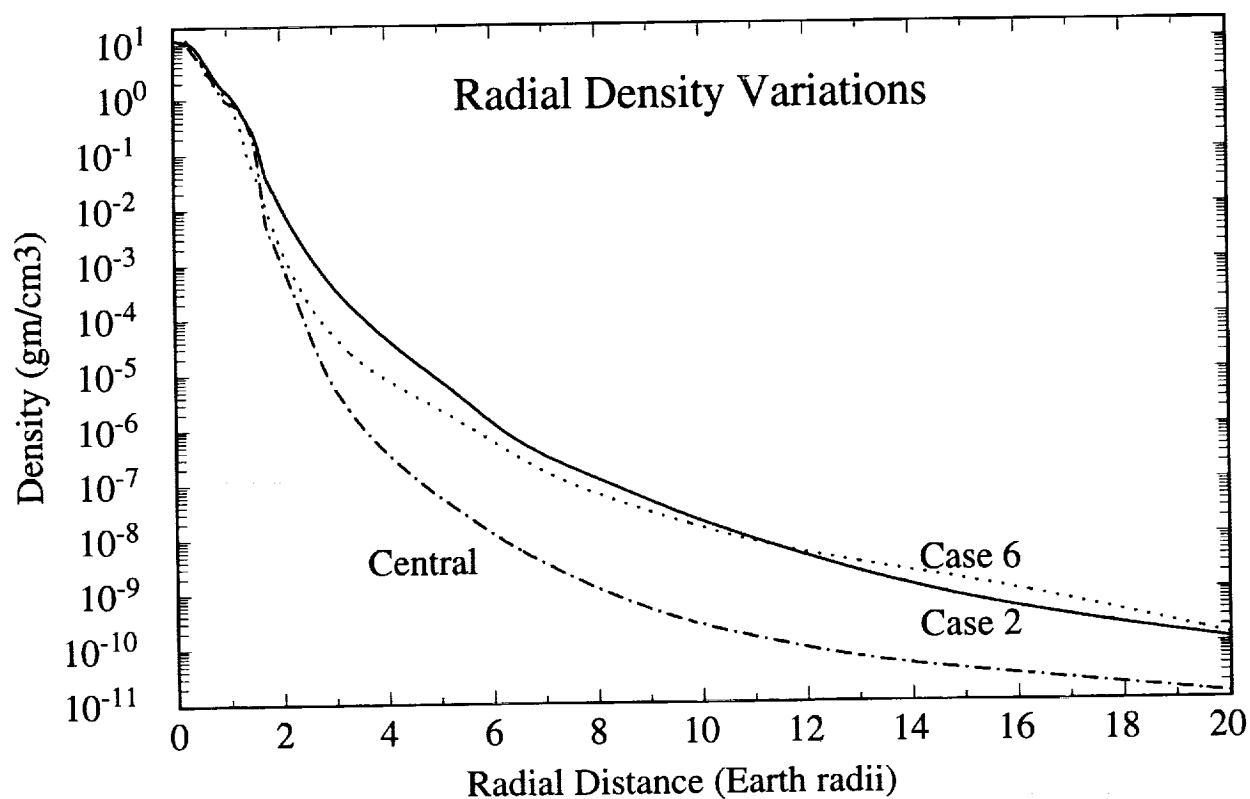
The bottom figure on the second page shows the angular velocity variations with radial distance for cases 2 and 6; the figure shows both the calculated results and what the angular velocity would need to be to place material in Keplerian orbit. Again the results for cases 2 and 6 (and other cases as well) are very similar; note that at small distances the condensed parts of the systems are in corotation. The angular velocities are subkeplerian in all cases. The central impact case (not shown) has deviations of both signs from zero angular velocity, presumably due to turbulence generated by the impact.

This work was supported in part by NAGW-1598.

References: (1) Benz, W., Slattery, W. L., and Cameron, A. G. W. (1986) *Icarus*, **66**, 515-535; (2) Benz, W., Slattery, W. L., and Cameron, A. G. W. (1987) *Icarus*, **71**, 30-45; (3) Benz, W., Cameron, A. G. W., and Melosh, H. J. (1989) *Icarus*, **81**, 113-131; (4) Cameron, A. G. W., and Benz, W. (1991) *Icarus*, **92**, 204-216.

COMPARATIVE RESULTS FROM GIANT IMPACT STUDIES

Cameron, A. G. W.



DIELECTRIC PROPERTIES OF VENUS: RESULTS FROM EMISSIVITY MODELING AND TERRESTRIAL FIELD MEASUREMENTS; Bruce A. Campbell, Center for Earth & Planetary Studies, National Air & Space Museum, Smithsonian Institution.

The two primary surface properties which control microwave scattering and emission are roughness and dielectric constant. Magellan synthetic aperture radar (SAR) measurements for Venus are strongly influenced by wavelength-scale roughness, while observations of the 12.6-cm brightness temperature are more dependent upon dielectric constant. Neither dataset, however, can be used in isolation to derive these physical quantities, since roughness changes affect the emissivity and reflectivity variations will be mirrored in the SAR return. This project examines the mean behavior of backscatter and emissivity data over the entire planet, and uses the observed relationships to derive a model which estimates the dielectric constant and a "surface roughness fraction". Use of this model may permit rapid separation of areas with actual dielectric variability from those whose emissivity variations are caused by roughness changes. The second portion of the work uses a field dielectric probe to determine the complex permittivity of terrestrial basalts, which are often characterized by vesicular upper layers. This field study was necessary to fill in a gap between lab measurements of powders and dense rock samples.

DATA. Magellan collected interleaved emissivity (E) and SAR measurements, and the ARCDR dataset contains values of E and "unfocused" (footprint-averaged) backscatter for each surface footprint of the high-gain antenna [1]. There are ~6 million footprints across the planet through Orbit 3900, with the incident/emitted angle varying as a function of latitude through Cycle 1 and held fixed through much of Cycle 2. The emissivity data were binned as a function of radar backscatter brightness (σ_0) within different incidence angle ranges to analyze the relative influence of roughness and dielectric changes on each parameter. Figure 1 shows the average H and V-polarized emissivity vs. σ_0 for angles $>30^\circ$ and elevations below 6053.0 km. The H-polarized data represent a global average, while the V data are from 10 orbits for which the spacecraft was rotated about its axis. In this plot, E_H increases linearly with $\log(\sigma_0)$ over a wide range of radar brightness, while E_V falls. These behaviors are attributed to the effects of roughness on both emissivity and radar backscatter. The rise in E_H and the decline in E_V with greater roughness (higher σ_0) are consistent with theoretical models for scattering and emission, which predict that, for angles $>30^\circ$ and dielectric constants below ~15, the rough-surface emissivity is approximately the average of the H and V plane-surface values [2].

Based on the observed behavior of E and σ_0 , a model was developed which treats each region within an antenna footprint as a checkerboard mixture of smooth and rough terrain. The surface is assumed to have a single dielectric constant within the footprint. With this "end-member" approach to the surface, we can use the SAR and emissivity data to derive values for the dielectric constant and "roughness fraction". This model, although dependent upon several assumptions, provides a first-order method for identifying areas which are truly anomalous in their roughness/dielectric properties.

MODEL RESULTS. The model was tested on areas for which Magellan incidence angles are $>30^\circ$ (54 N - 34 S). One obvious result is the lack of strong dielectric contrasts between the smooth plains and rough tessera, suggesting that the latter are simply deformed areas with essentially the same material composition as the plains. Most of the differences in plains emissivity fall along the best-fit E vs. σ_0 line in Figure 1, indicating that these variations are also due to roughness. The planetary average dielectric constant is ~4.15, which lies between the values found in lab studies for rock powders (~2) and dense basalt (5-8) [3,4]. In regions below 6053 km radius, there are many localized instances of higher and lower dielectric constants. High dielectric values (6-8) are found in some crater floors and in most of the extended crater "haloes", consistent with earlier analyses of these features [5, 6]. These high values may be caused by loading of impact melt material with conductive mineral phases [7]. If such loading is the cause of the high dielectric constant, then the crater haloes must be young enough to avoid weathering of these minerals by the

atmosphere. Low dielectric values (2-3) are found in a few crater-related mantling deposits (most notably east of Gula Mons) and in patches in the plains which may be more vesicular basalts or occasional accumulations of fine soil. The model dielectric results are in general agreement with those from the Magellan altimeter data, but appear to be more reliable in rough areas, where the Hagfors model breaks down.

FIELD DIELECTRIC DATA. Laboratory measurements of rock dielectric constants exist for powdered samples and for polished sections of dense basalt, but there is little information on the *in situ* density or dielectric constant of typical pristine terrestrial lava flows. To fill in this gap, a portable 6-cm dielectric probe was used on 14 Hawaiian volcanic surfaces (lava, ash, and weathered soil). Preliminary analysis shows that: (1) many Hawaiian basalts are characterized by a vesicular upper layer 5-20 cm thick which significantly lowers the effective density in the region "seen" by the radar, and (2) the lava flows have dielectric constants of 2.0-3.3, intermediate between lab values for powders and dense rock. The nature of the surface glass coating and the presence of patches of oxidized material had little effect on the bulk dielectric properties. The average estimated dielectric constant of 4.15 for Venus suggests that this surface is typically less vesicular than that of Hawaiian volcanoes (consistent with the higher atmospheric pressure), and that the global soil density must be rather low.

REFERENCES. [1] Pettengill, G.H., et al., JGR 97, 13091-13102, 1992. [2] Ulaby, F.T., et al., Microwave Remote Sensing, Addison-Wesley, 1987. [3] Campbell, M.J., and J. Ulrichs, JGR 74, 5867-5881, 1969. [4] Ulaby, F.T., et al., Univ. Michigan Rad. Lab Rep. 23817-1-T, 1988. [5] Plaut, J.J., and R.E. Arvidson, JGR 97, 16279-16292, 1992. [6] Campbell, D.B., et al., JGR 97, 16249-16278, 1992. [7] Pettengill, G.H., et al., JGR 93, 14881-14892, 1988.

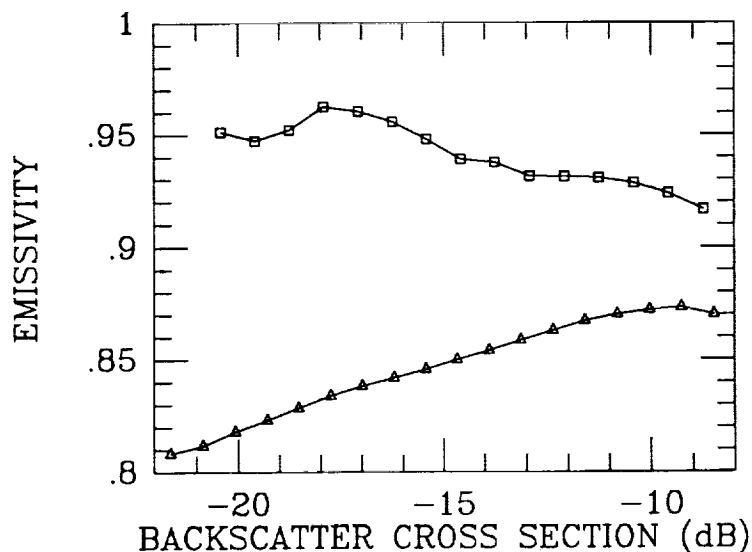


Figure 1. Average emissivity calculated for narrow bins of specific radar backscatter cross section (σ_0) from Magellan data for Venus. Upper line is V-polarized emissivity from 10 orbits; lower curve is H-polarized emissivity across entire planet from 54 N to 34 S (incident/emitted angle $>30^\circ$). Areas above 6053.0 km radius excluded from averaging to avoid contamination by the very-high dielectric mountaintops. Note the linear rise in E_h between -22 and -9 dB, and the drop in E_v over the same range.

MULTIPLE-WAVELENGTH LUNAR RADAR IMAGES: ANALYSIS OF REGOLITH PROPERTIES; Bruce A. Campbell, *Ctr. for Earth & Planetary Studies, Nat. Air and Space Museum*; B. Ray Hawke, *Planetary Geosciences, Dept. of Geology and Geophysics, University of Hawaii*.

Earth-based radar observations offer views of the roughness and dielectric properties of the lunar regolith which are complementary to multi-spectral analyses of the upper surface. Improvements in data collection and analysis methods have provided new opportunities for application of radar images, and in this work we utilize controlled mosaics of Zisk's 3.8-cm radar maps [1], the 70 cm nearside map of Thompson [2], and a restored version of Thompson's 7.5 m wavelength lunar image [3]. Our goals are to: (1) study the nature of absorption and scattering in the mare and highland regoliths, (2) define the location and extent of cryptomare deposits identified from multispectral data, and (3) evaluate the need for additional earth-based observations at 3, 12.6, and 70 cm wavelengths.

One of the major geologic questions about the lunar maria regards their relative abundances of Fe and Ti oxides. Spectroscopic techniques have been developed which estimate TiO_2 content from UV/Visible wavelength ratios [4, 5], but these methods typically can only separate the maria into a small number of broad classes. Uncertainties in the TiO_2 estimates increase for "redder" mare units ($<4\%$ TiO_2), and remote sensing evaluation of the Fe fraction in lunar soils is not well understood. Radar backscatter data provide a second means for estimating the FeO and TiO_2 content of the regolith. At 70-cm wavelength, the radar energy may penetrate several meters into the mare soil and be scattered from buried rocks or the sub-regolith lava flow surfaces. If we assume that the rock population does not vary systematically between the various mare units, then the differences in depolarized 70-cm echoes are a function of regolith attenuation and depth. This type of analysis was shown by Schaber et al. [6] to be useful in characterizing Mare Imbrium lava flows, and the availability of a calibrated nearside 70 cm map at 3-5 km spatial resolution makes it possible to compare the behaviors of many mare surfaces [2]. We coregistered the 70 cm map and a digitized version of the lunar color difference (0.61, 0.37 μm) image [7], and compared the relative dn values in the two datasets for several test regions. Figure 1 shows the results of this preliminary analysis. There is a general correlation between radar backscatter strength and the "redness" of the mare units, consistent with the bluer regions having a higher proportion of FeO and TiO_2 to absorb the radar energy. Higher Ti (bluer) surfaces have a wide range of radar backscatter values, while redder surfaces (higher color-difference dn) are limited to areas of high relative backscatter cross section. The departure of these parameters from a simple positive correlation may be useful in estimating the relative Fe and Ti abundances in mare soils.

Earth-based observations and Galileo images have shown that there are large patches of buried "cryptomare" material, many of which can be found near Mare Humorum [8, 9]. The longest wavelength radar data are particularly useful in studying these areas, since they tend to have the longest regolith path length and are thus most sensitive to changes in absorption properties. At 7.5-m wavelength, there is a marked area of low return in the region surrounding Schiller and Schickard craters, and additional smaller low-return patches north of Mare Humorum. In the 70-cm data, these areas can still be identified, but the magnitude of the low is much smaller, possibly indicating that the areas of highest loss are several tens of meters below the surface. The 70-cm data also show a marked dichotomy in radar brightness between the eastern and western highlands in the southern hemisphere. The higher radar return from areas closer to the Orientale basin may suggest the presence of large rocks derived from the impact event [2]. Analysis of the distribution of bright areas and the cryptomare patches may provide insight on the depth of basin ejecta and the degree to which Orientale has modified the southwestern nearside.

LUNAR RADAR IMAGES: B.A. Campbell and B. Ray Hawke

These results suggest that there are important lunar science issues which could be addressed with future high-resolution earth-based radar images. The upgraded Arecibo telescope will provide 12.6 cm images at resolutions of a few 10's of meters, and 70 cm images at the 300-500 m scale. The potential of the new 12.6 cm data for geologic applications appears very promising [10]. Higher-resolution 70 cm data should permit detailed analysis of mare lava flow boundaries, cryptomare areas, and pyroclastic deposits.

REFERENCES. [1] Zisk, S.H., et al., *The Moon*, 10, 17-50, 1974; [2] Thompson, T.W., *Earth, Moon and Planets*, 37, 59-70, 1987; [3] Thompson, T.W., *Icarus*, 36, 174-188, 1978; [4] Pieters, C.M., *Proc. LPSC 9*, 2825-2849, 1978; [5] Johnson, J.R., et al., *JGR* 96, 18861-18882, 1991; [6] Schaber, G.G., et al., *The Moon*, 13, 395-423, 1975; [7] Image by Whitaker, E.A., presented by Wilhelms, USGS Prof. 1348, 1987, page 98; [8] Hawke, B.R., et al., *GRL* 20, 419-422, 1993; [9] Head, J.W., et al., *JGR* 98, 17149-17182, 1993; [10] Stacy, N.J.S., PhD Dissertation, Cornell Univ., 1993.

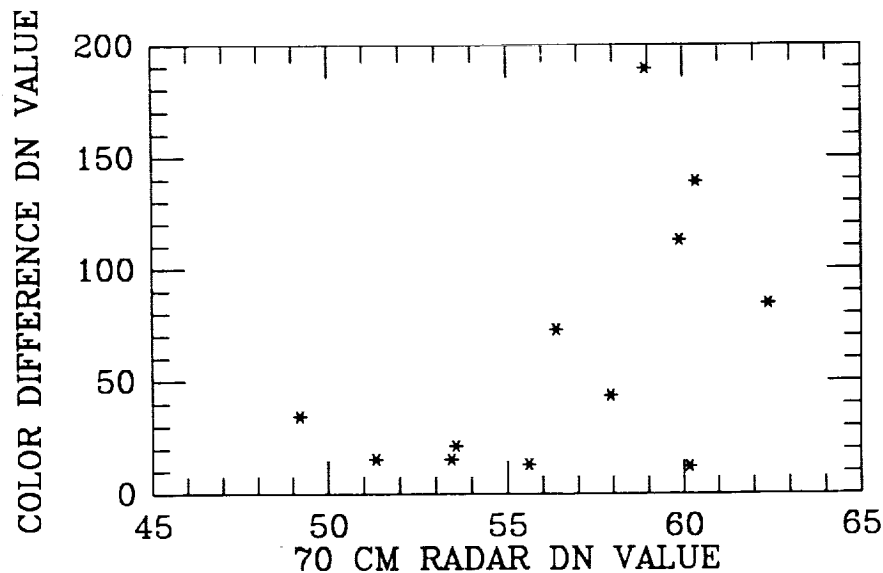


FIGURE 1. Plot of average color-difference dn values (higher dn corresponds to redder surfaces) versus average 70 cm depolarized dn values (each dn value is a 0.5 dB change in echo power). Sample areas in Serenitatis, Crisium, Fecunditatis, Humorum, Imbrium, and Procellarum basins.

SIDEROPHILE TRACE ELEMENTS IN SILICATE MELTS: SIGNIFICANCE AND STATUS OF UNUSUAL OXIDATION STATES C. J. Capobianco, J. A. DeAro, M. J. Drake and V. J. Hillgren, Lunar and Planetary Laboratory, University of Arizona, Tucson, AZ 85721

Current status of zero-valent and other unusual oxidation states for siderophile elements in silicate melts is discussed. New data on melt speciation of Ag and Sn are presented. Data consistent with unusual effective valences for Sn of 1+ and 0 in Fe-bearing melts are given. Preliminary data for Ag in Fe-free melts can be fitted to the expected 1+ state but we cannot yet entirely rule out significant zero-valent speciation at low oxygen fugacity.

Experimental evidence consistent with unusually low oxidation states for a variety of siderophile elements dissolved in silicate melts has been reported in several recent studies: Ir⁰ by Amossé et al. (1987); Ni⁰ by Colson, (1990), Steele et al. (1991), Colson, (1992), Ehlers and Grove, (1990), Ehlers et al. (1992) and Schmitt et al. (1989); Pd¹⁺ and Rh^{1.5+} by Capobianco et al., (1992); Ir²⁺ by O'Neill (1993); Pd¹⁺ by Borisov et al., (in press). The geochemical significance of such unusual speciation, particularly the zero-valent oxidation state, is discussed by Colson, (1992) and Capobianco et al. (1993). The presence of significant amounts of zero-valent species in silicate melts, a contentious issue, would produce greater than otherwise expected lithophility and incompatibility for the element during igneous processes. Such enhancements would be pronounced at high temperature or low oxygen fugacity and have been used to explain, for examples, Ni abundance in the mantle (Colson, 1992), Ni systematics from igneous systems on Earth (Morse et al., 1991) and the moon (Steele et al. 1992).

Zero-valent Ir in silicate melts has been implicated in the geochemistry of the association of chromite bodies and platinum group elements (PGEs) by Amossé et al. (1990 and 1992). Another hypothesis which does not necessarily involve zero-valent species, but which does recognize the importance of unusually low valence states for PGEs dissolved in silicate melt, has recently been suggested as an alternative explanation for the PGE-chromite association (Capobianco et al. in press).

However there has been some skepticism about the amounts of these unusual species in melts, particularly with regard to the zero-valent species proposed for Ni and Ir. Independent studies by Capobianco and Amelin (1992 and in press), Holzheid et al. (1993 and in press) and Dingwell et al. (1993) have failed to confirm the presence of significant amounts of zero-valent Ni or Co in simple Fe-free silicate melts. Neither were O'Neill et al. (1993) convinced by their Ir solubility experiments in Fe-free silicate melts that zero-valent Ir played a significant role.

On the other hand, for an Fe-bearing system in which a significant fraction of dissolved Ni⁰ was inferred from an olivine-melt partitioning study by Ehlers et al. (1990, 1992) some corroboration is provided by a single datum in Steele et al. (1991).

Zero-valent species must be present in any silicate melt having a finite activity of the element of interest; thermodynamics of partial molar entropies of mixing

mandate it. But whether the zero-valent concentration is ever an appreciable fraction of the total concentration of an element in a melt is a matter of chemistry over which opinions are unequally divided in the glass science and metallurgical literature, with those not believing in significant zero-valent speciation holding sway.

Among the early proponents of significant zero-valent solubility is Weyl (1953) who likens the physiochemical mechanism to a "frozen metallic vapor." To set a bound on the concentration of such a dissolved vapor we can use the metallic vapor pressure of an element, say for example, Ni, to calculate the density of Ni vapor at 1550° C and 1 bar. If we then assume that this vapor is completely contained in a silicate melt, a concentration for the metallic vapor near 10 ppb is calculated. This amount of dissolved Ni⁰ would amount to 10% of the total Ni concentration when the oxygen fugacity is approximately IW-8. Evidence for greater zero-valent concentrations than the above would imply that the zero-valent species is actually concentrated by the melt relative to the vapor and hence that there is some chemical stabilization of these species by the melt.

Along these lines Montana et al. (1993) argued against noble gases, such as Xe and Ar, being dissolved as species merely occupying voids in the melt structure, instead they suggest that specific melt sites control the solubility. One might ask, if noble gases chemically interact with a silicate melt then why not neutral metals?

Some indirect support for the presence of melt sites capable of housing zero-valent species comes from recent high P, T metal-silicate partitioning experiments of Walker et al. (1993) and Hillgren et al. (in press). They report decreasing metal-silicate partition coefficients for a variety of trace elements with increasing temperature. Although there may be other ways to explain this phenomenon, which was not anticipated from previous lower temperature metal-silicate experiments, enhanced solubility of zero-valent species at high temperature is one mechanism, as outlined in Capobianco et al. (1993).

Moreover, Walker et al. (1993) interpret their data in terms of the "closing of the solvus" between metallic liquid and liquid silicate. If this was not simply an uncontrolled oxidation-reduction process during their experiment, then closing the solvus implies that the silicate liquid can accept metallic components in

C-4.

SIDEROPHINE TRACE ELEMENTS IN SILICATE MELTS: Capobianco C.J. et al.

abundance, carrying the implication that such sites are plentiful at high enough temperature. And unless there is some qualitative transformation of a melt as temperature is increased then lower temperature melts should also contain sites capable of housing zero-valent species.

Because of the potential significance to geochemistry of zero-valent species in silicate melts a series of experiments is underway to try to reproduce the results of one of the better documented cases from the metallurgical literature (Richardson and Billington, 1956) of zero-valent speciation of Ag in silicate melts. Fig. 1 plots our new solubility data for Ag versus oxygen fugacity. These data were measured using the electron microprobe from glasses equilibrated (at 1293° C for at least 16 hrs.) in AgPd alloy crucibles in a gas mixing furnace (using CO-CO₂-N₂-O₂ gas mixtures).

Although these data are consistent with Ag dissolved as a 1+ species (see Schmitt et al. 1989 for explanation) the two most reduced runs are only marginally represented by the fitted univalent curve. Further experiments are underway to better quantify and extend the trend into more reducing conditions.

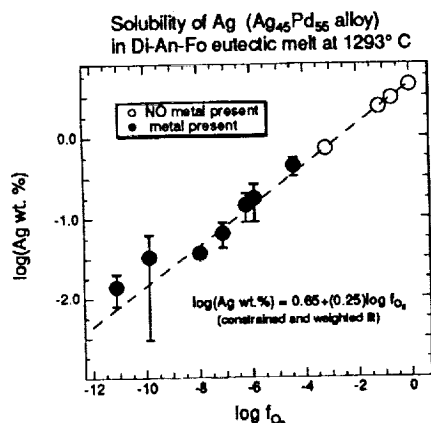


Figure 1. Fitted curve was constrained to a slope of 0.25 and was weighted by the reciprocals of the $\pm 2\sigma$ error bars. Filled symbols represent glasses which contained finely dispersed metallic particles. Although analytical errors in such runs are larger the univalent trend seems to be generally followed despite the presence of these particles, except perhaps for the two lowest oxygen fugacity points. This suggests that the metallic particles may be quench features.

We also present intriguing new data on Sn metal-silicate partitioning. Experiments which produced these data are part of a larger study to examine the metal-silicate partitioning of several chalcophile elements. However the results for Sn illustrate some novel melt chemistry attributable to a variable valence state for Sn in silicate melts.

Metal-silicate partition coefficients for Sn are plotted in Fig. 2 versus oxygen fugacity. Experimental techniques which produced these data are identical to those in Hillgren (1991) and are evacuated silica tube

experiments in which the oxygen fugacity is set by the Fe/Ni ratio of the metallic phase and its equilibration with the silicate.

The effective valence of Sn clearly changes with oxygen fugacity in these series of runs. However, apparent, but not necessarily real, valence changes for trace elements can be produced if the oxidation of the element is controlled by other than the reduction of molecular oxygen, which is the formalism usually adopted. For example, if metallic Sn were oxidized by Fe³⁺ in a system in which metallic Fe constrained the Fe³⁺/Fe²⁺ ratio (see Johnston 1964) then the Sn content of the melt, provided it was small, would also become buffered and independent of oxygen fugacity. Some process akin to this may explain the unusual flattening trend to the data in Fig. 2.

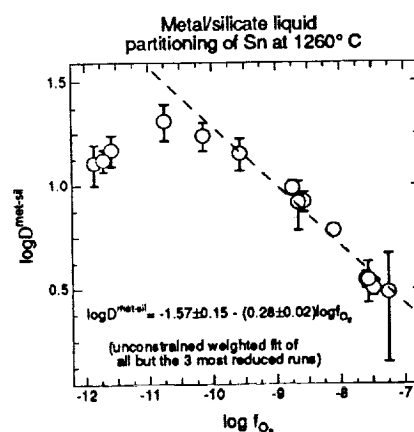


Figure 2. Linear curve was fitted only to data above an oxygen fugacity of 10^{-11} bars and was weighted by the reciprocals of the $\pm 2\sigma$ error bars. A slope of -0.28 ± 0.02 is consistent with predominantly Sn¹⁺.

Acknowledgment: NAGW 3348 and EAR93 03676.

References: Amelin, A., and Capobianco, C. (1992) LPSC XXIII, 29-30; Amossé, J. et al. (1987) C. R. Acad. Sc. Paris 304, 1183-1185; Amossé, J. et al. (1990) Chem. Geol. 81, 45-53; Amossé, J. et al. (1992) Comptes Rendus Acad. Sci. serie II-Mec. Phys. Chimie Sci. de la Terre et de l'Univers 315, 559-564; Borisov, A., et al. (in press) G. C. A.; Capobianco, C., and Amelin, A. (in press) G. C. A.; Capobianco, C. et al. (in press) Chem. Geol.; Capobianco, C. et al. (1992) EOS 73, 344; Capobianco, C. et al. (1993) J. G. R. Planets, 98, 5433-5443; Colson, R. (1990) GSA Abstracts 22, A164; Colson, R. (1992) Nature 357, 65-68; Dingwell, D. et al. (1993) EOS 74, 338; Ehlers, K., and Grove, T. (1990) EOS 71, 647; Ehlers, K. et al. (1992) G. C. A. 56, 3733-3742; Hillgren, V. (1991) G. R. L. 18, 2077-2080; Hillgren, V. et al. (in press) Science; Holzheid, A. et al. (1993) LPSC XXIV 667-668; Holzheid, A. et al. (in press) G. C. A.; Johnston, W. (1964) J. Am. Ceram. Soc. 47, 198-201; Montana, A. et al. (1993) Am. Min. 78, 1135-1142; Morse, S. et al. (1991) G. C. A. 55, 2373-2378; O'Neill, H. et al. (1993) EOS 74, 338; Richardson, F. and Billington, J. (1956) AIME 65, 273-297; Schmitt, W. et al. (1989) G. C. A. 53, 173-185; Steele, A. et al. (1991) LPSC XXII 1317-1318; Steele, A. et al. (1992) G. C. A. 56, 4075-4090; Walker, D. et al. (1993) Nature 262, 1858-1861; Weyl W. (1953) J. Phys. Chem. 57, 753-757.

LOW-TEMPERATURE COOLING HISTORIES OF VIGARANO CAIs: CONSTRAINTS FROM COMPOSITIONS OF METAL PARTICLES; I. Casanova^{1,2} and L. Grossman^{2,3}. ¹Department of Geology, Field Museum of Natural History, Chicago, IL 60605-2496. ²Department of the Geophysical Sciences and ³Enrico Fermi Institute, The University of Chicago, Chicago, IL 60637.

Abstract. Study of metal particles in Ca-, Al-rich inclusions not only provides information about condensation of siderophile elements in the solar nebula but also about the low-T cooling history of CAIs through analysis of their kamacite and taenite. We studied metal in four CAIs from Vigarano (two Type B1, Vig-1 and USNM 477-4; and two Type B2, Vig-2 and USNM 1623-8) as part of our work on the characterization of chemical compositions and inferred cooling histories of metal particles in CAIs from the reduced subgroup of CV3 chondrites (Casanova and Grossman, 1993a,b). Results suggest that metal from different inclusions cooled at different rates at subsolidus temperatures in localized zones of the solar nebula with different dust/gas ratios.

477-4 is an oval (5.2x3.7 mm) CAI that consists of a melilite mantle (300-600 μm thick) and a fassaite+anorthite core, all enclosing spinel poikilitically. Spinel grains in the mantle are smaller (<20 μm) than those in the center of the inclusion (20-60 μm). Two large spinel-free islands (SFI) are present, one roughly spherical, 1 mm in diameter, and the other irregularly-shaped, 2x1 mm. The spherical SFI is enclosed in a palisade body (continuous, closed chain of spinel crystals) and consists of roughly equal proportions of melilite and fassaite, with no anorthite. The melilite crystals in this SFI have homogeneous cores but display normal zoning in the outer 10-15 μm , where their compositions vary from Ak_{51} to Ak_{65} outwards. Fassaite is compositionally identical to that in the main inclusion, displaying a constant $\text{TiO}_2^{\text{tot}}$ content of 9.0 wt% ($\text{Ti}^{3+}/\text{Ti}^{\text{tot}} = 0.816 \pm 0.035$). The other SFI consists of a large single crystal of melilite, homogeneous in composition (Ak_{65-68}) with unzoned rims, poikilitically enclosing irregular grains of Al-rich pyroxene. Metal in the CAI is restricted to the fassaite+plagioclase+spinel-rich area, and makes up ~0.5 vol% of the whole inclusion. It occurs as generally well-rounded blebs that contain kamacite+taenite and occasionally have well-developed, continuous rims of Ca-phosphate (typically 1-3 μm thick). Only two of the 27 metal grains analyzed contain troilite, but in very minor amounts (two small inclusions of <1 and 2 μm). Bulk Ni and Co contents of the larger particles (>10 μm) determined by broad-beam analysis range from 24.5 to 27.8 wt% Ni and from 0.6 to 1.1 wt% Co. On the basis of their PGE (Ru, Os, Ir, Pt) concentrations, metal grains in this CAI can be subdivided into two groups: one with 0.2 wt% Ru, 0.2 wt% Pt, and Os and Ir <400 ppm each, and another with 0.2 wt% Ru, 0.5 wt% Pt, 0.1 wt% Os and 0.1 wt% Ir. There is no clear correlation between bulk Ni and PGE contents of the particles. Detailed microprobe traverses across kamacite-taenite lamellae on grains large enough for accurate analysis (typically >15 μm) show that all analyzed taenite grains have flat profiles, with concentrations between 30.3 and 31.2 wt% Ni; we have observed neither M-shaped Ni profiles in taenite grains nor PGE concentrations of a few wt% in the metal, both of which were reported by Caillet et al. (1988a) in their study of Vigarano 477B, another section of the same CAI. Kamacite exsolution is generally well-defined, with some grains displaying sets of 2-4 lamellae reminiscent of a Widmanstätten pattern. In the smaller grains, however, kamacite nucleates at the interface between the metal grain and its silicate host. Only one FeNi grain (1 μm) has been identified in the interior of the larger melilite-rich SFI. EDS analysis reveals that its bulk major element composition is identical to the metal in the rest of the CAI ($\text{Fe}_{72}\text{Ni}_{26}\text{Co}_1$).

Vig-2 is a comma-shaped fragment of a Type B1 inclusion, previously described by Simon and Grossman (1991). The metal is not as abundant as in 477-4 (<0.1 vol%), although texturally and compositionally it is very similar to the latter. The FeNi in this inclusion is also concentrated in the spinel+fassaite+plagioclase core, with only a few small particles in the melilite mantle. Metallic grains are usually well-rounded and display well-defined kamacite+taenite exsolution, although well-developed, Widmanstätten-like sets of kamacite lamellae were not found. Bulk compositions of single metallic grains range from 26.0 to 29.0 wt% Ni, 0.8-2.1 wt% Co, 0.1-0.3 wt% Ru, <400 ppm-0.6 wt% Os, <400 ppm-0.3 wt% Ir, and 0.1-0.5 wt% Pt. Unlike 477-4, however, there are no clearly distinguishable compositional groups among the metal particles in Vig-2. Microprobe traverses across kamacite-taenite grains show flat Ni profiles in the taenite at 32.0-33.1 wt%, and in kamacite at 5.0-6.1 wt% Ni.

The silicate mineralogy and chemistry of **1623-8** was studied by MacPherson and Davis (1993), and Casanova and Grossman (1993b) reported preliminary results on its metallic fraction. We have extended this study to fully characterize 19 metal particles. There are two compositionally distinct populations of metal in 1623-8. One is represented by 15 well-rounded FeNi grains similar in composition to M1, described by Casanova and Grossman (1993b). Their bulk compositions range from 23.1 to 29.0 wt% Ni and from 0.9 to 2.0 wt% Co, depending on the kamacite/taenite ratio. Total PGE contents are 4-5 wt%. Taenite in these metal grains shows flat Ni profiles, with contents in the interior of different crystals varying between 30.3 and 33.1 wt% Ni. The other 4 metal particles are very rich in PGE, with bulk compositions of 10 wt% Ni, 0.4 wt% Co, 0.6 wt% Re, 0.5 wt% Pt, 6.2-7.0 wt% Ru, 4.0-4.3 wt% Os, and 7.5-8.0 wt% Ir, similar to that of M2 (Casanova and Grossman, 1993b). They are irregular in shape and monomineralic.

Vig-1 is a complex Type B2 inclusion that contains palisade bodies that did not equilibrate with the CAI liquid,

LOW-TEMPERATURE COOLING HISTORIES OF CAIs: Casanova I. and Grossman L.

and abundant alteration products (Simon and Grossman, 1991). Unlike 477-4, Vig-2 and 1623-8, the metal particles in Vig-1 contain numerous Ca-phosphate grains, $<1\text{-}3\text{ }\mu\text{m}$ in size, sprinkled throughout the metal and, rarely, forming rims around it. These phosphate grains are most likely pseudomorphs of phosphide grains that exsolved from the metal and were later oxidized and reacted with Ca-rich minerals from the silicate host. Broad-beam analysis of bulk compositions of metal particles yielded consistently low totals (89-94 wt%), probably due to inclusions (commonly phosphate and occasionally an Fe-rich phase, possibly magnetite) and, consequently, grain boundary effects. Bulk Ni and P contents are 20.5-37.1 and $<0.02\text{-}0.15\text{ wt\%}$, respectively. The bulk PGE contents range typically from 0.1 to 0.9 wt% Ru, $<400\text{ ppm}$ -0.5 wt% of each of Os and Ir, and 0.2-0.6 wt% Pt. Kamacite and taenite are intergrown in submicron-to-micron-sized, plessite-like domains, and do not display clear grain boundaries as in the other CAIs. Nickel contents in taenite and kamacite (determined by point analyses with good analytical totals) are quite variable from grain to grain, showing ranges of 37.2-42.5 and 4.5-6.5 wt%, respectively.

Discussion. The solidus temperature of the silicate assemblages that host the metal is $\sim 1200^\circ\text{C}$ (Beckett, 1986). This precludes the possibility that the subsolidus cooling history of the metal is relict since kamacite and taenite intergrowths would have dissolved in one another in a few minutes at CAI solidus temperatures. For instance, given a diffusivity for Ni in $\alpha\text{-FeNi}$ at 1200°C of $10^{-6}\text{ cm}^2\text{sec}^{-1}$ (Dean and Goldstein, 1986), a $10\text{ }\mu\text{m}$ kamacite grain would completely dissolve in approximately 8 minutes. Since the volume fraction of metal ($<1\%$) is small, cooling of the FeNi particles was controlled by that of their host inclusions. Thus, the thermal history of the metal reflects the cooling history of the CAI at $T < 600^\circ\text{C}$. The well-developed kamacite+taenite lamellae and the flat Ni profiles of the taenite grains in 477-4, Vig-2 and 1623-8 indicate equilibrium crystallization at temperatures between ~ 600 and 500°C (corresponding to Ni contents in the bulk particles and in the taenite of 23-28 and 30-36 wt%, respectively). Attainment of equilibrium requires slow cooling at metal subsolidus temperatures. Although the influence of minor elements in Fe-Ni interdiffusion is not known, we assume that the amounts of PGEs in the metal particles of 477-4 and Vig-2 (total PGEs $<1\text{ wt\%}$ in all cases) have no significant effect on cooling rates calculated on the basis of Fe-Ni interdiffusion alone. The observed flat Ni profiles in taenite may be achieved through either (1) slow cooling at a rate of at most $50\text{-}100\text{ deg/Myr}$ (based on cooling rate curves by Saikumar and Goldstein, 1988) at temperatures $\sim 600\text{-}500^\circ\text{C}$ and subsequent fast cooling (to prevent further enrichment of Ni in taenite) or, (2) fast cooling to low temperatures followed by reheating (to $\sim 500^\circ\text{C}$) and subsequent quenching of the alloy. In either case, a long (maybe multi-stage) subsolidus cooling history for 477-4, Vig-2 (and perhaps 1623-8) is necessary (on the order of $10^4\text{-}10^6\text{ yr}$, as estimated by Caillet et al. 1988b).

On the other hand, the observed variability of Ni contents in taenite among metal particles in Vig-1 suggests non-equilibrium cooling at subsolidus temperatures. The taenite crystals in a single particle are homogeneous, but vary in composition from particle to particle. Since all of the particles consist of kamacite + taenite, the composition of taenite formed by equilibrium cooling would be controlled by the final closure temperature, and all of the taenite grains would have similar Ni contents. The metal particles in the other CAIs discussed above all underwent equilibrium cooling at $T \sim 500^\circ\text{C}$ and the taenite in each exhibits only a small range of Ni contents (0.9 wt% in 477-4, 1.1 wt% in Vig-2 and 2.8 wt% in 1623-8). The taenite grains in Vig-1, however, show a 5.3 wt% range in Ni content. If the taenite grains in Vig-1 cooled at equilibrium, then different equilibration temperatures (between 400 and $\sim 250^\circ\text{C}$) would be required for different particles in the same CAI. This is not plausible and implies that the compositional variability in Vig-1 taenite is due to non-equilibrium crystallization of kamacite and taenite. The cooling history of metal in Vig-1 is, consequently, very different from that of the other CAIs.

To reconcile the different cooling histories indicated by metal in the CAIs studied here, two different scenarios may be proposed: (1) the inclusions cooled at different depths in the Vigarano parent body (Vig-1 near the surface and the others at $\sim 20\text{ km}$ in a $100\text{-}200\text{ km}$ radius parent body), or (2) cooling of the CAIs occurred in different nebular environments at different rates. The first hypothesis would imply breakup and reassembly of the Vigarano parent body (or breakup of another one, fragments of which accreted later onto Vigarano), in order to mix materials cooled at different depths. It is difficult to envision, however, how the highly unequilibrated nature of the Vigarano silicates and volatile content of its matrix could be maintained at $\sim 500^\circ\text{C}$ for at least several thousand years, the conditions required for the slowly cooled metal grains. Instead, we favor nebular cooling, as such conditions may be possible if high dust/gas ratios existed in localized regions of the solar nebula. The materials that accreted to form Vigarano probably came from a variety of nebular environments with different thermal histories, perhaps regions with different opacities due to different gas/dust ratios.

REFERENCES: Casanova I. and Grossman L. (1993a) LPSC XXIV: 257-258. Casanova I. and Grossman L. (1993b) Meteoritics 28: 335. Simon S.B. and Grossman L. (1991) LPSC XXII:1261-1262. Caillet C., MacPherson G.J. and El Goresy A. (1988a) LPSC XIX: 156-157. Caillet C., Goldstein J.I., Velde D. and El Goresy A. (1988b) Meteoritics 23:262-263. MacPherson G.J. and Davis A.M. (1993) GCA 57:231-243. Beckett J. (1986) Ph.D. Thesis, University of Chicago. Zanda B. (1992) LPSC XXIII:1569-1570. Dean D.C. and Goldstein J.I. (1986) Met. Trans. 17A:1131-1138. Saikumar V. and Goldstein J.I. (1988) GCA 52: 715-726.

IMPACT CRATERS ON MARS: THE RELATIVE ROLES OF ATMOSPHERIC AND SUBSURFACE VOLATILES

Julie Cave and John Guest

University College London, U.L.O. Planetary Image Centre,
33-35 Daws Lane, Mill Hill, London NW7 4SD.

Nadine Barlow, Lunar and Planetary Institute, Houston, Texas.

Craters and their associated deposits provide a valuable means by which the properties of near-surface materials, particularly postulated sub-surface ice, may be examined (1). It is becoming increasingly apparent that the presence of a tenuous atmosphere may also have influenced the cratering process on Mars (2,3). It is difficult to evaluate the importance of atmospheric volatiles, however, because of the likely presence of a planet-wide ground-ice (4 and references therein) which is thought responsible for many of the characteristics of large martian craters, including rampart ejecta and central pits (1,5). Recent theoretical and experimental data (3) have further challenged the traditional interpretation of martian impact craters, having demonstrated the ability of atmospheric gases to produce fluid-like ejecta emplacement, and an evaluation of the importance of such processes on Mars from observational data is now required.

In previous work a database of over 7000 impact craters within a region roughly centered on Elysium was created from *Viking* data and analysed to investigate the distribution of martian ground-ice within this region by the variation of ejecta mobility and morphology with crater diameter, geology, latitude and altitude (6,7). The research indicated that sub-surface ice is likely to influence ejecta morphology strongly: the concentration of the postulated ice apparently varies according to the geological situation of an area, while its near-surface limit is latitude-dependent. This interpretation is strengthened by the observed distribution of other potentially ice-related landforms in the region, and theoretical predictions of ice-stability. The ejecta of many small craters, however, indicate signs of fluid-flow emplacement, and possible altitudinal trends in the variation of ejecta mobility of small and large craters were detected. Further analysis of this database and the re-evaluation of a globally comprehensive crater database is now underway in order to achieve a comprehensive assessment of the relative importance of atmospheric and sub-surface volatiles in the cratering process on Mars.

Conclusions from analysis of Elysium impact craters to date:

The initial analysis of the Elysium database (covering longitudes 245°-155° and latitudes 20°S-45°N) demonstrated that the ratio of ejecta diameter to crater diameter increased with increasing crater diameter. When the characteristics of sub-sets of the data were examined it was apparent that this increase in the ratio of ejecta to crater diameter, and hence increase in the mobility of the ejecta during their emplacement, generally occurred as a discontinuity (or break-point) at different diameters for different sub-sets of the data. A statistical technique was devised to locate the onset diameters of the enhanced ejecta mobility for datasets sorted by latitude, altitude and geological unit of the craters. The gradients of the data below and above the located break-points were taken as a measure of the ejecta mobility, and the percentages of craters with certain morphologies smaller and larger than the relevant break-points were determined in each case. This technique allowed the characteristics of craters which excavated material from the upper and lower parts of the martian sub-surface to be considered independently, and thus enabled a detailed prediction of the location of sub-surface ice at different depths to be made. A clear latitudinal trend in the depth of sub-surface ice was apparent in this region, despite the diversity of the surface units and the inferred concentration of the postulated sub-surface ice was shown to be consistent with the distribution of other geological features.

The importance of atmospheric and elevational variations was less clear, particularly since, in places, there were almost simultaneous variations in altitude and latitude. Within the Elysium study region there was some indication that craters of different sizes are differently influenced by the atmosphere, but further investigation is needed to verify and explain this observation. An important atmosphere-related implication arises from the observation that the various types of rampart ejecta occur at a wide range of altitudes, i.e., the formation of ejecta which shows signs of a fluid-like emplacement is not strongly influenced, or limited by the altitude of the target. This implies that either the atmosphere was previously more dense or that the flow-inducing processes are not highly critical upon atmospheric pressure. Alternatively, the results may indicate that any atmosphere-related emplacement mechanism *within the region studied* was negligible when compared with the ground-ice induced flow.

IMPACT CRATERS ON MARS: J.A. Cave et al.

Caution must be exercised in extrapolating these observations to Mars as a whole, however, because of the complexity of the study region, its particular location, and the limited accuracy of the craters' altitude estimates. An examination of the crater characteristics of other areas of Mars where either latitudinal or altitudinal variations are limited will provide further information on the relative importance of the two factors.

Current research on Elysium and global impact craters

The extended analysis of the Elysium database is concentrating on the variations of the detailed characteristics of the more common morphological types of crater in order to evaluate existing models of their formation. Owing to the complexity of the region a natural extension of this investigation is to display the average morphological characteristics in a 2-D grid (of variable dimensions and minimum crater diameter) for all craters in the region in order to show their spatial distribution and onset diameters. This approach will highlight any unusual concentrations of particular crater characteristics which may have influenced the systematic analysis, and hence may either have contributed to or masked any altitudinal trend.

It is important also to consider the global variation of impact crater characteristics. A major database by Barlow (e.g. 8) contains compatible data on the morphology, dimensions and latitude and longitude of all martian craters over 5 km in diameter. An estimate of the altitude of each crater will be incorporated into this database, using the geographical coordinates of the craters' locations and digital topographic data. This global crater database will then be analysed in a similar fashion to that used by Cave (6,7), which will allow the determination of underlying morphological trends in a wider variety of latitudes and terrain types. (The potential problem of the exclusion of the smallest craters from this global database will receive careful consideration, as it may not be possible to locate break-points accurately for all data sets.) To eliminate some of the ambiguity of the suggestions of altitude-related variations in ejecta morphology, the characteristics of craters will be examined as a function of altitude and of latitude for single, reasonably homogeneous geological units.

Targeted studies of impact crater characteristics are also being carried out in regions of specific interest, such as volcanic regions (9), using the highest resolution Viking images. It is anticipated that the combination of local, regional and global studies will facilitate a comprehensive assessment of the relative contribution of atmospheric and sub-surface volatiles to the observed variations in martian impact crater morphology.

References

- (1) Carr, M.H., L.S. Crumpler, J.A. Cutts, R. Greeley, J.E. Guest, H. Masursky, *Journal Geophys. Res.* **82**, 4055-4065, 1977.
- (2) Schultz, P.H. and D.E. Gault, *Journal Geophys. Res.* **84**, 7669-7687, 1978.
- (3) Schultz, P.H., *Geophys. Res. Planets*, **97**, 11623-11662, 1992.
- (4) Squyres, S.W., *Icarus* **79**, 229-288, 1989.
- (5) Greeley, R., J.H. Fink, D.E. Gault and J.E. Guest, In *Satellites of Jupiter*, ed. David Morrison, Univ. Arizona Press (Tucson), 1982.
- (6) Cave, J.A., Ph.D. thesis, University of London, 1991.
- (7) Cave, J.A., *Journal Geophys. Res. Planets* **98**, 11079-11097, 1993.
- (8) Barlow and Bradley, *Icarus*, 1990.
- (9) Cave, Guest, Moore, Carroll and Barlow, *L.P.S.C. XXV* (this issue), 1994.

IMPACT CRATER MORPHOLOGY ON MARTIAN VOLCANOES

Julie Cave, John Guest, Brendan J. Moore, John Carroll,
University College London, U.L.O. Planetary Image Centre,
33-35 Daws Lane, Mill Hill, London NW7 4SD.

Nadine Barlow, Lunar and Planetary Institute, Houston, Texas, U.S.A.

The distribution of impact crater characteristics and a number of other features imply the previous presence of ground-ice at depth within the Elysium lavas (unit Ael₁ [1]) and nearer the surface of the hummocky deposits to the northwest of Elysium Mons (unit Ael₃ [1])(2,3). It has been suggested that the inferred ice-distribution resulted from the concentration and subsequent redistribution of ground-ice (which possibly included an amount of juvenile water) as a consequence of local volcanic activity (2). In order to investigate this hypothesis further, and to determine whether the impact crater characteristics are unique to the Elysium province, a survey of impact crater morphology on all major martian volcanoes is in progress.

Ice in the Elysium volcanic region

Craters exhibiting central pits, double ejecta, partial extra ejecta lobes, jagged edges and high ejecta mobility may indicate the presence of ground-ice *at the time of their formation* (4). High proportions of these features generally occur in large craters (of over 9.4 km in diameter) within Elysium lava unit (Ael₁), suggesting that substantial quantities of ice were present at depth. In comparison, the near-surface layers of this unit appear relatively ice-poor: in particular, radial ejecta craters and a low average ejecta mobility are associated with Elysium Mons itself and areas immediately surrounding the construct (2). Further evidence suggesting the presence of an ice-rich layer capped by ice-poor material is provided by the signs of chaotic breakup of the surface to the west and north of Elysium Mons, and the concentration of outflow channels to the northwest. In addition, the deposits associated with these channels have been shown to be rich in ice (2), and to have morphologies consistent with their emplacement as lahars (5). Within the region studied here, with the exception of Hebrus Valles, the channels with Lowland sources are closely associated with Elysium Mons. This work has provided further evidence that this association is not coincidental, and strongly suggests that, in the case of *this* volcanic province, juvenile water contributed to the formation of a substantial sub-surface ice reservoir.

Implications for other martian volcanoes and crater formation

The strong correlation between the impact crater characteristics and the individual Elysium volcanic units is of relevance to the interpretation of the nature of volcanic materials and the causes of various impact crater morphologies. In particular, it is difficult to determine if the observed differences in crater morphology are due to a variable concentration of ice in differing geological situations or whether the physical nature of the rock could itself influence the ejecta range. While the interpretation that the morphological characteristics of small craters on the Ael₃ unit are the result of impacts into near-surface ice-rich deposits appears reasonable, it must be remembered that this rock-unit may have been particularly friable, and as such may have been strongly affected by atmospheric emplacement mechanisms (6) or other causes of fluid-like emplacement of ejecta (4). It is important, therefore, to consider the nature of impact craters on other martian volcanoes, and their associated deposits, some of which may have similar physical properties to the Elysium geological units.

The martian volcanoes are potentially useful targets for the detailed analysis of target nature implications for the formation of impact craters owing to their restricted size (each covering a limited range of latitude) and relatively homogeneous composition when compared with more expansive geological units. In addition, the volcanic constructs are of varied age, eruptive style and geographical location (7), which will enable useful comparisons between individual volcanoes, and types of volcano to be made. A comprehensive analysis of the characteristics and dimensions of impact craters on all major volcanoes is now underway using a classification scheme and techniques developed by Cave (2,3). The analysis will include all impact craters of 2 km diameter and over, and will simultaneously consider general and small-scale characteristics of the volcanoes. The project aims to determine whether target material (such as lava and ash deposits), the possible presence of ground-ice, volcano age, latitude or altitude has had the greatest influence on both interior and exterior impact crater morphology.

IMPACT CRATER MORPHOLOGY ON MARTIAN VOLCANOES: J.A. Cave et al.

This approach will yield information on whether the nature of the rock or the depth and concentration of sub-surface ice is the more important in determining the resultant crater morphology, and will also address the potential importance of volcanic activity in the generation and evolution of martian ground-ice.

References:

- (1) Greeley R. and Guest J.E., Map I-1802-B, U.S.G.S., 1987.
- (2) Cave, J.A., *Journal Geophys. Res. Planets*, **98**, 11079-11097, 1993.
- (3) Cave J.A., Ph.D. Thesis, University of London, 1991.
- (4) Carr, M.H., L.S. Crumpler, J.A. Cutts, R. Greeley, J.E. Guest, H. Masursky, *Journal Geophys. Res.* **82**, 4055-4065, 1977.
- (5) Christiansen E.H., *Geology* **17** 203-206, 1989.
- (6) Schultz, P. H., *Journal Geophys. Res. Planets*, **97**, 11623-11662, 1992.
- (7) Mouginis-Mark P.J., L. Wilson, M.T. Zuber, in *Mars*, ed. Kieffer *et al.*, University of Arizona Press, 1992.

EVIDENCE FOR EPISODIC TECTONIC CONSTRUCTION OF OVDA REGIO, VENUS; D. John Chadwick and Gerald G. Schaber, U.S. Geological Survey, Flagstaff, AZ 86001

Terrestrial continents grow laterally by the impingement of exotic terranes transported by the crustal movements of plate tectonics. Terrestrial-style plate tectonism apparently does not exist on Venus today [1], but significant lateral crustal movement has produced the linear fold and thrust belts that border many of the Venusian upland tesserae and Lakshmi Planum.

The cratering record on Venus suggests that the lowland areas of the planet were completely resurfaced by volcanism at about 0.3-0.5 Ga, and that subsequent volcanism was comparatively minor [2-4]. Thermal models suggest that Venus may have undergone such "catastrophic" resurfacing several times [5]. The distribution of the entire crater population is consistent with a statistically random one, both spatially and hypsometrically [3,4]. The highland tesserae regions of Venus must also have been resurfaced, largely by tectonism but supplemented by volcanism, during the same period as the volcanic resurfacing on the plains. Although all evidence of older resurfacing of the lowland plains was likely buried by the most recent resurfacing, the high elevation of the tesserae would have prevented inundation and may have preserved tectonic and volcanic evidence of older periodic global resurfacing episodes.

In this study, we are investigating Ovda Regio, a highland tessera region in the western part of Aphrodite Terra. Elevation of the tessera ranges from 1 to 4 km above surrounding Aino and Niobe Planitiae. Ovda is divided into two tectonic domains distinguished by the dominant trend in their compressive structures (Fig. 1). The western domain has experienced dominantly NNW-SSE compression; the eastern domain, mostly NE-SW and E-W compression. Each domain is subdivided into several subregions, based on the presence, abundance, and orientations of various lineaments, grabens, and folds. The tectonic fabric in the four western subregions appears to grow increasingly complex toward a central "core" region of the tessera. Two subregions to the north and one to the south are less complex, with the northernmost domain a relatively simple fold and thrust belt crosscut by orthogonal grabens. The western domain is bounded on the south by Ix Chel Chasma, an extensional rift. The eastern domain is divided into five subregions that also appear to grow in complexity toward an interior core (Fig. 1). One subregion to the west of this central region is composed of simple fold and thrust belts. To the east, three subregions whose tectonic complexity decreases progressively with distance from the core region. The eastern domain is bounded on the south by Kuanja Chasma.

We propose that the increasingly complex tectonic fabrics of discrete subregions in these two domains with distance from their tectonically simple and apparently young border-parallel fold and thrust belts suggest that Ovda Regio has been built in a piecemeal fashion, with fold belts adding to the lateral extent of the tessera during periods of high planet-wide tectonic and volcanic activity. The development of the fold belts may have accompanied downwelling and subduction under the tessera, as described by [6]. Interior subregions still contain border-parallel folds that are crosscut by younger grabens and possible strike-slip faults, suggesting that they were once simple fold and thrust belts like those now on the periphery of Ovda. In this model, interior subregions are "older" in the sense that they have existed as highlands for a longer period than other subregions, but extension within them has maintained a statistically random crater population on the tessera, as has volcanism on the plains. Crater destruction on the tessera is likely supplemented by volcanism; about 15% of Ovda is covered by relatively young volcanic deposits (Fig. 1).

In the youngest fold belts, a system of grabens--all orthogonal to the folds--has overprinted them. This pattern is similar to that in the Himalayas, where north-trending grabens have crosscut the east-trending mountain belts. Mercier and others [7] suggested that a change from compressive to extensional tectonism in the Himalayas in the late Miocene was the result of the change of the maximum principal stress direction from horizontal to vertical, due to the increase in the vertical principal stress caused by the weight of the elevated mass. In Ovda Regio, some subregions appear to have undergone several phases of such gravitational extension; in many cases, all traces of the original compressive fabric are gone. It is also possible that these core regions were once large, silicic, festoon flows, similar to the large flows south of Aphrodite Terra and atop Ovda itself, which are 400 m to 1.1 km high [8]. Such silicic piles would thicken the crust and behave as strain magnets, localizing compression during resurfacing events.

EPISODIC CONSTRUCTION OF OVDA REGIO: **Chadwick, D.J. and Schaber, G.G.**

References: [1] Solomon, S.C., and others, 1992, *J. Geophys. Res.*, 97, E8, 13,199-13,255; [2] Schaber, G.G., and others, 1992, *J. Geophys. Res.*, 97, E8, 13,257-13,301; [3] Strom, R.G., Schaber, G.G., and Dawson, D.D., in press, *J. Geophys. Res.*; [4] Strom, R.G., Schaber, G.G., and Chadwick, D.J., this conference; [5] Arkani-Hamed, J., Schaber, G.G., and Strom, R.G., 1993, *J. Geophys. Res.*, 98, E3, 5309-5315; [6] Lenardic and others, 1993, *J. Geophys. Res.*, 98, E10, 18,697-18,706; [7] Mercier and others, 1987, *Tectonics*, 6, 3, 275-304; [8] Moore, H.J., Plaut, J.J., Schenk, P.M., and Head, J.W., 1992, *J. Geophys. Res.* 97, E8, 13,479-13,493.

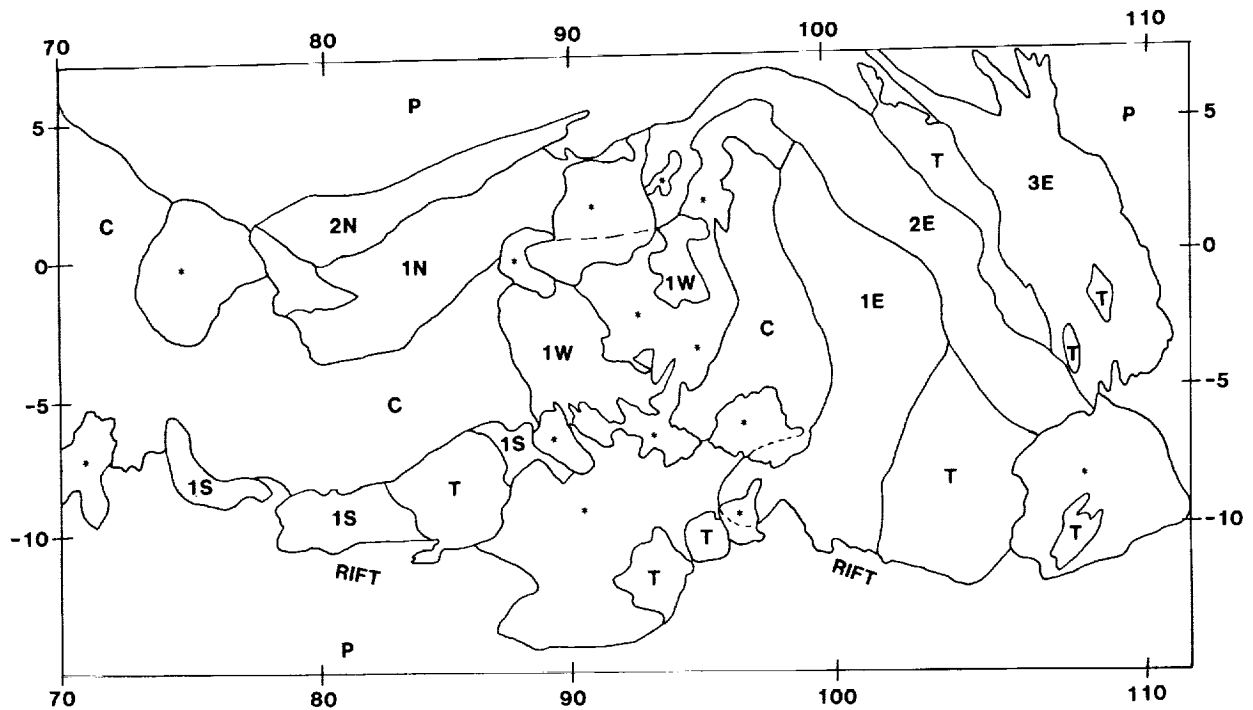


Figure 1. Sketch map of Ovda Regio, showing subregions in the western domain (C, 1N, 1S, 2N) and eastern domain (C, 1W, 1E, 2E, 3E). The core regions (C) have the most complex tectonic fabrics, whereas subregions near the borders (2N, 1S, 3E, 1W) of the domains are relatively simple fold and thrust belts. Border-parallel folds are largely destroyed by grabens but still visible in subregions 1N, 2E, and 1E, suggesting that they were once on the periphery of Ovda. The same number in different subregions (i.e. 1N, 1W, 1S, and 1E) does not necessarily imply the same age for these subregions. "T" denotes small, complex tessera blocks that are apparently entrained in the fold belts. An asterisk (*) shows areas where volcanic deposits, coronae and arachnoids have masked the tectonic pattern of the tessera. Dashed lines denote buried contacts between subregions.

REFINED VOLCANIC AND TECTONIC HISTORY OF THE VALLES MARINERIS, MARS; D. John Chadwick, Gregory J. Leonard, and Kenneth L. Tanaka; U.S. Geological Survey, Flagstaff, AZ 86001

The early formational history of the Valles Marineris must be largely deduced from the crosscutting relations of structures to surrounding plateau materials that can be dated, because mass wasting within the chasmata has erased craters that could have been used to determine relative ages. Previous crater counts [1] were not comprehensive, not taking full advantage of areas available for counting. We have performed more complete crater counts, based on the mapping of [1], for all larger units surrounding the Valles Marineris (Figure 1). These counts (Table 1) were made from the Mars Digital Image Mosaic (at a resolution of 231 m/pixel). We counted all craters larger than 2 km in diameter; however, our relative ages are based on densities of craters larger than 5 km because of their better preservation. Our results indicate extensive formation of smooth lava plains during the Late Noachian and Early Hesperian that waned in the Late Hesperian. Following wrinkle-ridge development, Valles Marineris faulting began in the later part of the Early Hesperian and continued into the Late Hesperian. Pit and trough formation primarily occurred during the Late Hesperian, at about the same time as the formation of the outflow channels that adjoin the Valles Marineris [1]. A brief history of the region follows.

Late Noachian: The oldest units adjacent to the Valles Marineris were probably flood basalts (units Q, P, and N, Figure 1), which were later deformed in places by grabens of several orientations that generally do not parallel the chasmata.

Early Hesperian: Flood basalts continued to be emplaced, embaying and partly burying the Noachian units. Wrinkle ridges then deformed the Noachian and Hesperian plains units, except for units E and F, where wrinkle ridges either did not form or were buried by later Lower Hesperian units. In later Late Hesperian time, faults and grabens began to form that are parallel to the present chasmata (in units E, F, and N), perhaps signalling incipient formation of the chasmata.

Late Hesperian: Emplacement of smooth plains units continued, though confined to the western part of the map area and locally near the chasmata. Note the progressive decrease in age from unit Q to J to B, suggesting either a waning of Tharsis-centered volcanism or a shift in source region with time. Faulting parallel to the Valles Marineris continued, perhaps more intensely than in the Early Hesperian. Pit crater chains and catenae, possibly indicative of the onset of collapse in the Valles Marineris, first appeared in the Late Hesperian. No partly buried catenae are visible in Upper Hesperian plains units, and catenae are developed equally well in Upper and Lower Hesperian units. Mass wasting of the chasmata walls, collapse, and minor tectonism probably continued into the Amazonian.

The appearance of grabens and faults that parallel the Valles Marineris in the Early Hesperian suggests that the chasmata began to develop at this time, but the apparent greater number of grabens and faults and the onset of catenae formation in the Late Hesperian suggest that most of the tectonism and collapse in the Valles Marineris took place in the Late Hesperian.

VALLES MARINERIS, MARS: Chadwick D. J. et al.

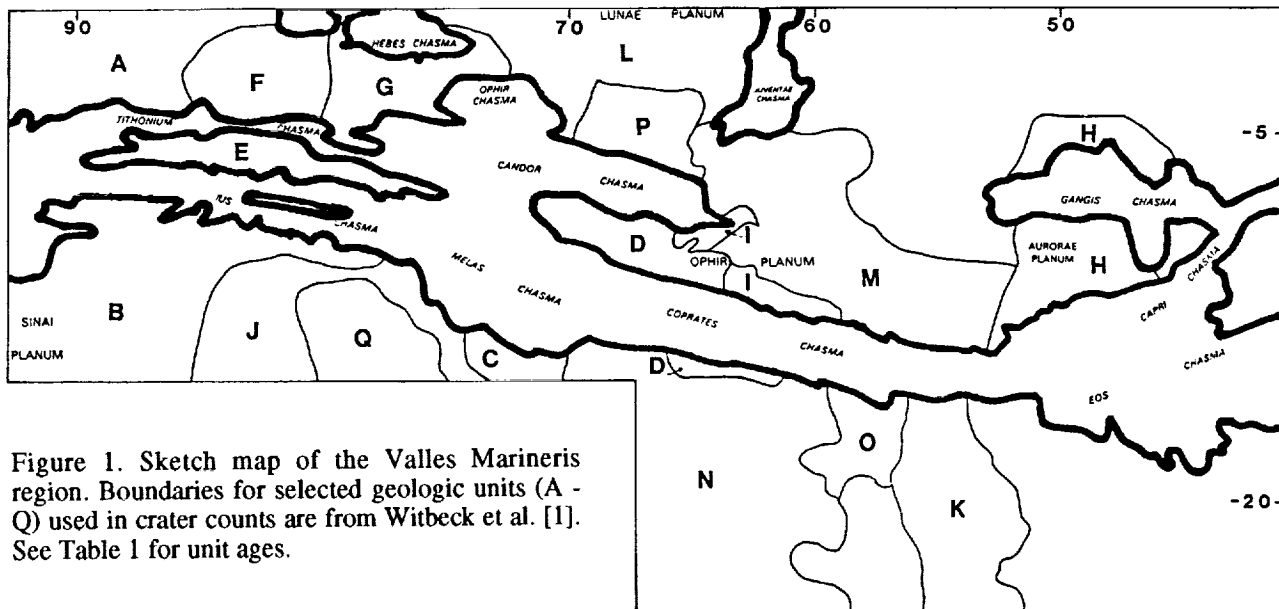


Figure 1. Sketch map of the Valles Marineris region. Boundaries for selected geologic units (A - Q) used in crater counts are from Witbeck et al. [1]. See Table 1 for unit ages.

Table 1. Cumulative crater densities and relative ages of geologic units in the Valles Marineris region of Mars.

Geologic unit ¹	Symbol	Crater density ² N(5)	Area (km ²)	Possible age range ³	Likely age ⁴
Syria Planum Formation					
Upper member	Hsu				
A		86±31	92,624	UH/LA	UH
B		119±32	117,342	LH/UH	UH
Plateau units					
Younger fractured material	Hf				
C		71±50	28,085	UH/MA	UH
D		106±40	66,029	LH/LA	UH
E		153±48	65,223	UN/UH	LH
F		164±47	73,069	UN/UH	LH
Smooth unit	Hpl3				
G		110±39	72,568	LH/UH	UH
H		273±54	95,221	UN	UN
I		332±105	30,079	MN/UN	UN
Ridged plains material	Hr				
J		155±40	96,860	LH/UH	LH
K		147±43	81,381	LH/UH	LH
L		163±31	165,404	LH	LH
M		190±31	200,091	UN/LH	LH
N		218±34	183,864	UN/LH	UN
Subdued cratered unit	Npl2				
O		122±55	40,846	LH/UH	UH
P		210±63	52,405	UN/LH	UN
Ridged unit	Nplr				
Q		234±57	72,800	UN/LH	UN

¹Units from Witbeck et al. (1991). ²Number of craters larger than 5 km in diameter per million square kilometers.

³Based on Tanaka (1986); reflects both material and modification ages. A = Amazonian, H = Hesperian, N = Noachian; U = Upper, M = Middle, L = Lower. ⁴Based on crater densities and superposition relations.

WAX MODELING OF THERMAL EROSION IN LOW-VISCOSITY LAVA FLOWS ; D. Challis, S. Williams, and R. Greeley, *Department of Geology, Arizona State University, Tempe, Arizona 85287-1404*

Summary: Potential thermal basal erosion of lava channels is greater beneath lava flowing under turbulent as opposed to laminar conditions because internal heat transport outward is much greater. This study assessed the qualitative differences in erosional features produced by hot fluid flows over a bedrock modeled by polyethylene glycol (PEG) wax. Erosion rates increased as the flow transitioned from laminar to turbulent conditions, but there was little change in erosional morphology until higher flow regimes were attained, in which irregular scallops were cut into the channel floor and sides.

Background: Lava flows can enlarge their channels by purely thermal erosion or by a combination of thermal and mechanical erosion. On Earth, thermal erosion has been observed in carbonatite flows [1] and has been inferred to occur at the base of komatiites [2], but has not been observed during active basalt flow emplacement. Thermomechanical erosion has been invoked for the formation of lunar sinuous rilles [3, 4] and long venusian channels [5]. In general, long sinuous channels suggest emplacement by a low-viscosity, rapidly-flowing fluid, but this raises a dilemma. The low flow viscosity implied by long flow distances implies that flow conditions were likely to have been turbulent, yet turbulence significantly increases the rate of internal heat loss, making long flows less likely. A turbulent flow may erode thermally more efficiently than a laminar flow because there is only a thin sub-laminar layer between the ground and the hottest fluid and there is a large quantity of heat being delivered to the top of the thermal boundary layer by the internal turbulence of the flow. There is a sharp temperature gradient over a short distance, the temperature at the flow/ground interface is above its solidus, and the ground melts. In a laminar flow the hottest part of the fluid is in the center of the flow, thus, the temperature gradient traverses a longer distance for the same flow thickness. The temperature at the ground interface is lower, making it harder to rise above the ground's solidus and so, basal melting is less certain. Even so, there was sufficient heat available in the 1988 carbonatite eruption to cause basal erosion, even though the flow was laminar [1]. This study focuses on modeling low viscosity lavas and whether turbulent conditions lead to thermal or thermomechanical erosion. The resulting morphologies are assessed for forms that are sufficiently different to be detectable in nature.

The assessment of terrestrial flow regimes utilizes two dimensionless parameters, the Reynolds number (Re) and the Froude number (Fr). Re is the ratio of the inertial forces acting on a given parcel of fluid to the internal viscous forces within the fluid that resist flow. A rule of thumb for open channel flows, is that when $Re < 500$ the flow is fully laminar and when $Re > 2000$ the flow is fully turbulent. Fr is the ratio of the inertial to gravitational forces acting on the flow. At $Fr < 1$, gravity forces are greater than inertial forces, the fluid's surface is relatively undisturbed and the flow is considered "tranquil". At $Fr > 1$, standing waves and other features may occur and the flow is said to be "rapid" [6]. Terrestrial basalts and komatiites have $Fr < 1$ and are, hence, tranquil flows at most places in their channels. The wax flow speeds required for turbulent flow also produce an $Fr > 1$; future modeling is required to assess thermal erosion under modeled tranquil flow conditions.

Procedure: Polyethylene glycol (PEG) waxes have been used to imitate lavas in several studies [2, 7, 8, 9]. PEG has been used before because it is a Bingham non-Newtonian fluid and it can form surface crusts under prevailing laboratory conditions. Several different weights of PEG were used in this study, including water and a 50% water/PEG 200 mixture, in order to simulate lavas of different viscosities. The model lavas were extruded into rectangular channels (3 cm deep x 6 cm wide x 170 cm long) in a base of solid PEG 3350. Test runs of different waxes were made with varying temperatures and slopes in order to cover the widest possible ranges of Re and Fr . Erosion runs were then made at a flow temperature of 100° and a slope of 10° for maximum thermal erosion and Re (see Table 1). Flow depths were measured along the length of the channel during a run and the surface flow velocity was measured by motion picture analysis.

Results: All runs produced erosion of the original channel. However, there were distinct differences in erosion rate and channel morphology with increasing Re . PEG 3350 (the most viscous wax) produced an Re of ~ 100 . Downward erosion was 2-5 mm and lateral erosion was 4-5 mm in ~ 10 minutes. The channel shape was smooth, with a rounded channel floor, similar in cross-section (Figure 1) to channels produced by [2]. Runs conducted with PEG 200 had an Re of 4000-6000, well into the turbulent range. The erosion rate was much higher than with PEG 3350, (with approximately double the amount of cutting in one third of the time), yet, the eroded channel shape was qualitatively the same as in the laminar flow. The 50% water/PEG 200 mixture had an Re of 7750 (despite having a slower velocity than the more viscous PEG 200). This run caused the same amount of sidecutting as the turbulent PEG 200 in the same time but the downcutting rate was three times as great. The channel morphology was also changed. Scallops ~ 3 cm in size were eroded into the base of the channel and irregular scallops were cut into the sides. The pure water run had an Re of 39000 and was the most erosive, downcutting 2-3 cm and sidecutting 0.5-1 cm in two minutes. The channel shape had many small, random scallops (~ 1 cm) on the base and sides (Figure 1).

WAX MODELING OF THERMAL EROSION; Challis, D., Williams, S. and Greeley, R.

Conclusions: Thermal erosion was produced under both laminar and turbulent conditions. The flow state controls the rate of erosion to a certain extent, but not the channel morphology. Instead, the style of erosion changes at high Reynolds number ($Re > 6000$); this behavior is analogous to sedimentary deposition where the style of deposition changes from plane beds to anti-dunes in the upper flow regime. Future work planned includes more accurate determination of model thermal properties for better quantitative modeling of natural thermal erosion.

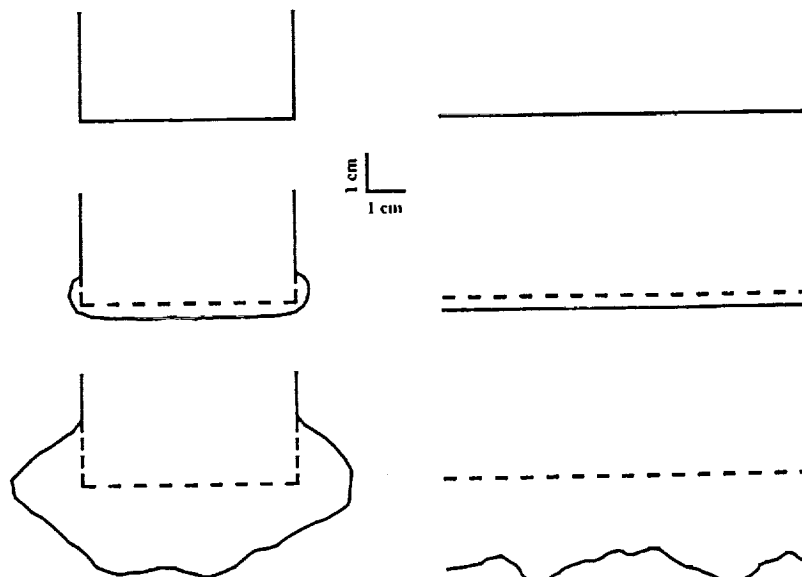
References: [1] Dawson, J.B. et al. (1990) *Geology*, 18, 260-3. [2] Huppert, H.E. and Sparks, R.S.J. (1985) *Journal of Petrology*, 26, 694-725. [3] Hulme, G. (1973) *Modern Geology*, 4, 107-117. [4] Carr, M.H. (1974) *Icarus*, 22, 1-23. [5] Baker, V. et al. (1992) *JGR*, 97, 13421-13443. [6] Briggs, L.I. and Middleton, G.V. (1965) in Middleton (ed.) *SEPM Special Publication* 12, 5-16. [7] Hodgson, G.W. (1981) Unpublished M.S. manuscript, Air Force Institute of Technology, Wright-Patterson AFB, Ohio. [8] Greeley, R. and Womer, M. (1981) *LPSC XII Proceedings*, 651-662. [9] Griffiths, R.W. and Fink, J.A. (1992) *JGR*, 97, 19729-19737.

Table 1. Summary of Erosion Runs

Run #	Material	Slope	L m	V m/s	ν m/s	Duration sec	Re VL/ ν	Fr V/\sqrt{Lg}	Erosion Rate mm/min		Comments
									SIDE	BASE	
501	PEG 3350	10°	9.4(-3)	0.84	7.0(-5)	544	110	2.8	0.4-0.5	0.2-0.5	Smooth floor and side erosion (U-shaped)
503	PEG 200	10°	1.4(-2)-9.2(-3)	1.85	4.3(-6)	219	4000-6000	5.0-6.1	1.9-2.5	1.4-2.7	Same morphology as in 501 but erosion rate was higher
504	50/50 mix of PEG 200 & H ₂ O	10°	6.3(-3)	1.59	1.3(-6)	210	7750	6.4	2.0-3.5	~8	Scalloped floor erosion; there is some periodicity to the scalloping downstream ($\lambda \sim 3$ cm)
502	H ₂ O	10°	7.0(-3)	1.61	2.8(-7)	136	3.9(4)	6.1	2.2-6.2	8.8-12.3	Severely scalloped (random) erosion
	Basalt	0-10°	3.3	1-5	1.8(-2)		180-890	0.17-0.87			
	Komatiite	0-10°	4.5-25	0.1-4.0	3.3(-5)-3.6(-3)		125-7.5(4)	0.015-0.6			

L = cross-sectional area / wetted perimeter, V = flow speed, ν = kinematic viscosity; Scientific notation exponents in parentheses.

Figure 1. Cross-section and longitudinal sections of typical erosion channel. The initial sections are shown at the top, the laminar/turbulent case in the middle, and the very turbulent case on the bottom. The laminar run duration was 550 seconds and the very turbulent run duration was 140 seconds. Dotted lines indicate the pre-flow surface.



2960

2
LUNAR MINERAL FEEDSTOCKS FROM ROCKS AND SOILS: X-RAY DIGITAL IMAGING IN RESOURCE EVALUATION John G. CHAMBERS, Allan PATCHEN, Lawrence A. TAYLOR, Stefan J. HIGGINS, Planetary Geosciences Inst. Dept of Geol. Sci., Univ. of Tennessee, Knoxville, TN 37996; and David S. McKAY, Mission Sci., & Tech. Office, Code SN14, Johnson Space Center, Houston, TX 77058. ✓

The rocks and soils of the Moon provide raw materials essential to the successful establishment of a lunar base (e.g., [1]). Efficient exploitation of these resources requires accurate characterization of mineral abundances, sizes/shapes, and associations of "ore" and "gangue" phases, as well as the technology to generate high-yield/high-grade feedstocks. Only recently, have x-ray mapping and digital-imaging techniques been applied to lunar resource evaluation ([2-6]). Our previous efforts have involved quantitative characterization of mineral liberation and beneficiation of hi-Ti basalt 71055 ([5-6]) with software from Oxford Inst. Inc. coupled with an EDS attached to a Cameca SX-50 EMP.

X-ray digital-imaging techniques supply a quantitative method of mineral resource evaluation ([5]), and therefore, application of these methods provide the best way to compare the mineral resource potential of soils and rocks. Previous studies have compared various soils, rocks, regolith breccias, and pyroclastic glasses as potential ilmenite feedstock sources ([2] and [4]), but no x-ray digital-imaging study has addressed the mineral feedstock potential of lunar soils. This is largely due to the difficulty of using chemical criteria to distinguish the complex impact-glass-welded components present in lunar soil. Integration of recent software development for digital-imaging combined with traditional petrographic methods has permitted "automated" characterization of lunar soil mineralogy and components (e.g., agglutinates) by Higgins et al. [9].

The use of lunar ilmenite as a reactant for hydrogen reduction to produce a Lunar-Liquid-Oxygen (LLOX) supply has received considerable study ([10]), and ilmenite concentrates will be used in this process. Therefore, it will be necessary to obtain beneficiated ilmenite feedstocks from either hi-Ti basalts or hi-Ti mare soils [4]. It is uncertain which raw material, rocks or soils, is the more feasible to beneficiate for an ilmenite concentrate ([2, 7, and 8]). By combining rock ([5, 6]) and soil [9] x-ray digital-imaging data it will be possible to quantitatively compare feedstock grade and yield.

Inherent Differences Between Lunar Basalts and Soils- Because of the complicated process of soil formation, a simple crushed lunar rock has many inherent differences as compared to lunar soil. Crushed lunar basalt consists primarily of monomineralic (i.e., clean) and multiminerale (i.e., lithic) particles. However, lunar soil is **not** simply comminuted rock material, but it is a complex array of primary and secondary phases (minerals and glasses) and particles (mineral and rock fragments and impact-glass welded particles). In fact, the lunar soil consists of monomineralic particles, basaltic microrocks, highland microrocks, impact glasses, meltrocks (i.e., impact glass + primary fragments), microbreccia, pyroclastic glasses, and agglutinates. These first-order differences are due to the complex weathering processes, comminution and agglutination, that create the lunar soil by meteorite and micrometeorite bombardment (e.g., [11]). In addition, while the amount of clean mineral fragments initially increases with soil exposure-time, the modal abundances and percentage of clean mineral fragments decreases as a soil approaches maturity, a function of agglutinate content ([8]). In addition, the magnetic properties of soil and crushed rock are very different due to the generation of native Fe^0 in the former. The process of auto-reduction during soil formation generates a myriad of single-domain (44-330 Å) native Fe^0 spheres, and this mineralogical change greatly increases the bulk magnetic susceptibility of a soil with exposure-time ([12]).

LUNAR MINERAL FEEDSTOCKS EVALUATION: J.G. Chambers et al.

Quantitative Comparison of Rock- and Soil-derived Ilmenite Concentrates- As an application, mineral distribution data were compared for the most ilmenite-rich magnetic splits from the 45-90 μm size fraction of 71055 (crushed hi-Ti basalt material) and 10084 (mature hi-Ti soil). The beneficiation of these materials was discussed in Taylor and Oder [1] and Taylor et al. [4]. Ilmenite in these splits was concentrated to 70 and 18 vol% by magnetic separation of this rock and soil, respectively. However, the yields of these concentrates are quite low at only 5 wt% for both raw materials. Figure 1 compares the distribution of ilmenite in the rock- and soil-derived feedstocks. The bars represent the percentage of particles with various amounts of ilmenite, and the curves are cumulative mineral liberation curves for ilmenite. The graph shows that ilmenite in the 71055 concentrate occurs mostly as clean fragments (i.e., 80 % of the ilmenite is in particles which are 80-100 % pure), but the ilmenite in the 10084 concentrate is not as clean (i.e., only 58 % of ilmenite is 80-100 % pure). Both concentrates show nearly bimodal particle distributions of 0-10 % and 90-100 % ilmenite particles, but the trends are opposite.

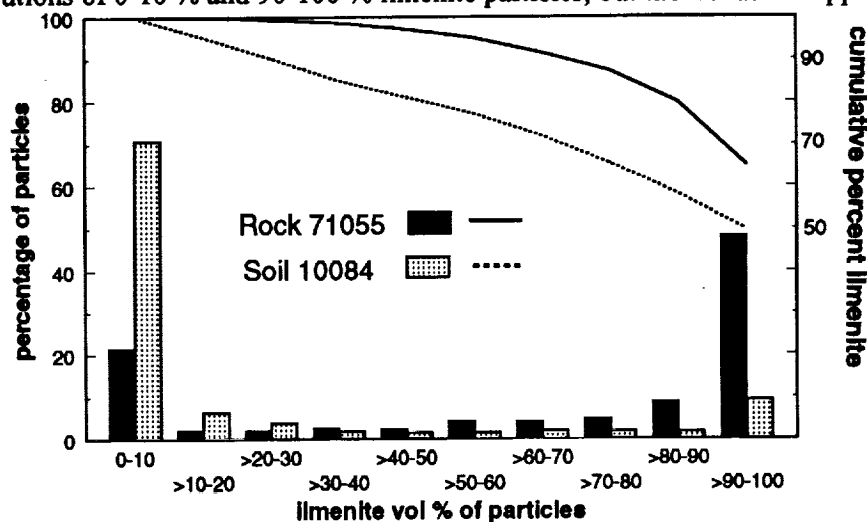


Figure 1. Comparison of the most ilmenite rich magnetic splits of the 44-90 μm fractions of hi-Ti rock 71055 and mare soil 10084.

Magnetic separation of rock material (71055) produced a richer ilmenite concentrate due to the simpler nature of the crushed rock. In both rock 71055 and soil 10084, ilmenite is attached to pyroxene, plagioclase, and olivine; however, the ilmenite 10084 is also associated with impact glass, Ti-glass, and pyroxene-like glass. Therefore, soils are more difficult to magnetically beneficiate due to impact glass which welds together minerals and rock fragments (agglutination).

Conclusions- X-ray digital-imaging characterization of lunar raw materials provides a quantitative comparison that is unattainable by traditional petrographic techniques. These data are necessary for accurately determining mineral distributions of soil and crushed rock material. Application of these techniques will provide an important link to choosing the best raw material for mineral beneficiation.

References [1] Taylor and Oder, 1990 *Space 90, ASCE*, 143-152; [2] Heiken and Vaniman, 1990 *PLPSC20*, 239-247; [3] Heiken et al., 1992, *Space 92, ASCE*, 555-564; [4] Taylor et al., 1992, *PLPSC23*, 1415-16; [5] Taylor et al., 1993, *PLPSC24*, 1409-10; [6] Chambers et al., 1994, *Space 94, ASCE*, in press, [7] DeLa'O et al., 1990, *Space 90, ASCE*, 177-186; [8] Taylor and McKay, 1992, *Space 92, ASCE*, 1058-1068; [9] Higgins et al., 1994, *PLPSC25*, in press, [10] Gibsen and Knudsen, 1990, *Space 90, ASCE*, 197-205; [11] Taylor, 1990, *Space 90, ASCE*, 68-77; [12] Taylor, 1988, *Space 88, ASCE*, 67-77.

2961

2
P. FIRST GALILEO IMAGE OF ASTEROID 243 IDA; C. R. Chapman (Planetary Science Inst., Tucson AZ), M. J. S. Belton (NOAO, Tucson AZ), J. Veverka (Cornell Univ., Ithaca NY), G. Neukum (DLR Inst. for Planetary Exploration, Berlin, Germany), J. Head (Brown Univ., Providence, RI), R. Greeley (Ariz. St. Univ., Tempe AZ), K. Klaasen (JPL, Pasadena CA), D. Morrison (NASA Ames Res. Ctr.), and the Galileo Imaging Team.

The second spacecraft encounter with an asteroid has yielded an unprecedentedly high resolution portrait of 243 Ida. On 28 August 1993, Galileo obtained an extensive data set on this small member of the Koronis family. Most of the data recorded on the tape recorder will be returned to Earth in spring 1994. A five-frame mosaic of Ida was acquired with good illumination geometry (phase angles about 50 to 60 degrees) a few minutes before closest approach; it has a resolution of 31 to 38 m/pixel and was played back during September 1993. Preliminary analyses of this single view of Ida are summarized here. When the data are returned, our color images of Ida will provide data on its compositional homogeneity and heterogeneity and may provide additional information relevant to the presence and geometry of a regolith. Also, we emphasize that much more definitive conclusions will be possible when we have images with somewhat different angles of illumination and perspective, and of the other sides of Ida.

Ida is at least 55 km long, perhaps slightly bigger than expected from groundbased data. Its general shape and orientation are consistent with pre-encounter predictions [1] for pole solution #2 of the two inherently ambiguous solutions from photometric lightcurves. Ida is clearly not a contact binary, contrary to some pre-encounter suggestions. It is not clear whether Ida is a monolithic body or a rubble pile, although views from other sides may clarify this issue. Ida appears to be more irregular in shape than does Gaspra, the first asteroid imaged by Galileo, or well-imaged small planetary satellites.

Unlike Gaspra, Ida is one of the most densely cratered objects yet observed in the solar system. Some of our preliminary crater frequency statistics are shown in Fig. 1 and comparisons with other bodies in Fig. 2; the preliminary conclusions that follow are based on these and other crater data. Ida's crater density (R-values of about 0.3) is similar to that attained on surfaces that are in equilibrium with a "saturation" cratering process. The slope of its differential size-frequency relation on a log-log plot is similar to, or perhaps a little steeper than, -3 for diameters smaller than 1 to 2 km.

For cratering production functions appreciably steeper than -3, studies of lunar cratering [2, 3] demonstrated that below the size where equilibrium sets in, the size-distribution should bend over to a -3 slope and there should be a full spectrum of crater morphologies from fresh to highly degraded. This is just what is seen on Ida for craters from 1 km down to at least 0.2 km diameter (Fig. 1). At larger diameters, preliminary counts show a steeper slope in the 2 - 4 km size range, possibly flattening at still larger sizes, consistent with the lunar crater production function [4]. Therefore, a consistent (though not unique) interpretation of the cratering histories of Gaspra and Ida is that the very steep production function recognized on Gaspra [5, 6] has cratered Ida 8 - 10 times more than Gaspra. It is expected, from orbital distributions of large main belt asteroids, that the inherent cratering rate by smaller asteroidal fragments should differ by much less than a factor of 2 between Gaspra and Ida. Accordingly, Ida's cratering age is 5 to 10 times older than Gaspra's age, which we estimated to be about 200 m.y. [6], or 1 to 2 b.y. old. If Ida is stronger than the rocky strengths assumed, its surface could date to the Late Heavy Bombardment (older than 3.5 b.y.). It may be inconsistent with Binzel's work [7] on the Koronis family that Ida is so old.

Ida seems to show more evidence for a regolith than Gaspra [8]. Downslope features (including "chutes"), small-scale albedo variations (e.g. dark floored craters), and the range of crater morphologies are all suggestive of regolith. There are some very large craters on Ida, which could be sources for the apparently more abundant regolith, particularly given Ida's stronger gravity and resulting greater retention of ejecta than is true for Gaspra. The spectral uniformity of Ida compared with Gaspra [9] could be due to ejecta from the latest big cratering event blanketing the entire surface with material from a single source region, or it could reflect underlying compositional homogeneity. Imaging

IMAGE OF ASTEROID 243 IDA; C.R. Chapman *et al.*

data in different spectral bands to be returned in 1994 will clarify if the compositional homogeneity extends to smaller spatial scales.

Various members of the Imaging Team [e.g. 8, 10] have described boulders visible on Ida, which may be ejecta blocks. Other geological features that have been recognized include grooves, crater chains, and various albedo features. Already, this single view of Ida shows more geological diversity than was found for Gaspra; although that partly reflects the better spatial resolution, Ida's larger size may facilitate processes not effective on smaller bodies or there may be other more fundamental differences between these two complementary members of the S-type.

Further clues that Ida may hold in store for us about the nature of S-type asteroids and about how the Koronis family parent body was disrupted await return of the bulk of the Ida encounter data, which is still stored on the Galileo tape recorder. It is presently expected that nearly all of that data can be returned prior to Galileo's preparation for its unique opportunity to observe the impacts of Comet Shoemaker-Levy 9 into Jupiter in mid-July.

References: [1] Binzel, R. P. et al. (1993), *Icarus* in press. [2] Gault, D. E. (1970), *Radio Sci.*, 5, 273. [3] Chapman, C. R., Mosher, J.A., and Simmons, G. (1970), *JGR*, 75, 1445. [4] Neukum, G., König, B., and Arkani-Hamed, J. (1975), *The Moon*, 12, 201. [5] Belton, M. J. S. et al., *Science*, 257, 1647. [6] Chapman et al. (1994), submitted to *Icarus*. [7] Binzel, R. P. (1992), *Icarus*, 100, 274. [8] Greeley et al. (1994), abstract, this meeting. [9] Carlson, R. et al. (1993), presentation at 25th AAS/DPS meeting. [10] Geissler, P., Petit, J-M., and Greenberg, R. (1994), abstract, this meeting.

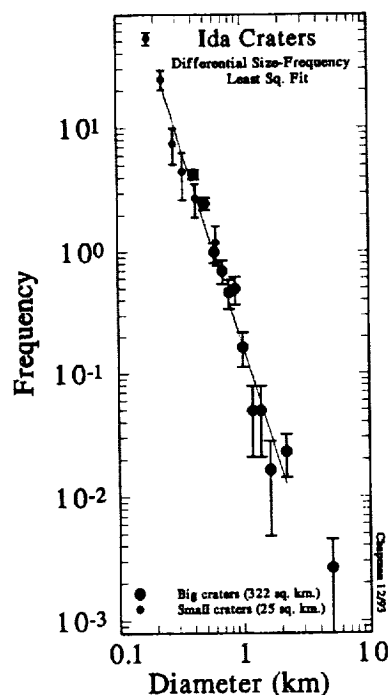


Fig. 1. Differential crater frequencies from 2 counting areas on Ida, with least squares fit power-law through reliable data points.

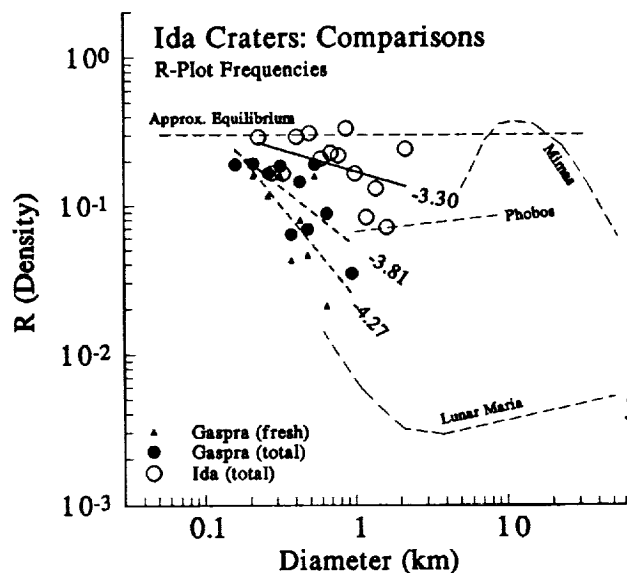


Fig. 2. R-plot crater densities for Ida and Gaspra (with least squares fits) shown in comparison with other satellite surfaces.

3-D PERSPECTIVE IMAGING: A TOOL FOR GEOLOGIC MAPPING OF VENUS; M.G. Chapman, R.L. Kirk, and J.M. Barrett, U.S. Geological Survey, Flagstaff, AZ 86001

The Galindo quadrangle (V40; 0°-25°S, 240°-270°E) is being geologically mapped at 1:5,000,000 scale as part of a Venus Data Analysis Program/Venus Geologic Mapping proposal, which is focused on Venusian geologic terrains containing assemblages of coronae, arachnoids, and novae. The map area, west of Phoebe Regio, contains a cluster of many asymmetric, multiple, and overlapping coronae, arachnoids, and novae that are randomly distributed. Geologic mapping of the quadrangle is being assisted by 3-D perspective views of geologically significant features [1].

Fig. 1
3-D view of corona
shown in Fig. 2



The 3-D renderings aid both geologic analyses and the subsequent explication of the results by depicting the radar characteristics, morphology, and vertical relations of these features (compare figs. 1 and 2). These three-dimensional relations are not apparent in raw SAR images; understanding of the morphology and history of superposition and deformation is enhanced by the perspective views of the radar-image and altimetric data. These views can also be color coded to show the relation between elevation and microwave emissivity, intermediate-scale surface roughness, or reflectivity data. In addition, the high-performance workstation and software used allow (1) rendering of views in almost real time for increased scientific visualization and (2) rotation, tilt, and zoom of the views so key features can be observed that allow placement of contacts on the map.

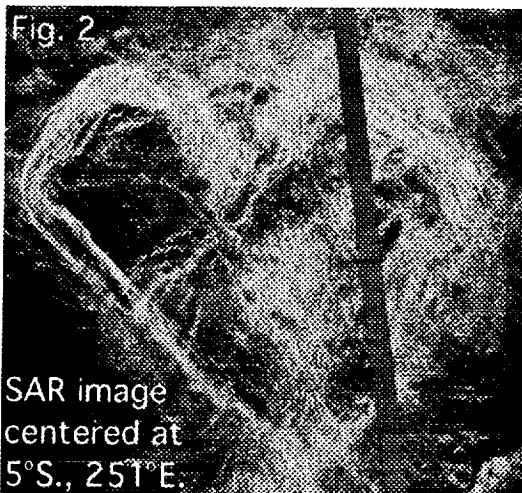


Figure 1 is a perspective rendering of an asymmetric corona overlapped by two novae in the foreground. The prominent high (arrow) in the corona is about the width of a single altimetry footprint and most likely represents an error. The 3-D view shows the widely varying slope morphology of the concentric scarp that

3-D IMAGING OF VENUS: Chapman, M.G. et al.

surrounds the corona. Furthermore, apparently rootless lava flows can be traced more easily to their sources by observing vertical relations in the perspective renderings.

V40 is an extremely "busy" quadrangle, and most of the important geologic relations are too detailed to be shown at the 1:5 million scale of the geologic map. Initial mapping has begun by dividing closely associated coronae and corona-like features into nine geographic groups. For each group, a small, more detailed, larger scale map has been generated by computer mapping over individual C1-MIDR tilelets imported from CD-ROM (56 tilelets per C1-MIDR) while hard copies of the perspective renderings were being viewed.

For example, five arachnoids (A-E) are included in group 9 (fig. 3). They form a rough question-mark shape with arachnoid A at the south end. The age relations shown by geologic mapping denote a clear, systematic age progression from A to E. Could this progression mean that the surface has moved above a stable plume? On the 3-D images, the relief of the features ranges from negative (A) to various heights (B-D) to relatively flat (E). Could the negative relief of arachnoid A be due to viscous relaxation of an older feature? Arachnoid B is the highest of the five and has produced the most lava, and the distance from A to B is the greatest among the group. Could these characteristics indicate an increase in plate movement or a "hiccup" in plume production between the formation times of A and B? The volume and asymmetry of the arachnoid group will be studied, and geologic relations from the mini-maps of V40 will be transferred to one large 1:5,000,000-scale final product to determine regional trends. (The mini-maps can be used as figures in the map text.) The combination of the 3-D synthesis of these Magellan datasets with the SAR images has clearly enhanced the interpretation of geologic relations in the map area.

The 3-D perspective renderings were generated by enhancing the image base from the Galindo quadrangle with spatial filtration, contrast exaggeration, and the addition of relief shading, as described by Kirk [2]. Elevation data from the Magellan global altimetric dataset (GTDR) [3] were merged with pre-Magellan data to fill gaps, reprojected to register to the image, and smoothed at the resolution of the altimeter. Rendering was performed on a SUN SPARCstation 10 model 512 with the Surveyor software package. The images (figs. 2, 3) were transferred to a VAX computer and copied to a Macintosh computer to generate hard copy.

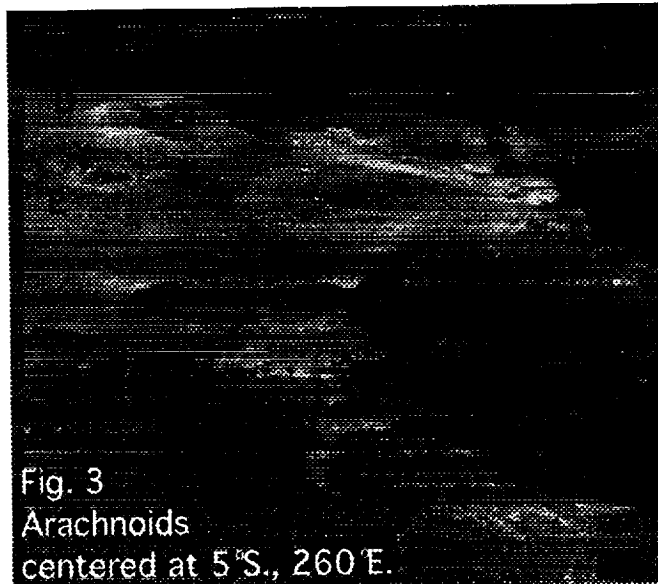


Fig. 3
Arachnoids
centered at 5°S., 260°E.

References: [1] Soderblom, L.A. et al. (1993) [abs.] NASA Planet. Data Visualization, San Juan Capistrano, CA, 38-39. [2] Kirk, R.L. et al. (1992) JGR, 97, 16,371-16,380. [3] Pettengill, G.H. et al. (1991) Science, 252, 260-265.

2962

SUBPIXEL RESOLUTION FROM MULTIPLE IMAGES**Peter Cheeseman, RIACS, Bob Kanefsky, Recom, John Stutz, NASA, and Richard Kraft, Recom**

Multiple images taken from similar locations and under similar lighting conditions contain similar — but not identical — information. Slight differences in instrument orientation and position produces mismatches between the projected pixel grids. These mismatches ensure that any point on the ground is sampled differently in each image. If all the images can be registered with respect to each other to a small fraction of a pixel accuracy, then the information from the multiple images can be combined to increase linear resolution by roughly the square root of the number of images. In addition, the gray-scale resolution of the composite image is also improved. We describe methods for multiple image registration and combination, and discuss some of the problems encountered in developing and extending them. We display test results with 8:1 resolution enhancement, and Viking Orbiter imagery with 2:1 to 4:1 enhancements.

Our problem is the inverse of computer graphics rendering. There, one is given a model of the relevant surfaces (shape and reflectivity), with associated viewing and lighting conditions. From this information, a graphics program projects an image of the scene. We have the inverse problem: given multiple images obtained under known lighting and viewing conditions, determine the most probable surface model subject to prior model constraints. Ideally, a planetary surface model would combine topographic information with multi-spectral reflectances at every point on the surface. Our current simplified approach is restricted to a single spectral band. We suppress topographic effects by requiring all images to be made from roughly the same direction under the same lighting conditions. Thus we combine the effects of varying ground slope and surface albedo into a 2-D model element ("mixel") grid. This mixel grid is made at some fraction of the projected pixel resolution, e.g., 20m instead of 80m.

Despite the above restrictions, we can achieve improved resolution in practical cases. For Viking Orbiter (VO), we can combine the overlapping margins and corners of high-resolution mosaics for a modest improvement. We can obtain dramatic improvement when dozens of images are available. Unfortunately, due to orbital mechanics, such sequences are always low-resolution.

Lacking geographic truth, our current work employs a relative registration. The mixel grid is initialized by interpolating values from one of the pixel images. Thus this image provides the geographic control. Successive pixel images are then registered by minimizing a mismatch function over the parameter space of the appropriate mapping transformation. For each pixel the mismatch function calculates the sum of mixel contributions over the projected pixel area, weighted by the instrument point spread function (PSF). The mismatch is then the sum of squared errors between the predicted and observed pixel values.

The choice of an appropriate geometric transform function is important. It must account for any inter-image distortions without introducing excessive degrees of freedom. For scanned images, rotation and translation are sufficient. With CCD detectors the addition of scale and shear will allow relative mapping, while projective transform is needed for geographic correction. The vidicon tubes on the Viking Orbiters and Voyagers introduce local and image wide readout distortions that we model with second order coefficients.

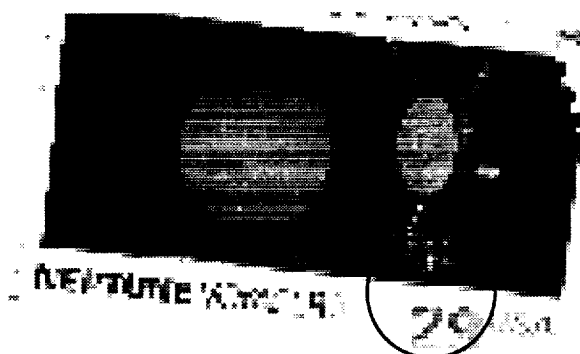
The final combined image is currently computed by setting each mixel to a weighted average of the pixel values influenced by that mixel via the PSF and registrations. This works surprisingly well, sufficiently to justify presenting the present technique. We are developing a full Bayesian solution to this inversion problem, to include PSF deconvolution and neighbor correlations.

There are problems with the current system. The registration search can only find local minima in the mismatch error space, so it is necessary to manually pre-register images to within a few pixels. Practically, registration requires that there be several prominent features distributed over the image. Also, the mismatch function is very sensitive to edge interaction of the mixel and pixel grids. These can be avoided.

In addition to readout distortion, the VO and Voyager vidicon images are subject to camera shading and uncertainties in exposure duration. Many pixels are blocked by data dropout and reseau marks. Others are corrupted by multi-bit transmission errors, quantization noise, blemishes, etc. These are all part of the camera model and could be reconstructed along with the surface model, but currently their effects are removed by preprocessing.

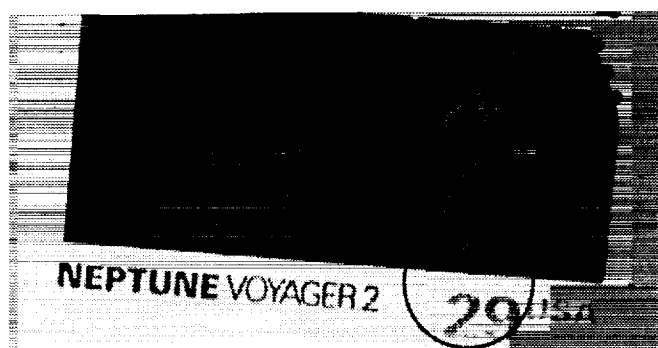
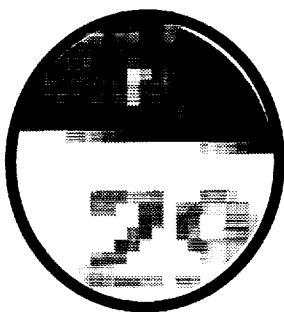
We hope, in the future, to have a full geometric model that will allow us to take advantage of the multiple high-resolution coverage that can be found among the 50,000 VO images, as well as long-range Voyager flyby sequences of certain moons, such as Iapetus.

SUBPIXEL RESOLUTION FROM MULTIPLE IMAGES — Cheeseman et al.

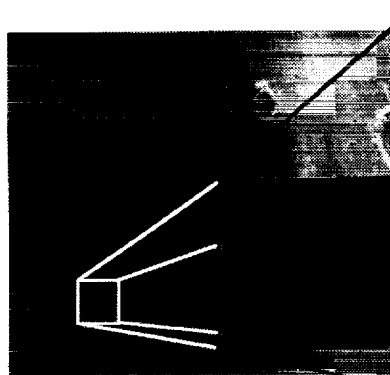


Postage stamp scanned
on an Apple scanner as
an 8-bit grayscale image.

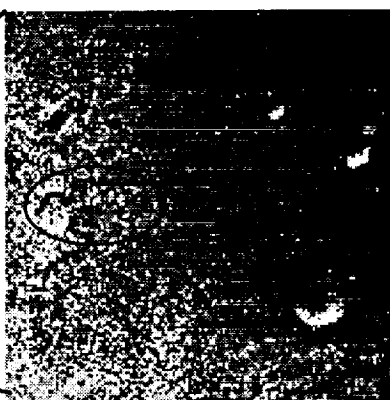
scanned at
72 pixels / inch



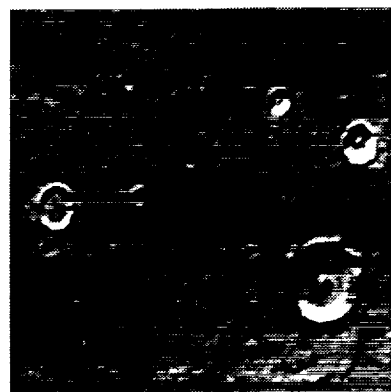
reconstructed at
576 pixels / inch



VO217S44, one of 24
wave-cloud frames



742
meters
/ pixel



186
meters
/ pixel



VO434S10, one of 4 overlapping images
from two mosaics of Gusev Crater.



69 meters / pixel



35 meters / pixel



HYPERVELOCITY IMPACTS AND THE MAGNETISM OF SMALL BODIES IN THE SOLAR SYSTEM

Guangqing Chen, Thomas J. Ahrens, Lindhurst Laboratory of Experimental Geophysics, Seismological Laboratory, California Institute of Technology, Pasadena, CA 91125
and Raymond Hide, Department of Physics and Earth Sciences, University of Oxford, Oxford OX1 3PU, England, U.K.

Magnetism of the Moon and other small bodies in the solar system has been a controversial topic (see, e.g. [1, 2]), and has only become more interesting since the recent flybys of the asteroid 951 Gaspra and the larger asteroid 243 Ida by the Galileo spacecraft, which have found that both of them may be sufficiently electrically conducting so as to perturb the interplanetary magnetic field, or they are magnetic [3]. Here we present a quantitative model evaluating the extent of magnetization by hypervelocity impacts—one of a few magnetizing mechanisms previously suggested—using shock and post-shock temperature calculations and a fracturing model by Housen and Holsapple [4]. We conclude impacts are generally incapable of magnetizing a planetary body throughout, but impact magnetization may offer a valid explanation for small magnetic asteroids like Gaspra or Ida which are thought to be impact fragments of larger bodies.

When rocks are shock heated to temperatures higher than the Curie point of their embedded ferromagnetic metals, and then cooled down through the Curie point, they can be magnetized strongly by the magnetic field that may present at the time. We calculated the shock and post-shock temperature as functions of shock pressure using the Tillotson equation of state for lunar rock [5] at several initial porosities. For solid rock, the needed shock pressure is about 50 GPa; for rocks of 50% porosity, the pressure is lowered to less than 10 GPa. From the Holsapple-Schmidt scaling of planetary impacts [6], the radius inside which the target is shocked above the threshold pressure in various impact conditions are obtained and shown as solid lines in Figure 1.

An important question in the model is whether the target can remain largely integral when it is shock-magnetized. Housen and Holsapple in [4] developed a catastrophic fragmentation (CF, defined as when the largest fragment mass is half that of the original target) threshold based on dimensional analysis and fragmentation experiments in the strength regime. The threshold was then extrapolated into the gravitational regime by replacing the impact-induced tensile stress (σ_I) with that in excess of the gravitational stress ($\sigma_I - \sigma_G$). A slightly relaxed threshold was given for larger bodies where fragments could reaccumulate under their own gravity. The fragmentation and reaccumulation limits for 1, 10, 100 and 1000 km-radius, solid or porous targets are shown in Figure 1 as broken lines. The magnetization zone is always within the CF limit, therefore our model predicts the target cannot be magnetized by an impact without breaking up. On the other hand, impact-induced magnetization on an unfragmented body (like the Moon) must be limited to the vicinity of impact center, and if it has been under multiple impacts, its magnetic field should have a "patchy" characteristic.

We further developed the model by Housen and Holsapple to predict the mass of the largest fragment when the impact is not at the CF threshold. The equation we used is:

$$\frac{M_L}{M} = 0.5 \times \left[\frac{\sigma_F}{\sigma_I - \sigma_G} \right]^\beta \quad (1)$$

where σ_F is the fracture strength at the prevailing strain rate, β is a constant and is determined from laboratory experiments in the strength regime ($\sigma_G = 0$). Another change we made from [4] is that we included the depth-dependence of the lithostatic stress σ_G :

$$\sigma_G(r) = \frac{2\pi}{3} G \rho^2 (R^2 - r^2) \quad (2)$$

Assuming both Gaspra and Ida were impact-magnetized, and they are remanent fragments from the same impacts that magnetized them, we can obtain a constraint on the minimum sizes of the impactors. Then, requiring the largest fragments be larger than Gaspra or Ida, lower limits on the pre-impact asteroid sizes can be set using Equation 1. At 5 km/s impact velocity, which is about the most probable in the asteroid belt, we obtained that the proto-Gaspra body was at least 91 km and the impactor at least 7.4 km in radius; For Ida, the minimum radii for parent body and impactor are 330 and 27.5 km respectively. The impactor radius is a strong function of impact velocity, while the parent body radius is almost constant with regard to impact velocity.

Based on geometrical considerations, Gradie *et al.* estimated the minimum radius of the parent body of the Koronis family should be 45 km [7]. Our minimum parent body radius reduced only by about a factor of 2 (to 138 km) when we artificially made its fracture strength 10^3 times the normal value in the calculations, therefore the reason for the surprisingly small size of the proto-Ida asteroid cannot be its strength. The present analysis thus suggests that if Gaspra and Ida are fragments from the impact on a protoasteroid and this impact magnetized them, their parent bodies had to have radii greater than 91 and 330 km, respectively. Or, the possible magnetization of these objects is unrelated to the impact process which created them from larger proto-asteroids.

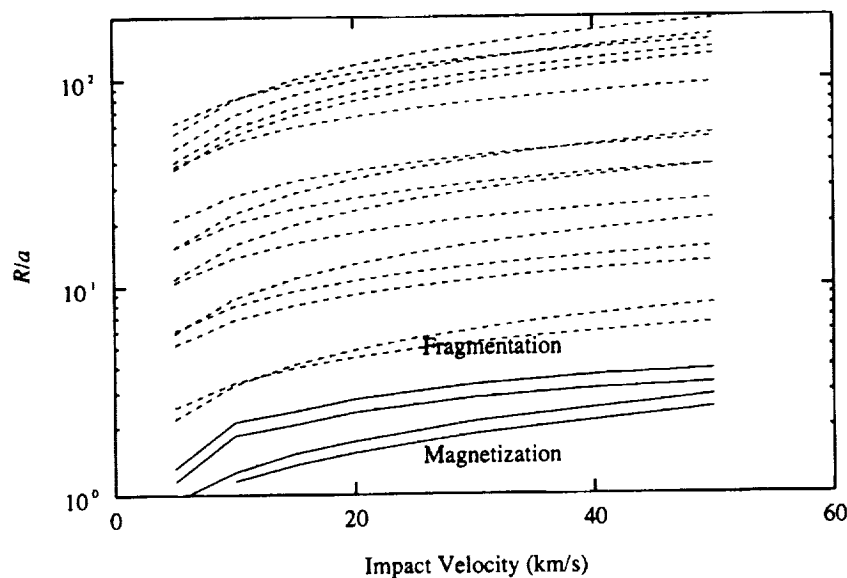


Fig. 1: Magnetization radius (solid lines) and catastrophic fragmentation threshold (broken lines) R , normalized to impactor radius a , plotted as functions of impact velocity. The four solid lines correspond to shock temperature or post-shock temperature based calculations for porous or non-porous rock; the 16 broken lines are fragmentation or gravitational reaccumulation thresholds for $R=1, 10, 100$ and 1000 km, porous or nonporous rock. The target will be magnetized if R/a lies below the solid lines; it will be fragmented if R/a is above the broken lines. All broken lines are above solid lines, meaning a planetary body cannot be totally magnetized while remaining integral.

- [1] L. L. Hood and Z. Huang, *J. Geophys. Res.* 96, 9837-9846 (1991). [2] D. W. Collinson, *Surveys in Geophysics* 14, 89-118 (1993). [3] M. G. Kivelson, L. F. Bargatze, K. K. Khurana, D. J. Southwood, R. J. Walker and P. J. Coleman, Jr., *Science*, 261, 331-334 (1993). [4] K. R. Housen and K. A. Holsapple, *Icarus* 84, 226-253 (1990). [5] T. J. Ahrens and J. D. O'Keefe, in *Impact and Explosion Cratering*, 639-656, Pergamon Press, New York (1977). [6] K. A. Holsapple and R. M. Schmidt, *J. Geophys. Res.* 92, 6350-6376 (1987). [7] J. C. Gradie, C. R. Chapman and J. G. Williams, in *Asteroids*, The University of Arizona Press, Tucson, Arizona (1979).

THE ABUNDANCE OF THALLIUM AND PRIMORDIAL LEAD IN SELECTED METEORITES - THE SEARCH FOR ^{205}Pb . J. H. Chen and G. J. Wasserburg. The Lunatic Asylum, California Institute of Technology, Pasadena, CA 91125

The presence of the short-lived nuclei ^{26}Al , ^{107}Pd , ^{129}I , ^{53}Mn , ^{60}Fe and ^{244}Pu in the early solar system is reasonably well established [1,2]. The nuclear astrophysical processes and stellar sources responsible for these diverse nuclei have been the subject of considerable discussion [3]. Of the above nuclei, only ^{107}Pd and ^{60}Fe are "s" process. Recent studies [3-5] presented analyses of "s" process products and predicted the abundances of all s-process radioactivities for a 1.5-3 M_{\odot} AGB star assuming $(^{107}\text{Pd}/^{108}\text{Pd})_{\odot} = 2 \times 10^{-5}$ after dilution with the ambient ISM. The predicted value of $(^{205}\text{Pb}/^{204}\text{Pb})_{\odot} = 6.5$ to 11×10^{-4} at the onset of solar system formation [5]. An incisive review of the nucleosynthesis of ^{205}Pb has been presented by [6], and previous searches for ^{205}Pb are in [7-10]. We had carried out studies on two iron meteorites which have primordial Pb(PAT) and thus have not suffered terrestrial Pb contamination. A hint of $^{205}\text{Tl}^*$ was found for sulfide from an iron meteorite [10]. It was evident that without a substantial improvement in $^{205}\text{Tl}/^{203}\text{Tl}$ measurements, that samples with higher $(^{204}\text{Pb}/^{205}\text{Tl})/(^{204}\text{Pb}/^{205}\text{Tl})_{\odot}$ were needed to obtain unambiguous results. In this study we determined Pb and Tl abundances and Pb isotopic compositions in the metal and sulfide phases of seven iron meteorites: Canyon Diablo (CD,IA), Bogou (B,IA), Derrick Peak (DP,IIB), Cape York (CY,IIIA), Trenton (T,IIIA), Nantan (N,IIICD) and Gibeon (G,IVA) (Table 1). Each sample was subjected to several etchings and the interior material dissolved and analyzed. Fractions of solutions were removed for Pb and Tl analyses. An interior sample of Canyon Diablo (CD) metal yielded a ^{204}Pb concentration of 18.88 pM/g ($^{204}\text{Pb}_m$) and a Pb isotopic composition which is $\sim 1.3\%$ more radiogenic than reported previously [11-13]. Assuming the excess radiogenic Pb was from terrestrial contamination, we estimated this CD metal sample had a primordial ^{204}Pb content ($^{204}\text{Pb}_p$) of 18.63 pM/g. From these results we calculate a $^{204}\text{Pb}/^{205}\text{Tl}$ ratio of 3.94 for the CD metal. An interior sample of CD troilite yielded a Pb isotopic composition indistinguishable from PAT. However, the leach has highly radiogenic Pb. The $^{204}\text{Pb}/^{205}\text{Tl}$ value for the sulfide (interior) is a factor of 3.2 higher than for the metal. Two other meteorites, Nantan and Bogou also have close to primordial Pb isotopic values and are plotted inside the insert of Fig. 1. The remaining meteorites contain varying amounts of radiogenic Pb and in some cases contain almost entirely terrestrial lead. We also analyzed a chondrite, Mezo-Madaras (MM) and an achondrite, Angra dos Reis (ADOR). These samples were not subjected to etching prior to analysis. The results show MM has close to primordial lead and ADOR has very radiogenic lead. The $^{204}\text{Pb}/^{205}\text{Tl}$ in MM (11.7) and ADOR (22) are quite high. The primordial $^{204}\text{Pb}/^{205}\text{Tl}$ ratios in both metal and sulfide of iron meteorites and two stony meteorites range from 0.15 to 22. Assuming $^{205}\text{Pb}/^{204}\text{Pb} = 5.4 \times 10^{-4}$ in the meteorite parent bodies, we estimated the amounts of possible $^{205}\text{Tl}^*$ to be from 0.1 to 12 ‰. We have established analytical procedures to determine $^{205}\text{Tl}/^{203}\text{Tl}$ ratios in Tl standards to a precision of $\pm 2\%$ [10]. Therefore, it may be possible to detect an isotopic anomaly in several of these samples. Experimental partitioning studies [14] showed that Pb and Tl are extremely incompatible in iron metal and troilite. The experimentally determined partitioning coefficients between troilite and metal (D) for Tl and Pb are 14 and 10 to 30 respectively. However the measured D_{Tl} (1.4 - 22) and D_{Pb} (1 - 32) show wide ranges, suggesting other factors affect the distribution of Pb and Tl in iron meteorites. It is not evident how our leaching procedure may alter the original Tl and Pb contents. The Tl and ^{204}Pb contents are plotted in Fig. 2. In this diagram, Allende samples form a linear trend which passes through the origin and Orgueil [9]. All our data, except Trenton troilite, plot to the right of this line, indicating enrichment of Pb relative to Tl. In summary, we found a general enrichment of Pb relative to Tl in most iron meteorites, a chondrite and an achondrite, as compared to the $(^{204}\text{Pb}/^{205}\text{Tl})_{\odot}$. However, only a few samples might be suitable candidates for detecting any $^{205}\text{Tl}^*$ at $> 4\%$ level. The study of Larimer [15] showed that Pb and Tl gas in equilibrium down to 500°K with Fe-Ni metal should have $(^{204}\text{Pb}/^{205}\text{Tl})/(^{204}\text{Pb}/^{205}\text{Tl})_{\odot}$ enhanced by ~ 40 . After the onset of Pb condensation, but before Tl condensation, the enhancement factor is up to ~ 200 . This suggests that there may be suitable candidates

The Abundances of Tl & Pb in Meteorites: Chen J. H. and Wasserburg G. J.

if one can find samples that equilibrated with nebular gases at the appropriate narrow temperature region. Such samples have not yet been identified and it is not evident that the fractionation found here can be simple related to a condensation model. Division Contribution 829(5354). Refs. [1]Wasserburg G.J. (1988) *Protostars and Planets II*, 703. [2]Podosek, F.A. and Swindle, T.D. (1988) *Meteorites and the Early Solar System*, 1073. [3]Cameron A.G.W. (1993) *Protostars and Planets III*, 47. [4]Wasserburg G.J., Gallino R., Busso M., Raiteri C.M. (1993) *LPSC XXIV*, 1487. [5]Wasserburg G.J., Busso M., Gallino R., Raiteri C.M. (1994) *ApJ* in press. [6]Yokoi K., Takahashi K. and Arnould M. (1985) *A&A* 145, 339. [7]Anders E. and Stevens C.M (1973). *JGR* 65, 3043. [8]Huey J.M. and Kohman T.P. (1973) *JGR* 78, 3227. [9]Arden J.W. and Cressey G. (1984) *GCA* 48, 1899. [10]Chen J.H. and Wasserburg G.J. (1987) *LPSC XVIII*, 165. [11]Tatsumoto M., Knight R.S. and Allègre C.J. (1973) *Science* 180, 1779. [12]Chen J.H. and Wasserburg G.J. (1983) *LPSC XIV*, 103. [13]Göpel M., Manhès G. and Allègre C.J. (1985) *GCA* 49, 1681. [14]Jones J.H., Hart S.R., and Benjamin T.M. (1993) *GCA* 57, 453. [15]Larimer J.W. (1973) *GCA* 37, 1603.

Table 1. Tl and Pb concentrations in meteorites

Meteorite	Wt. (g)	^{205}Tl (pM/g)	$^{204}\text{Pb}_m$ (pM/g)	$^{204}\text{Pb}_p$ (pM/g)	$\frac{^{204}\text{Pb}_m}{^{205}\text{Tl}}$	$\frac{^{204}\text{Pb}_p}{^{205}\text{Tl}}$	$^{205}\text{Tl}^*$ (‰) [†]	D(FeS/Metal) Tl	Pb
Canyon Diablo, M	5.33	4.73	18.88	18.63	3.99	3.94	2.1	1.35	4.33
Sulfide-L	0.98	29.26	275.16	79.43	9.40	2.71	1.5		
Sulfide-C	8.34	6.40	81.70	81.60	12.76	12.74	6.9		
Bogou, Metal	5.31	4.19	5.49	5.45	1.31	1.30	0.7	6.84	28.1
Sulfide	2.68	28.62	154.37	149.23	5.39	5.21	2.8		
Derrick Peak, Metal	8.45	0.07	0.08	0.02	1.10	0.33	0.2	4.09	3.29
Sulfide-C	2.59	0.30	0.27	0.04	0.88	0.15	0.1		
Cape York, Metal	8.12	0.06	0.59	0.42	9.48	6.73	3.6	9.51	3.77
Sulfide-L	0.20	2.37	252.16	22.12	106.61	9.35	5.1		
Sulfide-C	1.80	0.59	2.22	0.87	3.76	1.47	0.8		
Trenton, Metal	11.04	0.19	0.23	0.19	1.21	1.03	0.6	22.3	1.03
Sulfide-C	1.52	4.21	0.23	-	0.06	-	-		
Nantan, Metal	14.17	5.74	8.27	8.11	1.44	1.41	0.8	2.05	25.1
Sulfide-C	2.72	11.74	207.23	204.18	17.65	17.39	9.4		
Gibeon, Metal	17.01	0.02	0.04	-	1.62	-	-	2.73	32.1
Sulfide-C	3.07	0.06	1.22	0.05	19.03	0.75	0.4		
Mezo-Madaras (L3)	0.20	34.16	406.02	397.95	11.88	11.65	6.3		
ADOR (Achondrite)	0.24	0.24	5.30	-	22.02	-	11.9		
Orgueil[9] ^{26}Al	-	575	270	-	0.47	-	0.3		

Units in 10^{-12} Moles/g; subscripts: m = measured; p = primordial; L=Leach, C=Core;

[†]Note: $^{205}\text{Tl}^*$ calculated from $^{204}\text{Pb}_p/^{205}\text{Tl}$ assuming $^{204}\text{Pb}/^{205}\text{Pb}=5.4\times 10^{-4}$.

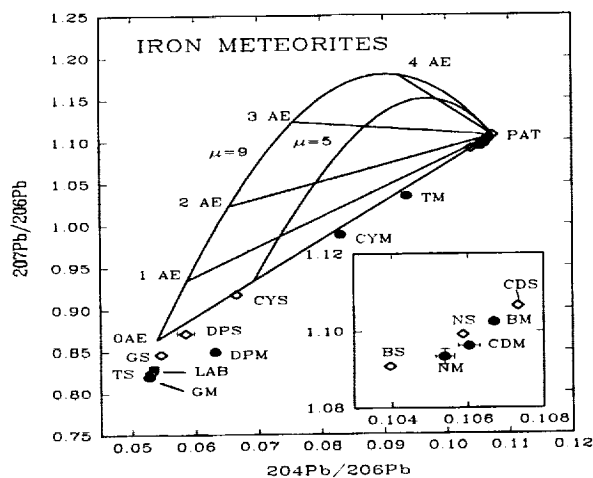


Figure 1. Pb Isotopic Composition in Irons

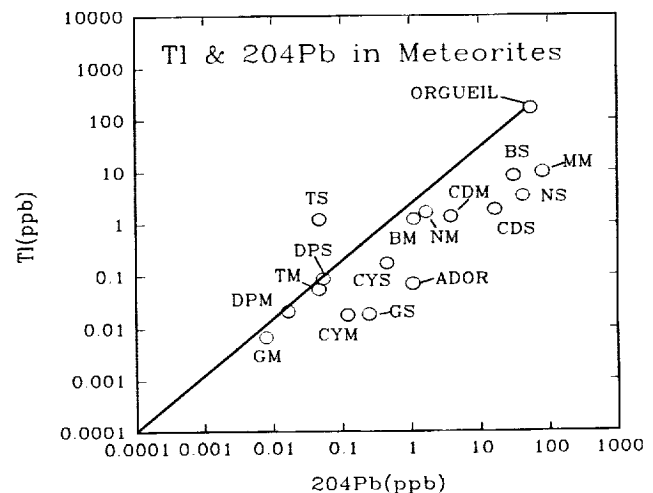


Figure 2. Tl vs. ^{204}Pb in Meteorites

THE ORBITAL EVOLUTION OF ORDINARY CHONDRITES OVER THE LAST 50 MILLION YEARS Yongheng Chen^{1,2}, Paul H. Benoit¹ and Derek W. G. Sears¹ ¹Cosmochemistry Group, Department of Chemistry and Biochemistry, University of Arkansas, AR 72701, USA ²Institute of Geological New Technology, Chinese Academy of Sciences, Wushan, Guangzhou 510640, PRC

Recent studies have suggested that the meteorite flux is subject to changes in its composition and possibly its intensity over various periods of time [1,2,3]. Many of these studies have concentrated on changes in the terrestrial flux using meteorite finds with large terrestrial ages (*i. e.*, Antarctic meteorites). In the present study we examine a collection of ordinary chondrite falls with terrestrial ages <30 years and for which cosmogenic nuclide data are available. We find that meteorites with long cosmic ray exposure ages apparently had smaller perihelia within the last 10⁵ years than those with smaller cosmic ray exposure ages. About half the spread in natural TL values of observed falls can be accounted for in terms of this secular evolution of their perihelia. Meteorite orbits apparently show an evolution of their perihelion to smaller values during the period represented by their cosmic ray exposure ages.

INTRODUCTION. Recent work has suggested that the ordinary chondrite meteorite flux is not constant with time, but displays variation in composition and possibly in intensity as well [1,2,3]. In a study of observed ordinary chondrite falls, Benoit *et al.* [4] observed that meteorites with cosmic ray exposure (CRE) ages <20 Ma showed a broad range of natural TL levels, including many with high TL levels. Meteorites with CRE ages >20 Ma, however, exhibited less variability in natural TL levels and none had high TL levels. They suggested that the restricted range of natural TL levels observed in meteorites with high CRE ages might reflect the extended orbital evolution of these meteorites; the low TL levels are interpreted as the result of recent orbits with perihelion < 1.0 AU. The dataset of Benoit *et al.* [4] included many observed falls with fairly large terrestrial ages, many of about 100 years. The initially rapid decay of TL under typical temperate climatic conditions means that significant scatter may be introduced in this dataset [4]. In order to examine the apparent orbital evolution of the ordinary chondrites in more detail, we have now measured the natural TL levels of a group of observed falls with very short terrestrial ages (<30 years). Our study included 17 equilibrated ordinary chondrites (11 H, three L, one LL and two L/LL chondrites).

RESULTS AND DISCUSSION. The new data also show a trend whereby natural TL levels decrease from 125 to 28 krad as CRE age increases from 0.9 to 51 Ma (Fig. 1). Our previous data show a similar trend [4], but is displaced to lower TL values as a result of terrestrial TL decay (Fig. 1). As noted by Benoit *et al.* [4], there is no basis for such a trend in the systematics of TL. Even under low temperature conditions, TL levels should reach equilibrium values in less than one million years. Other relevant factors, such as external radiation and dose-rate variation due to differences in shielding, are quantitatively unimportant for all but the largest and smallest meteoroid bodies [4]. The equilibrium value is therefore determined by temperature during irradiation in space, notably by the highest temperature experienced during a meteoroid's orbit which is at perihelion.

Making various assumptions about the albedo of meteoroid bodies, we can calculate an approximate perihelion for meteorites which represents an average perihelion for a period of time just prior to Earth impact. We find that, for our observed trend, perihelion decreases from about 1.0 AU (Zaoyang) to 0.90 AU (Xi Ujimqin) with increasing CRE age from 0.9 Ma to 51 Ma. This evolution of orbits among ordinary chondrites is summarized in Table 1. If we assume that the cosmic-ray exposure ages of meteorites largely reflect their irradiation while undergoing orbital evolution then one implication of these data is that the change in perihelia of meteoroid bodies is gradational and generally tends towards smaller perihelia. This, in turn, suggests that meteoroid bodies in Earth-approaching and Earth-crossing orbits do not generally exhibit chaotic orbital evolution over timespans of about 50 million years.

Two meteorites in the new database, Enshi and Laochengzhen, have very low natural TL levels (<1 krad) and do not plot along the TL vs. CRE age trend (Fig. 1). In all natural TL databases examined to date about 15% of meteorites also exhibit very low natural TL levels. It has been shown [4,5] that very small perihelion orbits (<0.85 AU) will drain TL levels to these low values. About 12% of observed falls had perihelia of <0.85 AU, as determined from their visual radiants [4]. Alternatively, TL levels could be drained to these low levels by shock-heating. Both Enshi and Laochengzhen have low TL sensitivities (0.62 and 0.16

ORBITAL EVOLUTION OF ORDINARY CHONDRITES: Chen Y. et al.

relative to Dhajala, respectively) which may be indicative of destruction of feldspar during shock. In either case, the thermal event which drained the TL of these meteorites must have occurred within 10^5 years before Earth impact so that natural TL levels did not rebuild to the higher "equilibrium" values. Enshi and Laochengzhen have also suffered ^3He and ^4He loss [6,7] which is indicative of thermal events. However, there are distinct differences between the response of TL and noble gases to thermal events. Natural TL is sensitive to fairly small thermal events but can recover from these events rapidly (about 10^6 years or less). Noble gas loss, however, requires fairly large thermal events and its "record" is retained throughout the cosmic ray exposure history of the meteoroid body. Therefore, the low TL and ^3He loss in Enshi and Laochengzhen indicate that the thermal event which affected both sets of data was (a) fairly intense and (b) occurred within the last 10^5 years. There are no ^3He data for two other meteorites with low TL levels in the present study (Peace River and Rochester).

Boxian seems to be an exception to the TL vs. CRE age trend in that it has a high TL level and a high CRE age (Fig. 1). This may indicate that LL chondrites do not follow the trend, although the dataset for meteorites with terrestrial ages >30 years does not support this suggestion [4]. Alternatively, it is possible that Boxian was "predosed" in a larger body. The noble gas data currently available [7] do not support a multi-stage irradiation history for Boxian, so perhaps this meteorite is a rare example of a meteoroid body with an unusual orbital history. Suizhou has a low natural TL but high equivalent dose [see 8], implying a sample heterogeneity problem.

CONCLUSIONS. We conclude that the natural TL levels of recently fallen meteorites correlate with their cosmic ray exposure ages, and this correlation is a result of orbital evolution in space. With increasing cosmic ray exposure age, meteoroid bodies tend to evolve to lower perihelia. The change in meteoroid perihelia as a function of time is not very large, generally between 1.0 to 0.90 AU over the last 50 million years but appears to apply to almost all ordinary chondrites.

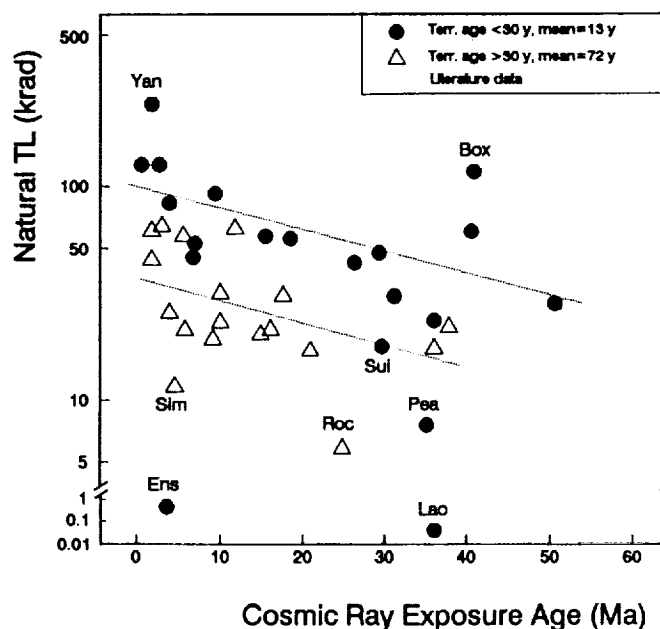
Acknowledgements: We wish to thank the Institute of Geological New Technology, Chinese Academy of Sciences and O. Eugster for samples and to D. Wang for suggesting this study. This work was supported by a grant from the Chinese Academy of Sciences and NASA grant NAGW-3519.

[1] Dodd *et al.* (1993) *JGR* 98, E8, 15105-15118. [2] Dennison and Lipschutz (1987) *GCA* 51,741-754. [3] Benoit and Sears (1993) *Icarus* 101, 188-200. [4] Benoit *et al.* (1991) *Icarus* 94, 311-325. [5] Benoit *et al.* (1993) *JGR* 98, B2, 1875-1888. [6] Wang *et al.* (1992) *Geochimica* (Chinese) No.4, 314-332. [7] Eugster *et al.* (1993) *GCA* 57, 1115-1142. [8] Hasan *et al.* (1989) *LPS* XX, 383-384.

Table 1: The evolution relationship among perihelion, natural TL level and CRE ages of ordinary chondrites.

Perihelion (AU)	Natural TL krad @ 250 °C	CRE age (Ma)
1.1-1.0	>100	<10
1.0-0.96	100-60	10-20
0.96-0.93	60-40	20-30
0.93-0.90	40-30	30-50
<0.90	<30	>50

Fig. 1 (Right). Natural TL levels (at 250 °C) vs. cosmic ray exposure age for ordinary chondrites with terrestrial ages <30 years. The correlation between natural TL and cosmic ray exposure age (excluding the two chondrites with natural TL <1 krad) is shown by the dotted regression line which has a slope of 0.01 ($r = -0.59$, $n = 18$). The chondrites are identified by the first three letters of their names.



EXPLORATION OF THE MORPHOLOGICAL DISTRIBUTION OF THE SPECTRAL UNITS IN THE GRUITHUISEN DOMES REGION.

Serge D. Chevrel ⁽¹⁾, Patrick C. Pinet ⁽¹⁾ and James W. Head ⁽²⁾.

¹ UPR 234/CNRS, Groupe de Recherche de Géodésie Spatiale, Observatoire Midi-Pyrénées, 31400 Toulouse, France; ² Brown University, Providence, R.I. 02912, USA.

The Gruithuisen domes δ and γ , located in the northwestern border of Mare Imbrium, are relatively high albedo features standing hundreds of meters higher than the mare and highland adjacent topography. Stratigraphic relations show that these features are of Imbrian age and that their formation is contemporaneous with the emplacement of the main sequence of mare deposits. High resolution Lunar Orbiter, color difference images, and reflectance spectra have shown that the domes are morphologically, texturally and spectrally distinct from the surrounding highland and mare materials (1). They show no obvious affinities with the highland background topography and although their origin is volcanic, their eruption style is distinct from mare basalt eruption styles (1,2). The morphology of the flows that are on and surrounding the domes clearly indicates that these flows are highly viscous in their emplacement and may also have been explosive in places. The similarities of the Gruithuisen domes δ and γ to terrestrial silicic domes, in terms of morphology and viscosity of lavas, has led to the interpretation that these features might possibly be related to plutons of granitic composition which may occur within or below the lunar crust (2).

An extensive spectral mapping (UV-visible-near-infrared domain) of the Gruithuisen domes region with high spatial (sampling: 0.7 km/pixel) and spectral ($R=100$) resolution CCD images has been made at the 2 meter aperture ($F/D=25$) telescope of the Pic-du-Midi Observatory (France). The region under study is centered on the Gruithuisen δ and γ domes. It extends from a mare region located south of the domes to the blanket ejecta of the crater Mairan A to the north, though the crater itself is not included in the image. It respectively includes to the West a portion of the highlands, and to the East, a portion of the western border of Mare Imbrium, approximately located between the craters Gruithuisen B and Mairan E.

The datasets, obtained in the October 1989 full-moon period, under 15° of phase angle, consist in repeated runs comprising 10 selected narrow-band images at 0.40, 0.56, 0.73, 0.91, 0.95, 0.97, 0.98, 0.99, 1.02 and 1.05 micron. The processing of the data allows for the production of a three-dimensional high quality spectro-imaging dataset, with each image pixel characterized by its spectrum ranging from 0.4 to 1.05 μm . Reflectance spectra retrieved from the three-dimensional dataset are normalized to a standard area taken in a mare region south of the domes. Depending on the information being considered (reflectance or reflectivity), these spectra are scaled or not to unity at 0.73 μm (3).

Mare materials:

In the near-infrared domain, spectral characteristics of the mare regions within the image are homogeneous and are spectrally identical to the standard area. Exception is for the northern portion of the western border of Mare Imbrium seen in the image, which shows depleted ratios about 4% relatively to the standard. However, mare regions show spectral variations relatively to the standard in the UV/VIS image. Both a portion of the mare located south of the domes, and of the western border of Mare Imbrium, have a 0.40/0.73 μm ratio slightly above (about 4%) the standard. For the northern portion of the western border of Mare Imbrium depicted above, this ratio is about 10 to 12% above the standard. This mare unit is therefore bluer than the mare unit taken as the standard. The observed distribution and the spectral characteristics of the basalt units within the image are consistent with the

GRUITHUISEN DOMES REGION: Chevrel S.D. et al.

previous global mapping of Pieters, and suggest that the standard area has a spectral type close to that of MS2 (4).

Domes:

Spectra retrieved in the dataset from both the Gruithuisen δ and γ domes (and also from the small dome located northwest of γ) are very consistent with those of red spots relative to MS2 (1), particularly in the case of Gruithuisen δ . In relation to the following, it is of interest to note that when not considering the UV spectral behaviour, these spectra are close to highland materials spectra (1).

Spectral mixing modelling:

Relying on this spectral information, a spectro-mixing analysis considering two endmembers (mare and dome endmembers) reveals that the image spectral variability both in reflectivity and reflectance can be globally explained, with an overall image residual at the level of 1.4%.

Nevertheless, spatially organized patterns display significant local residuals in the UV-VIS domain (0.40, 0.56, 0.73 μm) which are clearly distributed within or in the vicinity of identified morphological units (δ and γ domes, Gruithuisen A crater and the blue mare unit in Mare Imbrium described above). This is very likely related to UV-VIS spectral slope variations possibly due to different causes (TiO₂ content, maturation effects,...) which are not presently discriminated. On the basis of both the mixing results and the examination of the spectra across the dome units and surroundings, the dome δ appears fairly homogeneous with a possible extension of the same spectral unit to the north, including the high albedo linear morphological feature next to the dome and oriented NW-SE. The dome γ , as for it, displays a much more obvious spectral heterogeneity (0.40-0.56 μm region), spatially related to a crescent-like unit the morphology of which should be investigated in more detail. This crescent-like unit may connect to the small dome called "Northwest" (2) but is mainly located within the morphological unit of the dome γ , including the southwest area where the presence of flow units has been proposed (2).

Also, in the northern part of the image, one notes a specific spectral behaviour departing from the endmembers mixing results in the 1.05 μm region, in possible association with the southeast part of Mairan A ejecta.

To the west of the dome γ is an area physiographically located in the highlands. However, with the above modelling, it seems to be well taken into account by the spectral mixing, with the exception of the UV domain. In order to determine whether this is fortuitous or not, we are currently investigating, when introducing a highland spectral type endmember, the relative amount of highland materials which really contribute to the observed surface properties. It keeps open the possibility that this area may comprise dome-like material.

References:

1. Head J.W. and McCord T.B. (1978) *Science*, 199, 1433-1436.
2. Head J.W., Hess P.C. and McCord T.B. (1978), *LPSC IX*, 488-490.
3. Pinet P.C., Chevrel S.D. and Martin P. (1993) *Science*, 260, 797-801.
4. Pieters C.M. (1978) *Proc. Lunar Planet Conf.*, 9th, p.2825-2849.
5. McCord T.B. et al., (1972) *JGR*, 77, 8, p.1349-1359.

DETERMINATION OF NANOGRAM AMOUNTS OF C₆₀ BY HIGH PRESSURE LIQUID CHROMATOGRAPHY. L.P.F. Chibante¹, W.S. Wolbach², and D. Heymann³. ^{1,3}Departments of Chemistry and of Geology and Geophysics. Rice University, Houston TX 77251, USA. (713) 5274890. ²Department of Chemistry. Illinois Wesleyan University, Bloomington IL 61702-2900, USA.

The determination of nanogram amounts of C₆₀ in natural materials by high pressure liquid chromatography (HPLC) has the following strong features: a) the chemical preparation of samples is simple; b) the analysis is fast; c) quantitative analysis is simple; d) the technique itself can be used to separate C₆₀ from interfering substances prior to analysis.

Our own analytical system consisted of: 2 Waters model 510 pumps, the U6K injector, the Waters 996 Photo Diode Array detector, and the 3.9 mm x 300 mm Nova-Pak™ C-18, 4 μ m chromatography column. The mobile phase was a mixture of methanol and toluene, usually 50:50%, or 55:45%, at a flow rate of 2 ml/min. Increased proportions of methanol lengthen the retention time of C₆₀, increase the resolution of substances, and decrease the peak heights in the chromatograms. The photodiode array collected the UV/VIS spectra in the range 310-430 nm every 4 seconds; however, the chromatograms shown in this abstract are constructed from absorption at 330 nm. The volumes injected were 25 μ l.

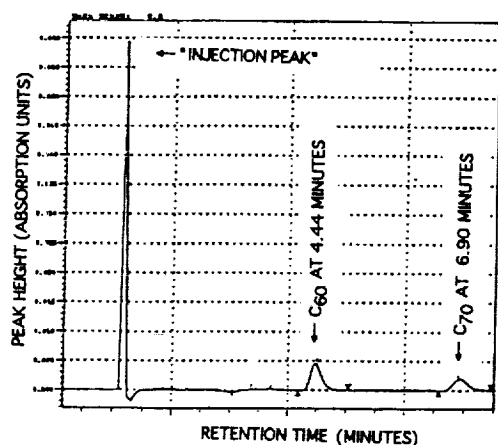
Fig. 1 shows the chromatogram for the injection of 50 ng C₆₀ (and C₇₀) in toluene. The sharp peak at 1.2 min. is due to the injection. The peaks at 4.44 and 6.90 min. are due to C₆₀ and C₇₀. Fig. 2 shows the calibration of sensitivity and linearity with a set of standards. Amounts as small as 0.5 ng injected can be determined. The accuracy for injections of more than 10 ng is mainly due to the error of the injection volume (\pm 8%). For smaller amounts, baseline corrections become the main source of errors.

Fig. 3 shows the chromatogram of a toluene-extract from a clay sample. The much higher and broader injection peak is typical for extracts from natural materials such as clays and shales. It is due to toluene-soluble hydrocarbons. One consequence is that small peaks from nanogram amounts of fullerenes are "riding" on the flanks of these hydrocarbon signals, hence may become completely masked by them. We have investigated whether it would be possible to reduce the hydrocarbon content without affecting the fullerene content by treating samples containing C₆₀ and C₇₀ as solids with 0.1 M K₂Cr₂O₇ in 2.0 M H₂SO₄ at 85 and 50 °C for up to 620.5 hours. The results show that this treatment destroys too much fullerenes even at 50 °C. C₆₀ was oxidized significantly faster than C₇₀. On the basis of results such as shown in figures 1 and 3, we concluded that it should be feasible to separate the hydrocarbons and fullerenes prior to analysis by HPLC. Since the retention times of the substances are known, one can collect the fluids emerging from the photodiode array in appropriate time intervals. The much diluted fullerene fractions must then be concentrated by evaporation. Preliminary experiments with the

DETERMINATION OF C₆₀. L.P.F. Chibante *et al.*

analytical column show that this is feasible. We will, however, do the actual separations on a semi-preparative column which accepts injections of sample volumes up to 2 ml.

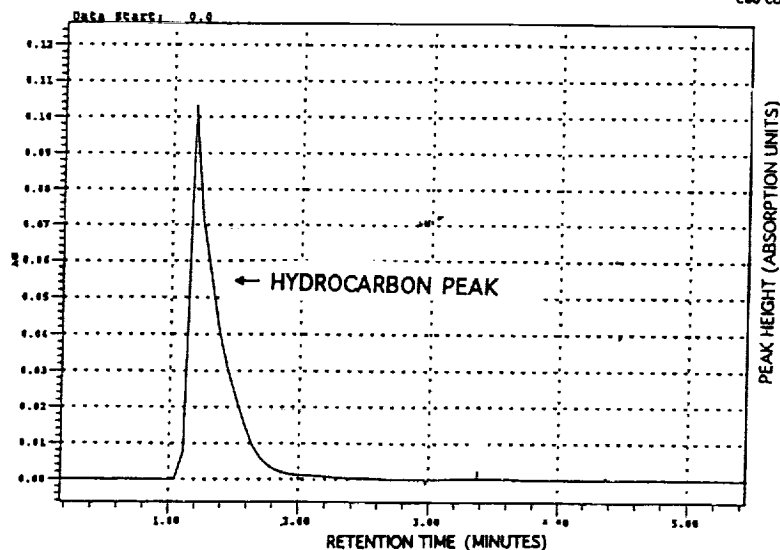
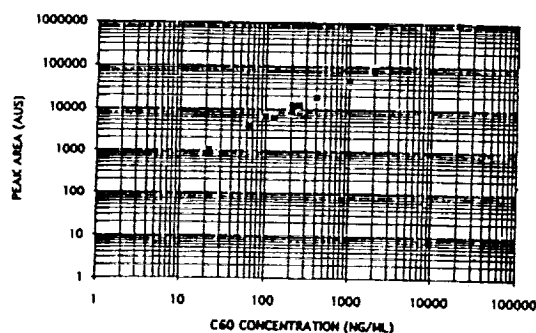
This research was supported by grants from NASA, NSF and the Welch Foundation.



← FIGURE 1

CHROMATOGRAM OF 50 ng EACH OF
C₆₀ AND C₇₀

FIGURE 2 ⇒
CALIBRATION OF INSTRUMENT
SENSITIVITY AND LINEARITY



← FIGURE 3

CHROMATOGRAM OF EXTRACT
OF A CLAY SAMPLE

MORO: A EUROPEAN MOON ORBITING OBSERVATORY

A.F. Chicarro (*) and G.D. Racca (*), Space Science Dept. (*), Scientific Projects Dept. (*), European Space Agency, ESTEC, Postbus 299, 2200 AG Noordwijk, The Netherlands.

Background:

The Moon ORbiting Observatory (MORO) mission is being studied by the European Space Agency as a candidate mission for the next medium-size (M3) project of ESA, in the framework of the Agency's Horizon 2000 scientific program. The available budget for such a mission is about 350 M\$ including launch. In the planetary field, MORO is in competition with a network of surface stations on Mars and a Mercury orbiter until the final selection in 1996. MORO could be the first step of an ambitious long-term plan for lunar exploration and utilization in ESA (1).

Scientific Objectives:

The global characterization of the lunar surface, together with investigations of the interior and the environment of our natural satellite, represent the main scientific objectives of MORO. The following disciplines will be addressed by the core scientific payload: geology and morphology (imaging system); geochemistry and mineralogy (γ -ray spectrometer, Vis-IR spectrometer); topography and heat flow (altimeter with radiometer capability). In addition, a number of instruments are also being considered for gravimetry (sub-satellite tracking), magnetism (magnetometer) and solar wind and electric field (plasma package).

Mission Scenario:

The stringent budgetary limitations, within the ESA plans for this class of mission, have imposed a limited spacecraft design and mission scenario on the study team. An Ariane-5 launcher will be shared by the MORO spacecraft with other payloads. The mission scenario includes a launch into geo-transfer orbit with subsequent transfer into a proper autonomous lunar trajectory. The dry mass of the spacecraft will be limited to about 600 kg. Several trade-off studies are currently being performed to select the simplest spacecraft configuration which would satisfy the mission scientific objectives. A feasible mission concept, based on a 3-axis stabilized spacecraft in polar orbit, will be presented at the conference.

Reference:

(1) ESA's Lunar Study Steering Group, *Mission to the Moon: Europe's Priorities for the Scientific Exploration and Utilisation of the Moon*, European Space Agency, ESA SP-1150, 190 pp., 1992.

1000

1000

1000

1000

1000

FORMATION OF IAB-IIICD IRON METEORITES; B.-G. Choi, and J.T. Wasson, Institute of Geophysics and Planetary Physics and Department of Earth and Space Sciences, University of California, Los Angeles, 405 Hilgard, Los Angeles, CA 90024.

Iron meteorite groups IAB and IIICD often contain chondritic inclusions rich in planetary-type rare gas whose presence tends to exclude the possibility of formation in a low-viscosity core of the sort that produced the magmatic groups such as IIIAB. Groups IAB and IIICD also differ from other groups in terms of their very high abundances of volatile metals (C, Ga, Ge, As) and in terms of their element-Ni distribution patterns [1]. The compositions of the IAB and IIICD irons differ only in terms of the Ga, Ge and Ir contents of their high-Ni members [1]; no element resolves them at Ni contents < 90 mg/g. We therefore will treat them as a single group in this paper, and use IAB to refer to the combined group. To successfully model IAB, one must explain a large set of unusual properties. The bulk composition of IAB is inferred to be the same as the mean of the low-Ni (Ni < 68 mg/g) members of the group. The O-isotope compositions ($\delta^{18}\text{O} \approx 5$, $\Delta^{17}\text{O} \sim -0.45$) of IAB silicates fall below the terrestrial fractionation line [2], suggesting a close link to carbonaceous chondrites such as CR or CM. Volatile abundances yield another link of IAB to carbonaceous chondrites; element/Ni ratios in IAB are high, similar to those in CI and CM chondrites, and higher than those in other chondrite groups, carbonaceous chondrites. In this abstract, we suggest that the Ga and Ge depletion in high-Ni IAB irons is related to the high C abundance in this group.

Several ungrouped irons are closely related to IIICD [3] and on some diagrams tend to fill the compositional gap between IAB and IIICD. If we substitute Ir for Ni as the reference axis in log-log plots, they are hardly resolvable. Like IAB members, they show enrichments of Au, As and Cu relative to magmatic irons. Another interesting observation is that on siderophile-Ir plots the IIE iron meteorites, which were produced by impact melting [4], plot with the dense high-Ir head of IAB. The enrichment of melt-favoring elements in IAB, IIICD, IIE and some ungrouped iron meteorites suggests that they originated by partial melting. It has been suggested that such partial melts were produced by impact melting in a megaregolith [1] or the incomplete melting of the interior of a parent body by an certain heat source [5,6]. Both models call for the melt to lie near the Fe,Ni metal-troilite cotectic in order to keep the melting temperature low.

Kracher [5,6] examined a fractional-crystallization model of a partially differentiated chondritic parent body. Assuming that the initial melt contained slightly less S than the cotectic composition, he explained the dense head of low-Ni portion in IAB and IIICD iron meteorites by compositional kinks in siderophile-Ni log-log plots. Cocrystallization of Fe,Ni metal and troilite changes the bulk distribution coefficient dramatically [7]. But one also expects compositional gaps to occur when cocrystallization begins. Troilite doesn't accept most siderophiles into its crystal structure. About four times (by mass) more troilite than metal forms during cotectic crystallization [8]. Because analysts avoid troilite, the concentration of a strongly siderophile element should jump up to a value five times higher. Such compositional gaps are not observed. Also if the IAB melts were nearly identical to the cotectic composition of Fe,Ni metal and troilite, the fraction

PRECEDING PAGE BLANK NOT FILMED

PAGE 254 INTENTIONALLY BLANK

FORMATION OF IAB-IIICD IRONS**Choi B.-G. and Wasson J.T.**

of melt may have been too small to segregate out and form a metallic core, and we do not expect efficient fractional crystallization in small melt pools.

We conclude that IAB siderophile element are better explained by different degrees of melting, plausibly formed by differing melting by impacts [1]. Because such melts have not experienced appreciable intermixing, they preserve more heterogeneous compositions than other iron meteorites formed in molten cores. This model can more easily account for the preservation of chondritic silicate inclusion because of the short duration of melting events. The densely populated low-Ni head head probably reflects almost complete melting. It is interesting and possibly significant that on siderophile-Ir plots IIE compositions are nearly identical to the low-Ni part of IAB.

According to the impact model [1], elements showing low concentrations in IAB remained sequestered in other phases during the impact generation of melt and the collection of these melts into puddles and pools. A problem question is to infer the siting of Ga, Ge and Ir that explains how element/Ni ratios could be 100-1000x lower in high-Ni melts than in the bulk chondrites. We suggest that this requires a strong nebular segregation into the different phases, i.e., the most refractory siderophiles and the most volatile siderophiles must be in phases distinct from the carriers of the common siderophiles. The high content of C and volatile siderophiles in IAB indicates that the precursor chondrite consisted of fine-grained matter that equilibrated with the nebular gas down to relatively low temperatures. In this case the high C content of these precursor materials probably reflects accretion as carbonaceous matter, similar to that in the CM or CI chondrites. We speculate that the Ga and Ge condensed together with this carbonaceous matter, and that it played an important role in sequestering them during the impact production of high-Ni members. This leads to the prediction that bulk C contents should also decrease with increasing Ni. A tentative examination of available data suggests that this may be correct, with bulk C contents dropping from ~20 mg/g at the low-Ni extreme to <0.5 mg/g in the high-Ni members.

Reference: [1] Wasson J.T. et al. (1980) *Zeit. Naturf.* 35a, 781-795; [2] Clayton R.N. (1983) *EPSL* 65, 229-232; [3] Malvin D.J. et al. (1984) *GCA* 48, 785 - 804; [4] Wasson J.T. and Wang J. (1986) *GCA* 50, 725-732; [5] Kracher A. (1982) *Geophys. Res. Lett.*, 412-415; [6] Kracher A. (1985) *PLSC* 15, C689-C698; [7] Kracher A. and Wasson J.T. (1982) *GCA*, 46, 2419 - 2426; [8] Kullerud G. et al. 1969, in *Magmatic Ore Deposits* (ed. H.D.B. Wilson) New Haven.

THERMAL-INFRARED MULTI-SPECTRAL OBSERVATIONS OF MARS;

Philip R. Christensen, Arizona State University, Tempe, AZ.

Thermal-infrared multi-spectral observations of Mars were made using the Mariner 9 Infrared Interferometer Spectrometer (IRIS) and Viking Infrared Thermal Mapper (IRTM) instruments during the 1970's. These data revealed a great deal about the physical nature of the surface (e.g. Kieffer et al., 1977) and the composition and dust loading of the martian atmosphere (Hanel et al., 1972; Conrath et al., 1973; Toon et al., 1977). However, they have not been fully utilized to study compositional variations in the surface materials. Vibrational spectroscopy is an excellent tool for studying the composition of solid materials, utilizing variations in the fundamental molecular vibrational modes associated with different bond strengths and atomic masses. These variations produce spectral features in the range from ~ 3 to $>50 \mu\text{m}$; the spectral region observed by the IRIS and IRTM instruments. Much of the reason for the long neglect of the existing data stems from the development of the Mars Observer Thermal Emission Spectrometer (TES) and the expectation that a wealth of new data would soon be available. Primarily out of frustration from the loss of this instrument, a reinvestigation of the existing data, initially undertaken many years ago (Christensen and Kieffer, 1984), has been performed. This analysis confirms the presence of strong absorption features clearly associated with surface materials in both the IRTM and IRIS data sets.

The IRTM and IRIS data provide an excellent combination of high spatial (IRTM) and high spectral (IRIS) observations. However, the IRTM data provide relatively poor spectral resolution (4 surface-sensing bands between 7 and $30 \mu\text{m}$) and the IRIS data have relatively poor ($>150 \text{ km}$) spatial resolution. Thus, the IRTM data can only provide spectral unit maps and cannot uniquely identify surface composition, and the IRIS data can only provide average compositional information over vast ($\sim 2 \times 10^4 \text{ km}^2$) areas. In addition, surface studies using the IRIS are greatly limited because the overwhelming majority of the total spectra ($\sim 21,000$) were acquired during high atmospheric dust opacity conditions, thus complicating surface observations. In fact, only 27 spectra were acquired during daytime (moderate signal-to-noise) conditions after the storm had cleared ($L_s > 0^\circ$).

Taken by themselves, absorption features in a single IRIS daytime spectrum can either be attributed to: 1) absorption/reemission by suspended dust particles that are cool relative to the surface; or 2) emission minima associated with normal emission from a solid surface. At night the situation is not ambiguous because suspended dust is warmer than the surface and results in an emission maxima in the $8\text{-}12 \mu\text{m}$ region due to suspended silicates, whereas surface emission will always produce an emission minima. An emission maxima was commonly observed in nighttime observations during the 1971 dust storms, leading to the correct inference that the observed spectral features were due to suspended silicate materials. These observations, however, have led to a perception that virtually all emission minima observed in daytime observations were also associated with suspended dust (option 2 above). However, the 140 spectra acquired at night under clear conditions by IRIS do not typically exhibit emission maxima between 8 and $12 \mu\text{m}$, suggesting that the atmosphere was relatively clear and the emission was originating from the surface.

The IRTM data provide additional, direct evidence that spectral features are due to surface materials. Data acquired by the Viking 1 IRTM between $L_s 10^\circ$ and 60° , local time 7 to 16 H have been processed to determine surface emissivity. (Nighttime data were excluded because spectral variations produced by non-uniform temperatures of sub-resolution rocks and fines complicate the interpretation of emissivity at night (Christensen, 1982). Data from the four IRTM wavelength bands were binned, the highest brightness temperature determined and assumed to be equal to the kinetic temperature (equivalent to assuming unit emissivity in this band), and the resulting emissivity calculated in the remaining spectral bands. These data show

THERMAL-INFRARED MULTI-SPECTRAL DATA OF MARS; P. Christensen

spatial variations in emissivity at 20 and 9 μm that closely follow surface albedo patterns. The correspondence with surface markings and the variations over small spatial scales rule out an atmospheric origin.

The next step in the analysis compared clear-period IRIS spectra with the IRTM data to determine if emission minima in the IRIS spectra could be unambiguously attributed to surface, rather than atmospheric, materials. This analysis was done by degrading the IRIS spectra to IRTM resolution using the IRTM filter transmission data. Because of the lack of IRIS data, this analysis could only be done for two regions. The first covers five spectra acquired at $\sim 50^\circ$ N latitude from Arabia, Acidalia Planitia, and Tempe Terra; the second covers a strip near 300° longitude from 15° N to -30° S. Degradation to IRTM resolution shows good agreement with the IRTM data, strongly suggesting a surface origin.

Once the surface origin of the IRIS spectral features can be established, it should be possible to compare the spectra of surface materials to spectra of minerals and rocks acquired in laboratory. Similar comparisons have been done using dust spectra (Hunt et al., 1973). Unfortunately, the IRIS data do not have sufficient radiometric resolution to allow detailed analysis. The surface data do show differences from the dust spectra and do reveal variation from place to place.

References

- Christensen, P. R., Martian dust mantling and surface composition: Interpretation of thermophysical properties, *J. Geophys. Res.*, **87**, 9985-9998, 1982.
- Christensen, P. R. and H. H. Kieffer, Analysis of martian surface compositional properties from IRTM and IRIS spectral observations, *Bull. Amer. Astron. Soc.*, **16**, 1984.
- Conrath, B., R. Curran, R. Hanel, V. Kunde, W. Maguire, J. Pearl, J. Pirraglia and J. Walker, Atmospheric and surface properties of Mars obtained by infrared spectroscopy on Mariner 9, *J. Geophys. Res.*, **78**, 4267-4278, 1973.
- Hanel, R., B. Conrath, W. Hovis, V. Kunde, P. Lowan, W. Maguire, J. Pearl, J. Pirraglia, C. Prabhakara, B. Schlachman, G. Levin, P. Straat and T. Burke, Investigation of the martian environment by infrared spectroscopy on Mariner 9, *Icarus*, **17**, 423-442, 1972.
- Hunt, G. R., L. M. Logan and J. W. Salisbury, Mars: Components of infrared spectra and the composition of the dust cloud, *Icarus*, **18**, 459-469, 1973.
- Kieffer, H. H., T. Z. Martin, A. R. Peterfreund, B. M. Jakosky, E. D. Miner and F. D. Palluconi, Thermal and albedo mapping of Mars during the Viking primary mission, *J. Geophys. Res.*, **82**, 4249-4292, 1977.
- Toon, O. B., J. B. Pollack and C. Sagan, Physical properties of the particles comprising the martian dust storm of 1971-1972, *Icarus*, **3**, 663-696, 1977.

2963

P-2
GRAIN RIMS ON ILMENITE IN THE LUNAR REGOLITH: COMPARISON TO VAPOR DEPOSITS ON REGOLITH SILICATES; R. Christoffersen, D.S. McKay, SN, NASA Johnson Space Center, Houston, TX 77058; L.P. Keller, MVA Inc., 5500 Oakbrook Pkwy., Norcross, GA, 30093.

Introduction. In efforts to understand regolith evolution on airless bodies increasing attention is now being paid to those processes and events that alter or "weather" the surfaces of regolith grains [1]. This attention has developed partly out of the ongoing need to optimize models of planetary reflectance spectra and the growing recognition that diverse types of grain coatings and surface alterations occur which can strongly influence mineral reflectance properties [1,2]. In addition to their implications for optical properties, surface features on regolith grains have provided useful clues to the basic thermal, chemical and radiation history of regoliths.

Ilmenite in the lunar regolith. Recent transmission electron microscope (TEM) studies have confirmed that silicate grains in the sub-20 μm fraction of lunar soils contain amorphous rims that likely formed by condensation of locally derived impact vapor [3]. These studies found no analogous rim deposits or coatings on ilmenite, but observations were limited by the low concentration of ilmenite relative to silicates in the bulk soils studied. We have re-examined ilmenites hand-picked from the sub-20 μm fraction of both submature and immature lunar soils and found that a large fraction do have outer margins that are highly altered and may contain vapor deposited material. The ilmenite rims have features that are also substantially different from those observed in silicates, and which we believe are influenced by solar radiation effects and subsolidus reduction, in addition to vapor deposition.

Samples and methods. Ilmenite grains 5 to 20 μm in diameter were hand picked from the sub-20 μm fraction of lunar soils 10084 ($I_s/\text{FeO}=48$), 67701 ($I_s/\text{FeO}=39$) and 61221 ($I_s/\text{FeO}=9.2$) [4]. The grains were prepared for TEM study by ultra-microtomy techniques that have been described elsewhere [3]. In addition to a combination of conventional and high-resolution imaging techniques, the TEM work utilized energy-dispersive X-ray spectroscopy (EDS) with light-element capabilities to perform chemical analyses at scales of 10-50 nm.

Results. The majority, but not all, of the ilmenites exhibit continuous outer rims 60 to 120 nm thick, which are shown to be nano-crystalline by selected-area electron diffraction (SAED). The average grain size within the rims is estimated to be between 4 to 10 nm, with a uniformly dense microstructure. Almost all rims show a 25-40% depletion in their atomic fraction of Fe relative to the grain interior. The very outer 10-50 nm of the rim contains Si (1.5-4.7 at.%), Al (0.4-1.4 %), Ca (0.4-0.8 %), and S (0.3-0.5 %) in various proportions; none of these elements occur in grain interiors.

SAED patterns confirm that nanocrystalline ilmenite makes up a portion of the rim material, but additional phases are required by the rim chemistry. We have noted two morphologically distinct types of crystallites within the rims. Type M crystallites are 8 to 10 nm in diameter with spherical or slightly elongate rounded shapes. Possibly due to interference from surrounding matrix their EDS analyses show a range of Fe/Ti ratios, although many show major Fe and minor Ti. The Type M grains are probably Fe metal, although some may also be small grains of ilmenite. The second class of rim components, Type R grains, occur as platelets 1 to 2 nm wide and 8 to 10 nm long, oriented parallel to the (001) basal plane of the ilmenite. Because they are less than 2 nm wide the platelets have been difficult to identify from EDS analyses or microdiffraction, but their crystallographic orientation and shape is identical to that of

GRAIN RIMS ON ILMENITE IN THE LUNAR REGOLITH, Christoffersen R. et al.

coarser precipitates of TiO_2 (rutile) known to form both in reduced and oxidized ilmenites [5]. Type R grains are typically highly concentrated in the outer 50 nm of a rim, with their concentration decreasing gradationally towards the interior of the ilmenite. In addition to Type M and R grains within the rims, the outer surfaces of some rims are decorated with spherical grains that we have positively identified as Fe metal. These are distinguished from Type M grains in that they are larger (10 to 20 nm in diameter) and occur as isolated blebs that protrude above the rim's outer surface.

Discussion. We believe the rims formed at least partly by alteration of the ilmenite grain's outer margin, rather than as deposited material. In particular the Type R grains are most reasonably interpreted as precipitates that formed within the original ilmenite, and along with the Type M grains represent the replacement of the ilmenite's original outer margin with a polycrystalline assemblage. This interpretation, however, does not account for the enrichments in Si, Al, Ca and S observed in the outer 5 to 10 nm of most rims. These elements would tend to indicate the presence of some type of thin surface deposit. In a few ilmenite grains we have been able to resolve a distinct, thin outer surface layer 2 to 5 nm thick, which may be the source of the anomalous elements. An interpretation of the Si and S in the rims as being derived from vapor deposition processes is consistent their known volatility [6], as well as with their presence in coatings on silicate grains now thought to be vapor deposits [3]. Ca and Al, although more refractory, should also occur in vapor deposits because they are major components of soil that is completely vaporized by micrometeorite impact.

The ilmenite rims differ from those on silicate grains in that they are *not* amorphous and, with the exception of their outer surface layers, differ in composition from their host grains only with respect to being Fe depleted. Although additional confirming evidence is needed, the phase assemblage within the rims appears to contain rutile and some Fe metal in the form of the type M grains. Both are established products of ilmenite reduction at 900-1000°C under H gas in the laboratory [7]. An alternative, low-temperature, reduction mechanism may be related to reactions discussed by [8] and [9], in which H^+ implantation by the solar wind causes *in situ* reduction.

An origin for the rims as the product of solar wind effects is consistent with the gradational nature of the rim alteration, but it is clear that their formation involved processes other than just radiation damage *per se*. As noted above, one of these processes involved the formation of a Si-enriched surface layer by vapor deposition. The surface blebs of Fe metal are distinctly coarser in grain size than the bulk of the ilmenite rim, and these may have formed when the grain's very outer margin was reduced in episodes of short duration, higher temperature heating. Such episodic heating may account for the Fe loss from the ilmenite rims by volatilization. Alternatively the Fe metal component might have been volatilized over time due to diurnal solar heating, which can produce temperatures of 100-120°C on the lunar surface.

The fact that ilmenites appear to have a thinner layer of vapor-deposited material relative to regolith silicates may be because the ilmenite surface is more *reactive*, and experiences volume changes, lattice strains and recrystallization associated with *in situ* reduction. Such processes may make ilmenite a less receptive substrate for acquiring and retaining vapor deposits.

References. [1] Hapke, B. et al. (1993) LPI Rpt. 93-01, LPI, Houston, TX, 14. [2] Hapke B. et al. (1975) *Moon*, 13, 339. [3] Keller, L.P. and McKay, D.S. (1993) *Science* 261, 1305 [4] Morris, R.V. (1978) *Proc. L. Planet. Sci. Conf. 9th*, 2287. [5] Haggerty, S.E. (1976) in *Oxide Minerals*, D. Rumble, ed., MSA S.Course Notes, 3, Hg-1. [6] DeMaria, G. et al. (1971) *Proc. L.Sci. Conf. 2nd*, 1367 [7] Allen, C. et al. (1994) this volume. [8] Housley, R.M. et al. (1974) *Proc. L. Sci. Conf. 5th*, 2623 [9] Yin, L. et al. (1975) *Proc. L. Sci. Conf. 6th*, 3277.

P-2
2964

BLOCK DISTRIBUTIONS ON THE LUNAR SURFACE: A COMPARISON BETWEEN MEASUREMENTS OBTAINED FROM SURFACE AND ORBITAL PHOTOGRAPHY; Mark J. Cintala⁺ and Kathleen M. McBride⁺ ⁺Code SN4, NASA Johnson Space Center; ⁺Code C23, Lockheed Engineering and Science Co.; both in Houston, TX 77058.

The distribution of blocks on the lunar surface is an important parameter not only in the interpretation of remote-sensing data such as those obtained from radar¹ and thermal² sensors, but also in operational activities, such as hazard evaluation for landing spacecraft and trafficability assessment for traverse planning. Unfortunately, few data exist that treat the distribution of blocky debris on the lunar surface. Those distributions that do exist either cover limited areas around landed spacecraft,^{3,4} treat relatively small fragments,^{3,4,5,6} or address "pathological" cases, such as distributions around impact craters.^{7,8} The ideal situation would permit assessment of block distributions over a wide area and a large range of sizes. This contribution resulted from an evaluation of the usefulness of high-resolution orbital photography in deriving the distribution of blocks on the lunar surface by comparing such data with those obtained from Surveyor photography of the same localities on the Moon.

Methodology: Enlargements of Lunar-Orbiter photography were used in conjunction with a digitizing tablet to collect the locations and dimensions of blocks surrounding the Surveyor 1, 3, 6, and 7 landing sites. Data were reduced to the location (latitude and longitude) and the major axis of the visible portion of each block;⁹ shadows sometimes made it difficult to assess whether the visible major axis corresponded with the actual principal dimension. These data were then correlated with the locations of major craters in the study areas, thus subdividing the data set into blocks obviously associated with craters and those in intercrater areas. A block was arbitrarily defined to be associated with a crater when its location was within 1.1 crater radii of the crater's center. Since this study was commissioned for the ultimate purpose of determining hazards to landing spacecraft, such a definition was deemed appropriate in defining block-related hazards associated with craters. Size distributions of smaller fragments as determined from Surveyor photography were obtained as measurements from the graphical data of [3]. Basic comparisons were performed through use of cumulative-frequency distributions identical to those applied to studies of crater-count data.

Data: The Surveyor data and least-squares fits passed through them are presented in Figure 1, along with the block distributions for the four areas as derived from the orbital photography. Three separate distributions are plotted for all but the Surveyor 7 site: one each for the blocks inside craters, those in the intercrater areas, and the sum of both subsets. The nature of the Surveyor 7 site, located on the near-field ejecta deposits of Tycho, precludes such a subdivision. In all cases, the slopes of the distributions determined from the orbital photography are greater than those obtained from the Surveyor photography, but there is a trend in the Surveyor 1 and 3 data toward lower slopes at the smaller size ranges. Only the number of large blocks at the Surveyor 3 site appear to be in agreement with the projected trend of the smaller fragments, although this agreement could be fortuitous, in light of the substantial differences in slopes. The densities of large blocks are overestimated by the distributions of smaller fragments at the other three sites.

Discussion: The reasons for the differences between the orbital and surface data are not clear. The nonlinear distributions for the three mare sites (Surveyors 1, 3, and 6) provide potential for partial reconciliation between the two, in that their slopes for the smaller sizes appear to be within the 95% uncertainty limits on the Surveyor fits. This decrease in slope, however, could be an artifact of deteriorating discriminability as the limit of resolution is approached. The Surveyor 7 data clearly deviate from the distribution of large blocks, and it is difficult to envision an effect related to resolution that could account for such a well-defined difference. Even given these uncertainties, it is clear that extrapolation of data obtained from surface photography has the potential to overestimate the density of larger blocks on the lunar surface, at least at the four sites studied here. Conversely, simple extrapolation of areal densities of large blocks cannot be justified in predicting the distribution of smaller fragments on the lunar surface.

References: [1] Thompson T.W. and Zisk S.H. (1972) *Progress Astron. Aeron.* 28, 83. [2] Mendell W.W. (1976) *The Apollo 17 Infrared Scanning Radiometer*. Ph.D. thesis, Rice University, 183 pp. [3] Shoemaker E.M. and Morris E.C. (1968) In *Surveyor Project Final Report - Part II. Science Results*, JPL Tech. Rep. 32-1265, 86. [4] Shoemaker E.M., Morris E.C., Batson R.M., Holt H.E., Larson K.B., Montgomery D.R., Rennilson J.J. and Whitaker E.A. (1968)

LUNAR BLOCK DISTRIBUTIONS: Cintala M.J. and McBride K.M.

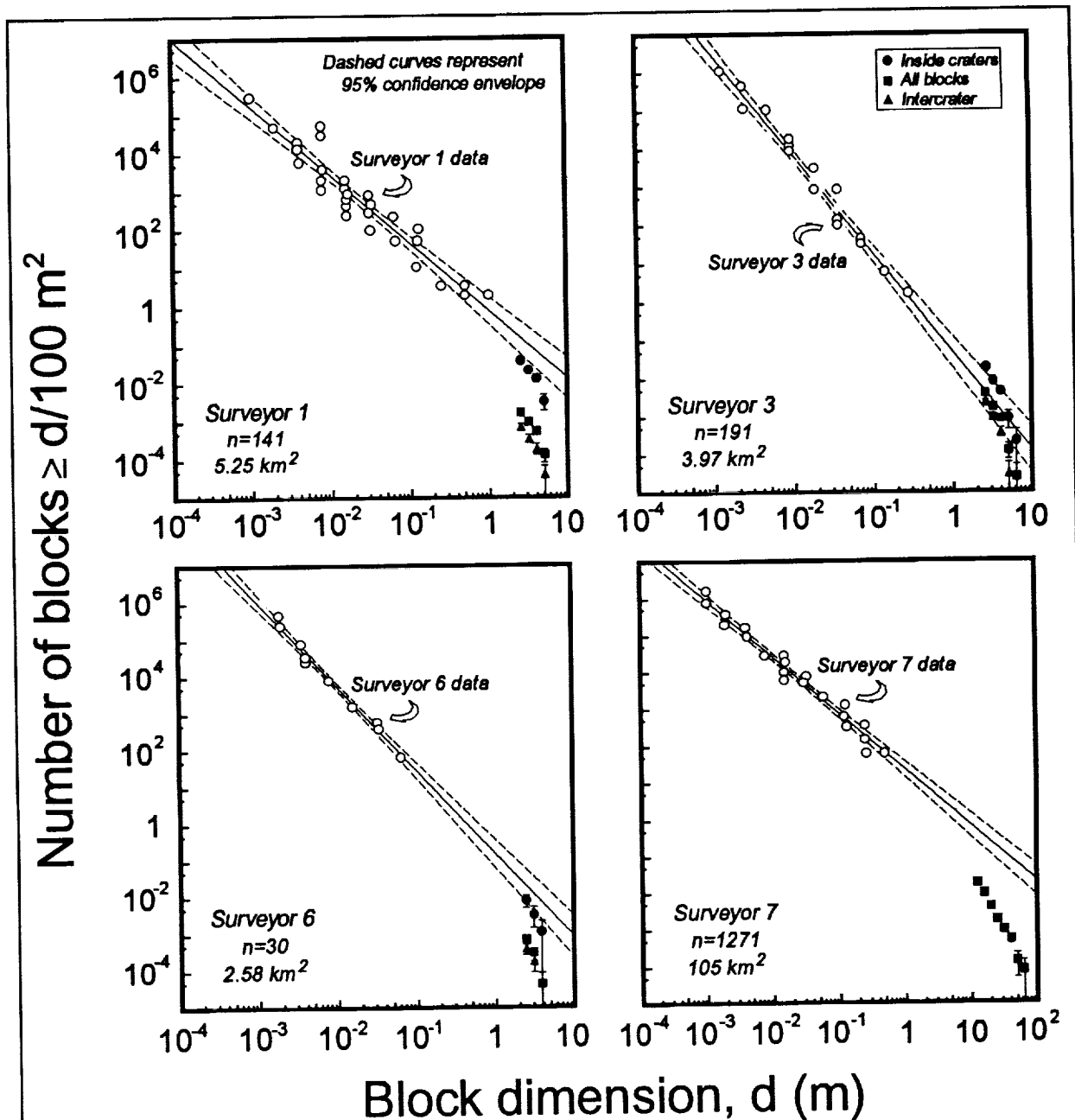


Figure 1. Block distributions as measured in the vicinity of the Surveyor 1, 3, 6, and 7 spacecraft. Only those blocks whose dimensions are larger than the effective resolution limit of the respective photograph are included in the plots. The number of blocks in each sample is indicated, as is the area on the lunar surface covered by each set of measurements. Note that the large blocks follow distributions that are invariably steeper than those of the smaller fragments measured on the Surveyor photographs.³ Error bars represent 1- σ confidence limits, assuming that the data can be represented by Poisson distributions.¹⁰

JPL Tech. Rep. 32-1265, 21. [5] Ulrich G.E., Moore H.J., Reed V.S., Wolfe E.W. and Larson K.B. (1975) *Lunar Sci. VI*, 832. [6] Ulrich G.E., Moore H.J., Reed R.S., Wolfe E.W. and Larson K.R. (1981) In *Geology of the Apollo 16 Area, Central Lunar Highlands* (eds. G.E. Ulrich, C.A. Hodges and W.R. Muehlberger), 160. [7] Cintala M.J., Garvin J.B. and Wetzel S.J. (1982) *LPS XIII*, 100. [8] Lee S.W., Thomas P. and Veverka J. (1986) *Icarus* 68, 77. [9] Grenander S.U., Cintala M.J., Wood C.A., Head J.W., and Mutch T.A. (1976) *DPS Abstracts*, 33. [10] Crater Analysis Techniques Working Group (1979) *Icarus* 37, 467.

ACID WATERS AS AGENTS OF CHANGE ON A COLD EARLY MARS; Benton C. Clark, Planetary Sciences Lab (B0560), Martin Marietta, Denver, CO 80201.

The concept of a "warm early Mars" depends upon the observation of widespread geomorphological changes via fluid processes early in Mars history. Acid waters, which seem inevitable on Mars because of the S-rich lithosphere [1] and a relatively high $\text{SO}_x/\text{H}_2\text{O}$ ratio [9], would allow a "cold" early Mars if neutralizing reactions were sufficiently slow.

Outgassing Source for Martian Volatiles. Volcanism on Mars has been widespread in both space and time. Notwithstanding important specific differences between the mantles of Earth and Mars, the geochemical similarities are such that the suite of gases emitted from martian volcanic activity should include H_2O , CO_2 , S-containing gases (e.g., H_2S and/or SO_2) and Cl-containing gases (e.g., Cl_2 and/or HCl). Both H_2O and CO_2 exist in the atmosphere of Mars. Both are also present as surface condensates. However, spectroscopic observations of the martian atmosphere clearly show that the S- and Cl-containing gases such as SO_2 , OCS , H_2S , and HCl are severely depleted, with upper limits of $\leq 10^{-7}$ to 10^{-8} of the abundance of CO_2 [2]. Likewise, there is no evidence of polar condensates of compounds of these elements, as there is for CO_2 and H_2O . Within the soil, on the other hand, there has been direct measurement of incorporated H_2O [3] and abundant compounds containing sulfur and chlorine [4]. Barring some as yet implausible geochemical sequestering process, the S/Cl ratio of about 6:1 in martian soils implicates a limit of 5% on the contribution of material of solar-like composition (e.g., carbonaceous chondrite or cometary matter) to these volatiles [5]. Hence, exogenous sources are minor or not yet observed, and the dominant source of observable volatiles at the surface of Mars is magmatic outgassing.

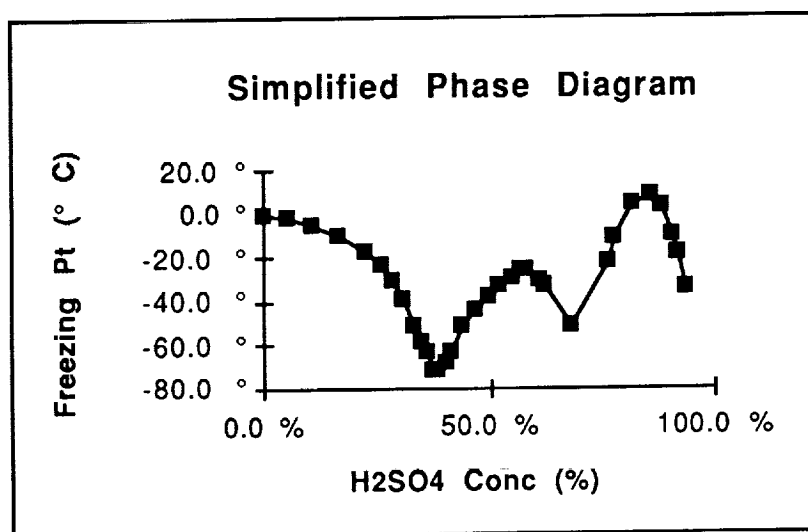
Amounts of Outgassed Water. Estimates for the total magma generated after crustal formation and the terminal stages of heavy bombardment have recently been updated. Although some 60 times lower than the current areal rate of extrusive lava resurfacing on Earth [6], the martian total is still equivalent to the release of 50 m of water averaged over the planet for every 1% (wt/wt) of H_2O released from extrusive and inferred near-surface intrusive magmas.

Model for Cold Hydrous Weathering and Fate of Martian Surface Volatiles

1. **Predominant source of volatiles is magmatic**
Only minor amounts exogenously imported, as evidenced by S/Cl ratio
2. **Magmatic gases are acidic (SO_2 , SO_3 , HCl), or convert photochemically to strong acids ($\text{H}_2\text{S} \rightarrow \text{SO}_2 \rightarrow \text{SO}_3 \rightarrow \text{H}_2\text{SO}_4$; $\text{Cl}_2 \rightarrow \text{HCl}$).**
3. **H_2O , HCl and H_2SO_4 form acid lakes. Via eutectic freezing point depression, portions remain liquid down to 200 K.**
4. **Chemical Weathering reaction rates are low**
(a) low temperatures; (b) armoring of mineral grains; (c) resistant minerals
5. **Physical Weathering reaction rates remain high**
Geomorphological modifications occur via hydrological processes
(a) erosion by flowing liquids; (b) infiltration/sapping; (c) freeze-thaw phenomena
6. **Eventually, chemical weathering becomes the sink for acids and H_2O**
Salt formation removes S, Cl; H_2O goes into clays, Fe oxyhydroxides, etc.

Acidity of Water. High acidity will result due to the preponderance of S and Cl components in magmatic emissions. On Mars, the acid/ H_2O ratio appears to be considerably higher than for Earth. Dreibus and Waenke [8] have pointed out that Mars mantle Cl/ H_2O may be nearly 1:1 (by weight). With the observed high S/Cl ratio in soil, the $\text{H}_2\text{SO}_4/\text{H}_2\text{O}$ ratio in surface waters could become quite high (0.1 to 10). Waenke et al. [9] have proposed, in fact, that SO_2 would be more abundant than H_2O and would be the dominant fluid for physical weathering on Mars. However, SO_2 rapidly converts via photochemically-driven atmospheric reactions into SO_3 , and subsequently into H_2SO_4 . Furthermore, S is removed from aqueous sulfuric acid solution more rapidly than H_2O in typical weathering processes.

ACID WATERS AS AGENTS OF CHANGE ON A COLD EARLY MARS: Clark B.C.



Physical Activity of Acid Waters. The phase diagram of $\text{H}_2\text{SO}_4/\text{HCl}/\text{H}_2\text{O}$ is highly complex, due to the existence of several solid hydrates of each of the strong acids, as well as H_2O ice. Pure HCl freezes at 161 K. Although pure H_2SO_4 itself freezes at 283 K, its aqueous solutions have extraordinarily depressed freezing points. Of great potential consequence for Mars is that the eutectic aqueous solution of 39% H_2SO_4 does not freeze until about 200 K, well below the diurnally-averaged temperatures at all latitudes on contemporaneous Mars during local summer (except on residual ice deposits). Eutectics form by freeze out of end-member or intermediate products. Thus, precipitation of ice or acid hydrates drive the residual liquid toward the eutectic point so that liquid remains present even at very low temperatures. Viscosity will be high because of the low temperatures and acid content. Erosion and sapping processes will still occur due to the transport properties of the fluid, augmented in part by increased density (1.3 g/cm^3 at the above eutectic). Analogs on Earth are difficult to come by, although erosive lavas and mud flows may represent better analogies than the extremes of fresh water or glacier ice.

Persistence of Acid Waters. Some minerals will be more susceptible to weathering than others, but reaction rates vary enormously as a function of temperature [7] and H_2O availability. Susceptible materials, such as olivines, glass, or carbonates, will be chemically attacked, while pyroxenes, feldspars, and Fe, Ti oxides will be much more resistant. The mineral assemblages of shergottites are in the second category. Initial acid-mediated weathering rinds typically form barriers to greatly slow further conversion of source material [8, 11].

Fate of Water. Chemical armoring and sediment sealing of lake beds can form a barrier to further attack. Infall of eolian transported debris will provide new material, but settling rates, grain size, composition-dependent reaction rates all affect the acid neutralization rate. If Mars' dominant soluble anion is SO_4^{2-} , then strong freezing-point depressors such as CaCl_2 would not be available for salt brines [10] because of spontaneous reaction to form poorly-soluble CaSO_4 . A pervasive drawdown of atmospheric volatiles would result from chemical reaction with abraded and comminuted surface materials and may be key to climatological evolution on Mars.

References: 1. Clark and Baird, *J. Geophys. Res.* **84**, 8395-8403, 1979. 2. Owen, T. in *Mars*, Ed. by H. Kieffer et al., U. Ariz. Press, 1992, p. 818-834. 3. Biemann et al., *Icarus* **34**, 645-665 (1978). 4. Clark et al. *J. Geophys. Res.* **87**, 11059-11067 (1982). 5. Clark, B. *Icarus* **71**, 250-256 (1987). 6. Greeley and Schneid, *Science* **254**, 996-998 (1991). 7. Burns, R. *Geochem. Cosmochem. Acta* **57** (1993). 8. Dreibus, G. and Waenke, H., *Icarus* **71**, 225-240 (1987). 9. Waenke et al., MSATT Conference, Kona, June 1992. 10. Clark, B. and van Hart, D., *Icarus* **45**, 370-378 (1981).

INFRARED SPECTRAL OBSERVATIONS OF SMALLER (50KM) MAIN BELT S, K, AND M TYPE ASTEROIDS; Beth E. Clark¹, Jeffrey F. Bell², Daniel J. O'Connor³ and Fraser P. Fanale², ¹McDonald Observatory, University of Texas at Austin, 78712, ²Planetary Geosciences, University of Hawaii at Manoa, 96822, ³Department of Physics, University of Siena.

INTRODUCTION

We report on our most recent observations of S, K, and M Type asteroids obtained with the seven color infrared filter system (SCAS) at the NASA Infrared Telescope Facility on Mauna Kea. Thirty-five new asteroid observations are presented, and bring the total of SCAS asteroid spectra to ninety-three. Among this collection are 81 S-types, 9 M-types, 1 C-type, 2 previously reported K-types and possibly 5 newly identified K-types. The average size of SCAS survey asteroids is about 50 km in diameter, compared to the average size of 102 km for the 52-color survey S-types [1]. Results of the analyses of these data are encapsulated as follows:

RESULTS

- 1) Asteroid 69 Hesperia has been observed with both the SCAS and the 52-color systems [1]. The 52-color data present Hesperia as a spectrally anomalous M-type. An average of four recent observations with SCAS however, show Hesperia to be a quite normal M-type, with a smooth spectral continuum slope of 0.24% (see Figure 1).
- 2) Asteroid 136 Austria, classified M-type by Tholen and Barucci [2], now appears to be more like an S-type upon analysis of integrated visible [3] and infrared wavelength spectra.
- 3) Asteroids 397 Vienna, 458 Hercynia, 642 Clara, 824 Anastasia, and 1186 Turnera, previously classified as S-types by Tholen and Barucci [2] actually appear to have K-type infrared spectral characteristics. A K-type asteroid, as described by Bell [4], is one which has S-type visible spectral characteristics and C-type infrared spectral characteristics. K-types have been proposed to be the CV/CO meteorite parent bodies.
- 4) Asteroids 513 Centesima and 633 Zelima, previously classified K-types by Granahan *et al.* [5], are verified as K-types with this data set.
- 5) Points 3 and 4 combined imply that a sampling of 83 S-Type asteroids as classified by the Tholen taxonomic system [6] will contain about 8% "misclassified" spectral K-types.
- 6) Spectral continuum slope ranges for the M-class asteroids as previously reported by Fanale *et al.* [7] based on the 52-color data have been extended from 0.04 - 0.33% to 0.03 - 0.39%. Continuum slopes known for laboratory samples of Fe,Ni metallic meteorites range from 0.22 - 0.64%.

ASTEROID INFRARED SPECTRAL REFLECTANCE: Clark B.E. et al.

CONCLUSION

These new observations are part of the growing database of asteroid reflectance spectra. This database is envisioned to eventually cover all observable size ranges of main belt, near earth and trojan asteroids. Integration of high and low resolution, visible and infrared data will be of invaluable use to compositional spectroscopists and planetary statisticians and will serve towards our goal of a more detailed understanding of the formation and geologic histories of small bodies in the Solar System.

REFERENCES

- [1] Bell J.F. et al. 1988, *LPSC XIX*, 57-58. [2] Tholen D.J. and Barucci M.A. 1989, *Asteroids II*, 298-315. [3] Chapman C.R. and Gaffey M.J. 1979, *Asteroids*, 655-687. [4] Bell J.F. 1988, *Meteoritics* 23, 256-257. [5] Granahan J.C. et al. 1993, *LPSC XXIV*, 557-558. [6] Tholen D.J. 1984, *Ph.D. Thesis*, Univ. Arizona. [7] Fanale et al. 1992, *Jour. Geophys. Res.* 97, 20,863-20,874.

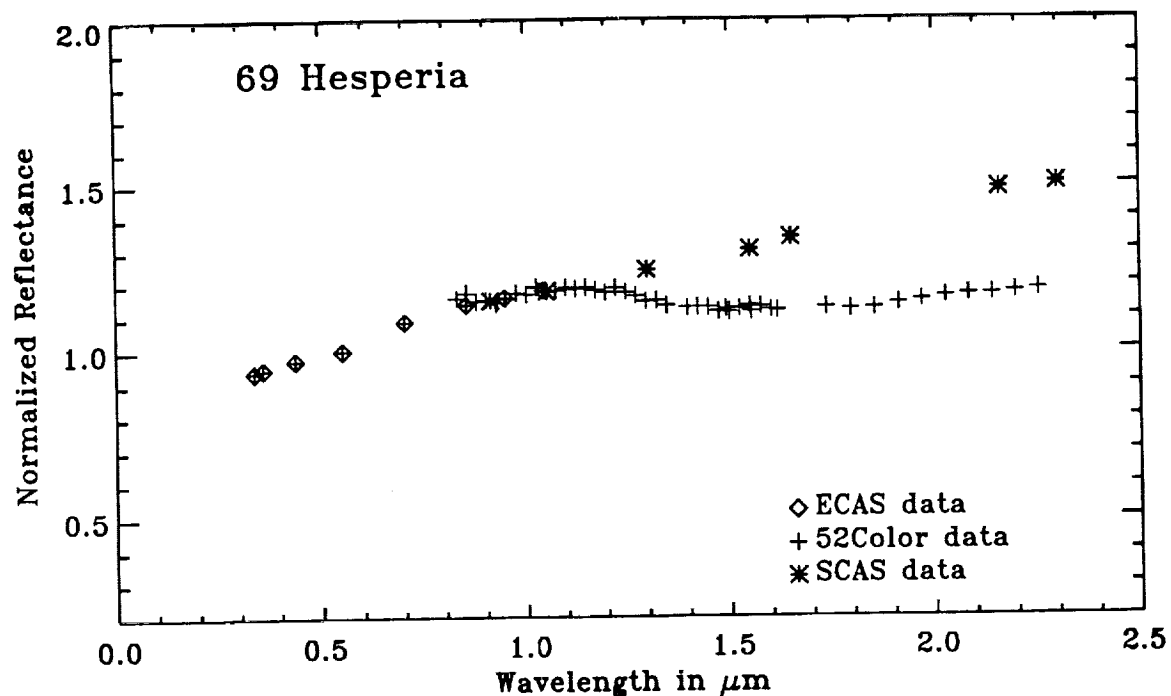


FIGURE 1 Spectral reflectance of asteroid 69 Hesperia, as obtained by the various systems shown. Note that four observations, separated in time, are averaged to produce the SCAS spectrum shown here.

P-2
525-89 ABS ONLY
2965

N94-35420

LPSC XXV

267

REMOTE GEOCHEMICAL EXPERIMENT PACKAGE FOR DISCOVERY CLASS MISSIONS

Pamela E. Clark, Catholic University, Washington DC; Larry G. Evans, Computer Sciences Corporation, Lanham-Seabrook, MD; Jacob I. Trombka, NASA/GSFC, Greenbelt, MD.

Remote sensing X-ray and gamma-ray spectrometers can be used to infer elemental composition on atmosphereless bodies, such as asteroids, the moon, and Mercury (1). The composition of the planetary body and variations in its surface chemistry are of fundamental importance in understanding the formation and dynamics of that body. Thus, for Discovery class missions, X-Ray Fluorescence (XRF), Gamma-Ray Spectrometer (GRS) or a combined Geochemical Experiment Package (GEP) have been proposed. These instruments can meet the mission science objectives, while still meeting the weight, power, and cost constraints. These missions include NEAR (Near Earth Asteroid Rendezvous), MASTER (Main-belt Asteroid Rendezvous), and others such as HERMES (Mercury Orbiter). This paper presents the results of calculations done to assess the sensitivity of a combined instrument to obtain elemental compositions of planetary bodies with an uncertainty small enough to be scientifically useful.

The first orbital experiment package was flown on the Apollo 15 and 16 missions in the early 1970s. The Apollo experiments were highly successful in providing surface compositional data of a solar system body without an atmosphere (2, 3, 4, 5). Orbital determinations of major and some minor elements of lunar petrological interest extended the 'ground truth' provided by the lunar sample collection (3, 6). Specifically, the experiment consisted of XRF spectrometers that provided maps of Al/Si and Mg/Si abundance ratios at 30 km resolution, and a GRS that provided maps of Fe, Ti, Th, and K abundances, and overall radioactivity at varying resolutions.

Analyses of lunar orbital geochemical data led to a greater understanding of the distribution and relative abundances of major rock types on the Moon. This work, involving correlation of compositional data with geological maps and in situ data from sample sites, has been done on various scales: a) global (scale of thousands of km), to provide average composition of the surfaces of highland, maria, and plains terranes (e.g., 7); b) regional (scale of hundreds of km), to demonstrate compositional variations within terranes, which has provided crucial evidence in support of highland volcanism (e.g., 3); and c) local (scale of tens of km), to study surface expressions of underlying chemistry as exposed by local impact and volcanic features at or near landing sites and in other places of geological interest (e.g., 9).

Technological improvements that have occurred since Apollo mean that such a package flown today would have additional capabilities, including inherently higher spectral resolution. An XRF instrument flown today could provide compositional maps of Al, Mg, Si, Ca, Fe, Ti, and in some cases S. A GRS instrument would provide additional data on Mg, Al, Si, Fe, K, O as well as H, Ni, Th, and U, in some cases.

Datasets from each of the two experiments provide independent and yet complimentary measures of elemental abundances. In the presently proposed GEP, the two instruments will in some cases generate abundance data for the same elements (Fe, Mg, Al), but at different resolutions and for different sample depths. Depths sampled (from which meaningful signals are received) by the XRF and GRS experiments are micrometers and tens of centimeters, respectively, although signals may originate from a depth of up to 0.5 m for naturally radioactive elements such as Th. Thus, the uppermost regolith, a mixture of gardened materials, would be sampled by the XRF measurements while bedrock may be included in the GRS measurements. Comparison of XRF and GRS derived datasets for the same element will give information on near-surface regolith stratigraphy and/or differences between local and regional expressions of major rock types.

Previously developed models of gamma-ray emission (8) used for the Mars Observer mission and XRF (9) used for the Apollo experiments were used to determine integrations times required to obtain

REMOTE GEOCHEMICAL EXPERIMENT: Clark, P.E., et al.

elemental compositions (with a 10% uncertainty at 2 sigma above background) for the targets of proposed Discovery class missions. These targets include both near-Earth and mainbelt asteroids.

The calculations were done for proposed orbital trajectories and time frames. The Sun, the primary source for fluorescent X-rays, was assumed to be at the mid-cycle level, appropriate for the years 1998-2003 proposed for these missions. The XRF instrument was assumed to have a field of view of 5° and 10° for NEAR and MASTER, respectively, while the GRS instrument was assumed to have a 45° field of view for both missions. Calculations shown here are for likely compositions for these targets: 1) Carbonaceous Chondrites Type 1 (CC1) and High Fe Chondrites (Chi) in the case of NEAR, and 2) Eucrites (Euc) for Vesta and Stony Irons (Pallasites) for Iris in the case of MASTER.

TIME TO MEASURE MODEL COMPOSITION TO 10% UNCERTAINTY

	NEAR						MASTER					
	MODEL			TIME			MODEL			TIME		
	CC1	XRF	GRS	Chi	XRF	GRS	Euc	XRF	GRS	Pal	XRF	GRS
Mg	9.6%	8 m	18 d	14.2%	6 m	4 d	4.3%	10 m	38 d	11.9%	4 m	5 d
Al	0.9%	6 h		1.0%	6 h		6.6%	9 m	180 d	0.2%	5 d	
Si	10.3%	9 m	21 d	18.1%	6 m	4 d	22.9%	3 m	2 d	8.0%	15 m	15 d
S	5.9%	15 m	140 d	2.0%	2 h		0.2%	3 d		0.0%		
Ca	1.1%	7 h		1.2%	7 h		7.4%	1 h		0.2%	11 d	
Ti	.05%	160 d		.08%	90 d		0.4%	7 d		.05%		
Fe	18.4%	55 m	8 d	27.6%	46 m	1 d	14.6%	3 h	4 d	54.5%	1 h	9 h
O	46.4%		35 d	33.9%		42 d	46.4%		23 d	19.5%		120 d
H	2.0%		2 d	0.1%			.01%			.01%		
Ni	1.1%		280 d	1.7%			0.5%			4.7%		120 d
K	430 ppm		19 d	800 ppm		6 d	350 ppm		29 d	100 ppm		350 d
Th	.032 ppm			.042 ppm			.45 ppm		75 d	.01 ppm		
U	.01 ppm			.014 ppm			.13 ppm		100 d	.002 ppm		

Where the times are given in m = minutes, h = hours, and d = days.

Our results indicate that surface mapping at up to tens of km resolution is potentially possible, and that asteroid classes should be readily distinguishable relatively early in a year-long mission: 1) carbonaceous chondrites on the basis of high H and S, and types within the class by variations in Mg, S, and H; 2) ordinary chondrites on the basis of high Mg, Si, K, Th, and U, and types within the class by variations in Fe; 3) achondrites on the basis of high Al, Ca, and Si, low Mg and Fe, and types within the class by variations in Al, Ca, and Fe; 4) stony irons on the basis of high Fe and Ti, and low Si and Al, and types within the class by variations in Fe and Si.

REFERENCES: (1) Adler and Trombka (1970) GEOCHEMICAL EXPLORATION OF THE MOON AND PLANETS; (2) Bielefeld et al (1976) PROC LUN SCI CONF 7TH 2661-2767; (3) Clark & Hawke (1981) PROC LUN PLAN SCI CONF 12TH 727-749; (4) Davis (1980) J. GEOPHYS. RES. 85 3209-3224; (5) Metzger et al (1977) PROC LUN SCI CONF 8TH 949-999; (6) Hawke et al (1985) EARTH MOON PLAN 32 257-273; (7) Clark et al (1978) PROC LUN PLAN SCI CONF 9TH 3015-3027; (8) Evans and Squyres (1987) J. GEOPHYS. RES. 92, 9153-9167; (9) Clark et al (1990) PROC LUN PLAN SCI CONF 20TH 146-160.

OXYGEN ISOTOPES IN KAIDUN; R.N. Clayton^{1,2,3}, T.K. Mayeda¹, A.V. Ivanov⁴, and G.J. MacPherson⁵. ¹Enrico Fermi Institute, ²Dept. of Chemistry, ³Dept. of the Geophysical Sciences, University of Chicago, Chicago, IL 60637; ⁴Vernadsky Institute of Geochemistry and Analytical Chemistry, Russian Academy of Sciences, Moscow 117975; ⁵Dept. of Mineral Sciences, Smithsonian Institution, Washington, D.C. 20560.

Kaidun is a complex chondritic breccia containing clasts and matrix representing several different lithologies. Some of these have been identified as CI- and CR-like carbonaceous chondrites, and others are related to enstatite chondrites. Oxygen isotopic compositions are reported here for 14 samples representing the various rock types. The compositions span a range of 15‰ in ^{18}O and have variable $\Delta^{17}\text{O}$, reflecting origins in two or more parent bodies prior to final assembly of Kaidun. There are systematic relationships to known CR and enstatite chondrites, but the Kaidun data extend the ranges of previous reported trends.

Table 1 presents brief sample descriptions and oxygen isotopic compositions. Fig. 1 shows the isotopic compositions of individual chondrules and chondrule-derived olivine fragments. Chondrule #05.05b is from the enstatite chondrite clast #05.05; #3.13a is a 5-mm diameter porphyritic olivine-pyroxene chondrule with extensive zoning in the silicates; #3.13e consists mostly of secondary phyllosilicates. The data for #3.13a and #3.13e extend the trend of carbonaceous chondrite chondrules from the region of CR chondrules toward lower ^{16}O compositions. Fig. 2 shows the isotopic compositions of various clasts of carbonaceous and enstatite chondrite type. The CR mixing line of Weisberg et al. [1] is shown for reference. Two samples of "Kaidun breccia" — #01.3.19b and #01.3.10h, consisting of clasts of CI- and CR-like material — fall on the CR trend but differ from one another by 4.5‰ in ^{18}O . These materials fall on a mixing line between chondrules (at the lower

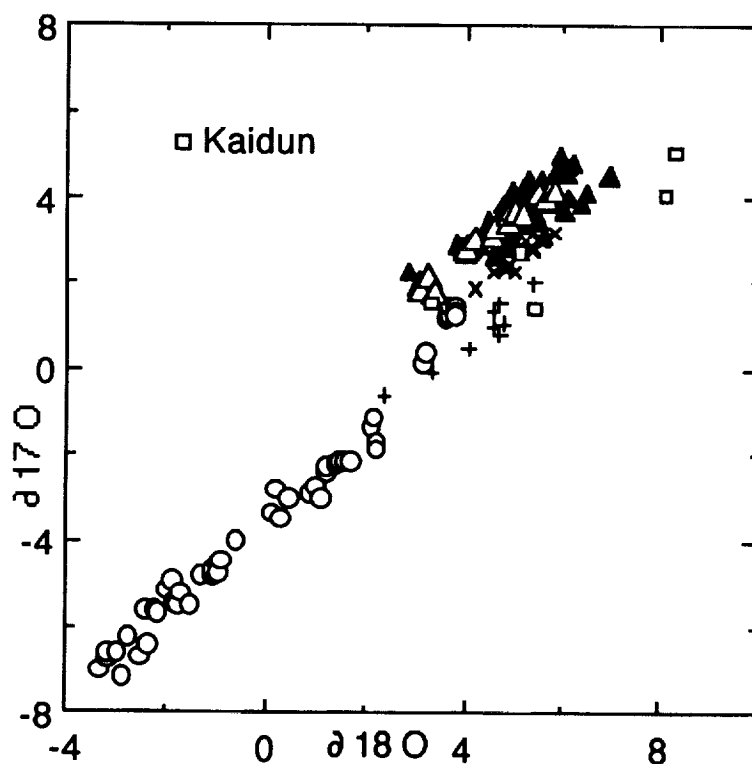


Fig. 1. Oxygen isotopic compositions of chondrules from various chondrite classes: circles — CM, CV, CO; triangles — O; crosses — E; plus signs — CR; squares — Kaidun.

left) and CI-like phyllosilicates, represented by the very fine-grained phyllosilicate-rich clast #56.03, at the upper right. The isotopic composition of #56.03 is very similar to that of Orgueil, and has not been observed in CR chondrites. The three E-chondrite/achondrite clasts fall along the terrestrial fractionation line, as do whole-rock compositions of enstatite chondrites and aubrites [2], but lie higher on the fractionation line than data from the E chondrites and achondrites. Clasts #05.05 and #3.06 are E chondrites; #3.01 is a unique "achondrite" consisting of angular enstatite fragments in a veined meshwork of Fe-Ni silicide or metal (7.6% Ni, 9.5% Si, Fe+Ni+Co/Si+P = 4.6); #05.05 is ^{16}O -rich relative to its enclosed chondrule #05.05b.

Clast 56.02 is a CM-like fragment with chondrules replaced by

OXYGEN ISOTOPES IN KAIDUN: Clayton R.N. et al.

phyllosilicates. Its isotopic composition lies 0.5‰ above the terrestrial fractionation line in a region unoccupied by any previous data. Clast #01.3.16b also consists largely of phyllosilicates and has a composition similar to CM matrix [3]. Most of the isotopic compositions reported here have recognizable counterparts in the data of Ivanov [4] for a different set of Kaidun samples. Together, the two data sets confirm that Kaidun is unique in containing such a diverse assemblage of carbonaceous and enstatite chondrites materials together with previously unrecorded types of meteoritic material.

REFERENCES: [1] Weisberg et al. (1993) *GCA*, 57, 1567; [2] Clayton et al. (1984) *JGR*, 89, C245; [3] Zolensky et al. (1994) *LPSC XXV*, this volume; Ivanov (1989) *Geochem. Inst.*, 26, No. 9, 84.

Table 1. Oxygen Isotopic Compositions of Kaidun Components

		δ^{18}	δ^{17}
<i>Chondrules and chondrule fragments</i>			
05.05b	from E-chondrite 05.05	8.12	4.08
01.3.13a	P.O.P.; zoned silicates; 5 mm	8.32	5.07
01.3.13e	phyllosilicate-rich	5.43	1.42
01.3.13d	olivine-rich	5.15	2.73
Oc	olivine crystals	3.30	1.52
<i>Enstatite-rich clasts</i>			
05.05	EL3	6.73	3.52
01.3.06	EH	7.71	4.23
01.3.01	achondrite	5.62	3.52
<i>Carbonaceous clasts</i>			
01.3.10h	CI-CR-like	10.52	4.76
01.3.19b	CI-CR-like	15.03	7.00
56.03	CI-like	19.01	9.64
56.02	CM-like	13.50	7.53
01.3.16b	CI-like	14.11	6.01
01.3.18a	pyrrhotite-magnetite-rich	6.43	1.24

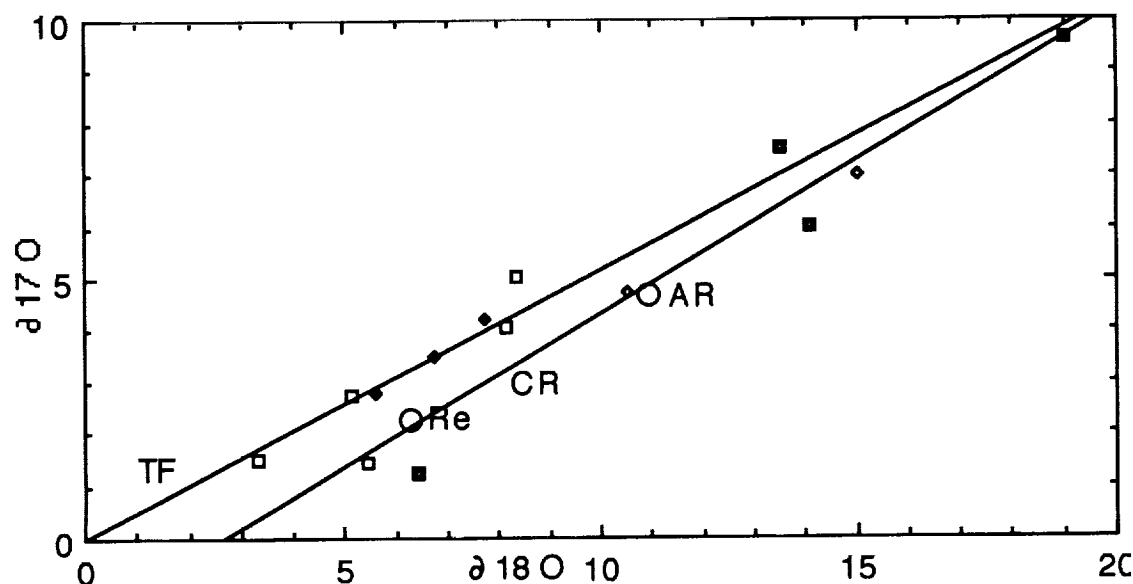


Fig. 2. Oxygen isotopic compositions of various Kaidun components. Terrestrial fractionation (TF) and CR mixing line shown for reference, along with whole-rock data for Al Rais (AR) and Renazzo (Re), Kaidun data from Table 1.

THE ROLE OF LOW TEMPERATURE HYDROTHERMAL CONVECTION IN THE PHYSICAL AND CHEMICAL EVOLUTION OF THE MARTIAN CRUST AND GROUNDWATER. S. M. Clifford, Lunar and Planetary Institute, Houston TX 77058, USA.

Given a water-rich Mars and climatic conditions resembling those of the present, the existence of a geothermal temperature gradient within the crust will give rise to a corresponding vapor pressure gradient that drives the diffusion of H_2O from the higher temperature (higher vapor pressure) depths to the colder (lower vapor pressure) near-surface regolith [1,2]. An important consequence of this geothermally-induced vapor transport is that the cold-trap represented by the pore volume of the cryosphere should remain saturated with ice for as long as a significant reservoir of subpermafrost groundwater survives on the planet. Under such conditions, a low temperature hydrothermal system will develop in the unsaturated zone between the water table and the freezing front at the base of the cryosphere (Figure 1) -- a process that has likely had important consequences for the physical and geochemical evolution of the crust, the composition and viscosity of groundwater, and local cryosphere thickness.

The development of a low temperature hydrothermal system within the unsaturated zone between the water table and the base of the cryosphere is a natural consequence of the thermally-induced origins of the diffusing water vapor. That is, as the crustal temperature gradient drives the upward migration of vapor from the water table, the vapor rises into the progressively colder crust above. This drop in crustal temperature results in a corresponding drop in saturated vapor pressure -- forcing some of the ascending vapor to condense and drain back to the water table as a liquid. In this way a dynamic balance of opposing fluxes is achieved, creating a circulation system of rising vapor and descending liquid condensate (Figure 1).

For reasonable values of crustal pore size ($1\text{--}10\ \mu\text{m}$) and porosity ($\sim 20\%$), a geothermal gradient of $15\ \text{K km}^{-1}$ can drive a vertical flux (per unit area) of $\sim 8.3 \times 10^{-5} - 2.8 \times 10^{-4}\ \text{m H}_2\text{O yr}^{-1}$ to the freezing front at the base of the cryosphere [1,2]. This is equivalent to the vertical transport of 1 km of water every $10^6 - 10^7$ years, or roughly $10^2 - 10^3$ km of water over the course of martian geologic history. However, there is reason to believe that this thermally induced vapor flux was even greater in the past. Models of the thermal history of Mars suggest that 4 billion years ago the planet's internal heat flow was $\sim 3 - 5$ times larger than it is today [3,4]. Because the vapor flux rate is directly proportional to the temperature gradient, this implies a similar increase in the volume of water cycled through the early crust.

The convective cycling of $10^2 - 10^3$ kilometers of water (per unit area) between the water table and the base of the cryosphere should have had a considerable effect on the geochemical and physical evolution of the martian crust and groundwater. On Earth, groundwater that resides within crustal rocks for hundreds of millions of years generally evolves into a highly mineralized brine consisting of a saturated mixture of chlorides, carbonates, sulfates, silica, and a variety of other dissolved species [5]. On Mars, this geochemical evolution will likely be augmented by the influx of minerals leached from crustal rocks by low-temperature hydrothermal circulation. The cycling of $10^2 - 10^3$ km of water through the unsaturated zone between the water table and the base of the cryosphere will deplete the intervening crust of any easily dissolved substances, concentrating many of them in the underlying groundwater to levels far in excess of their respective saturation points. The resulting precipitation of these minerals beneath the water table should lead to widespread diagenesis and to the development of a distinct geochemical horizon within the crust [6]. Where exposed by subsequent faulting or erosion, this horizon should appear as a relatively competent layer whose upper boundary conforms to a surface of constant geopotential. Although not diagnostically unique, such an observation is consistent with mineral deposition in an unconfined aquifer in hydrostatic equilibrium.

The concentration of soluble minerals beneath water table will also have a dramatic effect on groundwater viscosity. For example, at 290 K the viscosity of pure water is roughly 1 centipoise ($= 10^{-3}$ Pascal-second); however, naturally occurring brines on Earth can have effective viscosities that are many orders of magnitude higher. Since virtually all calculations of fluid flow, both above and beneath the martian surface, have assumed the unlikely pure-water value of viscosity, their results could be off by a factor of 10, 10^3 , or even more. Two examples of hydraulic properties that are highly sensitive to the value of viscosity are the Reynolds number (which is *inversely* proportional to the fluid's viscosity) and the permeability of a rock mass necessary to permit a particular discharge (which is *directly* proportional to groundwater viscosity). Thus, where a local permeability of 1 darcy may be required to permit a particular discharge for "pure" groundwater, a permeability as much as

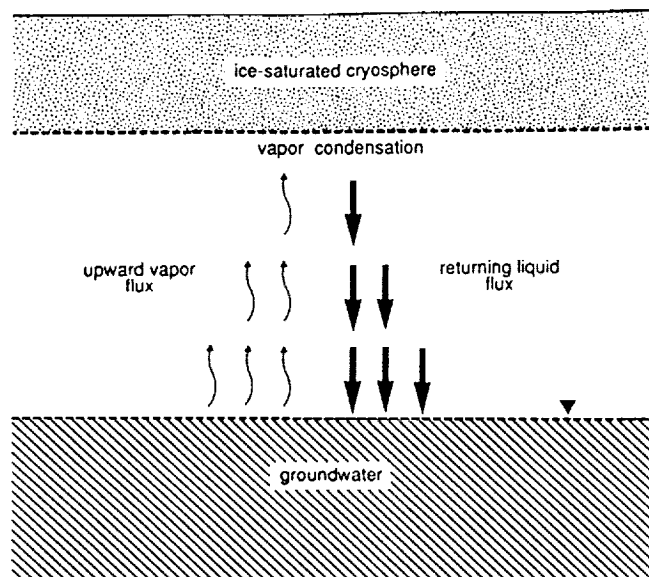


Fig. 1 . An example of low-temperature hydrothermal circulation driven by the Martian geothermal gradient.

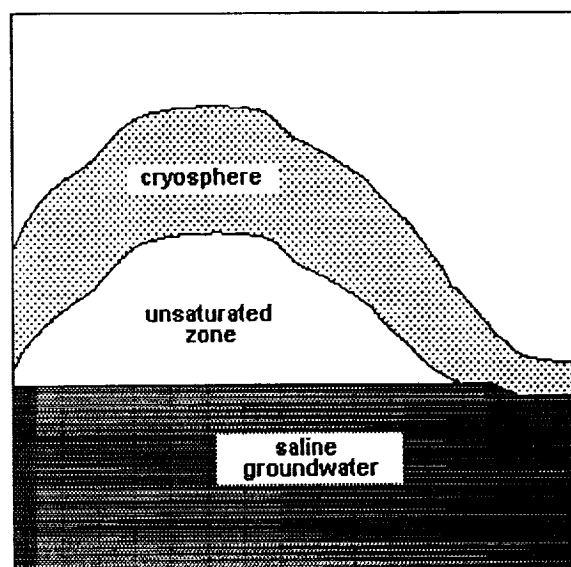


Fig. 2. A hypothetical cross-section of the crust illustrating the potential effect of low-temperature hydrothermal leaching on the local thickness of the cryosphere.

several orders of magnitude higher might be necessary to support that same discharge given a more realistic estimate of groundwater composition and viscosity.

Finally, the leaching of soluble salts from the crust -- and their concentration in the underlying groundwater -- will also have important consequences for the freezing point and local thickness of the cryosphere. For example, consider the cryosphere and groundwater relationships illustrated in the hypothetical crustal cross-section in Figure 2. In those regions where the water table and base of the cryosphere are not in intimate contact (e.g., see Section 2.3 of reference 2), the cleansing of salts from beneath the cryosphere will also eliminate any potential for a significant salt-induced depression of the freezing point -- thus, maximizing the cryosphere's local thickness. On the other hand, where groundwater is in contact with the base of the cryosphere, the freezing temperature of the salt-saturated groundwater (and, thus, the basal temperature of the cryosphere) could be depressed well below 273 K -- thereby minimizing the cryosphere's local thickness. For a groundwater system in hydraulic equilibrium, this suggests that the cryosphere of Mars will generally be thinner at lower elevations (where it is most likely in contact with groundwater) than it is at higher elevations. It also suggests that estimates of the total pore volume of the cryosphere that are based on the assumption of a globally depressed basal freezing temperature (e.g., Section 2.3 of reference 2) likely underestimate the total volume of water that could be stored as ice within the frozen crust.

A more detailed discussion of each of these points is currently in preparation.

References: [1] Clifford, S.M. (1991). *Geophys. Res. Lett.*, **18**, 2055-2058. [2] Clifford, S.M. (1993). *J. Geophys. Res.*, **98**, 10973-11016. [3] Davies, G.F., and R.E. Arvidson (1981). *Icarus*, **45**, 339-346. [4] Schubert, G., and T. Spohn (1990). *J. Geophys. Res.*, **95**, 14095-14104. [5] White, D.E. (1957). *Bull. Geol. Soc. Am.*, **68**, 1659-1682. [6] Soderblom, L.A. and D.B. Wenner (1978). *Icarus*, **34**, 622-637.

AN X-RAY DIFFRACTION AND REFLECTANCE SPECTROSCOPY STUDY OF IRON SULPHIDES

Edward A. Cloutis, ER Georesearch Ltd., 4 Huntstrom Road N.E., Calgary, Alberta, Canada T2K 5W3, and Michael J. Gaffey, Department of Earth and Environmental Sciences, Rensselaer Polytechnic Institute, Troy, New York 12180-3590

The reflectance spectra of some iron sulphides exhibit a range of spectral slopes and occasional Fe^{2+} absorption bands. The spectral and X-ray diffraction data suggest that the spectral differences are attributable to one or more of the following: iron content variations, crystal structure, and degree of crystallinity.

Introduction: The diffuse spectral reflectance properties (0.3–2.6 μm) of some powdered iron sulphides have been examined to determine how variations in composition, degree of crystallinity and crystal structure can affect iron sulphide spectra. Spectroscopy may be applicable to characterizing iron sulphides in various types of geological samples (e.g., thin sections, mineral separates) and has implications for geological remote sensing of iron sulphide occurrences and for pyrite-pyrrhotite geothermometry [1].

Experimental Procedure: 0–45 μm sized samples of natural pyrite (PRT101), marcasite (MAR101), pyrrhotite (PRH101), meteoritic troilite (TRO201) from the Canyon Diablo iron meteorite, and synthetic troilite (FeS ; TRO202) have been spectrally characterized. The 0.3– to 2.6- μm reflectance spectra were measured at the RELAB facility at Brown University [2] at $i=0^\circ$, $\theta=15^\circ$ and 5 nm resolution relative to halon. The compositions of the natural samples have been determined by electron microprobe (Table 1). The composition of the synthetic troilite sample is stoichiometric FeS (99.9% purity). The samples were also characterized by X-ray diffraction (XRD).

Results: XRD data indicate that the pyrrhotite (monoclinic) and synthetic troilite contain no measurable impurities. The meteoritic troilite sample contains a small amount (<5%) of graphite. The pyrite sample is contaminated with a small amount of quartz and the marcasite sample is composed of subequal amounts of pyrite and marcasite. The amount of small angle XRD scattering was used to assess relative degrees of crystallinity.

The sample reflectance spectra are shown in Figure 1. The pyrite (PRT101) spectrum exhibits 2 distinct absorption bands near 0.89 μm and 1.98 μm , similar to other pyrite spectra [3,4]. These bands are attributable to crystal field transitions in octahedrally coordinated Fe^{2+} [4,5].

The marcasite spectrum (MAR101) exhibits an absorption band near 0.9 μm , but no band near 2.0 μm . Because of the presence of appreciable pyrite in this sample, the marcasite spectral properties cannot be uniquely ascertained.

The pyrrhotite (PRH101) spectrum is relatively featureless. The overall spectral slope differs from other pyrrhotite spectra [4], suggesting that compositional and/or structural differences in pyrrhotite may be amenable to spectral analysis. The gradual reflectance increase suggests that this sample is somewhat disordered, consistent with the presence of low angle scattering in the XRD trace.

The meteoritic troilite spectrum (TRO201) is similar in shape to the pyrrhotite spectrum and to a previously measured troilite spectrum [6]. The synthetic troilite spectrum (TRO202) differs significantly from the TRO201 spectrum, with a distinct absorption band near 0.93 μm , a weaker band near 2.49 μm , a much flatter slope in the near-infrared and a more abrupt reflectance increase near 0.6 μm .

Discussion: The appearance of Fe^{2+} crystal field absorption bands is limited to the pyrite and synthetic troilite spectra. The absorption bands in the 0.3– to 0.6- μm region of the synthetic troilite spectrum are attributable to Fe^{2+} crystal field transitions [5].

The two troilite samples are compositionally similar. The XRD traces exhibit only small differences in low angle scattering and minor differences in relative peak heights. This suggests that spectral shape variations are largely attributable to differences in the degree of crystallinity. The presence of an Fe^{2+} band in the synthetic troilite sample near 0.9 μm suggests that small changes in composition can affect the appearance of this band.

All 5 spectra exhibit overall spectral shapes characteristic of powdered semiconductors [4]. The synthetic troilite sample exhibits the most abrupt reflectance rise near 0.6 μm , the flattest near-infrared slope and the least low angle X-ray scattering. This suggests that the degree of crystallinity affects spectral shape in the wavelength region associated with valence to conductance transition and that measures of spectral slope in the transition region may be most effective for assessing relative degrees of crystallinity.

Pyrite can be discriminated from the other natural sulphides on the basis of its well defined Fe^{2+} absorption bands. Comparisons of the compositionally similar PRT101 and MAR101

IRON SULPHIDE SPECTRA AND XRD: Cloutis, E.A. and Gaffey, M.J.

samples suggests that differences in the crystal structure [7] will control the appearance of Fe^{2+} bands while comparison of the two troilite samples indicates that composition may also be a factor.

The wavelength positions of minimum reflectance of the Fe^{2+} absorption bands in the pyrite and synthetic troilite samples differ (0.89 and 1.98 μm versus 0.93 and 2.49 μm , respectively) and may be due to differences in iron content and/or crystal structure; differences in degree of crystallinity are not likely to significantly affect band positions.

Conclusions: The data strongly suggest that the spectral properties of iron sulphides are a function of iron content, crystal structure and degree of crystallinity. Differences in degree of crystallinity may affect the shape of the reflectance rise. Differences in iron content can affect the appearance of Fe^{2+} absorption bands near 0.9 μm and 2.0 μm . Differences in crystal structure may also affect the appearance of Fe^{2+} absorption bands and overall spectral shape. The relative importance of each of these factors cannot however be deduced from the current sample set.

Acknowledgments: This study was supported by a grant-in-aid of research from the Geological Society of America (to EAC) and NASA Planetary Geology and Geophysics grant NAGW 642 (to MJG). Thanks to Dr. Carle Pieters and Stephen Pratt for acquiring the reflectance spectra at the NASA Reflectance Experiment Laboratory (RELAB) spectrometer facility in the Department of Geological Sciences at Brown University and to Diane Caird for acquiring the X-ray diffraction data in the Department of Geology at the University of Alberta.

References: [1] Deer, W.A. *et al.* (1966) An introduction to the rock-forming minerals. Longman, London. [2] Pieters, C.M. (1983) *JGR*, 88, 9534-9544. [3] Burns, R.G., and Vaughan, D.J. (1970) *Amer. Mineral.*, 55, 1576-1586. [4] Hunt, G.R. *et al.* (1971) *Mod. Geol.*, 3, 1-14. [5] Vaughan, D.J., and Craig, J.R. (1978) Mineral chemistry of metal sulphides. Cambridge University Press, Cambridge, England. [6] Britt, D.T., and Pieters, C.M. (1990) *LPSC XXI*, 127-128. [7] Tossell, J.A. *et al.* (1981) *Phys. Chem. Minerals*, 7, 177-184.

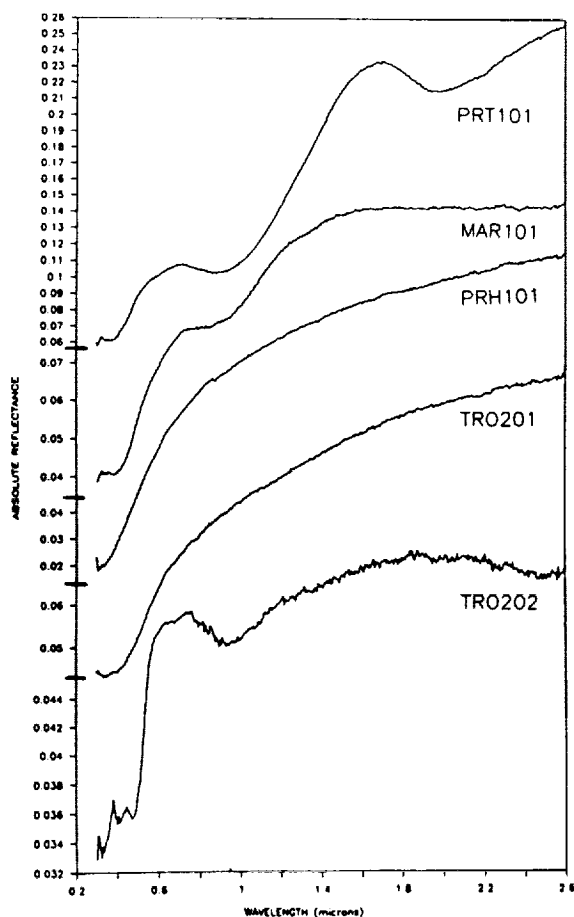


Table 1. Composition of the iron sulphides used in this study.

Wt%	Pyrite PRT101	Marcasite MAR101	Pyrrhotite PRH101	Troilite TRO201
Fe	45.97	45.45	58.53	61.50
Ni	0.00	0.00	0.70	0.03
Na	0.06	0.02	0.03	0.01
S	54.10	54.98	40.36	37.71
V	0.00	0.00	0.00	0.00
Co	0.01	0.04	0.07	0.02
P	0.00	0.00	0.00	0.00
Cr	0.00	0.00	0.08	0.32
Mg	0.08	0.00	0.04	0.00
Mn	0.00	0.00	0.00	0.00
Cu	0.00	0.00	0.00	0.00
Al	0.08	0.04	0.05	0.02
Pb	0.00	0.00	0.00	0.00
Zn	0.00	0.00	0.18	0.08
Ti	0.00	0.00	0.00	0.00
Total	100.30	100.53	100.04	99.89
Fe	7.84	7.71	10.80	11.56
S	16.07	16.26	12.97	12.35

Fig. 1. Absolute reflectance spectra (0.3-2.6 μm) of natural pyrite (PRT101), marcasite (MAR101), pyrrhotite (PRH101), meteoritic troilite (TRO201) and synthetic troilite (TRO202). Vertical scale varies for each sample.

Minimum Discharge Rates Required for Sustained Water Flow on the Martian Surface; G.D. Clow (U.S. Geological Survey, MS975, Menlo Park, CA 94025)

Small streams with depths $d \leq 1$ m are unstable on Mars under current climatic conditions and will freeze solid within 10 days [1]. One of the main factors affecting the energy balance of a river is the heat flux F_f associated with the conversion of gravitational potential energy to heat as the water flows downhill. Because F_f is proportional to $d^{5/3}$, stable perennially ice-covered rivers are expected to exist if water discharge rates can be maintained at sufficiently high levels. For such rivers, the rate at which ice accretes to the base of the ice-cover just balances the rate of sublimation loss from the surface. The objective of this study is to determine the minimum discharge rates that would be required to sustain water flow within a perennially ice-covered river. One of our motivations is to determine if moderate-sized ice-covered rivers could have flowed within the Martian outflow channels and hence participated in their modification.

For an ice-covered river to stably exist, the latent heat flux due to freezing within the river (F_L) plus F_f must exceed the rate at which heat is conducted out of the river bed into the cold surrounding terrain F_c , i.e. $F_L + F_f > F_c$. For equilibrium conditions, the freezing rate associated with F_L must equal the sublimation rate E_0 from the surface of the ice-cover. E_0 was evaluated for current Martian conditions in the Kasei Vallis region using the planetary boundary layer model described in [2,3]. At the latitude of Kasei Vallis, diurnal variations are far greater than seasonal variations. Thus, conditions were evaluated over one diurnal cycle on an "average" day ($L_s = 115^\circ$). During the day, atmospheric conditions were found to be very stable within 1 m of the ice-cover as warm air from the surrounding ice-free areas blow over the relatively cold ice-cover; at night, the situation is reversed. Taking into account the effects of atmospheric stability on the sensible and latent heat fluxes at the ice-cover's surface, the mean surface temperature of the ice was found to be $T_s = 201.6$ K, assuming an atmospheric optical depth $\tau_d = 0.4$, ice albedo $A = 0.6$, and a downwelling IR flux from the atmosphere taken from [4]. For a geostrophic windspeed of 10 m s^{-1} , sublimation rates peak at $1.12 \times 10^{-7} \text{ kg m}^{-2} \text{ s}^{-1}$ during midafternoon while mean daily sublimation rates are $5.26 \times 10^{-8} \text{ kg m}^{-2} \text{ s}^{-1}$. Thus, the flux F_L is quite small for current Martian conditions ($\approx 18 \text{ mW m}^{-2}$) and can be ignored in determining the minimum discharge rates. The conductive heat flux F_c was evaluated using a 2D steady-state thermal model and was found to be $F_c \approx c/w$ where w is the river's width and c is a constant that evaluates to 150 W m^{-1} for current Mars. The flux F_f is given by $F_f = \rho g Q S / w$, where ρ is the density of water, g is the gravitational acceleration of Mars, Q is the discharge rate, and S is the slope. Thus, the requirement for sustained water flow can be simply expressed in terms of the water discharge rate,

$$Q > c / (\rho g S). \quad (1)$$

If the discharge rate fails to satisfy this condition at any point along a river, the river will freeze solid at that point. In Upper Kasei Vallis, the regional slope is about 0.001 [5]. Based on Eq. 1, the minimum discharge rate for sustained water flow in this area is about $40 \text{ m}^3 \text{ s}^{-1}$. By comparison, the typical flow of the South Fork of the American River (Calif.) is $80 \text{ m}^3 \text{ s}^{-1}$.

Discharge Rates: Clow, G.D.

during the white-water rafting season.

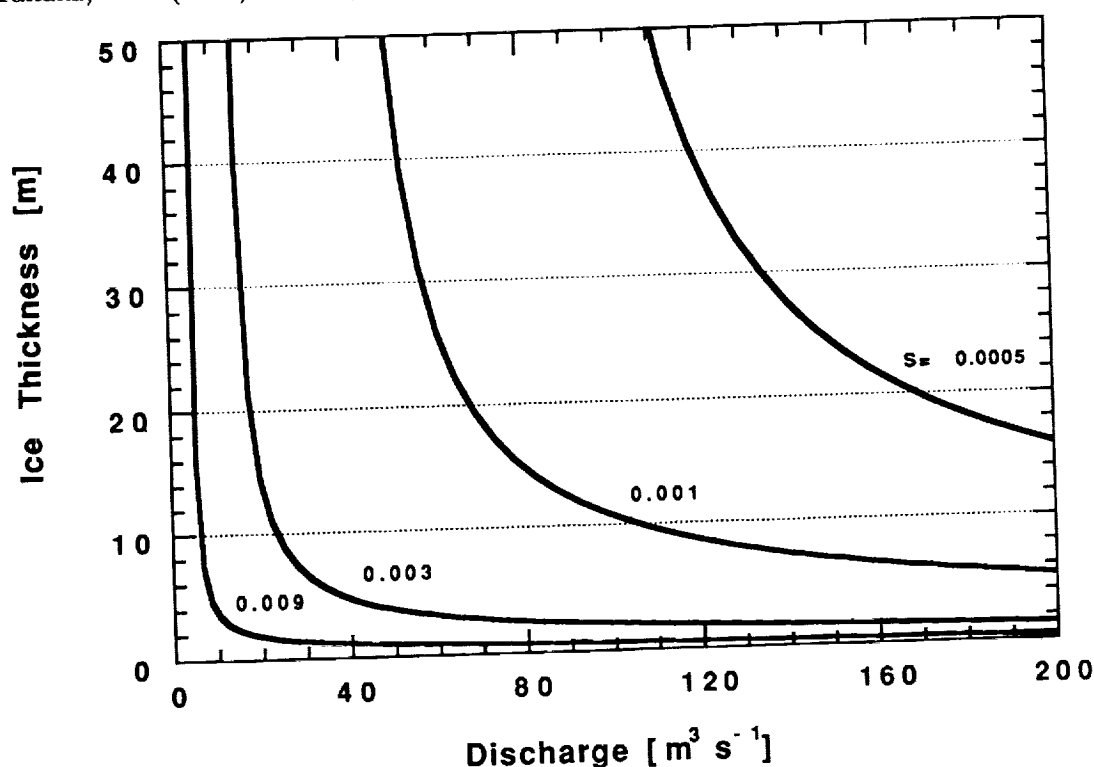
If Eq. 1 is satisfied, the equilibrium ice thickness at any point along the river is given by,

$$Z = \frac{(a/b)[e^{-bT_s} - e^{-bT_m}] - (1-A)S_o h}{F_L + F_f - F_c}, \quad (2)$$

where $a = 9.828 \text{ W m}^{-1} \text{ K}^{-1}$, $b = 0.0057 \text{ K}^{-1}$, T_s is the mean surface temperature, $T_m = 273 \text{ K}$, S_o is the mean incident solar flux, and h is the extinction pathlength for visible light in ice. Due to the presence of F_f in the denominator of Eq. 2, the equilibrium ice thickness is sensitive to the product of the discharge rate and the slope (QS). Fig. 1 shows the dramatic decrease in equilibrium ice thickness as the discharge Q is increased. Note that Z drops to about 10 m on a slope of 0.001 if the discharge rate can be maintained at $100 \text{ m}^3 \text{ s}^{-1}$. In the steepest portion of Kasei Vallis, the slope has been estimated to be 0.009 [5]. With discharges of only $40 \text{ m}^3 \text{ s}^{-1}$, the equilibrium ice thickness is predicted to be only 1.0 m in this area.

Finally, if the discharge rate should drop below that needed to sustain water flow, the ice-cover would sublime away during a time interval $\tau = Z\rho/E_o$. For a 10 m thick ice-cover, the expected lifetime is about 6 ka. A 1000 m thick glacier would potentially sublime away in 600 ka if its source was somehow cutoff. These lifetimes assume the ice is not protected by a layer of dust or other material.

References: [1] Carr, M.H. (1983) *Icarus*, 56, 476-495, [2] Clow, G.D. and Haberle, R.M. (1990) *LPSC XXI*, 209, [3] Clow, G.D. and Haberle, R.M. (1990) *LPSC XXI*, 210-211, [4] Haberle, R.M. and Jakosky, B.M. (1991) *Icarus*, 90, 187-204, [5] Robinson, M.S. and Tanaka, K.L. (1990) *Geology*, 18, 902-905.



TRITON'S LINEAMENTS: COMPLEX MORPHOLOGY AND STRESS PATTERNS;
Geoffrey Collins, Dept. of Geology, Carleton College, Northfield, MN, 55057; Paul Schenk,
Lunar and Planetary Institute, 3600 Bay Area Blvd., Houston, TX, 77058

Voyager 2 images of Triton, Neptune's largest satellite, revealed an icy moon with a variety of geologic features, including an impressive set of global-scale lineaments. Lineaments reflect the stress field on the crust at the time of their formation, preserving a record of global-scale processes. In our study, we have mapped the orientations and morphology of the lineaments to determine the stresses that caused them and to match them to theoretically predicted stress fields. The morphology and patterns of lineaments evades simple explanation. Through modeling of global stresses and morphological characterization, we shall attempt to place additional constraints on the history of Triton.

Because of Triton's retrograde orbit, it is believed to be a captured satellite [1] [2]. The initial highly irregular orbit was circularized within a short span of time after capture [3]. Triton was probably also despun during this time. These radical orbital changes produced a lot of heat within Triton, enough heat over a small enough time, some calculations say, to melt most of the planet [4]. Triton's heavily modified surface shows a very sparse distribution of craters [5], indicating that the surface is extremely young (<1 Gyr). Therefore, the lineaments we observe today must have also been formed recently and do not reflect stresses from the capture era. In this study, we explore three plausible mechanisms that could account for the formation of global-scale lineaments: change in the tidal figure, nonsynchronous rotation, and change in planetary radius.

As Triton's orbit decays, the spin rate increases and the tidal a axis lengthens, creating stresses on the crust [6, 7]. In the case of nonsynchronous rotation, the surface of the satellite is rotating slowly with respect to the a axis as a result of possible nonzero tidal torque [8], also placing stress on the crust as it adjusts to the changing shape of the surface. As a planet heats or cools, phase changes in its interior result in global volume changes which will stretch or compress the crust. Lineaments from planetary contraction or expansion should not have any preferred orientation. These general mechanisms don't necessarily work alone, however, and a combination of these predicted stress patterns may actually be manifested as lineaments on the surface.

OBSERVATIONS

Several distinct lineament types were identified, but two types are significant on a global scale: multi-ridge structures and lineated terrain. Multi-ridge structures, or 'sulci', are usually 10 km or so wide and can be thousands of kilometers long. They are composed of sets of 2-8 nearly parallel ridges trending along the lineament, with elevations on the order of a few hundred meters [9]. The other major lineament type is lineated terrain, which is characterized by short, narrow, parallel, and evenly spaced fractures or ridges. They occur over a wide area of the planet, but are generally concentrated in small regions, or 'packets', modifying the underlying terrain.

A few stratigraphic relationships can be resolved in the northern hemisphere. The cantaloupe terrain in the west seems to be one of the oldest units, followed by the sulci that cross it. These are both modified by the lineated terrain and all three of these units are embayed by the young volcanic terrain that covers most of the eastern section of Triton. In many cases, the intersections of individual sulci cannot be stratigraphically resolved, since some of them 'interweave' with each other. This suggests that some sulci formed concurrently.

The Voyager team initial reports [10] suggested that Triton's global lineament system was

TRITON' LINEAMENTS: Collins, G., and Schenk, P.

tensional in nature. They suggested that sulci are raised-rim graben into which some sort of viscous cryovolcanic material had been extruded. This does not explain the detailed lineament morphology. The relationships between the ridges can be complex in many areas, the middle ridge curving out to become the outer ridge, complex overlapping of crossing ridge sets, or sets of discontinuous diagonal ridges making up lineaments without outer boundary ridges.

Sulci morphology resembles the lineated fabric of three types of terrestrial features: fold belts, dyke swarms, and systems of strike-slip faults. The shape, elevation, and discontinuous nature of the ridges, the flattening of adjacent features, and the apparent amplification of intersecting ridges favor compressional folding. However, the seemingly concurrent formation of sulci at high intersection angles may make this less likely. The general pattern of ridges and discontinuities favor intrusive (and extensional) dyke swarms, but evidence for concurrent volcanism is rare. The narrow widths of the sulci and a tendency for ridges to occasionally exhibit a feather pattern tend to favor a shear mechanism, but do not explain the surface manifestation of ridges. At present, interpretation of these features is ambiguous, but their origins are not simple.

Structures within mapped areas of lineated terrain are preferentially oriented at N60W and N30E over a range of longitudes from 75°W to 50°E. These orientations do not fit any simple global stress model. Analysis of the orientations of sulci shows a weak tendency for both concentric and radial symmetry about the tidal axis, but we are handicapped by the limited Voyager coverage and the small number of sulci. Ongoing analyses include comparisons of sulci orientations to predicted stress fields from tidal distortion and nonsynchronous rotation models, particularly during periods of global expansion or contraction.

CONCLUSIONS

Global expansion or contraction may well have played a part in Triton's history, depending on the composition of the icy mantle and the planet's thermal history. Triton's decaying orbit indicates that there is a growing tidal bulge and a rotational spin-up deforming its shape. It is perhaps less likely that nonsynchronous rotation played a part in the planet's history. The morphological evidence is at present ambiguous regarding whether the stresses were tensional or compressional. However, it seems that the sulci may be related to tidal deformation and the lineated terrain may be related to a process such as spin-up that is symmetric about the rotational pole. The lineated terrain may also be related to global expansion, due to the terrain's usual appearance as narrow, evenly spaced fractures, its occurrence in a range of longitudes, and its superposition on many other types of terrain.

References: [1] McKinnon, W. B. (1984) *Nature*, 311, 355-358; [2] Goldreich, P. et al. (1989) *Science*, 245, 500-504; [3] McKinnon, W. B. (1992) Neptune and Triton Conference 54; [4] McKinnon, W. B. and Benner, L. A. M. (1990) LPSC XXI, 777; [5] Strom, R. et al. (1990) *Science*, 250, 437-440; [6] Melosh, H. J. (1980) *Icarus*, 43, 334-337; [7] Melosh, H. J. (1977) *Icarus*, 31, 221-243; [8] Helfenstein, P. and Parmentier, E. M. (1985) *Icarus*, 61, 175-184; [9] Schenk, P. and Jackson, M. P. A. (1993) *Geology*, 21, 299-302; [10] Smith, B. A. et al. (1989) *Science*, 246, 1422-1449.

2966

ON THE POSSIBLE ROLE OF ELEMENTAL CARBON IN THE FORMATION OF REDUCED CHONDRULES. ¹Harold C. Connolly Jr., ¹Roger H. Hewins, ²Richard D. Ash, ³Gary E. Lofgren and ⁴Brigitte Zanda. ¹Dept. of Geological Sciences, Rutgers University, New Brunswick, NJ 08901 USA. ²Dept. of Geology, University of Manchester, Manchester UK M139PL. ³SN-4, Johnson Space Center, NASA, Houston, Texas 77058, ⁴Laboratoire de Mineralogie, Museum National D'Histoire Naturelle, 61 Rue de Buffon, 75005 Paris, France.

INTRODUCTION Recent experiments(1,2) have been designed to produce chondrule textures via flash melting while simultaneously studying the nature of chondrule precursors. However, these experiments have only been concerned with silicate starting material. This is a preliminary report concerning what effects elemental carbon, when added to the silicate starting material, has on the origin of chondrules produced by flash melting.

EXPERIMENTAL TECHNIQUE A Type IA chondrule composition was synthesized from ground olivine (San Carlos), orthopyroxene, diopside and albite and sieved to form two grain sizes, 23-45 μ m and 125-250 μ m. The calculated liquidus (3) is 1703°C. Carbon, in the form of graphite (submicrometer to 200 μ m) and diamond (0.5 μ m), was added to the silicate precursor material. Amounts of carbon used were 1%, 3%, 5%, 7% and 10% by weight. Total weight of pellets before melting was 25mg. All charges were flash melted at 1750°C using the technique of (1,2) and the total time from initial melting to quenching was approximately 25 minutes. Experiments were performed at the Experimental Petrology Labs at the JSC. The fO_2 within the furnace was maintained with a mixture of CO and CO₂ at -1.5 log unit below the IW buffer. Samples were initially imaged as whole charges and metal grains were removed from the surface for later analysis. Charges were then sectioned and analyzed on a JEOL 8600 superprobe at the Rutgers University Microanalysis Lab.

EXPERIMENTAL RESULTS Imaging of uncut charges revealed that the surfaces of charges with no carbon added to the precursor contained no metal grains. However, charges that contained carbon in the precursor material often have numerous metal grains, up to several 100's of μ m in diameter, on their surfaces. Also present on the surfaces of some of the charges that contained graphite within the starting material was rare grains of graphite that were often associated with tiny metal and SiO₂ grains.

Experiments that used the 23-45 μ m grain size produced typical Type IA chondrule textures whereas the 125-250 μ m starting grain size produced PO textures similar to Type IIA chondrules. All charges that did not contain any carbon have olivine phenocrysts normally zoned from Fo₉₄ to Fo₈₉. These same charges contain numerous relict San Carlos olivines that are overgrown by the same, normally zoned, melt-grown olivine. Rare, inclusion-free, metal grains exist and the charges contain appreciable amounts of Na within the mesostasis.

Charges that contained carbon within the starting material all have textures similar to the control experiments. All of these charges contain phenocrysts that have compositions more reduced than the control experiments. Charges that contained 1% carbon have olivines zoned from Fo₉₆ to Fo₉₄. Charges that contained 3% carbon have olivines normally zoned from Fo₉₈-Fo₉₄. Charges that contained 5% carbon have olivines normally zoned from Fo_{99.50} to Fo₉₈. Charges that contained 7% and 10% carbon within the starting material have olivines with composition similar to charges that contained 5% carbon within the starting material. No difference in mineral chemistry was observed either between graphite or diamond and between fine and coarse grain sized starting material.

Relict San Carlos grains are present in all charges, however, in many charges the relict grains are not pure San Carlos olivine. Many relict grains have regions and veins of more reduced olivine and often have inclusions of metal grains and thin veins of Fe-metal. These charges all contain far more metal than the control charges and the metal often has inclusions of silica. The metal grains vary in composition from pure Fe-metal to Fe-metal with varying amounts of Ni and metal abundance appears to increase with increases in the amount of carbon in the starting material. The mesostasis of charges with carbon added to the starting

ELEMENTAL CARBON IN REDUCED CHONDRULES: Connolly H.C. et al.

material contain appreciable amounts of Na, analogous to the control charges, with no changes in Na correlated to variations in the amount of carbon added to the starting material.

DISCUSSION It is clear from our experiments that at 1 atm in a gas of IW -1.5 elemental carbon added to the silicate precursors produces a charge that is much more reduced in chemistry than charges without added carbon. The more carbon added to the starting material, the greater the reduction. However, as amount of carbon in the starting material exceeds 5%, no additional reduction of the silicates occurs. All of our experiments contain relict olivine grains, that have inclusions of metal and could be considered analogous to dusty olivines. Such relict grains have only been produced in the lab when carbon has been added to the silicate precursor. Most of these relict grains have zoning that is reversed from the center of the relict to the center of the overgrown olivine. However, the zoning then becomes normal from the center of the overgrowth to the edge of the overgrowth. We interpret this observation to be the product of initial reduction caused by the reaction of elemental carbon with oxygen in the charge to produce an initially more reduced intrinsic fO_2 than the surrounding gas. Once the carbon has all reacted, the charge equilibrates with the ambient gas, thus producing a more oxidized chemistry.

Another result of these experiments is the production of metal grains, many of which have inclusions of silica. Such inclusions in metal grains have been observed in natural reduced chondrules (4). Their formation has been argued to be the result of reduction followed by oxidation during chondrule formation (5). Unpublished results (6) show similar silica inclusions in metal in charges that were formed in a gas with an fO_2 of IW -4 without carbon added. However, these same experiments produce silicates that are more oxidized than either our experiments or natural, reduced chondrules. These same experiments have also not produced relict, dusty olivine grains that were produced in our experiments. Therefore, our data support the concept that the intrinsic fO_2 of the chondrule precursor may have played a more controlling role in the formation of reduced chondrules than the ambient nebular gas.

CONCLUSIONS Organic and elemental carbon were present within the early solar nebula (7,8). It has been postulated that organic material may be an important "glue" enabling the mineral grains of the chondrule precursor to stick together. Our experiments show that elemental carbon could have played a key role in the formation of reduced chondrules and that reduced chondrules, silica inclusion in metal grains, and relict, dusty olivine grains could be interpreted as evidence for carbon within chondrule precursors. Chondrule redox may therefore be controlled by the intrinsic fO_2 of the precursors and not the fO_2 of the surrounding nebular gases. However, we cannot rule out the possibility that the production of reduced chondrules may require both a reducing agent in the precursors and a reducing nebular gas.

REFERENCES (1) Connolly et al. (1993) *LPSC XXIV*, 329-330. (2) Connolly et al. (1993) *Meteoritics* **28**, 338-339. (3) Herzberg, C.T. (1979) *Geochim. Cosmochim. Acta* **43**, 1241-1251. (4) Perron et al. (1992) *Meteoritics* **27**, 275-276. (5) Hewins, R.H. and Zanda, B. (1992) *Meteoritics* **27**, 233. (6) Maharaj, S.V., personal communication. (7) Anders, E. and Zinner, E. (1993) *Meteoritics* **28**, 490-514. (8) Zinner, E. (1988) *Meteorites and the Early Solar System*, 956-983.

ASTRONOMY LABORATORY EXERCISES BASED ON SKYGLOBE (TM); M. Connors, Athabasca University

New exercises for a distance-education introductory astronomy course have been developed based on the SkyGlobe (TM) planetarium program, distributed as shareware by KlassM Software of Ann Arbor, Michigan. One aim of these exercises is to supplement the course text and enhance visualization of the orbital motions of Solar System objects. The use of graphs made from tables of measured data is also emphasized in what may be the only science course some students take. A sample laboratory and two assigned exercises stressing planetary motion are based on SkyGlobe (TM). The remaining three exercises in the course use stellar and extragalactic data from the Astronomical Data Centers' CD-ROM.

SkyGlobe (TM) is a program for PC-compatible computers which simulates views of the sky in a versatile and accurate manner. As such it is well suited for use by students using distance education, which in the Athabasca University course consists primarily of home study. The first laboratory exercises in the course, Introduction to Astronomy and Astrophysics [1], are concerned with the motions of Solar System objects, and also introduce methods of data presentation and analysis. The final exercises, not discussed here, are about stellar and extragalactic astronomy. To introduce students to the program and to presenting their findings in writing, the first laboratory exercise is provided with a solution in the form of a sample report. This exercise studies eclipses and introduces concepts ranging from the general aspects of motions of the Sun and Moon to that of the parameters of the orbit of the Moon, particularly its nodes and inclination to the Ecliptic. The concept of the parallax of the Moon is also illustrated, and it is interesting to note that the geometry of the November 3 1994 solar eclipse, as seen from Peru, leads to a simple calculation of the distance to the Moon. The first assigned exercise is less sophisticated than the sample, and focusses on the difference between sidereal and synodic periods. A plot of the angular distance travelled by the Moon each day is used in conjunction with Kepler's laws to deduce when it is closest to the Earth. The analemma is constructed by observing solar positions near sunset and the relation of day length to the declination of the Sun is deduced. In the second assigned exercise, the sidereal periods of the inner planets are computed through observation of the synodic period. For the Jovian planets the approximate sidereal period is obtained from observations of angular motion over the space of a year. These data are used to explore Kepler's third law and to deduce the mass of the Sun. Retrograde motion of Mars is also observed.

Through the use of a realistic and accurate sky simulation, concepts are presented to the students in a "hands-on" fashion. This approach is expected to clarify concepts which often present difficulties to beginning students.

Reference

- [1] Connors, M. (1992) *J. Royal Astr. Soc. Canada* 86, 59.

RETURN OF AN EARTH-GRAZING ASTEROID; M. Connors, University of Alberta

The Earth-grazing fireball of August 10, 1972 was sufficiently well observed to have an orbit determined. That orbit has been integrated forward, including planetary perturbations, to predict that the object will return to the vicinity of Earth in late July 1997. The object may be recoverable by directed telescopic searches at this approach.

A bright meteoric fireball observed widely in western North America on the afternoon of August 10 1972 remains the unique known natural object to have entered Earth's atmosphere and skipped off to return to interplanetary space. This encounter was also the closest passage of an asteroidal object by our planet, being at one Earth radius or approximately .000045 AU as opposed to .001 AU for the closest asteroid observed telescopically [1]. Analysis using meteor observing techniques permitted determination of the object's orbital parameters (with standard errors) before and after the encounter [2]. The semimajor axis (1.661 AU before; 1.4715(0.0009) AU after) and eccentricity (0.3904 before; 0.3633(0.0004) after) are typical of known near-Earth asteroids. Using the 1972 orbit, Ceplecha [3], while stressing the need to consider changes to this orbit from planetary perturbations, predicted another close approach to Earth between July 30 and August 16 1997. Precision calculations, using the RADAU integrator [4] and incorporating the effects of all planets except Pluto, support this prediction. Planetary positions retained an accuracy of 10^{-5} AU per ten years of simulation, so that limits on precision arise from the standard errors of the initial orbit. The most probable date of closest approach is found to be July 31 1997 with the approach distance being .08 AU. While this is not particularly close (being about 30 times the distance of the Moon), it is nearer than about 80% of encounters recently listed as radar observing opportunities [5]. The expected small size of the object (possibly only several meters diameter) would make it faint and random rediscovery unlikely. The object may be similar to asteroid 1991BA [6] and then would have a stellar magnitude at .08 AU of only about 24, a factor of 100 fainter than new asteroids being detected by present searches. The most favorable approach within the standard error given above (only the variation in semimajor axis of the orbit being of much consequence due to the associated change in period) is August 17 1997 at .05 AU. The object would be in twilight skies at nearest approach but would have a solar elongation of 138 degrees ten days later while still at .08 AU, possibly allowing dark sky detection. A search in the regions of sky indicated by an ephemeris based on the 1972 data would enhance chances of detection. The main return from such a detection would be determination of a good orbit for one of the very small objects which are the most numerous but hardest to detect among the near-Earth asteroids [7]. Further, the basic 1972 orbit is in 14:25 resonance with Earth. Near encounters with this object will continue to occur every 25 years but the resonance makes accurate prediction difficult without a precision orbit. In the case of an impact, the most likely mass and relative velocity of the object correspond to only 10^{13} to 10^{14} joules or roughly one kiloton of energy, near the low end of what could cause terrestrial effects. Nevertheless the evaluation of future impact probability (or study/deflection opportunity), based on a good orbit, would be of great interest. The 1997 encounter should pose little danger but may allow study of this interesting object.

EARTH-GRAZING ASTEROID: M. Connors

References

- [1] Green, D. *IAU Circular No. 5817*, 18 June 1993
- [2] Ceplecha, Z. (1979) *Bull. Astron. Inst. Czechosl.* 30, 349.
- [3] Ceplecha, Z. (1993) *Abstracts, Hazards due to Asteroids and Comets*, Tucson, p. 24.
- [4] Everhart, E. (1985) in *Dynamics of Comets* (eds. Carusi, A., & Valsecchi, G. B.) 185-202 (D. Reidel, Dordrecht).
- [5] Yeomans, D. K. et al. (1992) *Astr. J.* 103, 303.
- [6] Scotti, J. V. et al. (1991) *Nature* 354, 287.
- [7] Rabinowitz, D. L. (1993) *Astrophys. J.* 407, 412.

HAS THE TIDAL BULGE ON ARIEL SHIFTED IN LONGITUDE? Guy Consolmagno SJ, Vatican Observatory Research Group, Steward Observatory, University of Arizona, Tucson AZ 85721; Dan M. Davis, Department of Earth and Space Sciences, SUNY-Stony Brook, Stony Brook NY 11794; and Paul Nyffenegger, Department of Geological Sciences, University of Texas at Austin, Austin TX 78712

The orientation of cracks on Ariel is far from random, and these cracks probably arose from stresses due to the flexing of a tidal bulge and the despin of the planet. A statistical analysis of the cracks suggests that the location of the tidal bulge at the time of their emplacement may have been 60° east of the current sub-planetary point.

As reported elsewhere [1,2] we have performed an extensive statistical analysis of the tectonic features on the Uranian satellite Ariel. In those papers we concluded that many of the small linear features on Ariel could be strike-slip faults arising from stresses imposed as this moon was tidally flexed and despun, early in its history, while its orbit evolved outward from Uranus.

Where faulting occurs in a zig-zag pattern (conjugate faulting) it is possible to identify the direction of maximum and minimum stress with the direction of the line which bisects the conjugate faults. It is also possible to calculate from theory the direction that the maximum and minimum horizontal stresses ought to have if they result from the collapse of the tidal and equatorial bulges of a moon in synchronous spin as it recedes from its parent planet, or as it is flexed during an episode of tidal heating [3,4]. When these two sets of directions, observed and predicted, are compared for our Ariel data set, the resulting fit is not perfect but not too bad.

The fact that we don't get a perfect fit is not surprising. Any of a number of effects, ranging from anisotropies in the strength of the icy lithosphere due to pre-existing cracks or inhomogeneities in the ice-ammonia-rock composition, to errors in our selection and measurement of any given crack, would tend to make the orientation of stress features more random, and less controlled by tidal collapse alone. Clearly it is difficult to predict ahead of time how big these effects should be.

However, one possible non-random change can be tested. If the location of the collapsing tidal bulge were different from its present day location, then the direction of the predicted stress would be different. The easiest such shift to envision (and to calculate!) is to assume that the spin axis does not change, but that the location of the sub-planetary point does change its position in longitude along the equator.

It should not be too surprising that such a change could occur. The position of the sub-planetary point is presumably a function of asymmetries in the internal structure of the moon, and if the tectonic cracks were emplaced while the moon was undergoing internal evolution, one might well expect to find changes in the internal asymmetries. And, indeed, evidence for a 20° change in the location of the tidal bulge location on Europa has been suggested[5].

Figure 1 (on the next page) shows what happens when you plot the degree of mismatch between theory and observation (defined below) as a function of possible tidal bulge longitudes.

Notice, first, that the orientation of the cracks is far from random. The stress orientation is either strongly correlated, or strongly anticorrelated, with the predicted stress direction. This is seen both from how far the curve lies away from the shaded horizontal line, and by the how smoothly the curve varies from point to point.

Second, the least mismatch is found over a broad region of longitudes centered around longitude 60° East (and its symmetric antipode of 240° E); the worst mismatch (implying an anti-correlation) occurs at 90° away from these points, at 150° E and 330° E. This strongly suggests that the location of the tidal bulge during the emplacement of most of these features was located about 60° east of its present location (or, possibly, 120° west).

The mismatch is smaller for the stress field that includes both collapse of the tidal bulge and the despin of the planet, compared to the case where tidal flexing alone creates the stress. This is somewhat surprising. The amount of cracking depends on the rate at which the stress changes, and so one would expect a tidal flexing episode (when the moon is being heated by a resonance with another moon, pumping up its orbital eccentricity) to cause more cracking than

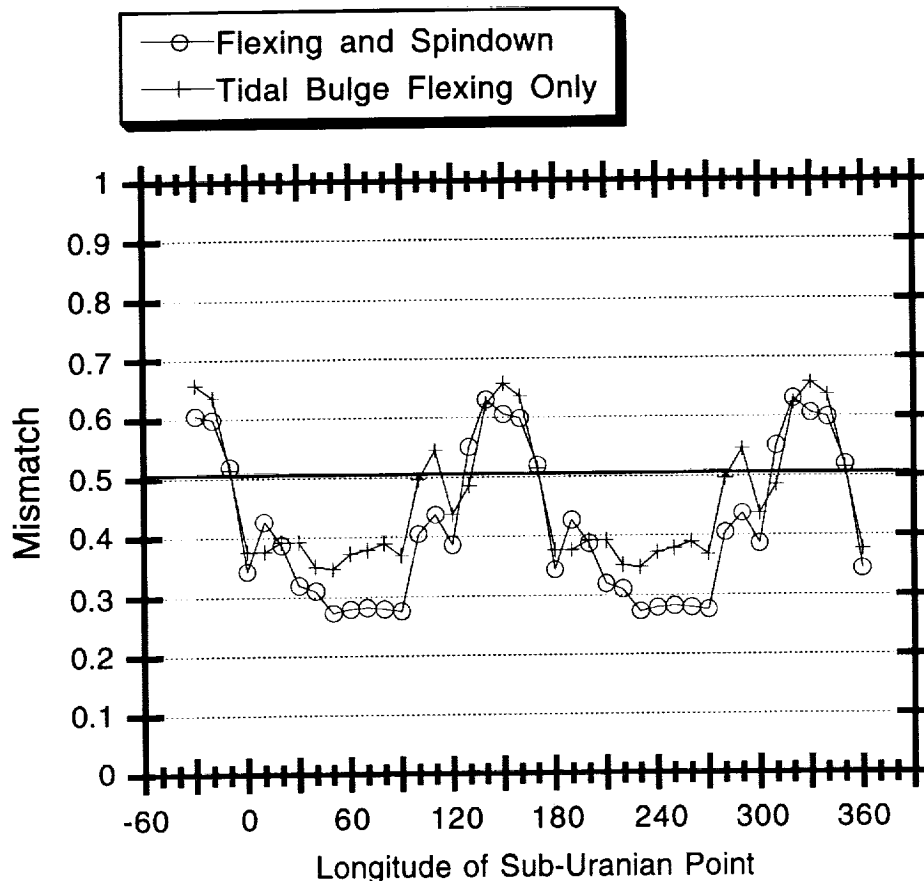


Figure 1 The mismatch between data and theory is the difference between the directions of maximum stress indicated by the orientation of tectonic features on Ariel and the directions predicted by a collapsing tidal bulge, weighted as described in the text, plotted as a function of the sub-Uranian point location. Today the sub-Uranian point is at longitude zero. The horizontal shaded bar is the level of mismatch expected if tectonic features were randomly placed on Ariel. The most likely longitudes are those with the minimum mismatch.

the slow collapse of both the tidal and equatorial (spin) bulges as the moon recedes from Uranus. However, it is not clear just how significant is the difference between these models' results.

Finally, there appears to be a local minimum in the mismatch right at the present-day location of the sub-Uranian point. An examination of the data shows that the mismatch near longitude 270°E is significantly smaller for the present-day case than for a case where the sub-Uranian point is located at 60°E. Perhaps the cracks in this region date from a later episode of tectonism, after the final sub-planetary point was established.

Appendix: How the mismatch was calculated We mapped 367 lineations on Ariel, divided them into 37 overlapping equal area sections, and binned the cracks by orientation relative to north-south. We then found azimuths of symmetry as the angle which gives the maximum of the autocorrelation of these data. These azimuths were subtracted from the predicted stress direction angle (and $\pm 90^\circ$ of this direction), and the difference was weighted by both the strength of the autocorrelation (so regions with lots of conjugate cracks counted more) and by the sine of the colatitude (to correct for the overlap of regions at high latitude).

References: [1] Nyffenegger P., Davis D. M., and Consolmagno G. J. (1991), *EOS (Trans. A. G. U.)* **72**, 184 (abstract). [2] Nyffenegger et al. (1994), *J. Geophys. Res. Planets*, (submitted). [3] Vening Meinesz F. A. (1947), *Trans. A. G. U.* **28**, 1. [4] Melosh H. J. (1980),

UNUSUAL CONCENTRATIONS OF RAMPART CRATERS AT THE MOUTHS OF OUTFLOW CHANNELS, MARS. F. Costard, Centre de Géomorphologie, CNRS, 14000 Caen, France.

Introduction : Several authors have hypothesized or described sedimentary plains at the mouths of outflow channels (1, 2, 3, 4). Jöns (5) suggested that a mud ocean covered the northern lowlands. Parker *et al.* (6) and Baker *et al.* (7) hypothesized the widespread deposition of marine sediments in the northern plains. According to McGill (8), sediments were deposited in Utopia Planitia as a result of mudflows or turbid floods that emanated from NW Elysium. Acidalia and Utopia Planitiae are interpreted to have contained water, as a consequence of outflow channel-forming floods, during the Hesperian Period (4, 9). In order to quantify the spatial distribution of ground ice in the northern plains, all rampart craters have been systematically measured and mapped, using the 1:2 M scale USGS photomosaics. That detailed morphological study have identified an exceptionally high incidence of rampart craters at the main terminations of outflow channels. These observations are interpreted to indicate the presence of an ice-rich sedimentary deposit, from nearby outflow channels, in Acidalia Planitia and Utopia Planitia.

Methodology : Fluidization of rampart crater ejecta seems to have been caused by impact melting of ground ice or other volatiles (10, 11, 12, 13, 14). In order to produce statistically significant results, all rampart craters that are visible in 1:2,000,000-scale Viking photomosaics have been taken into account. Data were collected for rampart craters in the size range 1-40 km. Each sample region covers an area of 5° x 5°.

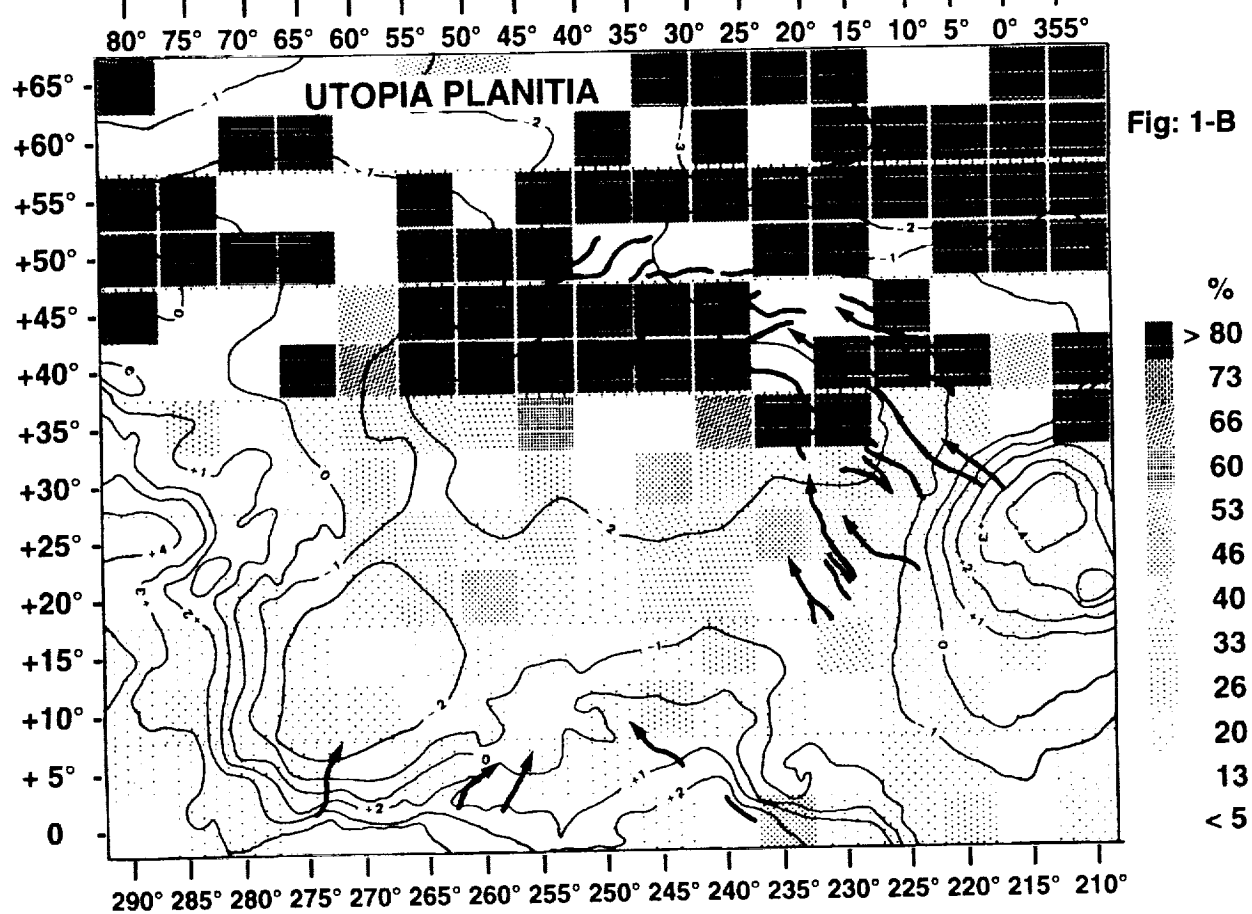
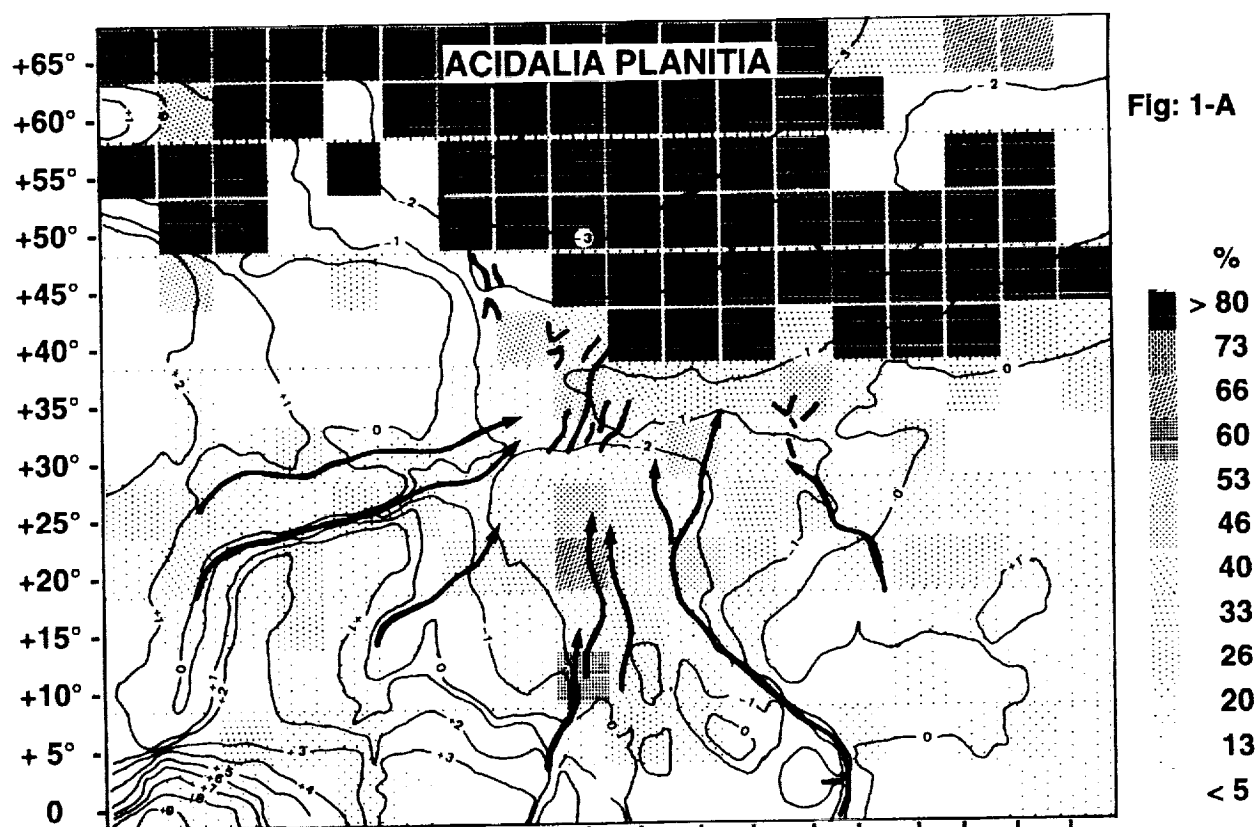
Description : Figures 1A and 1B show spatial relationships between the highest concentrations of fluidized ejecta, the elevation and the terminations of outflow channels. Particularly high concentrations of rampart craters (up to 80% of all craters) occur at latitudes higher than 40° near the mouths of the Chryse channels in Acidalia Planitia (Maja, Kasei, Tiu, Simud, Shalbatana and Ares Valles) and in the reentrant of Utopia Planitia where Elysium channels open into the plains (Tingar, Hebrus, Granicus and Hrad Valles). The statistical work shows a tendency for the highest percentages of rampart craters to occur in large topographic depressions near and below -1000 m, especially in areas that are close to the convergent terminations of outflow channels.

Interpretation : Previous investigators have noted that double-lobed ejecta, in particular, are most highly concentrated in the northern hemisphere, especially in Acidalia and Utopia Planitiae (15, 16, 17). The reason for this concentration of rampart craters may be that northern plains were the sites of accumulation of fluvial sediments and flood waters (18, 19, 20, 21). Large Martian basins (< -1000 m) that are associated with the main terminations of outflow channels were preferential areas for large lakes or seas (4, 6, 7, 22, 23, 24). At latitudes higher than 40°, channel terminations remain volatile rich because at those latitudes ground ice is in equilibrium with the atmosphere (25, 26).

References : (1) J.C. Pechmann 1980, *Icarus* **42**, 185. (2) B.K. Lucchitta *et al.* 1986, *JGR* **91**, E166. (3) R.S. Saunders 1988, MEVTV-LPI Tech. Rep. **89-04**, 45. (4) D.H. Scott *et al.* 1992, *Proc LPSC XXII*, 53. (5) H.P. Jöns 1987, *LPSC XVIII*, 470. (6) T.J. Parker *et al.* 1993, *JGR* **98**, 11061. (7) V.R. Baker *et al.* 1991, *Nature* **352**, 589. (8) G.E. McGill 1985, *LPSC XVI*, 534. (9) M.H. Carr 1986, *Icarus* **68**, 187. (10) M.H. Carr *et al.* 1977, *JGR* **82**, 4055. (11) P.J. Mouginiis-Mark 1979, *JGR* **84**, 8011. (12) J.S. Kargel 1986, *LPSC XVII*, 410. (13) V.M. Horner and R. Greeley 1987, *JGR* **92**, E561. (14) K.M. Wohletz and M.F. Sheridan 1983, *Icarus* **56**, 15. (15) P.J. Mouginiis-Mark 1981, *Icarus* **45**, 60. (16) F.M. Costard 1989, *Earth Moon and Planets* **45**, 265. (17) N.G. Barlow and T.L. Bradley 1990, *Icarus* **87**, 156. (18) F.M. Costard 1988, *LPSC XIX*, 211. (19) S.W. Squyres *et al.* 1992, in *Mars Book*, ed. H.H. Kieffer *et al.* 523. (20) J.S. Kargel and F.M. Costard 1993, MEVTV-LPI Tech. Rep. **93-04**, 7. (21) F.M. Costard and J. Kargel 1994, submitted to *Icarus*. (22) D.H. Scott and J.R. Underwood 1991, *Proc LPSC XXI*, 627. (23) M.G. Chapman 1993, LPI Tech. Rep. **93-04**, 4. (24) J.S. Kargel *et al.* 1993, submitted to *Nature*. (25) F.P. Fanale *et al.* 1986, *Icarus* **67**, 1. (26) B.M. Jakosky and R.M. Haberle 1992, in *Mars Book*, ed. H.H. Kieffer *et al.* 969.

This work was supported by P.N. Planetology of INSU.

UNUSUAL CONCENTRATIONS OF RAMPART CRATERS: Costard F.



AFFINITY AND PETROGENESIS OF A UNIQUE VITROPHYRIC OLIVINE-AUGITE MARE BASALT FROM THE APOLLO 15 COARSE FINES. Trina C. Cox¹ and Graham Ryder, Lunar and Planetary Institute, Center for Advanced Space Studies, 3600 Bay Area Blvd., Houston, TX 77058-1113. ¹Also Hardin-Simmons University, Abilene, Texas, 79698.

Fragment 15474,4 is a unique vitrophyre consisting of olivine and augite crystals in a fine-grained to glassy groundmass (Fig. 1). Despite its more than 20% of olivine, it appears to have crystallized rapidly and be close to a liquid composition. Both its bulk composition and its mineral chemistry suggest that it is not related by shallow-level fractionation to either of the two main series of Apollo 15 mare basalts (the olivine-normative and the quartz-normative mare basalts). Nor can it have been produced by impact melting of such rocks. Instead it represents an otherwise unsampled mare basalt type. Although it conforms to the local characteristic of being a low-titanium mare basalt and may represent part of the same magmatic pulse, the vitrophyre has a lower Mg/Fe than typical Apollo 12 or 15 basalts.

Fines 15470 were collected 30m outside the rim of a small crater superimposed on the rim of Dune Crater at Station 4. The olivine-augite vitrophyre was described by Powell et al. [1], after Powell [2] had separated it as a distinct "porphyritic olivine basalt (?)" from the sparse 4-10mm fragments. Its total mass was only 0.18g and its maximum dimension was about 5mm. In 1972 it was split for thin sections, a chemical analysis, and an argon analysis (the latter was never reported). The distinct character, particularly the high abundance of olivine (21.5%) and the pink "totem-pole" pyroxenes, led [1] to assign it to a distinct group of basalts (of which it is however at present the only identified member). Nonetheless the chemistry of the particle as determined by microprobe analysis of a bead of fused powder [1] is very similar to the other Apollo 15 mare basalts as also analyzed by [1], except that it is higher in FeO (22 wt %) and lower in SiO₂ (46.4 wt %).

Figure 1: Plane transmitted light image of part of thin section 15474,23. Image about 2 mm across. The white subhedral/euhedral phase is olivine (note circular and elongate trapped liquid). The "totem pole" gray phase is aluminous (6-10% Al₂O₃) augite. The dark groundmass contains Ti-oxides, pyroxenes, and glass(?).



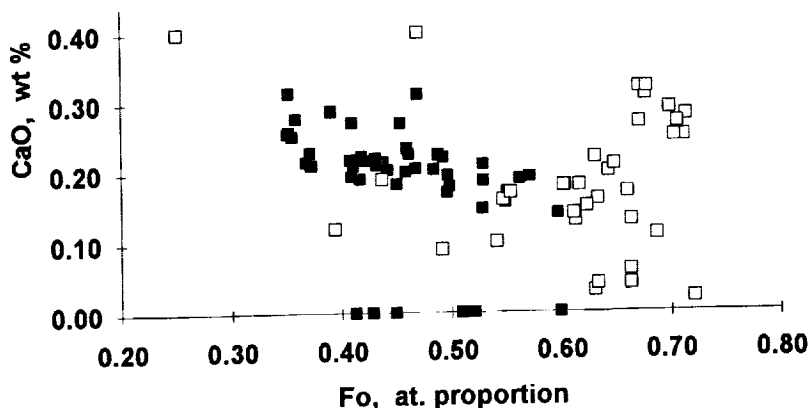
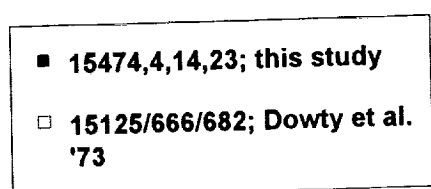
The vitrophyre appears to have been completely ignored since 1973, never appearing in reviews of mare basalts, despite its potential for being a distinct magma type and perhaps even a magma composition. The olivine abundance is greater than for any basalts except for some Apollo 12 olivine basalts, and no other Apollo 15 olivine-rich mare basalts (e.g. the olivine-normative group) have vitrophyric members. Thus we are making a re-study of the mineral chemistry and petrography of 15474,4 with the objective of illuminating any possible relationship with other lunar mare basalts, particularly the local olivine-normative and quartz-normative basalts, and understanding its petrogenesis. A tiny fragment has been approved for allocation for a chemical analysis. Enough of the fragment remains for potential Ar age determination using laser techniques.

We redetermined the mineral mode by point counting 1500 spots. Our results are similar to those of [1]: ol 22.8 (vol) %; px 32.8%; ox 1.6%; and gmass 42.8%. We derived a bulk composition from the mode and the average phase composition determined from our microprobe analyses (including rastering areas of the groundmass). This bulk is similar to that of [1] but we obtained even lower SiO₂. The olivines have a range in

PETROGENESIS OF VITROPHYRIC MARE BASALT, APOLLO 15: COX T.C. AND RYDER G.

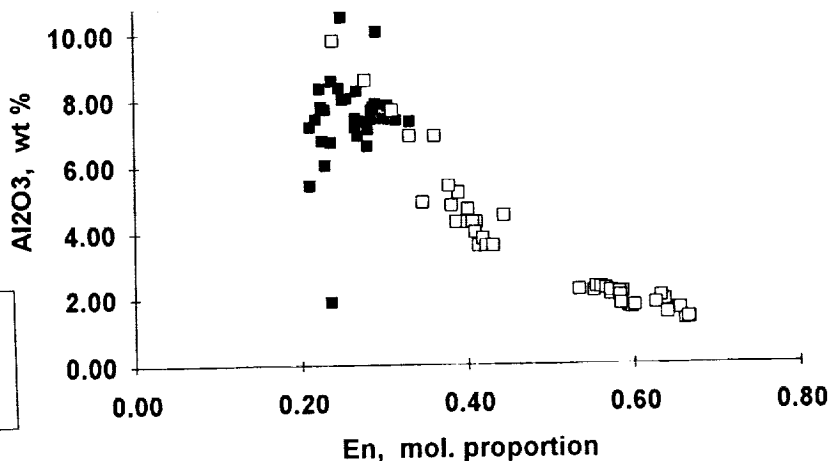
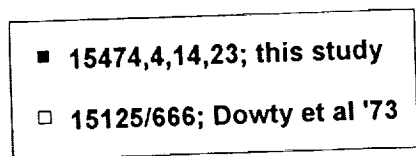
composition from $Fo_{0.60-0.35}$ (mol. prop.), with CaO about 0.25% (Fig. 2). There are no abrupt discontinuities in composition, suggesting (as does the petrography) that the olivines crystallized continuously, and are not xenocrysts. While some olivines have borders suggesting some reaction and resorption, many have euhedral to subhedral boundaries; a few show swallow tails indicative of very rapid cooling. The bulk Mg/Fe of the rock should crystallize equilibrium olivines of about $Fo_{0.70}$, not the $Fo_{0.60}$ we found. This suggests that either the cores re-equilibrated with the melt or that the olivine is partly cumulate, but neither explanation is particularly consistent with the inferred rapid cooling. Olivine that occurs sparsely in A15 QNB ranges to much more magnesian compositions and are much richer in Cr at a given Fo content.

Figure 2: CaO v. Fo for olivines in 15474,23 and those in some ol-bearing QNBs (the latter roughly corrected for an analytical error in CaO in data reported in [3]). Data this study and [3].



The pyroxenes evidently crystallized after at least the cores of the larger olivines had crystallized: none of the pyroxenes are embedded in olivine, and they do not include Mg-pigeonites such as are the typical early phase of the ONBs and QNBs (Fig. 3). They are Al- and Ti-rich augites, like the pyroxenes that developed in the later stages of crystallization of rapidly-cooled QNBs that contain olivine (Fig. 3). The chromites are also Al-, Ti-rich.

Figure 3: Al₂O₃ v. En content of augites in 15474,23 and those in some olivine-bearing QNBs. Data this study and [3].



The crystallization sequence was ol-->ol+cr-->px-->gmass chill. Neither plagioclase nor fayalite crystallized, but the groundmass does contain microcrystalline opaque phases. We can find no simple way to derive the olivine-augite vitrophyre sample from either an ONB or a QNB parent. It has lower SiO₂ and Mg/Fe than either, and abundant olivine cannot be obtained from either of them. We conclude that it represents a separate volcanic eruption and magma type, although it might be from the same magmatic pulse insofar as it is a low-titanium mare basalt with some characteristics of rapidly-cooled QNBs. Trace element and age determinations will shed light on the relationship of this basalt and its role in Apollo 15 site geology. Photogeologic and remotely-sensed chemical/mineral attributes around region demonstrate the presence of several mare basalt types that potentially contributed to Apollo 15 coarse fines, and this sample might be correlatable with one of them.

References: [1] Powell, B.N. et al. (1973) LPSC 4, 445-460 [2] Powell B.N. (1972) Apollo 15 Coarse-Fines (4-10 mm) Sample Classification, Description, and Inventory. NASA MSC 03228, 91 pp. [3] Dowty, E. et al. (1973) UNM Inst. of Meteoritics Spec. Publ. #9, 113 pp.

GEOLOGIC HISTORY OF ISIDIS PLANITIA AND SYRTIS MAJOR PLANUM, MARS; *Robert A. Craddock*, Center for Earth and Planetary Studies, National Air and Space Museum, Smithsonian Institution, Washington, D.C. 20560

Isidis Planitia is an extensive, semi-circular basin situated along the martian dichotomy boundary separating the southern cratered highlands from the northern smooth plains. Evidence for an origin by impact is clear: numerous mountains, morphologically similar to the massifs surrounding lunar basins [1], are aligned concentric to the Isidis plains. Concentric faults also appear to have originated from the Isidis impact, and these may have served as conduits for the volcanic material composing Syrtis Major [2]. High resolution Viking orbiter images (149, 150, and 151Sxx) show mounds ~500 m in diameter scattered on the floor of the Isidis basin. The origin of these features is less clear as various investigators have proposed volcanic cinder cones [3], pingoes [4], and glacial features [5] to explain them. In contrast, Nili and Meroe Paterae have only been examined in cursory studies [6, 7] despite their location within the classical albedo feature Syrtis Major and the limited number of highland volcanoes on Mars. 1:500,000 scale geologic mapping was undertaken to synthesize the broad-scale geology of both Isidis Planitia and Syrtis Major. The principal goals of this study are: (1) determine the geologic history of both Isidis Planitia and Syrtis Major Planum; (2) examine the nature of the dichotomy boundary separating Isidis Planitia from the southern cratered highlands; (3) interpret the most likely mechanism(s) for the formation of the small mounds and arcuate ridges on the floor of Isidis Planitia based on regional and local geology; and (4) because it is a simple area in which to land [8], determine the most feasible scientific objectives for a future surface mission. Because of the influence volatiles and aerosols released from volcanoes may have had in inducing or prolonging an early warm and wet martian atmosphere, the atmospheric contribution by Nili and Meroe Paterae is also being evaluated. Preliminary results are outlined and illustrated (Figure 1) below.

As the result of a giant impact [1], the Isidis Planitia topographic depression was formed during the Late Noachian (~4.2 Ga). The northeastern portion of the Isidis rim may have formed in a pre-existing topographic depression caused by the proposed Borealis basin [9]. Thus this portion of the rim would have been easily buried by subsequent northern plains volcanism. Alternatively, this portion of the rim may have been destroyed through local crustal thinning [10] during formation of the martian dichotomy. Crater age dates by Tanaka [11] suggest that Isidis (~1,100 km in diameter) is older than Argyre or Hellas, the other two large, well-preserved basins in the southern highlands.

Based on Earth-based radar elevation data, Nili and Meroe Paterae are best described as shield volcanoes [7]. Emplacement of the Syrtis Major Formation (Hs), the units comprising Nili and Meroe Paterae, occurred through the Hesperian (~3.3 to ~3.75 Ga). Detailed age-relations between Nili and Meroe Paterae have not been determined; however, age-relationships of flows suggest that Meroe may post-date the formation of Nili Patera. Topographic data also indicate that Meroe may have formed on the flank of Nili Patera, suggesting migration of the magma chamber. Using the base level of the volcanoes as the elevation of the surrounding cratered highlands, Schaber [7] calculated the volume of Nili and Meroe Paterae as being $\sim 0.2 \times 10^6 \text{ km}^3$. Assuming a basaltic composition with an average density of 2.6 g/cm^3 , the total mass of material erupted is $\sim 5.2 \times 10^{17} \text{ kg}$. Based on terrestrial values of 1 weight percent for the released water content, the amount of water released into the martian atmosphere from eruptions of Nili and Meroe Paterae is $\sim 5.2 \times 10^{15} \text{ liters}$, or $\sim 3 \text{ cm}$ of water distributed globally.

During the late Hesperian (~2.8 Ga), deposits interior to the Isidis basin formed (unit Hvr). These materials contain the enigmatic mounds mentioned above as well as curvilinear ridges and arcuate boundaries. Recently, these later features have been interpreted as shorelines and sediments deposited by a standing body of water in Isidis Planitia [12]. Apron materials (Am) formed along the boundary separating Syrtis Major from Isidis Planitia and were emplaced immediately after the Isidis plains materials. Interpreted as landslides, these units may be the result of mechanical failure due to loading from the formation of Nili and Meroe Paterae.

GEOLOGIC HISTORY OF ISIDIS PLANITIA AND SYRTIS MAJOR: Craddock R.A.

Alternatively, undermining of Isidis rim material from ponded water in the basin may have caused the Syrtis Major Formation to collapse catastrophically. Since that time, and continuing into the present, chemical weathering and aeolian redistribution of materials have created the classical albedo features visible from Earth today.

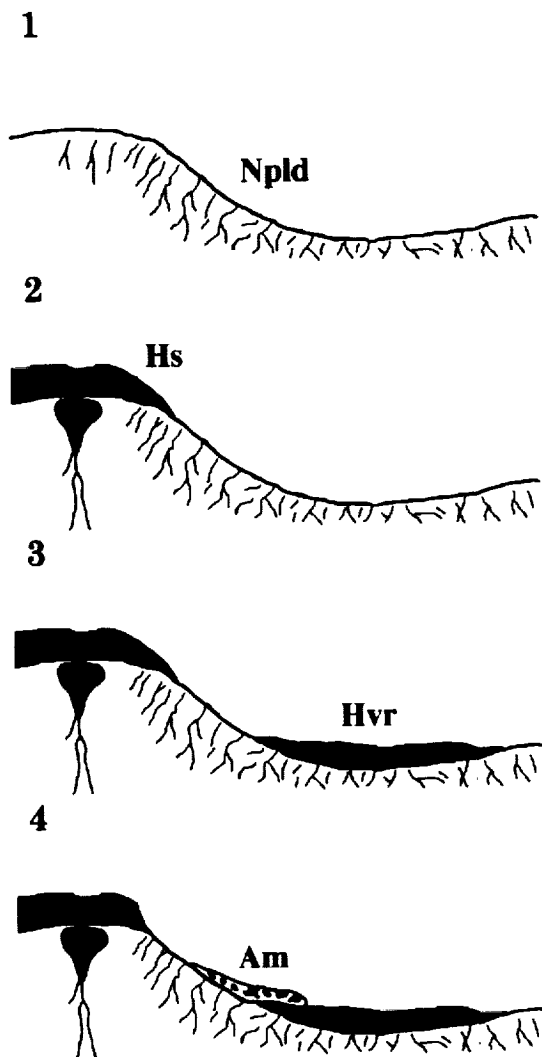


Figure 1. Generalized geologic history of Isidis Planitia and Syrtis Major Planum. Oldest is at the top. Profile is taken from the southwest to the northeast. Noachian: 1. Formation of the Isidis Planitia depression from an impact. Rim material remains visible in the cratered highlands as Npld materials. Hesperian: 2. Emplacement of Syrtis Major Formation (Hs). Meroe Patera appears slightly younger than Nili Patera. 3. Deposition of materials in the Isidis basin interior (Hvr). Presently, the origin of these materials is unclear. They are probably volcanic or sedimentary. Did they form in a standing body of water? Amazonian: 4. Apron materials (Am) form as the result of mechanical failure or undermining of Isidis rim material. Aeolian processes continued to redistribute materials within the region.

References:

- [1] Wilhelms, D.E., *J. Geophys. Res.*, 78, 4084-4095, 1973. [2] Comer, R.P. *et al.*, *Rev. Geophys.*, 23, 61-92, 1985. [3] Frey, H. and M. Jarosewich, *J. Geophys. Res.*, 87, 9867-9879, 1982. [4] Rossbacher, L.A. and S. Judson, *Icarus*, 45, 39-59, 1981. [5] Grizzaffi, P. and P.H. Schultz, *Icarus*, 77, 358-381, 1989. [6] Schaber, G.G. *et al.*, *Third Intl. Coll. Mars*, 223-225, 1981. [7] Schaber, G.G., *J. Geophys. Res.*, 87, 9852-9866, 1982. [8] Craddock, R.A., *Proc. Space '92 Conf.*, 3rd, 1488-1499, 1992. [9] Wilhelms, D.E. and S.W. Squyres, *Nature*, 309, 138-140, 1984. [10] McGill, G.E. and A.M. Dimitriou, *J. Geophys. Res.*, 95, 12,595-12,605, 1990. [11] Tanaka, K.L., *J. Geophys. Res.*, 91, E139-E158, 1986. [12] Parker, T.J. *et al.*, *J. Geophys. Res.*, 98, 11,061-11,078, 1993.

THE ORIGIN OF PHOBOS AND DEIMOS; *Robert A. Craddock*, Center for Earth and Planetary Studies, National Air and Space Museum, Smithsonian Institution, Washington, D.C. 20560

Determining the origin of Phobos and Deimos has remained problematic. Spectral analyses suggest that the composition of Phobos closely matches black or carbonaceous chondrites [1]. This combined with other physical properties such as their low densities ($\sim 1.7 \text{ g/cm}^3$ [2]) and low geometric albedoes (~ 0.05 [3]) has led many investigators to suggest that they are captured asteroids [e.g., 4]. However, the orbits of both moons are extremely circular and their Laplace plane is very close to the martian equatorial plane. Captured objects would be expected to have elongate orbits with randomly oriented orbital planes. Phobos may have been able to attain its circular orbit because it experiences tidal perturbations from its closeness to Mars and from libration. Deimos is too far away to experience much of either. Integrate Phobos' present eccentricity into the past, and it collides with Deimos [5]. The large number of elongate craters on the martian surface attest to the possibility that Mars may at one time have had many Phobos and Deimos size objects in orbit [6,7]. In addition, recent analyses of the spins of the terrestrial planets suggest that Mars has too much prograde angular momentum to be explained by the accretion of many small bodies [8]. The spin rate of Mars can only be explained by a collision with a planetesimal during accretion [8]. Could a giant collision have caused Mars to rotate at its present spin rate? Is it possible that such a collision vaporized enough material to form Phobos, Deimos, and other potential satellites as well?

The spin rate of the planet is expressed as the number of sidereal rotations per revolution around the sun, \mathfrak{R} . From Dones and Tremaine [8] the spin rate is written as

$$\mathfrak{R} = \frac{3\langle l_z \rangle}{2\Omega R_p^2} \quad (1)$$

where l_z is the specific angular momentum perpendicular to the orbital plane, Ω is the planet's orbital frequency ($1.06 \times 10^{-7} \text{ rad/sec}$), and R_p is the planetary radius ($3.39 \times 10^6 \text{ m}$). This is assuming that the dimensionless parameter r remains constant during accretion, expressed as

$$r \equiv \frac{R_p}{R_H} \equiv \frac{R_p}{(GM_p/\Omega^2)^{1/3}} \quad (2)$$

where R_H is the Hill, or tidal, radius of the planet, G is the acceleration of gravity (3.7 m/sec^2), and M_p is the mass of the planet ($6.43 \times 10^{23} \text{ kg}$). The Hill radius is simply the distance where centrifugal force balances the gravitational attraction from the planet. For Mars, $\mathfrak{R} = 670$ and is a positive value because Mars rotates in a prograde direction and $r = 0.0022$.

If a planet is formed by ordered accretion, then a maximum prograde or retrograde spin rate is possible. Dones and Tremaine [8] show that with ordered accretion, values for $\mathfrak{R}r$ should be between -2.2 and 0.3 . However, $\mathfrak{R}r = 1.5$ for Mars, which they argue is evidence that the rotation of Mars resulted from stochastic accretion. In stochastic accretion, a planet's final spin rate is determined by the imperfect cancellation of angular momentum between individual impactors. Simply, a single impactor more massive than the rest determines the final rotation rate and direction of the planet. They show that the typical rotation rate can be estimated from the equation

$$|\mathfrak{R}| \approx \frac{S_m}{r^{3/2}} \approx \frac{m_1}{M_p} r^{-3/2} \quad (3)$$

where S_m is the dimensionless effective mass of a planetesimal relative to the planet, m_1 is mass of a single impactor, which is more massive than all the rest, and M_p is the mass of the planet. From this equation, it follows that

$$S_m = \frac{m_1}{M_p} \quad (4)$$

With stochastic accretion and a planet spinning prograde

$$S_m \geq 0.3r^{1/2} \quad (5)$$

For Mars, $S_m \geq 0.015$, which implies that the minimum mass of the planetesimal (m_1) which induced the present spin rate of Mars, is $\sim 9.6 \times 10^{21} \text{ kg}$. Assuming a density of $\sim 3.0 \text{ g/cm}^3$, the diameter of this

impactor was ~1,800 km. Hartmann and Davis [9] calculate that the second largest object that would have formed near Mars' orbit at the end of accretion could have had a diameter of, coincidentally, 1,800 km. Assuming that this planetesimal struck Mars at escape velocity, the amount of energy involved in the collision would be $\sim 10^{36}$ ergs. This is the same amount of energy estimated to have formed the 7,700-km-diameter Borealis basin [10], suggesting, perhaps, that the collision ultimately responsible for the spin rate of Mars is recorded in the crustal dichotomy.

The mass of Phobos and Deimos is very small ($\sim 1.3 \times 10^{16}$ kg). If craters with asymmetric or elongate ejecta on the martian surface are the result of satellites whose orbits slowly decayed with time (similar to present-day Phobos), then the total mass of all martian satellites would have been $\sim 1.5 \times 10^{19}$ kg [6]. Determination of how much material is placed into orbit following the formation of a giant impact is not straight-forward. A majority of material ejected ballistically from an impact that explodes below the surface of a planet either escapes into space or falls back onto the surface. Cameron and Ward [11] proposed a solution for the formation of the Earth's Moon by suggesting that large amounts of vaporized material were released during collision. Vaporization of martian geologic material following impact with a large bolide is possible because the impact velocity must be between 7 to 12 km/sec to induce shock vaporization [12]. This is slightly higher than martian escape velocity and not an unrealistic value for an approaching planetesimal. Following impact, vaporized debris rising above the surface would continue to be accelerated by gas pressure effects and gravity. This mechanism allows much more material to be accelerated into orbit than by simple ballistic emplacement ($\sim 1/2$ the vaporized mass [13]) because the debris is given an added "kick." Vapor from both the planet and impactor need to mix efficiently, however, otherwise vapor from the impactor will exceed escape velocity and vapor from the planet will not reach orbit [13]. Thus only a narrow set of initial conditions are possible. Using a particle-in-cell hydrodynamic code, Cameron [14] found that a "successful" accretion disk formed when the velocity of the impactor slightly exceeded escape velocity and most of the vapor came from the impactor.

Phobos, Deimos, and all the other satellites which may have orbited Mars in the past are only a tiny fraction of the mass of the Borealis impactor (~ 0.001). For this reason alone it seems plausible that enough material from the formation of the Borealis basin could have been placed into martian orbit as an accretion disk. There are several other proposed impact basins on Mars which may have also been capable of placing debris into martian orbit: Daedalia (4,500 km), Chryse (3,600 km) or Utopia (3,300 km) are among the largest. Once an accretion disk is formed, gravitational instabilities prevent the particles from clumping [11]. Temporary mass concentrations would, however, cause a transfer in angular momentum from Mars to the accretion disk and the disk would begin to dissipate both towards the martian surface and out towards space. Once material in the disk emerged past the Roche limit, particles in the disk would begin to accrete. Small tides raised by this body would once again cause a transfer in angular momentum, and the small satellite would begin to recede from Mars. As the accretion disk continued to dissipate another small body would form in place of the first. In the formation of the Moon, the last body to form from the accretion disk would, by necessity, be more massive than the rest [13]. Thus this large satellite would recede from the proto-Earth faster, accrete the smaller satellites, and form the Moon. However, in the martian scenario this last, large satellite does not form, and Mars is left with a number of small, Phobos and Deimos-size objects in orbit. The impact responsible for creating the accretion disk would most likely have destroyed any atmosphere Mars had at the time of collision. Formation of a thick atmosphere subsequent to this event may have been enough to induce drag on some of the satellites, causing them to spiral into the surface. Alternatively, or perhaps in conjunction, removal of the accretion disk may have caused tidal perturbations in the satellites, causing their orbits to decay.

If the impactor was chondritic in composition, the spectrally derived compositions of Phobos and Deimos could be explained. Potentially the low densities of these satellites can also be explained by this scenario: the small accretion disk particles simply coagulated (i.e., aggregated) and remained loosely packed. This suggests that they have a significant amount of pore space and uniform density, agreeing with Phobos' libration [15]. Work will continue on creating a dynamic model to illustrate this hypothesis and constrain the initial conditions which must have been present. The true test of this hypothesis will not come from such models, however. Better compositional data from both Mars and its satellites are needed before the origin of Phobos and Deimos is truly understood.

References: [1] Murchie S.L. *et al.*, *JGR*, 96, 5925 (1991). [2] Avensov G. *et al.*, *Nature*, 341, 585 (1989). [3] Burns J.A. in *Mars*, 1283, U of A, 1992. [4] Burns J.A., *Vista. Astron.*, 22, 193 (1978). [5] Lambeck K., *JGR*, 84, 5651 (1979). [6] Schultz P.H. and A.B. Lutz-Garihan, *JGR*, 87, A84 (1982). [7] Strom R.G. *et al.*, in *Mars*, 383, U of A, 1992. [8] Dones L. and S. Tremaine, *Science*, 259, 350 (1993). [9] Hartmann W.K. and P.A. Davis, *Icarus*, 24, 504 (1975). [10] Wilhelms D.E. and S.W. Squyres, *Nature*, 309, 138 (1984). [11] Cameron A.G.W. and W. Ward, *LPSC*, VII, 120 (1976). [12] Ahrens T.J. and J.D. O'Keefe, *The Moon*, 4, 214 (1972). [13] Cameron A.G.W., in *The Origin of the Moon*, 609, LPI, (1986). [14] Cameron A.G.W., *Icarus*, 62, 319 (1985). [15] Duxbury T.C., *Icarus*, 78, 169 (1989).

THE INFLUENCE OF BODY SHAPE ON THE DEFORMATION AND BREAKUP OF COMET SHOEMAKER-LEVY 9 FRAGMENTS AS THEY ENTER THE JOVIAN ATMOSPHERE* D. A. Crawford, T. G. Trucano, M. B. Boslough, M. E. Kipp and J. M. McGlaun, Sandia National Laboratories, Albuquerque, NM, 87185.

The fascinating demise of periodic comet Shoemaker-Levy 9 as predicted for July, 1994 provides a wealth of observing possibilities and is a challenging problem for analytical and numerical simulations [1-5]. Likewise, the large amount of energy (possibly as much as 10^{24} J) expected to be released during the event(s) presents an unparalleled opportunity for the atmospheric modeling community to assess relatively long-term perturbations of the Jovian atmosphere that may occur. Jovian atmospheric modelers need predictions of the penetration depth of the individual cometary fragments, the amount of energy deposited and energy deposition rates within different regions of the Jovian atmosphere. To help constrain these predictions, we are performing 2-D and 3-D numerical simulations to investigate the influence of body shape during the early phases of the impact, in which the cometary fragments first strike the atmosphere, deform and break up. Preliminary 2-D investigations have been used to demonstrate that normally-incident, equal-mass spherical and cylindrical (length/diameter = 1) projectiles significantly differ in their deformation and breakup behavior as they enter the Jovian atmosphere. These differences suggest that in-depth investigation with additional 2-D and 3-D calculations is warranted.

We have used the CTH Eulerian shock physics code [6-7] to study 2-D, axisymmetric representations of the impact event. The cometary fragments are assumed to consist of water ice impacting an exponential graded-density hydrogen atmosphere at normal incidence (3-D calculations are being performed using a 40 degree incidence angle). The calculations are performed in a reverse-ballistic sense (the atmosphere impinges at 60 km/s on the initially stationary cometary fragment) in order to reduce numerical diffusion in the region of interest (i.e., the small region enclosing the fragment). To demonstrate the influence of body shape, two equal-mass cometary fragment shapes were chosen: (1) a sphere of 3-km diameter and (2) a cylinder of length = diameter = 2.62 km entering the Jovian atmosphere along axis.

The results of the two demonstration calculations are shown in Figs. 1-3. Figure 1 compares the configuration of the two projectiles very early in the calculation when the cometary fragments have penetrated to the 0.5 bar level in the Jovian atmosphere. Relatively little deformation has occurred at this time; the initial configuration is evident, and the formation of a bow-shock is apparent. Later, after the fragments have penetrated to the 20 bar level (Fig. 2), abundant deformation has occurred. Perhaps not surprisingly, deformation of the cylinder at this time is more extensive than that of the sphere. The intact portion of the cylindrical projectile is thinner and has spread to a greater lateral extent. The observations are quantified by the higher temperatures and pressures exhibited at the stagnation point of the cylindrical calculation and the higher internal pressure and greater rate of mass-loss experienced by the cylindrical cometary fragment (Fig. 3). These conditions will lead to greater deformation and energy deposition rates and, ultimately, a higher breakup altitude for the cylindrically shaped cometary fragment. A full exploration of 2-D axisymmetric shapes and representative non-symmetric 3-D shapes is being performed.

*This work performed at Sandia National Laboratories supported by the U. S. Department of Energy under contract DE-AC04-94AL85000.

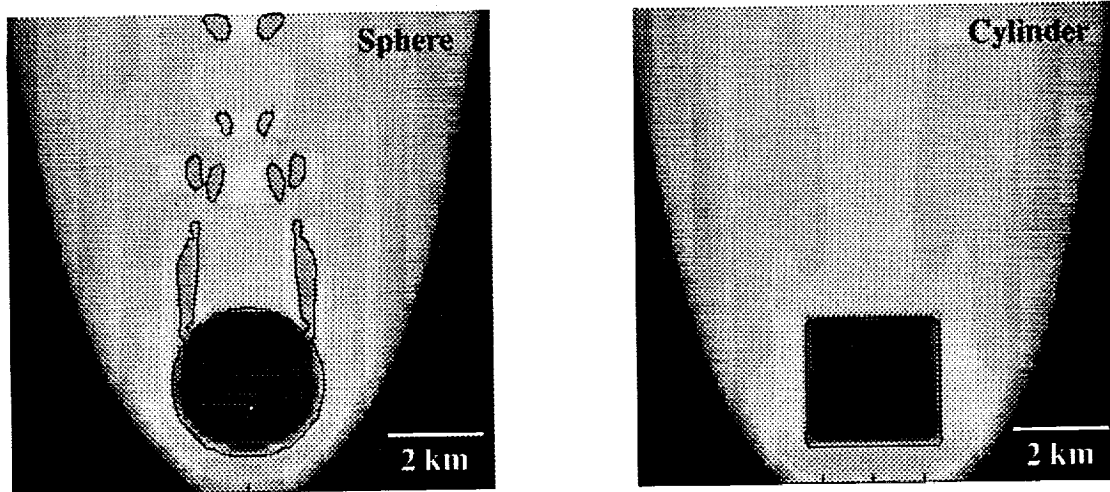
BREAKUP AND DEFORMATION OF SL9 FRAGMENTS: Crawford, D. A., *et. al.*

Fig. 1 Comparison of shape dependence 1 second into the calculation.

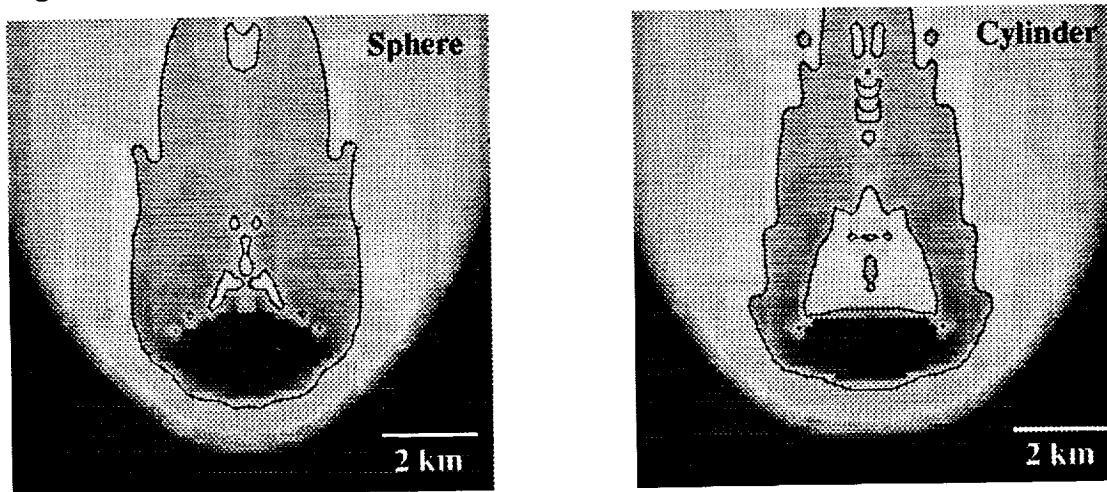


Fig. 2 Comparison of shape dependence 3 seconds into the calculation.

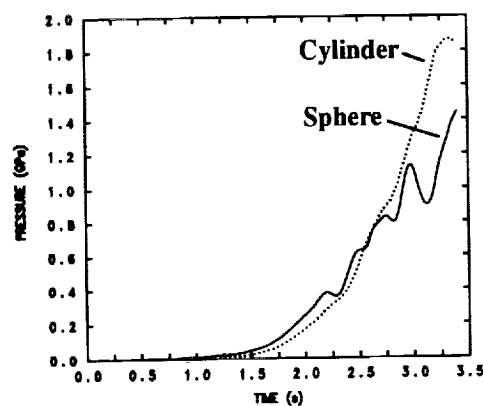


Fig. 3 The pressure at an internal point located near the edge of the projectile and its dependence on cometary fragment shape.

References: [1] C. R. Chapman, *Nature*, Vol. 363, pp. 492-493, June 10, 1993. [2] T. J. Ahrens, *et al.*, *Nature* (submitted). [3] R. A. Kerr, *Science*, Vol. 261, p. 552, July, 1993. [4] Corey S. Powell, *Scientific American*, pp. 26-27, Sept. 1993. [5] Zdenek Sekanina, *JPL D-10927*, 1993. [6] J. M. McGlaun, S. L. Thompson and M. G. Elrick, Sandia National Laboratories, *SAND89-0607*, Albuquerque, NM, 1989. [7] A. C. Robinson, *et al.*, *ASCE 8th Conference on Computing*, June 10-12, 1992.

Palimpsests on Ganymede: an endogenic origin?

Steven K. Croft, Lunar & Planetary Laboratory, University of Arizona, Tucson AZ 85721.

Introduction. One of the more enduring puzzles in the geology of the galilean satellites Ganymede and Callisto has been the interpretation and origin of the so-called palimpsests: quasi-circular light albedo patches with subdued interior topographic structure. Most hypotheses for the origin of palimpsests as a group have invoked some form of impact-related process, including: viscously relaxed "normal" impact craters (1), large, high velocity/high melt producing impacts (2), impacts with induced central endogenic diapirs (3), and impacts modified by cryovolcanism (4). Hypotheses of purely endogenic origin were proposed specifically for the Valhalla structure on Callisto soon after the Voyager Jupiter encounters (5,6). These specific models, however, could not be scaled to the observed dimensions of the palimpsests, and no further purely endogenic models have been considered. Reconsideration of the morphologies, classifications and statistical data of palimpsests, presented here, leads to inconsistencies with any kind of impact model for some palimpsests, prompting the proposal of a new, purely endogenic model for these features.

Morphologic classifications. One of the problems with interpretation of palimpsests has been the inclusion by various authors of different types of structures under the term "palimpsest." It is important to recognize different structure types, because different structures may be formed by entirely different processes. Based on a number of papers, features classed at times as palimpsests are differentiated as follows: 1) impact basins (e.g.: Gilgamesh, Nidaba, Hathor, 24N,182W on Ganymede) with a small central plain or dome, two (possibly 3) distinct concentric rings, secondary crater fields, and (sometimes) bright ejecta blankets, typically larger than about 150 km in diameter (1,2); 2) moat (7)/ anomalous pit (2)/ or (some) dome (3) craters (e.g.: Menhit on Ganymede) with subdued rims, prominent/oversize central pit rims with topographically prominent central domes, usually smaller than 100 km in diameter (2,3); ripple ring structures (e.g.: Valhalla and Asgard on Callisto, and 27S,153W on Ganymede [first described by (8), later rediscovered by (9)]) with rounded central smooth patches surrounded by inner annuli of concentric ridges and (only in the largest) outer annuli of concentric graben, usually larger than 300-400 km in diameter (8); and 4) "palimpsests" (e.g.: Memphis, Busiris, and Buto Faculae on Ganymede) with irregular central smooth patches surrounded by subdued, subconcentric ridges within a distinct, circular, sharp-edged light albedo patch, usually larger than about 100 km in diameter (1,2). [Hereafter, the term "palimpsest" will be restricted to class 4 features only.] Possible transition features between moat craters and small palimpsests exist, but the impact basins and palimpsests are distinctly different - one cannot be converted to the other by viscous relaxation (2). Ripple ring structures may be related to palimpsests, but only Valhalla has a bright albedo patch, and that is associated with the circular central plain. In contrast, the albedo patches of palimpsests extend considerably beyond any topographic structures, and they appear to be distinct deposits of non-negligible thickness overlying pre-existing terrain with sharp, raised, and sometimes slightly lobate edges. These characteristics led to their interpretation as ejecta blankets (1), melt sheets (2), or cryovolcanic flows (4).

Observations. Considering the [class 4] palimpsests as distinct features yields a number of interesting observational characteristics. A. The difference in crater statistics between large craters on Ganymede and Callisto is accounted for: if [class 4] palimpsests are assumed to be impact features and included in Ganymede crater counts (adopting a conservative rim diameter of 1/2 the diameter of the albedo patch), then the craters on Ganymede's dark terrain follow a roughly -2 differential slope between about 80 and 500 km in diameter. Over the same diameter range, there are actually fewer craters on Callisto (a much more heavily cratered object than Ganymede) and they follow a -4 differential slope. Removing the two dozen-odd palimpsests from the Ganymede statistics brings the crater counts on both bodies between 80 and 500 km into statistical coincidence - a result that might be expected for two bodies experiencing the same cratering flux (10). B. There are no unambiguous [class 4] palimpsests on Callisto. Except for Valhalla, virtually all of (1)'s proposed palimpsests turn out to be moat craters or fresh crater ejecta blankets. C. A few additional features (Siwah Facula, 19S,150W and 18S,156W) may be considered as palimpsests: they have the characteristic light deposit, but are irregular in shape. D. Palimpsests are not randomly distributed: they are concentrated in southern Galileo/eastern Marius Regio and eastern Barnard Regio. E. Palimpsests lack secondary crater fields and the sharp-edged bright deposit are difficult to interpret as ejecta. F. Palimpsests have a minimum diameter of 80-100 km; interior ridge systems and central patches (where identifiable) are, respectively, about 0.6-0.7 and 0.1-0.2 the diameter of the albedo patch.

Most of these observations are difficult to reconcile with any kind of impact model. The large impactor/high-velocity impact model of (2) is consistent with items E and F, but none of the rest, particularly the non-random areal distribution on Ganymede and the lack of palimpsests on Callisto. That palimpsests comprise the difference in large crater statistics between Ganymede and Callisto seems to be positive evidence that palimpsests are not crater-related, unless the putative crater is much smaller than any identifiable interior

PALIMPSESTS: Croft, S.K.

structure. On the other hand, the similarities in structure between palimpsests suggests that they were formed by a specific process. Therefore, consider a purely endogenic model.

Diapir/Plume Model. Several considerations motivate a diapir model: 1) Axisymmetric organization of most palimpsests are nominally consistent with expected isolated diapir shapes, yet diapir forms on Earth are flexible enough to account for irregular palimpsests. 2) Based on several studies (e.g.: 4,11), palimpsest bright materials are very thick (in excess of a few km) in the center near the central plain but much thinner (a few hundred meters) in and beyond the concentric ridges, suggestive of a massive upwelling of material in the center that flows viscously outward over the surface as might be anticipated from a large piercement diapir. 3) The existence of a lower diameter cut-off for palimpsests is consistent with diapirism, since diapirs have to be of some minimum size (dependent on mantle and plume viscosity and density relations) to reach and break through the lithosphere (12). 4) The edges of the bright material are sharp and slightly lobate and look like materials extruded from primary grooves (see groove at 15S,152W), suggestive of viscous flow. 5) The non-random area distribution of palimpsests is consistent with terrestrial analogs: diapirs form in groups where local conditions are favorable.

A scenario for palimpsest formation might be as follows: a large diapir, consisting of buoyant warm water ice or (more likely) mixtures of a number of low-melting point ices, nucleates at a boundary at depth (core-mantle, ice-phase change or ice-liquid?), rises through the mantle and pushes through the lithosphere to the surface. Near-surface materials buckle and fold, forming an incipient concentric ridge system (perhaps not unlike folds around Richat structure and Pilbara batholiths, see ref. 13). Viscous material then erupts from the central piercement and flows symmetrically outward. Collapse of the diapir "magma chamber" due to volume loss to the surface outflows would form concentric failure surfaces that may also contribute to the formation of the concentric ridge system. The irregular central plain marks the remnant of the central "vent", filled with cryovolcanic liquids or slushes. Ring dikes may also form, allowing local fracturing and flooding at large radial distances, forming some of the sharp, lobate boundaries and concentric depressions seen at the outer edges of some palimpsests (e.g.: Memphis Facula and 4S,222W). Alternatively, all of the flows may have originated from the central diapir, but a problem would be maintaining axial flow symmetry over such large distances.

Some comments can be made on the nature of the diapiric material. If Ganymede is only marginally differentiated (only a thin ice crust), the diapirs could consist of liquids and slushes. If Ganymede is largely differentiated (with a thick ice crust), then buoyancy considerations imply that liquids of likely composition would have difficulties reaching the surface and that the material should be warm, but solid, ice. The observed thicknesses (4) and distinct edges of the light deposits in the rugged terrain implies fairly viscous flows. Low viscosity liquid water or brine flows would be too thin and simply "get lost" in rugged terrain as they spread out from the source vent, unlike the observed deposits. Based on current understanding (14), the only icy magmas with viscosities high enough to form the observed deposits are liquids and slushes containing ammonia. Diapirs containing significant amounts of ammonia provide an additional plus for the model: depressurization melting (as occurs in terrestrial plumes) becomes possible. This allows the diapirs to buoyantly rise as warm solids and also provides a mechanism to initiate massive surface flows.

Light terrain formation on Ganymede was a distinct geologic episode. Based on morphology, light terrain emplacement may have been similar to dike swarm formation and flooding on the Earth. Dikes are now thought to propagate laterally from large diapir-like magma bodies (15). If Ganymede's grooved terrain was formed by a similar mechanism, then one would expect large diapirs in Ganymede's lower crust as well. Some of the diapirs should break through, forming surface features: I propose the palimpsests. Formation of the palimpsests as part of the same process as light terrain is supported by the similar appearance of materials forming some of the light terrain and palimpsest, and by their similar crater-count ages (1). This suggestion also accounts for the lack of both light terrain and [class 4] palimpsests on Callisto: it never went through the heating episode that produced both these features on Ganymede. The discussion of Ganymede's unique heating episode is beyond the scope of this paper, but possible explanations may come from special tidal heating mechanisms (16).

References. 1. Q. Passey & E. Shoemaker (1982) *Satellites of Jupiter*, U. of Arizona Press, p. 379. 2. S.K. Croft (1983) *JGR* (Suppl) 88:B71. 3. J. Moore & M. Malin (1988) *GRL* 15:225. 4. P.J. Thomas & S.W. Squyres (1990) *JGR* 95:19161. 5. W. Hale et al. (1980) *Conf. Multiring Basins (Abs.)*, p. 30. 6. C.A. Wood (1981) *Proc. Multiring Basins*, p173. 7. USGS Ganymede Mapping Program standard designation. 8. S.K. Croft (1985) *Rep.PGG Prog.* 1984, p.206. 9. P. Schenk & w.B. McKinnon (1987) *Icarus* 72:209. 10. S.K. Croft (1988) *LPS XIX*, p.227. 11. S.K. Croft et al. (1993) Geologic map of Tiamat Sulcus Quad, Ganymede, I-2328. 12. S.W. Squyres & S.K. Croft (1986) *Satellites*, U of Arizona Press, p. 293. 13. N.M. Short & R.W. Blair (1986) *Geomorph. from Space*, p. 98,124,158. 14. J.S. Kargel et al. (1991) *Icarus* 89:93. 15. H.C. Halls & W.F. Fahrig (1987) *Mafic Dyke Swarms*. 16. R. Malhotra (1991) *Icarus* 94:399.

POST-IMPACT HYDROTHERMAL SYSTEMS: MANSON IMPACT STRUCTURE,
MANSON, IOWA; L. J. Crossey, A. M. Kudo, P. McCarville, Department of Earth and Planetary
Sciences, University of New Mexico, Albuquerque, NM 87131

Re-equilibration after the disruption associated with large impacts includes: infilling of the crater depression, cooling of melt rocks, development of a hydrothermal circulation system, and mineralogical and geochemical alteration of target rocks, ejecta, and melt rocks. Emphasis has traditionally been devoted to establishing mineralogical and geochemical affinities among boundary layer clay, ejecta, impactor, and target rocks: little attention has been given to post-impact processes, though hydrothermal circulation is likely to chemically and mineralogically alter the composition of materials at the impact site. Based on mineralogical examination of material from the Manson Impact Structure (MIS), the presence of a high-temperature hydrothermal system operating within the central uplift is indicated (temperatures on the order of 300°C). Previous assessments of hydrothermal systems developed in impact craters have focused on thermal models of the impact melt sheet alone. In large impact structures, the formation of a central uplift represents an additional thermal perturbation of the system (several contributions must be considered: uplift of the geotherm, residual shock heat from the impact event, and rapid unloading). Utilizing previously-obtained temperature estimates for the impact melt-matrix layer and physical models for crater formation, a consideration of heat sources for a complex crater reveal that at the MIS the central uplift provides a greater caloric input than the hottest breccia material (approximately 60 cal/g compared to 170 cal/g respectively; but when relative volumes are considered, 0.9×10^{20} cal and 0.1×10^{20} cal, respectively). Although the calculation is sensitive to initial and boundary conditions, the volume of water heated by the event is considerably increased relative to an estimate considering only the melt rocks. Neglecting the thermal significance of the central uplift results in considerable underestimation of cooling time as well. A conductive cooling model for the melt-matrix breccia indicates that cooling would be largely completed (20% of initial temperature) in less than 100 years, depending on the thickness of overlying sedimentary clast breccia material. The central uplift (treated as a cylinder of 5 km diameter) requires approximately one million years to achieve the same degree of cooling. The observed mineralogy is best explained by the operation of a hydrothermal system driven by heat within the central uplift. The temperature necessary to produce the observed mineralogy is not likely to result from uplift alone: an additional heating component due to shock/unloading processes is required.

The operation of a post-impact hydrothermal system at the MIS has been previously reported [1, 2]. Lithologies encountered at the MIS are described elsewhere [3], as is the hydrothermal mineralogy [4]. The observed hydrothermal mineralogy (including garnet, ferroactinolite, zeolites, and chlorite) requires temperatures on the order of 300°C for times sufficient to grow cm-scale quartz and zeolite crystals. The pattern of increasing hydrothermal temperature with increasing core depth indicates a deeper heat source than the shallow melt-matrix breccia. Similar observations regarding a central uplift-sourced hydrothermal system have been reported for the 80 km-diameter Russian Puchezh-Katunki impact structure [5].

Previous quantitative impact cooling models [6, 7] have considered impact melt material and processes. Conductive cooling models were calculated for the melt-matrix breccia layer and the crystalline central uplift. Using equations from Jaeger [8] and Carslaw and Jaeger [9], the melt-matrix breccia layer was treated both as a lava flow and a sill (to assess the importance of depth of cover by subsequent sedimentary clast breccias). The central uplift was modeled as a cylinder. At the MIS, the melt-matrix breccia layer is estimated to be 30 m thick. The central uplift radius is estimated at 5 km. The thermal diffusivity for all lithologies is modeled at $0.01 \text{ cm}^2/\text{s}$. Model results for the relatively thin melt-matrix breccia reveal that, even under thick cover, the time required to cool to 20% of the initial temperature is less than 100 years. The central uplift is the most significant heat source, requiring over one million years to cool to 20% of the initial temperature. Figure 1 depicts the cooling profiles for the central uplift model. The model predicts that purely conductive heating of the crater fill is not substantial (about 25% of the

POST-IMPACT HYDROTHERMAL SYSTEMS: Crossey, L. J. et al.

initial uplift temperature attained 200,000 years after impact). Pervasive alteration of breccia materials at temperatures above 100°C would thus require convective heat transport. The central uplift retains 20% of its initial temperature for a time scale of one million years; sufficient to drive a hydrothermal circulation system. Note that the cooling time required to reach $T/T_0 = 0.5$ for the center of the uplift ($x/r=0$) is just under 400,000 years for the 5 km radius. Figure 2 shows model cooling times for a wide range of central uplift radii.

Though the melt-matrix breccia represents the hottest post-impact material deposited at the MIS, consideration of mineralogical and model results suggests that heat from the central uplift drives the long-term hydrothermal system. Uplift of the geotherm alone is insufficient to explain the hydrothermal mineralogy at Manson: residual heat from the impact or unloading phenomena are likely additional factors.

Acknowledgments: This research has been supported by the Department of Energy, Basic Energy Sciences to L. Crossey. **References:** [1] Crossey, L.J. and McCarville, P. (1993) *LPSC XXIV*, p. 351. [2] Crossey, L.J. et al. (1993) *GSA Abstracts with Programs*, p. A-23. [3] Anderson, R.R. et al. (1993) *LPSC XXIV*, p. 35. [4] McCarville, P. and Crossey, L.J. (1994) *LPSC XXV*, this volume. [5] Masaitis, V.L. and Naumov, M.V. (1993) *Meteoritics*, 28, p. 390. [6] Newsom, H.E. (1980) *Icarus*, 44, p. 207-216. [7] Onorato, P.I.K. et al. (1978) *JGR*, 83, 2789-98. [8] Jaeger, J.C. (1968) In *Basalts*, Vol. 2 (Hess, H.H. and Poldervaart, A., eds.), p. 503-536. [9] Carslaw, H.S. and Jaeger, J.C. (1959) *Conduction of Heat in Solids*, Oxford, 510 p.

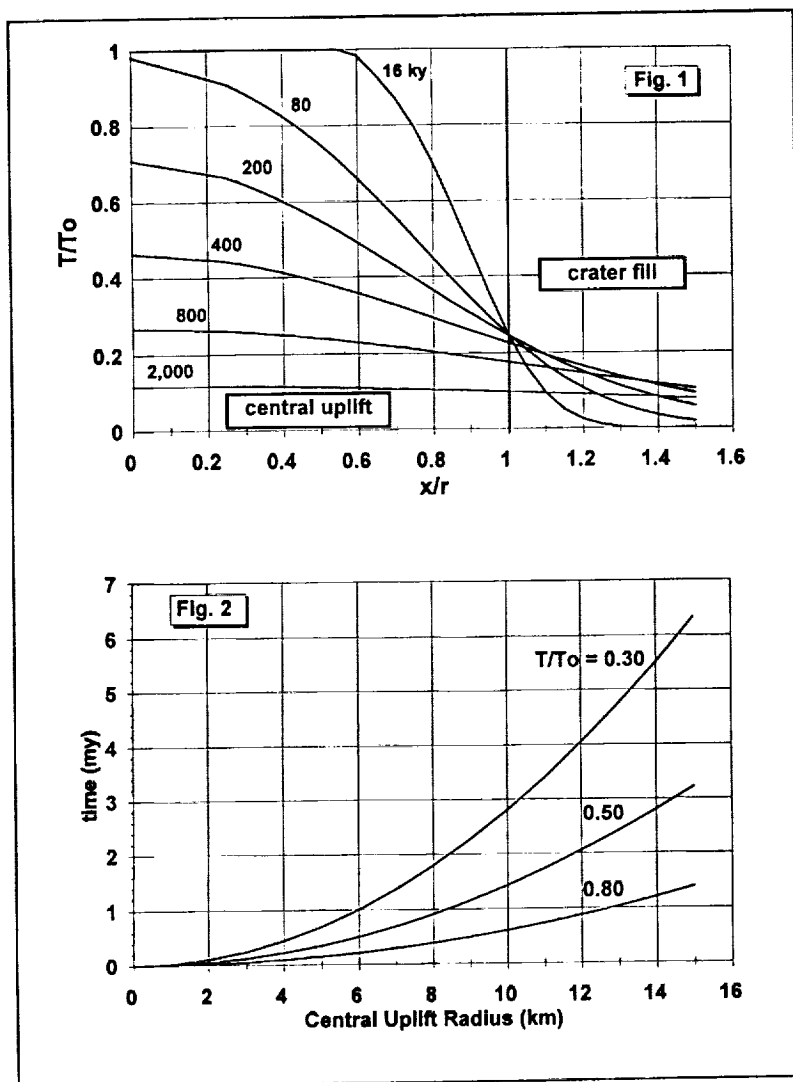


Figure 1. Model results for conductive cooling of a cylindrical central uplift. Cooling profiles are labeled in thousands of years (ky) elapsed since impact. The abscissa represents distance from the center relative to cylinder diameter (r). The ordinate (T/T_0) is temperature (T) relative to initial temperature (T_0). The outer boundary of the cylinder is indicated by a heavy vertical line at $x/r=1$. Thermal diffusivity is 0.01 cm^2/s and uplift radius = 5 km.

Figure 2. Conductive model results for time required for various degrees of cooling as a function of central uplift radius. Results are plotted for $T/T_0 = 0.30, 0.50$, and 0.80 .

GEOLOGY OF THE GUINEVERE PLANITIA QUADRANGLE OF VENUS; *David A. Crown, Department of Geology and Planetary Science, University of Pittsburgh, Pittsburgh, PA 15260; Ellen R. Stofan and Jeffrey J. Plaut, Jet Propulsion Laboratory, California Institute of Technology, 4800 Oak Grove Drive, Pasadena, CA 91109*

The Guinevere Planitia quadrangle (V30) of Venus is a low-lying region (0°-25°N, 300°-330°) located between the uplands of Beta Regio and Eistla Regio. Radar bright, dark, and mottled plains units, interpreted to be volcanic in origin, have previously been identified in Pioneer Venus, Goldstone, and Arecibo data of Guinevere Planitia, in addition to the arcuate fracture zones and lineament belt segments defining the Beta-Eistla deformation zone [1-5]. Analysis of Magellan SAR images has confirmed that volcanic landforms compose the majority of the surface of Guinevere Planitia [6]. The resolution of Magellan data allows detailed investigation of the geomorphic characteristics and stratigraphic relationships observed in the region in order to constrain its geologic history. Preliminary geologic mapping indicates that the Guinevere Planitia quadrangle consists of older, tectonically deformed complex ridged terrain, extensive volcanic plains, and volcanic flows. Volcanic materials in Guinevere Planitia have accumulated to form large shield volcanoes, lava flow fields, and small domes, cones, and shields.

Geologic Mapping of Guinevere Planitia

On the basis of geomorphic properties observed in Magellan SAR images, three types of geologic materials have been identified in the Guinevere Planitia quadrangle: complex ridged terrain, plains, and volcanic flows (Figure 1). Complex ridged terrain consists of embayed remnants of materials that have undergone intense deformation. *Lineated materials* contain one dominant orientation of tectonic features, and *complexly lineated materials* exhibit two or more tectonic fabrics. Prominent exposures of complex ridged terrain occur in a zone between 2.5-5.5°N and 315-317°E on the flank of a large volcano and at 12°N, 308°E in the center of a corona. Complex ridged terrain presumably includes the oldest materials preserved in Guinevere Planitia.

Extensive volcanic plains are evident throughout the Guinevere Planitia quadrangle. *Mottled, lineated plains* are generally large expanses containing a variety of small volcanic domes, cones, shields, and flows. Large eruptive centers possessing significant relief are not observed within this unit. Zones of tectonic disruption are common, as are outliers of complex ridged terrain. *Smooth plains* are low-lying regions which exhibit uniform radar brightness over large distances. Volcanic domes, cones, and shields are not abundant, but flow margins can be identified in many areas. Fractures and ridges are common and may extend for large distances (> 100 km). At 3°N, 304° a morphologically distinct network of irregular valleys appears to have formed by collapse of the surface due to the migration of subsurface fluids [7]. Typically, volcanic flows are superposed on the plains; however, locally, plains may embay the flanks of the major volcanoes in the region.

Two types of volcanic flow materials have been mapped in the Guinevere Planitia quadrangle. *Plains-forming flow materials* form extensive, radar bright or dark, relatively flat-lying sheets that can extend for hundreds of kilometers from their apparent source vents. Many exposures of plains-forming flows are associated with coronae or corona-like structures. *Lobate flow materials* form narrow, sinuous, overlapping, radar bright and dark deposits with lobate margins that form radial patterns around their source vents and have accumulated to form three broad, low-relief volcanic edifices in the region (A, B, and C in Figure 1). Numerous small domes, cones, and shields are observed within lobate flow materials on these large volcanoes.

Structures in Guinevere Planitia include numerous wrinkle ridges, fractures, and lineaments found primarily in plains units, coronae and corona-like structures, and the densely spaced ridges and troughs characterizing complex ridged terrain. Structures in plains units display a diversity of orientations, but usually occur in sets of similarly trending features. There does not appear to be a dominant tectonic fabric on the quadrangle scale; however, a large number of structures in the extensive smooth plains unit along the eastern margin of the quadrangle have trends between E-W and SE-NW. A prominent rift zone extends 250 km to the north from the summit of a large volcano (C) where it terminates in a series of arcuate fractures. In the central part of the quadrangle are several coronae and other structures with concentric ridges and/or fractures. The arcuate tectonic zones of these coronae and corona-like structures typically surround interior collapsed regions or clusters of small volcanic edifices. A group of 4 or more corona-like structures, with diameters between ~70 and 250 km, is partially embayed by lobate flow materials from the large volcanoes and also appears to be the source region for plains-forming flows.

Major Eruptive Centers and Regional Geologic History

Three large volcanoes dominate the recent volcanic history of the Guinevere Planitia quadrangle [6]. The northernmost (A in Figure 1) has a field of low shields at its summit and rises ~600 m above its surroundings. Its flanks (~600 x 800 km across) consist of a series of narrow, lobate flows which radiate from the summit region; a large flow field extends north onto the plains and coalesces with a secondary eruptive center consisting of small edifices and flows. Volcano B, ~1000 km across and exhibiting relief of ~1.4 km, consists of a large fan-shaped flow field which covers adjacent plains and lobate flows which embay a large corona and lineated materials. At its

summit radial flows surround a cone with a ~12 km diameter central pit. Volcano C, which rises ~2 km above its surroundings, has a complex summit region consisting of a shield field, a collapsed and embayed steep-sided dome, a large irregular dome, and summit flows that embay its prominent rift zone. The southern flank is composed of lobate flows which extend for ~500 km where they overlie radar dark, smooth plains with wrinkle ridges.

Relative age relationships both within and between the major eruptive centers in southern Guinevere Planitia are difficult to determine due to the complex nature in which volcanic flows interfinger and overlap. Each of the three large volcanoes appears to have had an extensive period of eruptive activity with several major phases emplacing large flow fields and more localized activity occurring both at vents on the flanks of the volcanoes and at their summits. Further geomorphic analyses and geologic mapping, including investigation of the radar properties of the flow units associated with the large volcanoes, will assist in documenting the types of volcanic activity which have occurred and the evolution of eruptive centers in the Guinevere Planitia quadrangle.

References: [1] Campbell, D.B., et al. (1989) *Science*, 246, 373-377. [2] Arvidson, R.E., et al. (1990) in *Proc. Lunar Planet. Sci. Conf., 20th*, 557-572, LPI, Houston. [3] Senske, D.A. (1990) *Earth, Moon, and Planets*, 50/51, 305-327. [4] Senske, D.A., et al. (1991) *Earth, Moon, and Planets*, 55, 163-214. [5] Stofan, E.R., et al. (1990) in *Lunar Planet. Sci. Conf., XXI*, 1208-1209, LPI, Houston. [6] Crown, D.A., et al. (1993) in *Lunar Planet. Sci. Conf., XXIV*, 355-356, LPI, Houston. [7] Baker, V.R., et al. (1992) *J. Geophys. Res.*, 97, 13421-13444.

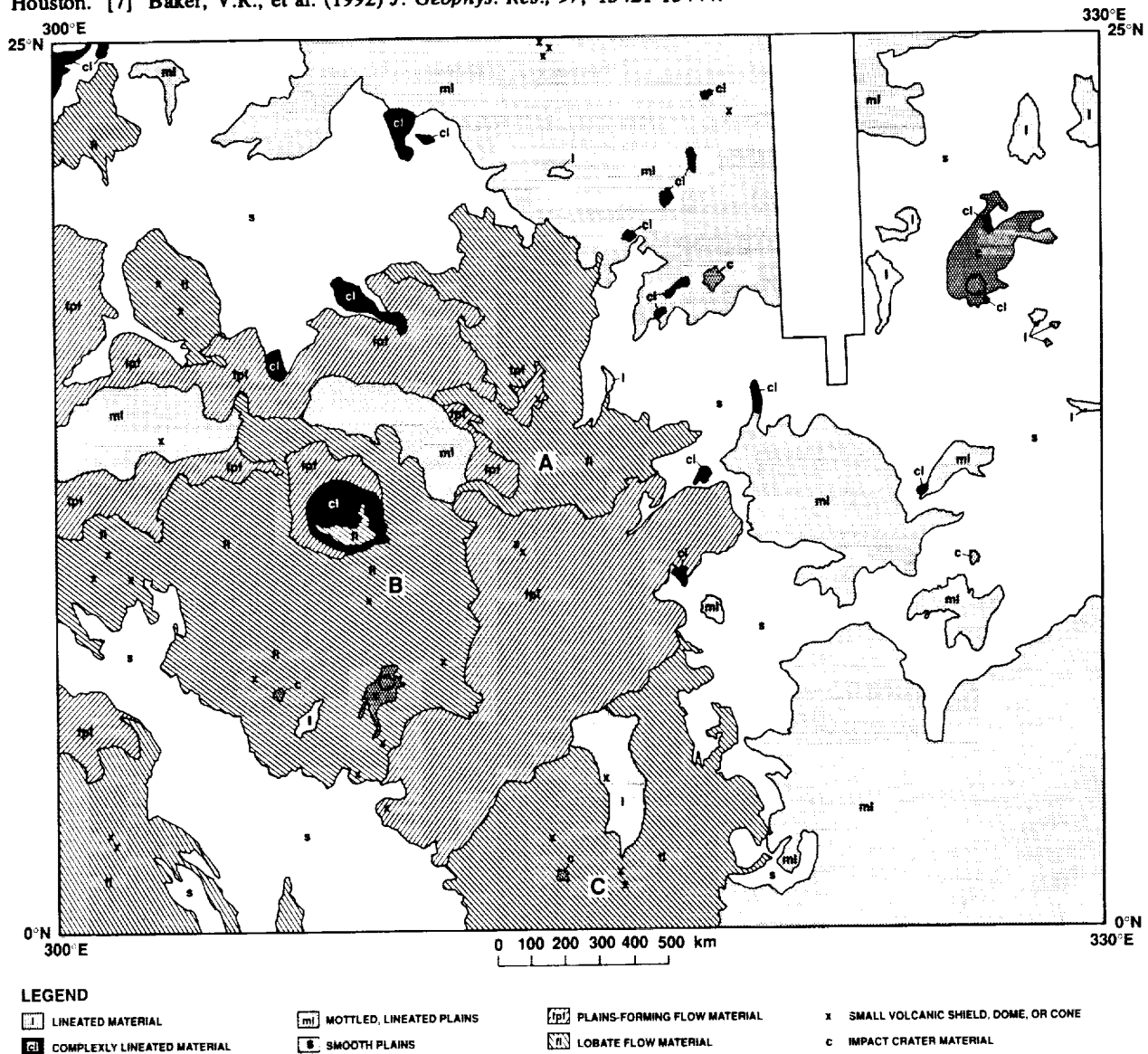


Figure 1. Simplified geologic map of the Guinevere Planitia quadrangle of Venus showing major geologic units (see text), impact crater materials, and small volcanic constructs. The summits of three large volcanoes are indicated by A, B, and C. Structures are not shown due to scale.

THE DISTRIBUTION OF HOT SPOTS AND ITS RELATION TO GLOBAL GEOLOGY: VENUS, EARTH, AND MARS;

L. S. CRUMPLER, Department of Geological Sciences, Brown University, Providence, RI 02912

INTRODUCTION. Completion of the Magellan spacecraft mapping of Venus [1] enables comparison of the global geologic characteristics of the three larger terrestrial planets. In this study it is shown that, despite the known dissimilarities in global geology and tectonic style, Venus, Earth, and Mars appear to share some large-scale similarities in the arrangement of fundamental geologic characteristics and the distribution of large magmatic centers.

CHARACTERISTICS AND SPATIAL DISTRIBUTION OF VOLCANISM. The distribution [2,3] of large volcanoes [4] and coronae [5] on Venus is non-uniform and is concentrated in the hemisphere between the highlands of Beta, Atla, and Themis Regions. Reconnaissance geologic mapping [4], and preliminary mission science reports [1] were used to establish the relationship between all major volcanic and magmatic centers larger than 100 km in diameter and global geologic characteristics. Similar maps of the distribution of volcanic and geologic characteristics were prepared from existing data for Earth and Mars. As plate boundaries associated with mobile tectonics are not present on Venus or Mars, only the intraplate hot spots are considered on Earth. Active intraplate volcanism on Earth is non-random and occurs in two hemispheric groups [6,7]. Volcanic centers on Mars occur in three settings, the Tharsis region, the Elysium region, and the Hellas basin region, the latter two occurring in the hemisphere opposite from the Tharsis region.

Inspection of the global maps shows that the distribution of volcanic centers on each planet, although non-uniform, is geometrically similar. To test this, the total number of magmatic centers was determined as a function of hemispheric caps of increasing area about a point on the surface on each planet (Figure 1), a method used previously [7] in describing the global abundance of hot spots on Earth. Steep changes in slope of the observed cumulative number-versus-area curve from the diagonal, which represents the distribution as it would appear if the existing population of hot spots were uniformly distributed, represent significant departures from a uniform distribution. A similar bipolar arrangement of volcanic centers occurs on each planet with three common characteristics: (i) a *primary group*, or a concentration of volcanic centers in which more than one-half of the global population occurs within less than 30% of the global area; (ii) a peripheral region where the density is less than or close to that expected for a uniformly distributed population, and (iii) a *secondary group*, occupying about 30% of the global area where the density is essentially similar to the uniform case.

GEOLOGIC CHARACTERISTICS OF MAJOR CONCENTRATIONS. The primary groups (*region i*) are areas of major thermal perturbations on all three planets. Concentration of thermal and magmatic processes of this dimension might be accompanied by distinctive boundary layer characteristics and styles and rates of tectonic deformation, resurfacing, crustal formation, and crustal modification. This association was checked by comparing the area of the primary group on each planet with corresponding global geologic maps using the appropriate circle (of area defined by the prominent breaks in slope of Figure 1) superimposed on the center of mass of each concentration (Figure 2). Based on these maps, hemispheric regions of anomalously concentrated volcanoes and magmatic activity are shown to occur in association with geologically distinctive global geologic characteristics.

On Venus the primary regional concentration of volcanic centers (*region i*) is characterized in Magellan SAR images by linear extensional deformation belts [3] whereas the geologic characteristics within the peripheral region, where volcanic

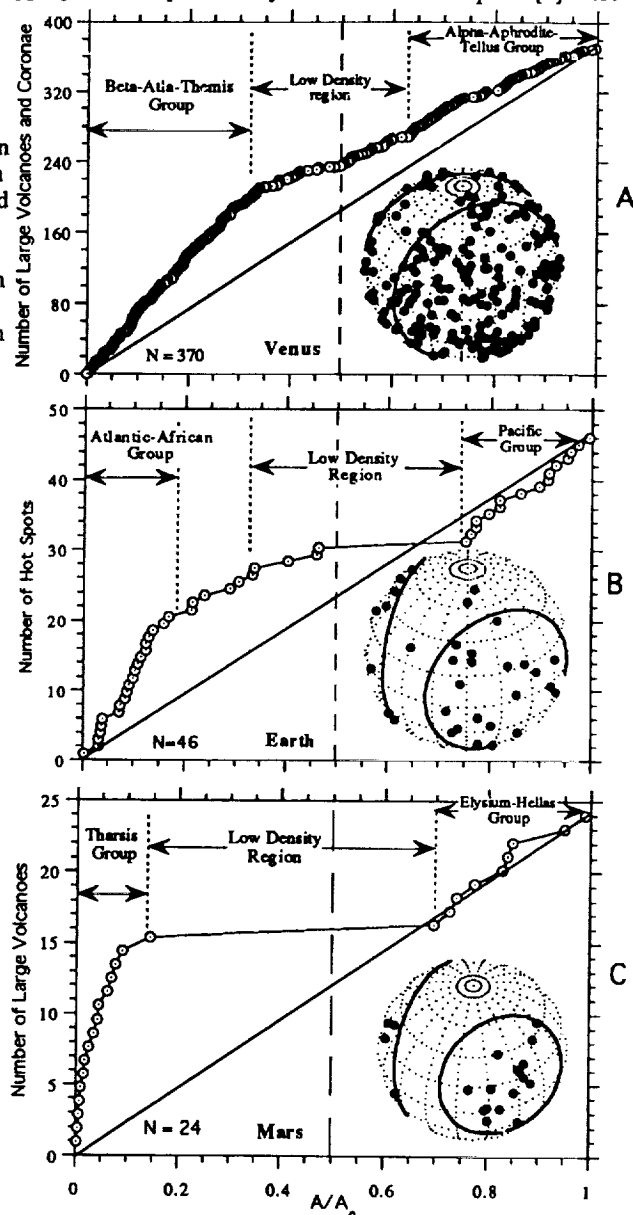


Figure 1. Cumulative distribution of volcanic centers about the centroid of the major concentrations on each planet. Insets are orthographic representations of the distribution centered at (A) 35N/240E (Venus), (B) 35N/20W (Earth), and (C) 45N/130W (Mars). Facing circles identify the boundary of the primary concentration anomalies.

HOT SPOTS ON VENUS, EARTH, AND MARS: CRUMPLER, L. S.

center abundance is low (*region ii*), include extensive lowland plains with the characteristics of flood lavas [10], frequent long linear ridge belts [11] interpreted to represent substantial crustal shortening [12], active orogenic belts surrounding complexly deformed highlands [13;14], and areas of proposed subduction-like behavior of the lithosphere [15].

The two-fold, African-Pacific global arrangement of intraplate volcanism on Earth (*region i* and *iii* respectively) correlates with prominent residual geoid highs [6] and large regions of anomalously low-seismic velocity mantle [16]. The intervening region (*region ii*) between hot spot groups corresponds to the location of plate convergence (Figure 2B), most of the current subduction zones, high seismic velocity upper mantle [16], and the current position of most of the continents [17]. The regions where most of the hot spots occur on Earth (*region i* and *iii*) includes most of the occurrence of large-scale global extension, and region *ii*, most of the examples of convergence.

The primary regions of extension on Mars occur in the Tharsis volcanic region (*region i*), a hemisphere characterized by high elevations, relatively youthful volcanism, and prominent geoid highs [18]. With the exception of minor occurrences of extensional features in the area of the Elysium-Hellas volcanic region (*region iii*), extensional tectonic features are relatively infrequent elsewhere on Mars (Figure 2C). In contrast, ridges of probable compressional origin [19,20] occur throughout *region ii*. Crustal shortening on Mars has been attributed to effects of subsidence associated with impact basins, gravity stresses associated with the Tharsis topographic dome, lateral effects of dynamic plumes associated with Tharsis, global contraction, or a combination of these influences [18;19;20].

CONCLUSIONS. On Earth it is as yet unclear whether the primary control on global patterns of interior convection are plates [17] or whether interior convection patterns control the pattern of surface tectonics [16;21;22]. In either model, hot spot type volcanism is likely to be suppressed in areas of subduction or down welling, and either enhanced or near that occurring in association with normal background levels of convection and volcanism in areas distal from subduction. The similarity among Venus, Earth, and Mars of the correlation between tectonism and hot spot concentration, regardless of the reigning global tectonic style, implies that the concentrations of volcanic centers in all three planets are deep-seated in origin rather than an influence of a mobile boundary layer alone. Plate tectonics could be influential in organizing the patterns of intraplate volcanism on Earth, but that mechanism alone will not work on Venus or Mars. Plates may be secondary as an influence on the global arrangement of intraplate volcanism on Earth.

- REFERENCES.** [1] Saunders, R. S., et al., 1992, *JGR*, 97, 13,067; [2] Head, J. W., L. S. Crumpler, J. C. Aubele, J. E. Guest, and R. S. Saunders, 1992, *JGR*, 97, 13,153; [3] Crumpler, L. S., J. W. Head, J. C. Aubele, 1993, *Science*, 261, 591; [4] Crumpler, L.S., J. C. Aubele, and J. W. Head, 1993a, *LPS*, XXIV, 363; [5] Squyres et al., 1992, *JGR*, 97, 13611; [6] Crough, S. T., and D. M. Jurdy, 1980, *EPSL*, 48,15; [7] Stefanick, M. and D. M. Jurdy, 1984, *JGR*, 89, 9919; Jurdy, D. M., and M. Stefanick, 1990, *GRL*, 17,1965; [8] Grimm, R. E., and S. C. Solomon, 1988, *JGR*, 93,11911; [9] Greeley, R., and B. D. Schneid, 1992, *Science*, 254, 996; [10] Baker et al., 1992, *JGR*, 97, 13,421; [11] Squyres et al., 1992, *JGR*, 97, 13579; [12] Solomon et al., 1992, *JGR*, 97, 13,199; [13] Crumpler, L. S. et al., 1986, *Geology*, 14, 1031; [14] Kaula et al., 1992, *JGR*, 97,16085; [15] McKenzie, D., et al., 1992, *JGR*, 97, 13533; [16] Richards, M. A., B. H. Hager, and N. H. Sleep, 1988, *JGR*, 93, 7690; [17] Anderson, D. L., 1982, *Nature*, 297, 391; [18] Phillips, R. J., and K. Lambeck, 1980, *Rev. Geophys.*, 18, 27; [19] Chicarro, A. F., and P. H. Schultz, 1985, *Icarus*, 63, 153; [20] Watters, T. R., 1993, *JGR*, 98,17,047; [21] Olson, G. Silver, and R. W. Carlson, 1990, *Nature*, 344, 209; [22] Schubert, G., D. Bercovici, and G.A. Glatzmaier, 1990, *JGR*, 95, 4105.

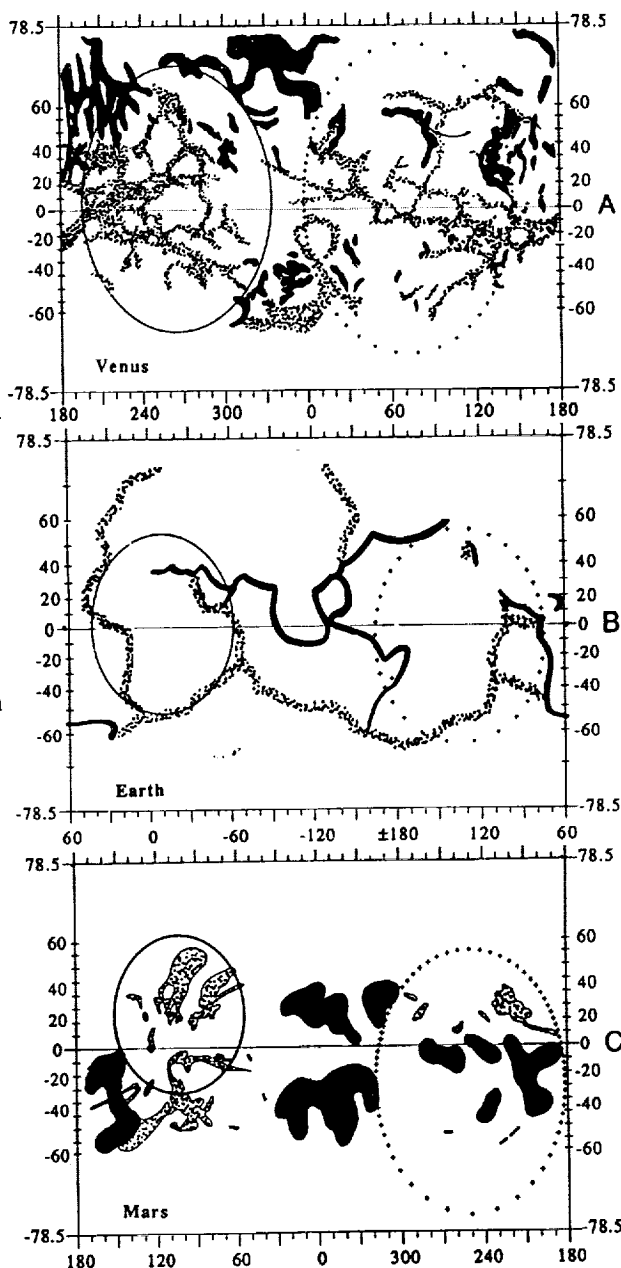


Figure 2. Arrangement of global volcanic and magmatic center concentrations (circles) relative to areas characterized by extension (stipple pattern) and significant contraction (black). Hemispheric organization occurs between concentrations of volcanic and tectonic features.

CALDERAS ON MARS: CLASSIFICATION, CHARACTERISTICS, AND PROCESSES RELATED TO MECHANISMS OF FORMATION;

L. S. CRUMPLER, J. W. HEAD, AND J. C. AUBELE, *Department of Geological Sciences, Brown University, Providence, RI 02912*

INTRODUCTION. Calderas represent records of magmatic processes associated with magma ascent, emplacement, storage, and evolution in planetary lithospheres. In addition to representing the surface manifestation of subsurface magma movement and changes in the state of subsurface magmas, calderas are evidence for differing conditions of crustal density and structure, variable volume rates of magma emplacement, and changing conditions associated with magmatic evolution.

A wide variety of calderas are observed on Earth and several hypotheses have been proposed for their formation [1,2,3,4], including volume decreases arising from evacuation of the magma reservoir, volume increases due to injection of new magma or vesiculation, and loading due to isostatic changes accompanying thermal evolution of the reservoir. Distinct surface characteristics are predicted to be associated with these differing mechanisms [10]. Recently the structure and distribution of associated features have also been used to infer the geometry and depth of the magma reservoir associated with the formation of the caldera of Olympus Mons [5]. As an initial step in comparing the observed characteristics of calderas with the predictions of from hypotheses, the characteristics and range of tectonic structures, their relation to associated volcanological features, and the stratigraphic relationships between the structures and sequences of events in the building of the edifice have been documented through detailed geologic mapping. In this study the calderas are first classified on the basis of the consideration of their geologic and topographic characteristics.

TWO FUNDAMENTAL TYPES OF CALDERAS. In a previous analysis of the tectonic structures and topographic characteristics associated with the summit of several volcanic edifices on Mars [6,7] we identified two fundamentally different types of calderas on Mars: the *Olympus-type* and the *Arsia-type*. In the *Olympus-type*, the pattern of faults defining the depression boundaries in map view occur frequently in sets of short arcuate scarps or as a nested sequence of depressions, the boundaries are sharply defined by a narrow inner slope, and the scarps associated with faulting are inward-facing, scalloped, and responsible for a terraced and chaotic appearance. In the *Arsia-type* the pattern of faults are primarily concentric, are distributed over a broad interval of radius from the center of the depression, and trace smoothly arcuate scarps with both inward and outward-facing slopes defining narrow graben along the topographic caldera rim.

The *Arsia-type* may be further distinguished in topographic profile from the *Olympus-type* caldera by a larger diameter in relation to the host volcano, a broadly concave and sag-like profile, gently-sloping marginal inner walls, and multiple boundary faults (rather than an abrupt bounding inner escarpment). The *Arsia-type* is a much larger scale of caldera development and appears not to have a morphologically or topographically equivalent counterpart on Earth, perhaps with the exception of the Taupo-type calderas [4] or the large depressions encompassing some volcanic fields [8]. Although the mobility of Earth's lithosphere may be a factor, these two examples suggests that the *Arsia-type* could occur in the terrestrial record, but may not be easily identified due to their extreme size and due to the obscuring effects of erosion.

MAP CHARACTERISTICS AND CLASSIFICATION. Structural maps of all of the calderas on Mars are illustrated at the same scale in Figure 1 based on detailed geologic mapping and consideration of previous work [5,6,7,9], and each caldera has been categorized according to the classification above. Inspection of the suite of maps reveals that whereas most of the calderas are of the *Olympus-type*, relatively few are strictly of the *Arsia-type*. This suggests that, as a rule, the *Arsia-type* may be size-dependent and associated with larger reservoirs.

Martian calderas may be further divided according to recurring minor characteristics relevant to potential modes of formation. Several calderas might best be described as transitional in morphology between the two main end members as the summits are characterized by an *Olympus-type* caldera enclosed within a larger annulus of faults and graben similar to that of the *Arsia-type* (Alba Patera, Biblis Patera, Tyrrhena Patera, Uranus Patera, Pavonis Mons, Hecates Tholus). The degree to which the annular graben are expressed varies from those with short arcuate segments on the flank (Hecates Tholus), to those in which numerous graben occur close to the boundary of an inner caldera and are characterized by listric-style walls (Biblis Patera), and to those with distinct enclosing summit sags (Pavonis Mons).

At least two of the edifices and their calderas are characterized by sector structure in which the calderas open onto and downwardly displace the adjacent flanks (Tharsis Tholus, Ceraunius Tholus). On several, a form of sector behavior occurs in which the calderas lie at the head of flank-inundating fans of fluidal deposits and channels (Ceraunius Tholus, Apollinaris Patera, and Hadriaca Patera). And although terraced, listric fault margins, and nested overlapping margins are common to the *Olympus-type*, several of the smaller calderas of the *Olympus-type* are to varying degrees simple, relatively circular, and characterized by steep walls (Albor Tholus, Ulysses Patera, Elysium Mons). Calderas on Mars are unusually circular across a wide range of dimensions. Despite the evidence for the influence of asymmetric stress fields in the form of sector structure and strong regional tectonic orientations, many of the calderas are unusually circular, and suggest relatively equant reservoir development. Small cones or shield volcanoes occur particularly along sector structures and *Arsia-type* graben arrangements, and represent evidence for circumferential fissures and lateral magma transport in at least four volcanoes.

Calderas on Mars are morphologically diverse, yet are characterized by several common features indicative of preferential mechanisms of development. These results, additional characteristics of edifices (flow sizes, volumes, magma reservoir geometry, etc.), and chronological relationships among calderas structures are being used to make inferences about the mechanism of magma ascent and emplacement, the timing of events associated with reservoir formation in planetary lithospheres, and the long-term evolution of isolated magmatic systems.

REFERENCES. [1] Williams, 1941, *Cal. Univ. Pub. Geol. Sci. Bull.*, 21, 51; [2] Gudmundsson, 1986, *Geology*, 14, 164; Gudmundsson, 1988, *Geology*, 16, 808; [3] Delaney et al., 1990, *Science*, 247, 1311; [4] Walker, 1988, *JGR*, 93,

CALDERAS ON MARS: CRUMPLER, L. S. ET AL.

14785; Walker, 1984, *JGR*, 84, 8407; [5] Zuber and Mouginis-Mark, 1990, *LPSC XXI*, 1318; [6] Crumpler, L. S., J. C. Aubele, And J. W. Head, 1991, *LPSC XXII*, 269; [7] Crumpler, L. S., J. C. Aubele, And J. W. Head, 1990, *MEVTV LPI Tech Rept 90-04,27*; [8] Heiken, 1976, *Geology*, 4, 568; [9] L.S. Crumpler, and J. C. Aubele, 1989, *MEVTV LPIU Tech Rept 89-06, 25*; L.S. Crumpler, and J. C. Aubele, 1978, *Icarus*, 34, 496; Zimbelman and Edgett, 1992, *Proc. Lun. Sci. Conf.*, 22, 31; Mouginis-Mark, 1981, *Proc. Lunar. Sci. Conf.*, 12B, 1431; Crown and Greeley, 1993, *JGR*, 98, 3431; Malin, 1977, *GSA Bulletin*, 88, 908; Wood, 1984, *JGR*, 89, 8391; [10] Ryan et al., 1981, *JGR*, 88, 4147.

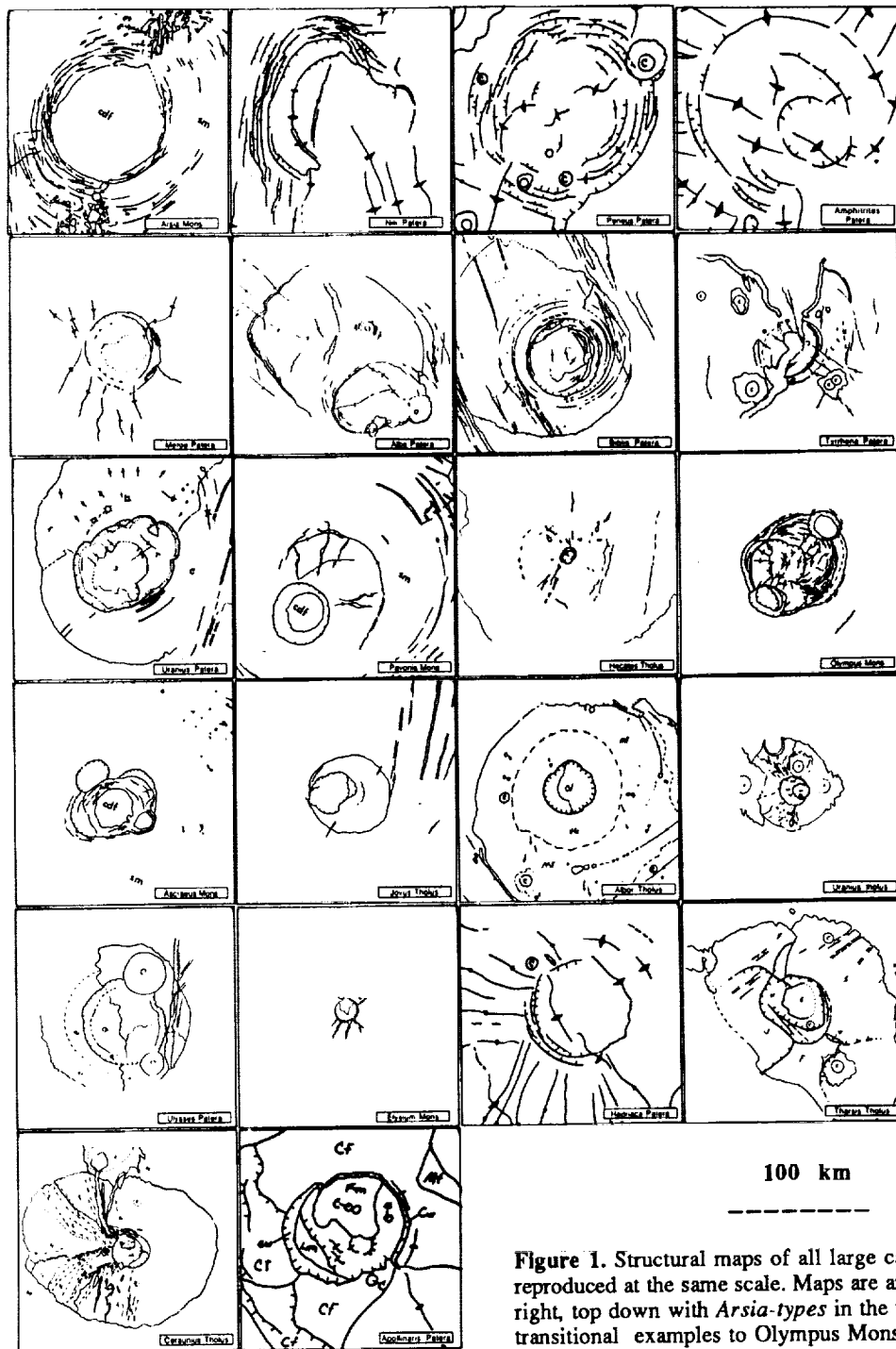


Figure 1. Structural maps of all large calderas on Mars reproduced at the same scale. Maps are arranged from left to right, top down with *Arsia*-types in the upper left, transitional examples to Olympus Mons in the middle, and modified *Olympus*-type (circular and sector-type) in the lower two rows.

P-2

2967

WHAT INITIATED PLANETESIMAL FORMATION? J. N. Cuzzi, A. R. Dobrovolskis, and R. C. Hogan; Space Science Division, 245-3, Ames Research Center, Moffett Field, California 94035-1000

The physical structure of primitive (chondritic) meteorites, even after some geological processing and modification, is thought by most to contain clues as to the first stage of accretion of solid matter into objects that might be called "planetesimals". However, theoretical understanding of the processes responsible for this important stage is shaky. We note what we believe are fundamental obstacles for the Goldreich-Ward version of rapid and direct planetesimal formation via gravitational instability in a settled particle layer [1], and describe an alternative scenario which might lead from grainy nebula gas to primitive planetesimals in a way that has intriguing connections to the meteorite evidence.

Primitive meteorite morphology appears to call for some specific, and geologically unusual, process of accumulation. Chondritic meteorite samples are fairly uniform (within a class) from the standpoint of constituent size distribution, arguing against "hierarchical" accumulation and in favor of a spontaneous coming together of constituents [2] which are very well size-sorted [3]. Recent work indicates that aerodynamic drag is the sorting mechanism [4], and raises the distinct possibility that the very earliest aggregates may be composed entirely of size sorted objects consisting of a solid object (chondrule or fragment, silicate or metal) covered with a fine-grained dust rim [5].

In its original form, the Goldreich-Ward (GW) scenario postulated that volumes of centimeter-sized objects could collapse directly (in a two-stage process) into solid, asteroid-sized objects; the similarity of the centimeter size scale to that of chondrules was encouraging. However, Weidenschilling [6] and subsequently we [7] have shown that the conditions for gravitational instability are difficult to achieve in the presence of nebula gas, at least while the typical particles are less than a meter or so in radius. This is due to the stirring effects of the turbulence that is generated around the differentially rotating dense midplane particle layer. Nevertheless, it is still commonly assumed that the particle layer instability will still occur, but at yet larger particle sizes for which turbulent diffusion is less effective.

We believe this is not the case. The GW instability requires not merely "marginal" gravitational instability, the criterion normally cited, but *extreme* instability in order for a volume fragment of particulates to collapse directly to solid density. The extremely large compression factor requires gravitational instability of initial fragment scales λ which are orders of magnitude smaller than the *critical* wavelength λ_c . As a fragment collapses, potential energy is converted to kinetic energy until a certain equilibrium fragment size λ' is reached. Equation 36 in [1], along with the standard definition of λ_c , shows that $\lambda/\lambda_c \sim \lambda'/\lambda$. GW require the equilibrium fragment to have achieved solid density; thus $\lambda'/\lambda \sim \lambda/\lambda_c \sim 10^{-2}$. Equation 37 of [1] then requires the particle random velocities to begin and remain far smaller than the "critical" random velocity $c_c = 2\pi G\sigma/\Omega$ which merely allows λ_c to be unstable. For the centimeter-sized particle layer originally described in [1], a combination of collisional damping and gas drag damping makes this a reasonable assumption. However, turbulent stirring prohibits the instability until the particles grow to meter-and-larger sizes for which both of these dissipation mechanisms become inefficient on a dynamical collapse time Ω^{-1} . Thus, while incipient fragments may become unstable at or near the critical wavelength, they are unable to shrink and collapse very far. These fragments are likely to be dispersed by differential rotation, or exist only as a standing wave

WHAT INITIATED PLANETESIMAL FORMATION? CUZZI J. N. et al.

or pattern with no capability of concentrating a specific ensemble of particles, much like the "wakes" in Saturn's ring system. Alternatively, Safronov [8] has proposed that *axisymmetric* or annular instabilities may initiate at close to the scale λ_c with random velocities c_c , and slowly compress radially until fragmentation densities (nearly 10 times higher) result. This process is much slower than a dynamical collapse time and not obviously relevant to meteorite structure or mineralogy, some of which indicates "short" accumulation timescales (perhaps comparable to or less than an orbit period) [e.g., 2].

A completely different mechanism that operates in very much the desired way, at least in terrestrial laboratories and numerical simulations, is turbulent *concentration* of appropriately sized particles [9]. The process appears to be capable of producing a substantial concentration of aerodynamically size-sorted objects into massive clumps, *and* of simultaneously providing the constituents with rims of fine dust. Order of magnitude concentration factors are already seen relative to the average particle density (and the gas density); considerably larger concentration factors are feasible in the nebula context. These are of mineralogical interest whether or not the process leads directly to planetesimals [e.g., 2, 10]. The primary uncertainties at present are in relating the time, length, and mass scales of the process to nebula and meteoritic scales, and in understanding the role of turbulence damping in stabilizing particle clumps. Turbulence now accessible to computational study has a Reynolds number which is orders of magnitude smaller than expected for the nebula, and we must understand the basic physics before being able to confidently extrapolate current results. It is in this area that we are devoting our current studies [11]. We present the scaling relations which we believe support this hypothesis as a candidate for the initial stage in the planetesimal formation process, and show how it could lead to concentrations with the mass equivalent of a 10 - 100 meter size object. Objects of this size would settle rapidly to the nebula midplane, and their subsequent growth and radial evolution may be modeled as "drift-augmented accretion" in which subsequent growth to asteroid radius r , at heliocentric distance R , can be geologically rapid (roughly $10^4(r/10\text{km})(R/1\text{AU})^2 \text{ yr}$) [7].

There are many unexplored and uncertain aspects of the turbulent clumping scenario. Solid chondrule-sized elements are merely presupposed, and the elusive intense thermal processing stage leading to chondrule formation is not addressed. Nor does this scenario explain evidence for high relative velocities between chondrule-sized objects, leading to considerable fragmentation *prior to* accumulation. Compression of loose agglomerations of chondrule-sized constituents to "rocks" is another "detail left to the reader". On the positive side, however, new physics has been introduced that appears to provide a fruitful direction for future study.

References: [1] Goldreich P. and Ward W.; *Astrophys J.*, 183, 1051-1061; [2]: Kerridge J. (1993) *Icarus* 106, 135-190; [3] Dodd R. T. (1976) *EPSL* 30, 281-291; Hughes D. W. (1978) *EPSL* 38, 391-400; [4] Skinner W. R. and Leenhouts W. (1993) *LPSC XXIV*, 1315-1316; Scott E. R. D. and Haack H. (1993) *Meteoritica* 28, 434; [5] Metzler et al. (1992); *GCA* 56, 2873-2898; [6] Weidenschilling S. (1980) *Icarus* 44, 172-189; (1984), *Icarus* 60, 555-567; [7] Cuzzi J. N. et al. (1993) *Icarus* 106, 102-134; [8] Safronov V. S. (1991) *Icarus*, 94, 260-272; [9] Squires K. D. and Eaton J. K.; *Phys. Fluids A2*, 1191-1203; *Phys. Fluids A3*, 1169-1178; [10] Wood J. and Hashimoto A. (1993) *GCA* 57, 2377 - 2388; [11] Cuzzi J. N. et al. (1993) *Meteoritica*, 28, 339; Dobrovolskis A. R. et al. (1993) *B.A.A.S.* 25, 1122, and *B.A.A.S.* 25, 1248

NMR SPECTROSCOPY OF EXPERIMENTALLY SHOCKED COCONINO SANDSTONE AND THE EFFECT OF PORE WATER; R. T. Cygan¹, M. B. Boslough¹, and R. J. Kirkpatrick², ¹Sandia National Laboratories, Albuquerque, NM 87185 and ²University of Illinois, Urbana, IL 61801

We have extended our solid state ²⁹Si nuclear magnetic resonance (NMR) spectroscopic study of shocked Coconino Sandstone from Meteor Crater, Arizona. Previously we showed that the NMR spectra of naturally-shocked samples taken from the crater are in excellent agreement with the classification scheme of Kieffer [1], and we identified a new hydroxylated amorphous phase [2,3]. To follow up that work, we have now collected data on Coconino Sandstone explosively shocked to independently-known pressure-temperature states. In addition, we performed identical explosive loading experiments on water-saturated samples to characterize the effects of groundwater in a natural impact. The magic-angle spinning (MAS) spectra for the shocked sandstone powders exhibit no additional phases; resonances for coesite and stishovite are not observed. However, a broadening of the quartz resonance is exhibited for both dry and wet samples relative to the narrow resonance for quartz in the unshocked material. The cross-polarization magic-angle spinning (CPMAS) NMR experiments exhibit an enhanced single resonance, probably associated with hydroxylated silicon in kaolinite clay. This peak broadens with shock-loading for both dry and wet samples. There is no clear distinction between the NMR spectra obtained for the dry and wet samples recovered from the shock-loading experiments.

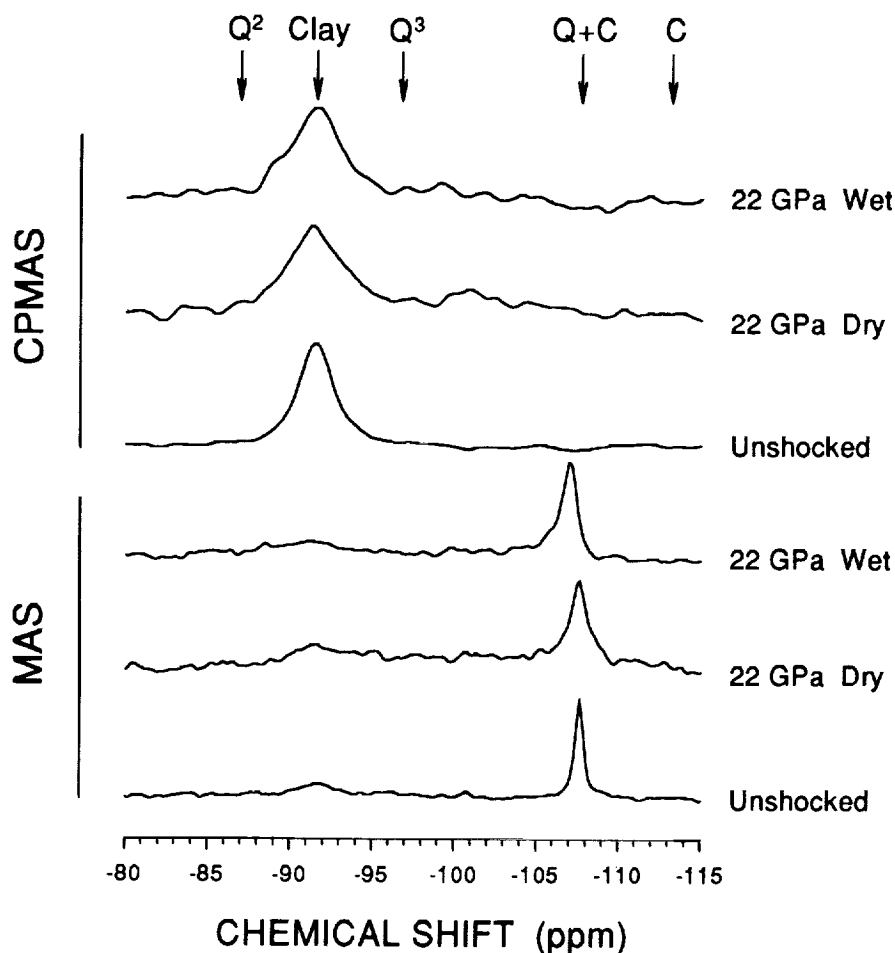


Figure 1. ²⁹Si NMR spectra of unshocked and experimentally-shocked (dry and wet) Coconino Sandstone samples. MAS (all Si sites) and CPMAS (hydrated Si species) spectra are presented for each sample. Arrows denote approximate chemical shift observed in previous studies [2,3] for quartz (Q), coesite (C), clay, and hydrated amorphous silica, including Q³ (one OH) and Q² (two OH) silicon sites.

NMR SPECTROSCOPY OF EXPERIMENTALLY-SHOCKED SANDSTONE: Cygan *et al.*

The present work is part of a continuing project to develop solid state NMR spectroscopy as a method of quantifying the effect of shock loading experienced by silicate minerals subjected to natural impact. We have previously suggested that NMR spectra be used as an unambiguous identification technique for shocked quartz, and have shown that it can be used as a "shock barometer" under some conditions [4,5]. In addition to finding a new densified amorphous phase, we have shown that NMR relaxation analysis can provide morphological information about shock-produced amorphous material [6]. However, our measurements to date have been limited to laboratory-shocked synthetic quartz samples, and to naturally-shocked sandstone. Moreover, other workers have obtained quantitatively different results using different starting materials (single crystals as opposed to powder) and different loading conditions [7]. By subjecting Coconino Sandstone to the same shock-loading histories as pure synthetic quartz in our earlier work, we are beginning to bridge the gap between natural and artificial shock-loading histories to help understand the differences. In addition, by using initially water-saturated samples, we attempt to 1) isolate the effect of the presence of water and 2) find out if the dense amorphous hydroxylated phase we found in naturally-shocked sandstone can be synthesized in the laboratory, and if so, under what conditions.

Samples of unshocked Coconino Sandstone were obtained from near Meteor Crater, Arizona and were subjected to explosive loading using the Momma Bear fixtures of Graham and Webb [8]. Wet experiments were performed by first saturating the sandstone powder with deionized water before sealing the copper sample fixture. The dry powder samples were subjected to peak shock pressures of approximately 7.5, 16.5, and 22 GPa. The corresponding pressure values for the wet sandstone samples are somewhat higher. The recovered materials were examined by optical and secondary electron microscopies, X-ray diffraction, and NMR spectroscopy. We use both standard MAS and CPMAS techniques in the NMR experiments to determine the resonances associated with ^{29}Si nuclei. Cross polarization transfers nuclear spin from protons to the ^{29}Si , thereby providing additional structural information and preferentially eliminating spectrum signal produced by anhydrous phases.

The MAS and CPMAS spectra obtained for the shocked sandstone samples do not exhibit any additional resonances compared to the spectra for the unshocked sample (Figure 1). Resonances for coesite (-108 ppm and -113 ppm) and stishovite (-192 ppm) are not observed. The strong four-fold coordinated silicon resonance, with a chemical shift of -108 ppm, dominates the MAS NMR spectra. A broadening of the quartz resonance for both dry and wet samples is observed with increasing shock pressure. These results are similar to our previous work on dry synthetic quartz powders [4,5]. A minor resonance in the MAS spectra, corresponding to the major resonance in the CPMAS spectra, is observed at -92 ppm. These resonances are associated with the hydroxylated silicon site in clay, probably kaolinite; X-ray diffraction analysis of the recovered material confirms this assignment. Some broadening of the clay CPMAS resonance occurs with increasing shock pressure for both dry and wet samples. There is no clear evidence for the formation of a dense hydroxylated amorphous phase in the material recovered from the wet shock-loading experiments. We previously observed for several naturally-shocked samples from Meteor Crater a very strong resonance with a chemical shift of -97 ppm, corresponding to Q^3 silicon [2,3]. These differences in the NMR spectra are related to the distinct loading and unloading histories associated with experimental shock-loading and natural impact events.

References: [1] Kieffer (1971) *J. Geophys. Res.* 76, 5449-5473. [2] Boslough *et al.* (1993) *Lunar Planet. Sci. XXIV*, 149-150. [3] Cygan *et al.* (1994) In *Shock Waves in Condensed Matter-1993*, in press. [4] Cygan *et al.* (1990) In *Proc. Lunar Planet Sci. Conf. 20th*, 451-457. [5] Cygan *et al.* (1992) In *Proc. Lunar Planet Sci. Conf. 22nd*, 127-136. [6] Assink *et al.* (1994) In *Shock Waves in Condensed Matter-1993*, in press. [7] Fiske *et al.* (1993) *Lunar Planet. Sci. XXIV*, 491-492. [8] Graham and Webb (1984) In *Shock Waves in Condensed Matter-1983*, 211-214.

Acknowledgments: John McHone and Susan Kieffer were instrumental in helping acquire samples of Coconino Sandstone from Meteor Crater. We thank Meteor Crater Enterprises, Inc. for allowing us access to the crater. Ed Dunbar performed the explosive loading experiments at EMRTC, Socorro, NM. Gary Turner obtained the NMR spectra. This work was partially funded by NASA's PMG program and was performed at Sandia National Laboratories by the U.S. Department of Energy under contract DE-AC04-94AL85000.

THE PLANETARY DATA SYSTEM EDUCATIONAL CD-ROM DEMONSTRATION; M. A. Dale-Bannister, McDonnell Center for the Space Sciences, Department of Earth and Planetary Sciences, Washington University, St. Louis, Missouri 63130-4899.

A chief purpose of the PDS Educational CD-ROM is to provide PDS-compatible data sets to the research and educational communities and help provide for an understanding of how planetary exploration and science are achieved. The Planetary Data System (PDS) Educational CD-ROM contains 5 analysis modules and a multimedia program called Journey to the Planets. The analysis modules are for use in planetary geology studies from the undergraduate through the graduate level. Journey to the Planets is an interactive, multimedia system that can be used with a more general audience and runs on Macintosh, personal computer systems running Windows, or Silicon Graphics work stations.

Journey to the Planets is a tool for presenting the excitement of planetary exploration to advanced and beginning students in planetary geology. Journey to the Planets is activated by clicking on the Journey icon within the file management system. The student chooses his own path through Journey to the Planets, using a "point and click" interface, by selecting first a planet or small body of interest. Individuals unfamiliar with "point and click" interfaces will find a brief user's guide in the Journey directory of the Educational CD-ROM. After selecting a planet or small body, the student may select an image from a menu, consisting of thumbnail renditions (very small, reduced versions) of the images available, for the selected planet or small body. Each image has a caption that appears on the screen, next to the image. By clicking buttons labeled with icons the student can guide himself, based on interest. Choices include having the computer read the caption aloud (volume control is available as a slider); selecting a "zoom-in" mode, where the student can get a high-resolution view of a feature of interest; selecting a spacecraft information mode, where the student learns about the spacecraft that acquired the image through another system of images and captions; or selecting the next or previous image in the stack available for the chosen planet.

The interactive interface makes Journey to the Planets easy to use and generates student interest because it allows the student to choose his own path. An instructor can also guide the student's path through the program by providing exercises in which Journey is used as a tool. For example, a set of questions about Venus might be prepared by the instructor in such a way as to guide the student through a path in the program that includes investigations of Venusian volcanology and the Magellan spacecraft.

The analysis modules include one module on photometric analysis of Voyager images of Titania using SPICE kernels and NAIF software. Another module involves an analysis and comparison of meteorite and asteroid reflectance spectra with reflectance spectra of minerals taken on Earth. There is a module that uses Viking

THE PDS EDUCATIONAL CD-ROM DEMONSTRATION; Dale-Bannister, M. A.

Orbiter images and topography combined with line-of-site gravity measurements to investigate gravity anomalies over Olympus Mons on Mars. A fourth module uses chemical analyses of Apollo 17 samples, an Apollo orbital image that covers the area in which samples were acquired, and linear mixing models to develop a scenario for the evolution of one area on the moon. A fifth module examines Magellan SAR mosaics, as well as altimetry and emissivity data sets covering Sapas and Maat Mons on Venus. The volinfo.txt file contains detailed text for each analysis module that explains the purpose of the module, and any software and data associated with it. A background discussion document is also included in the documentation directory of the CD-ROM. This document provides quantitative background material necessary for the student to take maximum advantage of the module exercises. Topics included in the background document include radiance, irradiance, Fresnel and volume scattering, the Planck Function, emissivity, Kirchhoff's Law, and the basics of radar backscatter theory. The use of SPICE for photometric analysis of Voyager 2 images of Titania is also discussed.

The Educational CD-ROM is available from the Planetary Data System through the Geosciences Node for NASA-sponsored researchers. To place an order contact Mary A. Dale-Bannister (internet: dale@wunder.wustl.edu; telephone: 314-935-6652). Individuals not sponsored by NASA should contact the National Space Science Data Center (NSSDC - internet: request@nssdc.gsfc.nasa.gov; telephone: 301-286-6695).

HIGH-RESOLUTION TRANSMISSION ELECTRON MICROSCOPY OF METEORITIC AND TERRESTRIAL NANO-DIAMONDS

T. L. Daulton¹, D. D. Eisenhour², P. R. Buseck², R. S. Lewis³, and T. J. Bernatowicz⁴, ¹Department of Physics, Geology, and Chemistry, Arizona State University, Tempe AZ 85287-1404, ²Departments of Geology and Chemistry, Arizona State University, Tempe AZ 85287-1404, ³Enrico Fermi Institute, University of Chicago, Chicago IL 60637-143, ⁴The McDonnell Center for Space Sciences and the Department of Physics, Washington University in St. Louis, St. Louis MO 63130

Introduction: Primitive meteorites contain within their bulk matrices a few parts per million of pristine interstellar grains that have survived the various mineral formation, accretion, and alteration processes that produced the meteorite parent bodies. These grains represent our only direct specimens of (surviving) physical material formed in past interstellar environments which we can subject to quantitative laboratory analysis. Interstellar grains were recognized from their isotopic compositions which are anomalous with respect to the solar mean and they were subsequently isolated and identified (graphite [1], silicon carbide [2,3], and diamond [4,5]). The most abundant of these carbon-rich components is diamond [6]. This abundance may not be representative of its distribution in the interstellar medium but most likely reflects its durability to pre-solar processing. The strong covalent tetrahedral bonds in the diamond structure make it highly resistant to alteration from: annealing, radiation damage, and chemical processing.

In this study, interstellar diamond crystallites isolated from acid dissolution residues of carbonaceous meteorites (Allende and Murchison) were systematically examined using high-resolution transmission electron microscopy (HREM). The distribution, density, and types of microstructural defects present in these nanocrystallites are heavily dependent on the details of the kinetics and energetics of the growth mechanism and are characteristic of the particular formation mechanism which produced them. Therefore, a detailed examination of the microstructures can be used to extrapolate information pertaining to the localized environments of diamond formation. To discriminate among the most likely formation mechanisms, microstructural features observed in the HREM images of the interstellar diamond crystallites are compared to those observed in terrestrially synthesized nano-sized diamonds formed from low pressure [4] chemical vapor deposition (CVD) and from high pressure shock waves [7] produced in controlled detonations [8].

Discussion: A JEOL JEM-4000EX high-resolution transmission electron microscope, operating at 400 KeV with a point-to-point resolution of 0.17nm equipped with a CCD video camera was used for the HREM imaging. The microstructures of the meteoritic diamonds exhibit extensive twinning. The most common and lowest energy twin boundary is a first-order $\Sigma=3$ (coincidence lattice site notation [9]) boundary with a {111} coherent twin plane. In a lower abundance, multiple $\Sigma=3$ twin boundaries are also observed. The most striking of these microstructures has a star configuration similar to those commonly observed in CVD diamond films [10] (Fig. 1a & 1b). Because of a 7.36° misalignment of the lattices, it is impossible to have five coherent $\Sigma=3$ twin boundaries sharing a common core. However a nano-sized structure can readily accommodate this misalignment by elastic strain at the twin interfaces (Fig 1a). Single and multiple $\Sigma=3$ twin boundaries are also observed in the terrestrially shocked diamonds, however no twin quintuplets (stars) have been observed. The shocked diamonds also differ in that they exhibit a large density of dislocations that are not observed in the meteoritic diamonds.

Type III hexagonal diamond (lonsdaleite) has been identified in the meteoritic acid dissolution residues (Fig. 1d). Lonsdaleite has been previously associated with meteorites; however, its formation there is attributed to terrestrial impact or recent meteoritic collisions in the early solar system [11, 12]. Since there is no evidence in Allende or Murchison for the shock levels necessary to produce lonsdaleite, the observed lonsdaleite is plausibly identified as an interstellar grain constituent. Although lonsdaleite is associated with shock processes, it is feasible that under certain CVD conditions that the kinetics would be favorable for the formation of the hexagonal polymorph [13]; this is further suggested from its observed nano-scale epitaxial growth on cubic diamond (Fig. 1c). This should impose additional constraints on the diamond forming interstellar environment. As expected, lonsdaleite is observed in diamonds synthesized in high pressure shock waves. It occurs as single crystals and in narrow (several unit cells wide) shock lamellae within cubic diamond nanocrystallites. These preliminary results indicate that the microstructures of the meteoritic diamonds are more consistent to those observed in CVD diamonds than those of shocked diamonds. This does not rule out shock processes as a diamond formation mechanism. However, it does suggest that the majority of observed meteoritic diamonds were formed from CVD-type low pressure processes.

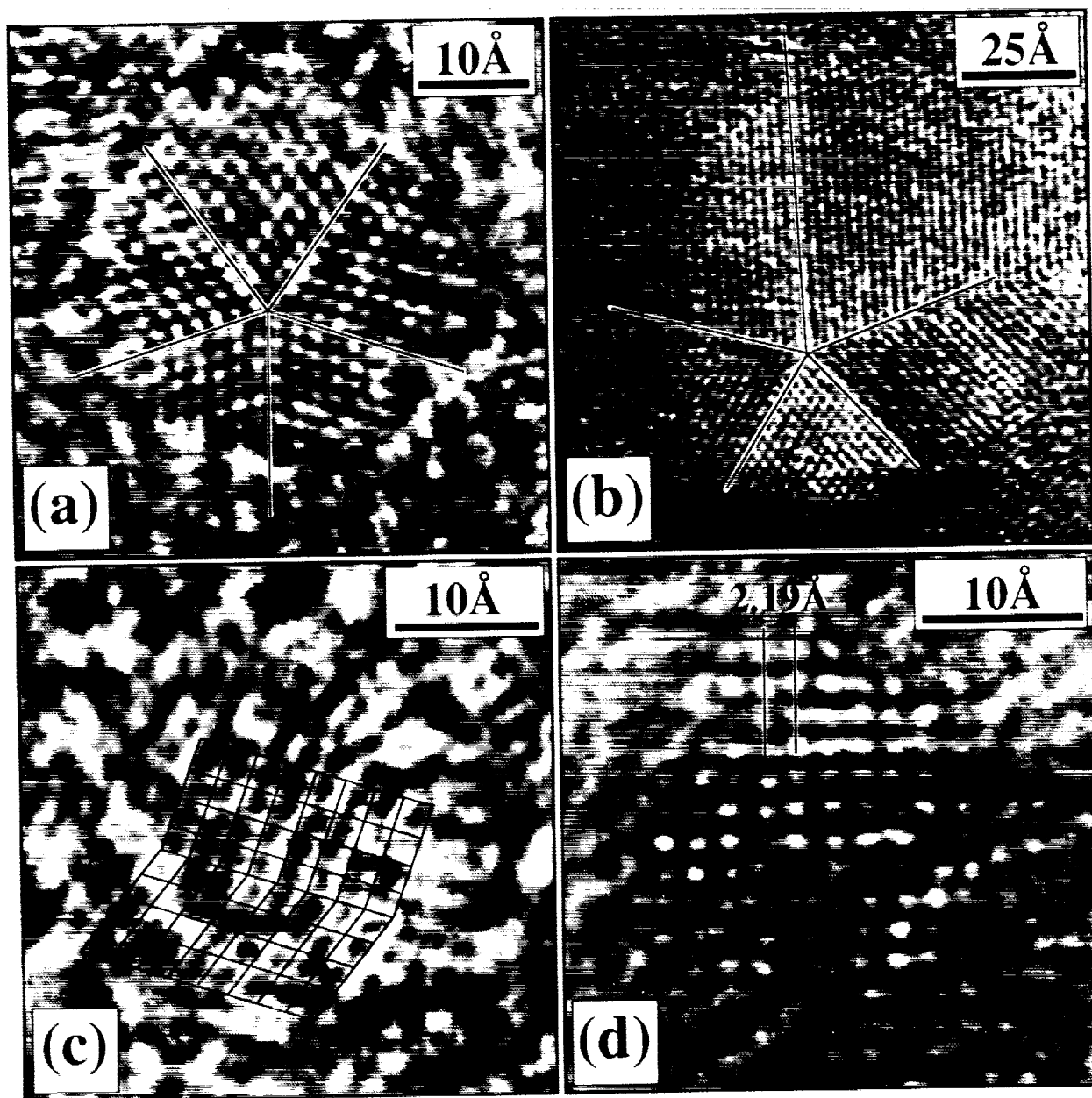
METEORITIC DIAMONDS: Daulton, T. L., *et al.*

Figure 1: HREM atomic resolution lattice images of meteoritic diamonds. (a) A twin quintuplet exhibiting pseudo five-fold symmetry in Allende DM. (b) A larger pentagonal multiple-twin microstructure in Murchison X. These nano-stars are presumably formed in the circumstellar shells of distant stars. (c) An epitaxial intergrowth of cubic and hexagonal diamond (lonsdaleite) in Allende DM. (d) Single crystal of lonsdaleite in Murchison X.

References: (1) Amari, S., Anders, E., Virag, A., & Zinner, E. (1990) *Nature* **345**, 238. (2) Bernatowicz, T., Fraundorf, G., Tang, M., Anders, E., Wopenka, B., Zinner, E., & Fraundorf, P. (1987) *Nature* **330**, 728. (3) Tang, M., Anders, E., Hoppe, P., & Zinner, E. (1989) *Nature* **339**, 351. (4) Lewis, R. S., Tang, M., Wacker, J. F., Anders, E., & Steel, E. (1987) *Nature* **326**, 160. (5) Lewis, R., Anders, E., & Draine, B. (1989) *Nature* **339**, 117. (6) Anders, E., Lewis, R., Ming, T., & Zinner, E. (1989) *Interstellar Dust* edited by Allamandola L. & Tielens, A., 389. (7) Tielens, A., Seab, C., Hollenbach, D., & McKee, C. (1987) *Astrophys. J. Lett.* **319**, L103. (8) Greiner, N., Phillips, D., Johnson, J., & Volk, F. (1988) *Nature* **333**, 440. (9) Ranganathan, S. (1966) *Acta Cryst.* **21**, 197. (10) Shechtman, E., Feldman, A., & Hutchison, J. (1993) *Mater. Lett.* **17**, 211. (11) Hanneman, R. Strong, H., & Bundy, F. (1967) *Science* **155**, 995. (12) Frondel, C. & Marvin, U. (1967) *Nature* **214**, 587. (13) Yarbrough, W. (1990) *Mat. Res. Soc. Symp. Proc.* **162**, 75.

Acknowledgments: Shocked diamonds were provided by N. Greiner, Los Alamos National Laboratory, Los Alamos, New Mexico, 87545. HREM was performed at the National Center for High Resolution Electron Microscopy at Arizona State University. This research is partially funded from NASA grant NAGW3386 awarded to P. R. Buseck.

ALTERATION OF ALLENDE TYPE B1 CAIs: WHEN, WHERE AND HOW; Andrew M. Davis¹, Steven B. Simon² and Lawrence Grossman^{1,2}. ¹Enrico Fermi Institute, ²Department of the Geophysical Sciences, University of Chicago, Chicago, IL 60637.

Abstract. We have undertaken a detailed petrologic, chemical and isotopic investigation of secondary alteration of the Allende Type B1 CAIs TS23 and TS34. ²⁶Al-²⁶Mg systematics show that alteration occurred at least 2.4 m.y. after crystallization of primary anorthite. Textural evidence shows that alteration occurred prior to incorporation of the CAIs into Allende. Trace element abundances and textures show that alteration is dominated by reaction of Mg-rich melilite with nebular SiO₂. Reaction between melilite and anorthite also occurred, as did loss of Sr and gain of volatiles.

Introduction. Although the crystallization history of Type B CAIs is becoming well-constrained by experimental petrology [1,2,3] and by detailed studies of trace element zonation [4,5,6,7], the very last stages of crystallization and the alteration that followed are not well understood. Phase equilibria [1] show that the last liquid should crystallize spinel + melilite + fassaite + anorthite. Ion microprobe analyses show that fassaite that crystallized late in Type B CAIs is enriched in LIL trace elements relative to early-formed fassaite, because they are incompatible in all crystallizing phases [6]. Application of partitioning data to REE abundances in CAI anorthite also indicates that this phase crystallized from a late, REE-rich liquid [8]. No mesostasis has ever been observed in a CAI, but the report of extremely REE-rich alteration products with chondrite-normalized abundances like that of very late fassaite (~1000 × CI) in the Allende Type B1 inclusion TS23 [6] led us to consider the possibility that fassaite or REE-rich mesostasis was altered, rather than melilite [9] or melilite and anorthite [10] as is commonly assumed. To investigate the extent to which melilite, anorthite, fassaite or mesostasis were altered, and to assess whether REE and other trace elements were internally redistributed, or lost or introduced during alteration, we have undertaken a detailed SEM, electron microprobe and ion microprobe study of alteration products in the Allende Type B1 CAIs TS23 and TS34.

Petrography. Both of these inclusions have melilite-rich mantles and spinel-, fassaite-rich cores. They also contain melilite with reversely-zoned bands, indicating that pyroxene crystallized before anorthite and making the latter the last major phase to join the crystallization sequence [2]. Mantle melilite is only lightly altered, with alteration products (predominantly grossular) present mainly along veins, whereas in the interior, patches of alteration products ~100 μm across are present. These patches mainly consist of 10–20 μm anhedral grains of wollastonite and monticellite and anhedral to nearly euhedral grossular. Point-counting of b.s.e. images of two such areas give ~50 wt% grossular, ~40 wt% monticellite and ~10 wt% wollastonite. All three alteration minerals are very close to end-member compositions. These intensely altered zones generally occur between ragged (partially altered) grains of anorthite and Mg-rich melilite (typically Ak_{72–76}) and clean, unaltered grains of fassaite and spinel.

Mg isotopes. Mg isotopic measurements on TS23 and TS34 show that most anorthite contains excess ²⁶Mg consistent with the canonical early solar system ²⁶Al/²⁷Al ratio of 4–5 × 10^{–5}, but some anorthite in altered zones of TS34 shows evidence of later disturbance, at least 3.3 × 10⁵ years after formation of primary anorthite. Grossular is the only secondary phase with high Al/Mg. One fairly clean grossular spot in TS34 contains no excess ²⁶Mg and must have crystallized at least 4.6 × 10⁵ years after primary anorthite. Hutcheon and Newton [10] reported a clean grossular spot in TS23 with no excess ²⁶Mg that must have formed at least 2.4 × 10⁶ years after primary anorthite.

In the previous discussion, we assumed that the ²⁶Al-²⁶Mg system can be used as a chronometer. Another possible explanation of the Mg isotopic data is that open system alteration occurred shortly after primary mineral crystallization in a region of the solar nebula with no ²⁶Al. If grossular formed at essentially the same time as anorthite, the ²⁶Al/²⁷Al ratio in it must have been diluted by at least a factor of ten compared to the reservoir from which the primary phases of TS23 and TS34 crystallized. Mass balance considerations require that most of the Al from breakdown was lost from the CAI and that most of the Al now in grossular was introduced from the ²⁶Al-free reservoir in which alteration occurred. Trace element data (below) do not suggest wholesale exchange of components with a reservoir external to these CAIs during alteration.

Trace elements. We measured major and trace elements in several profiles across alteration zones in the heavily altered interiors of TS23 and TS34. Alteration zones are light REE-enriched, with La enriched relative to CI chondrites by 20–100 times. The REE patterns resemble those of adjacent late-crystallized melilite. The altered zones are enriched in B, F, Na, K, Cl and Pb relative to adjacent primary phases and strongly depleted in elements that occur primarily in fassaite, Ti, Sc and Zr. Alteration zones are fairly high in Sr, Ba and Eu, like adjacent melilite and anorthite. A plot of chondrite-normalized Eu/Sr vs. Ba/Sr shows several interesting features. Fassaite and anorthite

ALTERATION OF ALLENDE TYPE B1 CAIs: WHEN, WHERE AND HOW; A. M. Davis et al.

have constant Eu/Sr, but variable Ba/Sr. Early-crystallized melilite has $\text{Eu/Sr} \times \text{CI}$ values of ~ 1 , but Eu/Sr and Ba/Sr drop for late-crystallized melilite. Alteration zones show a good correlation between Eu/Sr and Ba/Sr, with the trend line passing through the melilite points. Alteration zones appear to have inherited their trace element abundances from melilite; Sr was lost in varying amounts relative to Ba and Eu.

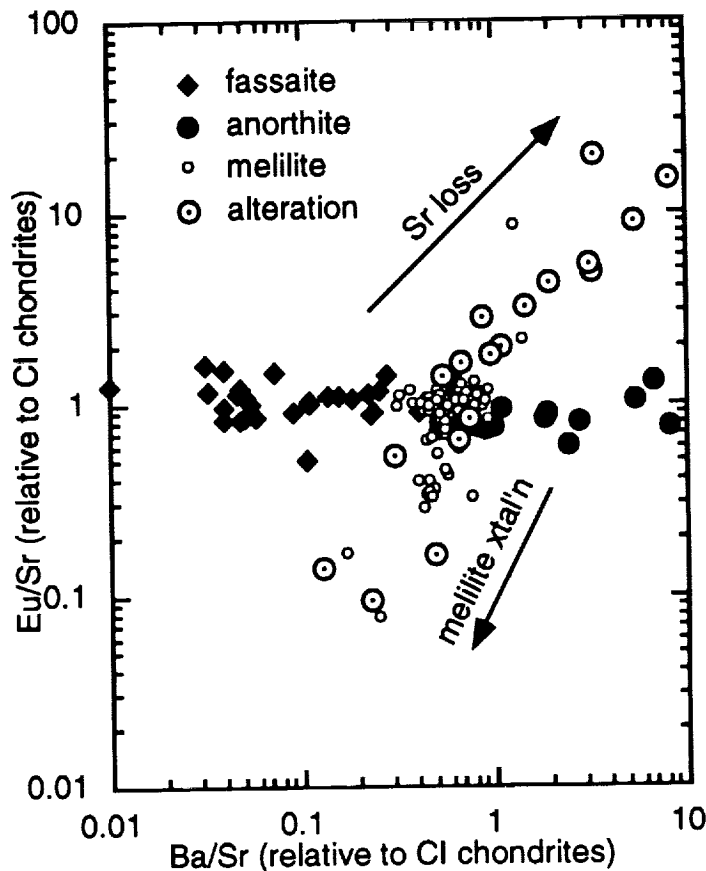
Discussion. It has long been assumed that most of the alteration products observed in CAIs were derived from melilite [9,11]. Our petrographic and trace element studies show that the precursor was largely Mg-rich melilite, but there is textural evidence that some alteration of primary anorthite also occurred. In addition, the partial resetting of the ^{26}Al - ^{26}Mg system in anorthite adjacent to an altered area in TS34 suggests that some elemental exchange can occur in primary anorthite. Hutcheon and Newton [10] proposed that melilite and anorthite reacted to form grossular + monticellite, based on the association of the former phases with intensely altered patches, but our data (Fig.) indicate little contribution from anorthite, and the bulk alteration products are more SiO_2 -rich than melilite + anorthite. We conclude that the alteration products were derived from Mg-rich melilite by reaction with a SiO_2 -, alkali-bearing fluid. The intense alteration in the interior of the inclusions vs. the light alteration of the gehlenitic mantles further suggests that Mg-rich melilite is more easily altered than gehlenitic melilite. The fact that altered zones do not have the high REE contents expected for the liquid from which primary fassaite and anorthite grew indicates that there was essentially no late-stage, residual mesostasis in Type B1 CAIs prior to alteration.

When? ^{26}Al - ^{26}Mg systematics indicate that alteration occurred at least 2.4 m.y. after crystallization of the primary minerals of Type B1 CAIs. The only way to accommodate a substantially shorter nebular lifetime is to have alteration occur in an ^{26}Al -free reservoir with wholesale exchange between ^{26}Al -free Al in the reservoir and ^{26}Al -rich Al released from breakdown of primary minerals.

Where? Textural evidence shows that alteration occurred prior to incorporation of the CAIs into the Allende parent body, presumably while the inclusions were still in the solar nebula.

How? Alteration occurred by reaction of nebular SiO_2 with åkermanite-rich melilite, but with some reaction between melilite and anorthite. LIL abundance patterns of altered zones were inherited from melilite with no exchange of these elements with an external reservoir. There is no evidence for alteration of fassaite, spinel or mesostasis. During alteration, SiO_2 and volatile elements were introduced and Sr was lost.

References: [1] Stolper E. (1982) *GCA* 46, 2159. [2] MacPherson G. J. et al. (1984) *J. Geol.* 92, 289. [3] Stolper E. and Paque J. M. (1986) *GCA* 50, 1785. [4] Kuehner S. M. et al. (1989) *GCA* 53, 3115. [5] Beckett J. R. et al. (1990) *GCA* 54, 1755. [6] Simon S. B. et al. (1991) *GCA* 55, 2635. [7] Davis A. M. et al. (1991) *LPS XXIII*, 281. [8] Simon S. B. et al. (1994) *GCA* 58, in press. [9] Wark D. (1981) *LPS XII*, 1145. [10] Hutcheon I. D. and Newton R. C. (1981) *LPS XII*, 491. [11] Beckett J. R. (1986) Ph. D. Thesis.



MORPHOMETRIES AND POSSIBLE TERRESTRIAL ANALOGS OF SMALL MARTIAN VOLCANOES; Philip A. Davis and Kenneth L. Tanaka, U.S. Geological Survey, Flagstaff, Arizona 86001.

Summary. Using Viking Orbiter images, we obtained photoclinometric profiles for over 1000 small (basal diameters less than about 5 km) Martian hills with summit craters; the hills are interpreted to be volcanoes. This morphometric database was compared with similar data compiled for various types of terrestrial volcanoes to determine the closest terrestrial analogs for the small Martian volcanoes. Our analysis indicates that the small volcanoes in many of the volcanic fields have morphometries that are closest to terrestrial cinder cones. However, some Martian volcanic fields are dominated by volcanoes whose morphometries are most similar to low-sloping and steep-sided terrestrial shield volcanoes, Icelandic lava shields, and tuff rings.

Introduction. We visually examined the entire inventory of Viking Orbiter images and selected all of the several hundred images containing small landforms that appear to be volcanic constructs on the basis of morphology (i.e., hills with summit craters) and geologic setting. Most of these landforms have been previously interpreted as volcanic constructs [1-7]. Most occur between 0 and 60 degrees north latitude; the individual volcanic fields cover a wide longitudinal range in the northern hemisphere [1-7]. In the southern hemisphere are relatively few small volcanoes; occurrences are isolated, scattered, and mostly in the west. We made a photoclinometric profile of each volcano in the selected Viking Orbiter images, using the methods described by [8], to obtain detailed topographic data for over 1000 small volcanoes. From each profile, we extracted summit-crater diameter and depth and flank width, height, and slope (Table 1). (Data for the 36 small volcanoes that occur in the southern hemisphere were examined in our analysis but are not shown.) We performed a preliminary statistical analysis of these data, comparing the morphometric characteristics of the small volcanoes to those compiled for terrestrial volcanoes by [9] in order to determine the most likely terrestrial analog for each of the small Martian volcanoes.

Morphometric Comparisons. Our preliminary morphometric comparisons of the small Martian volcanoes and possible terrestrial analogs show that (1) the volcanic fields located in Cydonia Mensae and southwest of Utopia Planitia have volcano morphometries most closely similar to terrestrial cinder cones, as suggested in a similar comparison by [3]; (2) two small volcanic fields (within Cydonia Mensae and within Chryse Planitia) have volcano morphometries most similar to steep-sided terrestrial shield volcanoes, as suggested by [10]; (3) a small volcanic field north of Olympus Mons and west of Alba Patera has volcano morphometries most similar to low-slope terrestrial shield volcanoes; and (4) small volcanoes on a plateau remnant between Tempe Fossae and Mareotis Fossae have morphometries most similar to low-sloping terrestrial shield volcanoes (as suggested by [6]), Icelandic lava shields, and terrestrial tuff rings.

Cinder Cone Relations. Terrestrial and lunar cinder cones generally have a crater-diameter/cone-basal-diameter ratio of 0.4 [3,11]. Our data for four different Martian cinder cone fields show a range in this ratio from 0.29 to 0.39 and an average for all cinder cones of 0.33; the two cinder cone fields southwest of Utopia Mensae have both the highest and the lowest average crater-diameter/cone-basal-diameter ratio. Wood [3] found that lunar cinder cones have a cone-height/cone-diameter ratio of 0.04, whereas terrestrial cinder cones have

SMALL MARTIAN VOLCANOES; Davis, P.A. and Tanaka, K.L.

an average ratio of 0.18 [11]. The cone-height/cone-diameter ratio obtained from a single Martian cinder cone by [3] is 0.06. Our data (from 969 measurements) show that the ratio for Martian cinder cones (0.033) is slightly lower than that of lunar cinder cones, despite the difference in lunar and Martian gravity. This result indicates that Martian cinder cones are constructed either at low rates, as proposed for lunar cones [3], or of different materials (e.g., mud volcanoes).

References. [1] Hodges, C.A. (1979) *NASA TM 80339*, 247; [2] Hodges, C.A., and Moore, H.J. (1979) *JGR 84*, 8061; [3] Wood, C.A. (1979) *PLPSC 10th*, 2815; [4] Hodges, C.A. (1980) *NASA TM 81776*, 181; [5] Moore, H.J., and Hodges, C.A. (1980) *NASA TM 82385*, 266; [6] Plescia, J.B. (1981) *Icarus 45*, 586; [7] Frey, H. and Jarosewich, M. (1982) *JGR 87*, 9867; [8] Davis, P.A., and Soderblom, L.A. (1984) *JGR 89*, 9449; [9] Pike, R.J. and Clow, G.D. (1981) *U.S. Geol. Survey Open-File Rpt. 81-1038*, 40p; [10] Greeley, R. *et al.* (1977) *JGR 82*, 4093; [11] Porter (1978) *Bull. Geol. Soc. Amer.* 83, 3607; [12] Scott, D.H. and Tanaka, K.L. (1986) *U.S. Geol. Survey Misc. Invest. Ser. Map I-1802-A*; [13] Greeley, R. and Guest, J.E. (1987) *U.S. Geol. Survey Misc. Invest. Ser. Map I-1802-B*.

Table 1. Averages and standard deviations of morphometric characteristics of small Martian volcanoes obtained by photoclinometric analysis of Viking Orbiter digital images for the northern hemisphere of Mars.

Geologic Unit ¹	General Location	Number Profiled	Crater Diameter [D _{cr}] (m±σ)	Crater Depth [d] (m±σ)	Cone Diameter [D _{co}] (m±σ)	Cone Height [h] (m±σ)	D _{cr} /D _{co} (m±σ)	h/D _{co} (m±σ)	Terrestrial Analog
Aal	Cydonia Mensae	414	306 ±76	6 ±4	866 ±236	26 ±15	0.361 ±0.079	0.030 ±0.011	Cinder Cone
Hvg	Cydonia Mensae	31	394 ±139	7 ±10	1164 ±259	37 ±25	0.338 ±0.086	0.031 ±0.019	Cinder Cone
Hvr	SW of Utopia Planitia	315	208 ±57	7 ±7	725 ±135	44 ±24	0.290 ±0.070	0.060 ±0.027	Cinder Cone
Apk	SW of Utopia Planitia	209	321 ±80	7 ±4	840 ±194	22 ±23	0.391 ±0.087	0.026 ±0.011	Cinder Cone
Aal	N of Olympus Mons	7	984 ±486	5 ±7	5035 ±1915	43 ±27	0.191 ±0.032	0.008 ±0.002	Low-sloping Shield
Hshp-Hch	Chryse Planitia	40	300 ±140	7 ±8	1345 ±397	72 ±54	0.229 ±0.109	0.039 ±0.021	Steep-sided Shield
Hvk	Cydonia Mensae	7	445 ±147	14	1926 ±242	59 ±20	0.225 ±0.048	0.034 ±0.011	Steep-sided Shield
Htu	Tempe-Mareotis Fossae	5	836 ±351	65 ±34	5393 ±803	203 ±59	0.150 ±0.042	0.039 ±0.014	Shields and Tuff Rings

¹Symbols for geologic units from [12, 13].

p-2 2968

THE OCCURRENCE OF BLUE LUMINESCING ENSTATITE IN E3 AND E4 CHONDRITES. John M. DeHart⁺ and Gary E. Lofgren*. ⁺1914 Amherst Ave., Casper, WY 82601. *SN-4, NASA-JSC, Houston, TX 77058. ✓

Introduction. Two compositional types of enstatite that emit Cathodoluminescence (CL) are known to exist in E3 and E4 chondrites. The first type consists of the most common enstatites that are relatively FeO-poor (Approx. En_{98}) and emit a red CL. Their CL is apparently activated by the presence of MnO and Cr_2O_3 in concentrations of 0.2 to 0.6 weight percent. The second type of enstatite is nearly FeO-free ($>\text{En}_{99}$), contains no MnO or Cr_2O_3 and emits a blue CL. The origin of these two types of enstatite and their accompanying chemical and CL differences has long been a subject of discussion. Leitch and Smith [1] first observed the two types and felt the compositional differences were too great to have formed under the same conditions. They postulated the two types of enstatite formed on separate parent bodies and were mixed when these bodies collided. McKinley et al. [2] observed a continuous range of compositions between blue luminescing and red luminescing enstatites and concluded the two types of enstatite formed by similar mechanisms (i.e. growth from a preexisting melt). Recently, Lofgren et al. [3,4] presented evidence that blue luminescing pyroxenes were relicts that did not completely melt during the heating event which melted other precursor grains, and are distinct from the red CL pyroxene in the chondrules in E chondrites. In order to further clarify the nature and origin of the pyroxene that emits blue CL, the sections listed in [5] were examined for the occurrence of blue luminescing enstatite.

Observations. In general, the blue luminescing enstatite we observed can be divided into three groups. There is a banded variety with bands of bright blue and pale pink to violet CL that appear to be associated with polysynthetic twinning. Occasionally, the pink to violet bands are replaced by duller blue luminescing bands. A second group of enstatites has CL that is uniformly blue over the entire area of the grain. The third type is similar to the enstatites that emit uniform blue CL, but has irregular, duller blue luminescing patches occurring throughout the grain.

Banded, blue luminescing enstatite occurs exclusively in MAC88136 and LEW87223. It is found as euhedral to subhedral grains in chondrules, clasts, refractory inclusions and grain fragments in the interchondrule matrix of MAC88136. It is likely that this type of blue luminescing pyroxene is unique to EL3 chondrites. This is also the only type of blue luminescing enstatite that has been produced in activator-depleted, dynamic crystallization experiments [4].

Unbanded, uniformly blue luminescing enstatite occurs most often as whiskers or grains embedded in kamacite. The proportion of enstatite to kamacite varies widely, from isolated 3 to 5 μm wide whiskers of enstatite that are embedded in isolated grains of metal, to chondrules 200 to 300 μm in diameter composed of grains of blue luminescing enstatite with interstitial metal and/or sulfide. While the latter cases are found only in the EL chondrites studied, the others are found in all E3 and E4 chondrites. It is unusually abundant in PCA82518, whose interchondrule matrix is dominated by metal/sulfide aggregates with grains of uniformly blue luminescing enstatite embedded in kamacite.

Uniformly blue luminescing enstatite also has three other notable occurrences. First, it is nearly the exclusive phase found in the interchondrule matrix of LEW87223. Second, it can be found as 5 to 10 μm wide overgrowths after red luminescing pyroxene in chondrules and clasts found in both EH and EL chondrites. Finally it can be found in association with other refractory minerals in objects identified as refractory chondrules and aggregates.

The third type of enstatite, the unbanded, uniformly blue luminescing enstatite with irregular, duller blue luminescing patches appear to be mostly relict grains. It is most often found in chondrules and as isolated grain fragments in EH chondrites. This enstatite occurs as isolated blue luminescing relicts surrounded by red luminescing enstatites which appear to have grown from the surface of the blue luminescing grain. These mottled blue luminescing enstatites often contain small inclusions of Mn-rich sulfides. Also, aggregates of this type of blue luminescing enstatite, metal and a dull blue luminescing quartz or nearly pure SiO_2 glass can be found surrounded by red luminescing enstatite that appears to have grown from their surfaces.

Pyroxene Emitting Blue CL in E Chondrites J.M. DeHart and G.E. Lofgren

Discussion. These three types of blue luminescing pyroxenes clearly have different histories. The variety with CL banding apparently formed from igneous melts depleted in activator cations and appear not to have experienced other alteration effects since their formation. In contrast, the history of the uniformly blue luminescing enstatite appears to be more complex. CL banding in blue luminescing enstatite grown in dynamic crystallization experiments can be eliminated by reheating [4]. This presumably can explain the uniform blue CL of the unbanded blue luminescing enstatite, but cannot explain the duller blue patches found in the mottled blue luminescing relict grains in E3 and E4 chondrites. In some instances (i.e. the blue luminescing pyroxenes included in kamacite), it may also indicate the enstatite formed by mechanisms other than growth from an igneous melt, such as gas-solid condensation. Both of these phases can condense from a gas of solar composition in the same range of temperatures and pressures [6]. It is possible the enstatite condensed first, then acted as nucleation sites on which the kamacite would nucleate and grow when conditions of the cooling gas became oversaturated in this phase.

Conclusions. No simple explanation can account for the occurrence of all blue luminescing enstatite in E-chondrites. While it appears blue luminescing enstatite with CL banding has the simplest history (i.e. formation from a preexisting melt), the unbanded blue luminescing enstatite appears to have a more complex history that involves either reheating or formation by mechanisms other than growth from a preexisting melt.

References: [1] Leitch and Smith (1982) *GCA* 46, 2083-2097. [2] McKinley et al. (1984) *Proc. 14th Lunar Planet. Sci. Conf., Part 2, J. Geophys. Res.* 89, Supplement, B567-572. [3] Lofgren G.E. and DeHart J.M. (1992) *Lunar and Planetary Science, XXIII*, pp. 801-802. [4] Lofgren G.E. et al. (1992) *Lunar and Planetary Science, XXIII*, pp. 799-800. [5] Lofgren G.E. and DeHart J.M. (1993) *Lunar and Planetary Science, XXIV*, pp. 893-894. [6] Grossman, L. (1972) *GCA*, 36, pp. 597-619.

Table 1. Representative electron microprobe analyses of the different varieties of blue luminescing enstatite in E3 and E4 chondrites. Values are in weight percent. B = banded, UB = unbanded, En = enstatite, refract = refractory, incl = inclusion, kam = kamacite

Sample Description	SiO ₂	Al ₂ O ₃	FeO	MgO	CaO	Total	No. Cations per 6 oxygens
MAC88136:							
B chondrule En	59.02	0.17	0.29	39.76	0.35	99.59	4.009
LEW87223:							
UB En in matrix clast	59.33	1.52	0.40	40.22	0.06	101.53	4.012
B En in refract incl	58.98	1.32	0.10	39.40	0.26	100.06	4.002
ALH84170:							
UB En after red En	59.93	0.12	0.16	39.91	0.05	100.17	3.999
UB relict En	59.75	0.12	0.49	39.36	0.05	99.77	3.997
UB En in incl in kam	60.42	0.10	0.46	39.91	0.07	100.96	3.997
PCA82518:							
UB En after red En	59.12	0.12	0.40	40.33	0.05	100.02	4.004
UB En in incl in kam	59.43	0.18	1.02	40.65	0.05	101.33	4.013

PONDING AND LACUSTRINE DEPOSITION IN LOWER MANGALA VALLES, MARS; R. A. De Hon, Department of Geosciences, Northeast Louisiana University, Monroe, LA 71209.

SUMMARY--Most martian outflows incorporated regions of temporary ponding as flood water traversed irregular terrain to lower elevations. Sedimentation and erosion in two large lakes attest to a prolonged history of lacustrine deposition and fluvial erosion in the lower part of Mangala Valles.

REGIONAL SETTING--The Mangala Valles outflow system is located in cratered plains of the Memnonia region of Terra Sirenum west of Tharsis Montes and Daedalia Planum and south-southeast of Amazonis Planitia. Mangala Valles appear to originate from a breach in the north wall of the largest of Memnonia Fossae grabens. The outflow is traced northward as a broad valley of upper Mangala Valles for 500 km where it splits into a complex system of anastomosing and divergent channels that extend 275 km northwestward as Labou Vallis and 350 km northward as lower Mangala Valles.

PREVIOUS STUDIES--The outflow system and surrounding region have been incorporated in a number of mapping and hydrologic studies [1-9]. Some early studies of Mangala Valles placed the source near the junction of Labou Vallis and Mangala Valles [10], but improved resolution allowed recognition that the valley extends far southward to an apparent source in a breach in Memnonia Fossae [8,9,11]. The difficulty of obtaining a high rate of discharge from the subsurface has lead some observers to suggest that the source was a surface impoundment south of the graben [12,13].

OBSERVATION--Lower Mangala Valles (north of the Labou Vallis junction) consists of a 120 km long by 35 km wide region of anastomosing channels within a topographic basin (South Basin of Fig. 1). At the north end of this region, Mangala diverges as a narrow channel of the eastern branch of Mangala Valles with a northerly trend and a western branch that widens to another region of anastomosing channels (North Basin, Fig. 1) approximately 150 km long and 45 km wide. Sabis Vallis and the western branch of Mangala Valles extend from this basin northward to Amazonis Planitia.

In both basins, plains material fill structural troughs formed by north-trending faults. The plains material exhibits an extremely smooth, level surface dissected by a complex pattern of channels that leaves isolated patches of plains material standing in terraces, streamlined islands, mesas, and plateaus as interfluves above the channel floors. North and South Basins exhibit inverted and resurrected topography as well as patches of chaotic terrain. Some channels within the dissected region exhibit local drainage to the south, opposite the regional trend. The sharpest channels tend to follow the margins of the basin deposits.

INTERPRETATION--The regions of extensive anastomosing channels-cutting plains material represents dissected lacustrine sediments deposited in ponded regions prior to establishing external drainage.

Remnant plains material, previously mapped as volcanic plains [5], is interpreted as lacustrine deposits based on the lack of an identifiable volcanic source, extremely smooth surface devoid of ridges or flow fronts, and apparent ease of dissection. Lacustrine plains are typically smooth, level surfaces within topographic depressions.

OUTFLOW HISTORY--The Mangala outflow is traced from Memnonia Fossae northward into the Labou Vallis region where incised channels are scarce and the outflow has ponded to form a large lake [12,13]. As the lake filled to capacity and flooded a large area of mid-Mangala Valles, water spilled

LOWER MANGALA VALLES: R. A. De Hon

northward as sheetflood flow across much of the cratered plains (unit chc of [1]). Outlets were cut westward to feed Labou Vallis and northward to feed lower Mangala Valles. Ponding on northernmost Terra Sirenum, along lower Mangala, created large lakes in South Basin and North Basin. Outlets were eventually established to Amazonis Planitia.

Discharge from the mid-Mangala lake continued to maintain lake levels in the lower Mangala basins for a long period of time (10's to 100's of years [9]). Lacustrine sedimentation formed smooth plains material. Falling lake levels and episodic discharge from mid-Mangala produced anastomosing drainage that dissected the lake sediments. Sapping channels recorded the last stages of dissection after the lakes were drained.

REFERENCES--[1] Mutch, T.A. and E.C. Morris, 1979, USGS Map I-1137; [2] Scott, D.H. and K.L. Tanaka, 1986, USGS Map I-1802-A; [3] Chapman, M.L. et al., 1989, USGS Map I-1962; [4] Chapman, M.L. and K.L. Tanaka, Proc. LPSC 20th, 531-539; [5] Chapman, M.L. and K.L. Tanaka, 1992, USGS Map I-2294; [6] Craddock, R.A. et al., 1990, LPSC XXI, 240-241; [7] Craddock, R.A. and R. Greeley, 1992, USGS Map I-2310; [8] Tanaka, K.L. and M.G. Chapman, 1990, JGR 95, 14,315-14,323; [9] Zimbelman, J.R. et al., 1992, JGR 97, 18,309-18,317; [10] Sharp, R.P. and M.C. Malin, 1975, GSA Bull. 86, 593-609; [11] Schumm, S.A., 1974, Icarus 22, 371-384; [12] Parker, T.J. and D.S. Gorsline, 1991, LPSC XXII, 1031-1032; [13] De Hon, R.A., 1992, Earth, Moon, and Planets 56, 95-122.

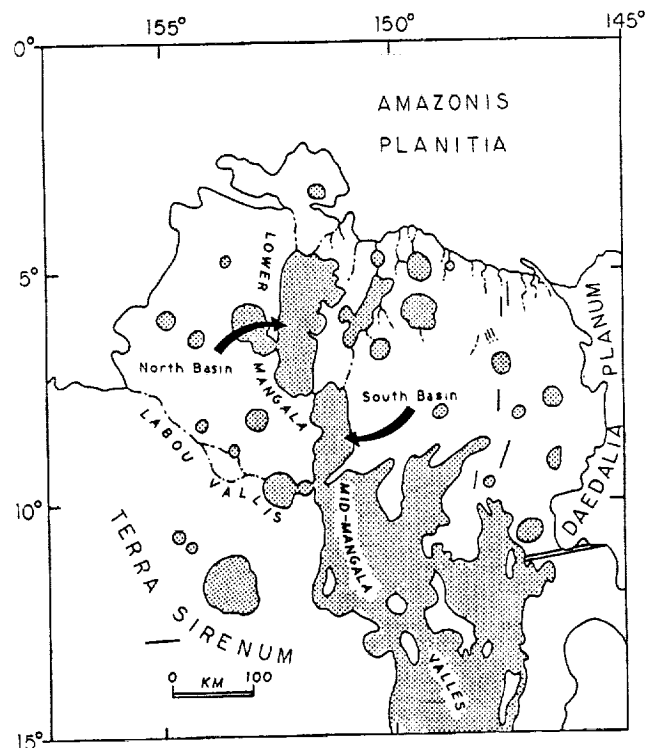


Figure 1. Lake basins in northern Memnonia. Stippled areas held standing water. North and South Basins are regions of highly-dissected smooth plains material.

An Oxygen Fugacity Grid For Nebular And Planetary Geochemistry.

Jeremy S. DELANEY¹; S.R. SUTTON² & S. BAJT²: (1) *Dept Geological Sciences, Rutgers University, New Brunswick, NJ 08903*; (2) *Dept Geophys. Sciences & CARS, University of Chicago, Chicago, Ill 60637*

The quantitative characterization of the oxidation states for a broad range of multivalent elements in micrometer scale volumes is now possible using x-ray absorption near-edge spectroscopy (XANES). Such measurements can be used to determine, directly and precisely, the oxygen fugacity at which many geo/cosmochemically relevant reactions occur. With data available for a comprehensive suite of reactions, a grid of oxygen fugacity sensitive reactions boundaries can be assembled that provide fundamental constraints on nebular and planetary processes. The ability to constrain reactions directly in oxygen fugacity space removes a major limitation from thermochemical modelling of P-T-X relations as the need to make assumptions about the oxygen fugacity will be removed.

INTRODUCTION: The early nebula has provided samples that were produced under an enormous range of physical conditions. Among the most critical parameters that must be determined for many nebular and planetary assemblages is the oxygen fugacity (or the equivalent fugacity for the relevant buffer species) under which reaction occurred. Generally, oxygen fugacity is inferred indirectly, as techniques for directly measuring its effect were unavailable. However, the application of a new microanalytical technique (x-ray absorption near edge spectroscopy, or XANES) makes measuring the oxidation state of multivalent elements possible (1,2,3). The application of this technique to the estimation of oxygen fugacity (as well as the fugacity of other gaseous species) in terrestrial and extraterrestrial materials becomes an important constraint on models of nebular processes. Because quantitative measurements of oxidation state will permit detailed calculation of oxygen fugacity in a great variety of nebular and planetary reactions, it will be possible to erect a systematic grid of fugacity sensitive reactions, that bracket and constrain assemblages observed in chondrites and achondrites.

Overview Of The Oxygen Fugacity Grid Approach: Reactions involving change of valence in multivalent elements such as Fe (as well as Cr, Ti, Nb, V, Eu, Ce, U etc.) are controlled by the oxygen fugacity of the systems in which they occur. In some cases the fugacity is imposed by external gas reservoirs such as subsystems of H-C-O-S but in other cases the oxygen fugacity will be internally buffered by the solid-solid or solid-liquid reactions occurring (4). In both cases, however, the abundance ratios of different oxidation states for multivalent elements will be controlled in whole or in part by the oxygen fugacity and measurement of these abundance ratios directly constrains the ambient fO_2 .

Because reactions involving these multivalent species occur throughout the range of probable nebular conditions, a grid of fugacity controlled reactions can, in principle, be created. A familiar subgrid of this oxygen fugacity grid is the fO_2 vs temperature plot for the "classic" Fe-buffer curves: iron-wüstite; quartz-magnetite-fayalite; magnetite-hematite. Buffer reactions involving other elements and other phases also contribute to the complete grid. Reactions controlling the Fe^{3+} , Fe^{2+} and Fe^0 contents of coexisting phases will be among the most important and informative in both terrestrial and extraterrestrial systems as iron is generally high abundant and often ubiquitous in most systems. Reactions involving oxidation state changes for minor and trace elements are unlikely to influence the ambient oxygen fugacity of a system but will reflect that fugacity in their abundance ratios. Such reactions act as tests of inferred fugacity based on major elements and/or dominant gas species.

Temperature estimates can generally be made based on thermochemical data for a broad array of element partitioning reactions as reliable compositional data are available for many samples. Pressure estimates are more difficult especially for systems involving gases where the gas phase is lost. The pressures for nebular processes were generally low and the most sensitive indicator for these low pressure reactions, the gas/vapor phase is never preserved. An aspect of the pressure regime, the fugacity of the reacting gases may be accessible in some cases as the gas fugacity of the system controls the relative abundances of different oxidation states of some multivalent elements.

Analytical Considerations: Commonly used analytical techniques provide abundance data for a wide range of elements and isotopes, but provide no data, about the oxidation state of the elements in any phase. A typical analysis of a bulk chondrite will present the abundance of iron in the sample but provides no information about the abundances of ferrous, ferric and native iron that are summed

Oxygen Fugacity Grid : Delaney, Sutton and Bajt

together in that analysis. A few techniques are capable of measuring the ratios of the different valence states of elements. Mössbauer spectroscopy is the most widely used of these techniques but it is limited to relatively large samples and to elements for which appropriate isotopes are available. Techniques capable of measuring valence states of atoms in micro-scale volumes comparable with those of the standard microanalytical techniques have been unavailable. In addition, the previously available techniques can only be applied to a limited range of multivalent elements. An ideal technique would allow non-destructive measurement of the valence state of any element in a volume comparable with that analyzed by geochemical microprobes (μm^3) so that both the variations within a single mineral grain and the partitioning of multivalent elements between coexisting phases can be measured. A technique for making these measurements is X-Ray Absorption Near Edge Spectroscopy (XANES) Applied With The Synchrotron X-Ray Microprobe (1). Although measurements carried out so far (1,2,3) have focussed on the elements Cr and Fe, this technique is applicable (in principle) to any element that occurs in multiple valence states. Oxidation state determinations using the microXANES technique is presently in its infancy but the potential exists for the development of a universally applicable method. The sensitivity of the technique is defined by the elemental concentrations and the brightness of available synchrotron x-ray sources. The accuracy is defined by the accuracy of interpretive methods for the XANES spectra and the availability of appropriate standards produced in experiments under controlled oxygen fugacity.

Applications: Elements whose variable oxidation states may be exploited as useful fugacity indicators include: Ti, V, Cr, Fe, Cu, Nb, Mo, W, (Ce,) Eu, U. Although the volatilities of most REE are sensitive to oxygen fugacity, the stabilization of multiple valence states in the solid phase (except Eu) may not be detectable. Terrestrial examples of the importance of $\text{Fe}^{3+}/\Sigma\text{Fe}$ measurements as part of the estimation of oxygen fugacity are well known (4,5). Extraterrestrial examples tend to be less obvious as systems involving ferric iron are less common. However, nebula conditions are so diverse that the existence of other elements in multiple oxidation states can be used to constrain oxygen fugacities in addition to Fe. Between the very reduced assemblages with Si^0 stable in metallic phases to C-chondrite matrix with stable hematite and magnetite almost every multivalent element is likely to be present in different oxidation states. Some reactions with possible relevance to meteoritic assemblages include $\text{Ti}^{3+}/\text{Ti}^{4+}$ in hibonite-fassaite assemblages and in various transition elements in refractory inclusions, rims, and fremdlinge; $\text{Cr}^{3+}/\text{Cr}^{2+}$ exchanges in ol-pyx-spinel assemblages; $\text{Fe}^{3+}/\Sigma\text{Fe}$ in fine grained matrix material from C-chondrites, including alteration products in Cl's, as well as partitioning between silicates and oxide minerals from chondrites and achondrites; and $\text{Eu}^{2+}/\text{Eu}^{3+}$ exchanges in phosphate/feldspar/ pyroxene assemblages.

If several reactions involving oxidation state changes can be identified within a single assemblage, the intersection of reaction boundaries in temperature - $f\text{O}_2$ space will define the P-T-X conditions under which reaction occurred. This approach cannot yet be applied as there are insufficient data for oxidation state changes in natural materials. With the availability of synchrotron microXANES, the characterization of relevant reactions can be initiated. Systematic studies of the partitioning behavior of elements in multiple oxidation states must be carried out to identify the critical reactions in the oxygen fugacity grid so that it may be used in conjunction with existing petrogenetic, phase equilibrium and element partitioning results. For the classical Fe-buffers (Figure 1) most reaction boundaries have roughly parallel slopes. To maximize the sensitivity of the oxygen fugacity grid, it is essential that reaction boundaries intersect at high angles to these reactions be identified. Thus, buffering reactions that do not liberate O_2 or other gases will be very important (i.e. reactions with very small volume changes.)

References: (1) Sutton et al. (1994) *this volume*; (2) Sutton et al. (1993) *GCA* **57**,461; (3) Sutton et al. (1993) *LPSC XXIV*, 1385; (4) Carmichael & Ghiorso (1990) *Rev. Mineral.* **24**,191; (5) Ballhaus C. (1993) *Nature*, **386**, xxx : Acknowledgements: NAG9-304

ABUNDANCE AND DIFFUSIVITY OF SULFUR IN LUNAR PICRITIC MAGMAS

J. W. Delano¹, B. Z. Hanson¹, and E. B. Watson². ¹Department of Geological Sciences, State University of New York, Albany, NY 12222; ²Department of Earth and Environmental Sciences, Rensselaer Polytechnic Institute, Troy, NY 12180.

SULFUR ABUNDANCES

The abundance of sulfur (S) has been measured (Table 1) by electron microprobe in fourteen varieties of picritic volcanic glass [1]. These abundances apply to the *interiors* of the volcanic glass spherules, and do not include the well-known surface-correlated sulfur [e.g., 2]. The electron microprobe was operated at 15 keV with a beam current of 50 nA. Counting times per analysis were 300 seconds on the peak position plus 150 seconds on each of the two background positions. A detection limit of 35 ppm S was achieved under these conditions. Mobility of S in the glass during the electron bombardment was explicitly looked for but not observed in these lunar glasses.

Although a correlation between Ti and S has been observed among the crystalline mare basalts [e.g., 3,4], no correlation is apparent among the picritic volcanic glasses (Figure 1). Note in Table 1 and Figure 1 that there is often a substantial range in abundance of S among glass spherules belonging to a single compositional group. Where bulk analyses of picritic glasses have been reported [3], the bulk S abundance is up to a factor of 4 greater than the mean abundance of S within the interior of the glass spherules. For example, in Figure 1, compare the "bulk 15427" and "bulk 74220" data with the interior S abundances measured in this investigation by electron microprobe. These higher bulk abundances underscore the importance of S-rich coatings on the exterior surfaces of the spherules. Although (a) the range of S abundances within individual suites of picritic glass and (b) S-rich surface coatings are consistent with diffusive loss of S from the spherules during their eruption in fire fountains, no well-defined diffusion profiles for S have yet been observed in any of the detailed linescans that have been made on individual volcanic glass spherules. A similar observation has been made previously for the Apollo 15 green glasses [5]. The lower S abundances in the picritic glasses compared to the crystalline, less primitive mare basalts are *not* due to their high normative olivine content or higher percentages of partial melting. *If* the picritic magmas represented by the volcanic glasses originally had S abundances comparable to those observed in the crystalline mare basalts (Figure 1), then up to 90% of the original S was lost from some of those picritic melts prior to quenching of the droplets.

DIFFUSIVITY OF SULFUR

The diffusivity of S has been experimentally determined in a lunar picritic composition (Apollo 15 yellow/brown volcanic glass) near its liquidus temperature of 1300°C at 1 atm pressure in a gas mixing furnace (CO+CO₂) and an oxygen fugacity of 0.5 log-unit below the iron-wüstite buffer. Spheres of synthetic mix made of reagent grade oxides were suspended on iron-doped Pt-wire loops in the furnace. One droplet was quenched after 40 minutes, and the other after 3 hours. Quenching was accomplished by electrically severing the Pt-loop and allowing the droplet to fall into a glass beaker of water at the bottom of the vertical furnace tube. Nominal oxygen fugacity was maintained during the quench procedure. Since the droplets (a) stopped glowing in <<1 second upon contact with the water and (b) contained no quench crystals, the quench is presumed to have been effective. The droplets had initial S abundances of 3000 ppm and radii of 500-750 microns. Linescans of these experimental glasses displayed diffusion profiles from center to edge indicating a S diffusivity of 6.6×10^{-8} cm²/sec.

IMPLICATIONS

There is convincing evidence that S, and other volatile elements [e.g., 6], were lost from these lunar picritic magmas during fire fountaining. The experimentally measured diffusivity for S in one of these lunar compositions indicates that 61-97% of the original S can be lost from melt droplets ($r=80$ -200 microns) at 1300°C in five minutes (Figure 2). The size-range of droplets modelled in Figure 2 is similar to that observed in suites of lunar volcanic glasses [e.g., 7]. For a melt droplet with a radius of 80 microns (i.e., median radius of Apollo 17 volcanic orange glasses from 74220 [7]), Figure 3 shows that 82-97% of the original S is diffusively lost from the 160-micron diameter spherule within a period of 2 and 5 minutes.

ABUNDANCE AND DIFFUSIVITY OF SULFUR: Delano J. W. et al.

Questions remain. For example, could droplets of picritic magma have remained at liquidus temperatures for a few minutes during fire fountaining? It should be kept in mind that the "free-flight" (i.e., radiative) cooling rate of an 80-micron melt droplet in a vacuum is about $1100^{\circ}\text{C}/\text{sec}$ [7], and that the critical cooling rates (i.e., the cooling rate below which crystals nucleate and grow) of lunar picritic compositions are between $1\text{--}100^{\circ}\text{C}/\text{sec}$ [e.g., 7]. Reconciling these experimental and observational constraints may require the following speculative view. A hot (i.e., near-liquidus temperature), turbulent plume of volcanic gas caused a mist of melt droplets to be suspended for periods of up to several minutes that resulted in the diffusive loss of S, and other volatile elements. Rapid cooling (i.e., greater than the critical cooling rate) to a glass occurred when the droplets travelled outside the plume. Based on experimental and textural criteria, Arndt and von Engelhardt [7] have previously demonstrated the requirement for a "a large mass of hot gas and/or a dense cloud of heat-radiating droplets."

REFERENCES: [1] Delano (1986) PLPSC 16, p. 201-213. [2] Butler and Meyer (1976) PLSC 7, p. 1561-1581. [3] Gibson and Andrawes (1978) PLPSC 9, p. 2011-2017. [4] Gibson et al. (1977) PLSC 8, p. 1417-1428. [5] Fogel and Rutherford (1992) LPS-XXIII, p. 377-378. [6] Meyer et al. (1975) PLSC 6, p. 1673-1699. [7] Arndt and von Engelhardt (1987) PLPSC 17, p. 372-376.

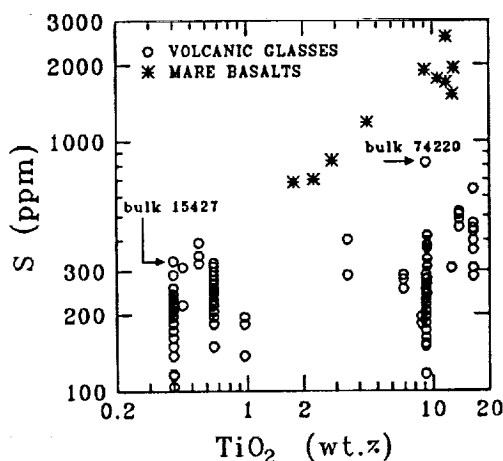


Figure 1. Sulfur abundances in mare basalts (*) and picritic volcanic glasses (o).

Table 1. Sulfur abundances in 14 varieties of picritic glass.

glass type	column # [1]	S (ppm)		
		observed range	mean	# analyses
Apollo 15 green	1, 2, 4-6	104 - 290	190	44
Apollo 14 green B	7	219 - 311	280	3
Apollo 14 VLT	8	322 - 391	360	4
Apollo 17 VLT	10	150 - 325	250	40
Apollo 14 green A	12	138 - 196	170	3
Apollo 15 yellow	13	288 - 403	350	2
Apollo 17 yellow	15	253 - 288	270	3
Apollo 17 orange I	16	184 - 196	190	4
Apollo 17 (74220)	17	116 - 288	210	24
Apollo 17 orange II	19	242 - 415	340	15
Apollo 14 orange	21	(308)	(308)	1 only
Apollo 15 red	22	449 - 518	490	4
Apollo 14 red/black	24	433 - 638	540	2
Apollo 12 red	25	285 - 467	390	7

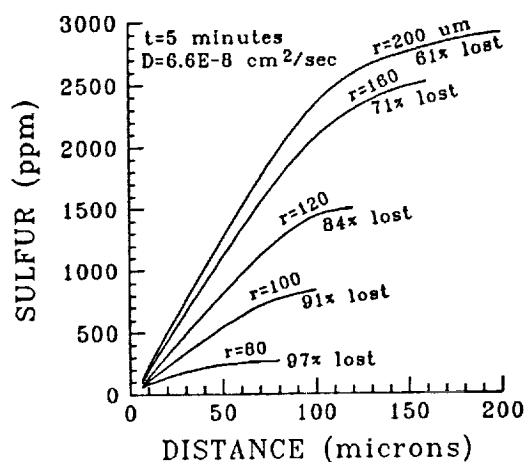


Figure 2. Radial concentration gradients caused by diffusive loss of S from droplets of various sizes in 5 minutes at 1300°C (initial $S=3000$ ppm).

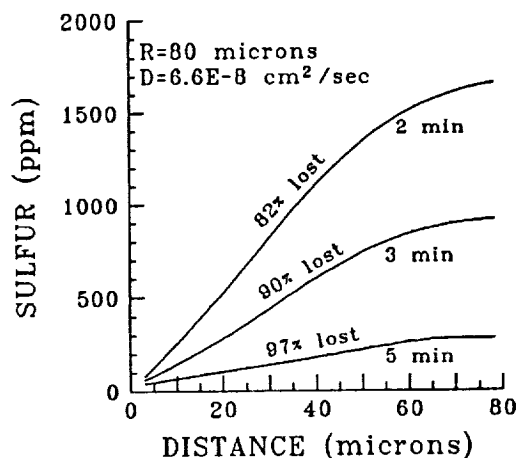


Figure 3. Radial concentration gradients caused by diffusive loss of S from a $160\mu\text{m}$ diameter droplet at 1300°C in 2, 3, and 5 minutes (initial $S=3000$ ppm).

p. 2

2969

THE FRETTED TERRAIN OF THE NILOSYRTIS MNSAE REGION OF MARS: CLUES TO THE TIMING OF DICHOTOMY FORMATION AND THE EMPLACEMENT OF THE NORTHERN PLAINS; Jeff E. DeTroye, *Mail Code AC, Johnson Space Center, Houston, TX 77058* and Steven H. Williams, *Department of Space Studies, University of North Dakota, Grand Forks, ND 58202*.

Geologic mapping of the fretted terrain of the Nilosyrtis Mensae region of Mars has revealed geomorphic evidence that the breakup of the plateau units to the south of Nilosyrtis occurred well before the plains units to the north were emplaced in late Hesperian time. The plains units were deposited against the fretted terrain, which has undergone some modification by mass wasting but not significant backwasting. The morphology observed at the contact between plains and the fretted terrain is consistent with that expected where the edge of a pile of sedimentary debris has undergone mass wasting and other erosion.

The Nilosyrtis Mensae region of Mars provides morphologic clues to the timing of two important events in martian geological history: the formation of the martian global crustal dichotomy and the emplacement of the northern plains. A preliminary geologic map at 1:500,000 scale of MTM quadrangle 35297, covering a box between latitudes 32.5 to 37.5° and longitudes 295 to 300°, was prepared to facilitate understanding of the sequence of geological events associated with the dichotomy boundary.

The plains units to the north of the Nilosyrtis Mensae are mapped by Greeley and Guest as HNu, undifferentiated materials of Noachian/Hesperian age [1]. The plains in the study quad more closely resemble the unit Hvk in [1], knobby plains of Hesperian age, part of the Vastitas Borealis formation. The plains are of late Hesperian age as determined from their N(5) crater population [1,2]. An additional age constraint is that the plains contain what are probably secondary craters from the Lyot impact basin [2], of early Amazonian age [3]. The nature and timing of dichotomy formation and plains emplacement places significant constraints on models of both internal and external processes (see [4, 5] for review). Questions addressed in this study include: When did the breakup of the plateau units on the dichotomy boundary into the fretted terrain occur? and: Has there been any appreciable retreat southward of the dichotomy boundary?

The portion of the contact between the Hvk plains and the fretted terrain contained within the study area is shown in Figure 1. There are several craters whose morphology indicates emplacement after the formation of the local mesas by the breakup of the plateau. Yet these craters clearly predate the emplacement of the Hvk; at one location (figure 1), a crater lies astride the contact between the Hvk plains, which bury its ejecta, and the mesas, upon which ejecta and scour are still visible. No similar craters can be found on the adjacent Hvk plains; presumably all such craters that were there were buried as thoroughly as was the ejecta blanket of the crater the plains partially bury (Figure 1). The plateau units to the south contain approximately the same distribution of younger craters. Unfortunately, the area in question and the number of craters involved are too small for accurate statistics, however, it is not likely that a geologically-short amount of time transpired between the formation of the frets and the emplacement of the Hvk plains because there are many craters of the 10-15 km size superimposed on top of the frets and none on the Hvk plains. Some mass wasting has occurred relatively recently on the mesas, as evidenced by the obliteration of ejecta that must have been plastered on their sides during emplacement (Figure 1), but there is little evidence that the fretted terrain has undergone much further erosion since the craters on them were formed. If backwasting occurred after plains emplacement, a similar population of craters would be expected for both the plains and the fretted terrain.

The edge of the Hvk plains at the point where the partially-buried crater is covered is fairly thick, on the order of hundreds of meters or more (Figure 1). If the fretted terrain to the south was fully developed when the Hvk plains were emplaced, then the observed thickness of the plains reflects the original thickness of the deposit; as there would have been no barrier to act as a

FRETTED TERRAIN OF NILOSYRTIS MENSAE: DeTroye, J.E. and Williams, S.H.

margin for the plains units and there is a relatively steep southward facing scarp at the contact. So it is likely that the plains margin was formed primarily by a single deposit rather than several thin units being emplaced with them all stopping at the same location without further overrunning the partially buried crater.

REFERENCES:

- [1] Greeley, R. and Guest, J.E., 1987, U.S.G.S. Map I-1802-B. [2] Stice, P. and Williams, S., 1991, LPI Summer Intern abstract. [3] Tanaka, K.L., 1986, *Journal of Geophysical Research*, 91, n.B13, p E139-158. [4] McGill, G.E. and Dimitriou, A.M., 1990, *Journal of Geophysical Research*, 95, n. B8, 12595-12605. [5] McGill, G.E. and Squyres, S.W., 1991, *Icarus*, 93, 386-393.



Figure 1. Shown is a section of martian fretted terrain in the Nilosyrtis Mensae area that lies between the Hvk unit of the northern plains assemblage and the Noachian age plateau units to the south. One crater (dark arrow) is partially overridden by the plains; its ejecta is partially covered by plains materials yet its rim allowed little, if any, material to flow into the crater directly.

HIGH-TEMPERATURE VAPORIZATION OF OLIVINE AND SERPENTINE. Yu.P. Dikov¹, O.I. Yakovlev², M.V. Gerasimov³, F. Wlotzka⁴. Russian Academy of Sciences: 1- Institute of Ore Deposits, Petrography, Mineralogy and Geochemistry; 2- Vernadsky Institute of Geochem. and Analytical Chemistry; 3- Space Research Institute; Moscow, Russia; and 4- Max-Planck-Institut für Chemie, Mainz, Germany.

Olivine and serpentine are the main ultramafic minerals which can represent the material of planetesimals impacting the growing Earth during the period of accretion. The transformation in chemical composition and structure of this material during impact processes and particularly during impact vaporization can result in global evolutionary trends during planetary growth. In order to simulate and study this process, we used a powerful laser beam focussed on olivine or serpentine samples (experimental setup and conditions are given below). The resulting vapor condensate was collected and analysed by XPS. The main result of our experiments is a notable enrichment of Si compared to Fe and Mg in the condensates (the (Mg+Fe) / Si ratio being close to 1 instead of 2, as in the starting material), that is a transformation of ultramafic silicates (olivine and serpentine) to mafic silicates (pyroxene) in the process of high-temperature evaporation-condensation. On a global scale of planetary formation it can be interpreted as a possible mechanism for transformation of ultramafic planetesimal matter into mafic (basaltic) material by impact vaporization and condensation processes.

Experimental conditions [1,2]: In two series of experiments samples of olivine or serpentine were placed in a hermetic cell and a beam of a powerful Nd-glass laser was focused through an optical window on their surfaces (~ 3 mm in diameter). The cell was filled either with helium or with air at room temperature and atmospheric pressure. Parameters of the laser pulse were: luminous energy ~600 J, density of luminosity ~ $5 \cdot 10^6$ W/cm², pulse duration ~ 10^{-3} s. The temperature of vaporization was estimated as ~4000 K. At a distance of ~5 cm from the sample a Ni-foil was mounted to collect products of condensation from a vapor cloud. Analyses of initial samples and of condensed films were performed using X-ray photoelectron spectroscopy (XPS). Condensed films were etched layer by layer (with a step of 200 Å) by a beam of argon ions and for every layer XPS analysis was performed providing an information of the cross-section of the film. XPS analyses gave both elemental chemical composition of the condensate and the distribution of elements between different phases (Tables 1 and 2).

A comparison of the cumulative composition of condensed films with the initial olivine shows that the condensates are enriched in Si and depleted in Mg and Fe. There is no significant difference in the structure of layers and bulk composition of condensed films precipitated in helium or in air. It is important that in both sets of experiments with olivine the molecular ratio of (Mg + Fe)/Si is between 1 and 1.13, i.e. the olivine condensates have a pyroxene type composition. Iron is also lower in the condensates than in the initial olivine and in recalculation to pyroxene corresponds to En 93-95. This indicates the shift of condensate composition during evaporation of olivine towards enstatite. These data do not confirm conclusions of other authors [3,4,5,6] who found a congruent evaporation of forsterite, but they agree with data by Sata et al. [7]. Condensed films contain noticeable quantities of reduced forms of Si and Mg (Si^{2+} , Si^0 , Mg^0), demonstrating redox processes inside the vapor cloud [8]. However, a relatively constant ratio of (Mg+Fe)/Si is obtained, when we consider all phases of Mg and Si, including reduced, non-silicate and silicate phases. This observation shows that volatilization of elements from a high-temperature melt probably occurs in form of molecular clusters having the observed ratio of Mg, Fe and Si. Redistribution of elements between different phases occurs in the hot spreading vapor cloud.

Experiments with serpentine resulted also in enrichment of Si and depletion of Mg in condensates similar to the experiments with olivine. Again the ratio of Mg/Si in the condensates is close to 1, showing the shift in condensate composition towards pyroxene. The concentration of water in the condensate calculated from the concentration of hydroxide is 14.4 mol%, that is only half of the concentration in the initial serpentine (28.5 mol%). The amount of trapped water increases from the bottom to the upper layers of the condensed film. No reduced Si and Mg was observed in contrast to the experiments with olivine. This effect is due to the oxidative role of water inside the vapor cloud [9].

VAPORIZATION OF OLIVINE AND SERPENTINE : Yu. P. Dikov et al.

There is a certain difference in the structural state of elements in condensed films for olivine and serpentine. About half of the Mg in the olivine condensate is present as oxide (MgO), whereas in the serpentine condensate MgO is absent and 1/3 of magnesium is present as Mg(OH)₂. The silicate structure of the olivine condensate is characterized by the absence of isolated silicon-oxygen tetrahedra and their polymerization to chain and framework structures, that is a total loss of the initial olivine structure and its transformation towards a pyroxene type structure has taken place. In the case of serpentine, the condensate contains layered silicates mixed with isolated silicon-oxygen tetrahedra.

- REFERENCES: [1] M.V.Gerasimov, et al. (1985) *Vestnic Akademii Nauk USSR* 9, 10-25 (in Russian).
 [2] M.V.Gerasimov et al. (1992) *LPSC XXIII*, 407. [3] B.O.Mysen, J.Kushiro (1988) *Amer. Miner.* 73, 1-19.
 [4] H.Nagahara et al. (1988) *Nature* 331, 516-517. [5] A.Hashimoto (1990) *Nature* 347, 53-55.
 [6] J.D.Kubicki, E.M.Stolper (1993) *LPSC XXIV*, 829-830. [7] T.Sata et al. (1978) *Rev. Houtes. Refract., Fr.*, 15, 237-248. [8] O.I.Yakovlev et al. (1992) *Geokhimiya* 12, 1359-1370 (in Russian).
 [9] M.V.Gerasimov et al. (1993) *LPSC XXIV*, 527-528.

TABLES: Chemical composition and phase distribution (in at.%) in different layers of condensed films from evaporation experiment of olivine in helium (Table 1) and serpentine in air (Table 2).

Table 1. Olivine condensate

	Si ⁰	Si ²⁺	Si ⁴⁺	Si ⁴⁺	Si ⁴⁺	Mg ⁰	Mg ²⁺	Mg ²⁺	Fe ²⁺	O ²⁻	O ²⁻	O ²⁻	Mg+Fe
			isol	chain	fw		silic	oxide	silic	n.s.	nbr	br	Si
Initial	-	-	14.3	-	-	-	26.1	-	2.5	-	57.2	-	2.00
Surface	-	1.3	-	13.9	4.6	-	11.8	9.1	1.0	10.3	19.5	28.4	1.11
200 Å	-	2.1	-	10.1	7.0	-	9.2	11.6	0.7	14.4	15.8	29.1	1.12
400 Å	-	1.7	-	11.4	5.9	-	11.0	9.7	1.0	12.4	19.0	27.9	1.14
600 Å	-	1.6	-	13.2	5.1	-	12.1	7.0	1.0	8.6	20.7	30.8	1.01
800 Å	1.5	-	-	10.3	5.8	1.7	8.4	10.5	1.3	11.6	18.0	30.9	1.24
1000 Å	1.9	-	-	11.1	6.1	1.2	13.5	5.8	1.2	7.2	20.3	31.2	1.14
1200 Å	1.1	-	-	11.8	6.2	1.0	10.9	8.4	1.1	9.5	18.8	31.2	1.13
Bulk			19.1				20.5		1.0		59.5		1.13

Table 2. Serpentine condensate

	Si ⁴⁺	Si ⁴⁺	Si ⁴⁺	Mg ⁰	Mg ²⁺	Mg ²⁺	O ²⁻	O ²⁻	O ²⁻	H	Mg/Si
	isol	layer	(OH)		silic	(OH)	(OH)	nbr	br		
Initial	-	11.1	-	-	-	16.7	22.2	7.0	20.9	22.2	1.50
Surface	5.5	7.3	2.7	-	10.1	5.5	14.4	24.8	13.6	14.4	1.0
200 Å	5.9	6.7	2.5	-	11.7	5.0	13.3	27.6	12.5	13.3	0.95
400 Å	6.2	6.5	2.3	-	12.5	4.8	12.5	29.0	12.5	12.5	1.15
600 Å	6.3	7.8	1.6	-	12.7	5.7	10.2	30.1	14.2	10.2	1.18
800 Å	6.0	8.7	1.3	-	11.9	6.4	9.8	29.3	16.1	9.8	1.14
1000 Å	6.2	9.5	0.7	-	12.3	7.1	7.5	30.6	17.7	7.5	1.18
Bulk		15.6			17.6			54.3		11.2	1.13

Note: isol = isolated; fw = framework; silic = silicate; n.s. = non-silicate; nbr = non-bridging; br = bridging;

GEOLOGIC HISTORY OF THE THAUMASIA REGION OF MARS; James M. Dohm and Kenneth L. Tanaka, U.S. Geological Survey, 2255 N. Gemini Dr., Flagstaff, AZ 86001

Introduction. Preliminary geologic mapping of the Thaumasia region (lat 15° to 50° S., long 55° to 115°) at 1:5,000,000 scale shows the temporal and spatial relations of a wide array of materials and structures, including those of early development of the Tharsis region [1,2]. The Thaumasia region (Figure 1) is dominated by the Thaumasia plateau, which includes the high plains of Syria, Sinai, Solis, and Thaumasia (provisionally named) Plana and the surrounding Thaumasia highlands that are fractured by Thaumasia, Claritas, Coracis, Melas, and Nectaris Fossae [3]. Our mapping methods are similar to those developed for unraveling the stratigraphic and structural histories of the Tempe Terra [4], Ulysses Patera [4], Alba Patera [5], and Syria Planum [6] regions of Mars. Thus far, we have identified more than two dozen geologic units and at least six fault stages, which, along with physiography, characterize eleven distinct geologic provinces (Fig. 1, Table 1). The extensive structural deformation of the map region occurred mainly throughout Noachian and Early Hesperian time [6,7,8]. It produced small and large extensional and compressional structures [8,9] that resulted from stresses related to Tharsis [1,2,6,10,11,12] and Valles Marineris [8]; from the Argyre impact [3]; and from local intrusions and uplifts [6,13]. Subsequent deformation in the Thaumasia region consisted mainly of the formation and reactivation of extensional structures radial to the Tharsis Montes volcanoes.

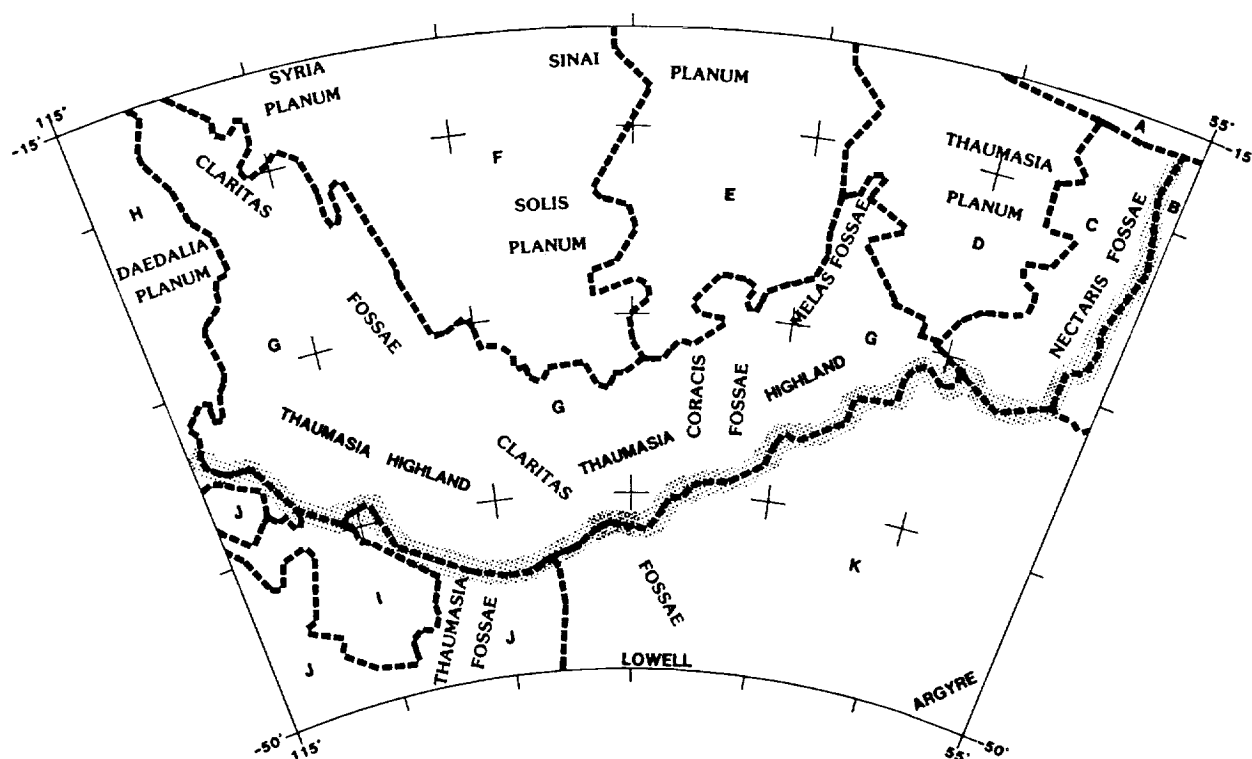


Figure 1. Geologic/physiographic provinces of Thaumasia region (see Table 1 for description). Edge of Thaumasia plateau shown by stippled line.

GEOLOGY OF THE THAUMASIA REGION, MARS: Dohm, J.M. and Tanaka, K.L.

Table 1. Characteristics of geologic/physiographic provinces of the Thaumasia region of Mars.

<u>Province/type</u>	<u>Features (interpretation) and relative age</u>
A.Valles Marineris/canyons	Rifting and collapse structures {broad uplift and extension}. Noachian - Early Hesperian
B.East of Coprates/ridged plains	Wrinkle ridges {compression}. Early Hesperian
C.Coprates/ridge belt	Broad ridges {lithospheric folds [14,15]}, tilted rock layers [14,16,17] {cuestas and hogbacks caused by tectonic tilting and differential erosion}, and wrinkle ridges {compression}; small (≤ 10 km wide) and large grabens and large faults ; trough-like depressions {collapse structures}; large valleys and valley networks {fluvial erosion/sapping; some related to volcanotectonic activity}; mountains {volcanoes}. Noachian-Early Hesperian
D.Thaumasia Planum/older ridged plains	Wrinkle ridges ; small grabens . Late Noachian - Early Hesperian
E.Sinai/younger ridged plains	Wrinkle ridges ; small grabens cut a few older areas. Mostly Early Hesperian
F.Syria-Solis/lava plains	Lava flows ; small grabens . Late Hesperian - Amazonian
G.Thaumasia highlands/highly deformed highlands	Small and large grabens , large faults , and intersecting dense concentrations of grabens {local uplift}; broad ridges {lithospheric folds [9]} and tilted rock layers {cuestas and hogbacks} along edge of Thaumasia plateau; mountains {volcanoes or basement complexes} and featureless plains {volcanic and sedimentary deposits}; valley networks and large valley forms {fluvial erosion/sapping; some related to volcanotectonic activity}. Noachian - Early Hesperian
H.Daedalia/young lava plains	Lava flows ; plateaus {high-standing outcrops of older materials} and mountains {volcanoes or basement complexes}; small grabens . Mostly Late Hesperian - Amazonian
I.Daedalia southeast/smooth plains	Featureless plains {volcanic flows}; small grabens ; wrinkle ridges . Hesperian
J.Sirenum/faulted highlands and plains	Small grabens ; large scarps {normal faults}; valley networks {fluvial erosion/sapping}; mountains {volcanoes}. Noachian - Early Hesperian
K.Argyre/impact-modified highlands	Featureless plains {many within topographic lows formed by impact}; mountains and plateaus {uplifted blocks; impact-related}; large scarps {normal faults; impact-related}; small grabens ; valley networks {fluvial erosion/sapping; some related to Lowell impact}; large ridges {folds} and wrinkle ridges near edge of Thaumasia plateau. Noachian - Early Hesperian

References cited. [1] Frey, H., 1979, *JGR* 84, 1009-1023. [2] Plescia, J.B., and Saunders, R.S., 1982, *JGR* 87, 9775-9791. [3] Scott, D.H., and Tanaka, K.L., 1986, *USGS Map I-1802-A*. [4] Scott, D.H., and Dohm, J.M., 1990, *PLPSC* 20, 503-513. [5] Tanaka, K.L., 1990, *PLPSC* 20, 515-523. [6] Tanaka, K.L., and Davis, P.A., 1988, *JGR* 93, 14,893-14,917. [7] Scott, D.H., and Dohm, J.M., 1990, *PLPSC* 20, 487-501. [8] Tanaka, K.L., and Dohm, J.M., 1993, *LPSC 24 Abs.*, 1399-1400. [9] Tanaka, K.L., and Schultz, R.A., 1993, *LPSC 24 Abs.*, 1401-1402. [10] Wise, D.U. et al., 1979, *Icarus* 38, 456-472. [11] Banerdt, W.B. et al., 1982, *JGR* 87, 9723-9733. [12] Banerdt, W.B. et al., 1992, in *Mars*, H.H. Kieffer et al., eds, Univ. Ariz. Press, ch. 8. [13] Tanaka K.L., and Dohm, J.M., 1989, *LPI Tech. Rept. 89-04*, 79-81. [14] Watters, T.T., 1987, *NASA TM 89810*, 481-483. [15] Tanaka, K.L., and Schultz, R.A., 1991, *LPSC 22 Abs.*, 1379-1380. [16] Plescia, J.B. et al., 1980, *NASA TM 81776*, 68-70. [17] Saunders, R.S. et al., 1980, *NASA TM 81776*, 74-76.

MAGNETIC FIELD IN THE PROTOSUN AND PROTOSTARS VICINITIES

A. Z. Dolginov, Lunar and Planetary Institute, 3600 Bay Area Blvd., Houston, TX 77058

Summary: It is shown that the proper magnetic field of the protostar that penetrates in the gaseous nebulae (or disk) embracing the star may be strongly increased by turbulent motions and differential motions in the star vicinity. For a star of the solar type the field may increase to the value 0.1 - 1 G in a few yrs at the distance of 10 stellar radius. This field may determine the accretion process, the possible collimation of the stellar wind blowing from the star polar regions, magnetic torque in the nebula, and magnetization of meteor bodies if their trajectories intersect regions with large field values.

Introduction: The process of accretion of matter from the protostar (protosun) nebula onto the star determines the star formation and is of great importance for the planet formation. In most cases the accretion disk is formed around the protostar. Apparently in some cases the accretion takes part in equatorial regions when the stellar wind is blowing from polar regions. The matter of the disk in the star vicinity is strongly ionized by the star radiation. Accretion of ionized substances, the stellar wind, and angular momentum transfer from the star to the disk are influenced by magnetic fields if such fields exist in the star vicinity. The proper magnetic field of the star in the star vicinity is a poloidal field (dipole in many cases). The field has quite a different structure if the ionized medium exists around the star. Only the dipole field, if any, has been considered in the literature as an important factor for accretion [1]. We will show that the field near the star not only has poloidal but also toroidal components and this field may be strongly amplified by differential rotation and turbulent motions in the matter around the star.

Dynamo action : Consider field \mathbf{B} in the star vicinity as a field that arises by the plasma motions in the presence of an external field that is the proper dipole field \mathbf{B}_0 of the star. Field \mathbf{B} is determined by the well known dynamo equation

$$\frac{\partial \mathbf{B}}{\partial t} - \nabla \times (\alpha \mathbf{B} + \mathbf{v} \times \mathbf{B}) - D_m \nabla^2 \mathbf{B} = \nabla \times \mathbf{v} \times \mathbf{B}_0 \quad (1)$$

where $(\alpha \mathbf{B} + \mathbf{v} \times \mathbf{B})$ is the electromotive force created by turbulent motion and differential rotation ($\alpha\omega$ dynamo), $\mathbf{v} = \omega(r) \times \mathbf{r} = e_\varphi \sqrt{GM/r}$ is the local Keplerian velocity. $\alpha \approx (\tau_c/3) \langle \mathbf{u}_t \cdot \nabla \times \mathbf{u}_t \rangle$, where \mathbf{u}_t is the turbulent velocity, and $\langle \dots \rangle$ determine the averaging over the turbulent motions. We use the simplest

MAGNETIC FIELD IN THE PROTOSUN AND PROTOSTARS VICINITIES

model $\alpha = \alpha_0 \sin \theta$ and $\alpha_0 \ll v_\phi$. The field of the star $\mathbf{B}_0 = (\mu/r^3)(3\mathbf{n} \cos \theta - \mathbf{n}_0)$, where μ is the star magnetic moment and $\mathbf{n} = \mathbf{r}/r$. Magnetic diffusivity $D_m = u_t \Lambda_t / 3$ is assumed due to turbulent motion with the average velocity u_t and average correlation length Λ_t . For estimations we will take $D_t \nabla^2 \mathbf{B} \sim \mathbf{B}/\tau$, and $(\nabla \times \mathbf{B})_\phi \sim (B_\theta/L_r) - (B_r/L_\theta)$, etc., where $\tau = L^2/D_t$ and L_i is the characteristic space scale of the field in the i -th direction. This assumption retains the structure of equation (1). The scales of \mathbf{B} are apparently larger than scales of \mathbf{B}_0 but not larger than scales of α and ω [2]. In this approximation

$$B_\phi = \frac{Q_\phi \tau}{4 - \lambda^2 \tau^2} \left\{ \frac{2}{\lambda \tau} [\sinh \frac{\lambda t}{2} + \frac{\lambda \tau}{2} \cosh(\frac{\lambda t}{2})] \exp(-\frac{t}{\tau}) - 1 \right\}, \quad Q_\phi = -\frac{7\sqrt{GM}}{2r^{9/2}} \mu \sin 2\theta \quad (2)$$

$$\lambda^2 = 4 \left\{ \left[\frac{\alpha_0^2}{L_\theta^2} + \frac{\alpha_0^2}{L_r^2} + \frac{\alpha_0}{L_\theta} \frac{\partial r \omega}{\partial r} - \left(\frac{\partial \alpha_0}{\partial r} \right)^2 \right] \sin^2 \theta - \frac{\alpha_0^2}{r^2} \cos^2 \theta - \left[\frac{\alpha_0}{r} \frac{\partial r \omega}{\partial r} + \omega \left(\frac{\partial \alpha_0}{\partial r} - \frac{\alpha_0}{L_r} \right) \right] \sin \theta \cos \theta \right\}$$

$$B_\phi \rightarrow \frac{Q_\phi \tau}{4 - \lambda^2 \tau^2} \left\{ \frac{2 + \lambda \tau}{2\lambda \tau} \exp\left(\frac{\lambda \tau - 2}{2\tau} t\right) - 1 \right\}, \quad (t \gg \tau) \quad (3)$$

The field increases if $\lambda \tau > 2$ that corresponds to criteria of the dynamo action. The radial component B_r differs from (2) by an additional factor $(2\alpha\tau/r) \sin \theta$ and B_θ by a factor $2\tau(\partial\alpha/\partial r) \cos \theta$. The common dynamo without the external field gives B_r and B_θ much smaller than B_ϕ . In our case all components of the field may be of the same order of magnitude in the star vicinity.

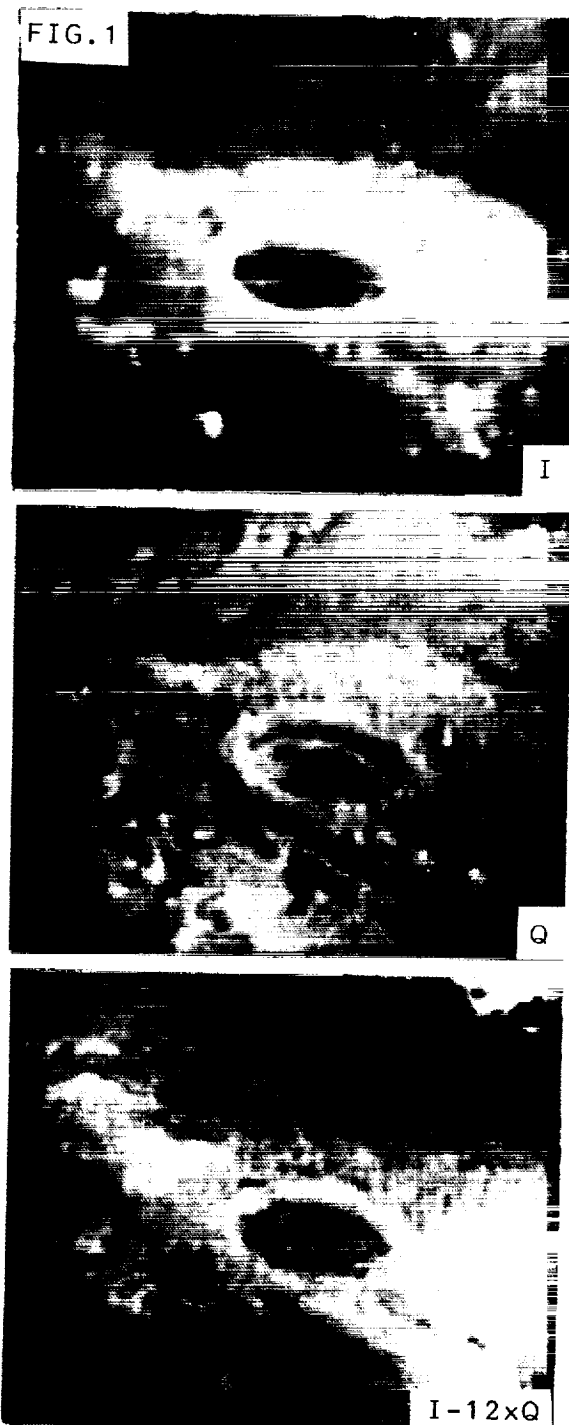
Qualitative estimations : Using the common accepted estimations [1] we will take $u_t \sim 10^4$ cm/s, $\alpha \sim 10^3$ cm/s, $\Lambda \sim 10^{11}$ cm, $M \sim M_\odot = 2 \cdot 10^{33}$ g, $\mu \sim \mu_\odot \sim 2 \cdot 10^{33}$. Consider a region at the distance $r \approx 10^{12}$ cm from the star. In this case $D_t = 3 \cdot 10^{14}$ cm²/s, $\tau = 100$ yr. λ is a function of r and θ and depends on the uncertain known values of $\alpha(r, \theta)$. As a rough estimation we can take $\lambda \sim 2\sqrt{\alpha\omega/r}$. At the distance 10^{12} cm we have $\lambda\tau \gg 2$, and $B_\phi \sim 10^{-3} \exp(t/\tau_{eff})$. Similar estimations for the distance $r = 10^{13}$ cm give $B_\phi \sim 10^{-7} \exp(t/\tau_{eff})$, where τ_{eff} is about a few years. We can see that the field in the ionized medium in the star vicinity will grow to the value of about 0.1 - 1 G both for toroidal and poloidal components in a relatively short time of about 10 - 100 yrs. The field increase stops by nonlinear effects. This field may be of great importance for the protostar (protosun) and protoplanetary system evolution.

References: [1]. *Formation & Evolution of Planet. Syst.*, ed. H. Weaver, L. Danly Cambridge Univ. Press.
[2]. T. Stepinski, E. Levy, (1991) *Ap.J.* 379, 343.

SOIL TEXTURE AT THE LUNAR SURFACE : REGIONAL ANALYSIS WITH POLARIMETRIC IMAGES; A. Dollfus, Observatoire de Paris, 92195 Meudon Cedex, France.

Images of the Moon are taken with CCD detectors through polarizer transmitting alternatively the linear polarizations perpendicular and parallel to the scattering plane. These images (I_1 and I_2 respectively) are combined to produce images with the polarized light only. The combination $(I_1 - I_2)/(I_1 + I_2)$ displays the degree of linear polarization over the lunar surface (Stokes parameter Q/I) which is an inverse image of the albedo plus additional departures produced by the texture at the lunar surface. These departures can be separated from the albedo by forming the image $(I_1 - I_2)$ which displays the Stokes parameter Q , in which the terrains are contrasted as a response to their surface properties only [1,2,3,4]. An image Q is essentially sensitive to grain size, slightly to compaction, and to large scale roughness (shadow effect on the luminence) depending of the phase angle. Models and laboratory works are available to decipher these contributions, for polarization [3,5] and for photometry [6,7]. Other combinations of images, such as $(Q/I - aQ)$ or $(I - aQ)$ enable, when optimizing the coefficient a , to enhance different types of terrains within the field of view. These results are related to the episodes of emplacement, surfacing and time evolution of the terrains.

Observations have been collected and processed, using the 100cm telescope at Meudon Observatory, over 25 lunar regions, some of them at different phase angles. New features are exhibited at the lunar surface, helping for deciphering the stratigraphic and geological histories of the areas. Examples for Mare Undarum, Messier and Plinius have already been presented [4].



SOIL TEXTURE AT THE LUNAR SURFACE. A. Dollfus

Fig. 1 refers to the vicinity of crater Plato, illuminated under incidence 63° at phase angle 31.5° on Dec. 20, 1988. The image Q shows the areas dark hued when the terrain is fine grained or rough, and light hued for coarser pieces on flat surfaces. The Plato floor has two types of surface textures and the inner rempart appears dark downhill, suggesting landslides. The image (I-12xQ), which combines albedo and surface texture, exhibits complex dark areas in Mare Imbrium (at bottom left), featuring specific soil properties and suggesting a multi-episods surfacing history.

Fig. 2 shows Ptolemaeus at phase angle 72.1° and illumination angle 69.1° , on Jan. 2, 1993. Image Q exhibits a bright aureola round crater A, requiring larger grains or a smoother surface. Its extension toward upper left is strengthened in the image (Q/I-2xQ) and suggests a flow. (Such kinds of features are also observed in Schickard, Copernicus, Cyrillus). The contrast enhanced version of this image identifies at least 4 types of surfaces within Ptolemaeus.

REFERENCES

- [1] Dollfus A. et al. (1989). *Compte Rendus Acad. Sci Paris*, **308**, II, 19-24.
- [2] Dollfus A. and Fauconnier T. (1989). *Proc. Int. Congress Optical Sci. Engineering*, Paris, SPIE, 25-28 April 1989.
- [3] Shkuratov Yu. G. and Opanasenko N.V. (1992). *Icarus* **99**, 468-484.
- [4] Dollfus A. (1990). *Proc. Lunar Planet. Sci. Conf. 25th*, Houston.
- [5] Geake J.E. and Dollfus A. (1985). *Mon. Not. R. astron. Soc.* **217**, 75-91.
- [6] Hapke B. (1981). *Jl. Geoph. Res.* **86**, B.4, 3055-3060.
- [7] Hapke B. (1984). *Icarus* **59**, 41-59.

FIG. 2



THE ROLE OF HAPKE'S BIDIRECTIONAL SURFACE REFLECTION MODEL
IN DETERMINING ATMOSPHERIC ABUNDANCES AT MERCURY; D. L. Domingue
(LPI), A. L. Sprague, D. M. Hunten (LPL)

This project investigates how knowledge of Mercury's surface reflection characteristics, as modeled using Hapke's theory [1,2,3], are used in the analysis of atmospheric emissions and how uncertainties in the values of the Hapke model parameters affect the interpretation of column abundance in the atmosphere of Mercury. The modeling of surface reflection is used in the reduction of observed emission spectra, in addition to the derivation of column abundances.

Atmospheric spectral measurements at Mercury are made by recording line emissions, typically on a CCD. The data numbers representing incident photons must then be translated in to radiance values. Thus a conversion or calibration factor is needed. If no calibration source is observed along with Mercury, then the surface of Mercury can be used as the calibration standard. Using Hapke's model, the radiance of Mercury within the continuum of a spectrum is calculated. The calculated brightness of Mercury is then "smeared" to various observing conditions and compared to the observed continuum. Comparisons made between the theoretically derived continuum and the observed continuum determine the amount of smearing in the observation in addition to providing the reflectance (R_r) used in calculating the calibration factor.

Veverka et al. [4] found two sets of values for the six Hapke parameters describing the disk-integrated brightness of Mercury using the whole disk observations of Danjon [5,6]. Thus, for a specific phase angle, the disk-integrated brightness of Mercury's whole disk can be calculated. If Mercury is observed using a CCD array then the disk-integrated brightness of the planet can be measured by summing DN over the entire disk of Mercury. Comparisons between the theoretically calculated radiance and the observationally measured DN provides a calibration factor. This method of calibration compares theoretical disk-integrated brightness (based on Danjon's observations) with observed disk-integrated brightness. Even though ground-based telescopic observations have some degree of smearing, if the total light from the disk is compared to the total reflected light calculated from the model, this method of calibration is valid.

However, if Mercury is observed using a slit spectrograph different considerations must be taken into account. A slit across Mercury measures the continuum over a portion of Mercury's surface rather than the whole disk simultaneously. A comparison of DN from a portion of the surface are then compared to R_r 's generated from whole disk measurements. Using these sets of Hapke parameters assumes that disk-resolved portions of Mercury's surface reflect light equivalently to the whole disk. This assumption is not necessarily valid and therefore needs to be tested.

HAPKE'S BIDIRECTIONAL SURFACE REFLECTION MODEL: Domingue D.L. et al.

Theoretical Mercurian surfaces were created for 110° solar phase angle using Veverka et al.'s [4] solution 1 and solution 2 Hapke parameters where the parameter B_0 was set to 1.0 for both solutions. These surfaces were then smeared to 0.3, 1.0 and 2.0 arcseconds radius of a seeing Gaussian, which correspond to smear factors typical of spacecraft, good ground-based telescopic, and worse-case, ground-based telescopic observations, respectively. Calibration factors were calculated for these surfaces using a north-south slit offset by 2 arcseconds from the sub-Earth meridian across the illuminated crescent. At 0.3 arcsecond smear there was a 6.5 % difference between the calibration factors of the solution 1 versus solution 2 surfaces. At 1.0 and 2.0 arcsecond smear the differences in the calibration factors were 2 and 3 percent, respectively.

Once the observations have been calibrated, the emission lines are examined. Emission due to the excitation of atmospheric atoms can be divided into two components, the emission due to incident solar flux and the emission due to surface reflected light. Using a complete frequency distribution atmospheric model that accounts for surface reflection and self absorption [7], we calculate atmospheric I/F values using solution 1 and solution 2 surfaces in the calculation. Atmospheric values were generated for $\tau = 1.0$ and $\tau = 0.1$, both are reasonable values for Na and K at Mercury. The percent of difference in column abundances is less than 1% for all smear factors. Thus the total uncertainties in calculated column abundances for this particular phase angle is less than 7% between solution 1 and solution 2 Hapke parameters, well within observational uncertainties for ground-based observations.

- [1] Hapke, B. (1981) *JGR*, 68, 4571.
- [2] Hapke, B. (1984) *Icarus*, 59, 41.
- [3] Hapke, B. (1986) *Icarus*, 67, 264.
- [4] Veverka et al. (1988) *Mercury*, U. of Arizona Press, 37.
- [5] Danjon, A. (1933) *Ann. Obs. Strasbourg*, 2, 170.
- [6] Danjon, A. (1949) *Bull. Astron. J.*, 14, 315.
- [7] Hunten, D.M. and Wallace, L. (1993) *Astrophys. J.*, 417, 757.

A SEARCH FOR FURTHER CONCENTRATIONS OF ORGANIC MATERIALS IN EET A79001; C.Douglas, I.P.Wright, and C.T.Pillinger, Planetary Sciences Unit, The Open University, Walton Hall, Milton Keynes, MK7 6AA, England. M.M.Grady, The Natural History Museum, Cromwell Road, London SW7 5BD, England.

EET A79001, an SNC meteorite believed to be of martian origin, is an unusual sample containing an igneous contact between two distinct lithologies: both are maskelynite-bearing feldspathic pyroxenites, one medium grained (lithology A) and the other coarser grained (lithology B). A third material is also present, generally referred to as lithology C [1], which consists of vugs and shock-melted glassy veins and is found throughout the meteorite. EET A79001 also contains numerous salts such as carbonates [1], sulphates and phosphates [2] and possibly nitrates [3]. The origin of these materials is the subject of continued research. Previous studies have also suggested an association of these salts with carbonaceous material burning at low temperatures presumed to be organic in nature [4, 5]. Herein we report further data concerning the lithology C assemblages.

Wright *et al.* [4] reported the presence of what were believed to be organic materials in EET A79001, sub-sample 239 (hereinafter 239). This material accompanied the calcium carbonate component known as "white druse" [1] found at a lithology A/C contact. Using stepped combustion, Wright *et al.* [5] found that 4682 ppm carbon was released from 239 between 200-700°C. The isotopic composition rose from $\delta^{13}\text{C}$ *ca.* -26.6‰ at 200°C to +8.9‰ at 600°C, before decreasing again to lighter values at higher temperatures. The profile was interpreted as a mixing of two components: (i) an isotopically light component (870-1540 ppm; $\delta^{13}\text{C}$ ~-30‰), combusting between 200 and 650°C; this temperature interval is consistent with the identification of organic materials and (ii) a carbonate ($\delta^{13}\text{C}$ ~+12‰) which decrepitated between 450 and 700°C. Since 239 was taken from deep within the meteorite, it is reasonable to assume minimal levels of terrestrial biogenic contamination. Indeed compared to 239, a sample from the surrounding lithology A was found to release more than an order of magnitude less carbon during combustion at temperatures up to 650°C. Furthermore, a sample of band-saw fines also from EET A79001, which has obviously suffered from extreme levels of contamination, contained only 1000 ppm carbon [6]. Nevertheless, the isotopic composition of the low temperature carbonaceous material in 239 is consistent with that of terrestrial organics, therefore a pre-terrestrial origin cannot be guaranteed.

Unfortunately, further analyses of 239 were not possible since the entire sample (5.35mg) was consumed [5]. Subsequently, more druse materials have been discovered in EET A79001 as pockets within lithology A. One such sample, EET A79001,323 (hereinafter 323), a whole-rock chip from lithology A which has been analysed by high resolution stepped combustion in

the current study. The sample 323 was found to have a total carbon concentration of 1888 ppm, with an average $\delta^{13}\text{C}$ of -12.4‰. The analysis revealed that 323, like 239, contained a large proportion of carbon that combusted at a low temperature (<650°C). Unlike 239, the two isotopically distinct components were partially resolved, as a result of the smaller temperature increments utilised in the experiment. Carbonate accounted for 850 ppm of the total carbon released, and reached a maximum $\delta^{13}\text{C}$ of +7.2‰ at 550-575°C. As this value was not maintained across several temperature steps, it can be assumed that the true isotopic composition of the carbonate is actually higher. The lower temperature component ($T < 550^\circ\text{C}$) accounted for ~ 990ppm calculated using an end-member $\delta^{13}\text{C}$ *ca.* -28.6‰. There are two possibilities for the nature and origin of the low temperature component: (i) Either the carbon is preterrestrial in origin or (ii) the carbon is a mixture of weathering products and organic contamination which has found its way deep within the sample along microfractures and between grains. The salt deposits do not appear to be distributed in boundary sites. An argument for the carbon components of 239 and 323 being of terrestrial origin is that both samples contained a highly labile $\delta^{13}\text{C}$ -enriched component, released below 200°C. This accounted for 10-15 ppm carbon in 323 and 60-70 ppm in 239, assuming a $\delta^{13}\text{C}$ of between 0 and -5‰. Components of this nature have appeared before in the analysis of many Antarctic meteorites. Another sample which contains large amounts of carbon released at low temperature is LEW 88516, which has three low temperature carbon components [7], one of which looks identical to the very low temperature carbon released during the analysis of 323. From isotopic considerations, the very low temperature carbon cannot be simply adsorbed air

If the carbonaceous components in 239 and 323 are truly martian organics, the implications for our understanding of Mars are immense. They may enable us to learn a great deal about the processes on Mars, both past and present, and perhaps even give clues to the origin of life. In order to ascertain that these materials are indeed martian organics further analysis is required, for example ^{14}C content would help to discriminate between terrestrial and preterrestrial organics. One such measurement of ^{14}C in salts from EET A79001 already exists, but the material analysed was collected from both the surface and the interior of the meteorite [8]. Weathering on the exterior of the sample may have produced terrestrial salts, which have a demonstrably different origin from the salts deep within the meteorite. Gas-chromatography-mass spectrometry techniques might be used to identify any organic compounds present in the samples and help discriminate between terrestrial contamination and other organic materials.

References: [1] Martinez R. and Gooding J.L. (1986), *Antarctic Meteorite Newsletter*, 9, 23-29; [2] Gooding J.L. *et al.* (1988), *Geochim. Cosmochim. Acta* 52, 909-915; [3] Grady M.M. *et al.* (1993) *Lunar Planet. Sci.* XXIV, 553-554; [4] Wright I.P. *et al.* (1989), *Nature* 340, 220-222; [5] Wright I.P. *et al.* (1988) *Geochim. Cosmochim. Acta* 52, 917-924; [6] Wright I.P. *et al.* (1993), *J. Geophys. Res.* 98, 3477-3482; [7] Wright, I. P. *et al.* (1993) *LPSC XXIV* 1541-1542; [8] Jull A.J.T. *et al.* (1992), *Lunar Planet. Sci.* XXIII, 641-642.

FOUND: STAR AND LINEAR DUNES ON MARS. *K. S. Edgett and D. G. Blumberg,*
Department of Geology, Arizona State University, Box 871404, Tempe, AZ 85287-1404.

Summary: The first star dunes identified on Mars occur at 8.8°S, 270.9°W. Unambiguous examples of linear dunes occur in a crater at 59.4°S, 343°W. While rare, dune varieties which form in bi- and multi- directional wind regimes are not absent on Mars. The directional variations of winds required to create these dunes are influenced by local topographic features.

Introduction: Linear and star dunes require bi- and multi- directional winds (respectively) in which to form. Linear dunes advance by elongation down wind and comprise half of all dune surfaces on Earth [1,2]. Star dunes cover about 5% of terrestrial dune areas and are typically pyramidal in shape with three or four arms radiating from a central peak [3]. Nearly all Martian dunes are barchan, barchanoid, transverse, or complex varieties that combine aspects of these dune types [4]. Such dunes generally result from unidirectional winds [5]. Linear and star dunes are very rare on Mars [6,7]. Incipient linear dunes formed by elongation of barchan horns have been observed in the Martian north polar erg [6,8], but sand seas composed mainly of linear dunes, as occur in Africa and Australia, do not occur on Mars [4].

Martian Star Dunes: The star dunes are shown in Figure 1. They are located in a valley created by the junction of two crater rims [7]. There are 11 distinct dunes showing various states of radial arm development. The dunes also have dark, wispy streaks emanating from them. The streaks are oriented toward the south-southeast, consistent with the present dominant wind direction [7]. The dark streaks might be evidence that these dunes are active under the present climate conditions. The dominant winds in this region flow from the north-northwest during southern summer [e.g., 9]. The valley opens out toward the north-northwest, thus the valley has probably acted as a funnel, bringing both wind and sand into it. The topography of the valley walls provide a local influence on wind conditions, which in turn provides the necessary multidirectional regime needed for star dune development.

Martian Linear Dunes: The linear dunes occur within a 70 km- diameter crater located at 59.4°S, 343°W (Fig. 2). The crater is in the Hellespontus region, a zone of thick intracrater sand accumulation. The entire dune field is about 25 km long, with a second smaller dune field occurring to the north-northeast after an ~ 8 km gap (T₂). The dunes considered to be linear (L) occur in the middle of the main dune field. They originate in a dune mass (M) and grade downwind into transverse dunes (T₁). The crater floor is pitted (P) upwind of the dunes, perhaps the result of aeolian deflation [7].

Discussion: The dunes in Figure 2 are similar to linear dunes in North America which we have examined in the field. The first example occurs among the Shifting Sand Dunes of eastern Christmas Valley, Oregon [7]; the second is in the Stovepipe Wells dune field of Death Valley, California. Four dune types, each characteristic of a different wind regime, are found at Stovepipe Wells: star, reversing, transverse, and linear dunes [10]. The occurrence of so many dune types in close proximity is attributed to local modification of the wind regime by the influence of the valley topography [10]. Local trapping of sediment and channeling of winds through gaps or corridors in topographic barriers are probably the main contributors to the observed dune morphologies [7]. The settings in which the star and linear dunes in Figures 1 and 2 occur do not resemble those of the large sand seas in Asia, Africa, and Australia [e.g., 11]. Instead, these settings are similar to those which contain the large dune forms and small sand seas found in North American deserts [12].

References: [1] Tsoar, H. (1989) *Progr. Phys. Geog.*, 13, 507-528. [2] Lancaster, N. (1982) *Progr. Phys. Geog.*, 6, 476-504. [3] Lancaster, N. (1989) *Progr. Phys. Geog.*, 13, 67-91. [4] Greeley, R., et al. (1992) In *Mars* (H.H. Kieffer et al., Eds.), p. 730-766. Univ. AZ Press. [5] McKee, E.D. (1979) *U.S. Geol. Surv. Prof. Pap.* 1052. [6] Tsoar, H., et al. (1979) *JGR*, 84, 8167-8180. [7] Edgett, K.S., and D.G. Blumberg (1994) Star and linear dunes on Mars, submitted to *Icarus*. [8] Lee, P., et al. (1993) *Bull. Amer. Astron. Soc.*, 25, 1038. [9] Greeley, R., et al. (1993) *JGR*, 98, 3183-3196. [10] Blumberg, D.G., and R. Greeley (1993) *Summaries 4th Ann. JPL Airborne Geoscience Wkshp., AIRSAR Workshop*, p. 9-12, JPL Publ. 93-26. [11] Breed, C.S., and T. Grow (1979) In *U.S. Geol. Surv. Prof. Pap.* 1052. [12] Smith, R.S.U. (1982) In *Reference Handbook on the Deserts of North America* (G.L. Bender, Ed.), p. 481-524, Greenwood Press, Westport, CT.

MARTIAN STAR AND LINEAR DUNES: Edgett, K. S. and Blumberg, D. G.

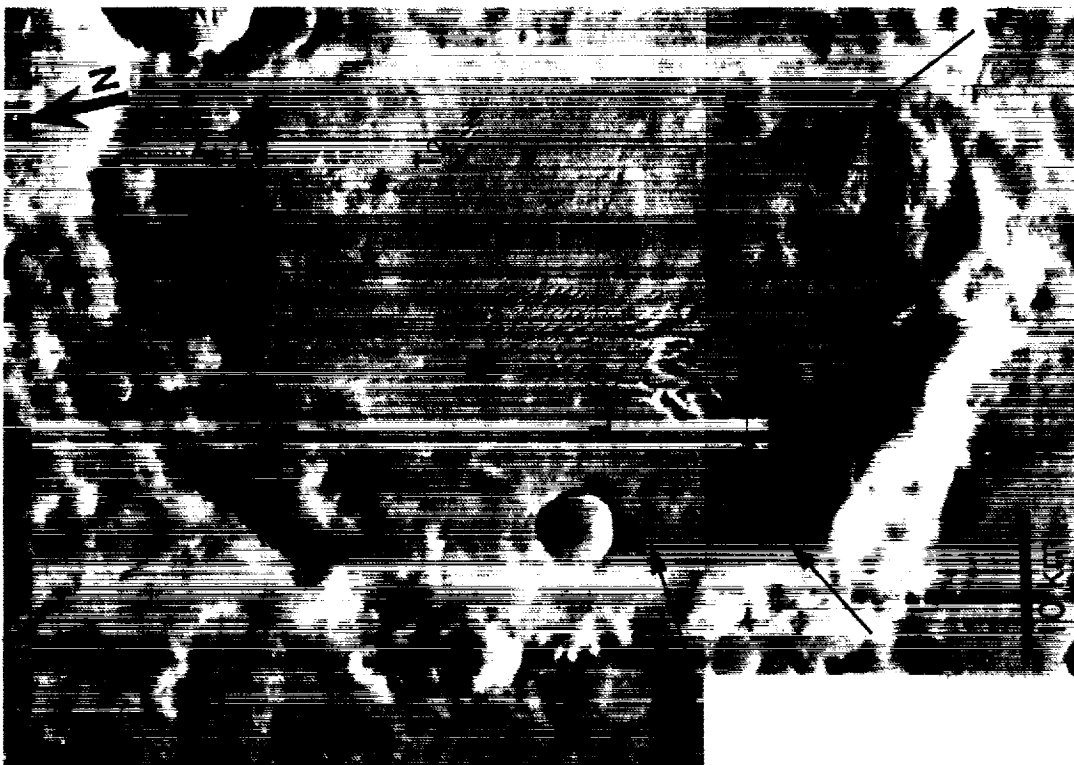


Figure 2. Martian linear dunes in a crater located at 59.4°S, 343°W. Interpreted wind flows are indicated by arrows. Mosaic of *Viking* images 753B 30 and 32.

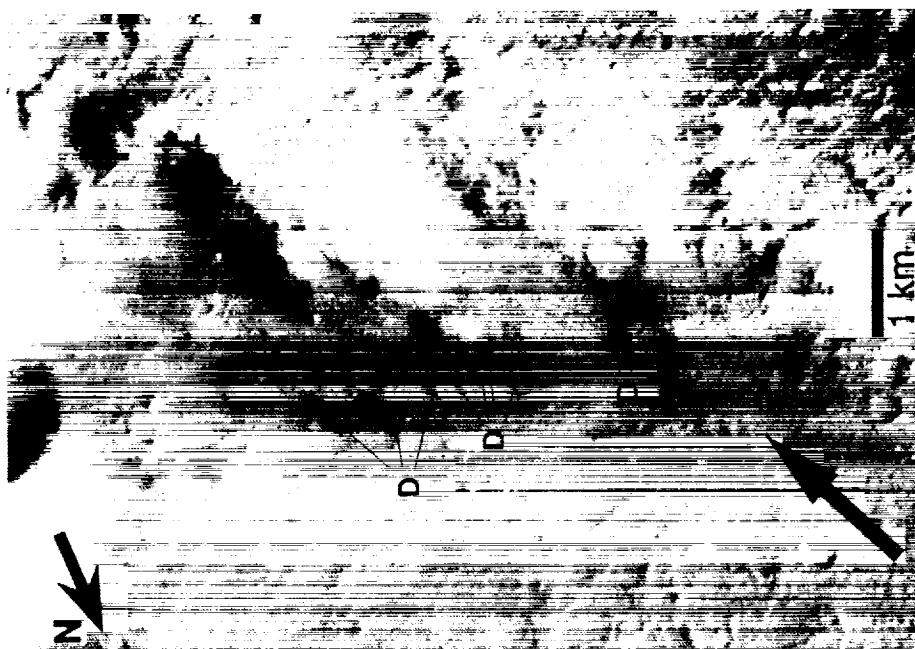


Figure 1. The star dunes (D). Dominant regional winds are indicated by arrow. Portion of *Viking* image 755A 19.

SUGGESTIONS FOR INTERACTION BETWEEN SCIENTISTS, K-12 STUDENTS AND EDUCATORS: MARS EDUCATION PROGRAM IN ARIZONA.
K. S. Edgett, P. R. Christensen, and S. Schmidt, Department of Geology, Arizona State University, Box 871404, Tempe, Arizona 85287-1404.

Summary: We have developed a science education outreach program based on the concept of sharing and interaction between a science research team, K-12 students, and their teachers. Student and teacher exposure to scientists and research offers them insight into how science is done and how groups consisting of scientists, engineers, and support staff, work together as a team. Our broad goal is to enhance education and scientific literacy by involving teachers and students in the exploration of the Solar System. This review provides examples for scientists who are planning educational outreach activities.

Introduction: The earth sciences are playing an increasing role in science education reform, in part because of popular recognition of environmental problems and because earth scientists are participating more in the education of young people [1, 2]. The exploration of our Solar System has led to a greater understanding of how Earth functions and how it has evolved through time. In addition, events such as the lunar Earthrise first seen by human eyes in December 1968, the landing of a robot on Mars in July 1976, and the portrait of our Solar System obtained by *Voyager 1* in February 1990, have provided us with the opportunity to consider the broader context in which we live [3]. Enhancement of education using planetary sciences as a "hook" has the advantage that it is a field of study which encourages and requires a global perspective. Fostering scientific literacy and global perspectives among non-scientists are important goals for improvement and understanding of the Earth's environment and in creating better political and economic relationships among Earth's people [3-5]. The description of the Mars Thermal Emission Spectrometer Education Outreach Program (below) should be considered as a potential model for education efforts that other science research teams may wish to develop in their communities.

Mars Observer TES Education Outreach: The *Mars Observer* mission presented a unique opportunity for enhancing science education through real-time participation in a planetary science project. Each *Mars Observer* instrument was controlled at the home institution of the instrument team leader. Thus, students and teachers living far from a NASA center but near one of the instrument teams would have a chance to become involved in the mission. The *Mars Observer* Thermal Emission Spectrometer (TES) [6] experiment was being conducted from a facility on the campus of Arizona State University (ASU) until the spacecraft was lost in August 1993. Located in a major metropolitan area (Phoenix, AZ), the ASU TES facility was designed with education of children and their teachers in mind. Thus, we developed an educational outreach program, centered on the real-time experience of exploration of Mars using TES, with the following foci: (A) local connection to real-time scientific discovery, (B) developing educational relationships between scientists, teachers, and students, (C) showing teachers and students how scientists and research teams work (breaking down stereotypes), and (D) learning the connections between Arizona and the geology, geomorphology, and historical study of the planet Mars [7]. Following the loss of *Mars Observer*, we found a great desire among the teachers and students in Arizona to continue our education program. The focus has shifted toward the process of recovery, planning, and building of a new spacecraft and TES, as well as increased emphasis on the similarities between our home state of Arizona and the landscapes and geology of Mars (and other planets).

Activities: The education program has reached hundreds of K-12 teachers across the state of Arizona. The two primary activities of the Mars TES education program are student visits and teachers' workshops (described below). We also send speakers on a limited basis to classrooms and astronomy club events. We are developing resources relating to Mars, Arizona, and TES, for teachers to borrow and/or copy. These resources include slide sets and a curriculum guide for the 1993-94 school year. A newsletter, *TES News*, is printed every 3 to 6 months, keeping teachers and their classes informed about the TES team efforts to study Mars.

K-12 EDUCATION OUTREACH: Edgett, K.S., Christensen, P.R., and Schmidt, S.

We have formed working relationships with the Challenger Center for Space Science Education and the Planetary Society to bring the benefits of their Marsville and MarsLink programs (respectively) to the teachers in our state. We also presented new remote sensing lab activities (still in development) to the Arizona Science Teachers Association annual conference [8].

During the academic year, an average of 300 students (K-12) visit the TES facility each month. A typical visit consists of 30 minutes of discussion and hands-on instruction about Mars, Arizona, and the activities of the TES science group at ASU. Students visit with a member of the TES team and thus get a glimpse of how the scientists, engineers, office staff, and college students all work together as a team to do their research.

The teachers' workshops occur every 6 months. The first three were held in February 1993, August 1993, and February 1994. Each of the first two workshops was attended by ~100 educators. The workshops are voluntary (*i.e.*, no college or district credit is given for attendance) and there is no registration fee. The workshops occur in a single day and include presentations by the teachers themselves. The workshops are forums for teachers to exchange ideas on how to incorporate childrens' excitement for space exploration into classroom activities. The workshops also give teachers an opportunity to follow TES activities and stay informed of developments in the earth and planetary sciences. All workshop announcements, hand-outs, and the *TES News* newsletters are designed to be photocopied and shared. Teachers have commented that the workshops have been exciting and informative, and they appreciate the personal interaction between themselves and the scientists, staff, and college students involved with the TES project.

Suggestions: We have learned that there are more schools that have computers in the classroom than we originally expected. At the same time, there are many more schools that have severely limited resources. The workshops and activities we have been developing attempt to take both of these realities into account. Much of the material shared at workshops is printed on paper so that it can be easily photocopied for student and colleague use. We try to be informative, showing teachers resource items produced by other organizations, such as the material available through NASA teachers resource centers and the NASA Spacelink Internet connection. We have also learned that many elementary and middle school teachers are uncomfortable teaching science, and therefore they value the direct contact with scientists who can teach them about the latest and most interesting discoveries as well as show them how science relates to their everyday lives. Much of what we have learned has come through (a) monthly meetings of an advisory group composed of local K-12 teachers, (b) surveys given to teachers during their student visits and the Saturday workshops, and (c) discussions with other scientists and graduate students involved with science education outreach [*e.g.*, 9]. The activities described here can occur within the context of a limited budget. There is a variety of sources for educational funding [see 10]. You are encouraged to contact us if you have questions about initiating a science education outreach activity in your community.

Acknowledgements: The Mars TES education program benefits from the patient assistance of numerous individuals. We especially thank Linda Jaramillo, Kathy Patoni, Dr. Don Anderson, Tiffany Montoya, Greg Mehall, and David Melendrez of the ASU TES group; Dr. Fred Staley, Mary Della Bourgeois, and Dr. Sheryl Santos of ASU; and the TES Education Advisory Group: Anthony Occhiuzzi (Tempe H. S.), David Harbster (Chandler, AZ), Mary Martin (Kiva Elem., Scottsdale, AZ), Steve Jones (J.B. Sutton Elem., Phoenix, AZ), Kathryn Nichols (Valley View Elem., Phoenix, AZ), Mary Palmer (Bethune Elem., Phoenix, AZ), and Addie Kinsinger and Harold Frederick (KAET-TV, ASSET). The help of Sue Cox-Kauffman (SAIC, Washington, DC), Carol Stadum (Planet. Soc.), and Lindy Pasos (Challenger Center) is also appreciated. This work is supported by an Educational Supplement to NASA grant NAGW 943.

References: [1] Mayer, V.J., *et al.* (1992) *J. Geol. Educ.*, 40, 66-73. [2] Carpenter, J.R. (1993) *J. Geol. Educ.*, 41, 304-311. [3] Mayer, V.J. (1990) *Sci. Teacher*, 57(1), 47-51. [4] Mayer, V.J. (1991) *Sci. Teacher*, 58(1), 34-39. [5] Hazen, R.M., and J. Trefil (1991) *Science Matters: Achieving Scientific Literacy*, Doubleday, New York. [6] Christensen, P.R., *et al.* (1992) *J. Geophys. Res.*, 97, 7719-7734. [7] Edgett, K.S. (1993) *Arizona Geol.*, 23, 10-11. [8] Edgett, K.S., *et al.* (1993) Abstr. present. to Arizona Sci. Teachers Convention, October 1993. [9] Edgett, K.S. (1993) Abstr. present. to Science Theatre Student Outreach Conf., Michigan State Univ., E. Lansing, MI, July-August 1993. [10] *NSTA Reports!* Sept. 1993, National Sci. Teachers Assoc.

HEATING BY LIGHT AND THE SIZE DISTRIBUTION OF CHONDRULES;

D. D. Eisenhour, T. L. Daulton, and P. R. Buseck, Departments of Geology and Chemistry, Arizona State University, Tempe, Arizona 85287.

Introduction: One of the most notable characteristics of chondrules is their limited sizes which range from ~0.1 to 3.0 mm in diameter with chondrules < 0.1 mm conspicuously rare [1]. Two commonly proposed explanations for this restricted size range are evaporation and sorting [2-4]. However, there are observational and/or theoretical difficulties with both of these interpretations. Sorting models provide a reasonable explanation for the chondrule population in any single meteorite but run into difficulties when all meteorites are considered collectively. Evaporation models have the advantage of relating the size distributions of chondrules to the heating events responsible for their formation but agree poorly with chondrule and chondrite compositions and are physically implausible. A more reasonable explanation is found in the formation of chondrules by electromagnetic radiation. When chondrules are heated by predominantly visible light, their size distributions are easily accounted for as a natural product of the heating process.

Discussion: Sorting theories assume that a broad chondrule distribution formed initially and that some physical process later separated them into different size bins. Regions containing different chondrule populations then supposedly accreted to form chondrites with the restricted chondrule distributions we observe today. This scenario reasonably explains the chondrule populations in individual chondrites but has difficulty explaining the chondrule population when all chondrites are considered collectively. Meteorites containing 0.1 to 3.0 mm chondrules are common, but those with chondrules < 0.1 mm are disproportionately rare. If sorting is responsible for the size distributions of chondrules in chondrites, then small chondrules are largely unaccounted for, posing a difficult problem for sorting theories. An additional difficulty with sorting is that the bulk compositions of chondrites are similar regardless of the proportion of chondrules (more refractory) to matrix (less refractory). This complementary relationship suggests that the chondrules and matrix of individual chondrites were derived locally without significant transportation and fractionation as is implied by sorting.

The complete destruction of chondrules < 0.1 mm through evaporation has also been proposed to explain the size distribution of chondrules. However, there is little support for this process, either observationally or theoretically. Two prominent problems exist: small surviving chondrules should be highly depleted in volatile elements, which is not generally observed, and more importantly, it is highly unlikely that evaporation would eliminate small chondrules from the population in the first place. The evaporation process could destroy small chondrules < 0.1 mm but would replace them by the incomplete evaporation of larger chondrules. Small chondrules would never be eliminated from the population!

Close examination of the heating properties of electromagnetic radiation provides a plausible solution to the difficult problem of chondrule size distributions. Chondrules with different sizes reach different peak temperatures when heated by predominantly visible light because larger chondrules absorb visible light more efficiently than do smaller chondrules, or stated more precisely, at a given temperature larger chondrules absorb visible light more efficiently relative to their ability to emit radiative energy than do smaller chondrules. This is not because larger chondrules have a larger geometric cross-section, but because their greater thickness makes them more opaque to visible light (visible light has a large extinction distance in chondrule-forming silicates). Over a limited size range, this means heating is roughly proportional to a chondrule's volume rather than its cross-section. Conversely, because both large and small chondrules emit a large portion of their energy in the infrared (~10,000 - 40,000 nm) where the extinction distance is small, cooling ability is roughly proportional to surface area. This translates to a radius dependence for heating; i.e., larger chondrules get hotter than smaller chondrules when heated by predominantly visible light.

Figure 1 shows the results from computer simulations of heating initially cold (400 K) chondrules for 300 seconds with predominantly visible light emitted from a 4000 K blackbody source. Calculations are based on both the wavelength-, and size-dependent absorption and emission efficiencies of typical olivine-pyroxene chondrules [5]. Peak chondrule temperatures are plotted as a function of chondrule

HEATING BY LIGHT: Eisenhour, D. D., et al.

size. Different curves represent heating at various distances from the light producing source and are labeled in units of flux normalized to the flux at the source (f/f_0). Note the mm-sized chondrule distribution that would be produced from this kind of radiative heating. Smaller chondrules reach lower peak temperatures because of their inability to efficiently absorb visible light, while very large chondrules remain cool because of the short exposure to heating (larger chondrules have greater thermal inertia). Similar results are obtained for a variety of heating conditions provided the incident radiation is predominantly located in the visible portion of the spectrum. Longer heating times simply stretch out the tail on the large chondrule end of the peak (which is only important if pre-chondrule aggregates of this size existed in chondrule formation regions initially).

For simplicity, grains were assumed to be spherical in the calculations for the temperature distributions shown in Figure 1. This assumption is well suited for chondrules, individual mineral grains, and roughly-spherical, compact grain aggregates. The temperature values shown in Figure 1 are less accurate for fluffy pre-chondrule aggregates, or aggregates with abundant opaque mineral inclusions. For the case of abundant opaque inclusions, the prominent heating peak would become less pronounced due to the preferential rise in temperature of chondrules, grains, or aggregates smaller than ~1.0 mm. For the case of fluffy aggregates, temperatures would be lower for all sizes and the heating peak would shift to the right as individual constituent grains would behave more like independent absorbers and emitters; the overall shape of the curve would remain the same, however.

The ability of light to produce chondrule-like size distributions through preferential heating is in itself compelling evidence for the existence of such a process, especially considering the apparently limited alternatives. However, additional support for this process is provided by the existence of inclusions of dispersed opaque minerals in chondrules, features which are characteristic of heating by intense visible light [5-7]. The ability of these unique opaque mineral assemblages to record the existence of intense visible light relies on the markedly different absorption properties of opaque minerals and silicates. Similar to the size-dependent heating described above, opaque minerals are preferentially heated because of their ability to preferentially absorb visible light; the difference being that for opaque minerals increased absorption is due to the small extinction distance for visible light rather than greater thickness as is the case for larger chondrules. Together, the existence of these characteristic, dispersed, opaque mineral inclusions and the size-dependent heating properties of light provide strong evidence for the formation of chondrules by radiative heating and suggest that the size distribution of chondrules is a natural consequence of the formation process.

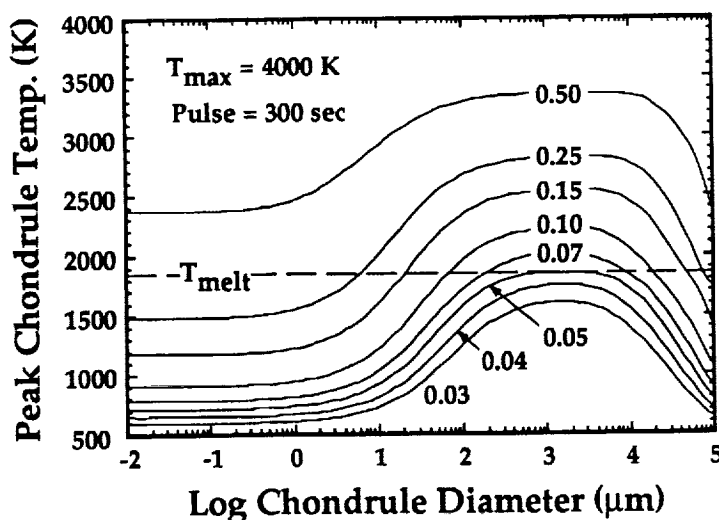


Fig. 1. Peak chondrule temperature as a function of size produced by heating chondrules for 300 sec. with light emitted from a 4000 K blackbody source. T_{melt} is the melting point of typical chondrules. Curves represent heating at different distances from the light producing source (see text).

References: [1] Grossman, J. N., et al. (1988) in *Meteorites and the Early Solar System*, J. F. Kerridge and M. S. Mathews eds., (University Tucson Press): 619. [2] Dodd, R. T. (1976) *Earth Planet. Sci. Lett.* 30: 281. [3] Rubin, A. E., et al. (1982) *Geochim. Cosmochim. Acta* 46: 1763. [4] Rubin, A. E., and Keil, K. (1984) *Meteoritics* 19: 135. [5] Eisenhour D. D., et al. (1994) *Science*: (submitted). [6] Eisenhour, D. D., and Buseck, P. R. (1993) *LPSC XXIV*: 437. [7] Eisenhour, D. D., and Buseck, P. R. (1993) *Meteoritics* 28: 344.

CARRIER PHASES OF ISOTOPICALLY ANOMALOUS NITROGEN IN ACAPULCO METAL: C- AND N-ISOTOPIC COMPOSITIONS VARY WITH GRAPHITE MORPHOLOGY; A. El Goresy¹, E. Zinner², K. Marti³; ¹Max-Planck-Institut für Kernphysik, Postfach 103980, D-69029 Heidelberg 1, Germany, ²McDonnell Center for the Space Sciences, Washington University, St. Louis, MO 63130, USA, ³Dept. of Chemistry, Mail Code B-017, University of California, La Jolla, CA 92093, USA

Graphite grains associated with metal in the Acapulco meteorite are rich in isotopically anomalous (light) nitrogen. Two morphologically distinct types, spherulitic graphite and feathery graphite, have distinct C- and N-isotopic signatures on a C vs N isotope plot. Both C and N in the metal appear not to be equilibrated

Introduction. Acapulco is a unique meteorite with a chemical composition similar to the average of H-chondrites. The meteorite is depleted in Al and the other refractory lithophiles in comparison to C1 chondrites [1]. It is depleted in K and Rb relative to the average H-chondrites but its Na-content is similar to that found in this chondritic group. The metal/silicate ratio in Acapulco is higher than in H-chondrites and the chemistry of its minerals is suggestive of formation at high temperatures (~1100°C) at f_{O_2} conditions intermediate between those of E- and H- chondrites. A cooling rate of >10°C/Ma was deduced from metallographic studies [1]. ¹⁴⁷Sm-¹⁴³Nd and ¹⁴⁶Sm-¹⁴²Nd chronological studies [2] have yielded an internal isochron age of 4.60 ± 0.03 Ga. Because of its old age Acapulco may have retained cosmochemical signatures from the earliest times of the solar system.

Analysis of bulk Acapulco has revealed two different nitrogen isotopic signatures [3]: The metal contains very light nitrogen ($\delta^{15}N \leq -130\text{‰}$) while the silicates contain heavy nitrogen ($\delta^{15}N = +20\text{‰}$). Heavy nitrogen has also been detected in the low temperature release of the metal [4]. Studies of the nitrogen isotopic compositions in taenite and kamacite concentrates indicated that nitrogen concentrations are higher in taenite (28 ppm) than in kamacite (4.5 ppm) [4]. The difference in the nitrogen isotopic composition between metal and silicates indicates lack of equilibration between these two components during melting and crystallization. Nitrogen appears to be lighter in taenite ($\delta^{15}N = -150\text{‰}$) than in kamacite ($\delta^{15}N = -130\text{‰}$) [4]. The lighter nitrogen is sited either in the metal phases or at high enrichment in minor phases closely associated with the metal.

We have initiated a detailed combined petrographic and ion probe study of Acapulco to address the following questions: (1) Is the light nitrogen in Acapulco confined to the metal or is it present in other phases associated with the metal? (2) If there are carriers, do they have identical nitrogen isotopic compositions or do they have distinct signatures which may have survived the melting and crystallization processes in the Acapulco parent body? Petrographic investigations were conducted on three polished thin sections using reflected light microscopy and scanning electron microscopy in the BSE mode. Quantitative electron microprobe analyses were also made to determine the chemical compositions of distinct phases encountered within the metal. The isotopic composition of C and N were measured by secondary ion mass spectrometry according to established procedures [5].

Petrography. Graphite grains of variable size (2-150 μm) were found intergrown with metal. In addition, we found rare cohenite, a phase not reported before from Acapulco. Since graphite was suspected to be the carrier of the light nitrogen, a detailed study was conducted on this mineral. This study revealed the presence of three morphologically distinct types of graphite: (1) Spherulitic graphite entirely sealed off inside of metal grains, coexisting with both kamacite and taenite. The spherulites consist either of radially arranged graphite platelets or fine-grained ($\leq 2 \mu\text{m}$) polycrystalline aggregate of graphite. (2) Feathery graphite intergrown with both metal and silicates. Large grains of this type are mainly enclosed in the silicates but are always in contact with the metal. (3) Graphite filigree. This type appears to be rare; it was encountered only once in all three sections. Like the spherulitic graphite, it is entirely enclosed within the metal.

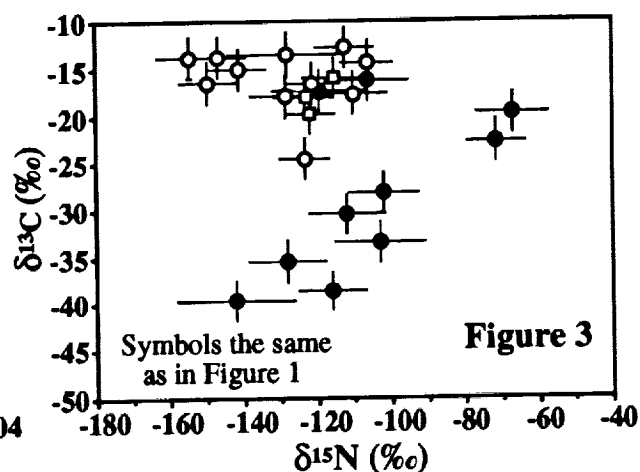
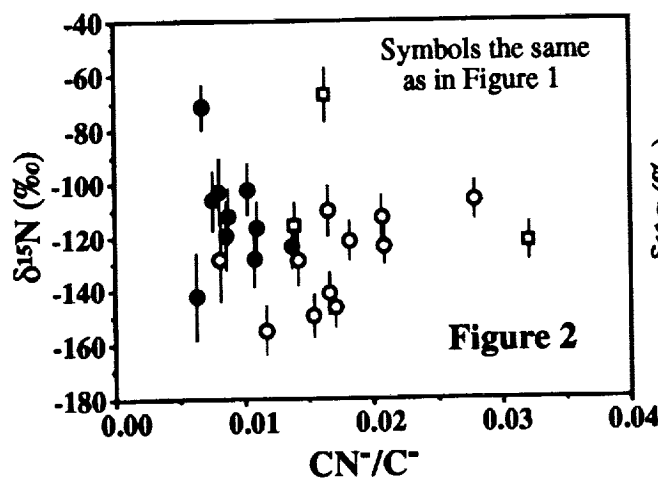
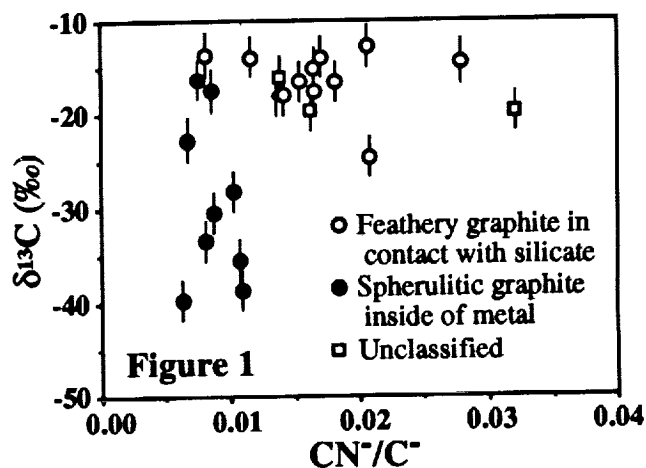
Isotopic analysis. Both in graphite and in cohenite nitrogen was measured as CN^- [5]. Nitrogen contents in cohenite were found to be very low. In contrast, all graphite grains measured are highly enriched in N ($0.002 < N/C < 0.01$). Spherulitic graphite contains less N ($N/C < 0.002$ vs

GRAPHITE CARRIES N ANOMALIES IN ACAPULCO: El Goresy et al.

≤ 0.05) than the feathery and filigree types (Fig. 1). Our measurements revealed distinct C- and N-isotopic characteristics of the various graphite types. The C-isotopic composition of the spherulitic graphite varies between $\delta^{13}\text{C} = -16\text{‰}$ and $\delta^{13}\text{C} = -40\text{‰}$ whereas the range of compositions for the feathery graphite is markedly narrower ($\delta^{13}\text{C} = -12\text{‰}$ to $\delta^{13}\text{C} = -25\text{‰}$) (Fig. 1). Feathery graphite has lighter nitrogen ($\delta^{15}\text{N} = -110\text{‰}$ to $\delta^{15}\text{N} = -154\text{‰}$) than the spherulitic graphite ($\delta^{15}\text{N} = -67\text{‰}$ to $\delta^{15}\text{N} = -141\text{‰}$) (Fig. 2). Figure 3 depicts the C- and N-isotopic compositions of both graphite morphologies. This diagram clearly shows that the data from the two graphite types fall into separate groups with distinct C- and N-isotopic signatures. While the feathery and filigree graphites plot in a region of heavier carbon, the spherulitic graphites plot on a linear array with a slope of ~ 3.25 that extrapolates to zero δ -values of both C and N. The $\delta^{13}\text{C}$ vs $\delta^{15}\text{N}$ trend in spherulitic graphite may represent either (a) a mixing line between two reservoirs, one with isotopically normal C and N, and the other with isotopically light C and N, or (b) correlated isotopic fractionation in both C and N (presolar?) and lack of subsequent equilibration.

Discussion. Several conclusion can be drawn from these results. (1) The two graphite types display distinct isotopic signatures thus indicating formation from different reservoirs before incorporation into Acapulco parental material. (2) Both types frequently occur in the same metal grain, yet no isotopic equilibration was attained between the two graphite morphologies during the melting and crystallization of Acapulco. (3) Because cohenite was found to be poor in N and its N-isotopic composition appears to be close to normal, it is quite unlikely that spherulitic graphite was formed by breakdown of cohenite to Fe + C during the cooling event. (4) The magnitude of the N isotopic anomaly is very similar to that previously reported [4] for the bulk metal (average $\delta^{15}\text{N} \approx -130\text{‰}$). Hence, it is not clear whether the light nitrogen component measured in the bulk metal [4] entirely resides in the graphite or the metal still contains a third carrier with a distinct isotopic composition or N is also contained in the metal. This issue can only be resolved by measurement of graphite-barren metal from Acapulco. The present study demonstrates the need for systematic C- and N-isotopic investigations of different graphite types in graphite inclusions in iron meteorites and other differentiated meteorites.

References: [1] Palme H. *et al.* (1981) GCA 45, 727; [2] Prinzhofer A. *et al.* (1990) LPS XXI, 981; [3] Sturgeon G. and Marti K. (1991) Proc. LPS 21, 523; [4] Kim Y. and Marti K. (1993) LPS XXIV, 801; [5] Zinner E. *et al.* (1989) GCA 53, 3273.



CARBONATES IN THE CI-CHONDRITE IVUNA: IMPLICATIONS FOR AQUEOUS ALTERATION PROCESSES ON THE CI-PARENT BODY.

M. Endreß and A. Bischoff, Institute of Planetology, Wilhelm-Klemm-Str. 10, 48149 Münster, Germany.

Chemically, CI-chondrites are regarded to be the most primitive chondrites; however, texturally and mineralogically they are strongly brecciated and altered. In a previous study it was demonstrated that distinct lithologies exist in the CI-chondrite Ivuna [1]. Many investigators already reported on the occurrence, mineral chemistry, and formation of carbonates and sulfates in CI-chondrites [2-6, and references therein]. In this course we examined two thin sections of Ivuna in order to find a relationship between the compositions of carbonates and the distinct lithic units. As a main result of this investigation we will demonstrate that each lithology has a characteristic carbonate composition.

Results: As mentioned above, among others several distinct lithologies were identified in the CI-chondrite Ivuna [1] (lithology I: carbonate-rich, up to 10 vol% carbonates; lithology II: sulfate-rich, no carbonates; lithology III: rich in coarse-grained phyllosilicate fragments). Recently, we discovered a fourth lithology (IV), which is characterized by a high abundance of olivine grains.

For this study we analysed 63 carbonate grains in Ivuna in order to shed light on the textural and compositional variability of carbonates in different lithologies. Carbonates in Ivuna are usually 10-70 μm in size. Two exceptions are (1) polycrystalline carbonate chunks intergrown with some magnetite in Ivuna described by [1], ranging in size from 60-300 μm (in the following referred to as carbonate fragments; Fig.1), and (2) carbonates in lithology IV, which are in general <15 μm in size. Magnetites (pure Fe_3O_4) within the carbonate fragments show typical morphologies known from CIs: platelets, spherules, framboids. The magnetites occur as inclusions or as lineaments (Fig.1), as also recently described by [7]. In contrast, carbonates in lithology I rarely show magnetite inclusions, but often are intergrown with nearly pure Ca-phosphates apparently evidence for a contemporaneous precipitation of carbonates and phosphates from the same fluid. Except for carbonate fragments, a common feature throughout the studied Ivuna sections is a small sulfate-rim around carbonate grains.

In general, dolomites (with up to 12 wt% MnO) are the dominant phase in the studied sections of Ivuna. Usually they exhibit a wide range of MnCO_3 -contents, but only a limited range of FeCO_3 -contents, as recently reported by [7] for dolomites in Orgueil and Ivuna as well. In addition to dolomite we observed minor amounts of calcite and breunnerite.

Dolomites within lithologies I, III, and IV exhibit very similar Ca/Mg-ratio (Fig.2a,b,c); however, important differences are obvious in a Mn vs. Fe-diagram based on formula units (Fig.3). The Mn-contents of carbonates in lithology I never exceed 0.20, whereas all carbonates analyzed in lithology III have Mn-contents above 0.20 (with both lithologies having generally low Fe-contents <0.30). Carbonates in lithology IV show either very low Mn-contents (<0.02) combined with intermediate Fe-contents (0.18-0.28) or intermediate Mn-contents (up to 0.20) with very high Fe-contents (0.62-0.73).

In contrast to the wide compositional range of carbonates in Ivuna, the carbonates in the carbonate fragments are quite homogeneous (Fig.2d).

Discussion: The observation that Ivuna carbonate compositions are linked to the lithologies in which they occur has strong implications for aqueous alteration processes generated on the CI-parent body(ies). It is suggested that distinct layers or units of the parent body were affected by aqueous alteration processes prior to brecciation and mixing of various rock types. Alternatively, but less probable in our view, the formation of carbonates with different compositions in distinct lithic units occurred after brecciation in the parent body regolith. McSween et al. [3] and Richardson [4] also proposed that fluids circulating in the CI-regolith must have experienced compositional changes locally and temporally, as also indicated by sulfate rims around carbonate grains. In general, our observations are in good agreement with most previous studies [4,6,7, and references therein] and match the predicted precipitation sequence of [4] with first crystallizing carbonates and then crystallizing Ca- and Mg-sulfates, respectively. Kerridge and Bunch [2] and Richardson [4] also stated that carbonate precipitation in CIs overlapped with a period of impact gardening, mainly based on the occurrence of "fresh" mafic minerals and the wide distribution of carbonate fragments, which [4] attributed to be remnants of former carbonate veins. Our observations in Ivuna are consistent with these suggestions. The homogeneous distribution of carbonate fragments throughout the studied sections, each up to several mm apart, and their small compositional variability compared to carbonates in distinct lithologies strongly implicates that all carbonate fragments share a common origin (e.g. precipitated from the same fluid) and were distributed by impact-related

CARBONATES IN THE CI-CHONDRITE IVUNA: M. Endreß and A. Bischoff

processes. The possibility that carbonate fragments in CIs could represent debris of former carbonate veins is evidenced by their fragmental appearance and shapes in Ivuna (comp. Fig.1). The elongated shape of the carbonate fragment as well as the partly fibrous texture of the outer rim implicates crystal growth perpendicular to a vein surface. Due to textural evidence we suggest that carbonate fragments in Ivuna originate from former carbonate veins subsequently destroyed during regolith processes.

References: [1] Endreß M. and Bischoff A. (1993), *Meteoritics* 28, 345. [2] Kerridge J.F. and Bunch T.E. (1979), In *Asteroids I*, pp. 745-764. [3] McSween H.Y. Jr. et al. (1993), *Meteoritics* 28, 396. [4] Richardson S.M. (1978), *Meteoritics* 13, 141-159. [5] Zolensky M.E. et al. (1989), *Icarus* 78, 411-425. [6] Fredriksson K. and Kerridge J.F. (1988), *Meteoritics* 23, 35-44. [7] Johnson C.A. and Prinz M. (1993), *GCA* 57, 2843-2852. [8] Zolensky M.E. et al. (1993), *GCA* 57, 3123-3148.

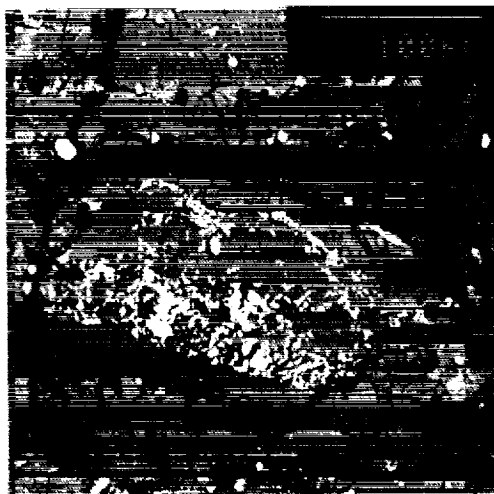
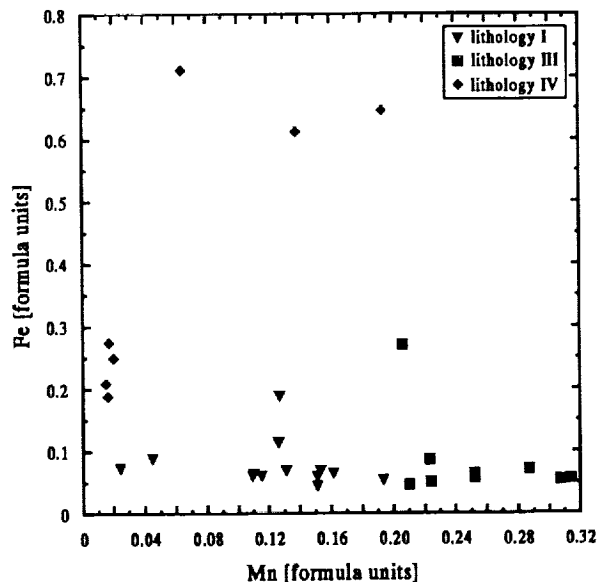


Fig. 1: An elongated carbonate fragment (light grey) in Ivuna indicating crystal growth perpendicular to a vein surface. The inner part of the fragment contains abundant magnetite (bright), showing all morphologies known from CIs.



APOLLO 16 LUNAR GLASSES: NORMATIVE COMPOSITION AND ORIGIN.
Wolf v.Engelhardt, Mineralogical Institute, University of
Tuebingen, Wilhelmstr.56, D-72074 Tuebingen, Germany.

Major element compositions have been determined by microprobe analysis of 322 glass particles in the 0.25-0.06 mm size fraction of soil samples from all Apollo 16 stations. To explore mineral compositions of potential source materials of impact glasses, the chemical data have been converted into weight percents of norm minerals anorthite (an), albite (ab), orthoclase (or), enstatite (en), ferrosilite (fs), wollastonite (wo), forsterite (fo), fayalite (fa), quartz (qu), ilmenite (il) and spinel (sp). The results are shown in Fig.1: each glass particle is represented by a point in triangles pl-px-ol and pl-px-qu, respectively (il and sp are neglected; $pl=an+ab+or$; $px=en+fs+wo$; $ol=fo+fa$). The 322 glasses form a continuum with some blurred clusters. As usual in other continuous complexes, e.g. magmatic rocks, the multitude of glasses must be classified by arbitrary or conventional dividing lines which are boundaries of certain compositional fields. Glass "groups" or "classes" must be defined by such boundaries, not by averages of chemical or normative composition. I tentatively distinguish 12 fields (Fig.1, Table 1). The applicability of this pattern was tested with 270 normative compositions of Apollo 16 individual glass particles and "glass groups", calculated from chemical analyses in the literature.

The glass particles are of different origin and had different histories of formation and cooling. They are either fragments of larger masses or quenched melt droplets and they cooled either rapidly to glass or more slowly to vitrophyric structures. The ratios fragments/droplets and glasses/vitrophyres show characteristic differences for particles of different normative fields. Some of the field I glasses, consisting of more than 95% plagioclase, are diaplectic glasses. Glass particles of field VIII are "green glasses" of volcanic origin. The majority of the analyzed glasses are quenched impact melts. Their normative compositions provide informations on shock-melted mineral aggregations.

Normative compositions of fine fractions of Apollo 16 regolith samples, of agglutinates from Apollo 16 soils and of 119 rock fragments collected at the Apollo 16 site do not cover the whole range of glass compositions: Fines and agglutinate particles occupy a restricted area in the center of glass field III. 85% of all rocks belong to the plagioclase-rich fields I, II, III and XI.

APOLLO 16 LUNAR GLASSES. Engelhardt W.v.

It follows that glasses of fields IV, V, VI, VII, IX, X and XII, i.e. 47% of the analyzed particles, can neither be derived from the fine fraction nor from the coarse rock components of the local regolith. One possibility would be that these olivine-rich, pyroxene-rich and quartz-normative glasses are exotic components which reached the Apollo 16 site by lateral transport. Another possibility is based on the observation at terrestrial impact craters that impact melts are formed from rocks deep below the original ground level. Examples are structures like Ries, Popigai, Lake St. Martin and Araguainha where the impact melts were formed from crystalline rocks, overlain by thick sedimentary sequences, whereas fragmental breccias consist mainly of weakly shocked materials from upper levels of the target. The consequence would be that in the Descartes region multiple impacts have produced the weakly shocked fine and coarse components of the regolith, predominately derived from upper levels of the lunar crust below the regolith, whereas impact glass particles represent in the average deeper levels. It follows that anorthosites (fields I, II, XI) and olivine-poor rocks of noritic composition (field III) prevail in upper levels, whereas troctolitic rocks with wo-rich pyroxene (field IV), and pyroxene-rich, ol-normative (fields V, VI, VII) and qu-normative rocks (fields IX and XII), some of them rich in ilmenite, are more abundant at greater depths.

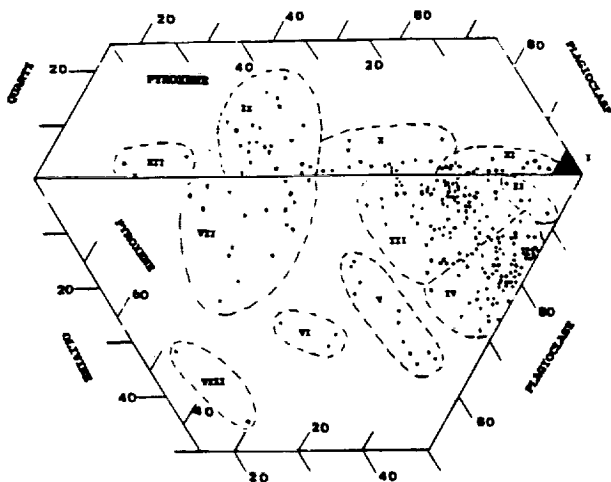


Fig. 1. Normative composition of 322 glass particles from Apollo 16 soils.

Field	Pl	Px	Ol	Qu	%
I	95-100	17
II	85-95	0-12	0-10	0	2
III	65-85	10-30	0-15	0	23
IV	65-87	0-15	10-30	0	29
V	50-60	5-30	15-35	0	4
VI	15-50	20-35	25-32	0	1
VII	30-60	40-60	0-25	0	6
VIII	20-30	30-50	30-50	0	0.6
IX	40-60	35-55	0	0-20	7
X	60-75	15-35	0	0-10	5
XI	75-95	5-20	0	0-10	6
XII	25-40	55-70	0	0-5	1

Table 1. Normative fields of Apollo 16 glasses.

GAMMA RAY SPECTRA FROM THE MARS OBSERVER GAMMA RAY SPECTROMETER: CRUISE DATA ANALYSIS

P.A.J. Englert^{a)}, N. Chakravarty^{a)}, O. Ivanova^{a)}, E.A. Beck^{b)}, J. Brückner^{c)}, S.H. Bailey^{d)}, F.C. McCloskey^{d)} and W.V. Boynton^{d)}.

a) Nuclear Science Facility, San Jose State University, San Jose, CA 95192-0163.

b) The Medical Physics Center, 9342 Technical Center Dr., Sacramento, CA 95826.

c) Max Planck Institut für Chemie, Abt. Kosmochemie, D-55020 Mainz, Germany,

d) Lunar and Planetary Laboratory, University of Arizona, Tucson, AZ 85721

This paper reports the preliminary analyses of special features of the gamma ray spectra acquired in the time period of Jan. 24, 1993 to July 30, 1993 by the Mars Observer Gamma Ray Spectrometer I (MOGRS I) in the flight of the spacecraft towards Mars. The purpose was to gather information on the electronic drift of the instrument, background photopeaks including the fingerprinting of new ones and the evidence on the radiation damage of the detector. Attempts have also been made via comparison with terrestrial simulation experiments, to arrive at crude estimates of the overall proton dose on the detector and the neutron fluence incident on it in the space environment.

Spectrum analysis was performed by the gamma spectrum deconvolution program GANYMED [1] and standard graphics, spreadsheet and statistical analysis packages utilising a Sparc 10/41 Workstation and IBM PC 486. Optimisation of baseline fitting and peak shape parameters within GANYMED allowed a reasonably invariant standard for these spectra. The linear calibration coefficients, a_0 (intercept) and a_1 (slope), of the detector were obtained from the benchmark 198, 271, 984, 1117 and 1312 keV gamma rays whose full widths at half maximums (FWHMs) were investigated for information on the resolution of the detector. The possible effects of solar flares, spacecraft and detector manoeuvres on these variables were examined. It was found that there was no functional correlation between a_0 and a_1 and the time elapsed in the C6 to C10 flight paths which shows the absence of instrument electronic drift. There is however some evidence of a slow progressive change of the coefficients in the C12 flight path which was the path placement of the spacecraft at the time of its disappearance. No correlation of the calibration coefficients with detector temperature and high voltage (HV) at constant time were seen. For the detector resolution, the expected decrease with temperature and increase with HV at constant time were observed. To inspect the time variation of the FWHMs, the spectra were normalised to the HV setting of 2500V and spectra with temperature variation were not considered at all. Average FWHMs were obtained for each flight path and plotted with respect to the average (julian) day of each flight path. The points were regressively fitted to the best polynomial. It was found that the detector resolution worsened with time which indicates progressive radiation damage, an idea of the rate of which was obtained from the coefficients of the polynomial fit.

For the purpose of determining overall spectral characteristics including unknown peak identification, the spectra in all the flight paths were summed up. It was possible to do so without special procedures because of the absence of instrument electronic drift. The FWHMs of all 42 peaks spanning 129-2222 keV in energy, were plotted as a function of gamma ray energy and the points fitted by polynomial regression. Figure 1 shows the plot in the 800-1500 keV region. Over this energy range the FWHM is found to increase almost linearly, if the small coefficients of the higher order terms are ignored. This conforms to the expected trend. However, implicit in this curve is the widening of the FWHMs due to the accumulated energetic particle dose. With the view to obtaining semi-quantitative information on the magnitude of this dose through the gamma spectrum alone, the controlled earth-bound experimental radiation-damage data of Bruckner et al

Gamma Ray Spectra from the Mars Observer: Englert P.A.J et al.

[2] were used. The FWHMs of the 1237 and 1312 keV peaks in the summed spectrum, chosen because of their proximity to the ^{60}Co peaks, were found to lie on or very close to one of the simulated radiation damage vs energy curves at a predetermined GeV proton dose. From this, a rough estimate of the accumulated Galactic Cosmic Ray dose on MOGRS1 can be obtained.

The summed spectrum was used to observe previously recorded background peaks and to identify new ones. The new activities were fingerprinted nuclide-wise on the basis of the most plausible nuclear reaction, the nuclide library NCC within the code GANYMED and other sources. This spectrum also showed the characteristic Ge(n,n' γ)Ge saw-tooth peaks, whose FWHMs were recorded with a separate set of fitting parameters in the code GANYMED. Beck's [3] data on such peaks obtained by quasi-monoenergetic neutron bombardments on the Ge crystal in an HPGe detector, were taken as a rough control data set and were reanalysed and appropriately arranged. The flight data FWHMs as obtained from the summed spectrum were compared to the values obtained from the control data. Within the large constraints of the geometrical mismatch of Beck's detector and the one on MOGRS1 and the fact that space provides a continuum of neutron energies, crude estimates of the average neutron fluence and energy encountered by the MOGRS1 were attempted. The neutron fluence value of $\lesssim 10^5$ neutrons/cm² was found to correspond, to a degree, with a rough estimate obtained by inserting the counts of the 693 keV peak in the standard empirical formula [4]. It will be interesting to compare this value with the actual average neutron fluences obtained from the neutron spectrometers aboard the MOGRS1.

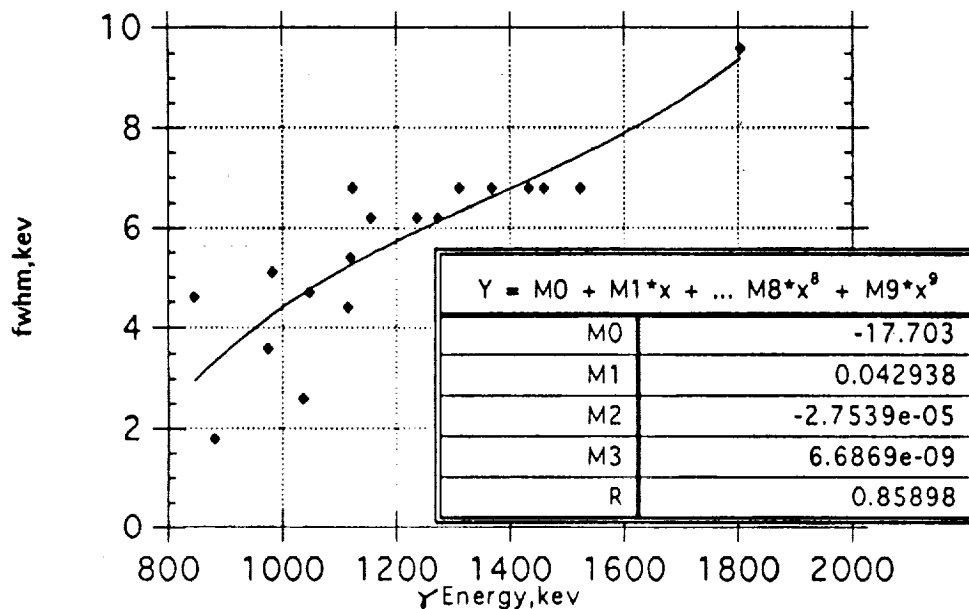


Figure 1.: FWHM of the gamma ray peaks versus gamma ray energy

REFERENCES: 1) Brückner J. and Kruse H., (1991), *GANYMED version 3.3, Technical Report*, Max Planck Institut fuer Chemie, Mainz, (unpublished). 2) Brückner J., (1993) *private communication*. 3) Beck E.A., (1991), "Neutron Energy Determination Using High Purity Ge Detector", *M.S. Thesis*, San Jose State University, (unpublished). 4) Knoll G.F., (1989), "Radiation Detection and Measurement", Second Edition, John Wiley and Sons, New York.

C/O ATOMIC RATIOS IN ANTARCTIC MICROMETEORITES : A PROGRESS REPORT.

C. Engrand, M. Perreau, (LEM CNRS/ONERA, BP 72, F-92322 Chatillon, France), M. Maurette (C.S.N.S.M. Batiment 104, F-91405 Orsay Campus, France).

We have measured C/O atomic ratios in Antarctic micrometeorites (AMMS) and two carbonaceous meteorites, Orgueil (CI) and Murchison (CM), to further assess similarities and differences between these primitive bodies [1,2].

Analytical transmission electron microscopy is used to measure the C/O ratios on a microscale of $\approx 1000 \text{ \AA}$. The C/O atomic ratios for AMMS from the 100-400 μm and 50-100 μm size fractions as given in reference [3] has been revised to average values of about $1,7 \times \text{CI}$ and $0,6 \times \text{CI}$ respectively. We also started to analyze the 25-50 μm size fraction, for a direct comparison with stratospheric IDPs. The preliminary average value is about $1 \times \text{CI}$ for this size fraction. The host phase of the carbonaceous matter has not yet been identified, as no correlation with other major elements was observed. The only exception is the COPS phase, enriched in P and S, and which seems to represent about 5% of the carbon rich phases [4].

Experimental

Micrometeorites are splitted into several fragments and processed as reported in [3]. One of the fragment is crushed on a gold electron microscope grid, between two glass plates, in order to avoid contamination [5]. This sample is further run in a JEOL 4000FX transmission microscope, and analysed both with an energy dispersive spectrometer (EDS) and an electron energy loss spectrometer (EELS).

Results and discussion

C/O atomic ratios range from 0 to $1,24$ for Orgueil and from 0 to $0,6$ for Murchison. The zero values corresponds to single crystals of olivine and pyroxene.

C/O ratios have been measured for 9 AMMs from the 100-400 μm size fraction. The comparison with Orgueil shows that about 15% of the total amount of grains exhibit a higher value of C/O than the highest of Orgueil. The mean value for these grains range from $0,1$ to $3,3 \times \text{CI}$, and the average value of the 125 grains is about $1,7 \times \text{CI}$.

We have analyzed 163 micrometer-sized grains from 11 AMMs from the 50-100 μm size fraction. The mean values for each micrometeorite range from 0 to $1,8 \times \text{CI}$. The average value for the 11 AMMs is only $0,6 \times \text{CI}$, as 2% of grains show a C/O amount higher than $1,24$.

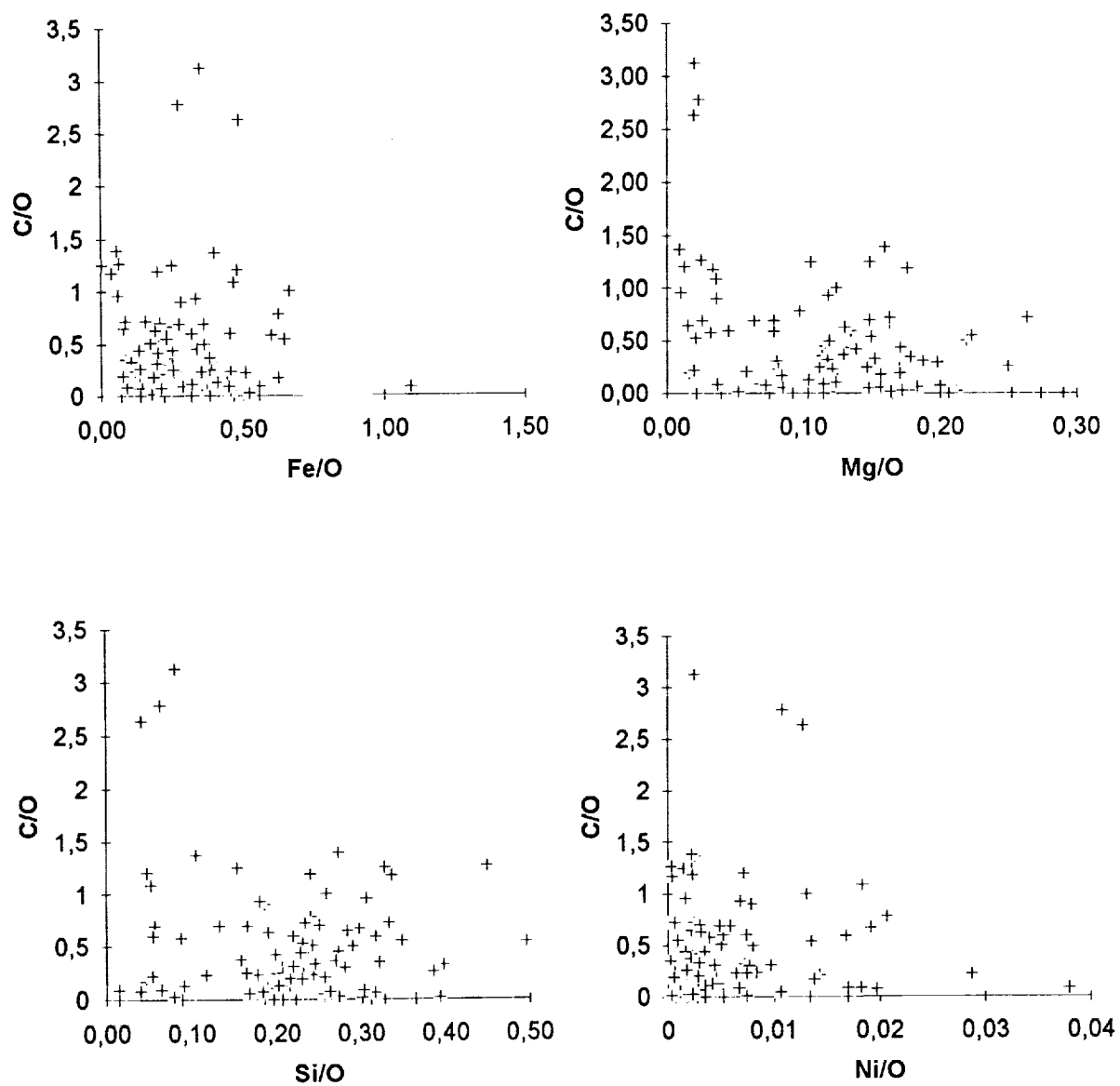
For stratospheric $\approx 10 \mu\text{m}$ IDPs, Thomas et al. [6] reported high carbon contents (between $0,7$ and $7 \times \text{CI}$). We obtain an average value of $1 \times \text{CI}$ for 58 micron-size grains from 3 micrometeorites from our 25-50 μm size fraction. The C/O ratios for these AMMs range from 0 to $2,3 \times \text{CI}$.

The C/O values seems to be independant of the AMMs size. Frictionnal heating (causing an eventual loss of carbonaceous material) during atmospheric entry cannot be the major process involved as AMMS from the 100-400 μm size fraction contain more carbon than smaller micrometeorites.

Complete EDS and C/O analyses have been made for 20, 68 and 19 micron-size crushed fragments from AMMs extracted from the 100-400, 50-100 and 25-50 micrometer size fraction respectively. So far, no clear correlation between C, Mg, Si, Fe and Ni contents of the grains is observed (see figure 1). As the C-rich material is always amorphous, it cannot be associated with crystalline phases such as diamond, carbides and carbonates. Its extraterrestrial origin is supported by the high Ni contents of some of the grains.

REFERENCES: [1] Maurette M., Olinger C.T., Christophe Michel-Levy C., Kurat G., Pourchet M., Brandstätter F., Bourot-Denise M. (1991) *Nature* 351, 44; [2] Presper Th., Kurat G., Maurette M. (1992) *Meteoritics* 27, 246; [3] Perreau M., Engrand C., Maurette M., Kurat G., Presper Th., (1993) *LPSC* 24, 1125; [4] Engrand C., Maurette M., Brandstätter F., Kurat G., Perreau M., (1993) *LPSC* 24, 441; [5] Maurette M., Bonny Ph., Brack A., Jouret C., Pourchet M., Siry P. (1990) *Lecture Notes in Physics* 390, 124; [6] Thomas K. L., Blanford G. E., Keller L. P., Klöck W. and McKay D. S. (1993) *Geoch. Cosm. Acta* 27, 1551.

C/O ATOMIC RATIOS IN ANTARCTIC MICROMETEORITES, C. Engrand et al.

Figure 1

EFFECTS OF AEROSOLS SCATTERING ON SPECTRAL CHARACTERIZATION
OF THE MARTIAN SURFACE Stéphane Erard *IAS - Planetologia, viale dell'Università 11,
00185 Roma, Italy.*

Introduction. Near-IR spectral observation has proven to be one of the most efficient ways to characterize the mineralogy of planetary surfaces. However, the main mineralogical absorptions have a typical depth of 1%, and in the case of Mars may be easily masked or subdued by light scattered by airborne particles. An estimate of this aerosols contribution to the light measured between 0.77 and 2.6 μm was previously derived from ISM imaging spectroscopic data acquired from the Phobos-2 spacecraft in 1989 [1] [2]. It makes it possible to investigate the effect of scattering on spectral parameters used to characterize the surface mineralogy.

Aerosols contribution. The Martian aerosols being very bright and strongly forward-scattering in the near-IR, the radiance factor can be approximated under low opacity as the sum of surface reflectance and aerosols backscattering [3]. This model made it possible to derive an estimate of the scattered spectrum, taking advantage of multiple observations of the same region (W of Pavonis Mons) under different viewing geometries [1]. The main hypothesis are: (a) the detected photons are scattered at most once in the atmosphere (b) the aerosols contribution is neglected above 2.6 μm (c) the photometric function of the surface is assumed independent of the wavelength (d) the difference between extinction and forward-scattering is supposed to be small compared to backscattering. The estimated spectrum is consistent with results of Phobos-2/Auguste data acquired in the same period (opacity at 1.9 μm $\tau \approx 0.23$, effective radius $\approx 1.2 \mu\text{m}$, effective variance ≈ 0.2 [4]) and contains weak features related to water-ice and hydrated phyllosilicates [1].

The image-cube covering Syrtis Major and Isidis Planitia ($400 \times 3000 \text{ km}^2$) was used to test the effect of scattering on the spectra. Statistical analysis of these 3000 spectra showed that the vertical opacity can be considered uniform on the whole region ($\tau \approx 0.17$ at 1.9 μm), with no altimetric dependence. This correction is probably overestimated on the darkest areas.

Surface properties. The main six spectral parameters related to the surface materials are: the reflectance at 1.09 μm ; the spectral slope estimated here as the derivative between 1.84 and 2.35 μm ; the strength of the 2 μm -pyroxenes band; a measurement of the depth of the 0.88 μm -ferric oxides band; the surface of the Fe^{2+} band, integrated from 0.86 μm to 1.09 μm . They were computed for the whole image-cube on calibrated spectra and on spectra corrected from scattering (estimate of the surface alone); their values are given in Table 1. The last three parameters were also used to establish a classification of the calibrated spectra [5]; the main spectral types are given in Fig. 1a. The spectra of the same pixels were averaged after subtraction of the aerosols contribution, and are given in Fig. 1b.

Discussion. The level of the scattered spectrum below 2 μm ranges from 0.02 to 0.05, which represents 5 to 15% of the albedo of the bright areas, and 15 to 30 % of that of the dark regions. This large contribution of scattering is similar to those inferred from IRTM observations for "clear atmosphere" [6] and from independent ISM analysis [7]. The negative spectral slope often ascribed to dark materials appears to be largely due to the aerosols scattering continuum, although intrinsic variations are recognized on the data, for example between the eastern and western parts of Syrtis Major (even enhanced by the correction in this case; see Fig. 1).

Although they are slightly subdued and shifted to longer wavelengths, the Fe^{3+} and 2 μm -pyroxene bands do not appear very sensitive to the addition of a low-opacity scattered component: their spatial distribution and relative contrast aren't deeply modified. Conversely, the Fe^{2+} band area is reduced by almost a factor of two, although the transformation is almost a linear stretch of

AEROSOLS SCATTERING ON MARS: Erard S.

the scale. This reduction may help explaining why the $1\text{ }\mu\text{m}$ -mafic feature is not always observed from the ground.

In the estimated surface spectra (Fig. 1b) the center of the $1\text{ }\mu\text{m}$ band is systematically shifted by some tens of nanometers towards the short wavelengths with respect to the measured spectra. This method also results in band centers located at shorter wavelength than a simpler but less physical correction (division by a linear continuum fitted on the data [8]). However, this latter shift isn't large enough to change dramatically the mineralogical interpretation of the surface: the absorptions are still compatible with hematite on bright regions (center at $0.86\text{ }\mu\text{m}$) and with calcic pyroxenes in Syrtis Major (center at $0.94\text{ }\mu\text{m}$), though probably less rich in Ca than previously inferred from ISM ($\text{Ca}/(\text{Fe}+\text{Ca}+\text{Mg}) \approx 0.20 \pm 0.08$ instead of 0.275 ± 0.075 [8]). Very calcic pyroxenes may have their bands shifted up to $1.05\text{ }\mu\text{m}$ by the addition of the scattered component, and could have been mistaken for olivine in early spectral data of Mars ranging only up to $1.1\text{ }\mu\text{m}$.

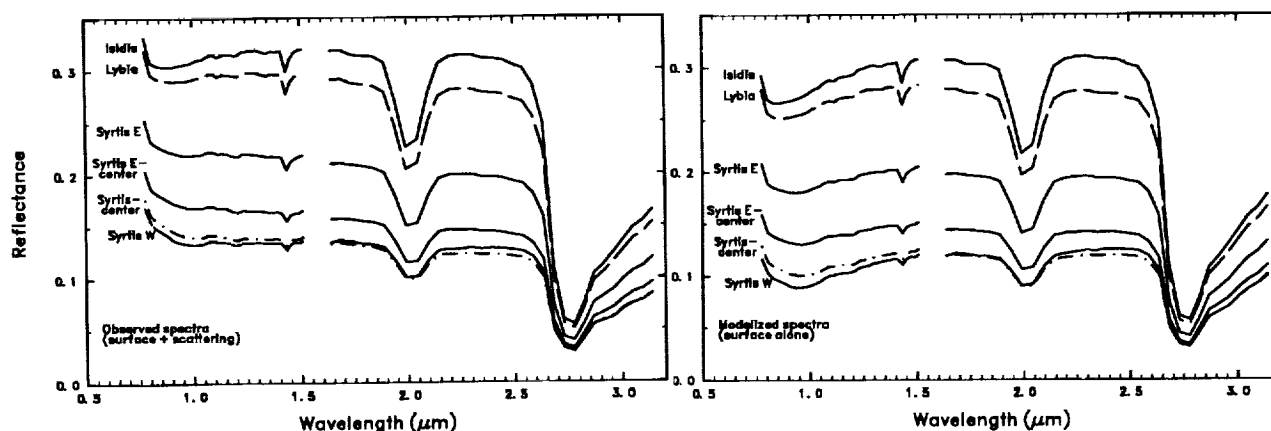


Figure 1. Average spectra of the six main spectral units in the Syrtis Major-Isidis Planitia image-cube: (a) calibrated spectra; (b) after removal of the estimated scattering.

Table 1: Range of variation of the spectral criteria in the Syrtis-Isidis image-cube.

	Surface + scattering (measured)			Surface alone (modelized)		
	min	max	Range/rms noise	min	max	Range/rms noise
Reflectance at $1.09\text{ }\mu\text{m}$	0.115	0.33	1200	0.08	0.30	1200
Spectral slope refl. units/ μm)	-0.025	0.0002	35	-0.010	0.020	30
$2\text{ }\mu\text{m}$ pyroxenes (band depth)	0.97	1.00	20	0.98	1.01	20
$0.9\text{ }\mu\text{m}$ Fe^{3+} (band depth)	0.965	1.055	50	0.955	1.055	60
$1\text{ }\mu\text{m}$ Fe^{2+} (band area)	0.0	0.40	85	0.0	0.70	150

References : [1] Erard *et al.*, *Lunar Planet. Sc. XXIV*, 445, 1993. [2] Erard *et al.*, *Icarus*, 1994, submitted. [3] Drossart *et al.*, *Annal. Geophys.* 9, 754, 1991. [4] Korabiev *et al.*, *Icarus* 102, 76, 1993. [5] Erard *et al.*, *Lunar Planet. Sc. XXIV*, 443, 1993. [6] Clancy and Lee, *Icarus* 93, 135, 1991. [7] Erard *et al.*, *Lunar Planet. Sc. XXIII*, 335, 1992. [8] Mustard *et al.*, *J. Geophys. Res.* 98, 3387, 1993.

PROJECTILE SHAPE AND VELOCITY: IMPACT ON EJECTA DISTRIBUTION AND COMPOSITION; Noreen Joyce Evans and Thomas J. Ahrens, Lindhurst Laboratory of Experimental Geophysics, Seismological Laboratory, California Institute of Technology, Pasadena, CA 91125

Ejecta scaling using the results of hypervelocity impact recovery experiments is critical to advancing our understanding of natural impact phenomenon such as the theory of the giant impact melting of the early Earth and formation of the moon, the proposed impact degassing of Mercury, the origin of tektites on the Earth and the mechanisms associated with impact-related extinction. However, before ejecta scaling from experiments can be accomplished, the dependence of ejecta volume, distribution, grain-size and composition (projectile-target mixing) on impact parameters such as projectile shape and impact velocity must be determined. A series of hypervelocity impact experiments with different impact velocities and projectile geometries have been performed. We have found that the exact configuration of the projectile (e.g., the presence of a sabot which holds the metal sphere or disc) greatly affects ejecta distribution and projectile-target mixing.

A two-stage light gas gun was used to launch 6-7km/s projectiles into Mo targets (see Table). Ejecta fragments were captured by 0.032 g/cm³ polystyrene foam (5cm thick) witness plates. After the impact, the witness plates were X-rayed and then sliced at regular longitudinal and transverse intervals to determine the depth of penetration and angular distribution of captured ejecta. Each section was dissolved in chloroform and the ejecta were recovered and weighed. Ejecta consisted of shards (unmelted) of target material (99% by mass) and melted ejecta which was composed of both target and projectile material, largely in spherical form. The spheres (<5-180 μ m diameter) have distinct quench textures and were analyzed by electron microprobe to determine the proportions of target (Mo) and projectile (Fe) material in each (Figure 1). Sphere fragment velocities were determined by equating the energy expended during passage through the polystyrene foam to the kinetic energies of the fragments (1). For all shots, sphere velocity increases with increasing angle from the target surface. Velocities range from <5km/s to a maximum value of twice the impact velocity.

In shots where both the flyer and sabot impact the target (shots 1, 2 and 3) the maximum total ejecta mass is found in a jetted zone between 50-60°. Flyer shape, therefore, is not a control on the angular position of the jetted zone when a sabot is present.

The correlation of projectile-target mixing and ejection angle for shots 1 and 2 is distinctly different. In shot 1 the high angle, high velocity ejecta contains a higher projectile component than low angle, low velocity ejecta (Figure 1). In contrast, approximately equal proportions of target and projectile components are present in the melted ejecta of shot 2. The spheres recovered from shot 3 show highly variable projectile-target mixing but are relatively enriched in the projectile component. Projectile energy is also highest in this shot (see Table).

When the sabot is stripped and the flyer impacts the target alone (shot 4), X-rays of the witness plates indicate that the jetted zone occurs at a higher ejection angle (60-75°) and that virtually all of the ejecta is concentrated in this zone. Because the sabot adds considerable mass to the projectile (sabot is 7 times more massive than the flyer), the projectile mass and energy for shot 3 (sphere + sabot) were 8.5 times greater than those for shot 4. Accordingly, in shot 3, the crater volume was 6.3 times greater than in shot 4. The spherical flyer produced a crater with a more conical cross-section and a more prevalent raised rim than the projectile composed of a sphere plus sabot.

The measured crater volumes correlate well with crater volume scaling in the strength regime [(2), Figure 10] and provide experimental data for a higher ultimate strength target (Figure 2). The representation developed in (2) for 6-8km/s metal projectiles and metal targets fits the current data within inherent scatter, although the cratering efficiency for shot 4 is somewhat higher than for the

Projectile Shape and Velocity...Evans N.J. and Ahrens T.J.

other shots (Figure 2).

These results indicate that, for cratering in the strength regime, when a sabot is present at impact, flyer shape exerts only minor control on the position of the jetted zone. Both projectile shape and impact velocity exert control projectile-target mixing. Whereas the disc + sabot impact at 6.6km/s led to an equal mixing of the projectile and target in the melted ejecta, the sphere + sabot impact at 6.9km/s produced spheres dominated by the projectile component. These shots fit well with crater volume scaling relationships developed in (2) and extend the previous data set to a higher strength regime. The energy partitioned to the impact by the sabot significantly effects crater morphology and ejecta distribution for high velocity experimental impacts in the strength regime. Since impact velocity and the presence of a sabot are critical controls on ejecta distribution and composition, ejecta scaling from experimental recovery experiments will only contribute to our understanding of terrestrial impact phenomenon if low strength targets and high velocity flyers without sabots are routinely used.

Shot	Flyer Composition	Projectile Shape	Impact Velocity (km/s)	Peak Shock Temperature and Pressure in Flyer	Projectile Energy ($J \times 10^3$)	Crater Volume (cm^3)
1	Fe-Ni-PGE ¹ alloy	disc + sabot ²	5.9	1740°C, 1.7Mb	7.9	0.78
2	Fe-Ni-PGE alloy	disc + sabot	6.6 ³	2944°C, 2.2Mb	9.9	0.92
3	stainless steel 302	sphere + sabot ⁴	6.9	3088°C, 2.4Mb	11	0.95
4 ⁵	stainless steel 302	sphere	6.9	3088°C, 2.4Mb	1.3	0.15

¹PGE = platinum-group elements (Ir, Ru, Pd, Pt) and Au. ³The velocity for shot 2 was calculated from figure 10 in (2). ²Disc inserted flush to impact face of sabot. ⁴Sphere protrudes from impact face of the sabot by half its diameter (0.11 mm). ⁵Weighing and microprobe analysis of the ejecta in shot 4 has yet to be performed. All targets were molybdenum.

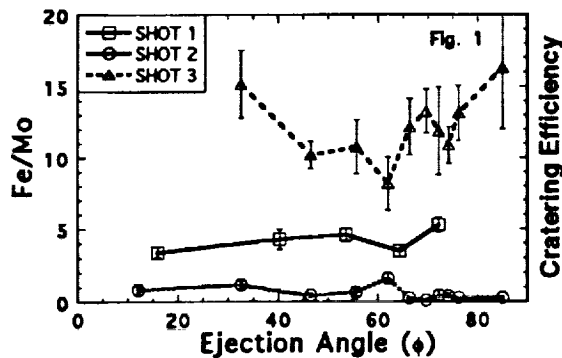


Figure 1. Mean Fe/Mo (mass ratio) versus angle of ejection (ϕ , angle from target surface). Error bars are standard deviation of the mean.

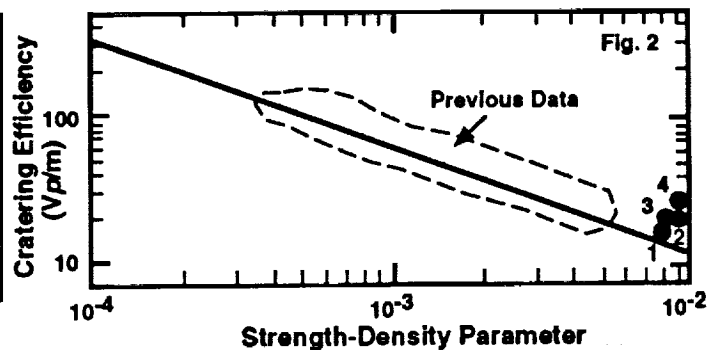


Figure 2. Crater volume scaling relationship (2) with present experimental data added.

(1) Evans, N.J., Ahrens, T.J., Shahinpoor, M. and Anderson, W.W. 1993. *Lunar Planet. Sci. Conf. XXIV*, March 15-19. (2) Holsapple, K.A. and Schmidt, R.M. 1982. *J. Geophys. Res.*, **87**, 1849-1870.

THEORETICAL ANALYSIS OF THE EXPLOSIVE EMPLACEMENT OF BASALTIC MAGMA IN LAVA FOUNTAIN ERUPTIONS: IMPLICATIONS FOR PYROCLAST DISPERSAL ON EARTH, VENUS AND MARS; S.A. Fagents and L. Wilson, Environmental Science Division, Lancaster University, Lancaster LA1 4YQ, England, UK.

Summary. A model has been formulated and implemented as a set of FORTRAN computer routines to simulate basaltic lava fountain eruptions. The model is used to make some predictions of the types of near-vent structure that should be formed for any given set of eruption initial conditions. It is found that the magma mass flux, exsolved volatile fraction and planetary environment most strongly control the dynamics of lava fountain activity. The fountain structure, in turn, determines the nature and morphology of the resulting volcanic feature, which may involve pyroclast coalescence into a lava flow, or the formation of spatter or cinder deposits. The model analyses are tested against terrestrial field and remote sensing data and some predictions for deposits on Venus and Mars are offered.

Introduction. It is well established that basaltic volcanism is a fundamentally important process operating on the terrestrial planets, both as a mechanism for heat transfer and as a resurfacing process. On Venus and Mars, the apparent absence of plate tectonics and surficial oceans implies that volcanic activity has even greater significance as a modifying process. Terrestrial explosive basaltic eruptions often manifest themselves as hawaiian style lava fountains, driven by the escape and expansion of magmatic volatiles, which tear the magma apart and eject the pyroclasts from the vent in a gas stream. On any given planet two factors, the exsolved volatile fraction and the magma mass flux, most strongly control the fountain dynamic structure and the pyroclast size distribution. These factors determine the amount of pyroclast cooling and the rate of accumulation at the ground surface [1], which together determine the extent, nature and morphology of the resulting deposit. Common deposits include: lava flows or ponds, spatter ramparts or cinder cones. In addition, planetary environmental factors (most importantly the atmospheric pressure and acceleration due to gravity) also significantly affect the style of eruption [2].

Fountain Model. A model has been formulated to simulate the ascent, fragmentation, eruption, flight and deposition of basaltic magma in order to explore the variations in the types of near-vent structure produced for any given set of magma initial conditions and planetary environment [3]. This draws on existing treatments of magma ascent and eruption [4,5] and computations of pyroclast trajectories [6], but also incorporates an approximation to the motions of volcanic and atmospheric gas induced by the erupting stream of gas and pyroclasts. There exist theoretical [7] and experimental [8,9] information on the way in which a jet of fluid interacts with a second fluid surrounding it. In this case the volcanic jet entrains the atmospheric gas, which causes a decrease in the upward motion of the jet and induces an inward and upward motion in the atmosphere. This information has been used to construct a model of the gas flow-field, and once the velocity and size distributions of the emerging pyroclasts have been specified, the paths of the pyroclasts through the gas flow-field can be computed, taking into account the details of the aerodynamic drag forces acting on the clasts. By keeping track of the landing sites of individual pyroclasts, a much more accurate prediction of the dispersal of pyroclasts from such eruptions than have been inferred by previous workers, who have ignored the presence of such a dynamic gas flow-field and computed pyroclast ranges as if in a vacuum [5,10,11]. Simulations have been performed for a wide range of values of magma mass flux and exsolved gas fraction, and for planetary environments representing the Earth, Venus and Mars.

Results and Discussion. The table below gives some results of the modeling for the Earth, Venus and Mars when the magma mass eruption rate is taken as 10^6 kg s^{-1} , the conduit geometry is cylindrical and the driving volatile is H_2O . The figures given for column height represent the height at which the upward gas velocity becomes equal to zero (left-hand figure) and 5 m s^{-1} (right-hand figure). For Venus the eruption velocity and column height are given for a total volatile content of 1.5 wt%, which is the minimum amount of magmatic gas required for magma fragmentation (and hence lava fountain activity) to occur. For the Earth and Mars values are given for volatile contents of 1.0 (in the upper end of the range of gas contents occurring in terrestrial basalts) and 1.5 (for comparison with Venus).

BASALTIC ERUPTIONS ON EARTH, VENUS AND MARS: Fagents, S.A. and Wilson, L.

Planet	Volatile content (wt%)	Eruption Velocity (m s^{-1})	Column Height (m)
Venus	1.5	57	>10000 / 2020
Earth	1.0	131	1900 / 1850
	1.5	167	2380 / 2300
Mars	1.0	226	4900 / 4750
	1.5	283	6970 / 6530

The values for the eruption velocity clearly show the effect of the planetary atmospheric pressure on the exsolution and expansion of magmatic volatiles during magma ascent: on Venus the high pressure suppresses gas expansion leading to low eruption velocities, whereas on Mars the low pressure leads to much greater exit velocities. Earth represents an intermediate case: a gas content of 1 wt% leads to an eruption velocity of $\sim 130 \text{ m s}^{-1}$ and a column height of $\sim 2 \text{ km}$. The computed deposit extends up to $\sim 150 \text{ m}$ from the vent, with by far the greatest proportion of material falling within a radius of $\sim 50 \text{ m}$. Within this annulus, the accumulation rate is likely to be sufficiently high for clast welding and/or coalescence to occur, which suggests that spatter deposits and lava flows will be formed. These predictions are in agreement with typical terrestrial deposits where the near-vent lava or spatter deposit is often surrounded by a halo of unwelded material.

On Venus the high atmospheric pressure will suppress gas expansion and retard clast flight outside of the fountain column. Within the column the smallest clasts will remain locked to the gas motion up to great heights since the upward velocity does not reach zero for a great distance ($>10 \text{ km}$ in the example given in the table). This is a result of the greater atmospheric density on Venus encouraging convection [10]. However, the coarser clasts making up the bulk of the fountain will fall out close to the vent (within a few vent radii) as a result of the low gas exit velocity (57 m s^{-1}) which will lead to far denser fountains and more localised deposits. The degree of clast cooling will therefore be minimal which, along with the greater accumulation rate of clasts in a more limited depositional area, implies a greater likelihood of clast coalescence and flow on landing.

On Mars, the low atmospheric pressure encourages gas exsolution and expansion in the conduit, hence greater eruption velocities. This, coupled with the low gravitational acceleration implies greater clast flights and would suggest that clasts undergo a greater degree of cooling. Thus one would expect commonly to observe widely dispersed pyroclastic deposits on Mars. However, the presence of very extensive lava flows suggests that this is not always the case which, in turn, suggests that the likely finer grain size of martian pyroclasts may be critical in maintaining column density and inhibiting cooling of the pyroclasts. An analysis of the dynamics of magma fragmentation may provide further insight into the importance of pyroclast size distributions on martian lava fountain dynamics.

We are currently working on the details of venusian and martian lava fountain models and will present a comparison of the results of analyses of lava fountain eruptions on the Earth, Venus and Mars with the aim of gaining a better understanding of the modes of formation of observed basaltic features.

References. [1] Head J.W. and Wilson L. (1986) *J. Volcanol. geotherm Res.*, **37**, 261-271. [2] Wilson L. (1984) *Vistas in Astronomy*, **27**, 333-360. [3] Fagents, S.A. Ph.D. thesis in preparation. [4] Wilson L. *et al.* (1980) *Geophys. J. Roy. astr. Soc.*, **63**, 117-148. [5] Wilson L. and Head J.W. (1981) *J. geophys. Res.*, **86**, 2791-3001. [6] Wilson L. (1972) *Geophys. J. Roy. astr. Soc.*, **30**, 381-392. [7] Prandtl L. (1954) *Essentials of Fluid Dynamics*, Blackie & Son Ltd., London. [8] Thring M.W. & Newby M.P. (1952) *4th Symposium on Combustion*, Cambridge, Mass., 798. [9] Morton B.R. *et al.* (1956) *Proc. Roy. Soc. Lond.*, **A234**, 1-23. [10] Head J.W. and Wilson L. (1986) *J. geophys. Res.*, **91**, 9407-9446. [11] Wilson L. *et al.* (1982) *ESA SP-185*, 107-113.

Mg and Ti Isotopic Compositions of CAI's from the Unusual Chondrite Acfer 214.

A. Fahey¹, and F. Wlotzka². ¹Lunatic Asylum, Division of Geological and Planetary Sciences, California Institute of Technology, Pasadena, CA 91125, ²Max-Planck-Inst. f. Chemie, Mainz, F.R.Germany.

Three Calcium-Aluminum-rich Inclusions (CAI's) have been identified in a thin section of Acfer 214. These inclusions have been examined in the S.E.M. and their major element compositions determined. Magnesium and Ti isotopic compositions were determined with the Caltech Ion Probe. Evidence for ²⁶Mg* was present in only one inclusion. Ti isotopes are normal in all 3 inclusions.

CAI-2 is ~120µm in diameter. The core region of CAI-2 consists mainly of hibonite that is intermixed with a Si-bearing, more Ca-rich phase similar to melilite. The divisions between these phases does not show obvious crystal boundaries. There are 3-5µm perovskite grains poikilolithically enclosed in the core and near the edge of the inclusion. The core region itself has a compact texture whereas voids are present around the periphery of the inclusion. CAI-3 is ~60µm in diameter and consists mainly of an intimate intergrowth of melilite and hibonite. The hibonite and melilite do not show sharp crystal boundaries. Perovskite crystals are poikilolithically enclosed in the melilite and hibonite. There are two regions that contain distinct hibonite crystals separated by voids. In addition, there is Fe-Ni-S-rich material in cracks and regions near the edge of the inclusion. CAI-4 (~130µm in diameter) has a compact texture and a core consisting mainly of melilite. Perovskite and spinel crystals are found throughout the melilite. Hibonite is also present near the rim and is intergrown with spinel. A perovskite-spinel rim surrounds part of the inclusion.

Magnesium isotopic measurements were made with the Caltech ion probe at a mass resolving power of $\Delta m/m \approx 3500$, sufficient to resolve interferences at the masses of the Mg isotopes. Madagascar hibonite was measured as a Mg isotope standard. The measured instrumental mass fractionation was: $F_{Mg} = -6.8 \pm 1.1 \text{ ‰}$. The measured $\delta^{26}Mg$ was computed via a linear mass fractionation law. The average $\delta^{26}Mg = 0.4 \pm 1.6 \text{ ‰}$ ($2\sigma_{\text{mean}}$) for Madagascar hibonite relative to $^{26}Mg/^{24}Mg = 0.13932$ [1]. Titanium isotopic measurements were made at a mass resolving power of $\Delta m/m \approx 6100$ sufficient to ensure that the interference due to the tail of ^{48}Ca at the center of ^{48}Ti was $\leq 1 \text{ ‰}$ (see Figure 2). The interference due to ^{48}Ca was monitored on the low mass tail of ^{48}Ti and by measuring ^{44}Ca . In addition, a correction for ^{46}Ca was made. Interferences at mass 50 due to V and Cr were monitored at masses 51, 52, and 53 respectively. Corrections were applied to the signal measured at mass 50. Corrections due to V and Cr were generally small for the meteoritic material (~1 ‰). Madagascar hibonite and terrestrial perovskite were measured as standards. A power law mass fractionation correction was applied to the interference-corrected isotopic ratios [2]. The measured values for Madagascar hibonite were $\delta^{47}Ti = -0.7 \pm 4.3$, $\delta^{49}Ti = -2.5 \pm 3.1$, and $\delta^{50}Ti = -0.4 \pm 3.3$, and for the terrestrial perovskite were $\delta^{47}Ti = -1.2 \pm 3.4$, $\delta^{49}Ti = 0.5 \pm 2.1$, and $\delta^{50}Ti = -0.3 \pm 1.9$ (errors are $2\sigma_{\text{mean}}$). The standard ratios were from Neiderer *et al.* 1981 [3].

Figure 1 shows the Al-Mg data for CAI-4. These data plot along a line of slope $(3.3 \pm 0.4) \times 10^{-5}$ ($2\sigma_{\text{mean}}$). The intercept of the line is not terrestrial within the errors. This is an indication that the inclusion may have been re-equilibrated during the decay of

CAI'S FROM CHONDRITE ACFER 214: Fahey A. and Wlotzka F.

^{26}Al . CAI-2 and CAI-3 show no excess ^{26}Mg within the errors of the measurement and show no significant intrinsic mass fractionation. Perovskite, and in some inclusions hibonite, was measured for its Ti isotopic composition in each of the three Acfer 214 inclusions. All of the inclusions measured show a "normal" Ti isotopic composition.

Acfer 214 CAI-4 was the only one of the three inclusion studied here that showed evidence of radiogenic ^{26}Mg . This is the first evidence of radiogenic ^{26}Mg in Acfer 214, although $^{26}\text{Mg}^*$ has been found in Acfer 182, which is generally considered part of the same meteorite (*e.g.* see [4]). CAI-4 has a significantly different texture than that of the other two inclusions. CAI-2 and CAI-3 have unusual intergrowths of hibonite and (perhaps) melilite where the two phases appear to "blend" into one another rather than showing sharp crystal boundaries. Further measurements, especially for REE abundances, will be made to further constrain the history of these inclusions.

[1]Catanzaro *et al.* (1966), *J. Res. Nat. Bur. Stand.*, **70a**, 453. [2]Fahey *et al.* (1987) *GCA*, **51**, 329.

[3]Neiderer *et al.* (1981), *GCA*, **45**, 1017. [4]Palme and Spettel (1993), *Meteoritics*, **28**, 272. Division Contribution #5360 (835). NASA NAGW-3297.

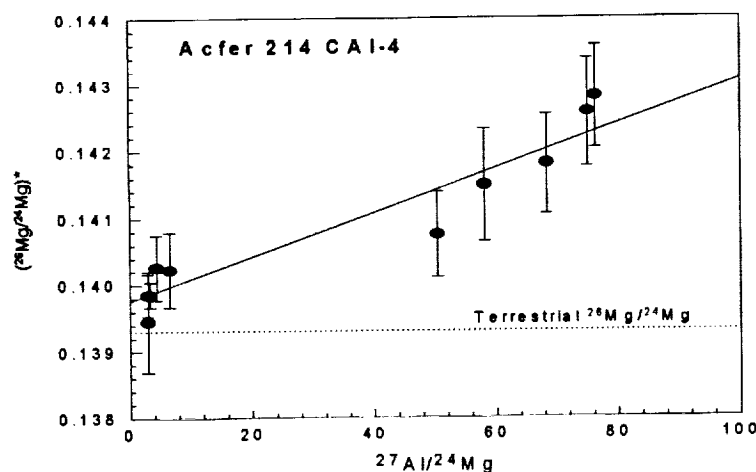


Figure 1.

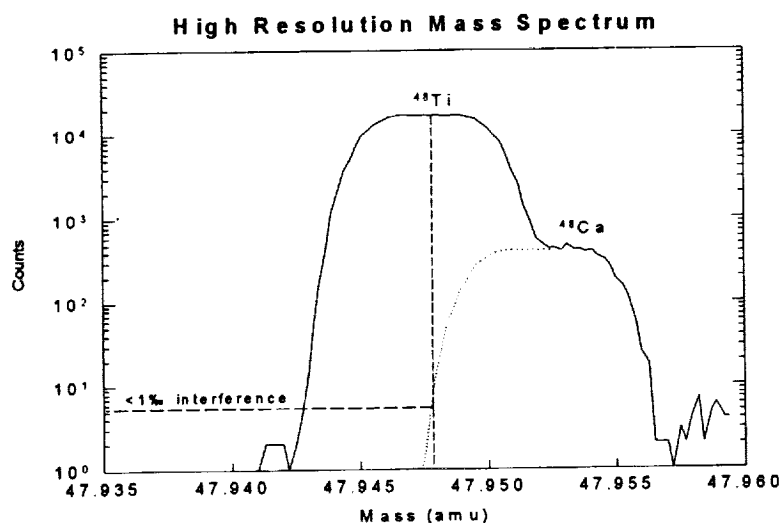


Figure 2.

WILL THE REAL ASTEROID SIZE DISTRIBUTION PLEASE STEP FORWARD

P. Farinella¹ and D. R. Davis²

1. *Observatoire de la Côte d'Azur, Nice, France*

2. *Planetary Science Institute, Tucson, Arizona*

The nature of the asteroid size distribution has been a question following the discovery of the second asteroid in the region between Mars and Jupiter, 192 years ago. Observationally based studies of the asteroidal size distribution have been carried out in the past 4 decades (Kuiper et al. 1958, Ap. J. Suppl. 3, 289, MDS; Van Houten et al. 1970, A&A Suppl. 2, 339, PLS; Cellino et al. 1991, MNRAS 253, 561). On the theoretical side, Dohnanyi (1969, JGR 74, 2531) showed how a collisionally relaxed system should be distributed assuming that the collisional outcomes were independent of size. Recently, with the Galileo encounters of asteroids Gaspra and Ida returning the first spatially resolved images of mainbelt asteroids, a number of interesting scientific questions arose whose answers depend on the asteroidal size distribution. Various workers have made a variety of assumptions about this distribution and we review these assumed distributions in light of what is really known about asteroids sizes.

The available sample of numbered asteroids is probably nearly complete only for diameters D larger than about 44 km (Cellino et al. 1991). According to the Cellino et al. work, some 600 – 700 asteroids exist with $D > 50$ km. Different models have been recently used to extrapolate the size distribution down to sizes of the order of 10 m (the projectiles producing the smallest resolved craters on Gaspra and Ida). Three recently used models are (see Fig. 1):

1. Farinella et al. (1992, A&A 257, 329) estimated the collisional lifetime of Gaspra by assuming a cumulative number $N(D > 50 \text{ km}) = 700$, and using the cumulative slopes -1 (as found by Cellino et al. between 44 and 145 km) for $50 \text{ km} > D > D_{tr}$ and -2.5 (the collisional equilibrium slope found by Dohnanyi) for $D < D_{tr}$. For $D_{tr} = 10$ and 25 km, this yields $N(D > 1 \text{ km}) = 1.1$ and 4.4 million, respectively. These are cases (1) and (2) in Fig. 1; cases (3) and (4) represent similar but more extreme assumptions, i.e. $D_{tr} = 1 \text{ km}$ and $D_{tr} = 40 \text{ km}$.
2. The size distribution for the current belt population derived by Davis et al. (1993, Planet. Space Sci., in press) by extrapolating the known population at $D = 44 \text{ km}$ with the geometric mean of results coming from the PLS cumulative slope assuming constant albedo (-1.95) and from a 'corrected random' albedo model according to Cellino et al.. The extrapolation was extended only down to $D = 5.5 \text{ km}$, with $N(D > 5.5 \text{ km}) = 64,300$. If this is further extrapolated with cumulative slopes of -1.95 and -2.5 (the best-fit PLS value and the Dohnanyi value), we get $N(D > 1 \text{ km}) = 1.8$ and 4.6 million, respectively.
3. The Galileo team (1992, Science 257, 1647) used differential slopes -2.95 (PLS) for $D > 0.175 \text{ km}$ and -3.5 (Dohnanyi) for $D < 0.175 \text{ km}$. From their assumed flux of $D > 0.1 \text{ km}$ projectiles on Gaspra, one can normalize the distribution and obtain $N(D > 1 \text{ km}) = 2.53$ million and $N(D > 50 \text{ km}) = 1230$. Thus their large-size population is overestimated by almost a factor 2 with respect to the real one. With a mean intrinsic collision probability of $P_i = 2.8 \times 10^{-18} \text{ yr}^{-1} \text{ km}^{-2}$, a mean radius $R = 6 \text{ km}$ and a minimum shattering projectile diameter of 0.35 km , the Galileo team population yields $N(D > 0.35 \text{ km}) = 1.96 \times 10^7$ and an expected lifetime of Gaspra $[P_i R^2 N(D > 0.35 \text{ km})]^{-1}$ of about 500 Myr, as stated in the Science paper — but this estimate should be viewed as very uncertain and population-dependent.

Actually, the available models suggest that the Galileo team population estimate is uncertain by about an order of magnitude in the diameter range between 1 and 10 km, and more so at smaller sizes, as different slopes can be used in the extrapolations. Note that the size distribution of fresh craters on Gaspra would suggest a very steep -3.3 cumulative slope for $0.01 < D < 0.1 \text{ km}$

ASTEROID SIZE DISTRIBUTION; P. Farniella and D.R. Davis

(Chapman et al., 1994, in press). On the other hand, Ida's craters give only a lower limit of about -2 to the cumulative slope in the same range, as the crater distribution is probably in equilibrium.

It is interesting to note that the size-frequency distribution of the observed asteroids does not follow the theoretical steady state slope predicted by Dohnanyi, i.e. a -2.5 cumulative diameter exponent. This is due at least partly to the violation of Dohnanyi's fundamental assumption about the size-independence of the collisional physics. Modern scaling theory suggests that collisional physics does depend upon size — and certainly gravity is a factor in how much collisional energy is required to disrupt a body. Also, variable slopes can result from a small-size cutoff of the distribution related to the production/removal of very small particles (Campo Bagatin et al. 1994, Planetary Space Sci., in press). Much further work is needed to: 1) determine observationally the size distribution of asteroids down to much smaller sizes and 2) understand theoretically what are the important physics for collisionally disrupting bodies of different sizes. Until we have such an improved understanding of the asteroids, authors should be aware of the implications of differing assumptions about the size distribution of asteroids on their calculations of cratering fluxes, asteroid lifetimes and ages, fragment yields to resonant orbits, etc.

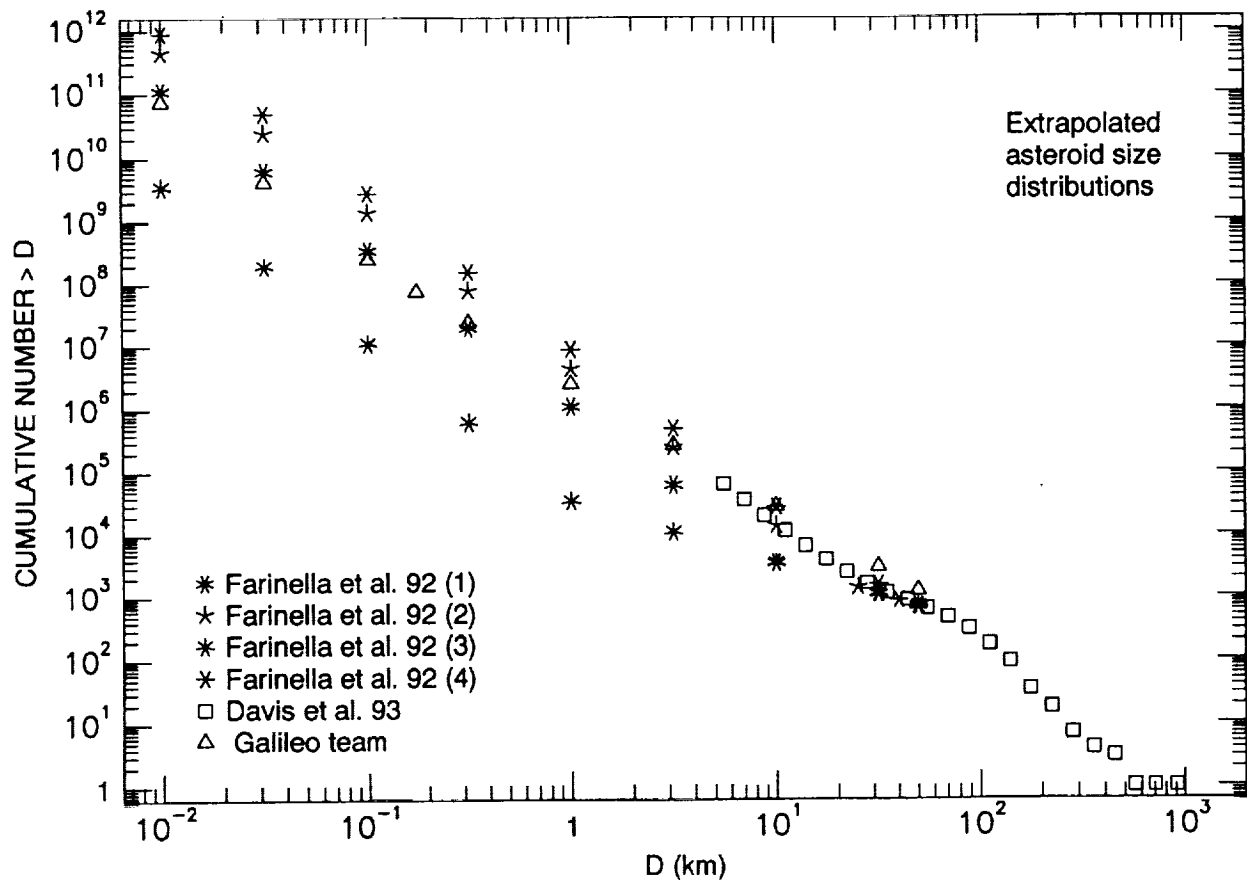


Figure 1. Various estimates of the asteroid size distributions.

EXOPALEONTOLOGY AND THE SEARCH FOR A FOSSIL RECORD ON MARS;
J. D. Farmer, D. J. Des Marais, NASA-Ames Research Center, MS 239-4, Moffett Field, CA 94035-1000

Although present Martian surface conditions appear unfavorable for life as we know it (1), there is compelling geological evidence that the climate of early Mars was much more Earth-like, with a denser atmosphere and abundant surface water (2). The fact that life developed on the Earth within the first billion years of its history (3) makes it quite plausible that life may have also developed on Mars (4). If life did develop on Mars, it is likely to have left behind a fossil record. This has called for a new subdiscipline of paleontology, herein termed "exopaleontology" (5), which deals with the exploration for fossils on other planets. The most important factor enhancing microbial fossilization is the rapid entombment of microorganisms by fine-grained, stable mineral phases, such as silica, phosphate or carbonate. The oldest body fossils on Earth are preserved in this way, occurring as permineralized cells in fine-grained siliceous sediments (cherts) associated with ancient volcanic terranes in Australia and South Africa (6,7). Modern terrestrial environments where minerals may precipitate in the presence of microorganisms include subaerial thermal springs and shallow hydrothermal systems, sub-lacustrine springs and evaporitic alkaline lakes, zones of mineralization within soils where "hardpans" (e.g. calcretes, silcretes) form, and high latitude frozen soils or ground ice.

Subaerial thermal spring deposits are key targets for a fossil record on Mars (8) because high rates of mineral precipitation may occur together with microbial activity. Volcanic terranes are widespread on Mars and some possess outflow channels that may have formed by spring sapping (9). The association of such features with potential heat sources, such as volcanic cones or thermokarst features, is evidence for the past existence of hydrothermal systems on Mars. Siliceous sinters are very favorable for preserving fossils because they are generally fine-grained and relatively insoluble under a neutral to alkaline pH. Common subaerial spring minerals include silica and carbonate, in addition to a number of hydrothermal clay minerals, formed by the alteration of host rocks. These minerals have characteristic spectral signatures in the Near- to Mid-IR. In addition, epithermal ore deposits have been identified using airborne magnetometers (10). The identification of thermal spring deposits from would greatly facilitate site selection for Mars exopaleontology.

Although rates of organic matter degradation appear to be quite high in thermal environments, a great deal of biological information is preserved in thermal spring sinters as macroscopic biosedimentary structures (stromatolites) and biogenic microfibrils (8,11). Many of the primary biogenic features of sinters survive diagenesis and we have recognized them in rocks as old as 350 Ma. The fluid inclusions contained in thermal spring deposits sample primary liquid and vapor phases, and potentially, also microorganisms and biomolecules (12).

Sublacustrine spring carbonates (tufas) are deposited at ambient temperatures where fresh water emerges as springs from the bottom of an alkaline lake. Precipitation rates are often high enough to entomb associated microbial mat communities. In contrast to sinter deposits, tufas often contain abundant microbial fossils and organic matter (5). Sublacustrine springs are also common in volcanic settings, in association with crater and caldera lakes. Such volcani-lacustrine deposits are frequently heavily mineralized and include some of our best examples of well preserved terrestrial communities (13). In pluvial lake basins in western North America, sublacustrine springs are particularly common along the distal edges of alluvial fans where they enter alkaline lakes. Fresh water typically enters the upper portions of alluvial fans, moving downslope through unconfined aquifers, and emerging at shallow depths along the lake shore margin (14). If lake basin shales are deposited on coarser deltaic sediments, say during a previous lake high stand, they may form an aquaclude, favoring the development of an artesian spring system and high rates of spring mineralization. With a confined aquifer, springs may emerge at a greater depths in the lake, rising along faults of other natural fracture systems. Fresh water may also be forced to the surface by density differences, rising over wedges of saline water formed during periods of intense evaporation (15). Such models are being applied in a general way to lake basins on Mars, in order to identify potential targets for orbital imaging and to develop strategies for surface exploration (16).

When evaporites crystallize from solution, they commonly entrap salt-tolerant bacteria within inclusions of brine. Evaporites have been suggested as potential targets for extant life on Mars (17), although debate persists regarding the long term viability of microorganisms in salt. Still, brine inclusions offer an excellent environment for preserving fossil microbes and biomolecules. The disadvantage of evaporites is that they are easily dissolved and tend to have short crustal residence times, particularly where there is an active hydrological system. Thus, most

MARS EXOPALEONTOLOGY: J.D. Farmer and D.J. Des Marais

Precambrian evaporites are known from crystal pseudomorphs that were preserved by early replacement with silica or barite. The most likely places for evaporites on Mars are terminal lake basins, including impact craters and volcanic calderas, where standing bodies of water may have accumulated under arid climatic conditions. Evaporites possess characteristic spectral signatures in the Near-IR (18) and such data could be acquired from orbit.

Most terrestrial soils contain abundant microorganisms, and microfossils and biogenic fabrics are often preserved in hard pan deposits (19). This occurs as surface water percolates downward through soils, soluble compounds are dissolved from upper zones and re-deposited at depth forming mineralized soil horizons or "hard-pans" of carbonate, or under wetter climates, Fe- and Al-oxides. The Viking biology experiments suggest that surface soils on Mars are highly-oxidizing and destructive to organic compounds. However, mineralized soil horizons could protect fossil organic matter from oxidation and should not be overlooked as potential targets for exopaleontology. Interestingly, at the Viking Lander 2 site, soil exhibit surface crusts suggestive of cementation (20).

Although ice may also afford protection to organic matter against oxidation, the long term "cryopreservation" of organisms seems unlikely given the tendency of ground ice to be lost by sublimation under the present Martian climate. Climate models, supported by geomorphic evidence, suggest that ground ice on Mars is presently unstable at latitudes <40 degrees (21). This restricts potential target areas for fossiliferous ice to high latitudes. Given the potential for periodic global warming on Mars, it difficult to evaluate the time range over which ground ice and frozen soils may have been stable; thus, ice is given a lower priority for exopaleontology than the other mineral deposits mentioned.

In exploring Mars for molecular fossils, priority should be given to sedimentary deposits that are the most likely to have maintained a closed chemical system after deposition. Fine-grained marine and lacustrine sediments (e.g. shales, mudstones) tend to exhibit higher organic contents and low permeabilities. Certain classes of clay minerals selectively bind molecules (e.g. biogenic ammonia) as interlayer cations, thereby retaining a signature of the original biological environment long after organic matter has been thermally degraded (22). Compaction of fine-grained sediments, accompanied by early mineralization (cementation), may further reduce permeability, promoting the preservation of organic materials. Precambrian microorganisms and even macroalgae are often preserved as organic impressions in shales or fine-grained volcanic ash, attesting to the ability of such sediments to protect organic materials from oxidation. Potential targets on Mars for organic-rich shales include prodelta and deeper water facies of terminal lake basins (16) and possibly volcanic ash deposits within volcanic-lacustrine sequences.

References: (1) Klein, H. P. (1992) *Orig. Life Evol. Biosphere* 21, 255-261; (2) Pollack, J. B., et al. (1987), *Icarus* 71, 203-224; (3) Oberbeck, V.R. and Fogleman, G. (1989), *Orig. Life Evol. Biosphere* 19, 549-560; (4) McKay, C.P. and Stoker, C.R. (1989), *Rev. Geophys.* 27, 189-214; (5) Farmer, J.D. and Des Marais, D.J. (1993), *Case for Mars V*, 33-34; (6) Awramik, S.M. et al. (1983), *Science* 20, 357-374; (7) Walsh, M.M. and Lowe, D.R. (1985), *Nature* 314, 530-532; (8) Walter, M.R. and Des Marais, D.J. (1993), *Icarus* 101, 129-143; (9) Carr, M.H. (1981), *The Surface of Mars*, Yale Univ. Press, 232 pp.; (10) Goetz, A.F.H. et al. (1983), *Econ. Geol.* 78, 573-590; (11) Farmer, J.D. and Des Marais, D.J. (in press), in Stal, L.J. and Caumette, P., eds., *Microbial Mats. Structure, Development, and Environmental Significance*, Springer-Verlag; (12) Bargar, K.E. et al. (1985), *Geology* 13, 483-486; (13) Rolfe, W.D.I. et al. (1990), *Geol. Soc. Amer. Spec. Paper* 244, 13-24; (14) Blevins, M.L. et al. (1987), Los Angeles Dept. of Water and Power, Unpubl. Rept. (March 1987); (15) Rogers, D.B. and Dreiss, S.J. (1993) *Geol. Soc. Amer., Abstracts* 25(6), 183; (16) Farmer, J.D. et al. (in press) in Greeley, R., ed., *Mars Landing Site Catalog*, NASA Ref. Publ. 124; (17) Rothchild, L.J. (1990), *Icarus* 88, 246-260; (18) Crowley, J.K. (1991), *Jour. Geophys. Res.* 96 (B10), 16,231-16,240; (19) Jones, B. and Kahle, C.F. (1985), *Journ. Sed. Pet.* 56, 217-227; (20) Moore, H. J. et al (1987), *U.S. Geol. Survey Prof. Paper* 1389, 22 pp.; (21) Squyres, S.W. and Carr, M.H. (1986), *Science* 231, 249-252; (22) Compton, J.S. et al. (1992), *Geochem. Cosmochem. Acta* 56, 1979-1991.

DIAPLECTIC TRANSFORMATION IN CLINOPYROXENE
(PUCHEZH-KATUNKY ASTROBLEME, RUSSIA). V. Feldman, S. Kotelnickov,
L. Sazonova, E. Guseva. Moscow State University, Russia.

Diaplectic transformation in clinopyroxene have been studied in the Vorotilovo core hole (Puchezh-Katunki astrobleme, Russia) at the depth of 0,5-5,2 km under $P_{\text{shock}}=0,5-50$ GPa respectively. Planar fractures, planar elements, mechanical twinnings, impact-thermal decomposition with the formation of new mineral aggregate have been observed in this pyroxene.

Puchezh-Katunki astrobleme is situated in the Volga region about 100 km, north from the town of Nizhnii Novgorod [1].

Clinopyroxene is one of the minerals of Archean amphibole-plagioclase schists which make the astrobleme target together with plagiogneisses and biotite gneisses. Clinopyroxene is a relict mineral of facies of granulite metamorphism and it is present in schists in quantities from tenth to 20-30%. The microprobe analyses have shown that the clinopyroxene composition in the studied samples has not gone essential transformations under the shock loading and changes in the following limits: $\text{En}_{34-42}\text{Fs}_{12-20}\text{Wo}_{42-47}$. The typical chemical composition of CPx has been given in table.

The shock loading has been estimated by quartz transformation [2] in gneisses interbedding with schists. With shock loading increase characteristic diaplectic transformations have been observed in pyroxene. Planar fractures and planar elements appear at shock loadings more than 15-20 GPa. Under all shock loadings the planes (110) and (001) are present, and the quantity of other planes - (121), (221), (100), (010), ($\bar{1}01$), ($2\bar{1}\bar{1}$), ($11\bar{1}$), ($01\bar{1}$), ($14\bar{3}$), ($\bar{3}21$), ($\bar{2}11$), ($21\bar{1}$) varies in different samples but in general has the tendency of increasing with P_{shock} increasing. Mechanical twinnings on (001) plane have often been observed, the part of grains with such twinnings increasing with P_{shock} increasing

DIAPLECTIC TRANSFORMATION...Feldman V. et al.

up to 30-35% at 35-40GPa. The angle of optical axes ($2V_{Ng}$) decreases from 62° at 0.5 GPa to 55° at 40-45 GPa .

Isotropization and diaplectic glasses are not observed in pyroxene. Instead of it impact-thermal decomposition of clinopyroxene with the formation of ultrathin grain (1-5 mkm) aggregate of secondary minerals begins approximately at 50 GPa. This aggregate includes amphibole, plagioclase, secondary clinopyroxene and magnetite (table). The ratio of gross aggregate composition and that of initial pyroxene have shown that secondary association require Si, Fe outward migration and on this account enrichment of it by Al. The temperatures of formation of such aggregates estimated by Amf-Pl and Amf-cPx thermometers [3] are 840° - 880° C. It should be noted that complete decomposition of pyroxene in the studied shock loading interval is seldom observed.

[1]. Feldman V.I. et al., Abstr. XXIII LPSC, Houston, 1992, p.351-352. [2]. Feldman V.I. Petrology of impactites, Moscow, MSU, 1990, 299p. (in Russian). [3]Perchuk L.L., Rjabchikov I.D. Phase correspondence in mineral systems. Moscow, 1976, 287p.(in Russian).

Chemical composition (weight %) of CPx and that of its shock-thermal decomposition products in the rocks of the Puchezh-Katunki astrobleme.

Oxides	CPx from target	Pl from target	Minerals from aggregate after Cpx, $P_{shock} = 50\text{GPa}$			
			CPx	Amf	Pl	Mgt
SiO ₂	51.39	61.13	51.67	54.55	56.15	0.20
TiO ₂	0.28	0.01	0.58	0.10	0.10	5.20
Al ₂ O ₃	2.43	23.69	2.61	24.58	26.65	1.84
FeO	11.41	0.08	8.02	3.42	0.96	91.01
MnO	0.32	0.19	0.46	0.09	0.07	0.85
MgO	11.33	-	15.51	2.40	-	0.30
CaO	21.82	5.88	20.43	9.74	9.85	0.43
Na ₂ O	0.87	8.08	0.59	4.77	5.92	0.16
K ₂ O	0.11	1.04	0.13	0.35	0.39	0.03

MODELING THE SPACE WEATHERING-INDUCED OPTICAL ALTERATION OF LUNAR SOILS: FIRST RESULTS; Erich M. Fischer, Carle M. Pieters and Stephen F. Pratt; Department of Geological Sciences, Brown University, Providence, RI 02912.

Introduction: On atmosphereless bodies such as the Moon, space weathering processes alter the optical properties of the surface material and consequently greatly interfere with accurate remote compositional interpretation. These optical effects increase systematically with increasing exposure and are superimposed upon spectral properties diagnostic of mineralogy. Because the optical properties of lunar soils are a function of both degree of surface exposure as well as composition, in order to accurately assess the composition of lunar soils using remotely acquired visible and near-infrared spectroscopic data, it is necessary to develop a physical model which quantitatively describes the alteration of lunar soil optical properties with exposure. A related issue is the need to determine what within the soil is responsible for altering the optical properties. Although work in the 1970's (i.e., 1;2;3;4;5;6) initially addressed these issues, recent work by Fischer and Pieters (7;8), Pieters et al. (9) and Hapke (10) have refocused attention on this subject and underlined the need for detailed analyses relating the petrographic and chemical features of soils at different evolutionary stages to their optical properties. To these ends, a consortium of collaborating scientists from Brown University (E.M. Fischer and C.M. Pieters), the Johnson Space Center (D.S. McKay, L.P. Keller, R.V. Morris and S.J. Wentworth) and Indiana University (A. Basu) has been formed. Described here are the first results of modeling lunar optical alteration using a suite of Apollo 16 soils.

The Apollo 16 soil suite: In order to investigate and model the source of lunar soil optical alteration, a suite of five Apollo 16 soils of similar chemical compositions, but varying exposure ages was identified by the spectroscopy group at Brown (soils 61221, 67461, 67701, 63321 and 64801). The assumption underlying this analysis is that these five soils can be considered to be equivalent soils observed at different stages of evolution (spectroscopically, this appears to be a tenable assumption with the exception of 67461, which will therefore be excluded from this discussion). A goal of the consortium is to characterize in detail the petrographic, chemical and optical changes a soil (or soil components) of given composition undergoes with increasing exposure at the lunar surface. Of particular interest is to quantitatively relate the physical and chemical properties of the soils to optical properties. To date, four of the five soils have been sieved in freon to a range of size fractions extending from 500-1000 μ m to <10 μ m, have been measured for I_S by ferromagnetic resonance (to characterize the degree of exposure), and have been spectroscopically measured from 0.3 μ m to 2.6 μ m (soil 63321 has not yet been analyzed). In addition, petrographic and chemical data are currently being collected.

Spectral properties of size fractions: Shown in Fig. 1 are spectra of the bulk and size fractions of sub-mature soil 67701 (obtained at incidence=30° and emergence=0° with the RELAB bi-directional spectrometer). The spectral systematics between the size fractions of 67701 are essentially identical to those of the other soils in the suite. These particle size analyses of the Apollo 16 soil suite substantiate the conclusion of Pieters et al. (9) from study of size fractions of Apollo soil 10084 and three Luna soils that the spectral properties of the fine fraction (particles <25 μ m or <45 μ m) are most equivalent to the spectral properties of the bulk soil. The Pieters et al. study, however, did not separate particles less than 25 μ m in diameter and thus did not address the role of the very finest fraction -- particles <10 μ m. In the current study, the soils are sieved to <10 μ m. The spectral properties of the <20 μ m, 10-20 μ m and <10 μ m fractions are found to be notably different from each other and from the systematics that characterize the spectral properties of the larger size fractions. Particles in the 10-20 μ m range exhibit among the steepest continuum slopes of the size fraction suite, and are characterized by slightly more prominent absorption bands than the bulk soil. The spectral properties of the <10 μ m fraction are the most unique -- characterized by a distinct flattening towards longer wavelengths and exhibiting virtually no 1 μ m and 2 μ m absorption features. Measurement of the <10 μ m fraction at forward scattering geometries as well as with various surface textures yields spectra of similar shape, indicating that the spectral character of the <10 μ m fraction is an inherent property of the material and not dominantly a sample surface effect.

Optical modeling: Shown in Fig. 2 are spectra of the bulk <1000 μ m soils 61221, 67701 and 64801. As described above, the fundamental assumption of this analysis is that these soils can be considered to represent different stages of soil evolution. To analyze the variation of optical properties with exposure, a model of the following form was developed:

$$\ln(R_{\zeta} \cdot 100) = (\ln(R_{\zeta=\text{mat}} \cdot 100))^{(1-k \cdot (70-\zeta))}$$

where ζ equals the value of I_S/FeO , R_{ζ} equals the reflectance of a soil of ζ I_S/FeO at a given wavelength, $R_{\zeta=\text{mat}}$ is the reflectance at the same wavelength of a mature soil of the same chemical composition, and k is an "optical alteration constant" for the given wavelength. For the purposes of this analysis, it is assumed that soils are at an "optical steady-state" at $I_S/\text{FeO} \geq 70$ ($\zeta=70$ for $I_S/\text{FeO} \geq 70$; see (8)). Performing a grid search to solve for k (and $R_{\zeta=\text{mat}}$) using the spectra and I_S/FeO values of the three soils in Fig. 2 as model inputs, the optical alteration constant curve illustrated in Fig. 3 was calculated. Use of the natural log of the reflectance rather than the reflectance alone appears to linearize the change of optical path length resulting from varying absorption coefficient; consequently, the optical alteration constant curve exhibits little to no residual absorption features. Using reflectance instead results in a curve for k which exhibits significant absorption features -- unrealistic for the concept of k as a rate constant in the model above.

MODELING LUNAR OPTICAL ALTERATION: Fischer E.M. et al.

Employing the optical alteration constant k in a forward modeling sense, a suite of spectra can then be calculated representing the optical evolutionary states of a soil of composition similar to soils 61221, 67701 and 64801 (Fig. 4). The optical alteration constant calculated for the three soils in Fig. 2, however, is not directly applicable to soils of other compositions (not shown). This indicates that the model in its present form requires modification in order to describe the optical alteration of lunar soils in a more generic manner. Nevertheless, this analysis shows extreme promise for providing the ability to normalize and eventually remove the optical contribution due to exposure at the lunar surface. This in turn will ultimately lead to the fundamentally important capability to accurately quantify lunar surface composition using remote visible and near-infrared spectroscopy.

Acknowledgements: This material is based upon work supported under a National Science Foundation Graduate Fellowship (EMF). EMF would also like to thank the Lunar and Planetary Institute for a summer LPI Visiting Graduate Fellowship, during which a portion of this work was undertaken. This research was also supported by NASA grant NAGW-3079 (CMP). RELAB is supported by NASA as a multi-user facility under Grant NAGW-748.

References: 1) Hapke B.W. et al. (1970) *Proc. Ap. 11 LSC*, 2199-2212; 2) Adams J.B. and McCord T.B. (1973) *Proc. LSC* 4, 163-177; 3) Gold T. et al. (1974) *Proc. LSC* 5, 2413-2422; 4) Hapke B. et al. (1975) *The Moon* 13, 339-353; 5) Charette M.P. et al. (1976) *Proc. LSC* 7, 2579-2592; 6) Adams J.B. et al. (1979) *LPSC X*, 1-3; 7) Fischer E.M. and Pieters C.M. (1993) *LPSC XXIV*, 477-478; 8) Fischer E.M. and Pieters C.M. (1994) Remote determination of exposure degree and iron concentration of lunar soils using VIS-NIR spectroscopic methods. To be submitted to *Icarus*; 9) Pieters C.M. et al. (1993) *JGR* 98, 20817-20824; 10) Hapke B. (1993) *LPSC XXIV*, 605-606.

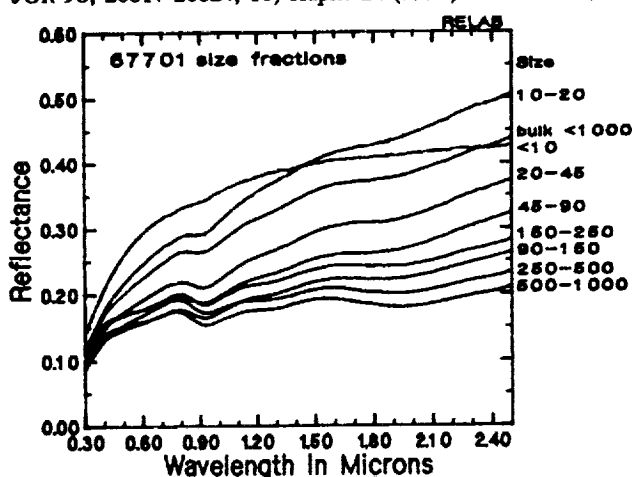


Fig. 1: Spectra of bulk soil 67701 and size fractions @ $i=30^\circ$ $e=0^\circ$. Particle size is shown in microns on the right. The $<20\mu\text{m}$ fraction is excluded for clarity.

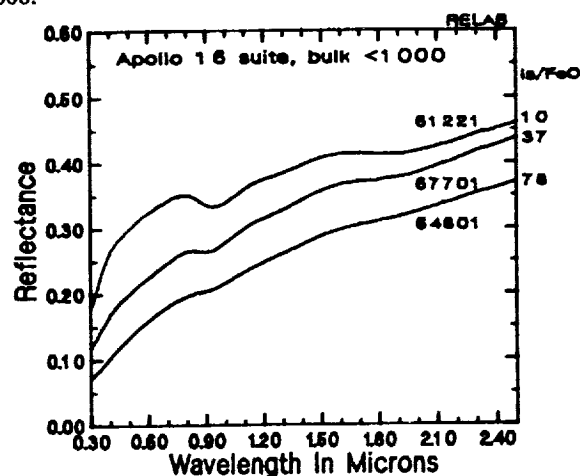


Fig. 2: Spectra of bulk soils 61221, 67701 and 64801. I_F/FeO measured for these analyses is shown on the right (R.V. Morris, unpublished data).

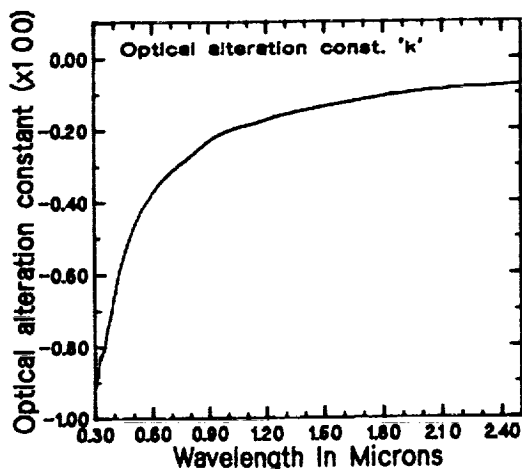


Fig. 3: The "optical alteration constant" k calculated for the soils shown in Fig. 2.

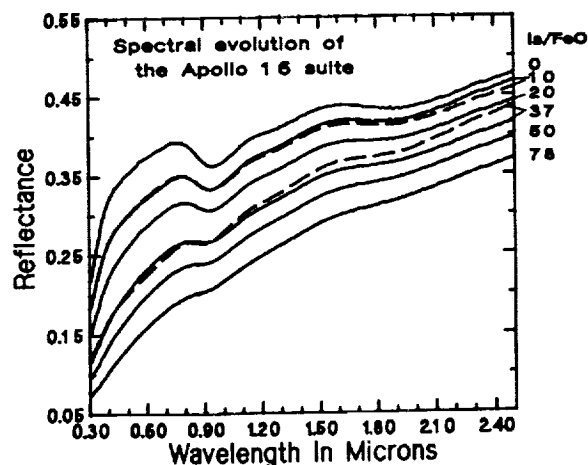


Fig. 4: A suite of calculated spectra (solid lines) representing the optical evolutionary states of the Apollo 16 soil suite. Dashed spectra are actual bulk soil spectra (see Fig. 2). I_F/FeO is given on the right. Actual and calculated spectra for $I_F/\text{FeO}=78$ are identical. Slight misfit results from the relative redness of 67701.

GRAIN-SIZE FRACTIONS OF SiC IN MURCHISON ARR: A METHOD FOR THE ANALYSIS OF CARBON AND ITS ISOTOPES BY STEPPED COMBUSTION; A.V. Fisenko, A.B. Verchovsky, L.F. Semjenova, J.W. Arden¹ and C.T. Pillinger². Vernadsky Institute, Moscow, Russia, ²Dept. of Earth Sciences, Oxford University, Oxford, U.K. ²Planetary Sciences Unit, Dept. of Earth Sciences, The Open University, Milton Keynes, U.K.,

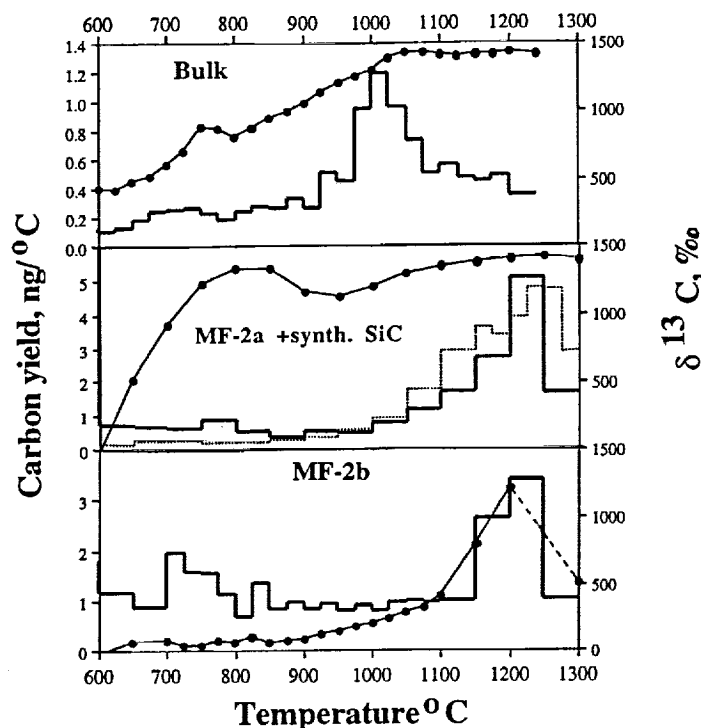
A technique is described for obtaining stepped combustion release profiles and isotopic measurements from small samples of silicon carbide separated according to grain size. Preliminary results for the 0.2 to 0.8 μm fraction of Murchison are presented; they suggest that the bulk of the SiC in this meteorite is $< 0.2\mu\text{m}$ in size.

It is now quite clear that interstellar SiC in primitive chondrites has a wide size distribution. Individual grains of different dimensions have been studied by ion probe [eg. 1] whilst aliquots of size separated material have been used from noble gas studies employing stepped heating for extraction purposes [eg. 2]. SiC has also been investigated on many occasions by the technique of stepped combustion. So far any effort to correlate the carbon yield and $\delta^{13}\text{C}$ measurements obtained by the combustion method with the ion probe and other data on size fractions has up to a point relied on intuitive or circumstantial arguments. The most relevant results derive from studies of an acid resistant residue (ARR) from the Indarch meteorite [3] and the analysis to two small ARR fractions from the Murray carbonaceous chondrite [4, 5]. Information of the type we seek is vital to the separation, understanding and characterisations of various types of interstellar grains so that the relative proportions of contributions to the early solar system can be established.

Now that static vacuum mass spectrometers are routinely employed for carbon and nitrogen isotope measurements at the picomole to nanomole level, it should be feasible to burn relative small (sub-microgram) aliquots of SiC to ascertain their stepped combustion properties, isotopic composition and trace nitrogen abundance and $\delta^{15}\text{N}$ values with an eventual aim of correlating with noble gas and other data. The major problem with pursuing such an ambition is processing small specimens without losing or contaminating them. Herein we describe a preliminary investigation of a procedure for treatment of acid resistant residues, which involves minimal handling of grain size fractions destined for analysis by the stepped combustion method.

The method is based on the use of Millipore (Millipore Corporation, Bedford, MA) membranes with the capability of filtering submicron particles. Murchison ARR was obtained by our usual $\text{HF/HCl/Cr}_2\text{O}_7^{2-}$ and HClO_4 (180°C) treatment. Before separation of SiC, the colloidal diamond was removed in aqueous ammonia. A suspension of the coarse fraction containing SiC and oxide grains was passed through a 1 cm diameter, 0.8 μm , Millipore filter and then a 0.2 μm filter, using a syringe and stainless steel membrane support. The material collected on the 0.8 μm membrane was designated MF-1; that on the 0.2 μm filter (grains between 0.2 and 0.8 μm) MF-2. After drying, sectors cut from the membrane MF-2 were taken for carbon isotope analysis but first they were treated with $\text{Cr}_2\text{O}_7^{2-}$ (80°C) and HClO_4 to destroy the organic substrate *in situ* in the quartz tube to be employed for the combustion. In one case MF-2A, perchloric acid at 80°C for 30 minutes was also used; in another, the sample MF-2B was left for 12 hours at 20°C with perchloric before heating to 80°C for 30 minutes. As a further precaution, the quartz vessel was combusted repeatedly at 600°C to remove any last vestige of filter material or other terrestrial contaminant, before the stepped combustion proper was carried out.

In the figure, we compare the stepped combustion analyses for MF-2A and MF-2B with the stepped combustion of a Murchison ARR similar to the one from which they were derived. Both the samples of 0.2 to 0.8 μm grains revealed a maximum carbon yield from combustion at between

GRAIN-SIZE FRACTIONS OF SiC; A.V. Fisenko *et al.*

1200 to 1250°C. MF2A gave a maximum $\delta^{13}\text{C}$ of +1414‰ at this temperature comparable to the plateau value for the bulk residue. We were unable to obtain isotope measurements for the maximum carbon released between 1200 and 1250°C for MF2B because of an analytical problem but the 1150 to 1200°C step, (the second largest yield) gave a $\delta^{13}\text{C}$ of +1224‰. The replicate release profiles we obtained for MF-2A and 2B are matched almost identically by that from a combustion performed for a sample of synthetic silicon carbide nominally less than 1 μm in size [6], (see dotted profile compared to MF-2B). A clear difference between MF-2A and 2B is the presence of a small amount of carbon with $\delta^{13}\text{C}$ up to +1345‰ burning at 800°C. Since the difference between the two samples is only the nature of the HClO_4 treatment, it is tempting to suggest that MF-2A contains a component of ^{13}C enriched carbon which had not been eliminated by the acid.

Perhaps the most surprising observation which can be made from the data is the lack of carbon burning at temperatures around 1050°C, the step with maximum carbon yield for the unseparated Murchison ARR. On the basis of this information, we can surmise that the greater part of the SiC mass in Murchison is in grains which are less than 0.2 μm in size. Although Stokes saw settling results from Amari *et al.* [7] are consistent with 0.1 to 0.2 μm SiC grains being most abundant by mass, these workers suggested that less than 0.2 μm particles constitute only *ca.* 30% of the overall mass complement of SiC. There are undoubtedly severe problems in manipulating tiny grains which may account for the observed discrepancy between the two sets of results.

In conclusion, the techniques reported here seem very appropriate for obtaining data for carbon and its isotopic composition from small SiC samples. Even if these highly resistant grains are deliberately contaminated by physical processing, a combination of chemical treatment and stepped combustion allows the information they contain to be recouped.

References: [1] Virag *et al.* (1992) *GCA* 56, 1715. [2] Lewis R.S. *et al.* (1990) *Nature* 348, 293. [3] Russell S.S. *et al.* (1993) *Meteoritics* 28, 425-426. [4] Wright I.P. *et al.* (1988) *Meteoritics* 23, 312. [5] Ash, R.D. Ph.D. Thesis, Open University [6] Pillinger C.T. and Russell S.S. (1993) *J. Chem., Soc. Farad. Trans.* 89, 2297-2304. [7] Amari S. *et al.*, submitted to *GCA*.

ISOTOPIC AND ELEMENTAL FRACTIONATIONS PRODUCED DURING EVAPORATION OF THE ALLENDE CARBONACEOUS CHONDRITE. C. Floss¹, A. El Goresy¹, G. Kransel², W. Rammensee², H. Palme³ and E. Zinner⁴ ¹Max-Planck-Institut für Kernphysik, 69029 Heidelberg, Germany; ²Mineral.-Petrograph. Institut, Universität Köln, 50674 Köln, Germany; ³Max-Planck-Institut für Chemie, 55020 Mainz, Germany; ⁴McDonnell Center for the Space Sciences, Washington University, St. Louis, MO 63130.

Refractory inclusions (CAIs) from carbonaceous chondrites have provided important clues to the processes active in the early solar system. Some CAIs exhibit mass-fractionated isotopic (Mg, Si and Ca) compositions that deviate from normal values by much larger amounts than can be accounted for through igneous differentiation processes [1,2]; enrichments in both the heavy and light isotopes are observed, as expected for evaporation residues from a homogeneous melt and condensates from the concomitant vapor, respectively. In addition, large mass dependent fractionations of O (along with Mg and Si) are observed in F (Fractionation) and FUN (Fractionation and Unknown Nuclear) inclusions. Although these fractionations are commonly interpreted as the result of Rayleigh distillation processes in the solar nebula, the data, particularly correlated data on several elements, require multi-stage processes [1,2]. Some inclusions also show trace refractory element fractionations that are consistent with a distillation origin [3], although isotopic fractionations generally are not obviously related to either bulk or trace element compositions.

We have begun a series of evaporation experiments in order to better understand the processes and conditions under which mass-dependent isotopic and elemental fractionations are produced. We used powdered bulk Allende as a starting material. Individual samples, ranging in weight from 23 to 75 mg, were suspended from Re wire loops and evaporated from the liquid state to varying degrees in a vacuum furnace at 10^{-8} bar. Temperatures ranged from 1450 – 1750° C and run durations were from 15 to 180 minutes. Major element compositions of the residues were determined with the electron microprobe, and isotopic and trace element analyses were made with the ion microprobe. In these initial runs, mass losses ranging from 13–96 % were observed. Most residues consist primarily of olivine and glass with occasional tiny euhedral spinels. However, two of the samples with the highest mass losses ($\geq 95\%$) have lost more than 99% of their Fe, Mg and Si, and consist of a heterogeneous mixture of submicroscopic grains of Ca-aluminates. Individual analyses (which are probably not on discrete grains) give compositions that correspond to linear mixtures of $12\text{CaO} \cdot 7\text{Al}_2\text{O}_3$ and $\text{CaO} \cdot \text{Al}_2\text{O}_3$, and $\text{CaO} \cdot \text{Al}_2\text{O}_3$ and $\text{CaO} \cdot 2\text{Al}_2\text{O}_3$ (calcium dialuminate), respectively (Fig. 1). The Ca/Al ratios of these two residues are 7% and 51% lower than those of bulk Allende (0.68 and 0.37 versus 0.73), reflecting a preferential loss of Ca over Al in these samples. The evaporation behaviors of the major elements are consistent with the results of Wang *et al.* [4], who conducted similar experiments using a synthetic starting material of CI chondritic composition.

Isotopic measurements show normal Ca and Ti compositions for all residues analyzed so far, whereas both Mg and Si exhibit fractionations favoring the heavy isotopes (up to 45‰ per amu for Si), consistent with a Rayleigh distillation model. Oxygen isotopic compositions, measured in two of the residues, also show a mass-dependent enrichment of the heavy isotopes. Determination of appropriate evaporation reactions in a complex substance such as the one used here is difficult, as several different reactions are likely to have taken place at various stages during the evaporation process. Calculated gas/liquid partition coefficients (α 's) for Si evaporation are similar within errors to those observed by Davis *et al.* [5] for forsterite evaporation, for which the appropriate reaction is $\text{Mg}_2\text{SiO}_4(\text{l}) \rightarrow 2\text{Mg}(\text{g}) + \text{SiO}_2(\text{g}) + \text{O}_2(\text{g})$ [6].

EVAPORATION OF THE ALLENDE CHONDRITE Floss C. *et al.*

This implies that most Si evaporated as SiO_2 , although the slightly higher α values determined from our experiment suggest the involvement of heavier gas species or isotopic inhomogeneity during evaporation, as was also true for the Davis *et al.* experiment [5]. Partition coefficients calculated for Mg evaporation, however, are much closer to unity than those reported by these authors and, furthermore, are higher than theoretical α 's based on evaporation of Mg as either the monatomic species or as MgO, suggesting complex evaporation behavior for this element.

Trace element measurements in one of the residues with the highest mass losses show enrichments up to $45 \times \text{CI}$ for most of the REE as well as for several other refractory lithophile elements (Fig. 2). Hafnium, expected to have an abundance similar to that of Zr, shows a 60% depletion relative to that element. Cerium and, to a lesser extent, Pr exhibit volatility-related depletions ($\text{Ce}/\text{Ce}^* = 0.002$; $\text{Pr}/\text{Pr}^* = 0.509$). Such depletions have been observed in several hibonite-rich inclusions [3] and in other laboratory evaporation experiments [3,4]. Wang *et al.* [4] noted that the oxidizing conditions implied by these depletions were probably due to the release of O during evaporation of major-element oxides. Despite their nominally similar volatilities under solar nebula conditions [7], Ba and Sr abundances differ, with the former being present at chondritic levels and the latter being enriched to $25 \times \text{CI}$. This is a further indication of oxidizing conditions during evaporation, because the volatility of Ba, relative to that of Sr, increases under oxidizing conditions [7]. Vanadium, which also becomes more volatile under oxidizing conditions, is present at less than chondritic abundances. Both elements are also depleted in HAL-type hibonite inclusions [3].

The results of these preliminary experiments are in good agreement with those of [4], despite the differences in starting materials, and show that isotopic fractionation effects as well as major and refractory trace element depletions observed in Ca-Al-rich inclusions can be duplicated through evaporation of chondritic material.

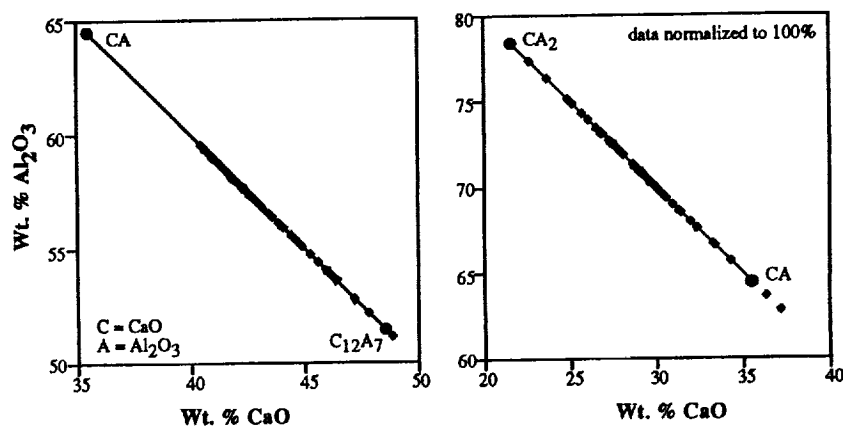


Figure 1

References: [1] Clayton *et al.*, (1985) In "Protostars and Planets II", 755-771. [2] Niederer and Papanastassiou (1984) *Geochim. Cosmochim. Acta* 48, 1279-1293. [3] Ireland *et al.* (1992) *Geochim. Cosmochim. Acta* 56, 2503-2520. [4] Wang *et al.* (1993) *Meteoritics* 28, 454-455. [5] Davis *et al.* (1990) *Nature* 347, 655-658. [6] Hashimoto (1990) *Nature* 347, 53-55. [7] Davis *et al.* (1982) *Geochim. Cosmochim. Acta* 46, 1627-1651.

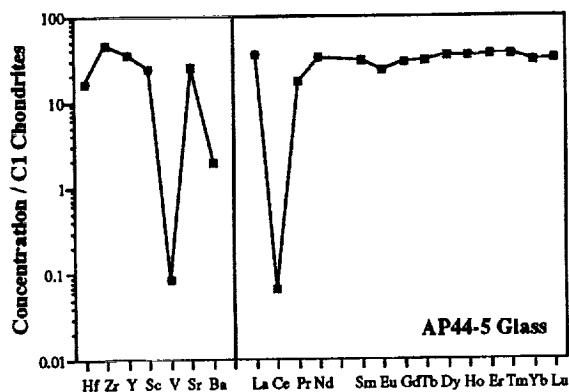


Figure 2

NARROW-FIELD IMAGING OF THE LUNAR SODIUM EXOSPHERE; B. Flynn and S. A. Stern, Southwest Research Institute, San Antonio, Texas

The lunar Na atmosphere has been observed from Earth since its discovery in 1988 [1]. Both spectroscopy and wide-angle imaging have been used [2-5]. We present results from a new imaging technique that takes advantage of a narrow-band Na interference filter, unique observing geometry, and good internal scattered light suppression to enable probing of the atmosphere over the lunar terminator. Preliminary results using this technique have been previously presented [6]. In this paper we present a thorough analysis of the original data set taken on 22-24 November 1991 and subsequent observations from 1 December 1993. Both sets of data were obtained at the University of Texas McDonald Observatory.

The narrow-field (4×4 arcmin) imaging technique involves taking images just to the dark side of the lunar terminator. The lunar surface within the field-of-view (FOV) is then illuminated only by earthshine. The varying illuminated path length due to the lunar shadow allows a measure of the atmospheric scale height. By taking image strips along the terminator as the terminator moves across the lunar surface, the structure of the atmosphere can be mapped out over approximately two thirds of the lunar surface visible from the Earth. By covering both lunar mare and highland surface units, spatial variations due to inhomogeneous surface composition may be characterized. Furthermore, temporal variations due to dynamical transport across the FOV can be detected by taking a time-sequence of images over the same surface regions.

The imaging technique described here complements other methods of observing the lunar atmosphere. Whereas spectroscopy is limited to observations off of the lunar limb, the narrow-field technique can measure the atmosphere over roughly 70% of the Earth-facing hemisphere. Furthermore, wide-angle coronagraphic imaging has so far observed only the extended lunar atmosphere at distances greater than ~ 0.5 lunar radii from the surface. The narrow-field imaging technique can observe the atmosphere down to within ~ 50 km of the surface.

The imaging data sets obtained in 1991 and 1993 have been thorough examined for detection of phenomena related to the lunar Na atmosphere. The data taken to date represents $<10\%$ of the visible lunar surface. Future observations will concentrate on obtaining data over the full extent of lunar surface that can be observed during the first quarter-full Moon and full Moon-last quarter observing windows. We will endeavor to: (1) Make lunar Na "movies" over specific surface areas; and (2) make full north-south Na image strips along the terminator over a wide range of lunar phases.

REFERENCES

- [1] Potter, A., and T. Morgan (1988), *Science*, **241**, 675.
- [2] Tyler, A., et al. (1988), *GRL*, **15**, 1141.
- [3] Potter, A., and T. Morgan (1988), *GRL*, **15**, 1515.
- [4] Mendillo, M., et al. (1991), *GRL*, **18**, 1351.
- [5] Flynn, B., and M. Mendillo (1993), *Science*, **261**, 184.
- [6] Stern, S. A. (1992), Proc. 23rd LPSC, Part 3.

DOES THE KUIPER BELT CONTRIBUTE SIGNIFICANTLY TO THE ZODIACAL CLOUD AND THE STRATOSPHERIC INTERPLANETARY DUST?; G. J. Flynn, Dept. of Physics, SUNY-Plattsburgh, Plattsburgh, NY 12901.

It is generally assumed that two major sources contribute to the Zodiacal Cloud: main-belt asteroids and active comets. However, direct measurement of the solar system dust population by the Pioneer 10 spacecraft suggests a large fraction of the interplanetary dust is in near-circular orbits (1) but that the dust flux does not decrease significantly outside the main-belt (1). The recent discovery of 100 km size objects in trans-Neptunian orbits (2), possibly associated with the Kuiper Belt, raises the possibility that collisions in the Kuiper Belt may contribute significantly to the Zodiacal Cloud and to the interplanetary dust collected from the Earth's stratosphere.

The smaller dust particles making up the Zodiacal Cloud are rapidly removed by Poynting-Robertson Drag while the larger particles are broken into smaller ones by catastrophic collisions. A constant source of resupply, estimated by Grun et al. to be 9×10^3 kg/sec (3), is required to maintain the Zodiacal Cloud in a steady-state. Until recently, active comets were presumed to be the major source of this dust (4). However, the degree of heating experienced by interplanetary dust particles (IDPs) collected from the Earth's stratosphere suggests a significant contribution by particles in near-circular orbits (5). Detailed examination of the evolution of the dust associated with infrared emission in the main-belt also indicates a significant asteroidal contribution to the Zodiacal Cloud (6, 7).

Constraints on Sources of the Zodiacal Cloud

Durmott et al. (7) suggest that the main-belt asteroids contribute about 30% of the dust to the Zodiacal Cloud, but find that the remainder of the cloud requires a source with a higher mean inclination to the ecliptic. They suggest that dust emitted by active comets is the source for the remaining 70% of the Zodiacal Cloud. However, Flynn (8) has pointed out that a cometary source that large should result in catastrophic collision lifetimes for large ($>200 \mu\text{m}$) micrometeorites which are too short to allow their survival during transport from the main-belt to the Earth. The collection of large micrometeorites having cosmic ray exposure lifetimes consistent with a main-belt origin (9) suggests the contribution of active comets to the Zodiacal Cloud is smaller (8). Taken together these results suggest the major contributor to the Zodiacal Cloud provides dust with a large range of inclinations but nearly circular heliocentric orbits.

Direct measurement of interplanetary dust with masses $>2 \times 10^{-9}$ grams by the Pioneer 10 spacecraft provides observational evidence of the orbital properties of the dust and constraints on its major source(s). Humes et al. (1) interpret the Pioneer 10 measurements to indicate:

- 1) that a large fraction of the dust near 1 AU is in near-circular orbits, and,
- 2) that the rate of dust impacts does not diminish significantly after passage through the main-belt (continuing well past the orbit of Jupiter).

The first observation suggests that active comets are not the dominant source of interplanetary dust, since the eccentricity of the orbits of cometary dust particles is still significant at 1 AU (5, 10). The second observation suggests that main-belt asteroids are not the dominant source of the interplanetary dust, since Poynting-Robertson Drag would cause the orbits of 2×10^{-9} gram dust produced in the main-belt to evolve rapidly inward, resulting in a sharp drop in the dust detection rate outside of the main-belt. The Pioneer 10 measurements seem to require a significant source for the Zodiacal Cloud which is located at a larger heliocentric distance than the main-belt, and provides particles in near circular orbits but a wide range of inclinations. In addition, this source must be invisible in the IRAS measurements, suggesting it might be at a large heliocentric distance.

DOES THE KUIPER BELT CONTRIBUTE?: G. J. Flynn

Kuiper Belt

The discovery by Jewitt and Luu (2) of large objects (>100 km) in trans-Neptunian, heliocentric orbits provides the first possible detection of the Kuiper Belt, which has been proposed as a source for short-period comets. Jewitt and Luu (11) have identified 6 trans-Neptunian objects. Because they sampled only a small fraction of the sky, they estimate the undetected objects >100km to number 10^4 (2,11), far exceeding the number of objects >100 km in the bias-corrected modeling of the main-belt. If so, then collisions with smaller objects should result in significant dust production in the Kuiper Belt. Modeling efforts by Jewitt and Luu (11) suggest possible dust production rates in the Kuiper Belt ranging from 10 to 10^5 kg/sec, depending on the assumed slope of the size-frequency distribution for larger objects. Thus the dust production in the Kuiper Belt could equal or exceed that required for replenishment of the Zodiacal Cloud.

Dust produced in the Kuiper Belt would be transported to the inner solar system on time scales short compared to the age of the solar system, however the perturbations experienced by these particles as they pass through gravitational resonances with Jupiter and the other large outer planets have not been studied. It is possible that resonance trapping, as calculated for dust particles passing Earth (12), would result in the production of a heliocentric dust ring outside the orbit of Jupiter. If so, detection of such a ring would provide confirmation of a Kuiper Belt contribution to the Zodiacal Cloud.

Conclusions

The assumption that the bulk of the Zodiacal Dust is derived from main-belt asteroids and/or active comets appears to contradict the observational constraints imposed by combining the Pioneer 10 and IRAS spacecraft measurements and physical observations or interplanetary dust recovered from the Earth's stratosphere and the polar ices. A source contributing particles whose orbits are nearly circular at 1 AU, but having a relatively large range of inclinations seems to be required.

If, as suggested by Jewitt and Luu (11), there are a significant number of undetected objects in the Kuiper Belt, then collisions, accompanied by the production of dust, must occur. Poynting-Robertson Drag would deliver the resulting particles to the inner solar system, unless they all experience significant orbital perturbations by the outer planets. Because their orbits would be nearly circular, these particles would have lower geocentric velocities at the Earth collection opportunity, and would experience significantly less thermal alteration on Earth atmospheric entry, than the particles emitted by active comets. Dust derived directly from the Kuiper Belt would appear to satisfy the orbital constraints imposed by the Pioneer 10 and IRAS spacecraft measurements as well as the physical measurements on the stratospheric and polar micrometeorites.

Detailed dynamical modeling of the rate of dust production in the Kuiper Belt and the subsequent orbital evolution of this dust will allow assessment of the magnitude of the Kuiper Belt contribution to the Zodiacal Cloud and the probability of stratospheric collection of nearly pristine samples of material stored at low temperature since the formation of the solar system.

REFERENCES: 1) D. H. Humes et al., J. Geophys. Res., 79, 3677-3684 (1974). 2) D. Jewitt and J. Luu, Nature, 362, 730-733 (1993). 3) E. Grun et al., Icarus, 62, 244-272 (1985). 4) L. Kresak, in Solid Particles in the Solar System, IAU Symp. 90, 211-222 (1980). 5) G. J. Flynn, Icarus, 77, 287-310 (1989). 6) W. T. Reach, in Origin and Evolution of Interplanetary Dust, 211-214 (1991). 7) S. F. Dermott et al., Asteroids, Comets, and Meteors 1991, 153-156 (1992). 8) G. J. Flynn, Asteroids, Comets, and Meteors 1991, 195-199 (1992). 9) K. Nishiizumi et al., Earth and Planet. Sci. Lett., 104, 315-324 ((1991). 10) A. A. Jackson and H. A. Zook, Icarus, 97, 70-84 (1992). 11) D. Jewitt and J. Luu, in Second International Conference on Planetary Systems: Formation, Evolution, and Detection, 9 (1993). 12) A. A. Jackson and H. A. Zook, Nature, 337, 629-631.

HYDRATED INTERPLANETARY DUST PARTICLES: ELEMENT ABUNDANCES, MINERALOGIES, AND POSSIBLE RELATIONSHIPS TO ANHYDROUS IDPs: G. J. Flynn¹, S. R. Sutton², S. Bajt², W. Klöck³, K. L. Thomas⁴, and L. P. Keller⁴. 1) Dept. of Physics, SUNY-Plattsburgh, Plattsburgh, NY 12901, 2) Dept. of Geophysical Sciences, The University of Chicago, Chicago, IL 60637, 3) Institut für Planetologie, Westfälische Wilhelms-Universität, Münster, Germany, 4) MVA Inc., 5500/200 Oakbrook Pkwy, Norcross, GA 30093.

The element abundances and mineralogies of six hydrated interplanetary dust particles, three having magnetite rims indicating they experienced significant entry heating, were determined. The unheated set shows significantly larger extremes of composition than the unheated, anhydrous IDPs examined previously. This suggests the hydrated IDP parent body is chemically heterogeneous on the 10 μm scale. The average trace element abundance pattern of the heated, hydrated particles is very similar to that of the heated, anhydrous particles. No mean depletion of Ca was observed, but a low Mn content may be a signature of hydrated IDPs.

We identified 6 hydrated interplanetary dust particles (IDPs) by transmission electron microscopy (TEM) and determined their trace element contents by Synchrotron X-Ray Fluorescence (SXRF). Each IDP was classified "cosmic" in the JSC Catalog. Independent evidence, either TEM observation of a magnetite rim on the particle or He content determined on another fragment of the same cluster, confirms the extraterrestrial origin of 4 particles (see Table 1).

Mineralogy

Three particles lack magnetite rims, indicating they experienced insignificant heating on atmospheric entry. L2005R7 contains Fe-rich smectite and sulfides but no anhydrous silicates. U2015G1 contains two mineralogically distinct subunits: one dominated by talc with minor smectite, and another by Fe-Ni-oxides and smectite, described by Stephan et al. (1). L2005D30 consists of smectite, other unidentified layer-silicates, SiO_2 crystals, TiO_2 crystals, and magnetite. Both the mineralogy and chemistry (see below) of L2005D30 are different from the other hydrated chondritic IDPs examined, and its identification as an extraterrestrial particle rests on the He content of another fragment of this cluster (2).

The mineralogies of the three heated particles were described previously by Thomas et al. (3). L2005L6 has a discontinuous magnetite rim <50 nm thick, while L2005P9 and L2005P13 have well-developed, continuous magnetite rims. L2005L6 is dominated by fine- and coarse-grained Fe-rich smectite with finely dispersed sulfides. L2005P9 contains poorly crystallized Fe-rich serpentine intergrown with fine-grained magnetite. L2005P13 contains poorly-crystallized Fe-rich phyllosilicates.

Chemical Abundances

The three hydrated IDPs without magnetite rims have widely varying trace element contents (see Table 1). Ni, Cu, Zn, Ga, Br, and probably Ge (only a Ge limit was determined for U2015G1) vary by over an order-of-magnitude in concentrations, with L2005D30 showing the most extreme variation. This is much wider than the range previously observed in a set of 5 unequilibrated, anhydrous IDPs (4). This suggests either the hydrated IDPs sample a parent body which is chemically heterogeneous on the size scale of the individual IDPs or multiple sources of diverse compositions.

The three hydrated IDPs which have experienced significant atmospheric entry heating show a much tighter clustering of their volatile trace element contents. Except for Zn, which is extremely sensitive to loss by entry heating (3, 4), and Br, which varies dramatically in all types of IDPs, the individual trace elements show variations of less than a factor of two among the three heated, hydrated IDPs. The average abundances of these elements (shown in Table 1) have been Fe-normalized and compared to the Fe-normalized abundances previously reported for heated, anhydrous IDPs (see Figure 1). There is a remarkable agreement between the average abundances of these two groups, though the average Ga and Br contents of the hydrated IDPs are significantly higher than those previously reported for the anhydrous IDPs.

HYDRATED INTERPLANETARY DUST: Flynn G. J. et al.

Table 1: CI Normalized SXRF Element Abundances in Hydrated IDPs

Particle	Ca ⁺	Cr	Mn	Fe ⁺	Ni	Cu	Zn	Ga	Ge	Se	Br	Evidence of Origin
Unheated												
L2005R7	0.1	1.0	0.4	1.1	1.4	3.0	2.7	2.0	2.5	1.9	50	-----
U2015G1	0.3	0.3	0.3	0.5	0.5	1.2	38	<3	<1	<2	28	-----
L2005D30	4.2	0.6	0.2	0.2	0.07	13	15	74	6.5	2.3	820	He/ClstFrg
Heated												
L2005L6	1.6	1.1	0.9	1.4	1.4	2.7	0.6	1.3	1.6	2.9	42	magnet.rim
L2005P9	0.1	0.6	0.6	1.2	0.7	2.0	0.5	1.4	2.2	3.1	121	magnet.rim
L2005P13	2.7	1.9	1.0	1.5	1.4	3.5	<0.03	0.7	1.8	2.9	40	magnet.rim
AVG. Heated		1.2	0.8	1.4	1.2	2.7	<0.4	1.1	1.9	3.0	68	

+ Ca contents of L2005R7, L6, P9, and P13 determined by EDS.

* Fe determined by EDS, except U2015G1 from JSC Catalog spectra.

The Ca contents of the 6 hydrated IDPs range from 0.1 to 4.2 X CI, showing no evidence for a depletion of the average Ca content of hydrated IDPs suggested by Schramm et al. (5). The most distinctive chemical feature of these 6 hydrated IDPs is their low Mn contents, with no particle having a Mn content above CI. The Mn average is about one-half that of the anhydrous group of IDPs we have previously examined. A similar Mn-depletion was reported by Kurat et al. (6) in a subset of unmelted, CI-like, hydrated micrometeorites from the Antarctic, but these particles also showed low Ca contents.

Interrelationships Between Anhydrous and Hydrated IDPs

Confirmation of chemical differences between anhydrous and hydrated IDPs will require analysis of a larger group of particles. This could test the suggestion that hydrated and anhydrous IDPs may be genetically related through aqueous alteration of anhydrous material to produce the hydrated material (7).

Conversely, anhydrous IDPs might be produced by alteration of hydrated IDPs experiencing extreme heating on atmospheric entry. Heating of phyllosilicates from Orgueil to 1200° C for a few seconds produces very fine-grained (<<100 nm) olivines and pyroxenes, similar in texture to the anhydrous IDPs L2006A24 and L2005A8. The fragments of these IDPs analyzed by SXRF were very small (<8 µm) resulting in incomplete trace element data, however both have Mn/Fe ≥ CI. Pulse heating experiments on both hydrated meteorites, as described by Klöck et al. (8) and hydrated IDPs are required to understand the alteration produced during entry.

REFERENCES: 1) T. Stephan et al. *Meteoritica*, 27, 292 (1992). 2) A. O. Nier and D. J. Schlutter *Meteoritica*, 28, 675-681 (1993). 3) K. L. Thomas et al. *LPSC XXIII*, 1427-1428 (1992). 4) G. J. Flynn et al. *Meteoritica*, 28, 349-350 (1993). 5) L. S. Schramm et al. *Meteoritica*, 24, 99-112 (1989). 6) G. Kurat et al., *LPS XXIII*, 747-748 (1992). 7) M. E. Zolensky and R. Barrett *Microbeam Analysis*, 2, 191-197 (1993). 8) Klöck et al. "Heating Experiments Simulating Atmospheric Entry of Micrometeorites," *LPSC XXV*, this volume.

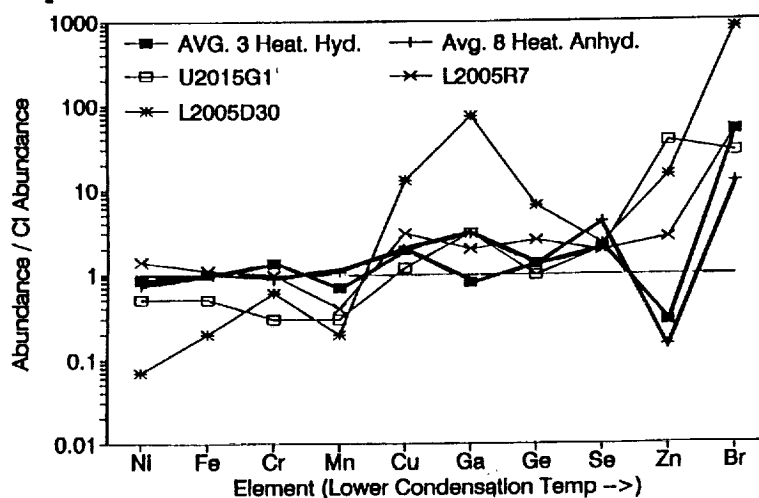


Figure 1: CI-normalized element abundances for 3 unheated, hydrated particles (narrow lines), and average CI- and Fe-normalized element abundances for the heated, hydrated and heated, anhydrous particles sets (wide lines).

NITROGEN SOLUBILITY IN AUBRITE AND E CHONDRITE MELTS. Robert A. Fogel, Dept. of Mineral Sciences., American Museum of Natural History, New York, NY

Introduction: Enstatite chondrites and aubrites are nitrogen-rich meteorite groups that contain the N-bearing phases TiN (osbornite; aubrites) and $\text{Si}_2\text{N}_2\text{O}$ (sinoite; E chondrites). An important feature that distinguishes the enstatite meteorites from the other meteorite groups is that *they are extremely reduced* (1,2). The reducing character of the enstatite meteorites is intimately linked to the stabilization of nitrides and N-bearing silicates.

Aubrites are basaltic achondrites derived from the melting of E chondrite-like reducing source material (3). E chondrites contain chondrule melts that formed in reducing parts of the solar nebula. Although the role of volatiles in silicate melts under oxidizing has been studied extensively, their role under reducing conditions is poorly understood. Melting and phase equilibria data from the material sciences suggest that the properties of silicate melts under reducing conditions are different from those under more oxidizing conditions ($>IW$). Under oxidizing conditions N acts as a trace element dissolving in ppm quantities; however, under reducing conditions, N can dissolve in minor element to major element amounts ($>1 \text{ wt}\%$) (4). I have been studying the solubility of N in geologically relevant silicate melts under reducing conditions in order to understand the importance of N in reducing igneous activity.

Experimental: A basaltic composition (NMIX-3) approximating an FeO-, K_2O -, Na_2O -, TiO_2 -free 1921 Kilauea basalt was formulated from component oxides. NMIX-3, thus, approximates a 1921 Kilauea basalt composition if it were melted under reducing conditions diagnostic of the enstatite meteorites ($IW -4-6$), since the FeO would be removed and partitioned into a separate Fe-Si phase. This assumption was verified by reducing experiments (similar to those described here) on the 1921 Kilauea basalt itself. Melts were equilibrated in graphite capsules under flow mixtures of pure CO gas and a 98% N_2 -2% H_2 gas mixture. Flow rates were monitored by flow meters and rigorously determined by timing experiments of the movement of bubbles through a 50 ml graduated burette under the respective gas flows. All experiments were conducted at similar N_2/CO fugacity ratios (≈ 22) at T's between 1500°C and 1600°C. Glass compositions were determined by electron microprobe with nitrogen and oxygen contents determined using a W-Si multilayer crystal.

Results and Discussion: Run products were clear light pink glasses. SEM examination showed that submicron spheres of an Fe-Si alloy were present and often concentrated near the graphite-silicate melt contact. Since the starting NMIX-3 contained FeO contents below probe detectability, spheres represent the reduction of trace quantities of FeO in NMIX-3 enhanced by the reduction of Si from the silicate melt. EDS analyses of the largest of these spheres (2 μm) show them to contain minor elements: Ti, Cr, Mn and Ni, which are strongly partitioning into the Fe-Si melt which scavenges the silicate melt for these trace elements under reducing conditions.

Glass major element contents show the loss of SiO_2 and the gain of MgO and CaO and are functions of T, time and amount of starting material. Relative to SiO_2 , however, MgO and CaO display clear linear trends (e.g., Fig. 1: MgO vs SiO_2). On a molar basis, the gain in MgO as a function of SiO_2 loss is $\approx 3\times$ that of the gain in CaO as a function of SiO_2 loss. Molar SiO_2 contents fell from 59.35% in NMIX-3 to 49.19% due to the high fugacity of SiO; MgO rose from 17.63% (NMIX-3) to 24.65%; CaO rose from 13.85% (NMIX-3) to 16.50%. Al_2O_3 contents did not vary appreciably from the starting composition (9.17%). Additionally, in two of the experiments that lost the most weight, TiO_2 contents rose from trace amounts in the starting material to 0.16 and 0.23 mole %. These trends are important indicators of relative cation volatility determined *experimentally*. In this silicate melt composition and under the experimental conditions investigated, volatility was thus: $\text{Si} > \text{Al} > \text{Ca} > \text{Mg} > \text{Ti}$. Interesting differences in this volatility scheme exist from those under more oxidizing conditions where,

Nitrogen Solubility in Aubrite and E Chondrite Melts, Robert A. Fogel

for example, Al is highly refractory instead of volatile. This reversal is consistent with the condensation calculations of (5) who show this difference as a function of nebular C/O ratio.

Nitrogen-solubility as a function of temperature is shown in Fig. 2 where it appears to be linearly correlated with $1/T$; lower T favoring increasing N content. N contents are as high as a 0.5 wt % or 2 mole % at 1500°C, showing that it plays a role far more important than a trace element at these T 's. The large *relative error* in two of the 1600°C runs is probably due to the lack of attainment of equilibrium (run times for these two were 1 hr.) as well as analytical uncertainties due to their low N-contents.

N is thought to speciate in very basic melts as a substitution for O (6). N incorporation by this method causes bridging O bonded to 2 Si to be replaced by N bonded to 3 Si (side panel).

$\begin{array}{c} \text{Si-O-Si} \\ " \\ \text{Si} \\ \text{Si-N-Si} \end{array}$	<p>This has a stabilizing effect on the melt and is correlated to increased glass transition T, liquidus depression and many other thermophysical properties (4). Previous experiments on very basic melts (25-38 wt% SiO_2) showed a positive T dependence of N solubility, contrary to that determined here. One explanation is the dependence of N solubility on SiO_2 activity which was previously shown to be positive(6). Since the melts here have SiO_2 contents in the 50-59 wt% range, it is possible that the nature of N speciation is different in the current melts. Alternatively, since the SiO_2 activity of the melts was variable in the run products due to high SiO fugacities, it is not yet possible to separate out this factor for the current experiments.</p>
---	---

These experiments show that the role of N in the petrogenesis of silicate melts of cosmochemical importance under reducing condition is of a proportion much greater than that of trace element. When viewed on a molar basis N plays the role of a major element dissolving over 2 mole %. The incorporation of N in silicate melts to such high concentrations will effect phase stability, liquidus depression and other parameters pertinent to igneous and plutonic activity under reducing conditions. Experiments are underway to elucidate these effects. The current experiments can also explain existing problems such as the stability of osbornite in aubrite meteorites. Retention of N in silicate melts generated by the melting of E chondrite-like precursor material containing sinoite, may help explain the appearance of osbornite on the aubrite liquidus. An understanding of E chondrite and aubrite melting events awaits a better understanding of silicate melt phase equilibria under reducing igneous conditions.

References & Acknowledgments: [1] Keil (1968) JGR 73, 6945-6976; [2] Watters & Prinz (1979) PLPSC X, 1073-1093; [3] Keil (1989) Meteoritics 24, 195-208; [4] Hampshire et al. (1985) Phys. Chem. Glas. 26, 182-186; [5] Larimer & Bartholomay (1979) GCA 43, 1455-1466; [6] Davies & Meherali (1971) Met. Trans 2, 2729-2733. Support of NASA: Origins grant # NAGW-2873 is gratefully acknowledged.

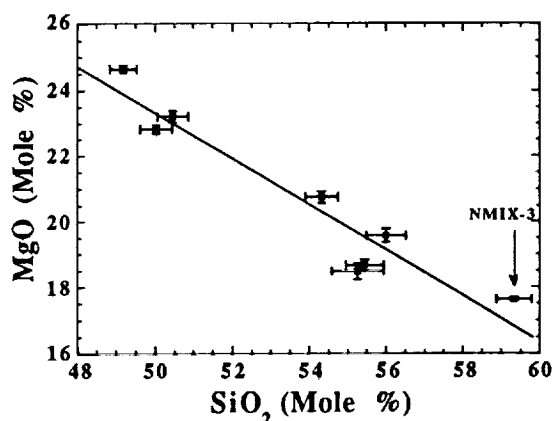


Fig. 1. MgO gain as a function of SiO_2 loss. Errors are 1σ and represent homogeneity of sample.

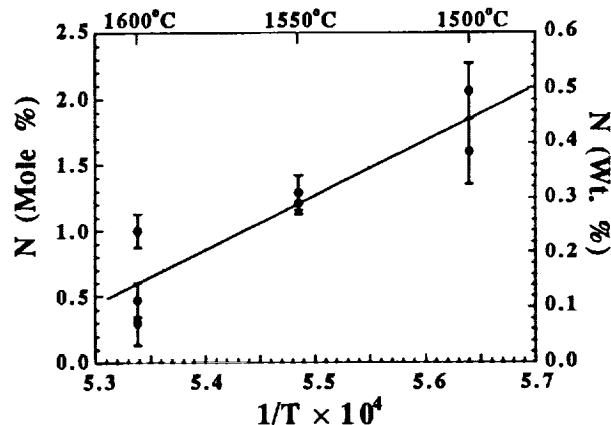


Fig. 2. Silicate melt nitrogen content as a function of $1/T$. Errors are 1σ and represent homogeneity of sample.

SIMS ANALYSIS OF ORTHOPYROXENE IN DIOGENITES: AN ATTEMPT TO DEFINE A FRACTIONATION SEQUENCE; G.W. Fowler, J.J. Papike, and C.K. Shearer; Institute of Meteoritics, Department of Earth & Planetary Sciences, University of New Mexico, Albuquerque, NM 87131-1126, U.S.A.

INTRODUCTION. Most diogenites appear to be cumulates that have crystallized from a single magmatic reservoir with only a few outliers that do not appear to fit into a single "fractionation" sequence. A recent study by Mittlefehldt [1] addressed this problem using EMPA and INAA techniques. We are attempting to add complimentary data and interpretations by using SIMS techniques on individual orthopyroxenes in a suite of diogenites. An advantage of this approach is that orthopyroxene can be analyzed in a microbeam mode and thus minimize the effects of contaminating phases including trapped melt. Here we report results for a suite of 15 diogenites for which we used a SIMS analytical package which included the elements Ca, Mn, Sr, Al, Cr, Ti, V, Zr, Nb, Y, Ce, and Yb. Figure 1 shows that Yb and Y are highly correlated (correlation coefficient = 0.96) and that a considerable compositional range of these elements is observed. Figure 2 represents a possible fractionation sequence based on Yb which is a REE that is relatively easy to measure in orthopyroxene by SIMS techniques. We here address the implications of the observed range of Yb, Y, and Zr.

RESULTS AND DISCUSSION. The ranges of Yb in orthopyroxene in our diogenite suite are shown in Figure 2. Yb in orthopyroxene varies by a factor of 27 from Ellement to LEW 88008. This contrasts with enrichment factors observed by Mittlefehldt [1] (less than a factor of 8) over the same range of meteorites and may be attributed to very small amounts of trapped melt in the orthopyroxene separates that were analyzed by INAA. This can have a substantial effect on the incompatible element depleted orthopyroxenes (e.g. Ellement) and much less of an effect on the incompatible element "enriched" orthopyroxenes (e.g. LEW 88008, Roda). Our ion microprobe data also shows that from Ellement to LEW 88008, Zr varies by a factor of 29 and Y varies by a factor of 32. We used LEW 88008 as an end member in our fractionation suite rather than Roda because Roda is anomalous and may not belong to the main sequence (e.g. very high Ti/Al). The 15 diogenites shown in Figure 2 have been "ranked" by average Yb concentrations in the orthopyroxene and put in order of increasing fractionation, assuming they are related by a single fractional crystallization process. Diogenites which plot in the lower left of this diagram (in a single reservoir model) appear to have crystallized early, while those plotting in the upper right appear to have crystallized late. It also is evident that orthopyroxene in a single diogenite show a range of incompatible trace element concentrations. We believe that this reflects both magmatic processes and local cumulate mixing. We calculated the extent of fractional crystallization needed to produce the orthopyroxene trace element array from Ellement to LEW 88008 assuming (1) a perfect fractional crystallization model, (2) that the trace element concentrations of the orthopyroxene in diogenites reflect orthopyroxene-basaltic melt equilibrium, and (3) that the D's selected for the calculation of the trace element characteristics of the EPB basaltic melts are appropriate for the conditions of crystallization. Based on these calculations, over 95% fractional crystallization of essentially orthopyroxene is required to generate a "LEW 88008 magma" from a parental "Ellement magma". This petrogenetic scenario is highly unlikely for basalts. Models tested by [1] also suggested high degrees of fractional crystallization were needed to produce this population of orthopyroxene through the crystallization of a single batch of magma. Although the predicted increase in partition coefficients during crystallization [1] lowers the extent of fractional crystallization in our models to 70 to 80%, this extent of orthopyroxene fractional crystallization is still too excessive without the crystallization of other phases (e.g. plagioclase). Three potential models are suggested by these data: (1) As suggested by [1], the magmas that are parental to the diogenites are of an unusual composition, essentially approaching orthopyroxene in composition; (2) The orthopyroxenes shown in Figure 2, do not represent a single fractional crystallization continuum, but represents fractional crystallization products of several batches of basaltic magmas produced by melting of different EPB mantle reservoirs (with elemental abundances ranging from ≈ 1 to $10 \times$ chondrite); (3) The trace element characteristics of the orthopyroxenes do not adequately preserve the magmatic history of the diogenites.

ACKNOWLEDGMENTS. We thank Graham Layne for technical help with the SIMS analyses. SIMS analyses were performed at the UNM/SNL Ion Microprobe Facility, a joint operation of the Institute of Meteoritics, UNM and Sandia National Laboratories. This research was funded by NASA grant NAGW-3347 and the Institute of Meteoritics.

REFERENCE. [1] Mittlefehldt, D.W. (1994) *G.C.A.*, **58**, in press.

SIMS ANALYSIS OF DIOGENITES: Fowler, G.W. et al.

Fig. 1

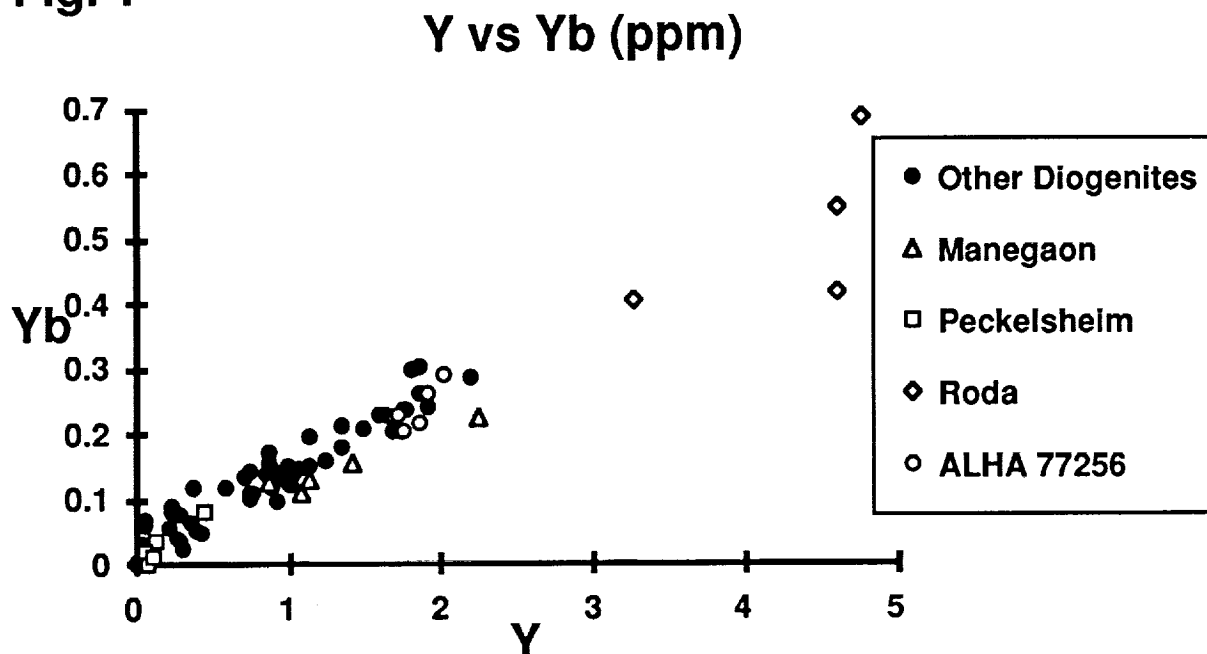
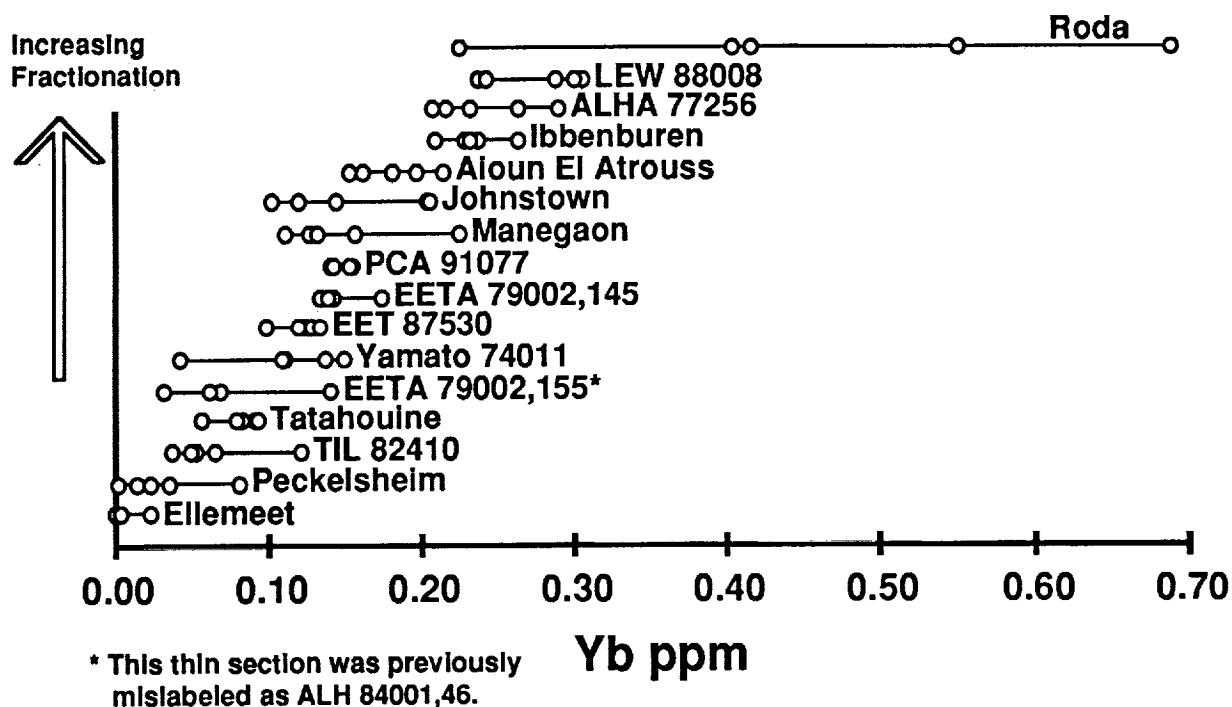


Fig. 2

Yb Ranges of Orthopyroxene in Diogenites

IMPACT BASINS IN SOUTHERN DAEDALIA, MARS: EVIDENCE FOR CLUSTERED IMPACTORS?

Herbert Frey¹ and James H. Roark², ¹Laboratory for Terrestrial Physics, Goddard Space Flight Center, Greenbelt MD 20771, 301-286-5450, ²Science Systems and Applications, Inc., Lanham, MD 20706.

The distribution of ancient massifs and old cratered terrain in the southern Daedalia region indicate the presence of at least two and probably three impact basins of large size. One of these is located near where Craddock et al. [1] placed their center for a Daedalia Basin, but has very different ring diameters. These basins have rings exceeding 1000 km diameter and overlap significantly with centers separated by 500 to 600 km at nearly identical latitudes of -26 to -29°. The smaller westernmost basin appears slightly better preserved, but there is little evidence for obvious superposition that might imply a temporal sequence. Recognizing the improbability of random impacts producing aligned, nearly contemporaneous features, we suggest these basins may have resulted from clustered impactors.

Introduction

Both Craddock et al. [1] and Schultz and Frey [2] suggested a major impact basin in the Daedalia Planum region. Craddock et al. [1] used orientations of grooved units, interpreted as impact materials, to locate a center at -26.0°, 125.0°, and suggested ring diameters of 1100, 1500, 2200, 3200, 4500 (main ring) and 6400 km. Schultz and Frey [2] looked to a broader distribution of a variety of mapped geologic units to infer a basin at -14.5°, 127.0° with ring diameters 1475, 2540 (main ring) and 3960 km, but acknowledged Craddock et al.'s fit was more consistent for many Noachian age features south of Daedalia Planum. We suggest neither of the proposed basins is a very good fit to the observed structures. Detailed study of not just the distribution but also the structure and orientation of features used to define basin rings suggests that at least two and more likely three impact basins of significant size exist in this area.

Evidence for Several Daedalia Basins

The sharply delineated scarp of *Nplh* material at 139°W between -22 and -30° is one of several large structures which suggest impact basin rings. Craddock et al.'s [1] second (1500 km) ring passes through this feature (Figure 1a), but fails to capture its true curvature: a smaller circle (diameter 850 km) centered at -26°, 131°W is a better fit to this feature and to outcrops of similar material farther south (SW Basin, Figure 1c). This smaller circle also lies along a textural boundary northeast of the scarp and passes through outcrops of *Nb* material near -30°, 125°W, features not explained by earlier proposed basins. Two additional rings (1180 and 1570 km) are well defined by similar outcrops of old material. Less but still intriguing evidence exists for two outer rings with diameters 1880 and 2375 km.

Outcrops of *Nb* material form a well-defined circle of diameter 420 km (SE Basin, Figure 1b), centered at -29.3°, 119.8°W, 500 km east of SW Basin described above. *Nb*, *Nplh* and *Npl1* units define a second and third ring with diameters 740 and 1015 km, and a major arcuate scarp-like structure of *Nplh* marks a fourth 1290 km diameter ring. Three or four additional outer rings may also exist, but are not so well marked by discrete outcrops of old material.

West of the SW Basin lies a complex uplifted region through which pass the three major rings of SW Basin (and possible outer rings of SE Basin?). Detailed study of this region suggests several large, overlapping craters or perhaps small (2-3 ring) basins (Figure 1d), one at -27.5°, 141.8°W with a diameter of 335 km and possible outer rings ($d = 690$ and 1125 km) passing through arcuate *Nplh* outcrops to the west, east and south. A 275 km impact crater overlaps this feature to the south, at -30.0°, 141.3°W.

Basin Spatial and Temporal Overlap

The combination of three basins explains the existing Noachian outcrops and many large, channel-like deposits of Hesperian-age plains-forming materials which lie between major rings. The ancient materials appear highstanding and well-preserved where positive re-inforcement

DAEDALIA, MARS IMPACT BASINS: Frey, H.V. and Roark, J.H.

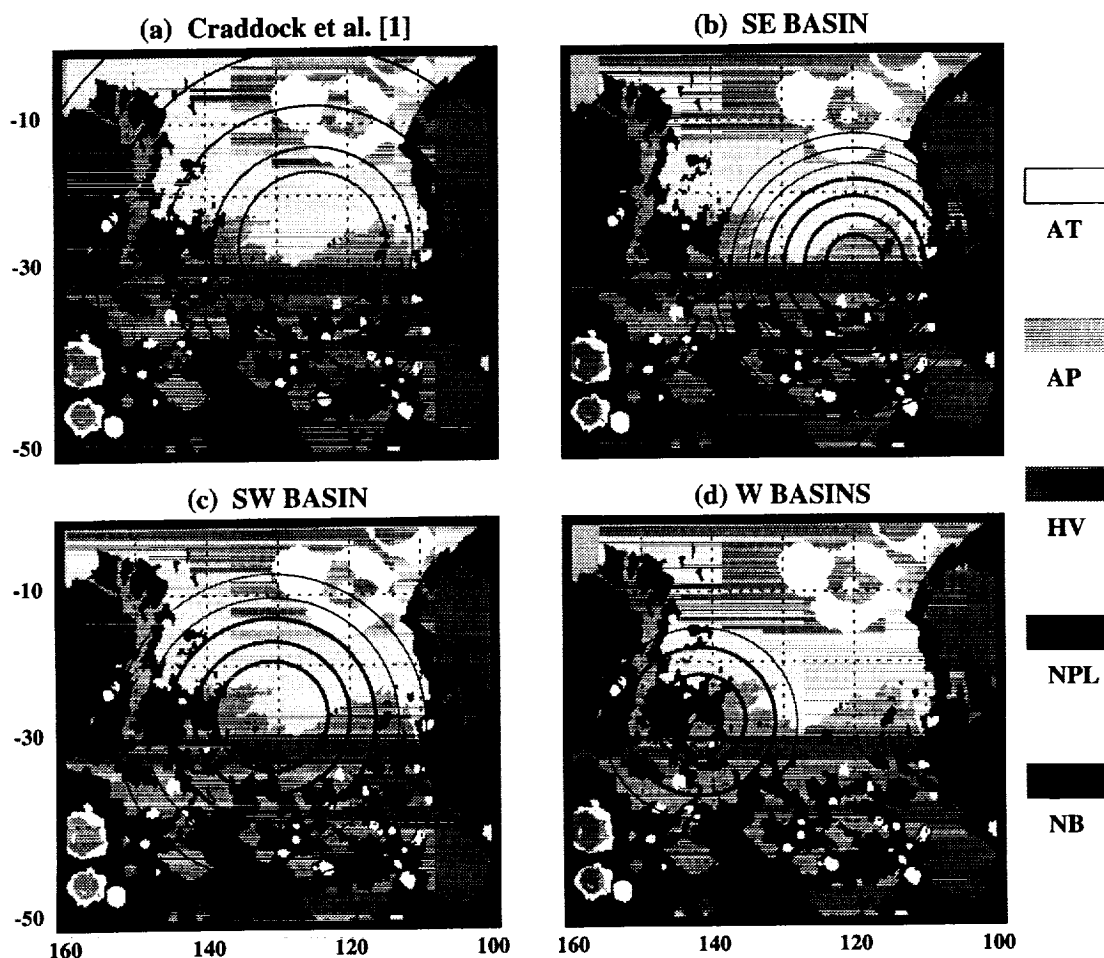
between two basins occurs (basin rings nearly tangent to one-another). Where rings cross at high angles, less survives in the overlap regions.

The basins show no obvious superposition relations that might indicate a temporal sequence in their formation. Many of the same structures are attributed to two different basins. Within the limits of the observational data, the two largest basins are of comparable age. The inner ring of the smaller W Basin is somewhat more complete, but the outer rings are best preserved where tangent to the overlapping SW Basin. If W Basin were significantly younger, better preservation of its outer rings on the eastern (Daedalia Planum) side might be expected.

The probability of random impacts producing three contemporaneous, aligned basins (two of similar large size) is very small. If all three basins really exist, the possibility they are genetically related should be considered. This might imply a nearly simultaneous impact by a closely spaced (recently disrupted?) group of objects. If the separation of the basins were due only to the rotation of Mars, the impacts would be separated in time by about 35 minutes.

REFERENCES: [1] Craddock, R.A. et al., JGR 95, 10,729-10,741, 1990. [2] Schultz, R.A. and H.V. Frey, JGR 95, 14,175-14,189, 1990.

FIGURE 1. Proposed impact basin rings superimposed on a simplified geologic map of the Daedalia region of Mars. (1a) Daedalia Basin as proposed by Craddock et. al. [1]. (1b) SE Daedalia Basin. (1c) SW Daedalia Basin. (1d) Western large craters or small basins.



2972

EFFECTS DUE TO OVERLAPPING LARGE IMPACT BASINS ON MARS

Herbert Frey¹, Anne Marie Reidy², James H. Roark³, and Stephanie Stockman³, ¹Laboratory for Terrestrial Physics, Goddard Space Flight Center, Greenbelt MD 20771, 301-286-5450, ²Astronomy Program, University of Maryland, College Park, MD 20771, ³Science Systems and Applications, Inc., Lanham, MD 20706.

Many ancient highly degraded large impact basins exist on Mars [1,2,3]. In many cases these basins overlap or are overlapped by more easily observed, presumably younger, impact basins. While impact basin overlap is becoming more recognized, the effects of such overlap have only occasionally been described. Such effects will depend on a variety of factors, including the absolute and relative size of the basins, the degree of overlap, the state of the lithosphere and its thermal gradient at the time of impact, and the time between impacts. There now exists enough evidence for overlapping basins of different sizes that some of these can be discussed. This paper highlights some examples of obvious effects of basin overlap.

Figure 1 shows several of the many examples now recognized on Mars. The Chryse-Acidalia Basins discussed in this volume [4] are shown in Figure 1a. Figure 1b shows the overlapping Utopia [5], Elysium [6] and Arcadia [3] Basins, and the overlapping Isidis, Scopolus [3] and Hellas Basins. We previously discussed the south polar region [7,8], where South Polar Basin is overlapped by Malea B and South Polar B as well as by the outer ring of Hellas.

Small impact basins affect only the upper structure of the lithosphere, so small basins overlapping the rim or edge of large impact basins have obvious and limited effects. There are several examples of such overlap, including Isidis-Utopia (Figure 1b). In such cases, the major effect is alteration of the surface structure, e.g. disruption of the larger basin rim. A second and larger example of this is the overlap of Acidalia with Chryse [4], which appears to have destroyed the northern portions of the Chryse rings (Figure 1a).

There are many cases where overlapping impact basins appear to control the extent of plains-forming units. Isidis-Utopia (Figure 1b) is one such example. Another may be the two larger basins in Daedalia, discussed elsewhere in this volume [9], where most of the (especially Hesperian age) plains in southern Daedalia lie within the overlap of two comparably sized basins. In the south polar region, the 40% overlap of South Polar and South Polar B, which are both of order 1000 km across but for which the area of deformation appears to be twice the main diameter, seems to control the off-axis deposition of polar deposits *Apl*.

A more complicated example of how basin overlap appears to control the distribution of plains-forming units is the Chryse-Acidalia pair. Topographic barriers associated with rings from the overlap of the comparably sized Acidalia Basin may have blocked the flow of volcanic and sedimentary materials draining northward from south of Chryse, causing ponding and subsidence in the southern portion of the Chryse Basin [4]. The distribution of Amazonian and Hesperian age plains units within Chryse-Acidalia also appears related to the location of Acidalia rings where they overlap the central portion of the Chryse Basin (Figure 1a). In particular the Amazonian units in central Chryse lie southward of the second Acidalia ring, and most of the Hesperian-age units lie within this ring.

In eastern Mars, most of the northern lowlands are confined within two very large (> 4000 km) Utopia [5] and Elysium Basins [6] (Figure 1b), the main rims of which form the crustal dichotomy boundary zone in this part of Mars [10,11]. The extension of Amazonian plains units into Utopia appears controlled by the topography in the overlap regions of the two basins, especially for the northwest trending *Ael3* unit. We have also suggested the combined deep-seated effects of two such large basins may have concentrated prolonged volcanic activity which gave rise to the Elysium tectono-volcanic complex [10] centered in the overlap region of the two basins. The central Elysium volcanoes are located close to the intersection of Utopia rings with inner Elysium rings, as given by [6].

Smaller examples of concentration of volcanic effects exist elsewhere. The Meroe and Nili Paterae lie along an outer Isidis ring where it passes through the center of the Scopolus Basin, and Hadriaca and Tyrrhena Patera may be associated with intersecting rings of a smaller Hesperia Basin and Hellas.

OVERLAPPING IMPACT BASINS ON MARS: Frey, H. et al.

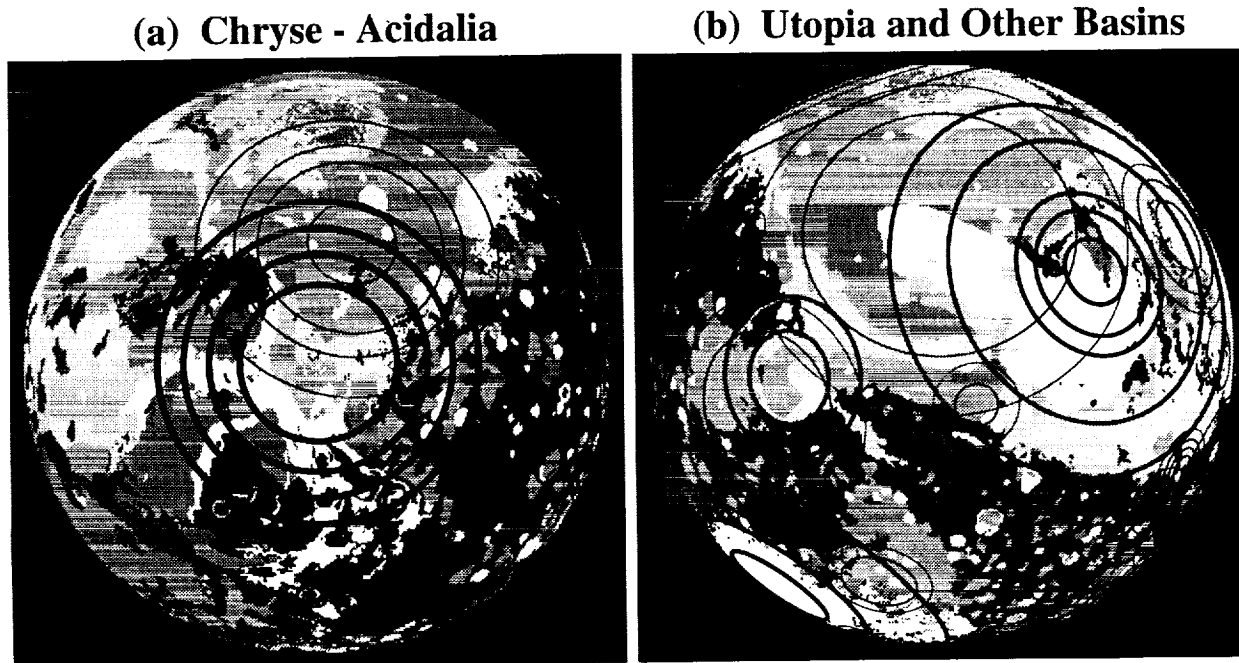
Structural effects also occur when distant rings of large basins cross inner rings of another basin. The outer ring of Hellas ($d \sim 4200$ km) may have influenced South Polar Basin, whose main ring is broken into segments at about the location of the Hellas ring. Perhaps gentle uplift along this zone raised this portion of the South Polar Basin rim and prevented its burial beneath polar deposits.

Near tangency of basin rings may provide positive reinforcement that elevates and helps preserve ancient terrains. Examples appear in the Daedalia region, discussed elsewhere in this volume [9] as well as in Chryse-Acidalia [4] where a lone outcrop of Noachian terrain in the northern lowlying plains appears to coincide with the one place where inner rings from the two basins are tangent (Figure 1a).

There are also many examples among the basin pairs where channel flow direction has been altered by overlapping rings of basins. Channel flow often widens between rings, running concentrically along what are presumed to be topographic lows, but may break through a ring or change direction abruptly where a ring from an overlapping basin crosses through. Examples in Chryse-Acidalia [4] and in western Daedalia [9] are discussed in this volume.

REFERENCES: [1] Schultz, P. H., et al., JGR, 86, 9803-9820, 1982. [2] Pike, R. J. and P. D. Spudis, Earth Moon Planets 39, 129-194, 1987. [3] Schultz, R. A. and H. V. Frey, JGR 95, 14,175-14,189, 1990. [4] Stockman, S. and H. Frey, Lunar Planet Sci XXV, (this volume), 1994. [5] McGill, G.E., JGR 94, 2753-2759, 1989a. [6] Schultz, P. H., Lunar Planet. Sci. XV, 728-729, 1984. [7] Reidy, A. M. et al., Lunar Planet. Sci. XXIII, 1137-1138, 1992. [8] Frey, H.V. and A.M. Reidy, MSATT Polar Processes, 1992. [9] Frey, H. and J. Roark, Lunar Planet. Sci. XXV, (this volume), 1994. [10] Frey, H. and R. A. Schultz, JGR, 95, 14,203-14,213, 1990. [11] Frey, H., Lunar Planet. Sci. XXII, 415-416, 1991a (abstract).

FIGURE 1: Examples of overlapping impact basins. (1a) The Chryse-Acidalia pair, discussed elsewhere in this volume [4]. (1b) Eastern Mars. Major basins [3] include Elysium, Arcadia, Utopia, Isidis, Scopolus and Hellas. See text for details.



CONSTRAINTS ON THE PHYSICAL DETAILS OF NAKHLITE FORMATION;

R.C. Friedman, T.J. McCoy, and G.J. Taylor, Planetary Geosciences, Dept. of Geol. and Geophys., Univ. of Hawaii, Honolulu, HI 96822.

Past studies of the nakhlites have concentrated on determining the magmatic source and interrelation of its constituent phases [eg.1,2]. In contrast, our interest in nakhlites concerns the physical setting of their formation to gain further understanding of volcanologic processes on Mars. We have begun by examining the heterogeneity of the original Nakhla meteorite. Modal analyses of eight sections demonstrate a significant variation in pyroxene:olivine ratios from 4:1 to over 17:1. There is no apparent correlation between olivine and mesostasis. This suggests that the amount of olivine is governed by a primary mechanism rather than later chemical interactions with remaining melt. We have also measured the crystal size distribution (CSD) of augites. Calculations based on CSD data suggest a growth period of about 1-5 yrs was necessary to produce the current grain sizes. This cooling period implies the host body was at least 11-26 m thick.

Modal heterogeneity

Previous workers have been limited to studying only one or two distinct Nakhla thin sections; we feel this ignores the real likelihood that the original Nakhla body, perhaps 30 cm on a side, may have been significantly varied in texture and chemistry. For example, recent studies of the shergottite Zagami have revealed a previously unnoticed 5 cm area (in a 15-20 cm body) that has a unique composition and displays crystals 50% larger than those in the main mass. We have, therefore, obtained 10 samples of different Nakhla stones to determine the extent of heterogeneity on a 10-cm scale. In principle, the extent of differences between nakhlites could help constrain magma-body size.

To date, we have determined the modes of eight Nakhla sections, from seven distinct stones; proper identification of olivines and mesostasis in weathered or disrupted sections was verified by backscattered electron imaging. As shown in Figure 1, pyroxene content varied by 15 vol%, olivine by 13 vol% and mesostasis by 6 vol%. These ranges reflect real heterogeneities beyond the inherent uncertainties of the method.

The ultimate source of these olivines has been hotly debated; they may be phenocrysts or xenocrysts or they may have grown in the magma after emplacement [1,2]. The increase in olivine correlates with a decrease in augite, but there is no definitive correlation with mesostasis content. This pattern suggests to us that the heterogeneity in olivine distribution is due to uneven mixing of phenocrysts. In fact, clumping of olivine grains is clearly visible in hand sample and thin section.

Textural analysis

A convenient method for quantifying textural properties of a sample is crystal size distribution (CSD) analysis. The method involves calculating population density of different size bins; theory predicts that steady-state growth would generate a negative linear correlation between the size and the log of the density [3].

For our study, widths of over 1000 augite grains were measured in Nakhla section USNM 2435. Figure 2 shows the observed distribution of grain sizes; note the nearly Gaussian distribution of the primary mode. From this data, a cumulative CSD was generated, plotting size vs. $\ln(n)$, where n is the number of crystals per unit length per unit area [3]. Figure 3 demonstrates the negative linear nature of the main body of the plot. We take this to indicate that the sample experienced a significant period of steady-state grain growth in contact with melt.

NAKHLITE FORMATION: R.C. Friedman *et al.*

There are two other features of note. First, the overabundance of large grains is perhaps due to the presence of augite phenocrysts. Second, the deficit at small sizes indicates a period of Ostwald ripening, in the presence of residual silicate melt, that preferentially removed smaller grains. Using an average initial grain size from the reciprocal of the slope ($80\mu\text{m}$) and a average final grain size from the measures distribution ($242\mu\text{m}$), a period of ripening can be calculated [4]. Using a diffusion coefficient of $10^{-6} \text{ cm}^2/\text{s}$, we get a ripening period of about 10 months.

We get alternate, but comparable, estimates of cooling time from diffusion considerations. Studies of mineral zoning in nakhlites have found Lafayette grains show no Fe or Ca zoning profiles [1], suggesting the grains reacted long enough with the melt to undergo complete diffusion. Using reasonable ranges of grain size, we calculate a time necessary for complete diffusion of 1-5 years, consistent with the above estimate. As a cooling time, this would imply a magma body at least 11-26 m thick.

References: (1) Harvey, R.P. and H.Y. McSween, Jr. (1992), *GCA* **56**, 1655-1663. (2) Treiman, A.H. (1990), *Proc. LPSC* **20**, 273-280. (3) Marsh, B.D. (1988), *Contrib. Mineral Petrol.* **99**, 277-291. (4) Taylor, G.J. *et al.* (1993), *Meteoritics* **28**, 34-52.

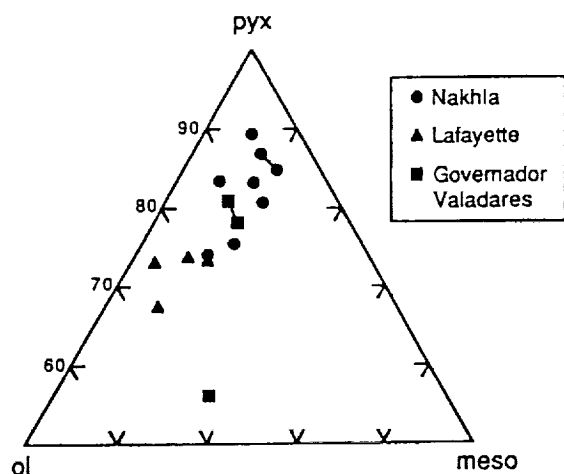


Figure 1. Modal properties of augite (pyx), olivine (ol), and mesostasis (meso) in nakhlites. Range in pyx:ol suggests variation in the abundance of primary phenocrysts in the nakhlite magma body.

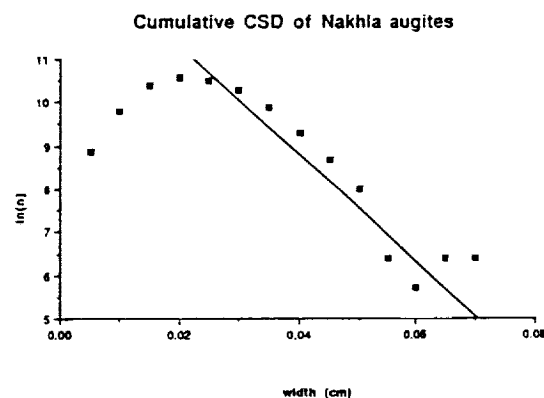
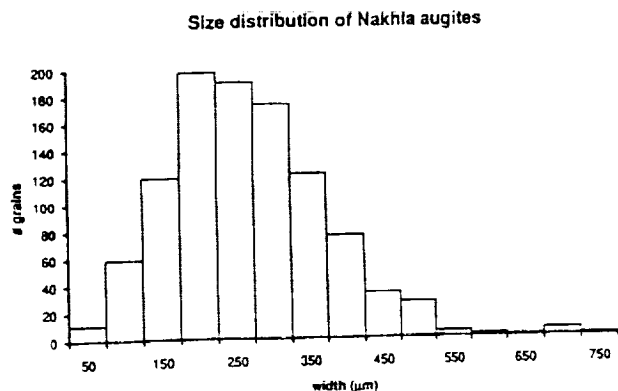


Figure 3. Crystal-size distribution (CSD) plot of augite widths. The line ($m=125/\text{cm}^3$) fits data in the main part of the trend and indicates steady-state nucleation and growth. The trail off at small sizes suggests coarsening before crystallization was complete. The overabundance at the largest sizes suggests the presence of primary phenocrysts.

Figure 2. Size distributions in Nakhla sample USNM 2435.

ESTIMATING SURFACE ROUGHNESS: EVALUATION OF AN EMPIRICAL BACKSCATTER MODEL

Lisa Gaddis, USGS, 2255 N. Gemini Dr., Flagstaff, AZ 86001

Overview: Comparison of radar backscatter coefficients (σ° , in dB), calculated using the empirical model of Oh et al. [1], to σ° extracted from AIRSAR data of four geologic units at Písgah volcanic field shows that the model is able to predict measured σ° to within ± 3 dB. The empirical model may be inverted to estimate rms height (s , in cm) from measured σ° for surfaces with $ks < 3$ [ks , or "electromagnetic roughness," is the wavenumber ($k = 2\pi/\lambda$, λ =radar wavelength) times s]. For example, model inversion for a platform pahoehoe unit at 30° - 50° incidence angles (θ) was able to estimate s to within ± 1 cm of the measured value of 3 cm. Work is underway to extend the applicability of this model to rougher natural surfaces and to apply these results to estimation of surface roughness on Venus through analyses of Magellan radar data.

The radar backscatter response of surfaces is a complex function of radar instrument parameters and surface characteristics. Theoretical radar backscatter models seek to characterize this response for cases that may have little or no applicability to most natural surfaces. For many natural surfaces, none of the commonly used theoretical models (small perturbation model [2], physical optics model [3], and their modified or combined versions [4,5]) is appropriate; natural surfaces are complex and may have both large- and small-scale roughness or a continuous distribution of roughnesses with respect to a given λ . Until appropriate theoretical backscatter models are available for natural surfaces, an empirical model relating measured surface characteristics to radar backscatter may provide a useful means of extracting physical parameters such as surface roughness from calibrated radar images of geologic surfaces.

I have compared calculated empirical backscatter values with calibrated data from the NASA/JPL Airborne Imaging Radar (AIRSAR) for four geologic units with a range of roughnesses. The four units occur at Písgah volcanic field, California. They are playa material ($s=0.83$ cm, dielectric constant $\epsilon_r=2.36$) [6,7]; "platform" pahoehoe ($s=3.0$ cm, $\epsilon_r=4.5$) [7]; hummocky pahoehoe ($s=6.0$ cm, $\epsilon_r=4.0$) [8,9]; and clinkery aa lava flows ($s=20.0$ cm, $\epsilon_r=4.0$) [8,9]. Písgah AIRSAR images were calibrated to accuracy of ± 3 dB [10]. Backscatter coefficients were extracted at L- and C-band wavelengths (24 and 5.6 cm, respectively) and at HH, HV, and VV polarizations.

The Model: The empirical radar backscatter model was developed by Oh et al. [1], who used polarimetric radar measurements collected with a scatterometer for bare soil surfaces under a variety of roughness conditions at L- (24 cm), C- (6.3 cm), and X-bands (3.16 cm) and at $\theta=10^\circ$ - 70° . Ground truth data (s , correlation length, and ϵ_r) were collected for each surface by using a laser profiler and dielectric probes. Radar measurements were made for dry and wet surfaces for surface roughnesses of $s=0.32$ - 3.02 cm; only the dry-surface data (moisture content ~ 0.15 wt.%) are considered here. Surface-height distributions for the four model surfaces were \sim Gaussian, with measured autocorrelation functions of exponential form for the three smoothest surfaces and of Gaussian form for the roughest surface. For the model surfaces s ranged from $s=0.32$ to 3.02 cm, and the "electromagnetic roughness" ranged from $ks=0.1$ to 6.01 .

For development of the model, the angular ($\theta \sim 10^\circ$ - 70°) backscattering behavior of the model surfaces was observed at VV, HV, and HH polarizations and at L-, C-, and X-bands [1]. For σ°_{VV} and $q=30^\circ$ - 70° , a sensitivity to surface roughness was observed; backscatter for $s=0.3$ - 3.0 cm increased in strength and decreased in slope, indicating a decreasing dependence on θ for increasing s . Also in this wavelength range, σ°_{VV} at X-band was observed to vary little with increasing s , indicating an insensitivity of σ°_{VV} to s for $ks > 2.0$. A strong similarity in angular behavior and backscatter strength was observed [1] between σ°_{HH} and σ°_{VV} , and the ratio of these values (the co-polarized ratio, $p = \sigma^\circ_{HH}/\sigma^\circ_{VV}$) is always ≤ 1 , approaching 1 as ks increases. For smoother surfaces, p is a function of θ , decreasing as θ increases. For rougher surfaces (e.g., $ks \geq 3$), $p \sim 1$ and is independent of θ . For co-polarized ratio data, these observations indicate a strong dependence on ks , an implicit dependence on ϵ_r , and (at higher θ) a weak dependence on θ . Although the behavior of σ°_{HV} and σ°_{VV} with respect to θ is very similar for a given λ and s , σ°_{HV} is always less than σ°_{VV} ; for increasing ks the separation between σ°_{HV} and σ°_{VV} decreases, and the cross-polarized ratio ($q = \sigma^\circ_{HV}/\sigma^\circ_{VV}$) increases with

ESTIMATING SURFACE ROUGHNESS FROM RADAR BACKSCATTER: Gaddis, Lisa

increasing ks . For dry surfaces, these observations of cross-polarized ratio data reflect a strong dependence on ks , an implicit dependence on ϵ_r , and a lack of dependence on θ .

Co- and cross-polarized ratio data (p and q) as functions of ks for a range of s and at $\theta=30^\circ$ - 50° were used [1] to derive empirical functions: q is a function of nadir Fresnel reflectivity (Γ_0 , and thus ϵ_r) and ks ; p is a function of q , Γ_0 , θ , and ks . The magnitudes of the backscattering coefficients are given by additional empirical relations: σ°_{VV} is a function of ks , p , and the horizontal and vertical components of the Fresnel reflectivities (Γ_h , Γ_v) of the surface at θ ; σ°_{HH} is a function of ks , p , Γ_h , and Γ_v ; and σ°_{HV} is a function of q and σ°_{VV} . Note that p is very sensitive to both ks and ϵ_r ; for dry, smooth surfaces with low ϵ_r and small ks , p approaches 0 very rapidly. Thus, the empirical model does not predict significant differences between σ°_{HH} and σ°_{VV} for most dry surfaces; for $ks \leq 2$, the factor p accounts for the small differences between σ°_{HH} and σ°_{VV} and includes a dependence on ϵ_r . Also, no attempt was made to include a coherent component in the empirical model, so its range of applicability does not extend to $\theta < 20^\circ$ for smooth surfaces. For rougher surfaces, a coherent component is expected to be negligible and so the model may be used at $\theta=10^\circ$ - 70° .

Application: Surface characteristics (s , ϵ_r) for four units at Pisgah were used in conjunction with the empirical backscatter model [1] to predict σ° at C- and L-bands. Predicted values were compared with σ° for the same sites. Agreement between the model and the measured values is influenced by the exact values of ϵ_r and s used in the model calculations. Tests indicate that the model is more sensitive to variation in s than in ϵ_r for smooth surfaces. For rougher surfaces (e.g., aa, $ks=22$), the model is less sensitive to changes in either s or ϵ_r , with only slightly more sensitivity to variation in ϵ_r than in s . Agreement between measured and model data is quite good for σ°_{HV} and σ°_{VV} , for which the empirical model predicted σ° to within ± 3 dB of the measured values (the estimated range of calibration accuracy of the AIRSAR data). However, the agreement between measured and model data is poorer for σ°_{HH} , for which the measured data are as much as 7 dB lower than the predicted values. As described above, the empirical backscatter model predicts little or no difference in σ°_{HH} and σ°_{VV} ; apparently the scatterometer data from which the empirical model was derived exhibited comparable σ°_{HH} and σ°_{VV} . As indicated by [2] for the general theoretical behavior of σ° at $\theta \sim 30^\circ$ - 60° for slightly rough surfaces, σ°_{HH} is expected to be lower than σ°_{VV} , suggesting that the AIRSAR data show more realistic backscattering differences at horizontal and vertical polarizations. This discrepancy between the scatterometer data and the AIRSAR data is under investigation.

The empirical model [1] may be inverted to estimate s from measured backscatter data for surfaces with $ks < 3.0$. Such an inversion was conducted for the platform pahoehoe by using L-band AIRSAR data ($ks=0.6$). All calculated s values are within ± 1 cm of the measured value of 3.0 cm. However, a different Γ_0 is required for each θ , confirming the complexity of modeling backscatter from natural surfaces (radar energy no doubt "sees" a single surface roughness differently at each θ for a given λ).

These promising results suggest that Magellan data can be used to infer surface roughnesses on Venus. Such roughness data can serve as a basis for comparison of the terrestrial and Venusian lava flow textures that are indicative of flow eruption and emplacement processes. Quantitative morphologic and surface textural analyses of lava flows can then be complemented by correlation of backscatter data with physical properties and/or composition as constrained by Magellan altimetry and emissivity data. Future work with this empirical backscatter model will involve modifications of the model to reflect accurate differences in HH and VV, as well as extension of the model to rougher surfaces ($ks > 6$).

References: [1] Oh, Y. et al., IEEE Trans. Geosci. Rem. Sens., GE-30, 370-381, 1992; [2] Ulaby, F.T. et al., Microwave Remote Sensing, Active and Passive, II, 1982; [3] Beckmann, P. and A. Spizzichino, The Scattering of Electromagnetic Waves from Rough Surfaces, 1987; [4] Brown, G.S., IEEE Trans. Ant. Prop., AP-26, 472-482, 1978; [5] Fung, A.K. and H.J. Eom, IEEE Trans. Ant. Prop., AP-29, 463-471, 1981; [6] Gaddis, L.R., GSA Bull., 104, 695-703, 1992; [7] van Zyl, J.J. et al., GRL, 18, 1787-1790, 1991; [8] Greeley, R. et al., submitted to Desert Aeolian Processes (Tchakerian, ed.); [9] Arvidson, R.E. et al., GSAB, 105, 175-188, 1993; [10] van Zyl, J.J., IEEE Trans. Geosci. Rem. Sens., 28, 337-348, 1990.

SPECTRAL UNIT MAP OF THE MOON WITH IMPROVED GALILEO SSI MOSAICS;

Lisa Gaddis, Alfred McEwen, and Tammy Becker, U.S. Geological Survey, 2255 N. Gemini Drive, Flagstaff, AZ 86001

Overview: We produced a mosaic of calibrated Galileo SSI data from EM1 and EM2, providing a nearly global multispectral map (~75% coverage) of the lunar surface. From this mosaic, we produced a spectral unit map by using supervised classification and a minimum-distance algorithm. Preliminary results of analysis of the spectral unit map include these observations: (1) exposures of nearly pure anorthosite are not distinguishable from immature highland soils with the SSI data; (2) the South Pole/Aitken basin interior has a very heterogeneous composition including several mare units and materials similar to Apollo 14 and Apollo 16 highlands; (3) cryptomare regions near Schiller/Schickard and Mendel-Rydberg are similar to the Apollo 14 mixed-lithology (highland/mare) unit; and (4) the previously published spectral-unit boundaries for nearside maria will require some refinements.

The Galileo Solid-State Imaging (SSI) experiment acquired multispectral images of the Moon in 1990 (EM1) and 1992 (EM2) [1]. SSI data were collected at wavelengths of 412, 560, 664, 731, 757, 888, and 990 nm. The EM1 data cover the western lunar hemisphere (Orientale), including ~45% of the farside, at resolutions of 4 to 30 km/pixel. The EM2 data cover the lunar north polar, eastern limb, and nearside regions at resolutions of 1.1 to 5.3 km/pixel. Altogether, the EM1 and EM2 data cover ~75% of the Moon's surface. Initial calibration and mosaicking of the datasets are described by [2]. More recently, we have updated the calibration and mosaicking of EM1 data in light of our experience and improved understanding of the SSI instrument and data characteristics after the EM2 encounter. In addition, a fully calibrated EM2 nearside and north polar mosaic (incorporating mosaic sequences LUNMOS-6 and -7, with 10°-40° phase angles) is now available. We have produced a combined EM1/EM2 mosaic of SSI data, providing a nearly global view of color variations on the Moon.

We conducted a preliminary analysis of the EM1/EM2 mosaic to examine major lunar color-unit boundaries and possible compositional affinities. Our analyses have used four of the seven SSI filters: (1) the 412/560 nm or "UV/VIS" ratio, related to TiO₂ content (high UV/VIS~high TiO₂ and vice versa) of mature mare soils [3]; (2) the 560/757 nm "continuum slope" (CS), related to TiO₂ content, composition, and maturity of soils; (3) the 757/968 nm 1- μ m "mafic mineral" (MM) absorption, related to the abundance of Fe-bearing minerals in soils; and (4) the 560 nm "visible albedo" data. We performed a supervised classification (using a simple minimum-distance classifier) of the color-ratio and albedo data from the EM1/EM2 mosaic. Spectral units used as training sites in the classification were (1) 11 mare basalts (distinguished by UV/VIS, albedo, and 1- μ m absorption

strength [4]); (2) 3 highlands units (the Apollo 14 and 16 landing sites and the Orientale ring anorthosite massif [5]); (3) 4 craters (Copernicus melt [6], the olivine-rich Bullialdus central peak [7], and the Aristarchus and Tycho interiors [2]); and (4) dark-mantle deposits (DMD; Aristarchus [8] and Apollo 17/Taurus-Littrow [9] DMD). Classification results indicate that the inferred feldspathic composition of the anorthosite massif [5] in the Inner Rook Mountains of Orientale cannot be readily distinguished from the high-albedo, immature soils associated with fresh highland craters such as Tycho (both units are distinguished by high albedo and similar color properties). The region of the farside South Pole/Aitken (SP/A) basin shows highly heterogeneous spectral signatures indicative of extensive lithologic mixing [3,10], with possible compositional affinities to Apollo 14 and Apollo 16 highland materials and an asymmetric distribution of mixed mare types. The southern region of SP/A shows a slightly stronger MM absorption than the northern region, suggesting a more mafic composition. Cryptomare deposits of the Mendel-Rydberg [3,10] and Schiller/Schickard [3,10,11,12] regions---as well as highlands units northwest of Mare Frigoris---show compositional affinities with the Apollo 14 highlands spectral unit. This highland affinity might be expected for compositionally mixed highlands/mare units such as those sampled by Apollo 14 [13]. DMD at Aristarchus Plateau and at Sulpicius Gallus are spectrally similar (low UV/VIS, strong MM) but are distinct from the DMD at Taurus-Littrow and Sinus Aestuum (~high UV/VIS, ~weak MM). These spectral affinities are consistent with previous results. Earth-based spectra for DMD at Aristarchus Plateau [8] and Sulpicius Gallus [14] show prominent iron absorptions, suggesting that these deposits have a significant component of Fe-bearing glass beads similar to those sampled at Taurus-Littrow [9]. Spectral signatures of DMD at Taurus-Littrow and Sinus Aestuum are thought to be dominated by black, devitrified beads identified by Apollo 17 [15].

Continued analyses of this multispectral Galileo SSI EM1 and EM2 mosaic will enable us to refine existing spectral unit boundaries and perhaps to identify previously unrecognized spectral classes among the lunar soils. It is also anticipated that analyses of these data will result in an improved baseline dataset for site selection, image targeting, calibration, and multispectral image analysis for the SDIO/NASA Clementine mission.

References: [1] Belton et al., 1992, *Science*, 255, 570; [2] McEwen et al., 1993a, *LPS XXIV*, 955; and McEwen et al., 1993b, *JGR*, 98, 17207; [3] Pieters, C.M. et al., 1993, *JGR*, 98, 17127; [4] Pieters, C.M., 1978, *PLSC* 9, 2825; [5] Hawke, B.R. et al., 1992, *LPS XXIII*, 505; [6] Smrekar, S. and C. Pieters, 1985, *Icarus*, 63, 442; [7] Pieters, C.M., 1991, *GRL*, 18, 2129; [8] Lucey, P. et al., *PLPSC* 16, *JGR*, 91, D344; [9] Pieters, C.M. et al., 1973, *JGR*, 78, 5867; [10] Head, J.W. et al., 1993, *JGR*, 98, 17149; [11] Mustard, J.F. et al., 1992, *LPS XXIII*, 957; [12] Greeley, R. et al., 1993, *JGR*, 98, 17183; [13] Wilhelms, D., 1987, *USGS Prof. Pap.* 1348; [14] Head, J.W. et al., 1980, *LPS XI*, 418; [15] Gaddis, L.R. et al., 1985, *Icarus*, 61, 461.

INFLUENCE OF VARIABLE OXYGEN AND SULFUR FUGACITY ON PARTITIONING OF Ni, Cu AND Cr AMONG OLIVINE, SILICATE MELT AND SULFIDE MELT. Glenn A. Gaetani and Timothy L. Grove, Dept. Earth, Atmospheric and Planetary Sciences, Massachusetts Institute of Technology, Cambridge, Mass 02139

Introduction. The absolute and relative abundances of siderophile elements in the silicate mantles of terrestrial planets provide constraints on the conditions under which their metallic cores segregated [1]. It has been recognized for nearly thirty years that the siderophile abundances in the Earth's upper mantle are inconsistent with simple metal/silicate equilibrium [2]. It has been suggested that a light element, such as S, dissolved in an FeNi metallic liquid may have affected the distribution of siderophile elements during segregation of the core [3,4]. Here we report the results of experiments designed to determine the influence of variations in the fugacities of oxygen (f_{O_2}) and sulfur (f_{S_2}) on the partitioning of Ni, Cu and Cr among coexisting olivine, silicate melt and sulfide melt. Our experimental results indicate that at a constant temperature the partition coefficients for Cu and Cr between sulfide melt and silicate melt increase as the ratio of f_{O_2} to f_{S_2} decreases. The sulfide melt/silicate melt partitioning behavior of Ni at low f_{O_2} /high f_{S_2} conditions is complicated by composition-related variations in the solubility of NiS in the silicate melt. The olivine/silicate melt partition coefficient for Cr increases with decreasing f_{O_2}/f_{S_2} ratio, while Ni becomes less compatible in olivine relative to silicate melt.

Experimental and Analytical Methods. Experiments were performed at 1 atm in crucibles fabricated from San Carlos olivine (Fo₈₉₋₉₁), with f_{O_2} and f_{S_2} controlled by mixing CO₂, CO and SO₂ gases. Starting compositions were a CaO-MgO-Al₂O₃-SiO₂-FeO-Na₂O analog for a chondrule from an ordinary chondrite (Fo86) [5] doped with FeS and NiO, and a synthetic Monroe Township komatiite (KOM) [6], containing Cr₂O₃, doped with FeS, NiO, and CuO. Experiments were performed at a single temperature, with f_{O_2} ranging from 1 log unit below the fayalite-magnetite-quartz (FMQ) oxygen buffer to the iron-wüstite (IW) oxygen buffer and f_{S_2} ranging from 1.7 to 2.7 log units above to FeFeS sulfur buffer. Experimental run products were analyzed by electron microprobe. Analytical conditions for trace elements were 15 kV accelerating potential and a beam current of 200 nA with counting times ranging from 250 to 700 s, depending on concentration of the trace element.

Results and Discussion. Table 1 reports the sulfide melt/silicate melt partition coefficients ($D_i^{sf/sil}$) determined experimentally for high f_{O_2} /low f_{S_2} and low f_{O_2} /high f_{S_2} conditions.

Table 1. Sulfide melt/silicate melt partition coefficients for Ni, Cu and Cr.

Experiment	T (°C)	Log f_{O_2}	Log f_{S_2}	$D_{Ni}^{sf/sil}$	$D_{Cu}^{sf/sil}$	$D_{Cr}^{sf/sil}$
Fo86-8s	1350	-7.9	-2.5	570	—	—
Fo86-10s	1350	-10.2	-1.5	2000	—	—
KOM-1s	1350	-7.9	-2.5	540	270	<0.01†
KOM-3s	1350	-10.2	-1.5	510	910	44

† Cr concentration in sulfide melt below detection limit of electron microprobe.

The sulfide melt/silicate melt partition coefficients for both Cu and Cr increase as the f_{O_2}/f_{S_2} ratio decreases. Further, the solubility of both elements decreases in the silicate melt, Cu by a

PARTITIONING OF Ni, Cu, AND Cr: Gaetani, G.A. and Grove, T.L.

factor of 12 and Cr by a factor of 6. The partitioning behavior of Ni appears to be more complicated. Experiments performed on the Fo86 composition show a factor of 3.5 increase in $D_{\text{Ni}}^{\text{sf/sil}}$, while Ni partitioning between sulfide melt and komatiite appears to be insensitive to the changing conditions. Table 2 reports the olivine/silicate melt partition coefficients measured in our experiments, along with the concentrations of nickel (Ni^{sil}) and sulfur (S^{sil}) dissolved in the silicate melt and the value of $D_{\text{Ni}}^{\text{ol/sil}}$ predicted from the composition of the silicate melt in a S-free system [8].

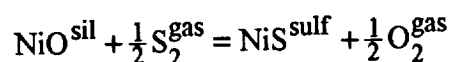
Table 2. Olivine/silicate melt partition coefficients for Ni, Cu and Cr.

Experiment	Ni^{sil}	S^{sil}	$D_{\text{Ni}}^{\text{pred}\dagger}$	$D_{\text{Ni}}^{\text{ol/sil}}$	$D_{\text{Cu}}^{\text{ol/sil}}$	$D_{\text{Cr}}^{\text{ol/sil}}$
Fo86-8s	0.102	0.031	7.9 ± 0.9	7.5 ± 0.2	—	—
Fo86-10s	0.006	0.080	7.1 ± 0.9	4.0 ± 0.4	—	—
KOM-1s	0.068	0.073	6.7 ± 0.9	6.74 ± 0.06	0.10	0.65
KOM-3s	0.014	0.155	6.1 ± 0.8	0.94 ± 0.02	‡	3.4

† Olivine/silicate melt partition coefficient predicted using the expressions of Kinzler et al. [8].

‡ Cu concentration in olivine below detection limit of electron microprobe.

The most striking results for olivine/silicate melt partitioning are the anomalously low $D_{\text{Ni}}^{\text{ol/sil}}$ values obtained at low f_{O_2} /high f_{S_2} conditions, while at high f_{O_2} /low f_{S_2} conditions the observed partition coefficients are within uncertainty of the predicted values. Selective retention of Ni in the silicate melt relative to olivine is attributable to the existence of NiS species in the silicate melt [9,10]. The deviation of the observed $D_{\text{Ni}}^{\text{ol/sil}}$ from the predicted values can be used to estimate the NiS/NiO ratio of the silicate melts at low f_{O_2} /high f_{S_2} conditions (0.78 for Fo86-10s and 5.4 for KOM-3s). If we then consider the sulfide melt/silicate melt exchange reaction:



and calculate simple Nernst distribution coefficients for the two sulfide melt/silicate melt pairs, we obtain similar values (3,700 for FO86 and 3,100 for KOM). Further, the estimated NiO concentrations of the two silicate melts are similar (0.004 for FO86 and 0.003 for KOM) despite significant differences in total Ni. The difference in NiS solubility between the Fo86 and KOM compositions may be due to differences in the degree of polymerization of the silicate melt, as Fo86 has a higher ratio of network formers to network modifiers. It therefore appears that at extremely reducing conditions, when the fugacity of sulfur is high, the NiS content of the silicate melt may have a significant effect on observed partition coefficients for both olivine/silicate melt and sulfide melt/silicate melt pairs. This implies that it is necessary to know something about the composition of the silicate melt, in addition to the ambient conditions, in order to model the evolution of siderophile elements in the mantles of terrestrial planets.

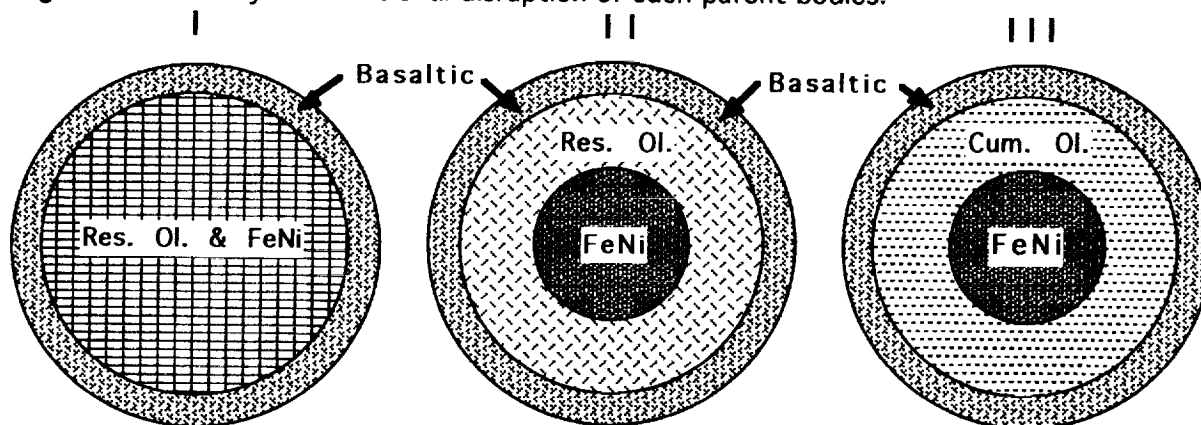
References. [1] Jones and Drake, 1986, *Nature*, 322:221-228; [2] Ringwood, 1966, *Geochim. Cosmochim. Acta*, 30:41-104; [3] Arculus and Delano, 1981, *Geochim. Cosmochim. Acta*, 45:1331-1343; [4] Brett, 1984, *Geochim. Cosmochim. Acta*, 48:1183-1188; [5] Ehlers et al., 1992, *Geochim. Cosmochim. Acta*, 56:3733-3743; [6] Kinzler and Grove, 1985, *Am. Min.*, 70:40-51; [8] Kinzler et al., 1990, *Geochim. Cosmochim. Acta*, 1255-1265; [9] Naldrett, 1989, *Magmatic Sulfide Deposits*, p. 36; [10] Gaetani et al., 1993, *EOS*, 74:337-338.

NATURE AND ORIGINS OF THE OLIVINE-DOMINATED A- AND S(I)-TYPE ASTEROIDS;
M. J. Gaffey, Dept. Earth Environ. Sci., Rensselaer Polytechnic Inst., Troy, New York 12181

Olivine is the most abundant mineral which can be unambiguously identified on asteroid surfaces. Olivine is also the most abundant mineral in anhydrous silicate bodies of chondritic (or solar) composition. In undifferentiated asteroids and in chondritic meteorite parent bodies, this olivine is intimately mixed with a variety of other mineral species. However, the A-type asteroids and a significant portion of the S-type asteroids exhibit spectra indicating the presence of large concentrations of nearly pure olivine produced by igneous processes. Consideration of the nature of these igneous processes leads to constraints on the size of the parent planetesimals of these olivine-rich asteroids and on the identification of additional fragments of those specific disrupted parent bodies.

Olivine can be concentrated in three general ways by igneous processes depending on the peak temperature attained within a parent planetesimal. These include: i) extraction of a melt containing the basaltic components (pyroxene & feldspar) at low degrees of partial melting to leave a residual intimate mixture of olivine and metal-metal sulfides; ii) gravitational segregation of metal melt from the solid or partially solid olivine at high degrees of partial melting; and iii) gravitational segregation of dense, early crystallizing olivine to form an olivine cumulate layer in bodies which had undergone complete or nearly complete melting [1-3]. Meteorites such as brachinites, lodranites and (some) ureilites appear to have been produced by the first process [3,4,5]. Pallasites apparently represent samples of the olivine-metal boundary region in bodies produced by the second or third processes. Residual or cumulate olivine achondrites produced by the second or third processes have not been unambiguously recognized in meteorite collections.

Three general types of differentiated parent bodies (shown schematically on the figure below) include large olivine-dominated regions: I) a residual intimate olivine-metal mixture [ol/metal ~ 1-5] in the interior underlying the basaltic crust of bodies which underwent low degrees of partial melting; II) a residual olivine layer sandwiched between the metal core and basaltic crust of bodies which underwent high degrees of partial melting; and III) a cumulate olivine layer sandwiched between the metal core and basaltic crust of bodies which underwent complete or essentially complete melting and magmatic differentiation. For smaller bodies with abundant volatiles the basaltic component may have been expelled from the body by explosive volcanism [3,5,6]. Olivine-dominated asteroids represent samples of these olivine-rich regions released by the collisional disruption of such parent bodies.



Assuming efficient basaltic melt extraction [2], the relative dimensions of the olivine-metal volume (case I: 0.80 to 0.94 of the body radius) or olivine layer (cases II & III: 0.29 to 0.47 of the body radius) depends on the initial composition of the parent body (i.e., chondritic types H to CV/CO). The metal cores for cases II and III have fractional radii of 0.47 and 0.31 for H-type and CV/CO-type precursors, respectively.

NATURE OF A- AND S(1)-TYPE ASTEROIDS: Gaffey M. J.

The A-type asteroids exhibit significantly stronger ($\sim 2\times$) olivine absorption features than the most olivine-rich S-asteroids (subtype S(1)) of comparable sizes [2]. It appears probable that the A-type assemblages represent fragments of case III parent bodies. The more strongly featured and higher albedo S(1)-objects (e.g., 113 Amalthea, 354 Eleonora) appear to represent fragments of case II parent objects, while the more weakly featured and lower albedo S(1)-object (e.g., 42 Isis) and associated objects (e.g., 9 Metis, 89 Julia) appear to sample case I parent planetesimals.

Based on the IRAS diameters of these olivine-dominated asteroids [7], the table below indicates the minimum diameter of their parent planetesimals assuming that they were derived from mantle layers in cases II and III and the maximum diameter of the parent planetesimals for objects which would still include the core of the parent body. For a case I parent object, the minimum diameter is indicated. In each case the diameters for H-type and for CV/CO-type parent compositions are indicated.

Parent Planetesimal Diameters as a Function of Parent Body Composition and Fragment Source

Object	Type	Case	<u>Minimum</u> Diameter if Mantle Fragment		<u>Maximum</u> Diameter if Core Included	
			H	CV/CO	H	CV/CO
289 Nenetta	A	III	285 km	175 km	90 km	135 km
446 Aeternitas	A	III	295 km	180 km	90 km	140 km
113 Amalthea	S(1)	II	330 km	205 km	100 km	155 km
354 Eleonora	S(1)	II	1120 km	690 km	345 km	520 km
42 Isis	S(1)	I	135 km	115 km	-----	-----
89 Julia	S(U)	I	200 km	170 km	-----	-----

Most are consistent with mantle fragments of 200 to 350 km parent planetesimals which fully melted (289, 446) or which extensively partially melted (113). 354 Eleonora probably still contains the core derived from a 350-520 km parent planetesimal.

Considerations of the relative survival probabilities of asteroidal bodies suggests that it is highly likely that the smaller case II and III objects (e.g., 298 Nenetta, 446 Aeternitas, 113 Amalthea) are not the largest remaining fragments of their respective parent bodies. Among the suite of fragments produced by the catastrophic disruption of a parent planetesimal, the larger and stronger (i.e., metal-rich) bodies have longer lifetimes against subsequent collisional destruction than smaller and weaker (i.e., silicate-rich) bodies. As noted above [2], the diameter of the cores ranges from 1.3 to 3.2 times the thickness of the overlying olivine-rich layer in cases II and III. The survival probability of such core objects (i.e., larger and metal-rich) is higher than that of the smaller, silicate-rich case II and III objects discussed above. Therefore it seems probable that each of these case II and III bodies (41-48 km) should have a large associated core fragment (an S- or M-type $>55 - 155$ km) located in a relatively nearby orbit. We are currently surveying the asteroid population near each of these case II and III olivine-rich asteroids to identify candidates for the associated cores.

Acknowledgements: This work was supported NSF Solar System Astronomy grant AST-9012180 and by NASA Planetary Geology and Geophysics grant NAGW-642.

References: [1] Taylor G. J. (1992) *JGR (Planets)* 97, 14717-14726. [2] Gaffey M. J. et al. (1993) *Icarus*, in press. [3] Taylor G. J. et al. (1993) *Meteoritics* 28, 34-52. [4] Nehru C. E. et al. (1992) *Meteoritics* 27, 267 (abstract). [5] Warren P. H. and Kallemeyn G. W. (1992) *Icarus* 100, 110-126. [6] Keil K. and Wilson L. (1993) *Earth Planet. Sci. Lett.* 117, 111-124. [7] Tedesco E. F. (1989) In *Asteroids II* (eds. R. P. Binzel, T. Gehrels and M. S. Matthews), pp. 1090-1138. Univ. Arizona Press, Tucson.

INTERSTELLAR GRAPHITE IN TIESCHITZ; X. Gao, C. Alexander, P. Swan and R. Walker, McDonnell Center for the Space Sciences and Department of Physics, Washington University, One Brookings Drive, St. Louis, MO 63130-4899.

In previous work on the CM meteorite Murchison, chemical and physical techniques were used to produce separates rich in spherical graphite particles [1]. Most grains exhibit highly anomalous $^{12}\text{C}/^{13}\text{C}$ ratios as well as anomalies in other, minor elements indicative of a circumstellar origin for the grains [2]. In this work, we report the first observation of similar interstellar carbon-rich spherules in separates from an ordinary chondrite. New separation and mapping procedures used to assess the concentration of these and other interstellar grain components are also described.

A 4.5 gm starting sample of Tieschitz was treated using a modification of the original methods developed by the Chicago group [3]. The modified methods were developed to produce samples enriched in the known interstellar phases (diamonds, SiC, graphite, corundum) more rapidly, and with smaller starting amounts of material, than previously done. The resulting interstellar grain-rich separates are smaller and less pure than those of the Murchison K series, but as we demonstrate here and in a companion abstract dealing with interstellar oxide grains [4], they contain enough interstellar material to measure in a variety of ways. A key element in the new method is the use of x-ray mapping [5] to locate interesting species at various stages in the separation procedure. Concentrations of different species are determined directly by a combination of weighing and mapping. The interstellar origins of various components are further assessed by ion probe isotopic measurements. This approach for determining the concentrations of interstellar dust species is thus fundamentally different than indirect methods used to infer the concentrations of various interstellar phases (based, for example, on noble gas measurements [6]).

After toluene-methanol extraction, the remaining Tieschitz sample was reacted with HF-HCl in a pressure bomb to dissolve silicates, and subsequently treated with $\text{Na}_2\text{Cr}_2\text{O}_7$ to remove reactive kerogens. A diamond-rich fraction was prepared by colloidal separation. The remaining material was separated by density and grain size into sub-samples enriched in various phases. SEM mapping of a density separate of 1.9-2.4 g/cm³ and nominal size > 0.2 μm showed that this fraction contains many carbon-rich spherulitic particles with morphologies similar to those previously shown to be interstellar graphite grains [2,7].

Thirty-eight of these grains, chosen on the basis of their external morphologies and high carbon x-ray count rates, were subsequently analyzed in the ion microprobe for their carbon and nitrogen isotopic compositions. As shown in Fig. 1, two of the spherules studied have highly anomalous $^{12}\text{C}/^{13}\text{C}$ ratios that fall within the (large) range previously measured in graphite grains from Murchison [2] and are similarly identified as interstellar material, probably graphite. One grain with normal C composition appears to be enriched in ^{15}N .

In contrast to the relative paucity of isotopically anomalous carbon-rich spherules found here (3/38), 50% to 95% of similar spherules from different density fractions of Murchison residues, encompassing about the same range as the Tieschitz separate studied here, are anomalous. The origin of these carbon-rich spherulites with isotopically normal carbon is unclear. Some such grains exhibit N and/or Mg anomalies and thus do not appear to have formed in the solar system. Whatever their origin, their abundance relative to that of the demonstrably interstellar graphite grains appears to be much higher in Tieschitz than in Murchison. However it must be noted that isotopic patterns are known to be associated with external morphologies [8] and we cannot rule out the possibility that the apparent difference results from selection biases used by different investigators in choosing which grains to measure in the ion probe. As we show in Fig. 2, grains of both normal and anomalous isotopic compositions can have similar "graphitic" appearances.

One of the primary purposes in developing the modified etching procedures described here was to survey, by direct measurement, the concentration of different interstellar phases in various meteorites. Based on the weight fractions of various residues and the proportion of isotopically

INTERSTELLAR GRAPHITE IN TIESCHITZ. GAO X. et al.

anomalous grains, we estimate that the bulk concentration of demonstrably interstellar graphite in Tieschitz is almost 100x less than that in Murchison. Considering that the interstellar material probably resides exclusively in the fine-grained matrix, there still appears to be an order of magnitude lower concentration in Tieschitz than in Murchison.

References: [1] Amari S. *et al.* (1990) *Nature* **345**, 238-240. [2] Amari S. *et al.* (1993) *Nature* **365**, 806-809. [3] Amari S. *et al.* (1993) *Geochim. Cosmochim. Acta* (in press). [4] Nittler L. *et al.* (1994) *LPSC XXV*, submitted. [5] Swan P. *et al.* (1989) *LPSC XX*, 1093-1094. [6] Huss G. (1990) *Nature* **347**, 159-162. [7] Bernatowicz T. *et al.* (1991) *Ap. J.* **373**, L73-L76. [8] Amari S. *et al.* (1993) *Meteoritics* **28**, 316-317.

Figure 1. Isotopic composition of Tieschitz graphite and comparison with that of Murchison graphite.

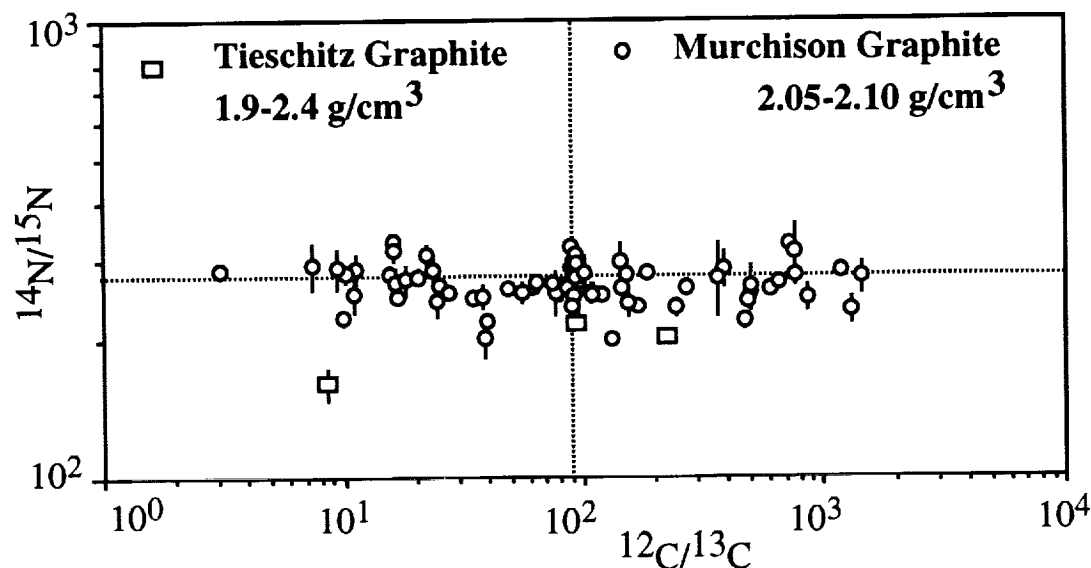
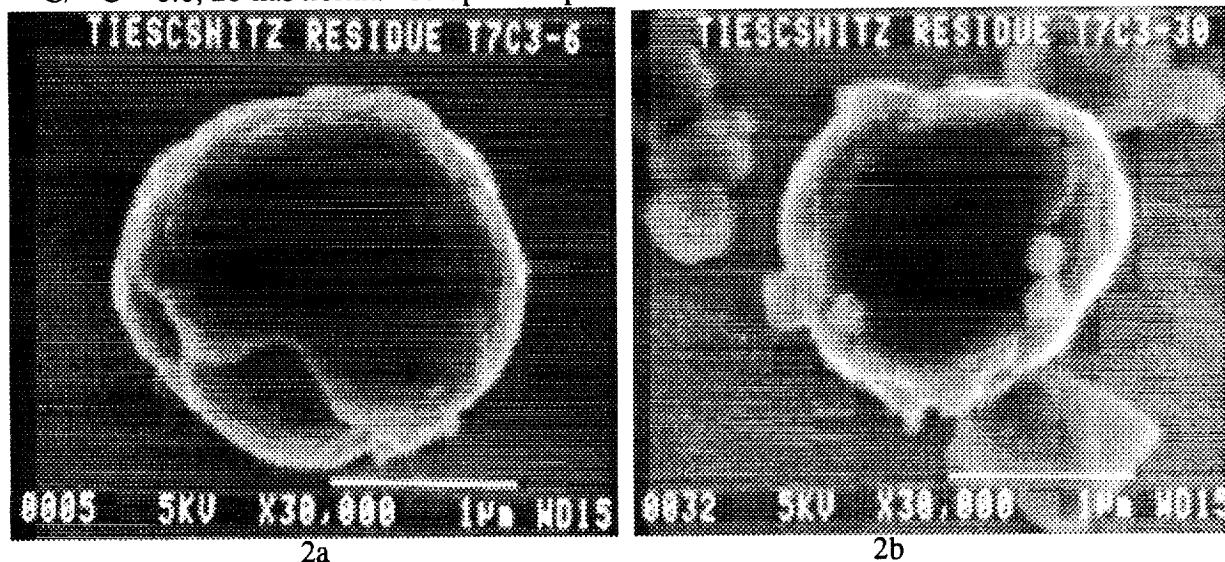


Figure 2. Two carbon-rich spherules from Tieschitz. 2a is isotopically anomalous with $^{12}\text{C}/^{13}\text{C} = 8.8$, 2b has normal isotopic composition.



SOLAR PROTON PRODUCED NEON IN SHERGOTTITE METEORITES

D. H. Garrison¹, M. N. Rao¹, and D. D. Bogard² (¹Lockheed-ES&C and ²Code SN1, NASA, Johnson Space Center, Houston, TX 77058)

Cosmogenic radionuclides produced by near-surface, nuclear interactions of energetic solar protons (~10-100 MeV) have been reported in several lunar rocks and a very few small meteorites. We recently documented the existence and isotopic compositions of solar-produced, or SCR Ne in two lunar rocks [1, 2]. Here we present the first documented evidence for SCR Ne in a meteorite, ALH77005, which was reported to contain SCR radionuclides [3]. Examination of literature data for other shergottites suggest that they may also contain a SCR Ne component. Existence of SCR Ne in shergottites may be related to a martian origin.

Solar-Produced Ne in ALH77005: To resolve SCR Ne produced near the surface of ALH77005 from galactic (GCR) Ne expected to dominate at depths below a few cm, we made temperature extractions of 7 samples from different shielding depths. A three-isotope Ne correlation plot (Fig. 1) indicates that most of the Ne is cosmogenic in composition; only the first (350°C) extractions, releasing a small fraction of the total Ne, plot outside of Fig. 1 and along the trend lines that connect with atmospheric composition. The cosmogenic $^{21}\text{Ne}/^{22}\text{Ne}$ ratio in ALH77005 appears variable, however, and gives values of 0.71-0.78 (for $^{20}\text{Ne}/^{22}\text{Ne} < 1.0$). These ratios are less than those shown by typical chondrites, e.g., the 31 H-chondrites plotted on the same $^{21}\text{Ne}/^{22}\text{Ne}$ scale in Fig. 1 [4]. The range of $^{21}\text{Ne}/^{22}\text{Ne}$ ratios shown by 30 of these chondrites (0.82-0.94) spans much of the range that is predicted to occur from significant variations in GCR shielding depths [5]. High $^3\text{He}/^{21}\text{Ne}$ ratios (ALH77005 is ~8) and $^{21}\text{Ne}/^{22}\text{Ne}$ ratios below ~0.8 are very difficult to obtain in chondrites from GCR shielding alone [5].

We conclude that ALH77005 contains, in addition to a GCR component, a SCR Ne component having the calculated composition (Fig. 1) for energetic solar protons over a shielding range of 0.5-10 g/cm² [6]. This is the first description of SCR Ne in a meteorite. In addition to having lower $^{21}\text{Ne}/^{22}\text{Ne}$ ratios, those ALH77005 samples believed to have resided nearer the meteorite surface also tend to have somewhat larger concentrations of total cosmogenic ^{21}Ne compared to more interior samples. This observation is consistent with an extra SCR component but not with GCR production as a function of depth. Because the predicted SCR/GCR production ratio for Ne varies ~1-0.1 over shielding depths of ~0.7-8 g/cm² (6), $^{21}\text{Ne}/^{22}\text{Ne}$ in ALH77005 is expected to vary ~0.70-0.80 over the same shielding range, in agreement with measured data. We recently showed very systematic correlations in cosmogenic ^{21}Ne concentrations, $^{21}\text{Ne}/^{22}\text{Ne}$ ratios, and subsurface depths for samples from lunar rock 61016; these were attributed to a depth-variable SCR component [1]. One H-chondrite (Fig. 1) gave $^{21}\text{Ne}/^{22}\text{Ne} = 0.74$ and high $^3\text{He}/^{21}\text{Ne} = 9$ indicative of irradiation under low GCR shielding [4]; we suggest that this chondrite also contains a SCR Ne component.

SCR Ne in Other Shergottites: Literature data [7, 8, 9, 10, 11, 12, 13, 14, 15, 16, 17] of Ne released during temperature extractions of shergottites EET79001, LEW88516, Shergotty, and Zagami also show $^{21}\text{Ne}/^{22}\text{Ne}$ lower than that for typical chondrites and suggest the presence of SCR Ne. A least squares fit to the EET79001 data (Fig. 2) defines cosmogenic $^{21}\text{Ne}/^{22}\text{Ne} = 0.76$ at $^{20}\text{Ne}/^{22}\text{Ne} = 0.85$ and passes near the atmospheric composition. Data for the other shergottites (Fig. 2 inset with the same $^{21}\text{Ne}/^{22}\text{Ne}$ scale) show a more cosmogenic composition and indicate $^{21}\text{Ne}/^{22}\text{Ne}$ of ~0.73-0.83. (One temperature extraction of Shergotty shows a chondrite-like $^{21}\text{Ne}/^{22}\text{Ne}$ of 0.88 but an unexplainably low $^{20}\text{Ne}/^{22}\text{Ne}$.) Measurements of cosmogenic radionuclides and tracks in shergottites suggest that they were irradiated as small objects and suffered low ablation losses averaging 1-3 cm [3, 18]. The cosmogenic $^3\text{He}/^{21}\text{Ne}$ ratio for ALH77005 and LEW88516 (~7-8) suggests that shielding was less than for the other three shergottites ($^3\text{He}/^{21}\text{Ne} = 4-6$) [17], and thus a larger SCR component might be expected in ALH77005.

Effects of Composition: Because ALH77005 and LEW88516 have chemical compositions similar to ordinary chondrites, observed differences in $^{21}\text{Ne}/^{22}\text{Ne}$ (Fig. 1) cannot be caused by target element effects. However, because other shergottites show considerable compositional differences compared to chondrites, we examined the compositional effects on cosmogenic $^{21}\text{Ne}/^{22}\text{Ne}$ in more detail (Fig. 3). Mg yields a considerably lower $^{21}\text{Ne}/^{22}\text{Ne}$ than do Al and Si, and the Mg/Mg+Si+Al parameter has been previously used to examine the effects of sample composition on cosmogenic $^{21}\text{Ne}/^{22}\text{Ne}$ [19, 20]. The oval field labeled "chondrites" shows analyses of silicate mineral separates from two chondrites [see 19], whereas the dashed line represents the variations in GCR shielding for the H-chondrite data shown in Fig. 1. Also plotted are data for three eucrites [21] and multiple depth samples of lunar rocks 68815 and 61016 [1, 2], the latter being pure anorthosite with

SOLAR PRODUCED NEON IN SHERGOTTITES: Garrison, Rao, & Bogard

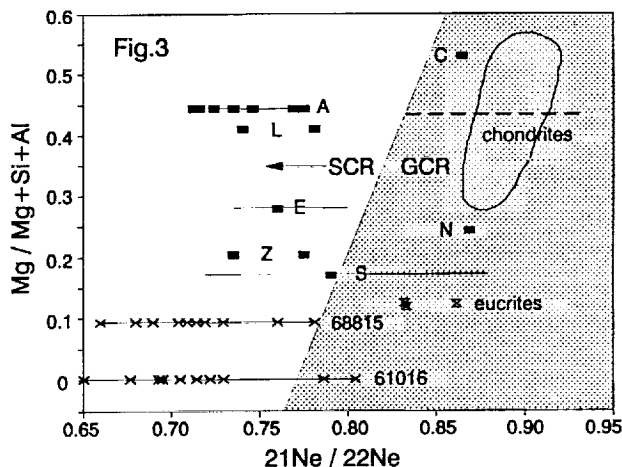
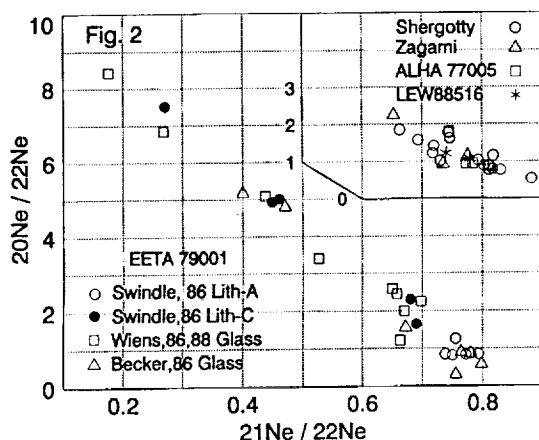
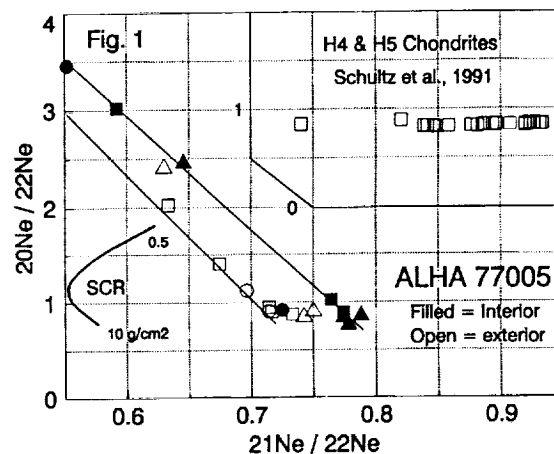
essentially no Mg. All samples of the two lunar rocks except those with the highest $^{21}\text{Ne}/^{22}\text{Ne}$ were shown to contain significant SCR Ne. These data suggest that GCR $^{21}\text{Ne}/^{22}\text{Ne}$ tends to correlate with Mg in silicates, but that even extreme compositional variations ranging from olivine to anorthosite cannot explain the ALH77005 data (labeled A in Fig. 3). We conclude that GCR Ne compositions generally would be limited to the shaded area of Fig. 3, and that increasing amounts of SCR Ne would move compositions to the left.

Literature data for other shergottites (L, E, Z, and S) as well as Nakhla (N) and Chassigny (C) are also shown in Fig. 3. The L and Z points are individual analyses, whereas the E and S points show the median values and total ranges of temperature extractions (Fig. 2). Although Chassigny and Nakhla give no evidence of SCR Ne, such a component appears to be present in LEW88516, EET79001, and possibly in some samples of Zagami and Shergotty.

It appears that all known shergottites, in contrast to chondrites, contain a cosmogenic Ne component with low $^{21}\text{Ne}/^{22}\text{Ne}$ that cannot be explained by shielding or composition; this suggests a Mars-related factor. Some evidence exists that the GCR $^{21}\text{Ne}/^{22}\text{Ne}$ ratio produced from pure Na is as low as 0.4-0.5. These shocked shergottites might contain such a cosmogenic component produced from Na-rich salts on the martian surface and shock-implanted by the process that has been invoked to implant Martian atmospheric gases into shergottites [22]. One sample of EET79001 showed variations in cosmogenic $^{21}\text{Ne}/^{22}\text{Ne}$ of 0.74-0.79 during temperature extractions [8, and Fig. 2], which might suggest separate release of cosmogenic Ne produced from Na compared to that produced within the silicate. Alternatively, orbital parameters of the shergottites during transit to earth may have produced more favorable conditions for SCR Ne production. Among the various possibilities are lower eccentricities or different inclinations of shergottites compared to chondrites to enhance the SCR/GCR production ratio, or smaller entry velocities into the earth's atmosphere to cause lower surface ablation of shergottites [H. Zook, pers. comm.]. In the latter case, the longer exposure ages of nakhlites and Chassigny compared to shergottites [7] may explain the absence of this SCR Ne in the former.

References: (1) Rao, Garrison, Bogard & Reedy, J.

Geophys. Res. 98, 7827, 1993; (2) Rao, Garrison, Bogard & Reedy, submitted G.C.A., 1993; (3) Nishiizumi, Klein, Middleton, Elmore, Kubik, & Arnold, G.C.A. 50, 1017, 1986; (4) Schultz, Weber & Begemann, G.C.A. 55, 59, 1991; (5) Graf, Baur & Signer, G.C.A. 54, 2521, 1990; (6) Reedy, LPSC XXIII, 1133, 1992; (7) Bogard, Nyquist & Johnson, G.C.A. 48, 1723, 1984; (8) Swindle, Caffee, and Hohenberg, G.C.A. 50, 1001, 1986; (9) Becker & Pepin, G.C.A. 50, 993, 1986; (10) Becker & Pepin, LPSC XXIV, 77, 1993; (11) Weins, Becker, and Pepin, E.P.S.L. 77, 149-158, 1986; (12) Weins, E.P.S.L. 91, 55, 1988; (13) Nagao & Matsuda, 11th Symp. Antarc. Met., 131, 1986; (14) Nagao, 12th Symp. Antarc. Met., 110, 1986; (15) Ott, G.C.A. 52, 1937, 1988; (16) Ott, unpublished 1989; (17) Bogard & Garrison, LPSC XXIV, 139, 1993; (18) Bhandari, Goswami, Jha, Sengupta, & Shukla, G.C.A. 50, 1023, 1986; (19) Begemann & Schultz, LPSC XIX, 51, 1988; (20) Masarik & Reedy, LPSC XXIV, 937, 1993; (21) Hampel, Waenke, Hofmeister, Spettel, & Herzog, G.C.A. 44, 539, 1980; (22) Bogard & Johnson, Science 221, 651, 1983.



2974

QUANTIFYING SHAPES OF VOLCANOES ON VENUS: J. B. Garvin,
NASA/Goddard, Code 921, Geodynamics, Greenbelt, MD 20771 USA

A large population of discrete volcanic edifices on Venus has been identified and catalogued by means of Magellan SAR images, and an extensive database describing thousands of such features is in final preparation [1-4]. Those volcanoes categorized by Head and colleagues [4] as *Intermediate to Large* in scale, while relatively small in number (~400), nonetheless constitute a significant volumetric component ($\sim 13 \times 10^6 \text{ km}^3$) of the total apparent crustal volume of Venus. For this reason, we have focused attention on the morphometry of a representative suite of the larger edifices on Venus, and in particular on ways of constraining the eruptive histories of these possibly geologically youthful landforms. Our approach has been to determine a series of reproducible morphometric parameters for as many of the discrete volcanoes on Venus that have an obvious expression within the global altimetry data acquired by Magellan. In addition, we have attempted to objectively and systematically define the mathematical essence of the shapes of these larger volcanoes using a polynomial cross-section approximation involving only parameters easily measured from digital topography, as well as with simple surface cylindrical harmonic expansions. The goal is to reduce the topological complexities of the larger edifices to a few simple parameters which can then be related to similar expressions for well-studied terrestrial and martian features..

Building on the results of a first-order morphometric comparison of Icelandic lava shields and selected venusian edifices [3], we have analyzed over 50 volcanoes on Venus, from which 7 have been chosen as representative end-member varieties: Tepev, Maat, Sapas, Sif, Gula, feature at 10.5N, 274E (V29 Quad), and a volcano at 46S, 215E (V51 Quad). The Table below lists some of the first order morphometric characteristics of these features as derived from Magellan altimetry data, polynomial approximations, and cylindrical harmonics. For comparison, classic terrestrial basaltic shields are also listed.

Volc. Name	D(km)	H(km)	Vol. (km^3)	H/D	shape n_x	V/D (km^2)	Flank Slope	Peak Amp.
Tepev	196	5.7	100000	0.030	2.8	508	3.3	800
Sapas	231	2.3	62000	0.010	3.6	267	1.1	410
V29 V	270	1.6	44000	0.006	1.9	161	0.7	1400
Sif	259	2.0	32000	0.008	0.9	124	0.9	520
Gula	233	2.5	41000	0.011	1.2	172	1.2	700
V51 V	186	2.4	30000	0.013	1.7	161	1.5	1280
Maat	312	7.5	355000	0.024	3.2	1136	2.7	740
Skjald	11	0.6	13	0.060	0.6	1.2	6.5	81
M.Loia	51	2.9	1620	0.060	0.7	32	6.5	210

The last two entries, *Skjald*, and *M. Loia* are representative of classical terrestrial shields at two different length scales; the M. Loia data describe only the subaerial component of the volcano. "Peak Amp." describes, in part, the shapes of all of the volcanoes in terms of the *degree one amplitudes* (in meters) of the nine-term cylindrical harmonic spectrum (CHS) for each feature (i.e., a 9x5 model rendered as a plot of amplitude vs degree).

The classic Icelandic lava shield Skjaldbreidur displays a degree 1 amplitude of only 81 m; all the other terms (degrees 2-9) have amplitudes less than or equal to 10. The spectra of Sif Mons displays an RMS variance of only 0.46 relative to that for Skjaldbreidur. Of the 50 volcanoes on Venus whose shapes we modelled using cylindrical harmonic expansions, only Sif and Gula displayed RMS variances (relative to that of *Skjald.*) less than 1.0. The best fitting power laws to the cylindrical harmonic spectra for the Venus and Earth volcanoes considered also illustrate the fundamental differences between most of the typical large-scale volcanoes on Venus and the lava shields of Earth. Again, only Sif and Gula Mons appear to display cylindrical harmonic spectra that resemble those of Earth shields. The Volumes listed in the Table were all computed from the CHS data and not directly from the Magellan GxDR altimetry. Variances in volume of up to 15% were observed when CHS results were compared with those measured from the altimetry directly. However, we believe the CHS-based Volume estimates are more reliable and objective, and they potentially permit analytical computation of volcano volumes independent of the initial data.

Our investigation of the shapes of volcanoes on Venus has illustrated several points. While there is little question that small "shield-field" volcanoes resemble monogenetic terrestrial basaltic volcanoes (and most especially lava shields [1,4,6,7]), the edifices larger than about 60 km that have been described in the literature as "shields" [1] do not in general display shapes that are shield-like in a morphometric sense [7]. Indeed, our volcano scaling studies have shown that while larger volcanoes on Mars do resemble scaled-up terrestrial basaltic shields (i.e., with basal diameters in the 500-800 km range), the larger so-called "shields" of Venus are noticeably more dome-like in cross-section (see n_x column in Table; values above ~ 1.5 tend to be more convex), and less voluminous. Terrestrial shields have edifice volumes which scale with basal diameter to the power of 2.9 to 3.2, while those on Venus scale at a power of 2.7. Only Maat and Tepev are close to the terrestrial shield volcano volume scaling trend. If volcanoes in the Solar System displaying terrestrial shield-like topography are effusive, basaltic varieties, then only a few of the larger venusian varieties that have been classified as such are likely to have been formed with eruptive histories and volume eruption rate patterns of landforms like Mauna Loa or Skjaldbreidur. The shape variability of the larger venusian edifices suggests a wide variation in the episodic eruption rate, and also points to a dominantly summit-area eruptive history. Reconciling the shield-like pattern of SAR backscatter features observed by Magellan at high resolution with the volcano topographic data, which does not indicate a shield-like morphometry, remains a problem we wish to address in our ongoing studies. {We acknowledge the support of the VDAP Program, RTOP 889-62-10-41, for this work; special thanks to S. Baloga for his support and to Jim Frawley}.

REFERENCES: (1) Head J. W. et al. (1992) *JGR* 97, p. 13153-13197. (2) Head J. and L. Wilson (1992) *JGR* 97, p. 3877-3903. (3) Garvin J. and R. Williams (1993) in *LPSC XXIV*, p. 523-524, LPI, Houston. (4) Crumpler L. et al. (1993) in *LPSC XXIV*, p. 361-362, LPI, Houston. (5) Pike R. and G. Clow (1981) *USGS Open File Report 81-1039*, 40 pp., Wash. DC. (6) Schaber G. (1991) *Proc. LPSC XXI*, p. 3-11, LPI, Houston. (7) Whitford-Stark, J. (1982) *Earth Sci. Rev.* 18, 109-168.

p. 2

2975

MESOSCALE ROUGHNESS OF VENUS: J. B. Garvin, NASA/Goddard, Geodynamics, Code 921, Greenbelt, MD 20771, and J. J. Frawley, Herring Bay Geophysics, Herring Bay, MD 20754

The global distribution of multi-kilometer (~9 km) length scale "roughness" (hereafter *mesoscale roughness* or MR) on Venus can be estimated from the Magellan global altimetry dataset (GxDR), and then compared with MR data derived for Earth from 5' ETOP5 data and for Mars (from USGS Mars DTM dataset). The mesoscale roughness parameter (MR) represents the RMS variance in meters of the actual planetary surface topography relative to the best fitting tangent plane defined on the basis of a 3x3 pixel sliding window [1]. The best-fit plane was computed using a least-squares solution which minimizes ΔH , the sum of the squares of the differences between the 9 local elevation values (H_i) and the elevation of best-fit plane ($ax_i + by_i + c$) at the same grid location:

$$-\Delta H = \sum_i [H_i - (ax_i + by_i + c)]^2 \text{ for } i = 1 \dots 9.$$

Using the best-fit plane and ΔH , we have computed the RMS "roughness" $var(\Delta R)$, given by:

$$var(\Delta R) = \sqrt{\{(1/9) * \Delta H\}},$$

where this parameter is always minimized on the basis of its calculation using least squares. We have called this "ruggedness" parameter the *Mesoscale Roughness* (MR) because it is directly related to the high-frequency variance of topography after mesoscale slopes and tilts (i.e., for Venus, the baseline over which MR is computed {dx} is ~ 8.8 km; dx for Earth is ~ 9.3 km) are removed. As such, MR represents the degree to which a planetary surface is more rugged than approximately 10 km scale facets or tilts. It should not be confused with the radar "RMS Roughness" parameter computed at 0.1 to 10 m length scales on the basis of the Magellan radar altimeter echo [2]. We will use our MR parameter to investigate the global ruggedness properties of Venus as they relate to geological provinces, and in comparison with the spatial pattern of MR for Earth and Mars.

Figure 1 illustrates the frequency distribution of the MR parameter for Venus, Earth, and Mars in a semi-log format. It is evident that there are broad similarities between the distributions for Venus and Earth, although the slopes of the frequency distributions are very different. The Venus MR distribution demonstrates a *mode* at ~5 m, unlike the monotonic Earth and Mars distributions. In addition, the Venus MR distribution crosses that of Earth first at 7 m, and then again at 40 m. The rapid, exponential decay of the Mars MR curve accentuates the extreme limitations of the dataset from which it was derived, reason more to return to Mars with a Mars Observer-class mission. From 7 to 40 m, the Venus distribution lies above that for Earth, and it represents some 23% of the surface area of the planet. Much of this intermediate level MR is represented by the flanks of the lattice-work of weakly connected uplands, especially those that interconnect Aphrodite and Beta-Atla-Themis. Perhaps the most intriguing aspect of the spatial pattern of MR on Venus relative to that of Earth is the paucity of extremely low (0 to 5 m) MR regions. On Earth, the continental cratons, the older patches of sediment-covered seafloor, and the continental shelves display MR values in the 1-5 m range; in contrast, Venus MR values are reduced by a factor of 4 in terms of occurrence at such low ruggedness levels. At least on Earth, the relative level of erosion and sediment cover exerts a strong control on the spatial pattern of MR; indeed, the most geologically active mountain belts and the mid-ocean ridge systems exhibit MR values in excess of 40 m. The limited spatial extent of low MR zones on Venus could provide evidence for the reduced role of erosion and basin-scale deposition.

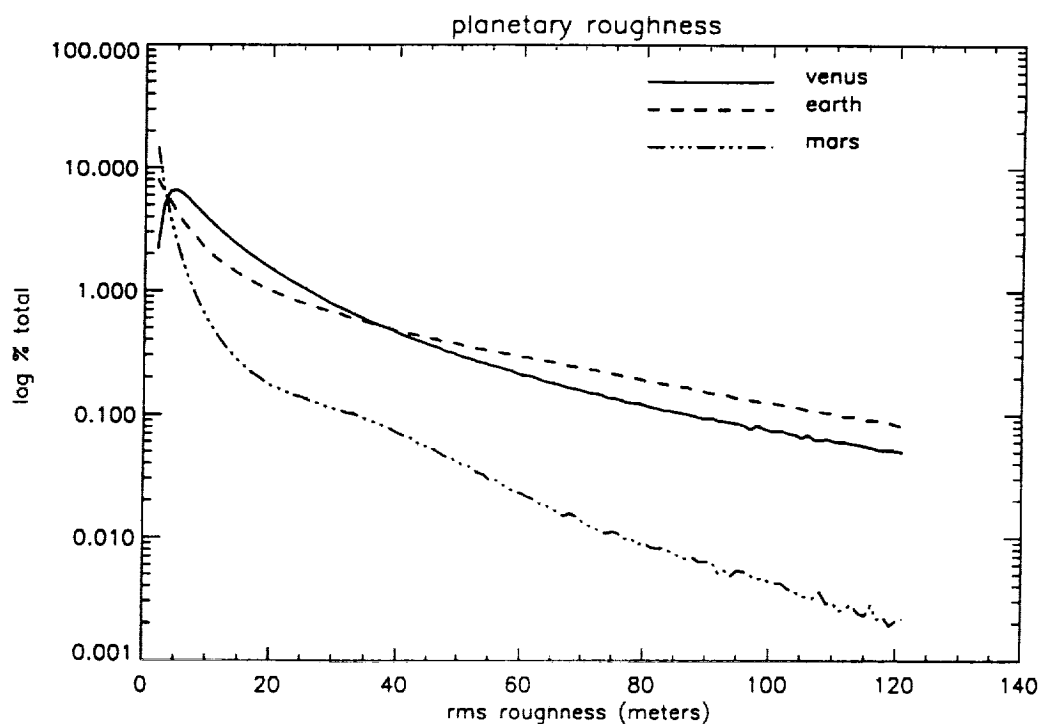
MESOSCALE ROUGHNESS OF VENUS: Garvin J. B. and Frawley J. J.

Another possibility is that the dominance of vertical tectonism associated with a global network of tectonized zones produces huge aprons of mass-wasted debris along the flanks of such regions at the requisite multi-kilometer (i.e., 9-19 km) length scales. Such debris covered surfaces, while sloped in relation to the source regions of the debris, could display an excess of roughness (in the 7-40 m range) relative to any simple facet model which describes them at ~ 10 km spatial scales.

These very preliminary findings for Venus indicate that a derived parameter such as mesoscale roughness (MR), even at spatial scales no smaller than 9 km, provides a potentially valuable new perspective on the intensity of global-scale surface processes [3,4]. Our analysis thus far of the MR pattern for Venus versus that for Earth reaffirms the dominance of degradational processes on Earth (erosion and sediment infill) and the lack of such effects at multi-kilometer length scales on Venus. (We gratefully acknowledge the support of VDAP, through RTOP no. 889-62-10-41).

REFERENCES: (1) Harding D. J. et al. (1994) in press, in *IEEE Trans. Geosci. Rem. Sens.*, 35 pp. (Satellite laser altimetry of terrestrial topography). (2) Ford P. and G. Pettengill (1992) *JGR* 97, p. 13103-13116. (3) Sharpton V. and J. Head (1986) *JGR* 91, p. 7545-7556. (4) Malin M. C. et al. (1993) in *LPSC XXIV*, p. 927-928, LPI, Houston.

FIGURE 1: Frequency distribution of Mesoscale Roughness in meters (*rms roughness* in the plot) for Venus, Earth, and Mars.



536-91 ABS. 6 N94-35431

2976

VOLCANO MORPHOMETRY AND VOLUME SCALING ON VENUS: J. B. Garvin¹, and R. S. Williams Jr.²; (1) NASA Goddard, Geodynamics Branch, Code 921, Greenbelt, MD 20771; (2) U. S. Geological Survey, Quisset Campus, Woods Hole, MA 02540

A broad variety of volcanic edifices have been observed on Venus, ranging in size from the limits of resolution of the Magellan SAR (i.e., hundreds of meters), to landforms over 500 km in basal diameter [1, 2]. One of the key questions pertaining to volcanism on Venus concerns the volume eruption rate or VER, which is linked to crustal productivity over time. While less than 3% of the surface area of Venus is manifested as discrete edifices larger than 50 km in diameter, a substantial component of the total crustal volume of the planet over the past 0.5 Ga is related to isolated volcanoes, which are certainly more easily studied than the relatively diffusely defined plains volcanic flow units. Thus, we have focused our efforts on constraining the volume productivity of major volcanic edifices larger than 100 km in basal diameter. Our approach takes advantage of the topographic data returned by Magellan, as well as our database of morphometric statistics for the 20 best known lava shields of Iceland, plus Mauna Loa of Hawaii [3]. As part of this investigation, we have quantified the detailed morphometry of nearly 50 intermediate to large scale edifices, with particular attention to their shape systematics. We found that a set of venusian edifices which include Maat, Sapas, Tepev, Sif, Gula, a feature at 46°S, 215°E, as well as the shield-like structure at 10°N, 275°E are broadly representative of the ~400 volcanic landforms larger than 50 km described by Head and colleagues [1, 4]. The cross-sectional shapes of these 7 representative edifices range from flattened cones (i.e., Sif) similar to classic terrestrial lava shields such as Mauna Loa and Skjaldbreidur [3], to rather dome-like structures which include Maat and Sapas. The majority of these larger volcanoes surveyed as part of our study displayed cross-sectional topographies with paraboloidal shapes, in sharp contrast with the cone-like appearance of most simple terrestrial lava shields.

In order to more fully explore the differences between large venusian edifices and volcanoes on the Earth and Mars, we developed a volume scaling algorithm which relies on conservation of volcano morphometry as basal diameter is varied; this approach suggests that virtually all of the venusian edifices that were examined are a factor of 5 to 15 less productive in terms of integrated edifice volume than well-constrained terrestrial structures such as Mauna Loa or Skjaldbreidur. Only Arsia Mons on Mars displays a pattern similar to venusian volcanoes such as Maat Mons. As a final demonstration of the fundamental differences between larger volcanoes on Venus and terrestrial shields, we have employed surface cylindrical harmonic series expansions to the Magellan topographic data for over a dozen features, in comparison with cylindrical harmonic models of two classic terrestrial lava shields, Skjaldbreidur (Iceland) and Mauna Loa (Hawaii). Results of this analysis convincingly demonstrate that only Sif Mons comes close to approximating the topology of canonical basaltic shields as found on Earth. Thus, our ongoing survey of the morphometric characteristics of large-scale volcanoes on Venus suggests that the vast majority of these features should not be classified as "terrestrial shield volcanoes", in spite of their shield-like SAR backscatter patterns [1-5].

On Earth, composite basaltic shield volcanoes such as Mauna Loa display integrated edifice volumes of approximately $10,000 \text{ km}^3$ (at a characteristic length scale of ~100 km). If a Mauna Loa style volcano were to be "scaled" to permit comparison with its 200 to 500 km diameter venusian counterparts, then a total volume of nearly 10 million km^3 would result if simple proportional growth in the absence of extensive erosion were in effect. We have developed an algorithm to facilitate both proportional and non-proportional shape and volume scaling of volcanoes, using as input an average volcano topographic cross-section or complete digital elevation model. When monogenetic lava shield volcanoes such as are found in Iceland (i.e., Sandfellshaed and Lambahraun) are scaled to venusian diameters, the resulting total edifice volumes fall in the range of 1-5 million km^3 (at Maat Mons length scales). Maat Mons itself displays a total edifice volume, as measured from Magellan GxDR topography, of $360,000 \text{ km}^3$ (with an error of +/- 10%). The proportional volume scaling parameter, here defined as the constant k in a power law growth function of the form: $V = k D^3$, where V is volume and D is basal diameter, ranges from 0.0005 to 0.0025 for most venusian volcanoes larger than 50 km, while typical Earth shields display k values in the 0.0105 to 0.0120 range.

VOLCANO MORPHOMETRY: Garvin J. B. and Williams R. S. Jr.

In contrast, the largest of the Tharsis edifices on Mars, Olympus Mons, has a k -value near to 0.0090, within 10% of those values derived for terrestrial shields.

Using these scaling laws, and the population of major volcanoes on Venus as described by Head and colleagues [1, 3], the order of magnitude cumulative volume of crustal volcanic materials on Venus contributed by discrete volcanoes is ~ 13 million km^3 . This represents a global layer thickness equivalent of 28-30 m over the past 0.5 Ga for Venus, which is probably on the order of 30 to 50 times less than the crustal production from flood "basaltic" eruptions. The several hundred larger-scale edifices on Venus, however, provide a useful perspective on the styles and rates of volcanism on the planet. For example, if Maat-style composite volcanoes represent one end-member eruption pattern for Venus, and if such edifices are the venusian equivalent of terrestrial basaltic shield volcanoes, then they would only require 0.13 to 1.3 Ma to construct, ignoring erosion. Even at the low average volume eruption rates typical of terrestrial shield-building eruptions (i.e., 10-100 m^3/s), the largest edifices on Venus would only require 1-10 Ma for complete construction. Thus, it is impossible that the population of larger volcanoes catalogued on Venus by Head, Crumpler and others [4] is the manifestation of only the last 10 Ma of localized volcanic activity on Venus. If the 20 to 30 lava shields that formed within the 103,000 km^2 area of Iceland over the past 15,000 years is only 10% of the total volume of extruded volcanic materials over the same time interval [6], then the total volume of those flood basalt eruptions on Venus that occurred simultaneously with the construction of the observed population of larger volcanoes could have exceeded 130 million km^3 , for a global layer thickness equivalent of almost 300 m (in only 10 Ma). Given the abundant evidence for extensive plains volcanic deposits on Venus, it is plausible that the crustal productivity over the past 100 Ma is enough to have overplated much of the rolling plains to a depth of several kilometers. This scenario, of course, assumes the dominance of basaltic volcanism on Venus, notwithstanding the lack of morphometric evidence for large-scale terrestrial-style basaltic shields on the planet, with the possible exception of Sif-like landforms. Perhaps relatively low volume eruption rate basaltic eruptions are commonplace and essentially continuous in any time interval on Venus, and there are other unique factors which explain the dissimilarity of major venusian edifices with respect to typical Earth shields [4, 5].

The normalized (to edifice basal diameter D) volume productivity trend for 21 venusian volcanoes can be compared against that derived for the record of post-glacial lava shield volcanoes in Iceland; for Venus $V \sim D^{2.7}$, while for Earth $V \sim D^{2.9}$. It is clear that only the largest of the Venus edifices (such as Maat and Tepev) come close to following the terrestrial shield trend, suggesting that most of the intermediate to large volcanic features on Venus are not constructed by means of sustained effusive activity, but instead involve sporadic high effusion rate episodes, perhaps including limited pyroclastic activity. Much of the anomalously high eruption rate activity that may be required to form large-scale edifices on Venus must occur in a localized summit region, in order to explain the shape trend (domical) displayed for most venusian volcanoes larger than 50 km in diameter. The significance of these observations with respect to the geologic history of volcanism on Venus is that the pattern is distinctively Earth-like; that is, the larger and greatest relief volcanic structures are perhaps geologically anomalous with respect to "average" eruption style plains volcanism, and may require pyroclastic activity. In addition, there is a reasonable possibility that the several hundred larger-scale edifices identified on Venus [4] are extremely recent features, and that these landforms are a window on the geologically most accessible record of volcanism. *(We gratefully acknowledge the support of the VDAF program, under RTOP 889-62-10-41; special thanks to Steve Baloga at PG&G).*

REFERENCES:

- [1] Head J. W. et al. (1992) *JGR* 97, p. 12153-13197.
- [2] Head J. W. and L. Wilson (1992) *JGR* 97, p. 3877-3903.
- [3] Garvin J. and R. Williams (1993) in *LPSC XXIV*, p. 523-524, LPI, Houston.
- [4] Crumpler L. et al. (1993) in *LPSC XXIV*, p. 361-362, LPI, Houston.
- [5] Pike R. and G. Clow (1981) in *NASA Tech. Mem. 84211*, p. 138-140 (PGPI).
- [6] Garvin J. and R. Williams (1992) *EOS Trans. AGU*, Vol. 73, no 43, p. 130.

IDA: DISTRIBUTION AND ORIGIN OF SURFACE BLOCKS

Paul Geissler, Jean-Marc Petit and Richard Greenberg, University of Arizona

At least 20 blocks or boulders have been discovered on the surface of Ida in the Galileo high resolution mosaic returned to Earth in September 1993. The block distribution fits a dynamical model in which the blocks are ejecta fragments that entered partial or temporary orbit about Ida before being swept up preferentially onto the leading surfaces. Thus the blocks may represent the first observational evidence of small "moons" of a main-belt asteroid.

Features interpreted as blocks are small, isolated objects with positive relief comparable to their horizontal scale, shown by shadows and illumination. Positive relief features found alongside craters are more likely to be rims and are not included in our mapping. A number of blocks can be unambiguously identified in the stereo pair formed by images 2339 and 2439, but because stereo coverage does not exist over most of Ida, the overall distribution was mapped using monoscopic coverage only. The spatial distribution of these 30 - 150 m diameter blocks is distinctly nonuniform (Fig.1), with most of the blocks found on or near the "leading surfaces" of the asteroid (the two regions which sweep through space as Ida rotates or, more precisely, where the local rotational velocity vector is directed outwards from the surface). None are found on the trailing region despite the excellent illumination and viewing geometry of images of this region (2313, 2326 and 2339). Although different sets of blocks have been identified by several mappers within the Galileo imaging team, depending upon subjective criteria, the spatial distributions have been similar.

The largest cluster is found near the site of two large (~10 km) craters on the leading surface. However, the blocks are not concentrated near the rims of these craters, and few blocks appear to be associated with the large craters near the middle of the mosaic. One or two trails leading to blocks have been tentatively identified; in each case, the implied direction of motion is away from the presumably high gravity potential at the ends of Ida. One small group of blocks visible in stereo images 2339 and 2439 may be the result of disruption of a single parent block.

The blocks were probably never small heliocentric asteroids, which would impact more uniformly over the surface, and most of which would be disrupted on impact at over 3 km/s [1]. Blocks of the observed size might have been ejected by 1-10 km craters [2, 3], but emplacement of blocks near their source craters would not explain their distinctive spatial distribution. Instead, we suggest that the large blocks were ejected at speeds near the escape velocity and went into temporary orbit about Ida, while smaller ejecta fragments were launched at higher velocities and escaped.

We have modeled the orbits of ejecta around a body with elongation similar to Ida's. The body consists of two contacting spheres of variable size and uniform density, connected by a massless cylinder. Tests with more realistic density distributions showed little difference from this model. In each numerical experiment, 10,000 particles are launched from random locations and tracked until they reimpact the surface. The launch direction for each particle can be randomly chosen, or assigned a fixed inclination. In a typical case, the two spheres in the model asteroid are each of radius 15 km and density 4 g cm^{-3} (so average overall density is 2.4 g cm^{-3}), rotating with period of 4.7 hr. All particles are launched at 32 m/s (near the average escape speed), inclined 45° to the surface, the predominant inclination for ejecta according to Melosh [4]. The material goes into temporary orbit around the asteroid for durations that are long in comparison to the rotational period. The fate of these small "moons" is strongly influenced by the irregular shape and rapid rotation of the asteroid.

Fig. 2 shows one side of the model asteroid, with the rotation axis in the plane of the paper and the leading surface on the right. The opposite side is similar by the symmetry of the model. Points show the impact sites of the 4% of particles that have returned to the surface after 10 revolutions of the model asteroid.

IDA BLOCK DISTRIBUTION AND ORIGIN: Geissler, P.E., J.M. Petit and R.J. Greenberg

The strong preference for collection on the leading edge is clearly shown. Similar results are found in all cases, except when the launch speed is so low that re-impact is immediate and local.

Blocks on Ida may be eventually destroyed by impacts of m-sized projectiles. Extrapolating the size distribution for small asteroids suggested by the Gaspra cratering record [5] down to 1 m suggests that the blocks survive on Ida for 30-80 million yr. Impacts by 50-350 m objects create the 1-10 km craters [6, 7] with blocky ejecta every 1-100 million yr. Thus block production probably keeps pace with block destruction.

References: [1] Bottke et al., *Icarus*, in press, 1994. [2] Moore, NASA SP-315, 1972. [3] Lee et al., *Icarus* 68, 77-86, 1986. [4] Melosh, "Impact Cratering", Oxford, 1989. [5] Belton et al., *Science* 257, 1647, 1992. [6] Nolan et al., *DPS*, 1992. [7] Greenberg et al., *Icarus*, in press, 1994.

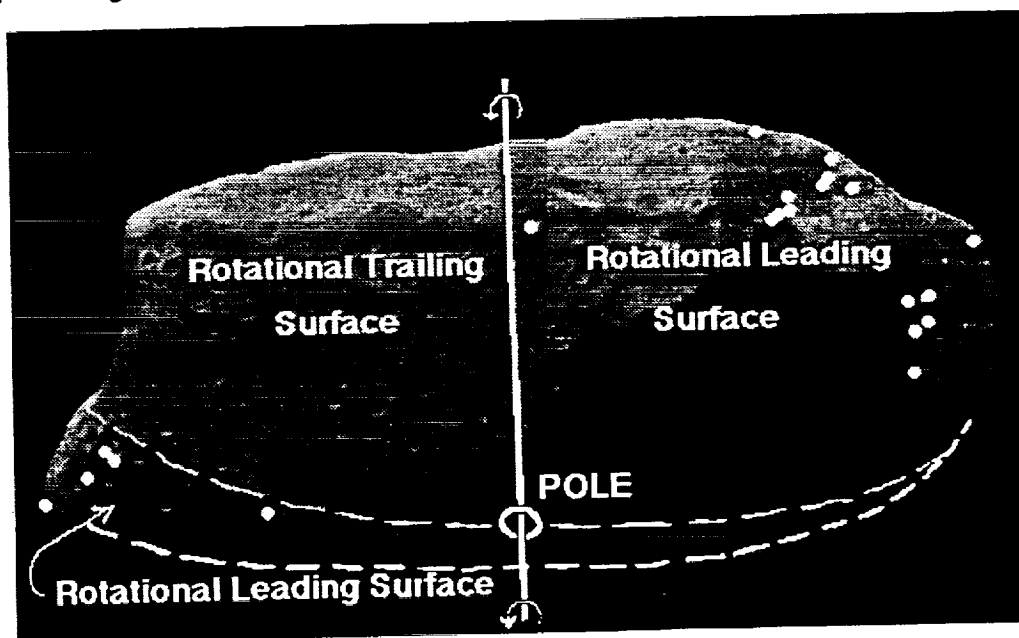


Figure 1: Locations of boulders and approximate boundaries of leading and trailing surfaces.

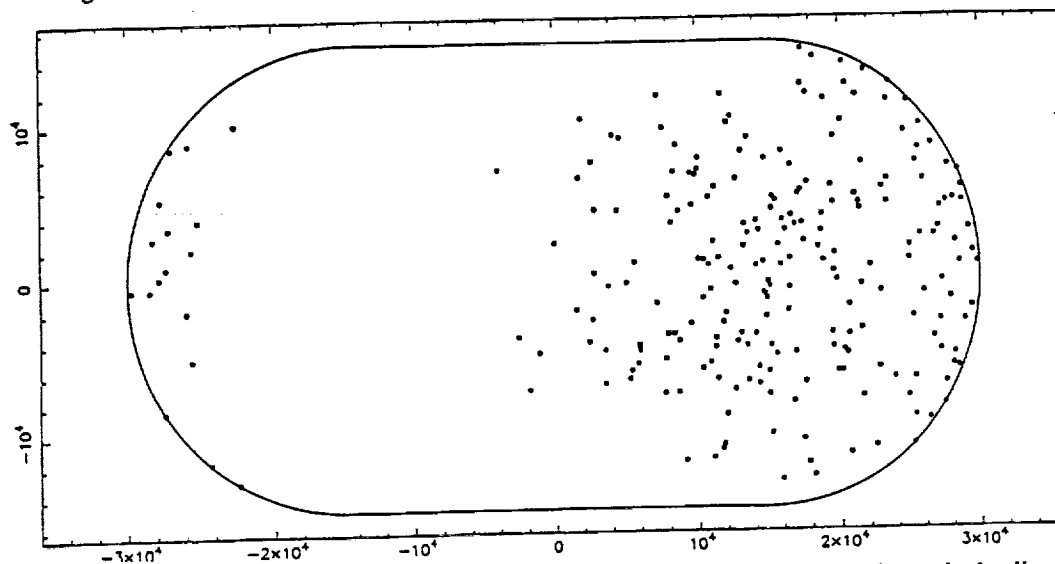


Figure 2: Ejecta launched uniformly from over the model asteroid reimpact predominantly on the leading surfaces.

HIGH-TEMPERATURE VAPORIZATION OF GYPSUM AND ANHYDRITE : EXPERIMENTAL RESULTS. M.V. Gerasimov¹, Yu.P. Dikov², O.I. Yakovlev³, and F. Wlotzka⁴. Russian Academy of Sciences, Moscow: 1-Space Research Inst., 2-Inst. of Ore Deposits, Petrography, Mineralogy and Geochemistry, 3-Vernadsky Inst. of Geochemistry and Analytical Chemistry, Moscow, Russia; and 4- Max-Planck-Institut für Chemie, Abteilung Kosmochemie, Mainz, F.R.Germany.

The possibility that enormous quantities of SO_2 and SO_3 evolved into the Earth's atmosphere during the formation of Chicxulub impact crater [1] encourages theoretical and experimental investigations of vaporization of sulphur-containing minerals [2,3]. Here we present preliminary results of experiments on high-temperature evaporation of gypsum $\text{CaSO}_4 \cdot 2\text{H}_2\text{O}$, and anhydrite, CaSO_4 . Experiments were performed using a pulsed Nd-glass laser and with a procedure described in [4,5]. High-temperature and dense initial state of an evaporated cloud with adiabatic expansion inside a cell could to a certain extent simulate the expansion of a vapor cloud during an impact process. The main mineral phases which were found in the condensates of vapor from anhydrite and gypsum are CaO and CaSO_4 . No hydroxides were detected. The CaSO_4/CaO ratio is significantly higher in the last layers of the condensate, deposited at a lower temperature, compared to the first, high temperature condensate.

Samples were vaporized in a hermetic cell filled with air at 1 atm. About 10 mg of sample was vaporized from a sample by the laser pulse. At a distance of 5 cm from the place of vaporization a Ni foil was mounted to collect products of condensation originating inside a cooling vapor cloud. Analyses of initial samples and of condensed films were performed using X-ray photoelectron spectroscopy (XPS). Condensed films were etched layer by layer (with a step of 400 Å) by a beam of argon ions and for every layer XPS analysis was performed providing an information of the cross-section of the film. XPS analyses gave both elemental chemical composition of the condensate and the distribution of elements between different phases.

The initial chemical composition of anhydrite was found to be: Ca- 16.8; S-17.9; O- 65.3 at.%; and for gypsum it was: Ca- 9.6; S- 9.9; O(-S)- 39.4; O(-H)-13.7; H- 27.4 at.%. In gypsum two states of oxygen were distinguished: oxygen in sulphate: O(-S), and oxygen which is bound in water: O(-H). The concentration of hydrogen was calculated based on the value of O(-H). The relative atomic concentrations of elements in gypsum were: Ca : S : O(-S) : H : O(-H) = 1 : 1 : 4.1 : 2.9 : 1.4. The deficit of water compared with the gypsum formula indicates that the sample was a mixture of gypsum (72%) and anhydrite (28%). The analysis of anhydrite gave a nearly stoichiometric ratio: Ca : S : O = 1 : 1.06 : 3.9.

The composition of condensed films is presented in Table 1 for gypsum and in Table 2 for anhydrite. We could distinguish during analyses: calcium in the form of pure oxide CaO (column 1), calcium bound with sulphur (column 2), sulphur in the form of sulphite (S^{4+} , column 3), sulphur in the form of sulphate (S^{6+} , column 4), sulphur adsorbed as SO_3 molecule (column 5), oxygen bound to calcium (column 6), oxygen bound to sulphur (column 7). The amount of calcium bound to sulphur (column 2) is approximately the same as the amount of sulphate sulphur (S^{6+} , column 4) in the condensate. This observation shows that anhydrite is the main form of sulphur in condensates from anhydrite as well as gypsum.

The presence of sulphur in the condensate shows that not all evaporated sulphur remains in the atmosphere, some part of it is trapped during condensation. A comparison of the chemical composition of the condensed film with the initial sample can give an evaluation of the amount of sulphur-containing gases which were evolved into an atmosphere. Taking into consideration that calcium is almost totally precipitated, the ratio of Ca : S in an initial sample and in its condensed film is informative about the amount of sulphur which is degassed into an atmosphere. Such a comparison for anhydrite shows that 17% of sulphur was degassed, and for gypsum this value was larger, amounting to 55%.

About 20% of sulphur in both condensed films is present in the form of adsorbed SO_3 . Only about 2% of sulphur is present in condensates in reduced form (S^{4+}). Such a small quantity of reduced sulphur is in contradiction to the proposed scheme of anhydrite decomposition [3,4] under the reaction: $2\text{CaSO}_4 = 2\text{CaO} + 2\text{SO}_2 + \text{O}_2$. A simple decomposition of anhydrite: $\text{CaSO}_4 = \text{CaO} + \text{SO}_3$ seems more likely. Another possibility is the oxidation of evolved SO_2 by atmospheric oxygen: $\text{SO}_2 + 1/2\text{O}_2 = \text{SO}_3$.

VAPORIZATION OF GYPSUM AND ANHYDRITE: M. V. Gerasimov et al.

The absence of hydrated phases in the condensate of gypsum and a relative deficit of sulphur in the condensate of anhydrite can be a result of formation of sulphuric acid (H_2SO_4). A possible way of gypsum decomposition can be presented by the reaction: $\text{CaSO}_4 \cdot 2\text{H}_2\text{O} = \text{CaO} + \text{H}_2\text{SO}_4 + \text{H}_2\text{O}$. It is uncertain which phase contains sulphur in reduced form (S^{4+}). Probably it is CaSO_3 , but its concentration cannot be evaluated. If we ignore adsorbed SO_3 , the composition of condensed films is: CaSO_4 - 64, CaO - 36 mol.% for anhydrite, and CaSO_4 - 40, CaO - 60 mol.% for gypsum. Surface layers of condensed films which are formed mainly by precipitation from a cooled vapor cloud after the end of the laser pulse have a ratio of CaSO_4/CaO notably higher than the inner parts of films which are precipitated at a hot stage of vaporization. This observation indicates that the efficiency of trapping of evolved sulphur containing gases is strongly temperature dependant and is higher at decreasing temperatures.

REFERENCES: [1] Brett R. (1992) *LPSC XXIII*, 157-158. [2] Chen G., Ahrens T.J. (1993) *LPSC XXIV*, 273-274. [3] Tyburczy J.A., Ahrens T.J. (1993) *LPSC XXIV*, 1449-1450. [4] Gerasimov M.V. et al. (1985) *Vestnik Acad. Nauk USSR*, No. 9, 10-25 (in Russian). [5] Dikov Yu.P. et al. (1994) *LPSC XXV*, this volume.

TABLES: Chemical composition (atom%) and chemical state of elements in different layers inside condensed films obtained in experiments with gypsum (Table 1) and anhydrite (Table 2).

Table 1: Gypsum condensate

Elements	Ca		S			O	
Chemical state	Ca-(O-Ca)	Ca-(O-S)	S^{4+}	S^{6+} -(O-Ca)	S^{6+} adsorbed	(O-Ca)	(O-S)
Column No	1	2	3	4	5	6	7
Surface	3.0	13.4	0.8	12.4	1.8	17.5	51.0
400 Å	16.0	7.8	3.3	7.2	1.4	24.6	39.7
800 Å	28.5	5.1	2.2	3.6	0.7	37.5	22.4
Average	15.8	8.8	2.1	7.7	1.3	26.5	37.7
	24.6		11.1			64.2	

Table 2: Anhydrite condensate

Column No	1	2	3	4	5	6	7
Surface	3.5	12.1	1.6	10.4	3.9	10.3	58.1
400 Å	6.0	11.4	3.5	9.6	2.9	11.3	55.4
800 Å	8.1	9.2	3.6	8.7	2.1	14.3	53.9
1000 Å	12.7	6.0	2.9	6.3	1.7	20.2	50.2
Average	7.5	9.7	2.9	8.7	2.9	14.0	54.4
	17.2		14.5			68.4	

TRAPPING OF CARBON DIOXIDE FROM A HOT ATMOSPHERE BY CONDENSING SILICATES.
 M.V. Gerasimov¹, Yu.P. Dikov², O.I. Yakovlev³, and F. Wlotzka⁴. Russian Academy of Sciences: 1 - Space Research Institute, 2 - Institute of Ore Deposits Geology, Petrography, Mineralogy and Geochemistry, 3 - Vernadsky Institute of Geochemistry and Analytical Chemistry, Moscow, Russia; 4 - Max-Planck-Institut für Chemie, Abteilung Kosmochemie, Mainz, Germany.

Planetary atmospheres are thought to be the result of release of volatiles during the bombardment of a growing planet by massive planetesimals. According to some models, the accumulation of impact-released water vapor and/or carbon dioxide can result in a dense and hot primordial atmosphere [1,2,3]. As a sink for atmospheric carbon dioxide only a post-impact formation of carbonates was considered [4]. In our experiments we show that the formation of carbonates is already possible during impact processes. In a previous set of experiments we investigated the trapping of water vapor from an atmosphere by condensing matter which originates during high-temperature pulse heating of pyroxene in a wet atmosphere, thus simulating the interaction of a wet atmosphere with ejected condensing matter during impact of a planetesimal [5,6]. An effective trapping of water vapor by condensed silicate matter was discovered, giving an amount of up to 10 wt% of trapped water. The activity of small condensing silicate particles in a spreading hot vapor cloud in a CO₂ atmosphere can also result in the formation of carbon bearing phases in the condensate leading to trapping of atmospheric carbon dioxide during an impact.

Here we present results of an experiment of interaction of a carbon dioxide atmosphere with condensing silicate matter which originated during high-temperature vaporization of clinopyroxene (Na- 1.95, Mg- 7.13, Al- 4.29, Si- 18.00, Ca- 6.05, Ti- 0.31, Fe- 2.51 atom%). As in our previous experiments [7,8,9], vaporization was achieved by a powerful neodymium laser pulse focused on a sample mounted in a hermetic cell with a volume of ~500 cm³. Parameters of the pulse are: luminous energy ~600 J, duration ~10⁻³ s, density of luminosity ~5.10⁶ W/cm². The estimated temperature of vaporization was 3000-4000 K. The cell was filled with 1 atm of carbon dioxide. A noticeable amount of condensed particles with dimensions from 50 to 1000 Å originated in a spreading hot cloud [5] which could mix and interact with CO₂ inside the cell. A part of the condensate was collected on a Ni-foil which was placed at a distance of 8 cm from the sample. Chemical analyses of the condensate were made using X-ray photoelectron spectroscopy (XPS) which provided both elemental chemical composition of the condensate and the distribution of elements between different phases. Condensed films were etched layer by layer (with a step of 200 Å) by a beam of argon ions and for every layer XPS analysis was performed providing an information of the cross-section of the film.

XPS analyses reveal the presence of a noticeable quantity of carbon which is trapped in the condensate. The main carbon-containing phases which we could distinguish in the condensate are: carbonates, carbides, amorphous carbon and chemisorbed CO₂. Carbonates are mainly formed with Ca and to lesser extent with Fe and Mg. Carbides are mainly formed with Fe. The concentration of trapped carbon-containing phases in bottom layers of the condensed film was ~1.5 wt% of CO₂ and ~0.5 wt% of carbon in amorphous and carbide phases, and in the upper layers it was ~4 wt% and ~2 wt%, respectively (Fig. 1). The bottom layers of the film represent the front part of the spreading vapor cloud which came to the Ni-foil and stuck to it first. The upper layers were formed by the last portions of evaporated matter and by sticking of condensed particles and radicals which were dispersed into the inner gas environment of the cell after the end of the laser pulse. In general the last portions of condensed films are formed at lower temperatures than front and inner parts of the film. The efficiency of CO₂ trapping is apparently higher during the last stages of condensation. The average total concentration of elemental carbon in the condensate is about 1 wt%, which is higher than in normal igneous rocks.

The same pyroxene was used in our previous experiments, where it was evaporated in an inert atmosphere of helium, and the condensed film was analysed in the same way by XPS [8]. An important difference between the experiments in helium and in CO₂ atmosphere is the presence of reduced forms of certain elements in the experiment in inert helium (~9% of silicon in the form of Si⁰ and Si²⁺, ~15% and ~7% of Al and Fe in metallic form, integrated through the volume of the film) and their absence in the experiment in CO₂. The same effect was observed after evaporation in a wet atmosphere [5], where water vapor provided for an effective oxidation of the condensate. The absence of reduced forms of elements in

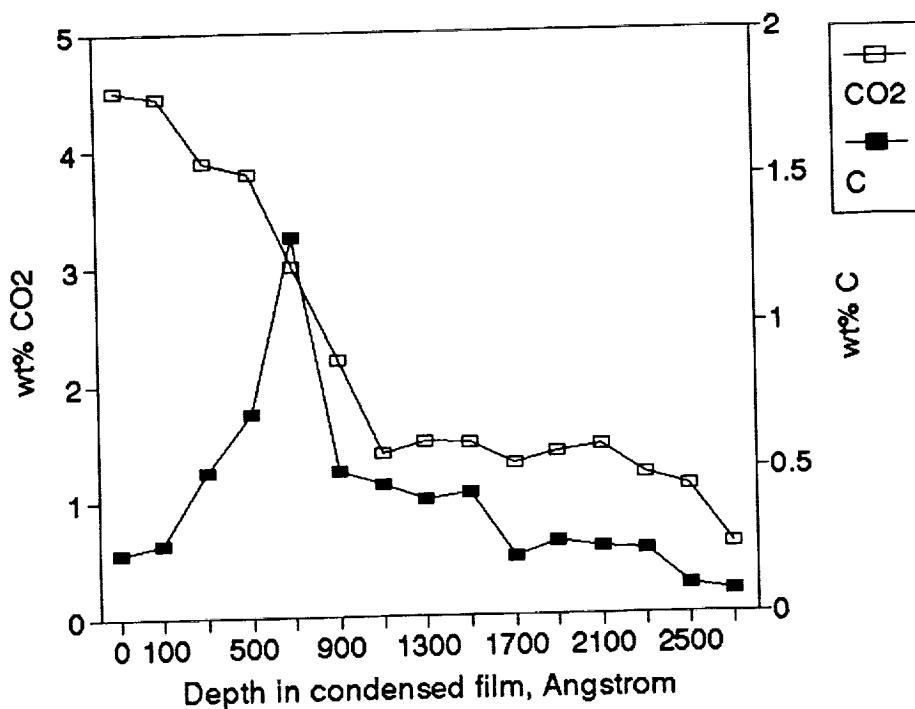
TRAPPING OF CARBON DIOXIDE: M.V. Gerasimov et al.

the experiment in CO_2 atmosphere also shows the oxidizing role of CO_2 molecules in the vapor cloud. The ratio $\text{Fe}^{3+}/\text{Fe}^{2+}$ for the whole condensed film in the CO_2 experiment is ~ 1.9 , that is twice as high as in the experiment in helium [8,10].

These experimental results prove the possibility of effective trapping of water vapor and of carbon dioxide from an atmosphere by dispersed hot condensing silicate matter. The trapping of gases proceeds with the formation of stable volatile-bearing phases. The concentration of trapped CO_2 can amount up to ~ 4 wt.% of the condensate. The efficiency of the trapping process suggests that it could be a feasible mechanism controlling the impact-induced formation of an atmosphere.

REFERENCES: [1] T. Matsui, Y. Abe (1986) *Earth, Moon and Planets*, 34, 223. [2] M.A. Lange, T.J. Ahrens (1982) *Icarus* 51, 96. [3] K.J. Zahnle, J.F. Kasting, J.B. Pollack (1988) *Icarus* 74, 62. [4] T. Matsui, E. Tajika (1990) *Lunar Planet. Sci.* XXI, 740. [5] M.V. Gerasimov, et al. (1993) *Lunar Planet. Sci.* XXIV, 527. [6] M.V. Gerasimov, et al. (1994) *Geokhimiya*, in press (in Russian). [7] L.M. Mukhin, M.V. Gerasimov, E.N. Safonova (1989) *Nature* 340, 46. [8] Yu.P. Dikov, et al. (1990) *Lunar Planet. Sci.* XXI, 289. [9] M.V. Gerasimov, et al. (1985) *Vestnik Acad. Nauk USSR* 9, 10 (in Russian). [10] O.I. Yakovlev, Yu.P. Dikov, M.V. Gerasimov (1992) *Geokhimiya* 12, 1359 (in Russian).

Fig.1. Concentration (in wt%) of trapped carbon in the form of carbonate (left axis) and of carbide and amorphous carbon (right axis) through the depth of the condensed film from its surface to the bottom.



PRELIMINARY ANALYSIS OF ASSOCIATIONS OF SMALL VOLCANIC EDIFICES WITH MAJOR GEOLOGIC FEATURES BY LATITUDE ON THE SURFACE OF VENUS-

Kyle Gerlach, Evergreen Senior High School, Vancouver, WA, Mike Safford, Sahuaro High School, Tucson, AZ, Evergreen High School Astronomical Research Class, Sahuaro High School Astronomical Research Class,,Advisors: G. Komatsu, J. Johnson (Univ. of Arizona, Tucson, AZ 85721), J. Lockwood (Sahuaro High School, Tucson AZ 85710), M. Ellison (Evergreen High School, Evergreen, WA 98682)

Introduction: The high resolution and global coverage of the Magellan spacecraft now allow a detailed study of small volcanic edifices on the surface of Venus. A simplified classification scheme for small volcanic edifices (less than 20 km in diameter) that was based on observations of 556 significant shield fields done by Aubele^[1] was used for this study by the astronomy research classes of Evergreen and Sahuaro High Schools. The four classes of small volcanic edifices located are shield-shaped (the most common type of small volcanic edifice on Venus)^[1]; dome-shaped; cone-shaped; and flat-topped (which are distinctive and similar to some sea-floor volcanoes imaged by GLORIA)^[1]. Some of these edifices are very similar to larger and less common Venusian volcanic land forms, implying a continuum of similar volcanic processes, materials, eruption rates, or conditions operating at different scales. ^[1]

Volcanic features are not evenly distributed on the surface of Venus. Head theorizes that the paucity of volcanic features in the lowlands may be due to an altitude dependent inhibition of volatile exsolution and the resulting production of neutral buoyancy zones sufficient to form magma reservoirs and favoring flood lavas at lower elevations.^[2]

Volcanic centers are rare within some geologic centers and occur heavily in others. Within tesserae volcanic centers are virtually absent, with the exception of a few small volcanic edifices. The reason may be due to evidence that tesserae is a thicker and older region of the crust that impedes magma ascent. Volcanic centers are also infrequent in areas characterized by ridge belts, mountain belts, and ridged plains. However, volcanic edifices are common within or around coronae, novae, and arachnids. These features are also commonly associated with each other.^[3]

This study was conducted to find a relationship between small volcanic edifice classes and major geologic features such as coronae, arachnids, novae, tesserae, and large and intermediate volcanoes. There are several questions raised by Aubele about small volcanic edifices, however, in this study we will only be dealing with two: (1) What type of volcanic activity is represented by these edifices? (2) What is the volume contribution of these numerous, but small volcanic source vents?^[1] Detailed mapping of the geologic relationships of these small volcanoes to the plains of larger volcanic features is essential to the exploration of these questions.

Methods: Student researchers at Evergreen High School in Vancouver, Washington, and Sahuaro High School in Tucson, Arizona, measured and located small volcanic edifices (1 to 20 km) in 16 F-MIDR's taken from 5 Magellan CD-ROMs. Most of the F-MIDR's were located along Venus's 0° longitudinal line. The diameter of each edifice was determined by taking measurements along the latitudinal and longitudinal axes and finding their average length. The latitude and longitude of the edifice was then recorded and used to locate the edifice on the GTDR images for measurement of the edifice's elevation.

The class of the edifice was determined by the above mentioned simplified classification scheme by J.C. Aubele^[1]. However, there are many subclasses of these types of volcanoes, and a supplementary catalog, also made by Aubele^[1], was used for clarification. This list included the morphologies of the different subclasses.

Results: Figure 1 clearly shows a deviance from a similar graph in Keddie and Head, 1992⁴ (Fig. 2). This deviance is most evident in the large peaks at -50 to -25 deg. S latitude and 50 to 75 deg N latitude. The major hindrance in the interpretation of this graph is the lack of data taken between 25 and 50 deg. N latitude. Other than this, the plot shows a sharp increase in the number

ANALYSIS OF SMALL EDIFICE DISTRIBUTION K. Gerlach, M. Safford, et. al.

of edifices at -50 deg. S lat., then a drop of roughly 50% that declines again slightly, then experiences an increase in edifice occurrence of about 40% from 25 to 75 deg. N lat.

Figure 2[4], in contrast, shows a smooth expected curve, and while the observed curve follows the expected curve in rough shape, it tends to peak in areas where Fig. 1 drops, and drops in areas that peak in Fig. 1.

Conclusions: The graph produced from the data collected by this year's Astronomical Research class does indeed hint at a possible relationship between latitude and small edifice occurrence. As evidenced by the peaks in the -50 to -25 deg. bin and the 50 to 75 degree bin. This may be due to the concentration of plateau areas corresponding to the bins that show a higher concentration of edifices as well as associations with larger volcanic constructs[5]. When compared to concentrations of features that may influence volcanic activity (such as coronae, large volcanoes, novae, and craters) as well as evidences of widespread volcanism (such as flow patterns), the areas of concentration of small volcanic edifices correspond very closely. In contrast, these small edifices are relatively sparse in areas covered by tesserae. This lack of an association with a particular type of large scale construct presents possibilities for future investigation. The most intriguing aspect of this graph is the apparent contradiction of Keddle and Head, 1992 with volcanic activity not being concentrated near the equator[4]. This, too, warrants further investigation. A high-resolution planetwide survey of small volcanic edifice distribution by latitude, in addition to the results of this investigation, would produce a result with a higher degree of accuracy.

References: 1-Aubele, 1993, *LPSC XXIV* pp. 47-48; 2-Head et. al. *JGR* vol. 97, no. E8, pp. 13153-13197; 3-Head et. al. *Science*, vol. 253, July 30; 4-Keddle and Head, 1992, *International Colloquium on Venus*, pp. 56-57; 5-Crumpler and Aubele, 1992, *LPSC XXIII*, pp. 275-276

Fig. 1-Frequency of Edifices by Latitude
Adjusted for Number of Samples per Bin

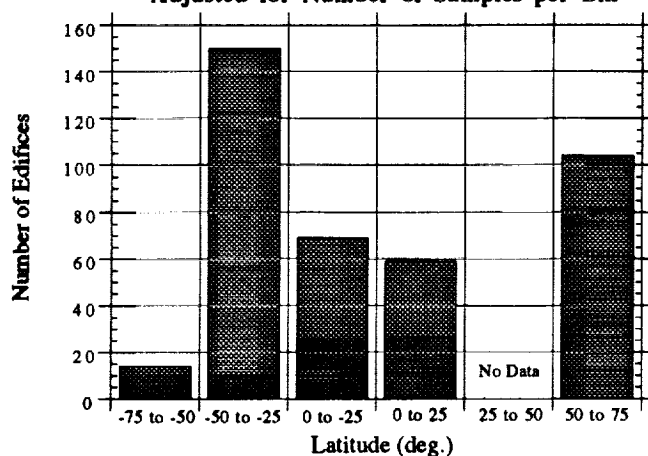
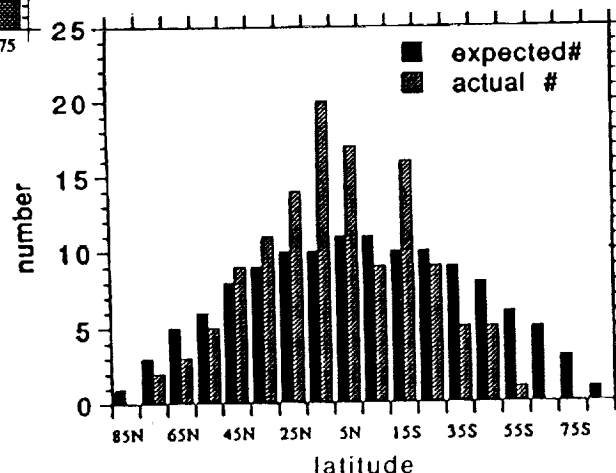


Fig. 2



MORPHOLOGICAL MAPPING OF TWO DISTINCT CORONA CHAINS:

R.C.Ghail, Environmental Science Division, Institute of Environmental and Biological Sciences, Lancaster University, Lancaster, LA1 4YQ, United Kingdom.

I have produced a 1 to 10 million scale morphological map of Parga Chasma corona chain, the Artemis-Latona-Atla (Dali) corona chain and the surrounding plains based up Magellan imagery and have mapped several representative and distinctive features at the full resolution of the Magellan S.A.R. images (70 m per pixel). Herein, the term Torques, meaning a chain or necklace, will be used in place of corona chain; hence the two corona chains will be referred to as Parga Torques and Dali Torques, respectively. Parga Torques consists of an irregular series of coronae of all types which lie on or close to a great circle joining Atla Regio at the equator to Themis Regio in the southern mid-latitudes. Although similar in length, Dali Torques is markedly different from Parga Torques, containing a fraction of the coronae that are present along Parga. However, these coronae are an order of magnitude larger in size and include Artemis Corona, the largest corona on Venus at 2 600 km diameter.

The fracturing throughout Parga Torques is syn-tectonic with regard to the coronae and often is deflected by the presence of individual coronae but may occasionally be found to cross-cut coronal annuli. Fracturing radial to coronae is often deflected to trend parallel to the external fracture trend. I estimate the extension across Parga Torques to be approximately 50% across a linear fracture zone 500 km across. However, the fractures are concentrated into linear zones across which there has been 50 to 150% extension separated by zones of approximately equal width which appear to have undergone limited extension of about 20%. The width of these zones is 18.2 ± 4.8 km. This style of zonal brittle deformation at the surface may be a result of pinch and swell deformation at depth in the crust. The characteristic width given above would correspond to a layer thickness of 3.8 ± 0.8 km, assuming a low viscosity contrast [1]. This layer may correspond to the whole thickness of the crust below the uppermost layers of flood basalts, equivalent to a thickness of 5.7 ± 1.2 km prior to stretching, or perhaps a layer within the crust itself. Occasionally there are also zones up to 50 km in width which appear to be free from any fractures at all. Several of the fracture trends align with deep trenches 500 to 1 500 m below mean planetary radius. However, Parga Torques is centred on a symmetrical topographic rise which extends 1 500 km in width from the level of the regional plains (500 m below mean planetary radius) to 500 m above the mean planetary radius at its crest. Atla and Themis Regiones both rise a further 500 to 1 000 m above the level of this crest. Radiometry data indicates metre scale slopes of 3° to 5° , greater than the planetary average of 2.5° but not comparable to the 10° to 30° slopes found at Aphrodite and Ishtar Terrae. However, both reflectivity and emissivity are average for the planet.

Volcanic features are present along Parga Torques but are generally small (typically shields less than 50 km in diameter) and occur almost exclusively in the interiors of coronae. The two important exceptions are Atla and Themis Regiones which are dominated by volcanic processes and structures and are believed to lie on volcanic rises generated by deep mantle convection. Several coronae within Parga Torques appear to have become distorted in shape through time as their centres of activity, marked by volcanic cones and tectonic radial ridges, have migrated across the interiors of the coronae. Southwest of Parga Torques are many tectonic ridges that appear to be the remnants of coronae. These two lines observations provide evidence that the line of plumes underlying Parga Torques are not stationary in relation to the crust, but are drifting in perhaps a somewhat random pattern locally, but generally in a northeastward direction, at an unknown rate. There is no evidence on Venus for crustal plate movement as there is on Earth, but this does not preclude mantle plume drift relative to the crust. Hot spots on Earth are known to drift in an absolute sense, even when plate motion is accounted for, and it seems likely that a similar drift occurs on Venus.

The ghost coronae southwest of Parga Torques appear to have fully relaxed since they lie at the level of the regional plains and are flooded by external lava flows. However, the topographic expression of these coronae is apparent and it appears that the lava flows covering them must be at

MAPPING OF TWO CORONA CHAINS: Ghail, R.C.

least several hundred metres thick. Given the great areal extent of the flows this implies enormous melt volumes, but where and how were such melts generated? It is paradoxical that the greatest melt volumes appear to have been generated just at the time when the most likely source, the mantle plume, had drifted away from the area. Perhaps the most likely explanation is that these flows have built up over long periods of time (hundreds of millions of years, based upon crater counts) from the small volcanic sources that seem to litter the Venusian surface.

At first sight, Dali Torques appears to be a scaled up version of Parga. Topographically, Dali Torques is centred on a symmetrical rise 2 to 2.5 km high, but contains trenches 4 to 5 km deep and includes Diana Chasma, the lowest point on Venus. Radiometry data indicate metre scale slopes of 10° to 20°, much steeper than the planetary mean, but reflectivity and emissivity are average. The scale of the coronae and regional fracturing is also greater, with two diverging fracture zones 200 to 500 km in width, across which extension is estimated to be 100 to 200%, separated by a zone up to 2 000 km wide across which extension appears to be less than 50%. These two fracture zones initially separate 1 000 km east of Latona Corona, the northern zone being incorporated into the annulus of Latona Corona and then continuing westward, where it again splits in two. One half continues westward and merges into the tessera of southern Thetis Regio, while the other transects the centre of Artemis Corona, forming a complex north-south trench which both cuts and is cut by the southern section of the annulus but then continues a further 650 km southwestward into Aino Planitia. The southern intense fracture zone appears to be older than its northern counterpart since it is cut by both Latona and Artemis Coronae. It follows a southwest trend as far as the eastern annulus of Artemis, from where it cuts due westward across the centre of the corona, partially diverting the north-south trench where the two cross. It extends as far as 90° E into Juno Planitia, its eastern-most portion containing several small coronae 150 to 200 km in diameter. Further fracture belts extend from the northern annulus of Artemis Corona, trending northeastward and merging into the tessera of Ovda Regio. Of the two large coronae, Latona appears to be the younger and more tectonically active. Artemis appears to have undergone several phases of activity linked with the growth and development of the major fracture zones, and may or may not be active at present. It appears that the fracture zones become progressively younger northward which may reflect a drift in underlying mantle circulation similar to that observed at Parga. However, the age relationship between the fracture zones of Dali Torques and the much more intense folding and fracturing of the tesserae of Thetis and Ovda Regiones is unclear. It is widely believed that tesserae represent the oldest fraction of crust present on Venus and are 500 Ma or greater in age, compared with the 300 Ma age estimate of the Dali fractures. These estimates are based on the limited data available from crater counts on Venus and are open to some considerable doubt particularly in the heavily deformed tesserae. Other observations, such as parallel fracture trends, support a contemporaneous age for the formation of tesserae and fracture belts. A contemporaneous formation age of the two features would, in part, alleviate the problem of accommodating the crustal extension across Dali Torques.

It is therefore apparent that the tectonic evolution of Dali Torques is both more complex and less organised than that of Parga Torques. The reasons for this are as yet unclear but may be due to a regional mantle heterogeneity in, for example, temperature or volatile content, or to variations in crustal thickness. Certainly the possibility that subduction is or has been occurring at the annuli of both Artemis and Latona coronae [2] must have a significant effect on the lithosphere and regional tectonism.

REFERENCES: [1] Price, N.J. and Cosgrove, J.W. (1990) *Analysis Of Geological Structures*, Cambridge Univ. Press. [2] Sandwell, D.T. and Schubert, G. (1992) *JGR* 97, 16069

PLATE TECTONICS, VENUSIAN STYLE; R.C.Ghail and L.Wilson, Environmental Science Division, Institute of Environmental and Biological Sciences, Lancaster University, Lancaster, LA1 4YQ, United Kingdom.

The topographic form and length of Parga and Dali Torques[†], and the fact that they lie on a great circles, has in the past led to the suggestion that these and similar features were spreading ridges. The higher resolution of the Magellan data has led to the rejection of this hypothesis on the basis that no significant horizontal motion is evident and that features such as transform faults that are typical of mid-oceanic ridges on Earth are not present on Venus. However, it is entirely possible, indeed probable, that the surface expression of a spreading ridge system would be different on Venus. The most popular hypothesis for corona formation and evolution postulates the impinging of a rising upper mantle diapir on the crust or lithosphere [1] but this model fails to explain the frequent occurrence of coronae in chains along tectonic rift zones. In addition, the proposed evolutionary sequence fails to account for the formation of arachnoidal structures and the observation that many coronae have either incomplete annuli or annuli that have been deformed by or incorporated into regional fracturing. This in part appears to have arisen as a result of the fact that the classification scheme of Stofan *et al.* [2] does not include arachnoids, and attempts to exclude coronae from the exterior environment (which clearly has a major impact on the morphology of coronae). Upper mantle upwelling and diapirism is thought to occur beneath terrestrial spreading ridges and we propose that a similar process may occur on Venus beneath torques.

Without subduction to provide a large horizontal stress, there would be no significant plate motion as found on Earth but even so mantle circulation patterns on Venus may be similar to Earth's [3]. Thus, upper mantle plumes may align themselves along great circles as is the case under terrestrial spreading ridges, resulting in the chains of coronae that are observed. Deeper mantle plumes (i.e., those generated at the core-mantle boundary) would generally be unrelated to these upper mantle plumes and would give rise to regional tectonic rises such as Western Eistla Regio. However, where deep mantle and upper mantle plumes interact (such as at Iceland on Earth), particularly pronounced activity may result. This may be the case at Atla Regio, which appears to be at the junction of several corona chains. Rabinowicz *et al.* [4] have modelled the three dimensional convection pattern beneath terrestrial spreading ridges using five distinct geophysical models of the upper mantle structure. For each case they have initially modelled the circulation pattern beneath a motionless upper plate, the results of which are in good agreement with the structures found on Venus and suggest an alternative evolutionary sequence, which we present below, to the diapiric model of Janes *et al.* [1].

Prior to the formation of the corona chain, the mantle is initially cool but is slowly heated from within by the decay of radioactive nuclei. Mantle circulation is initiated in a 65 km thick layer [4] immediately below the lithosphere by the formation of concentrated downwelling cold plumes surrounded by upwelling diffuse sheets of warm material. This circulation imposes stresses on the lithospheric plate which result in the formation of arachnoids above the downwelling plumes and extensive linear fracturing and graben formation above the diffuse upwelling sheets. Typical parameters [4] are a whole layer viscosity of 3×10^{19} Pa s and a Rayleigh number equal to 50 000, corresponding to an average arachnoid size of 90 km and a typical spacing (centre to centre) of 140 km, in close agreement with the observed size and spacing of arachnoids on Venus [5].

This pattern of circulation continues until the mantle layer has warmed sufficiently to undergo partial melting by adiabatic decompression in the uppermost third of the layer. This lowers the effective viscosity of the upper layer to approximately 1×10^{18} Pa s [4]. The lower viscosity upper layer reverses the circulation pattern so that upwelling occurs in large plumes and downwelling

[†] Herein, the term Torques, meaning a chain or necklace, will be used in place of corona chain; hence Parga Chasma will be referred to as Parga Torques and the Atla-Latona-Artemis corona chain will be referred to as Dali Torques

PLATE TECTONICS, VENUSIAN STYLE: Ghail, R. C. and Wilson, L.

material is concentrated into narrow sheets at the margins of the upwelling plumes. This circulation pattern results in the formation of coronae: the downwelling sheets correspond to the intensely deformed annuli of coronae which themselves are centred on upwelling plumes. These plumes supply large volumes of melt to the interiors of the coronae resulting in the flood volcanism which produces the interior plains and volcanic constructs. The average diameter of coronae produced by this model is 230 km, with an annulus 25 km wide. This is a little less than the average observed diameter of 250 to 300 km [2]. The spacing (centre to centre) of the coronae is typically 370 km (at Parga Torques) but each corona is connected to its neighbours by several narrow linear downwelling zones. Small downwelling plumes, usually about 30 km in diameter, are periodically generated within the coronae themselves and may result in localised radial fracturing in the interior. The limited crustal spreading that appears to be taking place at Parga Torques is apparently accommodated principally in the compressive fractures at the annuli of the coronae.

This is contrasted to Dali Torques, which is composed of exceptionally large coronae and has large amount of crustal extension. The region between Artemis Corona and Ovda Regio illustrates the interaction between the relatively young fracturing of northern Artemis Corona (estimated to be less than 300 Ma old) and the older tessera of southern Ovda Regio. This tessera is estimated to be more than 500 Ma in age and is believed to be the result of compressive folding and fracturing associated with mantle downwelling. The age determinations are derived from crater counts and are open to some doubt, given the unreliability of crater counts in general on Venus and in particular on the complex terrain within tesserae. It is therefore possible that both Artemis Corona and Ovda Tesserae are contemporaneous in age, with the compression in the tesserae accommodating the extension across northern Artemis. South of Artemis, however, there are no tesserae to accommodate the crustal extension within the corona. Here crustal extension appears to be accommodated entirely within the 100 to 150 km wide annulus of the corona which appears to have many features in common with terrestrial subduction zones and indicates that subduction is, or has been, occurring there.

It appears that while plate tectonic processes do not operate at a global scale on Venus, they may operate on a regional and local scale. Coronae appear to be linked closely to plate tectonic processes, and in fact Artemis Corona may be regarded as a micro-plate in itself. Thus Venus may represent an important link between Earth at the one extreme, where tectonic activity is dominated by plate motion, and the smaller, one plate terrestrial planets such as Mars, dominated by hot spot volcanic processes.

REFERENCES: [1] Janes, D.M., Squyres, S.W., Bindshadler, D.L., Baer, G., Schubert, G., Sharpton, V.L. and Stofan, E.R. (1992) *JGR* 97, 16055. [2] Stofan, E.R., Sharpton, V.L., Schubert, G., Baer, G., Bindshadler, D.L., Janes, D.M. and Squyres, S.W. (1992) *JGR* 97, 13347. [3] Crumpler, L.S., Head, J.W. and Aubele, J.C. (1993) Relationship Of Major Volcanic Center Concentrations On Venus To Global Tectonic Patterns, *Science* (in press). [4] Rabinowicz, M., Rouzo, S., Sempere, J.C., Rosemberg, C. (1993) *JGR* 98, 7851. [5] Head, J.W., Crumpler, L.S., Aubele, J.C., Guest, J.E. and Saunders, R.S. (1992) *JGR* 97, 13153

A REAPPRAISAL OF METAMORPHISM IN THE VREDEFORT DOME, SOUTH AFRICA, AND ITS IMPLICATIONS FOR THE ORIGIN AND EVOLUTION OF THE DOME. Roger L. Gibson¹, W. Uwe Reimold², Thomas Wallmach¹, and Wayne P. Colliston³; ¹*Department of Geology, University of the Witwatersrand, P O WITS 2050, Johannesburg, South Africa*; ²*E.G.R.U., University of the Witwatersrand, P O WITS 2050, Johannesburg, South Africa*; ³*Department of Geology, University of the Orange Free State, P O Box 339, Bloemfontein, South Africa*

Evidence of mid-amphibolite facies metamorphism in the collar of the Vredefort Dome has been used by some workers to support an endogenic origin for the structure [1,2,3]. Preliminary results of a new investigation contradict their findings, namely that the metamorphism is restricted to the vicinity of the Dome and that the metamorphic rocks are hornfelses which form part of a contact metamorphic aureole adjacent to a hidden pluton. Based on evidence of two syn-metamorphic deformation events, an anticlockwise P-T path, and overprinting of peak metamorphic assemblages by syn-doming structures, we propose that the metamorphism formed part of a regional dynamothermal event that culminated shortly before formation of the Dome. Given the presence of relict "shock" features and high-pressure polymorphs of quartz in the Dome, an impact origin remains the most plausible explanation for the formation of this structure.

Introduction: The Vredefort Dome is situated 100 km SSW of Johannesburg. It comprises a core of predominantly granitic Archean basement some 45 km wide which is surrounded by a collar of steeply-dipping to overturned metasedimentary and metavolcanic rocks belonging to the Dominion Group, the Witwatersrand and Ventersdorp Supergroups and the Transvaal Sequence (Fig. 1). The metamorphic rocks under discussion are from pelitic units in the Hospital Hill and Government Subgroups of the lower Witwatersrand Supergroup in the NW sector of the Dome. They contain assemblages involving biotite, andalusite, cordierite, garnet and/or staurolite which indicate peak metamorphic conditions of c. 600 °C, 4 kbar. In contrast, metamorphic grade in the equivalent stratigraphic horizons in the remainder of the Witwatersrand Basin does not exceed upper greenschist facies [4]. The local metamorphic "high" in the vicinity of the Dome, together with the paucity of evidence in outcrop for syn-metamorphic deformation fabrics, has led several workers to propose that the metamorphism is a local contact phenomenon developed adjacent to a hidden pluton [5,6,7,8].

Deformation fabrics: A study of 52 pelitic samples from the Hospital Hill and Government Subgroups showed that, despite the paucity of evidence in outcrop, the rocks contain two regionally-developed syn-metamorphic foliations [9]. The older foliation (S1) is defined by pervasive alignment of matrix biotite, opaques and lensoid quartz grains, and some biotite and cordierite porphyroblasts. The S2 foliation displays a more variable intensity. It developed by crenulation of S1 and is defined by matrix biotite and opaques and by aligned biotite porphyroblasts. Porphyroblast-matrix microstructural relations indicate that the bulk of porphyroblast growth, and the peak of metamorphism, occurred during the D2 foliation-forming event.

P-T path: Interpretation of the metamorphic mineral assemblages and reaction textures has enabled reconstruction of the P-T path followed by the rocks during metamorphism. The anticlockwise P-T path (Fig. 2) is deduced from evidence of (1) prograde breakdown of cordierite to andalusite and (2) retrograde breakdown of andalusite + biotite to staurolite.

Timing of metamorphism: The metamorphic rocks are cut by post-metamorphic fracture cleavages, often accompanied by pseudotachylyte, that are related to the doming event [3]. These cleavages are associated with two distinctive retrograde reactions. Samples containing an intense cleavage often display local retrogression of andalusite, staurolite and biotite to coarse-grained aggregates of chlorite + muscovite, testifying to rehydration of the peak assemblages while the rocks were still relatively hot. In some samples, however, the pseudotachylyte veinlets are bounded by cordierite aggregates which replace the peak assemblages (Fig. 3). The breakdown of staurolite + biotite to cordierite (reaction 3, Fig. 2) should only occur in anhydrous, chlorite-free assemblages and requires a significant drop in P from the peak metamorphic conditions. The development of cordierite associated with the pseudotachylyte-bearing cleavages thus suggests that (a) cleavage development (and, therefore, doming) occurred soon after the attainment of peak metamorphic conditions, before the rocks had cooled significantly, and (b) the decompression associated with doming must have been relatively rapid to prevent significant cooling during exhumation.

Discussion: The presence of syn-metamorphic deformation fabrics in the metapelitic rocks of the lower Witwatersrand Supergroup in the collar of the Vredefort Dome indicates that the rocks formed part of a dynamothermal terrane. This is supported by the P-T path followed by these rocks, which indicates that heating was accompanied by burial of mid-crustal levels. Such a path is not characteristic of contact metamorphic aureoles, which usually show near-isobaric heating and cooling [10]. It may, however, be indicative of loading caused by the intrusion of voluminous high-level magmas [11], or of thickening of crust characterized by a high basal heat flow [12]. In either case, the metamorphism is regional in extent. This

VREDEFORT DOME METAMORPHISM: Gibson R.L. et al.

implies that the lower-grade, upper greenschist facies metamorphism observed in the Witwatersrand Basin may correspond to shallower crustal levels than those exposed in the Vredefort Dome. Evidence of upper amphibolite and granulite facies conditions in the core of the Dome [13,14] is consistent with such a model and suggests that the Dome may expose a near-complete crustal profile through the metamorphic terrane.

It is difficult to reconcile the anticlockwise P-T path followed by the rocks with the endogenic cryptoexplosion or diapiric hypotheses proposed to explain the formation of the Dome [1,2,3], as these should lead to exhumation, not burial, of the rocks during heating. The post-peak timing of doming is indicated by the retrogressive assemblages associated with the syn-doming cleavages. Other evidence for rapid exhumation of rocks in the Dome is found in the core [13,14]. In conclusion, there does not appear to be a genetic link between the metamorphic and doming events, despite the partial overlap in their timing. Given the evidence of relict "shock" features and high-pressure polymorphs of quartz in the rocks, superimposition of a large bolide impact on a regional metamorphic terrane on the Kaapvaal Craton could reasonably account for the metamorphic and structural features of the Vredefort Dome.

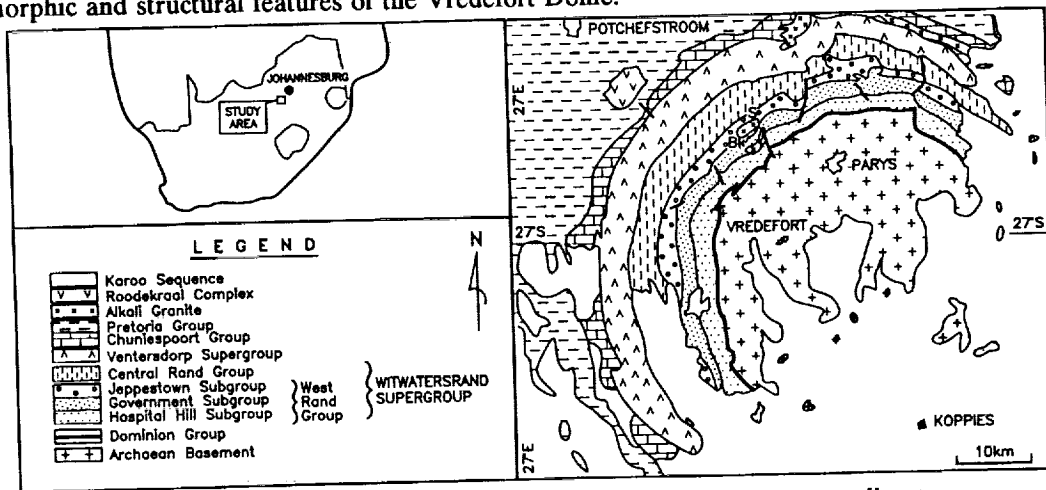


Fig. 1: Simplified geological map of the Vredefort Dome. A-F are sampling traverses.

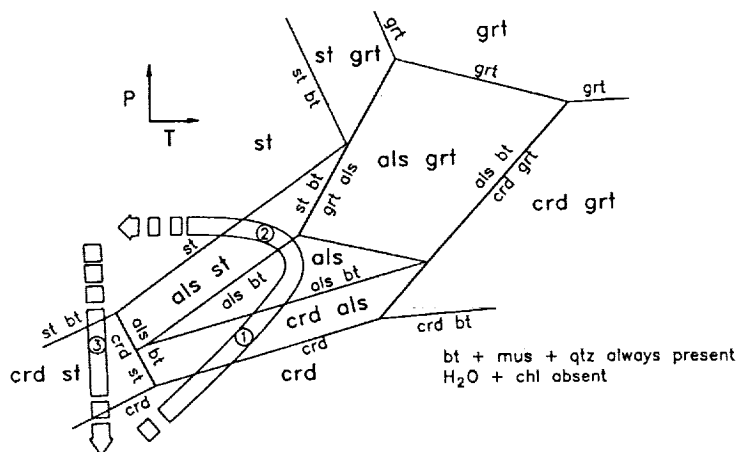


Fig. 2: Petrogenetic grid for pelites showing P-T path for the collar rocks.

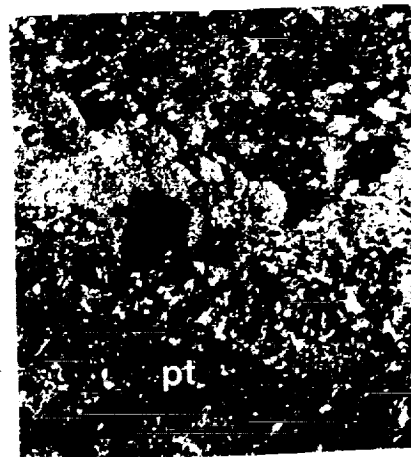


Fig. 3: Cordierite growth adjacent to pseudotachylyte.

- References:** [1] Nicolaysen L.O. (1985) *S. Afr. J. Sc.*, 81, 120-131; [2] Du Toit A.L. (1954) *The Geology of South Africa*, 611p; [3] Colliston W.P. (1990) *Tectonophysics*, 171, 115-118; [4] Phillips G.N. (1987) *JMG*, 5, 307-322; [5] Hall A.L. & Molengraaff G.A.F. (1925) *Verh. Kon. Akad. Wetenschap. Amsterdam*, 24, 183p; [6] Nel L.T. (1927) *Spec. Publ. geol. Surv. S. Afr.*, 6, 134p; [7] Bisschoff A.A. (1982) *Trans. geol. soc. S. Afr.*, 85, 43-57; [8] Schreyer W. (1983) *J. Petr.*, 24, 26-47; [9] Gibson R.L. (1993) *S. Afr. J. Geol.*, 96, 42-48; [10] Pattison D.R.M. & Tracy R.J. (1991) *Rev. Mineral.*, 17, 105-203; [11] Waters D.J. (1989) *Geol. Soc. Lond. Spec. Publ.*, 43, 357-363; [12] Loosveld R.J.H. (1989) *Tectonophysics*, 158, 191-218; [13] Schreyer W. & Abraham K. (1978) *CMP*, 68, 53-62; [14] Schreyer W. et al. (1978). *CMP*, 65, 351-361.

INTRATESSERA VOLCANISM OF ALPHA AND TELLUS TESSERAE ON VENUS: M. S. Gilmore and J. W. Head, Department of Geological Sciences, Brown University, Providence, RI 02912.

Tesserae represent some of the oldest terrain on Venus, comprising 8.35% of the surface of the planet [1]. Previous studies [2,3] have shown that tesserae display the following characteristics: 1) tesserae are stratigraphically older than surrounding plains; 2) the earliest deformational structures in the tessera are compressional in nature; 3) the compressional features are overprinted by graben and extensional faults; 4) tessera contain volcanic plains that are largely unmodified. Tessera may be formed by a downwelling mantle flow followed by long-term gravitational relaxation [4]. This study focuses on the morphology and extent of intratessera volcanism within Alpha and Tellus Regiones in order to further constrain this model.

Alpha Regio. Intratessera plains (ITP) cover 8% of the surface area of Alpha; individual patches range in size from 700 - 35,000 km². Most ITP are elongate to circular in shape and are confined by scarps an average of 1 km high. Lavas also passively embay the troughs of the tessera fabric itself; these unconfined flows often coalesce, forming irregularly-shaped plains. The ITP in Alpha contain one or more episodes of volcanism. In several ITP, the oldest flows are modified by extensional features continuous from the tessera fabric into the plains. Younger units are radar-dark and less deformed or undeformed. Volcanic edifices are discernable in most of the ITP, average 3 km in diameter, and are concentrated within the youngest flow units. Some flows can be traced to fissures up to 3 km wide and 20 km in length.

The intratessera plains in Alpha are larger in size and number in the northern and eastern sections of the plateau, the area with the lowest elevations of this tessera (6051 - 6052.5 km). The western part of Alpha contains very small and moderately tectonized ITP, and may have a history distinctive from the bulk of Alpha [5]. Intratessera volcanism is rare to absent in the southwest section of Alpha, which is dominated by broad zones of shear [3] and has the highest elevations of the plateau.

Tellus Regio. Intratessera volcanics cover 22% of the surface of Tellus. Most of the volcanics (64%) occur in a single, large flooded area covering 6.3×10^5 km² of northern Tellus. Contributing lavas to this flooded area are a steep-sided dome and an irregularly-shaped volcano $\approx 50 \times 100$ km in diameter; these types of edifices do not occur in Alpha. Confined ITP range from 400 - 17,000 km² and lie an average of 0.5 km below the surrounding scarps. These plains are frequently linked together into larger systems consisting of 2-5 individual ITP. The confined ITP have shapes similar to Alpha, four ITP however are shaped like very regular circles and ellipses ≈ 100 km in diameter. Their borders consist of several concentric ridges that cross-cut the tessera fabric, suggesting a tectonic component of ITP evolution. The ITP in Tellus have an order of magnitude more edifices per area of ITP than in Alpha. These volcanoes average 5 km in diameter and have contributed to flow units that frequently breach and engulf the bounding scarps. These lavas flood the lowest elevations of Tellus and may flow beyond the border of the tessera plateau itself. Some ITP display multiple episodes of volcanism. The oldest ITP lavas of Tellus are modified by extensional features; the oldest lavas in Tellus are more highly deformed than the oldest lavas in Alpha. Unlike Alpha, individual volcanoes up to 14 km in diameter and graben lined with pit craters and small shields occur independently of intratessera plains.

Evolutionary Models. We consider a model where tessera are formed by convergence due to mantle downwelling [4] generating the early compressional features of the tesserae. Magmatism could subsequently occur in two ways: 1) a crustal root could be thermally denser than the warm asthenosphere beneath it, or undergo a basalt-eclogite phase transition, and therefore become gravitationally unstable [6]. If the instability grows and detaches, warm asthenosphere will rise to replace the lost crust generating basaltic melts by adiabatic decompression and melting of the lower crust. 2) The crustal root may simply undergo melting when it thermally crosses its solidus. If the thermal gradient is 15°C/km this will occur at ≈ 60 km; if the thermal gradient is 25°C/km melting will occur at ≈ 30 km for basaltic compositions [7,8]. Melting a basalt can produce a variety of magma types depending on the pressure and the degree of melting [7]. The steep-sided dome within Tellus may be formed by melt generated by this process.

A delamination or widespread melting event would mark a change in the deformational style of the tessera as topography gravitationally relaxes. Melt migration and extrusion is easier in extensional

INTRATESSERA VOLCANISM: M. S. Gilmore and J. W. Head

regimes, resulting in the concentration of volcanism in topographic lows. The plateau continues to extend by gravitational relaxation allowing continued volcanism and extensional deformation. If dikes are propagated from overpressurized source regions, more will reach the surface in areas of thin crust than in thick crust [8], consistent with the predominance of ITPs and volcanic constructs in areas of lowest topography in Alpha and Tellus.

Intratessera Volcanism Source Region. The areal extent of intratessera volcanism is used to estimate the size of the magma reservoir (Table 1). We assume that ITP magma is a basalt erupting through a basaltic crust. The average thickness of the lava deposits is estimated to be 300 m based on the height of buried structures. The intrusion to extrusion ratio depends on crustal thickness, magma composition, rate of magma generation, and depth of any neutral buoyancy zone [8,9]. The ratios for terrestrial oceanic and continental crust have been estimated to be 5:1 and 10:1, respectively [9]; we adopt an intermediate value of 7:1 for tessera crust. Total magma produced can then be calculated and used to estimate size of the region of melt generation (reservoir) based on 25% and 10% partial melting. The reservoir volume is presented as a sphere and as a layer, where the area of the layer is equal to the surface area of the tessera.

A spherical reservoir that has undergone 10% partial melting will be far too small to distribute volcanism over the entire surface area of either Alpha or Tellus. If the reservoir volume is divided so that each ITP in the tesserae has its own spherical source region, the reservoirs would have a radius of 4 km; these spheres are at least an order of magnitude smaller in scale than the majority of volcanic features on Venus [10,11]. The areal extent of intratessera volcanism is more consistent with a tabular reservoir. A layer provides a good approximation of wide-spread melting of the lower crust beneath the tessera due to a delamination event or melting of a crustal root. Such reservoirs may be sites of magmatic differentiation, which could explain the correlation between steep-sided domes and tesserae on Venus [12]. The tectonic deformation associated with some ITP in Tellus may indicate that these features formed by negative diapirism rather than independent upwelling of the mantle from deeper sources. We are investigating the possibility that some ITP are the surface manifestations of negative diapirs.

Summary and Conclusions. Alpha and Tellus Regio both contain intratessera plains that are largely undeformed and must have been emplaced in relatively late stages of the history of the plateau. The greater abundance of volcanism in Tellus as compared to Alpha may be explained in terms of differences in crustal thickness, as Tellus has a lower average elevation than Alpha.

Table 1: Calculated volume of source reservoir for intratessera volcanism in Alpha and Tellus tessera. See text for details.

	Alpha	Tellus
Total Surface Area	$2.0 \times 10^6 \text{ km}^2$	$4.4 \times 10^6 \text{ km}^2$
ITP Area	$1.6 \times 10^5 \text{ km}^2$	$9.8 \times 10^5 \text{ km}^2$
Percent ITP	8%	22%
Volume of Extrusives	$4.8 \times 10^4 \text{ km}^3$	$2.9 \times 10^5 \text{ km}^3$
Total Magma Generated	$3.4 \times 10^5 \text{ km}^3$	$2.0 \times 10^6 \text{ km}^3$
Reservoir Size 25% Melt	$1.4 \times 10^6 \text{ km}^3$	$8.0 \times 10^6 \text{ km}^3$
10% Melt	$3.4 \times 10^6 \text{ km}^3$	$2.0 \times 10^7 \text{ km}^3$
Sphere Radius 25% Melt	69.4 km	124.1 km
10% Melt	113.0 km	168.4 km
Layer Thickness 25% Melt	0.72 km	1.82 km
10% Melt	1.74 km	4.55 km

- REFERENCES:** [1] Ivanov, M.A., and Head, J. W. (1994) submitted to *Icarus*. [2] Ivanov, M. A., and Head, J. W., (1992) *LPSC XXIII*, 581. [3] Bindshadler, D. L. *et al.* (1992) *J. Geophys. Res.*, 97, 13563. [4] Gilmore, M. S., and Head, J. W. (1992) *Abs. Int. Colloq. Venus*. [5] Bindshadler, D. L. *et al.* (1992) *J. Geophys. Res.*, 97, 13495. [6] Bird, P. B. (1979) *J. Geophys. Res.*, 84, 7561. [7] Hess, P. C., and Head, J. W., (1990) *EMP*, 57. [8] Head, J. W., and Wilson, L., (1992) *J. Geophys. Res.*, 97, 3877; (1992) *Geochim. Cosmo. Acta*, 56, 2155. [9] Crisp, J. A., (1984) *J. Volc. Geotherm. Res.*, 177. [10] Head, J. W. *et al.*, (1992) *J. Geophys. Res.*, 97, 13153. [11] Magee Roberts, K., and Head, J. W., (1993) *Geophys. Res. Lett.*, 20, 1111. [12] Pavri, B., *et al.*, (1992) *J. Geophys. Res.*, 97, 13445.

COMPOSITION AND PETROGRAPHY OF A MUONG NONG-TYPE GEORGIA TEKTITE; B. P. Glass, Geology Department, University of Delaware, Newark, DE 19716; C. Koeberl, Institute of Geochemistry, University of Vienna, A-1010 Vienna, Austria; H. Povenmire, 215 Osage Drive, Indian Harbour Beach, FL 32937.

A Muong Nong-type (MN) tektite was recently found in Washington County, Georgia, just south of Riddleville. This is the first MN tektite to be found in Georgia. It is also the largest Georgia tektite known and it is the only North American tektite known to contain zircons in addition to baddeleyite. Because of the uniqueness of the specimen a consortium was established to study it [1]. This report deals only with the composition and petrography.

An end piece weighing 5.2 g was cut off the specimen and then four 1-2 mm thick slices were cut. One slice was cut into four subsamples and given to members of the consortium. The slices show layering due to variations in color of the glass. The layering varies from indistinct and broadly curving to sharp and folded. The specimen exhibits extreme strain birefringence. Vesicles are generally common to abundant, but most are $< 200 \mu\text{m}$ in diameter and are therefore not obvious to the unaided eye. The largest vesicle observed is $740 \mu\text{m}$ in diameter. Lechatelierite is common and ranges from more or less equant to long (up to several millimeters) filamentous, highly-contorted inclusions. Some of the lechatelierite is bubbly, but frothy lechatelierite was not observed. Numerous rounded, white opaque inclusions, generally between $20\text{--}60 \mu\text{m}$ in size, were observed in each slice, otherwise the specimen is free of crystalline material. The end piece was crushed, sieved into two fractions ($74\text{--}149 \mu\text{m}$ and $< 74 \mu\text{m}$). The $74\text{--}149 \mu\text{m}$ size fraction was divided into different specific gravity fractions using heavy liquids in order to recover mineral inclusions and glasses of different composition. Nine glass fragments, each containing one white opaque inclusion, were recovered. The inclusions were similar in appearance to those observed in the slices. X-ray diffraction patterns, obtained using a Debye-Scherrer camera, indicate that all the white opaque inclusions are zircon, baddeleyite, or mixtures of zircon and baddeleyite.

Major oxide compositions were determined for numerous glass fragments from each of the specific gravity fractions using energy dispersive x-ray analysis. The SiO_2 content was found to vary from 67 to 88%. The range in composition is greater than for all the previously analyzed North American tektites combined; however, the oxide vs. silica trends are well defined and for a given SiO_2 content the weight percent of the other oxides are similar to those of previously analyzed North American tektites.

Some preliminary trace element data have been obtained for the Muong Nong-type Georgia tektite (MNGATek) using instrumental neutron-activation analysis (INAA) (see [2] for INAA technique and element precision) (Table 1). Unfortunately, very little trace element data have been published for North American

COMPOSITION AND PETROGRAPHY OF MNGATEK: Glass B. P. et al.

tektites. No As, Au, Br, or Sb data are available for Georgia tektites. The Ga concentration of the MNGaTek is within the range previously reported for Georgia tektites. As would be expected, the As, Br, and Sb concentrations are closer to those of bediasites than to MN Australasian tektites (Table 1).

Three measurements of the water content of the MNGaTek were made using a Perkin Elmer 1760X Fourier-transform-IR spectrometer. The specimen appears to be homogeneous at a 2-3 mm resolution with a water content of 0.007 wt. %. The water content of Georgia tektites is not known, but 0.007 wt. % is slightly lower than published values for most bediasites [6].

Muong Nong-type tektites are generally regarded as having formed at lower temperatures than the splash form tektites [7]. However, the lack of frothy lechatelierite and coesite and the fact that many of the zircons were converted either partly or completely to baddeleyite, and the higher water content compared with Muong Nong-type Australasian tektites indicate that this specimen was subjected to higher temperature than previously described MN Australasian tektites with crystalline inclusions [8]. The discovery of this specimen in the most northeastern part of the strewn field is consistent with previous suggestions that the source crater is probably on the Atlantic coastal plain or continental margin off the northeastern United States [9].

References. [1] Povenmire H. et al. LPS XXV (this volume). [2] Koeberl C. et al. (1984). Proc. Lunar Planet. Sci. Conf. 15th, C351. [3] Cuttitta F. et al. (1969) JGR, 72, 1343. [4] Weinke H. H. and C. Koeberl (1985) Meteoritics, 20, 783. [5] Glass B. P. and C. Koeberl (1989) Meteoritics, 24, 143. [6] Gilchrist J. et al. (1969) JGR, 74, 1475. [7] Koeberl C. (1989) Proc. 2nd Intern. Conf. Natural Glasses, Charles Univ.; Prague, p. 371. [8] Glass B. P. and R. A. Barlow (1979) Meteoritics, 14, 55. [9] Koeberl C. and B. P. Glass (1988) Earth Planet. Sci. Lett., 87, 286

Table 1. Trace Element abundances (ppm) for Muong Nong-type Georgia tektite (MNGaTek), selected North American tektites, and five Muong Nong-type (MN) Australasian tektites.

		Georgia Tektites [3]	Bediasites [4] BED8401	BED8402	MN Australasian [5]
	<u>MNGaTek</u>				
As	0.29		1	0.8	3.5 - 6.1
Au	0.3		-	-	0.8 - 1.6
Ga	9.3	5.7 - 10	-	-	10.0 - 21.8
Br	0.02		0.1	-	3.0 - 6.1
Sb	0.087		0.05	0.05	0.65 - 1.10

A THEORETICAL STUDY OF SO₂ TRANSPORT BY EXPLOSIVE VOLCANISM ON VENUS; Lori S. Glaze, Jet Propulsion Laboratory, California Institute of Technology, 4800 Oak Grove Dr., Pasadena, CA 91109

It has been proposed that explosive volcanism may occur on Venus, despite high atmospheric pressure and extreme surface temperatures, in an effort to explain the variability of SO₂ concentrations observed at the Venus cloud tops (40 mbar or ~70 km above mean planetary radius [ampr]) [1,2]. In support of this suggestion, recent geochemical studies of weathering processes on the Venusian surface indicate that ~1 km³/yr of magma would have to be erupted in order to supply SO₂ at a sufficient rate to remain in equilibrium with surface scavenging [3]. Even higher rates of volcanism are suggested by geophysical studies [4]. This study shows that volcanoes can erupt explosively under conditions found on the surface of Venus but that the buoyant plumes generated by these eruptions are very sensitive to the ambient atmospheric stability. Earlier theoretical studies of explosive volcanism have presumed simplistic atmospheric temperature and pressure profiles, however, there are several indications that the Venusian atmosphere is more stable than previously assumed. Extremely stable atmospheres are shown to have the most potential for producing the highest plumes. It may also be possible that tropospheric circulation is partially responsible for the transport of volcanic material, in which case, explosive volcanic eruptions would not be required to generate extremely high plumes in order to explain high concentrations of volcanic SO₂ at the Venusian cloud tops.

Ambient Sensitivities

Theoretical studies of explosive volcanism on Venus conducted in recent years have used a simple, globally averaged temperature and pressure model derived from the four Pioneer Venus probes sent into the Venusian atmosphere [6]. These studies concluded that it is unlikely that explosive volcanism on Venus could produce anything more than very small buoyant plumes. The dynamics of convective columns, however, are sensitive to atmospheric pressure and temperature profiles. Recent work [5,6] has shown that the final heights of volcanic plumes are very sensitive to the atmospheric lapse rate, and hence the degree of atmospheric stability. There are two problems with the simplistic atmospheric temperature model used in the past: there is significant uncertainty near the surface and latitudinal variations must be considered.

Near Surface Profile: Very little is known about the temperature structure near the surface of Venus because none of the four Pioneer Venus probes returned temperature measurements below 12 km altitude (ampr). Due to this lack of data temperatures near the surface have been extrapolated from higher altitude data. Recent work by D. Crisp and V. Meadows (pers. comm.), however, has shown that the near-surface lapse rate may be steeper than previously assumed, resulting in an atmosphere that is much more stable, thus increasing the rise potential of buoyant plumes.

Latitudinal Variation: Existing data [7] show that there is a significant latitudinal variation in the temperature gradient between 40 and 60 km (ampr). Seiff [7] reported that atmospheric temperatures in this region may drop much more sharply at higher latitudes (above 60°) than at mid and equatorial latitudes. This steeper lapse rate is indicated by both the 59° N Pioneer Venus probe and the radio occultation data from the Pioneer Venus Orbiter. This again indicates

a more stable regime and, therefore, is very important for volcanic plume rise and, hence, SO₂ transport. As an example, volcanoes erupting explosively with identical initial conditions are most likely to produce the highest plumes in the regions above 60°. Furthermore, some of the highest volcanoes on Venus are located in the northern latitudes, adding additional rise potential through the initial height as well as the difference in initial ambient pressure (50 bars at 8-9 km ampr as opposed to 90 bars at 0 ampr), again adding to the rise potential of an explosive volcanic plume. A volcano in the Maxwell Montes region, therefore, has a strong potential for producing a comparatively high plume. The higher a plume is able to rise in the atmosphere, the easier it is to explain the accumulation of SO₂ at the top of the troposphere.

Theoretical Calculations

The theoretical model used in this study to describe the rise of buoyant plumes is based on the Glaze and Baloga [5] buoyant plume model that assumes a system of ordinary differential equations describing the conservation of volume, mass, momentum and thermal energy as first describe by Morton *et al.* [8]. The ambient parameters have been modified for the conditions found on Venus and the plume composition has been assumed to be the same as the ambient atmosphere. For test purposes, I have assumed an initial plume radius of 300 m (which is within the reasonable range given current knowledge) and a vent height of 10 km (requiring the volcano to be located at one of the highest points on the planet's surface). I have then varied the initial velocity independently between 300 and 900 m s⁻¹. The initial velocity is integrally tied to the gas mass fraction, but the velocity has been allowed to vary for illustrative purposes. The first initial velocity of 300 m s⁻¹ is a realistic value for the chosen gas mass fraction of 0.03 [9]. The model plumes have then been released into several atmospheric regimes, including the simplistic, globally averaged atmosphere, a northern latitude profile [7] and a more stable near surface profile. The results for the globally averaged model indicate that even the physically implausible 900 m s⁻¹ initial velocity is incapable of maintaining a plume at 40 km altitude. This is nowhere near high enough for a direct injection of volcanic material into the cloud layer. The other atmospheric profiles show much more promise for direct injection.

It may not be necessary, however, to directly inject volcanic material into the top of the cloud layer. It is possible that atmospheric circulation may be at least partially responsible for transporting the volcanic SO₂. In this instance, explosive eruptions may only be required to generate plumes extending a few kilometers above the vent. Future research will include a study of the time and spatial scales for circulation in the Venus troposphere.

References:

- [1] Esposito, L.W. (1984) *Science* **223**:1072-1074.
- [2] Prinn, R.G. (1990) *Exploring Space* :94-101.
- [3] Fegley, B. and A.H. Treiman (1992) *Am Geophys Union, Geophysical Monograph* **66**:7-71.
- [4] Solomon, S.C. and J.W. Head (1982) *J Geophys Res* **87**:9236-9246.
- [5] Glaze, L.S. and S.M. Baloga (1994) in review
- [6] Thornhill, G.D. (1993) *J Geophys Res* **98**:9107-9111.
- [7] Seiff, A. (1983) in *Venus*, Chapter 11, 215-279.
- [8] Morton, B.R. *et al.* (1956) *Proc Roy Soc Lond* **A234**:1-23.
- [9] Wilson, L. *et al.* (1980) *Geophys J R Astr Soc* **63**:117-148.

HOT BELTS OF VENUS AND THE EARLY EARTH. M.Z.Glukhovsky, V.M.Moralev. Institute of Lithosphere, Russian Academy of Sciences, Staromonetny 22, Moscow 109180, Russia.

Introduction. Really wonderful global datum set from Magellan mission submitted to 22 and 23 LPSC stimulated the comparative study of the hot spot distribution on Venus and Earth. We conclude that the observed pattern of the distribution show their greatest density near the equator (in the interval $\pm 35^\circ$ latitudes), and such arrangement is the evidence for the development of equatorial "hot-belt" on Venus as well as on the Earth at the early stages of its geological evolution.

Analysis of distribution. Large volcanoes, calderas, arachnoids, coronae, novae and shield fields recognised on Venus are known to be clearly associated with rift-like structures within latitudinal regional uplift and are thought to represent the sites of crustal extension and intense mantle upwelling or hot spots [1, 2, 3]. A general equatorial-concentrated arrangement of volcanic centers on Venus [1] was compared with the hot spot distribution on the Earth. The calculation results based on the Herrick and Phillips data for Venus [4] and Burke and Wilson's catalogue for the Earth [5] treated by equal-area square-grid statistics are presented at the table and on the histograms (Fig. 1.)

Venus				Earth			
Volcanoes and coronae (250)				Hot spots (117)			
S	N	N ₁	D	S	N	N ₁	D
1 2.45x10 ⁸	163	65	67	2.6x10 ⁸	76	65	29
2. 2.35x10 ⁸	87	35	37	2.5x10 ⁸	41	35	16
3. 1.04	1.87	1.86	1.81	1.04	1.85	1.86	1.81

Notes: 1 - the data for equatorial belts ($\pm 35^\circ$ lat); 2 - the data for the surface of planets outside equatorial belts; 3 - the ratios 1/2; S-surface in sq.km; N - the number of features from the total given in brackets; N₁-the same in percentage; D - the density of features (for 10⁸ km²).

The statistical approach to the volcanic centers on Venus and to the hot spots which remains relatively stable on the Earth for the last 250 Ma [6] show that the equatorial-concentrated distribution can be recognised for both planets as well as the good correlation of the regions with high density of hot spots on the Earth with the geoid uplifts [7] and large volcanic centers with the equatorial belt of positive topography on Venus [2] (Fig. 2.).

Geological and paleomagnetic evidences. The sialic nuclei of ancient cratons on the Earth are supposed to be originated as the granitization centers in the basic protocrust representing the sites of mantle plumes in Early Precambrian. Hence, the major sialic nuclei can be considered as the indicators of the hot spot sites for the early stages of continental crust evolution on the Earth [8]. Paleomagnetic and paleotectonic reconstructions for the Late Proterozoic [9] evidence the location of the continents predominantly in the equatorial zone (Fig. 3) which corresponds to the position of the positive topography and volcanic centers on the present-day Venus.

Conclusion. The similarity in spatial distribution of hot spots on Venus and the Early Earth is believed to be initiated by the concentration of endogenic energy within the equatorial areas where the maximum rate of dissipation of gravity, tidal, and rotation energy could be observed. That was the stage of differentiation into heavy inner metallic and outer liquid iron core and the high thermotectonic and fluid activity in the mantle accompanied by intensive origination of the ancient continental crust within equatorial hot belts. The modification of primary hot belt into present-day hot fields on the Earth can be related to the plate tectonics while the distribution of hot spots on Venus reflect probably plume tectonic conditions transitional to plate tectonics.

References: 1.Crumpler L.S. & Aubele J.C. LPSC XXIII, Abst. Pap. Houston, Tex., 1992, P.1: 275; 2.Crumpler L.S. et al. LPSC XXIII, Abst. Pap. Houston, Tex., 1992, P.1: 277; 3.Senske D.A. & Head J.W. LPSC XXIII, Abst. Pap. Houston, Tex., 1992, P.3:1269; 4.Herrick R.R. & Phillips R.J. J.Geoph.Res., 1992, v.97, N B10: 1617; 5.Burke K. & Wilson J.T. Sci. Am., 1976, v.235: 46; 6.Zonenshain L.P. et al., Tectonophysics, 1991, v.199, N2-4:165; 7.Stefanick M. & Jurdz D.M. J.Geoph.Res. 1984, v.89, N B12:9919; 8.Glukhovsky M.Z. & Moralev V.M. LPSC XXIII, Abst. Pap. Houston, Tex., 1992, P.1:417; 9.Morel P. & Irving E. J.Geol., 1978, v.86, N5:535.

HOT BELTS OF VENUS AND THE EARLY EARTH.

M.Z.Glukhovsky, V.M.Moralev.

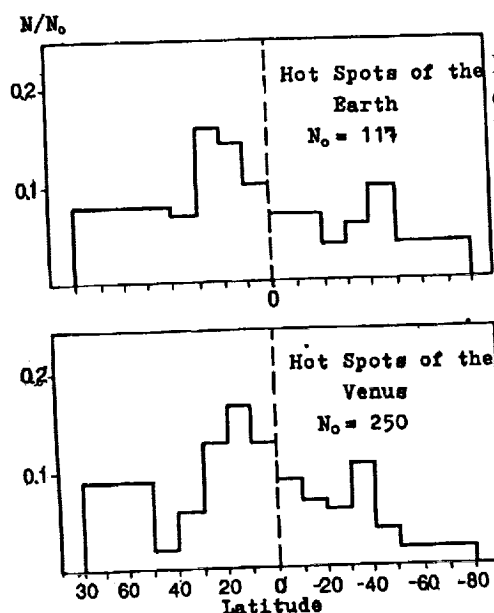
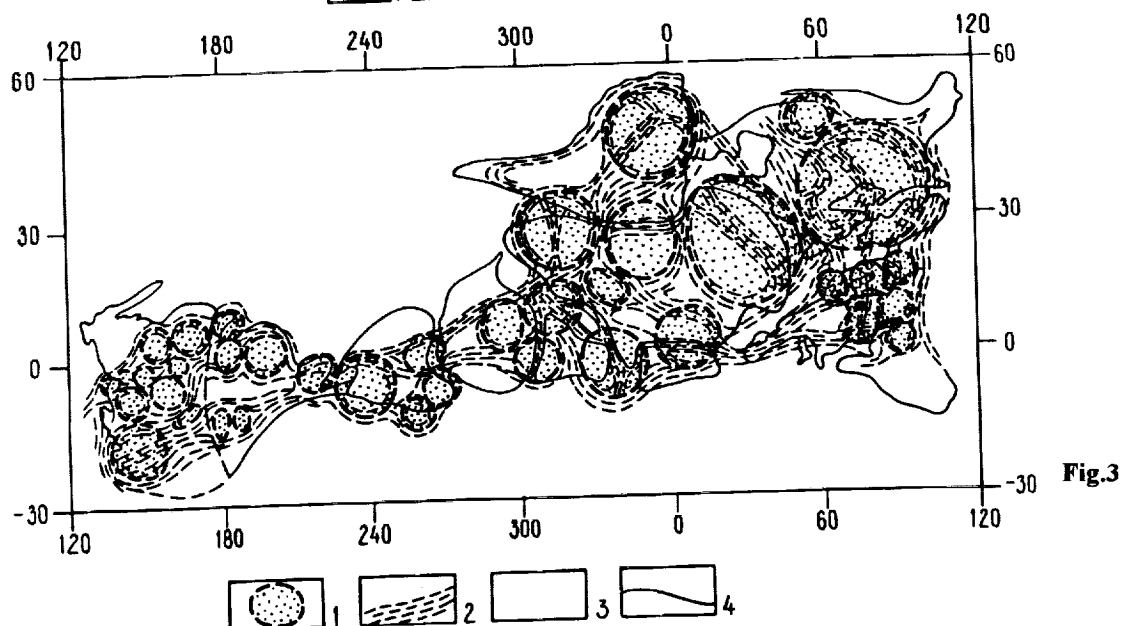
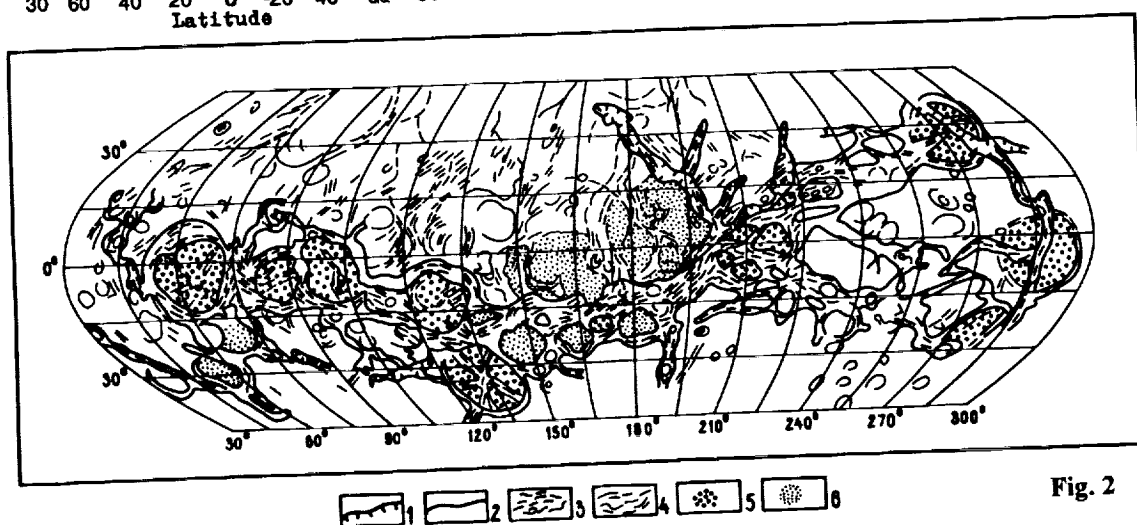
Fig.1. Histograms of hot spot (N_0) distribution in the latitude intervals (N).

Fig.2. Structural features on Venus, interpreted from radar images. 1-Boundaries of simple rifts, 2-boundaries of the belt of positive topography and major fractures, 3-structural features within the belt, 4-the same outside the belt, 5-positive volcanic features, 6-volcanic depressions.

Fig.3. Paleotectonic reconstruction of Proterozoic supercontinent on the Earth. 1-Sialic Early Precambrian nuclei of continents, 2-mobile belts, 3-internucleus simatic regions, 4-boundaries of present-day continents.



THE LINEAR POLARIZATION OF LIGHT SCATTERED FROM ICY SATELLITE SURFACES: THE DIAGNOSTIC POTENTIAL OF GALILEO PPR MEASUREMENTS

Jay D. Goguen, JPL/Caltech

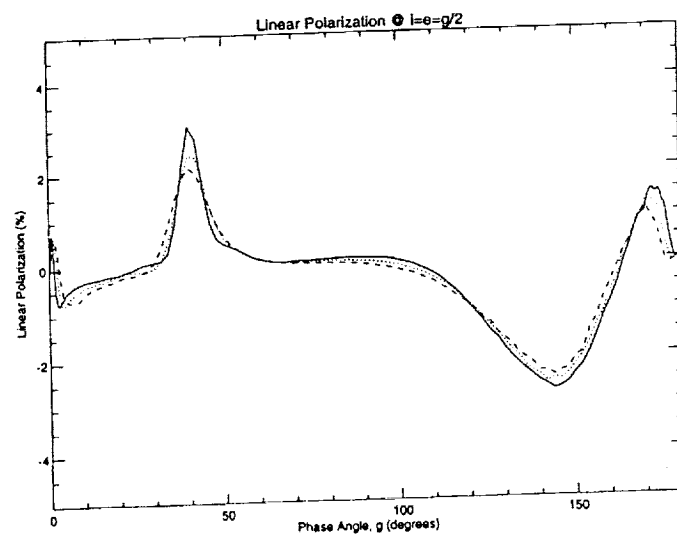
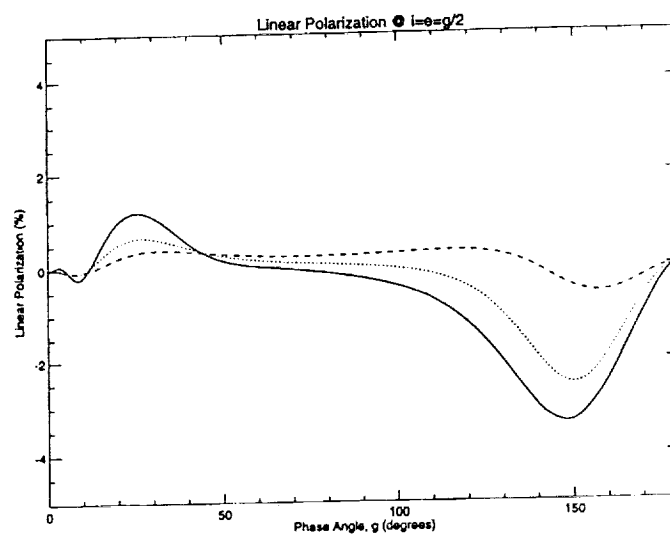
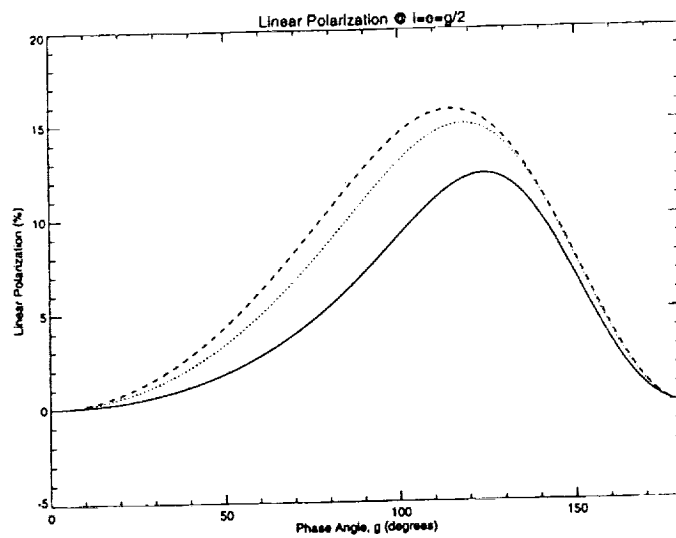
Goguen (1993, 1994) shows that for high albedo particulate surfaces, calculations combining Mie scattering with the doubling method give excellent agreement with laboratory measurements of the linear polarization of a carefully controlled sample of glass spheres. This approach is applied to investigate the expected linear polarization dependence on phase angle for water-ice regoliths at visible wavelengths. The Galileo Photopolarimeter/Radiometer (PPR) instrument (Russell et al., 1992) can accurately measure $\pm 0.1\%$ polarization in 3 bandpasses centered at 0.410, 0.678, and 0.945 μm . This study will examine the dependence of the linear polarization at these wavelengths, where water-ice is transparent ($k < 1.e-6$), on the mean particle size and width of the particle size distribution. The intended application is to anticipate which subset of the possible PPR icy satellite measurements will be most diagnostic of the physical state of the icy satellite regoliths. The results are applicable to Europa's relatively pure water-ice surface and should give valuable clues to features that may also be present in polarization measurements of Ganymede and Callisto.

Fig. 1 (opposite page) shows the approximate, modelling multiple scattering as isotropic (Goguen, 1994), linear polarization as a function of phase angle for 3 size distributions of water-ice spheres: small, $r \sim 0.07 \mu\text{m}$ (top); medium, $r \sim 0.7 \mu\text{m}$ (middle); and large, $r \sim 7.0 \mu\text{m}$ (bottom). Calculations for the 3 wavelengths of the PPR instrument are shown: solid line, $\lambda = 0.410 \mu\text{m}$; dotted line, $\lambda = 0.678 \mu\text{m}$; and dashed line, $\lambda = 0.945 \mu\text{m}$ in each panel. In each case, the width of the log-normal size distribution is the same, $\sigma_g = 0.47$ (Hansen and Travis, 1974) which corresponds to $\delta r/r \sim 0.5$. For small particles (top), the polarization approaches that due to rayleigh scattering with large positive polarizations near $g = 100$ degrees. For the wavelength sized particles (middle), the polarization is very different with neutral polarization near $g = 90$ degrees. Large particles (bottom) rapidly develop the expected "rainbow" feature near $g = 40$ degrees, show neutral polarization near $g = 90$ degrees, and large, negative polarization $g = 150$ degrees. Galileo PPR measurements in the phase angle ranges $g < 50$ degrees and $120 < g < 150$ degrees would easily discriminate between these surface models.

References

- Goguen, J.D. (1993). A Test of the Applicability of Independent Scattering to High Albedo Planetary Regoliths. *Lunar and Plan. Sci. Conf. XXIV*, 541-542.
- Goguen, J.D. (1994). A Quantitative Test of the Applicability of Independent Scattering to High Albedo Planetary Regoliths. *Icarus*, submitted.
- Hansen, J.E., and L. Travis (1974). Light Scattering in Planetary Atmospheres. *Space Sci. Rev.* **16**, 527-610.
- Russell, E.E., F.G. Brown, R.A. Chandos, W.C/ Fincher, L.F. Kubel (1992). Galileo Photopolarimeter/Radiometer Experiment. *Space. Sci. Rev.* **60**, 531-563.

DIAGNOSTIC POTENTIAL OF GALILEO PPR MEASUREMENTS: Gouguen J.D.



p-2 2977
APPLICATION OF AN ALKYLAMMONIUM METHOD FOR CHARACTERIZATION OF PHYLLOSILICATES IN CI CHONDRITES: D. C. Golden¹, D. W. Ming², M. E. Zolensky², and S. V. Yang³; ¹Dual Inc., ²NASA-JSC, ³Lockheed ESC, Houston, TX 77058

INTRODUCTION. Many meteorites and interplanetary dust particles (IDPs) with primitive compositions contain significant amounts of phyllosilicates, which are generally interpreted as evidence of protoplanetary aqueous alteration at an early period in the solar system [1]. These meteorites are chondrites of the carbonaceous and ordinary varieties. Characterization of phyllosilicates in these materials is important because of the important physico-chemical information they hold, e.g., from well characterized phyllosilicates, thermodynamic stability relations and hence the conditions of formation of phyllosilicates in the parent body of the meteorite can be predicted. Although we are at a rudimentary level of understanding of the minerals resulting from the aqueous alteration in the early solar nebula, we know that the most common phyllosilicates present in chondritic extraterrestrial materials are serpentines, smectites, chlorites and micas [2]. The characterization of fine grained minerals in meteorites and IDPs rely heavily on electron beam instruments, especially transmission electron microscopy (TEM). Typically, phyllosilicates are identified by a combination of high resolution imaging of basal spacings, electron diffraction analysis, and chemical analysis. Smectites can be difficult to differentiate from micas because the smectites lose their interlayer water and the interlayers collapse to the same basal spacing as mica in the high vacuum of the TEM. In high-resolution TEM (HRTEM) images, smectite basal spacings vary from 1 nm (fully collapsed) up to 1.5 nm, while micas show 1 or 2 nm basal spacings. Not only is it difficult to differentiate smectites from micas, but there is no way of identifying different classes of smectites (e.g., low-charged smectite, high-charged smectite, vermiculite, etc.) in meteorites and IDPs. To differentiate smectites from micas and also to recognize the charge differences among smectites, an alkylammonium method can be employed because the basal spacings of alkylammonium saturated smectites expand as a function of alkylamine chain length and the layer-charge density of the 2:1 expanding phyllosilicate, and the final product is significantly more stable under electron beam examination. Such a method was tested on standard clays and several meteorite samples using four alkylammonium salts ($N_c = 9, 12, 14$ and 18) [3]. This test clearly established the usefulness of alkylammonium technique in stabilizing the phyllosilicates under the electron beam and in expanding the layers to illustrate layer charge. However the alkylammonium saturation was carried out by equilibrating the sample thin sections with alkylammonium solutions for only 5 to 10 min. in the previous study. This equilibration time appeared to be too short to cause complete expansion. The current study was carried out to achieve complete saturation of the phyllosilicates by alkylammonium ions. A longer equilibration time of up to 4 hr was employed on thin sections of three meteorites and two standard clays. Alkylammonium solutions of a full range of N_c values from 6 to 18 were used to achieve complete expansion of the layers and hence permit complete characterization of the smectites with respect to layer charge density. The procedure presented discriminates the smectites from other minerals and allows the estimation of the smectite layer charge. The method therefore is suitable for studying the charge bearing phyllosilicates in meteorites and should be applicable to IDPs which cannot be examined by traditional mineralogical methods due to their sample size limitations ($< 100 \mu m$).

MATERIALS AND METHODS. Three CI chondrites (Alais, Ivuna, and CI clasts from Kaidun) and two standard clays (saponite from Ballarat, California and nontronite from Garfield, Washington) were embedded in Embed 812 epoxy and cut into 50-70 nm thin sections. The sections were placed on a C-coated holey plastic substrate mounted on Cu grids. Grid-

PHYLLOSILICATES IN CI CHONDRITES; Golden et al.

containing sections were dried and then transferred into an alkylammonium solution of predetermined concentration in a one-ml Eppendorf tube placed in an incubator set at 65°C. Samples were gently shaken for 30 sec at hourly intervals for 4 hr. At the end of 4-hr period the Eppendorf tube and the contents were quickly transferred into a beaker containing warm (65 °C) deionized water. The grid was picked up with tweezers and then repeatedly washed in warm deionized water three additional times and dried.

RESULTS AND DISCUSSION. HRTEM images were used to measure the layer spacings of the alkylammonium-treated standard phyllosilicates and meteorite samples. The phyllosilicate standards expanded to characteristic d-spacings depending upon the chain length of the alkylammonium ion and the interlayer charge density of the individual standard. For example, the saponite saturated with $N_c = 8$ alkylammonium ions had predominantly 1.3 nm spacing (monolayer) and as the N_c value was increased to 16, 1.75 nm spacings (bilayer) appeared more frequently. At $N_c > 16$ only 1.75 nm and higher d-spacings were visible. Similar changes were observed for nontronite, however, the monolayer to bilayer transition appeared at shorter chain lengths suggesting a higher average layer charge for nontronite than saponite. In the meteorite samples serpentine spacings were unaffected by the alkylammonium treatment (0.7 nm). Smectites in the meteorites expand to layer d-spacings according to the alkyl chain length and their layer charge. Typically, these d-spacings ranged from 1.35 to about 2.3 nm. A spacing of 1.35 nm corresponds to monolayer occupation of alkylammonium ions and 1.75 nm corresponds to bilayer occupation [4]. The presence of different spacings for a single alkylammonium ion saturated phyllosilicate in meteorites indicated charge heterogeneity among layers similar to that observed in terrestrial phyllosilicates [4].

The matrix of the Alais meteorite consisted mostly of phyllosilicates. It had uniformly stacked, slightly bent nanocrystals of smectite (saponite), consisting of 5 to 30 2:1 layers and ranged from 50 to 500 nm in diameter. Thin packets of serpentine layers (2 to 3 layers thick) appeared to be sparsely embedded in larger smectite crystals in concurrence with earlier observations [5,6], suggesting a genetic relationship between serpentine and smectite. The Ivuna meteorite contained predominantly smectite crystals, similar to those of Alais; the serpentine crystals observed here were larger (15 to 20 layers thick) than those observed in Alais. The Kaidun meteorite had fewer phyllosilicates in comparison to the other two. Phyllosilicate thickness here ranged from 2 to 15 layers and the diameter of the platy crystals ranged from 25 to 75 nm. An occasional 1 nm d-spacing was observed suggesting the presence of a mica. Otherwise the phyllosilicates were mostly smectites and serpentines. In addition to smectites, Kaidun contained pentlandite and pyrrhotite in agreement with earlier observations [5,7]. From the expansion of the phyllosilicates in the meteorite by alkylammonium ions, charge density variations in the smectites could be inferred. Ivuna and Kaidun matrices contained smectite nanocrystals of approximately similar low charge (<0.4 eq/ $(Si,Al)_4O_{10}$). Alais contained well-defined crystals of smectite with slightly higher charge and exhibited greater layer charge homogeneity. The layer charge heterogeneity of the former two samples, Ivuna and Kaidun, suggests complex reactions during the parent body aqueous alteration (hydrothermal?) process [8].

References: [1] Zolensky, M. E. and McSween, H. Y. (1988) in *Meteorites and The Early Solar System*, Arizona Press p. 114. [2] Zolensky, M. E. and Keller, L. P. (1992) *28th CMS Annual Meetings*, Houston, TX (abstract) p. 184 [3] Ming et al (1992). *LPSC XXII* pp. 913-914. [4] Lagaly, G. (1981) *Clay Miner.* 16:1-21. [5] Zolensky et al. (1993) *Geochim. Cosmo. Chim. Acta* 57:3123-3148. [6] Brearly A. J. (1992) *LPSC XXIII* pp.153-154. [7] Mackinnon I. D. R. (1985) *Meteoritics* 20:702-703. [8] Nadeau et al. (1985) *Am. Min.* 70:1004-1010.

p-2
2978

HIGH RESOLUTION TRANSMISSION ELECTRON MICROSCOPY (HRTEM) OF NANOPHASE FERRIC OXIDES: D. C. Golden¹, R. V. Morris², D. W. Ming² and H. V. Lauer, Jr³; ¹Dual Inc. ²NASA-JSC. ³Lockheed ESC, Houston, TX 77058

INTRODUCTION. Iron oxide minerals are the prime candidates for Fe(III) signatures in remotely sensed Martian surface spectra. Magnetic, Mossbauer, and reflectance spectroscopy has been carried out in the laboratory in order to understand the mineralogical nature of Martian analog ferric oxide minerals of submicron or nanometer size range [1,2]. Out of the iron oxide minerals studied, nanometer sized ferric oxides are promising candidates for possible Martian spectral analogs [1]. "Nanophase ferric oxide (np-Ox)" is a generic term for ferric oxide/oxyhydroxide particles having nanoscale (<10 nm) particle dimensions [1,3,4]. Ferrihydrite, superparamagnetic particles of hematite, maghemite and goethite, and nanometer sized particles of inherently paramagnetic lepidocrocite are all examples of nanophase ferric oxides. np-Ox particles in general do not give X-ray diffraction (XRD) patterns with well defined peaks and would often be classified as X-ray amorphous. Therefore, different np-Oxs preparations should be characterized using a more sensitive technique e.g., high resolution transmission electron microscopy (HRTEM). The purpose of this study is to report the particle size, morphology and crystalline order, of five np-Ox samples by HRTEM imaging and electron diffraction (ED).

MATERIALS AND METHODS. Five samples of np-Ox were analyzed: TNA13/210 and S6FN28 have been characterized by Mossbauer and reflectance data as np-Hm [2,6]. TNA13/260 based on the same data has larger oxide particles than TNA13/210. Sample TNA13/210 was prepared by oxidation in air of trinuclear acetato hydroxy iron(III) nitrate (TNA) at 210 °C, TNA13/260 was prepared in a similar fashion except that the oxidation was carried out at 260 °C. 6LSFEH 20 was prepared by dialyzing a dilute ferrous sulfate solution incubated at 70 °C for 5 hr against distilled water. 6LSFEH was prepared by heating the 6LSFEH to 400 °C. For HRTEM analysis sub milligram quantities of the samples were embedded in embed 812 epoxy resin and cut into 50 to 70 nm thin sections using a Microstar diamond knife mounted on a Porter Blum ultramicrotome. Thin sections were transferred on to carbon coated holey plastic substrates mounted on Cu grids. The sections were C-coated and observed under the JEOL 2000 FX transmission electron microscope operated at 200 kev.

RESULTS AND DISCUSSION. Sample TNA13/210 had a distinct ring ED pattern, with some spots due to discrete nanocrystals. The presence of rings at 3.67 and 2.72 Å (Table 1) confirmed the presence of hematite. However the very intense rings at 2.53 and 1.54 Å suggests the possible presence of an additional ferrihydrite like phase or smaller nanophase hematite particles. This observation was confirmed by the HRTEM images where a few nanocrystals of ~10 nm hematite crystals and a bulk of much smaller rounded particles with no discernible lattice structure (<5 nm) were observed. Presence of 2.72 and 3.67 Å lines in the ED pattern confirm the presence of hematite. TNA13/260 sample was similar to the above except that a stronger ED spot pattern suggesting more crystalline hematite than TNA13/210 was observed. HRTEM revealed the sample TNA13/210 to contain rounded hematite crystals of ~10 nm, although smaller areas consisting of much finer crystals were found. S6FN28 electron diffraction was masked by a diffuse broad central spot due to silica gel, however, the HRTEM images indicated the presence of very fine ferric oxide (~1 to 4 nm) particles dispersed in the silica gel matrix. No lattice fringes were observed. 6LSFEH had a few particles with lattice fringes corresponding to hematite (2.7 Å), whereas 6LSFEH20, the precursor to the above sample had only a two-line ED pattern (2.52 and 1.46 Å) typical of ferrihydrite. Out of the five np-Ox samples studied, TNA13/260 had predominantly hematite, TNA13/210 and 6LSFEH

NANOPHASE FERRIC OXIDES: Golden et al.

had hematite, and the rest were near amorphous ferric oxides exhibiting two or more ED lines in common with ferrihydrite (Table 1). By extrapolation, HRTEM-ED amorphous particles in all samples except 6LSFEH20 can be considered nanophase hematite which we were unable to confirm using our technique.

Because these np-Ox particles do not have defined ferric crystal field transitions, the reflectivity spectrum is unlike those for powders of crystalline ferric oxides. Also the lattice defects which cause the imbalance in two antiferromagnetic lattices give rise to a net magnetization [6]. The electron diffraction data indicates that the np-Ox particles studied here are large enough to be considered as particles, and the five samples provide a range of crystallinity near the amorphous end (Figure 1). The information on crystal structure obtained by HRTEM and ED in conjunction with earlier published spectral data [1,2,6] may help to constrain the Martian iron mineralogy with greater precision.

References: [1] Morris et al. (1989) *JGR* 94:2760-2778. [2] Morris et al. (1985) *JGR* 90:3126-3144 [3] Golden et al. (1993) *JGR* 98:3401-3411 [4] Bell et al (1993) *JGR* 98:3373-3385. [5] Towe, K. M. (1990), Origin, Evolution, and Modern Aspects of Biomineralization in Plants and Animals. Plenum Press. New York. [6] Morris et al. (1991) *LPSC XXII* pp. 927-928.

Table 1. Electron diffraction spacings in Angstroms for reference hematite (Hem), reference ferrihydrite (Fh) [5] and for the five np-Ox samples

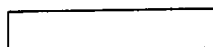
Hem ¹	Fh ¹	TNA13/210	TNA13/260	S6FN28	6LSFEH	6LSFEH20
-----Angstroms-----						
3.67(012)		3.67	3.67			
2.69(104)		2.72				
2.51(110)	2.54(110)	2.48	2.53	2.48	2.52	2.52
2.20(113)	2.24(200)	2.20	2.19			
	1.98(113)			2.01		
1.84(024)					1.80	
1.69(116)	1.72(114)		1.68		1.63	
1.64						
1.60(018,122)						
	1.51(115)					
1.48(214)	1.47(106)	1.48	1.47	1.49	1.6	1.46

¹Values in paranthesis are the Miller indices assuming a hexagonal lattice structure.

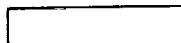
Figure 1. Particle sizes of the np-Ox samples as observed by high resolution transmission electron microscopy.

SAMPLE

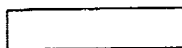
TNA13/260



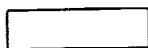
TNA13/210



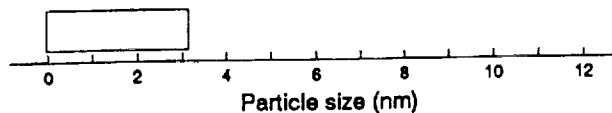
6LSFEH



S6FN28



6LSFEH20



Particle size (nm)

STRUCTURE AND RHEOLOGY OF PARTIALLY MOLTEN AMMONIA-WATER ICES ; D.L. Goldsby and D.L. Kohlstedt (Dept. of Geology and Geophysics, Univ. of Minnesota, Mpls, MN, 55455)

The physical properties of partially molten planetary materials, including permeability and rheology, are fundamentally dependent on the grain-scale distribution of the melt phase [1,2]. The results of high-pressure creep experiments on fine-grained partially molten ammonia-water ices reported in [3] have been analyzed in the context of recent observations of the wetting characteristics of the melt in two-phase ammonia-water ices. These creep experiments explored the effects of temperature T , strain rate $\dot{\epsilon}$, melt fraction ϕ , and grain size on creep strength. Experiments were conducted in a gas-medium apparatus designed for cryogenic use under the following conditions: $3.5 \times 10^{-6} < \dot{\epsilon} < 3.5 \times 10^{-4} \text{ s}^{-1}$, $160 < T < 220 \text{ K}$, and confining pressure $P_c = 50 \text{ MPa}$. Samples were prepared containing 1, 5 or 8 wt% ammonia, yielding calculated melt fractions, respectively, of 3-4, 15-20, and 24-32 vol% from the peritectic temperature $T_p = 176 \text{ K}$ to $T = 220 \text{ K}$. Partial melting of samples containing 1 wt% ammonia resulted in less than a factor of 2 decrease in strength over the entire experimental temperature range. Samples containing 5 and 8 wt% ammonia, however, exhibit a more dramatic loss of strength -- up to a factor of 5 -- at temperatures just above the peritectic temperature. Scanning electron microscope (SEM) micrographs of samples equilibrated at $T = 185 \text{ K}$ for 24 h at a confining pressure $P_c = 1 \text{ atm}$ reveal that at low melt fractions (e.g., 3 vol%) melt is confined to triple junctions, that is, grain faces remain melt-free. In contrast, at higher melt fractions, ammonia-water melt completely surrounds Ice I grains, so that the rheologically critical melt fraction ϕ_c is exceeded, as shown in Figure 1.

The presence of melt in a polycrystalline aggregate can have a profound effect on rheology, both in the dislocation and in the diffusion creep regimes [4,5]. Melt increases the rate of dislocation creep due to the stress enhancement caused by a decrease in load-bearing area. Likewise, melt increases the rate of diffusional creep due not only to an enhancement in stress but also to the presence of high diffusivity melt-filled pathways [6]. Thus, the distribution of the melt phase, often characterized by a dihedral or wetting angle θ , governs the creep strength of a partially molten aggregate. For $0^\circ < \theta < 60^\circ$, at low melt fractions, melt forms an interconnected network along three-grain and through four-grain junctions; at high melt fractions, the grains become completely surrounded by melt [1].

Previous microstructural analysis of ammonia-water ices deformed at high pressure has relied on replication of the outer sample surface by the indium jackets used to seal the samples [7]. This technique, however, does not provide adequate spatial resolution to measure the dihedral angle. A cryogenic temperature stage was developed for an environmental scanning electron microscope (ESEM) in the High Resolution Microscopy Center at the University of Minnesota that allows *in situ* microstructural characterization of ammonia-water ice samples. This cryosystem consists of a copper sample stage coupled to a self-pressurized liquid nitrogen (LN_2) dewar; subsolidus sample temperatures ($< T = 176 \text{ K}$) are maintained by circulating LN_2 through the sample stage at a controlled rate. The system provides stable temperature control in the range $100 \text{ K} < T < 273 \text{ K}$. The ESEM permits samples to be analyzed at much higher chamber pressures than is possible in a conventional SEM (i.e. $\sim 10^{-6} \text{ Torr}$ vs. $\sim 10^{-5} \text{ Torr}$). In addition, sputter-coating of a high-conductivity material on the ice surface is not necessary in the ESEM, as would be required in a conventional SEM. The higher chamber pressures in the ESEM, combined with the lower temperature environment, reduces the rate of sample

STRUCTURE AND RHEOLOGY OF PARTIALLY MOLTEN... Goldsby, D.L. and Kohlstedt, D.L.

sublimation to a negligible level. Condensation on the sample surface is minimized through the use of a dry imaging gas, such as N_2 , instead of water vapor; special sample exchange techniques are also used to minimize condensation.

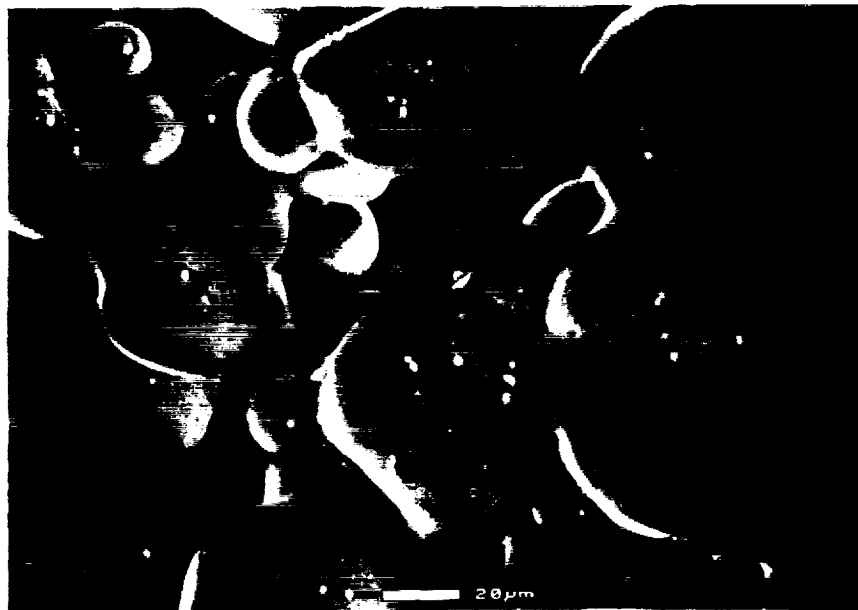


Figure 1- ESEM micrograph of 8 wt% NH_3 sample equilibrated for $t=24$ h at 1 atm pressure, $T=185$ K. Calculated melt fraction $\phi \approx 0.24$. Note that Ice I grains are completely separated by melt.

With this newly developed capability, SEM observations have been made in the ammonia-water system. At $T=185$ K for the composition $X_{NH_3}=0.01$, the dihedral angle is quite small, with $\theta \leq 20^\circ$. Hence, in the ammonia-water system, just above the peritectic temperature and for low melt fractions, melt forms a three-dimensional, interconnected network. At higher melt fractions, as in the $X_{NH_3}=0.05$ and 0.08 cases, Ice I grains are completely separated by melt, as shown in Figure 1. These SEM observations, coupled with the results of the creep experiments performed at hypersolidus temperatures for the samples with 5 and 8 wt% ammonia demonstrate that ϕ_c must be substantially less than 15 vol%. Consequently, partially molten ammonia-water ice near the surface and further within icy planetary bodies will undergo a dramatic loss of strength at relatively small melt fractions (i.e., at relatively water-rich compositions). These results also imply that the strength of partially molten ammonia-water ices will be critically dependent on the permeability, which will control the amount of melt retained in the ice body [8,9].

References

- [1] Bulau J.R. et al. (1979), *JGR*, 84, 6102-6108.
- [2] Kohlstedt D.L. (1992), in *AGU Geophys. Monogr.* 71, 103-121.
- [3] Goldsby D.L. (1993), *Proceedings of 24th LPSC Meeting*, 543-544.
- [4] Beeman M.L. and Kohlstedt D.L. (1993), *JGR*, 98, 6443-6452.
- [5] Chopra P.N. and Kohlstedt D.L. (1994), in *Magmatic Systems*, *in press*.
- [6] Cooper R.F. et al. (1989), *Acta Met.*, 37, 1759-1771.
- [7] Durham W.B. (1993) *JGR*, 98, 17667-17682.
- [8] Riley G.N. et al. (1990), *Geophys. Res. Lett.*, 17, 2101-2104.
- [9] Daines M.J. and Kohlstedt D.L. (1993), *Geophys. Res. Lett.*, *in press*.

CONSTRAINTS ON THE LARGEST MARSQUAKE

M. P. Golombek, Jet Propulsion Laboratory, Caltech, Pasadena, CA 91109

A recent estimate of martian seismicity through time has been made from the observed surface faulting on Mars (1), based on the definition of seismic moment, $M_0 = \mu SA_f$, where μ is uniform rigidity and S is average slip over fault area A_f . In this study, information on the extent and history of faulting on Mars was compiled to estimate the total moment release per year, which was then apportioned into different sized events based on likely moment-frequency relationships. One of the critical parameters needed to estimate the frequency of marsquakes is the size of the largest event. In this abstract, a number of arguments are made beyond those in Golombek et al. (1) that better constrain the largest marsquake. These arguments suggest the largest marsquake likely is limited to seismic moment of order 10^{27} dyne-cm, which is roughly equivalent to a body-wave magnitude 7 event on Earth (2); events larger than this are unlikely without subduction or plate tectonics. As in the earlier paper, the size of an event will be discussed primarily in terms of seismic moment, which is a more fundamental measure of seismic energy release than magnitude, and can be compared between planets without concern for specific seismic wave propagation characteristics or seismometer response.

The seismic events on Earth most likely to be analogous to events on Mars are intraplate oceanic earthquakes (2). These events make up a class of earthquakes that are due to lithospheric cooling and are relatively free from plate boundary effects. The largest intraplate oceanic earthquake since 1977 is under 10^{27} dyne-cm (actually 5.4×10^{26} dyne-cm, 3), excluding the Chagos Bank earthquake (1.8×10^{27} dyne-cm), which is believed to have occurred on a diffuse plate boundary (4). As a result, Golombek et al. (1) assumed the largest marsquake was $10^{26.5}$ dyne-cm. Note that even if the Chagos Bank event were included as an intraplate event the maximum moment would be limited to less than 2×10^{27} dyne-cm.

On Earth, seismic events of a particular moment typically have a limited range of fault areas and slips. Earthquakes of moment 10^{27} dyne-cm typically involve fault areas of a few hundred to a few thousand km^2 and slips of 1-10 m, for the nominal μ of 3×10^{11} dyne/cm². As examples, slip of 1 m on a fault a few hundred km long by 10 km wide would produce a 10^{27} dyne-cm moment event as would slip of 10 m on a fault a few tens of km long by 10 km wide. To further quantify these types of characteristics, earthquakes with well documented fault length (from field observations of surface breaks), width (from hypocenter distributions), slip (from field and geodetic observations of surface breaks) and moment (from waveform analysis) were extracted from the literature (these requirements purposefully excluded subduction related events). A couple of dozen examples show that in addition to the slip-area relationships just described, earthquakes with different focal mechanisms have different characteristic aspect ratios. Specifically, normal and thrust events typically occur on more equant shaped fault surfaces than strike-slip faults. Tabulation of about 8 normal fault earthquakes with well documented slip and fault plane information (5, 6, 7, 8) shows that they have an average aspect ratio of 2.3 (that is their fault length is on average 2.3 times greater than their width).

The size of a structure effectively limits the size of the quake that it could generate. Most grabens and wrinkle ridges on Mars are bounded by faults with widths that are <5 km (1). For fault rupture lengths of up to 10 km and slips of order 10 cm, the maximum moment event is $\sim 10^{24}$ dyne-cm. Larger grabens and faults bounding collapsed summit calderas of martian volcanoes probably extend up to 10 km deep (9 and refs. in 1). Fault rupture lengths of roughly 50 km with slip of about 50 cm could generate marquakes with moments of $\sim 10^{26}$ dyne-cm. Larger marsquakes require larger faults that cut the entire brittle lithosphere on Mars. Such faults bound rifts such as Valles Marineris and the Thaumasia rift on Mars (9). The brittle lithosphere on Mars has been estimated to be no more than 40 km thick based on assumed present-day heat flow and lithospheric strength envelopes (e.g., 9). For a normal fault with a width of about 40 km, the average length that would rupture during an individual marsquake is roughly 100 km, assuming an average aspect ratio for normal fault earthquakes. Geologic mapping of Valles Marineris, which

LARGEST MARSQUAKE: Golombek

has been active over most of martian geologic time, also indicates characteristic individual normal fault strands at the base of canyon wall scarps of about 100 km length (10). Slip of 1 m on a fault 100 km by 40 km would produce an event of moment $\sim 10^{27}$ dyne-cm. Slip of 10 m, which is possible for a fault of this size on Earth, would produce a moment release an order of magnitude greater than this (although a 40 km fault width is an upper limit). As a result, slip on large normal faults bounding canyons of Valles Marineris could reasonably be expected to generate marsquakes of moment $\sim 10^{27}$ dyne-cm.

Given that the largest marsquakes are generated on normal faults, a potential bound to such events on Mars could be the largest continental normal fault events on Earth. The largest continental normal earthquakes (excluding plate boundary or subduction-related plate bending events) release about 10^{27} dyne-cm (11). Among these is the particularly well documented 1959 Hebgen Lake, Montana (near Yellowstone) event (e.g., 5, 6). This event ruptured a 30 km long by 15 km wide fault plane, with a slip of about 10 m, for a moment release of $1-2 \times 10^{27}$ dyne-cm. Note that the Chagos Bank event that occurred in oceanic lithosphere, which is typically stronger than continental lithosphere (particularly when it is older than 10 Ma, 12), released about the same moment (1.8×10^{27} dyne-cm). These examples indicate that non-plate boundary normal fault events can be as large as about 2×10^{27} dyne-cm, but not much larger.

The arguments discussed above suggest that the largest moment marsquake that could be generated is about 2×10^{27} dyne-cm. This is the moment release of the largest intraplate oceanic earthquake as well as the largest intraplate continental normal fault earthquake. These two classes of earthquakes are relatively free of plate boundary effects and the oceanic events are primarily due to lithospheric cooling, both of which are likely attributes of the processes that generate marsquakes (2). Considerations of the largest faults on Mars, which bound Valles Marineris canyons, and typical aspect ratios and slips for normal events on Earth, also allow marsquakes of about this size. Using the moment-magnitude relationship derived earlier for purposes of illustration (1), suggests that an event of seismic moment 10^{27} dyne-cm is roughly equivalent to a body-wave magnitude 7 earthquake. This comparison and analysis clearly show that events equivalent to magnitude 8 or larger earthquakes, with moment release of order 10^{30} dyne-cm (which only occur between subducting plates on Earth, 11), are not possible on Mars. Subduction related events on Earth involve fault planes with widths of a few hundred km, lengths up to a thousand km and slips of 10-30 m, conditions that only can be met at subducting plate boundaries. For reference, note that large strike-slip events along transform faults on Earth only generate events of moment $\sim 10^{28}$ dyne-cm. It is interesting to note that an event of moment 10^{30} dyne-cm exceeds the total annual moment release of the Earth by 1 order of magnitude ($\sim 10^{29}$ dyne-cm/yr). The maximum moment release marsquake derived herein (10^{27} dyne-cm) exceeds our best estimate for the total annual moment release on Mars (1) by 2 orders of magnitude (10^{25} dyne-cm/yr). Finally, if the largest moment release event on Mars is 10^{27} dyne-cm, then the recurrence interval for marsquakes is 1.6 times longer than estimated in Golombek et al. (1). The recurrence interval for 10^{27} dyne-cm moment events, using the same assumptions for the entire seismogenic lithosphere (1) is 112 years (note that the recurrence interval for $10^{26.5}$ dyne-cm events, if these are the largest events for the entire seismogenic lithosphere, is really 35.6 years, rather than the 365 years mistakenly reported in Golombek et al., 1).

References: (1) Golombek et al., 1992, *Science* 258, 979-981. (2) R. J. Phillips, 1991, p 35-38 in Solomon et al., *Lunar Planet. Inst. Tech. Rep. No. 91-02*. (3) Bergman, 1986, *Tectonophys.* 132, 1-35 and S. C. Solomon catalog of 141 intraplate oceanic earthquakes, pers. com. (4) Wiens et al., 1985, *Geophys. Res. Lett.*, 12, 429-432. (5) Stein & Barrientos, 1985, *J. Geophys. Res.* 90, 11,355-11,366. (6) Doser, 1985, *J. Geophys. Res.* 90, 4537-4555. (7) Eyidogan & Jackson, 1985, *Geophys. J. R. astr. Soc.* 81, 569-607. (8) Jackson et al., 1982, *Earth Planet. Sci. Lett.* 57, 377-397. (9) Banerdt et al., 1992, p 249-297, in U Ariz. **MARS**. (10) Witbeck et al., 1991, *US Geol. Sur. Map I-2010*. (11) Pacheco & Sykes, 1992, *Bull. Seis. Soc. Amer.* 82, 1306-1349. (12) Lynch & Morgan, 1987, *Geol. Soc. Amer. Spec. Pub.* 28, 53-65.

EXTENSION ACROSS TEMPE TERRA AND SIRENUM PROVINCES ON MARS FROM MEASUREMENTS OF FAULT SCARP WIDTHS

M. P. Golombek¹, K. L. Tanaka², D. J. Chadwick², B. J. Franklin¹, and P. A. Davis²,

¹Jet Propulsion Laboratory, Caltech, Pasadena, CA 91109, ²US Geological Survey, Flagstaff, AZ 86001

A new method of determining extension across grabens and rifts on Mars has been developed and applied to the Tempe Terra and Sirenum provinces. In principle, determining extension across grabens and rifts is fairly simple provided that the structures are not heavily modified by subsequent geologic processes. Available evidence suggests that most extensional structures on Mars are bounded by steeply dipping normal faults (1). If the dip of the fault is known, or can be approximated, then the throw (vertical displacement) between the upthrown (footwall) and downthrown (hanging wall) blocks is directly related to the extension or horizontal slip between the blocks. To estimate the vertical relief or throw across a fault, methods such as measuring the length of shadows or photoclinoetry have been utilized (2, 3, 4). However, these methods have somewhat restrictive conditions for their use and can be both time consuming and impractical in certain situations. In this abstract, measurement of fault scarp widths are used with information on fault scarp slope and fault dip to estimate extension across normal faults in two provinces around Tharsis on Mars.

Most extensional structures on Mars are simple grabens, which are bounded by two inward dipping normal faults, with flat floors and equal scarps (1, 2, 3). As is the case for lunar simple grabens (5), mass wasting has considerably reduced fault scarp slopes on Mars (2, 3). Photoclinometric measurement of 628 simple graben scarp slopes throughout the western hemisphere of Mars (2, 3, 6) indicate an average slope of 8.6° (with a Poisson distribution-standard deviation $\pm 2.9^\circ$). Higher fault scarps that bound rifts on Mars appear to have a steeper slope. Photoclinometric measurements of 200 large slopes on Mars indicate an average slope of 20° (with a normal distribution standard deviation $\pm 9.6^\circ$). In addition, faults bounding simple grabens on Mars dip about 60° (with a loosely bracketed variability of 15° ; 3, 5).

Simple measurement of normal fault scarp width (perpendicular to surface strike) can then be used to estimate fault throw and extension. All simple graben fault scarps are assumed to slope 8.6° and all rift and larger, more heavily modified graben fault scarps are assumed to slope 20° . The width of the scarp, W_s , can then be used to calculate the extension, $E_x = (W_s \tan S_0) / \tan \alpha_0$, with an average slope, S_0 , and average fault dip, α_0 . The formal uncertainty in this estimate, assuming independent variables, is $\sigma_{E_x} = \{E_x^2 [dS^2 / (\cos^2 S_0 \sin^2 S_0) + d\alpha^2 / (\cos^2 \alpha_0 \sin^2 \alpha_0)]\}^{1/2}$

(7), where dS and $d\alpha$ are the uncertainties in the scarp slope and fault dip, respectively, which are taken from the standard deviations from the measured data set (given above). In practice, the width of all simple graben scarps and larger, more heavily modified faults scarps are measured and summed separately; the extension and uncertainty are then calculated. The formal uncertainty in extension is 0.7 to 0.8 times E_x . Note that this uncertainty is dominated by the uncertainty in the fault dip, which can easily vary by 15° . For example, uncertainties of up to 15% in determining height or slope from photoclinometry (2) only decreases the formal uncertainty in extension to 0.6 times E_x . As a result, the new method described in this abstract allows estimates of extension across normal fault structures on Mars that are only slightly more uncertain than estimates using photoclinometry. We apply this method of measuring extension to fault scarps in Tempe Terra and Sirenum Fossae, where lighting conditions in Viking images are not entirely favorable for photoclinometry.

Tempe Terra is a large plateau of cratered highland and plains (Noachian through Hesperian age) on the northeast flank of Tharsis. It is cut by a series of narrow northeast-striking grabens that are Noachian through Hesperian in age (8). A series of wider and deeper grabens and rifts formed along the axis of the plateau in the Middle to Late Noachian (8), along with a volcanic

center. Most of these grabens formed roughly radial to Tharsis during two main pulses of deformation (9, 10).

We measured fault scarp width across a northwest-southeast traverse through Tempe Terra (40.5°N, 89.5°W to 30.8°N, 76°W), which is roughly perpendicular to most of the structures and passes just to the south of the volcanic center but through the deep Tempe Terra rifts. A total of 272 scarp widths were measured; 201 simple graben scarp widths summed together to 71.4 km; 71 larger, more modified scarp widths summed together to 54.1 km. All together the scarps indicate about 17.6 km of extension with a formal uncertainty of ± 13.4 km. For comparison, Tanaka and Golombek (11) found about 19 ± 12 km of extension across Tempe Terra based on measured elongation of pre-existing craters.

Sirenum Fossae is located on the southwestern flank of the Tharsis rise. Twenty-six narrow structures are located at a distance of about 2500 km from the Pavonis tectonic center of Tharsis (9). These structures are oriented radially to this center and deform Noachian and Hesperian age rocks. The structures are very narrow in available Viking images (commonly comprising only a few pixels in the digital data base) and are either simple grabens or modified tension cracks. The region is devoid of local tectonic and volcanic centers and therefore may represent the circumferential extension due solely to Tharsis generated stresses.

We measured the perpendicular widths of each fault scarp, assuming each structure is a simple graben bounded by 2 scarps and determined a total scarp width of 28.9 km. Applying our method, the total extension is 2.5 ± 1.7 km across the region. This must be considered a minimum estimate of the extension, given that some of the structures may be tension cracks, which require more extension than similar width grabens. A total of about 1 km of extension was estimated by Tanaka and Chadwick (12), based on an oversimplified approach in which extension was assumed to be dependent on graben width.

The Sirenum and Tempe Terra regions each occupy about an eighth section of the roughly circular Tharsis rise. Nevertheless, the extensional strain accommodated by each is very different (roughly 3 km versus 18 km). Estimates of extension across other regions, such as Alba Patera (8 km; 4) and Valles Marineris (16 km, based on Chadwick and Lucchitta, 13, steep fault dip determinations and Schultz, 14, interpretations of structure), both of which also occupy up to an eighth section of Tharsis, further underscores this variation in circumferential extension around Tharsis. If Sirenum extension does, in fact, solely represent Tharsis regional stresses, then the total circumferential strain due to this stress source is only 20 km. However, total circumferential strain around Tharsis from the preliminary numbers cited above is roughly 45 km, not including the Thaumasia province. If the extension across Thaumasia is of the same order as the extension across Tempe Terra, total circumferential strain around Tharsis is of order 60 km. These results provide the first quantitative comparison of the heterogeneous strain among the various provinces around the Tharsis rise.

References:

- (1) Banerdt, Golombek, & Tanaka, 1992, p 249-297, in Univ. Ariz. book MARS.
- (2) Tanaka & Davis, 1988, J. Geophys. Res. 93, 14,893-14,917.
- (3) Davis & Golombek, 1990, J. Geophys. Res. 95, 14,231-14,248.
- (4) Plescia, 1991, J. Geophys. Res. 96, 18,883-18,895.
- (5) Golombek, 1979, J. Geophys. Res. 84, 4657-4666.
- (6) Davis, Tanaka & Golombek, 1993, Lunar Planet. Science XXIV, 381-382.
- (7) Bevington, 1969, Data Reduction and Error Analysis for the Physical Sciences, McGraw Hill.
- (8) Scott & Dohm, 1990, Proc. Lunar Planet. Sci. Conf. 20th, 503-513.
- (9) Plescia & Saunders, 1982, J. Geophys. Res. 87, 9775-9791.
- (10) Tanaka & Golombek, 1991, J. Geophys. Res. 96, 15,617-15,633.
- (11) Tanaka & Golombek, 1994, Lunar Planet. Science XXV, this volume.
- (12) Tanaka & Chadwick, 1993, Lunar Planet. Science XXIV, 1397-1398.
- (13) Chadwick & Lucchitta, 1993, Lunar Planet. Science XXIV, 263-264.
- (14) Schultz, 1991, J. Geophys. Res. 96, 22,777-22,792.

"FLINDERSITE" BEARING IMPACT EJECTA LAYER FROM SOUTH AUSTRALIA; V. A. GOSTIN & M. ZBIK, Department of Geology & Geophysics, University of Adelaide, Adelaide, South Australia 5005.

A thin (up to several centimeters) layer of coarse, feldspathic clasts and sand has been found in the Precambrian Bunyeroo Formation in central and northern Flinders Ranges. Such a characteristic and persistent marker bed was interpreted by Gostin et al [1,2] as an impact ejecta layer derived from bolide impact. The remnants of a huge impact structure have been found by Williams [3] in the Gawler Ranges, 300 km away from this ejecta layer. Coarse impact-metamorphosed clasts of acid volcanics that occur in the ejecta layer have been called "FLINDERSITES" [4]. Based on similarities between "Flindersites" and the Gawler Range Volcanics, a genetic link between this impact structure and the distal impactites has been established.

A sample of the impact debris layer several cm thick was collected for investigation from Bunyeroo Gorge in the central Flinders Ranges. The lowest layer (L-1) is a coarse clast-bearing [Flindersite] horizon. Mineralogy of this layer is determined by composition of the Flindersite clasts. The clay fraction of this layer consists of vermiculite and kaolinite, perhaps formed from the alteration and weathering of glassy components (Fig. 1). The dark red Flindersite clast, containing plagioclase phenocrysts surrounded by a felsic matrix, had sunk into the mudstone host rock (sample L-3). According to Gostin et al [1] this layer was deposited by vertical fall of ejecta through the water column shortly after impact.

The overlying sandstone layer (L-2) is high porous and more persistent compared to layer L-1, and represents finer impact debris that took longer to settle through the atmosphere and water column. A thin greenish-gray mudstone layer separates layers L-1 and L-2, and in composition is similar to host sediment L-3. The clay fraction of sample L-2 and L-3 (see Fig. 1) is rich in micas (illite) and clinochlorite which indicates that these layers had probably settled simultaneously. However the clinochlorite content in L-2 is significantly lower than in the host mudstone layer. Both layers L-1 and L-2 contain numerous grains displaying impact-produced features. These include several quartz grains displaying one or two sets of decorated PDF (planar deformation features, Fig. 2) and clasts with mixed melt developing along grain boundaries. Complete or partial isotropization of feldspar crystals (maskelynite formation) has occurred. Albite incrustated spherules and shard-like clasts described in [2] are present in both layers and in the intervening mudstone layer. They consist of secondary minerals which probably replaced primary glass of microtektite origin [Fig. 3].

Using basic geophysical principles and the results of our analyses, leads to a modified scheme of ejecta layer formation: 1- Due to the velocity of seismic waves in igneous rocks, a huge earthquake put sea-floor sediments into suspension about a minute after asteroidal impact in the Gawler Ranges. 2- Several minutes after this earthquake, coarse, impact-metamorphosed dacite rocks quickly dropped through the turbid watercolumn. Due to inhomogeneity of the ejecta curtain, the debris covered the sea-floor in patches. 3- The mud still in suspension settled on the sea-floor, covering the coarse ejecta. 4- At an indetermined time after impact, but probably when significant sediments were still in suspension, the finer impact debris settled through the atmosphere and water column. 5- After completing the sedimentation process, further sediment reworking occurred by turbidity currents. Since no debris finer than 0.1 mm in diameter occurs at Bunyeroo Gorge, this material was probably carried away by currents and deposited elsewhere.

Trace and minor element abundances in the above described layers [Fig.4], confirm the similarities between the impact ejecta layers, and the significant differences between these and the host mudstone. Moreover the diagrams show enrichment of impact ejecta layers in Cr and Ni,

IMPACT EJECTA LAYER FROM SOUTH AUSTRALIA; GOSTIN V. A. & ZBIK M.

especially in the clay fraction. Because these elements are not present in target rocks in such amounts, and because they follow the Ir anomaly [2], it is possible to investigate the type of impactor from studying the elemental ratios in the clay fraction of ejecta layers. Perhaps former impact glasses that were contaminated by impactor elements retained some elemental abundances of the impactor even after transformation of the glasses into clay minerals.

REFERENCES: [1]- V.A.Gostin et al. (1986) Science Vol. 233, pp. 198-200. [2]- V.A.Gostin et al. (1989) Nature Vol. 340, No. 6234, pp. 542-544. [3]- G.E.Williams (1986) Science Vol. 233, pp. 200-203. [4]- V.A.Gostin & M.Zbik (1994) 25th, LPSC Houston.

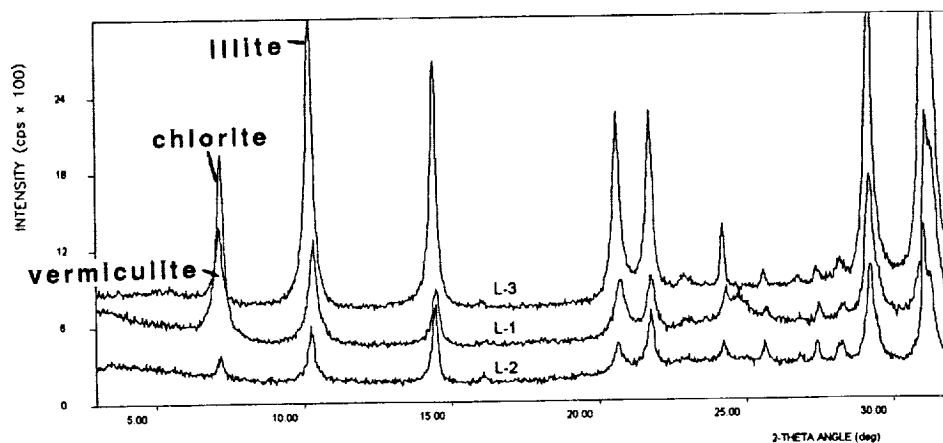


Fig. 1 Mineral composition of the clay fraction.

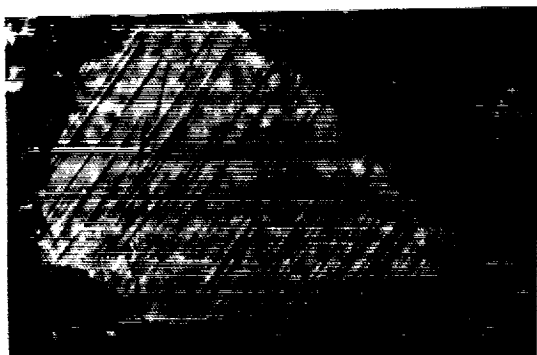


Fig.2 PDF in quartz grain from sandstone layer.

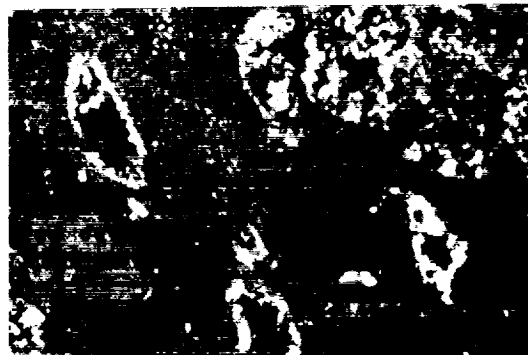


Fig. 3 Albite spherules from the thin layer between L-1 & L-2.

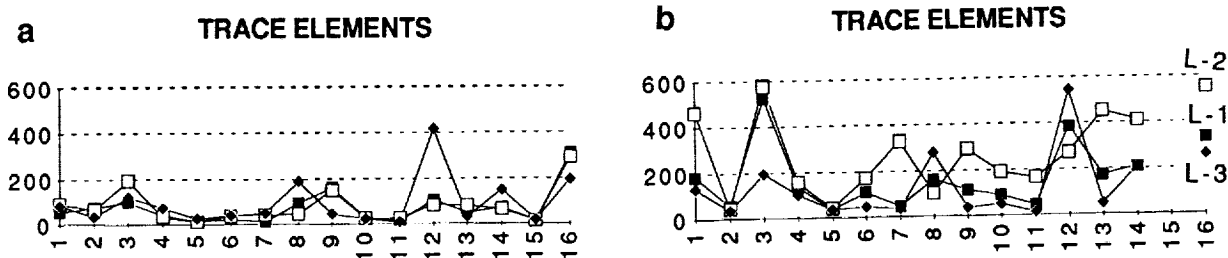


Fig.4 Trace and minor elements in: a- whole sample & b- clay fraction.

1-Ce, 2-Co, 3-Cr, 4-Ni, 5-Ga, 6-La, 7-Pb, 8-Rb, 9-Sr, 10-Th, 11-U, 12-V, 13-Y, 14-Zn, 15-Nb, 16-Zr.

"FLINDERSITES", DISTANT EJECTA IMPACTITES FROM SOUTH AUSTRALIA; V. A. GOSTIN and M. ZBIK Department of Geology and Geophysics, University of Adelaide, Adelaide, South Australia 5005.

Several clasts of dark red and strongly shattered dacites have been collected from the unique distant ejecta layer of the Lake Acraman meteorite impact structure [1]. Such clasts are extensively distributed along the iridium anomaly-bearing sedimentary horizon within the Precambrian Bunyeroo Formation outcropping in the central Flinders Ranges [2,3]. Petrology and chemical composition of feldspars from two clasts of distinctly different size have been studied. Results have been compared with chemical compositions of feldspars from pre-impact unshocked dacites (sample 1) and dacites from the central part of the Lake Acraman impact structure (sample 4).

Two clasts about 4cm (sample 2) and 40cm (sample 3) in diameter are dark red and strongly shattered (Fig.1). Hand specimens show a porphyritic texture, while in thin section large euhedral and subhedral phenocrysts of plagioclase, and rarely small quartz crystals are surrounded by a felsic matrix. Numerous cracks cross the phenocrysts and matrix. Green assemblages of fibrous chlorite which replace probable pyroxene are common, and small apatite crystals occur. Calcite, dolomite and Cu-bearing secondary minerals fill the porous system.

Numerous quartz crystals show multiple planar deformation features, many being decorated, probably by stishovite (Fig. 2). Plagioclase feldspar phenocrysts often display planar deformations, undulatory extinction and partial isotropization. Such isotropization probably led to maskelynite formation. Isotropic and partly isotropic feldspar grains are present in the matrix. Irregular pink dark turbid patches showing wavy extinction are sites of devitrified melt pockets and mixed melt along grain boundaries. All these features demonstrate that the studied samples were altered by shock metamorphism whose magnitude could be estimated as moderately shocked (shock stage S4), with shock pressures between 10 and 30 GPa [4].

Microprobe analyses showed the chemical composition of feldspars in both clasts were equilibrated and uniform. Large phenocrysts contain albite-rich plagioclase $Or_{0.5}Ab_{97.9}An_{1.6}$ with intergrowths of potassic feldspar $Or_{96.8}Ab_{1.1}An_{2.1}$ which dominate in the matrix.

In the studied samples, the K_2O/Na_2O ratios in albite show the opposite effect from that in orthoclase (see Fig. 3a and 3b). These ratios usually increase from target rocks to impactites, but in many cases the opposite tendency has been observed [5]. Enrichment of potassium occurs in albite whereas enrichment in sodium is noted in orthoclase. Perhaps during impact processes potassium in orthoclase and sodium in albite as the major elements have left the mineral structure quicker than the minor elements. A continuous sequence of chemical alterations are shown in Fig. 3c and 3d, where significant increases of the ratio SiO_2 and Al_2O_3 to volatiles suggest that samples chosen for investigation form a sequence within the same single impact event.

The uniqueness of such objects, which, for the first time have been found far away from remnants of the parent meteoritic impact structure, suggest that they be given a special name of "FLINDERSITES" from the mountain range where they occur. Furthermore, the similarity in origin between Flindersites and meteorites from the Moon and Mars provides a special occasion to study links between them.

"FLINDERSITES" FROM SOUTH AUSTRALIA: V.A. GOSTIN & M. ZBIK

REFERENCES: [1]- G.E.Williams. (1986) Science Vol. 233, pp. 200-303. [2]- V.A.Gostin et al. (1986) Science Vol. 233, pp. 198-200. [3]- V.A.Gostin et al. (1989) Nature Vol. 340. No. 6234, pp. 542-544. [4]- D.Stoffler et al. (1991) Geochim. Cosm. Acta Vol. 55, pp. 3845-3867. [5]- V.I.Feldman (1990) Petrology of Impactites. Moscow University Press. Moscow.

Fig. 1 Largest Flindersite from Bunyeroo Gorge, Flinders Ranges. Scale bar 35 cm.



Fig. 2 Planar deformation features in quartz crystal within Flindersite.

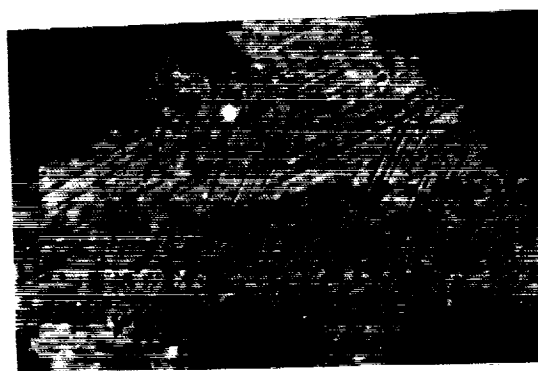
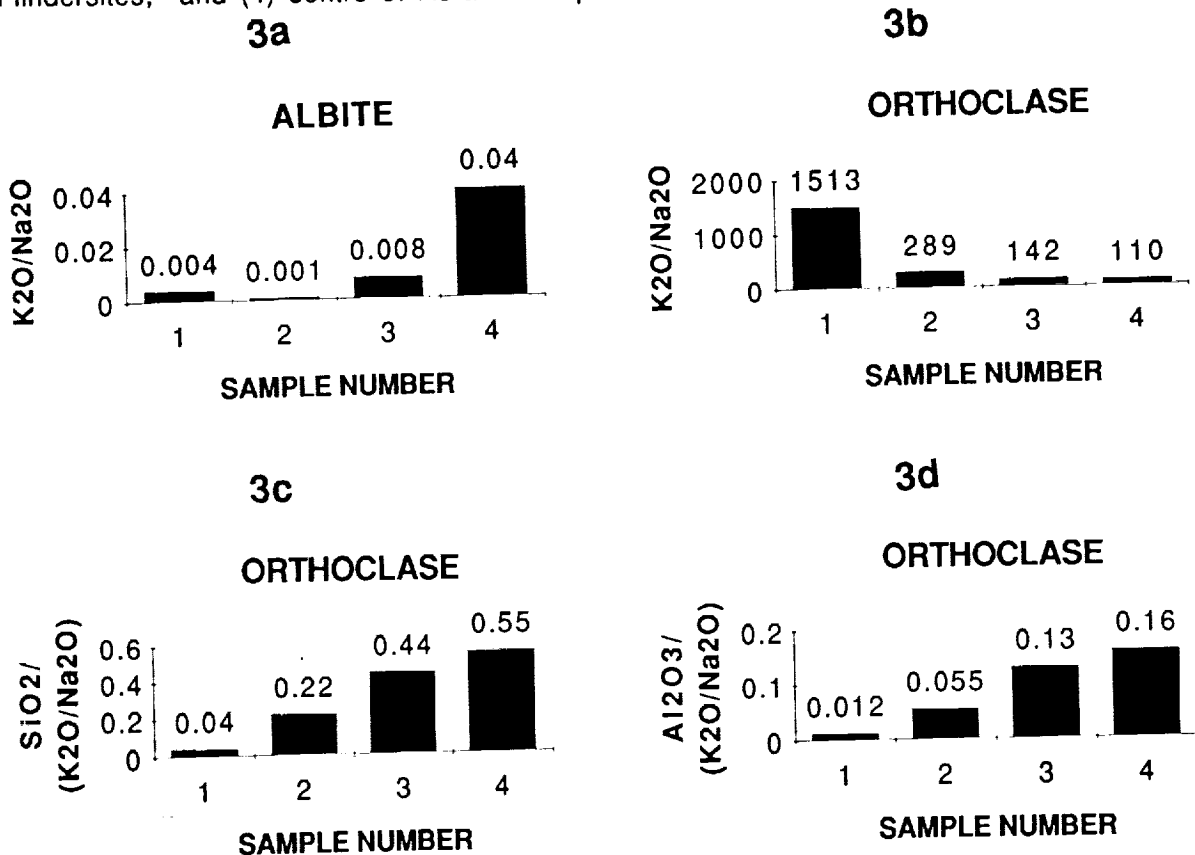


Fig. 3 Ratios of chemical components from (1) pre-impact dacite, (2) small and (3) large Flindersites, and (4) centre of Acraman impact structure.



DIAMONDS FROM ACFER 182: MORPHOLOGY, C & N STABLE ISOTOPIC COMPOSITION AND CATHODOLUMINESCENCE PROPERTIES, Monica M. Grady¹, M. R. Lee², C. M. O'D. Alexander³, J. W. Arden⁴ and C. T. Pillinger⁵. ¹Dept. of Mineralogy, The Natural History Museum, Cromwell Road, London SW7 5BD, U.K., ²Dept. of Geology & Geophysics, University of Edinburgh, Edinburgh EH9 3JW; ³McDonnell Center for Space Sciences, Washington University, St. Louis MO 63130, U.S.A.; ⁴Dept. of Geology, University of Oxford, Parks Road, Oxford; ⁵Planetary Sciences Unit, Dept. Earth Sciences, The Open University, Walton Hall, Milton Keynes MK7 6AA, U.K.

The occurrence of diamond in meteorites is well-documented, and much debate has ensued over their possible modes of formation. Sub-millimetre-sized diamonds located in iron meteorites and veins in ureilites are generally thought to be the result of collision, either during terrestrial impact [1] or between parent-bodies in space [2], although origin by chemical vapour deposition (CVD) has also been proposed [3]. The carbon and nitrogen isotopic compositions of these diamonds probably reflect their solar system origin [4]. Primitive chondrites also contain diamonds, although in this case they are nm-sized and play host to nitrogen and noble gas components with unusual isotopic compositions [5, 6]. These C δ diamonds are believed to be circumstellar grains. A third type of diamond, of unknown provenance, has recently been isolated from the Abee EH4 chondrite [7], as lath-shaped crystals with solar system carbon and nitrogen isotopic compositions. Since Abee is an unshocked meteorite, such diamonds are unlikely to be produced by collision. Thus far, all the samples studied have diamond of a single type, however, during study of the ungrouped chondrite Acfer 182, we have found diamond occurring in two morphologies. One is similar to C δ , the other we consider in more detail here.

Acfer 182 is an unusual chondritic breccia, characterised by its fine-grained nature, high metal content, small average chondrule diameter and abundant clasts of dark matrix [8]. It is relatively unshocked, most of the sample being S2, with only a few olivine grains exhibiting S3 features [8]. An outstanding feature of the meteorite is its elevated nitrogen isotopic composition, with whole-rock $\delta^{15}\text{N}$ values up to *ca.* +800‰, reaching +1600‰ in a single step [9]. In the hope that the elevated $\delta^{15}\text{N}$ values represented an abundant concentration of a new population of pre-solar grains, different from any so far recognised in other primitive chondrites, a suite of acid-resistant residues was prepared. After treatment with HF, HCl, Cr₂O₇²⁻ and HClO₄, a residue was obtained which represented 550 ppm of the original material. Combustion indicated that only *ca.* 7 wt. % of the residue was carbonaceous; EPMA confirmed that the bulk of the sample was in the form of the insoluble oxides corundum and spinel. Transmission electron microscopy (TEM) identified the carbonaceous material as diamond, most of which appeared as clumps of nm-sized grains, similar in appearance to C δ diamond. However, in addition to these aggregates, several large, micron-sized individual diamond platelets were present, the largest of which had dimensions *ca.* 8 μm x 5 μm .

Diamonds in Acfer 182

Grady, M. M. *et al.*

Stepped combustion of the residue indicated that almost all of the heavy nitrogen had been removed by the acid treatment. The major release of carbon and nitrogen occurred between 510°C and 550°C, with $\delta^{15}\text{N}$ down to -200‰, and mean C/N by mass *ca.* 85. The combustion temperature is higher by *ca.* 20°C than that of C δ isolated from CM chondrites [10], but the low absolute value of C/N and its variation with temperature is similar. These properties are consistent with identification of most of the residue as C δ -type diamond, or at least a close relation, modified by the presence of small residual amounts of ^{15}N -enriched material.

Between 625°C and 700°C, almost 14% of the carbon present in the residue combusts; this temperature range is appropriate for combustion of micron-sized diamonds [11]. Nitrogen isotopic composition is variable, with $\delta^{15}\text{N}$ rising from -5‰ to +21‰, then decreasing to -6‰. Nitrogen isotopic composition is therefore quite distinct from that of C δ diamond, as is the C/N ratio of *ca.* 1000. The combustion temperature, isotope characteristics and C/N ratio implies this material is also different from diamonds isolated from ureilites [12] and Abee [7].

Dark-field images obtained by TEM reveal that the largest diamond platelet found is morphologically different from Abee, exhibits symmetrical extinction features radiating from a void at the centre of one of the long edges. In an effort to determine whether this feature represented zoning associated with growth bands emanating from a "seed" nucleus, a scanning cathodoluminescence (CL) image was generated using a CL-SEM system with attached monochromator. The diamond luminesced only weakly, due to its size and transparency, but the CL exhibited was centred in the blue region of the spectrum, with strongest emission at 425nm. No sectorised growth zoning corresponding to the dark-field symmetry was observed: rather, the CL was strongest at edge defects, also visible in the secondary electron image. Inferences drawn from the CL imagery are that the large diamond is a single crystal, not an aggregate of lath-shaped diamonds, and that the visible structures are either growth defects or shock-induced during collisions.

We conclude that Acfer 182 is a source of yet another type of diamond with solar system characteristics, for which a shock origin cannot be eliminated. The diamonds are of a sufficient size for individual crystals to be used for ion probe studies.

Acknowledgements: Dr Paul Wright and Oxford Instruments Ltd., Eynsham, U.K., are gratefully acknowledged for carrying out the scanning cathodoluminescence analysis of Acfer 182 diamond.

References: [1] Lipschutz, M. E. and Anders, E. (1961) *Geochim. Cosmochim. Acta* **24** 83-105; [2] Vdovykin, G. P. (1970) *Sp. Sci. Rev.* **10** 483-510; [3] Fukunaga, K. *et al.* (1987) *Nature* **328** 141-143; [4] Grady, M. M. *et al.* (1985) *Geochim. Cosmochim. Acta* **49** 903-915; [5] Lewis, R. S. *et al.* (1983) *Nature* **305** 767-771; [6] Lewis, R. S. *et al.* (1987) *Nature* **326** 160-162; [7] Russell, S. S. *et al.* (1992) *Science* **256** 206-209; [8] Bischoff, A. *et al.* (1993) *Geochim. Cosmochim. Acta* **57** 2631-2648; [9] Grady, M. M. & Pillinger, C. T. (1993) *Earth Planet. Sci. Lett.* **116** 165-180; [10] Russell, S. S. *et al.* (1991) *Science* **254** 1188-1191; [11] Wright, I. P. and Pillinger, C. T. (1989) *USGS Bulletin* **1890** 9-34; [12] Russell, S. S. *et al.* (1993) *LPSC XXIV* 1221-1222.

A SEARCH FOR NITRATES IN NAKHLA; M. M. Grady¹, I. P. Wright² and C. T. Pillinger², ¹Dept. of Mineralogy, The Natural History Museum, Cromwell Road, London SW7 5BD, ²Planetary Sciences Unit, Dept. of Earth Sciences, The Open University, Walton Hall, Milton Keynes MK7 6AA, U. K.

Environmental conditions on Mars have been inferred from a variety of sources, *e.g.* theoretical modelling, satellite imagery, data from Viking landers etc. More recently, additional progress in constraining surficial processes has come from analyses of SNC meteorites. This small band of specimens has now increased in size to a total of ten, with the addition of samples from Antarctica [*e.g.* 1]. In the present study, one of the type SNC specimens, Nakhla, has been investigated in an effort to provide constraints on the nitrogen cycle on Mars.

The presence of low-temperature secondary minerals in SNC meteorites is well known. For instance, carbonates have been documented [*e.g.* 2], and their origin as martian weathering products deduced from carbon and oxygen isotope measurements [3, 4]. With a knowledge of the isotopic compositions of weathering products, coupled with additional data from magmatic sources and atmospheric gases, it should be feasible to derive models of the geochemical cycles on Mars. In this regard, efforts have been made to use carbon isotopic data to trace the evolution of martian atmospheric CO₂ [5]. Provided the requisite data are available for nitrogen species (*i.e.* low-temperature forms, magmatic volatiles, atmospheric gases *etc.*) an equivalent treatment could be attempted for the surficial nitrogen reservoirs on Mars. The occurrence of nitrates has been predicted on the martian surface [6]. If these are confirmed in SNC meteorites, isotope measurements acquired could be used in an analogous manner to data from carbonates. However, a pathfinder study seeking nitrates had only limited success [7]: data from the black glass lithology from EET A79001 were ambiguous. There was some evidence for the presence of nitrates, but the origin of the salts was uncertain, *i.e.* they might have been a result of Antarctic weathering processes. The search for martian nitrates has now been extended to Nakhla, an observed fall retrieved soon after it landed, which has therefore not suffered extensive terrestrial weathering in a temperate environment. Nakhla is known to contain materials thought to be produced by pre-terrestrial aqueous alteration: iddingsite [8], smectite, sulphates [9] and carbonates [3]. Hence, Nakhla was considered to be a prime candidate in which to search for nitrates.

A powdered whole-rock sample of Nakhla (*ca.* 2 mg) was mixed with spectroscopic-grade KBr and analysed by FTIR. The spectrum obtained was dominated by broad features below 1250 cm⁻¹, from the silicate minerals, with only a very minor peak around 1375 cm⁻¹. This latter feature occurs at the same wave-number as most synthetic nitrates [7]. To confirm that nitrates were indeed present in Nakhla, an attempt was made to concentrate these water-soluble salts by extracting *ca.* 500 mg sample with 2 ml triply-distilled, de-ionised water. From the resulting solution, *ca.* 0.5 ml was set aside for ion chromatography, to determine the concentration of the putative nitrates. The remaining solution, which also contained some fine mineral grains from the meteorite, was evaporated to dryness, yielding a poorly-crystalline

Search for nitrates in Nakhla
Grady, M. M. *et al*

residue, which was again mixed with KBr for FTIR analysis. The silicate features noted in the whole-rock were again present, but at reduced intensity. The adsorption at around 1375 cm^{-1} was more prominent - both broader and deeper than in the whole-rock spectrum, implying that the presumed nitrates had indeed been concentrated in the water-soluble extract. FTIR, however, does not absolutely distinguish between different nitrate species, hence XRD work is necessary to characterise the water-soluble salts.

Unfortunately, insufficient soluble material remained after FTIR for the nitrogen isotopic composition of the residue to be measured. However, it is known from previous work [7] that nitrates decrepitate over a narrow range of temperatures, between $300 - 500^\circ\text{C}$, hence it should be possible to assess the nitrogen isotopic composition of these minerals from measurement of a whole-rock sample of the meteorite. A preliminary analysis of Nakhla using stepped heating [10] showed a discrete release of nitrogen below 600°C , with $\delta^{15}\text{N}$ varying from -10‰ to $+10\text{‰}$. However, with the large step size (100°C) employed during the analysis, it was impossible to distinguish nitrates from any other components present, such as organic compounds (terrestrial or indigenous). Regardless, it is considered that should any nitrates be present in Nakhla, they have $\delta^{15}\text{N}$ values that are not far removed from 0‰ , as was the case in the study of EET A79001 [7]. The $\delta^{15}\text{N}$ value of the present-day martian atmosphere, has been determined by Viking to be $> +600\text{‰}$ [11], and from SNC's to be $> +300\text{‰}$ [12]. This is substantially different from that which is apparent for the supposed nitrates, therefore the latter could not have easily formed from martian atmospheric nitrogen (otherwise they would have large positive $\delta^{15}\text{N}$ values). Intuitively this is unexpected; if the results can be substantiated by further analyses, the whole subject of the nitrogen cycle at the surface of Mars may have to be reappraised.

The possibility, however, that the presumed nitrates are terrestrial, can not yet be ruled out. The recently recognised specimen ALH 84001, a new type of SNC [1], collected from a different environment from Nakhla, may provide another potential source of nitrates. If the isotopic composition of the nitrogen-containing salts from Nakhla, ALH 84001 and EET A79001 are all similar, and *ca.* 0‰ , then either the mechanism of nitrate production on Mars is more complex than has been presumed, or the formation of terrestrial nitrates with broadly similar isotopic composition is more widespread than anticipated. Hopefully, appropriate analyses of ALH 84001 can be made swiftly so as to enable results from this new rock type to be added to the data acquired from other SNC meteorites.

References: [1] Score, R. A. and Lindstrom, M. (1993) *Ant. Met. Newsletter* **16** No. 3 2-4; [2] Gooding, J. L. (1988) *Geochim. Cosmochim. Acta* **52** 905-915; [3] Carr, R. H. *et al.* (1985) *Nature* **314** 248-250; [4] Wright, I. P. *et al.* (1988) *Geochim. Cosmochim. Acta* **52** 917-924; [5] Wright, I. P. *et al.* (1990) *J. Geophys. Res.* **95** 14789-14794; [6] Yung, Y. L. *et al.* (1977) *Icarus* **30** 26-41; [7] Grady, M. M. *et al.* (1993) *LPSC XXIV*; [8] Ashworth, J. R. and Hutchison, R. (1975) *Nature* **256** 714-715; [9] Gooding, J. L. *et al.* (1991) *Meteoritics* **26** 135-143; [10] Wright, I. P. *et al.* (1992) *Geochim. Cosmochim. Acta* **56** 817-826; [11] Nier, A. O. *et al.* (1976) *Science* **194** 68-70; [12] Becker, R. H. and Pepin, R. O. (1984) *Earth Planet. Sci. Lett.* **69** 225-242.

A Galileo Multi-Instrument Spectral Analysis of 951 Gaspra

J.C. Granahan, F.P. Fanale, M.S. Robinson (Planetary Geosciences, Dept. of Geology and Geophysics, SOEST, University of Hawaii, 2525 Correa Rd., Honolulu, HI 96822), R.W. Carlson, L.W. Kamp, K.P. Klaasen, P.R. Weissman (Jet Propulsion Laboratory, 4800 Oak Grove Dr., Pasadena, CA 91109), M. Belton (National Optical Astronomy Observatories, P.O. Box 6732, Tucson, AZ 85725), D. Cook, K. Edwards, A.S. McEwen, L.A. Soderblom (United States Geological Survey, 2255 N. Gemini Dr., Flagstaff, AZ 86011) B.T. Carcich, P. Helfenstein, D. Simonelli, P.C. Thomas, J. Veverka (Laboratory for Planetary Science, Cornell University, Ithaca, NY 14853)

On October 29, 1991 the Jovian bound Galileo spacecraft encountered the asteroid 951 Gaspra. It was the first time any spacecraft encountered an asteroid. 951 Gaspra is a S-asteroid. The composition and evolutionary history of S-asteroids is somewhat of a controversy. S-asteroids are the most common asteroids known. Ordinary chondrites are the most common meteorites that are found on the Earth. Earth based telescopes obtained spectra that S-asteroids are composed of olivine, pyroxene, and reddish NiFe much like lodranites and mesosiderites. Ordinary chondrites are primarily composed of olivine, pyroxene, and NiFe. Hence many researchers subscribe to one of the following views: (1) S-asteroids may be composed of undifferentiated ordinary chondrite type material because meteorites and asteroids have common origins, and because S-asteroids and ordinary chondrites are respectively, the most abundant of each. (2) S-asteroids may be differentiated stony iron type material because S-asteroids are most spectrally similar to stony iron meteorites.

In order to further explore the composition of a S-asteroid the Galileo team collected images of 951 Gaspra through discrete visible wavelength filters (.41-.99 microns) with a solid state imaging camera (SSI) and in infrared wavelengths (.8-5.2 microns) via a near-infrared mapping spectrometer (NIMS). By combining these two data sets into a 3 dimensional array known as a spectral image cube, it is possible to analyze mineralogical composition and morphology simultaneously. At least two different spectral units are characterized in this data set. Figure 1 compares the spectra of "Typical Gaspra" with "Olivine Enriched Gaspra". The error bars of these spectra are equivalent or less than the symbols representing the data. Notice how the "Olivine Enriched Gaspra" has a more pronounced 1.05 micron feature than "Typical Gaspra". The "Olivine Enriched Gaspra" also has a significantly reduced 2 micron pyroxene absorption feature. The spectra plotted in figure 1 are representative spectra from "Typical Gaspra" and "Olivine Enriched Gaspra" and are not averages. The "Olivine Enriched Gaspra" corresponds with some of 951 Gaspra's craters.

A band area analysis developed by Cloutis et al.[1] was utilized in determining relative olivine/orthopyroxene abundances. Preliminary results indicate that the bulk composition of 951 Gaspra's surface has a relative olivine/orthopyroxene abundance ratio of 81% olivine/19% orthopyroxene (Note: the olivine/orthopyroxene abundance ratio does not indicate the relative abundance of 951 Gaspra's observed NiFe). A small fraction of the observed 951 Gaspra appears to have a relative olivine/orthopyroxene abundance ratio of 87% olivine/13% orthopyroxene. The uncertainty of these measurements is + or - 2%. Figure 2 compares these results with quantities derived by petrologic analysis of ordinary chondrites [2]. In order to verify that the spectral measurements of 951 Gaspra, an additional experiment was conducted. Spectra of ordinary chondrite meteorites were convolved to SSI/NIMS resolution and then measured utilizing the Cloutis et al.[1] band area techniques. The results were nearly identical to those portrayed in figure 2. This test validates the spectral analysis techniques that were applied to the 951 Gaspra data.

These observations are consistent with 951 Gaspra being a differentiated object. An undifferentiated asteroid is expected to be homogeneous in composition. 951 Gaspra possesses a heterogeneous composition. The spectra of 951 Gaspra have a redder spectral slope than ordinary chondrite spectra. It also contains materials which contain significantly higher abundances of olivine than ordinary chondrites. These are qualities consistent with the stony iron meteorites (like Pallasites).

A Galileo Multi-Instrument Spectral Analysis of 951 Gaspra: Granahan, J.C. et al.

Figure 1: 951 Gaspra SSI/NIMS Spectra

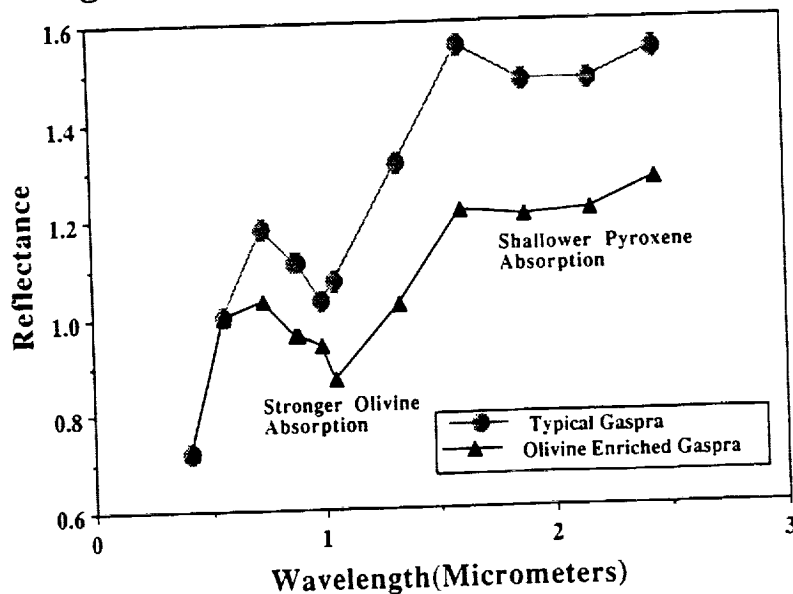
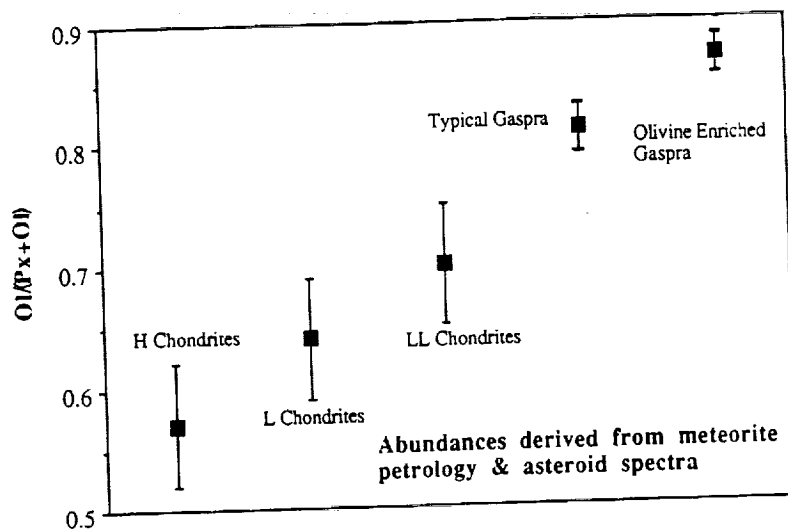


Figure 2: Olivine/(Olivine+Pyroxene)



[1]Cloutis, E., M.J. Gaffey, T.L. Jackowski, and K.L. Reed (1986) Calibrations of phase abundance, composition, and particle size distribution for olivine-orthopyroxene mixtures from reflectance spectra. JGR 94:11641-11653. [2]McSween, H.Y., M.E. Bennett, and Eugene Jarosewich (1991) The mineralogy of ordinary chondrites and implications for asteroid spectrophotometry. Icarus 90:107-116.

Ganymede and Callisto Spectral Data Cubes

J. C. Granahan, K. Polk, and F. P. Fanale, Planetary Geosciences, SOEST, University of Hawaii, 2525 Correa Rd., Honolulu, HI 96822.

Upon a successful orbital insertion of the Galileo spacecraft around Jupiter in December, 1995 there will be many spectral and imaging studies of the Galilean satellites. Unfortunately, due to the fact that this spacecraft is presently restricted by an approximately 40 bits per second downlink (about the same speed as a 2400 baud modem) and a finite onboard tape data storage many general observations of these moons will be restricted. Imaging instruments like the Solid State Imager (SSI) and the Near Infrared Mapping Spectrometer (NIMS) will be limited to making specific observations that have been previously unobtainable of specific targets. The purpose of this study is to utilize Voyager data sets to make a data set which can be integrated with Galileo data to provide supplementary spectral and spatial coverage of Callisto and Ganymede.

The primary data product of this exercise is a set of ISIS image/spectral data cubes which in summation are equivalent to a multiple wavelength cylindrically projected data set of Callisto and Ganymede. An image/spectral data cube is a three dimensional array in which the X and Y coordinates represent spatial (image) information and the Z coordinates contain spectral data. These data cubes consist of the 5 Voyager band data (see table 1) at a scale of 0.5 degrees/pixel of both moons. ISIS (Integrated Software for Imaging Spectrometers) is the standard data analysis software environment for the Galileo NIMS team. ISIS data cubes can easily be translated into PICS (Planetary Image Cartography System) and into VICAR image file formats. Both VICAR and PICS imaging processing software are being utilized by the Galileo SSI team. Hence, this data can readily be utilized by the Galileo project for planning and research activities. Table 1 shows the overlapping wavelength coverage of the Voyager, SSI, and NIMS data sets.

Table 1

<u>Voyager</u>	<u>SSI</u>	<u>NIMS</u>
0.35	0.41	0.69 -5.21
0.41	0.56	(with a maximum of 408
0.48	0.67	different wavelengths)
0.54	0.73	
0.59	0.89	
	0.99	

All quantities are effective wavelength values in units of micrometers.

Ganymede and Callisto Spectral Data Cubes: J.C. Granahan, K. Polk, and F.P. Fanale

Two versions of these data sets have been prepared. One is the calibrated using Voyager radiance values. The second correct the Voyager values to ground based observations.

What is the value of these data sets? Much analysis has already been conducted of the Voyager data color mosaics of Callisto and Ganymede ([1] for example). Aside from the Galileo orbiter observation sequence planning activities, it can be used to correlate a variety of data sets. Table 1 shows how the wavelength coverage of the Galileo SSI cameras complement the Voyager camera observations. These data sets can be used to create a more comprehensive visible wavelength spectral data set of the spatially resolved surfaces of Ganymede and Callisto than has previously existed. Photometric and Spectral trends found in the data restricted Galileo SSI images could also be modeled in regions and wavelengths only imaged by Voyager. Similarly trends observed in NIMS wavelengths and resolution found during its limited observation may be modeled in regions imaged by Voyager. A combination of the three data sets also may yield new insights into the surface composition via spectral analysis just as the combination SSI and NIMS data of 951 Gaspra demonstrated [2]. In addition to the compositional analysis suggested, the systematic software techniques used to construct these data cubes of Ganymede and Callisto can also be used to implement a variety of photometric corrective models to these moons to test a variety of photometric functions.

References:

- [1] Johnson, T.V., Soderblom, L.A., Mosher, J.A., Danielson, G.E., Cook, A.F. and Kupferman, P. (1983) Global multispectral mosaics of the icy Galilean satellites. *JGR* vol. 88, no. B7, p. 5789-5805.
- [2] Granahan, J.C., Fanale, F.P., Robinson, M., the SSI team, and the NIMS team (1993) *Bull. Am. Astron. Soc.* vol. 25, no. 3, p. 1139.

Early Fluvial Degradation in Terra Tyrrhena, Mars: Constraints from Styles of Crater Degradation on the Earth; John A. Grant and Peter H. Schultz, Brown University, Geological Sciences, Providence, R.I. 02912.

Evolution of valley networks across much of Mars during the early history of the planet is widely recognized (*e.g.*, 1-4), but whether their formation reflects incisement by precipitation-derived runoff or sapping by groundwater discharge remains debated (*e.g.*, 4-5). Because the geomorphic thresholds controlling fundamental degradation processes on the Earth can be directly measured, use of common scale templates on the Earth and Mars allows resolution of first-order degradation signatures on Mars (6-7). Previous comparative studies of degraded craters emphasized the role of fine-grained unconformable deposits in Hesperian degradation on Mars (6,8); the present study considers contrasting styles preserved from Noachian times. Results indicate that fluvial degradation near the crater Millochau was driven by runoff derived from precipitation events of magnitudes at least equivalent to those producing runoff and incisement at Meteor Crater, Arizona.

Broadly characterized as dissected cratered uplands (9,10), the Terra Tyrrhena region and crater Millochau (21.5°S, 274°W) are west of the Hesperia ridged plains and are characterized by a fairly high density of valley networks: drainage densities within a crater doublet just east of Millochau exceeds 1 km/km² (measured at ~60 m/pixel resolution) and is among the highest on the planet (3-4). Interpretation of crater densities (see 8) associated with the valleys places their formation in the Noachian shortly after formation of the Hellas Basin and concurrent with widespread evolution of valleys and concomitant crater destruction elsewhere on Mars (*e.g.*, 1,2,4,11,12). A later period of degradation also affected the region during the earliest Hesperian contemporary with ridged plains emplacement (10). This later activity is associated with a crudely layered and etched deposit whose remnants occur within and west of crater Millochau. The etched deposit buries some valley networks, is only exclusive of pristine craters, occurs over a range of relief, is not incised by intra-deposit valleys, and is morphologically similar to other contemporary deposits (6,8,13,14). Hence the deposit was likely created by deposition of a fine-grained air-fall deposit that was subsequently partially eroded during the early Hesperian.

Clues to the relative importance of runoff versus sapping processes in formation of valley networks during early degradation in Terra Tyrrhena can be gained by making similar-scale comparisons of morphology between martian craters and degraded craters on the Earth (6, 7). Of the ~10 terrestrial craters in varying states of preservation that have been examined to date, drainage densities and overall styles preserved in the crater doublet east of Millochau are most comparable to the fluvial features evolved by surface runoff of precipitation around the relatively degraded Talemzane Crater, Algeria (6). Similarities between the martian and Talemzane drainages include: numerous valleys up to several hundreds of meters wide that incise crater walls and increase in density as wall slopes decrease; observed headward erosion of some valleys through the rim to behead exterior drainages and segment the raised-rim; variable, but relatively lower drainage densities outside the crater (only 0.0-0.4 km/km² east of Millochau); exterior drainages best developed opposite locations where rim is least incised, otherwise poorly integrated valley segments common; variable wall slopes between 30° and 15° with drainage density inversely proportional to wall slope; possible coalesced alluvial fans flanking the base of the wall; and considerable crater fill. Based on these similarities, we conclude that fluvial degradation by runoff dominated Noachian valley formation: accordingly, wall backwasting in the crater doublet likely accounts for ~10% widening of the crater (6). Erosional reduction of slopes well below the angle of repose along the martian crater walls coupled with headward erosion of drainages

through the rim could not be accomplished by either a fixed or migrating point source discharge of groundwater. Features associated with mass-wasting and eolian activity (6,7,15) are absent from these martian craters.

The requirement that early valley network formation in Terra Tyrrhena was the result of surface runoff rather than groundwater sapping leads to important constraints on the climate that must have existed during early Noachian time on Mars. Whether warm or cold by terrestrial standards, there must have been an active hydrologic cycle capable of producing appreciable precipitation on a repeated basis. Because much of the area east of Millochau is likely underlain by a thick megaregolith, analogy with Meteor Crater implies infiltration capacities should be moderate to high, especially on ejecta surrounding the craters (7). Hence, in order to produce runoff, liquid precipitation events must have occasionally exceeded the one year 24 hour event (~3 cm, 12) that presently fails to produce significant runoff on the ejecta at Meteor Crater (16). If the martian valleys were formed as the result of rapid melting (e.g., 24 hours) of frozen precipitation, individual precipitation events may have been of lesser magnitude, but must have accumulated until the water content exceeded the one year 24 hour event (to a depth of at least 30 cm assuming a density of 0.10 gm/cm³ for snow) before rapid melting could produce appreciable runoff and incisement. Moreover, the incipient nature of drainage incisement at Meteor Crater (6, 7) indicates that such low magnitude events can only result in significant incisement only if recurrent over short timescales (e.g., annually) for periods of at least 10⁴-10⁵ years. Incisement of the martian valleys could occur more rapidly or much more slowly. Nevertheless, significant and repeated accumulation of precipitation is required to create the necessary runoff.

Similar scale comparisons between ancient degraded craters in Terra Tyrrhena and craters on the Earth indicate that local formation of valley networks on Mars reflects incisement by surface runoff rather than by discharge of groundwater. Although most of these martian valleys formed during Noachian degradation, they were likely buried during deposition of air-fall deposits in Hesperian times and subsequently exhumed. In many other areas on Mars (e.g. southern Ismenius Lacus, 6) this later eolian degradation effectively masked/destroyed any signatures of earlier degradation by alternative processes. Local survival of small scale fluvial features east of Millochau demonstrates the minimal net erosion occurring in some locales. Survival of these valley networks demonstrates that windows onto the record of earlier activity exist and comparisons between the preserved morphology viewed through these windows and that observed on the Earth can be used to constrain past degradation processes and climate on Mars.

References: (1) Carr, M.H., 1981, *The surface of Mars*: New Haven, Conn., Yale University Press. (2) Baker, V.R., 1982, *The Channels of Mars*: Austin, TX, Texas University Press, 198p. (3) Schultz, P.H. and Britt, D., 1986, 775-776, Lunar and Planet. Sci. XVII (abstracts), Lunar and Planetary Institute, Houston, TX. (4) Baker, V.R., et al. 1992, 493-522, in Kieffer, H.H., Jakosky, B.M., Snyder, C.W. and Matthews, M.S. (eds.), *Mars*, University of Arizona Press, Tucson, Arizona. (5) Laity, J.E. and Malin, M.C., 1985, *Geol. Soc. America Bull.*, 96, 203-217. (6) Grant, J.A. and Schultz, P.H., 1993, *J. Geophys. Res.*, 98, 11,025. (7) Grant, J.A. and Schultz, P.H., 1993, *J. Geophys. Res.*, 98, 15,033. (8) Grant, J. A. and Schultz, P. H., 1990: *Icarus*, 84, 166. (9) Schaber, G.G., 1977, USGS Map I-1020 (MC21). (10) Greeley, R. and Guest, J.E., 1987, USGS Map I-1802-B. (11) Schultz, P.H., 1988, 117-119, MEVTV Workshop on Nature and Composition of Surface Units on Mars (J.R. Zimbelman, S.C. Solomon, and V.L. Sharpton, eds.), LPI Tech. Rpt. 88-05, Lunar and Planetary Institute, Houston, TX. (12) Craddock, R.A. and Maxwell, T.A., 1993, *J. Geophys. Res.*, 98, 3453. (13) Schultz, P.H. and Lutz, A.B., 1988: *Icarus*, 73, 91. (14) Grizzaffi, P. and Schultz, P.H., 1989: *Icarus*, 77, 358. (15) Grant, J.A. and Schultz, P.H., 1993, *Geol. Soc. America Abs. with Programs*, 25, A141. (16) Miller, A.E., Fredrick, R.H., and Tracey, R.J., 1977, *Precipitation Frequency Atlas of the Western U.S.*, NOAA Atlas 2, U.S. Dept. Comm.

Erosion of Ejecta at Meteor Crater, Arizona: Further Constraints from Ground Penetrating Radar; John A. Grant and Peter H. Schultz, Brown University, Geological Sciences, Providence, R.I. 02912.

Ground penetrating radar (GPR) is an effective, non-intrusive, and easily deployed tool for defining the shallow stratigraphy around a variety of landforms (1-3). At Meteor Crater, Arizona (35°1'30"N; 111°1'15"W), GPR can be used to measure the accumulation of erosional products and place limits on the relative planation of exposed and adjacent buried ejecta surfaces. Such information constrains the preservation state of the ejecta deposits surrounding the crater and helps to distinguish between morphology related to primary emplacement and subsequent erosion. Previous GPR studies at the crater using a variety of transducer frequencies provided penetration depths of several meters around (4-6) and tens of meters inside the crater (7). The present study used a continuously profiling GPR with a 500 Mhz transducer along transects through alluvial and *in situ* ejecta deposits outside the crater. Results demonstrate that the ejecta deposit remains relatively undissected and largely preserved, thereby supporting recent estimates of low erosion at the crater (8).

Data were collected and processed using a fully digital SIR-10a subsurface profiling radar and RADAN III software. Transects were completed through alluvial and ejecta deposits on the west, southwest, south, southeast, and northeast sides of the crater at ranges between 0.4-3.0R (0.25-1.8 km). Intentional variations in strike along transects yielded continuous data collection over distances of nearly 3 km. Sample pits and discrete reflectors at known depth established groundtruth for the radar transects including dielectric constants and corresponding radar pulse travel times. For ejecta dominated by fragments of the Permian Kaibab Formation, the dielectric constant is fairly uniform around the crater (ranging between 4.0-5.3). Corresponding one-way pulse travel times are 13.0-14.5 cm/ns. Dielectric constants in alluvium derived from the ejecta are slightly higher at 7.3 and 10 for deposits containing significant Kaibab and Coconino ejecta debris, respectively. The one-way pulse travel time in Kaibab alluvium is 11 cm/ns, whereas a travel time of 9 cm/ns characterizes the Coconino alluvium. Such values are typical of dry blocky and sandy/silty materials (9).

GPR profiles through alluvium delineate stratigraphic relationships between the deposits and the surrounding *in situ* ejecta to depths of 1-3 m. Interpretation of these data indicate that buried ejecta surfaces are largely unincised by drainages. Consequently, deposition of the alluvium was not preceded by significant fluvial dissection of the ejecta. This conclusion is consistent with gradients of ejecta surfaces that can be traced continuously beneath the alluvium, thereby indicating minimal vertical denudation following alluvial deposition. Where not impeded by calcic soil development and/or high soil moisture, the GPR confirms the generally superficial nature of the alluvium and can generally distinguish deposits mapped as being Holocene versus Pleistocene in age (10). Transects crossing small alluvial fans on the southwest crater flank (~0.4-0.55R) indicate that the alluvium is less than 2 meters thick. Sediments comprising these deposits reflect relatively minor erosion of up gradient Coconino ejecta exposures. Not only do alluvial grains derived from erosion and transport of the Coconino ejecta decrease rapidly down the drainage, but the preserved volume represents a significant fraction of the entire inventory of fluvially transported Coconino ejecta.

GPR data collected at greater range west and south of the crater delineates the distal margin of the continuous ejecta at a range beyond that defined by surficial surveys. When confirmed by excavation, these data reveal that continuous ejecta remain preserved beneath a relatively thin veneer of colluvium (~20-40 cm thick) at

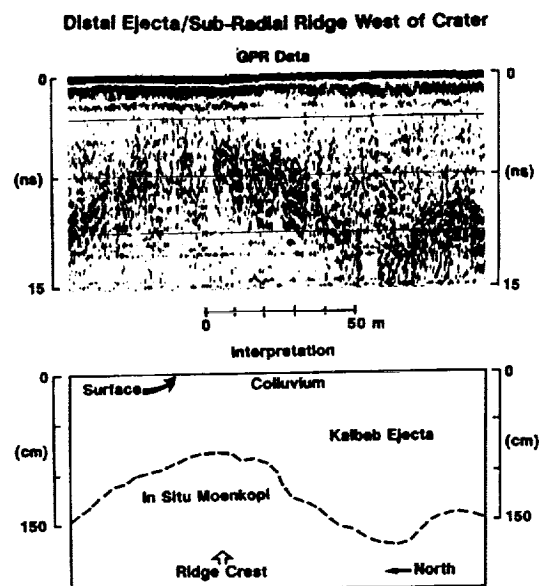
Erosion at Meteor Crater, Grant, J.A. and Schultz, P.H.

ranges exceeding $2.0R$. Local ejecta sections are in excess of 1.5 m in thickness at this range and varies due to emplacement over pre-impact relief on the *in situ* bedrock (Fig. 1). Transects completed across low sub-radial ridges (up to 5 m relief) on the ejecta west of the crater delineates cores of *in situ* bedrock (Fig. 1). As such, the ridges reflect ejecta emplacement over the existing topography on the pre-impact surface and are not the result of erosion-derived debris flow deposits were shed off the crater rim. Total ejecta thickness decreases by less than a meter across the ridge crests (likely resulting from the combined effects of emplacement over the ridge and subsequent erosion; Fig. 1), but continues to completely drape their outline. Moreover, there is no evidence for fluvial incisement or locations where the ejecta is locally breached by deflation or colluviation.

All of these observations indicate that there has been minimal erosion of the majority of the ejecta beyond the steep near-rim of the crater (ranges greater than $0.25-0.5R$ from the rim). Recent estimates place average vertical denudation on the distal ejecta at less than 1 meter (8). GPR data yield results that not only support this estimate, but demonstrate that much of the ejecta surrounding the crater retains a pristine form. Hence, the ejecta deposits around Meteor Crater should preserve key information regarding the subtleties of ejecta emplacement processes, as well as signatures of incipient degradation by fluvial and eolian processes.

References: (1) Ulriksen, C.P.F., 1982, *Application of Impulse Radar to Civil Engineering*, Ph.D dissertation, Lund University of Technology, Sweden. (2) Hanninen, P. and Autio, S., 1992, *Fourth International Conference on Ground Penetrating Radar*, Geological Society of Finland, Special Paper 16, 365p. (3) Brooks, M.J., Taylor, B.E., Grant, J.A., and Gaiser, E., 1993, *Annual Report of the DOE Savannah River Site Archeology Division*, Savannah River Site, S.C., Savannah River Archeological Research Program, New Ellenton, S.C., p. 27-37. (4) Grant, J.A. and Schultz, P.H., 1991, 481-482, in *Lunar and Planet. Science XXII (abstract)*, Lunar and Planetary Institute, Houston, Texas. (5) Grant, J.A. and Schultz, P.H., 1992, 5-7 in *MSATT LPI Tech. Rept. 92-07*, Lunar and Planetary Institute, Houston, Texas. (6) Grant, J.A. and Schultz, P.H., 1993, *GPR '94, Fifth International Conference on Ground Penetrating Radar* (in press). (7) Pilon, J.A., Grieve, R.A.F., and Sharpton, V.L., 1991, *J. Geophys. Res.*, 96, 15,563. (8) Grant, J.A. and Schultz, P.H., 1993, *J. Geophys. Res.*, 98, 15,033. (9) Fenner, T.J. and Smith, S.S., III, 1988, *Hazardous Waste Investigations Utilizing Subsurface Interface Radar*, Geophysical Survey Systems, North Salem, NH. (10) Shoemaker, E.M. and Kieffer, S.E. 1974, *Guidebook to the Geology of Meteor Crater, Arizona*: Arizona State University Center for Meteorite Studies Publication 17, Tempe, AZ., 66p.

Figure 1 Portion of GPR transect and interpretation from north to south on Chavez Pass Road at just over $1R$ from the crater rim. Transect crosses low (<5 m relief) ridge that is sub-radial to the crater and trends ENE-WSW. GPR data combined with groundtruth demonstrates that this ridge reflects buried relief on the pre-impact Moenkopi surface. Ejecta thins over the crest of the ridge but has not been breached by erosion. Because the radar defines the changing depth to reflectors, the surface is defined as horizontal and does not reflect actual topography. Colluvial thicknesses vary little between exposed highs and swales and demonstrates minimal lateral transport of debris.



SOLAR UV PHOTON INTERACTION WITH THE SURFACE OF MARS

R. Grard; Space Science Department of ESA/ESTEC, P.O. Box 299, 2200 AG Noordwijk, The Netherlands

A fraction of the solar photons with energies of up to 6 eV penetrate the Martian atmosphere and interact with the planetary surface. Photoelectrons are emitted with a mean kinetic energy of 0.4 eV and the current flux, averaged over one sol, is of the order of 20-140 nA per square meter at a latitude of 50 degrees North. These electrons are collisionally bound to the atmosphere and their dynamics is controlled by convection; they must all return to the surface in order to balance the flux of outgoing particles. Photoemission increases the atmospheric conductivity during the day; it may also play a significant role in the oxidation of the surface material.

INTRODUCTION. The solar photons which reach the surface of Mars have energies which are too small to ionize any gaseous constituents but their energy spectrum extends beyond the work function, W_f , of most solid materials; photoelectrons are therefore emitted from the surface. The solar flux, S , that reaches the planetary surface has been calculated by Kuhn and Atreya [1], for selected latitude, season and atmospheric model. Radiation with energy below 4.3 eV is hardly attenuated but carbon dioxide prevents photons with energies above W_c - 6 eV from reaching the surface.

PHOTOELECTRON EMISSION AND DYNAMICS. Photoemission has been studied in the laboratory and the electron yield per incident photon, Y , has been measured as a function of photon energy, W , for various types of targets [2,3]. The differential flux with respect to photon energy is equal to the product of the solar flux and material yield:

$$H(W) = S(W) Y(W); \quad (1)$$

the saturation flux, is given by

$$I_s = \int_{W_c}^{W_f} H(W) dW. \quad (2)$$

We make the following assumptions: (1) the flux and density of the outgoing particles are identical to those of the returning particles; (2) the energy distribution of the emitted electron flux for a fixed incident photon energy is constant from 0 to the maximum permissible energy, $W - W_f$, and (3) the irradiated surfaces are planar, horizontal and located at a latitude of 50°N.

Work function (eV)	Mean kinetic energy (eV)	Electron flux ($10^{10} \text{m}^{-2} \text{s}^{-1}$)	Current density (nA m^{-2})	Volume density (10^6m^{-3})	Electron shielding distance (m)
4.6	0.39	87/11	138/17	9.4/1.3	3.8/12.1

The figures recapitulated in the above table are averages of experimental results obtained for 9 different materials. It is not claimed that these materials are representative of the Martian surface, but it is expected that these results are indicative of the numbers which can be encountered in a practical situation. The incident solar flux is averaged over 1 sol. The first and second numbers correspond to spring and winter respectively. The mean kinetic energy is practically independent of the season and nearly the same for all materials. The electron flux emitted from the surface (Eq. 2) and the electron current density are much more sensitive to the nature of the surface and, of course, to the level of illumination. The electron volume density near

SOLAR UV PHOTON INTERACTION WITH THE SURFACE OF MARS; R. Grard

the emitting surface and the shielding parameter are also listed.

The photoelectron dynamics in a relatively dense gas is controlled by collisions, attachment processes, electrostatic forces, recombination and convection. It is estimated that the atmospheric motion plays a significant role, probably the most significant one, in the dynamics of the photoelectrons.

RELATED PHENOMENA. Solar photons extract electrons which leave a positively charged surface. Most photoelectrons reach an altitude which depends upon atmospheric convection and are subsequently collected by the surface. A small flux of photoelectrons recombines with positive ions or attach to neutral molecules and aerosols and returns to the ground under the form of negative ions and negatively charged aerosols. A possible net flux of atmospheric charged particles, resulting from the ionization of neutral molecules by cosmic rays, for example, is balanced by an equivalent flux of photoelectrons which escape into the atmosphere. On average, the flux of escaping photoelectrons equals the net flux of charged particles returning to the surface. The positive charges carried by the surface develop an upward electric field which has a polarity opposite to that of the fair weather field observed on Earth. The average magnitudes of the electric field and potential at the surface may vary with latitude and are functions of the rate at which the photoelectrons are removed and of the altitude at which they are carried by atmospheric convection. The atmospheric electrical conductivity in the vicinity of the surface is of the order of 10^{-11} U/m, which is at least 3 orders of magnitude larger than that found at the Earth surface, and has consequences for atmospheric electricity.

It is also proposed that solar photons play a significant role in oxidation-reduction reactions at the Martian surface by electron transfer. Photoelectrons are extracted preferentially from atoms with small electronegativities, such as iron, and are returned to the surface, where they are collected by surface compounds and possible adsorbed atmospheric atoms or molecules, such as oxygen, or radicals, such as OH, which have a much larger affinity for them. The negative ions subsequently desorb or migrate on the surface and then recombine with the positive ions, leading to the progressive production of a continuous layer of oxidized material.

In order to quantify the possible geological significance of this process, we shall now bring in three academic and somewhat extreme assumptions: (1) the oxidized surface is eroded as fast as it is produced, (2) this mechanism has been going on, unaltered, ever since the birth of the planet and (3) the oxidizing agents consist mostly of atmospheric constituents. These hypotheses entail the following consequences: (1) the accumulation of an oxidized regolith layer with a thickness of the order of 1 m over an area commensurate with that of the planetary surface and (2) the adsorption and chemical combination of a quantity of gaseous atoms or molecules, such as oxygen, comparable in number with the over-all volatile content of the present Martian atmosphere.

CONCLUSION. The significance of photoemission and its practical consequences for atmospheric electricity, surface chemistry and, possibly, dust electrostatic charging and dynamics are sufficiently important to justify the accommodation on a lander of a set of instruments entirely dedicated to the investigation of these phenomena. In-situ observations of the solar UV spectrum must be combined with the simultaneous measurements of photoemitted currents, conductivities of ground and atmosphere, quasi-static electric fields and electromagnetic activity. The direct detection of oxidation processes can be attempted by monitoring the evolution of the optical properties of selected sample surfaces. Still, this effect, which is nearly instantaneous on a geological time scale, is too slow to give rise to any noticeable modification during the life-time of the instrument; it might furthermore not be easily singled out from other surface phenomena such as erosion, adsorption and aerosol collection. This process must preferably be first studied in the laboratory, under accelerated conditions and in a controllable environment.

REFERENCES. [1] Kuhn, W.R. and Atreya S.K. (1979), *J. Mol. Evol.*, 14, 57. [2] Feuerbacher B. et al. (1972), *Geochim. Cosmochim. Acta, Suppl.* 3, 2655. [3] Feuerbacher B. and Fitton B. (1972), *J. Appl. Phys.*, 43, 1563.

THE CARSON QUADRANGLE, VENUS; R. Greeley, K. Bender, Arizona State University, Tempe, AZ, 85287, D. Senske, Jet Propulsion Laboratory, California Institute of Technology, Pasadena, CA 91109, J. Guest, University of London Observatory, London, NW7 4SD.

Over 75% of the surface of Venus is dominated by plains and lowlands at or near the mean planetary radius [1]. These regions are composed of lava deposits interpreted to be mainly basaltic [2] and contain a wide variety of volcanic features [3,4]. Understanding the mechanisms of plains formation is important for understanding the geologic evolution of the Venusian surface. To assess the modes of volcanism and to constrain local and regional stratigraphic relationships, the Carson Quadrangle (Fig. 1) is currently being mapped in detail.

Units are defined based on their texture, homogeneity, and presence of features such as fractures, small shields etc.. In many cases unit contacts are distinct and well defined by cross-cutting and superposition relationships. Additional factors used to characterize units are their radar properties, including rms slope, reflectivity, emissivity, and relationships to topography. The Magellan radar viewing geometry is important for interpreting the characteristics of surface units. Radar incidence angles for the Carson Quad range from 46° at the equator to 35.5° at 25° S latitude. Consequently, the returned signal is strongly modulated by surface roughness on the scale of a few tens of centimeters; units defined as "radar-bright" are generally rough while "radar-dark" units are smooth. Results from examining the radar scattering properties of Carson units are presented elsewhere [5].

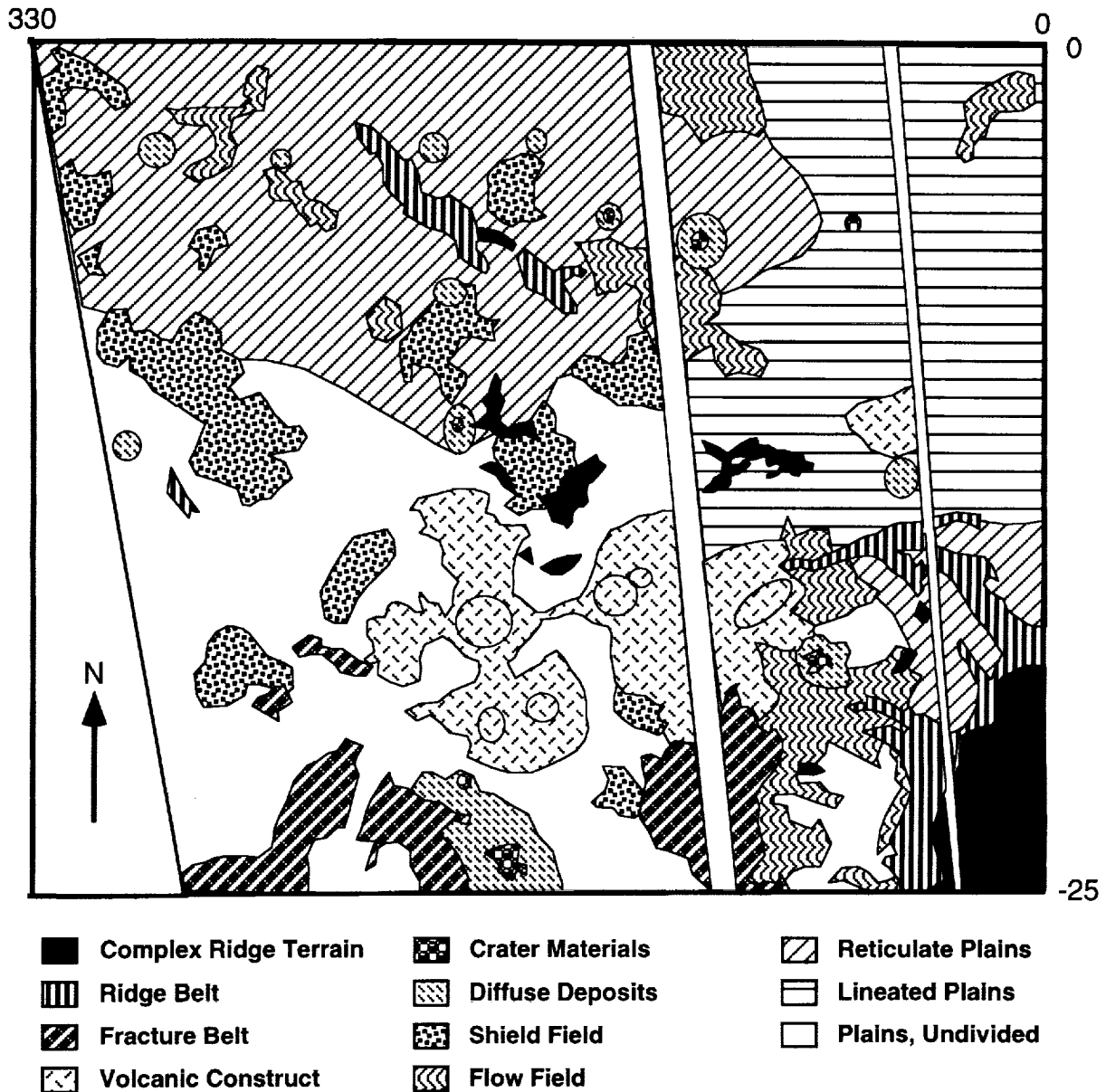
From preliminary mapping eleven major units have been identified, the most recent of which correspond to isolated volcanic centers, shield fields, and material associated with impact craters. Volcanic constructs >100 km across and ~1.0 km high consist of radar-bright material, radar-dark material and associated digitate lava flows that are superposed on the surrounding plains. Concentrations of smaller (~2 km diameter and greater) volcanic centers cluster in shield fields. These features and their associated deposits form locally radar-mottled surfaces whose boundaries with adjacent units range from distinct to diffuse. Other recent localized volcanic deposits, lava flow fields are made up of digitate, radar-bright and -dark deposits, some of which are associated with faults and fractures. Reticulate plains contain numerous sinuous ridges and have a moderate, homogeneous radar backscatter and few identifiable lava flow lobes. A major ridge belt cuts the reticulate plains as a deformation zone rising to an elevation >300m and composed of ridges spaced 10s of km apart. South of Heng-o, the reticulate plains embay a region of lineated plains; a unit with a homogeneous radar backscatter that contains abundant fractures which in some places form a gridded pattern. Closely related to this unit and located on a broad topographic rise to the west of Alpha Regio is a fracture belt. This deformational zone is 10s to 100s of km wide and is made up of linear, parallel fractures spaced from several to 10s of km. The most abundant plains are undivided, a large, homogeneous unit lacking ridges or lineations. The oldest unit, complex ridged terrain at Alpha Regio, contains ridges and fractures with multiple directions of deformation. Alpha Regio is rough at the 12.6 cm radar wavelength, and is extensively embayed by adjacent plains units. Two types of impact related units are mapped. Crater material form radar-bright, often lobate deposits extending .25 to 1 crater radii from the edge of inferred impact craters; in some places, the distal parts of the deposits appear to form flows. Diffuse deposits are localized, annular regions of bright or dark material that is typically centered on impact craters (in some places no crater is present and they form "splotches" [6]).

Stratigraphic relationships among units in the Carson Quad show that the most recent volcanic activity is associated with isolated volcanic edifices, lava flow fields, and shield fields. Earlier episodes of volcanism resulted in the emplacement of regional plains units, some of which are highly fractured. The earliest activity corresponds to the formation of complex ridge terrain in Alpha Regio.

Carson Quad, Venus; Greeley et al.

References. [1] Ford, P. G. and G. H. Pettengill (1992) *JGR*, 97, 13103. [2] Florensky, C. P., et al. (1977) *GSA Bull*, 88, 1537. [3] Guest, J. E., et al. (1992) *JGR*, 97, 15949. [4] Head, J. W., et al. (1992) *JGR*, 97, 13153. [5] D. A. Senske, et al. (1993) LPSC Abst. this issue. [6] Schaber, G.G., et al. (1992) *JGR*, 97, 13,257.

Fig. 1 General geologic sketch map of the Carson Quad.



DO LAVA FLOWS ERODE? PRELIMINARY ASSESSMENT; R. Greeley, R.S. Harris, S.D. Kadel, D.A. Williams, *Dept. of Geology, Arizona State University, Tempe, AZ 85287-1404*, J.E. Guest, *University of London Observatory, London NW7 4SD, England*

Summary. In the last decade or more, numerous studies have invoked erosion by flowing lava to explain various geological features on Earth and other planets. For example, economic deposits of NiS ore found in komatiite lavas were attributed to erosion of pre-flow, sulfur-rich sediment and assimilation into the high temperature, turbulently flowing lavas during emplacement [1]. In the planetary context, calculations were made to suggest that thermal melting of lunar crust by mare lavas could account for sinuous rilles [2, 3]; similarly, thermal erosion was used to explain the large sizes of lunar rilles by considering possible rates of effusion and vent geometry [4, 5, 6]. More recently, the discovery of long (>5000 km) channels on Venus that are inferred to be of volcanic origin has prompted consideration of thermal erosion by a variety of eruptive materials [7, 8, 9]. However, despite the frequent reference to erosion by lava flows in these models, little evidence is cited that flows actually do erode. Our analysis of "sheet flows" (komatiites and flood lavas) and lava tubes on Earth shows some local erosion, but thus far in the study, such erosion appears to be relatively limited.

Our goal is to collect field evidence for erosion by lava and where evidence is found: [1] determine the extent of the erosion, [2] assess the conditions favorable for erosion, and [3] use the results to constrain analytical models of lava erosion. Moreover, we hope to be able to distinguish thermal from mechanical erosion and to assess their relative importance. Two general environments are considered, erosion along the bases of sheet flows and erosion associated with channelized and tube-fed flows.

Sheet flows

The most likely candidates for erosion by sheet flows are lavas that were erupted at high temperatures and high rates of effusion, such as flood basalts and komatiite flows. In order to assess possible erosion, several kilometers of the lower contacts of flood basalt flows in the Columbia River Plateau were examined for evidence of downcutting into the underlying rocks and incorporation of pre-flow materials into the lavas. Except for an exposure near Soap Lake, Washington, where minor amounts (a few tens of cm) of pre-flow material were incorporated into the flow, little evidence of erosion could be found.

Komatiite lavas are ultramafic flows erupted primarily during the Archean and are considered to have produced very high temperature, perhaps turbulently flowing masses [10]. Although most komatiite flows are severely altered, localities in Canada and Australia include flow contacts that were examined for erosion. Evidence of possible erosion includes: truncation of horizontal rock units by channelized komatiite flows in the Abitibi belt, Ontario [11], and small amounts of entrained substrate fragments and geochemical anomalies suggestive of assimilation of substrate by flowing komatiite lava in the Yilgarn Craton, Western Australia [12, 13].

Tube-fed flows

In contrast to sheet flows, more definitive evidence for erosion by lava is found in association with basaltic lava tube flows. Several segments of the Ape Cave lava tube system on the southern flank of Mount St. Helens show undercutting of the pre-flow terrain by the lava tube [14]. Evidence is found for both mechanical erosion (evidenced by inclusions of pre-flow country rock incorporated into the flow) and a single occurrence of thermal erosion (a partly melted block of dacite). In general, sites of erosion occur in segments of the lava tube that have steeper flow gradients than elsewhere. Other localities of erosion by lava tube flows include northern California and possibilities in Hawaii, Idaho, and Iceland. In addition, at least two active flows in Hawaii suggest erosion through tubes, the Mauna Ulu flows in the early 1970s [15] and the current activity in Kalapana on the East Rift zone of Kilauea [16].

Preliminary conclusions suggest that erosion by sheet flows is very limited. Erosion by tube-fed flows appears to occur under some circumstances, but at this time the extent of erosion is not

DO LAVA FLOWS ERODE?: R. Greeley et al.

known. Ongoing work involves correlation of sites of erosion with local geological setting. Results from this study will be combined with the development of analytical models [17] and physical models [18].

REFERENCES:

- [1] Naldrett, A.J. (1981), *Econ. Geol. 75th Anniversary Volume*, 628-685. [2] Hulme (1973), *Modern Geology*, 4, 107-117. [3] Carr, M.H. (1974), *Icarus*, 22, 1-23. [4] Head, J.W. and L. Wilson (1980), *LPSC 11*, 426, 428. [5] Wilson, L. and J.W. Head (1980), *LPSC 11*, 1260-1262. [6] Head, J.W. and L. Wilson (1981), *LPSC 12*, 427-429. [7] Baker et al. (1993), *J. Geophys. Res.*, 97, 13,621-13,644. [8] Komatsu et al. (1993), *Icarus*, 102, 1-25. [9] Gregg and R. Greeley (1993), *J. Geophys. Res.*, 98, 10,873-10,882. [10] Arndt, N.T. and E.G. Nisbet (1982), *Komatiites*, Allen and Unwin: London. [11] Davis et al. (1993), *GSA Abstracts with Programs*, A-600. [12] Barnes, S.J. et al. (1988), *J. Pet.*, 29, 305-331. [13] Perring, C.S. et al. (1993), *IAVCEI* (abstract), 86. [14] Greeley, R. (1987), *U.S. Geol. Sur. Prof. Pap. 1350*, 1589-1602. [15] Tilling, R. et al. (1987), *U.S. Geol. Sur. Prof. Pap. 1350*, 405-469. [16] Jackson, D.B. et al (1987), *EOS*, 68, 1543. [17] Williams and Greeley (this issue). [18] Challis et al. (this issue).

DUST ON MARS: NEW VALUES FOR WIND THRESHOLD; R. Greeley, *Dept. of Geology, Arizona State University, Tempe, AZ 85287-1404*, M. Lacchia, B. White, *Univ. of Calif. at Davis, Davis, CA 95616*, R. Leach, D. Trilling, J. Pollack, *NASA-Ames, Moffett Field, CA 94035*

Summary. Dust storms on Mars have long been observed from Earth and spacecraft (1), and there has been much speculation on the requirements for entraining dust into suspension. Analytical models (2) and wind tunnel simulations (3) suggested that extremely high wind speeds are required to raise fine ($<10\text{ }\mu\text{m}$) particles into the low-density martian atmosphere. Because the Viking landers measured winds that were typically lower than threshold speeds for very fine grained material, many investigators invoked *ad hoc* mechanisms for raising dust on Mars, as recently reviewed (1,4). We have completed preliminary experiments which show that martian dust could be raised by wind friction velocities as low as 1.3 m/sec and explain why the previous estimates involve higher velocities.

Background

Previous aeolian threshold curves for Mars (Fig. 1) show that the size particle moved by lowest winds is about $100\text{ }\mu\text{m}$ in diameter, with larger and smaller particles requiring stronger wind friction velocities (u_*). Martian atmospheric dust is considered to be $<\text{few }\mu\text{m}$ in diameter (5). Particles this small are very difficult to handle, and few threshold experiments have been conducted for dust even for Earth conditions, let alone Mars. Previous threshold curves for this size particle were extrapolated from larger sizes on the assumption that threshold wind speeds would increase with decreasing particle size. Such a relationship is clearly indicated, at least for particles as small as $\sim 15\text{ }\mu\text{m}$. The difficulty in moving small particles is attributed to the increasing effects of inter-particle forces, such as cohesion, and aerodynamic effects (6). However, previous threshold curves were generated for particles entrained in saltation, rather than suspension, which is the principal mode for dust entrainment. Consequently, it may not be entirely appropriate to extrapolate threshold curves from large particles to those of a few μm in diameter and smaller.

Experiments

For the first time, experiments reported here involved $1\text{ }\mu\text{m}$ -size dust and martian atmospheric densities. Prior to running the experiments, suitable test materials were required, a technique for emplacing the material in the wind tunnel without introducing artifacts needed to be developed, and a method for detecting threshold was needed. Several lines of evidence suggest that martian dust is derived from the weathering of basaltic parent material, with nontronite clay being a good candidate composition. Consequently, we sought test materials that would have the physical properties of both nontronite and natural windblown dust of $\sim\text{few }\mu\text{m}$ size. Commercial potters clay (CRC) (particles = 1 to $2\text{ }\mu\text{m}$ diameter) met those requirements and was used in the experiments. SEM analyses showed that this clay has the same shape characteristics as both nontronite and natural windblown dust. After testing several methods for emplacing CRC in the Mars Surface Wind Tunnel (7), we found that the clay could be emplaced as an air-entrained cloud over the test bed. Experiments were then run at 10 mb pressure and ambient temperature, which produced the same fluid density as CO_2 on Mars at 6.5 mb pressure. Two test beds were used, one on which 250 mm sand grains were glued and the second on which pebbles $\sim 1\text{ cm}$ in diameter (spaced $\sim 1.5\text{ cm}$ apart) were glued. About 0.2 cm of clay was emplaced on each bed type.

Figure 1 shows threshold data points for various particles, along with the conventional saltation threshold curve. Also shown are results for CRC ("Mars dust"). All of the data points except the clay represent sustained saltation movement. Individual particles $\leq 10\text{ mm}$ typically do not saltate (8), but pass into suspension. In our low pressure experiments, *sustained* suspension threshold at a steady wind speed was not achieved and values shown in Figure 1 for dust correspond to initial, but sporadic, movement. It is important to note that particles of this size behave differently than larger grains. Dust movement on the "sanded" floor involved small ($\sim\text{mm}$) clumps of dust ("dust balls") which begin to roll along the surface. Rarely did these go into suspension but, more commonly, they rolled to the end of the test bed where they accumulated.

DUST ON MARS: R. Greeley et al.

Dust movement on the pebble floor was markedly different. Suspension threshold occurred for the particles that covered the tops of the pebbles; however, the friction velocity (u_*) at which this movement occurred was not consistent from one experiment to the next. Dust balls also formed in the pebble floor experiments; some dust balls developed on the tops of the pebbles then rolled or slid down the lee side of the pebbles where they accumulated. Other dust balls formed between the pebbles where they moved short (~few cm) distances until they reached a stable position.

These experiments pose several implications for Mars. Even though sustained threshold was not achieved, experiments show that micron-sized particles in a layer ~0.2 cm thick on top of small pebbles were removed by friction velocities of ~1.3 m/sec. Although precise translations of friction velocity to measurements of windspeed made by the Viking Lander anemometers is difficult, this value is well within the range of the higher recorded wind speeds on Mars. Particularly significant are the differences in the tests on the smooth and the rough test beds. The implication for Mars is that dust raising would occur in areas that are somewhat rocky; dust settled on the tops of the rocks would be removed; dust settled between the rocks would be trapped and accumulate until the rocks were buried or until some equilibrium surface roughnesses were achieved. As long as the tops of rocks remained exposed, this would provide elevated platforms for dust accumulation and removal, as in the experiments. Conversely, dust that settled on relatively smooth surfaces on Mars would require substantially higher wind speeds for entrainment; for example, the maximum MARSWIT speed is 160 m/sec and dust thresholds on the smooth floors were not achieved.

REFERENCES: [1] Kahn, R.A. et al. (1992), in *Mars*, Univ. Ariz. Press, 1017-1053. [2] Iversen, J.D., and B.R. White (1982), *Sedimentology*, 29, 111-119. [3] Greeley, R. et al. (1980), *Geophys. Res. Lett.*, 7, 121-124. [4] Greeley, R. et al. (1992), in *Mars*, Univ. Ariz. Press, 730-766. [5] Pollack, J.B. et al. (1977), *J. Geophys. Res.*, 82, 4479-4496. [6] Iversen, J.D. et al. (1976), *Icarus*, 29, 381-393. [7] Greeley, R. et al. (1981), in *Geol. Soc. Amer. Sp. Paper 186*, 101-121. [8] Pye, K. (1987), *Aeolian dust and dust deposits*. Academic Press, London.

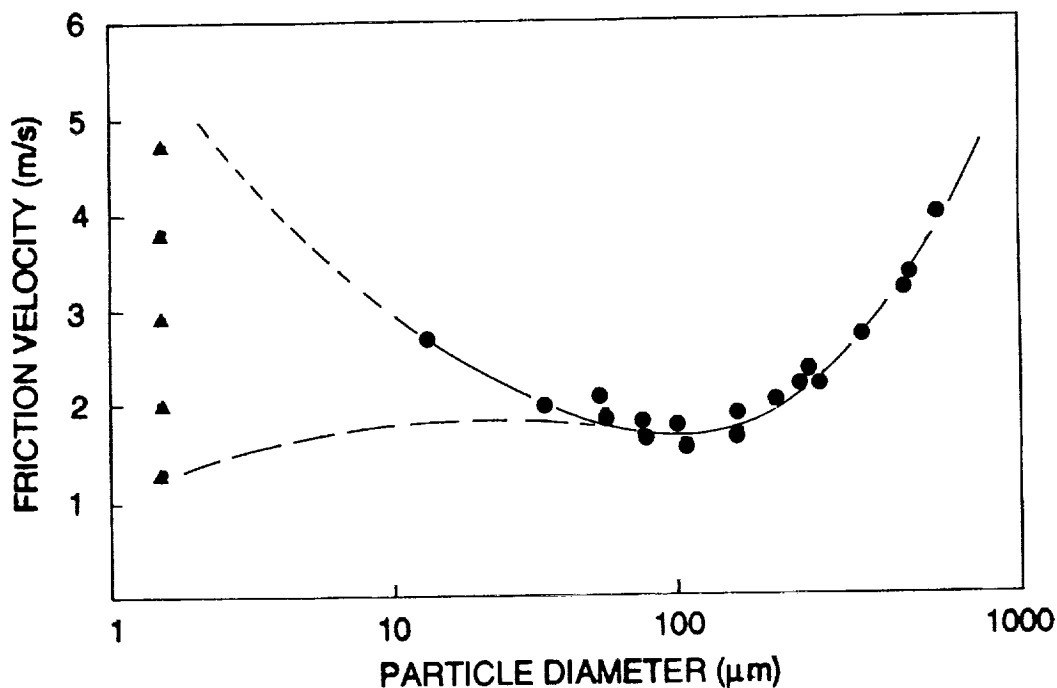


Figure 1. Threshold friction velocities (m/s) versus particle diameter from experiments run in the Mars Surface Wind Tunnel at 10 mb pressure. SOLID line shows "conventional" curve extrapolated to Mars dust sizes (~few μm); also shown are new experiment results using clay particles 1-2 μm in diameter. Although there is a wide range of threshold velocities, the lowest velocities (~1.3 m/s) correspond to dust removal from the tops of pebbles.

MORPHOLOGY AND GEOLOGY OF ASTEROID IDA: PRELIMINARY GALILEO IMAGING OBSERVATIONS; R. Greeley, R. Sullivan, R. Pappalardo, *Dept. of Geology, Arizona State University, Tempe, AZ 85287-1404*, J. Head, *Brown University*, J. Veverka, P. Thomas, P. Lee, *Cornell University*, M. Belton, *National Optical Astronomical Observatory*, C. Chapman, *Planetary Science Institute*

Summary. The Galileo spacecraft flew by asteroid 243 Ida on 28 August 1993 [1]. Five of the highest resolution (31-38 m/pixel) Solid State Imaging clear filter frames of Ida were returned for preliminary analysis (Fig. 1a); the remainder will be returned in 1994. Ida is classified as an S-type asteroid, inferred to be of pyroxene and olivine composition, and measures ~55 km in its longest dimension. At least seven categories of morphological features are mapped on Ida (Fig. 1b) which provide clues to the properties and geological evolution of the surface.

We have confidently identified 16 isolated positive relief features ("rocks"), none larger than 150 m in longest dimension. They are more concentrated in the upper part of the image mosaic, but it should be noted that their detection is strongly influenced by local slope and illumination. The four most prominent features are located within the rim of a large, partially illuminated impact crater in the upper part of the mosaic. Resolution is generally inadequate to determine confidently whether a given feature is "perched" on the surface or partly buried. These features may be blocks of impact ejecta. Less likely, they may be remnants of resistant "bedrock" (implying local heterogeneity of material strength) or fragments of impactor (implying very low energy impacts).

At least three shallow concavities (informally termed "chutes") are recognized on a steep slope near the top of the mosaic. The chutes are oriented with their long axes roughly parallel to local slope, and each ends downslope in a sub-circular crater. The largest chute is 1 km long and 400 m wide. Chutes could be scars produced by mass wasting of weakly cohesive material, possibly triggered by an impact. This interpretation suggests the presence of a regolith mantle, at least in the location where chutes occur. Alternatively, these features may represent extremely low-angle impacts, although their non-random distribution argues against this idea.

Lineations are recognized on the basis of albedo ("stripes") and topography ("grooves"). Stripes are 50 to 100 m wide, and 400 m to 2.5 km in length. Grooves are resolved as linear depressions of uniform width that in some places have subtle indications of raised and/or crenulated edges. Grooves are less than 100 m wide, and 400 m to 4 km in length. Some grooves and stripes cross craters, although they rarely intersect each other or bifurcate. Stripes are generally brighter than surrounding terrain, are more apparent in areas viewed at locally high sun, and are commonly oriented locally downslope; some "stripes" illuminated by high sun may be grooves. Grooves and stripes may have diverse origins. One group of bright stripes within a large bowl-shaped depression in the top third of the mosaic could represent tracks of mass-wasted debris; alternatively, they could be rays of ejecta from an impact crater which may be hidden from view. One groove terminates downslope adjacent to a "rock," and the groove might represent the track of this feature. Grooves could be fractures or joints resulting from stresses from large impacts, although a source crater(s) cannot be determined from the present mosaic.

Dark-floored craters, distinguished by low albedo floors, are seen in areas illuminated by high sun; most dark-floor craters occur in a cluster (lower left of the mosaic). Typically, dark material constitutes most of the crater interior. In a few cases, dark-floor material is surrounded by a halo of bright material lying at or just within the crater rim. Dark-floored craters could represent impacts through a thin, weak regolith to expose underlying low albedo material. Identification of this feature class is tentative, as their appearance could be an artifact of local illumination.

Three albedo features are tentatively identified; additional views of Ida available in Spring 1994 will show some of these features under different illumination and viewing geometries, allowing a more confident evaluation. (1) A triangular bright feature 2.5 km by 500 m wide is recognized in the top left of the mosaic; it is bounded on one side by the base of a local slope and on the other by a groove. The origin of this feature is unknown but it may represent mass wasting of debris from the adjacent slope. (2) A triangular dark patch nearly 2 km by 500 m wide is located near the terminator in the middle of the mosaic. A 200 m crater is located at the apex. The feature suggests either a thin, dark mantling deposit, possibly derived from the small crater at the apex, or a laterally extensive underlying darker material locally swept clear of a thin layer of brighter material, or an extensive exposure of anomalously dark material (no horizontal layering/mantling implied). (3) An irregular dark patch 200 m by 500 m is located among the cluster of dark-floored craters in the lower left of the mosaic (Fig. 1b). This feature may be a cluster of small dark-floored craters that do not display rim topography.

Craters are generally bowl-shaped, but some have flat floors; others appear to have small central mounds, and some have straight rim segments. There is a continuous range of degradation states. Craters lack distinct ejecta blankets, although deposits may be too thin to be recognized. A few of the freshest impact craters visible are bright and have one or two short rays. Many other craters with crisp rims do not have rays, although they do have narrow, raised rims. Under high sun, many craters are surrounded by a narrow bright ring immediately outside the rim (in contrast to the bright halo of some dark-floored craters, located mostly within the rim). The extremely low gravity on Ida probably precludes formation of distinct ejecta blankets and extensive fresh crater rays.

Crater chains are defined as consisting of three or more aligned craters of similar size separated by less than one crater diameter. Crater chains range from 500 m to 2.5 km in length, and component crater diameters range from 200 to 400 m. Orientations and locations are random across the mosaic. Crater chains may result from low-velocity impact of ejecta from a primary crater (although no crater chain can yet be linked to a larger primary) or from a string of original impactors.

MORPHOLOGY AND GEOLOGY OF ASTEROID IDA: R. Greeley et al.

Preliminary analysis of the types, morphologies, and distributions of surface features on the five-frame mosaic of Ida suggest the following:

1. Ida is geologically more complex than Gaspra, an asteroid imaged by Galileo in 1991. This may reflect its larger size or a different history.
2. Many of the morphological features suggest the presence of regolith, as evidenced by downslope movement of debris. Asymmetric distribution of these features may mean that the regolith is not present everywhere or is of variable thickness.
3. Preferred orientation of many of the lineations may be related to a stress field or as yet unseen craters.

We note that these observations are tentative and may be strongly influenced by local illumination and viewing geometry. Dimensions reported here are apparent and have not been corrected for foreshortening or local slope. When completed coverage from subsequent images is received, the distribution of morphological features and interpretation of surface geology will be improved.

REFERENCE: [1] C.R. Chapman et al., this volume.

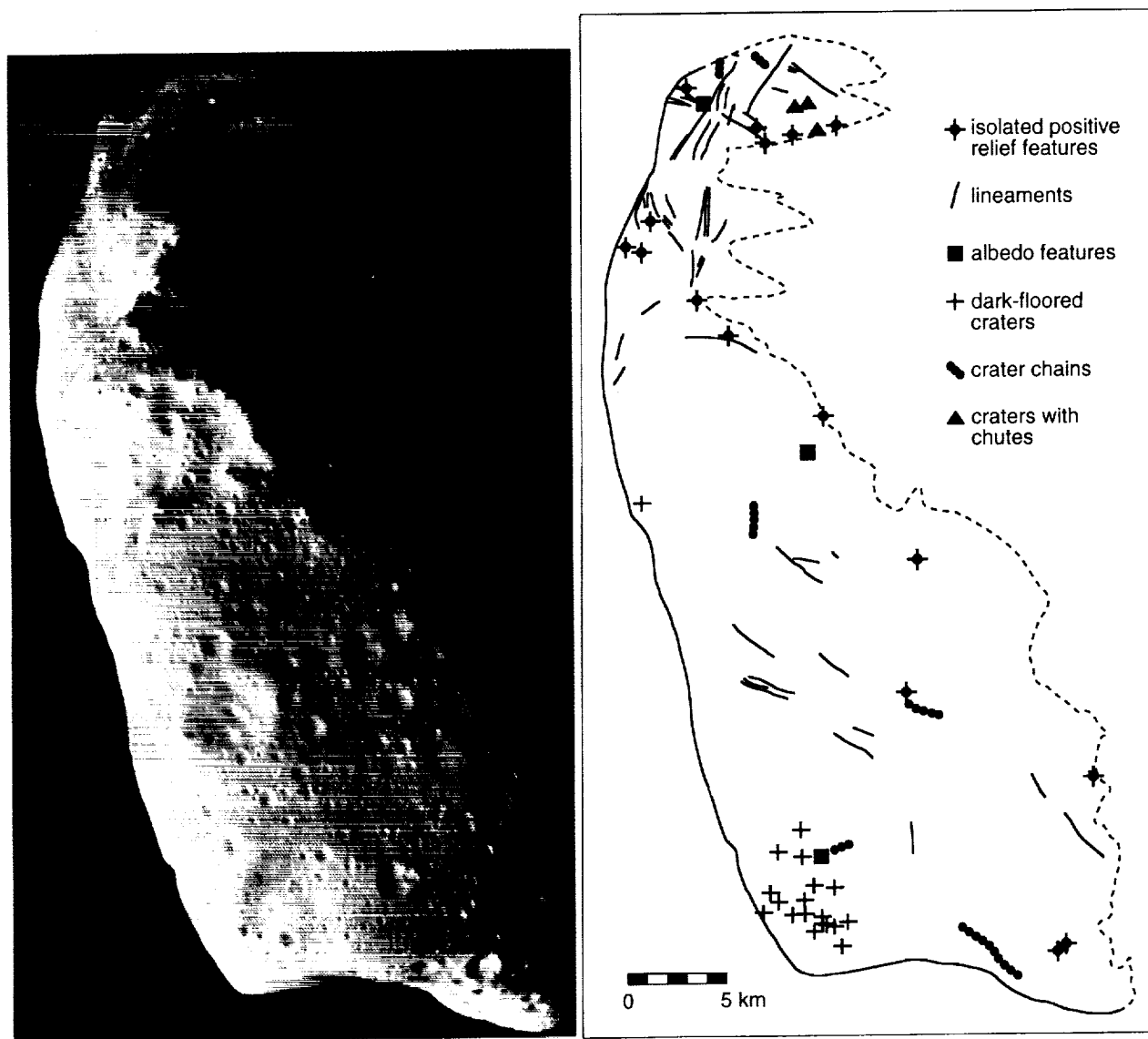


Fig. 1. a) Galileo photomosaic of Ida, b) sketch map corresponding to Figure 1a showing various surface features.

CONSTRAINTS ON FLASH HEATING FROM MELTING KINETICS.

James P. Greenwood and Paul C. Hess, Department of Geological Sciences, Brown University, Providence, RI 02912.

During a flash heating event, a mineral heated above its melting point will melt *in situ*, regardless of the minerals with which it is in contact. In contrast, melting paths controlled by phase equilibria are limited by diffusion in the liquid, and will therefore not necessarily control the melting kinetics. Melting will instead be rate limited by the kinetics occurring at the solid-liquid interface. It is then possible to predict melting rates for various amounts of superheating using a Wilson-Frenkel model[1].

Melting has historically been modeled as a continuous process. Intrinsic to this philosophy is the assumption that at the melting point the solid transforms to a liquid at all points in the lattice. The contrasting view of melting is that the solid transforms discontinuously via a nucleation and growth mechanism, similar to crystallization. If this is true, then melting can be modeled by existing theories of crystal growth, assuming the principle of microscopic reversibility. The principle difference between melting and crystallization is that the barrier to nucleation of melt on a crystal surface is considered negligible, while the nucleation of a crystal in a liquid is comparatively difficult.

The observation that metal crystals melt at even slight superheating has been cited as evidence to support the continuous transition theories. In contrast to these observations, studies on solids which melt to viscous liquids have shown that melt invariably nucleates on the external surface and interior boundaries (i.e. cleavage planes and fractures) and propagates inward[1-3]. Also, it is possible to superheat solids such as quartz[1,4] and albite[2] by hundreds of degrees for significant times. The melting rate and the amount of superheat a given solid can undergo is related to the viscosity of its liquid. It is not surprising that metal crystals are observed to melt almost continuously at slight superheating, because the kinetics of the melting process are very rapid and it would be difficult to measure (see below).

In choosing an appropriate model to describe melt growth, the rate controlling factor must be stipulated. If a crystal melts into a liquid of different composition, the melting rate will likely be controlled by diffusion of melted components from the interface into the liquid. When a crystal melts into a liquid of high fluidity, as in the case of a metal melting into a liquid of its own composition, the melting rate is generally controlled by the efficiency which heat can be transported to the interface. The melting rates in these cases will be time dependent. For a crystal which melts to a viscous liquid of its own composition, the rate is generally controlled by the kinetics at the interface. In this case, the melting rate will be time independent.

The melting kinetics of quartz[1,4], cristobalite[1,3], sodium disilicate[5,6], phosphorous pentoxide[7], albite[2], germanium dioxide[8], and diopside[9] have been studied to date. These studies involved single crystals or were melted into a liquid of the same composition. They were all found to have time independent melting rates. Also, the melting rate is linearly proportional to the amount of superheat. These two conditions must be satisfied in order to utilize a Wilson-Frenkel model for predicting growth rates[10-12]. The Wilson-Frenkel model attempts to predict growth rates for interface-controlled normal growth. Specifically for small superheating, $u = f\Delta H_f(T-T_m)/T_m 3\pi a^2 N_A \mu$, where u is the growth rate, f is the fraction of sites available at the solid-liquid interface ($f=1$ for normal growth), ΔH_f is the enthalpy of fusion, T is the temperature of interest (in kelvin), T_m is the melting point, a is the jump distance, N_A is Avogadro's number, and μ is the viscosity of the melt.

When the experimental melting rate is compared with the theoretical melting rate for P_2O_5 , GeO_2 , Na_2SiO_5 , albite, quartz, and cristobalite, the experimental rate is generally higher by an order of magnitude or less. Indeed, the melting rate of albite is predicted almost exactly [2]. These crystals melt to liquids with viscosities ranging from 10^2 to 10^7 Pa·s. But in the case of diopside, which melts to a liquid with a viscosity of 10^{-1} Pa·s, the theoretical melting rate is almost two orders of magnitude higher than the experimentally determined rate. The importance of viscosity on the melting rate can be illustrated by comparing the melting rates of cristobalite ($T_m=1726^\circ C$)

CONSTRAINTS ON FLASH HEATING: Greenwood, J.P. and Hess, P.C.

and diopside ($T_m=1665^\circ\text{C}$). The viscosities of cristobalite and diopside liquids at the melting points are 10^6 Pa·s and 0.9 Pa·s, respectively. The experimentally determined melting rate of diopside at a superheat of 12 degrees is 1×10^5 $\mu\text{m/hr}$. Though cristobalite melts at a higher temperature, its measured melting rate at the same amount of superheat is 3.9 $\mu\text{m/hr}$. The calculated rates for diopside and cristobalite at this superheat are 7.8×10^6 $\mu\text{m/hr}$ and 2.2×10^{-1} $\mu\text{m/hr}$, respectively.

The melting rates of forsterite, enstatite, akermanite, spinel, and anorthite have been calculated at various amounts of superheat. Some examples are shown in Figure 1. The melting rates of enstatite and akermanite are almost identical to diopside because these minerals melt to liquids with viscosities in the range of 10 to 10^{-1} Pa·s, similar to diopside melt. Also, the melting rates of spinel and forsterite are almost identical. Using diopside as an example, with 20 degrees of superheat, we calculate a melting rate of 3.78 mm/s, whereas the experimentally determined rate at this superheat is 500 microns/s. Clearly, minerals such as diopside cannot be superheated for great lengths of time. The presence of relict grains in chondrules and CAI's suggests that if they were melted by a flash heating event they were probably not taken above the nominal melting point of the minerals listed above. If they were superheated, it would be for very short duration ($\ll 1$ minute). The application of melting kinetics to placing constraints on chondrule precursor grain size, temperature, and duration of flash melting events can prove fruitful. Experimental determinations of the melting kinetics of relict grains can help clarify these important questions.

REFERENCES: (1) Ainslie, N.G., et al. (1961), J. Phys. Chem. 65, 1718-1724. (2) Greenwood, J.P., Hess, P.C., unpublished. (3) Wagstaff, F.E. (1969), J. Am. Ceram. Soc. 52, 650-654. (4) Scherer, G., et al. (1970), Phys. Chem. Glasses 11, 53-58. (5) Meiling, G.S., Uhlmann, D.R. (1967), Phys. Chem. Glasses 8, 62-68. (6) Fang, C.Y. and Uhlmann, D.R. (1984), J. Noncrystalline Solids 64, 225-228. (7) Cormia, R.L., et al. (1963), J. Appl. Phys. 34, 2239-2244. (8) Vergano P.J., and Uhlmann, D.R. (1970), Phys. Chem. Glasses, 11, 39-45. (9) Kuo, L-C., Kirkpatrick, R.J. (1985), Am J. Sci. 285, 51-90. (10) Turnbull, D., Cohen, M.H., (1960), in MacKenzie, J.D., ed., Modern aspects of the vitreous state: New York, Butterworth, p. 47-50. (11) Uhlmann, D.R. (1969), in: Kinetics of Reactions in Ionic Systems, Materials Science Research Vol. 4, New York, Plenum, p.172-197. (12) Kirkpatrick, R.J. (1975), Am. Min. 60, 798-814.

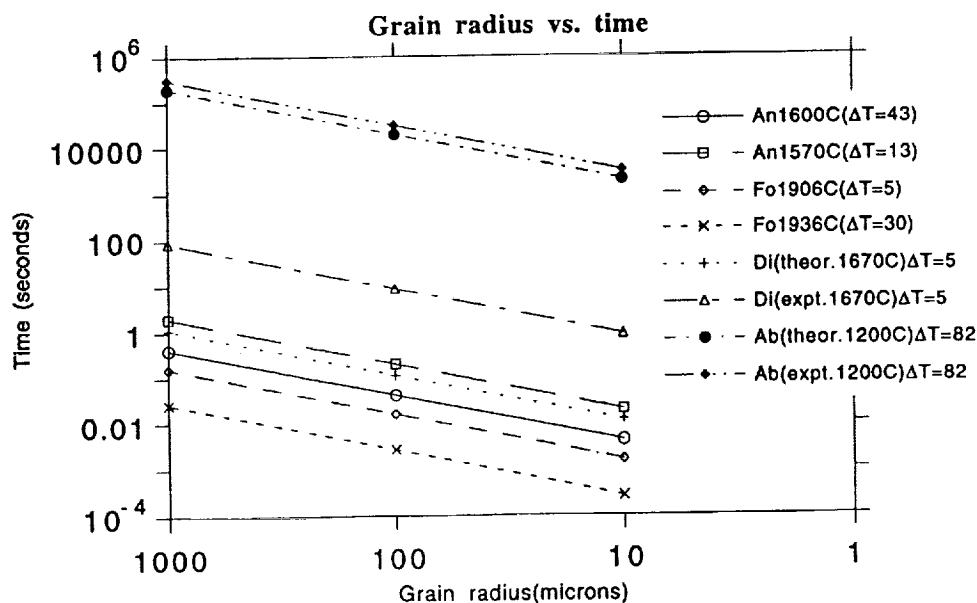


Figure 1: Melting kinetics as a function of superheat (ΔT) and grain radius.

RATIO OF FIRST AND SECOND GENERATION FOLD WAVELENGTHS ON LAVAS MAY INDICATE FLOW COMPOSITION; Tracy K.P. Gregg and Jonathan H. Fink, Department of Geology, Box 871404, Arizona State University, Tempe, AZ 85287-1404

The surface crust of an advancing lava flow will buckle transverse to the flow direction under sufficiently strong compression. Compression may be caused by an obstacle in the flow path, shear along flow margins, or by differential velocities in the downstream direction. Fold wavelength depends primarily upon the thickness and viscosity of the crust, and the viscosity of the flow interior [1]. Previous attempts to relate fold wavelength to lava composition have met with limited success [2, 3]. We have taken a different approach, focusing on the ratio of first-generation to second-generation fold wavelengths. We conclude that this ratio depends on the unique physical properties of the lava flow and surface crust, such as crystallinity, vesicularity, composition, and crustal strength and thickness.

By extruding polyethylene glycol wax (PEG) into a tank filled with cold sucrose solution, we can carefully observe the folding process. The distance from the vent at which first-generation folds appear depends primarily on eruption temperature, effusion rate, and underlying slope: the greater these parameters, the further from the vent folding takes place. Under certain conditions of sustained compression, multiple generations of folds may form. As the folded crust moves away from the vent, it cools and thickens. At some critical distance from the vent (which depends on cooling rate and flow velocity) the crust becomes too thick to accommodate additional compression by deforming into small, first-generation folds. Instead, a second generation of folds with longer wavelengths develops, superposed on the first-generation folds, appears. If compression continues as the crust thickens, a third generation may form. Alternatively, the crust may become too thick and brittle to deform in a ductile manner, and may break into a series of overriding plates.

We have examined fold wavelengths on flows of three compositions: rhyolite, basalt, and polyethylene glycol. (PEG is a commercially available wax, used in previous laboratory experiments to simulate lavas [4, 5, 6].) Comparing the wavelengths of the first (λ_1) and second (λ_2) generation folds observed in the laboratory simulations reveals a nearly constant ratio of $\lambda_2 / \lambda_1 \sim 8$. This ratio is independent of flow rate, flow temperature, underlying slope, or cooling rate. Examination of glassy rhyolite flows (e.g., Big Glass Mountain, California) reveals a ratio of fold wavelengths equal to ~ 3 . Hawaiian and Icelandic basalt flows give a ratio of wavelengths equal to ~ 5 (Figure 1).

This sequence suggests that some innate property of the lava crust--perhaps strength, which can be related to composition--limits the ratio of first- and second-generation fold wavelengths. We are currently examining surface folds on venusian and martian lava flows to determine if ratios are similar to those observed on terrestrial lava flows.

References. [1] Fink, J.H. and R.C. Fletcher (1978) *JVGR* 4, 151. [2] Fink, J.H. (1980) *Geology* 8, 250. [3] Porter, T.K. and P.H. Schultz (1990) *LPSC XXI*, 973. [4] Hallworth et al. (1987) *M. Geol.* 11, 93. [5] Fink, J.H. and R.W. Griffiths (1990) *JFM* 221, 485. [6] Griffiths, R.W. and J.H. Fink (1992) *JGR* 97, 19,739.

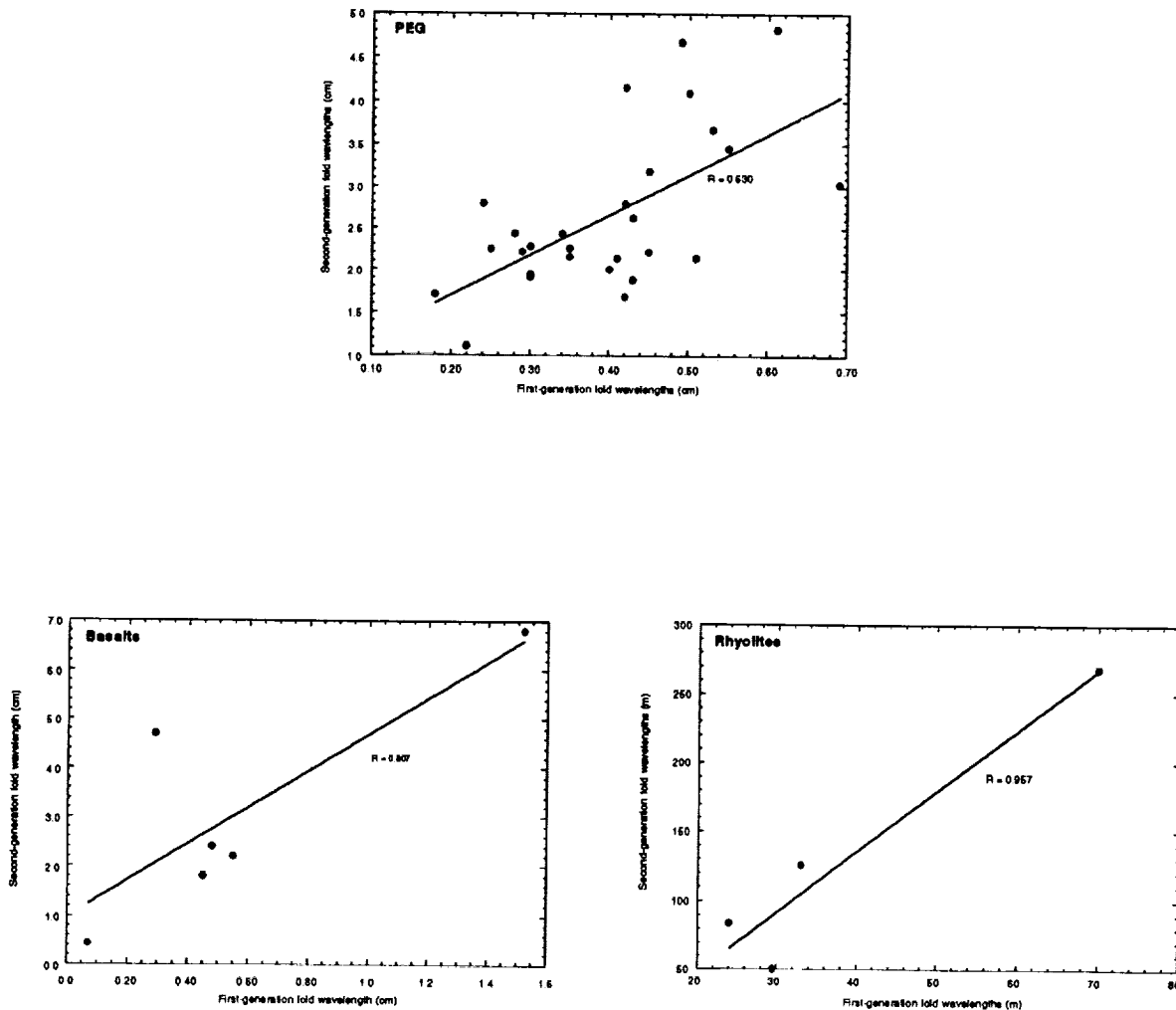


Figure 1. First and second generation fold wavelengths for basalts, rhyolites, and PEG.

$^{40}\text{Ar}/^{39}\text{Ar}$ DATING OF SAMPLES FROM THE CAT MOUNTAIN METEORITE

J.A. Grier, T.D. Swindle, D.A. Kring; Lunar and Planetary Laboratory, University of Arizona, Tucson, AZ 85721 USA.

Cat Mountain is a recently identified impact melt breccia containing shocked but unmelted L5 clasts in a completely shock-melted matrix [1]. Because less than 1% of recovered ordinary chondritic material is impact melted, this sample provides a rare opportunity to examine the collisional evolution of an asteroid. Exposure ages and dates of possible shock metamorphic events were determined for several samples. Our data appears to indicate an event affecting this meteorite at 850 Ma and perhaps another at 2700 Ma. Our calculated exposure age for Cat Mountain is about 20 Ma.

We analyzed Ne, Ar, Kr and Xe in two unirradiated samples; one each of the melt and a clast, and $^{40}\text{Ar}/^{39}\text{Ar}$ in irradiated samples of the melt and two clasts. Gases were extracted by stepwise heating in a resistance-heated double vacuum Ta furnace, and analyzed in an ion-counting VG5400 mass spectrometer. Figure 1 shows the apparent age spectrum of the melt sample. For up to 50% fraction of $^{39}\text{Ar}^*$ released, there is a good plateau in the apparent $^{40}\text{Ar}/^{39}\text{Ar}$ age at approximately 850 Ma. For higher fractions of $^{39}\text{Ar}^*$ released, the profile is consistent with diffusive loss, not surprising for a degassed melt sample. Similar to the melt sample, the clast samples (Figures 2-4) exhibit apparent $^{40}\text{Ar}/^{39}\text{Ar}$ ages with minimum values of approximately 850 Ma, for up to 50% fraction of $^{39}\text{Ar}^*$ released. Unlike the melt samples, the clast samples appear to achieve an additional plateau at approximately 2700 Ma. Although it is not unusual for L chondrites to have reset ages less than 1000 Ma, these usually fall in the 300 to 500 Ma range [2,3]. This pattern somewhat resembles the highly shocked chondrites Arapahoe (L5) and Lubbock (L5), and particularly the shock-melted Orvinio (L6) [2,4], which had minimum values from 800 to 1000 Ma, and values at higher $^{39}\text{Ar}^*$ release fractions of 3000, 2500 and 1900 Ma, respectively. The shape of the profile for these shocked chondrites has been described as "saddle-shaped". Lanphere and Dalrymple [5] concluded that "saddle-shaped" profiles such as these appear to indicated excess ^{40}Ar . Therefore minima in these profiles are usually interpreted as an upper limit for the crystallization, or in our case, shock age [2,5,6]. But other shocked samples were not paired with clearly degassed melt samples. The good plateau achieved by the Cat Mountain melt sample at approximately 850 Ma, the same age achieved by the minima in the clast samples, indicates that this may represent a meaningful event age. It is less clear whether the 2700 Ma age represents an actual event, partial resetting of phases, or perhaps excess ^{40}Ar . It is important to note that the shock veins going through the clasts may have been produced by the event at 850 Ma or an event at 2700 Ma. Continuing studies using a laser heating procedure may help distinguish which veins were created by which event.

From the unirradiated samples, we can determine cosmic ray exposure ages. Using the shielding-corrected production rates of Eugster [7], we calculate exposure ages of roughly 20 Ma for Cat Mountain (Table 1). By comparison, Orvinio has an exposure age of less than 10 Ma, while Lubbock and Arapahoe have exposure ages of 15 and 40 Ma respectively [8]. Thus Cat Mountain and Orvinio may have experienced the same shock event about 850 Ma ago, but the events that reduced them to m-sized objects were distinct.

We can construct a possible timeline for the events affecting the Cat Mountain meteorite. At 4500 Ma, chondrule formation and accretion occurred. At 2700 Ma, a shock metamorphic event may have occurred. At 850 Ma, a more energetic impact event took place, producing the impact melt breccia rock. Some time between 850 and 20 Ma ago, the material was jettisoned into space. At some other unknown time, the object containing Cat Mountain encountered an orbital resonance and was inserted into earth crossing orbit. As the Earth crossing orbit evolved, another collision at approximately 20 Ma took place, reducing the object to m-size; and finally the meteorite fell to Earth sometime in the 1980's.

$^{40}\text{Ar}/^{39}\text{Ar}$ DATING OF CAT MOUNTAIN METEORITE - J.A. Grier, T.D. Swindle, D.A. Kring

FIGURE 1 - 12B MELT SAMPLE

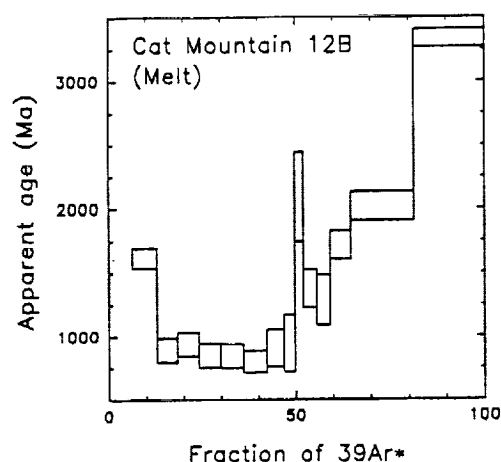


FIGURE 2 - 12D CLAST #2 SAMPLE

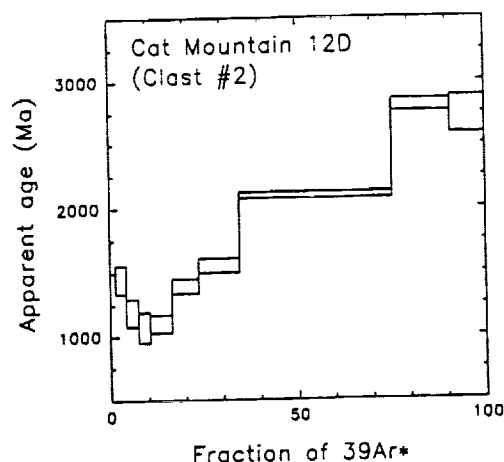


FIGURE 3 - 11B CLAST #1 SAMPLE

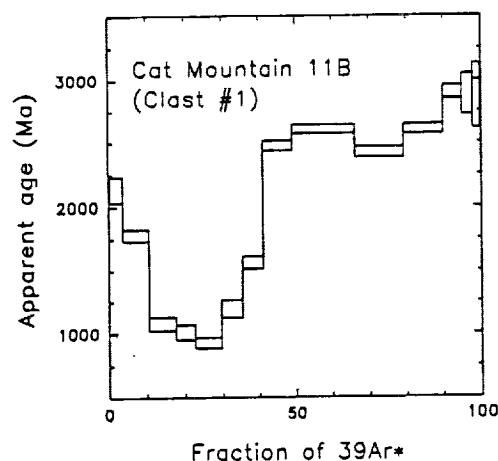


FIGURE 4 - 11C CLAST #1 SAMPLE

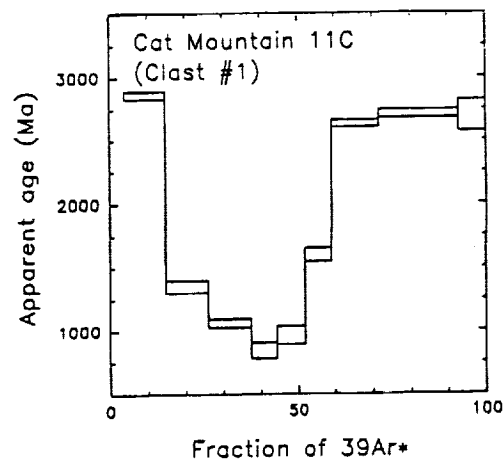


TABLE 1 - COSMIC RAY EXPOSURE AGES (Ma)

	T_3	T_{21}	T_{38}	T_{83}	T_{126}
Cat Mountain					
11A Clast #1			14.9	28.6	22.1
12A Melt		21.5	17.4	30.7	20.7
Arapahoe	50.2	41.4	40.1		
Lubbock	11.8	14.1	14.2		
Orvinio	5.7	6.0	6.5		

Cat Mountain from this study. Other data from [8]. Production rates from [7].

REFERENCES: [1] D. Kring (1993) *LPSC XXIV* 823; [2] D. Bogard and W. Hirsh (1980) *GCA* 44 1667; [3] G. Turner (1968) *Meteorite Research* (ed. Millman) 407; [4] M. Caffee et al. (1982) *LPSC Proc. 13th. JGR Supp.* 87 A318; [5] M. Lanphere and G. Dalrymple (1976) *Earth Planet Sci. Lett* 32 141; [6] R. Bottomly, D. York, R. Grieve (1990) *LPSC Proc. 20th* 421; [7] O. Eugster (1988) *GCA* 52 1649; [8] D. Heymann (1967) *Icarus* 6 189.

THE SUDBURY STRUCTURE: ADDITIONAL CONSTRAINTS ON ITS ORIGIN AND EVOLUTION; R. A. F. Grieve, Geological Survey of Canada and Institut für Planetologie, Munster, A. Deutsch, Institut für Planetologie, Munster, Germany, D-48149

The occurrence of shock metamorphic effects indicate an impact origin for the Sudbury Structure but the existence of the Sudbury Igneous Complex (SIC) and its non-circularity have posed problems for a simple impact origin and combined impact-magmatic models have been proposed (1,2,3). Recent studies have led to the suggestion that the SIC is part of a coherent impact melt sheet contained within a tectonised and eroded impact basin, which was originally ~ 200 km in diameter (e.g., 4,5). Most recently, the results of geophysical and allied structural studies, as part of the LITHOPROBE program, indicate that the SIC is, indeed, continuous beneath the Sudbury Basin (6) and there are no structures or bodies at depth (7), as would be expected for a feeder system for magmatism. They also indicate considerable NW shortening and that the SIC could have been originally circular (8,9). These results are consistent with the impact model (4,5) but suggest that the original diameter may have been as large as 250 km.

There is often a basic misunderstanding, which is still perpetuated (e.g., 10), on what constitutes the Sudbury Structure. It covers an area of > 15,000 km² and is not synonymous with the SIC. Formations related to the Sudbury Structure occur up to 80 km outside the SIC. Details of the recent comprehensive impact model can be found in (4,5) and can be summarised as: all breccia and "melt" formations can be explained by impact, and there is no chemical or physical reason for a magmatic component to formations directly linked to the formation of the Sudbury Structure. Beginning in 1991, a series of geophysical and associated studies were initiated across the SIC and the interior Sudbury Basin, as part of the LITHOPROBE program. Phase one is now complete and these independent results are to be published in an up-coming edition of GRL. Their implications for the impact model are summarised below.

Original shape It has been argued that the non-circularity of the SIC, and by implication the Sudbury Structure, is the greatest drawback to the impact interpretation (2). Reflection seismic data along a N-S traverse across the SIC indicate that it has been highly tectonised in the south and subjected to NW thrusting (6). This occurred following a period of ductile deformation and folding in the same direction (9). Thus, the present configuration of the SIC (Fig 1) has only indirect bearing on the original shape of the Sudbury Structure; although it is featured prominently in one recent impact model (10). Furthermore, pre-deformation reconstruction of the potential field anomaly patterns due to the SIC by removing a simple NW-directed stress field indicate that they were originally circular (8).

Subsurface characteristics Reflection seismic data, constrained by drill hole data, indicate that the North Range of the SIC dips 20° - 30° to the south as a coherent sheet under the Sudbury Basin (6). There is no indication of a magmatic feeder system (Fig 1). Similarly, reinterpretation of new and previous potential field data indicate no need for a "hidden mass" (11) of mafic-ultramafic material beneath the SIC, which in magmatic models (Fig. 1) was related to flanking intrusions associated with the SIC magma (2). The potential field anomalies can be explained by surface lithologies constrained at depth by the seismic data (7). Thus, except where tectonically disrupted in the south, the geophysical data indicate the SIC as a coherent sheet thickening towards the center, as would be expected in the impact model (4,5).

Original dimensions Previous estimates of the original dimensions of the Sudbury

THE SUDBURY STRUCTURE: Grieve, R. A. F. and Deutsch A.

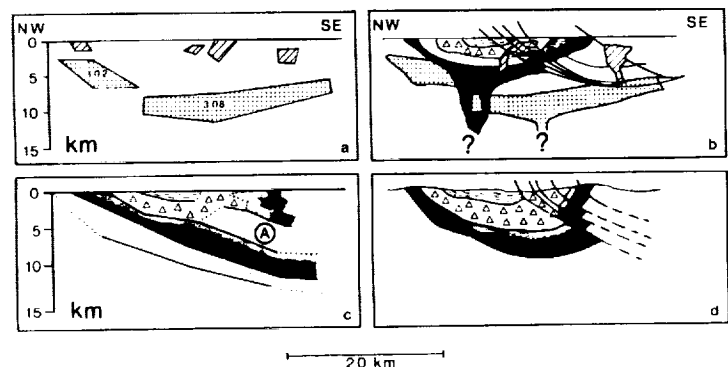
Structure were based on the radial distribution of various attributes, e. g., shock metamorphic features, dike breccias, with respect to the center of the structure, assumed to be the center of the Sudbury Basin interior to the SIC (4,5). These estimates depend strongly on the original diameter of the SIC, which was assumed to be 60 km. The present dimensions are 60 x 30 km and the seismic data suggest that there has been 50% shortening in a generally NW direction due to thrusting during the Penokean orogeny (6). This is a minimum, as the seismic data only imaged brittle deformation. The deconvolution of the potential field anomaly pattern (8) and the recent work on the extent of ductile deformation following the formation of the SIC (9,12) suggest that the SIC may have been 75 -80 km in diameter. This would revise these previous estimates of the original diameter of the Sudbury Structure up to 250 km or greater. That the effects of the Penokean orogeny extend further north than indicated by the seismic data alone is also suggested by the occurrence of reset Ar-Ar ages in some Sudbury Breccias up to 30 km north of the SIC (13).

Structural position of the South Range The NW thrusting of the southern portion of the Sudbury Structure indicates that the South Range of the SIC represents a deeper structural level than the North Range (Fig. 1). This is consistent with it being thicker, its greater range of in situ differentiation products (2) and with the rarity of Footwall Breccia compared to the North Range (2,14). At large impact structures, the basal breccia that floors coherent impact melt sheets is often missing below more central exposures of impact melt, having been eroded by the impact melt as it is driven downward and outward along the floor of the expanding transient cavity (15).

Concluding remarks The LITHOPROBE results have highlighted the tectonic evolution of the SIC and its environs and produced a three dimensional view that is consistent with previous impact models for the Sudbury Structure (4,5); although, perhaps favoring some what larger original dimensions. Previously, we have emphasised the implications of the SIC as part of an impact melt sheet for the interpretation of samples from the lunar highlands (4). It would also now appear that the Sudbury Structure has potential lessons for the recognition of impact structures on Venus, where both impact cratering and lateral tectonic processes have occurred.

REFERENCES (1) French, B. M. (1969) Bull. Vol., XXXIV, 466. (2) Naldrett, A. J. (1984) Ont. Geol. Surv. Sp. Paper 1, 533. (3) Norman, M. D. (1994) GSA Sp. Paper (in press). (4) Grieve, R. A. F. et al. (1991) JGR, 96, 753. (5) Stoffer, D. et al. (1994) GSA Sp. Paper (in press). (6) Milkereit, B. et al. (1992) Geology, 20, 807. (7) McGrath, P. H. and Broome, H. J. (1994) GRL (in press). (8) Roest, W. R. and Pilkington, M. (1994) GRL (in press). (9) Cowan, E. J. and Schwerdtner, W. M. (1994) Ont. Geol. Surv. Sp. Paper (in press) (10) Lowman, P. D. (1992) Rev. Geo., 30, 227. (11) Gupta, V. K. et al. (1984) Ont. Geol. Surv. Sp. Paper 1, 381. (12) Hirt, A. M. et al. (1993) Tectonophysics, 225, 231. (13) Thompson, L. M. et al (1993) EOS, 74, no.43, 389. (14) Dressler, B. (1984) Ont. Geol. Surv. Sp. Paper 1, 97. (15) Simonds, C. H. and Kieffer, S. W. (1993) JGR, 98, 14321.

Fig 1. (a) Subsurface model of SIC and its environs prior to the results of LITHOPROBE. (b) Geologic model of (a), with black being the SIC, stippled being hidden, related intrusions, dashes being the Onwatin and Chelmsford and the triangles the Onaping. (c) Post LITHOPROBE subsurface view, with symbols as in (b). "A" is an ambiguous zone of thickened units in the seismic data. (d) Geologic model of SIC as a tectonically



WANAPITEI IMPACT STRUCTURE: RECONSTRUCTION OF THE EVENT; R.A.F. Grieve, Geological Survey of Canada and Institut für Planetologie, Univ. Münster, and T. Ber, Univ. Ottawa, Canada.

The ~ 7.5 km diameter Wanapitei impact structure (46°45'N; 80°45'W) lies entirely within Lake Wanapitei in central Ontario, Canada. Impact lithologies are known only from glacial float samples. They consist of >50% suevite breccias, <20% glassy impact melt rocks, <20% highly shocked target lithologies, and <5% impact glass breccias, which may represent original fall-back material. The major element composition of the impact melt rocks can be modelled as a geologically reasonable mix of specific target lithologies. The melt rocks fall into two textural and mineralogical types, which also differ in their degree of meteoritic contamination. This begs the question of whether they would be recognized as coming from a single event if they were recovered from a situation with less geological control, as exists for extraterrestrial samples of impact melt rocks.

The potential target rocks at Wanapitei consist of Huronian meta-sediments of the Gowganda, Serpent, Espanola, Bruce, and Mississagi Formations (mostly arkosic quartzites and wackes), overlying Archean granite - greenstone and cut by Nipissing Intrusives [1]. Impact lithologies occur in glacial till at the south end of the lake [2]. From the till only lithologies with shock metamorphic effects could be assigned to having come from within the structure. From the examination of ~ 150 thin sections showing evidence of shock metamorphism, the recovered impact lithologies can be subdivided into:

1. Suevite breccias Lithic clasts show a range of shock features up to partial vitrification and constitute up to 40% by volume. They are Huronian meta-sediments and subordinate Nipissing Intrusives. No unequivocal Archean clasts were observed. Glass fragments contain vesicles and clastic debris and make up to 15%. They show a wide range of optical homogeneity but even when homogeneous contain areas corresponding to SiO_2 . Their bulk composition is, however, relatively constant and corresponds to no specific target lithology. The overall composition of the suevite breccias is variable, depending on clast content.
2. Highly shocked meta-sediments They are partially vitrified and vesiculated, with a density of ~ 2 g cm^{-3} , and can contain coesite [3]. They appear to be of a single lithology and correspond chemically most closely to the Mississagi Formation (Table 1). They occur as single cobbles but the presence of equivalent material as lithic clasts in the suevite breccias suggests that they too originated as large clasts in suevite.
3. Glass breccias These are relatively rare and resemble suevite breccias, except they contain up to 50% glass clasts and lithic clasts are dominated by highly shocked varieties. Their matrix is extremely fine grained and contains glass particles. They may represent samples of fallback material.
4. Impact melt rocks There are two variants. One has a colorless glass matrix, which may show perlitic fracturing. It contains ~ 5% round vesicles, up to ~ 25% mineral and rare lithic clasts, and microlites of hypersthene up to 1.0 mm long and containing up to 11.5% Al_2O_3 . The second consists of brown or mixed glass with ~ 15% elongate vesicles, up to 30% mineral and lithic clasts defining schlieren, and tabular crystals of hypersthene up to 0.05 mm with up to only 2% Al_2O_3 . Although there is abundant evidence of flow prior to solidification, the tabular hypersthene is randomly oriented. Both variants have similar major element bulk compositions (Table 1). Like the glasses in the suevite breccias, they have areas in the matrix corresponding to pure SiO_2 , which represent most likely ghost lechatelierite inclusions preserved because of the high SiO_2 content and high viscosity of the melt (Table 1) and the rapid chilling. The differences between the two variants is ascribed to different cooling histories, with the low Al_2O_3 hypersthene believed to have crystallized after the melt had quenched to a supercooled glass [4] that was then held at elevated temperature within the crater filling lithologies.

Reconstruction of the impact event The lithic clasts in the suevite indicate that only Huronian and Nipissing lithologies were within the transient cavity. This is consistent with the super-position of a transient cavity of ~ 5 km [5] on the present outcrop pattern extended across the Lake Wanapitei. The identification of the highly shocked meta-sediments as Mississagi restricts impact melting to lithologies stratigraphically higher than the Mississagi. Mixing models of the major element composition of the impact melt rocks (Table 1) suggest that they can be modelled as ~ 46% Gowganda, ~ 46% Serpent, and ~ 8% Nipissing. This is also generally consistent with the extrapolated outcrop pattern. Assuming the highly shocked meta-sediments are Mississagi, it begs the question of why the intervening Espanola and Bruce Formations were

WANAPITEI IMPACT STRUCTURE: Grieve, R.A.F. and Ber, T.

not within the zone melted. The Espanola is a calcareous siltstone and only one clast of such a lithology was observed in the suevite breccias. This would appear to confirm the most obvious explanation; namely, that these units thin dramatically along strike across the lake [1] and they were not a component of the target volume. Using the mixing model to correct for indigenous components, the Ni/Cr, Ni/Co, and Cr/Co ratios of the two impact melt rock types are 3-3.8, 15-20, and 5-5.2, respectively. These are similar to chondritic ratios and support previous interpretations based on siderophile [6] and PGE abundances [7] that suggest a chondritic impactor. The amount of meteoritic contamination in the impact melt rock with the tabular hypersthene, however, is a factor of five higher. Whether this difference in some trace elements and different mineral chemistry would be sufficient to erroneously ascribe these melt rocks to more than one impact event, in the absence of geological control [8], is a moot point. It does underscore, however, that not all the experiences gained in the study of large coherent impact melt sheets, e.g., [9], can be applied without caveat to smaller impact events.

Table 1. Chemistry of some lithologies at Wanapitei.

	1	2	3	4	5	6
SiO ₂	84.9	86.9	74.1	76.3	74.8	75.1
TiO ₂	0.07	0.10	0.19	0.20	0.20	0.27
Al ₂ O ₃	7.3	6.9	12.3	10.8	11.6	11.7
Fe ₂ O ₃	0.5	0.4	0.6	0.6	--	--
FeO	0.6	0.5	1.3	1.8	*2.3	*2.8
MnO	0.01	0.00	0.02	0.03	--	--
MgO	0.6	0.4	1.0	1.8	1.6	1.6
CaO	0.2	0.2	0.8	1.3	1.3	1.2
Na ₂ O	1.1	2.4	2.9	1.8	2.3	2.3
K ₂ O	1.7	1.7	2.8	2.3	2.5	2.6
H ₂ O	2.7	0.25	3.2	2.5	--	--
Total	99.68	99.75	99.21	99.43		

1. Average highly shocked and partially vitrified meta-sediments.
 2. Average Mississagi Formation, 3. Average impact melt rocks with high Al-hypersthene. 4. Average impact melt rocks with low Al-hypersthene. 5. Average all impact melt rocks. 6. Calculated impact melt rock from mixing model (see text). *All Fe as FeO.

- REFERENCES.** [1] Dressler, B.O. (1982) Ont. Geol. Surv. Rpt., 213, 131 p. [2] Dence, M.R. and Popelar, J. (1972) Geol. Assoc. Can. Sp. Pap. 10, 117. [3] Dence, M.R. et al. (1974) EPSL, 22, 118. [4] Grove, T.L. and Raudsepp, M. (1978) PLPSC 9th, 585. [5] Croft, S.K. (1985) PLPSC 15th, 828. [6] Wolf, S. et al. (1980) GCA, 44, 1015. [7] Evans, N.J. et al. (1993), CGA, 57, 3737. [8] Ryder, G. and Spudis, P.D. (1987) PLPSC 17th, 432. [9] Grieve, R.A.F. et al. (1977) Impact and Explosion Cratering, Pergamon, 791.

Mars - It's What's Inside That Counts: Laura L. Griffith and Raymond E. Arvidson, McDonnell Center for the Space Sciences, Department of Earth and Planetary Sciences, Washington University, St. Louis, MO 63130.

Spectral reflectance and emittance data covering the surface of Mars suggest a planet with basaltic bedrock covered with ferric-rich weathering products and only a few percent of carbonate material. This view of the surface may be biased by photo-oxidation and other weathering effects and thus may not be representative of the textural or mineralogical character of the crust. Hydrothermal alteration of the upper few kilometers of the crust may be widespread and may have occurred globally, even when surface temperatures were below the triple point of water. The main driving forces for the hydrothermal system would have been shallow intrusive and extrusive magmatic events. Extensive hydrothermal activity would have altered the properties of the upper crust and created subsurface reservoirs of volatile species, including carbonates. Physical and chemical modeling of hydrothermal systems on Mars provide predictions as to the nature and locations of altered crustal sections and suggestions as to where to make observations to test the hypothesis.

What is typically seen of Mars with imaging cameras, infrared instruments, radar, and even the Viking Lander *in situ* analyses necessarily involves aeolian sediment, local debris, and whatever bedrock is exposed. From various spectra (ISM [1], Mariner 9, IRIS [2], and ground-based [3]) the presence of ferric oxide or oxyhydroxide coverings or coatings on basalt is inferred. Ground-based spectra have also been used to deduce the presence of scapolites [4] and predict an upper limit of 10 - 15% of sulfates and carbonates in the airborne dust [5]. It has been estimated that 10 - 20 bars of CO₂ should have been outgassed by Mars; this amount of CO₂ is about equivalent to 225 - 450 m of calcium carbonate [6]. This CO₂ is in the polar caps, adsorbed onto the regolith, and in the atmosphere, but these reservoirs do not account for all the CO₂.

Kasting [7] has suggested that the martian surface temperature did not surpass the water triple point (i.e. 273 K) because CO₂ condensation in the upper atmosphere lowered the thermal gradient. In the absence of greenhouse gases other than CO₂ (e.g. SO₂), this result implies that rainfall and runoff were negligible. It has further been suggested that regional hydrothermal activity, instead of rainfall and runoff, was responsible for the runoff channels in at least the Hecates Tholus and Alba Patera regions [8]. Global hydrothermal alteration has also been sited for the "uniform" depth (~ 1 - 2 km) of erosion found at many scarp faces [9]. We propose that there has been extensive global hydrothermal activity on Mars that has affected the physical and chemical properties of the upper crust, even though rainfall and runoff did not necessarily occur on a global basis. Indeed, hydrothermal activity is a natural process accompanying intrusive and extrusive volcanism, both of which have occurred on Mars [10].

On Earth it is known that many hydrothermal circulation systems effect and alter their host rocks down to at least 2 km [11]. In most of these hydrothermal systems, calcite and/or aragonite and other carbonates are deposited along subterranean flow channels. Deposition occurs regardless of whether the hydrothermal water comes into contact with carbonate bearing rocks; in other words, the carbonate source constituents can be basalt or other volcanic rocks [11]. Greater than 15 wt% of altered volcanic rock may end up as carbonate [12]. Also, carbonaceous chondrite parent body alteration models have been run where the entire planetesimal is altered (up to ~ 35 km) [13]. These models, which start with a pseudo-basaltic composition (mostly olivine and pyroxene) and end up agreeing with meteorite mineralogies, also produce carbonates in a variety of Eh-pH and temperature regimes: Eh: -0.5 - -7.5 V, pH: 7 - >12, T: 1° - 150°C [14]. Volatiles other than carbon can also be sequestered in alteration phases [11]. If SNC's are assumed to be of martian origin, then fracturing and veining actually has occurred on Mars, since SNC's exhibit calcite and

Mars - It's What's Inside That Counts: L.L. Griffith and R.E. Arvidson

sulfate veins [15].

In our conceptual model three related heat sources are considered as forcing mechanisms: extrusive volcanism, intrusive magmatic emplacement, and an overall higher thermal gradient earlier in geologic time [16]. A frozen surface is assumed as a boundary condition. Thus, it is possible that carbonate and other volatile deposition have occurred in relatively large subterranean veins and not lakes, sequestering the carbonates along with other volatiles mostly below the surface. Frozen boundary conditions are also used in meteorite parent body circulation models [13], suggesting circulation patterns would be similar between the two models on regional scales. With a fixed amount of available fluid and the decreased porosity with depth (due to overburden pressure), the circulating systems would only be able to alter the crust to depths of several kilometers. Competing factors of available fluid, pressure, and porosity will be fairly uniform over the planet; therefore, planet-wide, a common base level of alteration would develop. This base level would explain the roughly uniform erosion depth observed in the fretted terrains [17]. In addition, variations in topography and magmatism will lead to regional-scale circulation systems and changes in physical and chemical properties of the crust. Consider a system in which aqueous fluids are in circulation away from an intrusion. Circulation patterns will be governed by the topography and local thermal characteristics. Fluids initially undersaturated with respect to carbonates might become saturated at a temperature $\sim 150^{\circ}\text{C}$ when the pH is ~ 7 and the Eh is ~ -0.4 V. At lower temperatures, $\sim 25^{\circ}\text{C}$, (further from the heat source) a wider range of pH is allowable for carbonate saturation, $\sim 7.5 - \sim 9.5$, along with Eh values between -0.5 and -0.75 V [14].

We are currently pursuing coupled physical and chemical modeling of hydrothermal systems on Mars, using 2D ground water flow and the EQ3/6 algorithm [18] to compute ionic concentrations and saturation states. The intent is to predict the nature and locations of hydrothermal products under a variety of topographic and heat source geometries and magnitudes. The predictions will also serve to focus attention on key areas on Mars to observe with the Gamma Ray Spectrometer and Thermal Emission Spectra, assuming a reflight of Mars Observer or another orbiter or orbiters. For example, the walls and interior layered deposits of Valles Marineris are prime candidates for exploring this hypothesis. These areas offer several advantages over areas of the planet: a) they are in an area where volcanism has been extensive, b) the canyon walls expose crustal sections, c) the interior layered deposits have various properties, including texture, topography, and coloration, which might be explainable by hydrothermal alteration, and d) the fretted terrain in the eastern end of the canyon shows features suggestive of fluvial activity.

- [1] Murchie, S. and J. Mustard (1992) LPSC XXIV, 1027-1028. [2] Hanel et al (1972) *Icarus*, **17**, 423-442. [3] Singer, R.B. (1982) *JGR*, **87**, 10159-10168. [4] Clark et al (1990) *JGR*, **95**, 14463-14480. [5] Pollack et al (1990) *JGR*, **95**, 14595-14627. [6] Carr, M.H. (1986) *Icarus*, **68**, 187-216. [7] Kasting, J.F. (1991) *Icarus*, **94**, 1-13. [8] Gulick, V.C. and V.R. Baker (1991) LPSC XXIII, 463-464. [9] Soderblom, L.A. and D.B. Wenner (1978) *Icarus*, **34**, 622-637. [10] Greeley, R. and Schneid, B.D. (1991) *Science*, **254**, 996-998. [11] Ellis, A.J. and W.A.J. Mahon (1977) *Chemistry and Geothermal Systems*. Academic Press: N.Y. [12] Fouillac et al (1989) *Chem. Geo.*, **76**, 271-289. [13] Grimm, R.E. and H.Y. McSween, Jr. (1989) *Icarus*, **82**, 244-280. [14] Zolinsky et al (1989) *Icarus*, **78**, 411-425. [15] Gooding, J.L. (1992) *Icarus*, **99**, 28-41. [16] Squyres (1989) 4th International Mars Conference. [17] Blasius et al (1977) *JGR*, **82**, 4067-4091. [18] Wolery, T.J. (1979) *Calculation of Chemical Equilibrium Between Aqueous Solution and Minerals: The EQ3/6 Software Package*. Lawrence Livermore Laboratory.

PROPOSAL FOR A TOPOGRAPHIC SURVEY OF GUSEV CRATER; E.A Grin, N.A Cabrol, Observatoire de Meudon France, G. Dawidowicz, Univ. Paris I France

The Gusev crater is considered as a high priority site for exobiology experiments for the future martian missions. In this perspective, the knowledge of the local relief appears of main importance. This survey uses the existant data and points out the local topography of the crater.

Data basis. The basic data used for the topographic study of the Gusev crater are :

- 1'- the topographic map of the Aeolis southeast quadrangle (MC-23SE) of the Atlas of Mars 1:2M, topographic series M2M-22/191T/, 1991 ;
- 2'- the Goldstone 1-13cm radar scan profile -14.89°, 10 aug.71, 0.376 Au (Roth et al., 1989) ;
- 3'- controlled photomosaics of the MTM-15182 quadrangle Ma'adim vallis region of Mars ;
- 4'- orthographic Viking Orbiter (VO) pictures of nominal image resolution from 68 to 71 meters per pixel.

Contours and elevation profiles. Contours were compiled on the topographic map MC-23SE and the controlled photomosaics maps I-2256 and I-2257 at 1:500,000 scale. Horizontal and vertical controls were established by the radar scan elevation profile. Additional detailed shadow length interpretation based on the VO pictures were used for specific areas near Ma'adim vallis outlet for the improvement of the basic topographic datum. Contour interval is 1000 meters. Estimated accuracy is approximatively one contour interval, with exception of the interpretation of radar scan elevation data, where a 200 meters accuracy is allowed.

The radar scan -14.89° aug.71 0.376 Au (Roth et al., 1989) was redrawn after its horizontal and vertical localization on the topographic map and labelled [RS]. A NE/SW elevation profile [AB] was compiled on the topographic map and correlated with the radar scan profile. These two elevation profiles show an inclined crater floor tilted east-westward, with a slope of less than .05 km/km (3'), and also tilted southeast/northwest, the lowest elevation being localised in the northwest side.

Discussion. During the process of compilation, the morphological map was used for contouring the rampart features of the Gusev crater. The final topographic contour map produced to illustrate the crater Gusev is compiled by using the above mentioned data. The results from the topographic map show that the Gusev crater floor is inclined towards the east highest rim. The west rim is less than 400 meters above the level of the surrounding plains. A 30 km young crater is superimposed on the south rim and give an elevated outlet to Ma'adim vallis. The elevation of the outlet is 1000 meters above the deepest point of the crater floor. The NW rim is obliterated by a 40 km diameter young crater. The Gusev crater rim which is lower in this section is deeply eroded at an approximative 1000 meters elevation. The results of this topography study -which could be reviewed by further topographic details from future missions- show the strong structural asymetry of the Gusev crater.

Implications of the topography for the crater history. The east rim is nearly 2400 meters above the level of the deepest point and only 400 meters above the surrounding plateau. On the north, the Gusev crater floor

TOPOGRAPHY OF GUSEV CRATER; E.A Grin, N.A Cabrol, G. Dawidowicz.

is 1000 meters below the crest level, when on the east, this floor is 2400 meters below the crest level. These results are in accordance with the localization of the crater on the highlands/lowlands boundary. But, the double-tilt of the crater floor appears more associated with the distribution of materials that constitute the floor than with its asymmetric location. The topography of the floor is consistent with episodic filling of various material (see Cabrol et al., 1994, and Landheim et al., 1994, this issue).

The outlet of Ma'adim vallis through the southern rim implies a water filling of the crater by fluvial activity. Considering the elevation of the northwest rim, and the level of the outlet of Ma'adim vallis, a lake may have been a local phenomenon related to the filling by Ma'adim vallis' flows, until the overtopping of the lowest northwest rim given an elevation of the lake surface of about 1000 meters.

The transections [RS] and [AB] cross each other near the center of the crater and may be used for a valuable illustration of the upper stratigraphy. Although the overlapping is delimited by photomosaics interpretation, the thickness of the deposits of the layers are more speculative. Meanwhile, two characteristic features of the cover of the Gusev crater bottom floor has been estimated by deduction based -one on measurements (Roth et al., 1989), the other by volume estimation of material deposition (Goldspiel and Squyres, 1991). A third type of information was used in the sketching of the deposit layers corresponding to episodic activity of Ma'adim vallis as underlined by Schneeberger (1989), Cabrol et al., (1993), Cabrol et al., (1994, *same issue*), Landheim et al., *same issue* (1994).

References.

Cabrol et al., *submitted to Icarus*, Cabrol et al., (1993), LPSC XXIV, Cabrol et al., (1994) *submitted to XXV LPSC*, Goldspiel and Squyres, (1991) *Icarus* 89 pp 392-410, Landheim et al., *submitted to XXV LPSC*, Roth et al., (1989), *Icarus* 79, pp 289-310 ; Schneeberger, (1989) LPSC XX

DIKE EMPLACEMENT AT ZONES OF NEUTRAL BUOYANCY ON VENUS.

Eric B. Grosfils & James W. Head, Dept. Geological Sci., Brown University, Providence, R.I. 02906

Overview: On the basis of their structure, plan view geometry and volcanic associations, we have interpreted formation of 118 large, radially lineated structures on Venus to occur in part through subsurface dike injection¹. On Earth, radiating dike swarms (irrespective of scale) are frequently emplaced laterally about a centralized magma reservoir located near the surface². Theoretically derived neutral buoyancy calculations for Venus³ predict an altitude-dependent distribution of magma reservoirs which is matched by observations of dike swarms across approximately 90% of the planet's surface; only those highland regions whose elevations exceed 6053 km appear anomalous. Previous analysis of the large volcano population yielded similar results⁴, and comparison between the dike swarm (intrusive) and large volcano (extrusive) populations supports the contention that depth to the level of neutral buoyancy increases systematically at altitudes above 6051 km. This suggests that, as observed on Earth, neutral buoyancy plays an important role in governing volcanic processes near the venusian surface, often facilitating radially configured lateral dike emplacement about shallow magma reservoirs.

Theory: Head and Wilson [1992] have proposed that the process of magma reservoir formation on Venus, and thus the development of related volcanic phenomenon such as dike swarms (intrusive) and volcanoes (extrusive), is controlled in part by neutral buoyancy. According to their calculations, high atmospheric pressure at low elevations (planetary radii <6051 km) minimizes volatile exsolution within ascending magma, and thus rock formed when this material erupts and cools will remain dense relative to the density of subsequent magma intrusions, inhibiting the development of neutral buoyancy zones and promoting continued surface eruption. At intermediate elevations (6051-6053 km) the relative decrease in atmospheric pressure permits volatile exsolution and subsequent formation of lower density vesicular rock at the surface. As layers of this material accumulate the resultant low density "cap" makes it increasingly difficult for buoyantly rising magma to reach the surface, and eventually magma will begin to stall within the substrate at a depth of neutral buoyancy. For magma of a given volatile content, the depth to this level of neutral buoyancy increases with elevation. This, in turn, has been shown to facilitate magma reservoir growth and lateral dike emplacement⁵. There should, therefore, be a gradual transition from extrusion- to intrusion-dominated volcanism as one progresses from intermediate to upper (>6053 km) elevations.

Observations: We tested the neutral buoyancy predictions by comparing the distribution of features interpreted to represent dike swarms¹ as a function of elevation with that expected if the population simply reflects the amount of surface area occurring at a given altitude (Figure 1). If swarms are uniformly distributed as a function of surface area, then approximately 12% should lie below a planetary radius of 6051 km, 79% should fall between 6051-6053 km, and the remaining 9% should be located at elevations >6053 km. The observed distribution, however, reveals no swarms located below 6051 km, 92% located between 6051-6053 km, and the remaining 8% at elevations >6053 km. A χ^2 test indicates a greater than 99% probability that the expected (uniformly distributed) and observed dike swarm populations are statistically different, with the greatest difference occurring from 6052-6053 km.

Discussion: The absence of dike swarms below 6051 km is predicted by the neutral buoyancy model since reservoir formation within the substrate, and thus intrusive volcanism, should be difficult to achieve at these altitudes. Those few reservoirs which do manage to form because of a particularly high magma volatile content, however, should do so very near the surface, a condition favoring the production of volcanoes or other extrusive products (as observed) rather than dike swarms in response to reservoir overpressurization.

At intermediate elevations, the enhanced concentration of dike swarms and large volcanoes⁴ suggests that magma frequently stalls to produce reservoirs, again in agreement with

DIKE EMPLACEMENT ON VENUS: E. B. Grosfils & J. W. Head

the neutral buoyancy model predictions. Conditions here should generally favor reservoir development within the upper several kilometers of the crust. Comparison between the distribution of large volcanoes and radiating dike swarms suggests that a transition from extrusive to intrusive reservoir volcanism occurs in this elevation range. At lower intermediate altitudes (~6051-6052 km), extrusive magmatism and volcano production is favored over dike swarm emplacement. At upper intermediate altitudes (~6052-6053 km), however, the formation of radial dike swarms clearly becomes predominant. This suggests that the depth to the magma reservoir, and thus the probability of an intrusive response to overpressurization, increases with elevation as predicted.

At elevations exceeding 6053 km the increased depth to the level of neutral buoyancy should continue to enhance magma reservoir formation and strongly facilitate an intrusive rather than extrusive response to reservoir overpressurization. The distribution of dike swarms observed resembles that expected if their occurrence simply reflects the available surface area, however, and a similar number of large volcanoes occur, suggesting that lateral dike intrusion is not favored over surface eruption. This implies that site-specific factors in addition to altitude-dependent pressure may govern magma behavior in many elevated areas on Venus. One way this could be accomplished is through mantle downwelling⁶: crustal thickening via ductile flow elevates higher density rock, formed through eruption at relatively low altitudes, to heights where low density (highly vesicular) rock would otherwise be expected to occur. The greater than expected density of the surface rock, therefore, would promote shallower magma chamber formation as observed at low and intermediate altitudes. Since elevated regions typically consist of heavily deformed highlands such as Aphrodite and Ishtar Terra, however, void production through spatially inhomogeneous fracturing or other site-specific processes may produce lateral density variations which modify the depth to the level of neutral buoyancy, thus affecting subsequent intrusive versus extrusive responses to reservoir overpressurization. Future consideration of reservoir development and evolution in highland areas across the planet should take into account the local geologic environment, and should provide additional insight into the neutral buoyancy mechanism which appears to satisfactorily account for the observed dike swarm (and large volcano) distribution across the remaining 90% of the venusian surface.

References: 1. Grosfils, E.B. & Head, J.W., *LPSC XXV* (this vol). 2. Halls, H.C., *GACSP v.34*, 483-492 (1987). 3. Head, J.W. & Wilson, L., *JGR v.97*, 3877-3903 (1992). 4. Keddie, S.T. & Head, J.W., *LPSC XXIV* 773-774 (1992). 5. Parfitt, E.A., *et al.*, *JVGR v.55*, 1-14 (1993). 6. Bindshadler, D.L., *et al.*, *JGR v.97*, 13563-13579 (1992).

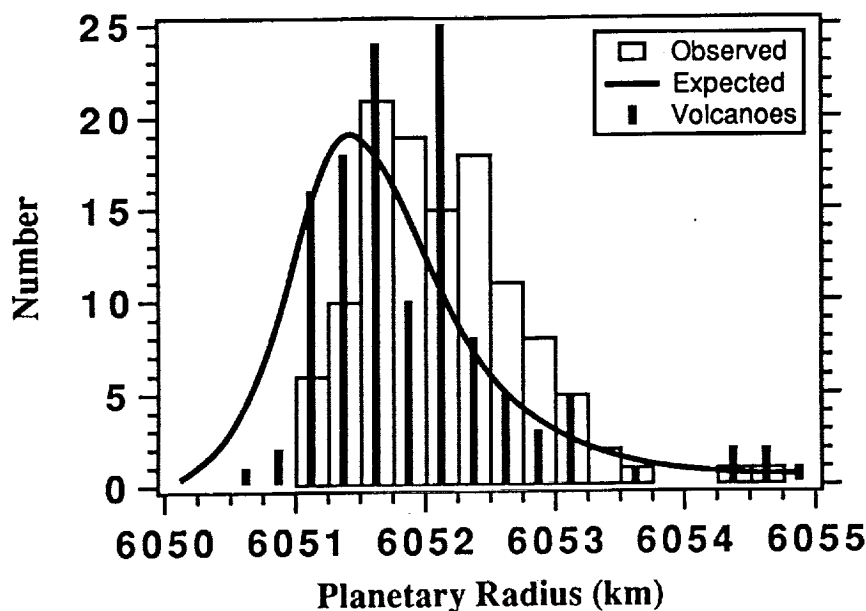


Figure 1: Observed distribution of giant radiating dike swarms as a function of altitude. Expected dike swarm population if distributed uniformly by surface area and distribution of large volcanoes⁴ are also shown. Dike swarms are absent below 6051 km, and a transition from extrusive- to intrusive-dominated magmatism occurs between 6051-6053 km.

MODES OF ORIGIN FOR GIANT RADIATING LINEAMENT SYSTEMS ON VENUS. Eric B. Grosfils & James W. Head, Dept. of Geological Sciences, Brown University, Providence, R.I. 02906

Overview: Two different interpretations have been proposed for the origin of the graben, fissure, and fracture elements which define 163 giant radial systems on Venus: 1) tensile deformation caused by the subsurface emplacement of radiating dikes^{1, 2}; and, 2) faulting accommodating uplift of a domical rise³⁻⁵. Both modes may be linked to a common process, *i.e.* the diapiric rise of mantle material, its impingement upon and deformation of the lithosphere, and pressure release melting which facilitates vertical and lateral magma emplacement. The broad morphological characteristics expected, however, differ sufficiently to permit a systematic evaluation of the relative occurrence of each mechanism. By comparing predictions with observations, we conclude that nearly three quarters of the lineament systems must have involved a significant component of subsurface dike swarm emplacement.

Observations: The individual graben, fissures, and fractures of which the radial systems are composed are typically less than several kilometers in width. Graben and fissures tend to cluster near the center, with fissures grading smoothly into fractures at greater distances to define the overall radial pattern. The lineament systems generally do not extend to equal lengths in all directions, and their maximum radii vary between a minimum of 40 km and a maximum of ≥ 2000 km, with an average of ~ 325 km (Figure 1A). The central topography is highly varied: 53% are domical, 9% are depressions, 15% are essentially flat, and the remaining 23% are indistinguishable from their surroundings (Figure 1B). For those with domical topography at the center, the ratio of dome radius to lineament radius is ~ 0.40 , *i.e.*, on average the radius of a given lineament system is 2.5x greater than that of the associated central dome (Figure 1C). In all, 53% of the radial systems are associated with one or more concentric structures, ranging from central, depression-bounding scarps only 25 km across to tectonic rings several tens of kilometers wide and up to 575 km in diameter. In 51% of these cases, the radial pattern originates within the annulus but also extends significantly beyond it. Only 9% of those radial features associated with annuli are confined within them, leaving 40% that are located entirely outside the outer rim of the annular structure. Finally, lobate finger-like flows emerging from radial lineaments, or groups of such flows characterized by a strong spatial correlation with multiple radial lineaments, occur for 45% of the radial systems.

Predictions: Deformation produced by diapiric impingement upon and domical uplift of the lithosphere³⁻⁵ is initially characterized by extensional stresses which generate radially aligned tensile lineaments upon the dome flanked by a zone of horizontal shear and potential strike slip faulting. As the rise evolves, whether gravitationally or in association with flattening of the underlying diapir, the role played by normal stress increases, and strike slip faulting should be superceded by annular compression at the base of the rise.

Radial elements formed by dike emplacement may be distinguished from those produced by domical uplift in several ways. First, even if domical central topography exists, dike lengths are typically controlled by magma supply rate and thermal factors², and thus radial elements produced by dike emplacement can potentially extend hundreds or thousands of kilometers beyond the lateral extent of the central topography and any associated annulus. Second, while dike swarm emplacement can be associated with a centralized uplift, this need not be the case, and thus the absence of a central dome favors a dike swarm interpretation of the radial elements, though caution must be used since thermal decay and isostatic adjustment might remove evidence of uplift over time. Finally, while a wide variety of volcanism can be expected, lineament-related volcanism (including small shields aligned along the lineaments and flows issuing from them) is particularly suggestive of dike swarm emplacement if it occurs in multiple locations toward the distal portions of the radial system, *i.e.* well away from any central topography.

RADIATING SYSTEM MODES OF ORIGIN: E. B. Grosfils & J. W. Head

Discussion: The fundamental evidence of uplift, namely central domical topography, is present for more than half the radial systems; however, in these instances the associated lineament patterns are far more laterally extensive (usually about 2.5x) than the domes themselves. This is inconsistent with predictions of radial lineament pattern formation through uplift alone, but is readily explained by lateral dike emplacement. In addition, since the remaining radial systems lack a central dome, uplift is unlikely to have been solely responsible for their generation unless the original topography has subsequently decayed through gravitational relaxation. This process, however, is predicted to produce annular deformation outside the dome periphery. Any radial system originally developed upon a rise due primarily to uplift should thus be contained within a tectonic annulus if topographic relaxation has occurred, contrary to the observation that few of the radial systems are so confined. It is therefore unlikely that uplift alone could have generated more than a few of the radial systems which currently lack the requisite topographic signature; however, the absence of central topography does not alter the feasibility of the dike emplacement mechanism.

Conclusions: By considering the topography at the center of each radial pattern, the lineament system radius relative to that of any central topography, the relationship between the radial system and any associated annulus, and the placement and style of volcanism observed, we conclude that formation of 72% of the radial systems must have involved a significant component of radial subsurface dike swarm emplacement. Uplift-derived lineaments are almost certainly present in many of these instances as well; however, only 9% of the radial systems appear to have formed predominantly as a response to production of a topographic dome, and data for the remaining 19% of the systems do not allow confident identification of a dominant mode of origin.

References: 1. McKenzie, D., *et al.*, *JGR* v.97, 15977-15990 (1992). 2. Parfitt, E.A. & Head, J.W., *EMP* v.61, 249-281 (1993). 3. Stofan, E.R., *et al.*, *JGR* v.96, 20933-20946 (1991). 4. Janes, D.M., *et al.*, *JGR* v.97, 16055-16067 (1992). 5. Cyr, K.E. & Melosh, H.J., *Icarus* v.102, 175-184 (1993).

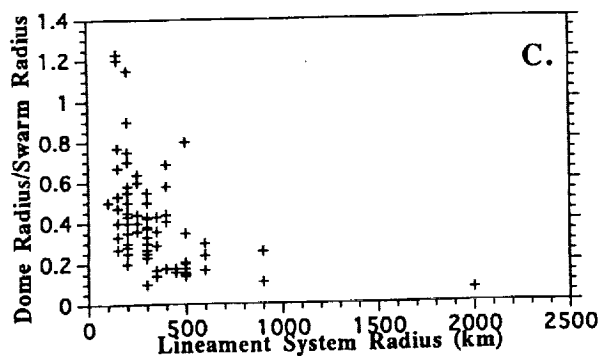
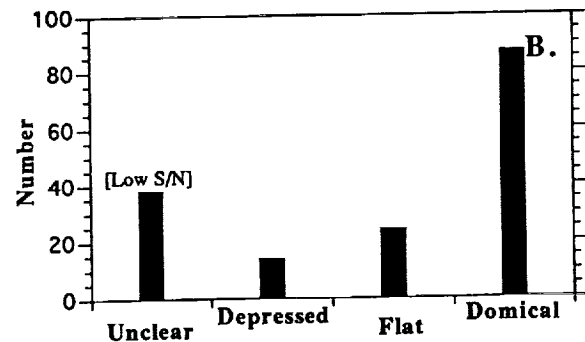
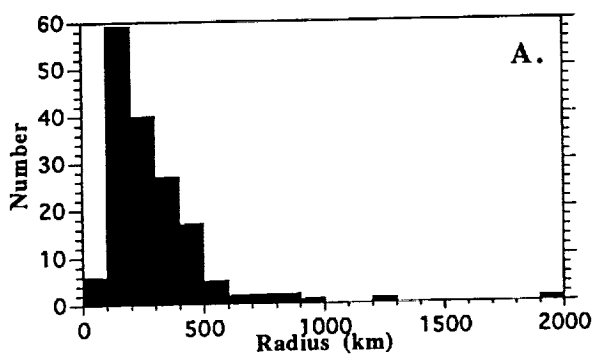


Figure 1: A) Histogram of giant radiating lineament system radii. Average radius is 325 km. B) Central topography associated with radiating systems. C) Plot of radiating lineament system radius versus dome-to-lineament radius ratio for those systems with domical central topography. The average ratio is 0.40.

RADIAL LINEAMENT SYSTEMS ON VENUS: CONSTRAINING MODELS OF GLOBAL STRESS

Eric B. Grosfils & James W. Head, Dept. Geological Sciences, Brown University, Providence, R.I. 02912

Overview: The stress dependent geometries of 163 giant radiating graben-fissure-fracture systems identified on Venus can be used to test existing models for the generation of a global stress field. The stress configuration recorded by these structures across the two-thirds of the planet between 330-210°E (Aphrodite Terra) is best matched by models of isostatic compensation of existing long wavelength topography or coupling between mantle flow and the lithosphere. The configuration across the rest of the planet, centered on the Beta-Atla-Themis region, is correlated with concentrated rifting and volcanism.

Observations: Each system's radial configuration is usually quite pronounced near the center: in 52% of the cases radiating lineaments fan through more than 270°, and 80% exceed 180° of arc. In their distal regions, however, the radiating elements in 72% of the systems continue along a purely radial trend, while distal elements in the remaining 28% curve gradually into unidirectional, sub-parallel geometries. Spatially, the systems as a whole are not randomly distributed across the venusian surface (Figure 1). Of the 163 identified, 79% lie within 40° of the equator, and there is a longitudinal concentration from 190-300°E. Globally, purely radial systems are widespread, but they tend not to occur in lowland and polar regions, and unusual concentrations occur within the Aphrodite Terra highlands, Eistla Regio, and along the Parga and Hecates rift zones. Systems which become unidirectional are also widespread, and avoid the lowland and polar areas, but their global distribution is otherwise different than the purely radial systems. Between longitudes 330-210°E (about two-thirds of the planet) the unidirectional systems principally occupy a broad swath north of Aphrodite Terra that curves around the eastern end of the highland area before terminating south of Atla. Throughout this region the unidirectional lineaments generally align perpendicular to the trend of the long wavelength topography. The remainder of the planet, between longitudes 210-330°E, is dominated by the concentration of rifts and volcanic features of the Beta-Atla-Themis (BAT) region. Unlike the Aphrodite Terra area, the unidirectional radiating structures within BAT do not appear to be geometrically related to the current distribution of long wavelength topography. Instead, these features are associated with the Parga, Hecates, and Devana rift zones, and their distal lineaments align parallel to the observed rift trends.

Discussion: Whether formed predominantly by subsurface dike swarm emplacement or domical uplift, the radiating tensile lineament geometries are stress dependent¹⁻³: those radiating systems which remain radial throughout are interpreted to have formed in the presence of a negligible regional differential stress field, while those systems which become more unidirectional were affected by a stronger regional differential stress, causing their distal lineaments to align in the maximum horizontal stress direction. This stress dependency implies that the geometry of the radiating systems observed on Venus can be used to constrain the orientation and relative magnitude of the planetary stress fields, thus providing a useful means of testing and further refining existing models for their generation. These include: 1) isostatic compensation of long wavelength topography^{4, 5}; 2) Earth-like plate tectonics⁶; and, 3) coupling between convective mantle flow and the lithosphere, either with⁴ or without^{7, 8} shear decoupling due to the presence of an asthenosphere. *Isostatic Compensation:* In considering the temporal evolution of the venusian surface, *Turcotte* [1993] argues that elevated topography on Venus is directly supported by a thick, isostatically compensated lithosphere. Using only long wavelength information, *Banerdt* [1986] calculated the stress field which would result under these conditions. His results predict topography-perpendicular stress orientations that agree quite well with those recorded by the unidirectional radiating systems across the two-thirds of the planet associated with the Aphrodite Terra highlands. The isostatic model, however, also predicts high differential stresses in the highlands and lower ones in the surrounding areas, contrary to the observation that purely radial systems dominate in the highlands while unidirectional ones occupy the adjacent regions. In addition, across the remaining third of the planet (BAT) the unidirectional orientations are only poorly approximated. We thus conclude that, while an isostatic model correctly predicts stress orientations across two-thirds of the planet, implying that the stress field and topography are correlated (this is suggested by wrinkle ridge alignments as well⁹), further refinement is required to account for both the differential stress magnitudes in highland and lowland areas and the observations within BAT. *Plate Tectonics:* On Earth, the maximum horizontal compressive stress direction at divergent oceanic plate boundaries is generally aligned perpendicular to the rift¹⁰. While morphologic evidence indicative of plate tectonics on Venus is not widespread¹¹, *McKenzie et al.* [1992] argue that many areas exhibit a plate tectonic signature like that of Earth.

CONSTRAINING MODELS OF GLOBAL STRESS: E. B. Grosfils & J. W. Head

Around Aphrodite Terra, given the consistency of the unidirectional system behavior, the simplest interpretation requires plates to spread approximately normal to the current highland topography, a situation not supported by existing data¹¹. Within BAT, the rift-parallel orientation of the unidirectional systems is also inconsistent with Earth-like plate boundary spreading; however, the geometry is characteristic of intraplate continental rifting on Earth, and may be linked to broad-scale upwelling¹². **Mantle-Lithosphere Coupling:** Coupling between mantle convective flow and the lithosphere can generate long wavelength topography and a global system of stress⁷. If an asthenosphere exists to decouple basal shear, the maximum compressive stress configuration expected on Venus is quite similar to that generated by pure isostatic compensation of a thick lithosphere⁴; it therefore accurately predicts the stress orientations recorded about Aphrodite Terra but fails to explain either the relative highland-lowland differential stress magnitudes or the radiating system behavior observed within BAT. In the absence of an asthenosphere, the addition of basal convective shear stress enhances the differential stress magnitude at the surface⁷, and may have promoted thermally dependent tectonic resurfacing⁸; however, as in the decoupled shear model the differential stresses should be higher in elevated areas, inconsistent with observations. While detailed predictions about the expected global stress configuration for this situation have not been made, the topography-perpendicular orientation of the systems about Aphrodite Terra suggest that mantle material flowed normal to the highland, a situation consistent with either mantle upwelling or downwelling beneath the currently elevated regions.

References: 1. Anderson, E.M., 206 pp., Oliver & Boyd: Edin. (1951). 2. Ode, H., *GSAB* v.68, 567-576 (1957). 3. Cyr, K.E. & Melosh, H.J., *Icarus* v.102, 175-184 (1993). 4. Banerdt, W.B., *JGR* v.91, 403-419 (1986). 5. Turcotte, D.L., *JGR* v.98, 17061-17068 (1993). 6. McKenzie, D., *et al.*, *JGR* v.97, 13533-13544 (1992). 7. Phillips, R.J., *JGR* v.95, 1301-1316 (1990). 8. Solomon, S.C., *PhysTod* v.46, 48-55 (1993). 9. Bilotti, F., *et al.*, *LPSC* 24, 107-108 (1993). 10. Forsyth, D.W. & Uyeda, S., *GJRA* v.43, 163-200 (1975). 11. Solomon, S.C., *et al.*, *JGR* v.97, 13199-13225 (1992). 12. Crumpler *et al.*, *Sci* v. 261, 591-595 (1993).

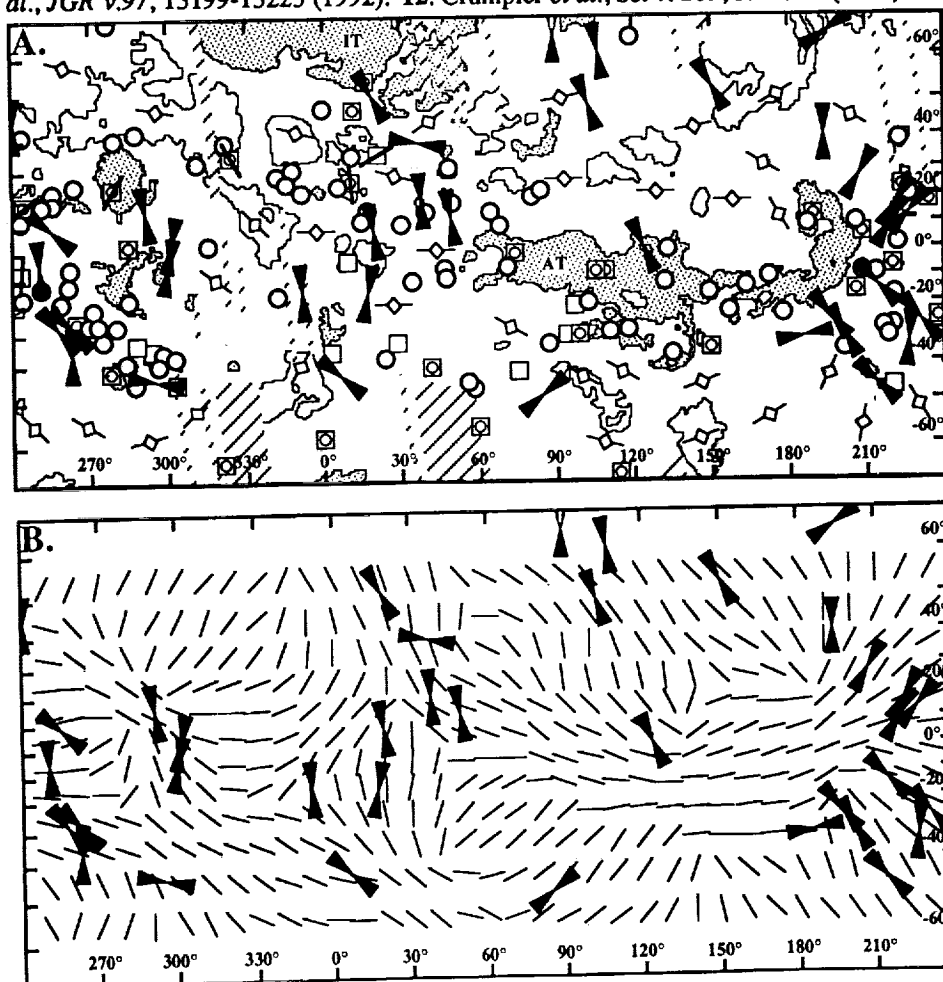


Figure 1: A) Distribution of radial graben-fissure-fracture systems on Venus. Those involving significant dike emplacement are circles (low regional differential stress) and black arrows (high differential stress, aligned with maximum horizontal compression), those dominated by uplift are squares, and those whose dominant contributing mechanism is not known are squares containing circles. Maximum compression directions indicated for the latter two cases are depicted by a solid line. Lines with diamonds show general wrinkle ridge trends⁹. 6051 km contour is shown and elevations above 6053 km are stippled. B) Unidirectional orientations compared with the maximum horizontal compressive stress directions (dashed lines) predicted by Banerdt [1986] for isostatic compensation of a thick lithosphere.

A POSSIBLE ATMOSPHERIC WATER SOURCE FOR THE FLUVIAL VALLEYS ON ALBA PATERA; Virginia C. Gulick and Christopher P. McKay (NASA/Ames Research Center, MS 245-3, Moffett Field, CA 94035; email: gulick@barsoom.arc.nasa.gov).

Erosion of the fluvial valleys on the north slope of the martian volcano, Alba Patera, seems to have required flow of surface water [1]. As such these fluvial valleys are of particular paleoclimatic interest since the surface upon which the valleys formed is of Amazonian age, forming well after the more numerous valleys in the heavily cratered terrain. One potential source for the water is precipitation derived from frozen lakes produced by outflow channel discharges. In this abstract we consider the atmospheric and geologic aspects of this hypothesis.

Several sources have been proposed for the water required to carve the valleys on Alba. Eruptions and explosive activity on Alba could have periodically transported water into the surface environment [2]. Ground-water outflow prior to surface water flow resulting from hydrothermal circulation within the water or ice-rich subsurface material underlying the unusually large, relatively low-relief volcano has been also proposed as a water source [1,3]. Numerical modeling [4] has demonstrated that the magnitude and duration of hydrothermal activity expected to result from the formation of Alba Patera could deliver sufficient quantities of ground water to the surface environment over time scales needed to form the observed fluvial valleys. Gulick and Baker [3] and Baker et al. [5] proposed that water vapor evaporated from a lake or sea created by outflow channel discharges might deliver water to the flanks of the volcano. Crater density studies indicate that the valleys on Alba are of similar age to outflow channel activity [6] and the formation of the proposed Oceanus Borealis [5].

The fluvial valleys on the north slope of Alba Patera cover approximately 30,000 km². The total volume of material removed from the 10⁴ km² area studied in [1] is estimated to be on the order of 10¹¹ m³. Assuming volume ratios of water to removed material of 1000:1, an equivalent depth of water of 10 km over the study region would be required for valley formation. Precipitation, with no atmospheric losses, of 1 cm/year could theoretically provide the necessary quantity of water in 10⁶ years. However it is doubtful that such low precipitation rates could actually induce valley development. The dry, leeward flanks of Hawaiian volcanos demonstrate that intensity as well as duration is important in valley formation. Regions of West Molokai receive approximately 20 cm/yr of rainfall and exhibit very little fluvial erosion. Widely-spaced linear streams with little to no tributary development dissect the approximately 2 million year old surface. Some regions on Mauna Loa receive an order of magnitude or more rainfall and show comparable or greater degrees of valley development on surfaces 10 times younger. However the degree of valley development on surfaces older than West Molokai receiving comparable amounts of rainfall is not appreciably greater. We conclude that rainfall rates less than some critical value, we estimate ~10 cm/year, are insufficient to erode valleys, even over long time periods.

Can precipitation deliver the required quantities of water to the north slope of Alba at rates sufficient to form valleys? Alba Patera is adjacent to the region in which outflow channel discharges would have ponded in the northern hemisphere. Transient seas as large as several 10⁷ km² have been proposed and are consistent with the observed geology of the northern plains [5,7]. Here we assume only that the frozen sea has an area comparable to that of the eroded flanks of Alba, or several 10⁴ km².

To estimate the rate at which water could be delivered to the flanks of Alba from the frozen sea, we consider air that has achieved saturation over the surface of an ice-covered lake. Winds with an initial relative humidity of 0% blow across the lake. The relative humidity of the air mass increases as the underlying ice sublimates. The rate of sublimation of the ice sheet depends primarily on the temperature and somewhat on the wind speed. For current martian conditions and wind speeds of 1 to 5 m/sec, sublimation rates are in the range of 0.3 to 3 cm/year. If mean conditions were 25 and 50 C warmer than current, the sublimation rate would be 10 and 100 times larger, respectively.

The saturated air then cools as it is lifted upward and part of the entrained water vapor condenses as snow. The fraction of water that is deposited as snow depends on the lapse rate and the height of the ascent - that is the altitude difference between the lake surface and the snowfield. For current martian mid-latitude temperatures, the snow accumulation rate over a 2 km altitude change is approximately 1 cm/year of equivalent

SNOWFALL ON ALBA PATERA: Gulick, V. and McKay, C.

water, if the snow accumulation area is comparable to the lake area. For a 6 km altitude change, appropriate for the summit caldera region of Alba Patera, the accumulation is 40% larger, assuming no precipitation at intermediate altitudes. The results depend linearly on the relative areas of the snowfield and lake.

The deposited snow, like the lake ice, is subject to sublimation. However, the sublimation rate is lower at higher altitudes due to the lower temperature. The estimated net annual snow production is of order 1 cm/year if the lake were formed under current martian conditions. The snow pack would be subject, however, to melting from below. A geothermal heat flux of 0.1 Watt/m² is required to melt a 1 cm annual water equivalent thickness production of snow. Such a heat flow is commonly measured over extensive (10⁴ km²) regions surrounding large terrestrial volcanic centers (e.g. Cascade volcanos). Heat flows of 1 W/m² are commonly measured over areas of 10³ km² in terrestrial hydrothermal regions with the more intense areas delivering on the order of 500 W/m² to the surface [8]. Therefore, the limiting factor in liquid water production on the slopes of an active volcano is snowfall, not delivery of latent heat from a local thermal source to melt the snow.

Upslope from the valleys on Alba and downslope from the summit caldera is an undissected wedge-shaped region that could potentially serve as a zone of snow accumulation. This region has an area of approximately 15,000 km², comparable to that of the valleyed area. Extrapolation of the major orientation of valley trends back to the summit region delineates the possible area of snow accumulation that would contribute to the formation of the observed valleys. The orientation of lava flows emanating from near the summit adjacent to this region suggest that fluid melted in this region would indeed flow into the valleyed area.

For snowfall on Alba to be an effective source of water for valley erosion, the production rate must exceed the calculated 1 cm/year. Warmer ambient temperatures would produce greater sublimation from the frozen lake and consequently greater snowfall. Greater effective water delivery rates might also be achieved if the snow field acts as a storage reservoir. During periods of little or no volcanic heating, the snow would accumulate. Periodic melting of the snow, perhaps due to greater heat flows associated with magma chamber inflation might produce periodic runoff rates comparable to precipitation of tens of cm per year. A combination of snow accumulation, melting, and erosion over appropriate time scales might result in fluvial valley development on Alba. Thus valley erosion would progress during times of snow melt and then effectively halt until a new melting episode. During the intervening time the snow pack would be replenished by additional snowfall. In this sense the snow field would act as a storage reservoir for water on the flanks of Alba.

In conclusion, sublimation of water from a frozen lake or Oceanus Borealis could result in delivery of snow to the flanks of Alba Patera at the rate ~1cm/year for current climatic conditions. The local heat flow was likely, at least periodically, capable of melting the delivered snow. However the calculated snow delivery rate is too low to permit valley development. For this mechanism to have been effective, the mean annual temperature must have been at least 25 C higher than at the present or the snow must have been stored on the flanks and melted episodically, providing shorter periods of more intense runoff. Given these limitations, ground water delivered to the surface by hydrothermal systems may have been a more effective fluid source. A combination of snowfall and hydrothermal discharge might better explain the observed valley morphology.

References: [1] Gulick, V.C. & Baker, V.R. (1989) *Nature* **341**, 514-516. [2] Mouginis-Mark, P. and Wilson, L. (1988) *Bull. Volcanol.* **50**, 361. [3] Gulick, V. & Baker, V. (1990) *J.G.R.* **95**, 14325-14344. [4] Gulick, V.C. (1993) Ph.D. Thesis, Univ. Ariz. 146pp. [5] Baker, V. et al. (1991) *Nature* **352**, 589-594. [6] Barlow, N. (1988) *Icarus* **75**, 285-305. [7] Parker, T.J., Saunders, R.S. & Schneeberger, D. (1989) *Icarus* **82**, 111. [8] Elder, J. (1981) *Geothermal Systems* (London: Academic Press).

FERROSILITE, FAYALITE AND MAGNESIOFERRITE FORMATION BY ISOTHERMAL ANNEALING OF AN IRON-CONTAMINATED Mg-SiO SMOKE.

Fu Guofei and Frans J.M. Rietmeijer, Department of Earth and Planetary Sciences, University of New Mexico, Albuquerque, NM 87131, USA.

Laboratory studies of thermally-annealed vapor condensates will advance the understanding of dust evolution in oxygen-rich protostellar environments. A previous analytical electron microscope (AEM) study of an annealed Mg-SiO smoke showed coarsening of forsterite and enstatite nanocrystals accompanied by equilibration of bulk Mg/Si (at%) ratios as a function of annealing time (2, 4, 8, & 39 hours) *in vacuo* at 1000°K [1]. This AEM study used dispersed, 3-dimensional "bulk" samples [1] in which it was difficult to obtain grain size distributions, and to perform electron diffraction and quantitative chemical analyses of individual nanocrystals. The introduction of serially-sectioned, ultrathin (80-100 nm) sections for AEM analyses of interplanetary dust [2] was the incentive to re-analyse the thermal-annealing history of the Mg-SiO smoke because the individual grains in ultrathin sections are accessible to quantitative chemical, electron diffraction and textural analyses. Traces of an unidentified Fe-bearing contaminant in the "bulk" samples did not react with the Mg-SiO smoke [1]. We exploit the greatly improved sample preparation to look for Fe-silicates that might have formed during annealing. Ultrathin sections of smoke samples annealed for 8, 30 and 167 hours were prepared for AEM analyses using a Jeol 2000FX AEM equipped with a TN-5000 energy dispersive spectrometer [cf. 3]. The samples appear dull-grey to black in white light, but ~40% of the 167h-sample has a yellow tinge that is probably due to ferric iron-bearing phases. We prepared ultrathin sections of the differently-coloured materials.

RESULTS. The annealed samples have an open cluster morphology. Relics of the crude network of interconnected ribbons of the original condensate [1] are still present in the 167h-sample (black fraction). All samples are dominated by equigranular (*i.e.* a narrow size distribution), poorly-crystalline Mg-SiO material with randomly oriented nanocrystals. Distinctly fine-grained (< 20 nm in diameter) polycrystalline materials are in variable proportions associated with coarse-grained material with nanocrystals of ~40-60 nm (8 hours) and ~60-80 nm in diameter (167 hours). The quantity of nanocrystals, and porosity of the Mg-SiO material, gradually increase with annealing time. The fine-grained domains are slightly Mg-richer than coarse-grained polycrystalline materials. The electron diffraction data are consistent with forsterite, enstatite and tridymite. Small amounts of amorphous silica-rich (>95 wt% SiO₂) areas and tridymite crystals (both up to ~200 nm in size) occur throughout the Mg-SiO material in all samples. The coarse-grained Mg-SiO material in each sample contains round to irregularly-shaped, platy single-crystal grains of ~100 nm up to ~500 nm in diameter. In the 167h-sample they tend to form subhedral single-crystal grains. The compositions of the Fe-SiO grains range from ~30-75 wt% FeO (8 hours) and ~30-95 wt% FeO (30 & 167 hours) with two clusters at 35 and 52 wt% FeO of ferrosilite and fayalite grains, and an a third cluster at 70 wt% FeO of hematite, and possibly maghemite, grains. In addition to equigranular Mg-SiO material, the 167h-sample's yellow fraction is characterised by (I) randomly-distributed, euhedral magnesioferrite single-crystals (< 300 nm long; ~18 wt% MgO) and euhedral, single-crystal brucite, Mg(OH)₂, up to 50-100 nm in size and (II) smoke-like domains of subrounded grains that include (a) euhedral periclase (MgO) grains with a Mg-SiO mantle (~16-65 nm in diameter) and (b) core-free Mg-SiO grains (~9-60 nm in diameter).

Fayalite and ferrosilite. In both iron-rich olivine and pyroxene $Fe^{2+}/(Mg+Fe^{2+}) = \sim 0.85 - 1.0$. These silicates generally contain ferric iron, *viz.* Fe^{3+} ions between 0.05 - 0.65 (calculated from stoichiometry), but mostly 0.05-0.10 (~70% of data). The $Fe^{2+}/(Fe^{2+} + Fe^{3+})$ ratios are 0.6-1.0 (olivine) and $fe = 0.90-1.0$ (pyroxene). In rare pyroxenes all iron is Fe^{3+} . We have not yet unambiguously identified laihunite (La) by electron diffraction but rare olivines in the 30h- and 167h-samples fit the structural formula of this 'ferrifayalite' mineral. These olivine are $Fe_{75}Fe_0La_{25}$ and $Fe_{54}Fe_0La_{46}$ (30 hours), and $Fe_5Fe_{90}La_5$ and $Fe_1Fe_{69}La_{30}$ (167 hours). We estimate $\log fO_2$ between -15 and -10 atm. at the FMQ and HM buffers.

DISCUSSION. Autoannealing describes post-condensation solid-state transformations that occur in a vapor-condensed smoke [4]. It will be difficult to identify nanocrystals as part of the condensation history or of later thermal annealing. For example, fine-grained Mg-silicates in poorly-crystalline material of the 8h-sample might be due to autoannealing. Otherwise the increased grain size and quantities of nanocrystals, and the formation and growth of Fe-silicates, are consistent with prolonged heating. Contrary to the earlier findings [1], an Fe-contaminant in the present allocations did react with the Mg-SiO smoke during isothermal annealing. The Fe-silicates might have formed by reaction of Fe-vapor with Mg-silicates or via solid-state reactions. Considering the boiling points of metallic iron and of various Fe-oxides and the thermal annealing conditions, we presently favour the latter explanation. The Fe-contaminant was probably steel from the collector plate. We propose that enstatite reacted to form fayalite and ferrosilite, viz. (a) $\text{MgSiO}_3 + 2\text{Fe} + 1/2\text{O}_2 = \text{Fe}_2\text{SiO}_4 + \text{Mg(g)}$, (b) $2\text{MgSiO}_3 + 2\text{Fe} = \text{Fe}_2\text{SiO}_4 + 2\text{Mg(g)} + \text{SiO(g)} + 1/2\text{O}_2$, and (c) $\text{MgSiO}_3 + 3\text{Fe} + 2\text{O}_2 = \text{FeSiO}_3 + \text{MgFe}_2\text{O}_4$, whilst forsterite formed Fe-silicates according to (d) $2\text{Mg}_2\text{SiO}_4 + 2\text{Fe} = 2\text{FeSiO}_3 + 4\text{Mg(g)} + \text{O}_2$, and (e) $\text{Mg}_2\text{SiO}_4 + 2\text{Fe} = \text{Fe}_2\text{SiO}_4 + 2\text{Mg(g)}$.

The reactions *a, b, d, & e* produce a metallic-Mg vapor consistent with earlier evidence [1] for evaporative Mg-loss during annealing. Reaction *b* also produces SiO vapor. The Mg-bearing vapor condensed into euhedral MgO crystals possible as the result of the vapore reacting with liberated 2O_2 . The euhedral MgO crystals indicate 3-dimensional growth at (local) high supersaturation ratio. They provided nuclei for Mg,Si-O deposition. Rare magnesioferrite spinel formed by reaction *c*. Magnesioferrite occurs naturally as a result of extreme and highly transient temperature gradients that yield disequilibrium mineral assemblages at a bulk scale but with domains of full thermodynamic phase equilibrium [5]. This type of environment is also conducive to laihunite formation via oxidation of fayalite wherein synthetic laihunite uniquely coexists with hematite and silica under atmospheric oxidation conditions [6,7]. Kinetically-controlled mineral formation rather than thermodynamic equilibrium for ultrafine assemblages also occurs during atmospheric entry flash-heating of micrometeorites wherein laihunite has also been observed [8,9]. The data support chaotic disequilibrium during isothermal annealing of an Fe-bearing, Mg-SiO smoke. After prolonged isothermal annealing, Fe^{3+} is no longer accommodated in the silicates which induces the formation of nonstoichiometric Fe-silicates, such as laihunite, and there is evidence for partial evaporation and condensation to produce the distinctly fine-grained Mg(Si-O) smoke. Brucite is probably a post-annealing artifact due to reaction of MgO with atmospheric moisture.

CONCLUSIONS. We exploit the inadvertent contamination of an Mg-SiO smoke with Fe-metal grains. Fayalite and ferrosilite with variable *fe*-ratios, rare laihunite and magnesioferrite occur alongside existing forsterite, enstatite and tridymite. The Fe-minerals form from their Mg-counterparts as a function of annealing time at 1000°K with (partial) evaporation and condensation of a metallic-Mg vapor after prolonged annealing. When thermal annealing of dust in protostellar regions is an important process, it follows that this dust may contain variable proportions of Mg-rich and Fe-rich olivines and pyroxenes and accompanying MgO and Mg,Fe-oxide minerals. In addition to metamorphism of the dust, partial evaporation and condensation events could occur. The opacity of silicate dust in the near-IR region depends on their $\text{Fe}^{2+}/(\text{Fe}^0 + \text{Fe}^{2+} + \text{Fe}^{3+})$ ratio. This ratio might provide an important constraint on the aging of astrophysical dust [10]. We have shown that thermal annealing of Mg-silicates in the presence of an "Fe-donor phase" tends to produce high *fe*-ratios in a small fraction of the silicate grains. This type of AEM analyses of astrophysical dust analogs may help elucidate the details of dust evolution in environments such as the primitive solar nebula.

REFERENCES. 1. Rietmeijer FJM et al. (1986) *Icarus* 66, 211-222; 2. Bradley JP & Brownlee DE (1986) *Science* 231, 1542-1544; 3. Rietmeijer FJM (1991) *EPSL* 102, 148-157; 4. Rietmeijer FJM & Nuth JA (1991) *Proc. LPS* 21, 591-602; 5. Foit, Jr. FF (1987) *Amer. Mineral.*, 72, 137-147; 6. Kondo, S et al. (1985) *Amer. Mineral.*, 70, 737-746; 7. Kitamura, M et al. (1984) *Amer. Mineral.*, 69, 154-160; 8. Keller LP et al. (1992) *LPSC XXIII*, 6765-6766; 9. Rietmeijer FJM (1992) *LPSC XXIII*, 1151-1152; 10. Nuth JA & Hecht JH (1990) *Astrophys. Space Sci.* 163, 79-94.

This work was supported by NASA grant NAGW-3646

AUTHOR INDEX*

Abell P.	1505	Bashkirov A.	1443
Adams J. B.	779, 1181	Basilevsky A. T.	63, 65, 67
Aeschliman R.	871	Bass D. S.	69
Agerkvist D. P.	1, 819	Basu A.	71
Agresti D. G.	1261	Batchelor J. D.	97
Aguirre-Puente J.	3	Batson R. M.	871
Ahrens T. J.	5, 243, 359, 1023, 1369	Baur H.	959
Akimov L. A.	1331	Beard B. L.	73
Alexander C.	7, 9, 11, 401, 449, 1005	Beck E. A.	353
Alexander W. M.	1381	Beck P.	75
Alexeev V. A.	13, 15, 17, 19	Becker R.	77, 815
Alexopoulos J. S.	1079	Becker T.	395, 871
Allen C. C.	21, 23, 937, 1415	Beckett J. R.	79, 755
Allen J.	795	Begemann F.	849, 1273
Allton J. H.	25, 1155	Bell J. F.	81, 83, 85, 87, 89, 265, 939, 1161, 1165
Amari S.	27, 103, 563	Belton M.	237, 453, 469, 787, 1395
Andersen D. W.	119	Bender K.	91, 463, 1243
Anderson F. S.	29	Benedix G. K.	865
Anderson R. C.	1133	Benner L. A. M.	93
Anderson R. R.	31, 719	Bennett M. E.	95
Anderson S. W.	33, 1091	Benoit P. H.	97, 99, 247, 573, 1367, 1545, 1547
Annexstad J. O.	891	Benz W.	43, 101
Antenenko I.	963	Ber T.	479
Antoine L. A. G.	847	Berg O.	1011
Antonenko I.	35	Bernatowicz T. J.	103, 105, 313, 1033
Arai T.	1373	Bernhard R. P.	107, 125, 567, 1233
Arden J. W.	373, 449, 1435	Bertka C. M.	109
Ariskin A. A.	37, 1071, 1073	Betts B.	111, 975
Arndt P.	139	Bilotti F.	1105
Arnold J. R.	1003	Bindschadler D. L.	113
Arriola S. T.	927	Binzel R. P.	1083
Artem'ev V. I.	41	Bischoff A.	115, 349, 1475
Artem'eva N. A.	39	Bish D. L.	121
Arvidson R. E.	157, 481, 605, 815, 1263, 1287	Bishop J. L.	117, 119
Ash R. D.	279	Blake D. F.	121, 621
Asphaug E.	43, 101	Blake G. A.	755
Aubele J. C.	45, 47, 305	Blake P.	1421
Bacon R.	837	Blanchard D. P.	71
Badjukov D. D.	601	Blaney D. L.	123, 1433
Bailey S. H.	353	Blanford G. E.	125, 1393
Baines K. H.	1095	Blewett D. T.	127, 515
Bajt S.	167, 323, 381, 713, 1361	Blum J. D.	719
Baker V. R.	627, 629, 631, 727	Blumberg D. G.	129, 341
Baloga S. M.	189	Bobe K.-D.	901
Balogh A.	49	Bobias S. G.	611
Banerdt W. B.	51, 155	Bobina N. N.	131, 1001
Banin A.	53	Bockstein I. M.	133
Banks M.	55	Boer R. H.	719
Bansal B. M.	1015, 1017	Boerner D.	1517
Barentine J. C.	57	Boesenberg J. S.	135
Barker B. M.	163	Bogard D. D.	137, 403
Barlow N.	59, 225, 227	Bohsung J.	139
Barnouin O. S.	61, 1213	Borisov A.	141
Barrett J. M.	239	Bornhoeft K.	83
Barrett R. A.	1565	Borunov S.	143

*Page numbers refer to the first page of an abstract on which an author appears.

Boslough M. B.	145, 295, 309	Chambers J. G.	235, 547
Boss A. P.	147, 149, 151	Chapman C.	237, 469
Bottke W. F. Jr.	153	Chapman M. G.	239
Bourot-Denise M.	543	Cheeseman P.	241
Bowman D. D.	155	Chen G.	243
Bowyer S.	749	Chen J. H.	245
Boynton W. V.	353	Chen P. C.	1501
Brackett R. A.	157, 1263	Chen Y.	99, 247
Bradley J. P.	21, 159, 185, 687	Chevrel S. D.	249
Brandstätter F.	979, 981	Chibante L. P. F.	251, 545
Brandt D.	161, 847	Chicarro A. F.	253
Brannon J. C.	1033	Choi B.-G.	255
Brazzle R. H.	163	Christensen P. R.	257, 343, 503, 1485
Brearley A. J.	165, 167, 641, 1069	Christoffersen R.	259
Bridges J. C.	11	Chryukina O. V.	909
Bridges N. T.	169	Chu W.-K.	1501
Brilliant D. R.	171, 173	Cielaszyk E.	647
Bringol L. A.	589	Cintala M. J.	107, 261, 567
Britt D. T.	175, 177, 785, 1135, 1293	Clark B. C.	263
Brookshaw L.	1397	Clark B. E.	175, 265
Brown C. D.	179	Clark P. E.	267
Brown R. H.	1419	Clayton R. N.	269, 579, 581, 865, 1063, 1457, 1459
Brown S. T.	647		
Browning L.	181, 645, 1565	Clemett S. J.	1391
Brownlee D. E.	21, 159, 183, 185, 809	Clifford S. M.	271
Brückner J.	187, 353	Cloutis E. A.	273
Bruno B. C.	189, 1383	Clow G. D.	275
Bruno L.	997	Cobban W. A.	607
Bullock M. A.	191	Coleman P.	1249
Bulmer M. H.	193	Collins G.	277
Bunch T. E.	565	Collison W. P.	423
Burba G. A.	131, 195, 1001	Connolly H. C. Jr.	279, 543, 1285, 1537
Burba G. G. Jr.	197	Connors M.	281, 283
Burbine T. H.	199	Consolmagno G.	285
Burch J.	795	Cook D.	453
Burke K.	201	Costard F.	3, 287
Burkett P. J.	801	Cox T. C.	289
Burnett D. S.	1075	Craddock R. A.	291, 293, 857
Burns R. G.	199, 203	Craig A. Y.	1421
Burt J. D.	205	Crawford D. A.	295
Buseck P. R.	345	Croft S. K.	297
Bussey D. B. J.	207	Crossey L. J.	299, 861
Busso M.	209	Crowell K.	795
Butler B. J.	211, 951	Crown D. A.	33, 301, 1091
		Crozaz G.	571, 1451
Cabrol N.	213, 483, 769	Cruikshank D. P.	85, 739, 1419
Caffee M. W.	1003	Crumpler L. S.	303, 305
Calvin W. M.	895	Cuzzi J. N.	307
Cameron A. G. W.	215	Cygan R. T.	309
Campbell B. A.	217, 219, 515		
Capobianco C. J.	221	Dale-Bannister M. A.	311
Carcich B. T.	453, 787	D'Aria D. M.	1191
Carlson R.	453, 807, 863	Daulton T. L.	313, 345
Carroll J.	227	Davis A. M.	315, 1063, 1457, 1459
Casanova I.	223	Davis D. M.	285
Cave J.	225, 227	Davis D. R.	365, 1175
Chadwick D. J.	229, 231, 443, 705, 1199	Davis P. A.	317, 443, 869
Chael E. P.	145	Dawidowicz G.	483
Chakrabarti S.	749	Dawson D. D.	1353
Chakravarty N.	353	Dawson J. B.	1087, 1089
Challis D.	233	DeAro J. A.	221
Chamberlain C. P.	719	DeHart J. M.	319, 801

De Hon R. A.	321	Fleming R. H.	1421
Delaney J. S.	135, 323, 831, 1361	Flores B.	655
Delano J. W.	325, 505, 639	Floss C.	375
Dembosky J.	811	Flynn B.	377
Des Marais D. J.	367	Flynn G. J.	379, 381, 713, 1391
DeTroye J. E.	327	Fogel R. A.	383
Deutsch A.	477, 497, 839, 1031, 1209	Foh J.	709
Dikov Yu. P.	329, 413, 415	Ford P. G.	67, 1279
Dobrovolskis A. R.	307	Forsyth D. W.	1407
Dohm J. M.	331, 1225	Foster P. N.	151
Dolginov A. Z.	333	Fowler G. W.	385, 1043, 1045
Dollfus A.	335	Franchi I. A.	171, 173
Domingue D. L.	337	Franklin B. J.	443
Donahue D. J.	647, 649	Frawley J. J.	407
Dong Q. W.	1389	Freedman R.	85, 87
Doose L. R.	1293	Frei R.	997
Dorofeeva V.	143	Frey H.	387, 389, 1345
Douglas C.	339	Fricke S. K.	791, 1291
Drake D. M.	899	Friedman R. C.	391
Drake M. J.	221, 551, 873, 1009	Froeschl H.	119
Drossart P.	143	Fry P.	1195
Duzheva E. A.	709		
Dymek R. F.	1253	Gaddis L.	393, 395, 577
		Gaetani G. A.	397
Eberhardt P.	563	Gaffey M. J.	273, 399, 689, 1117
Ebihara M.	1035, 1269	Galileo Imaging Science Team	237, 1395
Edgett K. S.	341, 343, 895, 1555	Galileo NIMS Science Team	575, 807, 863, 1019, 1235
Edwards K.	453, 1145	Galileo SSI Team	787
Ehlmann A. J.	865	Gallino R.	209, 583
Eisenhour D. D.	313, 345	Ganasan J.	555
El Goresy A.	347, 375, 1557	Gao X.	401, 1005
Ellison M.	417, 1187	Garbeil H.	1141
Emerson S.	55	Garrison D. H.	137, 403
Encrenaz Th.	143	Garvin J. B.	405, 407, 409
Endress M.	349	Geballe T. R.	85
Engel S.	511	Geiger T.	115
Engelhardt W. v.	351	Geissler P.	411
Englert P. A. J.	119, 353	Gektin Yu. M.	133
Engrand C.	355	Gerasimov M. V.	329, 413, 415
Epstein S.	1471	Gerlach K.	417
Erard S.	357	Ghail R. C.	419, 421
Eugster O.	997, 1479	Ghiorso M. S.	1183
Evans L. G.	267	Gibson E. K.	1155
Evans N. J.	359	Gibson R. L.	423
Evergreen High School		Giese R. F.	1445
Research Class	417, 1187	Gillis J.	1179
Evlanov E.	709, 819	Gilmore M.	425, 529
		Gilmour I.	1247
Fabian U.	187	Gladstone G. R.	749
Fagents S. A.	361	Glass B. P.	427, 1101
Fahey A.	363, 583, 585	Glaze L. S.	429
Fanale F. P.	265, 453, 455	Gliem F.	1293
Farinella P.	365, 495, 841	Glukhovsky M. Z.	431
Farmer J.	213, 367, 769	Goguen J. D.	433
Faurschou Hviid S.	819	Golden D. C.	435, 437
Fegley B. Jr.	157, 201, 707, 773, 1263	Goldsby D. L.	439
Feldman V.	369	Goldstein J. I.	1529
Fevig R.	1507	Golombek M. P.	441, 443, 1377
Fink J. H.	473	Gooding J. L.	25, 1021
Finkel R. C.	1003	Gorsline D. S.	1053
Fischer E. M.	371	Gostin V. A.	445, 447
Fisenko A. V.	373, 775	Goswami J. N.	1185, 1325

Grady M. M.	339, 449, 451	Head J. W. (cont.)	1359, 1495, 1531
Graf Th.	1093	Hechler M.	49
Granahan J. C.	453, 455	Held P.	709
Granovsky L. B.	909, 1559, 1561	Helfenstein P.	453
Grant J. A.	457, 459	Helgerud M. B.	531
Grard R.	49, 461	Henderson B. G.	533
Greeley R.	91, 129, 213, 233, 237, 463, 465, 467, 469, 769, 787, 1047, 1243, 1493, 1521	Herkenhoff K. E.	69, 535
Greenberg R.	153, 411	Herrick R.	537, 1399
Greenwood J. P.	471	Herzog G. F.	539, 1523
Gregg T. K. P.	473	Hess P. C.	471, 541
Grier J. A.	475	Hewins R. H.	279, 543, 825, 1535, 1537
Grieve R. A. F.	477, 479, 1085, 1347	Heymann D.	251, 545
Griffith L. L.	481	Hide R.	243
Grimm R. E.	29, 51, 179	Higgins J.	173
Grin E. A.	483	Higgins S. J.	235, 547
Grinspoon D. H.	191	Hildebrand A. R.	549
Grosfils E. B.	485, 487, 489	Hillgren V. J.	221, 551
Grossman J. N.	929	Hiroi T.	553, 941, 1375, 1567
Grossman L.	223, 315, 1275, 1533	Hofmann B.	997
Grove T. L.	397	Hogan R. C.	307
Guest J.	193, 207, 225, 227, 463, 465, 767	Hohenberg C. M.	105, 163, 683
Gulick V. C.	491	Holden T. C.	555
Gunnlaugsson H. P.	819	Holmberg B.	557
Guofei F.	493	Holsapple K. A.	559
Guseva E.	369	Honda M.	1269
Guyot F.	839	Hood L. L.	561
Haack H.	495	Hoppe P.	563, 763
Haberle R. M.	517	Horan M. F.	929
Hackbarth K.	497	Horn L. J.	985
Hackwell J.	123	Hornemann U.	839
Hager B. H.	1277	Hornshøj P.	889
Haggerty P.	525	Hörz F.	107, 183, 565, 567, 809, 1021
Hahn J. M.	1461	Houck J.	925
Haines E. L.	499, 899	Housen K.	569, 1207
Halliday A. N.	1299, 1305, 1307, 1309	Howell E. S.	785, 1135
Hamilton V. E.	501, 503	Howington-Kraus A.	869
Hanner M. S.	123	Howington-Kraus E. A.	1519
Hansen O. S.	889	Hrubsch L.	183
Hansen V. L.	681	Hsu W.	571
Hanson B.	325, 505, 639	Huang H.-P.	1515
Hapke B.	507	Huang S.	573, 1547
Harper C. L. Jr.	509, 613	Hui J.	575
Harris R. S.	465	Hultgrien L. K.	577
Hartmann W. K.	511	Humayun M.	579, 581
Harvey R. P.	513	Hunten D. M.	337
Haskin L. A.	635, 637, 729, 943, 1149, 1151	Huss G. R.	583, 585, 587
Hawke B. R.	81, 127, 219, 515, 1077, 1145	Hutcheon I. D.	587
Hayashi J. N.	517	Hutchinson R.	11
Hays J. E.	519	Hyde T. W.	589, 591
Hayward T.	925	Iancu O. G.	917
Head J. W.	35, 65, 205, 237, 249, 305, 425, 469, 485, 487, 489, 521, 523, 525, 527, 529, 675, 677, 679, 821, 823, 963, 1051, 1317, 1329,	Ip W. H.	1173
		Ipatov S. I.	593
		Israel E. J.	927
		Ivanov A. V.	269, 595, 1565
		Ivanov B. A.	41, 67, 597, 599, 991, 1095
		Ivanova O.	353
		Ivliev A. I.	601, 603
		Iwase Y.	1193
		Izenberg N. R.	605, 1079

Izett G. A.	607	Kilburn C. R. J.	805
Jackson A. A.	609	Kim J. S.	701
Jackson T.	611	Kim Y.	701, 703
Jacobsen S. B.	509, 613	King N. L.	809
Jakosky B. M.	517, 533, 615	Kipp M. E.	295
James O. B.	617	Kirk R. L.	239, 705
Janes D. M.	619	Kirkpatrick R. J.	309
Jansa L. F.	1085	Kissel J.	75
Jenniskens P.	621	Klaasen K.	237, 453
Jerde E. A.	1299, 1301, 1311	Klein J.	539, 1523
Jessberger E. K.	139, 1341	Klingelhöfer G.	707, 709, 819
Jha K.	623	Klöck W.	381, 711, 713, 1341, 1393
Johnson C. L.	625	Knudsen J. M.	1, 819, 1293
Johnson G. P.	933	Kobayashi Y.	1269
Johnson G. V.	1433	Kochemasov G. G.	715
Johnson J.	417, 627, 629, 631, 1187	Koeberl C.	119, 427, 549, 581, 717, 719, 721, 761, 847
Jolliff B. L.	633, 635, 637, 729, 1149, 1151	Koga A.	723
Jones J. H.	615, 639, 651, 653, 879, 1009, 1513	Kohlstedt D. L.	439, 817
Jones R. H.	641	Koike O.	723, 725
Jons H.-P.	643	Komatsu G.	417, 631, 727, 1187
Joseph L. H.	645	Konno T.	1527
Joswiak D. J.	185	Kono R.	1193
Jull A. J. T.	647, 649	Kononkova N. N.	595, 905
Jurewicz A. J. G.	639, 651, 879	Konopliv A. S.	1281
Jurewicz S. R.	653	Korokhin V. V.	1331
Jurgens R.	655	Korotaeva N.	1197
Kadel S. D.	465	Korotev R. L.	637, 729, 1149, 1151, 1223
Kadik A. A.	657, 659	Korotkova N. N.	669, 671, 1185
Kalinina G. V.	671	Korotkova Yu. Yu.	603
Kallemeyn G.	661, 663, 1465	Kosarev I. B.	731
Kamp L. W.	453	Koshiishi H.	733, 737
Kanefsky B.	241	Kotelnickov S.	369
Kankeleit E.	709, 819	Kotsarenko N. Ya.	735
Kano N.	665, 1363	Kouda R.	733, 737
Kargel J. S.	555, 667, 799	Kozlowski R. W. H.	739
Karner J.	1301	Kracher A.	719
Kashkarov L. L.	601, 603, 669, 671, 1185	Krähenbühl U.	741
Kauhanen K.	673, 1411	Kraft R.	241
Kawakami S.	1099	Kralik C.	119
Keddie S.	529, 675, 677, 679	Kramer J. L. A. M.	743
Keep M.	681	Kramers J. D.	997
Kehm K.	683	Kransel G.	375
Keil K.	495, 865, 1497	Krasnopolsky V. A.	745, 747, 749
Keller H. U.	1293	Kraus G. F.	1013
Keller L. P.	21, 159, 259, 381, 685, 687, 1391, 1393	Krauss R.	1195
Kelley M. S.	689	Kreslavsky M. A.	751, 1109
Kelley S. P.	1321	Kring D. A.	177, 475
Kenealy D.	897	Kronrod M. A.	133
Kent R. M.	691, 693	Krot A. N.	753, 1469
Kerridge J. F.	695	Kubicki J. D.	755
Keyser L. F.	1343	Kucinskas A. B.	757
Khodakovsky I. K.	143	Kudo A. M.	299
Khromov V. N.	819	Kukhareno Yu.	1443
Kidder J. G.	697	Kuramoto K.	759
Kiefer W. S.	699	Kurat G.	761, 763, 979, 981
Kieffer H. H.	575	Kurokawa H.	1099
Kik A. C.	743	Kuzmitcheva M. Ju.	765
		Lacchia M.	467
		LaFave N.	1499

Lal D.	649	Makalkin A. B.	827
Lancaster M. G.	767	Makhloufi N.	3
Landheim R.	213, 769	Malcuit R. J.	829
Langenauer M.	741	Mann J. L.	831
Lauer H. V.	437, 771, 939	Marchenko A. G.	833
Lauretta D.	773	Marín L. E.	1221, 1255
Lavrukhina A. K.	775, 777, 1429	Martel L.	835
Lawler M. E.	779	Marti K.	347, 701, 703, 1093
Lawson C. L.	499	Martin P.	837
Lawson S. L.	781	Martin T. Z.	87
Layne G. D.	1043, 1257	Martinez I.	839
Le L.	883, 907	Martinez R. R.	1221, 1417
Leach R.	467	Marzari F.	841
Leago K. S.	1233	Masarik J.	843, 845, 1003, 1119
Lebofsky L. A.	783, 785, 1117, 1135	Master S.	847
Lebofsky N. R.	783	Mathew K. J.	849, 851
Lee D.-C.	1299	Matson D.	1019, 1433
Lee E. M.	871	Matsubaya O.	1539
Lee M. R.	449	Matsui T.	759
Lee P.	469, 787, 925	Matsuzaki H.	665, 853, 1363
Lellouch E.	143	Matushima K.	733
Lemoine F. G.	789, 791, 1291	Maurer M. J.	855
Leonard G. J.	231, 1379	Maurette M.	355, 761, 763
Lerch F. J.	789	Maxwell T. A.	857
Lewis R. S.	27, 103, 313, 563, 793, 1063	May L.	549
Limaye S. S.	1195	Mayeda T. K.	269, 865, 1457, 1459
Lin C.	1455	Mazarik J.	899
Lindley P. M.	1421	McBride K. M.	261
Lindstrom D. J.	1221, 1417	McCallum I. S.	859
Lindström M.	1385	McCarville P.	299, 861
Lindstrom M. M.	795, 797, 1153	McCloskey F. C.	353
Lipschutz M. E.	941, 1183, 1229, 1567	McCord T.	863, 1235
Lockwood J.	417, 799, 1187	McCoy T. J.	391, 865
Lodders K.	707	McDonald J. S.	749
Lofgren G. E.	279, 319, 801	McDonnell J. A. M.	183, 867
Longhi J.	803	McEwen A.	395, 453, 869, 871
Lopes-Gautier R.	805, 807, 1297	McFarlane E. A.	873
Loseva T. V.	987	McGee J. J.	875
Love S. G.	185, 809	McGill G. E.	877
Lucchitta B. K.	811	McGlaun J. M.	295
Lucey P. G.	83, 127, 533, 1077, 1145	McGovern P. J.	1317
Lugmair G. W.	813	McGuire J. C.	879
Luhmann J. G.	615	McHone J. F.	881
Luksch R.	795	McKay C. P.	491
Lunar Working Group of Japan	915	McKay D. S.	21, 23, 71, 125, 235, 259, 547, 685, 687, 1391, 1393
Luo W.	815	McKay G.	639, 883, 907, 923
Lynch D.	123	McKinnon W. B.	93
Lynch R. A.	933	McLeod L. C.	163, 885
Ma Z.	1063	McSween H. Y. Jr.	95, 181, 1057
MacIsaac C.	813	Medveduk S. A.	41
Mackwell S. J.	817	Meeker G. P.	887
MacPherson G. J.	269, 595	Meibom A.	889
Madsen J.	819	Melchior R. C.	891
Madsen M. B.	1, 819	Melosh H. J.	153, 597, 893, 1201, 1203, 1425
Maehr S. A.	995	Merényi E.	895
Magee K.	529, 821, 823	Merrell J. A.	897
Magellan Flight Team	1401	Meshcherskaya V. A.	197
Magellan Science Team	1245	Messenger S.	1391
Maharaj S. V.	825	Metzger A. E.	499, 899
		Metzler K.	901, 1157

Meyer B. S.	903	Nichols R. H. Jr.	105, 683
Middleton R.	539, 1523	Nicholson P.	925
Migdisova L. F.	905	Niedermann S.	997
Mikouchi T.	907, 923	Nier A. O.	185, 999, 1391
Miles J.	925	Nikishin A. M.	1001
Milkereit B.	1517	Nishiizumi K.	1003
Ming D. W.	435, 437	Nittler L.	1005
Minnitt R. C. A.	1121	Nogami K.	1363
Misawa K.	935	Nolan M. C.	153
Mitchell J.	1303	Noll P. D. Jr.	995
Mitreikina O. B.	909, 1559, 1561	Noma M.	1363
Mittlefehldt D. W.	639, 651, 797, 911, 1167	Nordlie J.	1507
Miura Y.	913, 915, 917, 919, 1269	Norman M. D.	495, 1007, 1009
Miyamoto M.	921, 923, 1371, 1375	Nusbaum R. L.	1067
Moersch J.	925	Nuth J. A. III	1011, 1013, 1389
Moholy-Nagy H.	549	Nyffenegger P.	285
Mollard J. D.	1127	Nyquist L. E.	1015, 1017
Moore B. J.	227		
Moore H. J.	927, 1483	Oberbeck V. R.	565
Moralev V. M.	431	O'Brien H. E.	859
Morgan J. W.	929	O'Bryan M. V.	1467
Morgan P.	931, 933	Ocampo A.	1019, 1095, 1297
Morgan T. H.	1099	Ocker K. D.	1021, 1039
Morikawa N.	935	O'Connor D. J.	265
Morioka M.	967	Okada A.	1269
Morris R.	23, 71, 437, 771, 937, 939, 941, 1165, 1205, 1223, 1261	Okada T.	1269
		O'Keefe J. D.	5, 1023, 1369
Morrison D.	237	Olsen E. J.	1025
Morse A. D.	173	Opanasenko N. V.	1271
Moss B. E.	943	Oran W. A.	1027
Mostefaoui S.	945	O'Reilly S. Y.	931
Mouginis-Mark P. J.	947, 949, 1147	Orenberg J. B.	1163
Muhleman D. O.	211, 951	Ori G. G.	1029
Munro D. C.	953	Orton G. S.	5, 1369
Murchie S.	955, 957, 1399	Ostermann M.	1031
Murer Ch.	959	Otsuki M.	1375
Murray B. C.	111, 599	Ott U.	1033
Murty S. V. S.	851	Owen T. C.	1419
Mustard J.	519, 955, 961, 963, 1407	Ozaki H.	1035
Nagahara H.	723, 965	Paige D. A.	69, 1037
Nagao K.	919, 1269	Palma R. L.	1039
Nagasawa H.	725, 967, 1539	Palme H.	141, 375, 901, 981, 1563
Nakamura N.	935	Papanastassiou D. A.	1041, 1253
Nakamura T.	969	Papike J. J.	385, 1043, 1045, 1111, 1257, 1259
Namiki N.	971, 973		
Nash D.	897, 975	Pappalardo R.	469, 787, 1047
Nava D. F.	977	Parfitt E. A.	1049, 1051
Nazarov M. A.	905, 979, 981, 1185	Parker T. J.	1053, 1055, 1205
Neal C. R.	983, 1033, 1305	Parmentier E. M.	205, 541, 623, 1577
Nehru C. E.	1107	Patchen A.	235, 547, 1313
Nelson R.	985, 1297, 1389	Patel G. B.	789
Nemtchinov I. V.	731, 987, 989	Paterson B. A.	1057
Neuking K.	713	Pechernikova G.	1441, 1443
Neukum G.	237, 991	Pedroni A.	1059, 1061
Neumann G. A.	993	Pellin M. J.	1063
Newmann G. A.	1577	Pepin R. O.	77, 1065
Newsom H. E.	995, 1259	Permenter J. L.	1067
Newton J.	1435	Perreau M.	355
Ngo H. H.	1041	Perron C.	945
Nguyen T.	1261	Petaev M. I.	37, 1069, 1071, 1073
		Peters M. T.	1075

Peterson C. A.	1077	Rivkin A. S.	785, 1135
Petit J.-M.	411	Roark J. H.	387, 389
Pettengill G. H.	1279	Robertson B.	1517
Phillips R. J.	697, 885, 1079	Robertson D.	847
Phinney W. C.	1081	Robinett L.	655
Pieters C. M.	117, 119, 371, 1083, 1329, 1333, 1359, 1407	Robinson C. A.	1137, 1139
Pilkington M.	1085	Robinson M. S.	453, 1141, 1143, 1145, 1147, 1473
Pillinger C. T.	171, 173, 339, 373, 449, 451, 1247, 1435, 1515	Robinson R.	71
Pinet P. C.	249, 837, 1159, 1181	Rockow K. M.	637, 729, 1149, 1151
Pingitore N. E. Jr.	1513	Rode O. D.	1153, 1333
Pinkerton H.	691, 693, 1087, 1089	Roedder E.	513
Plaut J. J.	33, 301, 781, 1091, 1483	Romanek C. S.	1155
Plescia J. B.	1323	Romstedt J.	1157
Podosek F. A.	1033	Rong W.	1455
Polk K.	455	Rosenblatt P.	1159
Pollack J.	467	Rossman G. R.	1343
Pollack J. B.	85, 191, 747, 1521	Roush T. L.	87, 1161, 1163, 1165
Ponganis K. V.	1093	Rousset A.	837
Pope K. O.	1095	Rowan L. R.	1167
Popov S. P.	989	Rowland S. K.	1147
Popova O. P.	765	Rowlands D. D.	791
Porcelli D.	1097	Rubie D. C.	551, 873
Potter A. E.	1099, 1573	Rubin A. E.	1169
Povenmire H.	427, 1101	Rud N.	889
Powell R. A.	721	Ruff S. W.	1171
Pratt S. F.	371	Rulle H.	1341
Premo W. R.	1103	Russell R.	123
Presper T.	711	Rutherford M. J.	557
Price M.	1105	Ruzmaikina T. V.	1173
Prilutski O.	819	Ryan E. V.	1175
Prilutski O. F.	709	Rybakov V. A.	41
Prinz M.	1107, 1481	Ryder G.	289, 1177, 1179, 1255, 1399
Pronin A. A.	1109		
Pun A.	1111	Sabol D. E. Jr.	1181
Pybus G. Q. J.	1113	Sack R. O.	1183
Pyle D. M.	1087, 1089	Safford M.	417
		Sahijpal S.	1185
Quinn R.	1543	Sahuaro High School Astro- nomical Research Class	417, 1187
Racca G. D.	253	Saiki K.	1373
Radocinski R. G.	499	Sakimoto S. E. H.	1189
Raitala J.	1115	Sakurai H.	1363
Raiteri C. M.	209	Salisbury J. W.	1191, 1453
Rammensee W.	375	Sammis C. G.	155
Rao M. N.	403, 1039	Sandwell D. T.	625
Rappaport N. J.	51	Santek D.	1195
Rasmussen K. L.	889	Sasaki S.	1193
Reed K. L.	1117	Saunders R. S.	1055, 1195, 1245
Reedy R. C.	843, 845, 899, 1003, 1119	Sazonova L.	369, 1197
Reid A. M.	1513	Schaber G.	55, 229, 1199, 1353
Reidy A. M.	389	Schaller C. J.	1201
Reimold W. U.	161, 423, 717, 719, 721, 847, 1113, 1121	Schärer U.	839, 1031
Reyes-Ruiz M.	1123	Schenk P.	277, 1203, 1205
Reynolds S. J.	1047	Scherber D. S.	817
Rice J. W. Jr.	91, 1125, 1127	Schlichting F.	709
Richter W. M.	591	Schlutter D. J.	185, 999, 1391
Riciputi L. R.	1057, 1311	Schmidt R. M.	1207
Rietmeijer F. J. M.	493, 1129, 1131	Schmidt S.	343
Riley K. M.	1133	Schmitt R. T.	1209
		Schultz P. H.	47, 61, 457, 459, 1211,

Schultz P. H. (cont.)	1213, 1215, 1355	Snyder G. A. (cont.)	1305, 1307, 1309, 1311, 1313
Schultz R. A.	1217, 1219	Snyder K. D.	739
Schulz C. K.	125	Socki R. A.	1155
Schuraytz B. C.	1221, 1255, 1399	Soderblom L. A.	453, 807, 871, 1293
Schwarz C.	1223	Solomatov V. S.	1315
Scoon G.	49	Solomon S. C.	971, 973, 1277, 1317
Scott D. H.	1225	Sonett C. P.	561
Scott E. R. D.	495, 865, 1227	Sørensen S. A.	207
Sears D. W. G.	97, 99, 247, 573, 1229, 1367, 1545, 1547	Sorkhabi R. B.	881
Sears W. D.	1231	Souzis A. E.	539
See T. H.	107, 567, 1233	Speidel D. H.	1319
Segura M.	1235	Spettel B.	141, 901, 981, 1061
Sekine T.	969	Spilde M. N.	1043
Self S.	1383	Sprague A. L.	337, 739
Semenenko V. P.	1237, 1239	Spray J. G.	1321
Semjenova L. F.	373	Spudis P. D.	127, 1077, 1255, 1323
Senftle F.	549	Squyres S.	619, 925
Senske D.	463, 531, 1241, 1243, 1245	Srinivasan G.	1325
Sephton M. A.	1247	Sromovsky L. A.	1195
Sevier J.	1249	Stadermann F. J.	1327
Shaffer E.	1075	Staid M. I.	1329
Shapkin A. I.	1251	Starkey G.	1397
Sharma M.	1253	Starodubtseva O. M.	1331
Sharma P.	1003	Starukhina L. V.	1333
Sharpton V. L.	201, 537, 1221, 1255	Steele I. M.	1025, 1335, 1337, 1339
Shearer C. K.	385, 1043, 1045, 1257, 1259	Stein T.	1287
Shelfer T. D.	1261	Stephan T.	1341
Shepard M. K.	1263	Stephens S. K.	1343
Shervais J. W.	1265	Stephenson S.	1381
Shevchenko V. V.	1267	Stepinski T. F.	1123
Shih C.-Y.	1015, 1017	Stern S. A.	377
Shilobreeva S. N.	659	Stevenson D. J.	1315, 1343
Shima M.	1269	Stewart A. D.	1323
Shkuratov Yu. G.	1271, 1333	Stocco K.	795
Shukolyukov A.	813, 1273	Stockman S.	389, 1345
Shuvalov V. V.	39	Stofan E. R.	33, 301, 501, 503, 1091, 1245
Sidorov Yu. I.	1251	Stöffler D.	497, 901, 1209, 1347
Signer P.	959	Stolper E. M.	79, 755, 1471
Simmons E. C.	1303	Stooke P. J.	1349
Simon S. B.	315, 1275	Strait M. M.	1351
Simonelli D.	453	Strange R.	1101
Simons M.	1277, 1317	Strebel R.	563
Simpson R. A.	855, 1279, 1503	Strobert D.	655
Sims K. W. W.	995	Strom R. G.	55, 1199, 1353
Singer R. B.	895, 1293	Stutz J.	241
Sjogren W. L.	51, 1281	Sugita S.	1215, 1355
Skinner W. R.	1283, 1285	Sugiura N.	919, 1357
Slade M.	211, 655, 951	Sullivan R.	469, 787
Slavney S.	1287	Sunshine J.	553, 961, 1235, 1359
Smalley R. E.	545	Suppe J.	1105
Smith C. B.	161, 1113	Sutton S. R.	167, 323, 381, 713, 1361, 1391
Smith D. E.	789, 791, 1289, 1291	Suzuki Y.	1363
Smith M.	925, 1181	Svetsov V. V.	1365
Smith P. E.	549	Svitek T.	111
Smith P. H.	1293	Swaby B.	795
Smoliar M. I.	929	Swan P.	401
Smrekar S. E.	1295	Swann J. D.	871
Smythe W.	807, 985, 1297	Swindle T. D.	475
Snyder G. A.	73, 1299, 1301, 1303,	Symes S. J.	97, 1367

Takano A.	733	Veselova G. V.	709
Takata T.	5, 1023, 1369	Veverka J.	237, 453, 469, 787, 1395
Takeda H.	921, 969, 1371, 1373, 1375, 1525	Vickery A. M.	153, 1437
Talent D.	1099	Vilas F.	553, 1439
Tanaka K. L.	231, 317, 331, 443, 1377, 1379	Vis R. D.	743
Tanner W. G. Jr.	1381	Vistisen L.	1, 819
Tatsumara M. J.	189	Vityazev A.	1441, 1443
Tatsumoto M.	1103, 1409	Voelkel R.	1445
Taylor G. J.	189, 391, 835, 1077, 1383	Vorder Bruegge R. W.	1447, 1449
Taylor L. A.	73, 235, 547, 983, 1299, 1301, 1303, 1305, 1307, 1309, 1311, 1313	Vormaier A.	719
Tejfel V. G.	1331	Wacker J. F.	1275
Tertichnaya B. V.	1237, 1239	Wadhwa M.	1451
Teterev A. V.	989	Wagstaff J.	883
Teucher R.	709	Wald A. E.	1191, 1453
Thalmann Ch.	997	Walker R.	401, 929, 1005
Therriault A. M.	1385	Walker R. M.	1391
Thiemens M. H.	611, 1387, 1389	Wallmach Th.	423
Thomas K. L.	381, 687, 1341, 1391, 1393	Wang H.	1455
Thomas P.	453, 469, 787, 1395, 1397	Wang J.	1457, 1459
Thompson P.	1399	Ward W. R.	1461
Thompson R. N.	1063	Warren J.	1233, 1393
Thompson T. W.	1401	Warren P. H.	663, 1463, 1465
Thornhill G. D.	1139, 1403	Wasilewski P. J.	1467
Thorpe A. N.	549	Wasserburg G. J.	209, 245, 583, 585, 587, 1041, 1097, 1253
Tobola K.	795	Wasson J. T.	255, 753, 1469
Tomasko M. G.	1293	Watson G.	1105
Tomeoka K.	969	Watson L. L.	1471
Tomkinson K.-A.	1405	Watson W. B.	325
Tomobuchi M.	1375	Watters T. R.	1473
Tompkins S.	1407	Wdowiak T. J.	1143
Torigoye N.	1409	Weber D.	1475
Törmänen T.	673, 1411	Weidenschilling S. J.	1477
Träxler B.	719	Weigel A.	1479
Treiman A.	795, 797, 1413, 1415, 1417	Weisberg M. K.	1107, 1481
Trilling D.	467	Weiss J. R.	985
Trombka J. I.	267	Weissman P. R.	453
Trucano T. G.	295	Weitz C. M.	67, 1483
Tryka K. A.	1419	Wells E. N.	1541
Tsou P.	183, 1421	Wenrich M. L.	1485
Turcotte D. L.	757, 1423	Wentworth S. J.	25, 71
Turtle E. P.	1425	Wetherill G. W.	1487
Tyler G. L.	1503	Wharton R. A. Jr.	119
Ulyanov A. A.	1325	Whitaker E. A.	893
Ustinova G. K.	19, 777, 1427, 1429	White B.	467
Valter A. A.	1431	Wichman R. W.	1489, 1491
Van Cleve J.	925	Wieder M.	187
Vaniman D. T.	121	Wieler R.	959
van Oss C. J.	1445	Wiesmann H.	1015, 1017
Vanzani V.	841	Wilhelms D. E.	91
Vasavada A. R.	1037	Williams D. A.	465, 1493
Veeder G. J.	1433	Williams D. B.	1529
Vempati R. K.	771	Williams J.	183, 689
Verchovsky A. B.	373, 1435	Williams R. S. Jr.	409
Verkhoglyadova O. P.	735	Williams S.	233, 327, 1521
		Wills E. L.	1261
		Wilson D.	1205
		Wilson L.	361, 421, 527, 953, 1049, 1051, 1405, 1495, 1497
		Wilson T. L.	1499, 1501
		Winters R. R.	829

Witteborn F. C.	739	Yingst R. A.	1531
Witzke B. J.	31	Yoneda S.	1533
Wlotzka F.	329, 363, 413, 415, 1061	York D.	549
Wolbach W. S.	251, 545	Yu Y.	1535, 1537
Wong P. B.	1503	Yurimoto H.	723, 725, 1539
Wood C. A.	1491, 1505, 1507		
Wood J. A.	1071, 1073, 1509	Zanda B.	279, 543, 1537
Wood S. E.	1037	Zare R. N.	1391
Wooden D.	739	Zashu S.	1357
Woronow A.	1511, 1513	Zbik M.	445, 447
Wright E.	1195	Zellner B.	957, 1541
Wright I. P.	339, 451, 1435, 1515	Zent A. P.	1543
Wu J.	1517	Zhang Y.	1545, 1547
Wu S. S. C.	1519	Zheng F.	1455
		Ziglina I. N.	1549
Xu P.	1521	Zimbelman J. R.	1225, 1551, 1553, 1555
Xue S.	539, 1523	Zimmerman M. E.	817
		Zinner E.	27, 347, 375, 1005, 1475, 1557
Yakovlev O. I.	329, 413, 415		
Yamaguchi A.	1375, 1525	Zinovieva N. G.	909, 1559, 1561
Yamakoshi K.	665, 853, 1363	Zipfel J.	1563
Yanagisawa M.	1527	Zolensky M.	181, 435, 567, 595, 645, 941, 1233, 1565, 1567
Yanai K.	917, 935, 1409		
Yang C. W.	1529	Zolotov M. Yu.	1569, 1571
Yang S. V.	435, 595, 1565	Zook H. A.	609, 1573
Yaroshevsky A. A.	905	Zuber M. T.	789, 791, 993, 1289, 1575, 1577
Yen A. S.	599		
Yingst A.	529	Zubkov B.	819

SAMPLE INDEX*

10002	1299	15445	1305	68501	77, 1065
10010	1267	15474	289	68815	649, 1003
10011	1267	15495	579		
10020	97	15499	97	70001	97, 1367
10049	97	15505	579	70002	97, 1367
10084	235, 259, 371, 507, 547, 649, 685	15555	579, 1017	70003	97, 1367
10086	173	15556	579	70004	97, 1367
		15666	289	70005	97, 1367
		15682	289	70006	97, 1367
12002	97			70007	97, 1367
12005	97	20001	1267	70008	97, 1367
12009	579	20002	1267	70009	97, 1367
12011	97	20003	1267	70051	1181
12021	97, 1373	20004	1267	70135	1017
12023	173	24080-24102	1429	71055	235
12031	1373	24105-24114	1429	71501	77, 105, 959, 999, 1065
12034	1017	24118	1429		
12037	1267, 1373	24143	1153, 1429	72215	617
12038	1017	24160	1153	72235	617
12052	97	24184	1429	72255	617
12056	1017			72275	617
12064	1373	60006	125	72315	617
12070	507	60009	97, 125, 1267, 1367	72395	617
		60010	97, 1267, 1367	72443	637, 1149, 1151
14066	1305, 1307	60013	97, 1367	72503	637, 1149, 1151
14078	1017	60014	97, 1367	73215	617
14141	1267	60015	579	73221	649
14160	1307	60025	1103, 1309	73241	649
14161	633	60255	1301	73255	617
14163	579, 581	60315	97	73261	649
14303	1305	60635	1301	74001	21, 1181
14304	1307, 1311	60639	1301	74002	1003
14305	1265, 1305, 1307	61181	71	74220	21, 23, 325, 505, 579, 1181, 1267
14306	1305	61221	259, 371		
14310	97, 1017	61249	1301	74240	1267
14318	1311	62237	1103, 1309	74241	1181
14321	1305, 1307	62245	1301	74255	1017
		63321	371	75061	23
15001	1119, 1429	64515	1301	75075	1017
15002	1429	64801	371, 579	75081	1065
15003	1429	65795	1301	76015	617
15004	1429	65905	1301	76230	1525
15005	1429	67048	1301	76235	617
15006	1429	67075	859, 1103	76255	617
15009	1003	67235	1525	76315	617
15016	579	67461	371	76503	637, 1149, 1151
15041	579	67513	635	76535	579, 617
15058	97	67559	1301	77017	617
15065	579	67601	1267	77035	1045
15076	1017	67635	875	77135	617
15125	289	67637	875	77215	617, 1045
15386	557, 579, 1017	67701	259, 371, 1267	78235	617, 1045
15401	21, 1181	67747	1301	79001	1003
15403	1307	67915	875	79002	1003
15405	557, 1179, 1307	67975	633, 1307	79035	999, 1065
15415	875, 1103	68001	1223, 1313	79215	1525
15427	325	68002	1223, 1313	79221	1003
15437	875	68415	97		

*Page numbers refer to the first page of an abstract in which a sample is mentioned.

METEORITE INDEX*

Abee	449, 617	Allende (cont.)	1275, 1283, 1339,
Acapulco	347, 683, 703, 777,		1467, 1533, 1539,
	945, 1071, 1073,		1567
	1371, 1375, 1523,	Andreevka	1239
	1563	Angra dos Reis	245, 813, 1273
Acfer 094	115	Angrite	923
Acfer 111	959, 1061	Arapahoe	475
Acfer 153	1157	Asuka 881757	1017, 1373, 1463
Acfer 182	449, 1475	Atlanta	1545, 1547
Acfer 214	363	Ausson	95
Adhi-Kot	617, 1545		
Aioun El Trouss	385	Bachmut	1237, 1239
Al Rais	269	Barea	1529
Alais	349, 435, 713	Barringer	913
Alende	639	Barwell	587
Allan Hills 76004	1339	Belgica 7904	941
Allan Hills 76005	647	Belle Plaine	1169
Allan Hills 77005	403, 797, 911, 1417,	Bencubbin	1227
	1465	Benld	653
Allan Hills 77011	753	Bennett County	929
Allan Hills 77081	1523, 1563	Béréba	1273
Allan Hills 77156	801	Bholghati	981, 1015
Allan Hills 77214	573	Bielokrynitschie	1239
Allan Hills 77256	385	Binda	1111
Allan Hills 77257	647	Bishunpur	11, 583, 585, 945,
Allan Hills 77278	753		1229, 1481
Allan Hills 77296	801	Bjurböle	95, 977, 1467
Allan Hills 77307	165, 167	Bogou	245
Allan Hills 78019	647	Bouvante	639, 1273
Allan Hills 78084	99	Bovedy	587
Allan Hills 78132	647	Boxian	247
Allan Hills 78230	1073	Brachina	1183
Allan Hills 81005	97, 127, 797, 1463	Brenham	701
Allan Hills 81011	647	Bruderheim	1429
Allan Hills 81021	801, 1547		
Allan Hills 81101	611, 647, 663	Caddo County	1375
Allan Hills 81187	1523, 1563	Calcalong Creek	797
Allan Hills 81261	1073, 1523, 1563	Cañon Diablo	245, 273, 665
Allan Hills 82106	647, 663	Cape York	245
Allan Hills 82130	647	Carlton	1337
Allan Hills 84001	451, 647, 797, 911,	Cat Mountain	177, 475
	919, 1043	Cerro los Calvos	865
Allan Hills 84136	647	Chainpur	11, 743, 977, 1229,
Allan Hills 84170	801, 1545, 1547		1467, 1481
Allan Hills 84190	1523	Chassigny	403, 911, 1413, 1451,
Allan Hills 84206	1545, 1547		1471
Allan Hills 85001	647	Chico	495, 1017, 1169
Allan Hills 85045	1057	Chinguetti	1529
Allan Hills 85085	595	Clovis	587
Allan Hills 85119	1545, 1547	Coolidge	661
Allegan	1467	Cumberland Falls	611
Allende	79, 245, 313, 315,		
	375, 553, 579, 651,	Daniel's Kuil	1545
	665, 723, 725, 777,	Dengli	1185
	887, 957, 969, 977,	Derrick Peak	245, 929
	979, 1075, 1227,	Dhajala	573, 1429

*Page numbers refer to the first page of an abstract in which a meteorite is mentioned.

Dioux County	1273	Ikh rarene	587
Divnoe	1069, 1523	Imilac	921
Eagle Station	777, 1545	Indarch	585, 777, 1545, 1547
Efremovka	1325, 1557	Inman	585, 945
El Sampal	1337	Innisfree	1429
El Taco	849	Ivuna	349, 435, 1565
Elenovka	1237, 1239	Jilin	99
Elephant Moraine 79001	339, 403, 451, 911, 1413, 1417	Jodzie	979, 981
Elephant Moraine 79002	385, 647	Johnstown	385, 911
Elephant Moraine 79004	647	Juvinas	1273
Elephant Moraine 79005	647	Kaidun	269, 435, 595, 1185, 1565
Elephant Moraine 83213	25	Kainsaz	165, 167, 641
Elephant Moraine 83225	647	Kakangari	1523
Elephant Moraine 83230	1025	Kapoeta	37, 981
Elephant Moraine 83235	647	Kenna	137, 1409
Elephant Moraine 83254	1547	Khaipur	1545
Elephant Moraine 83322	1545	Khairpur	1547
Elephant Moraine 84302	703, 1073, 1371, 1375, 1479, 1523	Kho har	945
Elephant Moraine 87503	611, 1015	Knyahinya	843
Elephant Moraine 87511	663	Kota-Kota	1545
Elephant Moraine 87513	1015	Krymka	573, 1229, 1237, 1239, 1435, 1481
Elephant Moraine 87517	647	Kuleschovka	1239
Elephant Moraine 87521	97, 797, 1463	Kyushu	95
Elephant Moraine 87555	95	La Criolla	665
Elephant Moraine 87720	647	Lafayette	391, 911, 1471
Elephant Moraine 87746	1545	Lakangaon	639
Elephant Moraine 87770	1565	Lancé	641
Elephant Moraine 90004	1155	Laochengzhen	247
Elephant Moraine 90007	1155	Leonovka	1237, 1239
Elephant Moraine 90022	1155	Leoville	969, 1537
Elephant Moraine 90102	1545	Lewis Cliff 85300	981, 1015
Elephant Moraine 90299	1545	Lewis Cliff 85319	99
Ellemeet	385	Lewis Cliff 86001	647, 831
Enon	701	Lewis Cliff 86010	813, 1015, 1017, 1273
Enshi	247	Lewis Cliff 86024	1057
Erevan	979, 981	Lewis Cliff 87051	907
Esquel	921	Lewis Cliff 87119	1545, 1547
Fayetteville	959, 1061	Lewis Cliff 87223	319, 801, 1547
Flindersites	447	Lewis Cliff 87295	647
Forest Vale	701, 1057	Lewis Cliff 88008	385
Frontier Mountain 90011	703, 1479, 1523	Lewis Cliff 88135	1545
Frontier Mountain 90054	663	Lewis Cliff 88180	801, 1545, 1547
Galim	543	Lewis Cliff 88280	1479, 1523
Gibeon	245	Lewis Cliff 88516	403, 647, 797, 911, 1417
Gibson	1479, 1523	Lewis Cliff 88663	1169
Goalpara	1409	Lewis Cliff 88714	1545
Gorlovka	1239	Lewis Cliff 88774	663, 1107, 1465
Governador Valadares	391	Limerick	1057
Grant	539, 1025	Lodran	703, 1073, 1479
Hallingeberg	95	Lodranite	921
Happy Canyon	1545, 1547	Lombard	929
Haverö	137, 663	Loongana 001	661
Huittis	1545	Los Martinez	587
Ibbenburen	385	Lost City	99, 651, 879, 1429
Ibitira	651, 1273	Lubbock	475

MacAlpine Hills 88104	97, 1463	Pecora Escarpment 82506	647, 663, 1409
MacAlpine Hills 88105	97, 1463	Pecora Escarpment 82507	923
MacAlpine Hills 88136	319, 801, 1545, 1547	Pecora Escarpment 82518	319, 1545, 1547
MacAlpine Hills 88177	1371, 1479, 1523	Pecora Escarpment 86502	137
MacAlpine Hills 88180	1545	Pecora Escarpment 91002	1357
MacAlpine Hills 88184	1545	Pecora Escarpment 91020	801
Manegaon	385	Pecora Escarpment 91077	385
Manych	587, 945	Pecora Escarpment 91020	1545
McKinney	95	Pecora Escarpment 91085	1545, 1547
Meghei	957	Pecora Escarpment 91238	1545
Messenya	945	Pesyanoe	1065
Meteorite Hills 78008	1409	Pillistfer	1545
Meteorite Hills 78028	99	Pinnaroo	1529
Mező-Madaras	245, 753, 945	Pomozdino	1273
Mihonoseki	917	Pontlyfni	1523
Millbillillie	1273, 1525	Pribram	1429
Moama	1111	Pultusk	561
Monument Draw	1563		
Moorabie	865	Qingzhen	571, 665, 801, 1545, 1547
Moore County	1111, 1273	Queen Alexandra Range 90210	1057
Mount Edith	1025		
Mount Joy	929	Ragland	587
Mundrabilla	25	Ramsdorf	495, 1169, 1239
Murchison	27, 37, 103, 135, 181, 313, 355, 373, 401, 563, 583, 585, 639, 645, 651, 665, 793, 903, 941, 979, 1005, 1063, 1283, 1567	Reckling Peak 79015	1167, 1529
	979	Reckling Peak 80259	801, 1547
Murray		Renazzo	269, 543, 1537, 1565
		Rochester	247
		Rose City	1169
Nakhla	1, 391, 403, 451, 883, 911, 1413, 1451, 1471	Saint Sauveur	543, 617, 1547
Nantan	245	Saint-Séverin	99, 639, 651, 843, 879, 1429
Navajo	929	Sandia Mountain	929
Negrillos	929, 1041	Santa Cruz	1565
Netschaëvo	865	São Julião de Moreira	929
Noblesville	795, 1061	Saotone	917
Norton County	611	Saratov	1237, 1239
Novo Urei	137	Semarkona	11, 543, 573, 585, 587, 1227, 1229, 1481, 1537
Nuevo Laredo	639, 1273		
Nuevo Mercurio	665	Sena	1237
		Serra de Magé	1111
Ollague	979	Severenyi Kolchim	1185
Orgueil	269, 349, 355, 381, 579, 583, 585, 713, 761, 763, 777, 903, 957, 1033, 1435, 1565	Shallowater	683
		Sharps	11, 1481
Ormans	165, 167, 641	Shaw	95, 1169
Orvinio	475	Shergotty	403, 883, 911, 1413, 1471
		Shikhote Alin	849
Paranaiba	1169	Shirahagi	917
Pamallee	11	Sioux County	639, 651
Parsa	543	Smithsonian	929
Pasamonte	1273	Springwater	1335
Patuxent Range 91501	25, 95, 513, 1169	Stannern	639, 1273, 1525
Patwar	1529	Suizhou	247
Pavlodar	1335	Suwahib (Buwah)	865
Peace River	247, 1429		
Peckelsheim	385	Tadjera	957
Pecora Escarpment 82502	647, 1273	Tahara	917
		Taiban	1169

Taizhou	1455	Yamato 74356	1525
Tatahouine	385, 1479	Yamato 75011	1015
Theil Mountains 91714	1547	Yamato 75097	935, 1183
Thiel Mountain 91714	801	Yamato 790143	1169
Thiel Mountains 82410	385	Yamato 790964	1169
Thiel Mountains 91714	1545	Yamato 79097	95
Tieschitz	11, 401, 945, 1005, 1057, 1537	Yamato 791197	1463
Tocopilla	1041	Yamato 791491	1073, 1479, 1523
Toluca	509	Yamato 791493	1071, 1073
Torino	1017	Yamato 791538	663
Trenton	245	Yamato 792769	1015
Tsarev	905, 1185, 1239	Yamato 793164	1015
		Yamato 793169	1373, 1463
		Yamato 793241	935, 1183
Ucera	99	Yamato 793274	1463
		Yamato 793421	95
Vigarano	79, 223, 1075	Yamato 794046	935, 1183
		Yamato 82162	941
Warrenton	165, 167	Yamato 82192	97, 1463
Weatherford	1227	Yamato 8451	921
Weston	77	Yamato 86032	1463
Wiley	777	Yamato 86720	941
Willaroy	865	Yamato 92510	1015
Winona	1523		
Wray	865	Yanzhuang	1169
		Yilmia	1545
Xi Ujimqin	247	Zaborzika	1237, 1239
Yamato 691	801	Zagami	1, 403, 911
Yamato 74013	1371	Zaoyang	247
Yamato 74063	1073, 1523	Zhigailovka	1239
Yamato 74160	1169	Zvonkove	1239

KEYWORD INDEX*

Ablation	1365	Apollo 16	351, 635, 943, 1301, 1313
Abrasion	1285	Apollo 17	617, 637, 1151, 1181
Abriachan	1179	Apollo subsatellites	791
Abundances	1061	Aqueous alteration	349, 595, 1439
Acapulcoites	703, 1071, 1073, 1371, 1375, 1523, 1563	Archeology	549
Acapulco metal	347	Archives	1287
Accretion	57, 307, 509, 1259	Argon	137, 971
Accretional shock	1173	Ariel	285, 1193
Achondrites	647, 703, 901	Arsia Mons	1225
Acid etching	649	Artemis Corona	179
Admittance	1277	Artificial intelligence	1513
Adsorption	1543	ARTIST	783
Aerogel	183, 1515	Ascræus Mons	1225
AGB stars	151, 209, 583, 585	Asgard	91
Age dating	997	Assimilation	1511
Ages	19, 813, 1015, 1105	Asteroid breakup	1215, 1479
Agglutinates	71, 547, 685, 937	Asteroid families	689, 841, 1507
Alba Patera	491, 643, 1425	Asteroid genetic links	689
Albedo	1117	Asteroids	43, 89, 153, 175, 183, 185, 237, 243, 265, 365, 379, 399, 411, 453, 469, 495, 561, 609, 711, 785, 787, 795, 797, 991, 999, 1083, 1117, 1135, 1175, 1395, 1439, 1487, 1497, 1541
Alkali elements	1009	Asteroids, Earth-approaching	153
Alkali suite	1303, 1307, 1311	Astrobleme	369, 1197, 1431
Alkalies	753	Astronomy	1499, 1501
Alkylammonium	435	Atmosphere entry heating	381
Alluvium	459	Atmospheres	39, 143, 337, 377, 745, 747, 749, 987, 1023, 1093, 1331, 1397, 1437, 1569
Alpha Regio	425, 463	Atmospheric chemistry	201
Alteration	181, 299, 315, 645, 887	Atmospheric effects	1213, 1215
Alternative	1027	Atmospheric entry heating	711, 713
Altimeter topography	1055	Atmospheric evolution	615
Aluminum oxide, presolar	583	Atmospheric stability	429
Aluminum-26	27, 363, 539, 587, 1005, 1185, 1475, 1523	Aubrites	383
Ames Vertical Gun	61, 1211, 1213, 1215	Axial focusing	145
Ammonia	173	Axtell	1275
Ammonia-water	439, 555	Backscatter	627, 1483, 1503
Amorphous rims	105	Baddelyite	427
Analog	437	Barberton greenstone belt	717
Analysis, in situ	75	Barberton Mountain land	717
Ancient atmosphere, Mars	511	Barometry	1021
Angrite	907	Barringer impact crater	913
Anhydrite, vaporization	413	Barringerite	979
Annealing	95, 493	Basalt-eclogite	205
Anorthosites	875, 1077, 1103	Basaltic glass	505
Antarctic meteorites	13, 99, 941, 1035, 1155	Basalts	361, 1301, 1343, 1415, 1511, 1513, 1551
Antarctica	119, 917, 1125		
Antipodal focusing	145		
Apatite	881		
Aphrodite	229		
Aphrodite Terra	1405		
Apollo 11	1299		
Apollo 14	633, 1305, 1307		
Apollo 15	289		

*Page numbers refer to the first page of an abstract in which a term is mentioned.

Beast wave	41	Chemical fractionation	1183
Beneficiation	235	Chemical kinetics	707, 773
Bistatic	1279	Chemical mapping analysis	1373
Black chondrites	957	Chemical separations	401
Blanks	983	Chemical weathering	707
Blocks	261	Chemical zoning	907, 921, 1371
Blue CL enstatite	319	Chemistry	119, 685, 747, 1089, 1221, 1393
Bolides	5, 39, 1023, 1365, 1397	Chervony Kut	813
Borealis Basin	293	Chicxulub	537, 1095, 1201, 1211, 1221, 1255
Boulders	261	Chladniite	1337
Bromine, enrichment	139	Chondrites	11, 181, 279, 645, 661, 865, 905, 945, 1237, 1239, 1357, 1455, 1529, 1559, 1561
Bulk chemistry	981	Chondritic material	1457
Bulk composition	1563	Chondritic meteorites	561
Bulk regolith, composition	1153	Chondrule formation	573, 1229
Bunte breccia	31	Chondrule mesostases	11
Buoyant	623	Chondrule metamorphism	801
Bushveld complex	1121	Chondrule rims	1469, 1481
		Chondrule texture	801
Cadmium	1207	Chondrules	7, 279, 307, 345, 471, 543, 573, 587, 641, 723, 743, 753, 945, 965, 977, 1173, 1227, 1285, 1467, 1469, 1481, 1535, 1537
Calcium-aluminum-rich inclusions	79, 223, 315, 363, 471, 587, 725, 763, 825, 887, 965, 1075, 1283, 1475, 1533, 1539, 1557	Chrometers	683
Calderas	305, 527	Chromite	1107
Calibration	85, 87, 107, 567	Chromium	907, 1033
Callisto	91, 455	Chronology	475, 587, 1409
Camera	1573	Cinder cones	317
Canal	727	CK chondrites	1155
Canali	667	Classification	1347
Cap	69	Clays	53
Carbide	1465	Clementine	21, 1573
Carbon	659, 687, 945, 1107, 1435, 1515	Climate	69, 191, 933, 1543
Carbon abundance	1391, 1393	Clinopyroxene	369
Carbon dioxide, trapping	415	Clouds	747
Carbon isotopes	339, 373	Cloudy zones	1529
Carbon-14	647, 649	CM chondrites	115, 181, 645, 1131, 1565
Carbonaceous chondrites	199, 269, 645, 671, 957, 969, 979, 981, 1567	CM2 chondrites	181, 645, 665
Carbonaceous material	355	CO3 chondrites	165, 167, 641
Carbonates	201, 339, 349, 481, 687, 1343, 1485	Coagulation	1443
Carbonatite	667	Coarse fines	289
Carson Quadrangle	463, 1243	Cobalt	657
Carvon	759	Cohenite	663, 1465
Cathodoluminescence	319, 449, 571, 1339, 1547	Coherence	113
CD-ROM	311	Collision experiments	1175
Cementation	201	Collision integral	1549
Ceraunius Tholus	947, 1147	Collisions	569, 841, 1441
Channels	207, 631, 727, 885, 1029, 1493	Color	1145
Channels, depth	811	Combustion	171, 373, 793, 1435
Channels, floors	811	Comet Halley	1143
Channels, walls	811	Comet Shoemaker-Levy 9	5, 93, 101, 295, 597, 1023, 1369, 1527
Characterization	253	Cometary breakup	295
Chassigny	1451		
Chelmsfold turbidites	1517		

Cometary ionosphere	735	Cryovolcanism	555
Cometary nuclei	1527	Cryptomare	35, 127, 515, 523, 963, 1077
Cometary shells	735	Crystal fractionation	557
Comets	75, 93, 101, 147, 183, 185, 379, 597, 609, 621, 731, 841, 987, 989, 999, 1369, 1477, 1491	Crystal size	1315
Comminution	1445	Crystallization	37
Compensation	51	Crystals	659
Complex craters	559	Cumulate eucrites	1111
Complex ridged terrain	1553	Curriculum	783
Composition	81, 83, 167, 257, 661, 985, 1363	CV3 chondrites	1275
Condensation	493, 1227, 1251	Cydonia Mensae	1053
Condensation, silicates	329	Danu Montes	681
Condensation, sulfur	413	Dao Vallis	1029
Condensation, trapping	415	Dark-floored craters	1489
Contamination	339, 741	Dating	137
Continental crust	1009	Davy crater chain	1491
Contractional features	1473	Debris	915
Convection	697, 699, 1277, 1315	Decarbonation	839
Cooling	95, 921	Deconvolution	499
Cooling rate	859, 1315	Deformation	681, 817
Core	995	Deformation belts	1411
Core formation	141, 397, 509, 551, 653, 759, 1025, 1259	Degassing	971
Coronae	179, 239, 419, 421, 501, 503, 619, 673, 751, 823, 973, 1047, 1087, 1137, 1405, 1411, 1553	Deimos	293, 733, 1291
Correlations	757	Delamination	567
Corundum	1005	Deltas	1029
Cosmic dust	183, 185, 609, 711, 1381, 1515	Density	147
Cosmic ray exposure	247, 353, 1463	Depletion	995
Cosmic rays	19, 125, 845, 1429, 1479	Deposition	815
Cosmic spherule	761	Depth distribution	741, 1427
Cosmochemistry	1445	Depth profiles	1119
Cosmogenic isotopes	15, 17, 403	Detectability	1181
Cosmogenic material	853	Detection limits	983
Cosmogenic nitrogen	851	Diabese	817
Cosmogenic nuclides	701, 843, 1003, 1119, 1429	Diagenesis	1131
Cosmogenic profiles	99	Diamictite	565
Crater chains	893	Diamonds	449
Crater morphology	559	Diamonds, presolar	793
Cratering	89, 559, 857, 973, 1213	Diapirism	619, 751
Craters	43, 55, 237, 511, 599, 627, 629, 809, 893, 953, 991, 1105, 1201, 1355, 1483	Diaplectic	369
Cretaceous-Tertiary	31, 545, 607, 1095, 1221	Diaplectic talc	1431
Crisium Basin	127	Differentiated meteorites	813
Cross-sectional area	1117	Differentiation	873, 1185, 1251
Crust	271, 599, 697, 995, 1485	Diffuse reflectivity	771
Crustal history	877	Diffusion	859, 921, 1335
Crustal recycling	205	Diffusion coefficient	967
Crustal thickening	205	Diffusion profiles	1025
Cryosphere	271	Digital elevation model	1551
		Digital imaging	235, 547
		Dihedral angle	439
		Dike swarms	485, 487
		Dikes	523, 527, 693, 1497
		Diogenites	385, 639, 651, 1043
		Dione Regio	65, 675, 677
		Discharge rates	275
		Discovery missions	267, 951, 1323
		Dislocation	1455
		Disruption	495

Dissolution	983	Elysium	225, 227
Distinct lithologies	349	Emission spectra	1453
Distribution	417	Emissivity	217, 503, 605, 781, 1263, 1483
Distribution coefficients	907, 923	Empirical model	393
Dolomite	839	Energy partitioning	1175
Domes	193, 1189	Enstatite	319, 571, 683
Domical uplift	487	Enstatite chondrites	269, 319, 383, 801, 1545, 1547
Doppler data	1281	Entry	1215
Drag	1213	Environment	117
Drift potential	1521	Equation of state	731
DSC	25, 1021	Equilibrated ordinary chondrites	99, 247, 1035
Dunes	1171	Erosion	263, 459, 815, 1437
Dunes, linear	341	Eruptions	361, 1051, 1405, 1495, 1497
Dunes, Mars	341	Eucrites	135, 639, 651, 813, 831, 879, 901, 1015, 1273, 1525
Dunes, star	341	Eureca	867
Duricrust	955	Europa	1019
Dust	75, 257, 467, 493, 925, 1143, 1363, 1573	European Space Agency	49, 253
Dust collectors	107	Evaporation	375, 723, 755, 965, 1227, 1229, 1457, 1459
Dust grain charging	591	Evolution	493, 593
Dust subdisk	827	Exercise	281
Dusty plasmas	589, 591	Exobiology	367, 769
Dynamical evolution	841	Exopaleontology	367
Dynamical processes	411	Exospheres	377, 1099
Dynamics	189, 609	Experimental chondrules	825
E3 chondrites	665	Experimental crystallization	883
Early crust	1309	Experimental geochemistry	221
Early irradiation	671	Experimental petrology	639
Earth	407, 815, 829	Experimental study	109
Earth, analogs	457	Experiments	279, 653, 1343, 1535, 1537
Earth, differentiation	551, 1253	Exploration	733, 1177
Earth-grazing	283	Explosion	1369
Earth-Moon system	829, 1009	Exposure ages	15, 17, 475, 539, 1267, 1523
Earth, origin	215	Exsolution	1069, 1335
Eccentricities	593, 1549	Extension	29, 443, 993
Edifices	417	Extinct nuclides	849, 1185, 1325
Education	47, 163, 281, 311, 343, 783, 795, 835, 891, 897, 933, 1249, 1351, 1399, 1505	Extinct radionuclides	509, 613
Effusion	1551	Extraterrestrial matter	1429
EH chondrites	1545, 1547	Fassaite	1533, 1539
Eistla Regio	833	Faulting	441, 993, 1217, 1219
Ejecta	35, 41, 359, 459, 549, 787, 1201	Ferric oxides	1165
Ejecta deposits	565	Ferric oxyhydroxides	1165
Ejecta emplacement	61, 1355	Ferroan anorthosites	875, 1299, 1309, 1313
Ejection	987	Ferroelectric	1263
El chondrites	1545, 1547	Ferromagnetic resonance	71, 937
Electron diffraction	621	Ferrous/ferric ratio	323
Electron energy-loss spectroscopy	687	Festoon flow	1067
Electron microscopy	165, 355, 505	Field work	1177
Element ratios	1059	Fillowite	1337
Elemental depletions	761	First dredgeup	583
Elemental distribution	1375	Fission tracks	881
Elements	1563	Flash heating	471

Flood basalts	521, 821, 1383	Geology	535, 1329
Fluctuation	1441	Geology, surface	895
Fluid dynamics	693	Geometrical transformations	133
Fluidized	599	Geophysics	1085
Fluidized ejecta blankets		Georgia tektite	427, 1101
(FEB)	627, 629	Geothermal melting	491
Fluvial	321	Germanium detector	187
Fluvial processes	213	Giant impact model	613
Fluvial valleys	491	Gifted students	163
Flux	867	Giotto	1143
Flyby	1323	Glaciotectonics	799
Fold wavelengths	473	Glass	71, 351, 1181
Folds	331	Global	253
Formation of giant planets	1123	Global change	933
Forsterite	1339	Global geology	303
Found meteorite	917	Global properties	407
Fractals	1383	Global stress	489
Fractional crystallization	639	Global volcanism	303
Fractional melting	803	Glow	1573
Fractionation	375, 385, 723, 761, 873, 1457, 1459, 1511	Gold	997
Fracture patterns	155	Graben	331
Fracture spacing	155	Grain	1239
Fractures	1087	Grain charging	589
Fragmentation	243, 569, 597, 1365	Grain coagulation	591, 1011
Fragments	1157	Grain size analysis	373
Fremdlinge	223	Grain size distribution	1153
Fretted terrain	327	Grains	1237
Friction	1231	Grains, presolar	151
FTIR	451	Granite	557
		Granulites	1525
Gabbroic rocks	1077	Graphite	27, 103, 945, 1465
Gabbroonorite	633	Graphite, feathery	347
Galactic cosmic rays	17, 843, 851, 1003, 1119	Graphite, spherulitic	347
Galilean satellites	91, 433, 863	Gravitational constants	1291
Galileo	237, 243, 395, 411, 433, 453, 575, 807, 863, 869, 1019, 1235, 1359	Gravitational encounters	1549
Gamma rays	499, 845	Gravitational instability	827
Ganymede	297, 455, 575	Gravitational waves	1499
Garnet	803	Gravity	51, 113, 625, 699, 1281, 1295, 1401, 1551
Gas coalescence	1049	Gravity anomalies	789, 791, 1317
Gas-solid reaction	773	Gravity data	537
Gasptra	89, 453, 561	Gravity fields	789, 791
GCM	1521	Gravity regime	569
Generation	1427	Gravity relaxation	1109
Geochemical analysis	267	Green glass	21, 803
Geochemistry	157	Greenhouse effect	191
Geochemistry,		Grooves	953
martian meteorites	911	Ground ice	225, 227, 287
Geochronology	1113	Groundwater	271
Geoid	757, 1277	Group D	1299
Geologic history	833	Gruithuisen domes	249
Geologic mapping	65, 91, 239, 291, 463, 631, 677, 833, 1225, 1245	Guamote	1555
Geologic traverse	943	Guinevere Planitia	301
Geological processes	431	Gusev Crater	241, 483, 769
		GVDR	855
		Gypsum, vaporization	413

H chondrites	135, 1209	IIIAB irons	1025
H3 chondrites	1157	Ilmenite	105, 235, 259
Halogens	741	Image analysis	125
Hawaiian activity	1049	Image cube	455
Heat flow	1423	Image errors	779
Heat flux	1159	Image processing	241, 779, 1195, 1407
Heat transfer	691, 693	Imager	1293
Heating experiments	713	Images, color	871
Heating mechanisms	345	Imaging	81, 239, 655, 1271
Hecate Chasma, Venus	501	IMDR Regio	631
HED meteorites	651, 901, 981, 1083	Immiscibility	557
Helium	999	IMP	1293
Hellas	1379	Impact age	881
Hertha family	689	Impact basins	293, 387, 389, 537, 1211, 1345
Heterogeneity	1393	Impact breccias	1169, 1347
Hexagonal diamond (lonsdaleite)	313	Impact craters	59, 67, 201, 225, 227, 411, 559, 719, 721, 781, 847, 947, 1079, 1085, 1137, 1199, 1255, 1321
High pressure experiments	551	Impact events	607
High-micrometer sources	1103	Impact flash	5
Highbury structure	847	Impact frequency	1233
Highlands	97, 1265, 1305, 1307	Impact glasses	1039
History	1353	Impact heating	1169
Hole size	1207	Impact melt breccias	729, 1149, 1151
Hot belt	431	Impact melts	475, 477, 479, 513, 617, 753, 939, 1007, 1167, 1169, 1255, 1301, 1313
Hot spots	303, 431, 521, 877, 1295	Impact modeling	1095
Howardites	603, 979, 981, 1015	Impact origin	1121
HPLC	251	Impact origin, iron meteorites	255
Hubble Space Telescope	957	Impact processes	705, 1095
Hugoniot data	1209	Impact strength	1175
Human exploration	1177	Impact structures	299, 861
Humorum Basin	1077	Impact theory	579
Hydrated minerals	381	Impact, simulation	329
Hydrocarbons	251	Impactites	445, 447, 1347
Hydrodynamic effects	1231	Impacts	41, 43, 61, 145, 243, 295, 309, 359, 423, 495, 549, 565, 597, 599, 719, 787, 795, 809, 869, 989, 991, 1175, 1207, 1327, 1347, 1355, 1369, 1385, 1397, 1437
Hydrodynamic model	1381	Impacts, giant	215
Hydrodynamics	1231	Implantation	1059, 1093
Hydrogen isotopes	1155, 1471	Inclination	1549
Hydrothermal activity	481	Inclusions	905
Hydrothermal alteration	861	Infrared	123, 785, 975, 1135, 1191, 1433, 1453
Hydrothermal systems	299, 491	Infrared spectroscopy	519, 1161, 1163, 1165
Hyperion	1349	Inner solar system	991
Hypervelocity impact	1381	Inservice	783
Hyprometry	1159	Instrument	1261
Hypsometry	55	Instrumentation	709
IAB irons	255, 1375	Interdiffusivity	967
Ice	69, 211, 275, 433, 439, 621, 951, 1037		
Ice and frost	975		
ICP-MS	983		
Icy satellites	285, 555, 863, 1047, 1193, 1205		
Ida	89, 237, 411, 469, 787, 1395		
Igneous inclusion	935		
Igneous intrusion	1007		
Igneous processes	635, 1183		
IIE irons	865		

Interferometers	1499	Kawelu Planitia	531, 1553
Interior evolution	541	Kinetics	755, 1315
Interior processes	303	Kirchhoff's Law	1191
Interior structure	1295	Klapperkop member	1121
Interplanetary dust particles	139, 159, 185, 379, 381, 687, 853, 999, 1129, 1131, 1341, 1391, 1393, 1515	Komatiites	465, 1493
Interstellar diamond	775	KREEP	557
Interstellar dust	621, 1063	Kuiper belt	379
Interstellar grains	9, 27, 103, 313, 449, 563, 903, 1005, 1033	L chondrites	95, 495, 513, 1209
Interstellar graphite	401	L6 chondrites	665
Intrusives	161	Labrador	1303
Intrusives, gabbroic	1113	Lacustrine plains	321
Io	123, 807, 975, 1205, 1433	Lada Terra	821
Ion imaging	1005	Lafayette	1471
Ion microprobe	1057, 1451	Lake	213, 483
Ion probe	763, 1311, 1325	Lake basins	321
Ionization	149	Lakshmi	681
Iron	1361	Lamellar structure	1069
Iron grains	1011	Landform relief	927
Iron meteorites	245, 255, 539, 849, 929	Large igneous province	521
Iron mineralogy	709	Laser	683
Iron oxides	83, 1459	Laser ablation	1063
Iron sulfide	773	Laser fusion dating	1321
Irradiation	1157	Lava	189, 207, 361, 805, 1433
Irradiation dose	601	Lava channels	465, 667
Ishihara code	1551	Lava compositions	473
Ishtar terra	1447, 1449	Lava domes	33, 169
Isidis Planitia	291, 799	Lava erosion	465
ISM instrument	357	Lava flooding	525
Isolated grains	743	Lava flows	233, 391, 473, 531, 577, 691, 805, 1087, 1089, 1091, 1193, 1383, 1405, 1493, 1551
Isostasy	489, 757, 1317	Lava folds	473
Isotopes	173, 375, 903, 1057, 1409, 1457, 1459	Lava fountains	1049, 1051
Isotopes, carbon	347	Lava ponds	1531
Isotopes, magnesium	725	Lava tube	465
Isotopes, nitrogen	347	Lavinia	525
Isotopes, oxygen	965, 1389, 1539	Lavinia Planitia	529
Isotopic abundances	1391	Layered deposits	535
Isotopic anomalies	27, 401, 563, 585, 587, 611, 725, 775, 777, 903, 1033, 1185, 1325, 1387, 1389, 1539	Layered materials	955
Isotopic fractionation	615, 965, 1093	Lead-205	245
Isotopic ratios	579, 581, 701, 775, 1059	Light lithophile element	1257
Isotopics, oxygen	1387	Light plains	963
Isotopy	75	Lineament analysis	1133
Isua	1253	Lineaments	277
Japanese meteorites	917	Linear crater chains	1491
Johnsomervilleite	1337	Liquid immiscibility	1559, 1561
Jovian atmosphere	731	Liquidus boundary	803
Juno Dorsum	1241	Lithophile trace elements	1025
Jupiter	143, 295, 597, 1331	Lithosphere	113, 817, 931, 1203
Kaapvaal Craton	1113	Lithosphere thickness	1159, 1317
		LL chondrites	879
		Loading	525
		Lockne	1385
		Lodranites	703, 1071, 1073, 1371, 1375, 1479, 1523

Long Duration Exposure Facility (LDEF)	107, 567, 809, 867, 1207, 1233, 1327	Magnetic fields	149, 333, 561, 1123
Luminosity	1441	Magnetic grains	1011
Luna 20	1463	Magnetic properties	1, 977
Lunar anorthosite	635, 1081	Magnetism	709, 1467
Lunar basalt	1017	Magnetization	243
Lunar core	1223	Mahuea tholus	927
Lunar crust	875, 1007, 1045	Maja Vallis	1029
Lunar differentiation	1017	Mangala Valles	321
Lunar geochemistry	1151	Manson Impact Structure	31, 299, 607, 719, 729, 861
Lunar geochronology	1103	Mantle	657, 659, 699, 751
Lunar granites	1179	Mantle convection	489
Lunar gravity	791	Mantle flow	205
Lunar highlands	127, 249, 943	Mantle mineralogy	109
Lunar KREEP	1017	Mantle plumes	521
Lunar landing site	915	Mantle rare gases	1097
Lunar mantle	73, 1257	Mapping	305, 419, 499, 631, 1297, 1519
Lunar metal	77	Maps	1349
Lunar meteorites	797, 1373, 1463	Mare	523, 547, 1359, 1531
Lunar orbiters	791	Mare basalts	73, 219, 289, 1149, 1257, 1373
Lunar origin	579	Mare Crisium	127
Lunar project	915	Mare Orientale	715
Lunar regolith	1223, 1267, 1367	Marine impact	31
Lunar resources	737	Mariner 6,7	87
Lunar sample disk	835	Mariner 9	789
Lunar samples	637, 835	Mariner 10	985, 1145, 1297
Lunar shocked material	915	Marius Hills	1359
Lunar soil	23, 547, 685	Marquez Dome	881
Lunar surface	533	Mars	1, 3, 29, 53, 59, 69, 83, 85, 87, 109, 117, 119, 203, 211, 225, 227, 231, 257, 263, 271, 275, 287, 293, 305, 317, 367, 387, 389, 391, 403, 407, 437, 441, 443, 481, 511, 527, 535, 599, 615, 643, 709, 733, 745, 749, 759, 769, 799, 815, 845, 857, 871, 895, 925, 933, 939, 947, 955, 1043, 1053, 1125, 1127, 1141, 1147, 1171, 1205, 1217, 1219, 1261, 1289, 1291, 1343, 1345, 1377, 1379, 1383, 1413, 1425, 1437, 1473, 1495, 1521, 1541, 1543
Lunar symmetric tectonics	715	Mars, composition	961
Lunar volatiles	325	Mars, craters	61
Lunar volcanism	249	Mars, fluvial	457
Lunar wave tectonics	715	Mars, gravity	789, 1291
M asteroids	265	Mars, mineralogy	961
Ma'adim Vallis	769	Mars, nitrogen cycle	451
Maat Mons	405, 409, 949, 1139	Mars, remote sensing	961
Macromolecule	1247	Mars, thermal inertia	517
Magellan	129, 157, 625, 705, 1195, 1199, 1245, 1281, 1287, 1295, 1401, 1483, 1519, 1553	Mars, thermally derived albedo	517
Magma	361, 527, 1087		
Magma chamber	1405		
Magma evolution	1511		
Magma ocean	875, 1315		
Magma recycling	1051		
Magma rise speed	1049		
Magma sources	1103		
Magmatic evolution	541		
Magmatism	1497		
Magnesian suite	633, 1305		
Magnesiowustite	873		
Magnesium	1075		
Magnesium isotopes	315, 363, 539, 723		
Magnesium-perovskite	873		

Mars Observer	353	Mineralogy	85, 121, 165, 357, 785, 1131, 1135, 1393
Mars Observer, gamma ray spectrometer	353	Minerals, shocked	309
Marsquake	441	Minor planets	689
Martian meteorites	797, 911	Miranda	1047
Mass spectrometry	75, 1063	Mixing	963
Massif anorthosites	1303	Mixing analysis	1329
Material extraction, energy cost	737	Mixing model	479, 1129
Mathematical geology	1511, 1513	Mode of origin	487
Matrix	165, 167, 1481, 1525	Modeling	207, 361, 371, 815, 1403, 1493
Maturity	23, 937	Modeling, mineralogic	961
Mauna Loa	405, 409	Models	805
Maxwell Montes	1447, 1449	Modified Gaussian model	553
Mead Crater	51, 537	Montagnais	1085
Mechanical twin	1431	Monte Carlo simulation	845
Melilite	79, 825	Moon	81, 219, 253, 259, 335, 377, 395, 523, 541, 733, 829, 851, 869, 893, 1145, 1181, 1257, 1259, 1261, 1329, 1333, 1367, 1383, 1407
Melt inclusions	513, 1417	Moon, age	613
Melting	471, 1185	Moon, lunar cores	1367
Melting experiment	923	Moon, meteorites	97
Melting model	37	Moon, origin	215, 1259
Melting reactions	109	Moon, soils	97
Mercury	187, 337, 507, 533, 951, 985, 1037, 1099, 1145, 1203, 1297, 1323	Morphology	977, 1473
Mercury, surface composition	739	Mossbauer spectroscopy	1, 707, 709, 771, 939, 941, 1261, 1269
Meroe Patera	291	Mountain belts	1449, 1577
Merrihueite	753	Mountain building	1447
Mesosiderites	1167, 1529	Multikilometer roughness	407
MESUR	1293	Multimedia	311
Metal	223, 685, 695, 937, 945, 1061, 1237, 1239	Multiring basin	1255
Metal phases	1529	Multispectral	1145, 1359
Metal segregation	653	Multispectral images	1407
Metamorphism	165, 167, 423, 573, 941, 1169, 1545, 1547, 1567	Muong Nong-type tektite	427, 1101
Metasomatism	11, 641, 1305		
Meteor Crater	459	Nakhlites	391, 1451, 1471
Meteorites	13, 15, 17, 19, 37, 95, 149, 175, 177, 185, 265, 267, 279, 471, 561, 563, 777, 795, 843, 905, 917, 1409, 1427, 1525	Nanodiamonds	313
Meteorites, gas-rich	959	Nanophase	53
Meteoritic diamonds	313	Nanophase hematite	437
Meteoroid	183	Near Earth asteroids	153, 267, 283, 1319, 1505, 1507
Meteoroid and Debris Special Investigation Group (M&G SIG)	1233	Nebula	279, 543, 1251
Meteors	57, 765, 1397	Nebula heating	1227
Methane	1139	Nebular chemistry	773
MHD	735	Nebular processes	345, 827
Microcrater	867	Nebular solids	1469
Micrometeorites	71, 355, 713, 761, 763	Negative polarization	1271
Micrometeoroids	809, 1327, 1515	Neodymium-142	613, 1017, 1253
Mineral chemistry	633, 1183	Neon	403
Mineralization	367	Neon isotopes	1427
		Neutral buoyancy	485
		Neutron activation	1179
		Neutron flux distribution	899
		Neutrons	899

Nickel	657	Outflow channels	321, 811, 1029
Nickel chromites	717	Outreach	163
Nili Patera	291	Ovda Regio	229, 605, 1055, 1067
Nilosyrtris Mensae Region	327	Oxidation	199, 461
NIMS	453, 575, 807, 1019, 1235	Oxidation state	323, 1361
Nitrates	451	Oxygen fugacity	323, 657, 923
Nitrogen	77, 171, 173, 383, 701, 1419, 1435	Oxygen isotopes	269, 583, 1005, 1357
Nitrogen isotopes	449, 451, 703, 1357	P-sulfide	979
NMR spectroscopy	309	Palagonite	1485
Noachian	457	Palagonite, iron clay mixtures	1163
Noble gases	77, 683, 793, 919, 1039, 1065, 1093, 1269	Palagonitic soils	1161
Noble gases, solar	959	Palimpsests	297
Noble metals	141	Palisade bodies	1275
Nonisothermal	1251	Pallasite	921, 1335
Nonsteady ionization	765	Palmira	1555
Norite	633	Pancake domes	169
North Massif	1149	Parabolic halos	1201
North Ray Crater	635	Parent bodies	865
Nucleosynthesis	563, 665, 777, 903	Parent melt	883
Numerical modeling	623, 691, 693, 1503	Parental magmas	1513
Numerical simulation	843, 1397	Partial melting	639, 651, 653, 663, 803, 879, 1071, 1073, 1371, 1465
Nysa family	689	Particle	57, 1251
Oblique impacts	39, 1211	Particle cohesion	1445
Observing techniques	1505	Particle fluxes	843
Oceans	989, 1053	Particle sorting	1403
Offset dikes	1031	Partition coefficients	141, 883, 923, 1081, 1111
Oldhamite	571	Partitioning	79, 873
Olivine	399, 907, 909, 921, 923, 967, 1069, 1335, 1339, 1455, 1481, 1559, 1561	Pathfinder	1293
Olivine, isolated	723	Pavonis Mons	1225
Olivine, vaporization	329	Pentlandite	1565
Olympus Mons	1225	Percussion marks	1121
Optical alteration	371	Permafrost	3, 287
Orange glass	21, 23	Perovskite	1557
Orbital elements	853	Perseid	57
Orbital evolution	247	Petrogenesis	289, 1179
Orbiter spacecraft	187	Petrogenesis, martian meteorites	911
Orbits	93	Petrography	1269, 1285
Ordinary chondrite parent bodies	513	Petrology	493, 1129, 1131
Ordinary chondrites	7, 89, 175, 177, 651, 671, 701, 865, 879, 1057, 1169, 1183, 1481	Petrology, igneous	1511, 1513
Organic	1247	Petrology, martian meteorites	911
Organic materials	339	Phase equilibria	555, 879
Oriente Basin	515, 1077	Phobos	43, 111, 293, 733, 953, 957, 1291
Origin	749, 759, 1071, 1073, 1173	Phobos 2	357, 957
Orthopyroxene	385, 1045, 1371	Phoebe	1349
Orthopyroxenite	1043	Phosphate	1337
Oscillation	987	Phosphate minerals	1025
Oscillatory zoning	1339	Phosphides	595
Outer solar system satellites	863	Phosphorus	143
Outflow	3, 287	Photoabsorption	731
		Photochemistry	461, 745
		Photoclinometry	953, 1053, 1473
		Phyllosilicates	435, 763, 1565
		Picritic glasses	1257

Picritic magmas	1259	Procellarum	963
Piece-affine transform	133	Processes	3
Pioneer Venus	1139	Production rates	851, 1119
Plagioclase	641, 739, 831, 875, 1075, 1081, 1375, 1533	Projectile	359
Plains	45, 113	Projectile chemistry	1233
Plains deformation	767	Projectile residues	107
Planar deformation features	847, 1385	Projective	1221
Planar three-body problem	593	Proteus	1349
Planetary accretion	1009	Protoplanetary disk	827
Planetary data system	311	Protoplanetary nebula	333
Planetary differentiation	399	Protosolar nebula	777
Planetary evolution	431	Protosun	333
Planetary instrument	121	Provenance	1487
Planetary mapping	1243	Pseudotachylite	423, 1197, 1321
Planetary radar	515	Pyrite decomposition	707
Planetary science	897, 1351	Pyroclastic flow	1403
Planetary surface imaging	779	Pyroclastic glass	21, 23
Planetary surfaces	1407, 1453	Pyroclastics	1495, 1497, 1555
Planetary wave interference	715	Pyrolysis	171, 793, 1247
Planetesimal formation	827, 1011	Pyrope	909
Planetesimals	307, 399, 1283, 1441, 1477, 1549	Pyroxene	497, 859, 883, 909, 939, 1373, 1559, 1561
Planets	797	Pyroxene, plagioclase	669
Plasma instabilities	735	Q phase	979
Plasma stratification	735	Quantitative analysis	251
Plate tectonics	419, 421	Quartz	601, 1021
Pluto	1419	Quartz monzodiorite	557, 1307, 1311
Plutonium fission xenon	1065		
Polar	69, 535	Radar	211, 217, 219, 459, 577, 627, 629, 655, 951, 1091, 1279, 1401, 1503
Polar beaches	1125		
Polar caps	1323	Radar backscatter	393
Polar region	1331	Radar properties	927, 1243
Polarimetry	335, 1271	Radar scans	483
Polarization	433, 1331	Radial lineaments	485, 487, 489
Poles	1037	Radial pyroxene chondules	801
Polycyclic aromatic hydrocarbons	1391	Radially fractured domes	619
Polymict material	901	Radiation	1365
Polyoxymethylene	1143	Radiation damage	353
Post-impact alteration	861	Radiation effects	853
Post-impact processes	299	Radiative losses	765
Potassium	579, 581	Radiative signal	5
Preplanetary bodies	1443	Radio tracking	1281
Preplanetary disk	1441	Radioactivity, short-lived	151
Presolar diamonds	1435	Radiogenic Xe	703
Presolar grains	585	Radiometry	1433
Presolar SiC	373	Radionuclides	19, 1119
Pressure indicator	497	Radiothermal emissivity	1137
Pretoria Saltpan Crater	161	Raised channel systems	1127
Primitive achondrites	1071	Rampart craters	287
Primitive chondrites	1563	Rampart ejecta	59
Primitive mantle	995, 1009	Rare earth elements	315, 571, 725, 935, 1265, 1311, 1451, 1457
Primitive material	355, 1283, 1363	Rare gases	13, 997
Primitive meteorites	573, 1229	Rayleigh distillation	375
Principal components	1129	Recent volcanic activity	1139
Pristine highlands rocks	1007		

Recondensation	1229	Roughness	129, 393
Reconnaissance	1323	Rubidium-samarium isotopes	1309
Red giant stars	583	Runoff	457
Redox potential	1569, 1571	Rusalka Planitia	767
Reduction	23, 383, 543, 695, 1107	Rutile	771
Reflectance spectra	21, 177, 553, 939		
Reflectance spectroscopy	127, 159, 515, 519, 961	S asteroids	265, 553
Refractive index	507	S process	245
Refractory	1283	Salme Dorsa	1115
Refractory carbides	103	Saltation threshold	1521
Refractory elements	375	Samarium-146-	
Refractory inclusion	1325	neodymium-142	1015
Refractory inclusions	825, 1275	Sample representivity	1179
Refractory siderophiles	1035	Samples, lunar	371
Regional highlands	675	Samples, terrestrial	997
Regions	593	Sand	1555
Regolith	71, 97, 259, 261, 433, 469, 507, 695, 787, 943, 1059, 1061, 1083, 1157, 1301, 1313, 1333	Sandstone	309
Regolith breccias	1153	Sangay	1555
Regolith evolution	1153	Sapas Mons	679
Regolith maturity	1367	Satellites	43, 1541
Regolith processes	175, 177	Satellites, captured	93
Regolith properties	1191	Saturn	143
Relative ages	503	Scaling	359, 559
Relaxation time	1549	Scalloped margins	193
Relict enstatite	319	Scanning electron microscopy	125, 977
Remote sensing	249, 367, 533, 779, 837, 1191, 1263, 1267, 1407	Scapolite	11
Remote spectral sensors	737	Scattering	855
Reservoir	527	Schiller-Schickard	35
Residue	665	Science payloads	1249
Resolution	241, 625	Screen indicator	1427
Resonance ionization	1063	Sculpture	1237
Resources	235	Seafloor volcanos	169
Resurfacing	45, 191, 971, 973, 1079, 1199, 1353	Seamounts	1189
Resurfacing, global	1199	Secondary cratering	515
Rhea	1205	Sediment	119
Rhenium-osmium dating	1041	Sedimentary deposits	213
Rheology	189, 439, 1089, 1193, 1575	Sediments	1363
Ridge belts	529	Seismic images	1517
Ridges	1171	Seismic modeling	145
Rift zones	1105	Seismology	441
Rifting	29, 421, 623, 821, 823, 1047, 1241	Sekmet Mons	531, 1553
Rims	181	Semi-automated rover vehicle	737
Ring vortex	61	Semi-major axis	593
Riobamba	1555	Serenitatis melts	617
Robotic exploration	1177	Serpentine, vaporization	329
Robotics	1499	Shadow measurements	811
Rock mass	1217	Shatter cones	1121
Rocks, pelitic	423	Shear-lag model	155
Rocky	1027	Shergottites	1417
Roedderite	753	Shergottite meteorites	403
Rotational variations	1117	Shield volcanoes	405, 409
		Shock	177, 497, 603, 1021, 1209, 1239, 1431
		Shock experiments	839, 969
		Shock metamorphism	107, 309, 477, 497, 565, 607, 847, 1347
		Shock physics code	295

Shock processing	831	South Pole, Aitken Basin	715
Shock recovery	1167	Space debris	183
Shock temperatures	1209	Space grant program	47
Shock waves	39, 731, 777, 987, 1365	Space science	891
Shock, high temperature	969	Space weathering	175, 371
Shocked graphite	913	Spacewatch objects	153
Shocked quartz	913, 1385	Spare Environment and Effects Program (SEE)	1233
Shockwave interference	1463	Speciation	221
Siderophile elements	397, 551, 617, 663	Spectra	117, 119, 265, 455, 1329
Siderophiles	983	Spectral analysis	1235
Sif Mons	949	Spectral imaging	895
Silica	641, 753	Spectral mixture analysis	779
Silicate condensation	415	Spectral reflectance	249, 837
Silicate inclusions	849	Spectrophotometry	1135
Silicate liquid immiscibility	1303, 1305	Spectropolarimetry	1267
Silicate melts	221	Spectroscopy	81, 83, 85, 87, 123, 273, 357, 371, 519, 785, 975, 1333, 1419
Silicate minerals	603, 701	Spectrum of masses	1443
Silicates	1433, 1445	Spherule layers	717
Silicon carbide	585	Spherules	853, 1459
SIMS	385, 725, 1043, 1111, 1265, 1341, 1539	Spinels	553, 763, 1533
Simulation	569	Spotches	705
Sinuuous ridges	1127	Sputtering	1143
Sirenum	443	SSI	453
Site selection	943	Stereo	1205
Size analysis	1129	Stereotopography	1055
Size distribution	365	Stratigraphy	45, 65, 529, 677, 767, 769, 857, 1531
Size frequency	1319	Stratosphere, contamination	139
Size sorting	307	Stream	57
Slope failure	193, 1127	Strength	1217
Small bodies	469, 1027	Strike-slip faulting	1219
Small volcanic edifices	1187	Structural geology	179
Smoothed particle hydrodynamics	1527	Structures	277, 331, 501, 681
SNC meteorites	1, 391, 451, 647, 911, 919, 1043, 1413, 1451, 1463, 1471	Students	897
Sodium	79, 377, 887, 1099, 1535	Subduction	421
Soil	53, 117, 955	Subophitic basalts	1301
Soil, texture	335	Sudbury structure	477, 1007, 1031, 1517
Solar cosmic rays	851, 1003	Suevite	479
Solar energetic particles	125, 959, 999, 1059	Sulfide melt	397
Solar flares	649	Sulfides	273, 1061, 1537
Solar modulation	1429	Sulfur	325, 1057, 1155
Solar nebula	149, 151, 223, 755, 1123, 1173, 1283, 1469, 1477	Sulfur dioxide	123, 429, 975, 1139
Solar protons	403	Sulfur, condensation	413
Solar system	795	Sulfur, isotopes	611
Solar transit	1099	Sun dynamo	1429
Solar wind	77, 105, 171, 173, 259, 649, 959, 999, 1065	Superconductivity	1501
Solar wind implantation	1013	Supernovae	27, 903
Solar wind reduction	1013	Surface composition	187, 1235
Solidification	1027	Surface mineralogy	837
Solubility	383, 659	Surface processes	899, 1263
Sorting	1061	Surface properties	629
South Massif	1149	Surface reflection	337
		Surface thermodynamics	1445
		Surfaces	461, 855, 863, 925, 1237,

Surfaces (cont.)	1239, 1279	Tidal fracture	101
Surfacing	335	Tiger spectrography	837
Surveyor	261	Tikal, Guatemala	549
Synthetic aperture radar (SAR)	927, 951	Tillite	565
Syrtris Major	291	Timescales	1325
		Titan	1231
Taurus Littrow Valley	1149	Titanium	1075
Teachers	783, 835	Titanium isotopes	363, 1063
Tectonics	29, 113, 179, 285, 441, 673, 697, 817, 877, 885, 993, 1047, 1109, 1115, 1217, 1377, 1411, 1423, 1575, 1577	Titanium-iron-phosphides	595
		Topographic slopes	201
Tectonism	727, 1105	Topography	503, 727, 757, 1053, 1277, 1289, 1519
Tektite-like glaass	1269	Trace elements	221, 315, 385, 427, 761, 981, 1111, 1417, 1475, 1557
Tektites	549, 581, 741, 1039	Trace elements, partitioning	1075
Telescopic	81, 83, 85	Tracks	125, 1157
Tellus Regio	425	Trajectory calculation	1327
Tempe Terra	443, 643, 1377	Tranquillitatis	1329
Temperatures	149, 1501	Transform fault	1115
Temporal variations	19	Transient cavity	479
Tephra	1181	Transient heating	345, 1535, 1537
Termoskan	111	Transmission electron microscopy	685, 687, 1455
Terraces	213	Trapped gases	997, 1093
Terrestrial age	99, 647	Trapped xenon	1479
Terrestrial degassing	1097	Triangulation	133
Terrestrial planets	985, 1487	Triton	277, 555, 1419
Tesserae	229, 419, 425, 1001, 1133	Troctolitic	935
Tetrataenite	1529	Troilite	25, 773, 1057
Textures	825, 1285	Trojan asteroids	841
Thallium	245	Tropospheric circulation	429
Tharsis	111, 443, 1141, 1147, 1219	Trough	501
Tharsis-Sirenum dichotomy	837	Tsunamis	989
Thaumasia	331	Tungsten	995
Thermal conductivity	931	Turbulence	233, 307
Thermal emission	257, 533, 1161, 1163	Tusholi Corona	1115
Thermal erosion	233, 1493	Type B inclusions	79
Thermal gradients	1191		
Thermal history	223, 247, 1173, 1367	Ultramylonite	1197
Thermal infrared	925	Ultrarefractory inclusions	1475
Thermal isostasy	1159	Ultraviolet	461
Thermal models	931	Umov effect	1271
Thermochronology	1113	Unequilibrated chondrites	1185
Thermoluminescence	97, 99, 247, 601, 603, 1367, 1545	Unequilibrated enstatite chondrites	571
Thermometry	25	Unequilibrated ordinary chondrites	585, 1035
Three-body calculation	829	Unique chondrite	115
Threshold	129	Uranium-lead dating	1031
Threshold wind	467	Uranium-thorium-lead	1409
Thrust systems	1449	Ureilites	137, 663, 909, 1107, 1409, 1465
Thumbprint terrain	799, 1127	Ushas Mons	65, 675, 677
Tidal breakup	893		
Tidal capture	829	Valences	221
Tidal deformation	1527	Valhalla	91
Tidal disruption	147, 1491, 1527	Valles Marineris	29, 231, 955, 1219
Tidal effects	1231		

Valleys	331, 457	Volatiles	397, 1535, 1537
Vanadium	505	Volcanic activity	431
Vapor clouds	1355	Volcanic glasses	325
Vapor deposit	259, 695	Volcanic hazard	805
Vapor fractionation	581	Volcanic plains	155
Vapor impact	913	Volcanic rise	675
Vapor pressure	581	Volcanism	35, 45, 123, 193, 207, 301, 305, 325, 405, 409, 417, 425, 429, 463, 501, 521, 523, 525, 529, 623, 667, 679, 767, 797, 805, 807, 821, 823, 885, 971, 1079, 1087, 1089, 1091, 1105, 1189, 1423, 1447, 1489, 1495, 1531
Vaporization	413, 755	Volcanology	33, 1189, 1403
Vaporization, silicates	329	Volcanos	227, 305, 317, 679, 807, 947, 949, 973, 1141, 1147, 1317
Veins	169	Vortex flows	41
Velocity scaling	1207	Voyager	241, 455
Venera 15/16	1001, 1483	Vredefort	423, 1113, 1321
Venus	33, 45, 55, 63, 65, 67, 129, 155, 157, 179, 191, 193, 205, 207, 217, 229, 239, 301, 303, 405, 407, 409, 417, 419, 421, 429, 463, 485, 487, 489, 503, 525, 529, 531, 537, 577, 619, 627, 629, 631, 667, 673, 675, 677, 679, 697, 699, 705, 707, 727, 747, 749, 751, 757, 767, 781, 817, 821, 823, 833, 855, 877, 885, 927, 949, 971, 973, 993, 1067, 1079, 1109, 1115, 1133, 1137, 1159, 1189, 1195, 1199, 1201, 1213, 1215, 1263, 1277, 1279, 1281, 1295, 1317, 1353, 1355, 1411, 1423, 1447, 1449, 1519, 1569, 1575, 1577	Wake	39, 41
Venus, basalt	1415	Wanapitei	479
Venus, emissivity measurements	1509	Water	117, 275, 759, 785, 1037
Venus, impact craters	1489, 1509	Water of hydration	1135, 1439
Venus, major resurfacing event	1509	Waves	989
Venus, surface material	1509	Wax modeling	233
Vesta	1083	Weathering	53, 157, 263, 339, 937, 1035, 1137, 1155, 1415
Vesta Rupes	681	Wetting behavior	653
Vibrational (spectroscopy)	1485	White matrix	11
Viking	871	Wildfires	545
Viking missions	953	Workstation	1519
Viking Orbiter	241, 789	Wrinkle ridges	63, 1473
Viscosity	189	Wyoming	1303
Viscosity	699, 1089, 1193	XANES	323
Vitrophyre	289	Xenoliths	931
Volatile elements	617, 663, 713, 741	Xenon	1065
Volatile loss	579	Xenon isotopes	1097
		X-ray absorption spectroscopy	1361
		X-ray diffraction	121, 273
		X-ray fluorescence (XRF)	1261
		X-ray methods	1363
		Zimbabwe	847
		Zircon	427, 967, 1031
		Zodiacal cloud (or dust)	379

